

Flight Mechanics/ Estimation Theory Symposium 1994

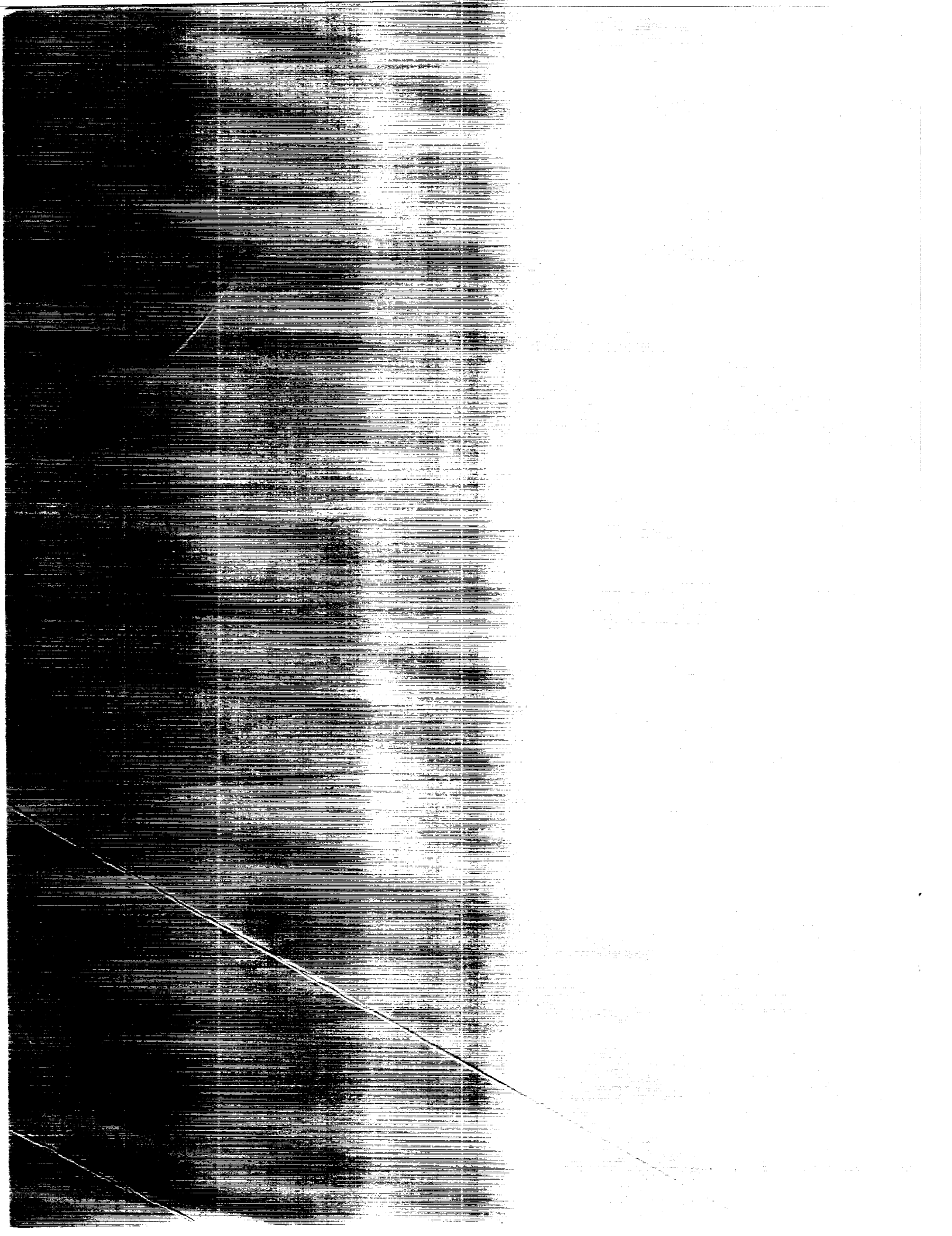
(NASA-CP-3265) FLIGHT
MECHANICS/ESTIMATION THEORY
SYMPOSIUM, 1994 (NASA, Goddard
Space Flight Center) 533 p

N94-35605
--THRU--
N94-35646
Unclass

H1/13 0009347

at
ter
nd
94





NASA Conference Publication 3265

Flight Mechanics/ Estimation Theory Symposium 1994

Kathy R. Hartman, Editor
*Goddard Space Flight Center
Greenbelt, Maryland*

Proceedings of a symposium sponsored by
NASA Goddard Space Flight Center and held
at Goddard Space Flight Center
Greenbelt, Maryland
May 17 - 19, 1994



National Aeronautics and
Space Administration

**Scientific and Technical
Information Branch**

1994

FOREWORD

The papers presented here have been derived primarily from speakers' summaries of talks presented at the Flight Mechanics/Estimation Theory Symposium held May 17-19, 1994 at the Goddard Space Flight Center. For completeness, abstracts are included for those papers which were presented but unavailable at the time of printing. Papers included in this document are presented as received from the authors with little or no editing.

CONTENTS

Page

SESSION 1

Modal Decomposition of Hamiltonian Variational Equations... W. Wiesel (Air Force Institute of Technology)	3
Low Encounter Speed Comet COMA Sample Return Missions..... P.Tsou, C. Yen, A. Albee (JPL)	15
High Earth Orbit Design for Lunar Assisted Small Explorer Class Missions..... M. Mathews, M. Hametz (CSC) J. Cooley, D. Skillman (NASA/GSFC)	17
Obtaining Coincident Image Observations for Mission to Planet Earth Science Data Return..... L. Newman, D. Folta (NASA/GSFC) J. Farrell (Ridge Technology)	33
Automated Maneuver Planning Using a Fuzzy Logic Algorithm.. D. Conway, R. Sperling(CSC) D. Folta, K. Richon, R. DeFazio (NASA/GSFC)	49
Reduction Procedures for Accurate Analysis of MSX Surveillance Experiment Data..... E. Gaposchkin, M. Lane, R. Abbot (MIT)	63

SESSION 2

Fixed-Head Star Tracker Attitude Updates on the Hubble Space Telescope..... M. Nadelman, J. Karl (CSC) L. Hallock (NASA/GSFC)	79
In-Flight Scale/Distortion Calibration of the HST Fixed Head Star Trackers..... R. McCutcheon, J. Boia, G. Welter (CSC) M. Gakenheimer, E. Kimmer, S. Murphy, (ATSC) L. Hallock (NASA/GSFC)	95
A Long-Baseline Method for HST Gyro Drift Rate Bias Calibration..... J. Boia, G. Welter (CSC) M. Gakenheimer (ATSC)	109

The In-Flight Calibration of the Hubble Space Telescope Fine Guidance Sensors-II (A Success Story).....	111
G. Welter (CSC), L. Abramowicz-Reed (Hughes)	
A. Guha (AKG), L. Hallock (NASA/GSFC)	
E. Kimmer (ATSC)	

In-Flight Estimation of Gyro Noise on the Upper Atmosphere Research Satellite (UARS) and Extreme Ultraviolet Explorer (EUVE) Missions.....	123
M. Lee, P. Crouse, R. Harman (NASA/GSFC)	
T. Leid, W. Davis, S. Underwood, (CSC)	

Operational Support for Upper Atmosphere Research Satellite (UARS) Attitude Sensors.....	139
M. Lee (NASA/GSFC), A. Garber, M. Lambertson, P. Raina, S. Underwood, C. Woodruff (CSC)	

Spacecraft Attitude Determination Accuracy From Mission Experience.....	153
D. Brasoveanu, J. Hashmall (CSC)	

SESSION 3

Compatibility of TOPEX/POSEIDON Trajectory Propagation with JPL and GSFC/FDF Operational Software.....	169
A. Salama, J. Guinn (JPL), M. Nemesure, D. Bolvin (CSC), R. Leavitt (Sterling)	

Improved Solution Accuracy for TDRSS-Based TOPEX/Poseidon Orbit Determination.....	179
E. Doll, G. Mistretta, R. Hart (NASA/GSFC)	
D. Oza, D. Bolvin, C. Cox, M. Nemesure, D. Niklewski, M. Samii (CSC)	

Implementation of a Low-Cost, Commercial Orbit Determination System.....	195
J. Corrigan, (Storm Integration, Inc.)	

Tracking System Options for Future Altimetric Satellite Missions.....	211
G. Davis, J. Ries, H. Rim, B. Tapley (Univ. Texas/Austin)	

Improved Solution Accuracy for Landsat-4 (TDRSS-User) Orbit Determination.....	225
D. Oza, D. Niklewski (CSC)	
C. Doll, G. Mistretta, R. Hart (NASA/GSFC)	

Optimum Satellite Relay Positions with Application to a TDRS-1 Indian Ocean Relay.....	237
A. Jackson (NASA/GSFC), P. Christopher (STel)	

TDRSS Onboard Navigation System (TONS) Flight Qualification Experiment.....	253
C. Gramling, R. Hart, D. Folta (NASA/GSFC)	
A. Long (CSC)	

SESSION 4

Atlas Solar Pointing Operations.....	271
C. Tyler (Teledyne), C. Zimmerman (NASA/MSFC)	
Overview of the Miniature Sensor Technology Integration (MSTI) Spacecraft Attitude Control System.....	281
R. McEwen (Integrated Systems)	
A Geometric Model of a V-Slit Sun Sensor Correcting for Spacecraft Wobble.....	297
W. McMartin, S. Gambhir (TASC)	
Overview of the MSTI 2 On-Orbit Alignment.....	303
C. Rygaard, F. Smith, M. Briggs (Integrated Systems)	
Measuring Attitude with a Gradiometer.....	315
D. Sonnabend (Analytical Engineering) T. Gardner (Univ. Colorado)	
Overview of the MSTI 2 Processor-In-the-Loop (PIL) Simulator.....	331
C. Rygaard (Integrated Systems)	
The Control of Satellites With Microgravity Constraints: The COMET Control System.....	341
W. Grossman (Madison) D. Freesland (CTA Space Systems)	

SESSION 5

Self-Rescue Strategies for EVA Crewmembers Equipped With the Safer Backpack.....	357
T. Williams (Univ. Cincinnati) D. Baughman (General Dynamics)	
Space Shuttle Orbit Determination Using Empirical Force Modeling of Attitude Maneuvers for the German MOMS-02/D2 Mission.....	373
C. von Braun (MIT), Ch. Reigber (GFZ)	
Application of a Monte Carlo Accuracy Assessment Tool to TDRS and GPS.....	385
M. Pavloff (MITRE)	

Evaluation of Semiempirical Atmospheric Density Models for Orbit Determination Applications.....	399
C. Cox, R. Feiertag, D. Oza (CSC)	
C. Doll (NASA/GSFC)	
Filter Parameter Tuning Analysis for Operational Orbit Determination Support.....	415
J. Dunham, C. Cox, D. Niklewski (CSC)	
G. Mistretta, R. Hart (NASA/GSFC)	
Comparison of Kalman Filter and Optimal Smoother Estimates of Spacecraft Attitude.....	431
J. Sedlak (CSC)	
Attitude Stability of a Spinning Spacecraft During Appendage Deployment/Retraction.....	447
N. Fitz-Coy, W. Fullerton (Univ. Florida)	

SESSION 6

Application of Star Identification Using Pattern Matching to Space Ground Systems at GSFC.....	451
D. Fink, D. Shoup (CSC)	
Color/Magnitude Calibration for National Aeronautics and Space Administration (NASA) Standard Fixed-Head Star Trackers (FHST).....	467
J. Landis, T. Leid, A. Garber (CSC)	
M. Lee (NASA/GSFC)	
Advantages of Estimating Rate Corrections During Dynamic Propagation of Spacecraft Rates - Applications to Real-Time Attitude Determination of SAMPEX.....	481
M. Challa, G. Natanson (CSC)	
D. Baker, J. Deutschmann (NASA/GSFC)	
MME-Based Attitude Dynamics Identification and Estimation for SAMPEX.....	497
J. De Pena, J. Crassidis, M. McPartland, T. Meyer, D. Mook (SUNY)	
A New Algorithm for Attitude-Independent Magnetometer Calibration.....	513
R. Alonso (CONAE), M. Shuster (APL)	
A Simple Suboptimal Least-Squares Algorithm for Attitude Determination With Multiple Sensors.....	529
T. Brozenec, D. Bender (Hughes Aircraft Co.)	
Motion Models in Attitude Estimation.....	545
D. Chu, Z. Wheeler, J. Sedlak (CSC)	

FLIGHT MECHANICS/ESTIMATION THEORY SYMPOSIUM

MAY 17-19, 1994

SESSION 1

Modal Decomposition of Hamiltonian Variational Equations

William E. Wiesel
Department of Aeronautics and Astronautics
Air Force Institute of Technology
2950 P Street
Wright - Patterson AFB, Ohio 45433

Abstract

Over any finite arc of trajectory, the variational equations of a Hamiltonian system can be separated into "normal" modes. This transformation is canonical, and the Lyapunov exponents over the trajectory arc occur as positive / negative pairs for conjugate modes, while the modal vectors remain unit vectors. This decomposition effectively solves the variational equations for any canonical, linear time-dependent system. As an example, we study the Voyager I trajectory. In an interplanetary flyby, some of the modal variables increase by very large multiplicative factors, but this means that their conjugate modal variables decrease by those same very large multiplicative factors. Maneuver strategies for this case are explored, and the minimum Δv maneuver is found.

1 Introduction

A Hamiltonian dynamical system can be written as a vector set of differential equations

$$\dot{\mathbf{X}} = Z \frac{\partial H}{\partial \mathbf{X}}, \quad (1)$$

where $\mathbf{X}^T = (q_i, p_i)$ is termed the state vector, and the matrix Z is

$$Z = \begin{Bmatrix} 0 & I \\ -I & 0 \end{Bmatrix}. \quad (2)$$

Introduce the small displacement $\mathbf{x}(t) = \mathbf{X}(t) - \mathbf{X}_0(t)$ from a known trajectory $\mathbf{X}_0(t)$. Then, to first order in small quantities, the displacement vector obeys the variational equations

$$\dot{\mathbf{x}} = A(t)\mathbf{x} = Z \left. \frac{\partial^2 H}{\partial \mathbf{X}^2} \right|_{\mathbf{x}_0} \mathbf{x}. \quad (3)$$

As a set of linear equations, the variational equations are formally solved by the fundamental matrix $\Phi(t, t_0)$, which satisfies

$$\dot{\Phi} = A(t)\Phi, \quad \Phi(t_0, t_0) = I. \quad (4)$$

Then, the general solution to (3) can be written as $\mathbf{x}(t) = \Phi(t, t_0)\mathbf{x}(t_0)$.

2 The Modal Transformation

In this section we will review the recent discovery of the modal transformation for general time dependent linear systems, Wiesel [6], and we will establish this transformation as a canonical change of coordinates.

The stability of a general trajectory of a linear system is determined by the Lyapunov exponents. These are the values

$$\lambda_i = \frac{1}{t_f - t_0} \log \frac{|\Phi(t_f, t_0)\mathbf{x}_i(t_0)|}{|\mathbf{x}_i(t_0)|}, \quad (5)$$

extremalized over all initial displacements $\mathbf{x}_i(t_0)$. Usually (5) includes a limit as $t_f \rightarrow \infty$, but not here. The restriction to finite time intervals is an absolute necessity, since prediction of chaotic systems is only possible for a finite time interval.

We wish to find the vectors $\mathbf{x}_i(t_0)$, which extremalize the growth of the norm of displacement vectors, $|\mathbf{x}(t_f)|$ with respect to the initial displacement $\mathbf{x}(t_0)$. This is a constrained maximization, since in a linear system we may specify $|\mathbf{x}(t_0)| = 1$ from the outset. Using a Lagrange multiplier μ , we have the optimization problem

$$J = |\mathbf{x}(t_f)|^2 - \mu (|\mathbf{x}(t_0)|^2 - 1). \quad (6)$$

Now, since $\mathbf{x}(t_f) = \Phi(t_f, t_0)\mathbf{x}(t_0)$, the scalar function (6) becomes

$$J = \sum_i \left\{ \sum_j \Phi_{ij} x_{0j} \right\}^2 - \mu \left\{ \sum_i x_{0i}^2 - 1 \right\}. \quad (7)$$

Partial derivatives can now be calculated as if all components of the initial conditions x_{0i} were independent, yielding

$$\frac{1}{2} \frac{\partial J}{\partial x_{0k}} = 0 = \sum_i \sum_j \Phi_{ij} \Phi_{ik} x_{0j} - \mu_i x_{0k}, \quad (8)$$

where $k = 1, 2, \dots, N$. But this is just the component form of

$$\{\Phi^T \Phi - \mu_i I\} \mathbf{e}_i(t_0) = 0. \quad (9)$$

That is, the $\mathbf{e}_i(t_0)$ are the real, orthogonal eigenvectors of the real symmetric matrix $\Phi^T \Phi$, or the right singular vectors of Φ . Comparison to (5) shows that the Lyapunov exponents over the time interval (t_0, t_f) are found from

$$\mu_i = \exp \{2\lambda_i(t_f - t_0)\}. \quad (10)$$

This has been recognized by Goldhirsch, Sulem and Orszag [1]. We will refer to our λ_i as *regional* Lyapunov exponents, since they pertain to the finite time interval (t_0, t_f) .

A matrix Φ is symplectic if it obeys $\Phi Z \Phi^T = Z$, or equivalently $\Phi^T Z \Phi = Z$. It is well known that the fundamental matrix Φ is symplectic for a Hamiltonian dynamical system, see, e.g., Wiesel and Pohlen [7]. But then examining $\Phi^T \Phi$, we find

$$\begin{aligned} \Phi^T \Phi Z (\Phi^T \Phi)^T &= \Phi^T (\Phi Z \Phi^T) \Phi \\ &= \Phi^T Z \Phi = Z, \end{aligned} \quad (11)$$

so that $\Phi^T \Phi$ is itself symplectic. The eigenvalues of a symplectic matrix occur as inverse pairs, $\mu_i, 1/\mu_i$, so by (10) the regional Lyapunov exponents occur as positive / negative pairs. Since the Lyapunov exponents are also real, at most half of the modes are unstable, while the other half are stable. The proof of Liouville's theorem follows from this as a very simple consequence.

Over a finite arc of the trajectory, the regional Lyapunov exponents may be used to factor the dynamics into separate modes. The initial conditions $\mathbf{e}_i(t_0)$ introduce N special solutions to the variational equations, $\mathbf{x}_i(t) = \Phi(t, t_0)\mathbf{e}_i(t_0)$, on which the average exponential rate of expansion or contraction is an extremum. But local variations in these rates can be quite large, Haubs and Haken [2], Nese [3], Sepúlveda, Badii, and Pollak [4]. We wish to use these N special solutions to the variational equations as basis vectors for the entire solution set, and it would be very inconvenient for them to be anything other than unit vectors. Their instantaneous rates of change of magnitude are given by

$$\sigma_i(t) = \frac{\mathbf{x}_i \cdot A \mathbf{x}_i}{|\mathbf{x}_i|^2}. \quad (12)$$

Since the regional Lyapunov exponents are the average of these instantaneous rates on these N extremal solutions, we have

$$\lambda_i = \frac{1}{t_f - t_0} \int_{t_0}^{t_f} \sigma_i(\tau) d\tau. \quad (13)$$

Then, define N new functions $\mathbf{e}_i(t)$ as the solutions to

$$\dot{\mathbf{e}}_i(t) = A\mathbf{e}_i - \sigma_i(t)\mathbf{e}_i \quad (14)$$

with initial conditions $\mathbf{e}_i(t_0)$ on the interval (t_0, t_f) . They are, by (14), trivially unit vectors on the entire interval $t_0 \leq t \leq t_f$, and orthonormal at $t = t_0$. That they must also be orthogonal at $t = t_f$ can be seen by realizing that $\mathbf{e}_i(t_f)$ must also be the extremal initial conditions for exponential growth of trajectories running *backwards* in time. So they are the eigenvectors of the symmetric matrix $(\Phi^{-1})^T(\Phi^{-1})$, and are orthogonal. But at other times in the interval (t_0, t_f) the $\mathbf{e}_i(t)$ vectors may not be orthogonal. We note that since the new vectors remain unit vectors,

$$\sigma_i(t) = \mathbf{e}_i \cdot A\mathbf{e}_i \quad (15)$$

is an alternate form of (12). The \mathbf{e}_i have the same direction as the special solutions \mathbf{x}_i throughout the time interval, differing from them only in magnitude.

Now, assemble the $\mathbf{e}_i(t)$ vectors by columns into the matrix $\mathcal{E}(t)$. The matrix analog of (14) is

$$\dot{\mathcal{E}} = A\mathcal{E} - \mathcal{E}J(t), \quad (16)$$

where $J(t)$ is the diagonal matrix whose entries are the $\sigma_i(t)$. This is a relationship which is very familiar from time-periodic systems.

We wish to use the $\mathbf{e}_i(t)$ vectors as the coordinate vectors for describing the solution to the variational equations. To this end, define new coordinates \mathbf{y} on the tangent space as

$$\mathbf{x}(t) = \mathcal{E}(t)\mathbf{y}(t). \quad (17)$$

Since $\mathcal{E}(t)$ is a nonsingular matrix function of time, at least for $t_0 \leq t \leq t_f$, all stability information resides within the \mathbf{y} variables. Again differentiating (17) and substituting into the variational equations (3) we have

$$\dot{\mathbf{y}} = \left\{ \mathcal{E}^{-1}A\mathcal{E} - \mathcal{E}^{-1}\dot{\mathcal{E}} \right\} \mathbf{y}. \quad (18)$$

But using (16), this easily reduces to

$$\dot{\mathbf{y}} = J(t)\mathbf{y}. \quad (19)$$

So, this transformation takes the variational equations (3), and replaces them with a set of *decoupled, time-dependent coefficient* differential equations for the variables \mathbf{y} , and another set of linear equations (16) for the coordinate vectors $\mathbf{e}(t)$. We will refer to \mathbf{y} as the *modal variables* for the system, and $\mathcal{E}(t)$ as the modal matrix.

The transformation (17) will be canonical if \mathcal{E} is a symplectic matrix for all time. It is possible to so normalize $\mathcal{E}(t_0)$ at the initial time, Siegel and Moser [5], Wiesel and Pohlen [7]. Then \mathcal{E} will stay symplectic if $\mathcal{E}^T Z \mathcal{E} = Z$ for all time. Taking a time derivative of this and substituting from (16) gives

$$\mathcal{E}^T A^T Z \mathcal{E} + \mathcal{E}^T Z A \mathcal{E} - J^T (\mathcal{E}^T Z \mathcal{E}) - (\mathcal{E}^T Z \mathcal{E}) J = 0. \quad (20)$$

Assuming that the modal matrix is at the moment symplectic replaces the quantities in parentheses with Z . For Hamiltonian systems the matrix $A = Z\partial^2 H/\partial X^2$, and since $\partial^2 H/\partial X^2$ is symmetric, the above reduces to

$$-J^T Z - ZJ = 0. \quad (21)$$

Simple calculation will show that this is an identity for any diagonal matrix J , so the modal transformation (17) is a canonical transformation if $\mathcal{E}(t_0)$ is symplectically normalized. The modal equations of motion (19) then come from a modal variational Hamiltonian

$$K(\mathbf{y}) = \frac{1}{2} \mathbf{y}^T Z^T J \mathbf{y}. \quad (22)$$

This is, of course, only a local approximation, ignoring cubic and higher order terms.

3 The Voyager 1 Trajectory

As an example, we have chosen to study an approximation to the Voyager I trajectory from earth past Jupiter, and onward almost to Saturn. The trajectory is only approximate, since it was constructed in the restricted problem of three bodies. But our method is general, and easily extends to more complex and realistic dynamics. The Hamiltonian function is

$$H = \frac{1}{2} (p_x^2 + p_y^2 + p_z^2) - p_x y + p_y x - \frac{1-\mu}{r_1} - \frac{\mu}{r_2}, \quad (23)$$

where

$$\begin{aligned} r_1^2 &= (x - \mu)^2 + y^2 + z^2, \\ r_2^2 &= (x + 1 - \mu)^2 + y^2 + z^2. \end{aligned} \quad (24)$$

Using Voyager I's known distance of closest approach to Jupiter of 780,000 km and the flight time of 544 days from the earth to Jupiter, a boundary value problem was posed: starting at Jupiter the trajectory was propagated backwards, and at "launch", it should be 1 A.U. from the sun, and moving tangentially. The initial conditions for this trajectory are listed in Table I. In addition, we give a point about 100 days prior to close approach.

Table I
Launch Initial Conditions

	x	y	z
q_i	$+3.762779457438691 \times 10^{-2}$	$+1.886728183030001 \times 10^{-1}$	0.0
p_i	$-2.991922520851858 \times 10^0$	$+5.825188979188912 \times 10^{-1}$	0.0
Intermediate Initial Conditions			
	x	y	z
q_i	$-8.775683982224044 \times 10^{-1}$	$-4.272485353294678 \times 10^{-2}$	0.0
p_i	$-8.227825491293955 \times 10^{-1}$	$-7.044554120116425 \times 10^{-1}$	0.0

Over this trajectory, a final time of 1.5 dimensionless time units will take the spacecraft from the earth almost to the orbit of Saturn. This is shown in Fig. 1, in the rotating reference frame usually used for the restricted problem. The regional Lyapunov exponents are ± 5.637879 , ± 5.08635 , and ± 2.251739 . Examining the eigenvectors, the first and third are modes in the orbital plane, while the second is purely an out of plane mode. This leads to amplification / contraction of initial errors by multiplicative factors of 4706, 2058, and 29.3. Over an infinite time interval we would expect two zero Lyapunov exponents, and the third mode is much the least dramatically unstable of the three. It probably corresponds to an initial displacement along the trajectory itself.

To gain further insight, adjacent trajectories have been examined in the modal space. Integrating the nominal trajectory and a nearby orbit, the difference $\mathbf{x} = \mathbf{X}(t) - \mathbf{X}_0(t)$ was converted into modal variables with $\mathbf{y} = \mathcal{E}^{-1}\mathbf{x}$. Initial conditions were chosen to excite only one mode at a time, and to explore the limit of the linearization inherent in our solution. A shorter arc of the trajectory, spanning ± 100 days before and after flyby was chosen in order to avoid the extreme differences between initial and final modal amplitudes. Initial conditions for this arc are also given in Table I, and the limits of this portion of the trajectory are indicated in Fig. 1. Over this interval, the first two modes expand/decay by a factor of about 400, while the third mode is nearly static with an expansion/contraction factor of 1.32. The corresponding Lyapunov exponents are ± 20.213590 , ± 20.161805 , ± 0.935968 . The study of a shorter, less violently expanding / contracting interval makes it possible to see the entire modal behavior on graphs. It also emphasizes that neither the Lyapunov exponents nor the modal vectors \mathcal{E} are invariant to changes in the trajectory arc studied.

Fig. 2 shows the behavior of the Lyapunov exponents through this time interval. That is, the figure plots the running values of $\lambda_i(t)$ starting 100 days before Jupiter approach, and ending 100 days afterwards. The final values are the Lyapunov exponents used to decouple the entire trajectory arc, but intermediate values show where error growth occurs. Obviously, the immediate vicinity of the close approach is a time of explosive error growth. But after the flyby some of this error growth decays again.

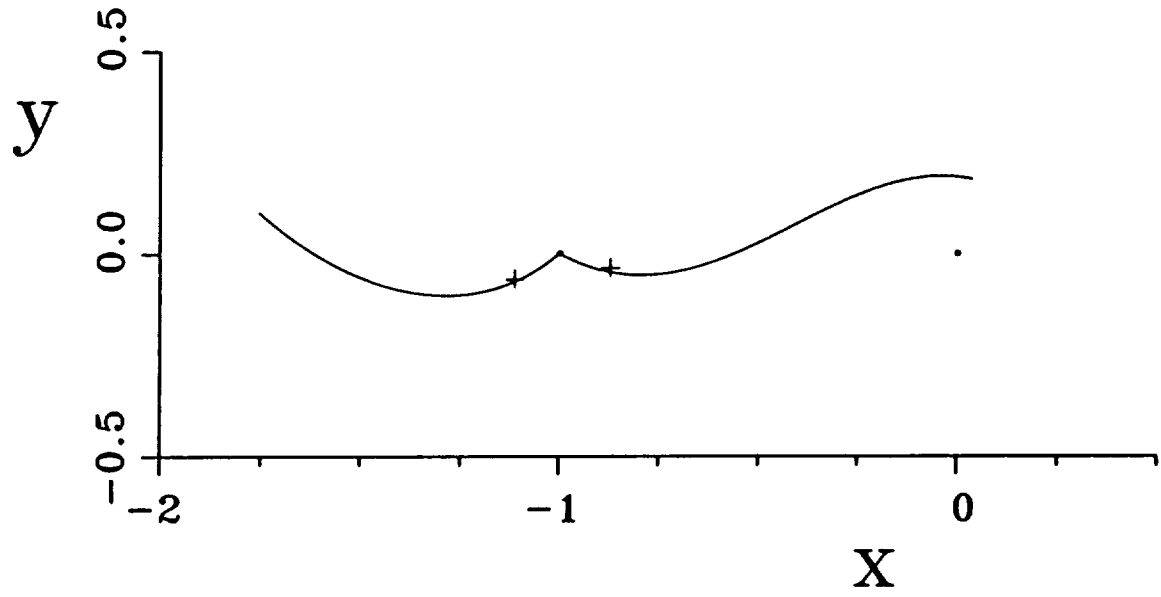


Figure 1: Voyager I flyby trajectory in the rotating frame of the restricted problem. Jupiter is at the cusp, while plus signs mark points ± 100 days bracketing close approach.

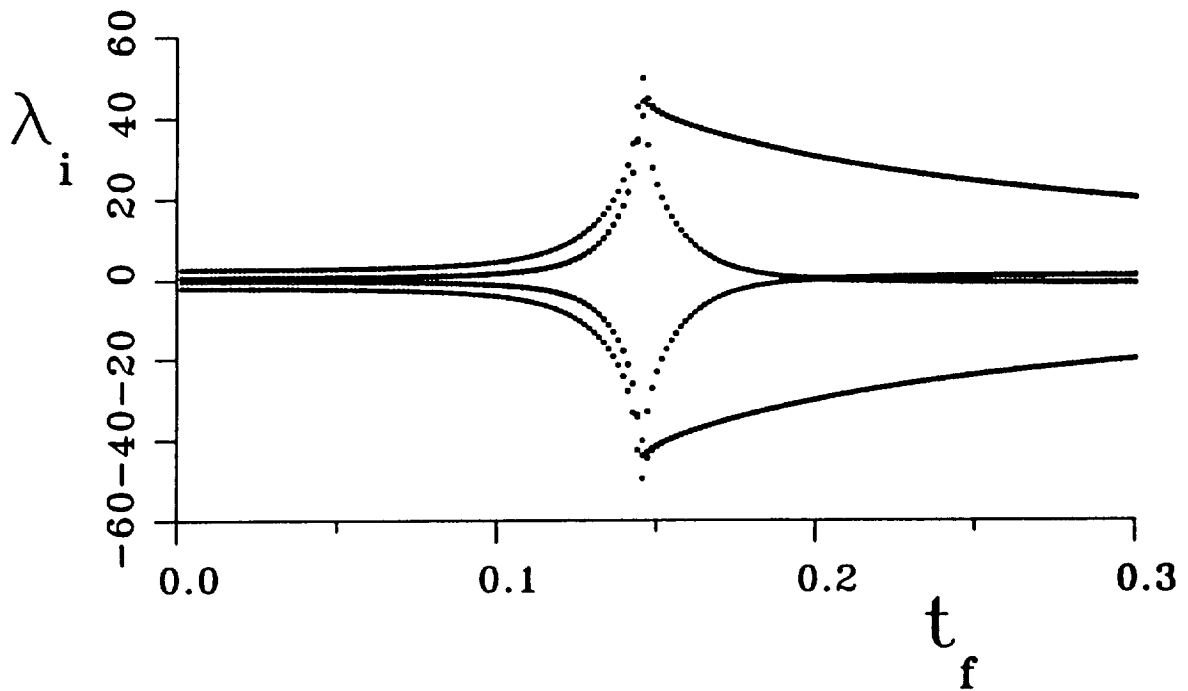


Figure 2: Lyapunov exponents $\lambda_i(t_f)$ throughout the ± 100 day interval bracketing flyby. The first and second modes (the outer curves after flyby) are superimposed at this scale.

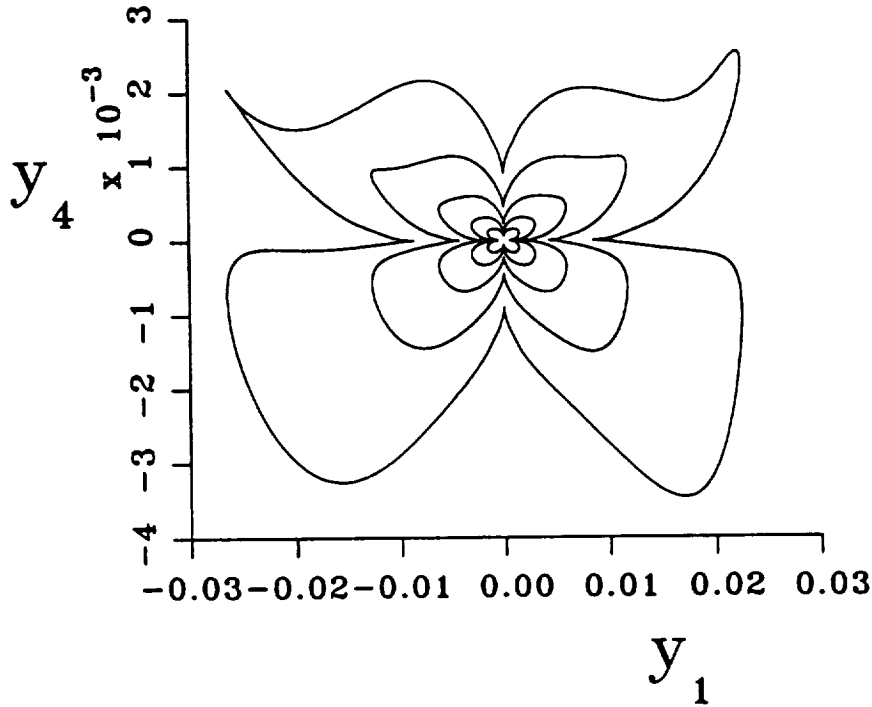


Figure 3: Modal trajectories on the tangent space for mode 1, with Lyapunov exponents ± 20.21359 .

Fig. 3 shows the behavior of the first mode over the ± 100 day arc. The modal vectors for this mode lie entirely within the orbital plane of Jupiter. Since the modal equations of motion (19) are time dependent, Fig. 3 is not a true phase portrait. Rather, initial conditions were scaled by a constant factor to find where the system visibly departs from linearity. Since y_1 grows by a factor of about 400 in this interval, while y_4 shrinks by the same factor, initial conditions are virtually on the vertical y_4 axis, while all trajectories terminate nearly on the horizontal y_1 axis. The linear regime appears at the core of the figure as a symmetric region where trajectories scale linearly. Most of the loop is traversed in a very short period of time about closest approach. Over most of the time interval trajectories are slowly departing from the vicinity of the y_4 axis before flyby, or converging towards the y_1 axis after closest approach. These trajectories were calculated with initial values of $y_2, y_3, y_5,$ and y_6 zero. These values stayed zero, confirming the success of the modal transformation.

Fig. 4 shows tangent space trajectories for the second mode. This mode lies entirely along the z, p_z directions in phase space, and the error growth / shrinkage factor is again about 400 over this trajectory arc. The truly linear regime again appears at the core of the figure, while the outer trajectories show visible departures from linearity. Also like mode 1, virtually all of the outer loops are traversed in a short time interval bracketing closest approach.

Mode 3 appears to span the in-track direction and the normal vector to the constant Hamiltonian surface. Since errors in these two directions are, in the long run, nearly static, the author suspects that if extended to infinity that this mode would generate the predicted pair of zero Lyapunov exponents. (A pair since in any autonomous system one Lyapunov exponent must be zero, and as a canonical system its Lyapunov exponents must occur as positive / negative pairs.) Fig. 5 shows some trajectories for this mode. The expansion / contraction of amplitude near close approach is so dramatic for this mode that all the initial and final points for this mode are at the origin on this scale plot. Actual initial modal amplitudes were of the order of 10^{-7} , and expand briefly by over four orders of magnitude near close approach. The individual trajectories seem to leave the origin, and then virtually retrace their outward path in returning.

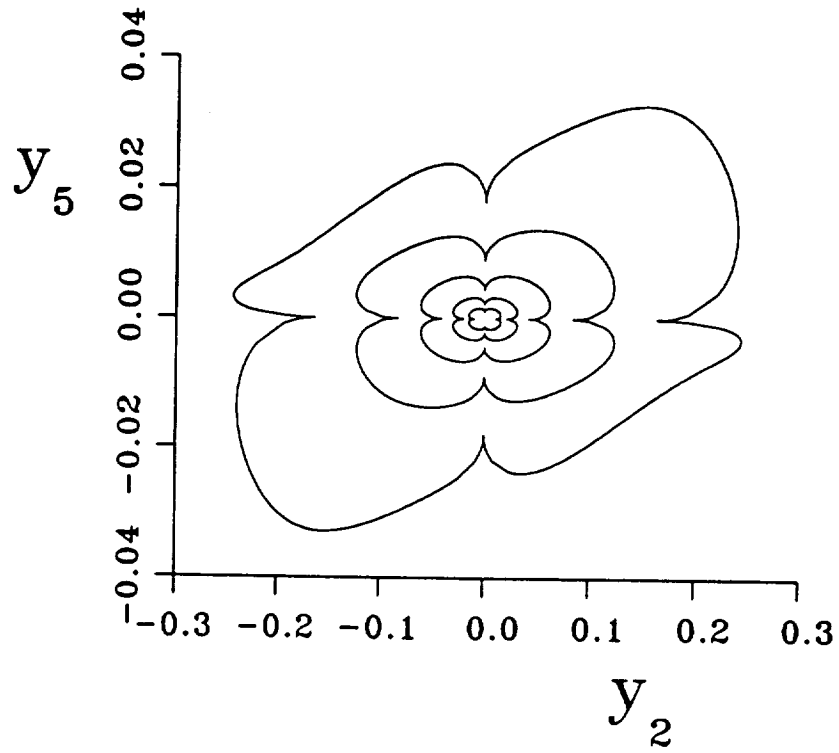


Figure 4: Tangent space trajectories for mode 2, the out-of-plane mode. The Lyapunov exponents are ± 20.16180 .

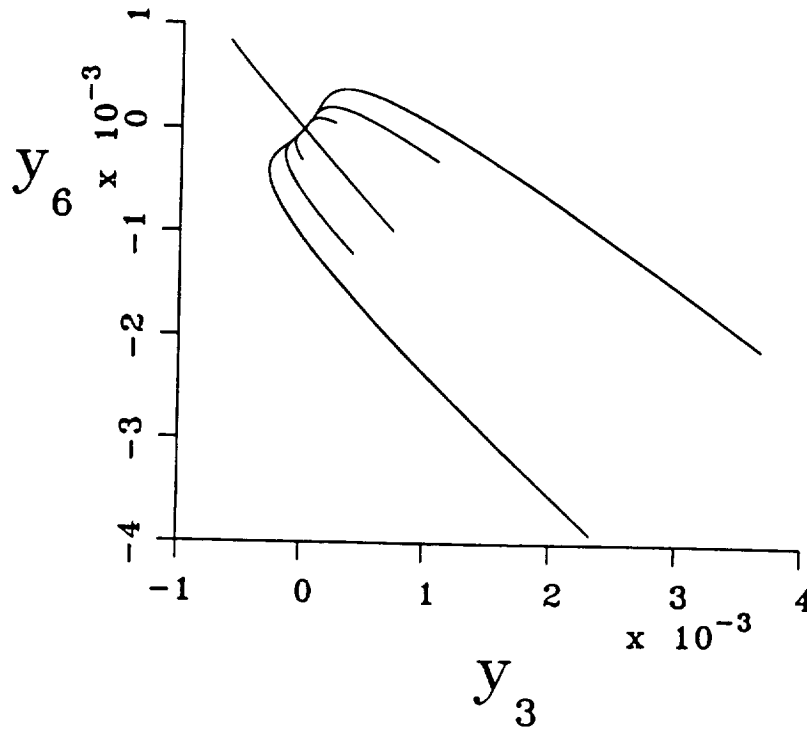


Figure 5: Tangent space trajectories for the third mode, with Lyapunov exponent ± 0.93596 . At this scale, all trajectories begin at and return to the origin.

4 Maneuvers

Since three Lyapunov exponents are positive, while three are negative, we have examined a maneuver strategy which attempts to zero the unstable modal amplitudes y_1, y_2, y_3 . The stable modal amplitudes are far less important, since they are decreasing any ways. However, we can only perform impulsive changes in velocity in the physical space, and we have just stated our maneuver goals in the modal space. Just before a maneuver, we have

$$\mathbf{x}(t^-) = \mathcal{E}(t)\mathbf{y}(t^-), \quad (25)$$

while just afterwards we have

$$\mathbf{x}(t^-) + \delta\mathbf{x} = \mathcal{E}(t)\mathbf{y}(t^-) + \mathcal{E}\delta\mathbf{y}. \quad (26)$$

Subtracting the two equations above produces $\delta\mathbf{x} = \mathcal{E}\delta\mathbf{y}$. Now, physically we must have $\delta\mathbf{x}^T = (0^T, \delta\mathbf{v}^T)$, since an impulsive maneuver cannot change the position vector, and since the momenta are really the components of the inertial velocity on the rotating frame axes. In partitioned form, then, the maneuver conditions become

$$\begin{pmatrix} 0 \\ \delta\mathbf{v} \end{pmatrix} = \begin{Bmatrix} \mathcal{E}_{11} & \mathcal{E}_{12} \\ \mathcal{E}_{21} & \mathcal{E}_{22} \end{Bmatrix} \begin{pmatrix} \delta\mathbf{y}_{1-3} \\ \delta\mathbf{y}_{4-6} \end{pmatrix}, \quad (27)$$

in three by three vector partitions. To zero the unstable modal amplitudes we must have

$$\delta\mathbf{y}_{1-3}^T = (-y_1, -y_2, -y_3). \quad (28)$$

The changes in the stable modal amplitudes are not within our control. The first three rows can be solved to yield

$$\delta\mathbf{y}_{4-6} = \mathcal{E}_{12}^{-1}\mathcal{E}_{11} \begin{pmatrix} -y_1 \\ -y_2 \\ -y_3 \end{pmatrix}. \quad (29)$$

Then, the second three rows give the desired maneuver as

$$\delta\mathbf{v} = \{\mathcal{E}_{21} + \mathcal{E}_{22}\mathcal{E}_{12}^{-1}\mathcal{E}_{11}\} \begin{pmatrix} -y_1 \\ -y_2 \\ -y_3 \end{pmatrix}. \quad (30)$$

An alternate strategy is suggested by the fact that only two of the modes experience significant expansion, while mode three is nearly static. Attempting to zero only the amplitudes of modes one and two enables us to minimize the velocity change required in the maneuver. Rewrite (27) as

$$\begin{pmatrix} \delta\mathbf{y}_{1-3} \\ \delta\mathbf{y}_{4-6} \end{pmatrix} = \begin{Bmatrix} \mathcal{E}_{11}^{-1} & \mathcal{E}_{12}^{-1} \\ \mathcal{E}_{21}^{-1} & \mathcal{E}_{22}^{-1} \end{Bmatrix} \begin{pmatrix} 0 \\ \delta\mathbf{v} \end{pmatrix}. \quad (31)$$

(The \mathcal{E}_{ij}^{-1} are three by three blocks of the inverse matrix \mathcal{E}^{-1} .) Then, we wish to minimize Δv^2 subject to the constraints $\epsilon_1\Delta\mathbf{v} = -y_1$ and $\epsilon_2\Delta\mathbf{v} = -y_2$, where the ϵ_i are the first and second rows of \mathcal{E}_{12}^{-1} . Using two Lagrange multipliers λ_i , the minimum amplitude maneuver is given by the solution to the five linear equations

$$\begin{aligned} 2\Delta v_i + \lambda_1\epsilon_{1i} + \lambda_2\epsilon_{2i} &= 0, \quad i = 1, 2, 3, \\ \epsilon_1\Delta\mathbf{v} &= -y_1, \\ \epsilon_2\Delta\mathbf{v} &= -y_2. \end{aligned} \quad (32)$$

To study this maneuver strategy, we have begun at 100 days before flyby with a unit error in either y_1 or y_2 . Of course, this is a linear problem, and scales linearly to other initial errors. Then the error was corrected at maneuver time t_m , and the new state, including nonzero amplitudes in the modal variables y_{4-6} , was propagated to 100 days after the flyby. The results for y_1 are shown in Figs. 6 and 7. Fig. 6 shows the required Δv maneuver amplitude as a function of the maneuver time in order to eliminate a unit error in y_1 at the start of the trajectory arc. As expected, the error is much cheaper to correct early in the trajectory, and becomes very expensive to correct after flyby. Fig. 7 shows the final values $y_{4-6}(t_f)$ as a function of the

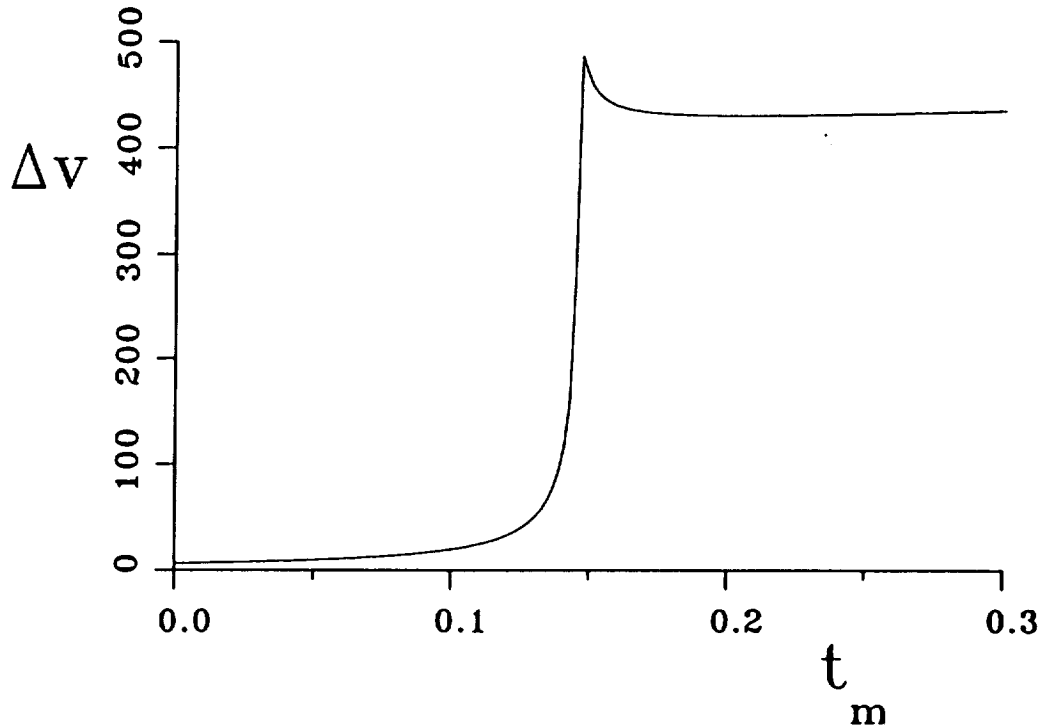


Figure 6: Maneuver magnitude Δv needed to correct an initial unit error in y_1 as a function of the time of the maneuver t_m . The error is vastly cheaper to correct before flyby.

time at which the maneuver is performed. Both y_3 and y_6 suffer a very large unwanted increase (again, at the final time) if the initial y_1 error is corrected any time around close approach. The conjugate variable to y_1 , y_4 , remains insensitive to y_1 corrections before close approach, since any error introduced into y_4 by an early maneuver has considerable time in which to decay. This is not true after the flyby, and the final error $y_4(t_f)$ shows a linear growth with t_m for maneuvers performed after the time of closest approach. The out of plane mode y_5 is decoupled from the planar modes, so it remains at its initial value of zero.

Figs. 8 and 9 show the analogous results for an initial unit error in the unstable vertical mode y_2 . The cost of correcting an out of plane error soars enormously just at the time of closest approach, and afterwards drops to a lower, nearly static value. The nearly static cost afterwards is due to the fact that most of the mode growth / contraction in this problem occurs very near the time of flyby. Afterwards most of the modal amplitudes themselves become almost static. Fig. 9 shows the final modal amplitudes as a function of the maneuver time. Since the z mode is decoupled from both planar modes, these are not excited from their initial zero values. However, the stable mode y_5 conjugate to the unstable vertical mode y_2 is excited by maneuvers performed after the close approach. As with the planar mode, this is due to the fact that y_5 can significantly decay if the maneuver is performed before the flyby, but does not greatly decay if the maneuver is performed after flyby.

5 Discussion and Conclusions

In this paper we have shown that the recently discovered modal separation for time dependent linear systems can be put on a canonical footing. A numerical example has been presented, showing the modal behavior and maneuver strategies for an approximation to the Voyager I flyby of Jupiter. The modal separation variables make it possible to assess the effects of initial errors and the steps taken to correct them without reference to the actual size of the errors, and making maximum use of the possible dynamical decoupling that the modal transformation offers.

This is just a beginning. There is no reason that the orbit determination process itself could not use the modal variables as the quantities to be determined. Also, the fact that the modal transformation is itself

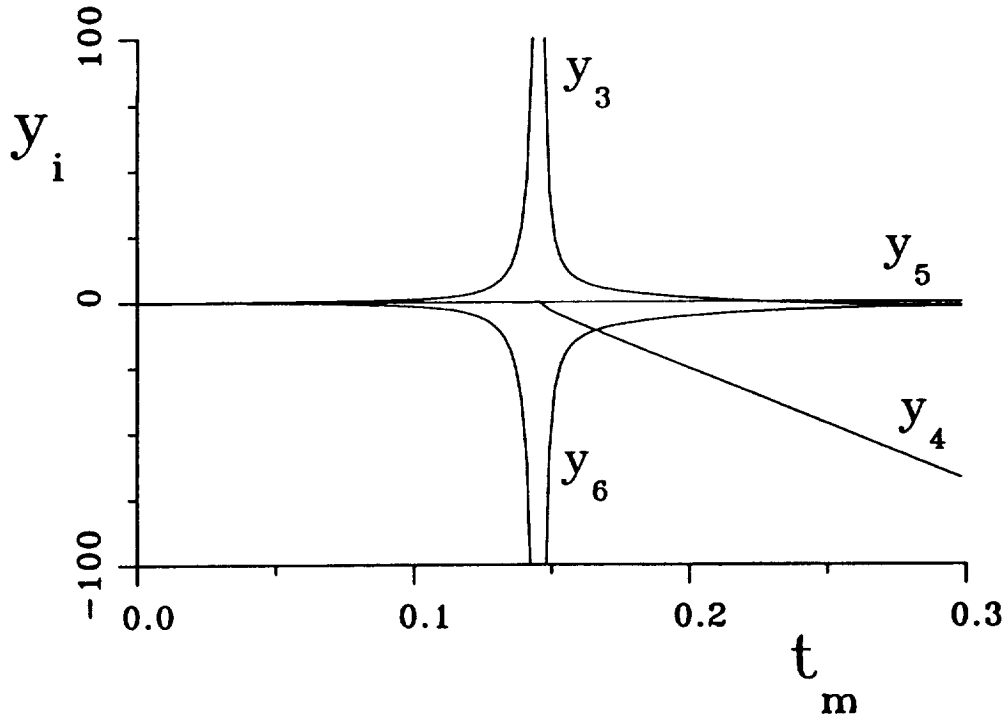


Figure 7: Final modal amplitudes $y_i(t_f)$ as a function of the time t_m a maneuver was performed to cancel an initial unit error in y_1 .

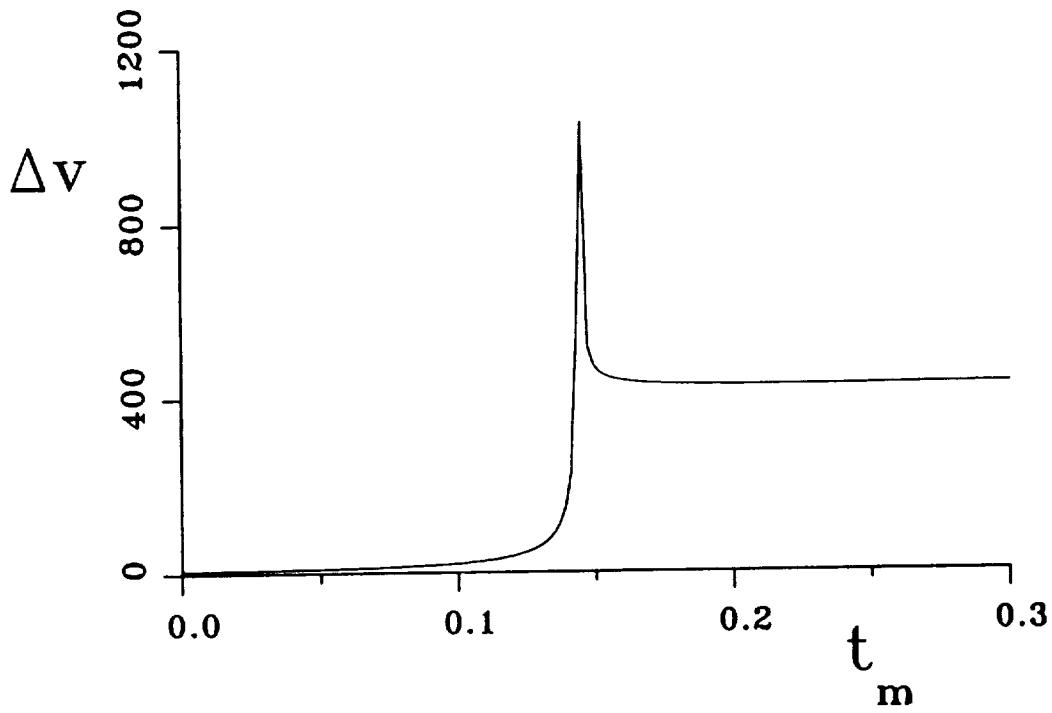


Figure 8: Maneuver cost Δv needed to cancel an initial unit error in the out of plane mode y_2 .

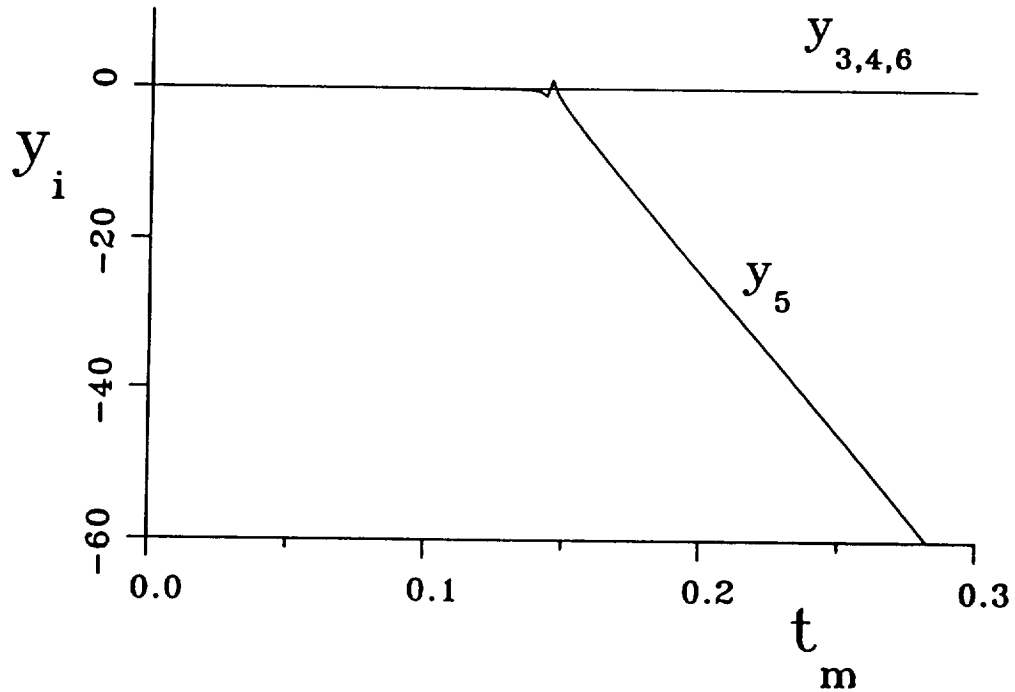


Figure 9: Final modal amplitudes $y_i(t_f)$ as a function of the maneuver time t_m used to correct an initial unit error in the unstable vertical mode y_2 .

a canonical transformation might be used to construct a *perturbation theory* about the underlying reference orbit, including higher order terms in the modal Hamiltonian (22) as the perturbation source. This might significantly extend the region of validity of the linearization of the trajectory.

References

- [1] I. Goldhirsch, P.-L. Sulem, and S.A. Orszag: 1987. *Physica D*, **27**, pp. 311-337.
- [2] G. Haubs and H. Haken: 1985. *Z. Phys. B*, **59**, pp. 459-468.
- [3] J.M. Nese: 1989. *Physica D*, **35**, pp. 237-250.
- [4] M.A. Sepúlveda, R. Badii, and E. Pollak: 1989. *Phys. Rev. Lett.*, **63**, pp. 1226-1229.
- [5] C.L. Siegel and J.K. Moser: 1971. "Lectures on Celestial Mechanics", *Springer-Verlag*, New York, pp 100-103.
- [6] W. E. Wiesel: 1994. *Phys. Rev. E* to appear, March 1994.
- [7] W. E. Wiesel and D. J. Pohlen: 1994. *Celest. Mech and Dynamical Astronomy*, **58**, 81-96, 1994.



LOW ENCOUNTER SPEED COMET COMA SAMPLE RETURN MISSIONS

P. Tsou¹, C. W. Yen¹ and A. L. Albee²¹ Jet Propulsion Laboratory, ² California Institute of Technology

Comets, being considered the most primitive bodies in the solar system, command the highest priority among solar-system objects for studying solar nebula evolution and the evolution of life through biogenic elements and compounds. The study of comets, and more especially, of material from them, provides an understanding of the physical, chemical, and mineralogical processes operative in the formation and earliest development of the solar system. These return samples will provide valuable information on comets and serve as a rosetta stone for the analytical studies conducted on interplanetary dust particles over the past two decades, and will provide much needed extraterrestrial samples for the planetary materials community since the Apollo program.

Lander sample return missions require rather complex spacecraft, intricate operations, and costly propulsion systems. By contrast, it is possible to take a highly simplified approach for sample capture and return in the case of a comet. In the past, we have considered Earth free-return trajectory to the comet, in which passive collectors intercept dust and volatiles from the cometary coma. However, standard short period cometary free-return trajectories results in the comet to the spacecraft encounter speeds in the range of 10 km/s. At these speeds the kinetic energy of the capture process can render significant modification of dust structure, change of solid phase as well as the lost of volatiles components. This paper presents a class of new missions with trajectories with significant reduction of encounter speeds by incorporating gravity assists and deep space maneuvering. Low encounter speed cometary flyby sample return will enable a marked increase in the value of the return science.

Acquiring thousands of samples from a known comet and thousands of images of a comet nucleus would be space firsts. Applying new approach in flight mechanics to generate a new class of low encounter speed cometary sample return trajectories opens new possibilities in science. A systematic search of trajectories for the first decade of the twenty-first century will be made. The target encounter speed is for less than 7 km/s to short period comets.

High Earth Orbit Design for Lunar Assisted Small Explorer Class Missions*

M. Mathews and M. Hametz
Computer Sciences Corporation (CSC)
Lanham-Seabrook, Maryland, USA

J. Cooley and D. Skillman
Goddard Space Flight Center (GSFC)
Greenbelt, Maryland, USA

Abstract

Small Expendable launch vehicles are capable of injecting modest payloads into high Earth orbits having apogee near the lunar distance. However, lunar and solar perturbations can quickly lower perigee and cause premature reentry. Costly perigee raising maneuvers by the spacecraft are required to maintain the orbit. In addition, the range of inclinations achievable is limited to those of launch sites unless costly spacecraft maneuvers are performed. This study investigates the use of a lunar swingby in a near-Hohmann transfer trajectory to raise perigee into the 8 to 25 R_E range and reach a wide variety of inclinations without spacecraft maneuvers. It is found that extremely stable orbits can be obtained if the postencounter spacecraft orbital period is one-half of a lunar sidereal revolution and the Earth-vehicle-Moon geometry is within a specified range.

Criteria for achieving stable orbits with various perigee heights and ecliptic inclinations are developed, and the sensitivity of the resulting mission orbits to transfer trajectory injection (TTI) errors is examined. It is shown that carefully designed orbits yield lifetimes of several years, with excellent ground station coverage characteristics and minimal eclipses. A phasing loop error correction strategy is considered with the spacecraft propulsion system ΔV demand for TTI error correction and a postlunar encounter apogee trim maneuver typically in the 30- to 120-meters-per-second range.

I. Introduction

The low Earth orbit environment presents significant problems for spacecraft that observe astronomical objects. The Earth is very bright and can scatter light into the telescope, so only objects toward the local zenith are unaffected. The apparent motion of the Earth soon causes the target to approach the bright Earth limb and target occultation soon follows. While in low Earth orbit the spacecraft experiences significant gravity gradient torques, atmospheric torques, and perhaps is exposed to radiation during passage through the South Atlantic Anomaly.

The target observability constraints severely limit the overall efficiency of the observatory. The environmental torques disturb the body orientation, which can blur the images. Radiation passages can cause a cessation of observing until the background count rate subsides.

Low Earth orbit is inevitable for observatories that optimize toward large optics or spacecraft complexity [as for the Hubble Space Telescope (HST)]. Smaller missions that concentrate on single instruments and modest apertures can take advantage of even small launchers to take them to higher orbits.

A higher orbit is optimal only if it can avoid Van Allen belt radiation, gravity gradient effects, and atmospheric torques. This implies that useful orbits should have perigee at or above the synchronous satellite altitudes ($\sim 6 R_E$). At these altitudes, there is only rare exposure to the radiation belts (during solar storms), small gravity gradient effects, and no atmospheric torques. At high altitudes the trapped radiation effects are largely absent, as are the gravity gradient and atmospheric effects.

* This work was supported by the National Aeronautics and Space Administration (NASA)/Goddard Space Flight Center (GSFC), Greenbelt, Maryland, under Contract NAS 5-31500

Some missions (Far Ultraviolet Spectroscopic Explorer) have taken the middle path via highly elliptical orbits that spend a large fraction of time above $6 R_e$, but which do suffer repeated loss of observing time while passing through the radiation belts twice each orbit.

Our goal was to find a high Earth orbit (HEO) that optimizes for the following:

- a) minimal atmospheric torques
- b) minimal exposure to trapped radiation
- c) minimal gravity gradient effects
- d) minimal line-of-sight interference by the Earth
- e) maximal observing time-on-target
- f) minimal eclipse time in Earth or Moon shadow
- g) minimal launch energy
- h) mission lifetime greater than 1 year
- i) data rate potential of at least 1 Mbs with modest RF system
- j) maximal inclination options
- k) minimal stationkeeping
- l) single station support.

Goals a and c impact the fine pointing ability of the spacecraft. Goal k is not really necessary for HEOs considered here since the orbits can be maintained without stationkeeping. However, some stationkeeping capability is assumed necessary in case the ability to avoid eclipses or perform other contingency maneuvers becomes necessary.

High Earth orbits, here defined to be an orbit with perigee radius greater than $6 R_e$, thus have the advantage of remaining above the radiation belts and generally providing excellent station coverage and communication links. Additionally, they can be advantageous for missions with constraints on the amount of time the spacecraft can spend in shadow. The relative freedom of the HEO from environmental disturbances (e.g., aerodynamic and gravity gradient torques) results in a stable observing platform with excellent pointing stability.

The principal disadvantages of traditional HEO concepts are that, typically, a ΔV on the order of 1 km/s or greater is needed to raise the perigee height of the transfer orbit to the final mission specific value and strong luni-solar perturbations can quickly drive perigee down and cause premature reentry unless the launch epoch is carefully chosen.

II. Concept Proposed in This Paper

The work described here expands the concept of perigee raising through a near lunar encounter developed in Reference 1 and explores the use of modest capability launch vehicles ($C_3 \sim -2 \text{ km}^2/\text{s}^2$) to place a spacecraft in a transfer orbit resulting in a low relative velocity lunar swingby targeted to meet other mission requirements than perigee height. Typical values of C_3 for the missions examined actually ranged from -2.2 to $-1.8 \text{ km}^2/\text{s}^2$. An example of such a mission would be the proposed Prometheus mission with a Pegasus-XL launch vehicle and a spacecraft of approximately 100 kg. The Prometheus mission, which will conduct a wide field ultraviolet sky survey, uses a lightweight, three-axis, sub-arcsecond stabilized spacecraft in a $19 R_e$ perigee, $57 R_e$ apogee, 15-day period orbit. The high angular resolution of the Prometheus instrument makes pointing stability an important concern, and weight limitations necessitate minimizing spacecraft propulsion system demands. It will be shown that using a lunar encounter permits launch of useful payloads with small expendable launch vehicles while achieving the desired perigee height without placing the demand for a perigee-raising maneuver on the spacecraft propulsion system. In fact, once transfer trajectory injection (TTI) errors have been corrected, no further spacecraft ΔV is required until one of the first few postencounter perigee passages. This scenario permits the control of orbit parameters to meet mission objectives and proper phasing with the Moon. Additionally, apogee can be moved out of the ecliptic plane to minimize the impact of shadows. Relatively large inclination changes can be produced as well. In fact, a swingby can be tailored to place the spacecraft in a polar orbit about the Earth, a mission with an, as yet, unexplored potential to the Earth observing community.

In general, after the lunar encounter the spacecraft will be in an elliptical Earth orbit with apogee distance somewhat greater than the mean lunar distance. Without further adjustment this orbit would, at times, produce long lived but chaotic orbits that are subject to strong lunar perturbations or even close encounters with the Moon that can result in reentry or even expulsion of spacecraft from the Earth-Moon system.

If, however, the spacecraft and Moon are approximately aligned along the line of sight from the Earth to the Moon when the spacecraft is at perigee and a maneuver is performed to lower apogee so that the resulting orbit has a period equal to half the lunar sidereal period of revolution, then at each subsequent apogee, the Moon will alternately lead or lag the spacecraft by 90 deg. Since the strongest lunar perturbations occur when the spacecraft is near apogee, this phasing will keep the spacecraft far from the Moon at apogee and the perturbative effects at one apogee will tend to be cancelled at the next.

With the proper phasing, a half-lunar period orbit is extremely stable for intervals up to several years, requiring essentially no stationkeeping for orbit maintenance. The secular variation of the Keplerian elements is small so that rotation of the line of apsides to bring apogee into the southern hemisphere with consequent impact on station coverage (the spacecraft spends much time near apogee and station coverage is better from the northern hemisphere) can be avoided.

Figure 1a shows, schematically, as viewed from the north ecliptic pole, the sequence of events involved in establishing a HEO mission. Starting from TTI at 1, the spacecraft encounters the Moon at 2, followed by an apogee adjusting maneuver at 3 to establish a one-half lunar period mission orbit. An important parameter for stability considerations is the angle between the spacecraft to Moon and the spacecraft to Earth vectors at the postencounter perigee. This Earth-vehicle-Moon angle is 180 deg if the Earth, vehicle, and Moon lie along a straight line, but a 180-deg Earth-vehicle-Moon angle can only be achieved if the spacecraft is in the Earth-Moon orbit plane at P1. Figure 1b shows the same sequence as viewed in the Moon's orbit plane. For this particular example, the mission was designed to have the final orbit in the Moon's orbit plane in order to achieve an Earth-vehicle-Moon angle of as close to 180 deg as possible.

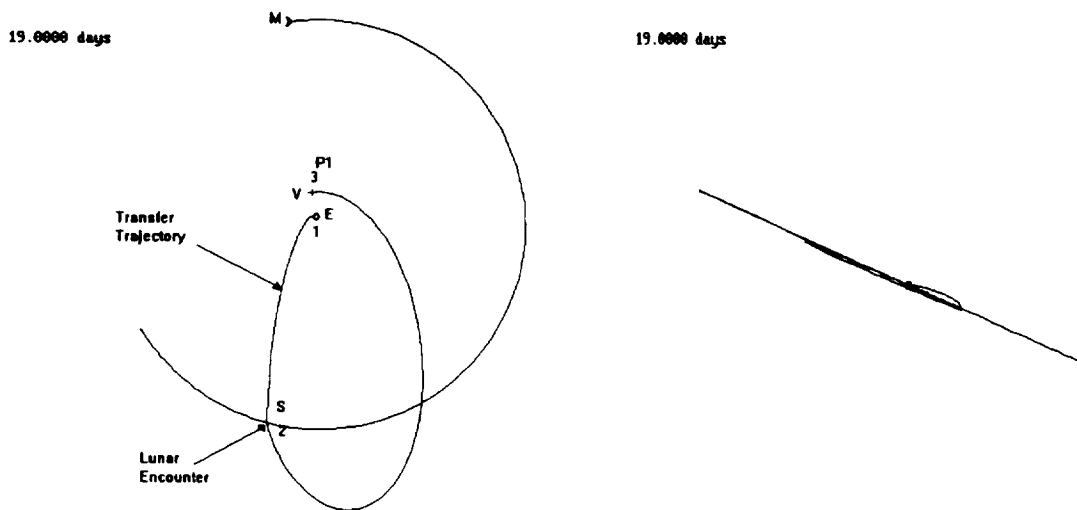


Figure 1a: View From Ecliptic Pole

Figure 1b: View in Plane of Moon's Orbit

Figure 1: HEO Transfer Trajectories to Mission Orbit

The work summarized here assumes insertion from a circular parking orbit into a 5-day lunar transfer trajectory. Such slow transfers require the minimum capability from the launch vehicle and result in an encounter with low spacecraft inertial velocity. The low velocity encounter permits large changes in perigee height in the postencounter orbit while keeping apogee near the lunar distance. Avoiding a large postencounter semimajor axis (SMA) is desirable to minimize the subsequent ΔV needed to establish the one-half lunar period orbit.

Actually, the total mission ΔV , including that provided by the launch vehicle is only less with the lunar assist if the final mission perigee radius is greater than a certain value. Below that limit, the lunar assist is more costly but, for all HEO, the lunar assist is the most economical means of establishing the orbit. Figure 2 compares the ΔV costs for our standard mission* using both a direct transfer to HEO (i.e., the spacecraft provides the ΔV for the perigee-raising maneuver) and a lunar assist (the Moon provides the ΔV for the perigee-raising maneuver) targeted to different postencounter perigee radii. No attempt was made to target to a particular value of inclination and in both instances the initial state used was a 300-km circular parking orbit. For the particular example selected here, the lunar assisted transfer is less costly whenever the mission perigee radius is greater than approximately 10,000 km. For comparison, the ΔV needed to establish a geostationary orbit via a Hohmann transfer from our parking orbit is included. Even though the geostationary radius is only $6.67 R_e$, its ΔV is significantly higher than that required to establish the HEOs because the geostationary orbit is circular.

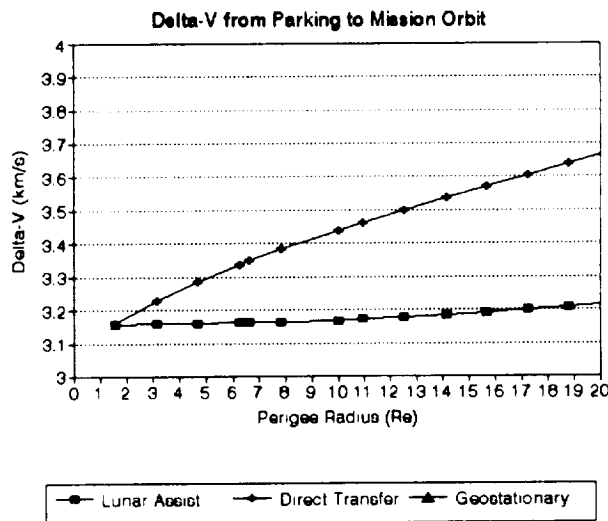


Figure 2: ΔV To Achieve HEO From Parking Orbit

Trajectories were modeled with the Mission Analysis and Design Tool, Swingby, using an eighth-order Runge-Kutta-Nystrom propagator with adaptive step size control through sixth order. Targeting to the initial lunar encounter conditions and then for various mission parameters (e.g., perigee radius and inclination) in the postencounter orbit was performed using the differential corrections targeting scheme in Swingby. For all calculations, point mass gravities were assumed for the Sun and Moon, and a 9×9 geopotential model was used for the Earth's gravity field. Solar radiation pressure and atmospheric drag were not modeled since their effects were found to be insignificant. Swingby was used to generate trajectory and ephemeris files which were then used as input to the Acquisition Data Program (ACQSCAN) to study shadows and station coverage.

III. Dynamics of the Lunar Encounter

A typical transfer orbit to establish a HEO type mission is shown in Figure 3. The transfer orbit is a Hohmann transfer in the sense that it has just sufficient energy for the apogee to be at approximately the lunar distance. The transfer requires approximately 4.7 days flight time from perigee of the initial state to lunar encounter. It is important to realize that the HEO transfer requires no ΔV capability of the spacecraft at the lunar encounter and

* Most of the figures in this document were created with data generated from trajectories derived from an initial state described by the following osculating elements: Epoch UTC 1993/12/16 12:00:00.0, $a=217831.93226$ km, $e=0.96934571$, $i=5.0$ deg, $\Omega=359.503048$ deg, $\omega=170.1790919$ deg, $TA=0$ deg, Mean-of-J2000 Earth equatorial coordinates. The encounter parameters were changed slightly to vary mission parameters for the particular situation to be illustrated. This initial state is referred to as our "standard mission."

the mission orbit is not circular. The ΔV needed to raise the perigee to the final mission value is provided by a momentum exchange with the Moon.

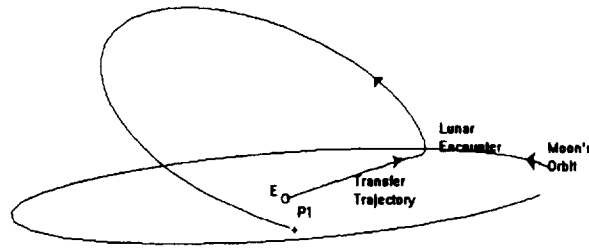


Figure 3. HEO Orbit Transfer to First Perigee

Although the results are not sufficiently accurate for detailed mission design, insight into the dynamics of the encounter can be gained by treating it as a classical two-body, zero sphere of influence collision of point masses. This approach is examined in some detail in Reference 7. Figure 4a shows the velocities of the spacecraft relative to an Earth-centered inertial reference frame just prior to the lunar encounter. In the Earth-centered inertial frame, the pre- and postencounter spacecraft trajectories are ellipses. In the selenocentric frame, however, the trajectory of the spacecraft is hyperbolic with an asymptotic approach velocity relative to the Moon given by

$$V_{br} = V_b - V_m$$

where V_b is the velocity of the spacecraft in the Earth-centered inertial frame before the encounter and V_m is the corresponding Earth-centered inertial velocity of the Moon. V_{br} and V_{ar} are the spacecraft velocities just before and just after the lunar encounter relative to the selenocentric frame. Since the spacecraft energy is conserved in the selenocentric frame during the encounter, the asymptotic departure velocity is equal in magnitude to the approach velocity, but from Figure 4b, it is apparent that the relative velocity vector has been rotated by the encounter through the angle Θ in the plane of relative motion even though its magnitude is unchanged.

Since the spacecraft velocity in the Earth-centered inertial frame after the encounter is

$$V_a = V_m + V_{ar}$$

it is obvious from Figure 4c that the encounter changes the spacecraft Earth-centered inertial velocity by ΔV where

$$\Delta V = 2 * V_{br} * \sin(\Theta/2)$$

where

$$\Theta/2 = \arcsin(1/e) \text{ and } e = 1 + R_p * V_{br}^2 / \mu$$

For the HEO considered in this analysis, with encounter distances ~ 15000 km and relative encounter velocities ~ 1 km/s, typically ΔV of approximately 500-1000 m/s are obtained from the encounter. This is sufficient to raise perigee to 10–25 R_e .

It is instructive to consider two special cases. If the motion is such that the result is a pure rotation of the relative velocity vector about the Moon's velocity vector, then the magnitude of spacecraft inertial velocity is unchanged. Such an encounter would change the trajectory plane (inclination) but not the energy (SMA). If the encounter were to take place so that the relative velocity vector is rotated entirely in the initial trajectory plane, then the

inclination is unaffected by the encounter. Usually, an encounter changes both the inclination and SMA and the change in each parameter can be controlled by appropriate B-plane targeting* of the incoming velocity asymptote.

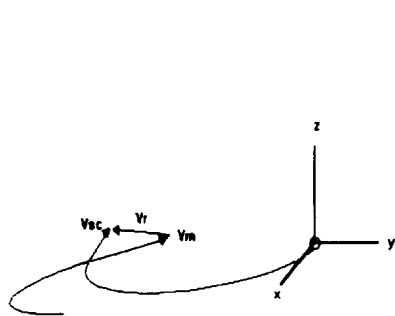


Figure 4a

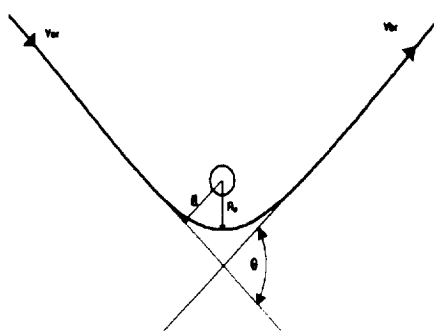


Figure 4b

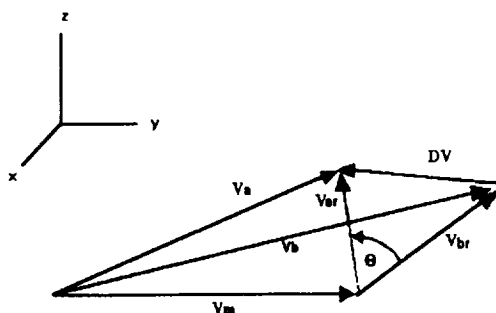


Figure 4c

Figure 4. Relative and Inertial Velocities During Encounter

Although the interrelationships of the orbital elements during the encounter are complicated, it is easy to show that the trajectory can be targeted to achieve the desired inclination to the Earth-Moon orbit plane and perigee radius by passing the Moon at the appropriate distance and height above or below the lunar orbit plane. The lunar swingby can be tailored to change the angular momentum and energy of the spacecraft to achieve the trajectory goals. Energy in the Earth-centered inertial reference frame is conserved but energy exchange between the Moon and spacecraft can produce large changes in the spacecraft orbit. A trailing edge swingby will add energy to the orbit, thus increasing the SMA and perigee height. The magnitude of the energy increase is controlled by appropriate choice of distance of closest approach. The closer the approach to the Moon, the greater the energy transfer and increase in SMA. The inclination of the postencounter trajectory is essentially controlled by varying the distance of the spacecraft above or below the Earth-Moon orbit plane while still achieving the targeted closest approach distance. Figures 5a and 5b show the behavior of the postencounter orbit inclination and perigee radius for the standard HEO as the targeted B-plane parameters are varied. To generate the data for Figure 5a, the lunar encounter was in the Moon's orbit plane, and only the miss distance was varied. In this case, the postencounter inclination changes only slightly while the perigee radius varies by more than a factor of 2. Conversely, in Figure 5b, the encounter distance projected in the lunar orbit plane was kept constant while the distance above or below

* A thorough discussion of B-Plane targeting parameters is given in Reference 8. The B vector is directed from the center of the targeted body to the point of closest approach the spacecraft would have if the target had no gravity. For targeting parameters, we frequently used the R and T components of B where \hat{R} is along the negative orbit normal and \hat{T} is perpendicular to \hat{R} and coplanar with B and \hat{R} . In our cases, \hat{T} lies essentially in the Moon's equatorial plane and is positive toward the trailing edge.

the plane at encounter was varied. Clearly this primarily affects the inclination while leaving the postencounter perigee radius unchanged.

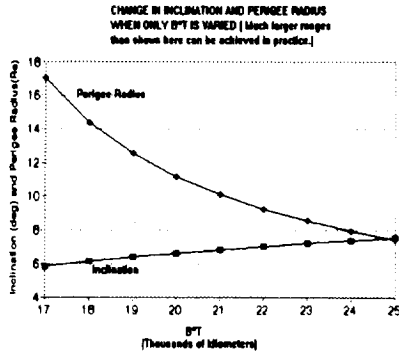


Figure 5a

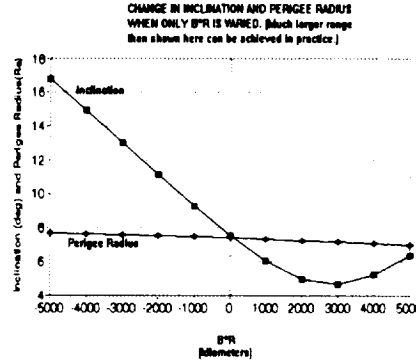


Figure 5b

Figure 5. Variation of Inclination and Perigee Radius With B-plane Parameters

The greater the number of elements that are targeted to specific values, the greater the difficulty in obtaining a suitable mission orbit. In general, it is not possible to target to an arbitrarily selected set of postencounter orbital elements and phase with respect to the Moon. This is a consequence of the constancy of the Jacobian integral in the restricted three-body problem.

This can be shown by considering the formulation of the Jacobian integral in the three-body problem commonly referred to as "Tisserand's Criterion for the Identification of Comets" (Reference 5). This can be expressed as

$$1/a + 2 * \sqrt{a * (1 - e^2) / p^3} * \cos(i) = \text{const}$$

where p is the mean Earth-Moon distance, a is the SMA, e is the eccentricity, and i is the inclination with respect to the lunar orbit plane. The constant retains approximately the same value in both the transfer orbit and the postencounter orbit. The expression can be written in terms of i , a , and initial perigee radius, R_p , by eliminating e with the aid of $R_p = a(1 - e)$. The end result is a constant of the motion involving only the SMA, inclination, and initial perigee radius. That this result constrains the achievable inclinations follows directly from the above equation. For a fixed postencounter perigee radius, the $1/a$ term contributes most for different choices of SMA. To achieve a high postencounter inclination, $\cos(i)$ should be small, which is most easily accomplished by decreasing the value of a . This was observed in the detailed mission design. For sequences of trajectories targeted to a fixed postencounter perigee radius, but with a range of inclinations, the postencounter SMA decreased with increasing inclination.

If particular values of perigee radius and inclination are selected from mission requirement considerations, then the SMA of the postlunar encounter orbit would be determined by the particular values selected. The resulting ΔV required to establish the final mission orbit of 241,000-km SMA after the apogee-adjusting maneuver would depend directly on the difference of the SMAs in the postencounter orbit and the final mission orbit.

In general, it will be found that if two of the mission parameters are fixed, then the choice of others is greatly restricted. For example, if perigee radius and Earth-vehicle-Moon angle are specified, then only a restricted range of inclinations may be achievable (fixing the Earth-vehicle-Moon angle is equivalent to choosing the postencounter SMA that determines the time of flight from encounter to $P1$). Conversely, precisely specifying perigee radius and inclination may make a viable Earth-vehicle-Moon angle unobtainable. Nevertheless, it is generally possible to find a wide range of orbits that meet mission objectives of lifetime and stability while, at the same time, having apogee rotated far enough out of the ecliptic plane and inclinations sufficient to minimize eclipses and maximize station coverage.

Typically we targeted pairs of elements. For example, perigee radius and inclination, or perigee radius and time of flight (phasing) to the first postencounter perigee were frequent choices for targeting parameters. Although most of the results presented in this paper are derived from a single example, many different trajectories and sets of

mission elements were considered in Reference 4. In this study (Reference 4), the relationship between targeting various mission parameters and the required spacecraft capability are examined in detail for ecliptic inclinations ranging from 0 to 75 deg and postencounter perigee radii ranging from 8 to 20 R_e . By choosing the launch geometry and epoch appropriately, we have found it possible to achieve inclinations relative to the Earth equatorial reference frame of 98 deg. Higher inclinations may be possible. Orbits with equatorial inclinations this high are tantalizing candidates for Earth observing missions that may want to study the polar regions of the Earth synoptically. To date, the emphasis of Earth observing missions has been on low Earth orbits.

IV. Error Correction Schemes

Detailed mission planning must consider and budget for maneuvers to correct TTI errors. Detailed analysis of the sensitivity of mission parameters such as perigee radius and Earth-vehicle-Moon angle to TTI errors is presented in Reference 4. It was found that the targeting of a typical HEO was quite sensitive to hot and cold burn errors along the velocity vector, but that a potentially useful HEO could still be reached without correction for pointing errors up to several degrees. Hot and cold burn errors of more than a few meters per second would probably need correction.

Two schemes for correcting TTI errors (hot and cold burns) are considered here. A transfer proceeding directly from the parking orbit in a transfer ellipse with apogee near the lunar distance and an encounter approximately 5 days after TTI is referred to as a "direct transfer." A transfer involving insertion into an orbit with apogee near the lunar distance in which the spacecraft completes one or more revolutions or "phasing loops" prior to the lunar encounter is referred to as a "phasing loop transfer."

Direct Transfer Post-TTI Error Correction

Figure 6 shows the ΔV needed to correct to the original targeted trajectory as a function of time from TTI for a representative mission assuming a 15 m/s under- or over-burn. Considering the previously demonstrated sensitivity to this kind of error, it is quite possible that correction may be necessary and, to avoid a sizable ΔV penalty (> 100 m/s after 20 hrs), the correction should be done soon after TTI; otherwise, a phasing loop mission scenario should be considered. It should be noted that corrections may not be as large or as critical as Figure 6 might seem to imply, because it may only be necessary to correct to any acceptable mission orbit and not necessarily to a precisely specified state. This concept is briefly considered in a subsequent section. There is considerable latitude if this is the case. An in-depth analysis of the various error correction scenarios should be explored in future studies.

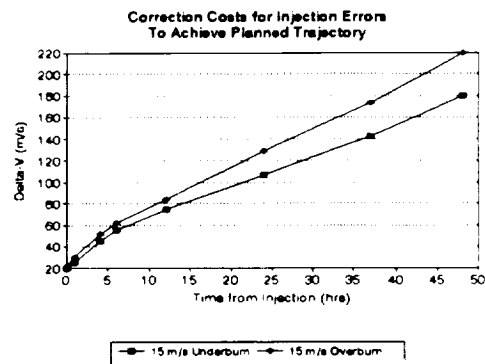


Figure 6. Direct Transfer Error Correction Costs

Phasing Loop Transfer Error Correction

Figure 6 indicates rapid growth with time from launch of the ΔV required to correct for hot or cold burns at TTI. Unless there are mission constraints to the contrary, correcting for TTI errors over two or more phasing loops could be a good strategy to avoid a potentially large fuel expenditure for error correction.

Essentially, a hot or cold burn results in a need for two corrections: phasing with respect to the Moon because the error results in early or late arrival at the lunar distance; and correcting energy so that the spacecraft has the proper velocity with respect to the Moon at encounter. A correction scheme using phasing loops would use burns at two perigee passes to correct the burn error. At the first perigee pass, a burn would be performed to adjust the period of the spacecraft so that the proper phasing can be regained by the time the spacecraft reaches the next perigee. At the second perigee pass, the spacecraft would then be given the proper energy for the encounter. Both the period change and the energy change can be accomplished by changing the size of the SMA.

To obtain a rough estimate of the total ΔV needed to implement this 2.5-loop phasing trajectory strategy, ± 15 -m/s impulsive ΔV perigee burns were applied at the initial epoch of a $15 R_e$ perigee, 50-deg initial inclination case to simulate hot/cold burn errors. The trajectories were then modeled with Swingby through the phasing loops with a period-changing maneuver performed at the first perigee to correct the arrival at the second perigee to the nominal epoch, and a final energy adjusting maneuver performed at the second perigee to correct to the proper energy for the lunar encounter. For the particular case and error correction strategy chosen, the total ΔV needed to correct for a 15-m/s overburn was found to be 65.8 m/s, while the amount needed to correct for the underburn was 36.0 m/s.

Although this was a simplified specific case, the results are consistent with results obtained for other missions such as the Geomagnetic Tail Laboratory (GEOTAIL) (Reference 6). It might be possible to reduce the ΔV by using other strategies, such as a 4.5-loop phasing trajectory strategy. For the purposes of this study, however, it seems reasonable to conclude that a phasing loop error correction strategy can be expected to require ΔV in the range of 20-80 m/s to correct TTI errors. In order to keep the direct transfer TTI error correction costs to this level, the corrections must be made within the first 10 hours after TTI. The disadvantage of the phasing loop strategy is that a time interval of approximately 35 days must elapse before the lunar encounter thus delaying the start of the science mission, as opposed to only 5 days if the errors are corrected during a direct transfer. This also results in some additional time being spent by the spacecraft in the radiation belts, but, because the spacecraft would be near perigee when this occurred, that time might not be excessive.

V. Shadows

ACQSCAN was used to determine periods when the spacecraft is in either Earth or Moon shadow. The cumulative eclipse summaries presented in this section are for a sequence of missions with $8 R_e$ perigee radius and ecliptic inclinations ranging from 0 to 70 deg that were analyzed in the course of the work done in preparing Reference 4. Figure 7 shows the total amount of time the spacecraft was in shadow during the 500-day interval covered by the ephemerides at each inclination. This was obtained by summing the individual eclipse durations for each 500-day mission at each inclination. No attempt was made to subdivide the totals into time spent in the umbral and penumbral regions. It is obvious from Figure 8 that eclipses become very infrequent when the orbit plane is tipped out of the ecliptic plane by only a small amount. Rotating apogee out of the ecliptic plane further reduces the likelihood of eclipses. The low-inclination orbits showed eclipses with durations of up to 10 hrs, but for inclinations above 20 deg, the longest eclipses observed were approximately 2 hrs, similar to the duration of total lunar eclipses.

It was initially thought that periods spent in the Moon's shadow might be significant. For the 0-, 10-, and 20-deg inclination cases, shadowing by the Moon for an interval of 36-42 min was observed approximately 5 days after launch during the lunar encounter. Only the $8 R_e$, 10-deg initial inclination case showed any shadowing due to the Moon at other times, and this was a single 33-min interval approximately 4.5 months into the mission lifetime. No shadowing by the Moon at all was observed for the $8 R_e$ perigee, inclinations greater than 20-deg cases.

One goal of the study described in Reference 4 was to determine whether it was possible to achieve a mission orbit with no eclipses during the first year. This is possible and is most easily achieved by choosing a mission orbit with an ecliptic inclination greater than 20 deg and apogee rotated out of the ecliptic plane. We targeted our standard orbit to an ecliptic inclination of 45 deg and a perigee radius of $25 R_e$ and then propagated the mission for 365 days. Figure 8 shows this trajectory propagated from the initial epoch to a stop on the first apogee after $P1$. The inclination of the orbit and the elevation of apogee above the ecliptic plane are clearly shown. No Earth shadows were encountered during the propagation, although the spacecraft did spend one 92-min interval in the Moon's penumbra.

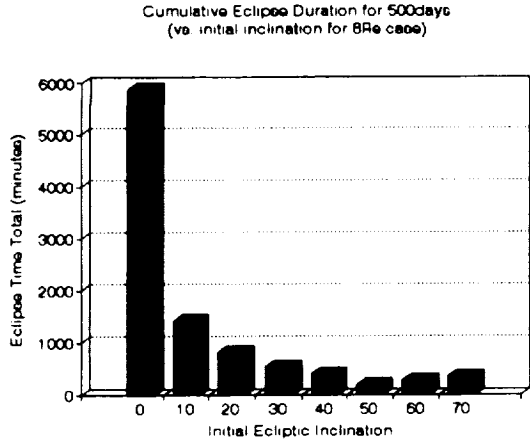


Figure 7. Cumulative Eclipse Duration for a 500-Day Mission

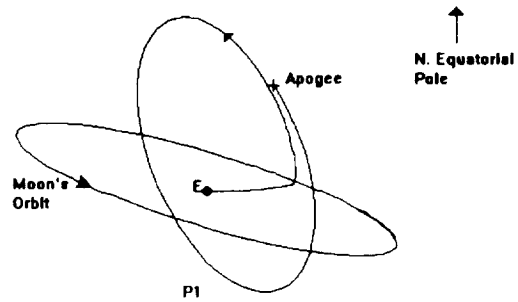


Figure 8. HEO for Eclipse and Station Coverage Analysis

VI. Station Coverage

ACQSCAN was used in conjunction with ephemerides generated with Swingby in order to obtain contact times for the Wallops Island and Canberra satellite tracking stations. The ephemerides used were obtained by starting from the initial state of the standard mission and retargeting to generate a mission orbit with a $28 R_e$ perigee radius and an Earth equatorial inclination of 70 deg. A plotting utility was used to graphically display the data for selected intervals during the mission lifetime. Figure 9 shows that the two stations selected complement each other quite well and generally provide from 20 to 24 hrs of combined coverage per day. The coverage provided by each station depends on the value of the argument of perigee (which determines whether apogee is located in the northern or southern hemisphere), the inclination, and the perigee radius (which determines the apparent angular rate of the spacecraft).

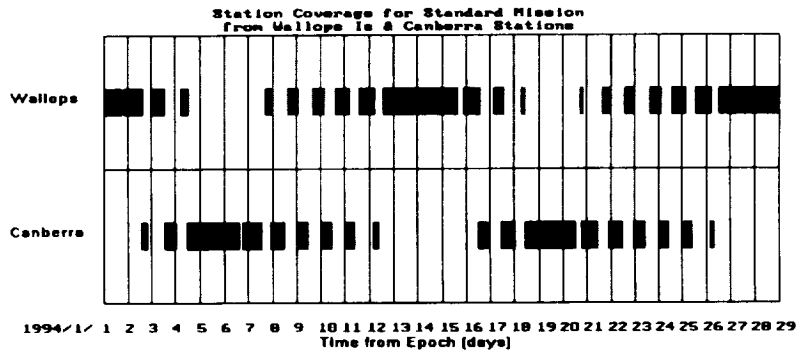


Figure 9. Station Coverage for the Standard HEO Mission

Because of its high altitude, even at perigee the spacecraft would be visible from approximately 92 percent of the hemisphere of the Earth facing it. Additionally, the apparent motion of the spacecraft is not great since, at perigee, its angular rate relative to the Earth-centered inertial coordinate system is only a few degrees per hour so that its diurnal motion is somewhat Moon-like.

Figure 10 shows the declination of the spacecraft over a complete orbit. Since Wallops Island is at a latitude of 38 deg, the spacecraft will be circumpolar when its declination is greater than approximately 52 deg. Thus for several days, the spacecraft will be continuously visible. From Canberra, at latitude 35 deg south, this situation will occur whenever the declination is south of approximately -55 deg. The longer contact times for Wallops are because, for this case, apogee is in the northern hemisphere and the spacecraft remains near apogee for a considerably longer period than near perigee.

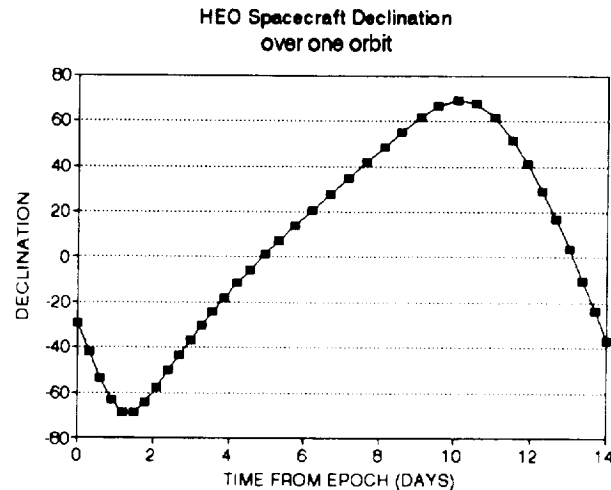


Figure 10. HEO Spacecraft Declination vs. Time From Jan. 4.5, 1994

The gaps in station coverage occur when the spacecraft is too far south from Wallops or north from Canberra to be seen. For two-station coverage, the choice of the Wallops Island and Canberra tracking stations is almost ideal since they complement each other extremely well. If tracking is to be done from a single station, an inclination could be chosen that avoids the coverage gaps and maximizes daily coverage for that particular station. In order to guarantee at least some coverage each and every day from Wallops Island, the equatorial inclination of the mission orbit would have to be less than 50 deg. Additionally, a lower perigee radius might be chosen to increase the time the spacecraft spends near apogee. This would shorten the periods of worst coverage.

VII. Orbit Stability

Were it not for the lunisolar perturbations, the Keplerian elements of a typical HEO would be quite stable since secular perturbations due to the geopotential are inversely proportional to the SMA raised to the 7-halves power (Reference 5, pg. 290), and the HEO SMA is large. Since the HEO examined here are designed to minimize such perturbations, they should show generally small secular changes in the elements. Figures 11a through 11e show the time variation of the elements for a 500-day propagation from the apogee-adjusting maneuver to establish the one-half period orbit. It is apparent that the changes are small compared to those customarily found for low Earth orbits.

Note the small secular component of the variation of the elements because of the large SMA. The phasing of the HEO orbit essentially cancels the strong lunar perturbations that would otherwise cause large variations.

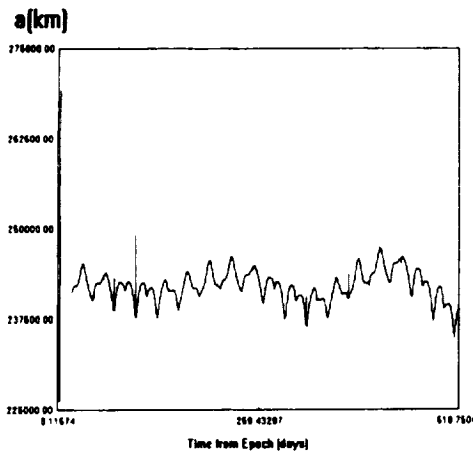


Figure 11a

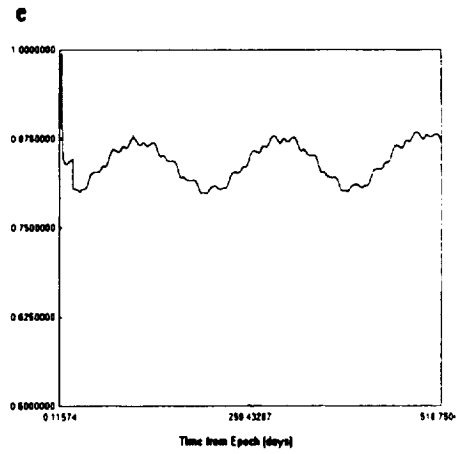


Figure 11b

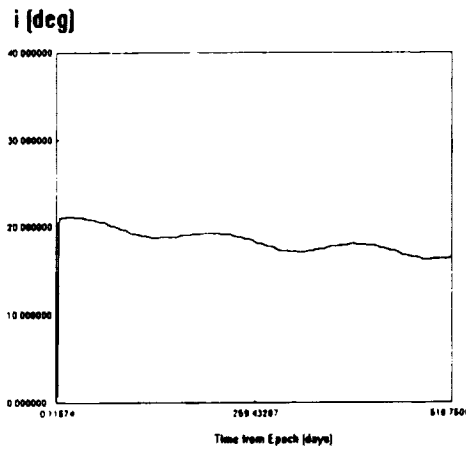


Figure 11c

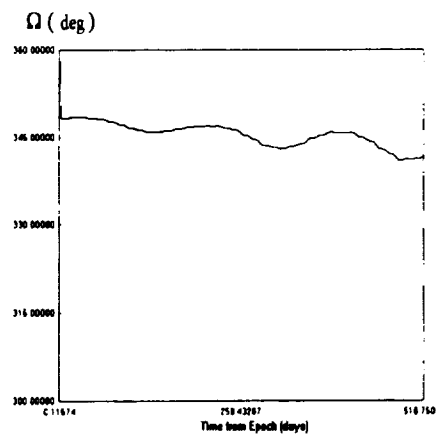


Figure 11d

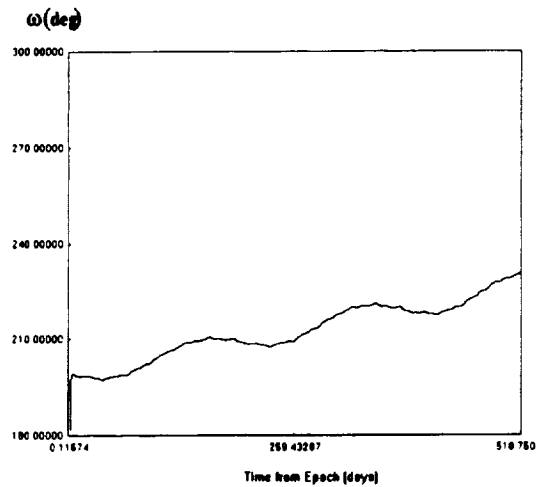


Figure 11e

Figure 11. Time Variation of HEO Orbital Elements

The long-term stability of a HEO is easily demonstrated by simply producing a trajectory plot of a propagation for the duration of the mission lifetime. Figures 12a and 12b show the trajectory propagated from the transfer trajectory through the apogee adjusting maneuver at the first post-encounter perigee and then for an additional 365 days. The time from TTI to P_1 is very nearly 19 days in all cases where a maximum Earth-vehicle-Moon angle was achieved. Figure 12a is a view from the north ecliptic pole while Figure 12b shows the trajectory as seen in the plane of the Moon's orbit. This particular case was purposely targeted to achieve a final mission orbit coplanar with the Moon's orbit in order to obtain an Earth-vehicle-Moon angle as near 180 deg as possible. The greatest Earth-vehicle-Moon angle obtained for this case was 179.5 deg.

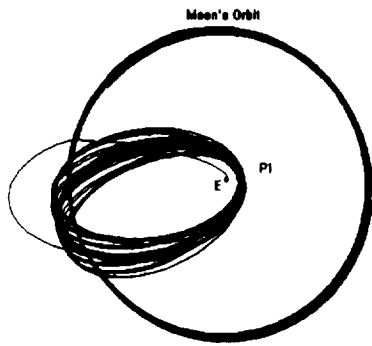


Figure 12a



Figure 12b

Figure 12. 365-Day Propagation of the Standard HEO

An interesting way of showing the stability of a HEO is to view the trajectory when propagated in an Earth-Moon rotating reference frame. Figure 13 is such a plot for the standard mission. Note that the spacecraft, when at apogee, clearly remains approximately 90 deg different in phase from the Moon for the entire mission duration.

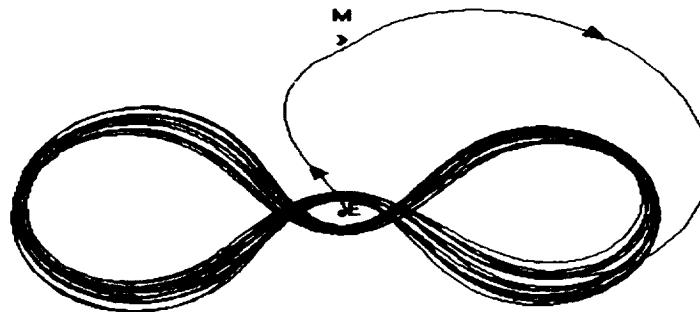


Figure 13. HEO Propagation for 365-Day Mission in Earth-Moon Rotating Coordinates

VIII. Other Possible Harmonic Orbits

It is certainly possible to establish orbits with fractional lunar periods that are ratios other than 1:2. The work described in Reference 1 examined orbits that had the lunar encounter at less than the lunar distance and were, thus, strictly speaking not swingbys, and it was not fully realized at that time that a one-half lunar period orbit gave the most stable mission configuration. The orbits of Reference 1 were not required to remain above $6 R_e$ perigee radius, so the lifetimes reported there were to impact and not really comparable to the ones studied here. Nevertheless, many of the desired HEO traits were obtained.

We looked briefly at orbital period ratios of 1:3 and 1:4 the lunar sidereal period. The 1:3 ratio orbit was not stable and its elements changed rapidly under the influence of lunar perturbations. The 1:4 ratio orbit was quite stable and could be a potential candidate for the appropriate mission. Figures 14a and 14b show the evolution of the 1:3 and the 1:4 ratio orbits in a co-rotating Earth-Moon reference frame for a 365-day propagation. The differences in stability are evident.

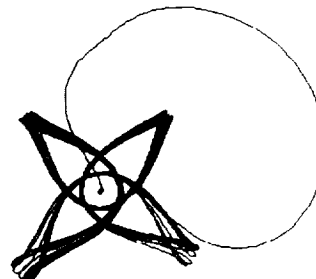
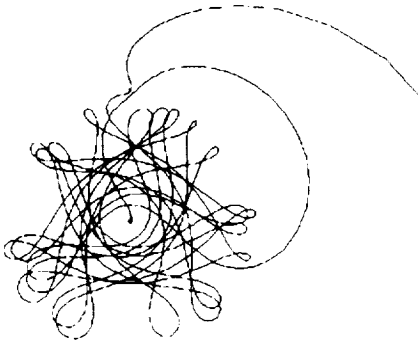


Figure 14a. 1/3 Lunar Period HEO Orbit

Figure 14b. 1/4 Lunar Period HEO Orbit

Figure 14. 365-Day Propagations of Non-Half-Period HEO Orbits

The ΔV required at *PI* to adjust apogee to the appropriate mission orbit value are 43.5 m/s, 109.5 m/s, and 169.8 m/s for the 1:2, 1:3, and 1:4 orbits respectively.

IX. Conclusion and Summary

We feel that the potential utility of high Earth orbits for future missions within the Earth-Moon system above the radiation belts has been convincingly demonstrated. Trajectories can be designed that show great stability for up to several years with no ΔV required either at the lunar encounter or for orbit maintenance maneuvers. The lunisolar perturbations that can cause dramatic changes in perigee height and other orbit parameters are effectively neutralized in these orbits. An additional benefit is that the long-term stability of the orbital elements for a properly designed trajectory can be used to enhance the already excellent ground station coverage in these orbits by maintaining apogee within a chosen hemisphere.

It would be presumptuous to say we had found orbits that optimize for all the parameters listed in Section I, but it seems clear that, with perigee radii near 100,000 km, the effect of environmental torques and the radiation belts should be minimal. With no ΔV required at the lunar swingby or for stationkeeping, and with C_3 near $-2 \text{ km}^2/\text{s}^2$, there are no great demands on either launch vehicle or spacecraft propulsion system. Adequate coverage from a single groundstation can be obtained by a judicious choice of inclination, but two stations can provide nearly continuous coverage. An orbit was easily found that did not result in eclipses for a nominal mission lifetime of 1 year, but that does not imply that the orbit was stable for only 1 year. The same trajectory was propagated for 10 years and, while the node and perigee cycled slowly, the SMA and Earth-vehicle-Moon angle at perigee changed by only 0.6 and 6.0 percent respectively, demonstrating great stability of the mission orbit.

Although this and other work have established the feasibility of high-Earth type orbits and many of their general properties, much analysis remains to be done. Further investigations into optimizing high-Earth orbit parameters through choice of launch date and various Earth-Moon-Sun configurations are needed, because only a handful of launch epochs have been considered. In-depth error and phasing loop analyses need to be performed to refine estimates of required mission ΔV budgets. Required specific launch vehicle energy (C_3) should be investigated for a variety of initial Earth-Moon configurations to identify favorable launch geometries. The work documented in Reference 4 revealed an apparent correlation between perigee

radius, inclination, and large Earth-vehicle-Moon angles. For larger perigee radii, the greatest angles occur for inclinations near 50 deg but lower inclinations tend to be favored for smaller perigee radii. Because the most stable orbits result from Earth-vehicle-Moon angles near 180 or 0 deg, this correlation should be investigated in greater detail and any dependence on launch date determined so that the most favorable launch dates may be identified.

Acknowledgments

The authors wish to gratefully acknowledge the preliminary efforts and insights of Peter Sharer, Bob Sperling, Steve Stalos, and Jeff Zsoldos.

References

1. Computer Sciences Corporation, CSC 53704 14, "HEO Orbit Analysis" (memorandum), S. Stalos, January 6, 1993
2. Computer Sciences Corporation, CSC 53704 49, "HEO Orbit Feasibility and Strategy Analysis" (memorandum), J. Zsoldos, and R. Sperling, June 17, 1993
3. Computer Sciences Corporation, CSC 53704 50, "Potential HEO Orbit Geometries" (memorandum), M. Hametz, J. Zsoldos, and R. Sperling, July 7, 1993
4. Computer Sciences Corporation, CSC 54704-08, "High Earth Orbit Study" (memorandum), M. Mathews and R. Sperling, December 30, 1993
5. A. E. Roy, *Orbital Motion*, p. 130, New York: Adam Hilger, 1988
6. D. W. Dunham and Shao-Chiang Jen, "A Launch Window Study for Geotail's Double Lunar Swingby Trajectory" International Astronautical Federation, 41st Congress Paper IAF-90-309, October 6-12, 1990
7. C. Uphoff, P. H. Roberts, and L. Friedman, "Orbit Design Concepts for Jupiter Orbiter Missions," *Journal of Spacecraft and Rockets*, Vol. 13, pp 348-355, June 1976
8. Goddard Space Flight Center, Flight Dynamics Division, 553-FDD-92/058R0UD0, *Mission Analysis and Design Tool (Swingby) Mathematical Principles, Release 1*, J. Carrico (CSC) and C. Schiff (CSC), prepared by Computer Sciences Corporation, July 1992

OBTAINING COINCIDENT IMAGE OBSERVATIONS FOR
MISSION TO PLANET EARTH SCIENCE DATA RETURNLauri Kraft Newman*, David C. Folta**, and James P. Farrell^o

One objective of the Mission to Planet Earth program involves comparing data from various instruments on multiple spacecraft to obtain a total picture of the Earth's systems. To correlate image data from instruments on different spacecraft, these spacecraft must be able to image the same location on the Earth at approximately the same time. Depending on the orbits of the spacecraft involved, complicated operational details must be considered to obtain such observations.

If the spacecraft are in similar orbits, close formation flying or synchronization techniques may be used to assure coincident observations. If the orbits are dissimilar, the launch time of the second satellite may need to be restricted in order to align its orbit with that of the first satellite launched.

This paper examines strategies for obtaining coincident observations for Mission to Planet Earth spacecraft. Algorithms are developed which allow the estimation of the time between coincident observations for spacecraft in both similar and dissimilar orbits. Although these calculations may be performed easily for coplanar spacecraft, the non-coplanar case involves additional considerations which are incorporated into the algorithms presented herein.

INTRODUCTION

The Mission to Planet Earth (MTPE) program provides a constellation of satellites which will monitor the earth's processes from a variety of orbits by combining the resources of many individual instruments on different satellites. Data from one spacecraft can then be used in a specific scientific process with data from other spacecraft to either compare data taken over the same geolocation by different types of instruments, or to calibrate one instrument with another identical one on a different spacecraft. In order to acquire measurements which can be used in a complementary manner, the satellites must take measurements of the same geolocation at approximately the same time. Taking measurements of the same location with satellites in different orbits at the same time is a challenge which has several possible solutions. Placing two spacecraft which want to obtain coincident measurements in a formation flying configuration (as described in Reference 1) would allow these coincident measurements to be taken almost constantly over the mission lifetime. However, because each satellite has unique mission requirements and is a collection of instruments of different types, the orbits are usually dictated by science requirements, causing the orbits of two spacecraft instruments which are interested in obtaining coincident measurements to be dissimilar.

* Flight Dynamics Engineer, EOS-Altimetry Project, Flight Dynamics Division, NASA Goddard Space Flight Center, Greenbelt, Maryland, 20771.

** Flight Dynamics Engineer, EOS Observatory Project, Flight Dynamics Division, NASA Goddard Space Flight Center, Greenbelt, Maryland, 20771.

^o President, Ridge Technology, Washington, D.C., 20010.

This paper presents results of a study of obtaining coincident measurements between satellites in various orbits. Possibilities for selecting spacecraft orbits to maximize the occurrence of coincidences while meeting the science requirements of all spacecraft instruments are examined, using MTPE spacecraft as examples. Algorithms are developed and verified for the Shuttle Solar Backscatter Ultra-Violet (SSBUV) experiment which allow the estimation of the time between coincident observations for spacecraft in both similar and dissimilar orbits. Although these calculations may be performed easily for coplanar spacecraft using equations presented in Reference 2, the non-coplanar case involves additional considerations which are incorporated into the algorithms presented herein.

BACKGROUND

MTPE program scientists are interested in obtaining coincident measurements between instruments on multiple MTPE spacecraft. However, while some of these spacecraft are in very similar orbits, some are quite dissimilar. Table 1 lists some of the MTPE spacecraft and their mean orbital characteristics, developed through Flight Dynamics Division (FDD) analysis. The spacecraft are the EOS 10:30 a.m. mean local time (MLT) of descending node spacecraft (EOS-AM), the EOS 13:30 p.m. MLT of ascending node spacecraft (EOS-PM), the EOS Altimetry (EOS-ALT) spacecraft, and the Tropical Rainfall Measurement Mission (TRMM) spacecraft. In addition to the information provided in Table 1, all of these spacecraft are in frozen orbits, which implies that the spacecraft altitude over a given geolocation remains constant. The spacecraft which are in sun-synchronous orbits have a fixed right ascension of node with respect to the mean sun, which means that the nodal regression rate is defined to be $0.9856^\circ/\text{day}$. The polar orbit which is not sun-synchronous has a different regression rate, and its orbit plane is not fixed with respect to the mean sun. Figure 1 shows a three-dimensional view of these orbits.

Several possible combinations of these spacecraft orbits can be considered to determine the coincidences which occur between them. These possible orbit combinations are two sun-synchronous spacecraft, one sun-synchronous spacecraft and one polar (but not sun-synchronous) spacecraft, and one sun-synchronous spacecraft and one equatorial spacecraft. The combination of the sun-synchronous spacecraft with the polar (but not sun-synchronous) spacecraft is of value since the nodal regression rates of these two spacecraft are different, as described above. This means that the orbit planes are moving with respect to each other. The combination of the polar spacecraft with the equatorial spacecraft is not considered, since it is virtually identical to the sun-synchronous/equatorial case. The following sections examine the natural coincidences which occur between these orbit combinations. A coincidence, the time during which each of the two spacecraft see the same location, is defined herein to be 10 minutes. This timing is considered realistic, since the EOS-ALT scientists are interested in obtaining coincident measurements between instruments on EOS-ALT and those on EOS-AM and EOS-PM within 10 minutes. Another assumption made throughout this analysis is that the coincidences occur between nadir-looking instruments with 0° fields-of-view (FOV). Currently, the capability does not exist to consider finite instrument FOVs; however, this capability will be implemented in the near future. Finite FOVs would increase the duration and occurrence of coincidences as explained in Reference 3. Therefore, the analysis presented herein represents a worst-case scenario.

Table 1: MTPE Spacecraft Mean Orbital Characteristics

	EOS-AM	EOS-PM	EOS-ALT	TRMM
Semi-major Axis	7077.79 km	7077.59 km	7076.28 km	6729.39 km
Eccentricity	0.0012	0.0012	0.0013	0.00054
Inclination	98.205°	98.145°	94.0°	35.0°
Right Ascension	255.356°	273.17°	310.0°	0.0°
Epoch	6/30/98	12/01/02	06/01/02	10/01/97
Type of Orbit	Sun-Synchronous	Sun-Synchronous	Polar	Equatorial

APPROACH AND CONSIDERATIONS

In order to evaluate occurrences of coincident measurements, algorithms were developed by Ridge Technology which estimate the time between coincident observations. These algorithms are implemented in an adjunct utility of the Orbit Works software designed by Ridge Technology. Orbit Works is a PC-based analytical tool which uses a U.S. Space Command (USSC)/North American Air Defense (NORAD) Simplified General Perturbations (SGP4) analytical propagator to create ephemerides from two-line orbit elements. The drag term is set to zero, and station keeping orbit adjustments are not modeled. This yields what might be termed "ideal" low earth orbit (LEO) models, since the time of interest spans several years. Hence, the result must be viewed as representative rather than absolute. Therefore, a more accurate calculation of coincidence times can be accomplished by propagating the spacecraft orbits with a propagator in operational software such as the Goddard Mission Analysis System (GMAS), which includes the effects of orbital perturbations such as geopotential effects, third body perturbations, atmospheric drag, and solar radiation pressure. However, data processing from the long propagations obtained with GMAS involves examining each time step of the propagation to determine the exact time at which the latitudes and longitudes of the spacecraft are equal. This process is time consuming and tedious, and does not take into account the desired time between coincidences. Orbit Works takes advantage of knowledge of the implications of orbit geometry to reduce the computation of coincident measurements from an exhaustive search of the time window to a more limited search.

One strategy is to seed numerical searches about key events such as equator crossings. A second strategy is to note the periodicity of coincidences and use this knowledge to jump (in time) to the vicinity of the next possible event. This allows long runs to be made quickly which indicate graphically and in tabular form the coincident time periods for two spacecraft. Two versions of the software exist - one for two high inclination spacecraft, the other for one low and one high inclination spacecraft. These software packages both use the position vectors of the two spacecraft to find places where the orbits are aligned, signaled by a maximum in the dot product of the vectors, or a minimum of the cross product. However, the starting point for the searches is determined differently for each version, as explained in more detail in specific examples which follow.

While Orbit Works does not itself include the more complicated models such as those present in GMAS, coincidences over specific periods can be determined by fitting a least-squares approximation of a two-line element set to a solution produced by GMAS. The same method can be applied to fit an element set to an orbit determination solution after launch to refine estimates of imminent coincidences. This approach and methods are being used with success for determining coincident measurements between a space shuttle based instrument and several LEO spacecraft based instruments, as detailed below.

Validation of Orbit Works with SSBUV

Orbit Works has been tested in an operational environment for the SSBUV experiment, a Space Transportation System (STS) payload bay experiment to assess the calibration of the Solar Backscatter Ultra-Violet (SBUV/2) instruments on the odd numbered LEO National Oceanographic and Atmospheric Administration (NOAA) weather spacecraft. The NOAA spacecraft are in sun-synchronous orbit with a MLT of 13:30, an altitude of 850 km, an inclination of 99°, and an orbital period of approximately 100 minutes. The STS orbiter is launched into a 299 km nominal orbit inclined 28°, 34°, 39°, or 57° depending on mission payload requirements. Calibration transfer is derived from SSBUV common view of the same latitude and longitude as SBUV/2 within one hour (± 60 minutes) and at an 88° or less solar zenith angle. The requirement is to obtain at least 32 coincident measurements per spacecraft per mission. To date, six SSBUV missions have flown, with one more scheduled for 1994 (further flights are planned each year for the out years). The mission profiles are summarized in Table 2.

A critical pre-flight activity is assessing whether the SSBUV experiment objectives can be met for the nominal STS flight plan, taking into account the launch window variation. Mission planning for SSBUV

consists of simulating the nominal mission profile to determine if the SSBUV success criteria are satisfied. If conditions are marginal, the simulation is run for the entire range of launch date and times to determine the effect of launch time on the number of coincident measurements. A critical post-flight activity is to rapidly assess the data take, given the actual launch time and orbit. The Orbit Works mission design, planning, and operations tools, as well as SSBUV mission/instrument specific tools are used to perform these analyses.

Table 2: SSBUV Mission Characteristics

SSBUV	STS Mission	Launch Date	Inclination (°)
1	STS-34	18 Oct 89	34
2	STS-41	06 Oct 90	28
3	STS-43	02 Aug 91	28
4	STS-45	24 Mar 92	57
5	STS-56	08 Apr 93	57
6	STS-62	04 Mar 94	39
7	STS-66	27 Oct 94	57

The computation of coincidences is based on the observation that the SBUV/2 orbits are near polar, while the SSBUV orbit is near equatorial. Sunlit NOAA equator crossings are computed first, then the STS orbit is propagated forward and back in time to align it with the longitude of the NOAA equator crossing. The latitude range to be searched is restricted by the STS inclination while the longitude range is determined by the NOAA inclination.

The SSBUV experiment has provided a unique opportunity to compare the pre-flight predicted coincidences with those derived from post mission spacecraft navigation data and the SBUV/2 and SSBUV instrument data streams. Excellent temporal and spatial agreement was confirmed by checking SSBUV 1-3 coincidence data versus the Orbit Works predictions. For SSBUV-4, all coincidences were compared, and excellent agreement was found for common coincidences. There were some predicted coincidences that were not found in the data and vice-versa. These could be due to instruments mode, data dropout, deviations from the STS mission earth view timeline, data processing errors, etc. These differences were resolved with the SSBUV Experiment Office as part of a quality assurance program. A single discrepancy remains, which is attributable to the Orbit Works software finding a relative minima rather than an absolute minima, since multiple minima can occur during the large temporal constraint of ± 1 hour.

Once the SSBUV goal of 32 coincidences with SBUV/2 is met, mission objectives change to acquiring coincident measurements with other spacecraft instruments, such as the Nimbus-7 and Meteor 3-5 Total Ozone Mapping Spectrometer (TOMS) instruments, as well as with the Upper Atmosphere Research Satellite (UARS) Cryogenic Limb Array Etalon Spectrometer (CLAES) and Microwave Limb Sounder (MLS) (limb looking) instruments. Coincident measurements with ground based (Dobson) instruments at Boulder, CO and Mauna Loa, HI are routinely planned. In addition, Sulfur Dioxide (SO₂) observation opportunities over eastern continental US, Europe, and eastern Asia (China, Japan, Korea) are identified and integrated into the data collection plan.

Post mission estimates of actual data take is accomplished by using the actual earth view session times (times when the SSBUV instrument was actually operating) and two line elements sets fitted to navigation data contained in the Johnson Space Center (JSC) state vector summaries.

Methodology for MTPE Coincident Measurement Cases

The extensive testing that the Orbit Works Coincident Viewing utility has undergone with SSBUV lends confidence in extending these algorithms for use with MTPE satellites. The algorithms developed for use in analyzing coincidences between two polar MTPE spacecraft orbits are developed from but slightly different than those used for the equatorial SSBUV. Even though these algorithms cannot be fully

acceptance tested until flight data from two polar spacecraft is available, the SSBUV testing allows a measure of confidence in the analysis results. Three cases involving representative MTPE spacecraft were examined. These are classified by orbit inclination. Case 1 involves one sun-synchronous spacecraft and one equatorial spacecraft, Case 2 considers one sun-synchronous spacecraft and one polar (but not sun-synchronous) spacecraft, and Case 3 includes two sun-synchronous spacecraft. Initially, Case 2 was thought to be included in the methods for Case 3; however, the converse proved to be true. That is, the methods developed to evaluate Case 2 also permit evaluation of Case 3. For all cases, a temporal constraint of observation within ten minutes was applied.

Case 1 (Sun-synchronous versus Equatorial)

The first coincident viewing case examined is the comparison between a high inclination, sun-synchronous spacecraft (EOS-AM) and a low inclination, equatorial spacecraft (TRMM). The methodology used in examining the coincidences which occur for this case is the same as that used for SSBUV, without some SSBUV mission specific extensions. For case 1, all equator crossings are checked, no sun angle constraint is applied, and the temporal constraint is 10 minutes.

The time and longitude of the ascending and descending equator crossings for the high inclination spacecraft are computed. The low inclination spacecraft position at the equator crossing time is then moved clockwise and counter-clockwise to the longitude of the high inclination crossing event. The time range to search, dt_1 , is defined by the time required for the polar spacecraft to transit the possible latitude range of the low inclination spacecraft. This is approximated from spherical trigonometry by:

$$dlat = \sin^{-1} \left(\frac{\sin i_2}{\sin i_1} \right)$$

$$dt_1 = \frac{dlat}{n_1}$$

where n denotes mean motion in radians per day, i denotes inclination, and $dlat$ denotes change in latitude in radians. Subscript 1 refers to the low inclination spacecraft (TRMM), and subscript 2 refers to the high inclination spacecraft (EOS-AM). Mean motion is calculated as:

$$n = \sqrt{\frac{\mu}{a^3}}$$

where μ is the earth's gravitational constant and a is the orbit semi-major axis.

The search range for the low inclination spacecraft is defined by the time, dt_2 , required for the low spacecraft to transit the same longitude range as the high spacecraft, in crossing the latitude range of the low spacecraft. This is estimated by:

$$dlon = \sin^{-1} \left(-\frac{\tan i_2}{\tan i_1} \right)$$

$$dt_2 = \frac{dlon}{n_2}$$

where $dlon$ denotes change in longitude in radians.

These times can be used to form a box over which a search can be performed for a position vector dot product maxima. The limits of the box, as shown in Figure 2, are from $t_1 - dt_1 - t_c$ to $t_1 + dt_1 + t_c$ on one axis

and from $t_2-dt_2-t_c$ to $t_2+dt_2+t_c$ on the perpendicular axis, where t_c is the time constraint of 10 minutes assumed for this analysis. An iterative search is then conducted to find a minima of the position vector cross product within this box. The box is divided into a grid of 625 equal sections. The section containing the minima is then further subdivided onto 625 equal sections, and so forth until the time intervals are both below a constraint (assumed to be one second). This refinement isolates the location of the minima. The one second criteria is justifiable, since the spacecraft position knowledge would be less than one second. This process is then repeated for the next node crossing to determine the next coincidence.

Case 2 (Sun-synchronous versus Polar)

This case involves two spacecraft: EOS-AM, a high inclination, sun synchronous spacecraft and EOS-ALT, a high inclination, polar spacecraft. The difference in the respective nodal regression rates means that the right ascension of the ascending nodes will cross about every two years, with a crossing while the spacecraft are traveling in opposite directions once per year. The method used for case 1 of determining a longitude box to seed the search for a cross-product minima could not be extended to cover this case, and the prediction of coincident measurement opportunities for this case proved to be somewhat challenging.

To investigate the nature and frequency of the coincidences, the behavior of the dot product of the position vectors of the two spacecraft was examined. This led to a methodology which entailed detection of the maximum extremae of the dot product or detection of the upper envelope of that function. Both orbits are propagated in steps of one minute using the analytic propagator, and the dot product of the geocentric inertial (GCI) position vectors is computed at each step. Figure 3 shows the value of the extrema over a five year period.

The time of the value of each maxima is then used to seed a search for a geocentric fixed (GCF) nadir trace crossing. The search is performed by bracketing the time of the maxima of the dot product by \pm the temporal constraint and performing a two-dimensional search for a minima of the cross product of the GCF position vectors. Figures 4 through 8 show the temporal and spatial distribution of the coincidences. The map shows the spatial distribution, while the timeline on the bottom of the figure shows when these coincidences occur during the year. Note that each figure contains a one year portion of the five year span shown in Figure 3, and that the temporal distribution of coincidences in each figure corresponds directly to the dot product maxima shown in Figure 3.

Case 3 (Sun-synchronous versus Sun-synchronous)

This case is a variant of case 2, with both spacecraft (EOS-AM and EOS-PM) in high inclination, sun-synchronous orbits. Since by definition the relative right ascension is constant (i.e. $\Omega_1 - \Omega_2 = C$), this case reduces to determining the longitude of crossings when they occur within the temporal constraint. The latitude of the coincidences can be computed from the orbit geometry - where the orbit planes cross - one in the northern hemisphere and one in the southern hemisphere. Passage of one spacecraft through the computed latitude can be used to seed a search for coincident observation by the second spacecraft. Since these passages are periodic, the searches are confined to the temporal constraint period of time twice a revolution. In practice, the methods developed for case 2 accommodated this case (but not necessarily vice-versa). For extensive application, an implementation capitalizing on the large (1/2 rev) jump between searches would economize computation time. The dot product extrema are shown in Figure 9.

RESULTS

This section discusses results of analyses of the three cases discussed above. The identified coincident measurement opportunities for each case are characterized by temporal characteristics, spatial characteristics, quantity of coincidences, and quality of coincidences (e.g. lighting conditions).

Case 1 (Sun-synchronous versus Equatorial)

Figure 10 shows a typical year of EOS-AM and TRMM coincidences. This represents several coincidences occurring daily on consecutive revs. On the average, half of these coincidences are sunlit. Note that in this case, the equatorial spacecraft was also at a much lower altitude than the sun-synchronous spacecraft. Figure 11 shows the relationship between the lighting conditions and the latitude at the coincidence location for a short (6 day) period during the year. Opportunities for coincidences in this case are characterized by a temporal characteristic of about 5 coincidences each day on consecutive revs, and a spatial characteristic of a full range of latitude and longitude locations within the orbit inclination constraints. The quantity of coincidences is about 2,200 coincidences per year for the EOS-AM and TRMM orbits, with a quality of 50% sunlit (the latitude varies with relative right ascension of node).

In fact, the availability of coincident measurement opportunities is dominated by the difference in mean motion of the EOS-AM and TRMM orbits of over one revolution (rev) per day. Coincident measurement opportunity analyses for other spacecraft which can be characterized as low inclination, low altitude, low eccentricity can be accommodated by this case. The algorithm must be further tested to determine its ability to handle low inclination spacecraft orbits which are high in either altitude or eccentricity.

Case 2 (Sun-synchronous versus Polar)

For the EOS-AM and EOS-ALT case, the results were somewhat surprising. The temporal pattern of coincidences is aperiodic in the five year interval we examined. Figure 5 shows a period of coincidences over seven (7) weeks which samples a wide range of earth locations. Figure 12 shows how this corresponds to a time when both the difference in right ascension of the ascending node and mean anomaly were near zero. Figure 13 shows the same information for the coincidences in Figure 7. Note that the availability of sunlit coincidences depends largely on the sun declination. Opportunities for coincidences in this case are characterized by a temporal characteristic of biannually for a period of either approximately 30 or 45 days, and a spatial characteristic which varies based on relative right ascension and mean anomaly. Opportunity exists for a period of observations which cover a full range (latitude and longitude) of geolocations at the times when the orbit planes intersect. The quantity of coincidences is approximately 600 to 1400 per year, with a quality of 50 % sunlit either all North or South latitude, except during right ascension of node crossover.

Polar or sun-synchronous spacecraft which fall into this category may be synchronized in mean anomaly or right ascension (if mission requirements are not violated) to maximize the number of coincidences. For instance, the right ascension of EOS-ALT was not specified by the science requirements. Therefore, some freedom in choosing this variable to maximize the coincidences with EOS-AM over the EOS-ALT lifetime is allowed. Figure 14 shows the coincidences between EOS-AM and EOS-ALT for a five year period, assuming that the EOS-ALT right ascension is chosen to be 310° . This choice was made by FDD to ensure that the first coincidence would occur after the initial EOS-ALT checkout period was complete (Reference 4). The fact that the spacecraft are traveling in the same direction the first year and opposite directions the second is clearly indicated by the long coincidences in the odd years (1, 3,...) followed by the multiple, short coincidences in the even years (2, 4,...). The lack of periodicity of the coincidences is also clearly evident.

Case 3 (Sun-synchronous versus Sun-synchronous)

For this case, the difference in spacecraft orbital periods results in a period of coincidences which occurs approximately once every 5 years for a period of about 12 months. Figures 15 and 16 show the spatial and temporal distribution of these coincidences. As expected, the coincidence location latitude is approximately 69.5° North and South of the equator. Figure 17 demonstrates that the variation of sun lighting conditions at the coincidence location depends solely on the sun declination. Opportunities for

coincidences in this case are characterized by a temporal characteristic of one twelve month period of coincidences during a five year mission, and a spatial characteristic which is confined to a single latitude North and South of the equator. The quantity of coincidences is approximately 11,000 coincidences, with a quality of 50% sunlit either North or South latitude, which reverses with annual variation of sun declination.

Again, polar or sun-synchronous spacecraft which are representative of this category may be synchronized in mean anomaly or right ascension (if mission requirements are not violated) to maximize the number of coincidences.

CONCLUSION

If coincident viewing requirements are levied on MTPE spacecraft orbits, numerical analysis must be performed to determine the coincidence times, since the co-planar coincidence algorithms presented in Reference 2 cannot be extended to cover the non-coplanar case. As evidenced by the above analysis, the PC-based Orbit Works tool provides a quick, easy, and economical way to numerically determine the coincident viewing periods for any two given spacecraft. Since spacecraft orbits are usually determined based on mission requirements, Orbit Works can be used to show the coincidence times which occur naturally between two given spacecraft orbits within a given temporal constraint. If the naturally occurring coincidences are inadequate, several options are available to ameliorate the situation. First, the launch of a second satellite can be planned to maximize coincidences with a satellite already on-orbit by varying the launch date and/or right ascension of the node of the second spacecraft. Secondly, the position of the second spacecraft in its orbit can be aligned with the position of the first such that each spacecraft passes through perigee at the same time. Finally, if the spacecraft are in similar orbits, close formation flying or synchronization techniques may be used to assure coincident observations. Orbit Works can be used to incorporate these coincident viewing considerations into future mission orbit selection, launch window analysis, operations and science planning for on-orbit spacecraft, or instrument calibration on multiple spacecraft.

The analysis presented herein assumes that both spacecraft orbits are fixed, and that the naturally occurring coincident periods (within the temporal tolerance) are sufficient to meet mission coincident viewing goals. No attempt was made to alter the mission orbits to maximize coincidences (with the exception of the EOS-ALT right ascension), as the orbits for MTPE spacecraft are specified by science requirements. It is also possible with Orbit Works to use the first spacecraft and a given temporal constraint to choose the orbit for the second spacecraft such that the number of coincidences is maximized. Choosing the second orbit to maximize coincidences is dependent on the ability of that orbit to meet the other mission science requirements.

REFERENCES

1. Folta, David, et al., "Considerations on Formation Flying Separations for Earth Observing Satellite Missions", AAS/AIAA Spaceflight Mechanics Meeting, Colorado Springs, CO, Feb. 24-26, 1992.
2. "Rendezvous/Proximity Operations Workbook", NASA JSC, Feb. 1985.
3. Scolese, Christopher, et al., "Field of View Location and Formation Flying for Polar Orbiting Missions", AAS/AIAA Spaceflight Mechanics Meeting, Houston, TX, Feb. 11-13, 1991.
4. "EOS-ALT Phase A Final Report Input," L. Newman to G. Smith, dtd. 12/23/93.

BIBLIOGRAPHY

Methods of Orbit Determination; P.R. Escobal; Krieger Publishing Company; 1976

Models for Propagation of NORAD Element Sets, Spacetrack Report No. 3; Felix R. Hoots & Ronald L. Roehrich; December 1980 (NTIS accession number: ADA 093554; Phone (703) 487-4650)

Orbit Works Reference Manual, Version 5.0, Ridge Technology, March 1994

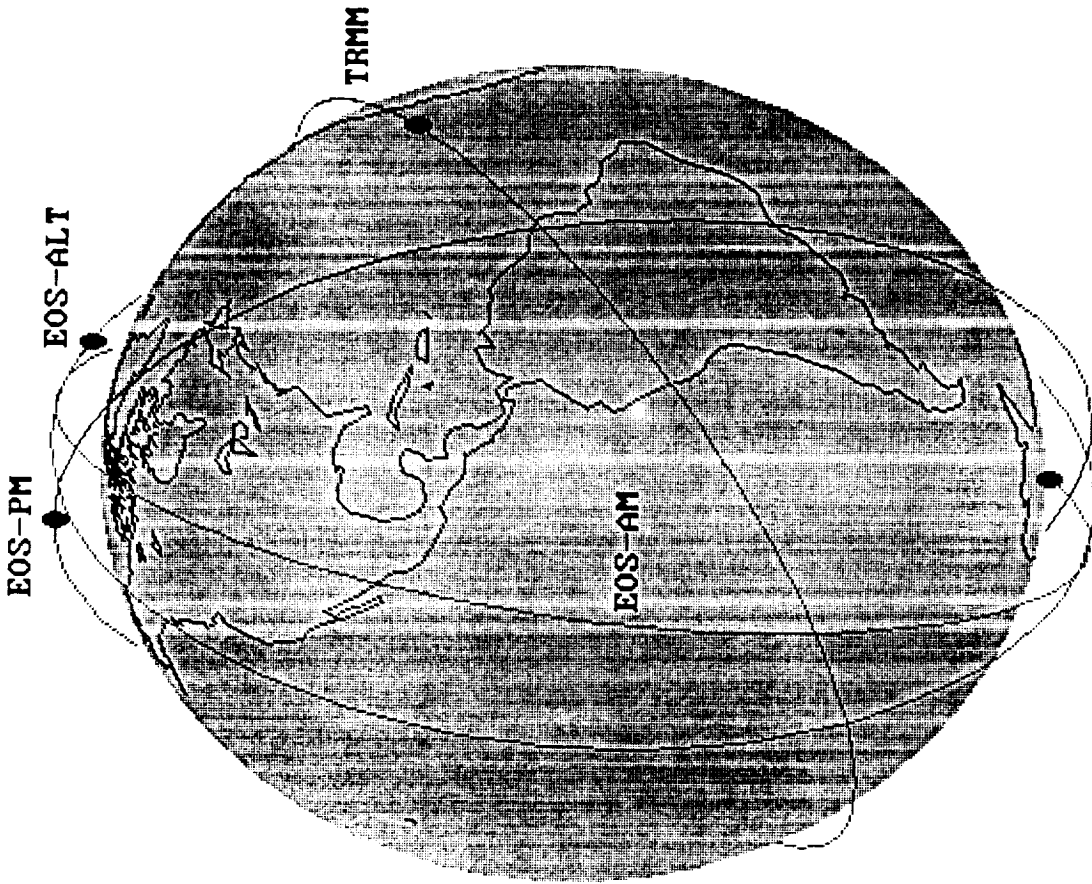


Figure 1: MTPE Spacecraft Orbits

Position Vector Dot Product
 Problem Set: CD318 System: CD318
 Date/time: Start: 81JAN2887 8888888 Stop: 81JAN2812 8888888
 Coincident measurement for alt bol w/raan=318

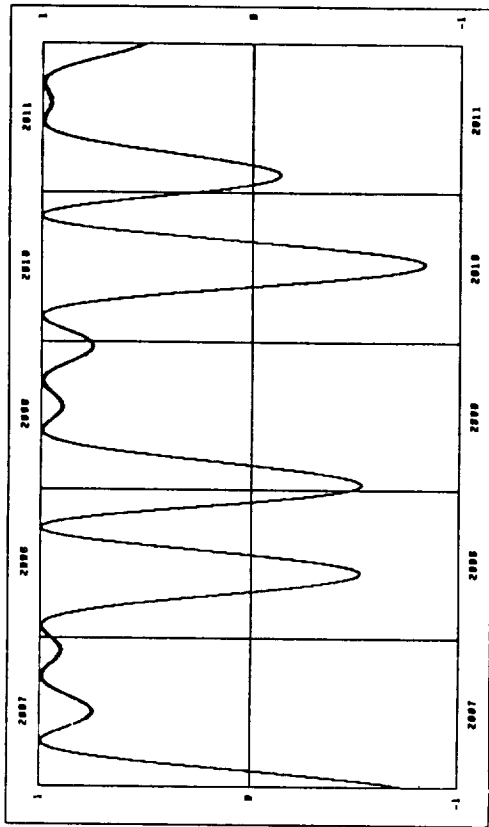


Figure 3: Position Vector Dot Products for EOS-AM and EOS-ALT

Instrument Track Coincident Earth Ulews
 Problem Set: cd318-88 System: CD318
 Date/time: Start: 81JAN2888 8888888 Stop: 81JAN2889 8888888
 Coincident measurement for alt bol w/raan=318 (2888)

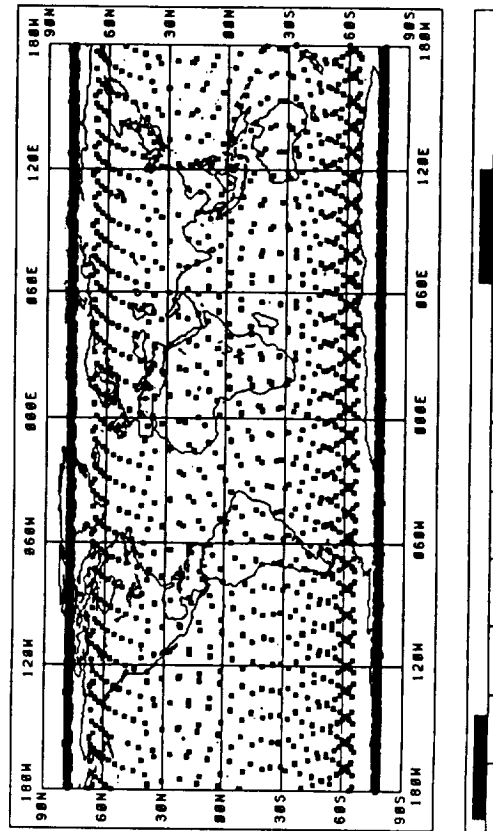


Figure 5: Case 2 Coincidences During 2008

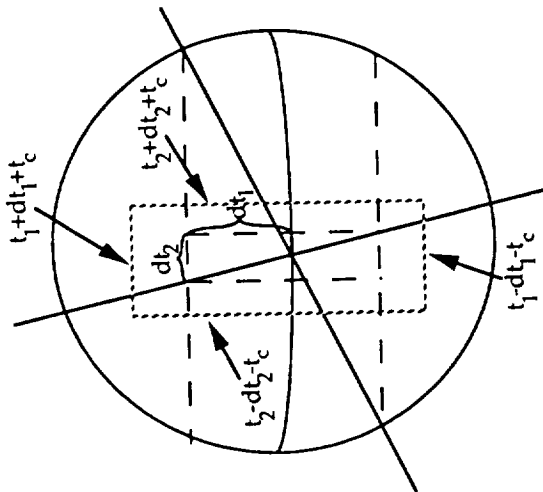


Figure 2: Case 1 Search Box

Instrument Track Coincident Earth Ulews
 Problem Set: cd318-87 System: CD318
 Date/time: Start: 81JAN2887 8888888 Stop: 81JAN2888 8888888
 Coincident measurement for alt bol w/raan=318 (2887)

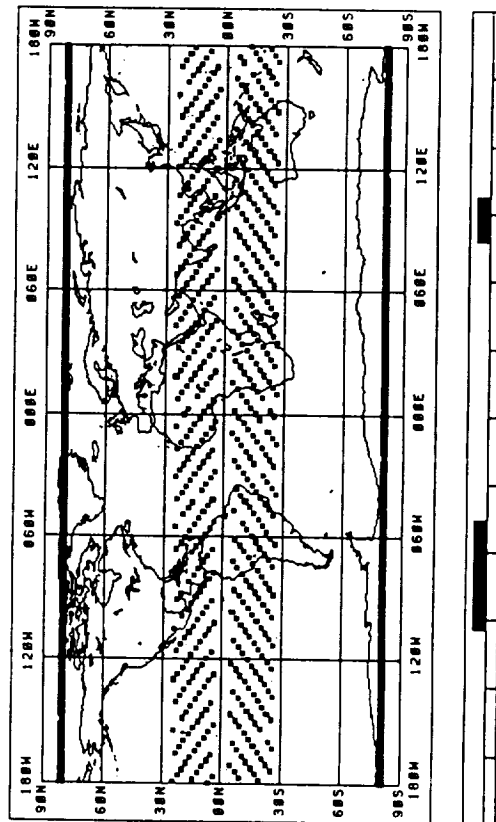


Figure 4: Case 2 Coincidences During 2007

Instrument Track Coincident Earth Ulcus
 Problem Set: cd318-10 System: CD318
 Date/time: Start: 01JAN2010 0000000 Stop: 01JAN2011 0000000
 Coincident measurement for alt bol w/raan=310 (2810)

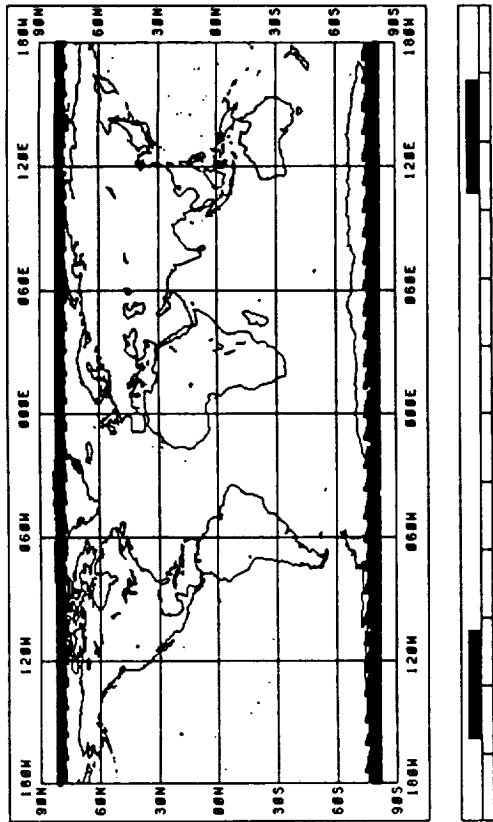


Figure 7: Case 2 Coincidences During 2010

Position Vector Dot Product
 Problem Set: AMPM2 System: AMPM2
 Date/time: Start: 01JAN2002 0000000 Stop: 01JAN2007 0000000
 coincident measurement for PM w/AM

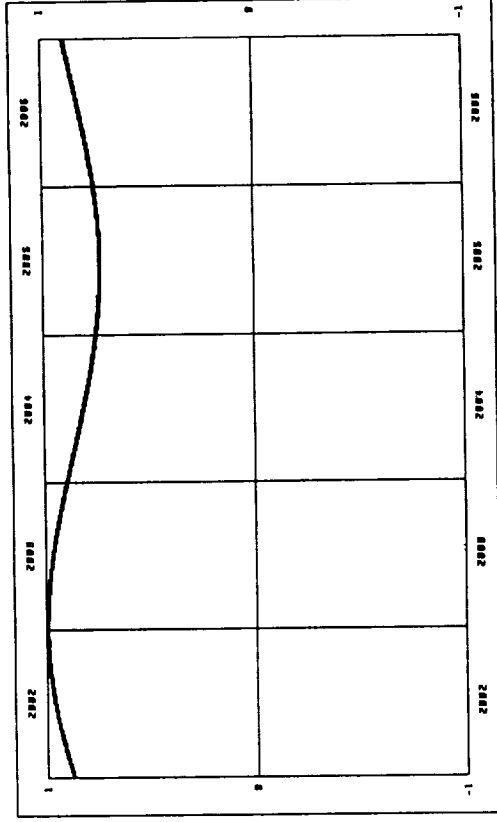


Figure 9: Position Vector Dot Products for EOS-AM and EOS-PM

Instrument Track Coincident Earth Ulcus
 Problem Set: cd318-09 System: CD318
 Date/time: Start: 01JAN2009 0000000 Stop: 01JAN2010 0000000
 Coincident measurement for alt bol w/raan=310 (2809)

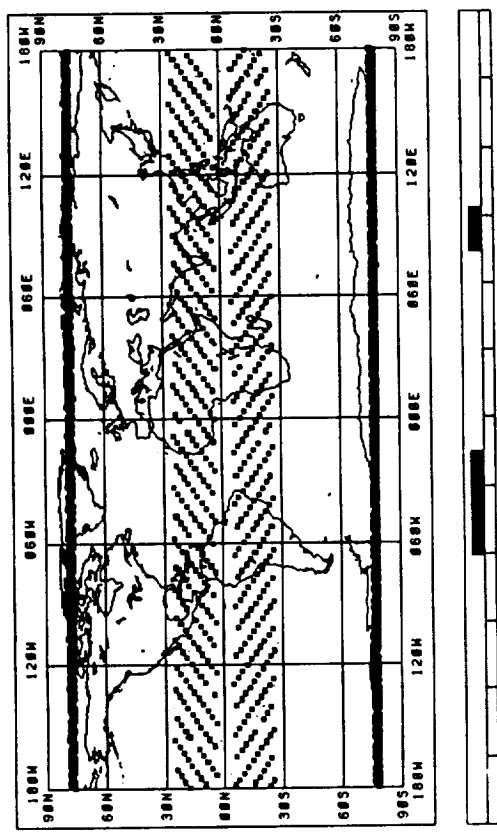


Figure 6: Case 2 Coincidences During 2009

Instrument Track Coincident Earth Ulcus
 Problem Set: cd318-11 System: CD318
 Date/time: Start: 01JAN2011 0000000 Stop: 01JAN2012 0000000
 Coincident measurement for alt bol w/raan=310 (2811)

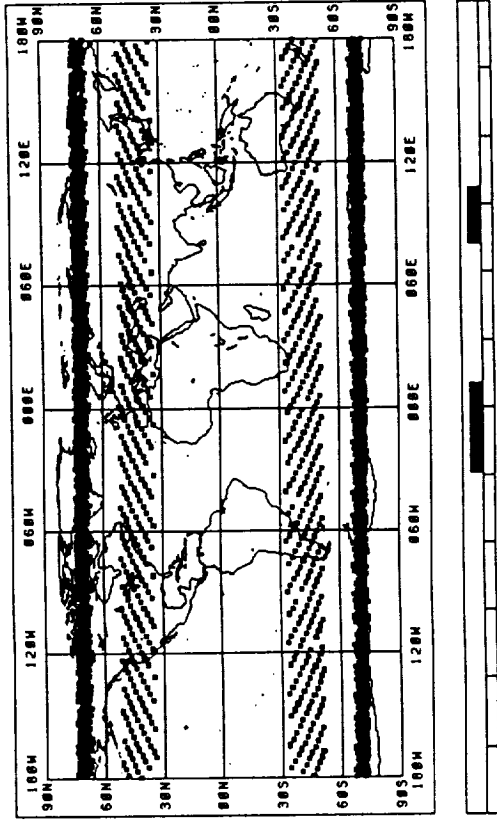


Figure 8: Case 2 Coincidences During 2011

Instrument Track Coincident Earth Uicvus
 Problem Set: astrum System: AMTRMM
 Date/time: Start: 01JAM1990 8606000 Stop: 01JAM1993 8606000
 coincident measurement for TRMM with AM

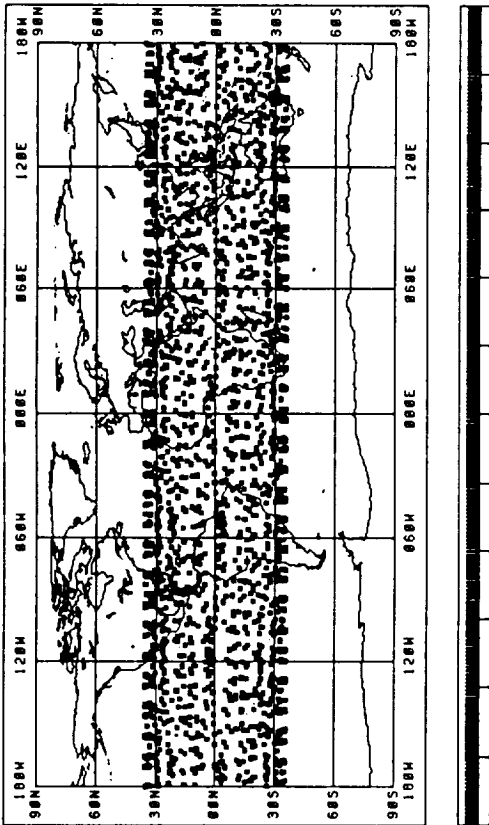


Figure 10: Case 1 Coincidences During 1998

Nadir Local Solar Time vs. Latitude
 Date: 01OCT2008 for 6 days Every 1.0 days System: CD310
 Sun right ascension: 187.51 Declination: -3.24

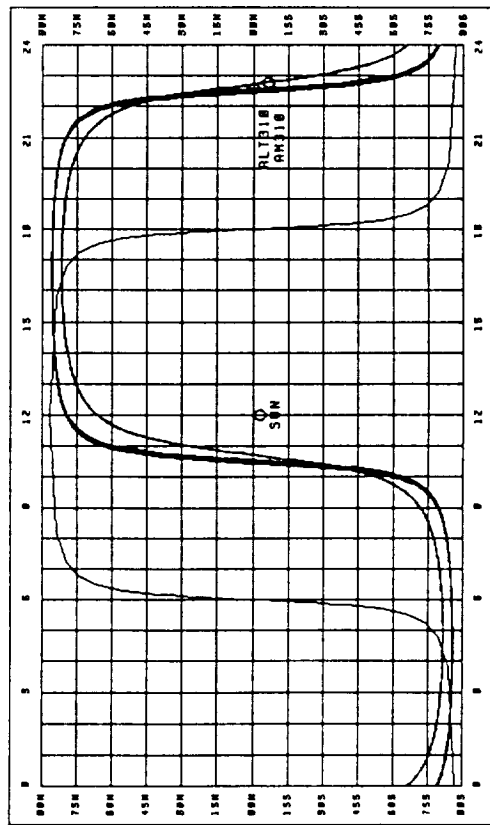


Figure 12: Nadir Local Solar Time Versus Latitude During 2008 (Case 2)

Nadir Local Solar Time vs. Latitude
 Date: 01JAM1990 for 6 days Every 1.0 days System: AMTRMM
 Sun right ascension: 281.26 Declination: -23.84

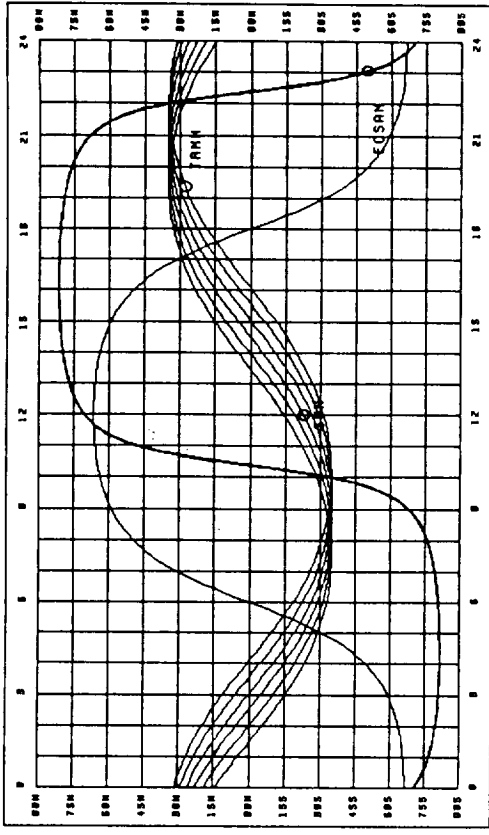


Figure 11: Nadir Local Solar Time Versus Latitude (Case 1)

Nadir Local Solar Time vs. Latitude
 Date: 01MAR2010 for 6 days Every 1.0 days System: CD310
 Sun right ascension: 341.80 Declination: -7.71

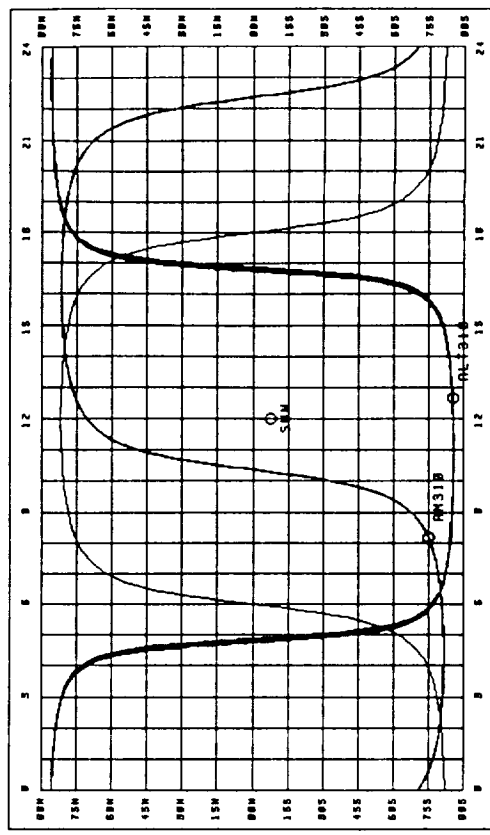


Figure 13: Nadir Local Solar Time Versus Latitude During 2010 (Case 2)

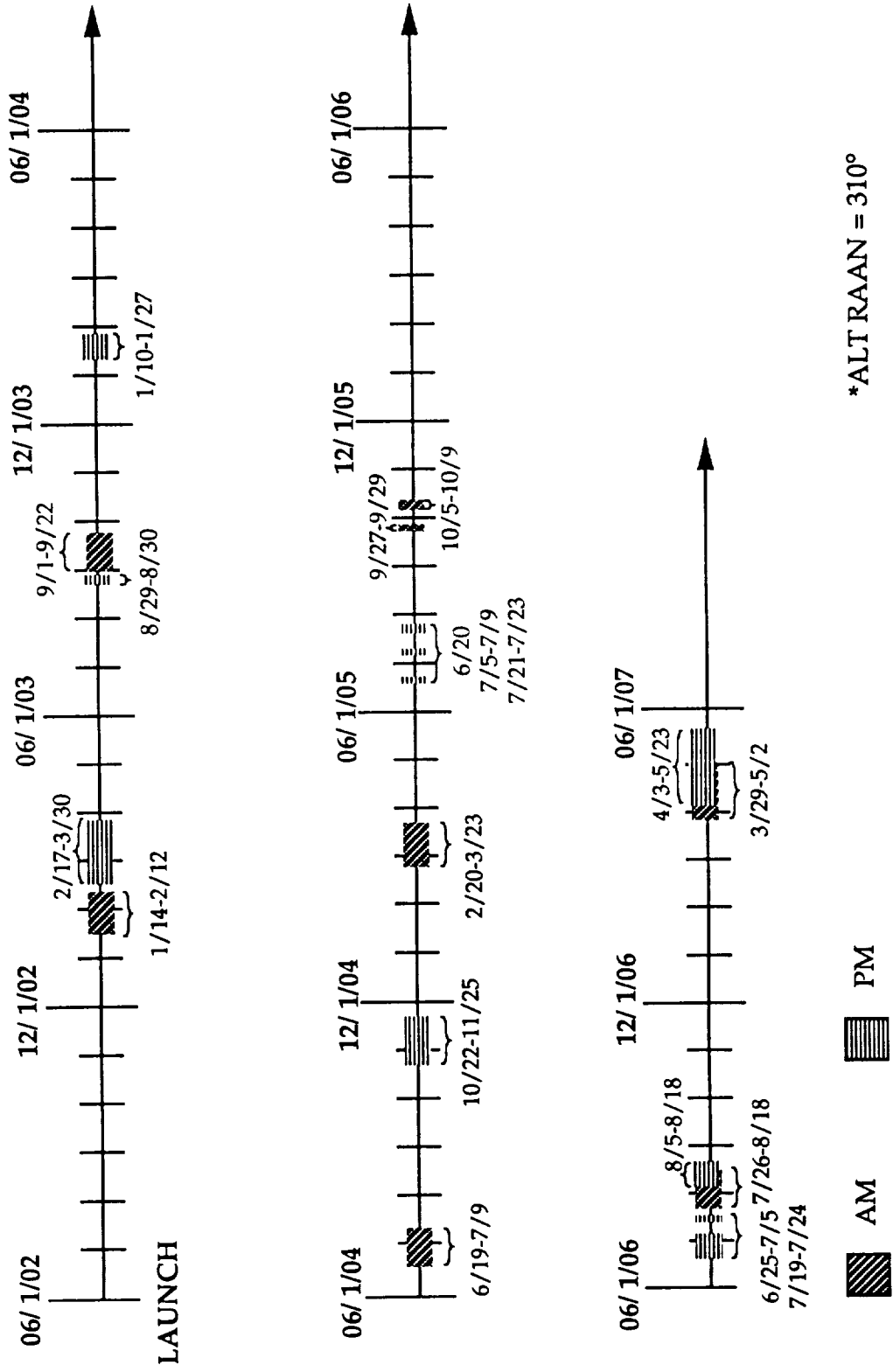


Figure 14: EOS-ALT Coincidences with EOS-AM and EOS-PM

Instrument Track Coincident Earth Views
 Problem Set: amp-B2 System: AMPH2
 Date/time: Start: 01JAN2002 0000000 Stop: 01JAN2003 0000000
 Coincident measurement for PM w/AM (2002)

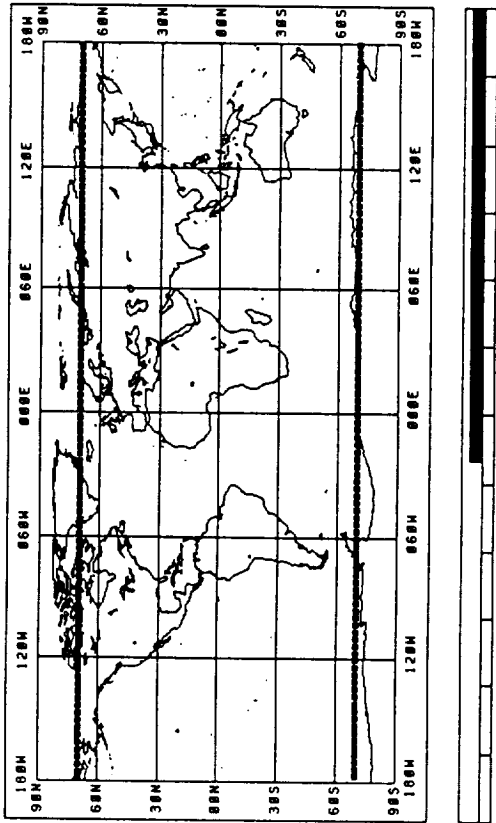


Figure 15: Case 3 Coincidences During 2002

Instrument Track Coincident Earth Views
 Problem Set: amp-B3 System: AMPH2
 Date/time: Start: 01JAN2003 0000000 Stop: 01JAN2004 0000000
 Coincident measurement for PM w/AM (2003)

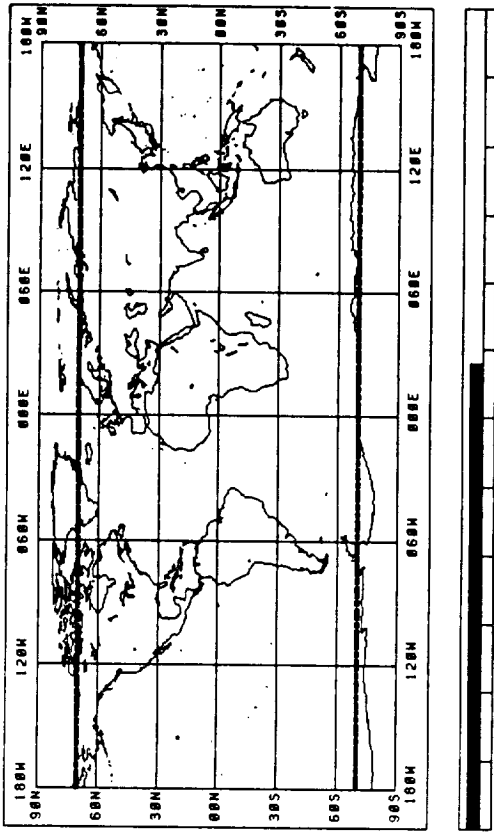


Figure 16: Case 3 Coincidences During 2003

Nadir Local Solar Time vs. Latitude
 Date: 01JAN2003 for 6 days Every 1.0 days System: AMPH2
 Sun right ascension: 281.83 Declination: -23.85

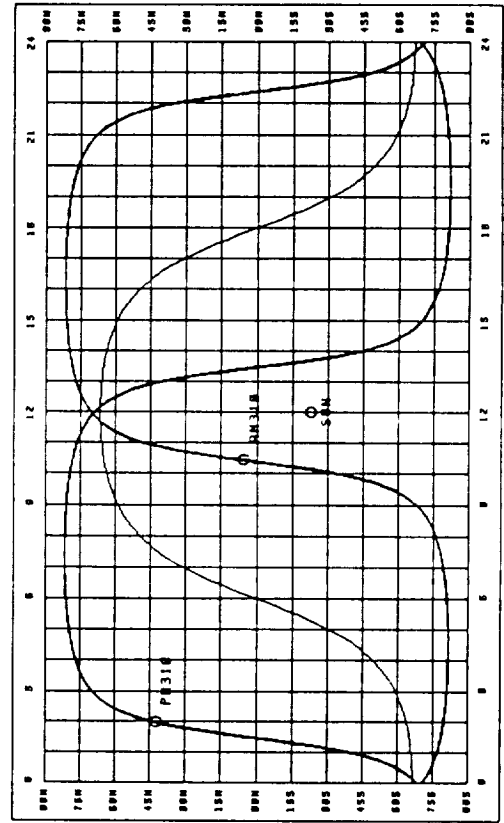


Figure 17: Nadir Local Solar Time Versus Latitude (Case 3)

Automated Maneuver Planning Using a Fuzzy Logic Algorithm*

D. Conway and R. Sperling
Computer Sciences Corporation (CSC)
Lanham-Seabrook, Maryland, USA

D. Folta, K. Richon, and R. DeFazio
National Aeronautics and Space Administration (NASA)
Goddard Space Flight Center (GSFC)
Greenbelt, Maryland, USA

Abstract

Spacecraft orbital control requires intensive interaction between the analyst and the system used to model the spacecraft trajectory. For orbits with tight mission constraints and a large number of maneuvers, this interaction is difficult or expensive to accomplish in a timely manner. Some automation of maneuver planning can reduce these difficulties for maneuver-intensive missions. One approach to this automation is to use fuzzy logic in the control mechanism. Such a prototype system currently under development is discussed.

The Tropical Rainfall Measurement Mission (TRMM) is one of several missions that could benefit from automated maneuver planning. TRMM is scheduled for launch in August 1997. The spacecraft is to be maintained in a 350-km circular orbit throughout the 3-year lifetime of the mission, with very small variations in this orbit allowed. Since solar maximum will occur as early as 1999, the solar activity during the TRMM mission will be increasing. The increasing solar activity will result in orbital maneuvers being performed as often as every other day. The results of automated maneuver planning for the TRMM mission will be presented to demonstrate the prototype of the fuzzy logic tool.

Introduction

Near-Earth missions flown during periods of high solar activity perform frequent maneuvers to overcome atmospheric drag. Missions mapping the Earth perform frequent maneuvers to maintain a precise groundtrack. Missions involving multiple spacecraft maneuver frequently to maintain the spacecraft formation over long periods of time. All of these missions contain a common control problem: for the spacecraft to maintain a precise orbit, frequent maneuvers must be planned and executed.

Maneuver plans are created well in advance of the maneuvers to facilitate fabrication of spacecraft commands and communications scheduling. As the time between maneuvers shrinks, the frequency of the planning function increases, and total costs rise. Automating maneuver planning can reduce these costs. If the constraints applied to a mission are simple and do not conflict, the control process is straightforward and can be implemented using simple checks on orbital parameters. As the complexity of the problem rises, this technique becomes intractable, and conflicting constraints become difficult to resolve. For such cases, bivalent logic employed for maneuver planning behaves poorly because the domain of the solution space shrinks quickly.¹ Multivalent logic systems overcome this difficulty by triggering appropriate actions as specified combinations of conditions are met.

An example of a mission that can benefit from maneuver automation is the Tropical Rainfall Measurement Mission (TRMM). TRMM is scheduled for launch in August 1997. The spacecraft must remain at a mean geodetic altitude of 350 km throughout its 3-year lifetime. Only very small variations in this orbit are allowed.

*This work was supported by the National Aeronautics and Space Administration (NASA)/Goddard Space Flight Center (GSFC), Greenbelt, Maryland, under Contract NAS 5-31500.

Since a solar maximum will occur as early as 1999, increasing solar activity during the TRMM mission will require frequent maneuvers. Figure 1 shows the evolution of the maneuver timing for the TRMM mission. Maneuvers will be performed nearly every other day during periods of high solar activity. Since station contacts and data collection must be planned 5 weeks ahead, TRMM is an ideal mission to test multivalent logic systems for automated maneuver planning.

Multivalent Logic Systems

Bivalent logic was introduced by the Greek philosopher Aristotle. Any statement in Aristotelian logic is either true or false. A system composed of such statements is simple to manipulate. Problems arise in Aristotelian logic systems when certain types of statements are combined: the resulting conclusions can be contradictory. The most common example where neither case can be true is the speaker who states "I am lying." If the speaker is lying, then the statement must be a lie. But if the statement is a lie, then the speaker must be telling the truth. Mathematical deduction can produce similar contradictions. Mathematicians began examining techniques for resolving this type of inconsistency in set theory in the early 1900s.² One of the resulting branches of mathematics is propositional calculus. It provides the basis for logic systems that allow for more flexibility than is available with bivalent (true/false) logic systems. An example of such a multivalent logic system is fuzzy set theory, often referred to as fuzzy logic.

Fuzzy logic was introduced in 1965 as a generalization of conventional set theory.³ It provides a mathematical structure for representing indeterminate results. In this paper, fuzzy logic is examined as a technique to automate maneuver planning for spacecraft missions. We begin by outlining fuzzy set theory and its application to control problems and discuss using fuzzy logic to automate frequent maneuvers. The maneuver constraints that fuzzy logic satisfies for TRMM are examined, and fuzzy logic is used to plan a sequence of maneuvers for the TRMM mission during a period of high solar activity. After examining this application, the strengths of fuzzy logic for maneuver planning are discussed, and some concluding remarks are offered.

The mathematics behind fuzzy logic are well founded. They provide crisp, reproducible results for a given application of the theory. The terminology used to describe fuzzy logic can be confusing.⁴ The basic building blocks of the theory are "fuzzy sets." The domain of each set is defined by a parameter in the real world. The "fuzziness" of the theory arises when evaluating values of the parameter. Any parameter value used in classical set theory would be either in the set or out of it. In fuzzy set theory, the set is defined such that parameter values may be partial members of a set. The "degree of membership," a number between 0 and 1, that the value takes determines the way that it is used in the fuzzy logic system. The process used to convert a measured value into a fuzzy set is called "fuzzification." This process takes the measured value and converts it into a fuzzy set. Once all of the fuzzification has been performed, a set of rules is applied to evaluate the consequences of the measured values, producing a fuzzy set. That set is converted into a number used in the real world through a process called "defuzzification." The details of this procedure are described below.

Fuzzification/Evaluation/Defuzzification:

The TRMM altitude constraint is not precise. It can be expressed in terms like "the mean geodetic altitude must be maintained at 350 ± 1.25 km," but the altitude specified is an averaged (mean) parameter and limits the amount of precision available for control. Fuzzy set theory evaluates such nebulous constraints by assigning a membership to each value in the domain of the problem. For example, the TRMM altitude constraint can be represented by the set shown in Figure 2. In this figure, each geodetic height is assigned a unique degree of membership in the set of "acceptable" altitudes. A geodetic height of 349.0 km with a membership 0.9 is more a member of this set than not a member. Similar statements can be made about any height value. Some geodetic heights belong completely in the acceptable altitude set and have a membership of 1.0; others belong only partially to this set and have a membership value between 0.0 and 1.0; still others do not belong at all—their membership value is 0.0.

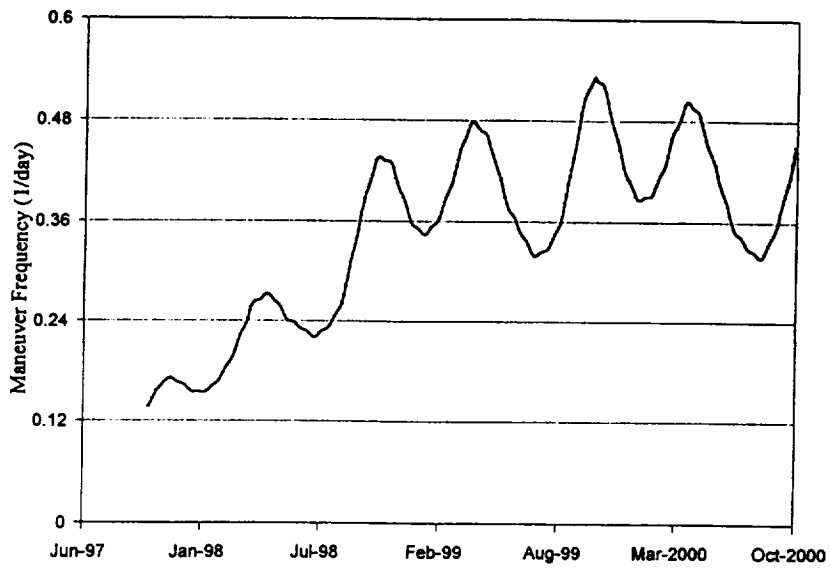


Figure 1. TRMM Maneuver Frequency

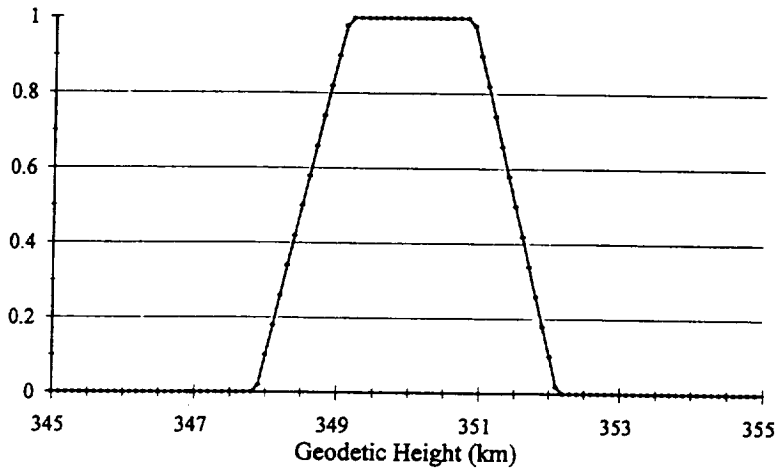


Figure 2. The Geodetic Height Set, H

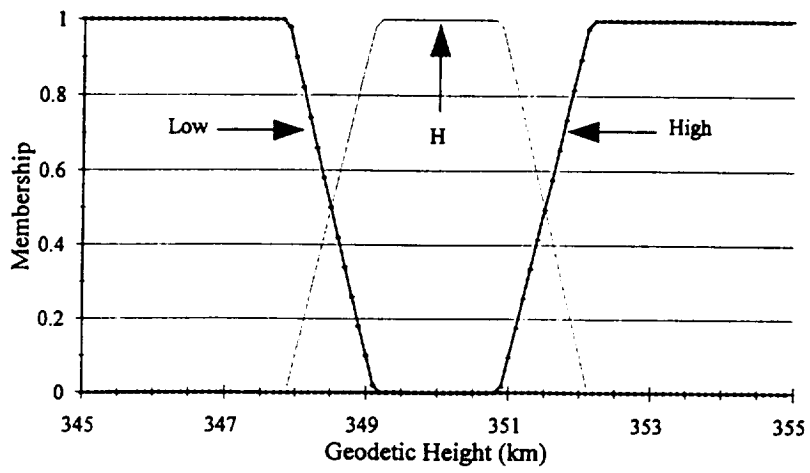


Figure 3. The *High* and *Low* Sets

Sets like the one described are the building blocks of fuzzy set theory. Once the appropriate sets have been constructed for a problem, they are manipulated to produce the desired results. To see how the sets produce the desired results, consider the action taken as the geodetic height decays for TRMM. If the geodetic height is low, a sequence of two maneuvers is performed to increase the apogee height and to circularize the orbit. Two sets describing low and high geodetic height are shown in Figure 3. The spacecraft is maneuvered according to the following rules:

- If the height is low and the apogee height is *not high*, then perform an apogee-raising maneuver.
- If the height is high and the perigee height is *low*, then perform a perigee-raising maneuver.
- If the height is acceptable (that is, in the acceptable geodetic height set—labeled *H* in the figures), then do nothing.

Each rule requires that three steps be taken.⁵ First, each parameter (height, perigee height, or apogee height in this case) is used to transform the appropriate fuzzy set or sets. This is the "fuzzification" step. Second, the resulting fuzzy sets are combined into a single entity for evaluation. This entity is the resultant, fuzzy set *R*. Finally, the set *R* is evaluated to determine what actions should be performed. The last step is "defuzzification."

We will use a satellite at a geodetic height of 348.7 km and an apogee height of 351.8 km to illustrate this process at a specific point in time. The fuzzification that we use is accomplished by determining to what degree the physical parameters are a member of each fuzzy set. These memberships are used to construct a new set that has membership values less than or equal to the membership values of the corresponding physical parameters. In this way, the physical parameters are converted into fuzzy sets. For our example, evaluation of the first phrase listed after the *if* in the first rule, *the height is low*, proceeds as follows. The membership of the height $h = 348.7$ km in the fuzzy set *low* is 0.34. This degree of membership is used to limit the *low* set to a maximum membership value of 0.34, producing the new fuzzy set shown in Figure 4. It is identical to the *low* set, except that the degree of membership has been restricted as discussed here. Similar fuzzification is applied to each antecedent clause in every *if/then* rule.

Points addressed below include evaluating clauses like *not high*. The ability of fuzzy logic to encompass such seemingly ambiguous clauses enhances their adaptability to diverse problems. The *not high* fuzzy set has the appearance one would expect: membership $\mu_{\text{not high}}(h)$ is given by

$$\mu_{\text{not high}}(h) = 1.0 - \mu_{\text{high}}(h) \quad (1)$$

After all antecedent clauses of a rule have been evaluated, the resulting sets are combined to form a fuzzy set for defuzzification. This set is formed from the intersection of all of the sets produced from fuzzification. For example, the final set for the first rule is constructed by taking the intersection of the sets described by *the height is low* and *the apogee height is not high*. Such a construction is illustrated in Figure 5 for a geodetic height of 348.7 km and an apogee height of 351.8 km. The final fuzzy set is shaded for clarity.

"Defuzzification" is performed by evaluating the location in the set of a single value representing the contents of the set.⁶ This evaluation can involve one of several methods. The simplest method is to find the point at which membership in the set has its maximum value. If more than one such point exists, as for the set in Figure 5, the center of the maximal region is taken as the representative value. For the set displayed in the figure, this maximum method yields a height value of 346.900 km. The representative value can also be determined from the centroid of the set. The centroid is defined as

$$R_{\text{centroid}} = \frac{\int r d\mu}{\int d\mu} \approx \frac{\sum r_i \mu(r_i)}{\sum \mu(r_i)} \quad (2)$$

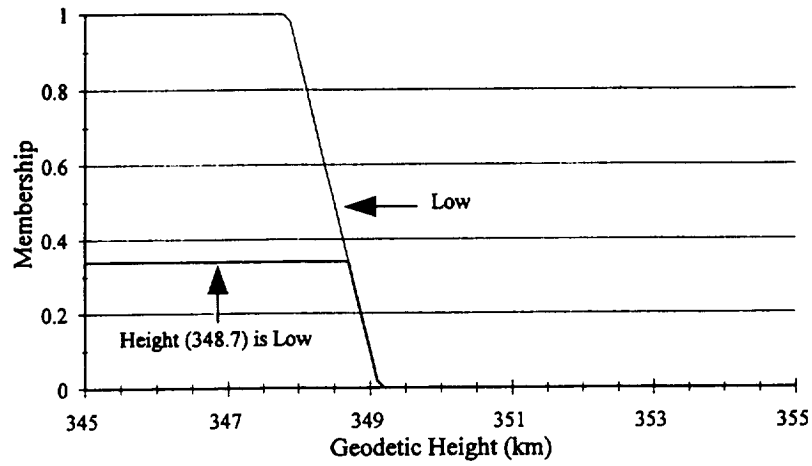


Figure 4. Fuzzification of $H = 348.7$

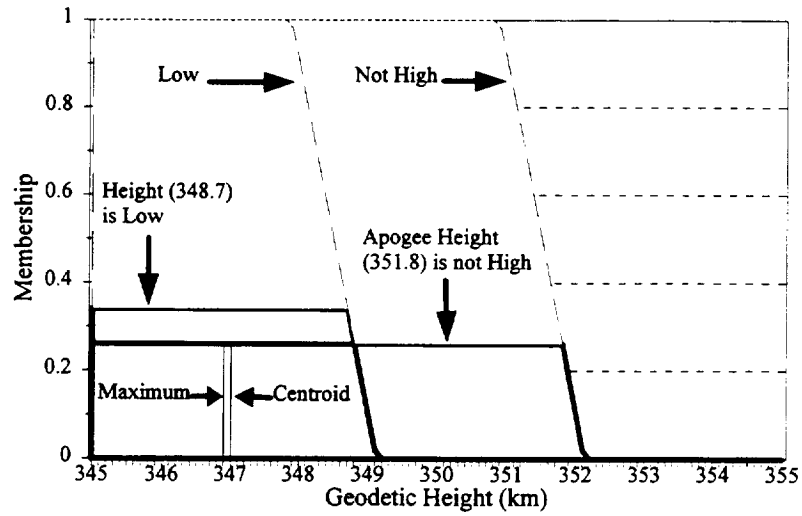


Figure 5. Fuzzified If Clause

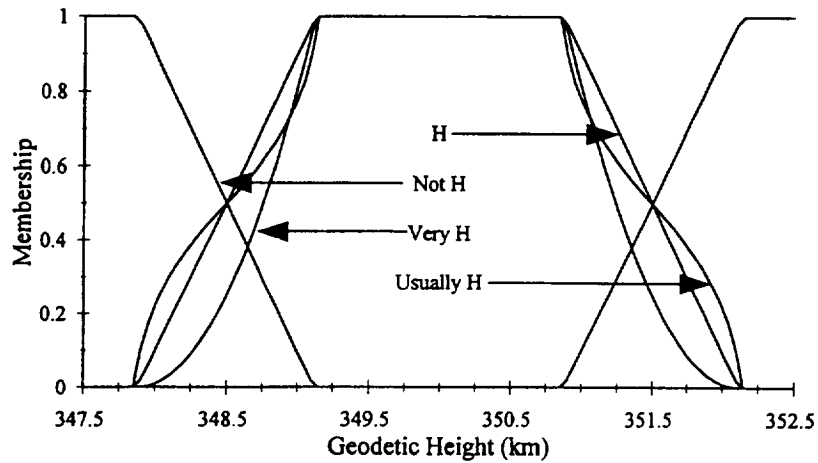


Figure 6. H and Some Hedges

The centroid of the set displayed in Figure 5 is at a height of 346.959 km. This point is labeled on the figure. Once the representative value has been determined, the degree of membership for that value is calculated and compared with a user-specified "threshold" value. The threshold value is chosen as the degree of membership required to trigger the consequence of the rule. If the membership is greater than or equal to the threshold value, the consequence of the rule is executed. For the set in Figure 5, the membership value both at the centroid and at the maximum is 0.26. If the firing threshold is set to 0.25, the consequence of the first rule (an apogee-raising maneuver) is executed; otherwise, it is not.

The procedure outlined above exemplifies the behavior of our fuzzy logic engine. Other methods of evaluation and defuzzification can be implemented for various types of problems. The method outlined here was chosen because it is simple and directly applicable to spacecraft control. The largest drawback to this approach is that it has no provision for a consequent action that contains variable parameters—for example, the spacecraft engines considered here are either on or off with no throttling. Variable throttling can be controlled with a fuzzy logic system.⁷

Although the fuzzy sets described above are simple, they are sufficient for spacecraft stationkeeping and orbit maintenance. Rather than design complicated fuzzy sets, we use simple sets that can be shaped to match our problems in a natural manner with linguistic hedges. The next section describes the techniques used to shape the sets.

Set Shaping and Hedges:

The fuzzy sets described above are coarse fits to the parameters that control a spacecraft maneuver. Precise control of a spacecraft with fuzzy logic requires that the sets be shaped to emphasize the parameters that control the spacecraft trajectory. Such shaping uses linguistic hedges.⁸

The set displayed in Figure 2 that describes acceptable geodetic height was constructed by piecing together five straight line segments between a height of 345 and 355 km with membership values between 0 and 1. These line segments may not be sufficient for the control problem. They form a rough picture of the region that defines the acceptable mean geodetic height for TRMM.

The control laws are composed of terms like *if the height is very low, then maneuver*. The word *very* modifies the meaning of *low*. It is a linguistic hedge applied to the set that describes low height. Such a hedge is implemented by taking the degree of membership at each value of the height, point by point, and squaring it. The degree of membership of the *very low* set is given by

$$\mu_{\text{very low}}(r) = [\mu_{\text{low}}(r)]^2 \quad (3)$$

This definition decreases the degree of membership of every point with partial membership in the set *low*. A point with membership 0.5 decreases to 0.25. Shaping matches the mathematical construction of the *very low* set to the linguistic meaning of *very low*. Direct mapping from natural language to a mathematical implementation is a key feature of fuzzy logic systems.

Three other types of hedges implemented in our maneuver planning tool, as well as the two hedges defined above, are listed in Table 1. The effects of these hedges are illustrated in Figures 6 and 7. Each hedge shapes the basic fuzzy set (*H* in the figure) to represent the meaning of the word attached to the hedge. The *not* hedge produces the inverse of the set. The *very* hedge sharpens the border of the sets by decreasing the membership of points with partial membership. The *somewhat* hedge broadens the border of the set by increasing the membership of points with partial membership. The *almost* hedge increases the membership of points with membership greater than 0.5 and decreases the membership of all other partial memberships. The *usually* hedge performs the inverse: points with nonzero membership less than 0.5 increase in membership, and those with partial membership greater than 0.5 decrease in membership. By implementing set shaping in this manner, the fuzzy logic system provides a direct

mapping from the linguistic description of the problem to the mathematics of the sets. This direct mapping makes the system easy to understand and use.

Table 1. Some Basic Hedges

Hedge	Formula
Not	$\mu_{\text{not}}(r) = 1.0 - \mu(r)$ (1)
Very	$\mu_{\text{very}}(r) = [\mu(r)]^2$ (3)
Somewhat	$\mu_{\text{somewhat}}(r) = \sqrt{\mu(r)}$ (4)
Almost	$\mu_{\text{almost}}(r) = \begin{cases} 2 \cdot [\mu(r)]^2 & \text{for } \mu(r) \leq 0.5 \\ 1.0 - 2 \cdot [1.0 - \mu(r)]^2 & \text{for } \mu(r) > 0.5 \end{cases}$ (5)
Usually	$\mu_{\text{usually}}(r) = \begin{cases} \sqrt{\mu(r)/2} & \text{for } \mu(r) \leq 0.5 \\ 1.0 - \sqrt{[1.0 - \mu(r)]/2} & \text{for } \mu(r) > 0.5 \end{cases}$ (6)

The Automated Maneuver Planning Tool

The purpose of maneuver automation is to calculate the timing and magnitude of spacecraft maneuvers from a set of general language rules determined by mission analysis personnel. The tool must calculate all necessary forces, integrate the spacecraft's equations, calculate relevant spacecraft events (orbital elements, shadow entry and exit, distances to appropriate bodies, and other geometric quantities), evaluate the maneuver rules with the fuzzy logic engine described above, compute thruster parameters, and include a user interface that provides access to data and parameters.

The force model implemented for the prototype automated maneuver tool contains a reduced representation of forces. The Sun, Earth, and Moon are treated as point masses. Oblateness of the Earth is included by using the J_2 through J_5 terms of the zonal expansion of the gravitational potential. Atmospheric drag is calculated from the Harris-Priester analytic drag model.⁹ The evolution of the spacecraft's orbit is calculated with a ninth-order Runge-Kutta numerical integration scheme with an adaptive stepsize control derived by Verner.¹⁰

The fuzzy logic engine in the prototype tool works as described above. The user describes the sets as ASCII data and saves them to disk. The tool reads these sets and shapes them with the hedges described above. Each set has one or more events associated with it. Each event is fuzzified using the technique described above. Once every event in a given rule is fuzzified, the range of each set is scaled to fit the closed interval [0, 1]. This step simplifies processing the rules. The intersection of the sets is found, and defuzzification proceeds as described above. The firing threshold is usually set to 0.30. When defuzzification detects that a maneuver should be performed, an impulsive maneuver is executed. These maneuvers are calculated by interpolation of the appropriate delta-V data.

Applications to TRMM

The principal constraint on the TRMM orbit is specified in terms of the spacecraft's geodetic altitude: the spacecraft must maintain a mean geodetic altitude of 350 km, with variations of no more than 1.25 km. Since the orbit is inclined 35 degrees to the equatorial plane, the oblateness of the Earth results in geodetic height variations of about 7 km for a circular orbit. The calculation of orbital elements for use in the control system is further complicated by the effects of perturbations in the gravitational potential of the Earth which arise from oblateness and non-uniform mass distribution. When the oblateness of the Earth and its non-uniform mass distribution are included, the osculating orbital elements vary by as much as 6 km around each orbit. The oblateness of the Earth and non-uniform gravitational field cause the geodetic height of the spacecraft to vary 7.5 km about an altitude of 350 km.

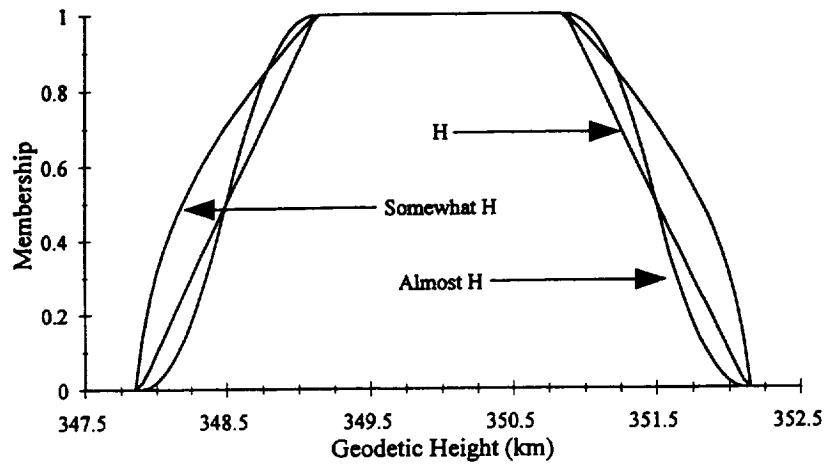


Figure 7. *H* and Some Hedges

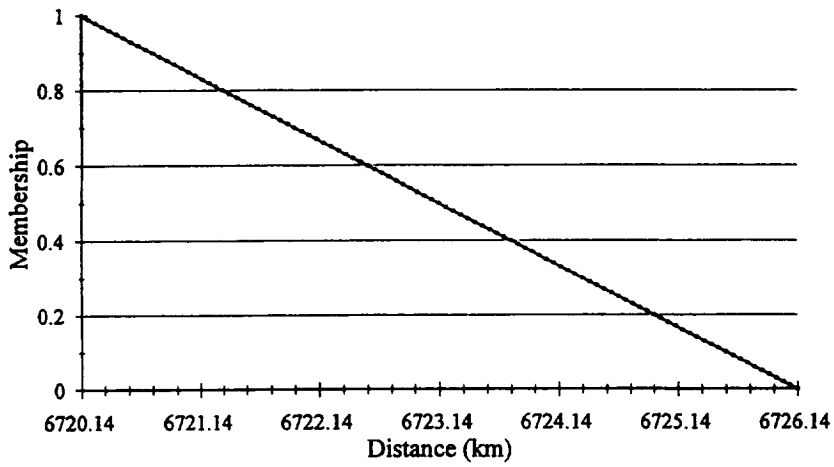


Figure 8. The *Low Set*

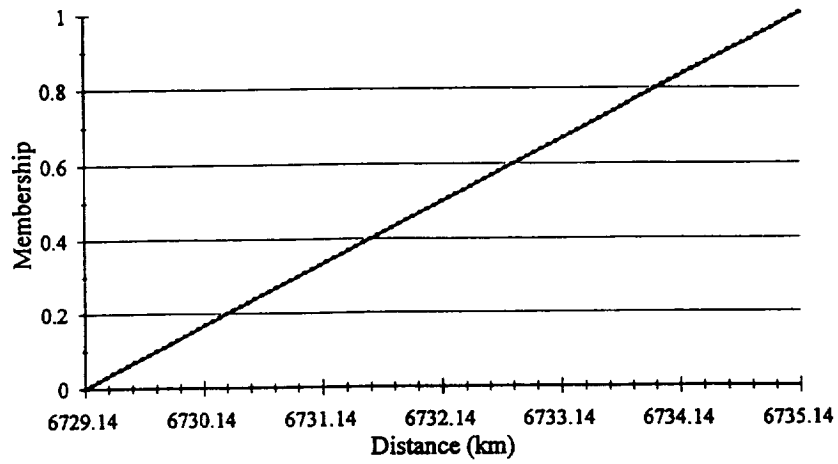


Figure 9. The *High Set*

We demonstrate below that automated maneuver planning can calculate the timing and magnitude of the maneuvers needed to maintain the TRMM mission orbit. We begin by describing the maneuver strategy and designing the appropriate sets required to implement this strategy for a force model that models gravitational effects as point mass effects only. This simplified force model will then be extended to include the effects of the zonal terms J_2 – J_5 in order to demonstrate the refinements that must be made to the control sets to account for the more complicated physics of the extended force model.

A typical TRMM orbital state is given in Table 2. For this analysis, we treat it as the initial state of the spacecraft. The spacecraft mass varies from 3500 kg fully fueled to 2893 kg upon reentry. Since we are interested in the maneuver sequence near the end of the mission, we use a mass of 3000 kg as the initial spacecraft mass. The nominal surface area of the spacecraft is 15 m². The table of coefficients for the analytic Harris-Priester atmospheric model used here represents moderate solar activity. The effects of high solar activity are mimicked by increasing the coefficient of drag.

Table 2. A Sample TRMM Spacecraft State

UTC Epoch: 10/01/1999 00:00:00.000	
Earth-Centered Mean of J2000.0 Earth Equator and Equinox Osculating Keplerian Elements	
Semimajor Axis, a	6724.524 km
Eccentricity, e	0.000228
Inclination, i	35 degrees
Right Ascension of Ascending Node, Ω	0 degrees
Argument of Perigee, ω	90 degrees
True Anomaly, TA	0 degrees

The maneuvers demonstrated here require fuzzy sets that describe low and high distances from the center of the Earth and other fuzzy sets that describe regions near perigee (true anomaly of 0 degrees) and regions near apogee (true anomaly near 180 degrees). The four fuzzy sets representing the control parameters of the problem are shown in Figures 8–11. Note that all of the sets are simple. The *high* and *low* sets were formed by assigning a membership of 1.0 to those points defining the TRMM altitude box. The boundary of the box was spread over a 6-km region. The geodetic heights were added to the mean orbital radius of the Earth (6378.14 km) to produce the endpoints for a straight line defining the set. The *low* set was defined based on a minimum height of 342 km, so that the distance 6720.14 km (6378.14 + 342.00) from the center of the Earth is the highest point with membership 1 in the set, and the point 6726.14 (6378.14 + 342.00 + 6.00) is the lowest point with membership 0. Similar reasoning was used to construct the *high* set. The *periapsis* and *apoapsis* sets were constructed by placing a sinusoidal function at true anomaly (TA) values of 0 and 180 degrees. The functions were shaped so that their full width at half maximum was 36 degrees. Only one cycle of the function was used to generate each set.

The TRMM orbit control problem is fairly simple: after the spacecraft orbit has decayed to a low altitude, it is boosted to a higher altitude through a pair of maneuvers that approximate a Hohmann transfer. This control is achieved through a pair of statements:

- If the perigee radius is *very very low* and the semimajor axis (A) is *low*, then perform a maneuver to raise the apogee height to the maximum height allowed.
- If the apogee distance is *somewhat high* and the semimajor axis is *somewhat low*, then perform a maneuver to raise the perigee height to the maximum height allowed and make the resulting orbit (approximately) circular.

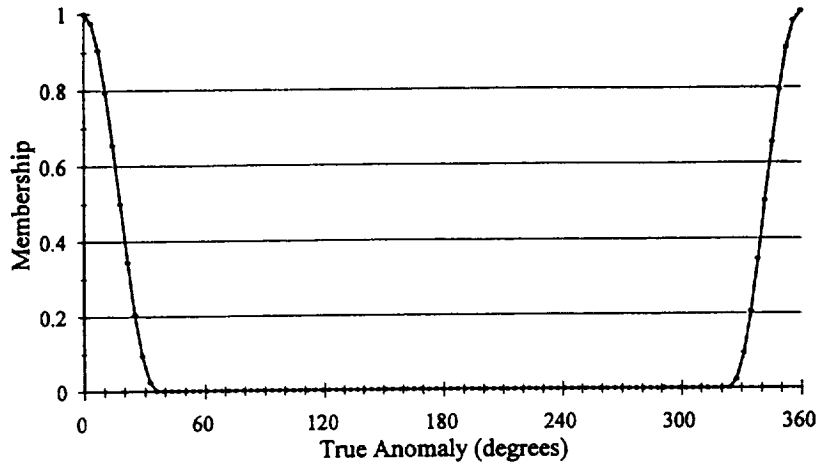


Figure 10. The *Perigee Set*

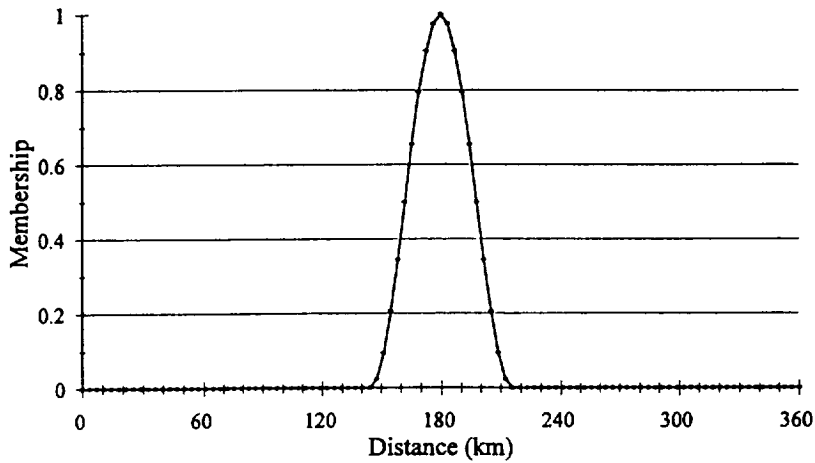


Figure 11. The *Apogee Set*

```

// This is a TRMM mission file propagating
// without the J2-J5 Zonal terms in the force model.
// Here is the command sequence...;

STATE = INITIAL_STATE;
//
// Propagate for two weeks;
WHILE EPOCH < 19991015.000000000;
  PROPAGATE;
  PLOT ELAPSED_DAYS APOGEE PERIGEE RADIUS A;
  PLOT ELAPSED_DAYS HEIGHT;

  IF PERIGEE IS VERY VERY LOW AND
  A IS VERY LOW AND
  TA IS PERLAPSE
  THEN VNB USING APOGEE FROM APOGEE.VNB;

  IF APOGEE IS SOMEWHAT SOMEWHAT HIGH AND
  A IS SOMEWHAT LOW AND
  TA IS APOAPSE
  THEN VNB USING PERIGEE FROM PERIGEE.VNB;

END;
FINAL_STATE = STATE;

```

Figure 12. Command Sequence for the TRMM Mission Without J_2 and Higher Terms in the Potential

The rules that perform this control are shown in Figure 12. Note the similarity of the statement of the orbit sequence (above) to the rules that control the fuzzy logic engine. Only the second rule differs. The statement description begins with the sequence *If the apogee distance is somewhat high. . . .* The corresponding rule begins IF APOGEE IS SOMEWHAT SOMEWHAT HIGH. . . . The second use of the hedge SOMEWHAT in the rule arose from experimentation designed to satisfy the mission constraints. If the second hedge is omitted, the second maneuver is not always performed, because the apogee height occasionally decays below the threshold value for the SOMEWHAT HIGH set before the spacecraft reaches apogee. This defect could be resolved by redefining the *high* fuzzy set. However, this would require regenerating the fuzzy set and retuning the logic engine. Instead, we used the SOMEWHAT hedge to shape the *high* set to match the observed apogee height data. This approach enabled us to experiment with and fine tune the control law without modifying the underlying algorithms or fuzzy sets, thereby demonstrating the simplicity and power of linguistic hedges.

The rules shown in Figure 12 are sufficient to drive the automated maneuver generation for the TRMM spacecraft. When these rules are applied to propagating the spacecraft from the initial state specification given above, under an Earth point mass gravitational force, maneuvers are performed as plotted in Figure 13. The geodetic height of the spacecraft is maintained between 344 and 359 km. The perigee height, semimajor axis, apogee height, and true anomaly of the spacecraft are computed at each propagation step. These parameters are fuzzified as described above and used to determine whether a maneuver is needed. When the defuzzification of the antecedent conditions specified in the *if/then* rule produce a value greater than the specified threshold, the consequent action is taken: in the TRMM case, a maneuver is performed to raise either apogee or perigee. For this analysis, the prototype interpolates the magnitude of the maneuver from a file of previously computed values and applies it impulsively to the spacecraft state.

The problem is more complicated when zonal terms of the Earth's gravitational field are included. The Keplerian orbital elements that act as control parameters oscillate with a magnitude comparable to the size of the box that defines the acceptable spacecraft orbits. Through experimentation, we found that the rules for orbit propagation using point masses can be modified to account for the effects of the zonal terms. These rules are shown in Figure 14. When these rules are executed using the TRMM initial state in Table 2, maneuvers are computed as displayed in the two graphs of Figure 15. The effects of atmospheric drag were exaggerated so that the behavior of the orbital elements could be seen. It was found that the osculating semimajor axis is not a good control parameter for the fuzzy sets defined in this section because at apogee it remains above the highest point in the *low* fuzzy set and never triggers consequences based on *low* semimajor axis values. Instead of using the semimajor axis value to control maneuvers, we use both the apogee and perigee distances to determine when the second maneuver of the Hohmann transfer should be performed. This method of control produces a sequence of maneuvers that maintains the TRMM orbit.

Because the maneuvers needed for TRMM are all nearly identical in nature, the maneuver strategy can be specified as a single set of conditions and consequences. Since the strategy is the same throughout the mission, a fuzzy logic controller can implement it repeatedly to automate maneuver planning tasks.

Strengths of Fuzzy Logic

Fuzzy logic controllers have several features that make them useful tools for maneuver planning automation. As is apparent from the preceding section, fuzzy logic control systems easily implement, in a simple manner, strategies for maneuvers that are nearly repetitive. Fuzzy logic does not require the conditions to be met identically each time for a maneuver to be generated. The fuzzy logic system evaluates the degree to which each constraint is met and triggers a maneuver based on this degree of membership.

A fuzzy logic control system can resolve conflicting constraints. Such a constraint would occur if TRMM maneuvers were to be performed only in sunlight. In such a case, the rules specifying that the first maneuver be performed at perigee must be relaxed. The periapsis and apoapsis fuzzy sets would be redefined to make them

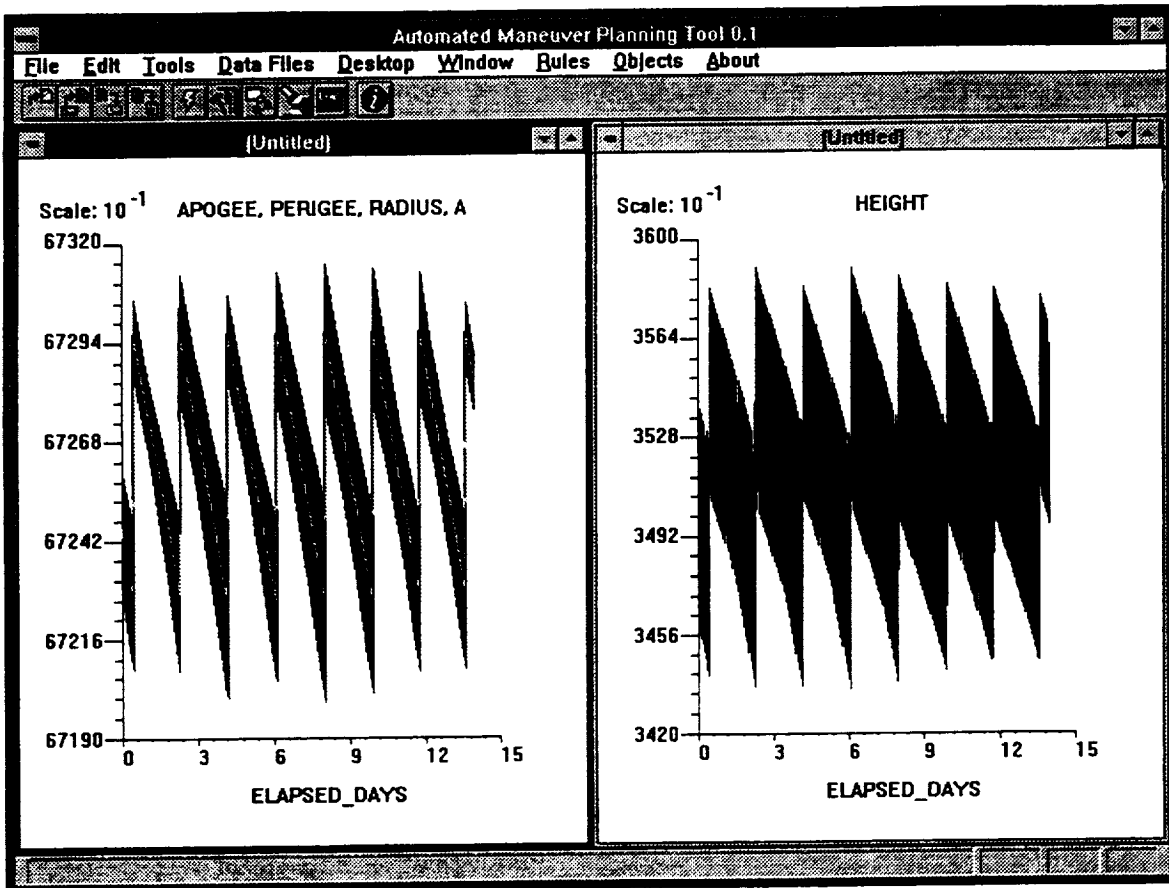


Figure 13. Two Weeks of the TRMM Mission (No Zonal Forces)

```

// This is a sample file for the automated maneuver planning tool. It is used to propagate the TRMM
// state;

STATE = INITIAL_STATE;

WHILE EPOCH < 19991005.000000000;
  PROPAGATE;

  PLOT ELAPSED_HOURS APOGEE PERIGEE RADIUS A;
  PLOT ELAPSED_HOURS HEIGHT;

  IF PERIGEE IS VERY LOW AND
    A IS LOW AND
    TA IS PERIAPSE
  THEN VNB USING A FROM APOGEE.VNB;

  IF APOGEE IS SOMEWHAT SOMEWHAT HIGH AND
    PERIGEE IS NOT VERY HIGH AND
    TA IS SOMEWHAT APOAPSE
  THEN VNB USING PERIGEE FROM PERIGEE.VNB;

  REPORT ELAPSED_HOURS HEIGHT RADIUS TO TRMM.DAT;

END;
FINAL_STATE = STATE;

```

Figure 14. The TRMM Mission Command Sequence for the Full Force Model

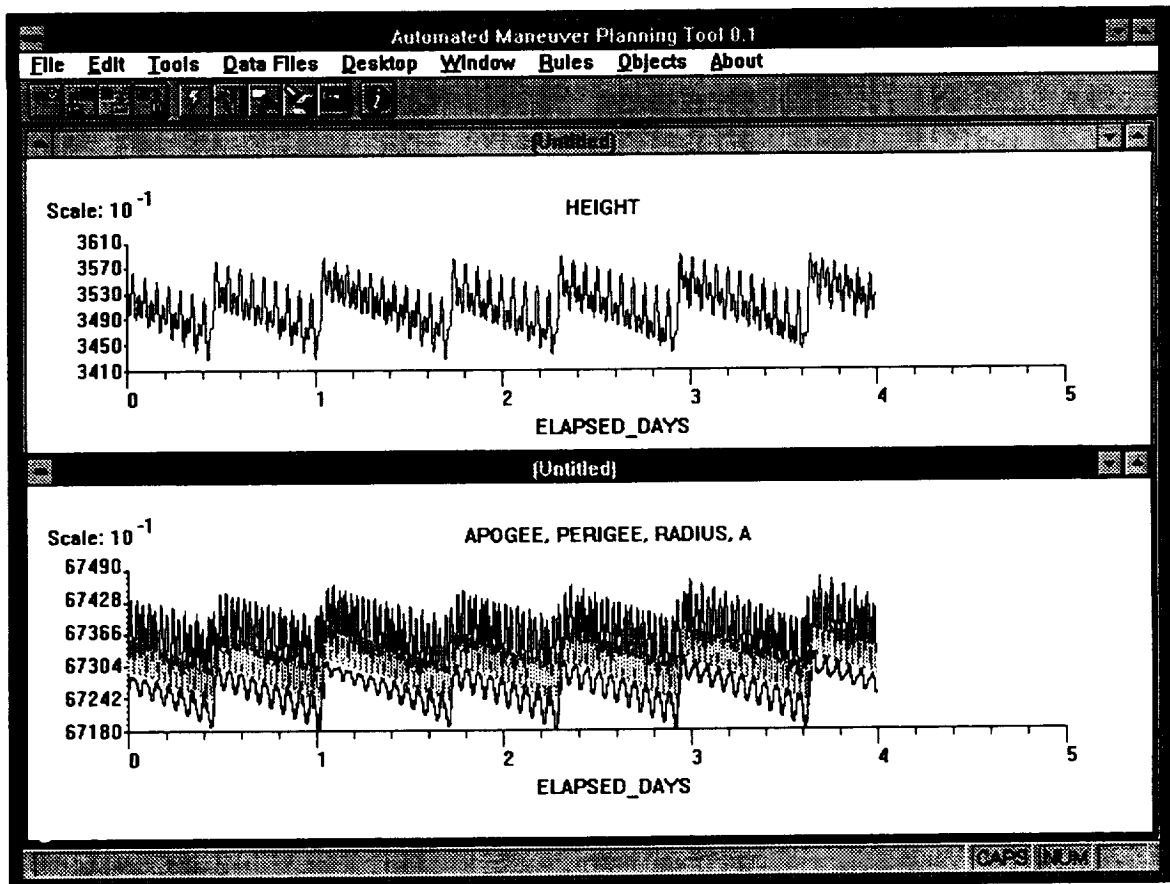


Figure 15. The TRMM Mission With Zonal Forces and Exaggerated Drag

broader than those shown in Figures 10 and 11. A new fuzzy set would be defined to match the Earth's shadow. Finally, the rules triggering the Hohmann transfer would be rewritten as follows:

IF PERIGEE IS VERY LOW AND A IS LOW AND TA IS PERIAPSE AND TA IS NOT SHADOW
 AND TA IS NOT ANTISHADOW
 THEN VNB USING A FROM APOGEE.VNB;

IF APOGEE IS SOMEWHAT SOMEWHAT HIGH AND PERIGEE IS NOT VERY HIGH AND TA IS
 SOMEWHAT APOAPSE AND TA IS NOT SHADOW
 THEN VNB USING PERIGEE FROM PERIGEE.VNB;

Note the use of the set ANTISHADOW. This set is used to keep the first maneuver in a region that allows the second maneuver of the Hohmann transfer (about 180 degrees away from the first) to be performed outside of shadow. This control strategy resolves the conflict between the shadow constraint and the Hohmann constraint on the location of the maneuvers. Similar techniques can be used to construct rules for other conflicting constraints.

Conclusions and Outlook

Fuzzy logic provides a linear mapping between maneuver planning and the way that maneuver strategies are specified. Linguistic variables and hedges make the control logic easy to define, use, and maintain. This ease of use encourages experimentation with the system and the development of innovative approaches to maneuver planning tasks. The resulting maneuver strategies are simple to interpret and tune to meet new mission constraints as mission plans evolve.

References

1. C. C. Lee, *IEEE Transactions on Systems, Man, and Cybernetics*, **20**, 404, 1990
2. H. Rasiowa, "Toward fuzzy logic," in *Fuzzy Logic for the Management of Uncertainty*, L. Zadeh and J. Kacprzyk (eds), New York: J. Wiley and Sons, 1992
3. L. A. Zadeh, *Information and Control*, **8**, 338, 1965
4. S. V. Kartalopoulos, *IEEE Communications Magazine*, **30** (9), 13, 1992
5. G. Viot, *AI Expert*, 26, November 1993
6. E. Cox, , *AI Expert*, 28, March 1992
7. B. Kosko, *Neural Networks and Fuzzy Systems*, Chapter 8, Englewood Cliffs: Prentice Hall, NJ, 1992
8. L. A. Zadeh, *IEEE Transactions on Systems, Man, and Cybernetics*, **SMC-3**, 1, 28, 1973
9. A. C. Long, J. O. Cappellari, Jr., C. E. Velez, and A. J. Fuchs (eds.), *Goddard Trajectory Determination System (GTDS) Mathematical Theory, Revision 1*, Goddard Space Flight Center, Flight Dynamics Division, FDD/552-89/001, prepared by Computer Sciences Corporation, July 1989
10. J. H. Verner, *SIAM Journal of Numerical Analysis*, **15**, 772, 1978

Reduction Procedures for Accurate Analysis of MSX Surveillance Experiment Data

E. Mike Gaposchkin⁺, Mark T. Lane and Rick I. Abbot^{*}

ABSTRACT

Technical challenges of the MSX science instruments require careful characterization and calibration of these sensors for analysis of surveillance experiment data. Procedures for reduction of Resident Space Object (RSO) detections will be presented which include refinement and calibration of the metric and radiometric (and photometric) data and calculation of a precise MSX ephemeris. Examples will be given which support the reduction, and these are taken from ground-test data similar in characteristics to the MSX sensors and from the IRAS satellite RSO detections. Examples to demonstrate the calculation of a precise ephemeris will be provided from satellites in similar orbits which are equipped with S-band transponders.

1.0 INTRODUCTION

The Midcourse Space Experiment (MSX) is scheduled for launch in 1994 and is a space flight program designed, in part, to demonstrate surveillance of the space and Resident Space Object (RSO) background from space (Mill et. al.). The technical challenges include cryogenic technology for cooling the Infrared sensor (SPIRIT III), low noise high performance focal planes, high off-axis stray-light rejection optics, on-orbit signal processing and data compression, and contamination control. The orbit is specified to be 898 km altitude circular at nearly a Sun-synchronous inclination of 99.16 degrees. The lifetime of SPIRIT III is expected to be 21 months, and the visible (SBV) and UV (UVISI) sensors have a planned operation period of 60 months. Primary science data will be stored on board using tape recorders and downlinked via 25 Mbit/s communications, and compressed science data will be downlinked via 1 Mbit/s communications. There will be two S-band transponders on board, which allow the S-Band Ground-Link Stations (SGLS) network to provide tracking data for precise ephemeris determination.

The SBV is the principal space surveillance sensor and uses a 15 cm aperture off-axis, re-imaging, all-reflective telescope, a thermo-electrically cooled, bare CCD focal plane, a signal processor and supporting electronics. The SBV focal plane contains four three side abutable frame transfer CCDs with 420x420, 27 μ m pixels each. The design characteristics are given in Table 1.

Table 1: SBV Characteristics	
Spectral Range	0.3000-0.9000 μ m
Spatial resolution	12.1 arcsec (60 μ rad)
Field of View	1.4° by 6.6°
Aperture, f/no.	15 cm, f/3
FPS size (four CCDs)	420 by 1680 pixels
Frame times	0.4, 0.5, 0.625, 1.0, 1.6, 3.125 sec.
Quantum efficiency	28%

The SPatial Infrared Imaging Telescope (SPIRIT) 3 sensor is the primary instrument on MSX, covering the spectrum from the midwave infrared (MWIR) to the very-longwave infrared (VLWIR). SPIRIT III consists of an off axis re-imaging telescope with a 35-cm diameter unobscured aperture, a six-channel Fourier transform spectrometer, a five-band scanning radiometer, and a cryogenic dewar/heat exchanger.

⁺ Senior Staff Member, MIT Lincoln Laboratory, Lexington, MA 02173 (617)-981-3403

^{*} Staff Members, MIT Lincoln Laboratory, Lexington, MA 02173 (617)-981-0973

This work was sponsored with the support of the Department of the Air Force under Contract F19628-90-C-0002. Review of this material does not imply Department of Defense endorsement of actual accuracy or opinion.

The sensitivity of the spectrometer limits its use for observing RSOs. The radiometer has five Si:As focal plan arrays of 8x192 pixels each, operating between 11 and 12 degrees Kelvin. It collects data in six color bands with a spatial resolution of 90 μ radians. The scan mirror can remain fixed or can operate at a constant 0.46 degree/sec scan rate with programmable scan fields of 1x0.75, 1x1.15 and 1x3.0 degrees. The radiometer focal plane assembly uses a combination of dichroic and bandpass filters to allow simultaneous measurements in bands A, D and E, and in band B and C. The band B focal plane is divided horizontally into two equal sections, each with a slightly different bandpass. Table 2 lists the half-power bandpass, number of active columns, and projected sensitivity for each array. Similar to the SBV, there will be an Onboard Signal and Data Processor (OSDP) for clutter rejection and data compression.

Radiometer Bands	Band A	Band B1 Band B2	Band C	Band D	Band E
Passband (μ m)	6.0-10.9	4.22-4.36 4.24-4.45	11.1-13.2	13.5-16.0	18.1-26.0
Active Columns	8	2	4	4	4
Sensitivity (NEFD) (10^{-18} W/cm ²)	1.1	10	0.8	0.7	1.7

The Ultraviolet/Visible Imaging and Spectrographic Imaging (UVISI) sensor system consists of five spectrographic imagers (SPIMS) and four imagers. Together the SPIMS cover a spectral range from far ultraviolet (110nm) to near infrared (900nm). The imagers include wide field-of-view (WFOV) and narrow-field-of-view (NFOV) sensors in the visible and ultraviolet. Surveillance investigations will concentrate on the NFOV imagers. The commandable filter wheel in each imager houses three bandpass filters and a neutral density filter, in addition to an "open" and "closed" position. The UVISI imager characteristics are given in Table 3.

Instrument	UV NFOV	Vis NFOV
FOV (deg)	1.28x1.59	1.28x1.59
Resolution (μ rad)	90	90
Passbands (nm)		
open	180-300	300-900
closed	--	--
ND filter	($\times 10^{-3}$)	($\times 10^{-4}$)
WB1 filter	200-230	305-315
WB2 filter	230-260	350-440
WB3 filter	260-300(polarization)	470-640

This report will focus on the reduction required for accurate analysis of the MSX space surveillance data. Three primary areas are identified: metric calibration, photometric and radiometric calibration, and calculation of the MSX precision ephemeris.

The SBV and SPIRIT III should provide metric measurements in the FK5 reference frame accurate to 15-20 micro-radians (3-4 arcseconds), and calibration will involve reference RSOs with well-known orbits (such as Lageos and EGP) and calibration of the sensor boresite, MSX fiducial reference frame, and sensor alignments. The UVISI sensors are not expected to provide high quality metric data.

The MSX sensors are designed to provide high quality radiometric data. The band-to-band ratios for calibrated SPIRIT III irradiance measurements are expected to be accurate to 5%. Radiometric calibration will involve RSO and stellar reference sources and multi-spectral comparisons from the different sensors.

The reduction of SGLS tracking data should provide an MSX orbit which is accurate to 15 meters. Obtaining this accuracy is difficult, however, and involves calibration of the SGLS tracking data, modeling of the MSX attitude and cryogen flow rate effects, and modeling other non-gravitational effects.

2.0 METRIC CALIBRATION

The SBV and SPIRIT III sensors should be able to provide good quality metric data. It is expected that the SBV metric data will be accurate to 4 arcseconds or better and that the SPIRIT III will be only slightly worse. This section will first describe the reduction that is required to produce the most accurate metric observations, and then techniques of calibrating the data will be presented involving the use of precise orbits of calibration RSOs. Test data similar to the SBV will be shown as examples of the reduction procedures and the means by which these data are calibrated.

2.1 Reduction of SBV Metric Data

The SBV involves highly distorted optics (which are not defraction limited) due to a design which attempts to maximize the rejection of stray light from the focal plane. The size of each pixel is approximately 13 arcseconds (60 micro-radians), and it is reasonable to try to sub-divide a pixel by a factor of 3-4 (or 4 arcseconds) using light which spills into neighboring pixels. SBV is a self-calibrating instrument, since it will be able to detect stars down to 15th visual magnitude. Therefore, a precise inertial location of the boresite and attitude map can be determined for the SBV at any instance by matching star detections to a star catalog and fitting attitude model parameters to the star map. Then, once an attitude model is updated for the SBV, the model can be inverted to focal plane locations for an RSO detection to produce right ascension and declination measurements. A metric error budget for the SBV involves accuracy of the reference star positions and number of stars observed, centroid error from the observed stars in SBV focal plane coordinates, (streak) endpoint error from the observed RSO detections in SBV focal plane coordinates, and model error from the SBV distortion map.

Any catalog of reference stars can be used for SBV metric reduction, and we have chosen several. Each reference star is to be anchored to the FK5 inertial reference frame, and therefore stars which do not come in that frame must be carefully transformed. This is adequately detailed in (Smith et. al.). The catalogs which are currently implemented in the reduction software for the SBV are the SAO catalog, the Astrographic all-sky star catalog, the Guide Star catalog, and the Landolt Special Area Fields catalog (see Landolt). The Landolt catalog positions are not intended for metric use, but the color information is useful for photometric calibration of the SBV. Stars in the reference catalogs typically have position accuracy of 0.5 - 2 arcseconds, and the use of dense catalogs often allows more than 100 observed stars from the SBV to be matched. Both annual and diurnal aberration are applied to transform mean to apparent place for each reference star, because diurnal aberration can produce an effect on the order of 5 arcseconds due to the velocity of the MSX about the Earth. The parametric model for the SBV attitude and distortion involves 37 coefficients.

The SBV will have a signal processor on board the MSX, which will detect linear streaks moving from frame-to-frame across the focal plane and stationary light sources. If the SBV is commanded to observe in a Sidereal mode, then the stars in the background will be stationary and streaks may represent RSO targets. If the SBV is commanded to track a particular RSO, so that the RSO is stationary in the SBV focal plane, then stars will be seen as streaking across the focal plane. Because the SBV optics are not defraction limited, a stationary point source will spill into neighboring pixels and a streak will actually appear as a swath of pixels between 3 and 5 pixels wide. This works to our advantage, however, since centroiding will allow the reduction software to sub-divide a pixel by a factor of three or four. Based on ground calibration of the SBV sensor, it is estimated that centroid error is less than 0.2 pixels (or 2.6 arcseconds).

The direct map between inertial coordinates and pixel coordinates on a particular CCD in the SBV focal plane is accomplished by a series of coordinate frame rotations about angles which characterize the

SBV attitude. If \mathbf{v} denotes an inertial unit vector and \mathbf{w} a unit vector of direction cosines on the focal plane, the direct map is described mathematically as

$$\mathbf{w} = R_1(-\mu)R_2(\xi)R_3(\Psi+90)R_2(90-\delta_0)R_3(\alpha_0)\mathbf{v},$$

where R_k denotes the rotation about the axis $k=1,2,3$ by the indicated angle, α_0 denotes the SBV boresite right ascension, δ_0 the boresite declination, Ψ the SBV roll angle, and μ and ξ denote off-axis angles which are designed to move the boresite vector from the center of the SBV focal plane to the center of a particular CCD. Once \mathbf{w} is calculated, direction cosines are input to the distortion map so as to convert (linear) direction cosines to CCD pixel coordinates.

The distortion map is expressed by a low-order polynomial in two direction cosine variables, U_z and U_y , involving 32 coefficients. The map can be described mathematically by

$$X_c = \sum_{m=0}^{15} a_m U_z^{p(m)} U_y^{q(m)}$$

and

$$Y_c = \sum_{m=0}^{15} b_m U_z^{p(m)} U_y^{q(m)}$$

where mathematical expressions for $p(m)$ and $q(m)$ are

$$p(m) = [m / 4]$$

and

$$q(m) = m - 4 p(m)$$

with $[k]$ being the integer portion of the number k . Initial calibration of the distortion map coefficients has been performed using the SBV optics on the ground, and it is found that this map is accurate to better than 0.15 pixels (or 2 arcseconds). The map described above can be inverted to transform pixel coordinates to inertial space, but the distortion map must be inverted using iterative techniques due to its non-linear nature.

2.2 Reduction of SPIRIT III Metric Data

In general, the SPIRIT III sensor will not be able to see enough stars in order to self-calibrate the pointing and attitude. Therefore, metric calibration will rely on alignment matrices between the SPIRIT III focal plane and an MSX fiducial frame. Alternatively alignment with the SBV focal plane can be used to determine the attitude of the SPIRIT III. The MSX is a rigid-body spacecraft, and there are no gimbaled mirrors. Therefore, pointing a sensor implies that the entire spacecraft must be pointed. The SPIRIT III and SBV sensors are co-aligned, and there exists a star camera on board the MSX which will be used to anchor the MSX fiducial frame. Whenever recognized stars are observed by the SPIRIT III, UVISI, and SBV sensors, then these data will be input to an algorithm to keep track of the alignment between sensors. This information will be steadily maintained throughout the lifetime of the instruments, and knowledge of the pointing for one sensor can be used in conjunction with the alignment information to determine the pointing for the other.

Distortion in the SPIRIT III optics will be modeled in a similar fashion to the SBV, and it is expected for the coefficients to change little from ground-calibration values since the temperature of the sensor will be kept nearly constant. Star data will be used periodically to check and update the SPIRIT III distortion model.

It remains to indicate how precise focal plane measurements of the RSO data are reduced from the SPIRIT III data. This task is performed by an On-Board Signal and Data Processor (or OSDP), which is to be

flown on board the MSX and can also be run on the ground with SPIRIT III raw data. The OSDP is a software and hardware system developed by the Hughes Aerospace Corporation, and involves two separate procedures. The first is known as the Time Dependent Processor, (TDP) which lines up the column data correctly from the SPIRIT III mirror scans (if necessary) and allows hot pixels to be grouped together. The second is known as the Object Dependent Processor (ODP), which detects a group of hot pixels and identifies star and streak data. These object sighting messages are prepared and attitude models are inverted for conversion into an inertial coordinate frame similar to the SBV detections.

2.3 RSO Calibration Orbits

Precision orbits of calibration RSOs are to be used to check the accuracy of the SBV and SPIRIT III metric data and to determine biases for the data. This section will identify RSOs that can be used for this procedure and will describe the independent data sets that are used to calculate the calibration orbits.

Good calibration RSOs are those which have stable orbits which are not difficult to model and which are routinely tracked by a variety of sites so that a dense sampling of tracking data is available. The Lageos calibration spheres are excellent candidates, because they are equipped with laser cube corner reflectors and serve as calibration RSOs for both radar and optical sites around the Globe. The Lageos orbits are stable and are routinely known to within 10 cm. They can also be routinely tracked by MSX sensors since viewing angles can be easily found which do not require tracking too close to the Sun or the Earth's limb. Other RSOs which make good calibration orbits are EGP, Etalon, ERS-1, and GPS. The GPS satellites make good calibration orbits because accurate samples of state vectors accurate to better than 5 m are available at all times.

The objective for calibrating the SBV and SPIRIT III data is to obtain an independent reference orbit for an observed calibration RSO which is accurate to better than 1 arcsecond in sensor right ascension and declination angles. The reference orbit is calculated using a special perturbation orbit determination program which can fit many types of data to the equations of motion using a detailed force model. Then this orbit is compared to the observed data and statistics are calculated from the pass. Biases are included in a historical database and incorporated into the calibration models for the metric data reduction.

The precision orbit determination software which is used for this procedure is known as DYNAMO, and it has a history dating back to the 1960s for use in calibrating sensor data and providing precision reference orbits. The capabilities and qualities of DYNAMO are highlighted in Figure 1.

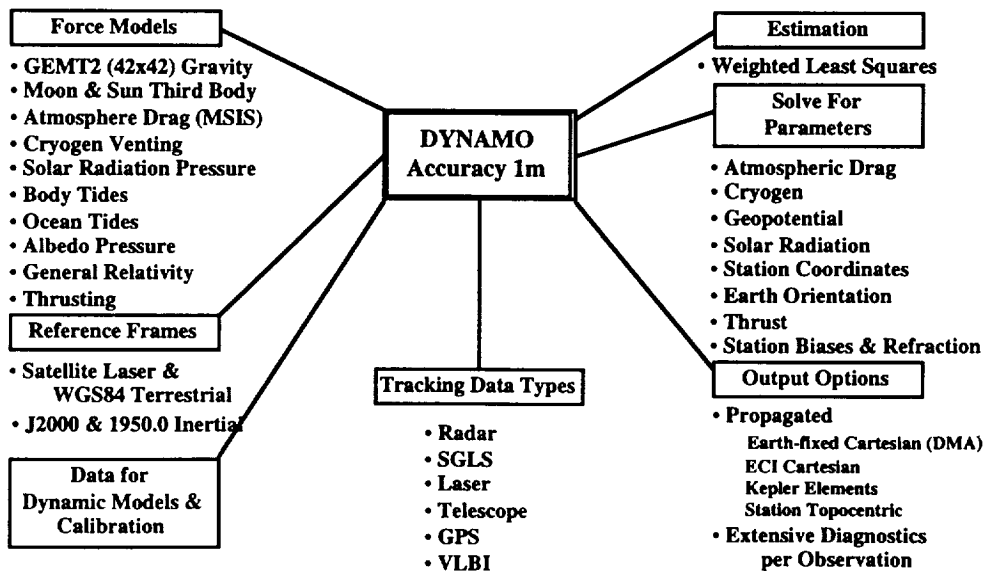


Figure 1: DYNAMO, A Precision Orbit Determination Software Package

2.4 Example of Metric Reduction and Calibration

In this section, an example of the metric reduction and calibration process will be presented. The raw data for this example are selected from a ground-test setup designed to be similar to the SBV. A 6 inch telescope system was attached to the 31 inch optical mount at the Experimental Test Site (ETS), located near Socorro, New Mexico. A 420 x 420 CCD focal plane was used to record the data employing parameters for the integration time and number of frames which are similar to the SBV. In November of 1991, a 32 minute pass of the Lageos I satellite was collected with this system using 29 sets of data with 8-16 frames for each set. The reduction and calibration steps for this set of data will be highlighted in this section, with the final objective being to characterize the accuracy of Lageos I metric observations.

First, the raw data must be passed through the SBV Signal Processor to detect the stationary point sources and streaks. In addition to the streak metric information, a type of signature data must be collected which labels frame and intensity data for each pixel near the best-fit line to the streak. The signature information is used in post-processing to refine the end points and deduce a visual magnitude measurement for each streak detection.

The next step is to match as many of the observed stars as possible to an on-line star catalog and to update attitude parameters for the sensor (boresite vector and focal plane scale). The results are shown in Figure 2, displaying a Bull's-eye plot of the residuals (in the focal plane) of the stellar position data after the fit. This chart shows that the root mean square (rms) of the residuals is close to 1 arcsecond in each direction. Outliers can be traced to saturation, double-star systems, or stars which are on the edge of the field of view.

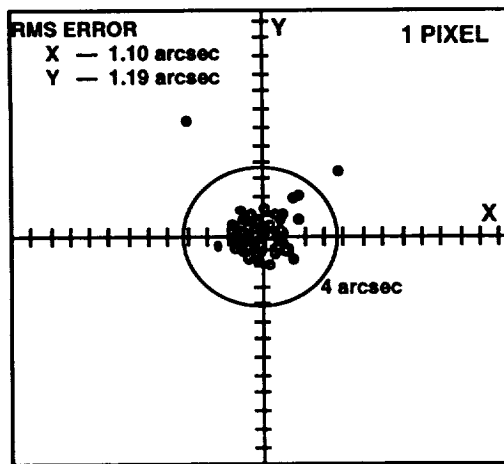


Figure 2: *Bull's-Eye Plot of Residuals (arcseconds) of Matched Star Positions Based on a Least Squares Fit of the Focal Plane Attitude Parameters*

Once an accurate attitude map is available, the end points of the observed streak must be refined using the signature data and the attitude map must be inverted to transform the streak end point measurements in focal plane coordinates to inertial right ascension and declination measurements. In order to characterize these measurements, a precision ephemeris for Lageos I must be determined. This is accomplished using DYNAMO and independent measurements of Lageos I from a time period spanning plus or minus three days about the epoch of the pass. The independent measurements are taken from laser radar and skin tracking from radars and optical sites in the Space Surveillance Network. This suite of observations allows an ephemeris for Lageos I to be determined to better than 10 cm, and this implies that the predicted sensor accuracy from a ground-based site is better than a fraction of an arcsecond. A comparison of the Lageos I observations to the precision ephemeris is shown in Figure 3. There is a strong bias in declination of

2.2 arcseconds, and this could be due to a time discrepancy since the inclination of Lageos I (109 degrees) causes along track orbit error to be manifested as a declination error. The standard deviations in right ascension and declination are larger than the desired 4 arcseconds, and the principal sources of error are not easily identified. Possible error sources include a (slight) shift of the mount from frame to frame and noise in the data.

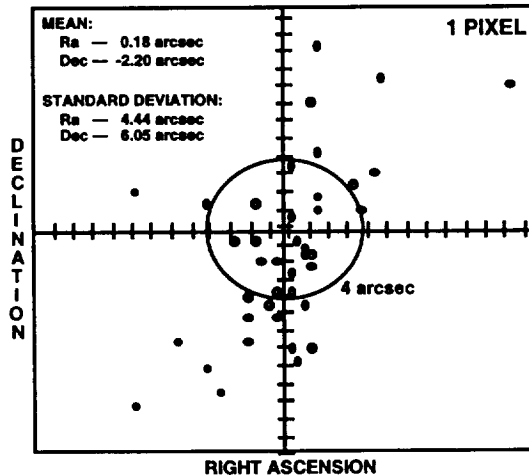


Figure 3: Bulls-Eye Plot of Residuals (arcseconds) of Lageos I Metric Observations as Compared to a DYNAMO Reference Orbit for a 32 Minute Pass.

3.0 RADIOMETRIC CALIBRATION

3.1 Introduction

The SBV, SPIRIT III, and UVISI sensors should be able to produce high quality photometric and radiometric data. Surveillance data will be used with high fidelity models of the reflected and self-emitted radiation from satellites, to develop methods for identifying RSOs, monitoring their status, and determining some of their physical properties. These high fidelity models account for such variables as: solar phase angle, sensor to RSO aspect angle, material properties, and temperature. The discussion here is limited to the methods of data reduction and calibration to be used with each of the MSX sensors, and an assessment of the expected accuracy.

Each of the MSX sensors is unique, and the data reduction and calibration will be different for each one. The MSX program intends to provide data that is certified to be calibrated to within specified limits. To this end, the Data Certification And Technology Transfer (DCATT) Principal Investigator Team is devoted to establishing calibration procedures and standard data reduction software. Even though fundamental differences between the MSX instruments require different calibration and data reduction methods, they do share some common elements. For example, there are three steps in the calibration process. Each instrument will have extensive preflight (or bench) calibration. It is hoped that this preflight calibration will be valid for the on-orbit data. Second, there will be a series of on-orbit observations taken for purposes of calibration. These include internal sources, used in each data set, to obtain corrections for each data set. Finally, some data sets will contain observations of objects with known luminosity, which will provide additional calibration information. These three sources of information will provide the calibration information necessary for photometric and radiometric analysis of MSX data.

3.2 SBV Radiometric Reduction and Calibration

The conversion of raw digital numbers to engineering units for the SBV is done for each pixel. The dark current (a function of temperature) is measured with the SBV cover closed, and is subtracted from the measurement. The responsivity conversion of digital numbers to Watts/cm² in band is done using ground-based calibration data.

The on-orbit calibration phase will be done using calibrated reference stars, primarily the Landolt fields (Landolt). The Landolt star fields have been established as astronomical photometric calibration standards. Since the SBV has a nonstandard and very broad spectral response, the relation between the SBV magnitude and the magnitude of a star must be known. From analysis of the SBV spectral response, the relation between the visual magnitude of a star, M_v , with color, B-V, and the SBV magnitude, M_{SBV} is given by an empirical relation (Beavers)

$$M_{SBV} = M_v + R_1(B-V) + R_2(B-V)^2 + R_3(B-V)^3 .$$

We expect this relation to have an accuracy better than 0.02 magnitude.

During the collection of RSO science data, many observed stars will have a visual magnitude and a color, though not of the accuracy and reliability as the Landolt calibration fields. The process of reducing the SBV data will start with a computed value, M_{SBV}^{cat} (as described above), for each detected star found in the star catalogue, and this is compared with the observed magnitude, M_{SBV}^{obs} , derived from the calibration. The mean difference between these two quantities becomes the zero-point correction for the frame set,

$$\Delta M_{SBV} = \Sigma (M_{SBV}^{obs} - M_{SBV}^{cat}) / n$$

and is subtracted from the observed RSO magnitude. In this way the SBV makes self-calibrating photometric measurements.

In processing SBV photometric data, a simple model is used for prediction of M_{SBV}^{RSO} . It is based on assuming that the satellite reflects the solar spectrum. We have adopted (Beavers)

$$M_{SBV}^{RSO} = -26.8 - \log_{10} (\rho A F(\phi) / r^2)$$

where ρ is the reflectivity, A is the effective area, $F(\phi)$ is the phase function, and r is the range to the target.

As an example of this process, a comparison of a pass of SBV like data taken on the Lageos satellite at the Lincoln Laboratory Experimental Test Site (ETS) is given in Table 4. This 32 minute pass is from the same example data discussed in the Section 2.4 on metric calibration, and photometric measurements were computed using the signature data collected by the SBV signal processor. These data were used to determine M_{SBV}^{RSO} using a zero-point correction calibrated by the stars, as described above. The area and reflective properties of the Lageos I sphere are used in the model. Shown in Table 4 are the solar phase angle and the residuals in SBV magnitude for each of the Lageos observations from the data set described in Section 2.4. The visible model used $\rho=0.15$ for the reflectivity, $A=0.5 \text{ m}^2$ for the effective area of the sphere, and $F(\phi)=2((\pi - \phi)\cos(\phi) + \sin(\phi))/(3\pi^2)$ for a diffuse sphere. The results illustrate modeling the photometric properties of Lageos sample to better than 0.4 magnitudes.

3.3 SPIRIT III Radiometric Reduction and Calibration

The on-orbit calibration phase for SPIRIT III will be done in two different ways. First, a ground based observing program has been conducted to determine a small number of stellar infrared reference calibration sources. These sources will be routinely observed and used to monitor the stability of the infrared sensor. As described below, calibration and analysis of infrared data involves knowledge of the source

temperature. For a star, the irradiance as a function of temperature depends in a fundamental way on the composition of the stellar atmosphere, a subject still under development. This proved to be an important issue in the calibration of IRAS (Beichman et al.). Therefore stars will provide a stable reference to monitor a change in the sensor, but another calibration method will be used. There are five emissive reference spheres that will be deployed from the MSX during the SPIRIT III lifetime. These two centimeter spheres, coated with Martin Black, are designed to have a well defined temperature, and to provide orbital geometry that will sample the full dynamic range of the SPIRIT III. The goal is to provide knowledge of the emissive reference sphere temperature with sufficient accuracy to determine the absolute irradiance to 15% and the band-to-band ratio to 5%.

Table 4: Comparison of an Observed Pass of Visible Data for Lageos with a Photometric Model

OBJECT	YR	DAY	HR	MN	PHASE	RANGE	SENSOR MAGNITUDES			
							OBS	PRED	RES	
8820	91	312	2	6	+	26.1	7581.1	12.10	12.21	-0.11
8820	91	312	2	6	+	25.6	7548.4	11.98	12.20	-0.22
8820	91	312	2	6	+	25.3	7534.7	11.93	12.19	-0.26
8820	91	312	2	7	+	24.4	7480.7	12.10	12.17	-0.07
8820	91	312	2	8	-	22.7	7382.1	11.72	12.13	-0.41
8820	91	312	2	8	-	22.7	7382.1	11.58	12.13	-0.55
8820	91	312	2	9	-	21.6	7312.9	12.02	12.10	-0.08
8820	91	312	2	9	-	20.9	7270.0	12.13	12.08	0.05
8820	91	312	2	15	-	17.9	6880.7	11.71	11.95	-0.24
8820	91	312	2	16	-	18.7	6851.9	11.92	11.94	-0.02
8820	91	312	2	18	-	20.7	6814.4	11.90	11.94	-0.04
8820	91	312	2	18	-	21.7	6804.7	11.88	11.95	-0.07
8820	91	312	2	19	-	22.9	6798.8	11.76	11.95	-0.19
8820	91	312	2	20	-	25.0	6798.1	11.55	11.97	-0.42
8820	91	312	2	21	-	27.0	6806.4	11.54	11.99	-0.45
8820	91	312	2	22	-	29.2	6823.4	12.06	12.01	0.05
8820	91	312	2	23	-	31.6	6850.9	12.13	12.04	0.09
8820	91	312	2	24	-	34.2	6891.0	12.53	12.08	0.45
8820	91	312	2	25	-	36.3	6930.2	12.80	12.11	0.69
8820	91	312	2	26	-	38.6	6981.5	12.67	12.15	0.52
8820	91	312	2	27	-	41.2	7045.6	12.81	12.20	0.61
8820	91	312	2	28	-	43.6	7114.7	12.37	12.26	0.11
8820	91	312	2	37	-	64.2	8068.4	13.55	12.86	0.69
8820	91	312	2	38	-	65.2	8131.8	13.24	12.90	0.34

For surveillance data analysis, a simplified calculation is needed for the automated processing and a quick check of the observed RSO radiometry. The following describes such a process. Tables have been developed for processing the six SPIRIT III wavebands and the four IRAS wavebands. These can be augmented for other wavebands as necessary. The analysis involves conversion of the input observation for each band in Watts/m² in band to any other band, and conversion to standard units such as Jansky's (W/m²/Hz) and Naj's (W/m²/micron). The basic relations are as follows: If the telescope response is R(λ), the filter + blocker + detector response for band B is τ_B(λ), the Planck function radiation is ℑ_λ(T), and T is the absolute temperature, then we define the object in-band radiance as

$$F^B(T) = \int_0^{\infty} R(\lambda) \tau_B(\lambda) \mathcal{I}_\lambda(T) d\lambda \quad \left(\frac{W}{m^2} \right)$$

where the Planck flux density is

$$\mathcal{I}_\lambda(T) = \frac{3.74185 \times 10^8}{\lambda^5 \left(e^{\frac{14388.3}{\lambda T}} - 1 \right)} \quad \left(\frac{W}{m^2 \mu} \right)$$

and λ is in microns (Allen). For convenience we call this flux density unit a Naj. A generally used alternate flux density unit is the Jansky defined as 10⁻²⁶ W/m²/Hz. Using the relation that fλ=c=2.99792458x10¹⁴ microns/sec, we can convert Naj's to Jansky's with Naj's=Jansky's*2.99792458x10⁻¹²/λ². We can now compute the observed flux (in-band) irradiance as

$$F_0^B(T) = \frac{\epsilon A}{\pi r^2} \int_0^\infty R(\lambda) \tau_B(\lambda) \mathcal{S}_\lambda(T) d\lambda \quad \left(\frac{W}{m^2} \right),$$

where A is the area of the object, ϵ the emissivity, and r the range to the object.

The temperature of an object can be found as follows. The temperature dependence of the observed flux, $F_0^B(T)$, depends on the band. It also depends on ϵ, A , and r . Assuming ϵ is independent of λ , the ratio

$$\mathfrak{R}(T) = \frac{F_0^x(T)}{F_0^y(T)} = \frac{F^x(T)}{F^y(T)}$$

for bands x and y, is a monotonic function of T. Figure 4 displays this ratio for a number of bands for the SPIRIT III sensor. Therefore, given this function an observed in-band flux ratio immediately determines the temperature, independent of object size, range, and emissivity. With the measurement of n in band fluxes, $n(n-1)/2$ determinations of temperature are possible.

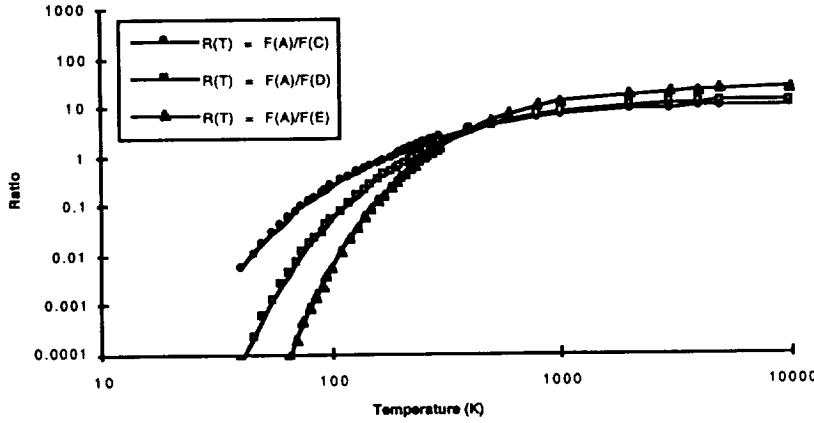


Figure 4: Ratio of Flux Densities for SPIRIT III Wave Bands

Given a temperature, the observed in-band flux can be expressed in Naj's at a reference wavelength, λ_0 , as

$$N_0^{\lambda_0} = F_0^B \left(\frac{\mathcal{S}_{\lambda_0}(T)}{F^B(T)} \right) \quad \left(\frac{W}{m^2 \mu} \right)$$

It is customary (though not necessary) to select λ_0 in the band. This can be converted to Jansky's, as described above, with

$$J_0^{\lambda_0} = N_0^{\lambda_0} \left(\frac{\lambda_0^2}{2.99792458 \times 10^{-12}} \right)$$

As an example of this process, we show some data from the IRAS satellite. The InfraRed Astronomy Satellite (IRAS) was operational for about 10 months in 1983. The IRAS sensitivity is very similar to that expected from SPIRIT III, although the IRAS observing geometry resulted in measurements at a phase angle near 90 degrees. However, a number of observations on medium to high altitude satellites were made over the lifetime of IRAS, and they are illustrative. In Table 5, we give the results of analysis of an observation sequence for the Lincoln Calibration Sphere (LCS) 1 (SSC #1361). This is a 1 meter square area sphere in a circular orbit at a range of 1900 km. Three measurements were taken in each of the 12, 25, and 60 micron bands, and if a value of $\epsilon = 0.032$ is used, then we see the comparison of the measurements to the model is good to better than 0.5 Jansky's. The largest residual is for the 60 micron measurement, and the temperature inferences from the ratios with this measurement appear to be high. It is reasonable for this

methodology to be able to provide temperature data from SPIRIT III measurements to $\pm 5^\circ\text{K}$ in temperature and $\pm 2\%$ in emissivity and absorbtivity.

3.4 UVISI Radiometric Reduction and Calibration

The on-orbit calibration phase for UVISI will be done using calibrated reference stars. There are two issues involved here. The first is the algorithm for detecting and extracting the aperture irradiance. In contrast to the SBV, a star will generally fall in only one pixel. The detection will be based on finding the pixels with exceedences greater than some threshold and correlation with detections from the SBV signal processor. Secondly, since the UVISI has a non-standard spectral response, the relation between the UVISI magnitude and the magnitude of a star must be known. From analysis of the UVISI spectral response, the relation between the visual magnitude of a star, M_v , with color, B-V, and the UVISI magnitude, M_{UVISI} is given by an empirical relation similar to that for M_{SBV} (Beavers).

Table 5: Comparison of an Observed Pass of IRAS Infrared Data for LCS-1 with a Radiometric Model

OBJECT	YR	DAY	HR	MN	BND	RANGE	CORRECTED JANSKYS			FLUX DATA (W/SQ METER)		
							OBS	PRED	RES	OBS	PRED	RES
1361	83	72	11	56	I12	2001.1	16.55	16.42	0.132	0.11E-11	0.11E-11	0.89E-14
1361	83	72	11	56	I25	2001.1	8.97	8.75	0.212	0.29E-12	0.28E-12	0.68E-14
1361	83	72	11	56	I60	2001.1	1.82	2.27	-0.449	0.11E-13	0.14E-13	-0.27E-14
3 TEMPERATURE MEASUREMENTS:							479.51	561.76	958.71			

During the collection of RSO science data, each UVISI frame will detect many stars will have a visual magnitude and a color, though not of the accuracy and reliability as the calibration fields. The process of reducing the UVISI data will be similar to SBV: Compute $M_{\text{UVISI}}^{\text{cat}}$ for each detected star found in the star catalogue and compare with the observed magnitude, $M_{\text{UVISI}}^{\text{obs}}$, derived from the calibration. The mean difference between these two quantities becomes zero-point correction for the frame,

$$\Delta M_{\text{UVISI}} = \Sigma (M_{\text{UVISI}}^{\text{obs}} - M_{\text{UVISI}}^{\text{cat}}) / n$$

and is subtracted from the observed RSO magnitude. In this way the UVISI makes self-calibrating photometric measurements, similar to the SBV.

In processing UVISI photometric data, a simple model is used for prediction of $M_{\text{UVISI}}^{\text{RSO}}$. It is based on assuming that the satellite reflects the solar spectrum. We have adopted (Beavers)

$$M_{\text{UVISI}}^{\text{RSO}} = -26.8 - \log_{10} (\rho A F(\phi) / r^2) + \Delta M ,$$

where ρ is the reflectivity, A is the effective area, $F(\phi)$ is the phase function, and r is the range to the target. The function ΔM will color correct the model for each UVISI waveband.

4.0 THE MSX EPHEMERIS

4.1 Description of the Problem and Method of Attack

The metric accuracy of the MSX sensors critically depends on the ephemeris or position accuracy of the MSX satellite platform. This section will be describe the required ephemeris accuracy for the MSX and how it can be achieved.

The ephemeris accuracy requirements are dependent on the required metric data quality for the SPIRIT III and SBV. It is required that the ephemeris error for MSX be a small part of the overall error budget, and (more specifically) 3-10 times less than the error of the data. An example of one of the more stressful demands on the MSX ephemeris accuracy will be when the SBV or SPIRIT III is viewing an object at the Earth's tangent height, a range 2500 km, in a 90 minute parking orbit. A simple calculation indicates

that with 4-arcsecond sensor data quality and a requirement that the ephemeris error be at least 3 smaller implies that the ephemeris accuracy for MSX must be better than 15 meters.

There were three methods considered for providing the required ephemeris accuracy: 1) an on-board GPS receiver, 2) ground (or skin) tracking from the Space Surveillance Network (SSN) radars, or 3) ground tracking from the Air Force S-band Ground Link Stations (SGLS). A GPS receiver on board the MSX was the most attractive choice; but it was eliminated because of power, weight, and space requirements. Radar (skin) tracking of the required accuracy could come from the Millstone radar in Massachusetts and from the ALTAIR radar in the Marshall Islands (in the near equatorial Pacific). These provide accurate enough measurements, but they are heavily tasked already and the amount of tracking that would be required for MSX would demand too much of their resources. The SGLS network is used by the Air Force for satellite communications, and the S-band tracking data is obtained to support acquisition. The MSX satellite will have a coherent S-band transponder and will be controlled by the SGLS network. Tracking data from this network become an attractive source for calculating a precision ephemeris for the MSX. The SGLS network is a globally distributed network of stations, measuring range, range rate, azimuth, and elevation for satellites with a coherent transponder.

To determine if the SGLS tracking data could suitably meet the 15 meter accuracy requirement for MSX, a number of evaluations of the data have been made. The original studies were made in late 1989 and through 1990. These studies involved SGLS data from two satellites with similar orbital parameters to MSX. Table 6 compares these with one column devoted to the expected orbital parameters for MSX. The two test satellites were lower, however, and their attitudes were not well-determined, which implied that atmospheric drag was more difficult to model than is expected for MSX. The remaining dynamical complication that could not be considered during these tests arises from the fact that MSX will have cryogen gas venting during the useful lifetime of the SPIRIT III sensor. This phenomenon will constitute a significant perturbation of the MSX orbit and is absent in the test satellites.

Table 6: Orbit Comparison of MSX and the Evaluation Test Objects: #19911 and #20497

	MSX	19911	20497
ALTITUDE (km)	888.	490.	460.
ECCENTRICITY	0.001	0.00133	0.00161
INCLINATION (deg)	99.	47.7	43.1
DRAG	YES	HIGH	HIGH
MANEUVER	NO	OFTEN	NO
SATELLITE ASPECT	KNOWN	NOT KNOWN	NOT KNOWN

The objectives of the sample evaluations were to establish how accurately an orbit could be determined for the two satellites with SGLS data. The stated precision of SGLS data is 6 meters in range, 3 cm/s in range rate, and 20 millidegrees for the angle measurements. These values are potentially good enough to meet the orbit accuracy requirements. Related questions which were addressed by the test evaluations include: how much tracking is required?, how well are the data calibrated?, and what additional processing has to be done in order to use the data to its potential?

The late 1989 and 1990 studies took place during periods of major solar activity. For these low altitude satellites, it was found that three day orbit fits were most suitable for the SGLS data. Besides solving for the satellite state vector, drag scale factors at half day intervals were also estimated. The orbit accuracy was evaluated using high accuracy radar measurements and also by comparing overlapping orbits. The radar measurements were from the Millstone Hill L-Band radar (with a range accuracy of 1 meter) and from the ALTAIR UHF radar (with a range accuracy of 10 meters).

The SGLS data had a nominal range bias correction applied (none for the angles) and a troposphere refraction correction based on an empirically derived mapping function and monthly surface refractivity values. No ionosphere refraction correction had been applied, and so we applied corrections based on the best

available global model (Bilitza, Klobuchar). The range rate had to be converted to a range difference measurement to be properly used. Additional biases in the range data were determined thereby improving the calibration and accuracy of the data. The angles were also calibrated.

With an enhanced calibration and an average of 8 tracks per day, the evaluation showed that the two satellites have orbits computed to an accuracy of 15 meters. This is illustrated in Figures 6 and 7. Figure 6 provides a sample of the data quality from one of the SGLS tracking stations (Guam) using an orbit computed with the radar data, and Figure 7 shows range residuals for the radar data using an orbit computed with the SGLS data. The plots display the mean and $\pm 1 \sigma$ error bars for each of the tracks. The means from Figure 7 are within 15 meters and are due to a combination of measurement error and orbit error. These evaluations indicate that the SGLS network can provide the necessary tracking data for the MSX orbit computation.

SAMPLE ACCURACY OF DATA (Guam)

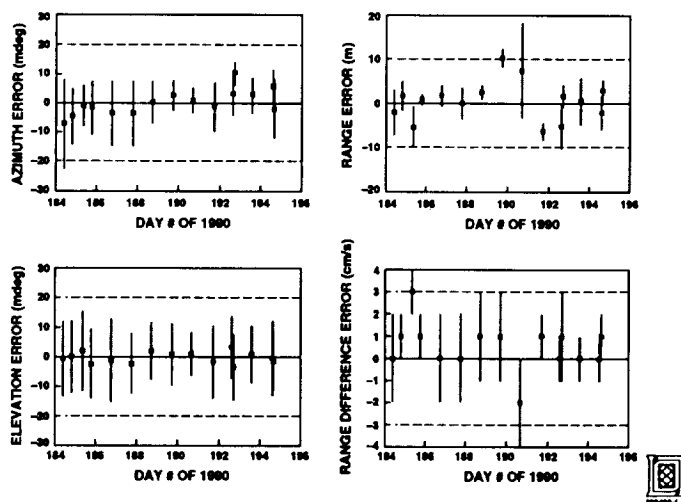


Figure 6: *Residuals of SGLS Tracks from an Orbit Determined with Radar Data*

SGLS ORBIT ACCURACY EVALUATED USING RADAR RANGE MEASUREMENTS

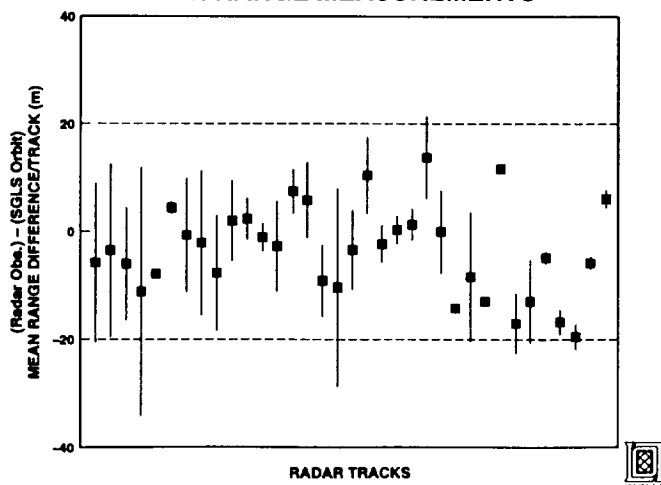


Figure 7: *Residuals of Radar Tracks from an Orbit Determined with SGLS Data*

4.2 Modeling the MSX Orbit

In order to produce a 15 meter orbit for the MSX on a routine basis, accurate modeling of the forces acting on the MSX orbit is required. The gravitational forces are well known and already incorporated in the DYNAMO software. The non-conservative forces which are more difficult to model include radiation pressure, atmospheric drag, and the force induced by the venting of the gas created by the sublimation of a solid hydrogen block within the cryo-stat. Two important data types that must be obtained and input to the MSX force model are the satellite attitude and the venting flow rate of hydrogen gas from the cryogen cooling system. The attitude data is necessary for the drag, solar radiation pressure, and cryogen venting models. The cryogen flow rate data will be measured and provided by Utah State University (the manufacturers of SPIRIT III), and details are still being worked out.

The cryogen gas venting model is the remaining dynamical complication for the MSX satellite. The cryo-system on the MSX contains a large mass of solid hydrogen, which is used to keep the instruments at the required temperature. As heat is added to or generated by the satellite, the hydrogen escaping through the venting system produces a low thrust on the satellite. Depending on the detailed geometry of the venting system, the effect of the resulting force can be large when integrated over the course of a day. Details on the exact nature of this force are yet unclear, but an exact or an empirical model (which will be parametrized and updated from the orbit fits) is critical to achieving a 15 meter orbit for the MSX on a routine basis.

5.0 SUMMARY

The MSX science instruments cover a wide range of the spectrum from the ultra-violet to the long-wave infrared and will be able to provide useful metric, photometric, and radiometric data for surveillance of the Resident Space Object background. Careful characterization and calibration of the sensor data is required for accurate analysis of space surveillance experiment data. Procedures for reduction and refinement of the metric and radiometric (or photometric) data have been presented and methods of calibration have been described. Examples from ground-test data similar in characteristics to the MSX sensors and from the IRAS RSO detections have been presented to support the reduction and procedures outlined in this report. In addition to the reduction of the MSX sensor data, it is crucial to calculate a precise MSX ephemeris. The ephemeris is calculated using SGLS tracking of data from one of two S-band transponders on board the MSX and sophisticated models of the MSX orbit. Examples to demonstrate the techniques for this calculation have been provided from satellites in similar orbits equipped with S-band transponders.

6.0 REFERENCES

- Allen, C.W., **Astrophysical Quantities**, The Athlone Press, London, 310pp, 1973.
- Beavers, W., Private Communication, 1989.
- Beichman, D., *Infrared Astronomical Satellite (IRAS) Catalogs and Atlases. Vol I: Explanatory Supplement*, Jet Propulsion Laboratory, NASA RP-1190, 455pp., 1987.
- Bilitza, D., *International Reference Ionosphere: Recent Developments*, Radio Sci., **21**, 343, 1986.
- Klobuchar, J.A., Private Communication, 1989.
- Landolt, A., *UBVRI Photometric Standard Stars in the Magnitude Range $11.5 < V < 16.0$ Around the Celestial Equator*, Astron. J., **104**, 340 - 371, July, 1992.
- Mill, J.D., O'Neil, R.R., Price, S., Romick, G.J., Uy, O.M., Gaposchkin, E.M., Light, G.C., Moore Jr., W.W., and Murdock, T.L., *The Midcourse Space Experiment: Introduction to the Spacecraft, Instruments, and Scientific Objectives*, J. Rockets and Spacecraft, In Press, 1994.
- Smith, C.A., Kaplan, G.H., Hughes, J.A., Seidelmann, P.K., Yallop, B.D., and Hohenkerk, C.Y., *Mean and Apparent Place Computations in the New IAU System. I. The Transformation of Astrometric Catalog Systems to the Equinox J2000.0*, The Astron. J., **97**, 265-273, January, 1989.
- Wyatt, C.W., *Acceptance Test Data and Algorithms for Predicting SPIRIT III Radiometric Performance*, SDL/92-048, Space Dynamics Laboratory/Utah State University, Logan Utah, June, 1992.

FLIGHT MECHANICS/ESTIMATION THEORY SYMPOSIUM

MAY 17-19, 1994

SESSION 2

**FIXED-HEAD STAR TRACKER ATTITUDE UPDATES
ON THE HUBBLE SPACE TELESCOPE***

Matthew S. Nadelman and Jeffrey B. Karl
Computer Sciences Corporation
1100 West Street, Laurel, MD 20707
and
Lou Hallock
National Aeronautics and Space Administration
Goddard Space Flight Center
Greenbelt, MD 20771

ABSTRACT

The Hubble Space Telescope (HST) was launched in April 1990 to begin observing celestial space to the edge of the universe. National Aeronautics and Space Administration (NASA) standard fixed-head star trackers (FHSTs) are used operationally onboard the HST to regularly adjust ("update") the spacecraft attitude before the acquisition of guide stars for science observations. During the first 3 months of the mission, the FHSTs updated the spacecraft attitude successfully only 85 percent of the time. During the other periods, the trackers were unable to find the selected stars — either they failed to find any star, or worse, they selected incorrect stars and produced erroneous attitude updates. In July 1990, the HST project office at Goddard Space Flight Center (GSFC) requested that Computer Sciences Corporation (CSC) form an investigative "tiger" team to examine these FHST update failures. This paper discusses the work of the FHST tiger team, describes the investigations that led the team to identify the sources of the errors, and defines the solutions that were subsequently developed, which ultimately increased the success rate of FHST updates to approximately 98 percent.

INTRODUCTION

On April 24, 1990, the Space Shuttle Discovery was launched by the National Aeronautics and Space Administration (NASA) to deploy the Hubble Space Telescope (HST). HST contains a Ritchey-Chretien design Cassegrain telescope with a 94.5-inch primary mirror. The attitude control of the telescope is performed by HST's pointing control subsystem (PCS) (Reference 1). The PCS is supported by eight types of sensors and actuators, including fixed-head star trackers (FHSTs), fine guidance sensors (FGSs), and rate gyro assemblies (RGAs). The process whereby FHSTs update spacecraft attitude, which resulted in errors early in the HST mission, is the focus of this paper.

The NASA standard FHSTs on the HST are analog devices used to assist the ground in verifying the onboard attitude and to update the spacecraft attitude after large maneuvers. Each tracker can scan its 8.0-degree by 8.0-degree total field of view (FOV) (TFOV) to map out stars whose data can be subsequently used by ground software for attitude determination. It can also be commanded to search an approximate 1.5-degree by 1.5-degree reduced FOV (RFOV) region for a preselected reference star whose position error can be used to correct the spacecraft's attitude.

FGSs are used to obtain the precise pointing necessary during HST's science observations and as scientific instruments while in astrometry mode. Their FOV is along the telescope axis. Although variable, the accuracy of the attitude of the spacecraft is typically expected to be known to within 60 arcseconds for FGSs to acquire their guide stars and allow the HST to perform science observations.

The RGAs provide control for the vehicle during maneuvers. They also provide primary guidance for the telescope while the FGSs are occulted. Accurate calibrations of the RGAs and FHSTs are critical to the successful acquisition of guide stars by the FGSs. For more information on calibration of the HST attitude sensors, see Reference 2.

* This work was performed under NASA GSFC contract NAS 5-31500. This paper is declared a work of the U.S. Government and is not subject to copyright protection in the United States.

Because of the unique value of HST science observing time, science observations are scheduled as efficiently as possible to make maximum use of unocculted time periods. To achieve this goal, vehicle attitude errors must be reduced as much as possible before FGS guide star acquisitions to minimize FGS search time and increase FGS guide star availability. In terms of FHST performance, these conditions place much more stringent demands on FHST accuracy and reliability than those experienced on previous missions. It therefore became a source of major concern when, soon after launch, it was discovered that FHST updates were correctly updating the spacecraft attitude only 85 percent of the time. The remaining time, updates resulted in two basic types of failures: timeouts and spoilers. A *timeout* failure occurs when the FHST fails to acquire the reference star or acquired the star later than the flight software (FSW) data base setting. A *spoiler* failure occurs when the FHST acquires an incorrect star or object (a spoiler), which results in the calculation of an inaccurate attitude update. These failures prevent HST's FGSs from acquiring guide stars, which in turn leads to missed science observations. The HST project at Goddard Space Flight Center (GSFC) directed CSC to form a special "tiger" team to investigate the cause of these failures. This team, which was expanded to include personnel from GSFC and other contractors, was also tasked to find solutions for this 15-percent failure rate. This paper discusses the use and "reliability calibration" of the FHSTs in their attitude update mode, the approach to the problem, investigations, solutions, and the current status of the problem.

FHST OPERATIONS ON THE HST

One of the keys to performing science observations with the HST is to first obtain an accurate attitude. After a viewing period has been completed, the spacecraft will slew to the next target and perform an FHST update. As stated previously, HST depends on calibrated RGAs to accurately reach this target. The pre-launch gyroscope scale factor alignment accuracy requirement was such as to permit errors on the order of 1 arcsecond/degree of slew following large maneuvers. In-flight calibration of the gyroscopes in July 1990 provided an accuracy on the order of 0.5 arcsecond/degree. Since the First Servicing Mission (FSM) of HST in December 1993, the accuracy has been improved to approximately 0.3 arcsecond/degree. The purpose of performing FHST updates is to remove the attitude errors that can accumulate over time (while HST maneuvers and when the FGSs are occulted) due to gyroscope errors. FHST updates typically bring the spacecraft attitude to within 15 arcseconds (1 sigma) of the planned target attitude, thereby permitting guide star acquisitions using the FGSs. The HST issues approximately 70 FHST updates per week.

The analog NASA standard FHSTs on HST work by raster scanning (see Figure 1) using the instantaneous FOV (IFOV) in both TFOV (map) mode and RFOV mode. For more detail on the FHST hardware, see References 3 and 4. There are some differences between the scan modes. The TFOV mode works by scanning in an increasing positive vertical direction and across, right to left or left to right horizontally. When a star is encountered within the previously set magnitude threshold (discrete settings assigned from the ground), the FHST begins a cross-scan on the star (track mode). If five cross-scans are made, star presence is triggered and acquisition occurs (0.5 second). The star is tracked for the FSW data base time limit and then the IFOV of the tracker jumps more negatively by 0.4 degree (approximately four analog scan lines) and "blanks" (essentially ignoring all light) approximately 0.6 degree (approximately six analog scan lines) in a positive vertical direction, thereby effectively blanking in a positive vertical direction by 0.2 degree.

The RFOV also works by raster scanning toward the positive vertical direction of the RFOV. The scan begins with an offset command at the vertical center, blanks six vertical lines (including the center), and then goes to the top (vertical negative). It takes 1.5 seconds to scan an empty RFOV and 11 seconds to scan an empty TFOV. Track mode works the same way in RFOV as in TFOV, except that the intent in RFOV mode is to remain fixed on the predetermined reference star for the remainder of the FHST update period. If the scan fails to find the star or finds a star that is not within the voltage (magnitude) tolerance set by ground command, the FHST continues its search across the RFOV with no blanking or jumping. If a break track command is issued, the tracker blanks approximately 0.6 degree (flight experience has shown 0.72 degree to be a more accurate value) in a positive vertical direction before scanning continues (Reference 5). The spacecraft remains fixed on the star after acquisition so the onboard software can compare the current position of the preselected star (within the tracker frame) with the expected position of the star (uplinked to the spacecraft) at that attitude. This difference is considered to be the attitude error. The HST then updates the attitude by issuing a slew to correct for this error. When two trackers are used, the error is combined to give a three-axis attitude error that has typically been within 15 arcseconds (1 sigma) of the desired attitude as measured relative to the FGSs. Problems result when the star is not acquired or an object other than the reference star is acquired and an errant update is performed.

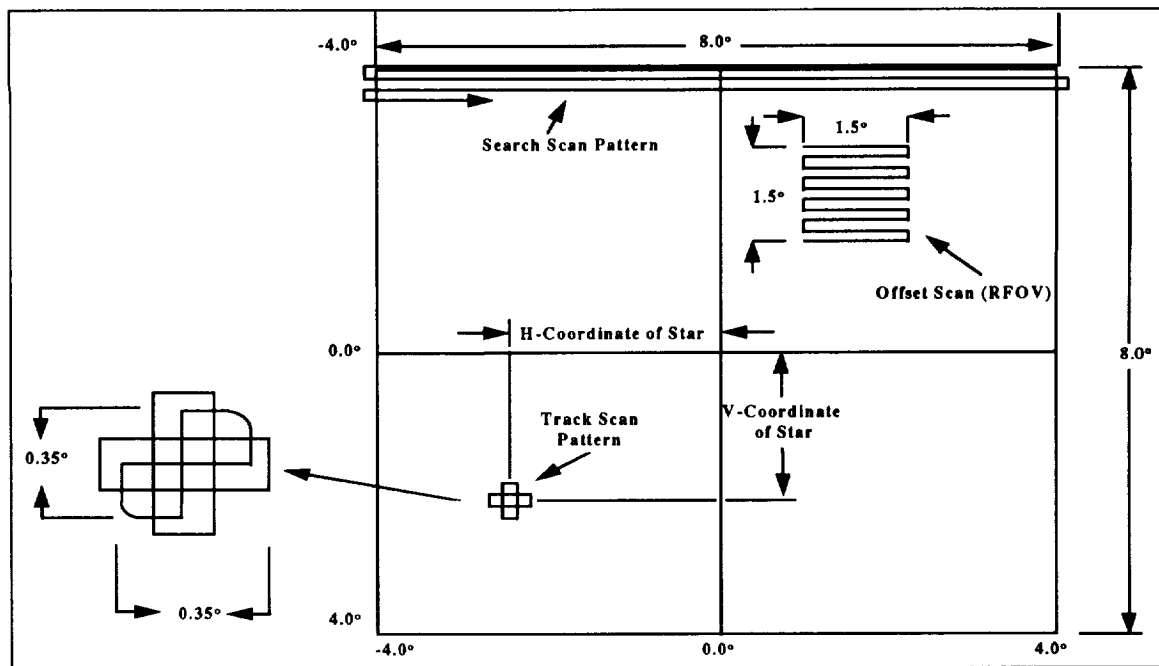


Figure 1. Generic FHST Description Diagram

UPDATE PROCEDURES

Fundamentally, FHST updates are requested through a science mission specification (SMS). The SMS acts as a script for the HST, typically describing a week's worth of activities. Among other things, it tells the spacecraft when to slew, when to perform science observations, and when to perform an FHST update. The SMS is read by the Payload Operations Control Center (POCC) Applications Software Support (PASS) command management software, which verifies constraints and generates commands. In this context, PASS plans the FHST updates. The following steps are performed by the PASS mission scheduling software to schedule an update:

1. *Check FHST availability.* The scheduling software checks to see which FHSTs are available or unavailable due to Earth and Moon occultations and Sun constraints.
2. *Determine candidate stars.* For the expected attitude, the ground software will look for candidates that are within the TFOV, between the bright and dim limits set (originally between $2.0 m_v$ and $5.7 m_v$, currently between $2.0 m_v$ and $6.0 m_v$), are not variable or double stars, do not have a large proper motion or position uncertainty, and are not in the BADSTARS file. The BADSTARS file is a sequential file that can be updated to exclude undesirable stars from reference star consideration. The star information used to support ground-based predictions and processing is generated from the PASS SKYMAP run catalog. This run catalog is a subset of the SKYMAP master catalog that is generated by the National Space Science Data Center and contains approximately 250,000 stars. The ground software for HST requires a subset of this catalog. Only stars that the trackers are capable of seeing are necessary for this run catalog.
3. *Determine reference stars.* The software chooses one of the stars from step 2. It verifies that the star is within a data base distance of the boresight, that its RFOV center is within an allowable range, that it is within a data base value of the edge of the RFOV, and that it is well isolated from potential spoiler stars.
4. *Determine the best reference star.* If several stars pass step 3, one star is chosen based on its not being in an undesirable region (a region where update failures have been known to exist or where the tracker is determined to be less sensitive) of the FHST TFOV, being furthest from the TFOV and RFOV edges (within data-base-specified tolerances), being furthest from its potential spoilers (within a data-base-specified tolerance), and being the brightest star.

If all of these tests are passed, the reference stars are chosen and commanding is generated for uplink to the HST. If none are chosen, then no update is performed. If a three-axis update (two FHSTs) is requested, but only one star passes the reference star tests, then the FHST update becomes a single-axis update using only one tracker. The following information, contained in the commands for the FHST update, is then prepared for uplink to the HST DF-224 onboard computer (OBC), to be used in conjunction with tracker alignment data:

- *Location of desired star at expected attitude* – The position of the star, in horizontal and vertical counts, in FHST coordinates, are taken from steps 3 and 4 of the previous procedure.
- *RFOV center coordinates* – The ground software chooses a RFOV (from a discrete set of values, each offset from the previous value by 0.5 degree) that can best isolate the chosen reference star. This will increase the chances of acquisition.
- *Reduced set of distortion coefficients* – Distortion effects are computed for each reference star and packaged in a format appropriate for use by the OBC. A discussion of the calibration of FHST distortion and scale is presented in Reference 3.
- *Type of update* – The onboard software needs to know whether a three-axis (two FHSTs) or one-axis (one or two FHSTs) update is expected to be performed and whether to issue the resulting attitude correction at the time of computation (maneuver mode) or wait until requested to issue the update (delayed mode).
- *Magnitude threshold setting for the FHST* – The FHSTs have four threshold settings, each of which is hardware-voltage dependent. The voltages correspond, approximately, to magnitudes 3, 4, 5, and 6 (commonly referred to as a "wide open" value). When set to these values, the FHST will be sensitive to stars brighter than the limit. For example, if the tracker is set to a threshold of 5, it will be capable of seeing any star that is brighter than the original hardware voltage setting, which, if set perfectly, would mean any star brighter than $5 m_v$. A setting of 6 means that the FHST is capable of seeing down to the hardware creation limit of the internal photocathode tubes. The first sensitivity study of the trackers discovered that FHSTs 1, 2, and 3 had seen stars as dim as $7.12 m_v$, $6.80 m_v$, and $6.64 m_v$, respectively (see Reference 6). Hardware acceptance test data showed that the threshold voltages differ significantly from the voltage values that actually map to the integer values of 3, 4, 5, and 6 for the magnitude.

The spacecraft then executes the stored commands (and therefore, the attitude updates). It was at this point that problems were first noticed. Additional information on the PCS is presented in *HST Flight Software Examination for the PCS* (Reference 7).

PROBLEM APPROACH

On July 6, 1990, GSFC requested that CSC assemble a "tiger team" to investigate, and, if possible, solve the FHST update failure problem. The team decided that the best approach to the problem was to create a data base of FHST update failures and successes, analyze successful updates to obtain the correct signature of an update, analyze all failures and categorize them, perform correlation studies, and publish a weekly report to keep the customer (GSFC) apprised of the situation.

To fully analyze and categorize FHST update failures, a system of data collection that included both predictive and post-failure data was used. All of the predictive data for FHST updates were provided by reports from the PASS mission scheduling subsystem. The PASS mission scheduling subsystem selects the appropriate reference star(s), generates the predictive horizontal and vertical coordinates for that star, the RFOV center, the FHST threshold setting, and the reference star's SKYMAP number, visual magnitude, and right ascension and declination from the PASS SKYMAP run catalog. The mission scheduling subsystem also provides FHST scheduling timelines and a predictive TFOV plot that includes the RFOV, the reference star, and all nearby spoiler stars.

Once the update is executed onboard HST, near-real-time data concerning the event can be monitored or snapped from a PCS console display or plotted on a strip chart plotter in the HST Mission Operations Room (MOR). If an FHST anomaly is observed, a console engineer writes an HST anomaly report (HSTAR). FHST failure analysis begins after the tiger team receives the HSTAR.

Examination of FHST failures can be accomplished in several ways. The raw horizontal and vertical counts and the observation intensity (volts) of the FHST scan can be reviewed, after the fact, using plots created by the PASS fine attitude determination software. The position and magnitude data of the FHST scan can also be provided by plots generated by the HST engineering support system. It is typically from these data, in comparison with the predictive data, that a failure can be categorized. The DF-224 Analysis and Software Development Facility (DASDF) real-time graphics system was used by the tiger team to obtain history data of FHST updates that had occurred weeks and months in the past. This system replays the HST engineering telemetry stream using history tapes and outputs MOC console PCS displays. The DASDF system was used extensively to create a history of early FHST successes and failures.

In cases where spoiler objects were acquired, many resources were available for the spoiler object's identification. The SKYMAP and Smithsonian Astrophysical Observatory (SAO) catalogs were commonly used to identify spoiler stars acquired during the update. For other spoiler objects, the Astrophysics Data System (ADS), and the Atlas Coeli 1950.0 and SAO sky atlases were used. ADS is an on-line, Internet-accessible data system, supported by NASA, that provides access to astrophysics catalog data.

The first determination resulting from this analysis revealed that HST's FHSTs were more sensitive than originally expected. It had been documented that FHSTs could see down to a magnitude of 5.7 and the first reference star catalog contained stars down to 6.7 m_v . Spacecraft data clearly showed that it was necessary to extend the SKYMAP run catalog to include dimmer stars. Although reference stars dimmer than 5.7 m_v were not selected, dimmer stars (down to 7.1 m_v) that were being seen within the RFOV acted as spoilers, forcing attitude update failures. The catalog was adjusted to include stars down to 7.1 m_v . An earlier change to the catalog and selection algorithm was to prevent double stars, variable stars, and stars with large proper motion from being chosen as reference stars, but to retain them as potential spoiler stars. This action thereby allowed the software to choose an alternate reference star if one of these spoilers was in the RFOV, bringing the success rate up to approximately 90 percent.

The data base of update successes and failures was begun on July 12, 1990. It consisted of 3,515 updates at completion. The following information was kept on each update: date, time, FHST number, telemetry slot, category, SKYMAP number, expected position (right ascension and declination) of star, expected and observed position of star in FHST, magnitude, intensity, threshold setting, RFOV center coordinates, and spacecraft attitude (right ascension, declination, and roll). By reviewing these updates, the tiger team was able to define 13 distinct update failure categories that required investigation; subsequent analysis identified two additional categories. Each category is described in detail in Appendix A. The following studies were set up to analyze these failures:

- FHST sensitivity (References 6, 8, 9, and 10)
- Data correlations (stellar magnitude versus failure, RFOV position versus failure, RFOV position versus success, day/night transitions versus success/failure, solar array angle versus success/failure)
- Examination of stars from updates that failed, using information from other star catalogs (e.g., SAO)
- Discussions with the hardware manufacturer
- Possible algorithmic modifications
- Creation of a FSW reference star quality test (the "error box")
- Tuning the ground star selection algorithm

Reports and status summaries of these studies were presented by the tiger team on September 7, October 25, and October 26, 1990; and on February 22, 1991 (References 11, 12, and 13).

By studying the data and the various categories, solutions were developed. Solutions were reduced to the following main subject areas:

1. *Star catalog issues*, where the PASS SKYMAP run catalog had to be updated twice to account for the dimmest stars the trackers could see, which acted as spoilers, and an additional time to correct for magnitude errors in the master catalog.
2. *Hardware properties*, which ranged from gaining operational experience (e.g., in flight calibrations) for the sizes of the TFOV, RFOV, and voltage (magnitude) threshold limits, to supporting less sensitive areas on the trackers, to making corresponding software algorithmic and data base changes to accommodate these updates.
3. *Commanding problems*, which ranged from command group information corrections to command timing modifications.
4. *Implementation of an error box* to add a flight-proven [on the High-Energy Astronomy Observatory (HEAO)] check in the FSW. This allowed the ground software to better isolate a reference star (the size of the error box is smaller than the RFOV), and to increase the likelihood of finding the correct star.

These solutions may be useful to others with similar problems with FHSTs, or for review before designing a new system with FHSTs. A detailed list of these solutions containing a description, the category affected, the problem solved, and a description of new problems created is presented in Appendix B.

CURRENT STATUS

On December 2, 1993, the Space Shuttle Endeavour embarked on HST's FSM to correct the telescope's optical errors, replace failed equipment, and add the new wide field/planetary camera (WFPC). Although no FSM repairs were performed on the FHSTs, there was concern that the trackers might be accidentally damaged or misaligned because they are located in the same local compartment on the HST as the gyroscopes that were replaced. Following the FSM, it was verified that FHST calibration and response characteristics remained unchanged and FHST updates and maps worked as expected.

From October 1993 to March 1994, 1,326 attitude updates were issued with 22 recorded failures. Six of these failures were caused by attitude errors in excess of 300 arcseconds following the FSM. The ground system has been set up to assume that during normal operations, attitude errors are well contained and should never exceed 300 arcseconds. Due to the changeout of uncalibrated RGAs during the FSM, these types of errors were not unexpected. These failures were therefore not due to errors within the FHST hardware or software systems. Excluding these failures from computations gives a success rate of 98.79 percent over the most recent 130 days. The breakdown of the 16 remaining failures is as follows (the category number is as indicated in Appendix A):

- Seven category 2 failures, all on the same reference star, which was located less than 400 arcseconds from the RFOV edge
- Two failures of the same back-to-back spoiler acquisition caused by a RFOV problem
- Two delayed-mode update duration problems
- Two blanking problems
- Two potential Artificial Earth Satellite (AES) acquisitions
- One category 9 failure, when the FHST acquired a bright open cluster

Of all of these failures, only the potential AES acquisitions cannot be solved with simple data base changes. Figure 2 shows a plot of FHST update successes versus time. Each point on the plot represents the success rate for a 1-month period. Note that no data were collected for May and June 1991 and September 1992 through September 1993. The anomalous point in December 1994 contains the seven category 2 failures of the same star. Data base changes are being made to prevent this failure from occurring again.

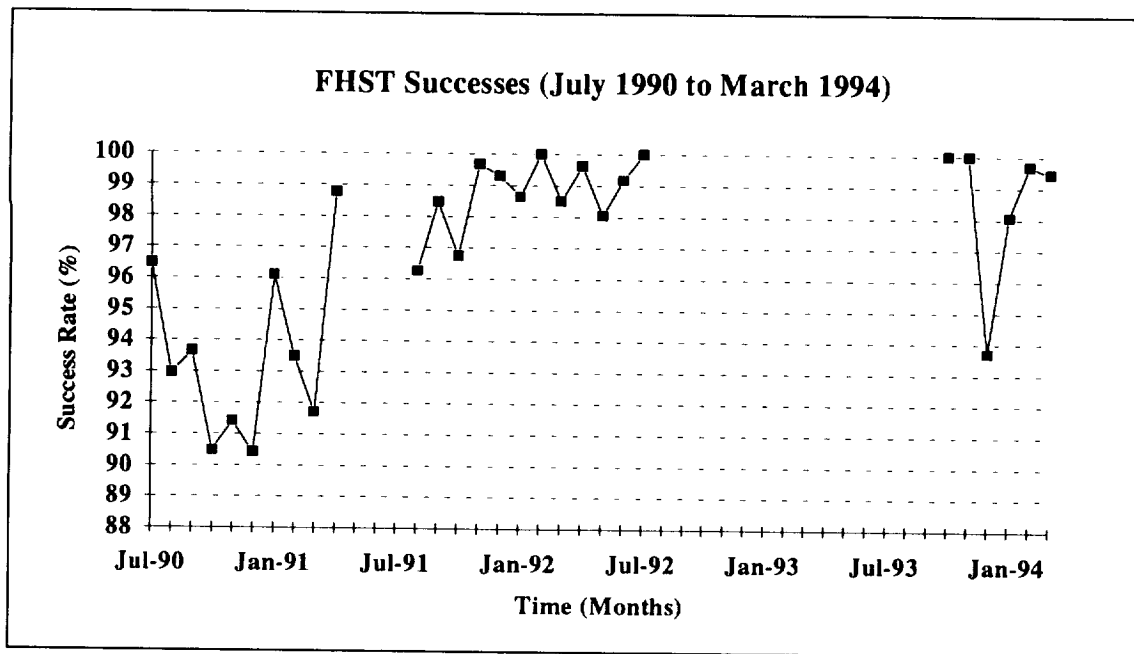


Figure 2. FHST Successes (July 1990 to March 1994)

Analysis of FHST failures will continue on HST. Adjustments may need to be made to RFOV and error box blanking sizes to reduce or eliminate these failure categories. Category 9 spoiler problems can be solved with updates to the BADSTARS file or by installing future versions of the SKYMAP catalog that will contain updated star information. No software or data base changes are planned to prevent potential AES problems because they occur too infrequently (only three have occurred in the last 2 years) to impact FHST operations. Further work on the least understood failure types (categories 1, 2, and 3) is in progress. Many category 2 failures have been reclassified as other anomalies, including the recent discovery and fix of the delayed-mode update duration problem. The last category 1 and 3 failures were recorded in September and July of 1993, respectively. These failure types are not currently impacting FHST operations. As of March 1994, the FHST update success rate was approximately 99 percent.

SUMMARY

This paper has presented a review of investigations undertaken to improve the reliability of FHST attitude updates performed by the HST. An update failure rate of roughly 15 percent, with an associated significant loss of science, was experienced during the beginning of the HST mission. Extensive investigations have led to a categorization of the 15 types of update failures and the development of operational solutions that have reduced the failure rate to roughly 1 percent. Investigations continue with the goal of improving FHST update reliability even further.

APPENDIX A - FHST FAILURE CATEGORIES

This appendix lists the FHST failure categories that were determined by the tiger team. Each failure that was examined was analyzed and assigned a category. For each category, the symptoms of the failure are described, the causes or suspected causes listed, and the current status (as of March 1994) is given.

Table A-1. FHST Failure Categories (1 of 2)

Category	Title	Symptoms	Causes	Status
1	RFOV Excursions With Noise Spikes	The raw data show a noisy scan in both horizontal and vertical directions with excursions outside the RFOV. Intensity spikes greater than the expected reference star intensity are seen.	Under study. The noise in the data implies that bright light is in the RFOV. Stray light from reflections off the sun shades or solar arrays has been considered a possible source.	Under analysis. These failures are responsible for 8% of all failures since April 1992.
2	Star Not Acquired in RFOV; No Noise on Magnitude	Clean, blank scans in both horizontal and vertical directions are observed with no recorded intensity beyond typical background noise.	Under study. The blank scan and lack of intensity imply that the RFOV is empty or that the shutter for the FHST is closed. Some category 2 anomalies have been attributed to commanding errors, reference star magnitude errors, and large HST attitude errors.	Partially corrected. Software and data base changes have eliminated some of these failures but other unexplained ones continue to occur. Category 2 failures are responsible for 16% of all failures since April 1992.
3	Star Not Acquired in RFOV; Magnitude Spikes	Clean, blank scans in both horizontal and vertical directions are observed with recorded intensity spikes typically up to the expected reference star intensity.	Under study. The intensity spikes for this anomaly imply that some object with brightness close to the reference star is in the RFOV, but for whatever reason cannot be acquired. Many of these anomalies have been caused by thresholds being improperly set.	Partially corrected. Software and data base changes have eliminated some category 3 failures identified as threshold problems (see below) but other unexplained category 3 failures continue to occur. Category 3 failures responsible for 16% of all failures since April 1992.
4	Acquired Spoiler Star Outside RFOV; No Intensity Noise	A spoiler star is acquired outside the predicted RFOV.	The true FHST RFOV sizes are not precisely known.	Corrected
5	Reference Star Outside RFOV Due to Attitude Error	Clean, blank scans in both horizontal and vertical directions are observed with no recorded intensity beyond typical background noise (similar to category 2)	The reference star selected had a predicted position too close to the edge of the RFOV. Large HST attitude errors positioned the reference star outside the RFOV.	Corrected
6	Flight Software Command Timing Error	The A channel for FHST data appears empty while the B channel contains the expected A channel data.	Internal FSW had a A/B channel, DF-224 40Hz/1Hz processor timing problem.	Corrected
7	Ground Commanding Error	The FHST update was not issued. No data were available (FHST shutters closed).	An error existed in the set-up of ground software command groups.	Corrected
8	Spoiler Star; Uncertainties of Attitude Position	The acquisition of a spoiler star inside the predicted RFOV.	The spoiler star, with a predicted position outside the RFOV, was relocated inside the RFOV due to spacecraft attitude error.	Corrected

Table A-1. FHST Failure Categories (2 of 2)

Category	Title	Symptoms	Causes	Status
9	Spoiler Object; Not Identified in PASS Star Catalog	The acquisition of a spoiler object inside the predicted RFOV.	1) A star too dim to be in the PASS reference star catalog but bright enough to be acquired by the FHSTs; 2) open clusters, globular clusters, and bright galaxies (none of which are in the PASS star catalog); or 3) very bright planets or stars not predicted to be located in the RFOV, but inside due to large FHST distortion calculation errors.	Corrected for causes 1 and 3. Cause 2 failures can be corrected on a case by case basis using the BADSTARS file. Cause 2 failures of category 9 account for 14% of all failures since April 1992.
10	RFOV Outside the TFOV	Clean, blank scans in both horizontal and vertical directions are observed with no recorded intensity beyond typical background noise.	RFOVs were allowed to extend outside the TFOV. Reference stars could be scheduled outside the TFOV and therefore not acquired.	Corrected
11	Catalog Magnitude Error	Clean, blank scans in both horizontal and vertical directions are observed with no recorded intensity beyond typical background noise (similar to category 2).	The SKYMAP Master catalog, used as the source for the PASS reference star catalog, contained magnitude errors for some reference stars used. Updates using reference stars whose magnitude were too dim to be acquired could be scheduled.	Corrected
12	Potential Artificial Earth Satellite (AES) Interference	A good acquisition of reference star; interruption by bright, moving object, is observed.	Possible AESs. Past suspects included the Space Shuttle, GRO, and TDRS.	Uncorrected. Category 12 failures account for 5% of all failures since April 1992.
13	Threshold Problem, Reference Star Not Observed in RFOV	Clean, blank scans in both horizontal and vertical directions are observed with recorded intensity spikes typically up to the expected reference star intensity (similar to category 3)	The PASS software assigned a FHST threshold setting (3,4,5, and 6) for reference stars assuming the hardware used 3.0, 4.0, 5.0, and 6.0 magnitudes, respectively, as accurate threshold cutoffs. A reference star could be scheduled with an incorrect threshold setting and therefore not acquired.	Corrected
Blanking	FHST Error Box Blanking Problem	A spoiler star, with an expected position inside the RFOV but outside the allowable reference star region, is acquired. FHST breaks track off the spoiler but the reference star is not acquired.	The blanking sizes of each FHST are not precisely known.	Partially corrected. True blanking sizes are currently being studied. Blanking failures account for 24% of all failures since April 1992.
TFOV Problem	Reference Star Too Close to the TFOV Edge	Clean, blank scans in both horizontal and vertical directions are observed with no recorded intensity beyond typical background noise (similar to category 2).	The FHST update was scheduled with the reference star too close to the TFOV edge. The TFOV sizes of each FHST are not precisely known and large flat-field distortion exists near the edges.	Under analysis. TFOV problems account for 6 % of all failures since April 1992.

APPENDIX B - FHST FAILURE SOLUTIONS

This appendix lists the FHST failure solutions that were determined by the tiger team. For each solution, a title and description is provided along with a list of the categories (from Appendix A) affected and descriptions of problems solved and created during the solution process. Solutions are grouped according to the following types:

1. Star catalog issues
2. Hardware properties
3. Commanding problems
4. Implementation of an error box

Table B-1. FHST Failure Solutions - Star Catalog Issues

Title	Description	Categories Affected	Problems Solved	Problems Created
Modified BADSTARS File	Stars were added to a PASS software namelist to prevent a particular star from being selected as a reference star.	3, 9, 11	Stars with SKYMAP catalog magnitude errors (category 11) were placed in the BADSTARS file until SKYMAP master catalog and then run catalog updates became available. Many stars were added as a result of comparing SKYMAP with the TYCHO star catalog. Reference stars located near bright stellar objects not in the PASS star catalog were placed in the file on a case-by-case basis to solve category 9 failures. Particular troublesome reference stars with category 3 failure behavior were also placed in the BADSTARS file to prevent their selection in the future.	The reduction of the number of reference stars available can make FHST update scheduling slightly more difficult.
Updated PASS Star Catalog	The PASS reference star catalog was updated to increase the limiting star magnitude from 6.7 m_v to 7.1 m_v (containing close to 25,000 stars) and finally to 7.5 m_v (containing over 40,000 stars). This magnitude limit was increased based on stars observed by the FHSTs. This change allowed inclusion of stars where the catalog listed a them as very dim but with large errors on the magnitude or variables.	9	The catalog updates eliminated many of the category 9 failures where the spoiler star was too dim to be in the PASS star catalog (see References 6, 8, 9, and 10).	The increased number of potential spoilers for sensitive FHSTs reduced the number of available updates.
Installed SKYMAP Star Catalogs, Versions 3.5 and 3.7	SKYMAP master star catalog has been updated twice since the launch of HST. These newer versions of SKYMAP contained more accurate star data as well as corrections to previous errors in star magnitudes and positions.	11	The SKYMAP updates prevented all previous category 11 failures from reoccurring and allowed the removal of many stars from the BADSTARS file.	None

Table B-2. FHST Failure Solutions - Hardware Properties (1 of 2)

Title	Description	Categories Affected	Problems Solved	Problems Created																																				
Modified FHST Threshold Tolerances	The PASS software data base was modified to increase the tolerances on FHST threshold settings. These tolerances are used to isolate reference stars from spoiler stars.	1, 2, 3	This fix, implemented shortly after launch, greatly reduced the number of timeout failures. By increasing these threshold tolerances, many reference stars previously selected when there were spoilers inside the RFOV were now rejected.	The number of updates that could be scheduled was reduced.																																				
Increased FHST Update Search Times	The FSW data base was modified to increase the FHST update search time for a reference star from 20 seconds to 45 seconds.	1, 2, 3	Some of these time-out failures appeared to have eventually acquired their reference stars. This increase in FHST update search time was thought to eliminate those failures.	None																																				
Used FHST Undesirable Regions	The PASS software data base was modified to apply an undesirable region to the one-third most negative horizontal portion of the FHST-3 FOV. This allowed a reference star to be selected in this region only if no other candidate stars existed.	1, 2, 3	A large number of time-out failures occurred in this region of FHST-3. Avoiding this region was thought to have helped schedule better updates.	By not selecting a reference star in the undesirable region, the reference star selection algorithm was forced to attempt to select a star that may be less preferred by other predetermined criteria.																																				
Installed Rectangular RFOVs	<p>The PASS software was modified to model the dimensions of each FHST's RFOV as rectangles instead of 1.5-degree squares. Hardware acceptance test data show these modifications:</p> <table border="1" data-bbox="347 1115 678 1247"> <thead> <tr> <th>FHST</th> <th>H°</th> <th>V°</th> </tr> </thead> <tbody> <tr> <td>1</td> <td>1.65</td> <td>1.52</td> </tr> <tr> <td>2</td> <td>1.64</td> <td>1.53</td> </tr> <tr> <td>3</td> <td>1.56</td> <td>1.41</td> </tr> </tbody> </table> <p>Operational experiences show the RFOV to be the following for reference star selection and spoiler protection, respectively:</p> <table border="1" data-bbox="347 1360 678 1478"> <thead> <tr> <th>FHST</th> <th>H°</th> <th>V°</th> </tr> </thead> <tbody> <tr> <td>1</td> <td>1.338</td> <td>1.340</td> </tr> <tr> <td>2</td> <td>1.300</td> <td>1.300</td> </tr> <tr> <td>3</td> <td>1.380</td> <td>1.240</td> </tr> </tbody> </table> <table border="1" data-bbox="347 1499 678 1625"> <thead> <tr> <th>FHST</th> <th>H°</th> <th>V°</th> </tr> </thead> <tbody> <tr> <td>1</td> <td>1.818</td> <td>1.553</td> </tr> <tr> <td>2</td> <td>1.808</td> <td>1.563</td> </tr> <tr> <td>3</td> <td>1.728</td> <td>1.443</td> </tr> </tbody> </table>	FHST	H°	V°	1	1.65	1.52	2	1.64	1.53	3	1.56	1.41	FHST	H°	V°	1	1.338	1.340	2	1.300	1.300	3	1.380	1.240	FHST	H°	V°	1	1.818	1.553	2	1.808	1.563	3	1.728	1.443	4	The PASS software change eliminated most of the category 4 failures. The change also greatly improved the quality of update scheduling by allowing better spoiler protection control via data base parameters. It also eliminated awkward data base workarounds.	Occasional update failures caused by the true RFOV sizes not being consistent with the hardware acceptance test data still occur.
FHST	H°	V°																																						
1	1.65	1.52																																						
2	1.64	1.53																																						
3	1.56	1.41																																						
FHST	H°	V°																																						
1	1.338	1.340																																						
2	1.300	1.300																																						
3	1.380	1.240																																						
FHST	H°	V°																																						
1	1.818	1.553																																						
2	1.808	1.563																																						
3	1.728	1.443																																						

Table B-2. FHST Failure Solutions - Hardware Properties (2 of 2)

Title	Description	Categories Affected	Problems Solved	Problems Created
Restricted Reference Star RFOV Positions	PASS software data base modifications were made to restrict the position of reference stars sufficiently away from the RFOV edge.	2, 5	The PASS software change eliminated the category 5 failures. Forcing the reference star towards the interior of the RFOV was also thought to have reduced category 2 failures.	None
Added TFOV Pad	The PASS software was modified to include a pad around the TFOV for spoiler checking. This pad is used when a FHST RFOV is selected near the edge of the TFOV.	8	Eliminated category 8 failures where the spoiler was expected to be outside the TFOV (and therefore not in the RFOV) but came in due to attitude error. (Discussions with the manufacturer revealed that the TFOV can actually extend to 8.5 degrees, although it is not usable for placing reference stars.) The software modification allowed for more control on the size of the TFOV and the removal of complicated data base workarounds.	None
Improved Magnitude to Intensity Conversion Model	The PASS software was modified to more accurately convert very bright planets' and stars' visual magnitudes to voltage intensities for FHST FOV distortion calculations. This improvement eliminated large predicted position error for bright objects.	9	The PASS software change eliminated all category 9 failures caused by very bright planets or stars.	None
Restricted FHST RFOV Centers	The PASS software data base was modified to prevent FHST RFOVs from overlapping the TFOV.	10	The data base modification eliminated all category 10 failures.	None
Improved FHST Threshold Settings	The PASS software was modified to allow the FHST reference star selection algorithm to use more accurate voltage intensity threshold settings instead of rough magnitude approximations. These threshold settings were assigned values based on FHST hardware acceptance test data and operational experience.	13	The PASS software change eliminated category 13 failures and allowed the removal of complicated data base workarounds.	None

Table B-3. FHST Failure Solutions - Commanding Problems

Title	Description	Categories Affected	Problems Solved	Problems Created
Increased Delayed-Mode Update Durations	The PASS software data base was modified to increase the duration of delayed-mode updates to allow sufficient time for full onboard processing.	2	Special time-out failures where a delayed-mode update was scheduled shortly before the HST entered occultation were eliminated. Several of these failures were initially placed in category 2.	None
Corrected Flight Software Command Timing	The FSW was modified to correct the DF-224 40 Hz/1 Hz processor timing problem.	6	The FSW change eliminated all category 6 failures.	None
Modified Ground Command Groups	The operational ground software command groups were changed to prevent a known FHST update commanding error.	7	The modified command groups eliminated all category 7 failures.	None

Table B-4. FHST Failure Solutions - Implementation of an Error Box

Title	Description	Categories Affected	Problems Solved	Problems Created
Implemented FHST Error Box Checks	<p>The error box check is a method implemented in both the ground and FSW to allow the OBC to quickly determine whether or not the desired reference star is being observed by the FHST. The PASS software schedules an update with a reference star inside a special data-base-sized isolation region within the selected RFOV.</p> <p>This isolation region should be equal to the expected FHST hardware blanking size plus the expected HST attitude error. This new reference star isolation algorithm allows for spoiler stars to reside within the RFOV as long as they are outside the specified isolation region. Once isolated, the reference star position in observation coordinates are uplinked to the spacecraft. When the FHST observes a star, the error box check requires that the observed coordinates be directly compared with the uplinked coordinates. If the comparison is successful within the bounds of the anticipated attitude error, the FHST can proceed with the attitude update. If the error box check fails, a break track command is issued, the FHST blanks six or seven scan lines (approximately 0.72 degree) (as described in the RFOV description in the BACKGROUND section), and the search for the reference star continues. Currently, three error box checks are issued each update. The third of the checks must be successful or the update fails. (see Reference 14). This operation was verified in a spacecraft test that occurred during the week of August 12, 1991 (see References 14, 15, and 16).</p>	4, 8, 9	Most spoiler problems occur where the spoiler object is located outside the error box. This change in PASS software increased the number of reference stars available for an FHST update because the required reference star isolation region was reduced.	Spoiler star failures caused by improperly predicted blanking by the FHSTs (blanking category) were introduced.

REFERENCES

1. National Aeronautics and Space Administration (NASA), *HST 1st Servicing Mission Reference Guide*. Sunnyvale, California: Lockheed Missiles & Space Company, Inc.
2. G. L. Welter, "The In-Flight Calibration of the HST Attitude Sensors," *Proceedings of the GSFC Flight Mechanics/Estimation Theory Symposium 1991*, May 1991
3. R. McCutcheon et al., "In-Flight Scale/Distortion Calibration of the Fixed Head Star Trackers," *Proceedings of the GSFC Flight Mechanics/Estimation Theory Symposium 1994*, May 1994
4. Ball Aerospace Systems Division, TM 79-04A, *Users' Guide for the Standard Star Tracker*, June 1981
5. Computer Sciences Corporation (CSC), *Minutes of the Fixed-Head Star Tracker Update Tiger Team Meetings With Ball Aerospace (Final)*, M. Nadelman, October 19, 1990; based on meetings of September 5 and 6, 1990
6. P. Davenport, "HST FHST Intensity to Visual Magnitude Calibration," CSC, Internal Memorandum, August 31, 1990
7. CSC, CSC/TM-88/6103, *Hubble Space Telescope Flight Software Examination for the Pointing Control Subsystem (Revision 2)*, L. Hallock, March 1990
8. P. Davenport, *HST FHST Intensity to Visual Magnitude Calibration II*, CSC, Internal Memorandum, June 6, 1991
9. G. Welter and J. Karl, *HST FHST Intensity to Visual Magnitude Calibration III*, CSC, Internal Memorandum, March 17, 1992
10. G. Welter and J. Karl, *HST FHST Intensity to Visual Magnitude Calibration IV*, CSC, Internal Memorandum, April 15, 1993
11. CSC, *Hubble Space Telescope (HST) POCC Applications Software Support (PASS) FHST Tiger Team Status*, September 7, 1990
12. --, *Hubble Space Telescope (HST) POCC Applications Software Support (PASS) FHST Tiger Team Status*, October 25, 26, 1990
13. --, *Hubble Space Telescope (HST) POCC Applications Software Support (PASS) FHST Tiger Team Status*, February 22, 1991
14. M. Nadelman, *Test SMS and Expected Results for the FSW FHST Error Box Test*, CSC, Presentation, August 1991
15. NASA/Goddard Space Flight Center (GSFC), *Plan for the On-Orbit Test of the Flight Software FHST Error Box Modification*, A. Leibowitz and C. Turner (GSFC) and M. Nadelman (CSC), August 1991
16. M. Nadelman, *Analysis of Results and Recommendations for the FSW FHST Error Box Test*, CSC, Presentation, August 1991

ACKNOWLEDGMENTS

We extend our thanks to the FHST tiger team, which, in addition to the authors, was made up of the following analysts from the HST community: Bill Collier, Paul Davenport, Ray Kutina, Robert McCutcheon, Tom Pfarr, and Milt Phenneger of CSC; Kevin Grady, Joe Hennessy, Bill Ochs, and Mike Wright of GSFC; Mike Brunofski of AlliedSignal Technical Services Corporation; and Theresa Gaston of Jackson & Tull.

We also thank Dick Deters, James McQuerry, and Dave Wagner of Ball Aerospace for their assistance in providing vital information about how FHSTs work and for their assistance in the analysis of some early anomalous data. Special thanks are extended to Michael Gross and Marilyn Newhouse for investigation of software workarounds and checking for software errors. Thanks also go to Robert McCutcheon and Gary Welter for their advice and review, and to Joan McFarland for her tireless efforts in the editing of this paper.



In-Flight Scale / Distortion Calibration of the Hubble Space Telescope Fixed-Head Star Trackers¹

R. McCutcheon,² J. Boia,² M. Gakenheimer,³
L. Hallock,⁴ E. Kimmer,³ S. Murphy,³ and G. Welter²

ABSTRACT

This paper describes an in-flight scale and distortion calibration procedure that has been developed for the Ball Aerospace Systems Division Fixed-Head Star Trackers (FHSTs) used on the Hubble Space Telescope (HST).

The FHST is a magnetically focused and deflected imaging sensor that is designed to track stars as faint as $m_v = 5.7$ over an 8-degree by 8-degree field of view. Raw FHST position measurements are accurate to approximately 200 arcseconds, but this can be improved to 10-15 arcseconds by processing the raw measurements through calibration polynomials that correct for flat field, temperature, intensity, and magnetic field effects. The coefficients for these polynomials were initially determined using ground test data.

On HST the use of three FHSTs is an integral part of the preliminary attitude update procedure required before the acquisition of guide stars for science observations. To this end, FHST-based attitude determination having single-axis errors no worse than 22 arcseconds (1σ) is required.

In early 1991 it became evident that one of the HST FHSTs was experiencing a significant change in its optical scale. By mid-1993 the size of this error had grown to the point that, if not corrected, it would correspond to a maximum position error on the order of 100 arcseconds. Subsequent investigations demonstrated that substantial, uncompensated cubic distortion effects had also developed, the maximum contribution to position errors from the cubic terms being on the order of 30 arcseconds. To ensure accurate FHST-based attitude updates, procedures have been developed to redetermine the FHST scale and distortion calibration coefficients based on in-flight data gathered during normal HST operations. These scale and distortion calibrations have proven very effective operationally, and procedures are in place to monitor FHST calibration changes on a continuing basis.

INTRODUCTION AND BACKGROUND

The Hubble Space Telescope (HST) was launched into low Earth orbit on April 24, 1990. Equipped with an Optical Telescope Assembly (OTA) capable of providing image resolution 10 times sharper than that provided by ground-based telescopes, HST must be able to place science targets into scientific instrument (SI) apertures as narrow as 0.1 arcsecond and maintain stability to an accuracy as high as 0.007 arcsecond averaged over 24 hours.

¹ This work was performed under National Aeronautics and Space Administration (NASA) Goddard Space Flight Center (GSFC) contracts NAS 5-31000 and NAS 5-31500. This paper is declared a work of the U.S. Government and is not subject to copyright protection in the United States.

² Computer Sciences Corporation (CSC), Laurel, Maryland, USA

³ AlliedSignal Technical Services Corporation

⁴ NASA/GSFC, Greenbelt, Maryland, USA

HST is equipped with a variety of attitude sensor and control devices: three Rate Gyro Assemblies (RGAs), three Fixed-Head Star Trackers (FHSTs), three Fine Guidance Sensors (FGSs), five Coarse Sun Sensors (CSSs), two three-axis Magnetic Sensing Systems (MSSs), four Magnetic Torquing Systems (MTSs), and four Reaction Wheels (RWs). Figure 1 shows the locations for most of these instruments and defines the HST V_1 - V_2 - V_3 reference frame. The FGSs, FHSTs, and RGAs provide attitude information during normal operations, whereas the CSSs and MSSs are used as attitude sensors mainly during initial HST deployment and also when the spacecraft is in safemode. The RWs serve as the primary attitude torquing mechanism, and the MTSs are used as momentum dumping devices.

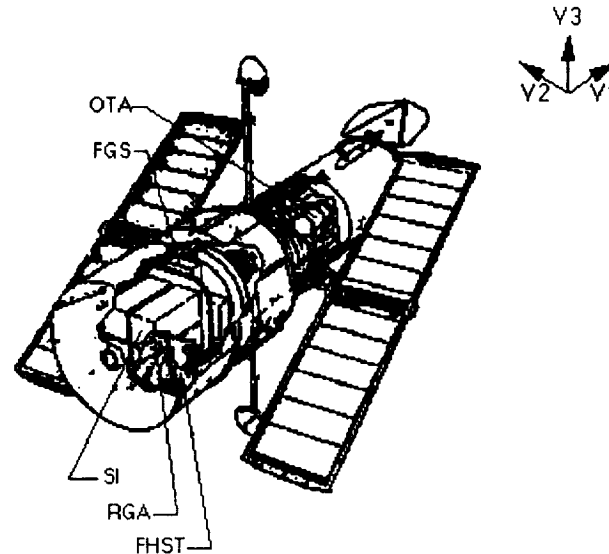


Figure 1. HST and the HST V_1 - V_2 - V_3 Reference Frame

The FGSs are the dominant instruments for attitude control during science operations. They are capable of tracking stars between $m_v = 9$ and $m_v = 14.5$ with a differential accuracy of $\sim .003$ arcsecond after calibration (Welter, 1991b and 1994), and the alignments of the combined FGS field of view (FOV) relative to the SIs currently are known to within ~ 1 arcsecond. At present FGS guide star acquisition requires preacquisition attitude knowledge that is accurate to within ~ 60 arcseconds. Failure to acquire a guide star will result in the loss of a scheduled science observation.

The FHSTs are the primary attitude sensors for determining HST attitude before FGS guide star acquisition. FHST-1 is mounted with its boresight approximately along the $-V_3$ axis, whereas FHSTs 2 and 3 are mounted pointing downwards and backwards in the HST reference frame with boresights that are located in a plane rotated approximately 45 degrees around the V_2 axis away from the V_2/V_3 plane and 30 degrees to either side of the V_1/V_3 plane.

The HST FHSTs are used in two modes. In map mode the trackers scan their FOVs and provide position information for all stars detected over a fixed period of time. The fine attitude determination function of the ground-based HST Payload Operations Control Center Applications Software Support (PASS) system uses these map data to compute an attitude that can be used to initialize (e.g., after initial release from the shuttle) or reinitialize (e.g., during recovery from safemode) the onboard computer's attitude knowledge.

In update mode one or two FHSTs are commanded to locate and track preselected reference stars (one star per tracker), and the flight software uses these stars' measured positions to compute either roll or three-axis attitude updates. Roll updates usually are performed before large slews, and attitude updates are performed following large attitude slews and before attempting FGS guide star acquisition. ([Hallock, 1990] provides a thorough description of how the HST flight software uses FHST data.)

As can be seen from this description, improper knowledge of reference star positioning within the FHST FOV will lead to degraded onboard attitude knowledge and potential failure of FGS guide star acquisition. Failure of FGS acquisition, in turn, will cause a loss of science data. Hence it is critical that the FHSTs be calibrated to perform at the limit of their measuring potential. To this end, FHST-based attitude determination having single-axis errors no worse than 22 arcseconds (1σ) is required (Fallon, 1983).

The present paper describes an in-flight calibration of the HST FHSTs that was undertaken in response to uncompensated scale factor and distortion phenomena that were noted in the FHST measurements following launch--phenomena that on occasion were causing FGS guide star acquisition failures. The following sections provide a general description of the FHST hardware and FHST calibration procedures, an historical recounting of how the scale factor and distortion effects were uncovered and the steps that were taken to reduce these effects to a minimum, and a brief description of future FHST calibration activities along with recommendations for FHST calibrations on other spacecraft missions.

DESCRIPTION OF FHST AND FHST DATA PROCESSING ON HST

The FHST, also known as the NASA standard star tracker, was developed by Ball Aerospace Systems Division (BASD) and has been used as an attitude sensor on numerous NASA missions beginning with the Solar Maximum Mission (SMM). At present, FHSTs are in use on the Compton Gamma Ray Observatory (GRO), the Upper Atmosphere Research Satellite (UARS), and the Extreme Ultraviolet Explorer (EUVE) in addition to HST. A complete description of the FHST can be found in (BASD, 1981).

Employing a 70mm, f/1.2 objective lens, the FHST uses an electronic scan to search its FOV and acquire reference stars. The heart of the FHST is an ITT F4012 RP image dissector. The objective lens forms an image on the dissector's photocathode (Figure 2). Light from star images on the photocathode generates an electron stream that is deflected toward a fixed receiving aperture by magnetic coils. As the magnetic deflecting coils' currents are varied, different active portions of the photocathode direct their electrons toward the aperture and from there to an electron multiplier. Therefore, through proper selection of the coil currents, the light impacting any portion of the photocathode surface can be sampled. The size of the region sampled is the FHST's instantaneous FOV (IFOV) and is defined by the size of the fixed aperture to be 9-arcminutes-by-9-arcminutes.

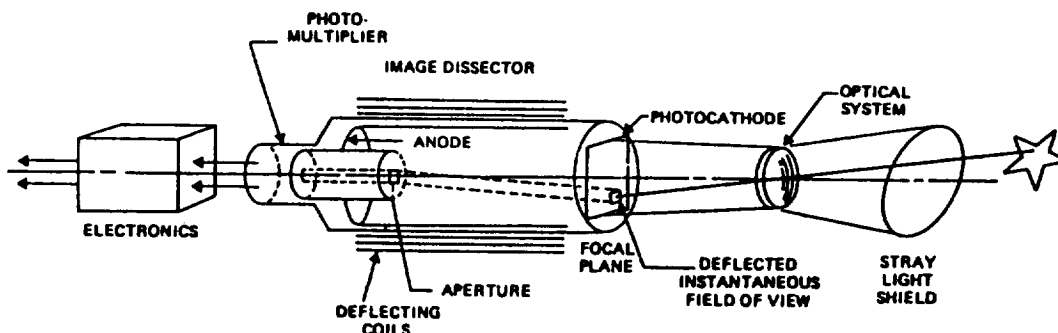


Figure 2. Cutaway Diagram of an FHST

As illustrated in Figure 3, when first turned on or when so commanded, an FHST scans either its 8-degree-by-8-degree total FOV (TFOV) or a ground-commanded 1.5-degree-by-1.5-degree reduced FOV until it encounters an object brighter than a commanded threshold. (These FOV dimensions are approximate. Although BASD designed the FHST to observe stars to $m_v = 5.7$, one of the HST FHSTs has regularly tracked stars as dim as $m_v = 7$ [Davenport, 1991, and Welter, 1992].) The FHST then enters a smaller cross-pattern scan centered on this object and forms output position and intensity information. The FHST will continue to track the object until it leaves the TFOV, its observed intensity falls below the commanded threshold, or a command is issued to break track.

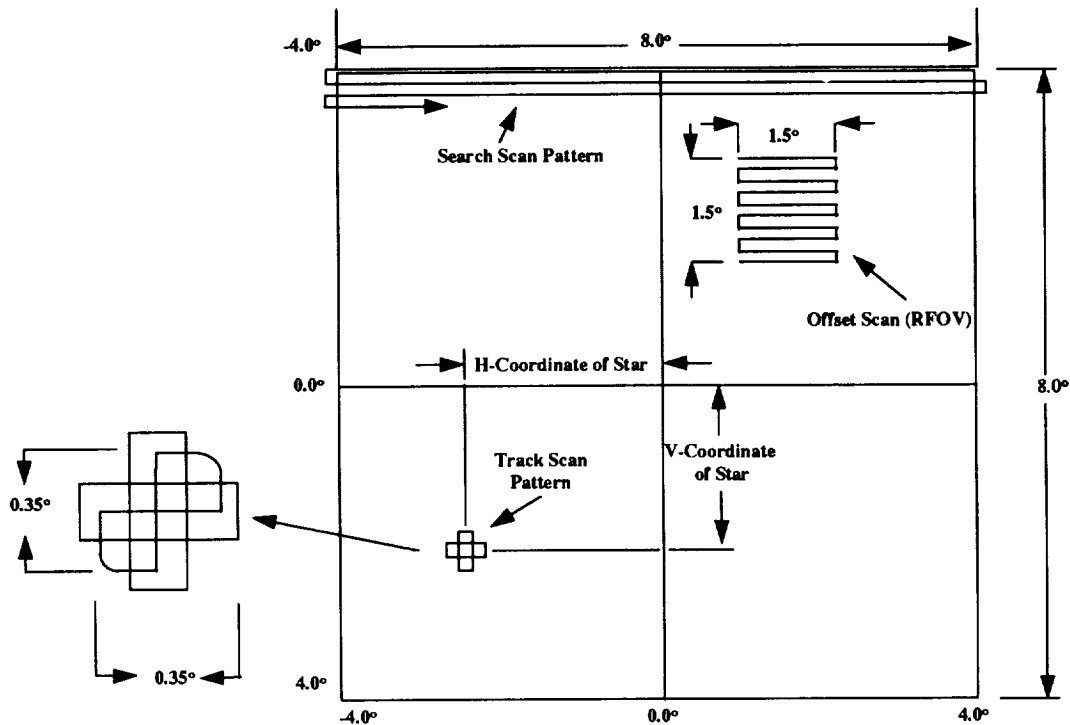


Figure 3. FHST Scan Geometry

Raw FHST vertical (V) and horizontal (H) positions are measured over a range of ± 2048 counts, which can be converted to angular measurements through application of a standard BASD-specified scale factor of 0.002079 degrees per counts. The raw measurements are subject to a variety of distortions that can offset a star's observed position by several hundred arcseconds from its true position. The largest of these are the flat field effects, which result from aberrations in the objective lens and the fact that the positions of stars on a curved celestial sphere are being measured on a plane surface (the photocathode). For the HST trackers, flat field effects are in the range of 300-500 arcseconds.

Temperature changes produce the second largest distortion in raw FHST measurements. At the center of the TFOV, for example, a change in temperature from the operational minimum (-10°C) to the operational maximum ($+50^{\circ}\text{C}$) will result in an apparent position shift of up to 110 arcseconds.

Intensity and magnetic field effects produce smaller distortions in the raw FHST position measurements. For example, a star's position as measured when there is a -0.5 -gauss magnetic field component parallel to the tracker boresight may differ by as much as 5-10 arcseconds from the same measurement made in a $+0.5$ -gauss field. Changes in a star's measured intensity over the tracker's operational range produce shifts that are on the same order.

For any given FHST, BASD characterizes the distorting influences of flat field, temperature, intensity, and magnetic field effects through an extensive series of ground tests whereby the tracker observes a grid of artificial "stars" that are evenly distributed over the TFOV under varying conditions of temperature, intensity, and magnetic field strength. Based on these observations, one can determine a set of distorted-to-true coefficients that can be used in a polynomial calibration function to remove the effects of distortion. BASD traditionally has used a polynomial that requires 190 coefficients per FHST (BASD, 1981). Based on operational experience with the SMM trackers (McCutcheon, 1982), a somewhat simpler version requiring only 48 coefficients per tracker has been adopted for the HST mission:

$$\begin{aligned}
 V_c &= (\alpha_{00} + \alpha_{01}T + \alpha_{02}T^2 + \alpha_{03}I + \alpha_{04}I^2 + \alpha_{05}I^3) + \\
 &\quad (\alpha_{10} + \alpha_{11}T + \alpha_{12}T^2 + \alpha_{13}B)V + (\alpha_{20} + \alpha_{21}T + \alpha_{22}T^2 + \alpha_{23}B)H + \\
 &\quad (\alpha_{30} + \alpha_{31}T)V^2 + (\alpha_{40} + \alpha_{41}T)VH + (\alpha_{50} + \alpha_{51}T)H^2 + \\
 &\quad \alpha_{60}V^3 + \alpha_{70}V^2H + \alpha_{80}VH^2 + \alpha_{90}H^3 \\
 \\
 H_c &= (\beta_{00} + \beta_{01}T + \beta_{02}T^2 + \beta_{03}I + \beta_{04}I^2 + \beta_{05}I^3) + \\
 &\quad (\beta_{10} + \beta_{11}T + \beta_{12}T^2 + \beta_{13}B)V + (\beta_{20} + \beta_{21}T + \beta_{22}T^2 + \beta_{23}B)H + \\
 &\quad (\beta_{30} + \beta_{31}T)V^2 + (\beta_{40} + \beta_{41}T)VH + (\beta_{50} + \beta_{51}T)H^2 + \\
 &\quad \beta_{60}V^3 + \beta_{70}V^2H + \beta_{80}VH^2 + \beta_{90}H^3
 \end{aligned}$$

where

$$\begin{aligned}
 V, H &= \text{raw vertical and horizontal position (counts)} \\
 V_c, H_c &= \text{calibrated vertical and horizontal positions (counts)} \\
 T &= \text{temperature (volts)} \\
 I &= \text{intensity (volts)} \\
 B &= \text{magnetic field component parallel to tracker boresight (gauss)} \\
 \alpha_{ij}, \beta_{ij} &= \text{distorted-to-true calibration coefficients}
 \end{aligned}$$

GSFC Flight Dynamics Facility (FDF) personnel used the original BASD test data for the HST trackers to determine coefficients for this simplified calibration equation (Challoner, 1983 and 1984; McLaughlin, 1989). After application of the computed coefficients to the test data, they found root-mean-square (rms) residuals over all observations in the range of 6-9 arcseconds for the three HST FHSTs. Similarly, they found maximum residuals in the range of 23-38 arcseconds, with the maximum residuals generally located in the corners of the TFOV. (When the computed coefficients were applied only over an 8-degree circular FOV, the maximum residuals were reduced to between 17 and 19 arcseconds.)

In addition to determining distorted-to-true calibration coefficients (α, β), FDF personnel determined inverse true-to-distorted coefficients (α, β)⁻¹ that can be used to add the corrupting distortion effects to ideal, "true" star positions (Challoner, 1984; McLaughlin, 1989). The HST PASS mission scheduling (MS) software is responsible for selecting FHST reference stars. For each reference star, the MS software in combination with the flight software uses these inverse coefficients to determine where a selected reference star should appear in the FHST TFOV (Hallock, 1990). The flight software then computes attitude updates based on a comparison of expected with actual reference star positions. Any inaccuracies in the FHST calibration coefficients will translate directly into attitude errors that will reduce the efficiency of FGS guide star acquisition.

HISTORY OF FHST SCALE FACTOR/DISTORTION CHANGES ON HST

The requirements for HST attitude determination and attitude sensor calibration (Hallock et al., 1987) made no provision for in-flight updates to the FHST scale factors and/or distortion coefficients. These were to be used "as is," and only the FHST alignment matrices were to be updated regularly based on in-flight data. (For a discussion of the post-launch calibration of the HST attitude sensors, see [Welter, 1991a]. For a discussion of early postlaunch difficulties with the HST FHSTs, see [Nadelman, 1994].)

By early 1991, however, it had become apparent that ground attitudes computed using FHST-3 data were less accurate than those computed using data from the other two trackers. In addition, on occasion FHST-3 was having difficulty locating its commanded reference stars. By computing angular separations between observed FHST-3 stars and comparing these to angular separations computed from reference star catalog information, it was determined that the baseline FHST scale factor, 0.002079 degrees per count, understated the true scale by about 0.25 percent. From this point forward, PASS personnel began monitoring the scale factors for all three FHSTs on a regular basis.

Figure 4 shows the development of scale factor changes from shortly after launch through the middle of 1993. This figure shows clearly that the FHST-1 and FHST-2 scale factors have remained essentially constant, albeit differing slightly from their design values, whereas the FHST-3 scale factor increased rapidly through the end of 1991. Since that time the scale factor has continued to increase, although somewhat more slowly, and by August 1993 it had reached a level 0.45 percent above its original value. For a star near the corner of the FHST TFOV, such an increase corresponds to a position change on the order of 100 arcseconds; errors of this magnitude are quite large in comparison to the attitude accuracy required for successful FGS guide star acquisition.

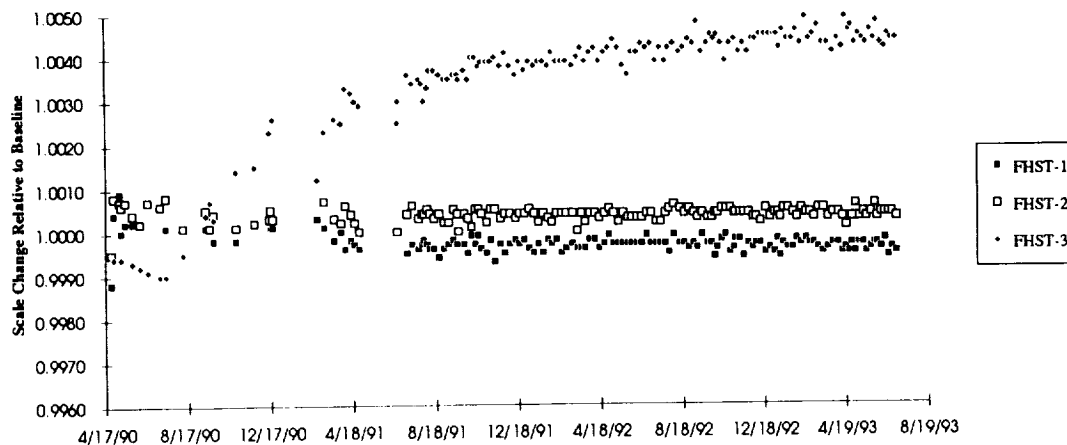


Figure 4. FHST Scale Factor Changes Relative to Baseline Value

PASS personnel made appropriate changes to the HST project data base (PDB) to reflect these increases in the FHST-3 scale factor, and these changes greatly improved the accuracy of attitudes computed using FHST-3 data, thereby improving the reliability of FGS guide star acquisition. By the middle of 1992, however, it became apparent that even with PDB updates for the new scale factor, FHST-3 still was not performing at the same level as FHST 1 or 2. This led to the suspicion that the FHST-3 calibration coefficients themselves had changed since launch.

To investigate possible changes in the FHST-3 coefficients, PASS personnel modified the FHST alignment software (FALIGN) to compare observed and reference FHST star positions. The input to FALIGN consists of observed and reference star vectors as well as attitude information generated by the PASS fine attitude determination software (FINATT). (The observed vectors have already been corrected for distortion within FINATT.) FALIGN begins by separating the observations into constant

attitude frames, and for each frame it then performs an optimal rotation to transform the reference vectors from the geocentric inertial (GCI) reference frame to the FHST reference frame. (The data for the PASS analysis were usually taken with the vehicle under RGA control. RGA bias characteristics ensure attitude stability on the order of 2.5 arcseconds maximum average error over the time frame of a typical FHST map.) FALIGN next converts the vectors to V and H coordinates and forms residuals by taking the differences between the observed and reference positions.

Figures 5, 6, and 7 show the residual plots in V and H for all three trackers using post-HST Servicing Mission data from 1993.351 through 1994.062. (Data in these figures were processed using the updated FHST-3 scale factor. The plots were subjected only to minimal editing and include data for 3015, 2868, and 2005 stars for FHSTs 1, 2, and 3, respectively.) These figures show, first of all, the expected result that the largest residuals for all three trackers are at the edges of the TFOV. The slight slope in the residuals for FHSTs 1 and 2 may reflect the effect of slightly off-nominal scale terms already observed in Figure 4. Most dramatically, however, Figure 7 clearly shows the effects of uncompensated distortions as large as 30 arcseconds in regions that are still far from the edges of the TFOV.

With this evidence of uncompensated distortion in hand, PASS personnel made further modifications to FALIGN to allow it to compute new FHST flat field coefficients (α_{i0}, β_{i0} , $i=1-10$) using a standard linear least-squares approach. To carry out this solution, it is necessary first to "de-calibrate" the observed star positions using the inverse (i.e., true-to-distorted) coefficients in order to recover the original raw FHST V and H positions. Temperature, intensity, and magnetic field data are not readily available to FALIGN, and thus it was not possible to consider effects due to these factors in this analysis.

PASS personnel used FALIGN to compute new coefficients, and the distortion coefficients in the HST PDB were updated with this new solution in December 1993. That the new coefficients improve the accuracy of FHST-3 measurements is shown in Figure 8, which plots residuals for the same data as in Figure 7. It should be noted that the largest FHST-3 residuals are now at the edges of the TFOV and that the general character of Figure 8 is now similar to that of Figures 5 and 6.

Figures 9 and 10 provide a three-dimensional visualization of the combined V and H residuals (using the same data as in Figures 7 and 8) over the FHST-3 TFOV using the old and new distortion solutions. Now, however, the TFOV has been subdivided into roughly 1-degree-by-1-degree squares, and the residuals for stars in each square have been combined to form local rms residuals. These figures demonstrate the "flattening" effect of the new solution in the inner portions of the TFOV, and they also clearly show the expected result that the corners of the TFOV are subject to the largest distortions.

Operational experience with the new FHST-3 calibration solution confirms what is illustrated by Figures 8 and 10: the new scale factor and distortion coefficients have improved the accuracy of attitudes computed using FHST-3 data. With this new distortion solution, HST can continue its science operations with increased confidence that FGS guide star acquisition will not fail because of degraded FHST performance.

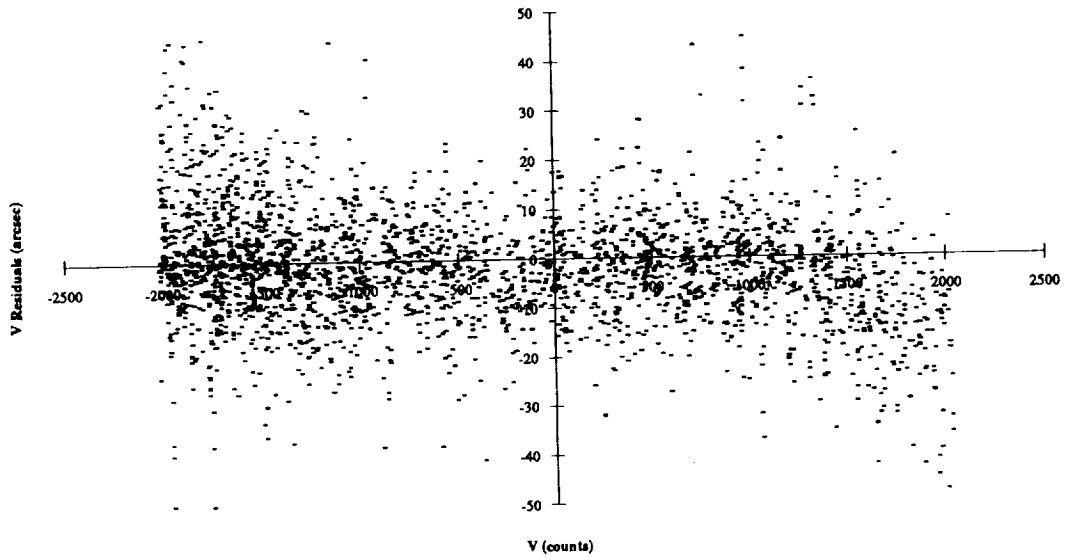


Figure 5a. FHST-1 V Residuals vs. V

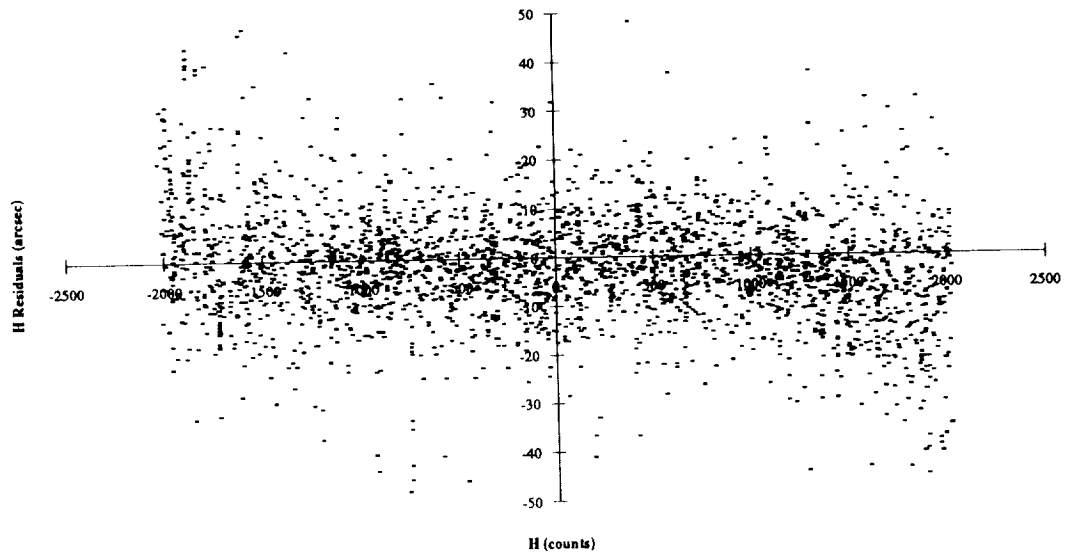


Figure 5b. FHST-1 H Residuals vs. H

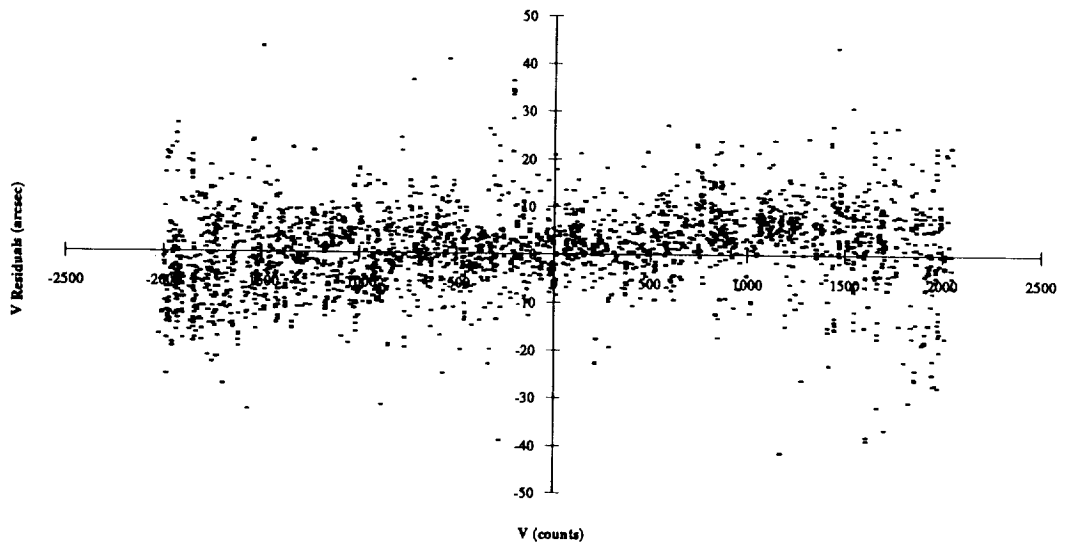


Figure 6a. FHST-2 V Residuals vs. V

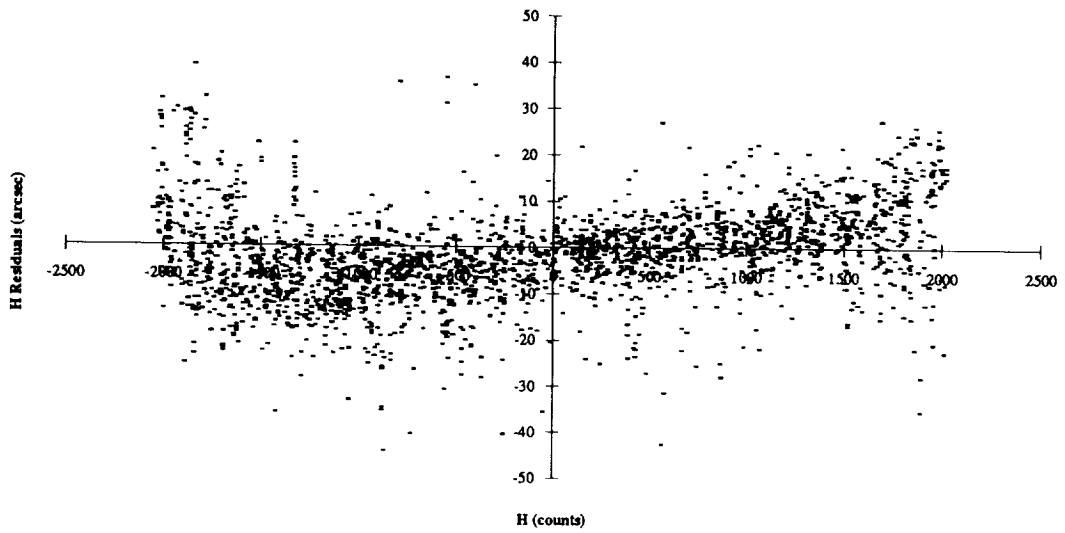


Figure 6b. FHST-2 H Residuals vs. H

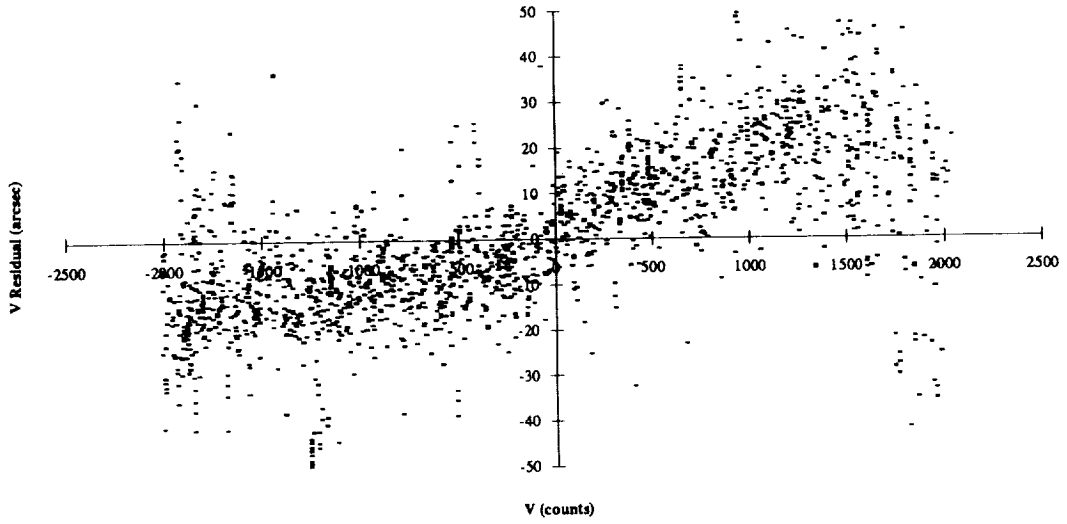


Figure 7a. FHST-3 V Residuals vs. V

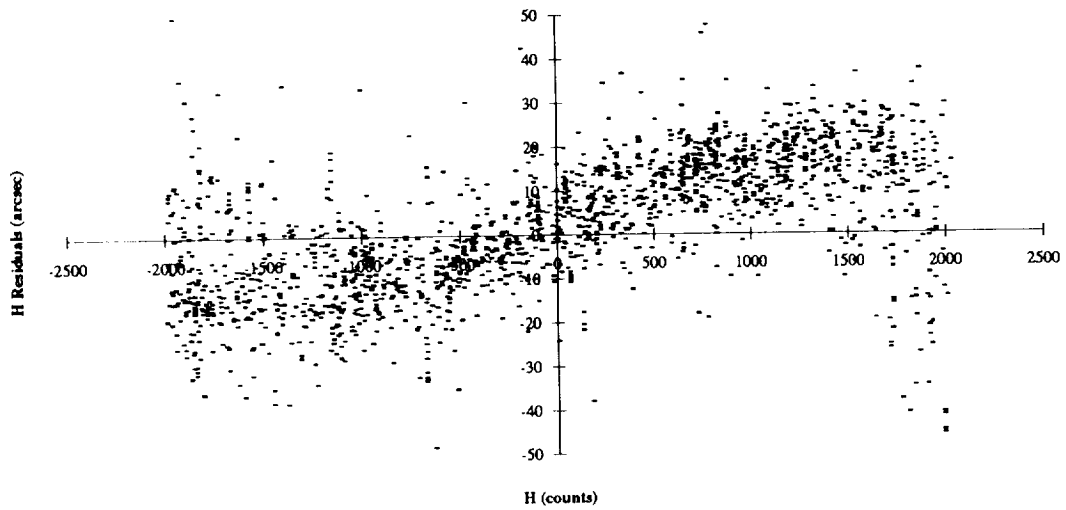


Figure 7b. FHST-3 H Residuals vs. H

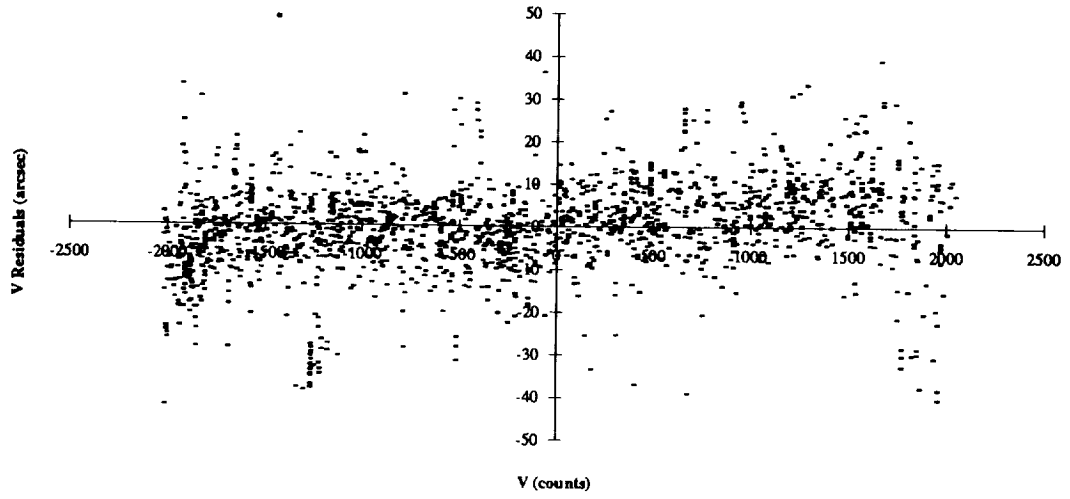


Figure 8a. FHST-3 V Residuals vs. V With New Calibration

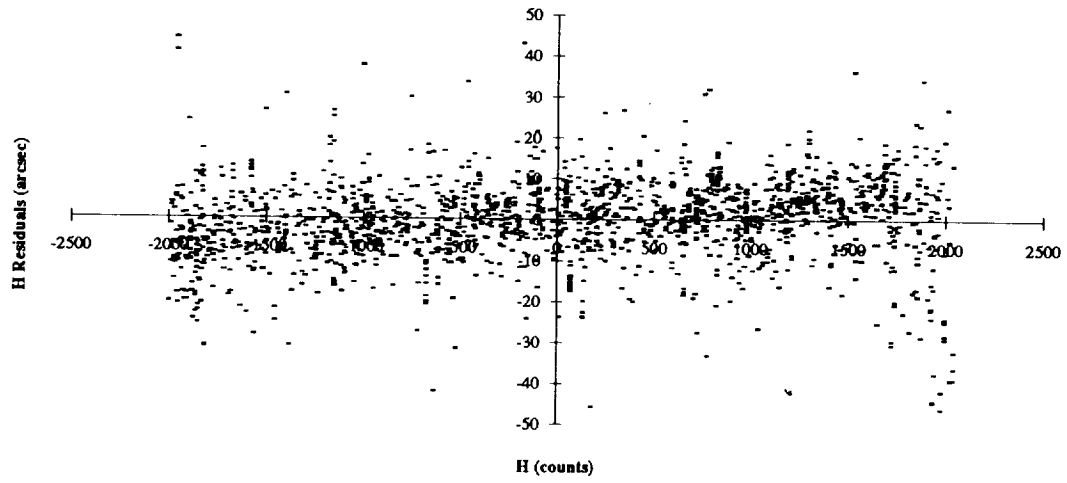


Figure 8b. FHST-3 H Residuals vs. H With New Calibration

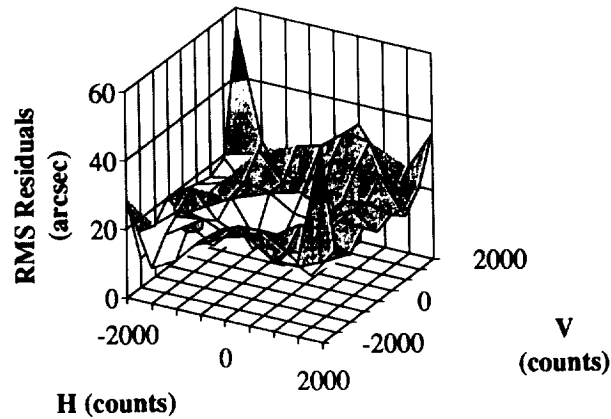


Figure 9. FHST-3 Local rms Residuals With Old Calibration

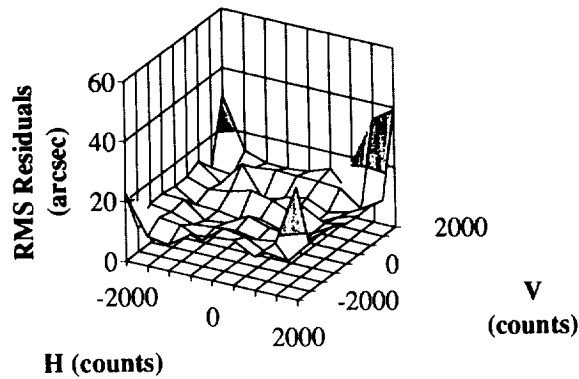


Figure 10. FHST-3 Local rms Residuals With New Calibration

CONCLUSIONS

The in-flight FHST scale factor and distortion calibration described in this paper has greatly improved the reliability of FHST-3 for use in HST attitude determination and control. To ensure trouble-free acquisition of FGS guide stars and, hence, science data, HST PASS personnel intend to monitor the scale and distortion of all three FHSTs throughout the rest of the HST mission.

The primary conclusion to be drawn from this experience with the HST FHSTs is that the distortion and scale characteristics of FHSTs under flight conditions may differ from those on the ground. Further evidence in support of this conclusion comes from the GRO, EUVE, and UARS missions (Davis, 1992 and 1993; Hashmall, 1993), which have reported similar changes in their FHSTs. GRO, in particular, has experienced FHST scale factor changes far above those described here for FHST-3. A secondary conclusion is that it is possible to adjust the FHST calibration coefficients by performing a calibration using in-flight data, confirming the experience of Davis (1992 and 1993) and Hashmall (1993).

The recommendation that follows from these conclusions is that future missions equipped with FHSTs should be prepared to verify scale factor and distortion characteristics as part of the normal post-launch

attitude sensor alignment and calibration sequence. This monitoring process and, if necessary, recomputation of scale and distortion should be repeated at periodic intervals.

A new generation of charge-coupled device (CCD) star trackers may ultimately replace FHSTs as the standard NASA star tracker, and it is uncertain how many more NASA missions will be equipped with FHSTs. Whether or not the new CCD trackers will have scale and distortion characteristics similar to those of the FHST has yet to be seen, but it would be prudent for users of these new trackers to be prepared for possible postlaunch calibration changes.

ACKNOWLEDGMENT

The authors wish to acknowledge the work done by the HST PASS operations team that gathered the data used in this study.

REFERENCES

- BASD, "Users' Guide for the Standard Star Tracker," TM79-04A, June 1981.
- E. Challoner and S. McLaughlin, *Results of Processing Space Telescope (ST) Fixed-Head Star Tracker (FHST) Calibration Data*, CSC, CSC/TM-83/6111, December 1983.
- E. Challoner, S. McLaughlin, and S. Talukdar, *Final Space Telescope Fixed-Head Star Tracker Inverted Calibration Coefficients*, CSC, CSC/TM-84/6073, June 1984.
- P. Davenport, *HST FHST Intensity to Visual Magnitude Calibration II*, CSC memorandum, June 6, 1991.
- W. Davis, J. Hashmall, and R. Harman, *Recent Goddard Space Flight Center (GSFC) Experience with On-Board Calibration of Attitude Sensors*, 43rd Congress of the International Astronautical Federation, IAF-92-0049, August 1992.
- W. Davis, J. Hashmall, and R. Harman, *Postlaunch Calibration of Spacecraft Attitude Instruments*, AAS/GSFC International Symposium on Space Flight Dynamics, AAS 93-325, April 1993.
- L. Fallon, *Space Telescope POCC Applications Software Support (PASS) Functional Requirements (Revision B)*, CSC, CSC/SD-82/6069, September 1985.
- L. Hallock et al., *Space Telescope POCC Applications Software Support (PASS) Requirements Specification (Revision E)*, CSC, CSC/TM-82/6045, September 1987.
- L. Hallock, *Hubble Space Telescope Flight Software Examination for the Pointing Control Subsystem (Revision 2)*, CSC, CSC/TM-88/6103, March 1990.
- J. Hashmall, W. Davis, and R. Harman, *The Attitude Accuracy Consequences of On-Orbit Calibration of the Extreme Ultraviolet Explorer Attitude Sensors by the Flight Dynamics Facility at Goddard Space Flight Center*, AAS/AIAA Spaceflight Mechanics Meeting, AAS 93-103, February 1993.
- R. McCutcheon and C. Anderson, *Analysis of Calibration Procedures for the Space Telescope Fixed-Head Star Trackers*, CSC, CSC/TM-82/6173, December 1982.
- S. McLaughlin and J. Epelboim, *Calibration of Fixed-Head Star Trackers (FHSTs) Using STARCAL*, CSC, CSC/SD-89/6164, September 1989.

M. Nadelman, J. Karl, and L. Hallock, *Fixed-Head Star Tracker Attitude Updates on the HST*, Proceedings of the GSFC Flight Mechanics / Estimation Theory Symposium 1994, May 1994.

G. Welter, *The In-Flight Calibration of the Hubble Space Telescope Attitude Sensors*, Proceedings of the GSFC Flight Mechanics / Estimation Theory Symposium 1991, NASA Conference Publication 3123, May 1991.

G. Welter, L. Abramowicz-Reed, A. Guha, L. Hallock, and E. Kimmer, *The In-flight Calibration of the Hubble Space Telescope Fine Guidance Sensors*, Proceedings of the Third International Symposium on Spacecraft Flight Dynamics, ESA Publication SP-326, October 1991.

G. Welter and J. Karl, *HST FHST Intensity to Visual Magnitude Calibration III*, CSC memorandum Ref: 20:0292-058-GW, March 1992.

G. Welter, L. Abramowicz-Reed, A. Guha, L. Hallock, and E. Kimmer, *The In-flight Calibration of the Hubble Space Telescope Fine Guidance Sensors II (A Success Story)*, Proceedings of the GSFC Flight Mechanics / Estimation Theory Symposium 1994, May 1994.

A Long-Baseline Method for HST Gyro Drift Rate Bias Calibration*

John J. Boia
Gary L. Welter
Computer Sciences Corporation

Martin F. Gakenheimer
AlliedSignal Technical Services Corporation

ABSTRACT

The routine on-orbit calibration of the Hubble Space Telescope (HST) rate gyro assemblies (RGAs) has depended on several related algorithms for drift rate bias calibration. The gyros have exhibited time-varying biases, which must be regularly corrected to maintain pointing stability. Currently, gyro drift parameters are uplinked to the spacecraft every 1-2 days for low rate mode and every 7 days for high rate mode. In order to minimize the impact of frequent calibrations on the HST science schedule, we have refined the gyro calibration algorithms and data collection schemes to reduce the amounts of telemetry data and processing time required for accurate bias calibration. We present a review of the evolution of the gyro calibration algorithms, with particular attention to what we have called the long-baseline bias (LBBIAS) technique, and describe the relative success of these methods in maintaining spacecraft stability.

*This work was supported by the National Aeronautics and Space Administration (NASA) / Goddard Space Flight Center (GSFC), under Contract NAS 5-31500.

**THE IN-FLIGHT CALIBRATION
OF THE HUBBLE SPACE TELESCOPE FINE GUIDANCE SENSORS - II
(A SUCCESS STORY)**

G. Welter
Computer Sciences Corporation

L. Abramowicz-Reed
Hughes Danbury Optical Systems

A. Guha
AKG Incorporated

L. Hallock
National Aeronautics and Space Administration / Goddard Space Flight Center

and E. Kimmer
AlliedSignal Technical Services Corporation

ABSTRACT

The Hubble Space Telescope's fine guidance sensors (FGSs) are unique in the performance levels being attempted; spacecraft control and astrometric research with accuracies better than 3 milliarcseconds (mas) are the ultimate goals. This paper presents a review of the in-flight calibration of the sensors, describing both the algorithms used and the results achieved to date. The work was done primarily in support of engineering operations related to spacecraft pointing and control and secondarily in support of the astrometric science calibration effort led by the Space Telescope Astrometry Team. Calibration items of principal interest are distortion, sensor magnification, and relative alignment. An initial in-flight calibration of the FGSs was performed in December 1990; this calibration has been used operationally over the past few years. Followup work demonstrated that significant, unexpected temporal variations in the calibration parameters are occurring; provided good characterization of the variations; and set the stage for a distortion calibration designed to achieve the full design accuracy for one of the FGSs. This full distortion calibration, using data acquired in January 1993, resulted in a solution having single-axis residuals with a standard deviation of 2.5 mas. Scale and alignment calibration results for all of the FGSs have been achieved commensurate with the best ground-based astrometric catalogs (root-mean-square error ~ 25 mas). A calibration monitoring program has been established to allow regular updates of the calibration parameters as needed.

1. INTRODUCTION AND BACKGROUND

The Hubble Space Telescope (HST) began its mission in April 1990. The ultimate scientific goals require relative pointing accuracy of order 3 milliarcseconds (mas) for target objects within the telescope's 0.5-degree-diameter field of view (FOV). This high accuracy is achieved using the spacecraft's fine guidance sensors (FGSs), manufactured by Hughes Danbury Optical Systems (HDOS), which allow the spacecraft to maintain pointing relative to a preselected set of guide stars. The milliarcsecond-level pointing requirements dictate equally demanding requirements for the FGS calibration algorithms and procedures. Refs. 1 and 2 presented a summary of the status of our calibration efforts as of mid-summer 1991, at which time calibration results had not yet achieved the design accuracy level. This paper presents the results of our continued calibration work through the time of the HST First Servicing Mission (FSM) at the end of 1993.

Besides a calibration error level an order of magnitude above the design level, Refs. 1 and 2 also reported initial indications of unexpected temporal variations in the FGS calibration parameters. The variations, based on a comparison of data taken in December 1990 and May 1991, were noted in both optical field angle distortion (OFAD) of the individual FGSs and the relative alignments of the FGS FOVs. The OFAD changes were detected at essentially the 1σ noise level (~ 30 mas) of the reference catalog used for the calibrations, whereas the alignment changes were about a factor of seven above the noise. Because of the low level of

certainty in the initial OFAD change detection, precise differential analysis of apparent motions of the same target stars from the preceding year was performed in December 1991. This analysis, being independent of the ground-based catalog, was able to verify the previously detected OFAD change rate at a level an order of magnitude above noise.

Section 5 discusses the results of our December 1991 and subsequent analyses of FGS calibration variation. At the time of our verification of the sensor changes, the HST Project System Engineering Board (HPSEB) found the detected level of variation significantly disturbing and consequently established a special working group to analyze, characterize, and, if possible, explain the changes. Significant support for the efforts of the FGS Working Group (FGSWG) was provided from many sources. Besides the current authors, the group consisted of, or received support from, HDOS optical analysts and engineers, members of the Space Telescope Astrometry Team (STAT), representatives of the HPSEB, and staff scientists at the Space Telescope Science Institute (STScI). The efforts of the working group over the past 2 years have resulted in substantial advances in our understanding of the functioning of the FGSs and our ability to maintain a precise level of calibration for them. We believe that this enhanced understanding will prove particularly important for the operation of the HST during the post-FSM era.

Each of the various subgroups within the FGSWG had its own area of particular concern. Not surprisingly, these areas overlapped to a considerable extent. The particular goal of the authors of this paper was to establish an FGS calibration program adequate to meet the operational needs of the HST mission as a whole. The calibration software used for this work is part of the HST Payload Operations Control Center (POCC) Applications Software Support (PASS) system developed by Computer Sciences Corporation (CSC); Ref. 3 documents the PASS system requirements. Analyses by the STAT were analogous to our own but focused on the use of the FGS system, and particularly FGS-3, as a tool for doing high-precision astrometric science. To distinguish our work from that of the STAT, we refer in this paper to the results of the two groups as the PASS and STAT solutions, respectively. HDOS analysts provided technical expertise for understanding the hardware, both of the FGSs and of the primary and secondary mirror structure of the telescope. The calibration analyses performed by

the PASS and STAT groups were done in friendly competition. The work was a competition in that the details of the algorithms and software were developed independently and thus could be used for mutual verification. The competition was friendly in that the verification and exchange of results were done on a regular basis. This approach provided valuable feedback for both groups, allowing early detection of analysis errors and a more timely arrival at our mutual goals.

2. THE FINE GUIDANCE SENSORS

The heart of the HST's pointing control system (PCS) is the set of FGSs manufactured specifically for use on the HST by HDOS. A description of FGS design and operation is available in Ref. 4, with indepth descriptions available in Ref. 5. We limit ourselves here to a high-level summary needed as a foundation for the results presented in the rest of the paper. The FGS FOVs are restricted to the outer 4-arcminute annulus of the HST's full FOV. Each FGS FOV is an arc with an azimuthal range of 82 degrees and a radial range extending from 10 arcminutes to 14 arcminutes relative to the primary optical axis of the telescope. Figure 1 illustrates the FOVs of the FGSs as they look out to the celestial sphere. The axis labels (V2,V3) indicate the HST coordinate frame; the third axis, referred to as V1, corresponds to the optical axis and points out to space. The visual magnitude (m_v) range for guide stars usable by the FGSs is approximately 9 to 14.5 m_v . The precision of the FGS system, ~ 3 mas when fully calibrated, follows from its design as an amplitude interferometer using

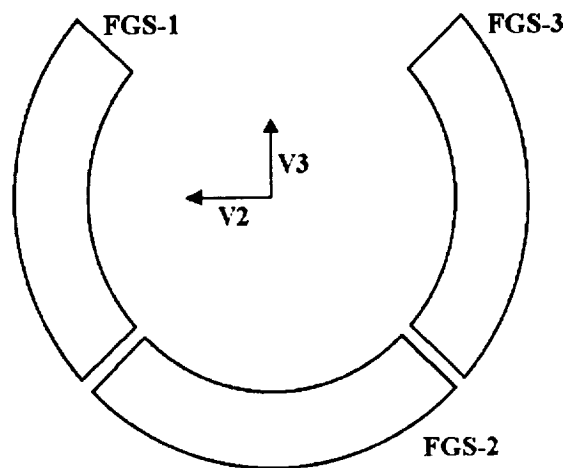


Figure 1. FGS fields of view (looking out to the celestial sphere)

Koester's prisms combined with photomultiplier tubes. Standard pointing control procedure during scientific observations is to use two of the FGSs to maintain guidance of the spacecraft. The remaining FGS is available for precise astrometric observations, the dim limit for astrometry being $\sim 17 m_v$.

Figure 2 illustrates the coordinate system of an FGS as it maps to the actual hardware and telemetry from the spacecraft. Each FGS coordinate frame is defined as a right-handed $x/y/z$ system with the z -axis pointed approximately along the HST optical axis. Each FGS has a 5-arcsecond-by-5-arcsecond instantaneous field of view (IFOV) that can be commanded to a selected position within the total FGS FOV. The instantaneous position of the center of the IFOV is determined by the angles θ_A and θ_B in Figure 2. The lengths of the "lever arms" δ_A and δ_B indicated in Figure 2 map onto specific aspects of the hardware design; for the purposes of this discussion the lever arms may be thought of as rigid, hinged rods whose rotations move the IFOV about in the total FOV. Using spherical trigonometry (e.g., see Ref. 6), the equations that transform the angles θ_A and θ_B into standard spherical polar coordinate angles ρ and ϕ can be derived:

$$\rho = \cos^{-1} [\cos(\delta_A) \cos(\delta_B) - \sin(\delta_A) \sin(\delta_B) \cos(\theta_B - (\theta_A - \theta_{A0}))] \quad (1)$$

$$\phi = (\theta_A - \theta_{A0}) + \cos^{-1} [(\cos(\delta_B) - \cos(\delta_A) \cos(\rho)) / (\sin(\delta_A) \sin(\rho))] \quad (2)$$

where θ_{A0} is an offset parameter to be determined via the calibration process. (An analogous offset parameter for θ_B is not required because any constant term added to both θ_A and θ_B is observationally indistinguishable from a rotation of the sensor; this can be absorbed in the subsequent alignment calibration.) The FGS can detect star light only through the IFOV. A star image falling within the inner 20 mas of the IFOV will produce a significant interferometric signal. The FGS is said to be in fine lock (FL) when so measuring a star's direction. Further spherical trigonometric manipulation is needed to adjust for the star's measured position relative to the center of the IFOV. Although included in our data analysis, these complications will not be considered here; rather the coordinates ρ and ϕ will be treated as if they were the coordinates of the measured star position in the FGS FOV. The equations that transform ρ and ϕ

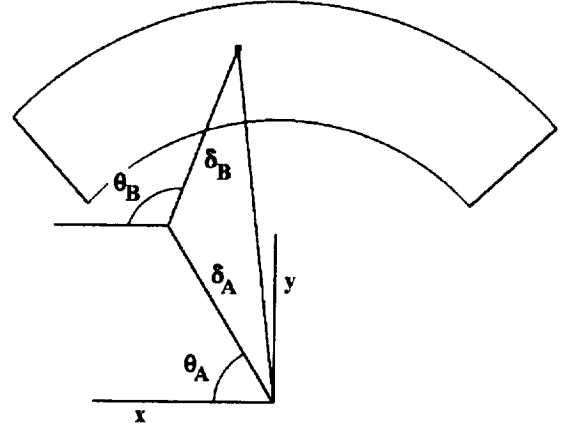


Figure 2. FGS coordinate system

into the x and y Cartesian elements of an object space unit vector are

$$x = \sin(\rho/M) \cos(\phi) \quad (3)$$

$$y = \sin(\rho/M) \sin(\phi) \quad (4)$$

where M , the magnification of the HST/FGS system, is approximately 57.3. We have found that M may be taken as fixed during calibration of the sensors, with scale adjustments being introduced via changes to the parameters δ_A and δ_B .

A second mode of FGS operation, coarse track (CT) mode, is also available. In this mode the center of the IFOV is commanded to nutate about the true star position in such a way that the edges of the IFOV cut across the image of the star in a symmetric pattern. The coordinates ρ and ϕ are then estimated as the center of the nutation circle. The estimated design accuracy of determining star positions using CT mode is approximately 20 mas. Because CT mode is less sensitive to spacecraft-jitter-induced loss of lock than is FL mode, it is sometimes used in observing situations for which extreme pointing precision is not required.

3. CALIBRATION ALGORITHMS

3.1 Distortion and Scale Determination

The distortion and scale calibration of the FGSs is divided into two phases. The first (also called "mini") phase uses ground-based astrometric observations as reference information and is thereby limited by the accuracy of those data. The second

(also called "full") phase goes beyond the limitations of ground-based astrometric work, the goal being to achieve the design precision of the FGS system. To date, full-OFAD calibration has been performed only for FGS-3, the FGS selected for use in astrometric science. A phase 1 scale calibration for an FGS follows immediately as part of a mini-OFAD calibration; the ground-based observations serve to define the absolute scale for the solution. Phase 2 scale determination, which is planned to be based on asteroid observations and associated precise theoretical ephemerides, has not been performed for any of the FGSs as of the time of this writing. Refs. 1 and 2 describe the algorithm and procedures intended for that calibration.

The algorithm used for OFAD calibration is a constrained two-dimensional least-squares algorithm based on the technique presented in Ref. 7. The fundamental input data are FGS observations of stars in an open cluster. The data are taken over a number of spacecraft pointings. Any given star may therefore be observed in multiple locations in the FGS FOV during the course of the entire sequence. Before being processed through the calibration algorithm, the data are corrected for the effects of velocity aberration using a fully relativistic formulation (e.g., see Ref. 8). The approach thereafter is to minimize a loss function, L , subject to certain constraints applied to the associated state vector. The loss function can be expressed as

$$L = \Sigma \{ [W_{ij} - D(W_{ij}, S) - A_j X_i]^2 / \sigma_{ij}^2 \} \quad (5)$$

where

- W_{ij} = object space position of star i in observation set j (as determined by equations 1 through 4)
- $D(W_{ij}, S)$ = OFAD correction vector function
- S = OFAD correction function parameter set
- A_j = attitude transformation matrix between attitude frame j and an arbitrarily specified standard frame
- X_i = "true" direction vector for star i in the standard frame
- σ_{ij} = measurement uncertainty for star i in set j

and the summation is done over all stars and frames. (The term "frame" here refers to data taken in a single orbit, during which a single pair of guide stars is used to control the vehicle's attitude.) For HST

OFAD calibration, the correction function $D(W_{ij}, S)$ has been parameterized as separate polynomials in the x and y Cartesian projections of W ; the set $\{S\}$ is the corresponding set of polynomial coefficients.

The state vector for a mini-OFAD calibration (which can in principle be done with a single spacecraft pointing and each star observed only once) consists of the set $\{S, A, \delta_A, \delta_B, \theta_{A0}\}$, i.e., the polynomial coefficients, attitude transformation matrices, and three star selector parameters. The vector set $\{X\}$ is provided as a priori knowledge from ground-based observations. It need be accurate only differentially; any systematic errors in $\{X\}$ will be absorbed in the matrices $\{A\}$. Three constraints must be applied because any average translation or rotation introduced into the function D via changes to $\{S\}$ would be indistinguishable from a systematic rotation of the spacecraft applied to all matrices $\{A\}$; without constraints, the associated matrix inversion problem would be singular (or nearly so) with a nullity of 3. To select a unique solution from an infinite potential family of solutions, we impose constraints on the elements $\{S\}$ such that the calculated change in D relative to an initial estimate has zero translation and rotation content when averaged across the FGS FOV.

The full-OFAD calibration procedure extends the mini-OFAD procedure so as to include the vector set $\{X\}$ as part of the state vector, thereby eliminating all errors associated with ground observations. Because the reference frame for $\{X\}$ is arbitrary, one of the attitude matrices is eliminated by selecting the associated observation frame as the standard frame. Unlike mini-OFAD calibration, full-OFAD requires multiple frames of data and significant variation of the spacecraft attitude between frames. In particular, the full-OFAD algorithm requires that there be significant variation in spacecraft roll to detect any shear effects in distortion. It is by moving the various target stars through locally different distortion variation in the FGS FOV that the relative distortion across the entire FOV becomes observable. Numerical simulations performed by the STAT have demonstrated that roughly 20 observation sets are required to achieve milliarcsecond accuracy for the function D . As with mini-OFAD computations, full-OFAD calibration requires that constraints be applied to the state vector. In addition to the three constraints discussed for the mini-OFAD algorithm, two constraints related to solution scale are used in the PASS software. Because the set $\{X\}$ is part of the

state vector of the problem, true scale is intrinsically nonobservable to the full-OFAD algorithm. To first order in the state vector elements, a change in the scale of $\{X\}$ (i.e., in the calculated angular distance between cluster members) can be compensated for by a change in the polynomial set $\{S\}$ and/or the star selector parameters $\{\delta_A, \delta_B\}$ with no increase in the loss function. To remove this second-order singularity from the full-OFAD problem, one constraint each is applied to the sets $\{S\}$ and $\{\delta_A, \delta_B\}$. The constraint on $\{S\}$ is applied in a manner analogous to those used to prevent $\{S\}$ from introducing changes in translation or rotation; it prevents D , when averaged across the FGS FOV, from changing its scale properties. The constraint applied to $\{\delta_A, \delta_B\}$ is simply that the sum $\delta_A + \delta_B$ remain unchanged. These constraints are adequate to allow the full-OFAD algorithm to pick out a unique solution.

Although the algorithm described in the previous paragraph is able to select a solution that is both unique and a minimum of the full-OFAD loss function, the scale content for the solution so produced is only approximately correct. This occurs primarily because the unconstrained parameter θ_{A0} is capable of introducing both scale and distortion contributions to the solution. Given that, to date, astrometric ground-based catalogs represent the best source of true scale information for the target clusters that we have been using, we have chosen to rescale our full-OFAD solution using the mini-OFAD algorithm. The data are reprocessed with the state vector restricted to the set $\{A, \delta_A, \delta_B\}$ subject to the constraint that the ratio δ_A/δ_B remain unchanged. With the set $\{\{S\}, (\delta_A/\delta_B)\}$ fixed to that found by the full-OFAD solution, and the rescaling introduced via the change to $\delta_A + \delta_B$ kept small, we find that this rescaling procedure introduces a negligible change to the distortion aspect of the solution. Finally, to produce a rescaled catalog of star positions based on the FGS observations, we rerun the full-OFAD algorithm using the restricted set $\{A, X\}$ as the state vector.

3.2 Alignment Determination

To date, the relative alignment of the FGSs has been determined only with an accuracy commensurate with astrometric ground-based observations. Before HST launch, plans had been made to eventually perform this alignment calibration to the full design accuracy of the sensors; Refs. 1 and 2 discuss the

algorithm intended for this purpose. As a consequence of the fairly rapid temporal variations that we have found in the relative alignments of the FGSs, it has been decided that the effort that would be required to achieve full FGS accuracy is unwarranted. Rather, procedures and software have been developed that permit monitoring of the changes in the alignments as a function of time. The approach begins with an alignment determination that uses ground-based observations of target stars as fiducial points. With the relative alignments specified, observations from all three FGSs can be used to construct a catalog against which future observations of the same stars can be compared. Apparent changes in angular separation between stars observed in different FGSs during repeat visits to the target cluster are then used to determine relative alignment shifts between the FGSs.

As described in Refs. 1 and 2, there exists a systematic offset for each FGS between a star's position as determined using CT mode and that found using FL mode. These offsets must be accounted for during relative alignment determination if any of the data were taken with one or more of the FGSs operating in CT mode. HST operating conditions were sufficiently degraded during the first year of operations as to mandate the use of CT guidance during FGS calibration data takes. Our fiducial data set for relative FGS alignment determination was taken during this time period and was corrected for the CT/FL offset effect with data obtained concurrently. Because the 20-mas accuracy level of coarse track guidance is comparable to the best ground-based astrometric catalogs, degradation of alignment results as a consequence of using CT guidance is not severe.

4. REFERENCE CATALOGS

Two target clusters have been used for FGS calibration work to date: the open clusters NGC 5617 (r.a. $\sim 217^\circ$, dec. $\sim -60^\circ$) and M35 (r.a. $\sim 93^\circ$, dec. $\sim 24^\circ$). An NGC 5617 astrometric quality reference catalog based upon ground observations was provided for mini-OFAD and alignment calculations by the astrometry group at Yale University (Ref. 9). An analogous catalog for M35, based upon the observations of McNamara and Sekiguchi (MS, Ref. 10), was provided to us by the STAT. The estimated 1σ random error levels associated with the Yale and MS catalogs are 30 and 24 mas, respectively, based upon an intercomparison of results from separate plates. Both catalogs

contain proper motion estimates for the included stars. We used these estimates to correct for the effects of proper motion when comparing any sets of data taken on different dates.

One result of the FGS OFAD analysis over the past few years is the discovery that the position coordinates for the stars in both ground catalogs were subject to significant magnitude and color dependencies relative to the FGS data. The levels of these systematic dependencies were such that the standard deviations of residuals to mini-OFAD fits were 70 and 41 mas for NGC 5617 and M35 data, respectively. Because FGS data are intrinsically more accurate than ground observations, the scatter of mini-OFAD residuals should be essentially the same as the estimated intrinsic catalog error level; larger mini-OFAD residuals are an indication of systematic catalog error. This effect was first recognized for the Yale catalog a few months after associated FGS observations were made in December 1990. The Yale group subsequently corrected its catalog, using the results of a preliminary FGS full-OFAD calibration as a basis for the correction. The resulting standard deviation for mini-OFAD residuals was reduced to 35 mas, in reasonable agreement with the estimated intrinsic random catalog error. The corrected Yale catalog was used in the analysis reported in this paper.

As a consequence of the discovery of the magnitude and color dependencies in the original Yale catalog, the PASS system was augmented to include software to compare star catalogs for relative magnitude and position dependencies. The use of this utility became a planned feature in the cycle of mini-OFAD and full-OFAD calibration processing. The first step is to produce preliminary mini-OFAD and full-OFAD solutions based upon a completely independent ground catalog. The catalog produced as part of the full-OFAD solution is then used as a reference against which the ground catalog may be compared for determining magnitude and color dependencies. Corrections for any so-detected dependencies may then be removed from the ground catalog, after which the cycle of mini-OFAD and full-OFAD processing is repeated. This procedure was applied during our analysis of observations of M35, with the result that the standard deviation for associated mini-OFAD residuals was reduced to 22 mas, in good agreement with the 24-mas estimate from interplate comparisons. This corrected version of the MS catalog was used in our subsequent analysis.

The reader may reasonably ask how it is known that the errors to be corrected are within the ground data as opposed to the FGS data. As a first point, when performing a mini-OFAD calibration with multiple frames of data, we find that the postfit observation residuals are strongly correlated in both size and direction in sky coordinates for all observations of any individual star; this indicates that the error source is associated with the individual stars and not with FGS FOV position. Second, with respect to NGC 5617 data, the same correction relative to sky coordinates was found for all three FGSs. Given that the FGSs had different relative orientations on the sky during the observations (see Figure 1), it is unlikely that the FGSs themselves could produce such an effect. Finally, with respect to M35 data, a single correction relative to sky coordinates is found to be appropriate irrespective of spacecraft roll. This eliminates both the FGS used for these observations (FGS-3) and the HST primary and secondary mirror system as possible sources of the magnitude/color effects. For these reasons, we find it appropriate to attribute the effects to the ground catalogs.

5. CALIBRATION RESULTS

5.1 Distortion and Scale Results

5.1.1 Previous Results

Several unanticipated operational constraints significantly affected the ability of HST in general, and the FGSs in particular, to acquire FGS calibration data during the first years of HST operations. Of these, the most serious from our perspective was the spacecraft jitter induced at day-night transitions by the thermal flexing of the original solar arrays. Jitter-induced loss-of-lock for FGS guide stars remained a serious problem until a guide star recentering algorithm was implemented in the flight software in December 1992. As a consequence, all FGS calibration data were taken using CT guidance during the first 2 years of the mission. During this period, peak-to-peak spacecraft pointing changes as high as 100 mas were noted, although at a sufficiently high frequency that averaging across the 1-minute observation periods for each astrometry star significantly reduced the pointing error. Maximum average displacements of the guide stars during a single orbit were typically on the order of 10 mas. Using this level of performance, the first reasonably successful mini-OFAD calibration was completed in December 1990.

In Refs. 1 and 2, we discussed calibration results for data taken in December 1990 and May 1991, reporting that the measured values for the distortion coefficients agree reasonably well with their design values for all three FGSs, but the parameter θ_{A0} differs significantly from its design value of zero for both FGS-2 and FGS-3. θ_{A0} is approximately 0.57° and -0.63° for FGS-2 and FGS-3, respectively. Prelaunch analysis indicated that ground-to-orbit changes in θ_{A0} would be less than 0.1° . The cause of these large deviations remains unexplained. A comparison of the OFAD results between December 1990 and May 1991 indicated that significant changes had apparently occurred during the 5-month interval. Given the restricted accuracy of the data sets, it was possible then to characterize the change only to first order — and only as an approximate scale change. The largest change was detected for FGS-1, for which the effective scale change corresponded to 100 mas over 14 arcminutes. The estimated accuracy of the December 1990 and May 1991 mini-OFAD calibrations is about 10 mas over FOV regions separated by no more than about 4 arcminutes and about 30 mas across the whole FOV of any single FGS.

5.1.2 New Results

Since the writing of Refs. 1 and 2, three major advances in our analysis of FGS distortion have occurred. First, via differential studies of apparent changes in star positions during repeat visits to the calibration target clusters, we have been able to better quantify the nature of the long-term "scale" variations previously reported. Second, via repeat observations of selected "check" stars during periods of continuous astrometric observing, we have found significant apparent changes in the effective relative alignments of the FGSs over time periods short compared with a single orbit. Finally, because of the operational improvements in fine lock guiding performance made possible by flight software enhancements, a full-OFAD calibration observing sequence for FGS-3 became possible and was successfully executed in January 1993. The advances in our understanding of FGS performance occurred over a period of months, with improvements in each area providing a better foundation for analysis in the others. Although we discuss each area separately below, their interdependence is readily apparent.

5.1.2.1 Long-Term Variations in Distortion

Our studies of the long-term variations of the FGS distortion calibration are based on two sequences of

OFAD data sets. The first provided us with a 2-year baseline starting with our original December 1990 mini-OFAD calibration observations of the star cluster NGC 5617. As previously noted, the accuracy of this initial calibration is estimated to be about 10 mas over small regions of each FGS FOV and about 30 mas over each complete FOV. To take advantage of the relatively good calibration accuracy over small FOV regions, we based our analysis of calibration changes on differential studies of apparent changes in star positions during repeat visits at 1-year intervals to the same target cluster. The 1-year interval was dictated by spacecraft operational pointing constraints; spacecraft roll relative to the sunline is constrained to prevent illumination of the underside of the spacecraft. By repeating the observations at 1-year intervals, we were able to place the various target stars in essentially the same position in the FOV as during the initial calibration. After compensating for proper motion effects, we determined the adjustments to our December 1990 solution needed to restore the original relative positions. We found, to within the accuracy of our data, that the FGS calibration changes are well modeled as changes to the star selector parameters δ_A and θ_{A0} . Although adjustment to both parameters is in general required for good modeling at the data noise level, we find that the FGS-1 variation is greatly dominated by changes to θ_{A0} ($\Delta\theta_{A0} \cong -0.044^\circ$ over 2 years), whereas that for FGS-3 is greatly dominated by changes to δ_A ($\Delta\delta_A/\delta_A \cong 2.9 \cdot 10^{-4}$ over 2 years). The 2-year variation over baselines of about 12 arcminutes was roughly 200, 30, and 100 mas for FGSs 1, 2, and 3, respectively.

Because of the long-term changes in distortion calibration observed for all three FGSs, it was decided that a high-accuracy monitoring program should be established for FGS-3, the FGS selected for astrometry work, as a companion activity to its full-OFAD calibration. This long-term stability (LTSTAB) program began 1 month before the January 1993 full-OFAD observing sequence. M35 is the selected target for both the full-OFAD and the LTSTAB calibration work. Because M35 is located near the ecliptic plane, spacecraft roll constraints dictate two possible principal roll orientations of the spacecraft relative to the target. Using data from any specific orientation, it is possible to conduct purely differential studies of FGS distortion changes; such studies are not subject to errors in a specific OFAD solution or a selected reference catalog. With only slightly greater error, a

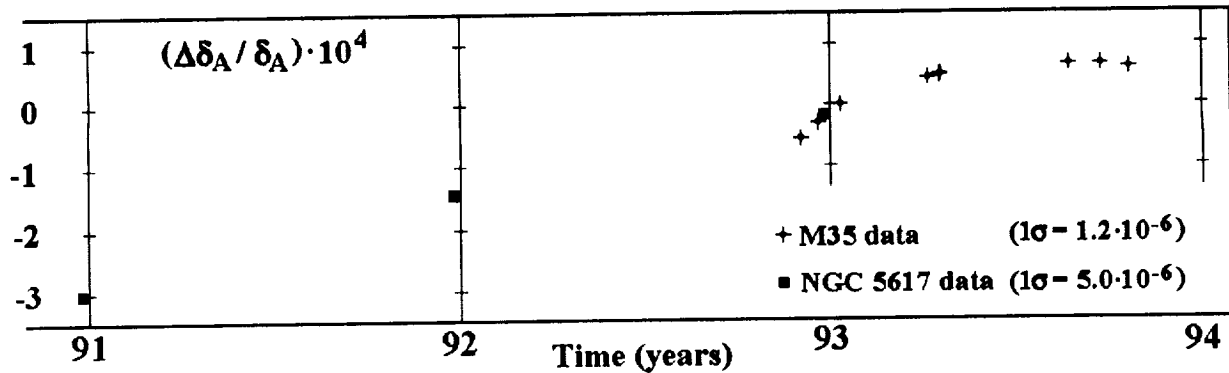


Figure 3. For FGS-3, long-term variation of parameter δ_A as a function of time

combined LTSTAB study can be performed using data from both orientations by taking advantage of the results from a full-OFAD calibration; the OFAD solution is used to correct for distortion, and the FGS-generated catalog serves as an orientation independent set of reference points. We have selected the latter approach for the results presented here, using our analysis of the January 1993 full-OFAD data set as our fundamental reference.

As was the case for the NGC 5617 observations, most of the temporal changes in FGS-3 distortion are fairly well modeled by adjustments to the single parameter δ_A . Figure 3 presents a plot of the change in δ_A as a function of time, with δ_A treated as the only free distortion parameter. The plot combines the results of the differential studies using observations of stars from both NGC 5617 and M35. Relative normalization of the two data sets was accomplished by placing the NGC 5617 December 1992 data point on a smoothly interpolated position within the M35 sequence. (The normalization is consistent with the scale of both ground catalogs to within their error levels.) The results suggest that the variation of δ_A is significantly nonlinear for time scales between a few months and 1 year but fairly linear for time scales of order 2 to 3 years. LTSTAB monitoring of FGS-3 distortion will continue for the indefinite future, with the results being used for both engineering analysis of FGS performance and correction of astrometry data obtained with that sensor.

5.1.2.2 Short-Term Alignment Variations

The second area of analysis advancement pertains to the apparent change in relative FGS alignments over time periods comparable to a single orbit. For all of our recent OFAD calibration data sets, and in particular for the full-OFAD data obtained in

January 1993, the astrometry observing sequence includes repeat observations of three well-separated stars during the course of each orbit. The function of these "check" star observations is to detect any systematic change in the astrometry FGS FOV with respect to translation, rotation, or scale during the course of a single orbit. With a perfectly operating optical system, after compensation for velocity aberration effects, all of the check stars would maintain their angular separations relative to each other and to the guide stars monitored by the other two FGSs. (With an ideal pointing control system, the star positions — not merely their angular separations — would also remain fixed.) In practice, the angular separations do not behave as they should for a perfect system; significant systematic motion of the check stars relative to the two "fixed" guide stars is regularly seen to occur. The effective change in alignment during a typical 40-minute observing sequence is on the order of 10 mas, although one orbit showed a change as large as 17 mas. Changes in the effective alignment of the astrometry FGS relative to the guiding FGSs over a single observing period result in a motion of the astrometry FOV relative to the background stars. If left uncorrected, this effect would corrupt the OFAD calibration.

Investigation of the phenomenon of short-term FOV motion has been undertaken from two perspectives: (1) to model and remove the effect from FGS calibration data (or astrometry science data, for that matter) and (2) to understand the physical cause of the phenomenon. Clearly the latter objective can be an important intermediate goal on the way to the former, but achieving complete success in that area is not necessary to make significant first-order corrections to the data. We have found that the check star motion for FGS-3 astrometry orbits is fairly well modeled as constant velocity translation

of the whole FOV, the model being extremely good for about two-thirds of such orbits. We have therefore used this model in conjunction with check star data to establish FOV-motion parameters for each orbit of our full-OFAD and LTSTAB data sets and thereafter applied the model to correct all of the remaining astrometry observations within each orbit.

The cause of this apparent motion of the astrometry FOV relative to the FOVs of the guide FGSs is not yet well understood. A conjecture was made a couple of years ago that differential heating of the secondary mirror support structures could cause the mirror to move and produce focus and coma changes that would result in the observed behavior. Christ Ftaclas at HDOS has developed an optical model for the implied effects for FGS observations and found it to work well for about half of the January 1993 OFAD calibration orbits. The motions in the remaining orbits are incompatible with the model, being either wrong in direction or containing sharp changes. This may indicate the existence of yet another mechanism. A PCS/FGS coupling study has been initiated recently and may shed some light on this phenomenon. Evidence for secondary mirror "breathing" has also been seen in the data from the other HST scientific instruments (SIs). Investigating the conjecture that there is a thermal driver for the effect, Pierre Bely of the STScI has shown that there is a correlation between the temperature of HST's forward light shield and the changes observed by some SIs (Ref. 12). He further computed the changes to secondary mirror position needed to model these changes. Unfortunately, the amount of secondary mirror motion needed to model the changes in SI response is only about half of that needed in the Ftaclas model to explain concurrent apparent motions of the FGS FOVs. This difference is being investigated. If no significant error is found in either analysis, that may be taken as an indication for the existence of some mechanism that has an effect on the FGSs but not on the SIs. Again, the PCS/FGS coupling study may resolve this question.

Within the context of the Ftaclas model for FGS pointing changes, we find that the simplicity of our linear-motion correction procedure for FGS-3 astrometry data is somewhat fortuitous. The model predicts that effective rotation and scale changes also occur in the astrometry FGS FOV, but these effects happen to be below noise level for cases when FGSs 1 and 2 are used for guiding.

5.1.2.3 Full-OFAD Calibration

With the phenomenon of short-term alignment variation reasonably well modeled, and with the problem of jitter-induced loss-of-lock solved, a full-OFAD calibration at the level of FGS design accuracy became possible. For reasons of economy (i.e., because the amount of data required for the full calibration of a single FGS is large), it was decided to perform the calibration only for that FGS selected for use in astrometric science. Twenty frames of M35 observations for this calibration were acquired on January 10 and 11, 1993. Analysis was restricted to data obtained with all three FGSs in FL mode. Each star vector was constructed as an average over approximately 25 seconds of data. The observing period for each frame was roughly 35 minutes. Data from 2 of the 20 orbits were removed from consideration because of commanding and guidance problems.

We processed the data for distortion calibration using the algorithms discussed in Section 3. We began with an FGS-3 mini-OFAD solution based on data from the December 1990 and December 1992 observations of NGC 5617. The distortion portion of the state vector for this solution was restricted to the parameters $(\delta_A, \delta_B, \theta_{A0})$, the polynomial coefficients being held at their design values. Values for the three star selector parameters were first determined using the 1990 data; adjustments to (δ_A, θ_{A0}) were then determined based upon a differential comparison of the 1990 and 1992 data. The star selector parameters alone were adequate to define deviations from design distortion to roughly the accuracy of the ground catalog (~ 30 mas, 1σ), whereas adjustments to (δ_A, θ_{A0}) captured the 2-year differential changes to within the accuracy of the 1990 FGS data (~ 8 mas, 1σ).

Using the NGC 5617 mini-OFAD solution as an initial estimate, we processed the M35 data through the full-OFAD algorithm to generate an intermediate solution star catalog with which to correct the MS catalog (Ref. 10). The state vector for this solution consisted of coordinates for the 91 observed stars, 3 star selector parameters, 14 polynomial distortion coefficients (up to third order), and attitude Euler angles. The single-axis standard deviation of residuals for the fit was 3.3 mas. As described in Section 4, we used the FGS-generated star coordinates catalog to correct the MS catalog. (The correction was dominated by the dependency on magnitude, the size being 36 ± 6 mas / m_V .) The

corrected MS catalog and the 18 frames of FGS M35 data were then used in a mini-OFAD calculation. The state vector for this solution consisted of the star selector parameters, 15 distortion polynomial coefficients, and attitude Euler angles. As described in Section 3, three constraints were applied to the distortion polynomial to prevent any meaningless change in translation or rotation content. The single-axis standard deviation for the postfit residuals of this solution was 22 mas.

The state vector for the subsequent full-OFAD calculation consisted of the 3 star selector parameters, 21 polynomial coefficients, 51 Euler angles, and coordinates for the 91 stars. Five constraints were applied: the four translation, rotation, and scale polynomial constraints and the single ($\delta_A + \delta_B$) constraint. The single-axis standard deviation of residuals for this fit was 2.5 mas. (After adjustment for the dimension of the state vector, this translates into an estimate for the intrinsic root-mean-square FGS measurement error of 2.8 mas.) As discussed in Section 3, rescaling of this OFAD solution using the mini-OFAD algorithm was required because changes in θ_{A0} generate scale changes as well as distortion changes. Based on the accuracy of the MS catalog and the number of stars observed, we estimate the scale accuracy of our final OFAD solution to be good to 1 part in $2.5 \cdot 10^5$ (roughly 3 mas over a 12-arcminute arc). A final FGS-based M35 catalog was then generated using the full-OFAD software with the state vector restricted to the attitude Euler angles and the relative star coordinates. The 2.5-mas standard deviation of residuals was preserved through this rescaling process, verifying the basic validity of the approach.

Our final results agree well with the independent calibration work performed by the STAT (Ref. 13), which found a solution characterized by a standard deviation of the residuals of 2.3 mas. The slightly tighter residuals found in the STAT solution are probably a consequence of the team's incorporation into their algorithm of a spacecraft jitter correction based upon observations of the guide stars at time points coincident with the astrometry observations. The two-axis root-sum-square error in a single observation implied by the calibration results is 3.5 and 3.2 mas for the PASS and STAT solutions, respectively, which agrees well with the prelaunch expectation of 2.7 mas.

5.2 Alignment Results

Refs. 1 and 2 presented our early relative alignment determination results for the three FGS FOVs. The first determination was based on 17 frames of NGC 5617 data taken in December 1990. Each frame contained observations of 2 guide stars and about 10 astrometry stars, FGS-2 being used for astrometry. Corrections for velocity aberration, distortion, scale, and CT/FL offset were applied before determination of the relative FOV alignments. The Yale catalog was used to provide the fundamental reference set of angular separations. The postcalibration standard deviation of residuals for the difference between measured and reference star separations was found to be 35 mas, consistent with the estimated accuracy of the reference catalog. Subsequent observations in January 1991 and May 1991 indicated apparent relative shifts of the FGS FOVs. The alignment change was manifest primarily as motions in opposite directions parallel to the V3-axis by the FGS-1 and FGS-3 FOVs relative to FGS-2, the magnitude of the shifts being of order 200 mas after 5 months.

The repeat visits to NGC 5617 in December 1991 and December 1992 have allowed a continued monitoring of the long-term changes in the relative alignments of the FGSs. Specification of the changes in the relative alignments of the FGSs is coupled to the assumed form of any changes to the individual responses of the FGSs. Different effective alignment shifts are seen depending on the model used to represent distortion changes. Our decision to represent distortion changes using the parameters δ_A and θ_{A0} influences our alignment change results significantly, but ultimately only at a level of order 10 percent of the detected alignment change. Our differential method for determining the relative alignment changes from December 1990 to December 1991 and December 1992 is discussed in Section 3. The December 1991 data were acquired in a repeat of 4 of the previous year's alignment determination orbits; the December 1992 data were acquired in a repeat of 3 of the December 1990 OFAD determination orbits, with each FGS in astrometry mode once. The December 1991 ($\Delta V2$, $\Delta V3$) shifts in effective coordinate grids for FGS-1 and FGS-3 relative to FGS-2 were (110, -160) mas and (370, 690) mas for FGS-1 and FGS-3, respectively; the December 1992 shifts were (120, -660) mas and (530, 1030) mas for FGS-1 and FGS-3, respectively. Roll changes were small and have not been included here. The standard deviation for the residuals in

these differential fits was about 10 mas. The relative shear between FGS-1 and FGS-3 increased from about 850 mas in December 1991 to nearly 1700 mas in December 1992.

The physical cause of this continued change in the relative alignments of the FGSs remains under investigation. Some significant progress has been made by HDOS optical engineers via a study of data taken using the internal test source (ITS) for each FGS. Ideally, the coordinates of each ITS should remain fixed with time. HDOS has found that the ITS coordinates are changing and that appropriate differences between the coordinate changes for FGSs 1 and 2 and for FGSs 3 and 2 are strongly correlated with the changes reported for the relative alignments of the FGS FOVs. (Three of the four comparable coordinate differences agree to within about 20 percent for the two different procedures.) This suggests that the effective alignment changes are occurring as a result of changes internal to the individual FGSs. As part of its general effort to characterize the on-orbit changes in the HST/FGS system (Ref. 14), HDOS conducted an optical sensitivity study that indicated that motion of the FGS asphere could cause relative alignment changes of the detected size. The physical mechanism that drives the motions remains unclear.

6. SUMMARY

This paper has presented a review of the procedures and algorithms used for the calibration of the HST FGSs, as well as a discussion of the results obtained through the end of 1993. Despite the well-publicized problems with HST discovered shortly after launch in April 1990, significant progress has been made in calibrating the system to achieve good pointing performance. Design-level (~ 3 mas) distortion calibration for FGS-3 was achieved with data taken in January 1993. Distortion calibration at the 30-mas level has been achieved for the remaining two FGSs. Long-term trends in distortion variation have been measured and characterized for all three FGSs, and a long-term stability monitoring program has been put in place for FGS-3. Short-term (intraorbit) variations in the effective alignments of the FGS FOVs have been observed and adjusted for in the distortion calibration for FGS-3. Relative alignment calibration for the FGSs has been achieved at the 30-mas level. Systematic long-term changes in the relative FGS FOV alignments with rates on the order of 0.5 arcsecond per year have been found. Continued monitoring of,

and adjustment for, these changes in FGS distortion and alignment calibration will be an important feature of routine HST engineering calibration maintenance as HST scientists strive for full design performance from the telescope during the post-FSM era.

A great many individuals and organizations have been involved in the efforts that ultimately resulted in the successful calibration of the HST FGSs. Besides those already alluded to in the body of this paper, we would like to explicitly acknowledge the efforts of two individuals. Paul Davenport (GSFC/CSC) served as lead system engineer for the HST operations management system through the years of its development before launch; his analytic insights provided the basis for, or extensions of, many of the algorithms in the PASS system. Keith Kalinowski (GSFC) served as the chief representative of the HST project office to the FGSWG. His dedicated efforts and technical insights were invaluable to all aspects of the FGSWG investigations, but particularly with respect to the selection and preparation of the M35 observing scenarios used for the OFAD calibration.

The work reported in this article was supported in part by NASA contracts NAS 5-31500 (Welter), HB80E4940N (Abramowicz-Reed), NAS 5-31786 (Guha), and NAS 5-31000 (Kimmer), which enable CSC, HDOS, AKG, and ATSC to provide systems engineering, analysis, and operations support to NASA/GSFC.

7. REFERENCES

1. G. Welter, *The In-Flight Calibration of the Hubble Space Telescope Attitude Sensors, Proceedings of the GSFC Flight Mechanics / Estimation Theory Symposium - 1991*, NASA Conference Publication 3123, May 1991.
2. G. Welter, L. Abramowicz-Reed, A. Guha, L. Hallock, and E. Kimmer, *The In-Flight Calibration of the Hubble Space Telescope Fine Guidance Sensors, Proceedings of the Third International Symposium on Spacecraft Flight Dynamics*, ESA Publication SP-326, October 1991.
3. L. Hallock et al., *Space Telescope POCC Applications Software Support (PASS) Requirements Specification (Revision E)*, Computer Sciences Corporation Document CSC/TM-82/6045, September 1987.

4. A. Bradley, L. Abramowicz-Reed, D. Story, G. Benedict, and W. Jefferys, *The Flight Hardware and Ground System for Hubble Space Telescope Astrometry*, Publications of the Astronomical Society of the Pacific, March 1991, vol. 103, p. 317.
5. OAO Corporation, Hubble Space Telescope Astrometry Operations Handbook, Marshall Space Flight Center Document SMO-1040, March 1987.
6. W. Smart, Text-Book on Spherical Astronomy, Cambridge, England: Cambridge University Press, 1971.
7. W. Jefferys, *On the Method of Least Squares*, The Astronomical Journal, February 1980, vol. 85, no. 2, p. 177.
8. C. Misner, K. Thorne, and J. Wheeler, Gravitation, San Francisco: W. H. Freeman & Co., 1973.
9. T. Girard, C. Heisler, Y.-W. Lee, C. Lopez, W. van Altena, and P. Ianna, *Astrometric Calibration Regions with Proper Motion Membership Estimates in the Open Clusters NGC 188 and NGC 5617*, Poster Presentation at the January 1990 Meeting of the American Astronomical Society held in Washington D.C.
10. B. McNamara and K. Sekiguchi, *A Proper Motion Analysis of the Cluster M35*, The Astronomical Journal, March 1986, vol. 91, no. 3, p. 557.
11. C. Ftacilas and L. Abramowicz-Reed, *OFAD, Breathing, and the Shift Model*, Hughes Danbury Optical Systems Memorandum ST-SE-7160, April 6, 1993.
12. P. Bely, *Progress Report on Focus Change Study ('Breathing')*, Space Telescope Science Institute Technical Memorandum, December 4, 1992.
13. W. Jefferys, A. Whipple, Q. Wang, B. McArthur, G. F. Benedict, E. Nelan, D. Story, and L. Abramowicz-Reed, *Optical Field Angle Distortion Calibration of FGS3*, Proceedings of the HST Calibration Workshop, Space Telescope Science Institute, November 1993.
14. L. Abramowicz-Reed, R. Basedow, R. Crout, W. Freeman, C. Ftacilas, J. Tausanovich, and R. Zarba, Hubble Space Telescope Assembly Project - FGS Working Group Tiger Team Final Report, Hughes Danbury Optical Systems Report PR J14-0105, June 1992.

ACRONYM LIST

CSC	Computer Sciences Corporation
CT	coarse track
FGS	fine guidance sensor
FGSWG	FGS Working Group
FL	fine lock
FOV	field of view
FSM	First Servicing Mission
GSFC	Goddard Space Flight Center
HDOS	Hughes Danbury Optical Systems
HPSEB	HST Project System Engineering Board
HST	Hubble Space Telescope
IFOV	instantaneous field of view
ITS	internal test source
LTSTAB	long-term stability
M	Messier (catalog entry, e.g., M35)
mas	milliarcsecond
MS	McNamara and Sekiguchi (Ref. 10)
m_v	visual magnitude
NGC	New General Catalog (e.g., NGC 5617)
OFAD	optical field angle distortion
PASS	POCC Applications Software Support
PCS	pointing control system
POCC	Payload Operations Control Center
SI	scientific instrument
STAT	Space Telescope Astrometry Team
STScI	Space Telescope Science Institute

G. Welter, CSC, 1100 West Street, Laurel MD 20707

L. Abramowicz-Reed, HDOS, 100 Wooster Heights Road, Danbury CT 06810

A. Guha, AKG Inc., Post Office Box 10135, Silver Spring MD 20914

L. Hallock, Code 512.0, Goddard Space Flight Center, Greenbelt MD 20771

E. Kimmer, ATSC, Code 519.1, Goddard Space Flight Center, Greenbelt MD 20771

In-Flight Estimation of Gyro Noise on the Upper Atmosphere Research Satellite (UARS) and Extreme Ultraviolet Explorer (EUVE) Missions*

M. Lee, P. Crouse, and R. Harman
National Aeronautics and Space Administration (NASA)
Goddard Space Flight Center (GSFC)
Greenbelt, Maryland, USA

T. Leid, W. Davis, and S. Underwood
Computer Sciences Corporation (CSC)
Lanham-Seabrook, Maryland, USA

Abstract

This paper characterizes the low-frequency noise response of the Teledyne dry rotor inertial reference unit (DRIRU) gyroscopes on the Upper Atmosphere Research Satellite (UARS) and the Extreme Ultraviolet Explorer (EUVE). The accuracy of spacecraft attitude estimation algorithms that use gyro data for propagating the spacecraft attitude is sensitive to gyro noise. EUVE gyro data were processed to validate a single-axis gyro noise model, which is used onboard various spacecraft. The paper addresses the potential impact of temperature effects on the gyro noise model and the overall impact on attitude determination accuracy. The power spectral density (PSD) of the gyro noise is estimated from UARS in-flight data by Fast Fourier Transform (FFT). The role of actuator dynamics on the PSD function is also discussed.

Introduction

The algorithms that use gyro data to propagate the spacecraft attitude over a period of time are affected by the estimation of the gyro noise. This paper attempts to characterize that noise by using in-flight data for the Upper Atmosphere Research Satellite (UARS) and the Extreme Ultraviolet Explorer (EUVE). Both UARS and EUVE have Teledyne dry rotor inertial reference unit (DRIRU)-II gyroscopes on board. The description and specifications of this hardware are presented below.

One goal of this paper is to use in-flight data to validate a single-axis gyro model that is commonly used in the Kalman filter attitude estimation process on board various spacecraft (the Gamma Ray Observatory (GRO), EUVE, and UARS, for example) to estimate gyro rate and drift rate noise. Since EUVE has redundant measurements on all three axes, it is proposed that the difference of the two measurements will strip the true rate information and leave the noise. This noise then can be evaluated to determine if the model is accurate. A second goal of this work is to attempt to identify the source of signatures in the gyro data for the UARS spacecraft. The solar array drive is known to cause real spacecraft motion that is reported in the gyro data. It has been suggested that components of the gyro data that appear to be measurement noise may be due to science instrument operation. The power spectral density (PSD) of the gyro noise will be obtained by Fast Fourier Transform (FFT) to evaluate this suggestion. The goal is to be able to reduce the estimate of gyro noise to a value that is only the true noise so that attitude determination accuracy can be improved.

*This work was supported by the National Aeronautics and Space Administration (NASA)/Goddard Space Flight Center (GSFC), Greenbelt, Maryland, under Contract NAS 5-32500.

IRU Description and Specifications

The DRIRU II consists of three gyroscopes, each with a spinning rotor mounted on two gimbals to provide 2 degrees of freedom and rate information along two body axes (two channel output), for a total of six channels of information. Each gyroscope has internal temperature compensation, and the temperature of each is reported in the downlinked telemetry. The gyroscopes are configured to provide dual redundancy along each body axis. When the spacecraft attitude is noninertial, the IRU gimbals are reoriented to maintain a null deflection from an inertial orientation. The current required to produce the magnetic torque to accomplish this reorientation is proportional to the angular rate about the corresponding axis. This torque current is converted to a series of pulses, which are counted and reported as accumulated rotation angles. The IRU itself provides rate information as incremental angles every 64 milliseconds, and a separate electronics unit converts this to accumulated angles reported every 128 milliseconds for the EUVE. In contrast, the UARS IRU reports digital rates every 128 milliseconds and accumulated angles every 1.024 seconds. In our following analysis, the IRU and the electronics unit are considered together as the IRU.

The IRU can operate in two rate ranges. The high-rate mode allows for rates of up to 2.0 degree/second (deg/sec); low-rate mode allows rates of up to 400 arcsec/sec (.11 deg/sec). The digital resolution of the IRU is 0.8 arcsec in high-rate mode and .05 arcsec in low-rate mode. The specified angular rate bias stability (Reference 1) for the DRIRU is on the order of 0.003 arcsec/sec over a period of 6 hours and 0.02 arcsec/sec over a month. The long-term noise characteristics of the DRIRU differ from the short term, so the random walk noise model is appropriate only for relatively short timespans (on the order of at least 6 hours). Only the short-term noise performance is pertinent for the onboard attitude determination processing.

The IRU accumulated rotational angle measurements are reported in the EUVE telemetry as integer counts at 0.128-sec intervals. The Flight Dynamics Facility (FDF) ground system unpacks and converts the counts to engineering units (deg/sec) while also (optionally) correcting the measurements for known misalignments, scale factors, and biases.

Noise Model and Rate Noise

A common model for IRU rate noise (documented in Reference 2 and used in the onboard Kalman filter for attitude determination) uses the sum of two noise processes:

$$r(t) = v(t) + b(t)$$

where $r(t)$ is the rate noise as a function of time, $v(t)$ is a rapidly varying random process that is modeled by a white-noise source, and $b(t)$ is a slowly varying random process that is modeled by a random walk process (see Reference 2), with the rate white noise, $v(t)$, corresponding to the float torque noise and the bias white noise, $u(t)$, corresponding to the float torque derivative noise. We intend $b(t)$ to be the variations of the rate bias. It is the amount of accumulated bias error since the beginning of some timespan. As the initial bias will be calculated and adjusted for in our processing, the value of $b(t)$ can be taken as zero at the start time, t_0 , of the timespan under consideration. The autocorrelation of the white-noise source has the following form:

$$\langle v(t)v(t') \rangle = \sigma_v^2 \delta(t-t')$$

where σ_v^2 has the dimensions of angle squared per time and $\langle \dots \rangle$ is the statistical expectation operator. The random walk process is the integral of another independent white-noise source. Let $u(t)$ be the white noise source that drives the random walk of the rate such that

$$\langle u(t)u(t') \rangle = \sigma_u^2 \delta(t-t')$$

where σ_u^2 has the dimensions of angle squared per time cubed. Then, the random-walk process is then given by

$$b(t) = \int_{t' = t_0}^{t' = t} u(t') dt'$$

$$\langle b(t)b(t') \rangle = \int_{t_1 = t_0}^{t_1 = t} dt_1 \int_{t_2 = t_0}^{t_2 = t'} dt_2 \langle u(t_1)u(t_2) \rangle$$

$$\langle b(t)b(t') \rangle = \sigma_u^2 \min((t - t_0), (t' - t_0))$$

where $\min((t - t_0), (t' - t_0))$ is the smaller of $t - t_0$ and $t' - t_0$. For independent random processes, the autocorrelation of the rate noise is given by

$$\langle r(t)r(t') \rangle = \sigma_r^2 \delta(t - t') + \sigma_r^2 \min((t - t_0), (t' - t_0))$$

Observable Consequences of Rate Noise

The rate output of the IRU for each channel has the following form

$$\Omega(t) = \omega(t) + r(t)$$

where $\Omega(t)$ and $\omega(t)$ are the observed and true rates, respectively. The IRU converts this rate to an accumulated angle

$$\Theta(t) = \int \Omega(t) dt = \int \omega(t) dt + \int r(t) dt$$

Let the rate be integrated from time t_0 . Let $q(t)$ be the noise of the integrated rate as a function of time. Then,

$$q(t) = \int_{t' = t_0}^{t' = t} r(t') dt' = \int_{t' = t_0}^{t' = t} v(t') dt' + \int_{t' = t_0}^{t' = t} b(t') dt'$$

Note that because the integral of a white noise source is a random walk, the rate white noise source becomes a random walk process for the accumulated angle. Also, the rate random walk process becomes a double random walk for the accumulated angle. The phrase "random walk" by itself becomes ambiguous. It could mean either the random walk of the rate, which is produced by the u-process, or the random walk of the angle, which is caused by the v-process.

The variance of the noise of the angle accumulated from time t_0 is

$$\begin{aligned} \langle q(t)^2 \rangle &= \int_{t' = t_0}^{t' = t} dt' \int_{t'' = t_0}^{t'' = t} dt'' (\langle v(t')v(t'') \rangle + \langle b(t')b(t'') \rangle) \\ &= \sigma_v^2 (t - t_0) + \int_{t' = t_0}^{t' = t} dt' \int_{t'' = t_0}^{t'' = t} dt'' \sigma_u^2 \min(t' - t_0, t'' - t_0) \\ &= \sigma_v^2 (t - t_0) + \frac{1}{3} \sigma_u^2 (t - t_0)^3 \end{aligned} \quad (1)$$

The verification of the above equation is the goal of our gyro noise processing. For EUVE, all six gyro channels are reported in the downlinked telemetry. This luxury allows us to observe the gyro noise directly. If timespans of data

are used where the spacecraft is undergoing constant rate motion and if small effects due to the slight differences in alignments of the gyro channels are neglected, then the result of differencing the primary and backup gyro signals for a given axis will be to subtract the true rate information. One is then left with a quantity equal to the difference of the two channels' rate biases and rate noises. If the initial bias of these quantities is removed, a source of pure noise is left that theoretically is described by the above equation, but with the root mean square (RMS) strength of the random walk sources for the gyros given by

$$\sigma_v / (\sqrt{2}) \tag{2}$$

and

$$\sigma_u / (\sqrt{2})$$

An additional quadratic term can be included in Equation (1), $\sigma_b^2 (t - t_0)^2$, which is due to the 1-sigma uncertainty, σ_b , in the initial bias calculation. The bias uncertainty is discussed later in this analysis.

Results from Applying the Noise Model to Observed Data

Both low-rate mode and high-rate mode gyro noise were investigated. To minimize contributions to noise and bias changes due to spacecraft motion and gyro misalignment coupling, only timespans where EUVE was rotating at a constant rate were processed. For the low-rate mode, this implies that EUVE is inertially pointing, while for high-rate, the survey phase data could be used. During the survey phase, EUVE is rotating at a constant rate of 3 revolutions per orbit most of the time. As discussed below, because finding inertial data for this analysis was difficult, eventually timespans when EUVE was in the survey phase were used exclusively.

In Figure 1, the square of the propagated error due to the noise differences from the primary and backup X channels is shown as a function of propagation time in seconds for a span of data on December 11, 1993. At this time, the gyros were in the low-rate mode. Comparison of the shape of the variance plot over time (Figure 1) versus the temperature plot (for the primary X channel, Figure 2) suggests that the gyro parameters might be affected by temperature changes. Further investigation into the data shows that for the data taken on that day, the apparent bias (computed at 5-minute intervals), is roughly linear with respect to the average (over the prime and backup channels) temperature as shown in Figure 3. As the bias is the average difference between two gyro signals for a given axis, both gyros must have constant temperatures to avoid temperature-variation induced effects. From the data processing performed for this analysis, it is unclear whether other gyro parameters, such as the gyro scale factor for conversion of the telemetered counts to engineering units or the random noise strengths, are also functions of temperature. Previous analysis for the Cosmic Background Explorer (COBE), Reference 3, has shown gyro parameter dependence on gyro temperatures, although the gyros flown on COBE were not the DRIRU II. The COBE experience was that a variation in drift rate was seen approximately 320 seconds after a change in gyro base plate temperature. Note that the bias variation, as a function of time, appears correlated to the gyro temperature change, and the propagation error plotted in Figure 1 is the integral with respect to time of the bias. Further analysis is planned to characterize the relationship of the changes in the DRIRU II parameters with temperature variation.

In general, the gyro temperature varied more when EUVE was inertial than when EUVE was in survey mode. Because of the rotation during the survey phase, the gyro temperatures are more likely to remain constant over several hours in time. For this reason, only EUVE survey mode data were used.

Another problem, one that plagued previous attempts (Reference 4) to fit the gyro noise model to on-orbit data, is that the best cubic fit to the data often entails negative coefficients for the fitting polynomial if the bias uncertainty term (the quadratic term) is allowed free rein. Negative values of these coefficients are not physically meaningful in the noise model. To circumvent this problem, the quadratic term that models the contribution of uncertainty in the initial bias to the propagated error is analyzed in detail.

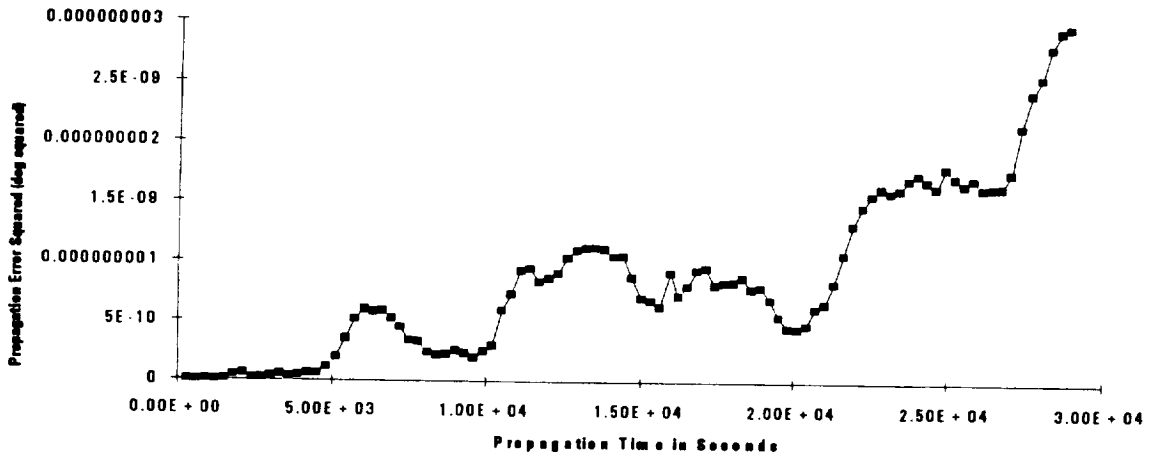


Figure 1. X Propagation Error Squared for December 11, 1993 (Low Rate)

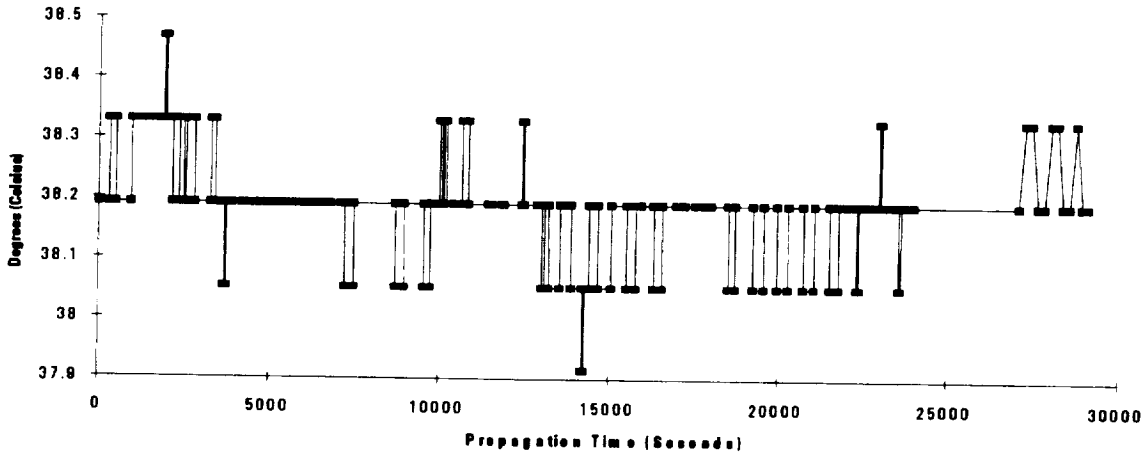


Figure 2. Prime and X and Y Channel Temperature for December 11, 1993

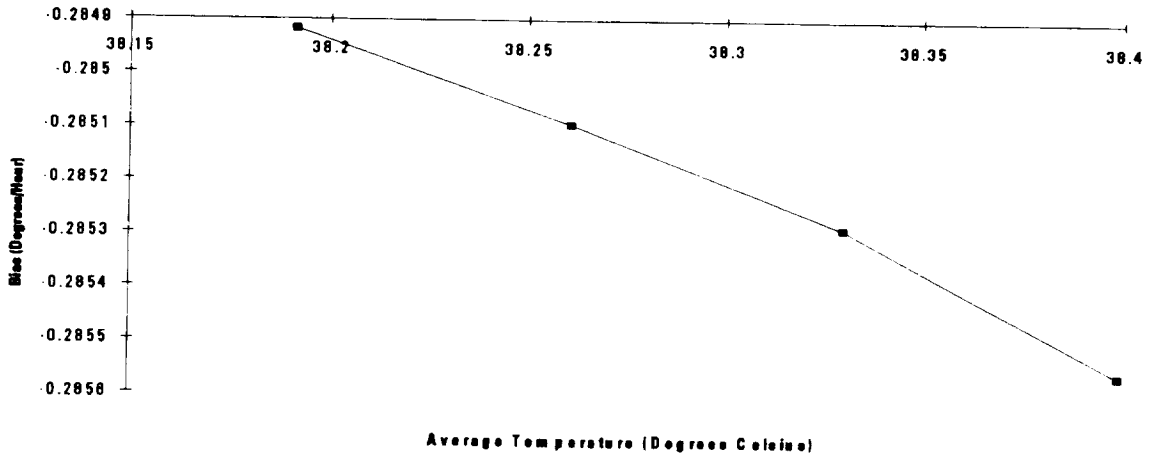


Figure 3. X Channel Bias Versus Average (Prime and Backup) Temperatures

The initial bias used is the average gyro signal over the first 5 minutes of data taken. The one-sigma error in an individual bias computation due to accumulated noise, telemetry quantization, and variation of the bias over the first 5 minutes (using the random walk noise model) can be estimated. This error is dominated by the error caused by the rate white noise, with strength denoted by σ_v . Over a 5-minute interval, the accumulated angle error variance is given by $\sigma_v^2 \cdot 300(\text{sec})$, with the resultant bias variance, σ_b^2 , given by $\sigma_v^2 / 300(\text{sec})$. This results in the final equation for the variance of the noise of the angle accumulated from time t_0 given by

$$\langle q(t)^2 \rangle = \sigma_v^2 \left[(t - t_0) + (t - t_0)^2 / 300(\text{sec}) \right] + \frac{1}{3} \sigma_u^2 (t - t_0)^3 \quad (3)$$

Survey data from September 5 through September 11, 1992, was processed for this analysis. The FDF received slightly over 4 hours of continuous data for each of these days, and all of the available data for these days were used. The average over all of the gyro channels for each of the days processed (seven intervals) of the propagation variance was assumed to be of the form

$$Q(\Delta t)^2 = a_1(\Delta t + \Delta t^2 / 300\text{sec}) + a_3(\Delta t)^3 \quad (4)$$

and a least squares fit to the parameters a_1 and a_3 was performed. The temperature dependence of the white noise strength parameters is neglected. The parameters computed will reflect the RMS of the white noise strength parameters over all the gyro channels. The final procedure is described below:

1. Find timespans of data that are at a nearly constant rate for the entire timespan; for EUVE, we used the playback survey mode data from September 5 through September 11, 1992.
2. Ensure that there are no extreme temperature variations of the gyros. By visual inspection of the data, the temperature varied no more than 1 sensor count (.14 deg Celsius) from its median value for the days chosen (with the exception of infrequent, short-lived peaks of 2 counts, which are possibly noise in the temperature sensor output).
3. Process the primary and backup channel information for each axis, differencing the backup channel from the primary channel to remove the signal and leave only the value of the backup channel's noise subtracted from the primary channel's noise and the difference in the two channels' biases.
4. Compute the initial bias using a 5-minute timespan and compensate for the initial bias throughout the timespan of data used.

The cubic equation describes the model for the variance of the accumulated angle due to gyro noise or equivalently the expected value of the noise-driven propagation error squared. The gyro noise samples are accumulated (or propagated) over time, and a least squares fit to Equation (4) is performed on the average (over all timespans and over all gyro axes) square of the gyro noise propagation error. The white noise strengths σ_v and σ_u indicated by the data taken can then be calculated and compared to expected values.

A total of 21 sample points of the propagation variance (3 axes and 7 days) is available for propagation times over 4 hours. The 4-hour length is constrained by the length of the data routinely provided the FDF on a given day. The 21 points give an average propagation error (squared) that can be fit to Equation (2) with results depicted in Figure 4. Data points are indicated by the squares; the fitting curve is the dark line.

The 1-sigma white noise strengths for an individual channel that corresponds to the cubic fit shown above are

$$\sigma_v = 0.12 \text{ arcsec} / \text{sec}^{1/2} \quad (5)$$

and

$$\sigma_u = 5.21 \times 10^{-5} \text{ arcsec} / \text{sec}^{3/2}$$

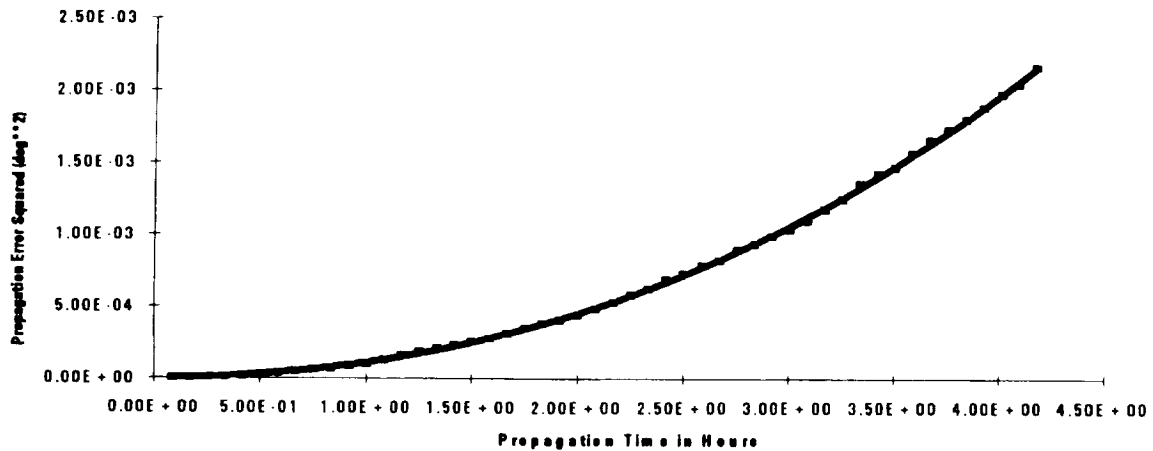


Figure 4. Average Variance Over All Channels (High Rate)

Typical values used for the DRIRU II in low-rate mode, (for GRO and EUVE, for example), are

$$\sigma_v = 0.042 \text{ arcsec}/\text{sec}^{1/2}$$

and

$$\sigma_w = 4.44 \times 10^{-5} \text{ arcsec}/\text{sec}^{3/2} \tag{6}$$

Our values are for the DRIRU II in high-rate mode, so no direct comparison can be made except that the computed values are higher and on the same order of magnitude. This comparison to the onboard numbers, which are based on ground analysis for the low-rate mode, is made mainly to verify our results. Since our results are for the DRIRU II in the high-rate mode and the EUVE and GRO values are for the low-rate mode, attempting to draw any further conclusions about the accuracy of the onboard numbers would be specious because the parameters could differ depending on the rate mode. Based on these data, the onboard white noise strengths used by the EUVE onboard Kalman filter when the gyros were in the high-rate mode should have been increased from the expected values of gyros in the low-rate mode.

Discussion of Results

The first goal, to validate the noise model using on-orbit data, can be considered accomplished, although only for the DRIRU II in high-rate mode and for EUVE in survey mode so that temperature effects are reduced. The cubic fit to the average covariance of the propagation error due to noise is accurate enough from a practical sense for onboard processing. Furthermore, early in the mission, when EUVE was using the gyros in the high-rate mode (necessary for the survey phase), the gyro noise parameters used by the onboard Kalman filter were for the low-rate mode. Based on the white noise strengths computed for the high-rate mode, this could cause a decrease in the accuracy of the onboard attitude determination algorithm, and was, in fact, seen (Reference 5). Based on recommendations from the FDF, the low-rate mode was used when possible for EUVE to improve the onboard attitude determination. Another solution would have been to tailor the noise parameters to the high-rate case when the gyros were in high-rate mode.

However, the difficulties due to changing gyro temperatures do cause concern. As discovered during our analysis, the gyro parameters appear to be temperature dependent to a degree that might impact the usefulness of the noise model. Further analysis is necessary, using low-rate data when EUVE is inertially fixed, to quantify the impact of the temperature dependence on the noise model accuracy for the low-rate scenario.

Potential topics for further analyses are as follows:

1. Investigate the temperature effects on the gyro parameters
2. Continue analysis of the low-rate mode to determine the impact of the temperature dependence on the applicability of the noise model
3. Process further data and compute the statistical confidences of the results

Power Spectral Analysis

The aim in using the power spectra of the gyro noise is (1) to identify the signals associated with the operation of the solar array and science instruments and (2) to obtain a baseline signature of the gyro noise as a diagnostic aid. It has been the experience of the FDF (GSFC) that gyro failure can be predicated from an increase in gyro noise. Signal detection is best accomplished by using frequency analysis rather than time domain analysis. Power spectra method has an extensive literature base (References 6 and 7), but we follow basically the development in Reference 7.

For a continuous function, $h(t)$, there exists a Fast Fourier Transform (FFT) $H(f)$ if the integral over all times, t , of the absolute value of the function (time series) is bounded or if the function $h(t)$ is monotonically decreasing function of t or if the $h(t)$ can be represented by a curve of finite height in any finite time. Since the gyro data are sampled discretely, rather than continuously, the FFT is correctly represented only with the range of the Nyquist frequency, $-f_c$ to f_c , or that the transform is band limited. The Nyquist frequency is defined as $(1/2T)$, where T is the sampling interval.

If the function $h(t)$ is continuous, then a sample of $h(t)$ at times separated by T can be represented as

$$\sum_{n=-\infty}^{n=\infty} h(t) \delta(t - nT) \quad (7)$$

and is an infinite sequence of equidistant impulses (from the delta function) each of whose amplitude is given by the value of $h(t)$ at the time of occurrence. A truncation function, $x(t)$, must be used since the sample signal is of finite duration. The truncation (or window) function is defined below for a given duration T_0 .

$$\begin{aligned} x(t) &= 1 & -T/2 < t < T_0 - T/2 \\ &= 0 & \text{otherwise} \end{aligned} \quad (8)$$

Thus, the expression $h_s(t)$

$$h_s(t) = \sum_{n=-\infty}^{n=\infty} h(t) \delta(t - nT) x(t) \quad (9)$$

represents $N = T_0/T$ sample points of the function $h(t)$. The truncation of the time series introduces rippling in the FFT. The discrete FFT of truncated sample wave form is given by

$$H(n/NT) = \sum_{k=-\infty}^{k=N} \sum_{n=-\infty}^{n=\infty} h(t) \delta(t - nT) x(t) e^{j2\pi kn} \quad (10)$$

We use the FFT algorithm, popularized by Cooley and Tukey, to compute the FFT of the truncated sampled gyro signal. To obtain the power spectral density function of $h_s(t)$, suppose that the number of observations $N = 2q + 1$ is odd. If we use a Fourier series to model the time series, such as,

$$z(t) = \alpha_o + \sum_{i=1}^q \{\alpha_i \cos(2\pi f_i t) + \beta_i \sin(2\pi f_i t)\} + \varepsilon(t) \quad (11)$$

where $f_i (= i/T)$ is the i^{th} harmonic of the fundamental frequency ($1/T$) and $\varepsilon(t)$ is the random noise with zero mean and constant variance σ^2 . The terms in the curly bracket represent the signals produced by the solar array movement and the operation of the science instruments. A least squares estimate of the coefficients α_o , α_i , and β_i yields for $i = 1$ through q

$$\begin{aligned} a_o &= \text{gyro bias } \langle z(T) \rangle \\ a_i &= (2/N) \sum_{m=1}^N z(mt) \cos(2\pi f_i t) \\ b_i &= (2/N) \sum_{m=1}^N z(mt) \sin(2\pi f_i t) \end{aligned} \quad (12)$$

The spectral power or amplitude in the i^{th} harmonic is

$$P(f_i) = (N/2)(a_i^2 + b_i^2) \quad i = 1, 2, 3, \dots, q \quad (13)$$

and result for even N is similar except that the b_i are zero. The FFT of the gyro rates would yield the harmonic content of the gyro rates, i.e., the a_i and, subsequently, the power spectral density. The expectation value of the variance of the time series is related to the PSD in a simple way.

$$\sum_{t=1}^N (z(t) - \langle z(t) \rangle)^2 = \sum_{i=1}^q P(f_i) \quad (14)$$

If the times series consisted only of white noise, then the amplitude of $P(f)$ would be equal to

$$P(f_i) = 2\sigma^2 \quad (15)$$

and its amplitude would be independent of frequency. White noises ordinarily defined as noise that possess a flat power density spectrum for all frequencies. Evidently, if the PSD has a constant value for all frequencies, the total power represented by the noise would be infinite. In practice, we defined white noise as a flat power spectral density over the frequency range of interest. However, any harmonic content in the times series would add to the value of variance at those harmonic frequencies.

$$P(f_i) = 2\sigma^2 + N(a_i^2 + b_i^2)/2 \quad (16)$$

In practice, it is not very probable that the frequency of the unknown sinusoidal component would match any of the calculated FFT frequencies. More likely, the variance would be spread among several frequencies and resemble a peak with finite width more than a delta function spike.

The PSD is related to the autocorrelation $R_x(t)$ by

$$PSD = \int_{-\infty}^{\infty} R_x(t) e^{-2\pi i f t} dt \quad (17)$$

We assume the autocorrelation to be described by

$$\langle v(t)v(t') \rangle = \sigma_v^2 \delta(t-t') \quad (18)$$

and perform the integration to obtain

$$PSD = \sigma_v^2 \quad (19)$$

where the units of σ_v^2 are $\text{arcsec}^2/\text{time}$ ($\text{arcsec}^2/\text{sec}$). The PSD will have the units of the quantity being analyzed (rad/sec) squared per freq (sec^{-1}). So, our units should be $\text{rad}^2/\text{sec}^2$. However, we are performing the discrete Fourier Transform. The relation between the discrete Fourier transform (H_n) of a set of numbers and their continuous Fourier Transform ($H(f_n)$) when they are viewed as samples of a continuous function sampled at an interval dt can be rewritten as $H(f_n) \approx dt \cdot H_n$. As we are computing the discrete Fourier Transform of the rates and using the square of the magnitudes to represent the PSD, we need to multiply by dt^2 squared to get to an approximation to the continuous PSD, which is related to the continuous autocorrelation (with the delta function) as above.

For low rates, the $0.042 \text{ arcsec}/\text{sec}^{1/2}$ value for the white noise and the equation

$$P(f) = 2\sigma^2 \quad (20)$$

gives a value for our discrete PSD of

$$\begin{aligned} PSD &= 2 \cdot \sigma_v^2 / (.128\text{sec})^2 \\ &= 2 \cdot (57.296)^{-2} \cdot 3600^{-2} \cdot 0.042^2 / (0.128)^2 \\ &\approx 5 \cdot 10^{-12} \end{aligned} \quad (21)$$

Two criteria are used to identify significant peaks in the power spectral density. First, only peaks that have amplitude that are at least an order of magnitude larger than the background level are considered. This criterion establishes the signal peak as statistically significant. Secondly, signal peaks that have finite bandwidths are indicative of complex physical processes.

The two main practical limitations for applying the power spectra method are as follows: (1) the length of the times series should not be a multiple of the frequency of interest and (2) the frequency of interest must be below half of the sampling frequency. However, in most cases, one does not know the frequency of interest. The most reasonable way to analyze the power spectra is to obtain spectra for different sample lengths. In this way, the occurrence of false periodicities are minimized.

Power Spectra of UARS Gyroscopic Rates

Data from UARS were used for two basic reasons: (1) the solar array motion was known to induce motion in the spacecraft and (2) some of the scientific instruments were suspected of causing motion in the spacecraft. A search was made of the archival data for timespans in which investigators could isolate noise associated with the quiescent spacecraft from that of the operation of the solar arrays, the science instruments, and nominal operations. For the quiescent period, June 4, 1992, was selected since the science instruments were turned off, and the solar array was parked. On August 8, 1993, there was an extended period when only the solar array was in operation. Three days later, on August 11, at 17:50 Greenwich mean time (GMT), the UARS science instruments were turned on. February 6, 1994, was selected to represent nominal operations.

On board the UARS spacecraft, the gyroscopes' digital rates are sampled every 0.128 sec, which is subsequently sent to the FDF for ground processing. On the ground, the digital rates are converted to gyro rates in units of

rad/sec. These data are ordinarily used to determine the spacecraft's attitude. We applied the FFT to computed gyro rates samples that were of different lengths (15 and 30 min) and different sampling times (.152 and .128 sec, respectively). The units of the PSD are $\text{rad}^2/\text{sec}^2$.

In Figures 5, 6, and 7, we have the power spectra density function from the quiescent period. The spectra indicates that the noise level of the PSD is about $10^{-12} \text{ rad}^2/\text{sec}^2$. This implies a white noise level corresponds to a digital rate of about 0.2 arcsec/sec. On the X and Z-axis, there are four peaks that are in common to both plots, namely, .24, .97, 1.95, and 2.93 Hertz (Hz). The major difference between these axes is that the peak at .24 Hz on the X-axis is 10 times larger than one on the Z-axis. The Y-axis, which is the pitch axis, is the axis about which UARS rotates once an orbit (1 rpo) and its power spectra does not have a well-defined peak at 0.24 HZ. The pitch axis does, however, have several frequencies of interest. The frequencies are as follows: 0.479 , 0.956 , 1.43, 1.95, 2.44, 2.93., 3.43 Hz.

Data from August 8, 1993, in which only the solar array is operating, shown in Figures 8, 9 , and 10, indicates a large increase in the amplitude on all three axes of at least three orders of magnitude at .24 and .956 Hz. In addition, there is a small peak at 2.15 Hz in the power spectra of the X and Z axis. The pitch axis does not contain this frequency.

Data from August 11, 1993, in which all the science instruments are turned on, does not indicate any new frequencies with a finite width. Likewise, the data from February 6, 1994, does not indicate any significant new frequency information other than a slight increase in the noise level. Figures 11 and 12 are representative samples of the data from the period when the science instruments were turned on and off from nominal operations.

Discussion of Results

The immediate goal of the power spectra analysis, which was to determine whether the method can be used to identify spacecraft motion due to the solar array and science instrument, has been obtained. The signature of the solar array consists of large amplitude noise at 0.24 and 0.967 Hz. Additionally, there is a small peak at 2.15 Hz. There does not seem to be a noise signature associated with the operation of the science instruments.

However, further analysis is needed to explain the presence of a large number of peaks with very narrow frequency bandwidth. The occurrence of these frequencies may be related to bandwidth. It is well known that high-frequency resolution (small bandwidth) leads to large variances of the estimate of power spectra while low-resolution (wide bandwidth) produces a stable estimate (Reference 7). On the other hand, presence of these frequencies may be related to how we compute the gyro rates. The basic time step in both these cases is .128 sec. Finally, the sharp peaks may indicate aliasing or over sampling. The presence of increased noise levels near the Nyquist frequency is the standard indicator of aliasing.

A comparison between the UARS and EUVE power spectras was performed to determine if EUVE gyros had a similar signature to UARS. The calculation of EUVE gyro rates is completely different from that of UARS. The data in Figure 13 indicate well-defined signal peaks at 0.976, 1.953, and 2.93 Hz. The EUVE power spectra in Figure 13 represents FFT of 8,192 points from a time series of 16,384 points. Since the Telemetry Processors (TPs) for EUVE and UARS are so different, but mathematically equivalent, the weight of evidence indicates that the abovementioned peaks may be characteristic of the Teledyne DRIRU II gyroscopes and/or multimission spacecraft.

The presence of similar peaks in both power spectral densities rules out computational error in the way rates are computed but does not rule out aliasing. The FFT computer program does not calculate FFT above the Nyquist frequency of the time series, but the time series has not been filtered to remove frequencies above the Nyquist frequency. Note that every point in the time series contributes, in principle, to the amplitude of every harmonic. Further work needs to be done to construct a time series filter that would provide a definitive answer about the significance of the narrow peaks.

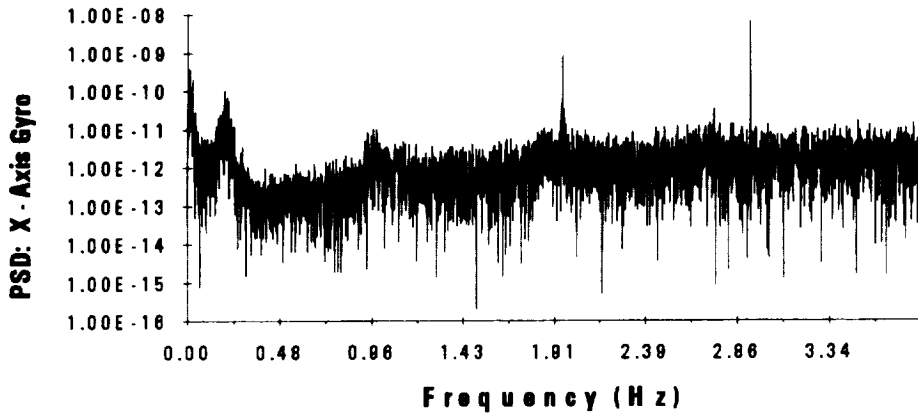


Figure 5. Power Spectra of the X Axis: 920604: (Sample = .128 sec)(N = 8192)

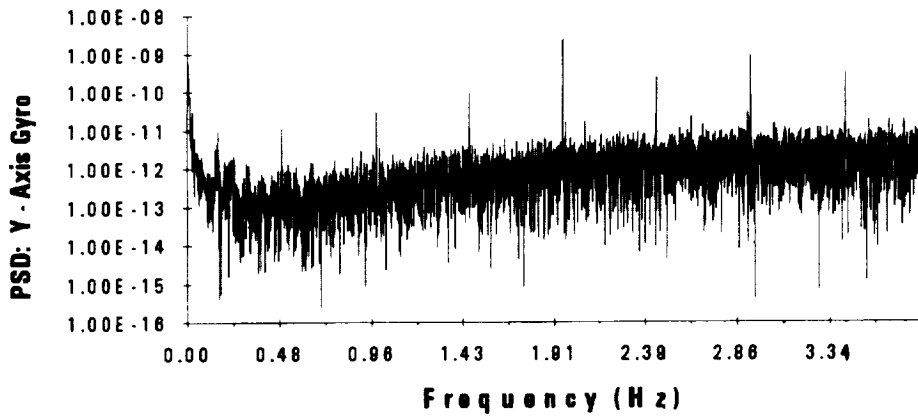


Figure 6. Power Spectra Y Axis: 920604 (Sample time = .128 sec)(N = 8192)

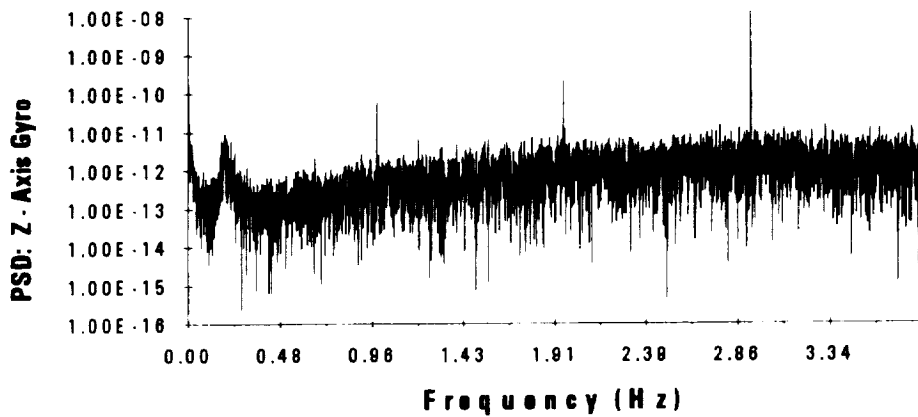


Figure 7. Power Spectra Z Axis: 920604 (Sample time = .128 sec)(N = 8192)

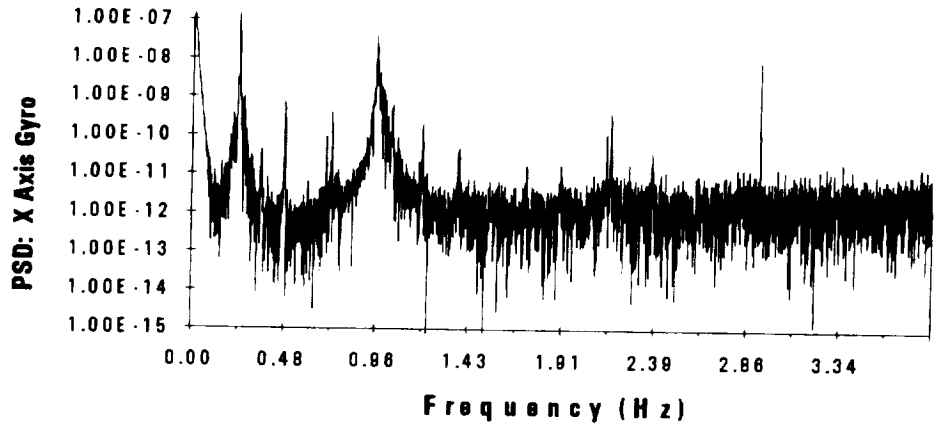


Figure 8. Power Spectra X-axis: 930808 (Sample time = .128 sec) (N = 8192)

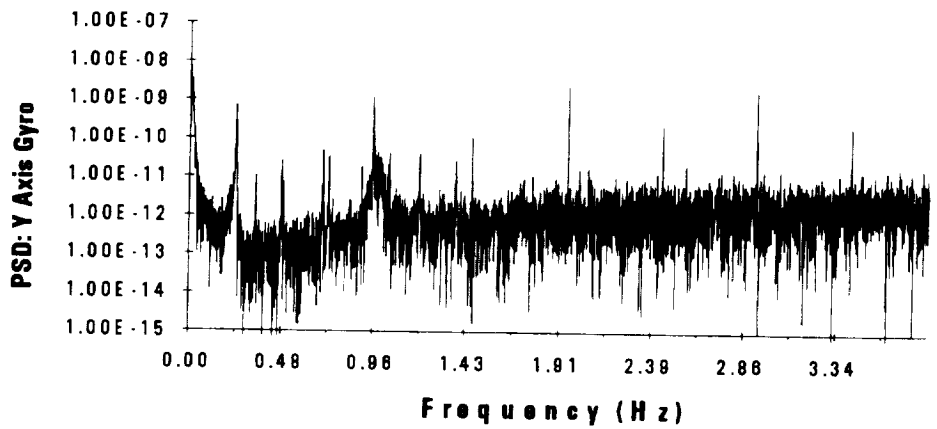


Figure 9. Power Spectra Y-axis: 930808 (Sample time = .128 sec) (N=8192)

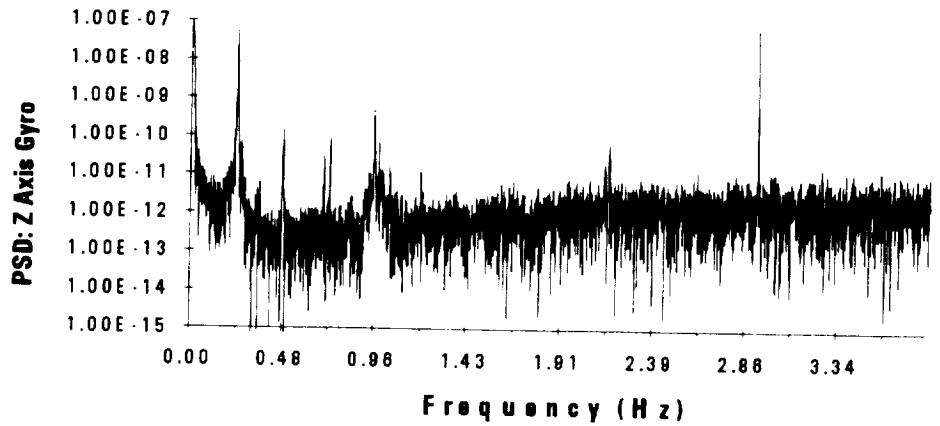


Figure 10. Power Spectra Z-axis: 930808 (Sample time = .128) (N = 8192)

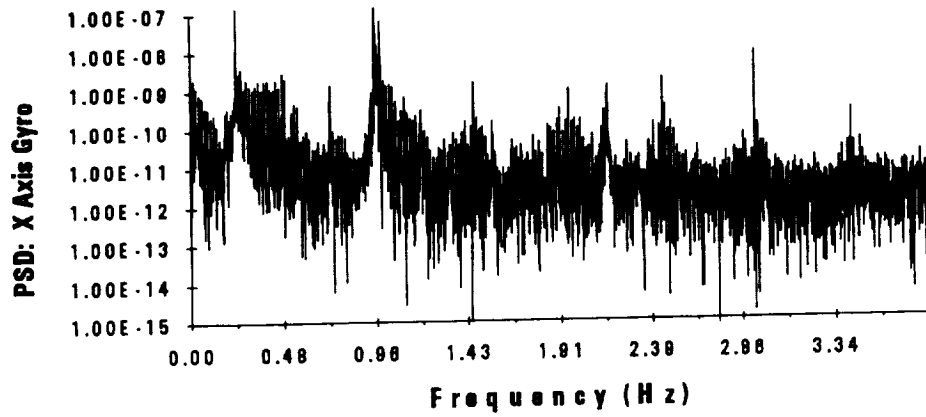


Figure 11. Power Spectra X-axis: 930811 (Sample time = .128 sec) (N = 8192)

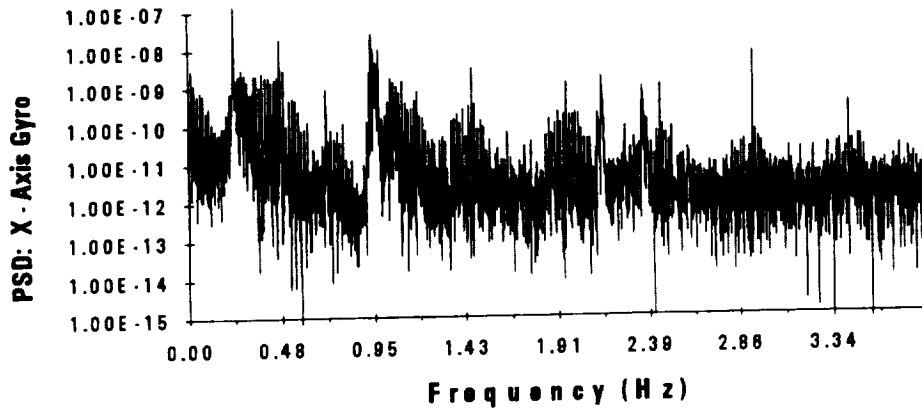


Figure 12. Power Spectra X-axis: 940206 (Sample time = .128 sec) (N = 8192)

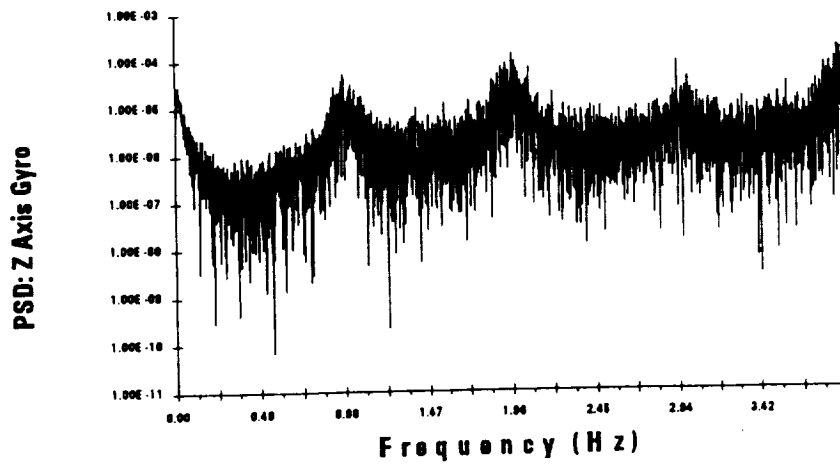


Figure 13. EUVE Coefficients for Z Channel (7/2/92) (N = 16384)

References

1. Teledyne Systems Company, Equipment Specification for High Performance Dry Gyro Inertial Reference Unit (DRIRU II), November 9, 1979
2. R. L. Farrenkopf, "Generalized Results for Precision Attitude Reference Systems Using Gyros," AIAA Mechanics and Control of Flight Conference, Anaheim, CA, August 5-9, 1974, AIAA Paper No. 74-903
3. V. K. Kumar, E. L. Wright, and F. S. Patt, "COBE Ground Segment Attitude Determination," Proceedings of Flight Mechanics and Estimation Theory Symposium, May 21-23, 1991
4. T. Z. Willard, O. H. Filla, D. Chu, and J. Deutschmann, "In-Flight Estimation of Gyro Noise," Proceedings of Flight Mechanics and Estimation Theory Symposium, May 22-24, 1990
5. M. Lee, Memorandum from 553.1/Attitude Section (the Flight Dynamics Facility) to 513/Project Operations Branch/K. Hartnett, January 4, 1993
6. R. B. Blackman and J. W. Turkey, Dover Publications, The Measurement of Power Spectra, Inc., New York, 1959
7. E. O. Brigham, The Fast Fourier Transform and its Applications, Prentice Hall, Englewood Cliffs, New Jersey, 1988

Operational Support for Upper Atmosphere Research Satellite (UARS) Attitude Sensors*

M. Lee

National Aeronautics and Space Administration (NASA)
Goddard Space Flight Center (GSFC)
Greenbelt, Maryland, USA

A. Garber, M. Lambertson, P. Raina, S. Underwood, and C. Woodruff
Computer Sciences Corporation (CSC)
Lanham-Seabrook, Maryland, USA

Abstract

The Upper Atmosphere Research Satellite (UARS) has several sensors that can provide observations for attitude determination: star trackers, Sun sensors (gimbaled as well as fixed), magnetometers, Earth sensors, and gyroscopes. The accuracy of these observations is important for mission success. Analysts on the Flight Dynamics Facility (FDF) UARS Attitude task monitor these data to evaluate the performance of the sensors, taking corrective action when appropriate. Monitoring activities range from examining the data during real-time passes to constructing long-term trend plots. Increasing residuals (differences) between the observed and expected quantities is a prime indicator of sensor problems. Residual increases may be due to alignment shifts and/or degradation in sensor output. Residuals from star tracker data revealed an anomalous behavior that contributes to attitude errors. Compensating for this behavior has significantly reduced the attitude errors. This paper discusses the methods used by the FDF UARS attitude task for maintenance of the attitude sensors, including short- and long-term monitoring, trend analysis, and calibration methods, and presents the results obtained through corrective action.

Introduction

UARS Mission Description. UARS carries 10 science instruments that perform its mission objectives: to study (1) energy input and loss in the upper atmosphere, (2) the global photochemistry and dynamics of the upper atmosphere, (3) the relationships among these processes as well as the coupling between the upper and lower atmosphere (Reference 1). To achieve its mission goals, UARS is flying at approximately 585 kilometers (km) altitude in a nearly circular orbit, which has a 57-degree (deg) inclination and an Earth-oriented attitude. The UARS attitude is expressed as a 3-1-2 (yaw-roll-pitch; Z-X-Y) Euler rotation, with reference to the Orbital Coordinate System (OCS). The OCS is defined as having the yaw axis parallel to the negative of the Earth-to-spacecraft vector and the pitch axis pointing parallel to the negative of the orbit normal vector. The estimation and control requirements for the attitude are 60 and 108 arcseconds (arcsec) (3 standard deviations (3σ)), respectively, for each axis.

An important parameter related to the orbit is the solar beta angle. The solar beta angle is the complement of the angle between the orbit normal vector and the Earth-to-Sun vector. The beta angle is constantly changing due to the combined motion of the UARS orbit precession and the Sun in the celestial sphere. The changing solar beta angle forces UARS to perform an attitude maneuver approximately monthly. The Sun must be kept in the hemisphere bounded by the X-Z plane and containing the solar array for power considerations and science instrument protection. As the beta angle passes through 0 deg, UARS must perform a yaw maneuver of 180 deg. UARS is said to be flying forward when its positive X-axis is aligned with its velocity vector and backward when its negative X-axis is aligned with its velocity vector.

* This work was supported by the National Aeronautics and Space Administration (NASA) Goddard Space Flight Center (GSFC), Greenbelt, Maryland, under Contract NAS 5-31500.

Engineering support for the mission is provided by a standard Multimission Modular Spacecraft (MMS) bus. The MMS, built by Fairchild Space Company, consists of a communications and data handling (C&DH), power, signal conditioning, propulsion, and attitude control subsystems. The Modular Attitude Control Subsystem (MACS) has Earth sensors, fine and coarse Sun sensors, magnetometers, fixed-head star trackers (FHSTs), and inertial reference units (IRUs (gyroscopes)) available for use in attitude estimation. The Earth sensors are Ithaco-manufactured Earth sensor assemblies (ESAs), which perform conical scans and sense the infrared horizon of the Earth; UARS has two ESAs. The coarse Sun sensors (CSSs) are manufactured by Adcole. These are backup sensors for safehold situations and are not analyzed in this paper. The pair of three-axis magnetometers (TAMs) are flux-gate units manufactured by Schoenstadt. Besides providing safehold attitude support, they give information used to adjust the FHST measurements. There are three fine Sun sensors (FSSs): one mounted on the MACS, called the MACS FSS, and two mounted on the Solar-Stellar Pointing Platform (SSPP), called platform Sun sensors (PSSs). These are two-axis digital sensors manufactured by Adcole. The SSPP provides pointing control for some of the science instruments. The FSS and the PSSs differ in that the FSS has a 64-by-64 deg field-of-view (FOV) and is a backup to the FHSTs, while the PSSs have only a 4-by-4 deg FOV and are used primarily to determine the pointing of the SSPP. The PSSs are also much more accurate than the FSSs. The two FHSTs manufactured by Ball Electro-Optics/Cryogenics Division (BECD) (Reference 2) are the primary attitude sensors. The onboard computer (OBC) normally computes attitudes and gyro rate biases using star observations from the FHSTs, along with rates determined by the Teledyne dry rotor inertial reference units (DRIRU IIs) (Reference 3) in a Kalman filter.

Flight Dynamics Facility Support for UARS Attitude Sensors. The Flight Dynamics Facility (FDF) at Goddard Space Flight Center (GSFC) provides orbit and attitude support for GSFC-managed space missions. FDF attitude support responsibilities for the UARS mission include

- Real-time and near real-time attitude monitoring
- Trend analysis of sensor and onboard attitude determination performance
- Production of definitive attitudes as requested by the scientist
- Attitude and high-gain antenna contact predictions
- Attitude sensor calibration/alignment
- Science and mission planning aids

The software systems used by FDF to provide this support are the attitude determination system (ADS), the calibration and attitude validation systems, and several utilities that run exclusively in batch (noninteractive) mode. Most of the software is part of the Multimission Three-Axis Stabilized Spacecraft (MTASS) Flight Dynamics Support System (FDSS), which was developed by Computer Sciences Corporation (CSC) under a GSFC-managed National Aeronautics and Space Administration (NASA) contract (Reference 5). The MTASS system provides functions that are common to three-axis stabilized spacecraft support. (It is currently used to support two other operational missions: the Extreme Ultraviolet Explorer (EUVE) and the Solar, Anomalous, and Magnetospheric Particle Explorer (SAMPEX) missions; several upcoming missions also plan to use parts of the MTASS system for their attitude support.)

The ADS processes the spacecraft telemetry sequentially through a mission-unique telemetry processing subsystem and mission-independent data adjustment, star identification, and attitude determination subsystem. The onboard-determined attitude can then be compared to that computed by the ADS; the differences are a measure of OBC attitude determination and control accuracy. The definitive attitude determination system (DADS) is designed to create a file containing 24 hours of UARS attitude from ADS solutions in the event of OBC attitude estimation problems. So far this has actually been needed only once.

There are six calibration systems. The FHST/Earth sensor/FSS calibration system (FEFCAL) computes alignments according to an attitude-independent method developed by Shuster, Chitre, and Niebur (Reference 8) and later refined by Shuster and Bierman (Reference 9). Gyro biases and the gyro scale factor/misalignment matrix are computed by the IRU calibration system (IRUCAL) using an algorithm developed by Davenport and documented by Keat (Reference 10). The

TAM calibration system (TAMCAL) computes the biases and TAM scale factor/misalignment matrix based on an algorithm developed by Lerner and Shuster (Reference 11). The FSS field of view system (FSSFOV) calculates the nine parameters required for the Adcole FSS; both the MACS FSS and the PSSs can be calibrated. Finally, the SSPP gimbals can be calibrated using SSPPCAL. Each system uses processed telemetry and/or the adjusted data. Calibration results are typically confirmed by before and after comparisons of sensor residuals in the coarse/fine attitude determination system (CFADS). Following verification, the calibration results may be made available for processing in the ADS and for uplink to the spacecraft.

The attitude verification system (ATTVAL) compares Euler angles for any two attitudes. Operationally, the OBC determined attitude is compared to the ADS-determined attitude. Statistics for the differences in the Euler angles are displayed for the analyst's interpretation.

Attitude Data Trending and Problem Analysis. The Attitude task processes 2 hours of data three times each week and trends the results over the life of the mission. The ground ADS uses star tracker data and gyro rates in a batch least-squares algorithm to determine the attitude and the gyro biases (assumed constant over the 2-hour interval). Values that are trended include sensor root-mean-square (RMS) residuals, which are computed from a comparison of the observed vectors to the reference vectors; the onboard versus ADS attitude comparison results; the ground-based (ADS-computed) gyro bias correction; and the TAM bias correction. Parameters from the planning aids software, such as star density, are also trended for use in analysis.

Plots of these data are examined for anomalies; however, the causes must be carefully discerned because anomalies can result from operational errors as easily as from real problems with the attitude sensors or may result from the ill behavior of another component of the system. It is important to recognize that the residuals are based on the ground processing because the sensor alignments are updated more frequently on the ground than onboard the spacecraft. To accomplish the proper validation of the OBC attitude, the most accurate sensor calibration is used in the ground processing to account for potential shifts in the sensor performance over time. Updates in the ground sensor parameters are often visible in the plot of the sensor residuals discussed later in the paper.

Fixed Head Star Trackers

The primary sensors used for attitude determination by the UARS spacecraft are the FHSTs. In addition to this function, they are used to produce high-quality attitudes that are used to perform gyro calibrations and to evaluate calibrations of the coarser sensors. Correct calibration of the FHSTs is, therefore, considered of utmost importance to the mission.

These sensors search for, detect, and track stars as they pass through an 8-by-8 deg FOV. By focusing light from the star being tracked on the photocathode of an image dissector tube, the position and intensity of the star can be determined. The UARS FHSTs can track stars from magnitude 2.0 to 5.7. They are mounted on the MACS with approximately a 76-deg angle between boresights. The digital resolution of the sensors is 7.78 arcsec with a manufacturer's specified accuracy of 10 arcsec inside an 8-deg circular central FOV. Star positions are given as the distance from the center of the FOV in two orthogonal directions referred to as H and V. The parameters are converted to a unit vector in the data adjustment process.

For UARS, one of the Ball FHSTs (designated FHST1) is experiencing scale factor drift. The scale factor is a counts-to-degrees conversion factor that is applied to the two star position parameters H and V in the data adjustment process. Changes in this scale factor had been seen in previous missions and was, therefore, anticipated for the UARS FHSTs. An apparent rotation of the FHST about its boresight accompanies this drift and is believed to result from the same source (Reference 12).

An analysis utility, developed by Joseph Hashmall and William Davis of CSC, determined new scale factors for the trackers. This utility performs a least-squares fit of the horizontal and vertical position errors. The slope of this linear fit is then used as a multiplicative correction factor for the nominal scale factor value to eliminate these position errors.

Methods

The star tracker residuals are trended as discussed previously, and plots are generated. New alignments and scale factors are computed and the ground processing of the tracker observations updated to the new values as needed. In addition, the onboard parameters are updated but less frequently, based on FDF recommendations as to when the onboard attitude determination is becoming too inaccurate. Due to the scale factor drift of FHST1, the FHST1 alignment is being updated much more frequently than is normally expected.

Results

Figure 1 shows a steady increase of FHST1 residuals (from flight days 450 to 679), which appeared to correspond to the pitch axis attitude residuals shown in Figure 3. The FHST residuals shown are the difference between the observed vectors and the reference vector if the ground attitude is assumed to be true. This gives a measure of sensor and ground determined attitude accuracies. Figure 2, however, shows that the residuals for the FHST2 observations did not have a systematic change over time, which indicated that the problem was endemic to FHST1 rather than in the ground attitude determination. Both scale factors for FHST1 were also shown to be changing nearly monotonically, as can be seen in Figure 4. An analysis by Lee (Reference 13) proved that this scale factor drift could cause the pitch axis errors evident in Figure 3.

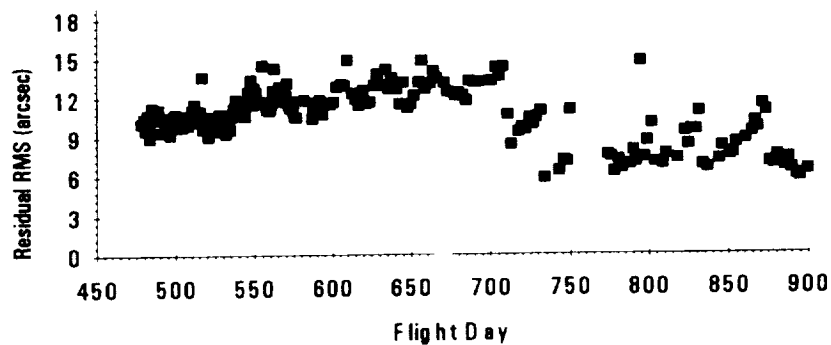


Figure 1. FHST1 RMS Residual (arcsec)

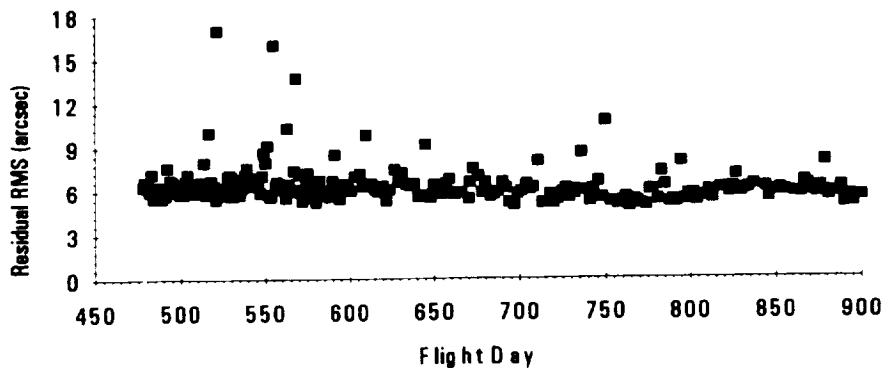


Figure 2. FHST2 RMS Residual (arcsec)

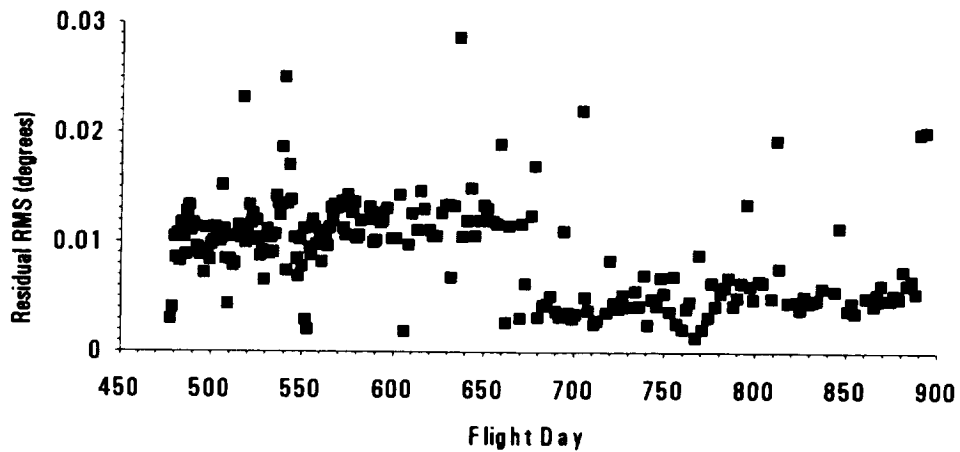


Figure 3. Errors in Pitch Axis Euler Angle

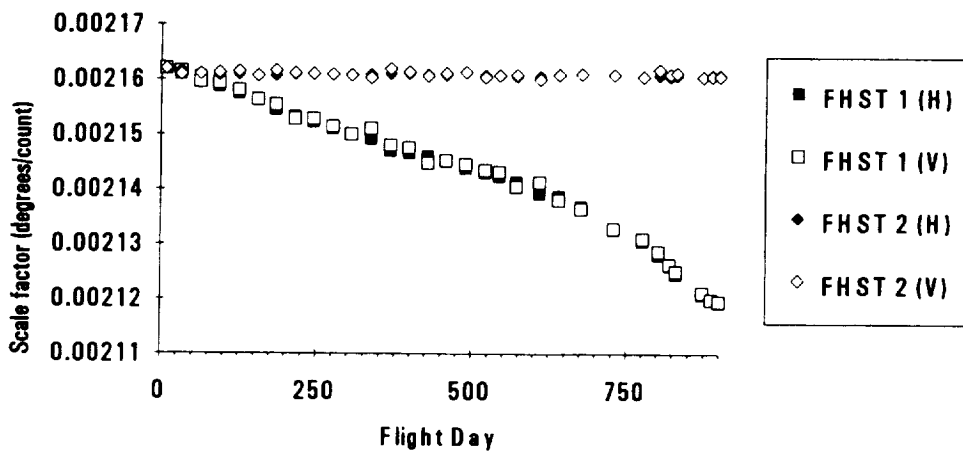


Figure 4. FHST1 Scale Factors Changing with the Flight Day

On flight day 679 (July 21, 1993), new H and V scale factors computed by the FDF were uplinked to UARS by the FOT for use in the onboard computations. This corrected the OBC-computed pitch attitude, as can be seen in Figure 3. This was followed by an uplink of the FHST1 alignment calibration on flight day 709. The alignment and scale factor calibrations were also updated in the ground system on day 709. This resulted in the reduction of the star observation residuals illustrated in Figure 1.

Based on the apparently more rapid degradation of FHST1 seen in Figure 3, the Attitude Operations task began to perform scale factor updates and alignment updates in the ground system more frequently. Figure 1 shows a decrease in FHST1 sensor residuals each time the scale factor was updated on the ground (flight days 817 and 888). Using the current scale factors and alignments in the ground system reveals the attitude error due to use of outdated FHST information in the OBC computations. The operations analysts can then determine when the onboard calibrations need to be updated by comparing the residuals to the OBC attitude estimation requirements.

The success of the corrections made on flight days 679 and 709 along with the increased monitoring has resulted in subsequent uplinks of FHST scale factors and alignments. The procedure is to uplink the scale factors, confirm their corrections by reviewing playback data, and then uplink the alignments a few days later. Uplinks occurred again on flight days 814 and 817. The corrections from these uplinks are not as obvious in the pitch residuals as from the first uplink because the error had not been allowed to grow as large.

Fine Sun Sensors

The FSS provides two-axis Sun direction information with respect to the sensor axes as FOV parameters α and β . The sensor consists of two orthogonally mounted single-axis sensor units. Each unit contains two reticles: one coarse and one fine. The reticles are composed of two thin fused silica plates separated by a fused silica spacer. Reticle patterns are located on the insides of the plates. Silicon photocell arrays are located below each reticle, which are used to provide the angle data (Reference 7). The overall accuracy of the FSS is specified to be within 60 arcsec within a 60-deg circular FOV, and 120 arcsec outside the 30-deg FOV.

The FSS residuals were seen to be steadily increasing, prompting calibration of the FSS alignments.

Methods

The UARS FSS alignment is calibrated using the same Shuster algorithm and at the same time as the FHSTs. The FSS is also calibrated for FOV variations. The FOVCAL system uses the Levenberg-Marquardt method (Reference 13) to solve a nonlinear least-squares model for the calibration coefficients. These coefficients are used in constants in a transfer function to convert the counts to the FOV parameters α and β . The current operational transfer function was provided by Adcole.

Results

The UARS FSS alignments have been updated onboard and in the ground system each time the FHST alignments have been uplinked. Figure 5 shows that the RMS residuals for the FSS dropped almost in half due to the new alignment uplink that occurred on flight day 708. However, with the next calibration uplink on flight day 817, the FSS residuals increased back to near the original levels. This indicates that the alignment may be inaccurate. A new FSS alignment was put in the ground system on flight day 888 resulting in reduced residuals.

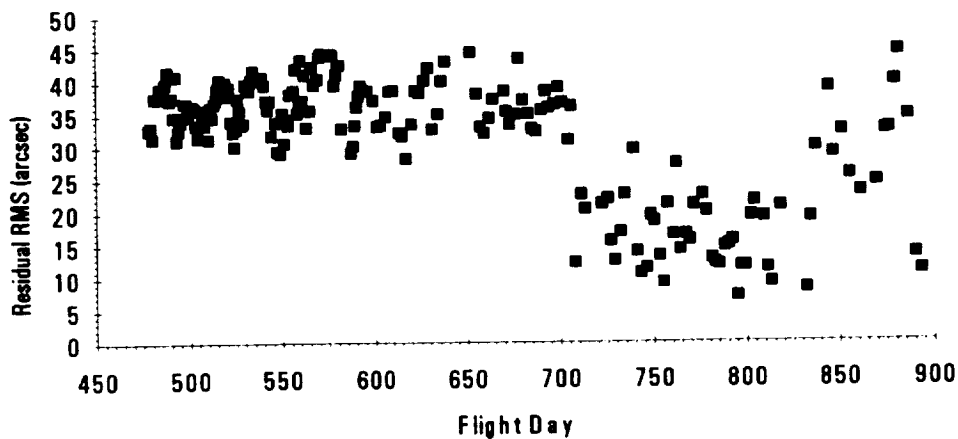


Figure 5. FSS Residuals

The calibration of the FOV coefficients has met with mixed success. The postlaunch on-orbit calibration of the FOV resulted in only a slight improvement over the prelaunch values. Systematic variations of residual magnitudes as a function of the sun's position in the FOV can still be observed even after the postlaunch calibration. As a result, the Sensor Studies task from FDF has undertaken an extensive analysis into this calibration problem (Reference 15).

The original transfer function defined for the FSS involves two equations (one for each axis α and β) with nine coefficients each to convert counts to position in the FOV. The Sensor Studies task developed equations with three additional constants for each axis. Initial analysis by the task shows a reduction in α residuals from an RMS of 73 arcsec to 13, and a reduction in β residuals from 46 arcsec to 15 as reported by Hashmall (Reference 15). Investigation into the possible use of these new transfer function to improve FSS accuracy continues. These results are significant because of the possibility of using the FSS as a replacement for a degraded FHST to maintain the spacecraft attitude within accuracy requirements.

Gyroscopes

UARS has one attitude rate sensor onboard consisting of a strap down gyro package that measures inertial vehicle rates about the sensor axes. The Teledyne DRIRU II consists of three gyroscopes, each with a spinning rotor mounted on two gimbals to provide two degrees of freedom and rate information along two body axes (two channel output) for a total of six channels of information. This allows the IRU to provide dual redundancy along each body axis. To maintain a null deflection on a given gimbal, a current is required to produce a magnetic torque that is proportional to the angular rate about the corresponding axis of that gimbal. This torque current is converted to a series of pulses, which are counted and reported as accumulated rotation angles. The torque current can also be differenced after small time intervals to generate analog rates.

The IRU can operate in two rate ranges. The high-rate mode allows for rates of up to 2.0 deg/sec; low-rate mode allows for rates of up to 400 arcsec/sec (0.11 deg/sec). The digital resolution of the IRU is 0.8 arcsec in the high-rate mode and 0.05 arcsec in low-rate mode. The specified angular rate bias stability for the DRIRU II is on the order of 0.0012 arcsec/sec over a period of 6 hours and 0.0008 arcsec/sec over a year (References 16 and 17).

ADS computes any unresolved body rates as a gyro bias correction in the state vector. The trends for gyro bias corrections from the CFADS state vector exhibited strong dependencies on UARS flight direction, as shown in Figure 6. A possible source of these bias corrections was a ground system timetagging error discovered through investigation of another problem seen in the ground system processing.

Methods

The spacecraft angular rate vector is computed from the following equation:

$$\bar{\omega} = [A]([S]\bar{\Omega} - \bar{B})$$

where $\bar{\omega}$ is the angular rate vector in body coordinates, $[A]$ is an alignment matrix, $[S]$ is a diagonal matrix that produces IRU scale factor adjustments, $\bar{\Omega}$ is the raw unadjusted angular rate vector, and \bar{B} is a bias vector. The alignment part of the IRU calibration, $[A]$, consists of the unit vector of each of the three physical axes. This feature allows the measurement axes to be nonorthogonal. It also incorporates an overall rotation of all three axes. Such a matrix has six degrees of freedom. The transfer function part is parameterized by $[S]$ and \bar{B} . The scale factor for each axis of the sensor and the alignment matrix are combined into a single 3-by-3 alignment/scale factor matrix, $[G] = [A][S]$. The angular rate vector is then given by

$$\bar{\omega} = [G]\bar{\Omega} - \bar{b}$$

where $\bar{b} = [A]\bar{B}$. All nine components of the G matrix can vary independently. Combined with a bias vector, a total of 12 degrees of freedom are to be determined. This is done using an algorithm described by Keat (Reference 10).

Observability in the gyro rates is required for all degrees of freedom solved for in the application of the gyro calibration algorithm. For the calibrations performed by the FDF, nine periods of data spanning three roll offset maneuvers and two yaw maneuvers were used for the gyro calibration. The yaw maneuvers rotate the spacecraft 180 deg. The roll offset maneuvers were first to -5 deg, remained at constant body rates for about 3 hours, then rotated to 5 deg, again remaining at constant body rates for about 3 hours, and finally rotated back to its initial orientation. Calibration was performed with the IRUs at low rate only. The accuracy of the results depends on the accuracy of the ground attitude solutions contained within the timespans of the data used. For this reason, the FHST alignment accuracy impacts the solved for gyro parameters. Additionally, in the ground ADS, the bias correction to the nominal calibration parameters is solved for, and this correction also depends on the star tracker alignments.

Results

The most recent calibration accounts for the timetag error. The new calibration was introduced to the system on flight day-553, and the improvement is easily seen in Figure 6. Changes in the nominal spacecraft rotation rate due to yaw maneuvers can couple with inaccuracies in the gyro to star tracker alignment to appear as discontinuities on the bias correction plot. This is clearly seen for times previous to flight day 553. Table 1 shows the change in the gyro parameters from the prelaunch values to the current gyro alignment.

On flight day 709, the alignment for FHST1 was updated, and an increase can be seen in the Z component of the gyro bias corrections. Based on the FHST and FSS residuals, this most likely indicates that the gyro calibration was performed using a tracker alignment that had some inaccuracies. In general, the gyro bias corrections will respond to tracker performance changes (the actual alignment and scale factors change with time) and as to FHST1 alignment updates.

Table 1. Change in IRU Alignment and Scale Factor Between Prelaunch and In-Flight Calibration

Alignment Change in arcsec			Percent Change in Scale Factor		
X axis	Y axis	Z axis	X axis	Y axis	Z axis
117	103	109	-0.017	-0.103	-0.081

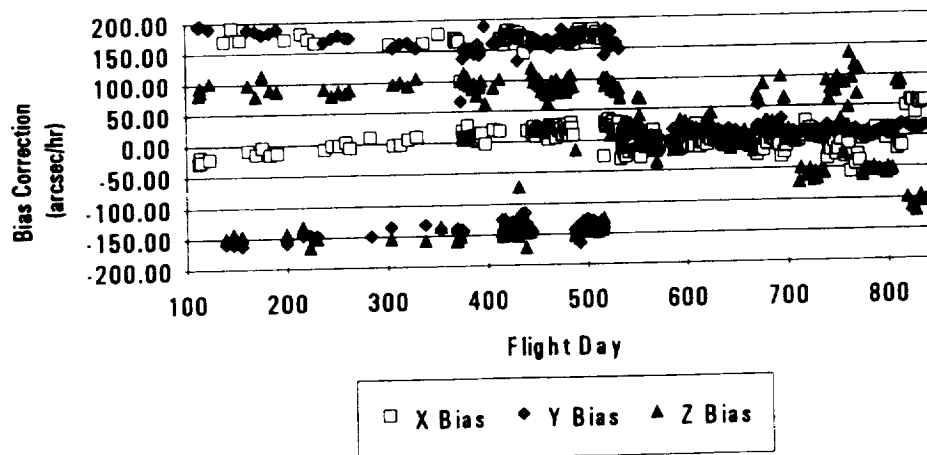


Figure 6. UARS Gyro Bias Corrections Versus Flight Day

Solar Stellar Pointing Platform (SSPP) and Platform Sun Sensors

The SSPP provides pointing for three science instruments. This consists of pointing at the Sun during daytime portions of each orbit for solar observations and pointing toward selected bright stars for calibration during spacecraft night.

The SSPP subsystem includes a two-axis gimbal assembly with redundant drive motors and shaft encoders, a control electronics box, and associated control software in the OBC. The OBC can use data from the one of two PSSs for closed-loop Sun tracking. For star tracking, it is limited to using data derived from OBC attitude knowledge and platform gimbal position encoders. The OBC can also point the platform toward the Sun using onboard ephemerides and attitude knowledge.

Correct pointing of the SSPP is, therefore, dependent on gimbal angle and PSS calibrations, attitude knowledge, and sometimes ephemerides (Reference 1).

Method

The PSS residuals had been approaching the 60 arcsec accuracy limit required for the SSPP science. To improve the PSS accuracy, a gimbal angle calibration was undertaken in November 1993. Unfortunately, this was shortly after the FHST1 alignment of flight day 817. This is the alignment that has not proven well in the sensor trending, and the SSPP results are based on this alignment. Therefore, the PSS calibration was not uplinked and will be redone for the more recent FHST1 alignment, which was proven. The results for this PSS calibration are presented to indicate the expected accuracy that can be achieved by updating the gimbal angle alignment parameters.

The PSS transfer function to convert from counts to the FOV parameters has the same form as the UARS FSS transfer function. The FDF has the capability to calibrate the PSS FOV transfer function; however, the PSS boresights are normally pointed directly at the Sun. Therefore, there has been no need to calibrate across the whole FOV, and no data are available for that purpose.

Results

The initial validation was performed by observing PSS Sun observation residuals obtained using the old calibration parameters to those obtained with the new calibration. This validation was done on six segments of data from the actual calibration timespan, spread out to include three periods each of positive and negative solar beta angles. Timespans and residuals of for the initial validation are listed in Table 2 below. The old calibration solutions show residuals ranging from 18 to 48 arcsec, compared to the residuals from the new calibration, which range from 6 to 20 arcsec.

The calibration was then confirmed by examining residuals for contemporary data that were not used in the actual calibration. The results of this exercise shown in Table 3 confirm that the new calibration is an improvement over the old one.

Finally, data from the beginning of the mission were examined to determine if the errors in the gimbal angles were a result of calibration drift or procedure. The results from this analysis are shown in Table 4. The residuals for the beginning of mission data are comparable to the contemporaneous data, indicating that the improvement is due to calibration procedure. The calibration at the beginning of the mission was performed on data that included only negative beta angles because data for positive beta angles were not available at the time the calibration was needed. This analysis indicates that inclusion of data for one full period of both negative and positive solar beta angles is a better procedure for gimbal angle calibration.

Table 2. Initial Validation Using Actual Calibration Timespans

Greenwich Mean Time (YYMMDD.HHMM)	Solar Beta Angle (deg)	Old Calibration (arcsec)	New Calibration (arcsec)
931025.1831 - .1905	2.8	48	20
931106.2232 - .2309	40.0	31	7
931124.1730 - .1804	2.8	33	9
931126.0200 - .0250	-2.8	19	12
931218.1204 - .1256	-75.0	29	6
940104.2105 - .2140	-2.8	18	14

Table 3. Validation Using Early Mission Data

Greenwich Mean Time (YYMMDD.HHMM)	Solar Beta Angle (deg)	Old Calibration (arcsec)	New Calibration (arcsec)
911119.1200 - .1400	37.4	35	7
911225.1200 - .1400	-80.4	15	7

Table 4. Calibration Validation Using Most Recent Data

Greenwich Mean Time (YYMMDD.HHMM)	Solar Beta Angle (deg)	Old Calibration (arcsec)	New Calibration (arcsec)
931205.0300 - .0500	-40.0	26	5.
931215.1130 - .1330	-80.0	37	13
931216.1930 - .2130	-40.0	38	16
940105.1000 - .1200	0.0	17	14
940110.1200 - .1400	18.0	34	6
940121.1200 - .1400	37.0	27	8
940120.1930 - .2130	18.0	31	7
940204.0900 - .1100	1.5	32	8

Magnetometers

The type of TAM used on UARS consists of three mutually orthogonal, single-axis fluxgate magnetometers. These TAMs measure the strength and the direction of the Earth's magnetic field and can be used to compute magnetic torquing commands to control the spacecraft angular momentum. The magnetic torquing contributes to the ambient magnetic field at the TAM.

The TAMs on UARS are normally considered a backup sensor for safehold situations and do not require highly accurate calibrations. However, some unexplained trends in the magnetic field bias corrections computed by the ADS and the possibility that reasonable attitude accuracy could be provided by the TAMs provided the motivation to improve on the existing TAM calibrations.

Methods

The calibration algorithm derived by Lerner and Shuster (Reference 11) determines the scale factor/misalignment matrix and biases and the coupling matrix for the influence of the magnetic torquer assembly (MTA) on the TAM. The misalignments, scale factors, and biases are used to convert TAM measurements in the true sensor frame into the MACS

frame and to compensate for static spacecraft magnetic fields. The coupling matrix compensates for the magnetic field due to the MTA.

The TAMCAL utility uses the spacecraft ephemeris and an accurate Earth magnetic field model to compute a reference magnetic field vector each time sensor data are available. It converts the reference field into MACS coordinates using the spacecraft attitude at that time. It performs a least squares minimization of the difference between the measured and reference magnetic fields with reference to the parameters to be determined.

To compute the alignment and scale factor matrix, TAM calibration requires an FHST-determined attitude and adjusted TAM data. The OBC-computed attitude was considered to be sufficiently accurate. The calibration data were taken over a 12-hour span in which UARS performed a yaw maneuver to obtain good observability of the magnetic field. However, the MTA data were not available for analysis in the ground system. Therefore, the coupling matrix could not be determined.

Results

The calibration was first examined by computing a fine attitude using the FHSTs and gyros in the ADS batch least squares algorithm, with the magnetometer measurements included in the processing but weighted so that they did not influence the attitude. This allows a good estimate of the residuals for the TAM measurements to be obtained. The variances and RMS residuals for the calibrated and nominally aligned and unbiased TAMs are in Table 5. These results show improvement for the calibration primarily in the spread of the residuals, as shown by the variances.

The attitude accuracy obtainable from the calibrations was then examined. The TAMs and gyros were used to compute attitudes that were then validated against the attitude obtained using the FHSTs. The RMS and maximum errors for the attitudes computed from the calibrated and nominally aligned and unbiased TAMs are in Table 6. TAM2 again shows the most improvement, but using the current calibration, it is not capable of determining the attitude as well as TAM1, as would be expected from the results shown in Table 5.

These results also indicate that the calibration was not significantly affected by magnetic torquer activity. This is probably due to the influence of the magnetic torquers being small.

Table 5. Magnetometer Measurement Residuals and Variances

Magnetometers	Variance (mG) for Spacecraft Axis			Residual RMS (mG)
	X axis	Y axis	Z axis	
TAM1, Nominal	23	8	27	3
TAM1, Calibrated	9	7	8	2
TAM2, Nominal	21	18	57	4
TAM2, Calibrated	17	8	26	3

Table 6. Residuals From Magnetometer-Only Attitudes

Magnetometer	Residual RMS, deg for Spacecraft Axis			Maximum residual, deg for Spacecraft Axis		
	X-axis	Y-axis	Z-axis	X-axis	Y-axis	Z-axis
TAM1, Nominal	0.5437	0.3030	0.6571	0.7920	-0.5569	1.033
TAM1, Calibrated	0.1958	0.0589	0.0767	0.2368	-0.0761	0.1166
TAM2, Nominal	1.0180	0.9175	2.2140	-1.623	1.792	3.010
TAM2, Calibrated	0.3170	0.1101	0.3113	0.6031	0.2153	0.5009

Earth Sensors

Earth sensor data are received in telemetry as roll and pitch angles. These angles are computed onboard using a model based on a round Earth with UARS assumed to be flying at 600 km altitude. This model varies significantly with reality: the Earth is not perfectly round and UARS does not constantly fly at 600 km. Furthermore, the ESAs trigger on the infrared horizon of the Earth, which varies from the solid Earth horizon in a complex way. The ground system modeling for adjustment of ESA data currently accounts for Earth oblateness and non-nominal altitudes. It is being modified to account for radiance effects from the Earth's infrared horizon. A complete analysis of the ESA behavior will be performed and presented later in another paper after the ground system modeling is satisfactory.

Conclusion

Monitoring attitude sensor data is critical for the success of the UARS mission. Maintaining a database of sensor and attitude data parameters derived from ground system processing is a valuable aid in monitoring long-term trends. The ground system must be kept as error free and as well calibrated as possible to properly reveal problems in the trends. The trend data must be carefully interpreted to derive the correct meaning.

The scale factor drift problem in FHST1 was revealed through the increasing residuals for the star observations. A corresponding trend was also seen in the OBC pitch axis attitude estimation error. FDF has devised procedures that are currently sufficient to compensate for this sensor problem. However, an FHST onboard the Gamma Ray Observatory (GRO) has exhibited erratic behavior in scale factor drift (Reference 18). The scale factor for this sensor increased rapidly, and then returned to a constant, stable value. The return to a constant value is encouraging, but FDF must carefully monitor the FHST for any rapid changes in the scale factor.

The results of the Sensor Studies task (Reference 15) may allow replacement of the FHST by the FSS should the FHST fail. The FDF will continue working to improve the attitude accuracy attainable from the UARS attitude sensors.

Acknowledgments

The authors are indebted to the other members of the UARS Attitude task for their contributions in support of this work: Jenny Moore, Davood Ashrafi, Terry Leid, Jon Landis, and Jim Klein. In particular, Jon Landis computed the FHST scale factors that appear in Figure 4.

The work of Joseph Hashmall and William Davis of CSC has been critical for the analysis of UARS attitude sensors. They have applied their years of experience in FDF attitude support to several missions with remarkable success.

References

1. General Electric Astro-Space Division, *Upper Atmosphere Research Satellite Project Data Book*, April 1987
2. S. Torgow, *User's Guide to the Standard Star Tracker*, Ball Aerospace Division, TM 86-02, April 1986
3. Teledyne Systems Company, *NASA Standard High Performance Inertial Reference Unit, DRIRU II*, Northridge, CA, January 1988
4. J. Hashmall and J. Garrick, "GSFC Flight Dynamics Facility (FDF) Calibration of the UARS Sensors," *Proceedings of the Flight Mechanics Estimation Theory Symposium*, May 1992
5. J. Langston, K. Krack, and W. Reupke, "A Multimission Three-Axis Stabilized Spacecraft Flight Dynamics Support System," *Proceedings of the Flight Mechanics Estimation Theory Symposium*, May 1992
6. M. D. Shuster and S. B. Oh, "Three-axis Attitude Determination From Vector Observations," *Journal of Guidance and Control*, Vol. 4, No. 1, January 1981

7. J. R. Wertz, (ed.), *Spacecraft Attitude Determination and Control*, Dordrecht, The Netherlands, D. Reidel Publishing Co., 1985
8. M. D. Shuster, M. D. Chitre, and D. P. Niebur, "In-Flight Estimation of Spacecraft Attitude Sensor Accuracies and Alignments," *Journal of Guidance and Control*, Vol. 5, No. 4, 1982
9. M. D. Shuster and G. J. Bierman, "Spacecraft Alignment Estimation," 27th IEEE Conference on Decision and Control, 1988
10. J. E. Keat, *Gyro Calibration Analysis for the High Energy Astronomy Observatory-a (HEAO-A)*, Computer Sciences Corporation (CSC), CSC/TM-77/6082/, June 1977
11. G. M. Lerner and M. D. Shuster, "In-Flight Magnetometer Calibration and Attitude Determination for Near-Earth Spacecraft," *Journal of Guidance and Control*, Vol. 4, No. 5, September-October 1979
12. W. Davis, J. Hashmall, J. Garrick, and R. Harman, "Postlaunch Calibration of Spacecraft Attitude Instruments," *Advances in the Astronautical Sciences*, Vol. 84, Part II, Paper number 325, April 1993
13. M. Lee, "FDF Report on Impact of UARS Star Tracker Scale Factor Shift on Onboard Attitude Determination," internal memorandum, June 1993
14. W. H. Press, B. P. Flannery, S. A. Teukolsky, *Numerical Recipes: The Art of Scientific Computing*, Cambridge Press, 1986
15. J. Hashmall, *Determination of a Modified Transfer Function for the Fine Sun Sensor (FSS)*, Goddard Space Flight Center, Flight Dynamics Division, FDD 553-FDD-94/002R0UD0, prepared by Computer Sciences Corporation, January 1994
16. R. Harman and M. Lee, "Extreme Ultraviolet Explorer Attitude Determination Support With a Multimission Three-Axis Stabilized Spacecraft Flight Dynamics Support System," *Spaceflight Dynamics 1993*, Vol. 84, Part II, 1993
17. Y-T Sheu, *Upper Atmosphere Research Satellite (UARS) Dynamics Simulator Engineering Model Specifications*, Computer Sciences Corporation (CSC), CSC/TM-88/6071, November 1988
18. Z. Wheeler, "GRO FHST Anomaly Report Update", Computer Sciences Corporation, Internal Memorandum, March 1994

Spacecraft Attitude Determination Accuracy From Mission Experience*

D. Brasoveanu and J. Hashmall
Computer Sciences Corporation (CSC)
Lanham-Seabrook, Maryland

Abstract

This paper summarizes a compilation of attitude determination accuracies attained by a number of satellites supported by the Goddard Space Flight Center Flight Dynamics Facility. The compilation is designed to assist future mission planners in choosing and placing attitude hardware and selecting the attitude determination algorithms needed to achieve given accuracy requirements. The major goal of the compilation is to indicate realistic accuracies achievable using a given sensor complement based on mission experience. It is expected that the use of actual spacecraft experience will make the study especially useful for mission design.

A general description of factors influencing spacecraft attitude accuracy is presented. These factors include determination algorithms, inertial reference unit characteristics, and error sources that can affect measurement accuracy. Possible techniques for mitigating errors are also included. Brief mission descriptions are presented with the attitude accuracies attained, grouped by the sensor pairs used in attitude determination. The accuracies for inactive missions represent a compendium of mission report results, and those for active missions represent measurements of attitude residuals. Both three-axis and spin stabilized missions are included. Special emphasis is given to high-accuracy sensor pairs, such as two fixed-head star trackers (FHSTs) and fine Sun sensor plus FHST. Brief descriptions of sensor design and mode of operation are included. Also included are brief mission descriptions and plots summarizing the attitude accuracy attained using various sensor complements.

Introduction

This paper summarizes a report for the National Aeronautics and Space Administration Flight Dynamics Division (FDD) entitled *Attitude Determination Accuracy From Mission Experience* (Ref. 1). The report is a compendium of information about the attitude determination accuracies attained using various sensor complements. It is based on flight data available to the Attitude Section of the FDD at Goddard Space Flight Center. The report is expected to be useful in the early mission planning and design stages for future spacecraft.

The three-axis stabilized missions included in the report are the Upper Atmosphere Research Satellite (UARS); the Heat Capacity Mapping Mission (HCMM); the Gamma Ray Observatory (GRO); the Stratospheric Auroral and Gas Experiment (SAGE); the Ocean Studies Satellite 1 (SEASAT-1); the Solar Maximum Mission (SMM); the Magnetic Field Mapping Satellite (MAGSAT); Dynamics Explorer 2 (DE-2); the Extreme Ultraviolet Explorer (EUVE); the Solar, Anomalous, and Magnetospheric Particle Explorer (SAMPEX); and the Topographic Explorer (TOPEX). The spin stabilized missions included are the Communications Technology Satellite (CTS), Dynamics Explorer 1 (DE-1), the Small Scientific Satellite 1 (SSS-1), the Interplanetary Monitoring Platform 8 (IMP-8), the International Sun-Earth Explorer 3 (ISEE-3), the International Ultraviolet Explorer (IUE), Geostationary Operational

*This work was supported by the National Aeronautics and Space Administration (NASA)/Goddard Space Flight Center (GSFC), Greenbelt, Maryland, under Contract NAS 5-31500.

Environmental Satellites 3 and 5 (GOES-3 and GOES-5), the Atmospheric Explorer 3 (AE-3), the Small Astronomy Satellite 2 (SAS-2), and the Italian Experimental Communications Satellite (SIRIO).

Attitude Sensors

The attitude determination accuracy depends on sensor types, sensor placement, sensor calibration, attitude determination algorithm, data quantity and quality, and mission design. The attitude sensors used on board the three-axis stabilized spacecrafts included in the survey are: the Charge-Coupled Device Star Tracker (CST), the Fixed-Head Star Tracker (FHST), the Fine Sun Sensor (FSS), the Fine-Pointing Sun Sensor (FPSS), the Digital Sun Sensor (DSS), the Horizon Sensor (HS), the Stationary Earth Sensor (SES), and the Three-Axis Magnetometer (TAM). The attitude sensor measurements are propagated using gyro data. CST models CT-601 and CT-401 and the NASA standard star tracker FHSTs are manufactured by Ball Aerospace Systems Group, formerly known as Ball Brothers Research Corp. (Ref. 2). The Sun sensors are manufactured by ADCOLE. The integral horizon scanner/momentum wheel systems are manufactured by Ithaco Corp. Body-mounted horizon scanners and SES systems are manufactured by Barnes Corp. Most spacecraft use fluxgate magnetometers manufactured by Schonstedt Co.

Two types of conventional gyroscopes are used on spacecraft to measure changes in the orientation: rate gyros (RGs) and rate-integrating gyros (RIGs). Usually, several gyros are grouped together in an inertial reference unit (IRU). Most gyros are supplied by Teledyne Systems Company; Bendix Corp.; Honeywell, Inc.; and Northrop Corp. For three-axis stabilized missions, the sensor measurement accuracies ranged from 0.001 to approximately 0.7 degree (1σ). The most accurate sensor is the CST (3 arc sec measurement accuracy, 1σ), followed by the FPSS (5 arc sec, 1σ), the FHST (10 arc sec, 1σ) and the FSS (60 arc sec, 1σ). The DSS has a measurement accuracy of approximately 0.15 degree. Using an Earth infrared emission model, the HS can attain an accuracy of 0.2 to 0.3 degree. The SES can attain an accuracy of approximately 0.1 degree. Due to current Earth magnetic field modeling limitations, TAMs can attain an accuracy of only 0.3 to 0.5 degree (Ref. 2). Further Earth magnetic field modeling refinements may significantly improve accuracy, since the instrument design itself does not impose such a poor accuracy limit.

The advantages of the CST are its high accuracy and its ability to provide enough information for complete three-axis attitude determination. Its disadvantages are its small FOV; Earth, Sun, and Moon interference; its high computational overhead; and little mission experience. The FHST is advantageous for its high accuracy. Except for mission experience, it has the same disadvantages as the CST. The advantages of the FSS are its moderate accuracy and a moderately wide FOV. The disadvantages of the FSS are that it can track only a single target and that it experiences Earth occultations and horizon distortions. The DSS has a larger FOV but, in addition to the disadvantages of the DSS, a limited accuracy. The HS and the SES need no target acquisition and can take measurements anywhere in orbit. Their disadvantages are their incomplete compensation for seasonal and latitudinal perturbations in the infrared horizon height, their limited accuracy, and their susceptibility to Sun interference. In addition, these sensors can take measurements only when the attitude and orbit are near the design values. The advantages of the TAM are that attitude measurements can be taken anywhere in orbit and that, when combined with gyro data, the TAM measurements provide complete information for three-axis attitude determination with a small amount of data (over time). The TAM suffers from very limited accuracy and significant biases (up to ± 10 mG) that must be removed correctly.

The attitude sensors used on board spin stabilized spacecrafts included in the survey are the single-axis FSS, the single-axis DSS, the V-slit Sun sensor, the single- and multiple-slit star scanner, the Body-Mounted Horizon Sensor (BHS), and the TAM. The single-axis Sun sensors are manufactured by ADCOLE (Ref. 2). The star scanners are manufactured by Ball Aerospace Systems Group and Honeywell. Their accuracies range from 0.02 to approximately 1 degree. The most accurate sensors are the single-axis FSS (60 arc sec, 1σ) and the multiple-slit star scanner (0.033 degree, 1σ). Like the double-axis DSS, the single-axis DSS can attain a measurement accuracy of approximately 0.15 degree. The BHS is similar in performance to the HS, attaining an accuracy of 0.2 to 0.3 degree. The single-slit star scanner achieves an accuracy of approximately 0.3 degree.

The advantages of the multi-slit star scanner are its accuracy, wide coverage, and ability to acquire both angle and phase measurements. Its disadvantages are that it can track only a few targets and suffers from Earth, Sun, and Moon interference. The single- and double-axis FSSs behave similarly, as do the single- and double-axis DSSs. The BHS behaves like the HS. The advantages of the multi-slit Sun sensor are its wide coverage and its ability to acquire both angle and phase measurements. Its disadvantages are that it can track only a single target and experiences Earth occultation.

A single sensor producing a single observation vector (the Earth vector or the Sun vector, for example) does not provide enough information to determine all three axes; therefore, the sensor complements include at least two attitude sensors. Usually, the sensors for three-axis stabilized missions provide two angular measurements. In general, the sensors for spin stabilized satellites provide only one measurement, either the arc length separation between the spin axis and a known reference vector or a rotation angle around the spin axis between two known vectors. Therefore, spin stabilized missions also use at least two attitude sensors.

When selecting the sensors and their placement, care must be taken to avoid Earth, Sun, and Moon interference. In addition, the TAMs should be placed as far away as possible from instruments that generate magnetic fields. Maximum attitude determination accuracy is attained when the instrument boresights are perpendicular, since the attitude uncertainty depends on the sine of the angle between the observations.

The listed accuracies can be achieved only after calibration and in optimum circumstances. Calibration includes alignment and transfer function correction. The launch shock can produce misalignments of about 0.1 degree. Missions requiring attitude accuracy of this order or better require in-flight alignment. The TAM calibration should take into account the effect of magnetic torquer assemblies (MTAs) and other electrical instruments. The HS, SES, and BHS transfer function should model the effect of the infrared horizon height variations due to latitude and seasonal changes.

The attitude determination accuracy also depends on the attitude determination algorithm and the amount of data used. Single-frame solutions are more rudimentary and provide less accuracy than multiple-frame methods such as the batch least-squares and sequential filter methods. Multiple-frame methods require data propagation; therefore, the gyro errors must be included in the analysis. The use of large amounts of data is always recommended, since the random error is inversely proportional to the square root of the number of measurements. Biases and misalignments are to be removed through proper calibration, and anomalous data should be discarded.

A variety of error sources can degrade accuracy. The most important error sources are measurement noise generated within the sensor, residual misalignments, stray light and bright objects, the South Atlantic Anomaly, measurement time uncertainty, star magnitude, near-neighbor interference, variation in the temperature of the Earth atmosphere, Earth atmospheric refraction, telemetry data precision, the Earth magnetic field, the spacecraft residual magnetic field, and bit flipping. Increasing the number of measurements mitigates the first of these error sources, and in-flight alignment reduces the effect of the second. Additional precautions must be taken to mitigate the other error sources. Stray light can disable an FHST. It can induce errors of up to several arc seconds in single- and double-axis FSS measurements (Ref. 3). The error induced in HS and SES measurements can reach up to 0.4 degree. The South Atlantic Anomaly can induce errors of up to 100 arc sec in the FHST position measurements. For 1-rotation-per-orbit missions, the measurement time uncertainty can produce errors of up to 12 arc sec in the FHST and double-axis FSS position measurements.

For spinning missions, the measurement time uncertainty can produce errors of up to 10 arc sec in single-axis FSS measurements and 0.01 degree in multiple-slit star scanner measurements.

In FHSTs, dim star position measurements can have random errors of up to 15 arc sec using a reduced circular field of view (FOV), or up to 25 arc sec through the entire FOV. The FHST position measurement errors quoted are for stars not dimmer than magnitude 5.7. The FHSTs are not designed to track stars dimmer than magnitude 5.7. If used to track stars dimmer than the design limit, the FHST position measurement random errors can be much larger than the values given above. Even when the stars for the mission catalog are carefully selected, near-neighbor stars induce FHST and CST measurement errors of up to 7 arc sec.

Variation in the temperature of the Earth atmosphere can induce errors of up to 0.1 degree in SES measurements and up to 0.3 degree in HS and BHS measurements. Earth atmospheric refraction can produce errors of up to 0.1 degree in single- and double-axis FSS and DSS measurements and of several arc minutes in both FHST and multiple-slit star scanner measurements. The current telemetry data precision is responsible for errors of up to 8 arc sec in FHST measurements, 0.003 degree in single- and double-axis FSS measurements, 0.13 degree in single- and double-axis DSS measurements, 0.005 degree in BHS measurements, and from 0.05 to 0.2 degree in TAM measurements. The modeling errors produced by an Earth magnetic field model of degree 6 or higher can induce errors of up to 1.0 degree in the TAM measurements. Bit flipping can affect any sensor, and the errors can be very large.

Some common techniques used to mitigate the error sources affecting the FHST and CST are providing sunshades; avoiding pointing the instrument near the Sun, Earth, or Moon; limiting the star reference catalog to brighter stars; removing any catalog star with bright neighbors; and correcting sample time for spacecraft rotation. In addition, measurements should be discarded if taken when the target star is near a planet, when the instrument is occulted by the Earth, when the spacecraft is in the South Atlantic Anomaly, or when the target star image is near the Earth limb. To mitigate the error sources affecting the FSS and single-axis FSS, the analyst should discard anomalous data and data acquired when the Sun is near the Earth limb, correct the sample time to reduce the measurement time uncertainty, and consider a large number of observations. To moderate the effect of the error sources affecting the HS and the BHS, the analyst should discard anomalous data, use an Earth radiance model or atmospheric temperature measurements, and select the correct Earth oblateness model.

In addition, attitude determination accuracy can be improved for the SES by changing the operation mode in order to avoid measuring in the quadrant containing the error sources. DSS measurements taken near the Earth limb should not be used. TAMs should not be used in the South Atlantic Anomaly, and the most accurate available Earth magnetic field model should be used for their calibration. TAM calibration should include coupling with magnetic torquers, and the magnetometers should be placed as far away as possible from instruments that generate magnetic fields. Star scanner measurements taken near the Sun, Moon, and Earth limb should not be used. Time corrections and a large number of observations can reduce the effect of the measurement time uncertainty. All anomalous sensor data should be discarded.

The mission design factors affecting the data quality include planned attitude motion and rates, desired pointing directions, planned attitude maneuvers, data rates used for attitude sensors and for the IRUs, spacecraft orbit, launch time, Sun position with respect to the spacecraft, and communication constraints.

Attitude Determination Accuracies From Flight Data

The important attitude results from flight data are presented in Figs. 1-12. Each of these graphs displays the attitude uncertainties corresponding to rotations about the roll, pitch, and yaw attitude axes (Refs. 4-30).

The results presented are generally determined differently for active and inactive missions. For inactive missions, the only information available is contained in reports of mission attitude performance. The best estimate determined from mission reference documents is given. Often, attitude accuracies must be inferred from reports on sensor performance (since sensor performance may be attitude accuracy dependent). Data from inactive missions, especially ones that have been inactive for a considerable period of time, may be less reliable than results for active missions because of inconsistency in the reference sources consulted and methods used for attitude accuracy estimation.

For active missions, information from mission reports can often be supplemented or even replaced by direct measurements of the spacecraft data and the attitudes determined from these data. The most accurate pair of sensors is considered a reference pair. Attitude uncertainty for the reference pair is determined by statistically combining the measured uncertainty of the attitude at epoch (from the Attitude Determination System (ADS)) with known uncertainties that are not included in the ADS attitude uncertainties. The ADS uncertainties chiefly reflect the effects of measurement noise and must be combined with terms reflecting the effects of postcalibration alignment uncertainties, FOV variances, and other parameter uncertainties to provide a more accurate estimate for attitude determination accuracy.

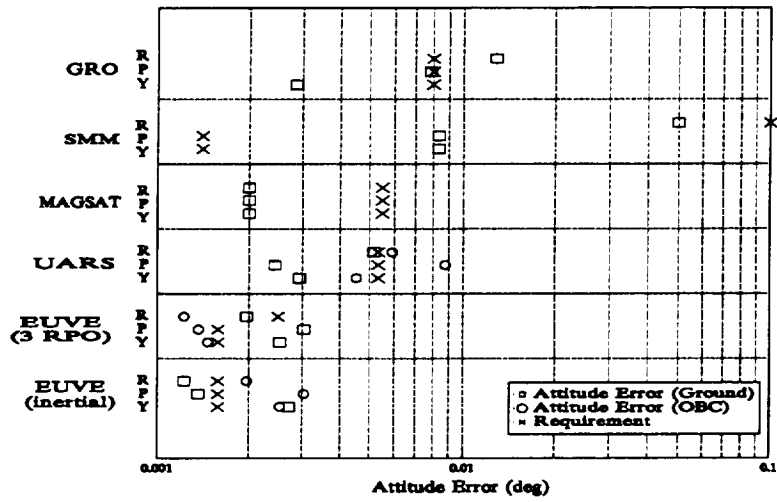


Figure 1. Attitude Accuracies (1σ) Using Two FHSTs

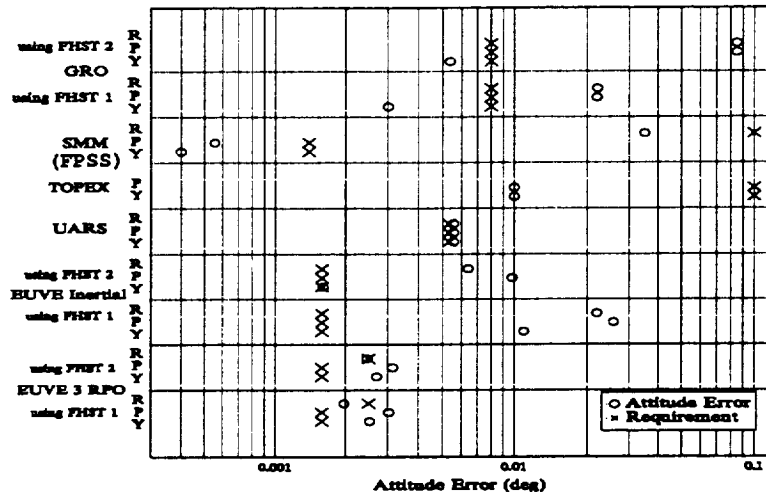


Figure 2. Attitude Accuracies (1σ) Using an FHST and an FSS

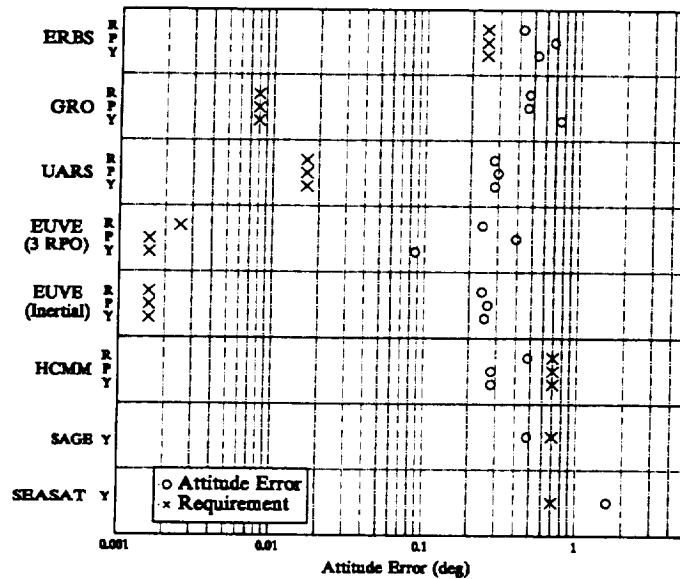


Figure 5. Attitude Accuracies (1σ) Using a TAM and Another Sensor (FHST, FSS, or DSS)

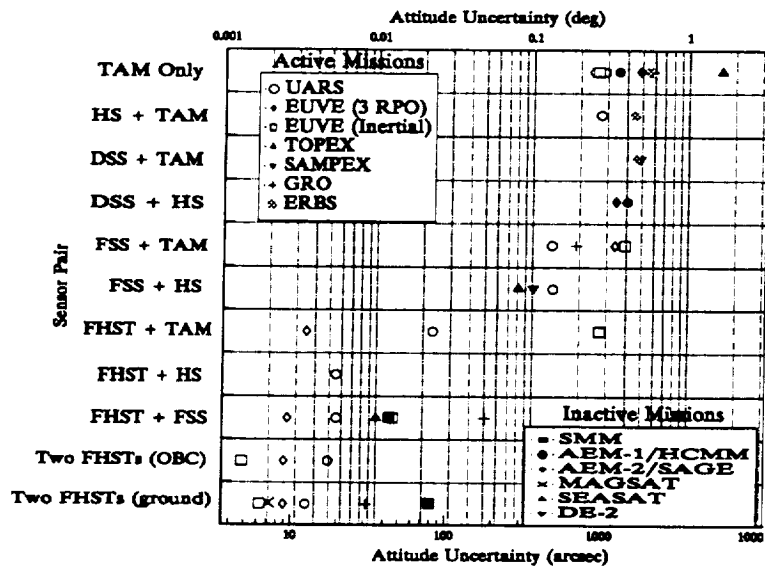


Figure 6. Summary of Three-Axis Stabilized Attitude Accuracies (1σ)

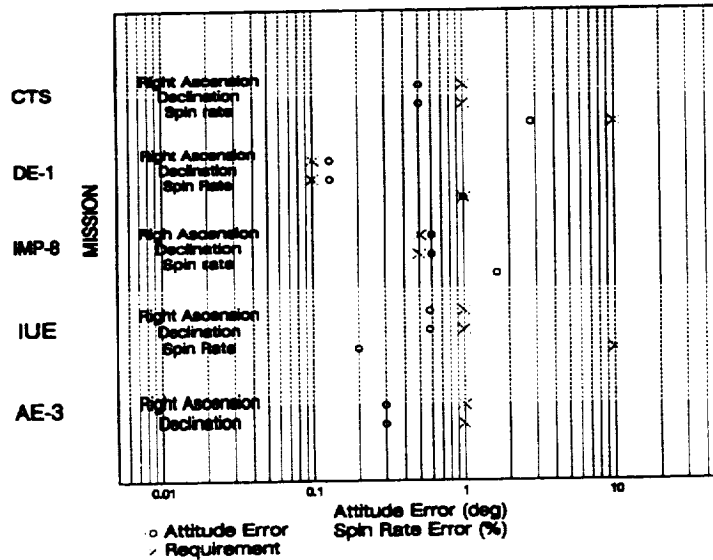


Figure 7. Attitude Accuracies (1σ) of Spin Stabilized Satellites Using a DSS and an HS

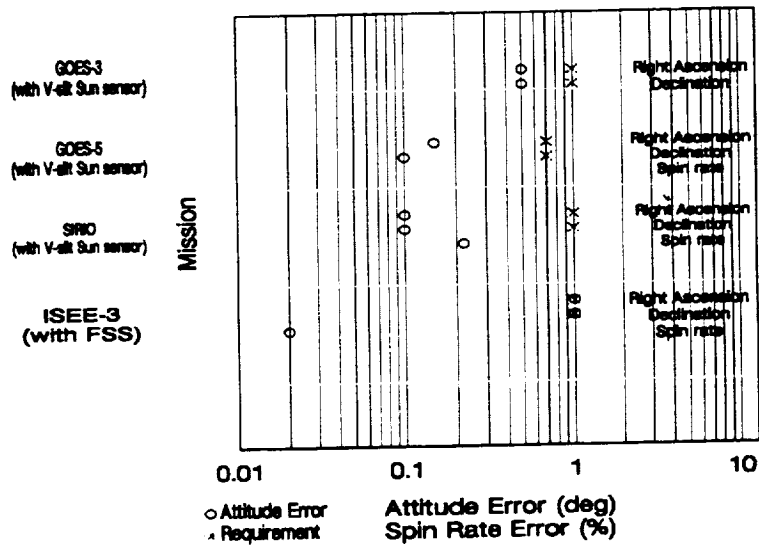


Figure 8. Attitude Accuracies (1σ) of Spin Stabilized Satellites Using an HS and Another Sensor

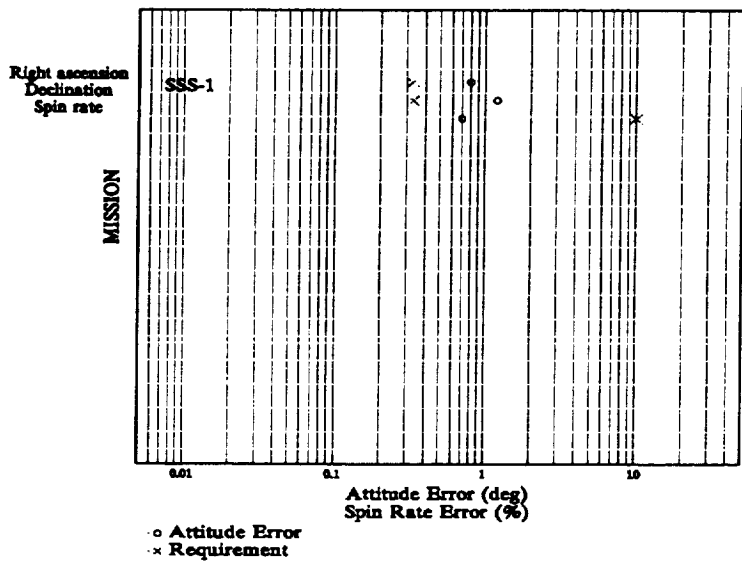


Figure 9. Attitude Accuracies (1σ) of Spin Stabilized Satellites Using a Single-Slit Star Scanner and a Single-Axis DSS

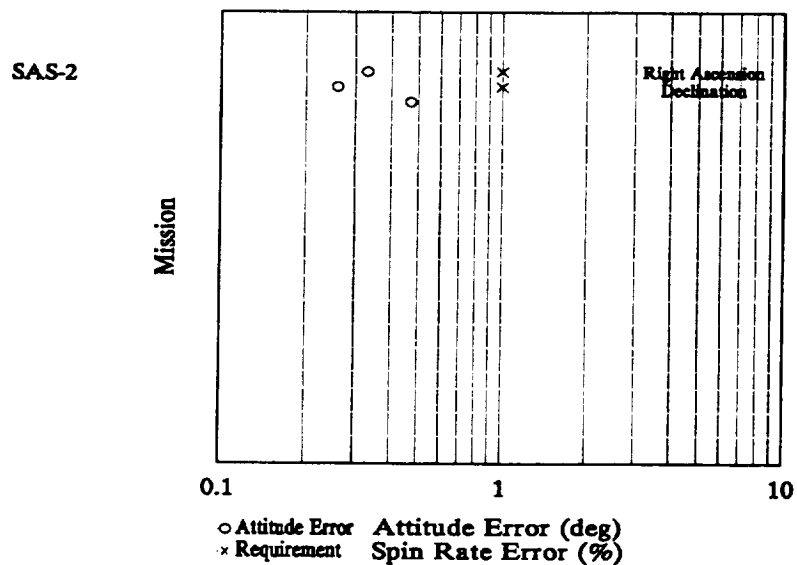


Figure 10. Attitude Accuracies (1σ) of Spin Stabilized Satellites Using a Multiple-Slit Star Scanner and a Single-Axis DSS

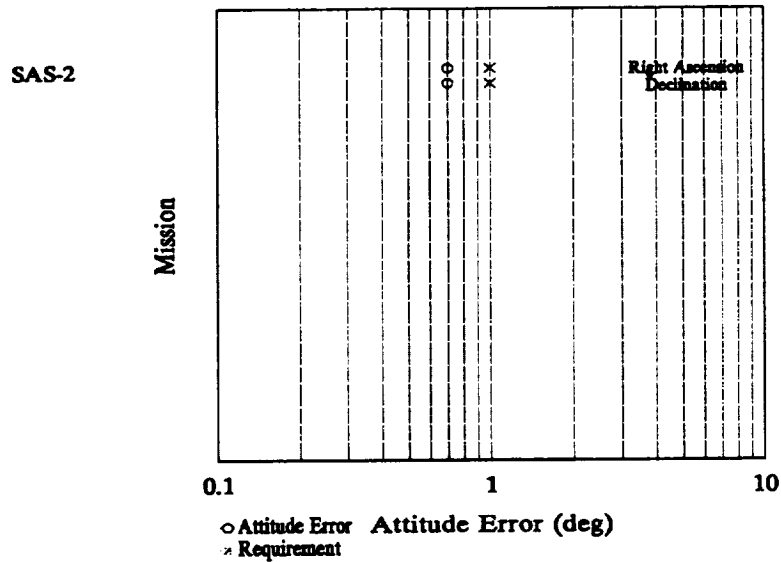


Figure 11. Attitude Accuracies (1σ) of Spin Stabilized Satellites Using TAMs Only

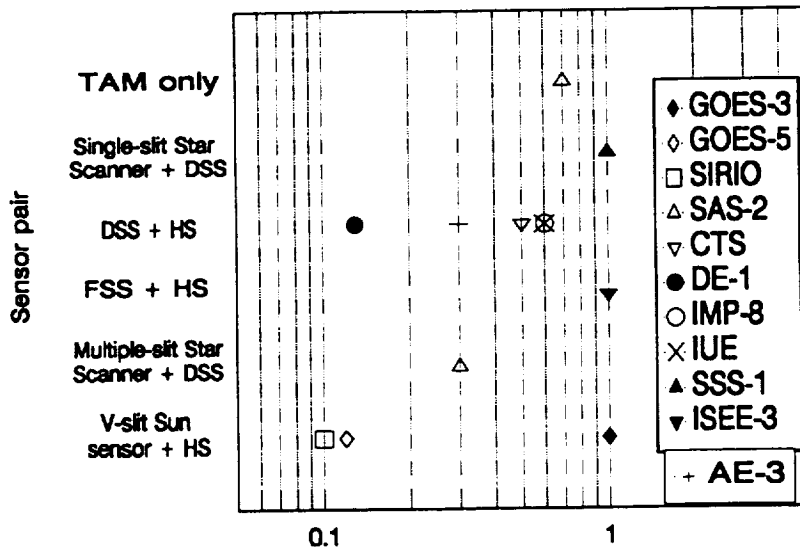


Figure 12. Summary of Spin Stabilized Attitude Accuracies (1σ)

Once reference attitudes have been determined using the most accurate sensor pair, they can be used to estimate the error of less accurate attitudes computed using a less accurate sensor pair. The attitude uncertainty of the less accurate case is determined by statistically combining the root mean square (RMS) attitude residual (between the reference and less accurate attitudes) with the uncertainty in the reference attitude. Attitude accuracies of this type are presented below. In some cases, the reference attitude is not significantly more accurate than the attitude calculated using a different pair. In these cases, because comparison with the reference attitude does not give accurate estimates of attitude error, the attitude accuracy is estimated using the same method as that used for the reference pair.

For the three-axis stabilized missions, the sensor complements analyzed are two FHSTs, one FHST and one FPSS, one FHST and one FSS, one FHST and one HS, one FHST and one TAM, one HS and one FSS, one HS and one DSS, one TAM and one HS, one FSS and one TAM, one DSS and one TAM, and TAMs only. The sensor measurements were propagated using gyro data whenever these data were available. The attitude determination accuracies attained using these sensor complements are shown in Figs. 1–5. Fig. 6 presents a summary of attitude determination accuracies attained by the three-axis stabilized missions surveyed. This plot shows the RMS of the attitude determination accuracies observed per axis. For spinning missions surveyed, the sensor complements analyzed are one single-axis DSS and one BHS, one single-axis FSS and one BHS, one single-axis DSS and one single-slit star scanner, one BHS and one V-slit star scanner, one single-axis DSS and one multiple-slit star scanner, and TAMs only. The attitude determination accuracies attained using these sensor complements are shown in Figs. 7–11. The attitude determination accuracies attained in spin-axis stabilized missions are summarized in Fig. 12. RMS values for three-axis stabilized mission attitude determination accuracies ranged between 2 arc sec and 2 degrees (1σ). EUVE and SMM achieved the most accurate attitude determinations: 4 arc sec per axis for EUVE using two FHSTs and 2 arc sec for SMM using an FHST and an FPSS. The spinning missions achieved spin-axis attitude determination accuracies in the 0.1–1.0 degree range (1σ). Among spinning spacecraft, the best attitude determination accuracies belong to SIRIO and GOES-5 (approximately 0.1 degree) using a V-slit Sun sensor and an Earth sensor.

Missions using two FHSTs attained accuracies in the 4–180 arc sec range. Spacecraft using an FHST and an FPSS attained accuracies between 2 and 120 arc sec. Missions using an FHST and FSS attained accuracies in the 6–300 arc sec range. Missions using an FHST and an HS achieved accuracies ranging from 12 to 40 arc sec. Those using an FHST and a TAM achieved accuracies ranging from 0.002 to 0.65 degree. Spacecraft using an FSS and an HS achieved accuracies between 0.045 and 0.2 degree. Missions using an FSS and a TAM achieved accuracies between 0.1 and 0.6 degree. The DSS plus HS sensor complement produced accuracies in the 0.1–0.6 degree range. The single mission equipped with a DSS and a TAM included in the survey attained an attitude determination accuracy of approximately 0.5 degree. The spacecraft using an HS and a TAM attained accuracies between 0.3 and 0.6 degree. The TAM-only accuracies ranged from 0.09 to 1.1 degree.

Spinning missions using a DSS and an HS achieved attitude determination accuracies in the 0.1–0.6 degree range. The single spinning mission using a single-axis FSS and an HS achieved an accuracy of about 1.0 degree. Those missions using a multiple-slit Sun sensor and an HS attained attitude determination accuracies in the 0.1–0.5 degree range. The single mission using a single-slit star scanner and a single-axis DSS achieved an accuracy between 0.7 and 1.1 degree. The only mission equipped with a multiple-slit star scanner and a single-axis DSS attained accuracies ranging from 0.25 to 0.5 degree. The single spinning mission surveyed that used TAMs only achieved an attitude determination accuracy of 0.7 degree.

Conclusions and Recommendations

The attitude determination accuracy survey included 10 spin stabilized and 11 three-axis stabilized missions. The sensors used by the three-axis stabilized missions include FHST, FSS, the digital Sun sensor, the Earth sensor, and magnetometers. Most of the recent three-axis stabilized missions use gyros to propagate measurement data. The attitude sensors used by the spin stabilized missions surveyed include the single and multi-slit star scanner, single-axis DSS, single-axis FSS, BHS, and TAM.

The overall accuracy of the attitude sensors used on spin-stabilized satellites ranges from 0.02 to about 1 degree (1σ). For the three-axis stabilized missions, the sensor accuracy ranges from about 0.001 to about 1 degree (1σ). The most accurate sensors used on board the three-axis stabilized missions are the FHST, the related CST, and the FPSS. These instruments achieve high accuracy but at high cost.

Because sensors commonly used on three-axis stabilized missions are more accurate than those used on spin stabilized missions, the three-axis stabilized missions achieved the best attitude determination accuracies. For spinning missions, the attitude determination accuracy ranged from 0.1 to 1 degree (1σ). For three-axis stabilized missions, the attitude determination accuracy ranged from 0.001 to 3 degrees (1σ).

The following recommendations are offered based on the above analysis and experience. These recommendations cannot be considered absolute rules because of the mission design factors mentioned above, which may or may not be negotiable (spacecraft altitude and inclination, for example). However, these recommendations may still serve as useful general guidelines for mission planning. To reduce cost, 1-revolution-per-orbit missions that require an attitude determination accuracy of less than 0.2 degree (1σ) could use digital Sun sensors and horizon sensors. To attain the same accuracy, inertial missions could use digital Sun sensors and magnetometers.

For attitude determination accuracies of less than 0.1 degree, FHSTs or CSTs are required. If an attitude determination accuracy of less than 5 arc sec is required, CSTs and fine-pointing Sun sensors are recommended. Spin stabilized missions that require an accuracy no better than 0.2 degree could use horizon sensors and digital Sun sensors. If a spin-axis determination accuracy of better than 0.2 degree is required, a multi-slit star sensor and a single-axis fine Sun sensor could be used. Missions requiring an attitude determination accuracy no better than 0.4 degree could use magnetometers only.

Multi-frame algorithms are recommended for missions requiring attitude determination accuracies of 0.1 degree or better. Large amounts of data (at least several hundred measurements) should be used. Error source mitigation techniques should be used routinely. IRU errors should be taken into account. In-flight alignment (Refs. 31-33) and transfer function calibration is recommended for missions requiring an attitude determination accuracy of 0.1 degree or better.

References

1. Goddard Space Flight Center, Flight Dynamics Division, 553-FDD-93/098R0UD0, *Sensor Studies Task Spacecraft Attitude Determination Accuracy From Mission Experience*, D. Brasoveanu (CSC), J. Hashmall (CSC), and D. Baker (GSFC), prepared by Computer Sciences Corporation, January 1994
2. J. R. Wertz, ed., *Spacecraft Attitude Determination and Control*, Dordrecht: D. Reidel Publishing Company, 1985
3. Computer Sciences Corporation, CSC/TM-77/6264, *SIRIO Attitude Analysis Postlaunch Report*, L. C. Chen and J. J. McEnnan, October 1977
4. ———, CSC/SD-77/6017UD1, *Applications Explorer Mission-A/Heat Capacity Mapping Mission (AEM-A/HCMM) Attitude System Functional Specifications and Requirements*, R. Byrne, J. S. Legg, J. W. Wood, et al., January 1977
5. ———, CSC/TM-78/6221, *Applications Explorer Missions-A/Heat Capacity Mapping Mission (AEM-A/HCMM) Postlaunch Report*, D. Niebur, F. Baginski, and R. Byrne, September 1978
6. ———, CSC/TR-84/6008, *Infrared Horizon Sensor Modeling for Attitude Determination and Control*, T. H. Lee, M. C. Phenneger, S. P. Singhal, and T. Stengle (GSFC), November 1984
7. ———, CSC/TR-79/6008, *SEASAT-1 Postlaunch Attitude Analysis*, S. Bilanow, K. W. Chan, G. F. Manders, and M. C. Phenneger, June 1979

8. ———, CSC/TM-79/6073, *AEM-B/SAGE Attitude Analysis*, C. B. Spence, G. Lerner, D. Niebur, et al., March 1979
9. ———, CSC/TM-79/6223, *Application Explorer Missions-2/Stratospheric Aerosol and Gas Experiment (AEM-2/SAGE) Postlaunch Report*, D. P. Niebur, September 1979
10. ———, CSC/TM-81/6043, *MAGSAT Infrared Horizon Scanner Data Evaluation Report*, S. Bilanow, March 1981
11. ———, CSC/SD-78/6077UD1, *MAPS/MAGSAT Attitude System Functional Specifications and Requirements*, M. B. Baker, R. N. Collier, Y. S. Hoh, et al., September 1978
12. ———, CSC/TM-81/6036, *High Precision Attitude Determination for MAGSAT*, G. Abshire, R. McCutcheon, G. Meyers, et al., April 1981
13. Goddard Space Flight Center, Flight Dynamics Division, FDD/553-90/016, *Solar Maximum Mission (SMM), Summary of Operational Attitude Support*, D. S. Pitone (CSC), prepared by Computer Sciences Corporation, April 1990
14. OAO Corporation, *Dynamics Explorer-A and -B Attitude System Functional Specification and Requirements*, December 1979
15. Computer Sciences Corporation, CSC/TR-85/6703, *Earth Radiation Budget Satellite (ERBS) Attitude Support Postlaunch Report*, E. Burges, R. Pendley, and J. Rowe, August 1985
16. ———, CSC/SD-82/6013, *Earth Radiation Budget Satellite (ERBS) Attitude Ground Support System (AGSS) Functional Specifications and Requirements*, B. Fang, K. Liu, M. Radomski, and S. Smith, September 1982
17. Goddard Space Flight Center, Flight Dynamics Division, 554-FDD-91/114R0UD0, *Gamma Ray Observatory (GRO), Flight Dynamics Analysis Team Support, Postlaunch Report*, L. Kulp (CSC), prepared by Computer Sciences Corporation, February 1992
18. Computer Sciences Corporation, CSC/TR-89/6022, *Gamma Ray Observatory (GRO), Flight Dynamics Support System Specifications: III. Mathematical Specifications, Revision 1*, L. Snyder, March 1989
19. ———, CSC/TM-76/6001, *Communications Technology Satellite (CTS) Attitude Analysis and Support Plan*, M. Joseph, J. Oehlert, G. Page, et al., February 1976
20. ———, CSC/TM-76/6104, *Communications Technology Satellite (CTS) Postlaunch Report*, P. M. Smoth and G. K. Tandon, May 1976
21. ———, CSC/TR-73/6022, *Evaluation of SSS-1 Star Sensor Attitude Determination*, D. F. Alderman, B. M. Beard, H. S. Gotts, and J. E. Kronenfeld, September 1973
22. ———, CSC/TM-79/6061, *ISEE-3 Attitude Postlaunch Report*, P. Batay-Csorba and J. N. Rowe, April 1979
23. ———, CSC/TR-78/6102, *International Sun-Earth Explorer-C (ISEE-C) Attitude Analysis and Support Plan*, J. N. Rowe, P. A. Batay-Csorba, S. K. Hoven, and G. Repass (Goddard Space Flight Center), May 1978
24. ———, CSC/TM-78/6072, *IUE Attitude Analysis Postlaunch Report*, S. Bilanow, W. Boughton, C. Hsieh, and J. McEnnan, March 1978
25. ———, CSC/TM-77/6305, *International Ultraviolet Explorer Attitude Analysis and Support Plan*, D. R. Sood, December 1977

26. ———, CSC/TM-78/6198, *Flight Dynamics Postflight Report for the Geostationary Operational Environmental Satellite-3 (GOES-3)*, W. Boughton and D. Haley, September 1978
27. ———, CSC/TM-81/6149, *Geostationary Operational Environmental Satellite-5 (GOES-5) Attitude Postlaunch Report*, S. Bilanow, H. L. Hallock, R. McCuthcheon, et al., July 1981
28. ———, CSC/TM-75/6004, *Horizon Sensor Behavior of the Atmosphere Explorer-C Spacecraft*, C. F. Gartell, M. E. Plett, and K. S. Liu, May 1975
29. ———, CSC/TM-74/6158, *SAS-2 Attitude Processing Study*, V. Norrod, May 1978
30. Goddard Space Flight Center, Flight Dynamics Division, FDD/544-90/121, *Study of the Earth Albedo Interference on Sun Sensors*, H. Arabshahi (CSC), D. Brasoveanu (CSC), and M. Phennegar (CSC), prepared by Computer Sciences Corporation, September 1990
31. M. D. Shuster, D. S. Pitone, and G. J. Bierman, "Batch Estimation of Spacecraft Sensor Alignments: I. Relative alignment Estimation," *Journal of the Astronautical Sciences*, Vol. 39, No. 4, pp. 519-546, October-December 1991
32. M. D. Shuster and D. S. Pitone, "Batch Estimation of Spacecraft Sensor Alignments: II. Absolute Alignment Estimation," *Journal of the Astronautical Sciences*, Vol. 39, No. 4, pp. 547-571, October-December 1991
33. M. D. Shuster, "Inflight Estimation of Spacecraft Sensor Alignment," *Advances in the Astronautical Sciences*, Vol. 72, pp. 252-274, 1990

FLIGHT MECHANICS/ESTIMATION THEORY SYMPOSIUM

MAY 17-19, 1994

SESSION 3

COMPATIBILITY OF TOPEX/POSEIDON TRAJECTORY PROPAGATION
WITH JPL AND GSFC/FDF OPERATIONAL SOFTWARE

Ahmed Salama¹, Michael Nemesure², Joseph Guinn¹,
Dave Bolvin², and Robert Leavitt³

ABSTRACT

Two independent trajectory software systems are used to perform the TOPEX/Poseidon operational orbit determination and propagation: the Goddard Trajectory Determination System (GTDS) at the GSFC/FDF and the Double Precision Trajectory System (DPTRAJ) at JPL. GTDS is used for operational tracking and TDRS-based orbit determination. DPTRAJ is used for ephemeris generation necessary to conduct day-to-day mission operations. This paper describes the DPTRAJ/GTDS trajectory comparison analysis conducted jointly by JPL and GSFC to ensure the compatibility of these two independent trajectory software systems.

INTRODUCTION

The Ocean Topography Experiment (TOPEX)/Poseidon spacecraft was launched on August 10, 1992 to study ocean circulation and its interaction with the atmosphere, to improve our knowledge of climate change and heat transport in the ocean, and to study the marine gravity field. These objectives are accomplished through accurate mapping of the ocean surface with a dual-frequency on-board altimeter and precision orbit determination.

Two independent Orbit Determination (OD) processes are associated with the mission. A Precision Orbit Determination (POD) process which is used to support analysis of the altimeter data, and an Operational Orbit Determination (OOD) process which is used to support the daily satellite operations. This paper is concerned only with the utilization of the OOD solutions in daily operational navigation. The OOD is the responsibility of the Goddard Space Flight Center (GSFC) Flight Dynamics Facility (FDF). Using tracking data from the Tracking and Data Relay Satellite (TDRS) System (TDRSS), the FDF produces TOPEX/Poseidon and TDRS state vectors for transmission in the Extended Precision Vector (EPV) message format. These EPV solution sets are transferred to the Jet Propulsion Laboratory (JPL) via National Aeronautics and Space Administration Communications Network (Nascom) to be used by the Navigation Team (NAVT) as initial conditions for propagating the Operational Orbit Ephemeris (OOE). Operational navigation support procedures have been developed to ensure the compatibility of the FDF-estimated TOPEX/Poseidon and TDRS state vectors and the NAVT-generated OOE's (Fig. 1). The objective of this paper is to present the results of this activity for only TOPEX/Poseidon trajectories.

Two independent trajectory software systems are used to perform the above task: the Goddard Trajectory Determination System (GTDS) at the GSFC/FDF and the Double Precision Trajectory System (DPTRAJ) at JPL. GTDS is used for operational tracking and TDRS-based OD. DPTRAJ is used for OOE generation necessary to conduct day-to-day mission operations.

¹ Jet Propulsion Laboratory, California Institute of Technology

² Computer Sciences Corporation

³ Sterling Software, Inc.

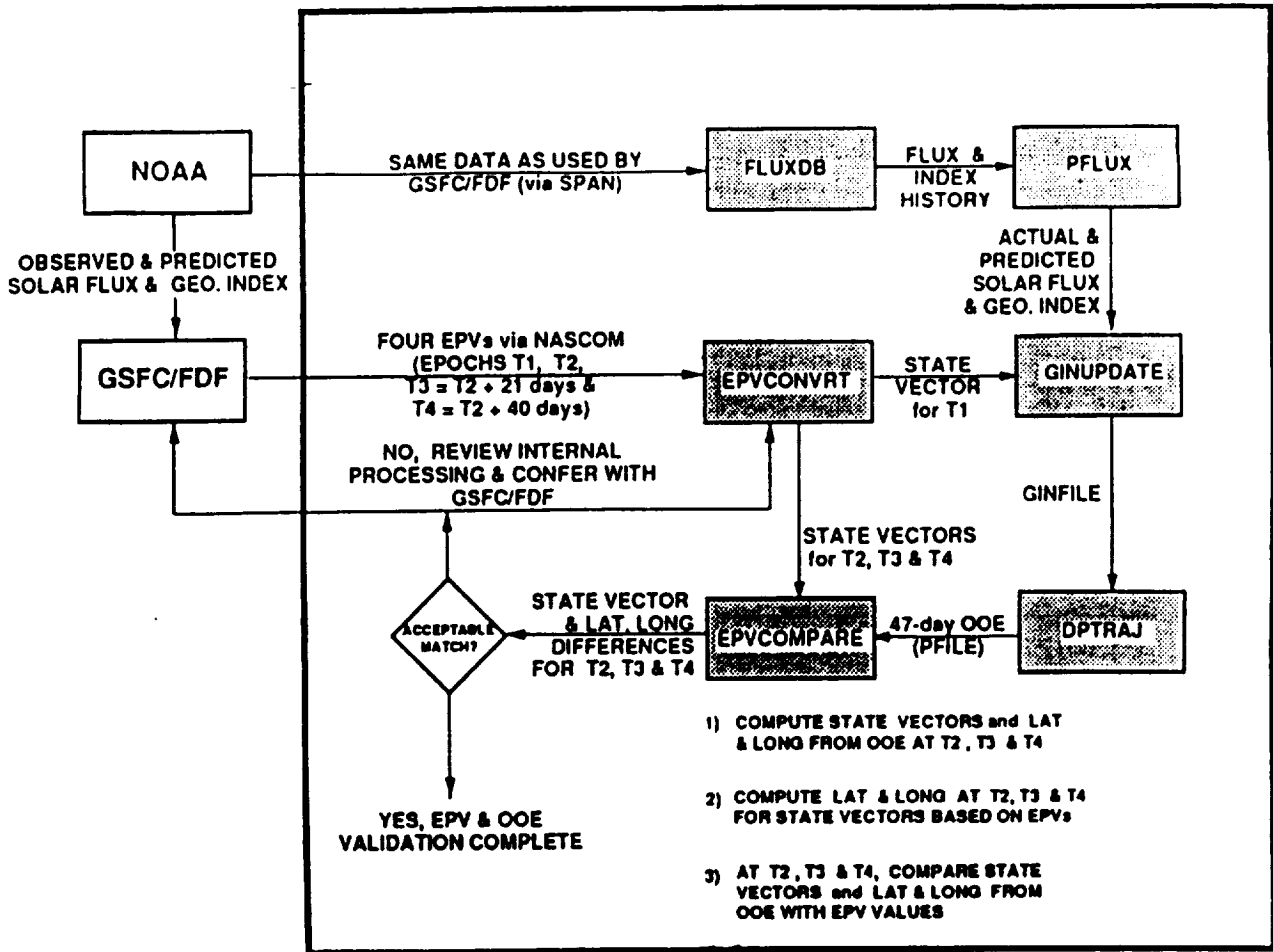


Figure 1. OOE Generation & EPV Validation Procedure

This paper describes the GTDS/DPTRAJ trajectory comparison analysis conducted jointly by the authors and their colleagues. The paper discusses both the TOPEX/Poseidon mission requirements as they related to OOE accuracy requirements and the error budget developed to meet these requirements. The operating procedures used to generate orbit solutions at GSFC/FDF, to transfer these solutions to JPL, and to process the solutions at JPL are also addressed. A description of each force model enhancement to GTDS and DPTRAJ motivated by the TOPEX/Poseidon mission is presented followed by a discussion of the DPTRAJ/GTDS comparison tests and test results. Finally, the lessons learned from JPL and GSFC/FDF experiences, providing joint flight dynamics operational navigation support for TOPEX/Poseidon are presented.

ACCURACY REQUIREMENTS ON THE OOE

The TOPEX/Poseidon project has imposed several accuracy requirements on TOPEX/Poseidon operational navigation support. The primary driver behind these requirements is a ± 1 km error tolerance on the equator crossings of the satellite ground track to maintain ground track repeatability. Orbit Maintenance Maneuvers (OMM) used to maintain this ground track must be planned and evaluated to a

commensurate accuracy level based on the OOE's. More specifically, a 30-day OOE must have a 1σ error of no more than 250 meters in equator crossing location. To ensure this level of accuracy, an error budget was prescribed (Ref. 1) that apportioned the overall error allowance for the OOE's among the identified error sources. The one error source of interest here is the trajectory software modeling errors. Ref. (1) indicates that the 1σ value of this error must be no more than 40 meters in equatorial crossing longitude after 30 days (Table 1). A 5 meter (out of the 3σ 120 meters) longitude difference at equator crossings after 30 days was allocated as a derived requirement for JPL-FDF trajectory prediction software comparisons. This 5 meter tolerance was chosen during software development as an achievable objective. It is more of a goal than a requirement. Joint mission support by the NAVT and GSFC/FDF thus demands a high level of consistency between GTDS and DPTRAJ. Both systems must, for example, model atmospheric drag and geopotential forces consistently and utilize common drag and solar radiation pressure spacecraft cross-sectional area profiles.

Table 1. Predicted Ephemeris Error Budget

ERROR COMPONENT	Equator Crossing Error at 30 days (1 Sigma Random or max. systematic) (m)
Definitive OD (all sources)	75
Prediction error (Nature's unpredictability after the definitive OD interval: density, UTI)	130
Prediction Trajectory Software Modeling Errors	40
Maneuver Execution	70
Geopotential tuning limitations	<u>10</u>
Total error (Uncorrelated errors)	171
Total error	<u>221</u>
Allowable error	<u>250</u> (TBR)
Margin available: (Uncorrelated)	79
(Correlation - 1)	29

BACKGROUND

Extensive effort was made during the mission development phase to ensure the compatibility of DPTRAJ and GTDS. This effort began in 1987 (Ref. 2 and 3) by identifying the force models to be used in the two organizations to support TOPEX/Poseidon operational navigation. Over the years many cases have been established to allow for a model-by-model comparison between DPTRAJ and GTDS.

Although extensive effort was made during the software development phase to eliminate inconsistencies between the two systems (Ref. 4 and 5), it was not feasible to eliminate all inconsistency. DPTRAJ and GTDS utilize different modeling design implementations, input/output interfaces, numerical strategies, and, in some cases, different force models. For example, DPTRAJ uses a variable-step integrator with the terrestrial dynamical time as an independent variable whereas GTDS uses a fixed-step integrator with A.1 time as an independent variable. In addition, DPTRAJ uses a conical umbra shadow model for solar radiation pressure modeling whereas GTDS uses a cylindrical umbra shadow model. A paramount objective of this work was to quantify the effect on OOE error of system inconsistency and to ensure conformity with the error budget. To this end, ten tests were designed and performed during the pre-mission phase to allow for a model-by-model comparison between DPTRAJ and GTDS. After launch, upon the discovery of an unanticipated thrust-like perturbation, an eleventh test was devised to ensure consistency of thrust modeling.

SOLUTIONS AT FDF

TOPEX/Poseidon operational navigation is supported by TDRSS, which consists of a set of five geostationary relay spacecraft, called TDRSs, the White Sands Ground Terminal (WSGT) located at White Sands, New Mexico and the Bilateral Ranging Transponder System (BRTS). Routinely, TOPEX/Poseidon is supported by two of the five TDRSs, an "east" and a "west" TDRS, which provide two-way range and one-way and two-way Doppler tracking measurements, as well as spacecraft commanding and telemetry support. BRTS provides ground-based range and two-way Doppler measurements for use in TDRS orbit determination.

The FDF generates OOD solutions for TOPEX/Poseidon using the GTDS. GTDS uses a batch weighted least-squares estimation algorithm, in conjunction with TDRSS one-way and two-way Doppler tracking measurements, to minimize the summed-squared differences between observed and calculated values of selected tracking measurements over an OOD solution arc. TOPEX/Poseidon range measurements are excluded from the solutions because of current limitations in solving for uncorrected biases which have been found to reduce the orbit solution quality. The estimated parameters consist of the TOPEX/Poseidon position, and velocity, onboard ultrastable oscillator frequency bias and drift, and a single along-track thrust scaling parameter. TDRS OOD solutions are generated prior to and separately from the TOPEX/Poseidon OOD solutions using BRTS tracking measurements. The TDRS OOD solutions are then used in generating the TOPEX/Poseidon OOD solutions.

DATA TRANSFER TO JPL

EPV state vectors are transmitted from GSFC/FDF to JPL via Nascom in series of 4800-bit data blocks with each block containing an EPV message. During routine operations, the TOPEX/Poseidon OOD solution arc is 7 days 10 hours long and OOD is performed every Monday, Wednesday, and Friday. For each of these OOD solutions, four state vectors are transmitted via Nascom in the EPV format to the TOPEX NAVT at JPL. These vectors have epochs at the start and end of the OOD arc, the start of the OOD arc plus 24 hours, and the end of the OOD arc plus 7 days. On Wednesdays, the vector with epoch at the end of the OOD arc plus 7 days is replaced with a vector with epoch at the end of the OOD arc plus 14 days. These vectors are used to monitor the spacecraft ground track and produce trajectory products as well as to quality assure the OOE's generated by the NAVT.

In addition to routine OOD, the FDF provides special OOD support for TOPEX/Poseidon OMMs. TOPEX/Poseidon OMMs occur every 4 to 6 months in the current low-solar-activity environment and are designed to raise the semi-major axis to maintain the groundtrack to within the required ± 1 kilometer band. In support of these maneuvers, the FDF generates and delivers a set of premaneuver state vectors and several sets of postmaneuver OOD state vectors to the TOPEX NAVT in addition to the routine OOD. For each OOD maneuver solution, state vectors are delivered with epochs at the start and the end of the OOD arc. These state vectors are used to assist the NAVT in evaluating maneuver performance and calibrating the thrusters.

JPL PROCESSING

An ephemeris file for either TOPEX/Poseidon or a TDRS is generated by DPTRAJ for each set of EPV state vectors provided by GSFC/FDF. In addition to EPV state vectors, other inputs to this process include general navigation input parameters, gravity field coefficients, solar and geomagnetic activity data, polar motion and timing parameters, and anomalous thrust model parameters. All of these inputs are incorporated into the process by the software module GINDRIVE, which produces a Namelist-type file for DPTRAJ.

Each set of EPV state vectors is validated using the generated ephemeris. The first EPV state vector of the set supplies DPTRAJ with its initial epoch and state vector to integrate the satellite's equation of motion over the required time span. For validation, the remaining EPVs are compared with their corresponding state vectors extracted from the ephemeris.

PROPAGATION MODELS

The following are the major force models used in DPTRAJ and GTDS for TOPEX/Poseidon (Models used as a rapid preliminary orbit propagation tool to condition maneuver requirements for subsequent precision prediction can be found in Ref. 6):

- Geopotential Model

The model that had been used during the pre-launch analysis phases was Goddard Earth Model (GEM)-T3. Subsequently, a slightly refined version of GEM-T3, referred to as Joint Gravity Model (JGM)-2, was selected for mission support. JGM-2 models the Earth's geopotential using an expansion of the solution to the Laplace equation, $\nabla^2\Psi(r,\phi,\lambda) = 0$, in spherical harmonics with respect to a body-fixed frame up to degree and order 70. A truncated 20 x 20 version is used for operational navigation because of computational limitation at JPL.

- Luni-Solar Gravity

The gravitational perturbations of the Sun and Moon can be modeled adequately by considering these perturbing bodies as point masses in both systems.

- Solid Earth Tides Model

The solid Earth Tides model provides an adjustment to the quadrupole term of the geopotential model to compensate for the deformation of the solid portion of the Earth induced by the combined tidal effects of the Sun and the Moon. The model includes a lag angle between the azimuthal component of the position of the disturbing body and the stretching axis. The model also includes a Love number which serves as a proportionality constant for the effect. As implemented in GTDS and DPTRAJ, the model yields an additive adjustment to the gravitational force on the spacecraft.

- Atmospheric Drag

The greatest influence of atmospheric drag on TOPEX/Poseidon is the orbital decay in terms of semi-major axis reduction. It is modelled as a function of atmospheric density and the velocity of the satellite relative to the atmosphere. Density is a complicated function of solar and geomagnetic activity, satellite geometric parameters, and diurnal, annual, and latitudinal-seasonal variations. Both DPTRAJ and GTDS use the same solar and geomagnetic activity data supplied by the National Oceanic and Atmospheric Administration (NOAA). The Jacchia-Roberts atmospheric density model is used in both systems.

- Solar Radiation Pressure:

The solar radiation pressure (SRP) has effects on TOPEX/Poseidon that exceed those of atmospheric drag, however, this perturbation can be modeled reasonably well. The effect of the numerical integration due to the extremely rapid changes in the radiation pressure perturbation when the satellite passes through the Earth's shadow has been investigated. A conical model that allows for no integrator restarts has been implemented in the JPL DPTRAJ software. GTDS does not restart the integration either upon entry to or exit from its cylinder shadow model.

- Variable Mean Area Model

The variable mean area (VMA) model allows for a variable mean spacecraft cross-sectional area for the purpose of computing perturbations due to atmospheric drag and SRP. The model provides for distinct SRP and atmospheric drag area profiles. Either area profile is driven by a parameter called β' , which is the complement of the angle between the Earth-sun vector and the spacecraft orbital angular momentum vector. Based on nominal attitude control, referred to as "full sinusoidal steering yaw", a table of atmospheric drag and SRP cross-sectional area values at integral values of β' has been developed as an input to GTDS and to DPTRAJ. Area values at intermediate points are obtained through linear interpolation. When the spacecraft is under fixed-yaw steering attitude control, the VMA drag area profile is overridden with constant area values.

- Thrusting Effects

Shortly after launch, OD solutions indicated orbital decay levels about 60 times larger than could be explained by atmospheric drag (Ref. 7). Later, orbit trend analysis indicated a presence of body-fixed residual along-track forces comparable to drag which caused either orbital decay or boost depending on the satellite attitude and solar array articulation mode. Consequently, plans with the FDF were made to estimate an along-track thrust τ , instead of the drag multiplier, where the along-track thrust is measured in $(1 + \tau)$ micro Newtons. To ensure the compatibility of thrust modeling between DPTRAJ and GTDS, the NAVT added to the DPTRAJ force model a continuous finite burn with duration equal to the length of the OD arc and force equal to $(1 + \tau)$ micro Newton.

TRAJECTORY COMPARISON TESTS

In all, eleven trajectory comparison tests were conducted in preparation for this paper. They are similar, though not identical, to the tests originally performed during the pre-launch analysis phases of TOPEX/Poseidon. The current set of tests is in line with the present operational support configuration (the configuration has evolved somewhat since the original tests were performed). The tests provide a model-by-model comparison between GSFC and JPL trajectory software. Each test involves propagating for 30 days a single initial state vector independently with DPTRAJ and GTDS. A comparison of the ascending node equator crossing longitude and time of crossing were examined at regular intervals during the 30-day period.

The first test in the series utilized the simplest force model (all perturbations were turned off). With successive tests, various combinations of force models were included. The last test duplicates the operational support configuration.

The tests were as follows:

1. Point mass earth

This test excludes all perturbations; only the point-mass effect of the Earth is modeled. Ephemeris discrepancies will arise only from integration and implementation differences.

2. Earth gravitational perturbations

This test adds to Test 1 terms of the JGM-2 geopotential model up to 20×20 . Additional ephemeris discrepancies will arise from differences in geopotential model implementation and in inertial to earth-fixed coordinate transformations.

3. Earth, Sun, and Moon gravitational perturbations

This test adds to Test 2 the point-mass effects of the Sun and Moon. Close agreement for this test would confirm consistency in solar and lunar ephemerides.

4. Solid-Earth Tides

This test adds to Test 3 the solid-Earth tides effects on the geopotential. Additional ephemeris discrepancy would be negligible because of the simplicity of the tides model.

5. Expanded Gravity Field

This test adds to Test 4 terms of the JGM-2 geopotential model up to 26×26 . Ephemeris discrepancy somewhat more than that seen for Test 4 would be expected.

6. Solar Radiation Pressure

This test adds to Test 1 perturbations due to SRP on the satellite. Additional ephemeris discrepancy would arise from shadow model differences (conical umbra for DPTRAJ and cylindrical umbra for GTDS), both directly and from interplay between the shadow crossings and the numerical integrator. In this test, constant spacecraft cross-sectional area is used in the SRP computations. As Ref. (3) indicates, a small difference is expected in this test.

7. Variable Mean Solar Radiation Pressure Area Model

This test adds to Test 6 the VMA model for the SRP. Additional ephemeris discrepancy would be negligible because VMA implementations in DPTRAJ and in GTDS are virtually identical.

8. Atmospheric Drag

This test adds to Test 1 perturbations due to atmospheric drag. The Jacchia-Roberts atmospheric density model is used for both systems. Common solar flux values and geomagnetic indices are input. Additional ephemeris discrepancy would arise from minor implementation differences. In this test, constant spacecraft cross-sectional area is used in the drag computations.

9. Variable Mean Atmospheric Drag Area Model

This test adds to Test 8 the VMA model for the atmospheric drag. Additional ephemeris discrepancy would be negligible because VMA implementations in DPTRAJ and in GTDS are virtually identical.

10. Combined

This test combines all perturbations and modeling configurations used for the operational support of the mission with the exception of thrust modeling. Ephemeris discrepancy must not exceed the allowance prescribed by the error budget.

11. Operational Test

This test incorporates all perturbations and modeling configurations currently used for the operational support of the mission. It adds to Test 10 a thrust model. The need to account for thrust-like perturbations was not identified until after launch.

RESULTS AND FUTURE CONSIDERATIONS

Excellent model-by-model agreement between GTDS and DPTRAJ has been achieved. This allows either system to be used for operational navigation support. Figure (2) shows that differences in Earth-fixed longitude at equator crossings after 30 days were less than 75 centimeters. While good orbit prediction agreement between the two systems was observed, the above figure is not necessarily a worst case. Sometimes longitude difference between the two systems exceeded the 5 meter goal. Figure (3) shows a one-year statistics of the longitude difference.

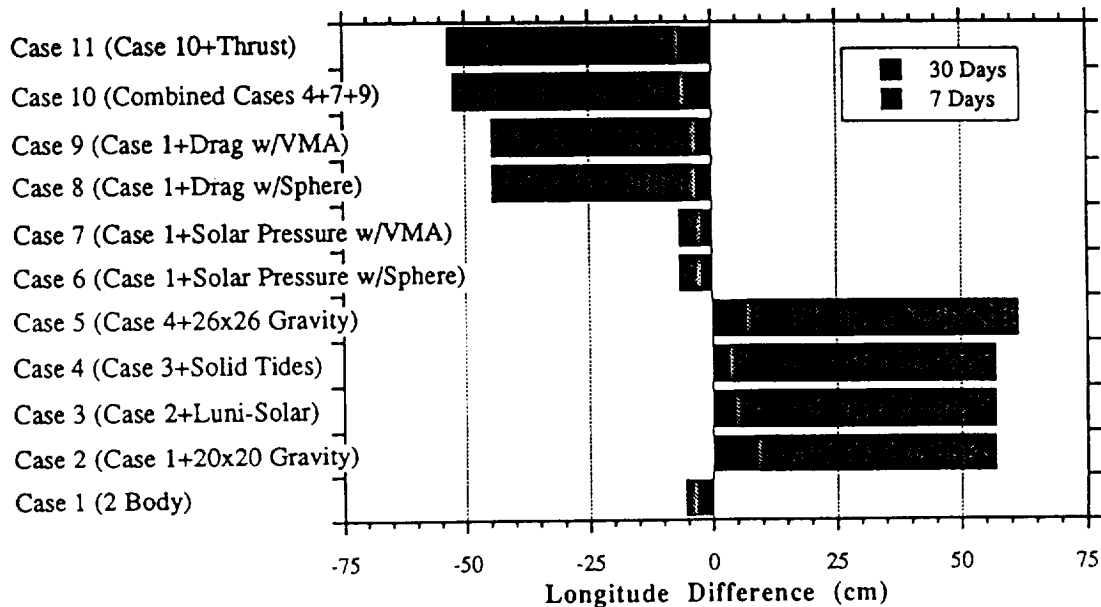


Figure 2. Trajectory Comparison Results
JPL (DPTRAJ) - GSFC (GTDS)

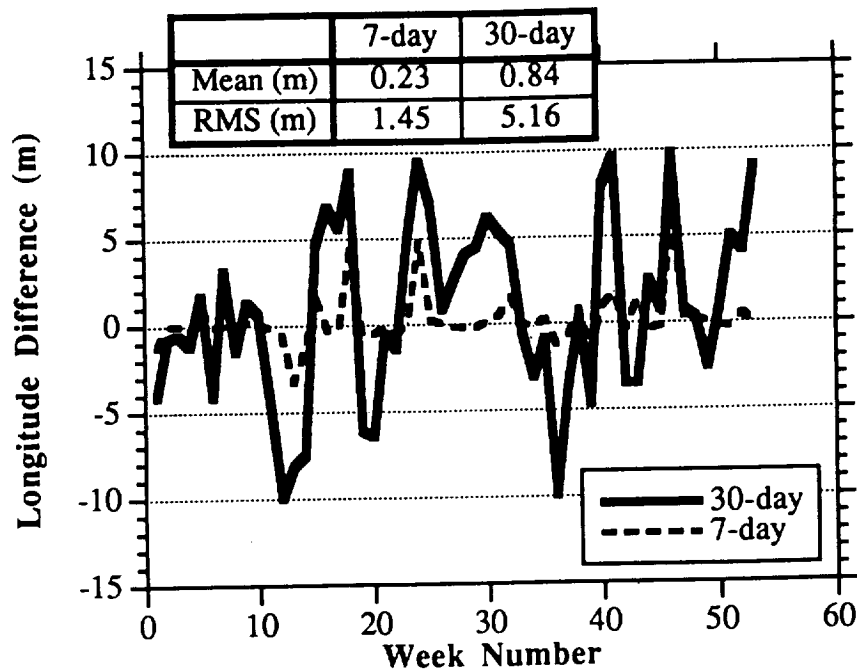


Figure 3. One-Year Trajectory Comparison Results

LESSONS LEARNED

Below are the lessons learned while performing the DPTRAJ/GTDS trajectory comparisons:

Lesson 1: Perform the trajectory calibration analysis as early as possible.

Calibrating any two complex software systems such as DPTRAJ and GTDS can be a tedious and time-consuming process because of the large number of variables involved. Recognizing this fact, the FDF and the NAVT initiated the trajectory calibration effort almost three years before launch. As a result of this early start, both teams had more than sufficient time to identify, analyze and correct several discrepancies between DPTRAJ and GTDS.

Lesson 2: When software is developed, all constants should be user modifiable.

When performing a trajectory calibration analysis, it is critically important to ensure that both software systems use the same modeling constants. It is equally important that the user be able to easily modify any constants which must be changed for compatibility. In the case of the DPTRAJ/GTDS trajectory calibration, most modeling constants were easily modified, since the constants were input by the user and not hardcoded within the software. Had the constants been hardcoded, the trajectory calibration analysis would have required significantly more time and effort.

ACKNOWLEDGMENTS

The research described in this paper was carried out by the Jet Propulsion Laboratory, California Institute of Technology, under a contract with the National Aeronautics and Space Administration. The authors would like to acknowledge Ray Frauenholz for his valuable discussions and suggestions and Bryan Brown for his useful input to and review of this paper.

REFERENCES

1. TOPEX/Poseidon Mission and Systems Requirements, 633-103, April 1989 (Internal Document).
2. Frauenholz, R.B., "Plan and Schedule for Trajectory Propagation Software Comparison Between GSFC and JPL for TOPEX", IOM 314.5-1061, 16 January 1987, JPL (Internal Document).
3. Frauenholz, R.B., "Summary of GSFC/JPL Trajectory Propagation Software Comparison for TOPEX", IOM 314.5-1061, 2 July 1987, JPL (Internal Document).
4. Guinn, J., A Presentation at TOPEX/Poseidon Navigation Development Review 4, April 10, 1991 (Work is done with Mike Nemesure's help), Internal Document.
5. Salama, A., A Presentation at TOPEX/Poseidon Operational Navigation Meeting No. 9 at GSFC, November 19-20, 1991 (work is done with Mike Nemesure's help), Internal Document.
6. Bhat, R.S., R.B. Frauenholz, and P.E. Cannell, "TOPEX/Poseidon Orbit Maintenance Maneuver Design", AAS/AIAA astrodynamics Specialist Conference, Stowe, Vermont, Aug. 1989.
7. Fraueholz, R.B., T.W. Hamilton, B.E. Shapiro, and R.S. Bhat, "The Role of Anomalous Satellite-Fixed Accelerations in TOPEX/Poseidon Orbit Maintenance", AAS/AIAA astrodynamics Specialist Conference, Victoria, B.C., Canada, Aug. 1993.

Improved Solution Accuracy for TDRSS-Based TOPEX/Poseidon Orbit Determination*

C. E. Doll, G. D. Mistretta, and R. C. Hart
Goddard Space Flight Center (GSFC)
Greenbelt, Maryland, USA

D. H. Oza, D. T. Bolvin, C. M. Cox, M. Nemesure,
D. J. Niklewski, and M. V. Samii
Computer Sciences Corporation (CSC)
Lanham-Seabrook, Maryland, USA

Abstract

Orbit determination results are obtained by the Goddard Space Flight Center (GSFC) Flight Dynamics Division (FDD) using a batch-least-squares estimator available in the Goddard Trajectory Determination System (GTDS) and an extended Kalman filter estimation system to process Tracking and Data Relay Satellite (TDRS) System (TDRSS) measurements. GTDS is the operational orbit determination system used by the FDD in support of the Ocean Topography Experiment (TOPEX)/Poseidon spacecraft navigation and health and safety operations. The extended Kalman filter was implemented in an orbit determination analysis prototype system, closely related to the Real-Time Orbit Determination System/Enhanced (RTOD/E)** system. In addition, the Precision Orbit Determination (POD) team within the GSFC Space Geodesy Branch generated an independent set of high-accuracy trajectories to support the TOPEX/Poseidon scientific data. These latter solutions use the Geodynamics (GEODYN) orbit determination system with laser ranging and Doppler Orbitography and Radiopositioning Integrated by Satellite (DORIS) tracking measurements.

The TOPEX/Poseidon trajectories were estimated for November 7 through November 11, 1992, the timeframe under study. Independent assessments were made of the consistencies of solutions produced by the batch and sequential methods. The batch-least-squares solutions were assessed based on the solution residuals, while the sequential solutions were assessed based on primarily the estimated covariances. The batch-least-squares and sequential orbit solutions were compared with the definitive POD orbit solutions. The solution differences were generally less than 2 meters for the batch-least-squares and less than 13 meters for the sequential estimation solutions. After the sequential estimation solutions were processed with a smoother algorithm, position differences with POD orbit solutions of less than 7 meters were obtained. The differences among the POD, GTDS, and filter/smoothing solutions can be traced to differences in modeling and tracking data types, which are being analyzed in detail.

1.0 Introduction

This paper assesses the Ocean Topography Experiment (TOPEX)/Poseidon orbit determination accuracy of the Tracking and Data Relay Satellite (TDRS) System (TDRSS)-based orbit solutions using an operational batch-least-squares system and a prototype sequential orbit determination system within the Goddard Space Flight Center (GSFC) Flight Dynamics Division (FDD). The TDRSS-based orbit solutions are compared with the high-precision orbit solutions obtained by the GSFC Space Geodesy branch using laser and Doppler Orbitography and Radiopositioning Integrated by Satellite (DORIS) tracking measurements.

TDRSS is a geosynchronous relay satellite network, which currently consists of five geosynchronous spacecraft and the White Sands Ground Terminal (WSGT) at White Sands, New Mexico. Of the five TDRSSs, three (TDRS-East, TDRS-West, and TDRS-Spare, located at 41 degrees, 174 degrees, and 62 degrees west longitude, respectively) actively support tracking of TDRSS-user spacecraft. Of the two remaining TDRSSs, one TDRS (located at 275 degrees west longitude) is used only for satellite communications, while the other TDRS (located at 46 degrees west longitude) is being reserved for future use. TDRSS can provide 85-percent to 100-percent coverage, depending on spacecraft altitude.

The Bilateral Ranging Transponder System (BRTS) provides range and Doppler measurements for determining each TDRS orbit. The ground-based BRTS transponders are tracked as if they were TDRSS-user spacecraft. Since the positions of the BRTS transponders are known, their ranging data can be used to precisely determine the trajectory of the TDRSSs.

* This work was supported by the National Aeronautics and Space Administration (NASA)/Goddard Space Flight Center (GSFC), Greenbelt, Maryland, under Contract NAS 5-31500.

** RTOD-E is a copyrighted product of Applied Technologies Associates, Incorporated (ATA).

The accuracy requirements on the Space Geodesy Branch Geodynamics (GEODYN) (Reference 1) orbit determination solutions, used to analyze the sea surface height measurements obtained by the TOPEX/Poseidon radar altimeter, are extremely stringent. The definitive orbit determination requirements for the TOPEX/Poseidon mission science data include a maximum 13-centimeter (1σ) radial position error. The accuracy of the precision orbit ephemerides (POEs) is being verified through the use of the TOPEX/Poseidon science data. Radar altimeter measurements over known overflight verification sites and the ocean surface are taken and then compared with coincident definitive TOPEX ephemerides generated using the ground-based laser and DORIS tracking. The resulting high-accuracy ephemerides are used to assess the accuracy of FDD-generated orbit determination solutions. The availability of the independent orbit determination solutions generated by the Space Geodesy Branch provides a unique opportunity to evaluate the accuracy of the orbit determination systems used by the FDD for operational navigation and analysis support.

This paper presents recent results of the TDRSS-based orbit determination accuracy analysis using the batch-least-squares method that is used for operational orbit determination support in the GSFC Flight Dynamics Facility (FDF). The batch-weighted-least-squares algorithm implemented in the Goddard Trajectory Determination System (GTDS) (Reference 2) estimates sets of orbital elements, force modeling parameters, and measurement-related parameters.

The sequential estimation algorithm is implemented in a prototype system, referred to as the Prototype Filter Smoother (PFS) filter. The PFS filter, which is closely related to the Real-Time Orbit Determination/Enhanced (RTOD/E) system (Reference 3), simultaneously estimates the TDRSS user and relay spacecraft orbital elements and other parameters in the force and measurements models at each tracking measurement time (Reference 4). It performs forward filtering of tracking measurements using the extended Kalman filter with a process noise model to account for serially correlated, geopotentially induced errors (Reference 4), as well as Gauss-Markov processes for drag, solar radiation pressure, and measurement biases. The PFS filter incorporates the same essential estimation algorithm as RTOD/E. It differs from RTOD/E in four significant ways: (1) the PFS filter executes on a mainframe computer whereas RTOD/E executes on a personal computer (PC); (2) the PFS filter lacks a maneuver model; (3) the PFS filter does not process one-way return Doppler TDRSS measurements; and (4) PFS includes a smoother and does not have a spacecraft antenna offset. The main features of RTOD/E can be found in Reference 5. To gain further insight into the comparison results, auxiliary sequential estimation solutions were generated with a smoother algorithm implemented in a system referred to as the PFS smoother. These solutions were compared with the POD solutions as well.

The estimated TOPEX/Poseidon ephemerides were obtained for the period November 7 through November 11, 1992. This timeframe was chosen because this period was relatively free of TOPEX attitude events and was well characterized through previous analyses (Reference 6). Independent assessments were made to examine the internal consistencies of results obtained by the batch and sequential methods.

This paper describes the POD solutions (Reference 7), describes the batch-least-squares and sequential orbit determination and evaluation procedures used in this study, provides an accuracy assessment of the POD solutions, describes the results obtained by the batch-least-squares and sequential estimation methods, provides the resulting consistency and comparisons with the POD solutions, and presents the conclusions of this study.

2.0 Analysis Procedures

This section describes the analysis procedures used in this study and provides a description of the tracking measurements and orbit determination and modeling methods.

2.1 Tracking Measurements

The TOPEX/Poseidon spacecraft was launched on an Ariane 42P expendable launch vehicle in August 1992. In October 1992, maneuvers were completed that moved the spacecraft into its operational orbit, which is circular with an inclination of 66 degrees, an altitude of 1336 kilometers, a period of 112 minutes, and a 10-day ground track repeat period. The time period chosen for this study was from 00:00 hours coordinated universal time (UTC) on November 7, 1992, through 21:33 hours UTC on November 11, 1992, which corresponds to the latter portion of the fifth 10-day ground track repeat cycle, hereafter referred to as Cycle 5.

Tracking measurements from TDRSS, used for TOPEX/Poseidon operational orbit navigation support by the FDF, were used to estimate the GTDS and filter definitive ephemerides. The GTDS orbit solutions were obtained using two-way range and one-way return and two-way Doppler data from TDRSS in addition to two-way range data from BRTS for estimation of the TDRS locations. The sequential estimation solutions were generated using two-way range and two-way Doppler data from TDRSS and BRTS, but no one-way return Doppler data were used. This restriction was necessary because the PFS

filter/smoothing combination, currently the only means available for studying smoothing processes, does not accommodate one-way return Doppler tracking measurements. The inability of the PFS filter/smoothing to accommodate TDRS maneuvers imposed an additional restriction on the time period processed.

The tracking consisted of an average of 10 passes of one-way return Doppler measurements and 11 passes of two-way range and Doppler measurements per day, with the average pass lasting 40 minutes. During selected tracking passes, TOPEX/Poseidon science data are downlinked. A representative daily TDRSS tracking data distribution is shown in Figure 1. Passes labeled "2" consist of two-way range and Doppler measurements, while passes labeled "1" consist of one-way return Doppler measurements. BRTS tracking coverage of each TDRS spacecraft typically consists of twelve to fifteen 5-minute passes per day.

The POD team uses ground-based laser ranging and one-way forward Doppler measurements from the DORIS system to generate the POEs. The laser tracking data network consists of approximately 50 ground stations located around the world. Fifteen of these stations are specifically designated to support TOPEX/Poseidon tracking. Most of the stations are located in the United States, Europe, and Australia. For Cycle 5, 171 tracking data passes were taken from 25 laser tracking stations. A typical pass of laser ranging data lasts from 10 to 15 minutes.

The DORIS tracking system, developed by the Centre Nationale d'Etudes Spatiales (CNES), consists of a global network of approximately 50 ground-based transmitter beacons that provide one-way ground-to-spacecraft Doppler tracking measurements. During a typical 10-day cycle, tracking measurements are obtained using approximately 40 of these ground beacons, which generate a total of about 1300 tracking passes per cycle. For Cycle 5, 1071 tracking data passes were taken using 42 DORIS tracking stations. Each pass is approximately 10 minutes in duration.

2.2 Orbit Determination Methods and Modeling

This section describes the orbit determination methods and the modeling used to generate the POEs and the GTDS batch-least-squares, and sequential estimation TOPEX/Poseidon solutions and ephemerides.

2.2.1 Precision Orbit Ephemerides

The POEs are generated by the Space Geodesy Branch POD team using the GEODYN program. Each POE spans a 10-day period coincident with a project-defined beginning and end of a repeatable ground track cycle. GEODYN, like GTDS, uses a batch-least-squares estimation process to fit the tracking measurements and estimate a solution. The POE used in this analysis covers the period from 17:32 hours UTC on November 1, 1992, through 21:33 hours on November 11, 1992. This timespan corresponds to the fifth 10-day ground track repeat cycle. The POEs for Cycles 4 and 6 were also used for additional comparisons with the filter/smoothing solutions.

The POEs used in this study represent the most refined POD solutions used to support the TOPEX/Poseidon science data. The quality of these POEs is discussed later in the paper.

The important force models and parameters used in the POE are given in Table 1. The TOPEX/Poseidon dynamic solve-for parameters consist of the TOPEX/Poseidon spacecraft state vector, one once-per-revolution along-track acceleration per day, one once-per-revolution cross-track acceleration per day, and one constant along-track acceleration per day. These

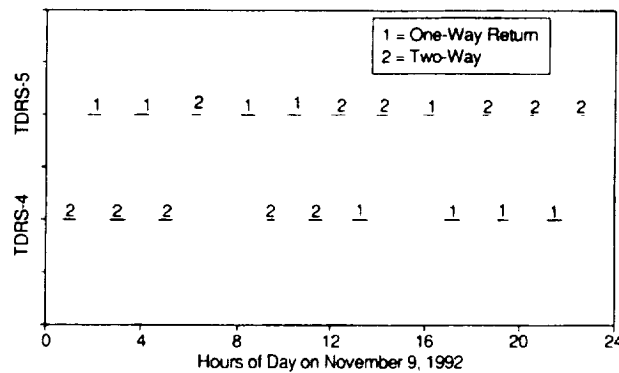


Figure 1. Typical TDRSS Tracking Scenario for TOPEX/Poseidon

Table 1. Force Modeling and Parameters Used in the POEs

Orbit Determination Parameter or Option	POE Values
Estimated parameters	Orbital state, along-track accelerations, cross-track acceleration
Integration type	11th-order fixed-step Cowell
Coordinate system of integration	True-of-reference
Integration step size	30.0 seconds
Tracking data	Ground-based laser ranging and DORIS data
Data rate	1 per 30 seconds
Differential correction convergence parameter	2 percent between iterations
Editing criterion	3.5 σ
Satellite area model	Box/wing model
Geopotential model	70 x 70 Joint Gravity Model-2 (JGM-2)
Atmospheric density model	Drag temperature model (DTM)
Coefficient of atmospheric drag	2.3
Coefficient of solar radiation pressure	1.0
Solar and lunar ephemerides	JPL Developmental Ephemeris-200 (DE-200)
Tropospheric refraction correction	Yes
Polar motion correction	Yes
Solid Earth tides	Yes
Ocean tides	Yes
Plate motion	Yes
Earth radiation pressure	Yes

once-per-revolution along-track and cross-track accelerations were introduced to better model an anomalous spacecraft body-fixed acceleration discovered shortly after launch. Atmospheric drag and solar radiation forces are applied but are not solved for. The constant along-track acceleration was introduced as an adjustment for atmospheric drag.

2.2.2 Batch-Least-Squares Estimation

The batch-least-squares estimation algorithm used by GTDS for this analysis is the same as that used for operational navigation support of the TOPEX/Poseidon mission by the GSFC FDF. The procedure used for operational support includes solving for the TOPEX/Poseidon spacecraft state, onboard ultrastable oscillator (USO) frequency bias and drift parameters, and an along-track thrust estimation parameter using two-way and one-way return Doppler measurements. TOPEX/Poseidon range measurements are excluded from the solutions because covariance analysis shows no improvement in accuracy and to avoid operational limitations in solving for uncorrected biases, which have been found to reduce the orbit solution quality. TDRS spacecraft trajectories are determined separately using the BRTS ranging and Doppler measurements.

The modeling and state estimation parameters used for this analysis have been modified and enhanced to provide more accurate results and to take advantage of modeling and techniques not currently in operational use. Specifically, the TOPEX/Poseidon state space was expanded to include estimation of the coefficient of solar radiation pressure in addition to multiple along-track thrust parameters that were intended to compensate for the anomalous acceleration acting on the spacecraft. Analysis of the operational TOPEX/Poseidon orbit solutions has indicated the presence of an unmodeled spacecraft body-fixed force with a day-to-day variability. Analysis performed by the Jet Propulsion Laboratory (JPL) has indicated that the unmodeled force is dependent on the angle between the orbit plane and the Sun (Reference 8). Consequently, in addition to an applied drag force, a series of thrust scale factors (referenced to a 1-micronewton continuous along-track thrust) was estimated.

TDRS Orbit Determination

TDRS spacecraft trajectories were estimated simultaneously with TOPEX/Poseidon using both BRTS range and TOPEX/Poseidon two-way range and two-way and one-way return Doppler data to determine the best possible TDRS trajectories for use in the TOPEX/Poseidon-only batch estimation. The modeling, data types, and other orbit determination options used for the TDRSs and TOPEX/Poseidon in the simultaneous solution are presented in Table 2. The data span chosen was 5 days, with one thrust correction factor per day. The simultaneous TDRS/TOPEX solution arcs were selected to avoid all maneuvers and angular momentum unloads, where possible, while maintaining the longest possible data spans. In addition, central angle editing was used to mitigate the effects of ionospheric refraction on the TDRS-to-TOPEX/Poseidon tracking link. The central angle chosen was designed to eliminate all data below the TOPEX/Poseidon local horizon.

Numerous transponder delay corrections were necessary to resolve biases between the BRTS and TOPEX/Poseidon range measurement types in the simultaneous solutions. These transponder delays included the individual transponder delays for each BRTS ground transponder and a transponder delay on each TDRS. In addition, a TOPEX/Poseidon spacecraft transponder delay correction value was applied to reduce the effects of ranging calibration errors on the TDRS and TOPEX/Poseidon orbit solutions.

Table 2. Parameters and Options Used in the GTDS Solutions

Orbit Determination Parameter or Option	GTDS Values*	
	TOPEX	TDRS-East, TDRS-West
Estimated parameters	Orbital state, thrust coefficients, coefficient of solar radiation pressure (C_R), USO bias and drift	Orbital state, coefficient of solar radiation pressure (C_R), spacecraft transponder delay, BRTS transponder delays
Integration type	Cowell 12th order	Cowell 12 th order
Coordinate system of integration	Mean-of-J2000.0	Mean-of-J2000.0
Integration step size (seconds)	60 seconds	600 seconds
Tracking measurements	TDRSS two-way Doppler TDRSS one-way return Doppler TDRSS two-way range	BRTS two-way range
Data span	See text	See Section 3.2 of text
Data rate	1 per minute	1 per 20 seconds
DC convergence parameter	0.00005	0.00005
Editing criterion	3 σ	3 σ
Ionospheric editing criterion	Central angle greater than 79.48 degrees	-
Measurement weight sigmas	Doppler: 10 millihertz Range: 1.5 meters	2 meters
Satellite area model	Variable mean area model	Constant, 40 meters ²
Satellite mass	2417.2 kilograms	TDRS-6: 1973.1 kilograms TDRS-4: 1853.6 kilograms
Geopotential model	50 x 50 JGM-2	20 x 20 JGM-2
Atmospheric density model	Jacchia-Roberts	N/A
Solar and lunar ephemerides	DE-200	DE-200
Coefficient of drag (C_D)	2.3 applied	N/A
Ionospheric refraction correction		
Ground-to-spacecraft	Yes	Yes
Spacecraft-to-spacecraft	No (central angle edit instead)	N/A
User-spacecraft antenna offset correction	Constant radial, along-track, cross-track	No
Tropospheric refraction correction	Yes	Yes
Polar motion correction	Yes	Yes
Solid Earth tides	Yes	Yes
Ocean tides	No	No
Plate motion	No	No
Earth radiation pressure	No	No

*JGM = Joint Gravity Model; N/A = not applicable

Application of at least a single BRTS transponder delay is necessary to prevent the orbit solutions from being ill-determined. Residuals analysis, supported by comparison with the precision ephemerides, indicated that the default WSGT BRTS transponder delays provided optimal TOPEX/Poseidon estimation. Estimation of the Alice Springs, Australia, BRTS site transponder delay was found to have little impact on the TOPEX/Poseidon estimation accuracy. The applied TOPEX/Poseidon transponder delay correction was modeled as a range bias and was determined based on an auxiliary solution where BRTS and TOPEX/Poseidon range measurement biases were estimated instead of the BRTS and TDRS transponder delays.

Topex/Poseidon Orbit Determination

After the TDRS trajectories were estimated in the simultaneous solution, they were applied in a TOPEX/Poseidon-only solution that used the one-way and two-way Doppler data only. This was done to minimize the effect of TOPEX/Poseidon range data bias modeling errors on the TOPEX/Poseidon trajectory. The span of this solution was only 4 days, and it was selected to reduce the dynamical modeling errors and to simplify the thrust estimation parameter selection. Force modeling for the TOPEX/Poseidon-only solution is the same as that used for the simultaneous solutions with TDRS (see Table 2), with the exception that only two thrust correction factors were estimated for the 4-day data span.

Solution Evaluation

Since adjoining and overlapping solutions were not calculated for this analysis, evaluation of the solution quality was performed based on comparison with the POEs and the final solution observation residuals. This was performed using average and standard deviation summary statistics and was shown graphically using plots of the individual data point residuals. Only data points that were not edited from the solution due to data validity flagging, 3σ editing, user editing, or central-angle editing were used in the evaluation of the residuals. However, the graphical evaluation did consider the possible need to use data eliminated by the 3σ editing, to preclude the elimination of potentially useful data that may have been edited as the result of a mismodeled bias.

2.2.3 Sequential Estimation

The improvement in the POE-filter comparison results brought about by application of a smoother was studied using Cycle 4, 5, and 6 POEs and the PFS filter/smoothing system. The general approach was to generate several PFS filter and smoother solutions for portions of Cycles 4, 5, and 6 and to compare these solutions with the respective POEs. The PFS filter was run for a period several days long, and a series of PFS smoother runs was made for progressively longer spans, each ending at the same epoch. Previously, sequential TOPEX orbit solutions for the same time period were generated using RTOD/E (Reference 6). A more realistic operating mode was achieved for these earlier solutions, for example, by processing for extended periods (more than 1 month) and by suspending RTOD/E execution at various points to accommodate maneuvers and adjust tuning parameters and, when necessary, for complete reinitialization. The PFS filter/smoothing system is currently the only means to study the smoothing process, a paramount objective of the current study. Although limitations of the PFS filter/smoothing system (i.e., inability to process one-way TDRSS measurements and lack of a maneuver model) precluded replication of the RTOD/E solutions used in the earlier study, ephemeris consistency tests showed that solutions generated with the PFS filter were essentially reproducible with RTOD/E when common tracking data sets were used. Valid conclusions about the potential for improvement in RTOD/E solutions (for example, those discussed in Reference 6) could thus be drawn.

The filter was initialized for TOPEX, TDRS-Spare, and TDRS-West for October 22, 1992, 19:00:00 UTC, and run to October 27, 1992, 00:00:00 UTC (no two-way TOPEX measurement data were encountered until October 24, 1992, 03:32:00 UTC). The smoother was run from October 27, 1992, 00:00:00 UTC back to October 24, 1992, 00:00:00 UTC. This period is contained within Cycle 4. Although tracking measurements from both TDRS-Spare and TDRS-West were included, TDRSS and BRTS tracking measurements for TDRS-West that occurred after a TDRS-West maneuver at about 14:00:00 UTC on October 26, 1992, were rejected by the editing process due to the inability of the software to model maneuvers. A second filter run was initiated for TOPEX, TDRS-East, and TDRS-West for November 5, 1992, 00:00:00 UTC, and run for 14 days. This second processing period overlaps Cycles 5 and 6. For either run, two generic initial orbit RIC [radial, in-track (along-track), and cross-track] covariance matrices, one for TOPEX and one for the TDRSSs, were used for each initialization.

Tables 3 and 4 provide detailed information on the models and options used for the filter-smoothing solutions. The solution state included orbital elements for TOPEX and each of two TDRSSs. Other estimated quantities included a coefficient of atmospheric drag for TOPEX and a coefficient of solar radiation pressure for each of the three satellites.

Table 3. Parameters and Options for PFS Solutions

Orbit Determination Parameter or Option	PFS Filter/Smoother Values	
	TOPEX	TDRS-East/TDRS-West/TDRS-Spare
Estimated parameters	Orbital state, coefficients of drag and solar radiation pressure, TDRSS range and Doppler tracking measurement biases	Orbital state, coefficient of solar radiation pressure, BRTS range and Doppler tracking measurement biases
Integration type	Variation of Parameters (VOP)	VOP
Coordinate system of integration	Mean of 1950.0	Mean of 1950.0
Integration step size	60.0 seconds	60.0 seconds
Tracking data	TDRSS two-way range and Doppler	BRTS range and Doppler
Data rate	1 per minute	1 per minute
Editing criterion	3 σ	3 σ
Gravity error autocorrelation values	R: 2.828 minutes I: 0.001 minute C: 5.611 minutes Errors of omission and commission	Not applicable (N/A)
Measurement sigmas: Range Doppler	0.50 meter 0.010 hertz	0.25 meter 0.002 hertz
Gauss-Markov parameters: Drag half-life Drag sigma C_R half-life C_R sigma Range bias half-life Range bias sigma Doppler bias half-life Doppler bias sigma	840.0 minutes 0.400 1440.0 minutes 0.200 60.0 minutes 6.0 meters 8 minutes 0.034 hertz	N/A N/A 11520.0 minutes 0.200 60.0 minutes 7.0 meters 60 minutes 0.030 hertz
Standard deviation of the Earth's gravitational constant	0.005 kilometers ³ /second ²	0.005 kilometers ³ /second ²

Table 4. PFS Force and Measurement Model Specifications

Model or Options	PFS Values	
	TOPEX	TDRS-East/West
Geopotential model	GEM-T3 (50 x 50)	GEM-T3 (8 x 8) (truncated)
Atmospheric density model	CIRA 72*	N/A
Solar and lunar ephemerides	Analytic	Analytic
Coefficient of drag	Estimated with a priori value of 2.3	N/A
Coefficient of reflectivity	Estimated with a priori value of 1.25	Estimated with a priori value of 1.4
Ionospheric refraction correction	No	No
Tropospheric refraction correction	Yes	Yes
Antenna mount correction	No	No
Polar motion correction	Yes	Yes
Earth tides	No	No

*CIRA = Committee on Space Research (COSPAR) International Reference Atmosphere; GEM = Goddard Earth Model

A comparison between the filter, smoother, and the POEs, resolved in orbit-plane principal directions, provided the primary means of gauging the sequential orbit determination accuracy. The comparisons were performed in the J2000.0 true-of-date (TOD) coordinate frame. Other indicators of solution quality were provided by the diagonal elements of the state error covariance matrix (Reference 9), the integrity of the drag coefficient estimates, and an examination of the residual statistics.

3.0 Results and Discussion

This section presents the TOPEX/Poseidon accuracy assessment analysis results, an assessment of the consistency of the TOPEX/Poseidon ephemerides, and the ephemeris comparison results.

3.1 Accuracy Assessment of the POEs

To support the science objectives of the TOPEX/Poseidon mission, the POD team is required to produce POEs that are accurate to 13 centimeters (1σ) in the radial component. Comparisons of the POEs with actual TOPEX/Poseidon radar altimeter data show agreement to within 12 centimeters. These comparisons, in conjunction with a battery of other verification tests, provide strong evidence that the POEs are sufficiently accurate to meet the 13-centimeter (1σ) requirement. The tests also indicate that the along-track component is three to four times less accurate than the radial component, while the cross-track component is one to three times less accurate than the radial component (Reference 7).

One aspect of the POE verification involves performing overlap comparisons to assess solution consistency between the POEs and specially generated overlap solutions. A special 10-day overlap solution, which overlaps the first 5 days of the Cycle 5 POE, was generated and compared with the Cycle 5 POE in the common interval. The results show an average root-mean-square (RMS) overlap radial position consistency of 0.6 centimeter, which is substantially less than the 13-centimeter (1σ) accuracy requirement. In addition, the average RMS overlap along-track and cross-track position consistencies are 3.3 and 3.8 centimeters, respectively (Reference 7).

3.2 Summary of the Batch-Least-Squares Estimation Results

The simultaneous TDRS/TOPEX solution spanned November 7 through November 12, 1992. This period was chosen since it provided TDRS data spans with few momentum unloads, which normally occur every 1.5 to 2.5 days. The separate TOPEX/Poseidon-only solution spanned November 7 through November 11, 1992, maximizing the measurement span for which there were two valid TDRS trajectories available from the simultaneous solution. Shortening the solution span to 4 days also reduces the effect of known dynamical modeling errors by approximately 20 percent compared with a 5-day span.

Solution residuals are presented for the simultaneous TDRS/TOPEX orbit solution, used primarily for the TDRS trajectory estimation, and for the separate TOPEX/Poseidon orbit determination solution. Both solutions correspond to the latter half of the TOPEX/Poseidon ground track Cycle 5. There were three TDRS momentum unloads during this period, each having a different impact on the orbit determination performance. A TDRS-West momentum unload on November 10 at 17:00 UTC had a significant impact on the solution residuals; therefore, all TDRS-West tracking data after that time were edited from the simultaneous solution, but the residuals were calculated to illustrate the effect of the momentum unload. TDRS-East momentum unloads on November 7 at 06:35 UTC and November 9 at 19:45 UTC had little impact on the residuals. Exclusion of the TDRS-East momentum unloads was found to reduce the solution quality because of the shortened TDRS data spans and the lack of significant two-TDRS tracking of TOPEX/Poseidon.

Figure 2 illustrates each TOPEX/Poseidon two-way range residual from the simultaneous solution. Tracking data from both TDRS-West and TDRS-East are included. The edited data after the TDRS-West momentum unload was the result of the manual exclusion of the TDRS-West data due to the momentum unload. The mean of the accepted data residuals is approximately 0 meters, and the residuals are generally within ± 4 meters. The residual statistics reported from the solution were 0.022 ± 2.219 meters (in the form of the mean \pm the standard deviation). There appears to be a 24-hour periodicity to the residuals until the TDRS-East momentum unload on November 9 at 19:45 UTC. Given the 24-hour periodicity, the most likely cause is a modeling error common to both TDRS spacecraft trajectories. Further analysis is needed to positively identify the cause. The TDRS-West momentum unload on November 10 at 17:00 UTC resulted in either an increase in the amplitude of the residuals from ± 5 meters to ± 10 meters, assuming that the pass with a residual of 10 meters near noon on November 11 was good, or an introduction of a secular rate of approximately -5 meters per day in the residuals, assuming the pass was randomly biased. Either way, inclusion of the TDRS-West data after the momentum unload degraded the solution. The TDRS-East momentum unloads on November 7 at 06:35 UTC and on November 9 at 19:45 UTC had little effect on the magnitude of the residuals.

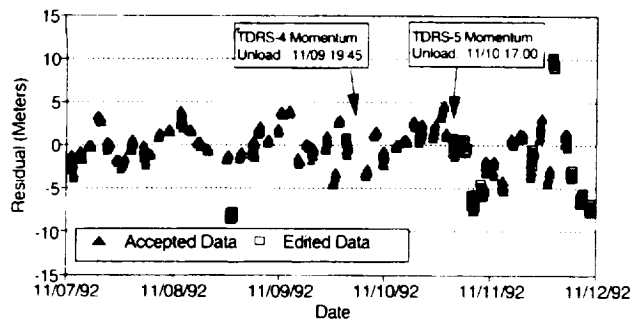


Figure 2. TOPEX/Poseidon Two-Way Range Residuals (Simultaneous Solution)

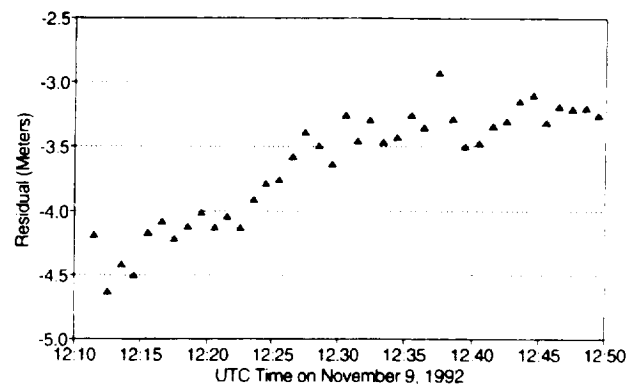


Figure 3. TOPEX/Poseidon Two-Way Range Residuals From TDRS-East (Simultaneous Solution)

A representative pass of TOPEX/Poseidon two-way range data residuals from TDRS-East is plotted in Figure 3. The data used in the solution were sampled at the rate of one point every minute out of data that were available at 10-second intervals. No smoothing was performed in the sampling of the 10-second data. As can be seen, there is still significant structure to the residuals with evidence of very little noise.

Two-way BRTS range residuals for TDRS-East are given in Figure 4. As with the TOPEX/Poseidon range data, the residuals generally do not exceed 5 meters. There is a significant amount of structure left in the residuals, which exhibit a 24-hour periodicity. Unlike the TDRS-West momentum unload on November 10 at 17:00 UTC, which resulted in an increase in the amplitude of the residuals, the TDRS-East momentum unloads did not. Each vertical block of data points typically represents two 5-minute adjacent passes. Assuming that the geostationary TDRS spacecraft are not moving significantly with respect to the ground during the passes, the vertical scatter in the data points is the result of noise in the data. Inspection of the passes on a pass-by-pass basis confirms that the 3σ noise is approximately 1 meter. The BRTS range measurement weight sigma was 2 meters. Some discontinuities are evident in the data, implying that there are biases in the data that are not entirely constant over the solution data span. The cause of the bias changes needs to be investigated further. The combined TDRS-East and TDRS-West BRTS range residual average is -0.016 ± 3.008 meters, slightly larger than the TOPEX/Poseidon range values.

The S-Band (2287-megahertz) return-link two-way TOPEX/Poseidon Doppler tracking residuals for the simultaneous solutions were generally bounded by 30 millihertz, with the average being 0.0 ± 9.7 millihertz. One-way return residuals averaged 0.0 ± 12.8 millihertz. These values correspond to range-rate values of 0.0 ± 1.27 millimeters per second for the two-way Doppler and 0.0 ± 1.68 millimeters per second for the one-way return Doppler. Most of the residuals have structure, implying that mismodeling, rather than noise, is the dominant source of error. Overall, these figures are approximately 40 percent of the values from previously reported results (Reference 6).

Two-way Doppler residuals for the 4-day TOPEX/Poseidon-only orbit solution average to 0.0 ± 8.5 millihertz, a little more than 10 percent better than the simultaneous solution. The one-way Doppler residuals average was 0.0 ± 12.7 millihertz. A representative pass of two-way Doppler data is given in Figure 5, illustrating the structure left in the residuals. Noise in the Doppler data appears to be limited to 1 to 2 millihertz, making noise only 10 percent of the observed residuals. Since the observed residuals appear to be highly structured, it should be possible to improve the modeling to minimize solution errors.

Overall, the solution range residuals show an approximately 2.0-meter 1σ error for the TOPEX/Poseidon range data, while the TDRS BRTS range data had an approximately 3.0-meter 1σ error. The cause of the higher error level for the BRTS range data appears to be the result of noise; otherwise, it is comparable to the TOPEX/Poseidon range data in quality. Based on the presence of a 24-hour periodicity in the residuals, most of the user range residual structure appears to be caused by TDRS trajectory error. The TOPEX/Poseidon Doppler residuals were of the order of 10 millihertz (1σ), with most of the residuals having significant structure and little noise. Some improvement in the Doppler residuals was observed when the TDRS estimation and range data were eliminated from the solution, using the previously estimated TDRS trajectories.

3.3 Summary of Sequential Estimation Results

Several indicators were available to assess the quality of the filter solutions independent of other orbit determination systems. Among such performance criteria are the diagonal components of the state error covariance matrix, more specifically, the square root of these values (standard deviation) (Reference 9). Figure 6 shows the time-evolution of the 1σ root-sum-square

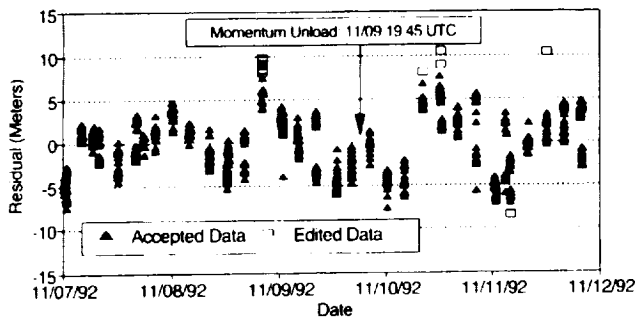


Figure 4. TDRS-East Two-Way Range Residuals From BRTS (Simultaneous Solution)

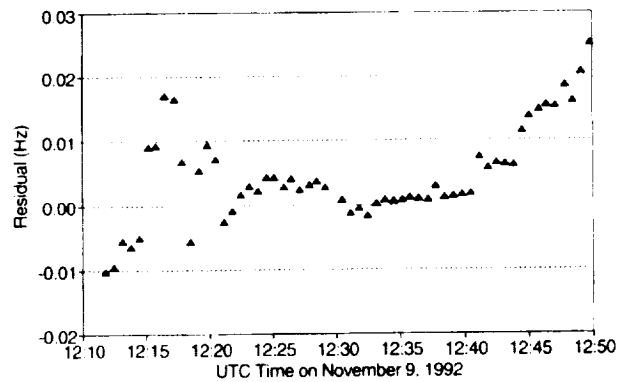


Figure 5. TOPEX/Poseidon Two-Way Doppler Residuals via TDRS-East

(RSS) position error estimate for TOPEX during the 4-day period beginning at 00:00:00 hours UTC on November 7, as computed by the PFS filter and the PFS smoother. Filter settling is apparent throughout the 4 days shown in Figure 6. Correspondingly, improved solution quality is expected as the smoother interval is increased. The root-variance estimates shown in Figure 6 indicate optimum accuracy near the middle of the smoother span, a characteristic predicted by theory. Averages of the standard deviations over the orbital periods (112 minutes) were computed to produce this plot. Perfect agreement in smoother and filter covariance at the start of a filter run, as evident in the figure, is a direct reflection of the smoothing algorithm.

Additional evidence of solution quality was sought by examining the residual statistics. Smoother postfit residual standard deviations for the period from November 7, 00:00:00 UTC, to November 8, 00:00:00 UTC, are shown in Table 5. These are typical for the timespan studied. A high degree of similarity can be seen among the values for the various smoother runs.

Excessive variations in the estimates for the coefficient of the solar radiation pressure and the coefficient of atmospheric drag for TOPEX can indicate problems with solution quality. When properly tuned, the estimated values of the drag and solar radiation coefficients should accommodate mismodeling of the atmospheric density and uncompensated variations in the solar radiation force model, respectively. In addition to atmospheric modeling and solar flux level uncertainties, changes in the spacecraft attitude can be expected to induce variation in the coefficient estimates (the PFS filter uses a constant-area cross-section for both the drag and solar radiation pressure computations). Given these factors, the observed variation in the coefficient estimates was judged to be reasonable, although a nonoptimum process noise tuning parameter C_D is indicated.

3.4 Results of POE and GTDS Solution Comparisons

Two GTDS ephemerides, spanning the latter portion of Cycle 5, were compared with the Cycle 5 POE. The ephemerides were compared at 10-minute intervals in orbit plane coordinates over their common definitive spans.

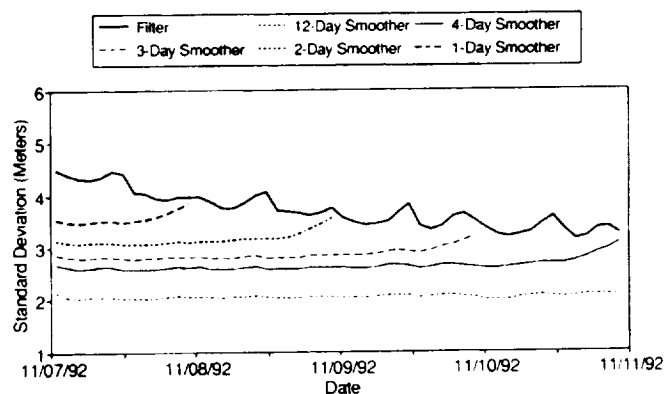


Figure 6. TOPEX/Poseidon Filter/Smoother RSS Position Error Estimates

Table 5. Typical PFS Filter/Smoother Residual Statistics

Estimation Type	Residual Statistics			
	TDRSS Range σ (meters)	TDRSS Doppler σ (hertz)	BRTS Range σ (meters)	BRTS Doppler σ (hertz)
Filter (prefit)	0.38680	0.011474	0.79318	0.014827
Filter (postfit)	0.08234	0.002383	0.12289	0.002569
Smoother (12-day)	0.10093	0.002406	0.17754	0.002893
Smoother (4-day)	0.10052	0.002352	0.17690	0.002866
Smoother (2-day)	0.10051	0.002223	0.17570	0.002903
Smoother (1-day)	0.10172	0.002463	0.17471	0.002986

NOTE: The values in the table above are for all residuals between 11/7/92 00:00:00 and 11/8/92 00:00:00 UTC, except for the first ones in passes. Thus, all are based on the same set of measurements over a 24-hour period. There were 450 TDRSS measurement pairs in this sample and 90 BRTS measurement pairs.

The first GTDS ephemeris, which corresponds to the TOPEX/TDRS simultaneous solution used to obtain the optimal TDRS orbits, is approximately 5 days long and spans the period 00:00 hours UTC on November 7, 1992, through 21:33 hours UTC on November 11, 1992. The RSS position differences between this GTDS ephemeris and the Cycle 5 POE are shown in Figure 7. The average RSS position difference is 1.1 meters, with a maximum difference of 2.9 meters.

The second GTDS ephemeris, which corresponds to the separate TOPEX solution and represents the best currently available TOPEX orbit, is 4 days long and spans the period 00:00 hours UTC on November 7, 1992, through 00:00 hours UTC on November 11, 1992. The RSS position differences between the second GTDS ephemeris and the Cycle 5 POE are shown in Figure 8. The average RSS position difference is 1.0 meter, with a maximum difference of 2.0 meters.

Note that the GTDS/POE differences shown in Figures 7 and 8 are similar except near the ends of the solution arc, where the differences for the separate GTDS solution/POE ephemeris comparison are somewhat smaller. This can be attributed to the reduced number of solved-for thrust coefficients in the separate TOPEX solution, which allows for the increased observability of, and a better estimate for, the unmodeled along-track accelerations acting on the spacecraft in addition to uncertainties related to the TDRS estimation.

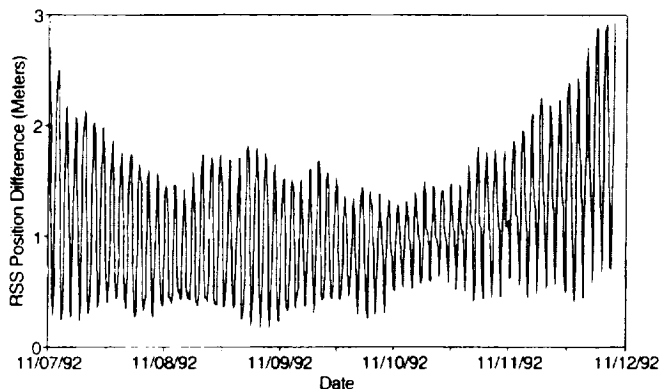


Figure 7. Position Differences Between POE and GTDS TOPEX Ephemerides (Simultaneous Solution)

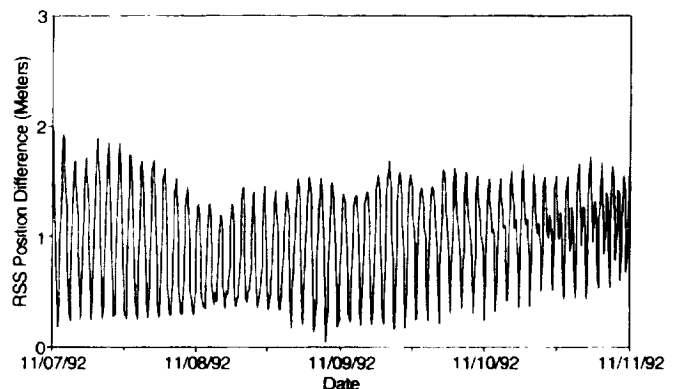


Figure 8. Position Differences Between POE and GTDS TOPEX Ephemerides (Separate Solution)

Figure 9 shows the representative differences in the radial, cross-track, and along-track directions for the separate TOPEX solution, on November 9, 1992. The maximum radial difference is 0.5 meter, while the maximum cross-track difference is 1.6 meters. The maximum along-track difference, which is the largest of the three components, is about 1.9 meters. The differences in the along-track and cross-track components have an average value of -0.5 meters and 0.3 meter, respectively, while the average difference in the radial component is nearly zero.

Some of the difference in the along-track component is likely due to differences in the modeling of along-track accelerations. The POEs estimate a daily once-per-revolution along-track acceleration, consisting of two solved-for parameters per day, and a daily constant along-track acceleration to accurately model the effects of the anomalous spacecraft forces as well as atmospheric drag perturbations. This represents a total of 30 solve-for parameters to characterize the along-track accelerations. The separate GTDS TOPEX solution, however, estimates only two thrust scale factors to characterize the along-track forces. Similarly, the POEs estimate a daily once-per-revolution cross-track acceleration, consisting of two solved-for parameters per day, to characterize the cross-track accelerations. The separate GTDS TOPEX solution, however, estimates no cross-track accelerations. Along-track and cross-track component differences can, in part, also be attributed to the differences in the modeling of the attitude changes resulting from the yaw-steering feature. These would affect both the measurement modeling and the atmospheric drag and solar radiation pressure force modeling. The POEs model the instantaneous changes in the spacecraft cross-sectional areas for drag and solar radiation pressure evaluation resulting from the yaw steering. The separate GTDS TOPEX solution uses the variable mean area model, which provides mean orbital values of the drag and solar radiation pressure cross-sectional areas.

3.5 Comparison Between POEs and Sequential Ephemerides

Ephemeris comparison results for the Cycle 5/6 period are illustrated in Figures 10 and 11. Figure 10 shows the TOPEX position difference between the POEs and the filter ephemeris and between the POEs and the smoother ephemerides for a 12-day span. The position differences are represented with an orbital average of the RSS position difference computed over 110-minute periods (the TOPEX orbital period is approximately 112 minutes). The figure also displays results for smoother runs of 1 through 12 days, each ending on November 7, 00:00:00 UTC. Figure 11 shows the radial, cross-track, and along-track components of the position difference between the Cycle 5 POE and the 4-day smoother ephemeris during a representative day (November 9, 1992).

The average 1-day RSS position difference was under 7 meters for all but the 1-day smoother run. In Figure 10, a reduction in the position difference is evident. The maximum difference for the filter was approximately 15 meters, while for the smoother it was approximately 8 meters (after the smoother settled). Thus, a categorical improvement in agreement with the POEs resulted from the application of the smoother to the sequential estimation solutions.

As seen previously for RTOD/E results, a significant cross-track position difference is observed for the PFS filter results. While at a reduced level, the cross-track component is proportionately similar for the smoother results.

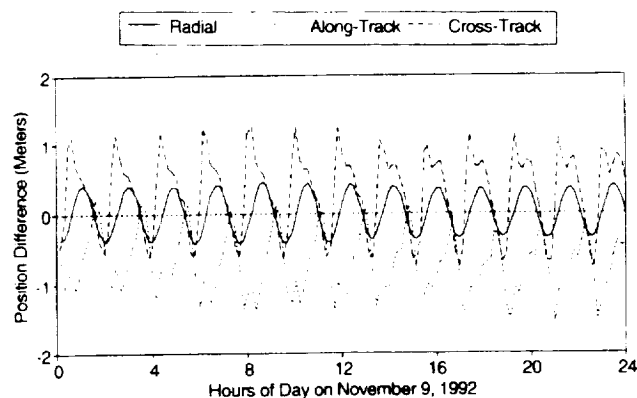


Figure 9. Position Differences by Component Between POE and GTDS Ephemerides for November 9, 1992

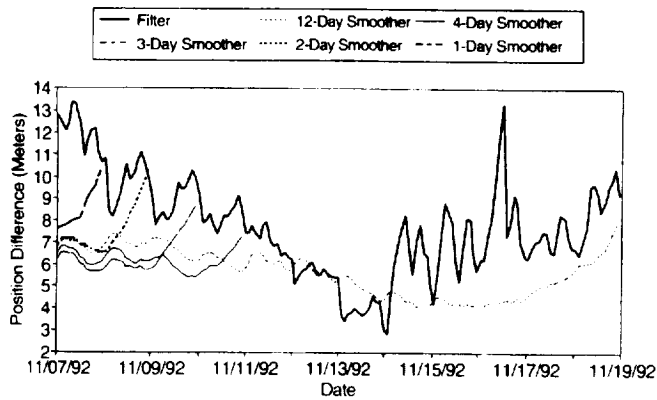


Figure 10. Position Differences Between POE and PFS Filter/Smother Ephemerides

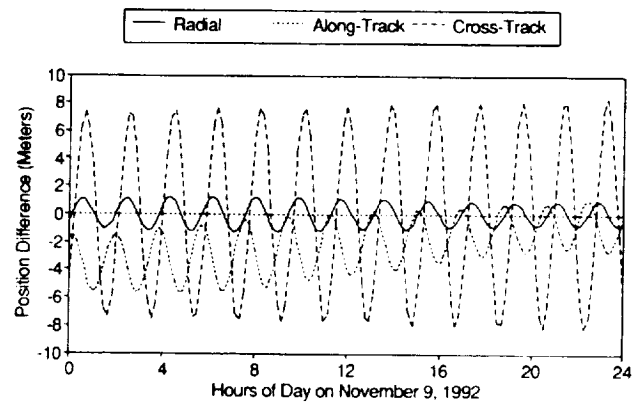


Figure 11. Position Differences by Component Between POE and PFS Filter/Smother Ephemerides for November 9, 1992

3.6 Remarks on Supporting Analysis

Batch-least-squares covariance analysis was performed to analyze the GTDS solutions. The modeling for the covariance analysis was made as close as possible to the GTDS modeling. The 3σ RSS position uncertainty was found to vary between 7 and 15 meters. By components, the maximum 3σ position uncertainties were 3 meters, 5 meters, and 14 meters in the radial, cross-track, and along-track directions, respectively. The differences between the GTDS solutions and the POEs are less than the uncertainties obtained by covariance analysis. At the maximum 3σ RSS position uncertainty of 14.9 meters, the major contributors to the errors are the uncertainty in the ionospheric refraction correction at WSGT (11.6 meters) affecting TDRS position accuracy and the geopotential (6.0 meters).

The batch-least-squares procedures used in this analysis are being applied to the processing of a longer (20-day) span of data. Preliminary results indicate that the results presented here are reproducible when moderately good conditions are prevalent, such as when the TDRS spans are undisturbed by significant momentum unloads and maneuvers. More frequent momentum unloads and shorter data spans have been observed to have a significant detrimental effect on the TOPEX/Poseidon orbit determination.

GTDS orbit determination solutions have been obtained using state vectors from the Cycle 5 POE as the measurements. This form of orbit determination solution eliminates all observational and TDRS spacecraft dynamical force modeling, thereby making it possible to estimate the amount of error resulting from the dynamical modeling used in GTDS for TOPEX/Poseidon. The solution span corresponds to the same span used for the TOPEX/Poseidon-only orbit determination solution, which was presented earlier. The solution is 4 days long and spans the period 00:00 hours UTC on November 7, 1992, through 00:00 hours UTC on November 11, 1992, and used state vectors at 12-minute intervals. The RSS position differences between this special solution and the Cycle 5 POE are shown in Figure 12. The average RSS position difference is 0.4 meter, with a maximum difference of 1.1 meters. The maximum radial, along-track and cross-track differences are 0.4 meter, 0.9 meter and 1.0 meter, respectively. The average component differences are all zero.

The differences illustrated in Figure 12 reflect the force modeling errors between the GTDS dynamical force modeling and the Cycle 5 POE. Comparison with Figure 8 reveals that the force modeling errors and the measurement modeling errors both contribute approximately 1 meter to the total error, on average. GTDS solutions using 10-day spans from the POEs yielded errors of 2 meters. The error appears to be a function of the solution span, incurring error at the rate of 20 centimeters per day of solution. The nature of the errors implies that GTDS is performing a best average fit to a time-varying term in the dynamics modeling. This is supported by preliminary analysis which has eliminated constant errors in the geopotential terms, including those affected by dynamic polar motion and constant errors in the $C_{2,0}$ term. Likewise, preliminary analysis has indicated that the effect of the $C_{2,0}$ rate term is too small to produce the observed effects.

The validity of the secular trends of the GTDS dynamic modeling was also verified by performing GTDS solutions for arc lengths of 1 day through 10 days, with increasing arc lengths by a day each for Cycle 5. The characteristics of the comparison of the 10 solutions with the POEs did not change from the short (1-day) arc length to the long (10-day) arc length. This demonstrated that the effects of dynamical mismodeling are small compared with the other errors. Corresponding covariance analysis solutions with the same tracking schedules as the 10 GTDS solutions supported the GTDS solutions.

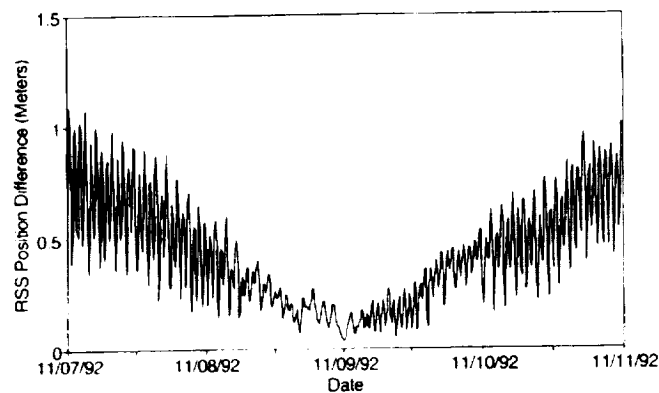


Figure 12. Comparison of Special GTDS Solution With the POE

The accuracies achieved here using batch-least-squares and sequential estimation methods are different, in most part, due to differences in modeling and the effectiveness with which the modeling is used; they are not a reflection of the inherent potential of either estimation technique.

It is important to note that TDRSS tracking does not have a requirement to yield orbit solutions with accuracy comparable to laser-tracked orbit solutions. However, a major objective of this work is to assess the achievable TDRSS orbit determination accuracy.

3.7 Future Analysis

Several areas in the batch-least-squares modeling and orbit determination processing could be improved to yield better results. First, the area modeling of TOPEX itself should be improved. At present, only mean areas are used for the solar radiation and drag force computations. Second, the antenna offset model could be improved to incorporate the effects of the sinusoidal yaw steering mode. The ability to automatically estimate TDRS trajectories through momentum unloads would possibly allow for operational support using the procedures present herein. Finally, better treatment of the unmodeled body-fixed force should help improve the accuracy of the batch-least-squares solutions.

Although the tunable parameters used for the PFS filter runs were close to optimal, the smoother nevertheless provided appreciable improvement in the comparison results. It is thus reasonable to suppose that a similar improvement in ephemeris comparison results would be achieved if a smoother were applied to solutions from an optimally tuned filter.

While appreciable, neither tuning nor smoothing improvements has resulted in POE comparisons commensurate with the inherent filter accuracy implied by the filter's covariance estimates. This indicates that further optimization of the filter's tunable parameters would be worthwhile. The substantial improvement in comparison results for GTDS ephemerides that has been achieved through refinement of the predetermined TDRS solutions suggests that additional analysis involving the simultaneously estimated TDRS orbit solutions would result in further improvement. Other factors limiting agreement with the POEs include dissimilarities in modeling and tracking data types.

4.0 Conclusions

This study analyzed the TDRSS-user orbit determination accuracy using a batch-least-squares method and a sequential estimation method. Independent assessments were performed of the orbit determination consistency within each method, and the estimated orbits obtained by the two methods were compared to the POEs.

In the batch-least-squares analysis, the solution range residuals show an approximately 2-meter, (1σ) mean value for the TOPEX/Poseidon range data, 3 meters for the TDRS BRTS range data, and TOPEX/Poseidon Doppler of the order of 10 millihertz. Virtually all of the observed residual patterns have significant structure and display little noise. These solutions compare with the POEs at less than 2 meters in maximum total position difference. The radial component compares to within 0.5 meter, slightly less than four times the 13-centimeter (1σ) POE accuracy requirement. Dynamical TOPEX/Poseidon modeling errors in GTDS have been shown to cause approximately 1 meter of the observed error in the solutions. Given the observed residuals and the known level of dynamical mismodeling in the current GTDS solutions, it can be stated that the TDRSS tracking measurement data have sufficient quality to support orbit determination to levels better than 2 meters in accuracy, provided issues of sufficient tracking coverage and accurate orbit determination modeling are addressed.

The reduction of the differences, as compared with an earlier analysis (Reference 6) was the direct result of the use of the improved TDRS orbits obtained from the TOPEX/TDRS simultaneous solutions. This demonstrates that the treatment of the relay orbit determination has a significant impact on high-accuracy orbit determination in the TDRSS environment.

After allowance is made for filter settling, the near-optimally tuned filter produced orbit solutions that were within 13 meters of the POEs. Application of a smoother algorithm to these filter solutions reduced the difference with the POEs to within 7 meters. These results demonstrate that smoother postprocessing offers the potential for appreciable improvement in sequential estimation solution accuracy, even when the filter is near-optimally tuned. Additional improvement in sequential orbit determination accuracy would be expected from further refinement of tunable parameters and enhancement of force modeling.

In summary, the differences between the TDRSS/GTDS-derived definitive batch-least-squares ephemerides and the POEs were no larger than about 2 meters. The differences between the smoothed sequentially estimated ephemerides and the POEs were no larger than 7 meters. Further analysis is in progress to understand the magnitudes of the differences. The differences among the POEs, GTDS, and sequential solutions can be traced to differences in modeling and tracking data types, which are being analyzed further.

References

1. Hughes STX Systems Corporation, STX Contract Report, *GEODYN II Systems Description, Volume 1*, J. J. McCarthy et al., Lanham, Maryland, February 26, 1993
2. Goddard Space Flight Center, Flight Dynamics Division, FDD/552-89/001, *Goddard Trajectory Determination System (GTDS) Mathematical Theory, Revision 1*, A. C. Long and J. O. Cappellari, Jr. (CSC) and C. E. Velez and A. J. Fuchs (GSFC) (editors), prepared by Computer Sciences Corporation, July 1989
3. Goddard Space Flight Center, Flight Dynamics Division, FDD/554-91/064, *Enhanced RTOD Demonstration System User's Guide*, W. Chuba (ATA), prepared by Applied Technology Associates (ATA), Inc., March 1991
4. J. R. Wright, "Sequential Orbit Determination with Auto-Correlated Gravity Modeling Errors," *Guidance and Control*, Vol. 4, 1981
5. D. H. Oza, T. L. Jones, S. M. Fabien, G. D. Mistretta, R. C. Hart, and C. E. Doll, "Comparison of ERBS Orbit Determination Using Batch Least-Squares and Sequential Methods," NASA Conference Publication 3123, *Proceedings of the Flight Mechanics/Estimation Theory Symposium*, National Aeronautics and Space Administration, Goddard Space Flight Center, Greenbelt, Maryland, May 21–23, 1991
6. C. E. Doll, G. D. Mistretta, R. C. Hart, D. H. Oza, C. M. Cox, M. Nemesure, and D. T. Bolvin, "Accuracy Assessment of TDRSS-Based TOPEX/Poseidon Orbit Determination Solutions," Paper No. AAS 93-572, presented at the AAS/AIAA Astrodynamics Specialist Conference, Victoria, B.C., Canada, August 16–19, 1993
7. B. H. Putney et al., "Precise Orbit Determination for the TOPEX/Poseidon Mission," Paper No. AAS 93-577, presented at the AAS/AIAA Astrodynamics Specialist Conference, Victoria, British Columbia, Canada, August 16–19, 1993
B. Putney, J. Teles, W. Eddy, and S. Klosko, "Comparison of TOPEX/Poseidon Orbit Determination Results Using Laser, DORIS and TDRSS Data," Paper No. AAS 93-267, presented at the AAS/GSFC International Symposium on Space Flight Dynamics, Greenbelt, Maryland, April 26–30, 1993
Private communication with Nikita Zelenski, Precision Orbit Determination Team, January 1994
8. R. B. Frauenholz et al., "The Role of Anomalous Satellite-Fixed Acceleration in TOPEX/Poseidon Orbit Maintenance," Paper No. AAS 93-570, presented at the AAS/AIAA Astrodynamics Specialist Conference, Victoria, British Columbia, Canada, August 16–19, 1993
9. A. Gelb (editor), *Applied Optimal Estimation*. Cambridge, Massachusetts: M.I.T. Press, 1974

Implementation of a Low-Cost, Commercial Orbit Determination System

N94- 35621

Jim Corrigan
Storm Integration, Inc.
2025 Gateway Place, Suite 118
San Jose, CA 95110
(408) 451-0620 FAX (408) 451-0622

Abstract

This paper describes the implementation and potential applications of a workstation-based orbit determination system developed by Storm Integration, Inc. called the Precision Orbit Determination System (PODS)[™]. PODS is offered as a layered product to the commercially-available Satellite Tool Kit (STK)[®] produced by Analytical Graphics, Inc. PODS also incorporates the Workstation/Precision Orbit Determination (WS/POD)[™] product offered by Van Martin Systems, Inc. The STK graphical user interface is used to access and invoke the PODS capabilities and to display the results. WS/POD is used to compute a best-fit orbit solution to user-supplied tracking data.

PODS provides the capability to simultaneously estimate the orbits of up to 99 satellites based on a wide variety of observation types including angles, range, range rate, and Global Positioning System (GPS) data. PODS can also estimate ground facility locations, Earth geopotential model coefficients, solar pressure and atmospheric drag parameters, and observation data biases. All determined data is automatically incorporated into the STK data base, which allows storage, manipulation and export of the data to other applications.

PODS is offered in three levels: Standard, Basic GPS and Extended GPS. Standard allows processing of non-GPS observation types for any number of vehicles and facilities. Basic GPS adds processing of GPS pseudo-ranging data to the Standard capabilities. Extended GPS adds the ability to process GPS carrier phase data.

1. Introduction

1.1. Problem Background

The Precision Orbit Determination System (PODS)[™] grew out of a need to process antenna tracking data to determine a spacecraft orbit. The determined orbit can then be used to generate antenna pointing commands to control a ground antenna. Such a system is necessary for full "closed-loop" satellite command and control (i.e., from processing of telemetry and tracking data to the transmission of commands) and augments commercial command and control systems such as Storm's Intelligent Mission Toolkit (IMT)[™].

1.2. Requirements

A workstation-based capability is desired for compatibility with other workstation-based products, including the IMT. The system should function stand-alone, but offer interfaces for integration with other products. A Commercial Off-the-Shelf (COTS) product approach is desirable for potential resale either alone or integrated with other command and control products. Finally, the development and certification costs must be kept low, which suggests incorporation of existing, proven COTS products in the design as much as possible.

1.3. Solution Approach

Storm has chosen two commercial products for incorporation into PODS: Satellite Tool Kit (STK)[®] by Analytical Graphics, Inc. (AGI) of King of Prussia, PA, and Workstation/Precision Orbit Determination (WS/POD)[™] by Van Martin Systems, Inc. (VMSI) of Rockville, MD. PODS consists of these products as well as the additional code and data required to integrate the products, accept user inputs and provide output data in operationally useful formats.

In order to support customers with different requirements, PODS is available in three options:

1. Standard - Provides basic capability for parameter estimation using the ground-based measurement types (angles, range and range-rate). Does not process any Global Positioning System (GPS) data types besides position vectors.
2. Basic GPS - Includes the capabilities of Standard PODS and adds the ability to process GPS pseudo-range and navigation data.
3. Extended GPS - Includes all of the capabilities of Standard and Basic GPS PODS, and adds the ability for processing of GPS carrier phase data.

The remainder of this paper discusses the two commercial products (STK and WS/POD), how they are used within PODS, an operational description of PODS, and suggestions for application of PODS to different missions.

2. COTS Product Descriptions

2.1. Satellite Tool Kit

STK is a workstation-based, interactive system for analyzing the relationships among satellites, Earth-bound vehicles, ground stations and targets. STK incorporates both text-based tables and graphics to display satellite orbits, periods of visibility, access times, and sensor coverage patterns for multiple satellites, ground stations and targets. The graphics allow animation of satellite constellations to see how sensor coverage and visibilities change over time and with orbital position.

STK allows the input of initial orbit conditions for satellites, facility and target coordinates, and Earth- and satellite-based sensor parameters via ASCII text file or Motif-based user interface panels. Output is displayed via graphical ground traces on a variety of map projections, and tables of access angles and ranges over windows of visibility. Both text and graphics output can be sent to files for printing and/or incorporation into other systems.

STK allows the specification of different orbit propagation methods, including two-body, J2 and J4 perturbations, processing of NORAD 2-Line Mean Element Sets (2LMES), and the optional High-Precision Orbit Propagator (HPOP) from Microcosm, Inc., which performs numerical integration of the satellite equations of motion based on a high-fidelity environmental force model. All propagation methods require input of initial conditions at a specified epoch time. The 2LMES (which can be loaded automatically through an external interface) contain an epoch time, initial orbit conditions, and other modeling parameters.

The STK user interface uses an object-oriented approach for defining and manipulating data. For example, a Scenario object consists of multiple Vehicle, Facility and/or Target objects. Each of these in turn may have one or more Sensor objects. Objects are created, saved, and restored

separately. Data for objects are stored in individual ASCII files with pre-defined extensions (e.g., ".v" for vehicle files, etc.).

Through the addition of optional add-on modules, STK provides a highly accurate and sophisticated operational mission planning capability. For example, Pacific Sierra Research, Inc. (PSR) offers an scheduling capability known as the Generic Resource Event and Activity Scheduler (GREAS), which combines STK-generated orbit and visibility information with user-entered events to construct mission time lines. AGI's Visualization Option (VO) offers high-resolution three-dimensional graphic visualizations of vehicle attitudes, orbits, and relationships to ground targets and other vehicles. Other products like these can be added in a modular fashion to construct a mission planning environment to meet specific requirements.

2.2. STK Programmer's Library

The Satellite Tool Kit/Programmer's Library (STK/PL)[™] offers C application programmers access to the underlying functionality of the STK runtime version. The STK/PL includes header files and selected source code modules to allow programmers to develop add-on applications that are seamlessly integrated with the STK user interface, or stand-alone applications that use STK/PL as a library of functions. The STK/PL includes access to the object manager, user interface, and graphics, as well as astrodynamics libraries, time and coordinate conversion functions, and the orbit propagators. The STK/PL is written in an object-oriented manner which allows rapid modification and addition of new functionality. The PODS User Interface is being developed using the STK/PL.

2.3. Workstation/Precision Orbit Determination

WS/POD is a state-of-the-art precision orbit and geodetic parameter determination software system derived from the GEODYN II Version 8609 software used by NASA's Goddard Space Flight Center (GSFC). Van Martin Systems, Inc. has ported the GEODYN II software to numerous workstation platforms, enhanced it in the area of GPS data processing, and packaged it as a commercially available and supported product.

WS/POD processes satellite tracking data using a Bayesian weighted least-squares data reduction algorithm and detailed environmental modeling using a Cowell-type numerical integration scheme to determine precisely various quantities related to the satellite orbit and tracking stations. Specific capabilities include the following:

Physical Models

- Atmospheric drag using the Jacchia 1971 atmospheric density model
- Solar radiation pressure
- Earth gravitation (up to 180 x 180 geopotential matrix)
- Polar motion
- Earth rotation
- Solid Earth tides
- Third body gravitation
- Earth precession and nutation
- Tropospheric refraction

Measurement Types

- Laser and radar range
- Radar range rates and dopplers (including single and double differences)
- Radar altimeter range
- Topocentric right ascension and declination
- East and north direction cosines
- X/Y angles relative to the tracking station
- Azimuth/elevation angles relative to the tracking station
- GPS pseudo-range and carrier phase, including single, double and triple differences

Parameters Estimated

- Orbit state vectors
- Parameters of atmospheric drag and solar radiation pressure
- Measurement and time tag biases
- Tropospheric refraction scale parameters
- Satellite and station clock polynomials
- Earth gravitational coefficients
- Tracking station coordinates

Algorithms and Capabilities

- Cowell-type numerical integration
- Bayesian weighted least-squares estimation algorithm
- Batch data processing
- Automatic data editing with criteria specified by the user
- Simultaneous estimation of up to 99 satellite orbits in a single run

WS/POD is implemented as a series of stand-alone programs as detailed below. When a WS/POD run is performed, the required programs are executed in sequence, with the outputs from one forming the inputs for the next.

1. FixClock - Corrects GPS data for transmitter (GPS vehicle) and receiver clock errors. Estimates carrier phase ambiguities and resolves carrier phase cycle slips (GPS options only).
2. GPS Data Formatter (GDF) - Performs selection and correction of GPS receiver data and navigation information. This program is used only for applications requiring processing of GPS tracking data.
3. Tracking Data Formatter (TDF) - Performs data selection and editing for non-GPS tracking data.
4. WS/POD Control (CNTL) - Performs the input/output intensive portions of the WS/POD processing and accepts most of the user-control information.
5. WS/POD Executive (EXEC) - Performs most of the numerical work, including integration of the equations of motion and the statistical data fitting process.

Figure 1 shows the processing and data flow for a complete WS/POD run. The programs receive input and produce output exclusively through files. There is no user interface provided. Program control is provided by input files of 80-column card images with data in rigidly-defined column format. Data is provided and produced in ASCII text and binary files, with the file formats defined in the WS/POD documentation.

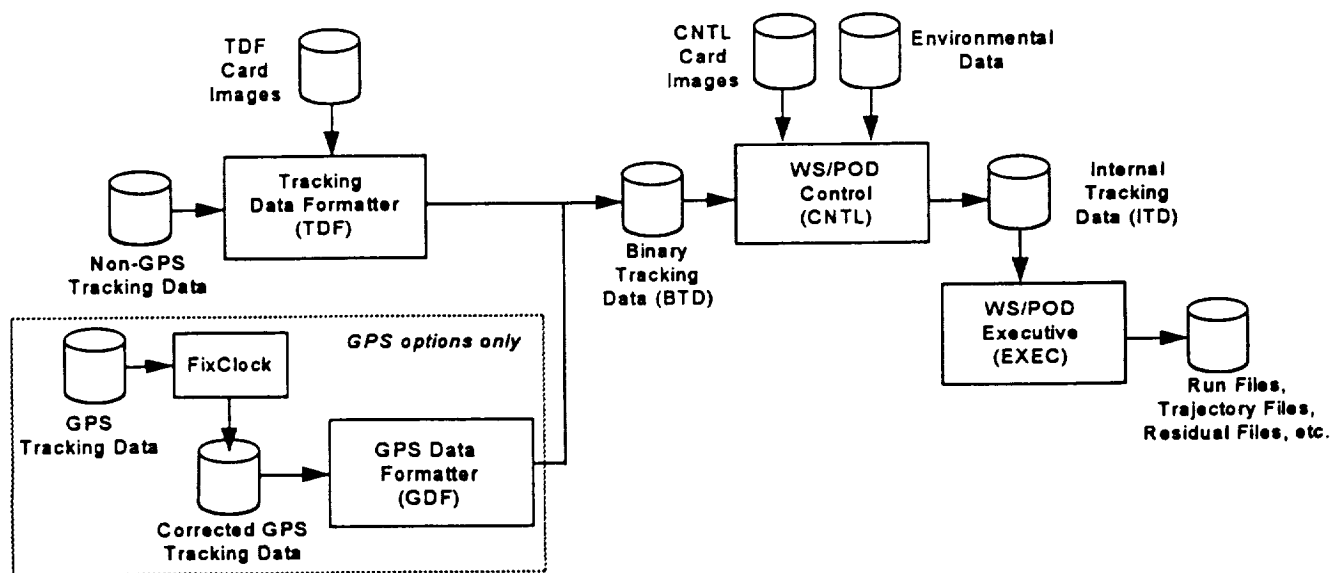


Figure 1: WS/POD Execution and Data Flow

2.4. Summary of Products

Both STK and WS/POD are true COTS products, each with an established customer base, full documentation, vendor support for questions/problems, and available maintenance and upgrades. STK offers a state-of-the-art graphical user interface that has been perfected through many years of development, upgrades and customer feedback. WS/POD offers more algorithmic and data processing capabilities than any other commercially-available orbit estimation system. WS/POD also benefits from its NASA heritage, which assures that the algorithms have been tested using a wide range of operational scenarios over a span of decades. The combination of the two products in PODS results in an orbit estimation system with unmatched ease-of-use and computational power.

3. Solution Approach and Features

The PODS design separates the PODS functionality into two components: PODS User Interface and the PODS External Procedure (PODS/XP). PODS User Interface is implemented using STK/PL. PODS/XP is a stand-alone program independent from STK that provides a C-language interface to WS/POD. The PODS functional breakdown is shown in Figure 2 and further described below.

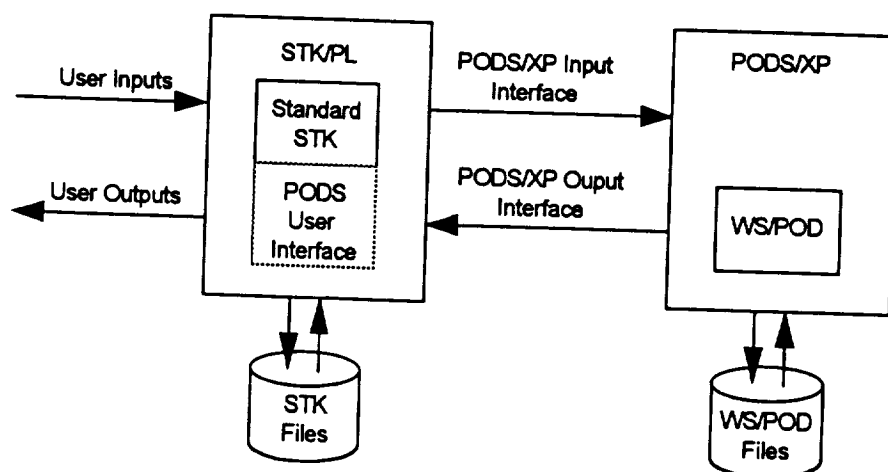


Figure 2: PODS Functional Breakdown

3.1. PODS User Interface

PODS operations are implemented as extensions to the existing STK operations and are invoked via the pull-down menus on the STK Browser Window. Input data panels appear in the STK Utility Window. The PODS input panels are similar to the existing STK panels, providing a Motif look-and-feel, pull-down menus, context-sensitive help, and standardized range and data format checking. A sample PODS input panel is presented in Figure 3.

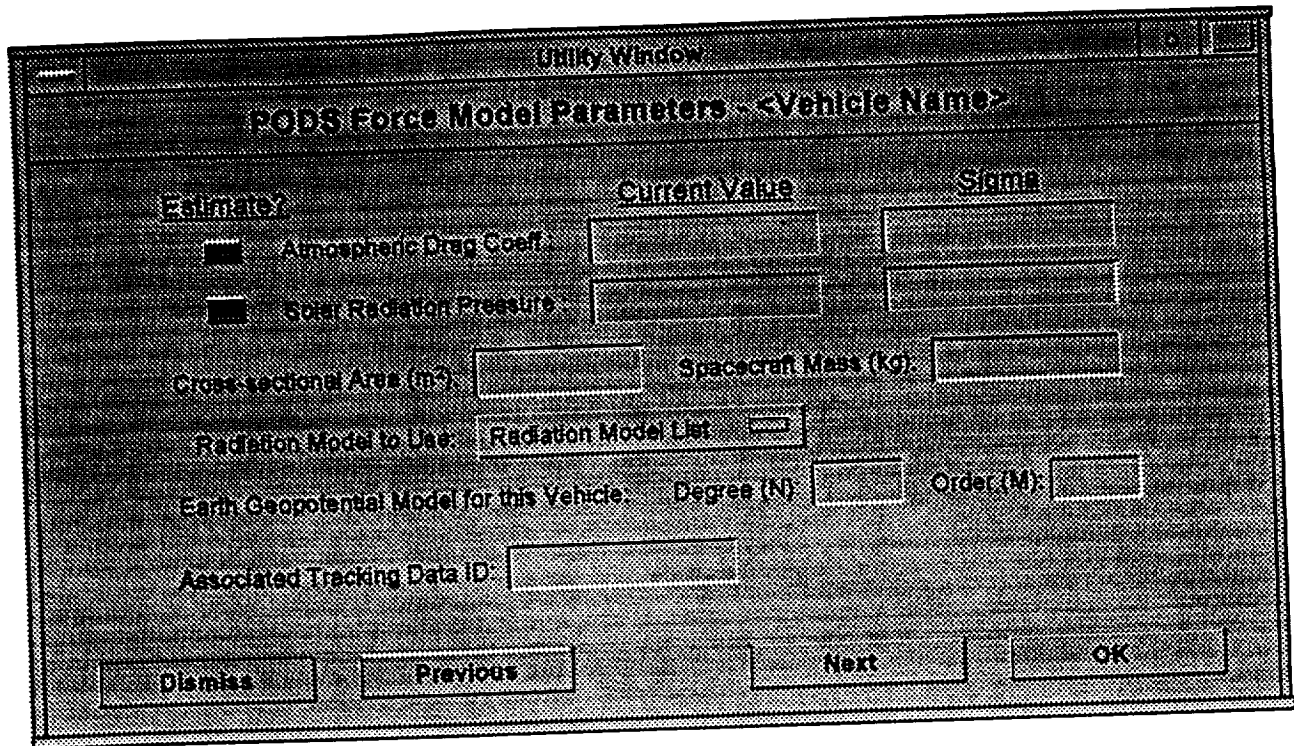


Figure 3: Sample PODS Input Panel

The PODS interface offers the capability to access panels in sequence or directly. Accessing the next or previous panel in a sequence is accomplished using the NEXT and PREVIOUS buttons respectively. The DISMISS button removes the current input panel from the display with no values saved. The OK button updates all the values in the current panel sequence. For data requiring an indeterminate number of entries, a MORE button is provided which accepts the inputs on the current panel and re-displays a blank panel to allow more entries.

STK provides an object-oriented user interface in which the data entered on the panels in the Utility Window applies to the object (either Vehicle, Facility or Scenario) selected in the Browser Window. PODS data is treated as an extension to the data for the existing STK object class. PODS input panels are accessed using a "PODS Data" operation added to the STK *Utilities* menu for each object. This allows STK to store the PODS user inputs in the STK object files and use previously-entered values as defaults for subsequent runs. This approach also allows PODS input data to be specified in the ASCII object files instead of through the user interface.

Numerical outputs from PODS are displayed in the standard STK output data window which allows scrolling through the output data, exporting to files, queuing to a system printer, and real-time units and time format conversions. Selected PODS data (e.g., ephemeris and facility locations) are entered into the existing STK data structures, allowing STK to display the data graphically and use it as the basis for accesses and other computations.

In addition to the input panels for each object type, PODS offers two entry points for the STK user: Orbit Determination and Orbit Propagation. The interface to each is described further below.

Orbit Determination

The PODS Orbit Determination capability is invoked as an option from the Scenario-level STK *Utilities* menu. The Orbit Determination options presented are:

- **Modify Estimation Parameters** - This option gives the user access to a series of input panels which allow specification of the data applying to the entire run, including editing controls, force modeling controls and environmental parameters.
- **Select Tracking Data** - This option brings up an input panel allowing the user to select the tracking data files and the specific tracking data types and data spans to use for this run.
- **Select Output Files** - This option allows the user to select and specify names for optional output files and to select options pertaining to the contents of the selected output files.
- **Perform Estimation** - This option invokes WS/POD to perform the statistical data fitting process. Estimated parameters are displayed numerically in the STK output data window and graphically in the STK map window.
- **Perform Database Maintenance** - This option allows the user to specify the files containing environment data including solar/lunar/planetary ephemeris, Earth gravitational field model coefficients, Earth polar motion parameters, and solar and magnetic flux values. This option also provides a utility for updating the polar motion, UT1 and flux data tables.
- **Select Optional Outputs** - This option presents a menu which allows the user to select a variety of optional outputs to display after the estimation run.
- **Specify GPS Data** - This option allows the user to specify the data selection and editing parameters for the processing of GPS data. This option is only offered as part of the GPS options of PODS.

Orbit Propagation

The orbit propagation capability of PODS is implemented in STK as an additional propagator type and is accessed from the STK *Utilities/Orbiting* menu in the same manner as the other propagator types (Keplerian, J2, J4, etc.). The orbit propagator is used to extend the ephemeris span of previously-determined orbits. Note that the initial orbit state must be generated via a previous PODS run; i.e., it cannot be entered directly on the PODS orbit propagation panel. The current orbit state and epoch is shown on this panel as a display-only field for reference.

3.2. PODS External Procedure

The PODS External Procedure (PODS/XP) provides a C-language interface to the WS/POD product. It is designed to be independent from the specifics of the user interface, which allows the use of other user interfaces or calls from external applications.

PODS/XP provides four major operations:

- **Provide Tracking Data Summary** - This operation accepts the tracking data file names as input and produces a summary of the data for display to the user. The TDF and other utilities of WS/POD are used to read the tracking data files and extract the summary data.
- **Update Tables** - This operation accepts updates to the flux, polar motion and UT1 data in ASCII format and produces a new binary data file used by WS/POD. Off-line WS/POD utilities are used to read the data and produce the updated binary file.
- **Perform Orbit Determination** - This operation accepts tracking data, a priori parameter estimates, editing controls and selection criterion and uses WS/POD to compute a best-fit solution along with ephemeris and other optional outputs.
- **Propagate Orbit** - This operation uses WS/POD to extend the ephemeris span of an existing vehicle orbit.

The interface data are consolidated in a series of structures in header files that are incorporated by the application providing the data (initially STK/PL). PODS/XP is designed such that calls to it can be made from any C program that makes use of the PODS structures.

4. PODS Product Description

4.1. Processing Levels

PODS is offered in three levels to support users with a variety of mission requirements. All levels provide the STK-based graphical user interface and input/output capabilities. The different levels are licensed externally, allowing users to upgrade without re-installation of the PODS software. Each level is described in more detail below.

4.1.1. Standard

The Standard level provides the capability to determine all of the parameters and process all of the measurement types listed in 2.3. Workstation/Precision Orbit Determination with the exception of GPS pseudo-range and carrier phase data. Position vectors obtained using GPS receivers (or by any other means) can be processed by this level.

Sub-meter orbit accuracies are achievable depending on spacecraft altitude, tracking data accuracy/coverage, and physical models invoked.

4.1.2. Basic GPS

The Basic GPS level provides all of the capabilities of the Standard level and adds the ability to process GPS pseudo-range data from any number of GPS satellites and receivers. The receiver data is entered in the form of standard ASCII Receiver Independent Exchange (RINEX) files. Accompanying navigation data files also in standard ASCII RINEX format allow automatic correction of the GPS receiver clocks. The RINEX file formats are documented in GPS bulletins published by the National Oceanic and Atmospheric Administration (NOAA).

To achieve a more accurate solution using GPS data, PODS estimates the orbits of the GPS satellites based on the tracking data rather than using the satellite positions in the navigation files. The Basic GPS option contains parameterizations by Aerospace Corporation of detailed solar radiation pressure models developed by the satellite manufacturer (Rockwell International) to improve the accuracy of the determined GPS orbits.

4.1.3. Extended GPS

The Extended GPS level offers all features of the Standard and Basic GPS levels plus the ability to process carrier phase data. The Extended GPS level provides sophisticated algorithms to combine carrier phase data with other measurement types to resolve range ambiguities and remove cycle slips. Input GPS receiver data is provided in the RINEX file format as with the Basic GPS option.

With the addition of carrier phase data, orbit position accuracies within 10 cm and ground station coordinate accuracies within 1 cm are possible.

4.2. Inputs

The type, format and purpose of all PODS inputs are documented in the PODS User Manual. This section summarizes the available inputs.

4.2.1. Inputs from User

PODS user inputs are provided per STK object (Scenario, Vehicle, or Facility). Scenario inputs apply to all vehicles and facilities in the Scenario. Inputs per object type are listed below.

Scenario Inputs

- Input tracking data file names and formats
- Selection criteria for tracking data by time span, measurement type, vehicle or facility, etc.
- Earth flattening coefficient
- Earth gravitational constant and sigma value (if being estimated)
- Maximum geopotential model degree and order for all vehicles
- Earth gravitational model coefficients and sigma values (if being estimated)
- Solar flux data and times
- Magnetic flux data and times
- Coordinate system reference date
- Data pass definitions
- Minimum and maximum number for both arc and global iterations
- Arc and global convergence criteria
- Arc and global sigma editing criterion
- Arc and global initial RMS values
- Orbit integrator step size
- Selection of optional output reports as listed in 4.3.1. Outputs to User

Facility Inputs

- Minimum elevation angle before data is rejected
- Facility coordinates (in a variety of coordinate systems) and sigma values (if being estimated)
- Coordinate system for station adjustments
- Facilities which are constrained in position relative to one another
- Earth semi-major axis and flattening overrides for geodetic conversion per station
- Antenna mounting type and displacement

Vehicle Inputs

- Transponder delay
- Geopotential model degree and order to be used in the force model for this vehicle
- Vehicle area and mass
- Initial orbit state vector in a variety of coordinate systems and element forms (Cartesian, Keplerian, non-elliptical forms, etc.)
- Span for orbit estimation and/or propagation
- Optional unmodeled acceleration and sigma values (if being estimated)
- Solar pressure coefficient and sigma value (if being estimated)
- Atmospheric drag coefficient and sigma value (if being estimated)
- Biases and sigma values (if being estimated) for all measurement types, including
 - Simple (additive) biases
 - Scale (multiplicative) biases
 - Simple (additive) time bias
 - Satellite clock drift up to third order (GPS options only)
- Covariance matrix for initial orbit elements
- Selection of optional output files

Additional GPS Inputs (GPS options only)

- Names of RINEX files containing GPS tracking data
- Names of navigation files containing GPS navigation data
- Time span and/or measurement type criteria for selection/deletion of GPS data
- Radiation pressure model name for GPS orbit perturbations
- Identification of hub receivers used in construction of single differences

Facility Inputs (cont.)

- Nominal received wavelength
- Turn-around factor (ratio of wavelength transmitted to wavelength received)
- Biases and sigma values (if being estimated) for all measurement types (see list for vehicles above)
 - Simple (additive) biases
 - Scale (multiplicative) biases
 - Tropospheric refraction scale bias
 - Simple (additive) time bias
- Override sigma values for normal equations and data editing
- Temperature, pressure and humidity at facility and time spans over which the data applies

Additional GPS Inputs (GPS options only), cont.

- Allowed tolerances between receiver times when forming differences
- Selection of optional output data

4.2.2. Inputs from Files

4.2.2.1. Observation Data Files

PODS supports processing of observation data supplied in the following file formats:

- PCE Data Format
- GEODYN Binary Format
- GEOS-C Card Image Format
- Binary Metric Tracking Format
- RINEX Format (GPS options only)

The PCE and GEOS-C formats are ASCII. The others are binary. All formats are described in detail in the PODS documentation.

4.2.2.2. Environmental Files

Geopotential Model File

The Geopotential Model File is an ASCII file containing values for the coefficients of the Earth geopotential matrix. A default version is supplied with PODS and new versions may be created by the user using estimated coefficient values from PODS runs.

Flux, Polar Motion and UT1 Tables File

This is a binary file containing information relating to solar and magnetic flux, polar motion, and time conversions. The file contains the following information:

- A1-UTC data
- A1-UT1 data
- Polar motion data
- Solar flux data
- Magnetic flux data

This file must be periodically updated by the user as new information becomes available. PODS provides a table update utility for updating the binary file when new information is obtained. The format of the data is described in the PODS documentation.

JPL Planetary Ephemeris Data File

This is a binary file of solar/lunar and planetary ephemeris in the range January 18, 1957 to December 31, 1999. It is supplied with the PODS delivery and cannot be changed by the user. New versions of the file are supplied to the user by the PODS vendor as necessary.

4.2.2.3. STK Object Files

The user input data is stored as extensions to the STK object class definitions. Each STK object class has an associated ASCII file format in which the STK and PODS inputs are stored. The file formats are described in the STK and PODS documentation.

4.3. Outputs

4.3.1. Outputs to User

All user outputs are displayed through the STK user interface. STK provides the ability to change display units and time systems, export data into a format suitable for use by a spreadsheet program, and send data directly to a system printer. The Mandatory Outputs are displayed during or after every PODS run, and the Optional Outputs can be displayed in addition to the Mandatory Outputs at the user's choice. The items in each output type are listed below.

Mandatory Outputs

- Tracking data summary, including:
 - Vehicles, facilities and observation types for which tracking data exists in the selected files
 - Start and stop time of selected tracking data by vehicle, facility and observation type
 - Number of passes
 - Time span for each pass
 - Vehicle, facility and observation types per pass
- Convergence status (converged/diverged) for global and arc solutions
- Convergence criterion for global and arc solutions
- Number of global and arc iterations performed

Optional Outputs

- Correlation and covariance matrices for solved-for parameters
- Last iteration residuals
- Number of observations per type used in each iteration
- Summary per observation type, including:
 - Name
 - Units
 - Total number of measurements in tracking data
 - Number used
 - RMS and mean value of both the residual and weighted residual
- RMS history per iteration
- GPS vehicle orbit elements (GPS options only)

Mandatory Outputs (cont.)

- List of parameters estimated
- For each estimated parameter:
 - A priori value
 - Estimated value before last iteration
 - Final estimated value
 - Difference between final and a priori values
 - Difference between final and last iteration values
 - Final sigma value
 - Final sigma value multiplied by the RMS value
 - Epoch times (for estimated orbits)
- List of STK objects updated
- Ephemeris data (including ground traces) for each estimated orbit
- New locations for each estimated facility

Optional Outputs (cont.)

- WS/POD TDF Run File
- WS/POD TDF Block Summary File
- WS/POD GDF Run File (for GPS options only)
- WS/POD FixClock Run File (for GPS options only)
- WS/POD CNTL Run File
- WS/POD EXEC Run File (132-column)
- WS/POD EXEC Terminal Output File (80-column)

4.3.2. Outputs to Files

4.3.2.1. Solution Files

PODS allows the user to specify any of the following WS/POD files to save after the PODS run along with path names for the files. Note that the estimated orbits and other parameters, vehicle orbit ephemeris and facility locations are automatically stored in the STK object files.

TDF Files

- Binary Tracking Data (BTD) Format File
- ASCII TDF Run File
- ASCII Block Summary File

EXEC Files

- Binary Trajectory File
- Binary Residual File
- Binary Partial Derivative File
- Binary V-Matrix Format File (Force Model Partial Derivatives)
- Binary S-Matrix Format File (Solution Matrix) *or* Binary E-Matrix Format File (Normal Equations)
- ASCII Inertial Cartesian Ephemeris
- ASCII Keplerian Ephemeris
- ASCII Earth-Fixed Cartesian Ephemeris
- ASCII EXEC Terminal Output File (80-column)
- ASCII EXEC Run File (132-column)

CNTL Files

- ASCII CNTL Run File

FixClock Files (GPS options only)

- ASCII FixClock Run File

GDF Files (GPS options only)

- ASCII GDF Run File

The formats and contents of these files are outlined in the PODS documentation.

4.3.2.2. Environmental Files

PODS provides the ability to update the Geopotential Model File with the latest estimates of the Earth geopotential model coefficients. In addition, the PODS Flux, Polar Motion and UT1 Tables File update capability outputs a new ASCII master file and a new binary Flux, Polar Motion and UT1 Tables File. See 4.2.2.2. Environmental Files for a further description of these files.

4.3.2.3. STK Object Files

The STK object files containing PODS data are updated when the corresponding STK objects are saved in the same manner as the baseline STK. Saved input data appears as panel defaults for the associated object in the next PODS run.

5. Applications

5.1. Single Satellite Maintenance

One potential application for PODS is the Air Force Satellite Control Network (AFSCN), which determines the orbit of individual satellites using azimuth, elevation and S-band range and range-rate from a world-wide network of Remote Tracking Stations (RTSs). Tracking data is generated by the stations and sent to a Mission Control Complex where an orbit estimation is performed. The new orbit is used to generate antenna pointing angles, which are in turn sent to the RTSs to drive the antenna for subsequent contacts with the vehicle.

A typical sequence of events using PODS is as follows:

- The analyst creates the vehicle in the STK database including the initial orbit estimate. This can either be the result of a previous PODS run propagated to the present time, or generated by STK using NORAD 2LMES inputs.
- The tracking data from the RTSs are reformatted into a PODS data format. This can be accomplished using a database management system, custom program, or text formatting tool such as UNIX *awk*.
- The analyst produces a tracking data summary as necessary to display the types and spans of tracking data available.
- After approval of the tracking data contents, the analyst sets the estimation parameters and performs a PODS estimation run, resulting in a display of solution data and a ground trace for the new vehicle orbit.
- After examination of the output, the analyst can elect to accept the results by saving the vehicle object in STK, or can delete the results by reloading the original vehicle object from the data base.
- The analyst invokes the standard STK *Access* operation against the saved orbit ephemeris data to generate antenna pointing angles for the RTSs.
- After viewing the pointing angles, the analyst can export the data to a file for use in controlling an antenna in real-time.

The saved PODS results supply the input field defaults for the next PODS run for the same vehicle. The PODS-generated ephemeris data is used by other STK utilities including VO and GREAS. The analyst can also at any time extend the ephemeris span of a PODS orbit by invoking the PODS orbit propagator from the STK *Vehicle/Orbiting* menu.

5.2. Automated Constellation Management

One of the powerful features of the PODS implementation is the ability to process the data for many satellites simultaneously. This allows management of entire constellations from a single workstation. The nature of the STK interface and object file storage capability allows inputs to be specified by an automatic process, eliminating the need for a user to manually enter data for each run.

As an example of such a process, consider a constellation of several dozen low-flying satellites at high inclination (as is proposed for several commercial global cellular communications networks). Tracking data for the satellites is collected by multiple ground stations around the world. A process utilizing PODS is as follows:

- Collect the tracking data for the different stations.
- Using a network management system (such as Storm Integration's IMT) perform the following:
 - Reformat into PODS tracking data types. Data from multiple stations and/or vehicles can be included in a single PODS tracking data file.
 - Automatically generate the PODS inputs and build the STK ASCII object files containing the PODS inputs per object.
 - Invoke PODS for the entire constellation. Graphical results for the entire constellation appear in STK and can be displayed in high-resolution 3-D graphics using STK/VO.
 - Automatically save the estimated results for the entire constellation.
 - Use the Inter-process Communication (IPC) features of STK to automatically generate scheduling information, ground station access times and antenna pointing angles for the constellation.
- The analyst can perform periodic updates of the solar and magnetic flux information, Earth polar motion and UT1 coefficients using the PODS database management utilities, or these can also be automated.
- Manual overrides can be used at any time, entered either through the user interface or the object files.

Initial orbit estimations may require multiple passes of data in order to accurately estimate the effects of solar pressure, atmospheric drag, and the Earth gravitational field per vehicle. Longer data spans using multiple stations can also be used to precisely determine the location of the tracking stations as well as any biases associated with the measurements from the individual tracking stations. The best estimates of these parameters can be used in the automated scenario described above and can be updated at any time.

5.3. GPS Data Processing

PODS provides a variety of options for GPS data processing. The simplest option is supported by the Standard level and involves incorporation of GPS receiver point position vectors into an orbit solution. Vehicles with on-board GPS receivers generally telemeter the position vectors computed by the receiver. These position vectors can be combined with ground-based measurement types (e.g., range, range-rate, etc.) to form a single set of data for which PODS will compute the orbit that best fits the available data. The GPS receiver data can supplement ground-based measurement types, which can reduce the number and/or required coverage areas of ground stations while still achieving high accuracy. The GPS data can also be used as a reference to calibrate the ground-based receivers.

A more sophisticated approach can be supported when the on-board GPS receiver passes along the raw pseudo-range and carrier phase data. The GPS options of PODS can process these data types directly to obtain user satellite position solutions with 10 cm accuracy. Processing of pseudo-range and carrier phase data from ground-based receivers allows determination of ground receiver locations as well as orbit solutions for the entire GPS constellation with uncertainties below 1 m.

6. Summary

PODS combines two powerful COTS products, STK and WS/POD, into a single integrated system combining ease-of-use with high-fidelity algorithms. STK provides a modern graphical user interface and seamless integration of the estimated parameters with a wide range of existing mission planning and analysis tools. Current STK users will find PODS to be a natural extension of the existing STK capabilities, while new users will find the user interface easy to learn. WS/POD provides powerful computational capabilities with demonstrated reliability due to the heritage from NASA programs.

The COTS nature of PODS provides an end user with toll-free help lines, commercial-quality documentation, and available maintenance and upgrades. Costs of bug fixes and upgrades are spread out over the entire install base rather than being absorbing by a single customer. The system is designed so that it can be entirely configured by the end user with minimal assistance from the vendor.

Applications of PODS range from single satellite control to constellation management. The three different processing levels based on inclusion of different types of GPS data allow the user to choose the level of support appropriate for mission requirements. The open nature of the PODS/STK interfaces allow easy integration with existing command and control systems.

7. References

- Volume 1, MicroCosm® Systems Description, Version 9302.00, February 1993 published by Van Martin Systems, Inc., Rockville, MD.
- Volume 2, MicroCosm® File Description, Version 9302.00, February 1993 published by Van Martin Systems, Inc., Rockville, MD.
- Volume 3, MicroCosm® Operations Description, Version 9302.00, February 1993 published by Van Martin Systems, Inc., Rockville, MD.
- Volume 1, MicroCosm® Installation and Tutorial, Version 9302.00, February 1993 published by Van Martin Systems, Inc., Rockville, MD.
- Satellite Tool Kit® User's Manual, Version 2.0 for Engineering Workstations, published by Analytical Graphics, Inc., King of Prussia, PA.
- Satellite Tool Kit/Programmer's Library (STK/PL)™ Programmer's Guide, published by Analytical Graphics, Inc., King of Prussia, PA.
- Satellite Tool Kit/Programmer's Library (STK/PL)™ Programmer's Reference, published by Analytical Graphics, Inc., King of Prussia, PA.

Tracking System Options for Future Altimeter Satellite Missions

G. W. Davis, H. J. Rim, J. C. Ries, and B. D. Tapley
 The University of Texas at Austin/Center for Space Research
 2901 North I.H. 35, Suite 300
 Austin, TX 78722

Abstract

Follow-on missions to provide continuity in the observation of the sea surface topography once the successful TOPEX/POSEIDON (T/P) oceanographic satellite mission has ended are discussed. Candidates include orbits which follow the ground tracks of T/P, GEOSAT or ERS-1. The T/P precision ephemerides, estimated to be near 3 cm root-mean-square, demonstrate the radial orbit accuracy that can be achieved at 1300 km altitude. However, the radial orbit accuracy which can be achieved for a mission at the 800 km altitudes of GEOSAT and ERS-1 has not been established, and achieving an accuracy commensurate with T/P will pose a great challenge. This investigation focuses on the radial orbit accuracy that can be achieved for a mission in the GEOSAT orbit. Emphasis is given to characterizing the effects of force model errors on the estimated radial orbit accuracy, particularly those due to gravity and drag. The importance of global, continuous tracking of the satellite for reduction in these sources of orbit error is demonstrated with simulated GPS tracking data. A gravity tuning experiment is carried out to show how the effects of gravity error may be reduced. Assuming a GPS flight receiver with a full-sky tracking capability, the simulation results indicate that a 5 cm radial orbit accuracy for an altimeter satellite in GEOSAT orbit should be achievable during low-drag atmospheric conditions and after an acceptable tuning of the gravity model.

Introduction

The very successful TOPEX/POSEIDON (T/P) oceanographic satellite mission has demonstrated the ability to monitor the Earth's sea surface topography from space with very high accuracy (Fu et al., 1994). The radial orbit accuracy of the T/P precise orbit ephemeris is estimated to be 3-4 cm root-mean-square (rms), which is more than a factor of three better than the mission objective (Tapley et al., 1994, Nerem et al., 1994). With the end of the T/P mission in 1997, continuous, high precision observations of the sea surface will be interrupted. Studies of long term variations in the sea surface topography, particularly those related to global change, will thus be negatively impacted. As a result, the oceanographic community has recommended a follow-on mission to provide continuity in the observation of the sea surface topography.

To link new altimeter observations to existing data sets, it is useful to select an orbit which follows the ground track of a previous altimeter mission, such as GEOSAT, ERS-1 or T/P. If continuous, high accuracy monitoring of the sea surface is desired, then a logical choice would be the T/P orbit. The unprecedented accuracy of the T/P orbit ephemeris is due to the extensive force model development efforts, the robust and precise tracking provided by satellite laser ranging (SLR) and the French doppler tracking system DORIS (Nouel et al., 1988), and the low atmospheric drag associated with the 1300 km altitude. Combined with the 2 cm precision of the TOPEX altimeter, it is an ideal platform from which to study the temporal evolution of the ocean circulation. A follow-on mission in the T/P orbit would provide the long term, contiguous observations needed to study such phenomena as the secular increase in mean sea level. To date, over fifty ten-day repeat cycles of TOPEX altimeter data have been collected, and by the projected mission end the data set will span five years. A follow-on mission in the T/P orbit would expand this time frame, making it the preeminent altimeter data set for oceanographic studies.

Another mission option under consideration is the GEOSAT orbit. With a 108° orbit inclination, a greater altimeter coverage of the polar regions is provided. This would allow more complete study of the circumpolar currents and the ice fields. Although the GEOSAT altimeter data set is of lower quality than the T/P data set, it has been studied extensively and can still provide many opportunities for long term studies. The 800 km altitude of the GEOSAT orbit, however, results in increased drag and geopotential perturbations on the satellite, making it

difficult to obtain an orbit with the T/P precision. The orbit errors associated with the geopotential can be reduced to some extent by tuning the gravity field with tracking data from the first few months of the mission, but the orbit errors due to atmospheric drag will be more difficult to overcome. Such effects will be exacerbated by the expected increase in solar activity in the late 1990's. The ERS-1 orbit would have similar modeling problems, with possible additional difficulties due to the sun synchronous orbit.

To illustrate some of the problems already encountered with these altimeter missions, the current estimate of the GEOSAT radial orbit accuracy is 14 cm rms (Chambers et al., 1994). The low accuracy of this orbit relative to the T/P orbit results primarily from the mismodeling of the accelerations due to gravity and drag at low altitudes, but it also results from the noise level of the doppler tracking systems supporting the satellite (primarily U.S. Navy OPNET tracking plus some French, Canadian and Belgian TRANET tracking). These systems have instrument noise levels that are an order of magnitude larger than that of DORIS, the doppler tracking system on T/P, and their measurement noise contributes to the uncertainty in the GEOSAT orbit. Similarly, the estimated radial orbit accuracy of the ERS-1 orbit is on the order of 10 cm rms (Kozel et al., 1994). Due to the failure of PRARE on ERS-1, only a limited amount of SLR tracking data is available for the ERS-1 orbit computation and efforts are being made to supplement the SLR tracking with dual satellite cross-over measurements that take advantage of the precise T/P orbit. The use of altimeter information for orbit improvement, however, can lead to aliasing of oceanographic signal into the orbit. It is thus important that a tracking system that consistently produces well distributed, high precision observations of the satellite motion be available to support future missions with low altitude orbits such as GEOSAT and ERS-1.

The T/P experience has shown that tracking data from a combination of SLR and DORIS or from the Global Positioning System (GPS) can be used to obtain independent orbits that agree with each other at the 2-3 cm level. To illustrate the success of the T/P orbit determination effort, a revised orbit error budget is provided in Table 1. It is observed that the pre-launch sources of orbit error have been substantially reduced, resulting in an overall radial orbit accuracy that is more than three times lower than that of GEOSAT or ERS-1. If a follow-on mission occupies the T/P orbit, it is very likely that this level of orbit accuracy can be maintained using any combination of the above tracking systems. Orbit determination at the lower altitude, however, is more difficult. As previously discussed, the most recent experience with SLR at the 800 km altitude is that of ERS-1. Undoubtedly the ERS-1 orbit uncertainty would be decreased significantly if more SLR tracking were available, but it is the near continuous coverage provided by radiometric data of the DORIS or GPS systems that is needed to fully cope with the atmospheric drag perturbations. Experience with DORIS at the 800 km altitude comes from tracking of the SPOT-2 satellite, where it is estimated that a radial orbit accuracy of approximately 10 cm rms is attainable (Nouel et al., 1993). Since DORIS provides only range-rate information, it is difficult to calibrate this accuracy without the benefit of an absolute measure of range such as SLR. If DORIS were used to support a follow-on mission in either the T/P or the GEOSAT orbit, the addition of corner cube reflectors is necessary so that SLR data may be used for strengthened orbit and altimeter calibration purposes. While there is little experience with GPS tracking at GEOSAT altitude, the success of its use on T/P is undeniable (Yunck et al., 1993, Bertiger et al., 1994), and improvements in the flight receiver hardware and software in the near term will make it an even more attractive system for the support of future altimeter missions. Projecting the DORIS and the GPS orbit accuracy capability downwards to the GEOSAT altitude is thus an area of interest.

In summary, the achievable radial orbit accuracy for a follow-on mission in the T/P orbit has been established at the 3 cm rms level. Clearly, such unprecedented accuracy should serve as the standard for future altimeter missions. The expected radial orbit accuracy for a follow-on mission in an 800 km altitude orbit, however, has not been established, and achieving an accuracy commensurate with T/P will pose a great challenge. As a result, this investigation focuses on the radial orbit accuracy that can be achieved at this altitude, with the GEOSAT 17-day repeat orbit used as an example. Given the tracking systems available to support such a mission, the orbit accuracy attainable will tend to be dominated by force model errors rather than measurement model errors. Emphasis is thus given to characterizing the effects of force model errors on the estimated radial orbit accuracy, particularly those due to gravity and drag. The importance of global, continuous tracking of the satellite for reduction in these sources of orbit error is demonstrated with simulated GPS tracking data. Effective orbit determination strategies are presented for mitigating the effects of drag errors, and a gravity tuning experiment is carried out to show how the effects of gravity error may be reduced.

Precise Orbit Determination Considerations

Historically, uncertainty in the geopotential has been the largest source of orbit error for oceanographic satellite missions. However, tremendous improvements made specifically for the T/P mission in modeling the static and time-varying components of the gravity field have substantially reduced these errors. As a result, orbit errors due to gravity are roughly equivalent to those due to surface forces at T/P altitude. Such improvement is best illustrated through the rms radial orbit error predicted by the gravity field covariance (Rosborough, 1986). Results for the T/P pre-launch gravity models, TEG-2B (Tapley et al., 1991) and JGM-1 (Nerem et al., 1994), and for the post-launch tuned models, JGM-2 (Nerem et al., 1994) and JGM-3 (Tapley et al., 1994) are provided in Table 2. It is observed that the radial orbit error due to the JGM-2 gravity model, which is the reference model for the T/P precise orbits produced by NASA, is about 2 cm. The JGM-3 model, which is a refinement of the JGM-1 model with additional information from tracking of T/P (SLR, DORIS, and GPS), Stella, Lageos-2, and SPOT-2, yields about 1 cm rms of radial orbit error. The JGM-3 gravity model also yields improvement for the ERS-1 and GEOSAT orbits, with predicted rms radial orbit errors of about 4-5 cm. Such will be the level of pre-launch radial orbit error due solely to the geopotential for a follow-on mission that occupies either of these orbits. Previous gravity model solutions have demonstrated that post-launch tuning of the gravity field can reduce this error, but the level of success depends on the data quality and the ability to separate gravity effects from surface force effects. It should also be noted that additional radial orbit error can be expected from the time-varying component of the gravity field. Bettadpur and Eanes (1994) have shown that at the 1300 km T/P altitude, the rms radial orbit error due to ocean tides is about 1 cm, and increases to about 3 cm at 800 km altitude. These errors may be reduced through improvements of the ocean tide model with altimeter data being obtained from T/P.

Surface forces have also been large sources of orbit error for oceanographic satellite missions, especially atmospheric drag. A major contributor to the T/P orbit precision is the low atmospheric density associated with the 1330 km altitude, as well as the relatively low solar and geomagnetic activity occurring throughout the mission. These elements have combined to provide T/P with a low drag environment favorable for computing very accurate orbits. For example, at the T/P altitude, the atmosphere is very tenuous, and the accelerations due to solar, terrestrial and thermal radiation pressure are one to two orders of magnitude greater (Ries et al., 1992). At the 800 km altitude of GEOSAT and ERS-1, where the atmosphere is much more dense, drag accelerations may exceed those due to radiation pressure. To illustrate these concepts, typical accelerations due to surface forces at both altitudes are provided in Table 3. These accelerations were computed from daily averages for the first day of each month in 1992 and are based on the precise force models used in the UT/CSR orbit determination software. It is observed that at the 1300 km altitude, the acceleration due to drag is much smaller than that due to solar and terrestrial radiation pressure, and that the variation in the drag acceleration from minimum to maximum is usually no more than an order of magnitude. However, at the 800 km altitude, the acceleration due to drag can exceed that due to solar and terrestrial radiation pressure and exhibits very large fluctuations with the maximum being two orders of magnitude greater than the minimum. Despite the fact that the acceleration due to drag is often smaller than that due to radiation pressure, it is drag that has the most dramatic effect on the orbit. Rapid density fluctuations that can occur several times within a day make modeling the effects of atmospheric drag very difficult at low altitudes.

Simulation Description

The simulation performed in this analysis is intended to provide a preliminary assessment of the radial orbit accuracy that can be achieved for a satellite in GEOSAT orbit, with emphasis on the impact of gravity and drag errors and how the tracking system technology can be used to overcome them. The fidelity of the simulation is dependent upon realistic sources of dynamic and measurement model errors, and effort must be made to ensure that the error models are neither overly optimistic nor pessimistic. Thus, it is necessary that the orbit error models be calibrated against those observed in real data analysis. The dynamic and measurement model errors used in this simulation are generated through differences between the models used in the data generation and the data processing. Random stochastic effects are added in the data generation phase. The residual rms radial orbit difference that remains after the data is processed is the radial orbit error. This simulation makes extensive use of the error models developed for GPS applications by Rim et al. (1993). Improvements to some of these error

models were made with updated information from recent satellite missions. Similarly, error models specific to the GEOSAT orbit were developed for this analysis with knowledge gained from the processing of real satellite data, especially T/P and SPOT-2.

Calibration of the dynamic error model is carried out by integrating the spacecraft equations of motion with the reference force model and then processing the resulting satellite states as observations in a batch filter. This is equivalent to having continuous, perfect observations of the spacecraft position, or "idealized" tracking, and thus considers only force model errors. For example, gravity model error can be simulated by generating a satellite ephemeris using the JGM-1 gravity model, and then processing the resulting satellite positions with the JGM-2 model. Adjusting only the satellite epoch state provides an estimate of the power of a particular source of error, which in this case is the error implied by differences between JGM-1 and JGM-2. Adjusting additional parameters over various arc lengths provides insight into parameterizations that are helpful in absorbing or accommodating such errors. It is this effort to properly calibrate the dynamic model error that receives the most attention in this study, because as previously discussed, measurement errors are not expected to be major contributors to the overall orbit error for the tracking system(s) being considered. Most of the measurement model errors were generated based on uncertainties obtained from the current literature.

The GPS measurement assumed for the simulation was the dual-frequency carrier phase observable in the double-differenced mode. Effects of selective availability, multi-path, phase center migration and ionospheric dispersion on the radial orbit accuracy are neglected. Assumptions for the flight receiver and the ground network are summarized in Table 4. Furthermore, it was assumed that a GPS flight receiver capable of tracking all GPS satellites in view will be available to support the orbit determination.

An assumption on the satellite design is also necessary because knowledge of physical attributes such as the area-to-mass ratio and solar array size are necessary to properly scale the surface forces acting on the satellite. Physical descriptions of some relevant satellites are provided in Table 5. It is observed that the T/P, SPOT-2 and ERS-1 designs are similar in maximum area-to-mass ratio. These satellites are configured in a "box-and-wing" design, where the spacecraft is treated as a combination of flat plates arranged in the shape of a box with an attached solar array. The SPOT-2 model was chosen for the 800 km altitude option because its satellite bus is very similar to the ERS-1 design but does not have the large synthetic aperture radar antenna. The smaller solar panel is also more appropriate because it is unlikely that the follow-on mission satellite will have as large a power requirement as ERS-1.

Error Model Description

The important sources of dynamic model error for any oceanographic satellite are gravitational and surface forces, and at GEOSAT altitude, the atmospheric drag error model is particularly important. Gravitational errors included a bias in the knowledge of the Earth's gravitational coefficient, GM, errors in the geopotential and ocean tide model coefficients, and a bias in the dynamic solid Earth tide parameter. The errors for the geopotential are based on JGM-2 and TEG-2B gravity model differences, and the errors for the ocean tide model are based on differences between selected ocean tide models.

Non-gravitational errors for both the altimeter satellite and the GPS satellites included solar, terrestrial and thermal radiation pressure and atmospheric drag. Such errors are much different for the GPS satellites, compared to a satellite in GEOSAT orbit, because at the 20,000 km altitude of the GPS constellation, the dominant sources of non-gravitational error are direct solar radiation and thermal imbalances, particularly during periods of eclipsing of the Sun by the Earth. The complete dynamic error model employed in this simulation is summarized in Table 6.

The important sources of observational error include instrument noise, clock errors, and media biases due to tropospheric refraction and ionospheric dispersion. Reference frame errors also contribute to the measurement model error, and include errors in the Earth orientation parameters, nutation and precession errors, and station coordinate errors. The basic data type assumed was the GPS dual-frequency carrier phase measurement in the

double-differenced mode. The effects of clock error including selective availability, multi-path, phase center migration and ionospheric dispersion were neglected. Table 7 summarizes the measurement model errors.

Error Model Calibration

As previously discussed, the dynamic error model consists of force model differences between the perturbed orbit and the reference orbit, with random stochastic effects added. The level of orbit error generated in this manner is examined by integrating the spacecraft equations of motion with the reference force model and then processing the resulting satellite states with the perturbed model. Dynamic model parameters are estimated over various arc and sub-arc lengths to absorb the force model errors, and the residual radial orbit differences that remain are compared to the expected level of orbit errors derived from real data experience.

The calibration results for the dynamic error model is given in Table 8, where the dominant error sources are examined individually. For each case considered, a ten day ephemeris was generated with five minute spacing. Two arc epochs were utilized to highlight the effects of low and high atmospheric activity on the drag error model. The ephemeris was processed such that the satellite state was adjusted once over the entire ten day arc, and the empirical 1-cpr transverse (T) and normal (N) parameters were adjusted for each day. In the case of the GEOSAT error model calibration, drag scaling parameters were adjusted every six hours, while for T/P, along-track accelerations (C_T) were adjusted every six hours.

In Case 1, the gravity error due to JGM-2 and TEG-2B differences is examined. The model differences for these two fields are much too large to be realistic at T/P altitude, but appear to generate very realistic radial orbit errors for GEOSAT altitude. As given in Table 2, the rms radial orbit error predicted from the JGM-2 covariance is 7.4 cm, and residual rms orbit error obtained with the model differences yields the same result. In Case 2, the gravity error due to JGM-2 and JGM-1 differences is examined. These model differences result in 2.1 cm rms radial orbit errors for T/P, which is compared to value of 2.2 cm from the JGM-2 covariance. The 3.6 cm rms radial orbit errors generated for GEOSAT with these model differences is about half of that predicted by the JGM-2 covariance, and is more representative of what tuning the gravity model might provide. Accordingly, the errors generated by the aforementioned model differences will be termed the "pre-launch" and "tuned" gravity model errors. In Case 3, the error due to a bias in GM results in about 0.5 cm of radial orbit error regardless of the orbit altitude. In Case 4, ocean and solid Earth tide errors result in about 3 cm of radial orbit error at GEOSAT altitude. In Case 5, the drag error model was examined. It is observed that drag is negligible at T/P altitude, regardless of the epoch. However, at GEOSAT altitude, the rms radial orbit error increased by more than a factor of three for the highly variable atmosphere of the March, 1991 epoch. Moreover, this level of radial orbit error is about twice as large as the gravity error from the "tuned" model and is commensurate with the gravity error from the "pre-launch" model. In Case 6, the solar, terrestrial, and thermal radiation pressure error model is examined. It is observed that level of rms radial orbit error, which was generated from a fairly pessimistic error model, is small in comparison to both the gravity and the drag error. This again demonstrates the ability of the empirical accelerations to absorb mismodeled or unmodeled accelerations, especially those that have distinct 1-cpr signatures such as radiation pressure errors.

The aggregate effect of these individual dynamic error sources on the rms radial orbit accuracy is shown in Table 9. The final dynamic error model for GEOSAT orbit was selected to emulate "pre-launch" dynamic errors, and the final dynamic error model for T/P orbit was selected to emulate the current dynamic errors that have been observed in real data processing. The effect of arc length was investigated to illustrate the impact of dynamic model error build-up on the rms radial orbit accuracy. Long arcs, on the order of a few to several days, provide dynamical constraints through the satellite equations of motion, but suffer from the build-up of non-conservative surface force model errors. Short arcs, on the order of a day or less, tend to attenuate long-period and resonant gravity errors and reduce the build-up of non-conservative surface force model errors. For each arc length used, initial conditions were adjusted at arc epoch and C_D 's for GEOSAT and C_T 's for T/P were adjusted every six hours. The 1-cpr T and N accelerations were adjusted daily, except in Case 4, where they were adjusted every six hours. From Cases 1 through 3, it is observed that for both T/P and GEOSAT shortening the arc length from one ten-day arc to ten one-day arcs has little effect on the rms radial orbit error, although a slight benefit was gained

for GEOSAT in the March, 1991 time frame where the drag model error was greater. It is thus seen that one day arcs essentially contain all the dynamic orbit error that is present in the longer arcs, mainly because of the power of the 1-cpr T and N accelerations in absorbing slowly changing accelerations. This implies that long arcs, such as the ten-day arc length used to generate the precise T/P orbits, can be parameterized in a manner that does not result in significantly increased orbit error relative to one-day arcs. In Case 4, the sub-arc length of the 1-cpr T and N parameters is reduced to six hours, and such a parameterization begins to approach the "reduced dynamic" filtering technique used successfully with GPS data on T/P (Bertiger et al, 1994). It is observed that the parameterization in Case 3 results in a significant reduction in the rms radial orbit error generated for both GEOSAT and T/P in the February, 1993 time frame, and for T/P in the March, 1991 time frame. However, only a negligible reduction in the March, 1991 time frame was realized for GEOSAT, indicating that additional C_D 's are needed to further reduce the drag error. For T/P, it is observed that the time frame of the simulation has little impact on the rms radial orbit error, indicating the drag model error is not a major consideration for this high altitude. Finally, it is observed that the dynamic error model yields rms radial orbit errors for GEOSAT orbit at the 8-9 cm level for a benign atmosphere and at the 9-11 cm level for a volatile atmosphere when arc lengths of one day or longer are used.

GPS Error Model Calibration

Calibration of the GPS error model was carried out by comparing the data fits for the simulated GPS data with those observed in real GPS data processing. This was done using GPS data collected during a twelve-day period beginning February 2, 1993. Orbits were obtained for the GPS satellites using two different parameterizations, one utilizing the classical approach and the other utilizing the empirical acceleration parameters. In both cases, the twelve days of data were processed in four three-days arcs. In the first case, initial conditions, a Y-bias parameter and a scale factor for the box-wing radiation pressure model were adjusted at arc epoch. The real and simulated data fits showed excellent agreement, with residuals on the order of 2.2 to 2.5 cm. The smallest difference in residual rms observed between the real and simulated data fits was 0.01 cm, and the largest was 0.1 cm. In the second case, initial conditions, a C_T and a 1-cpr T and N were adjusted at arc epoch. The real and simulated data fits again showed excellent agreement, with residuals on the order of 1.4 to 1.6 cm. The smallest difference observed was 0.02 cm and the largest difference was 0.12 cm. In either case, the simulated data did not fit consistently below that of the real data, indicating the error models are not too optimistic. In Tables 10 and 11, one-day orbits are compared against the three-day orbits discussed above using the Y-bias and radiation pressure scale factor parameterization. The similarities between the results is striking, especially considering the agreement for GPS satellites 2 and 20 which were being eclipsed by the Earth. Thus the dynamic error model used for the GPS component of this simulation emulates quite well that which is observed in real data processing.

Simulation Results

Eighteen days of GPS double-differenced phase data were simulated for a SPOT-2 type satellite in the GEOSAT orbit beginning February 2, 1993 with the comprehensive dynamic and measurement error models previously described. The epoch was selected to provide atmospheric conditions conducive to the separation of drag effects from gravity effects, so the results will be somewhat optimistic. To test the effectiveness of tuning the gravity field for a satellite in this orbit, information equations from the first twelve days of the data were obtained with four three-day arcs. This provided six days of data withheld from the tuned field for comparison purposes. Orbits for the altimeter satellite and all GPS satellites were adjusted simultaneously along with the positions of twelve of the fifteen GPS ground stations. The three stations with the smallest random position errors were held fixed as fiducial sites. The parameterization used for the altimeter satellite was six-hour C_D 's and a daily 1-cpr T and N, while that for the GPS satellites was a daily Y-bias and a three-day C_R . Recall that JGM-2 is the reference gravity field and TEG-2B is the field used to generate gravity errors through the model difference. The recovery of the JGM-2 field in this experiment is shown by plotting the degree difference variance (DDV) in Fig. 1. The heavy line with solid dots represents the DDV of TEG-2B with respect to JGM-2, and the dashed lines with open dots represents the DDV of the tuned field. If the JGM-2 gravity field were perfectly recovered, the DDV would be zero for all degrees. It is observed that TEG-2B and JGM-2 agree well for the dominant zonal terms such as J_2 ,

J_3 , etc., but that the differences become large for degrees above four. Partial recovery of the JGM-2 model is obtained in the tuning process for degrees up to about 24, with much of the improvement attributed to the resonant terms. Above degree 24, the DDV of the tuned field surpasses that of TEG-2B until about order 38, suggesting that some of the surface force errors may have slightly contaminated the gravity model. When all eighteen days of data are included in the gravity model, the results were essentially the same. This demonstrates that tuning the gravity field with the satellite tracking data is effective in reducing the radial orbit error due to the geopotential, particularly that which is attributed to the low degree and order terms. Only twelve days of tracking data were used to tune the gravity field in this experiment, so further improvement could be realized with the additional information provided by a few months of data. This would provide the much needed data redundancy required to average out the random components of the surface force model errors.

The results obtained from processing the simulated GPS double-differenced phase data with the pre-tuned and tuned gravity models are given in Table 12. The eighteen days of data were processed in six three-day arcs using the daily Y-bias and three-day radiation scale factor parameterization for the GPS satellites, and the six-hour C_D and daily 1-cpr T and N parameterization for the altimeter satellite. It is observed that for the pre-tuned field, the rms of the double-differenced phase residuals is on the order of 5-7 cm, and is subsequently reduced to 3-5 cm rms with the post-tuned field. It is interesting to note that although the last two three-days arcs were not used to tune the gravity field, improvement in those residuals was still obtained. Furthermore, comparison of the best fit orbits to the reference orbit shows that radial orbit errors of about 8-11 cm rms are generated with the pre-tuned gravity field and all other dynamic and measurement errors, while about 6-7 cm rms error are generated with the post-tuned field. The reduction in rms radial orbit error due to gravity tuning is thus significant, especially when it is considered that only twelve days of a single 17-day GEOSAT repeat orbit was used for the tuning. Further improvement is obtained when one-day arcs are used to reduce the contribution of drag error, as shown in Table 13. It is observed that for both the pre-tuned and post-tuned cases, the residuals are reduced roughly by half when one-day arcs were used. The reduction in rms radial orbit error is about the same for both cases, indicating that short arcs on the order of one day may be needed to contend with the level of drag error associated with the GEOSAT altitude.

Conclusions

A study was conducted to predict the rms radial orbit error that could be achieved for an altimeter satellite in GEOSAT orbit being tracked by GPS. The numerical simulation technique was used to generate realistic sources of orbit error with dynamic and measurement error models calibrated with knowledge from real data processing. The GPS tracking scenario assumed a constellation of 21 Block II satellites, with flight and ground receivers that can track all GPS satellites in view. A gravity tuning experiment was conducted to demonstrate how the rms radial orbit error due to the geopotential can be reduced, and orbit determination tests were conducted to examine strategies effective in reducing the atmospheric drag error. From this study, it was found that the expected radial orbit error due solely to the geopotential can be reduced with post-launch tuning of the gravity field. Only twelve of the eighteen days of simulated tracking data were used to tune the field, yet a significant reduction in the radial orbit error was obtained. The radial orbit error due to drag, however, will be more difficult to mitigate. The simulation results suggest that, in a low drag environment and with a tuned gravity field, about 5 cm of rms radial orbit error can be expected when one-day arcs are used. This also assumes that robust tracking is provided by a GPS flight receiver capable of tracking all GPS satellites in view. The dynamic error model calibration showed that the drag error can increase substantially when high atmospheric density variations exist. Adjusting the geopotential model in this high-drag environment will be more difficult and is a topic for further study.

Acknowledgments

The research was prepared under NASA contract JPL-959737. Additional computing resources were provided by the University of Texas System Center for High Performance Computing.

References

- Bertiger, W. I., Y. E. Bar-Sever, E. J. Christensen, E. S. Davis, J. R. Guinn, B. J. Haines, R. W. Ibanez-Meier, J. R. Jee, S. M. Lichten, W. G. Melbourne, R. J. Muellerschoen, T. N. Munson, Y. Vigue, S. C. Wu, T. P. Yunck, B. E. Schutz, P. A. M. Abusali, H. J. Rim, M. M. Watkins, and P. Willis, GPS precise tracking of TOPEX/POSEIDON: Results and implications, submitted to *J. Geophys. Res.*, 1994.
- Bettadpur, S. and R. J. Eanes, A tidally coherent geographically correlated representation of orbit error due to ocean tide model error, submitted to *EOS Trans. AGU*, Spring, 1994.
- Chambers, D. P., C. K. Shum, J. C. Ries, and B. D. Tapley, Precise ephemerides for the Geosat exact repeat mission, manuscript in preparation, Center for Space Research, The University of Texas at Austin, 1994.
- Fu, L. L., E. J. Christensen, M. Lefebvre, and Y. Menard, TOPEX/POSEIDON mission overview, submitted to *J. Geophys. Res.*, 1994.
- Kozel, B. J., C. K. Shum, J. C. Ries, and B. D. Tapley, Precision orbit determination using dual satellite altimeter crossover measurements, *Proc. of AAS/AIAA Spaceflight Mechanics Meeting*, Cocoa Beach, Florida, February 1994.
- Nerem, R. S., F. J. Lerch, J. A. Marshall, E. C. Pavlis and B. H. Putney, J. C. Chan, S. M. Klosko, S. B. Luthcke, G. B. Patel, N. K. Pavlis, R. G. Williamson, B. D. Tapley, R. J. Eanes, J. C. Ries, B. E. Schutz, C. K. Shum, and M. M. Watkins, R. H. Rapp, R. Biancale and F. Nouel, Gravity model development for TOPEX/POSEIDON: Joint Gravity Model-1 and 2, to appear *J. Geophys. Res.*, 1994.
- Nouel, F., J. Bardina, C. Jayles, Y. Labrune, and B. Troung, DORIS : A precise satellite positioning doppler system, *Astrodynamics 1987, Adv. Astron. Sci.*, J. K. Solder et al. (Eds.), 65, 311-320, 1988.
- Nouel, F., M. Deleuze, C. Valorge, P. Laudet, Improvement of the ERS-1 orbit precision by using the drag effect on SPOT-2, *Proc. of AAS/AIAA Astrodynamics Specialist Conference*, Victoria, B. C., Canada, August 1993.
- Rim, H. J., B. E. Schutz, B. D. Tapley, Error modeling for GPS geodetic applications, *Proc. of AAS/AIAA Spaceflight Mechanics Meeting*, Pasadena, California, February 1993.
- Ries, J. C., C. K. Shum, and B. D. Tapley, Surface force modeling for precision orbit determination, *Environmental Effects on Spacecraft Positioning and Trajectories*, Geophysical Monograph 73, IUGG Vol. 13, 1993.
- Rosborough, G. W., Satellite orbit perturbations due to the geopotential, CSR-86-1, Center for Space Research, The University of Texas at Austin, 1986.
- Tapley, B. D., C. K. Shum, D. N. Yuan, J. C. Ries, R. J. Eanes, M. M. Watkins, and B. E. Schutz, The University of Texas Earth gravitational model, XX General Assembly of the IUGG, Vienna, Austria, August 1991.
- Tapley, B. D., J. C. Ries, G. W. Davis, R. J. Eanes, B. E. Schutz, C. K. Shum, M. M. Watkins, J. A. Marshall, R. S. Nerem, B. H. Putney, S. M. Klosko, S. B. Luthke, D. Pavlis, R. G. Williamson, and N. P. Zelensky, Precision orbit determination for TOPEX/POSEIDON, submitted to *J. Geophys. Res.*, 1994.
- Tapley, B. D. et al., The JGM-3 gravity model, manuscript in preparation, Center for Space Research, The University of Texas at Austin, 1994.
- Yunck, T. P., W. I. Bertiger, S. C. Wu, Y. Bar-Sever, E. J. Christensen, B. J. Haines, S. M. Lichten, R. J. Muellerschoen, Y. Vigue, and P. Willis, First assessment of GPS-based reduced dynamic orbit determination on TOPEX/POSEIDON, to appear in *Geophys. Res. Lett.*, 1993.

Table 1. TOPEX/Poseidon Orbit Error Budget

Error Source	Mission Specification (cm)	POE Estimate (cm)
Gravity	10	2
Radiation pressure (solar, terrestrial, thermal)	6	2
Atmospheric drag	3	1
GM (Earth's gravitational constant)	2	1
Earth and ocean tides	3	1-2
Troposphere	1	< 1
Station positions	2	1
RSS absolute error	12.8	3-4

Table 2. RMS Radial Orbit Error Predicted by Gravity Covariance

	TOPEX (cm)	ERS-1 (cm)	GEOSAT (cm)
TEG2B	10.1	19.2	15.3
JGM1	3.4	8.3	8.2
JGM2	2.2	7.9	7.4
JGM3	1.0	4.0	5.3

Table 3. Typical Accelerations Due to Surface Forces

Satellite	Altitude (km)	Average Solar Radiation (10^{-9} m/sec ²)	Average Earth Radiation* (10^{-9} m/sec ²)	Min / Max Atmospheric Drag (10^{-9} m/sec ²)
T/P	1300	60	3	0.2 / 1.7
GEOSAT/ERS-1	780	70	9	3 / 136

Table 4. GPS Tracking Assumptions

- GPS constellation consists of 21 Block II satellites
- Flight and ground receivers track all GPS satellites in view
- 15° elevation cut-off for ground stations; 5° elevation cut-off for altimeter
- 15 GPS ground stations
- 2 minute observation sampling time

Table 5. Altimeter Satellite Orbit and Spacecraft Geometry

Satellite	Alt. (km)	Inc (deg)	Mass (kg)	Max Area/mass (m ² /kg)	Projected Areas			
					Roll (m ²)	Pitch (m ²)	Yaw (m ²)	Solar Panel (m ²)
T/P	1330	66	2417	0.012	4.7	8.2	8.3	25.5
SPOT-2	820	98.7	1875	0.013	6.5	3.5	9.0	18.5
ERS-1	770	98.5	2400	0.014	5.0	5.0	15.0	28.0
GEOSAT	780	108	662	0.008	5.0			

Table 6. Dynamic Error Models used in Simulation

- Altimeter satellite and GPS gravitational errors :
 - GM error of 0.0008 km³/sec²
 - Geopotential errors from JGM-2 vs. TEG-2B
 - Ocean tide errors from CSR tide model differences
 - Solid earth tide errors from 3% error in k₂
- GPS non-gravitational errors :
 - Radiation pressure
 - > box-wing reflectivity randomly perturbed by 5%
 - > thermal acceleration with amplitude of 1 nm/sec², on vs. off
 - > 5 km random error in Earth shadow radius
 - > integration step size, 500 sec vs. 600 sec
 - Y-bias acceleration stochastically perturbed by 5%, 6-hour correlation time
 - Constant 1° solar panel misalignment, constant 1° solar panel pitch angle error
- Altimeter satellite non-gravitational errors :
 - Radiation pressure
 - > 50% error in solar reflectivity, Earth albedo and emissivity
 - > Earth albedo and emissivity also randomly perturbed by 3%
 - > 50% error in thermal model acceleration and time decay
 - > 5 km random error in Earth shadow radius
 - > integration step size, 50 sec vs. 60 sec
 - Drag error from constant flux, random 3-hour K_p vs. standard flux and K_p
 - Constant 1° solar panel misalignment, constant 1° solar panel pitch angle error

Table 7. GPS Measurement Error Model used in Simulation

- Observational Errors :
 - 5 mm random error for each phase range
 - time tag errors from two-point Allan variance model with
 $\sigma_f = 5 \times 10^{-13}$, $\tau_1 = 1 \times 10^3$, $\tau_2 = 1 \times 10^5$ for TPFO receiver
 $\sigma_f = 1 \times 10^{-13}$, $\tau_1 = 1 \times 10^5$, $\tau_2 = 1 \times 10^7$ for GPS ground receivers
 - troposphere error from modified Hopfield model vs. Chao's model, with 0.8% stochastic tropospheric biases added
 - Phase center errors via satellite attitude errors of 1° in roll, pitch, yaw
- Random precession and nutation errors
 - 0.1 mas/yr random error in precession
 - 1.0 mas noise in 1-day values of nutation
 - 0.1 mas random errors in long period of nutation
 - 0.05 mas random errors in short period components of nutation
- 1 mas random noise in 5-day values of Earth orientation (x_p , y_p , UT1)
- 3 cm random errors in station coordinates
- 3% random errors in individual station tide corrections
- 8 mm/yr random error in all tectonic plate velocities

Table 8. Altimeter Satellite Dynamic Error Model Calibration Using 10-Day Arcs

Case	Error Source	RMS Radial Orbit Differences (cm)			
		Epoch 2/1/93		Epoch 3/12/91	
		T/P	Geo	T/P	Geo
1	"pre-launch" gravity model error	n/a	7.4	n/a	7.4
2	"tuned" gravity model error	2.1	3.6	2.1	3.7
3	GM error	0.5	0.5	0.5	0.5
4	ocean and solid Earth tide error	1.0	3.4	1.2	3.3
5	atmospheric drag error	0.0	1.8	0.1	7.1
6	radiation pressure error	0.2	0.7	0.1	0.5

Table 9. Final Altimeter Satellite Dynamic Error Model Calibration

Case	RMS Radial Orbit Differences (cm)			
	Epoch 2 / 1 / 93		Epoch 3 / 12 / 91	
	T/P	Geo	T/P	Geo
1	2.4	8.9	2.4	10.6
2	2.4	8.6	2.4	10.1
3	2.3	8.1	2.3	9.5
4	1.6	6.7	1.5	9.4

**Table 10. Error Model Calibration for GPS Satellites
3-day vs. 1-day Orbit Solution Differences using Real Data**

GPS Satellite	Radial RMS (m)	Transverse RMS (m)	Normal RMS (m)	RSS (m)
1	0.2634	0.7123	0.3910	0.8541
2	0.4284	1.1245	0.5433	1.3203
3	0.2510	0.5016	0.3004	0.6363
11	0.1980	0.6501	0.3796	0.7784
12	0.2324	0.6680	0.3091	0.7719
13	0.2008	0.5326	0.2975	0.6422
14	0.2656	0.5521	0.2726	0.6705
15	0.2764	0.8046	0.4113	0.9450
16	0.2787	0.8108	0.3393	0.9220
17	0.3383	0.8126	0.3526	0.9482
18	0.1738	0.4004	0.2630	0.5096
19	0.1763	0.4771	0.2488	0.5663
20	0.4459	1.2239	0.4165	1.3676
21	0.2743	0.7410	0.2823	0.8390
23	0.1971	0.5730	0.2962	0.6745
24	0.2967	0.7115	0.3656	0.8532
25	0.2668	0.8509	0.3786	0.9688
26	0.2118	0.6973	0.3655	0.8153
27	0.2113	0.6229	0.3151	0.7293
28	0.2606	0.7045	0.3521	0.8296
29	0.2735	0.5825	0.3535	0.7342

**Table 11. Error Model Calibration for GPS Satellites
3-day vs. 1-day Orbit Solution Differences using Simulated Data**

GPS Satellite	Radial RMS (m)	Transverse RMS (m)	Normal RMS (m)	RSS (m)
1	0.2021	0.6088	0.3536	0.7325
2	0.4454	1.2733	0.5832	1.4696
3	0.2526	0.5433	0.3302	0.6841
11	0.1878	0.6441	0.3184	0.7427
12	0.1812	0.5483	0.2990	0.6503
13	0.1578	0.4224	0.2212	0.5022
14	0.2369	0.4815	0.2404	0.5880
15	0.2699	0.7739	0.3912	0.9082
16	0.2676	0.7449	0.2984	0.8459
17	0.3427	0.8260	0.3077	0.9457
18	0.1478	0.3470	0.2635	0.4601
19	0.1744	0.5760	0.2775	0.6627
20	0.4916	1.3548	0.4643	1.5142
21	0.2638	0.6340	0.3163	0.7561
23	0.1737	0.5282	0.2835	0.6241
24	0.2604	0.6162	0.3105	0.7375
25	0.2409	0.8529	0.4322	0.9860
26	0.1459	0.6022	0.3692	0.7213
27	0.2017	0.6303	0.3061	0.7291
28	0.2911	0.8480	0.3687	0.9695
29	0.2651	0.5459	0.3443	0.6978

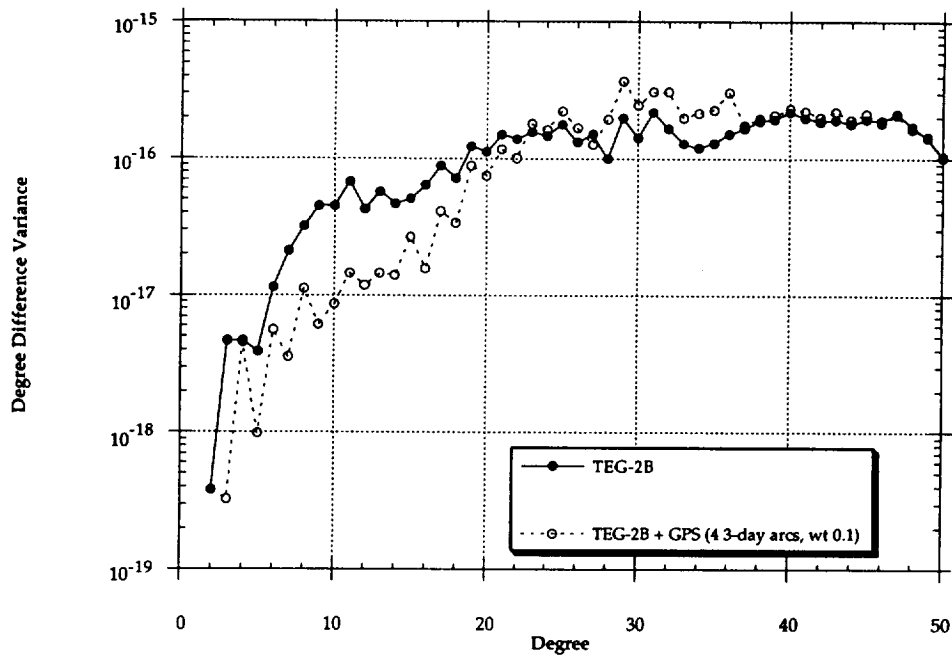


Fig. 1 GPS-Tuned Geopotential Model Evaluation

Table 12. Results of GPS Tuning Experiment using 3-day Arcs (solar activity of 2/1/93)

Arc	Pre-Tune				Post-Tune			
	Residual RMS (cm)	RMS Orbit Differences (cm)			Residual RMS (cm)	RMS Orbit Differences (cm)		
		R	T	N		R	T	N
1	5.7	8.7	34.1	17.4	3.6	5.9	17.3	7.9
2	5.5	9.8	29.6	22.9	4.0	6.2	18.4	10.8
3	6.2	10.8	37.8	20.6	4.0	6.7	17.1	7.2
4	7.0	10.0	42.8	21.4	4.6	6.5	19.8	13.2
5	6.2	7.5	40.0	17.6	4.5	5.9	22.3	8.0
6	5.5	7.9	27.5	15.5	4.8	6.8	27.4	8.6

Table 13. Results of GPS Tuning Experiment using 1-day Arcs (solar activity of 2/1/93)

Residual RMS (cm)	Pre-Tune			Residual RMS (cm)	Post-Tune		
	RMS Orbit Differences (cm)				RMS Orbit Differences (cm)		
	R	T	N		R	T	N
3.3	8.2	25.5	18.5	1.8	4.5	12.6	8.6

Improved Solution Accuracy for Landsat-4 (TDRSS-User) Orbit Determination*

D. H. Oza and D. J. Niklewski
Computer Sciences Corporation (CSC)
Lanham-Seabrook, Maryland, USA

C. E. Doll, G. D. Mistretta, and R. C. Hart
Goddard Space Flight Center (GSFC)
Greenbelt, Maryland, USA

Abstract

This paper presents the results of a study to compare the orbit determination accuracy for a Tracking and Data Relay Satellite System (TDRSS) user spacecraft, Landsat-4, obtained using a Prototype Filter Smoother (PFS), with the accuracy of an established batch-least-squares system, the Goddard Trajectory Determination System (GTDS). The results of Landsat-4 orbit determination will provide useful experience for the Earth Observing System (EOS) series of satellites. The Landsat-4 ephemerides were estimated for the January 17-23, 1991, timeframe, during which intensive TDRSS tracking data for Landsat-4 were available. Independent assessments were made of the consistencies (overlap comparisons for the batch case and covariances for the sequential case) of solutions produced by the batch and sequential methods. The filtered and smoothed PFS orbit solutions were compared with the definitive GTDS orbit solutions for Landsat-4; the solution differences were generally less than 15 meters.

1.0 Introduction

This paper compares the orbit determination accuracy of a prototype sequential orbit determination system with the accuracy achieved using an operational batch-least-squares system for a Tracking and Data Relay Satellite (TDRS) System (TDRSS) user spacecraft. This analysis also evaluates the effect of applying a smoother algorithm to the filter solutions.

TDRSS is a geosynchronous relay satellite network which currently consists of five geosynchronous spacecraft and the White Sands Ground Terminal (WSGT) at White Sands, New Mexico. Of the five TDRSs, three (TDRS-East, TDRS-West, and TDRS-Spare, located at 41 degrees, 174 degrees, and 62 degrees west longitude, respectively) actively support tracking of TDRSS-user spacecraft. Of the two remaining TDRSs, one TDRS (located at 275 degrees west longitude) is used only for satellite communications, while the other TDRS (located at 46 degrees west longitude) is being reserved for future use. TDRSS has the operational capability to provide 85-percent to 100-percent coverage, depending on the spacecraft altitude.

The Bilateral Ranging Transponder System (BRTS) provides range and Doppler measurements for maintaining each TDRS orbit. The ground-based BRTS transponders are tracked as if they were TDRSS user spacecraft. Since the positions of the BRTS transponders are known, their ranging data can be used to precisely determine the trajectory of the TDRSs.

The focus of this paper is an assessment of the relative orbit determination accuracy of the batch-least-squares method, used for current operational orbit determination support, with that of a sequential method implemented in a prototype system, used for analysis in the GSFC Flight Dynamics Facility (FDF). The batch-weighted least-squares

* This work was supported by the National Aeronautics and Space Administration (NASA)/Goddard Space Flight Center (GSFC), Greenbelt, Maryland, under Contract NAS 5-31500.

algorithm implemented in the Goddard Trajectory Determination System (GTDS) estimates the sets of orbital elements, force modeling parameters, and measurement-related parameters that minimize the squared difference between observed and calculated values of selected tracking data over a solution arc (Reference 1).

The sequential estimation algorithm implemented in a prototype system, the Prototype Filter Smoother (PFS), simultaneously estimates the TDRSS user and relay spacecraft orbital elements and other parameters in the force and observation models at each measurement time. The PFS filter is closely related to the Real-Time Orbit Determination/Enhanced (RTOD/E)* system (Reference 2). PFS performs forward filtering of tracking measurements using the extended Kalman filter with a process noise model to account for serially correlated, geopotential-induced errors, as well as Gauss-Markov processes for drag, solar radiation pressure, and measurement biases. The main features of RTOD/E are summarized in Reference 3.

An orbit determination analysis of Landsat-4 using TDRSS is reported here. Motivation for an orbit determination evaluation of Landsat-4 derives from the fact that the orbital characteristics of Landsat-4 are similar to those of the Earth Observing Satellite (EOS) series of missions, planned for launch starting in 1998. The results of a study for Landsat-4 will provide useful experience and verification of EOS flight dynamics support requirements. Early assessment of conclusions regarding meeting EOS support requirements will provide adequate opportunity to develop comprehensive support scenarios.

The estimated Landsat-4 ephemerides were obtained for the January 17–23, 1991, timeframe. This particular timeframe was chosen because dense TDRSS tracking data for Landsat-4 were available. Independent assessments were made to examine the consistencies (overlap comparisons for the batch case and state error covariances and the measurement residuals for the sequential case) of results obtained by the batch and sequential methods.

Section 2 of this paper describes the orbit determination and evaluation procedures used in this study, and Section 3 presents the results obtained using the batch-least-squares and sequential estimation methods and provides the resulting consistency and cross comparisons. Section 4 presents the conclusions of this study.

2.0 Orbit Determination and Evaluation Procedure

This section describes the analysis procedures used in this study. The TDRSS and BRTS tracking data characteristics are presented in Section 2.1, and the orbit determination evaluation methodology and options used are described in Section 2.2.

2.1 Tracking Measurements

Landsat-4 was deployed by Delta-3920 in July 1982. It has a nearly circular orbit, an altitude of approximately 715 kilometers, an inclination of 98 degrees, and a period of approximately 99 minutes. The time period chosen for this study was from 0 hours universal time coordinated (UTC) on January 17, 1991, through 10 hours UTC on January 24, 1991. During this interval, unusually dense TDRSS tracking of the Landsat-4 satellite was made available. The tracking consisted of an average of 15 passes of two-way TDRSS range and Doppler observations each day, each pass ranging from 3 minutes to 45 minutes in duration. The normal TDRSS tracking of Landsat-4 (less dense) typically consists of about six 5-minute passes each day. A timeline plot of the TDRSS tracking data distribution is given in Figure 1.

The typical scenario for BRTS tracking of the TDRSSs during the period of study included approximately 4 or 9 minutes of range and two-way Doppler measurements from two ground transponders for each relay every 2 to 3 hours, consisting of an average of 12 BRTS passes per TDRS each day. BRTS stations for TDRS-East are located at White Sands and Ascension Island. BRTS stations for TDRS-West are located at White Sands, American Samoa, and Alice Springs, Australia.

* RTOD/E is a copyrighted product of Applied Technologies Associates, Incorporated (ATA).

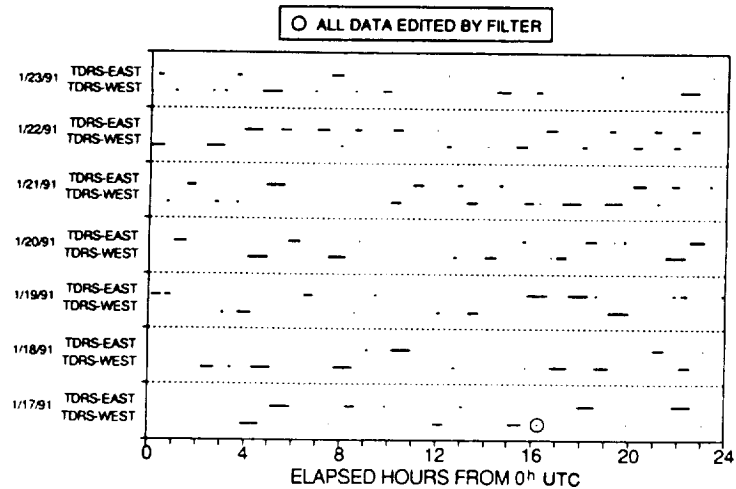


Figure 1. Tracking Data for Landsat-4

2.2 Evaluation Methodology

The evaluation methodologies for the batch-least-squares and sequential estimation methods are described below. Since there are some known differences between the GTDS and PFS models (estimation method, solar and planetary ephemerides representation, solid Earth tides, ionospheric refraction corrections to the measurements, and process noise modeling), and since the PFS TDRSS and BRTS measurement models were implemented independently from GTDS, the two systems are not expected to provide identical results. Therefore, this study assumes that each system is used in its optimal configuration. Table 1 gives the parameters and options for the simultaneous solutions of the user and relay spacecraft. Table 2 gives the force and measurement model specifications.

Batch Least-Squares Method

Except for the variations noted, the computational procedures and mathematical methods used in this study are identical to those used for routine operational orbit determination in the GSFC FDF. The choice to expand the state space of the least-squares solutions to include measurement biases was motivated by the fact that the PFS orbit determination algorithm estimates an equivalent set of bias parameters. The batch-weighted-least-squares algorithm implemented in GTDS (Reference 1) solves for the set of orbital elements and other parameters that minimizes the squared difference between observed and calculated values of selected tracking data over a solution arc. Parameters solved for, other than the spacecraft state at epoch, include free parameters of the force model and/or the measurement model.

A detailed study of the Earth Radiation Budget Satellite (ERBS) with the batch-least-squares estimation method was reported in Reference 4, and it was further refined in Reference 5. The models and options found optimal in the previous study of ERBS are used here for Landsat-4. The options used for the study described in this paper are summarized in columns 2 and 3 of Tables 1 and 2.

To evaluate the orbit determination consistency achievable with a particular choice of options using least-squares estimation, a series of seven 34-hour definitive solutions was performed with 10-hour overlaps between neighboring arcs. The GTDS Ephemeris Comparison Program was used to determine the root-mean-square (RMS) position differences between the definitive ephemerides for neighboring solutions in the 10-hour overlap time period. These "overlap" comparisons measure the adjacent solution consistency, not the absolute accuracy.

Sequential Estimation Method

PFS has been developed to address future increased TDRSS-navigation accuracy requirements and to provide automation of some routine orbit determination operations. The goal for future orbit determination accuracy is 10 meters total position error (1σ) for the user and 25 meters total position error (1σ) for the TDRSSs. PFS provides a

Table 1. Parameters and Options for the Simultaneous Solutions of User and Relay Spacecraft

Orbit Determination Parameter or Option	GTDS Values		PFS Values	
	User (Landsat-4)	Relay (TDRS-East & TDRS-West)	User (Landsat-4)	Relay (TDRS-East & TDRS-West)
Estimated parameters	State, drag scaling parameter (ρ_1), range and Doppler measurement biases for tracking via each ground station	State, transponder delays for each BRTS transponder, solar reflectivity coefficients	State, coefficient of drag, range and Doppler measurement biases for tracking via each TDRS	State, solar reflectivity coefficient (C_R), range and Doppler measurement biases for tracking via each transponder
Integration type	Fixed-step Cowell	Fixed-step Cowell	Variation of parameters	Variation of parameters
Coordinate system of integration	Mean of 1950.0	Mean of 1950.0	Mean of 1950.0	Mean of 1950.0
Integration step size (seconds)	30.0	600.0	60.0	60.0
Tracking data	TDRSS	BRTS	TDRSS	BRTS
Data rate	1 per 20 seconds	1 per 10 seconds	1 per 30 seconds	1 per 10 seconds
DC convergence parameter	0.005	0.005	N/A	N/A
Editing criterion	3σ	3σ	3σ	3σ
Measurement σ 's: Range Doppler	30.0 meters 0.25 hertz	10.0 meters 0.003 hertz	0.4 meter 0.004 hertz	0.4 meter 0.003 hertz
Gauss-Markov parameters: Drag half-life Drag sigma C_R half-life C_R sigma Range bias half-life Range bias sigma Doppler bias half-life Doppler bias sigma	N/A	N/A	840 minutes 0.500 N/A N/A 60 minutes 6 meters 8 minutes 0.034 hertz	N/A N/A 11520 minutes 0.2 60 minutes 4.5 meters 60 minutes 0.02 hertz
Satellite area	12.2644 meters ²	40 meters ²	12.2644 meters ²	40.0 meters ²
Satellite mass	1900.32 kilograms	1990.76 kilograms (TDRS-East) 1735.46 kilograms (TDRS-West)	1900.32 kilograms	1990.76 kilograms (TDRS-East) 1735.46 kilograms (TDRS-West)

N/A = Not applicable

Table 2. Force and Measurement Model Specifications

Orbit Determination Parameter or Option	GTDS Values		PFS Values	
	User (Landsat-4)	Relay (TDRS-East & TDRS-West)	User (Landsat-4)	Relay (TDRS-East & TDRS-West)
Geopotential model	GEM-T3 (50 × 50)	GEM-T3 (8 × 8)	GEM-T3 (50 × 50)	GEM-T3 (6 × 6)
Atmospheric density model	Jacchia-Roberts daily solar flux values (209, 203, 199, 204, 202, 225, 223)	N/A	CIRA 1972 daily solar flux values (209, 203, 199, 204, 202, 225, 223)	N/A
Solar and lunar ephemerides	JPL DE-118	JPL DE-118	Analytical	Analytical
Solar reflectivity coefficient (C_R)	1.5	Estimated	1.5	Estimated
Coefficient of drag (C_D)	Estimated	N/A	Estimated	N/A
Ionospheric refraction correction:	Bent Model	Bent Model	No	No
Ground-to-spacecraft	N/A	Yes	—	—
Spacecraft-to-spacecraft	Yes	N/A	—	—
Tropospheric refraction correction	Yes	Yes	Yes	Yes
Polar motion correction	Yes	Yes	Yes	Yes
Earth tides	Yes	No	No	No

GEM = Goddard Earth Model
 JPL = Jet Propulsion Laboratory
 N/A = Not Applicable

proof of concept for the use of sequential estimation techniques for orbit determination with TDRSS tracking data and offers the potential for enhanced accuracy navigation. PFS is a research tool for assessing sequential estimation for FDF navigation applications in realistic operational situations.

PFS uses the extended Kalman filter form for sequential orbit estimation. With the sequential estimation method, each tracking measurement can be processed immediately upon receipt to produce an update of a spacecraft's state vector and auxiliary state parameters. This fact makes it well suited for realtime or near-realtime operation. Sequential estimation is particularly well suited to the development of systems to perform orbit determination autonomously on the spacecraft's onboard computer (Reference 6). Spacecraft orbit determination during and just after a maneuver is a critical support function for which orbit determination is needed in near realtime. Therefore, sequential estimation is also well suited for such an application. In addition, the forward filter can be augmented with a backward smoothing filter to further improve the overall accuracy, especially during periods without tracking data.

PFS employs a sequential estimation algorithm with a process noise model to stochastically account for gravity model errors (Reference 7). In addition to the spacecraft orbital elements, the filter estimates free parameters of the force model and the measurement model, treating these parameters as random variables whose behavior is governed by a Gauss-Markov stochastic process. The specific options used in PFS for this study are listed in the last two columns of Tables 1 and 2.

A good indicator of the consistency of the sequential estimation results is provided by the state error covariance function generated during the estimation process (Reference 8). In addition, the relationship of the first predicted measurement residual of each tracking pass to the associated predicted residual variance provides an indication of the physical integrity of the state error covariance of the filtered orbits. These parameters were monitored during the sequential estimation process.

3.0 Results and Discussion

The results of this study for the Landsat-4 and TDRSS relay spacecraft are presented in this section, along with an analysis of the results. Greater emphasis is placed on the Landsat-4 results, since the primary objective is to study TDRSS user orbit determination. The orbit determination results using batch-least-squares calculations and sequential estimation are given in Sections 3.1 and 3.2, respectively; the comparisons are presented in Section 3.3.

3.1 Batch-Least-Squares Results

In general, all data arcs for Landsat-4 solutions consisted of 34 hours, beginning at 0 hours UTC of each day from January 17 to January 23, 1991, with one exception. The exception was made for the arc beginning at 0 hours UTC on January 20, 1991. There is a long data gap of about 5 hours (see Figure 1) at the end of the nominal 34-hour period, resulting in a predicted solution for the last 5 hours instead of a definitive solution. Therefore, for this particular solution, the arc length was extended by 2 hours to 36 hours so that the next tracking pass was included in the solution.

The RMS values of six Landsat-4 overlap comparisons are summarized in Figure 2. The RMS overlap differences vary from about 3 to 5 meters. The mean and sample standard deviation of this distribution, in the form of mean \pm standard deviation, is 3.9 ± 0.8 meters. The maximum total position differences over the same distribution vary between 5 and 9 meters, with a mean and standard deviation of 6.5 ± 1.3 meters. The maximum position difference values for Landsat-4 are typically a factor of 1.7 larger than the RMS values.

A batch-least-squares covariance analysis was performed to identify the major sources of error. The actual tracking data distribution was used for the covariance analysis. For the seven covariance analysis solutions, six RMS overlap comparison values were obtained. The mean and standard deviation of the overlap comparisons were 5.4 ± 0.5 meters, which is comparable to the GTDS-based orbit determination overlap comparison results. The agreement between the covariance analysis and the GTDS overlap values establishes confidence in the error models used in the covariance analysis. The dominant orbit determination error source was due to the geopotential model error, with the error magnitude significantly larger than the next largest error source.

The RMS values of six TDRS-East and TDRS-West overlap comparisons are summarized in Figure 3. The overlap values for TDRS-East vary from about 11 to 17 meters. The mean and sample standard deviation of this distribution is 14.9 ± 2.3 meters. The maximum total position differences over the same distribution vary between 14 and 25 meters, with a mean and standard deviation of 18.7 ± 4.0 meters. The overlap values for TDRS-West vary from about 10 to 49 meters. The mean and the sample standard deviation of this distribution is 20.8 ± 13.3 meters. The maximum total position differences over the same distribution vary between 13 and 67 meters, with a mean and standard deviation of 24.9 ± 19.1 meters. The maximum position difference values for the TDRSs are typically a factor of 1.1 larger than the RMS values.

The possible advantage of varying the estimation arc lengths to exclude periods of TDRS angular momentum unloads was evaluated. These momentum unloads are designed to use opposing thrusters so that the effects on the orbit are minimized. However, earlier analysis on the Ocean Topography Experiment (TOPEX) satellite indicated

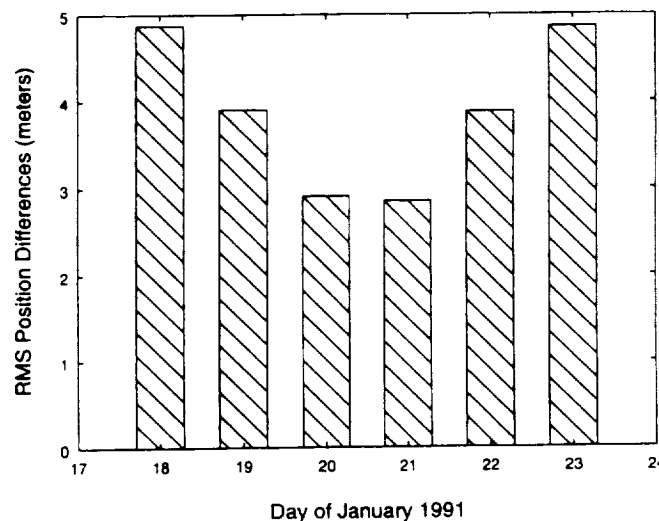


Figure 2. Landsat Overlap Comparisons

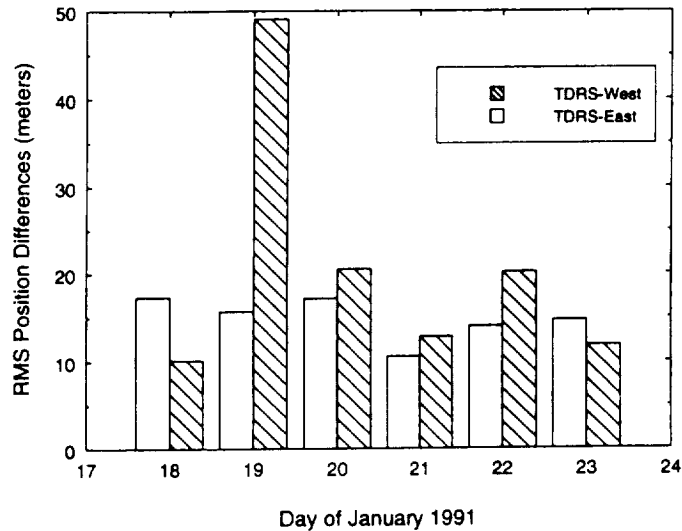


Figure 3. TDRS-East and TDRS-West Overlap Comparisons

that by excluding momentum unloads from the estimation arcs, solutions with greater accuracy were possible (Reference 9). Five TDRS momentum unloads were performed during the period covered by this study—three by TDRS-East (at UTC 1/17/91 20:25:00, 1/20/91 20:00:00, and 1/22/91 21:00:00) and two by TDRS-West (at UTC 1/19/91 09:20:00 and 1/19/91 12:30:00). These momentum unloads were excluded by performing five solutions with arc lengths of about 20, 37, 31, 49, and 27 hours, respectively. A period of about 3 hours between the TDRS-West momentum unloads was excluded entirely. Predicted periods of 10 hours at both ends of the solution arcs were used in overlap comparisons to judge consistency. These overlap comparisons were less favorable than for similar predicted overlap comparisons for the 34-hour solution arcs presented above. In particular, it appeared that the initial 20-hour arc may have been too short to accurately estimate all 21 parameters in the state vector. The GTDS solutions using 34-hour arc lengths will be used in the comparisons presented in Section 3.3.

3.2 Sequential Estimation Results

During sequential processing of the TDRSS and BRTS measurements using the PFS filter/smoothener, the position component standard deviations from the state error covariance function (σ) were closely monitored. The filter was started with high initial diagonal values in the covariance matrix. The smoother was of the Rauch-Tung-Striebel type and was therefore started at the end of the time period of investigation (UTC 1/24/91 00:00:00) with the same covariance as the final filter covariance.

The root-sum-square (RSS) position standard deviations (1σ) for both the filter and smoother runs for Landsat-4 are plotted in Figure 4. The filter standard deviations initially increase to about 2 kilometers. This is not unusual before the filter has reached steady-state performance, especially considering that there are no TDRSS data for Landsat-4 in the first 4 hours (see Figure 1). After an initial filter settling period (about 24 hours), the 1σ values varied from about 2.9 to 13.2 meters in the RSS position for Landsat-4. The 1σ values for Landsat-4 dropped to their lowest levels during a tracking pass and then gradually rose to the maximum values during the time update phase (propagation phase). (The duration of the time update phases can be seen in Figure 1). The smoother RSS standard deviation remained fairly constant at about 2.8 meters, with greater values at either end, a result predicted by theory.

Unlike Landsat-4, the filter 1σ RSS values for TDRS-East and TDRS-West continued to decline gradually for about 4 days. Near the end of the filter run, the 1σ RSS position standard deviations for TDRS-East and TDRS-West remained relatively steady at about 10.8 meters and 7.2 meters, respectively. The smoother RSS standard deviations for the TDRSs were fairly constant at about 6.9 meters for TDRS-East and 6.6 meters for TDRS-West, with slight increases at either end.

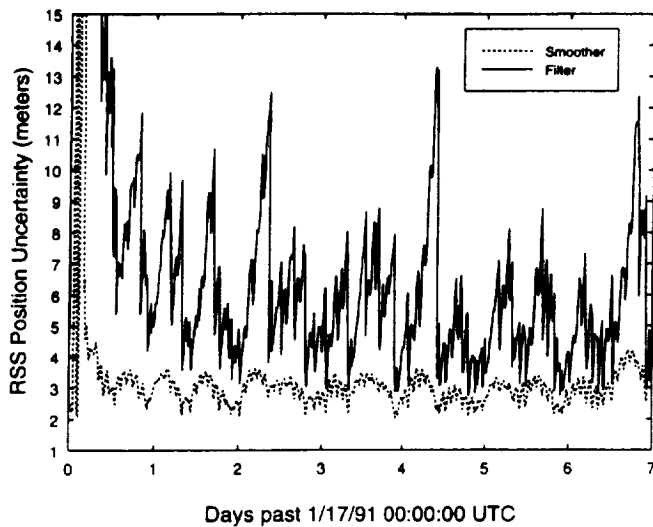


Figure 4. RSS Position Standard Deviation (1σ) for Landsat-4 PFS Filter/ Smoother

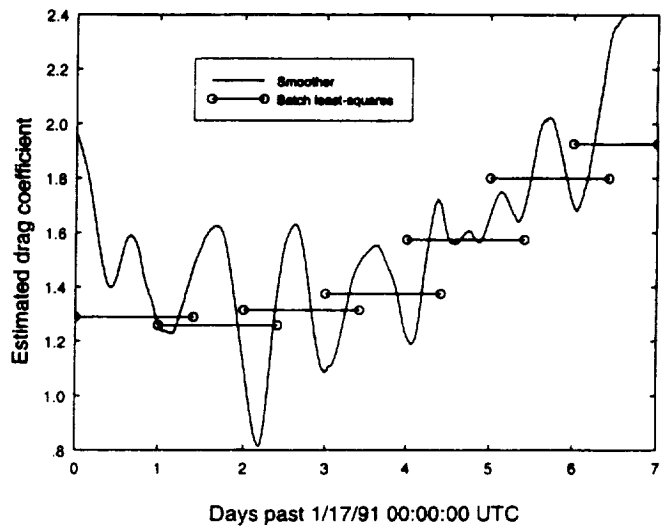


Figure 5. Coefficient of Atmospheric Drag (C_D) for Landsat-4

The estimated force model parameters varied as a function of time and were updated after each measurement was processed. The time variation of the atmospheric drag coefficient for Landsat-4 is shown in Figure 5 for the smoother solution. The drag coefficients estimated by the batch-least-squares solutions (34-hour arcs) are also indicated in Figure 5. The drag coefficient estimate from the smoother varied from a low of about 0.8 to a high of about 2.5. Throughout most of this interval, the smoother's drag coefficient standard deviation (1σ) remained fairly constant at about 0.18, increasing to about 0.35 at both ends of the interval. The upward trend in the drag coefficient indicated by the batch-least-squares results is reflected in the smoother results as well.

The time variation of the smoother's estimate of solar reflectivity coefficients for TDRS-East and for TDRS-West are shown in Figures 6 and 7, respectively. The corresponding batch-least-squares results are indicated on these figures as well. The solar reflectivity coefficient varied from about 1.34 to about 1.44 for TDRS-East and from about

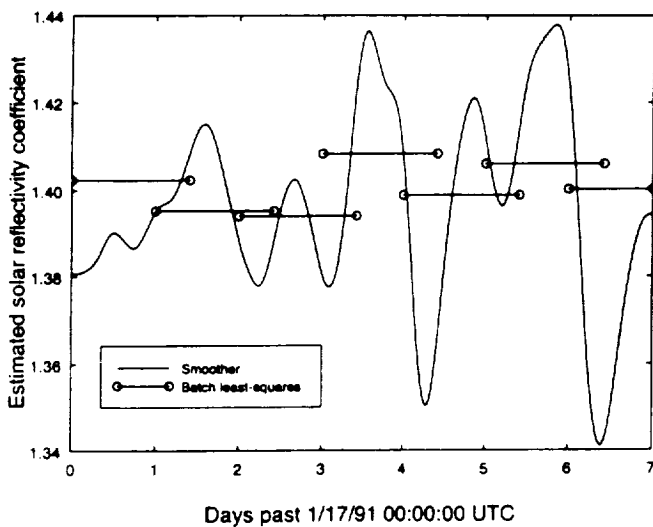


Figure 6. Coefficient of Solar Radiation Pressure (C_R) for TDRS-East

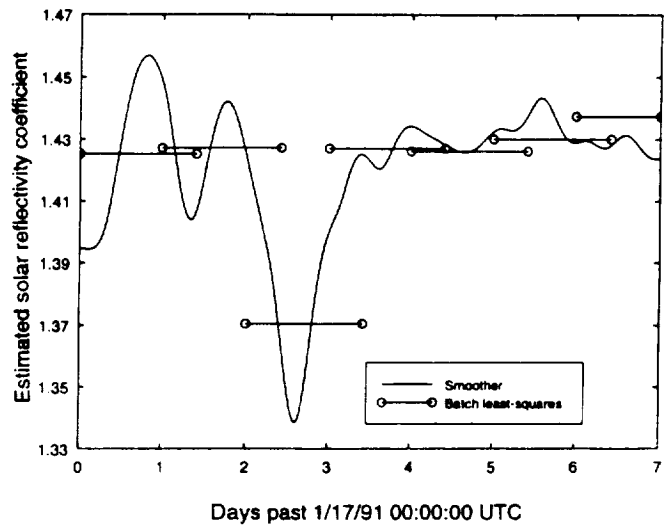


Figure 7. Coefficient of Solar Radiation Pressure (C_R) for TDRS-West

1.34 to about 1.46 for TDRS-West. During most of this time interval, the smoother's solar reflectivity coefficient standard deviations (1σ) remained fairly constant at about 0.02 for TDRS-East and 0.02 for TDRS-West. There appears to be fairly good agreement between the smoother and batch-least-squares results for the solar reflectivity coefficient. In particular, an excursion on the 19th of January for TDRS-West is reflected in the results of both systems.

The solar flux values are input to the PFS filter/smoothing on a daily basis. The time variation of the flux value over the 24-hour period is not input. Therefore, the atmospheric drag coefficient must be adjusted to compensate for the variation (Figure 5). The filter/smoothing also models the area of the TDRS to be a constant throughout the day, whereas in actuality the TDRS surface area exposed to the solar flux varies with a 24-hour period. An oscillatory signature of the variation in C_R values with a period of 1 day is evident in the smoother results.

3.3 Comparison of Batch and Sequential Estimation Results

Comparisons of the estimated Landsat-4 orbits between GTDS solutions and PFS filter/smoothing solutions are presented in Figures 8 and 9. Both figures show the radial, along-track, and cross-track differences, as well as RSS differences over a single day in the middle of the period under investigation (January 20, 1991). Figure 8 shows the comparisons for the filter solution, and Figure 9 shows comparisons for the smoother solution. Both figures are plotted on the same vertical scale so that differences between them are readily apparent. The maximum RSS difference between the filter and the batch-least-squares solution over this time period is about 32 meters, while for the smoother comparison to batch, it is about 12 meters.

In Figures 10 and 11, comparisons of the estimated TDRS-East orbits between GTDS solutions and PFS filter/smoothing solutions are presented. These comparisons are for the same time interval as for the Landsat-4 comparisons. Radial, along-track, cross-track, and RSS comparisons are provided. Figure 10 shows the comparisons for the filter solution, and Figure 11 shows a similar comparison for the smoother solution. The most striking feature is the relatively constant 90-meter along-track offset seen in the filter solution that is not present in the smoother solution. Such an offset ordinarily might have been attributed to coordinate system differences between the two systems or to measurement model discrepancies. Since this offset does not appear in the smoother solution, these explanations are not valid for this case (the smoother uses the same coordinate system and measurement model algorithms as the filter). The origin of the along-track offset in the filter solution for TDRS-East is not known at this time, but further analysis is in progress to identify the cause. The discontinuity in the comparisons at around 5 hours into the day arises because two separate batch-least-squares solutions from different arcs were appended.

Finally, in Figures 12 and 13, comparisons of the estimated TDRS-West orbits between GTDS solutions and PFS filter/smoothing solutions are presented. Figure 12 shows the comparisons for the filter solution, and Figure 13 shows a similar comparison for the smoother solution. The along-track offset in the filter solution is smaller than it was for TDRS-East (here it is about 30 meters). The smoother solution also shows an along-track offset, although it is much smaller than for the filter (about 10 meters).

A significant part of the difference between the batch and sequential orbit determination results can be attributed to the differences in the force and measurement models used for GTDS and the PFS filter/smoothing. Quantitative estimates for some of these model difference effects are available from previous studies using GTDS. It was reported in Reference 4 that the maximum position differences observed in the definitive ERBS orbits due to the presence and absence of ionospheric refraction correction in the measurement model for the spacecraft-to-spacecraft leg can be 2.6 ± 0.9 meters. The maximum position difference due to solid Earth tide effects on ERBS was measured at 7.0 ± 3.2 meters. A detailed analysis of the influence of polar motion and solid Earth tides on ERBS orbits is given in Reference 10. ERBS is at an altitude of about 600 kilometers, whereas Landsat-4 is at an altitude of about 715 kilometers. Therefore, all the stated effects above for ERBS should be somewhat diminished in magnitude for Landsat-4. However, Landsat-4 has a polar orbit, which has a significant adverse effect on the tracking geometry. Due to the inclusion of a process noise model for geopotential errors in the PFS and its absence in GTDS, the impact of differences in the geopotential models used would be different in the two systems.

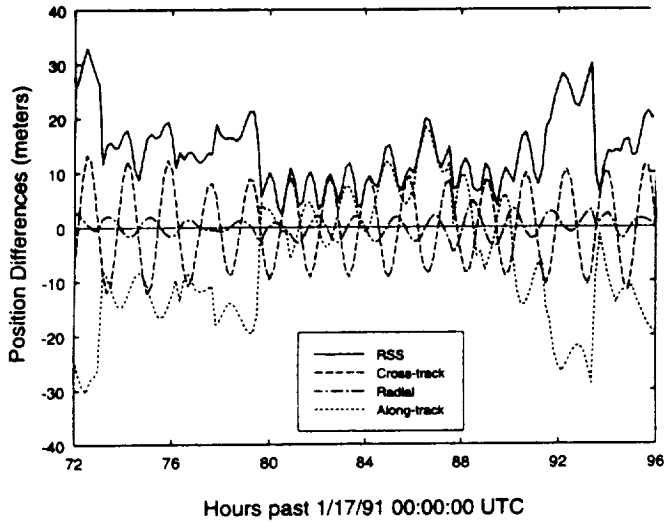


Figure 8. PFS Filter and GTDS Ephemeris Differences for Landsat-4 (Day 4)

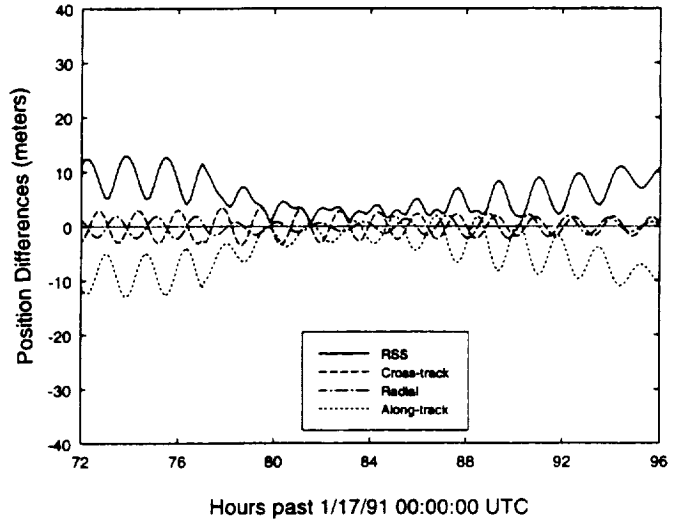


Figure 9. PFS Smoother and GTDS Ephemeris Differences for Landsat-4 (Day 4)

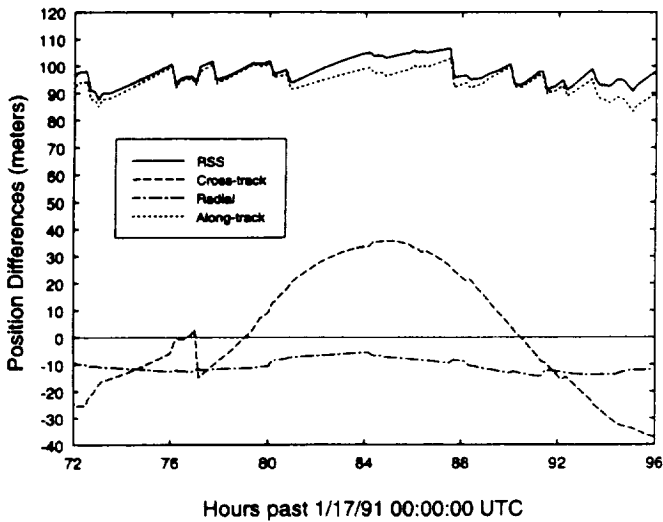


Figure 10. PFS Filter and GTDS Ephemeris Differences for TDRS-East (Day 4)

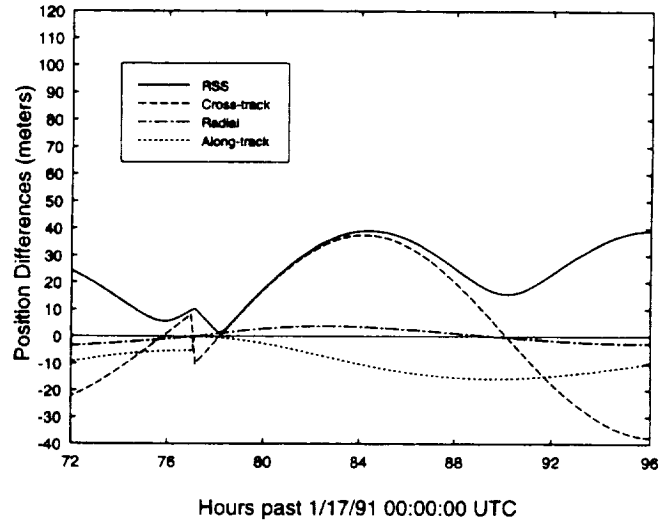


Figure 11. PFS Smoother and GTDS Ephemeris Differences for TDRS-East (Day 4)

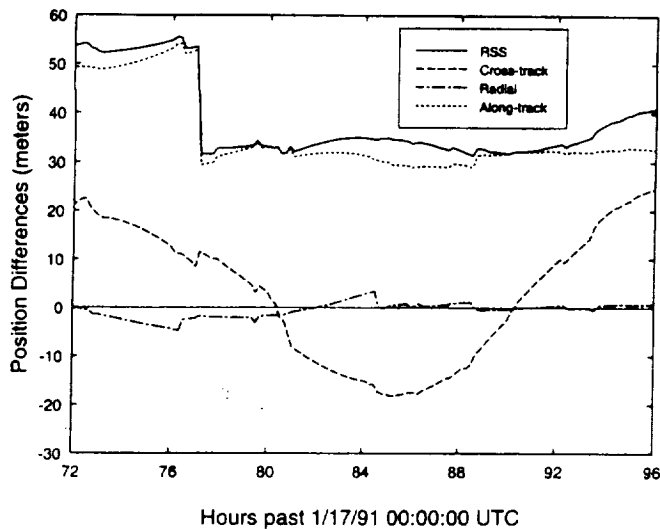


Figure 12. PFS Filter and GTDS Ephemeris Differences for TDRS-West (Day 4)

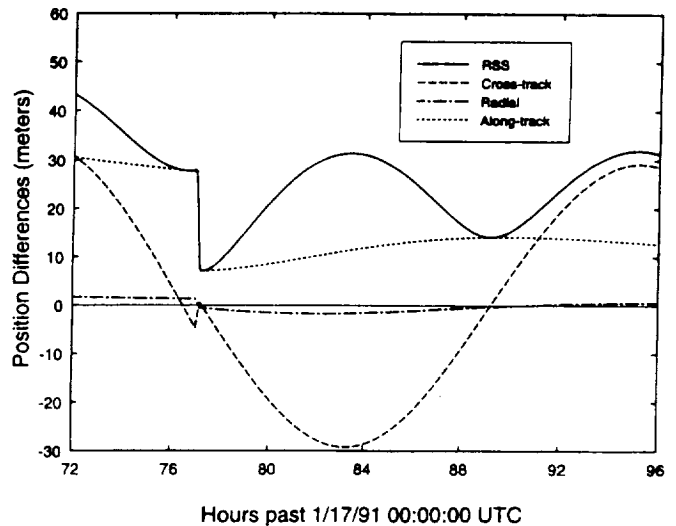


Figure 13. PFS Smoother and GTDS Ephemeris Differences for TDRS-West (Day 4)

Another source of the difference between the GTDS and PFS filter/smoothen estimated ephemerides is due to the fundamental difference in the way the estimated parameters are obtained in the batch-least-squares and sequential estimation techniques. In the batch-least-squares method, a single set of parameter values is estimated over an entire arc. In the sequential estimation process, the set of estimated parameter values is updated at each measurement time. The time variations in selected estimated parameters are shown in Figures 5 through 7.

Based on the magnitude of these differences and the differences in the estimation techniques, the maximum position difference of about 12 meters between the GTDS and PFS smoother results is not unusual. Also, as expected, the smoother provides more accurate solutions since it utilizes data occurring both before and after a given time to estimate the state at that time.

The sensitivity of orbit determination accuracy to varying tracking schedules was reported in Reference 11. The corresponding covariance analysis was also reported in the same paper. The results of a study that successfully processed through orbit-adjust maneuvers were reported in Reference 12.

4.0 Conclusions

This study presented an analysis of TDRSS user orbit determination using a batch-least-squares method and a sequential estimation method. Independent assessments were performed of the orbit determination consistency within each method, and the estimated orbits obtained by the two methods were also compared. This assessment is applicable to the dense-tracking measurement scenario for tracking Landsat-4.

In the batch-least-squares method analysis, the orbit determination consistency for Landsat-4, which was heavily tracked by TDRSS during January 1991, was found to be about 4 meters in the RMS overlap comparisons and about 6 meters in the maximum position differences in overlap comparisons. In the sequential method analysis, the consistency was found to be about 12 meters in the 3σ state error covariance function for the smoother and 30 meters for the filter; and, as a measure of consistency, the first residual of each pass was within the 3σ bound in the residual space for the filter.

After the filter/smoothen had reached steady state, the differences between the definitive batch-least-squares ephemerides and the sequentially estimated forward filter ephemerides were no larger than 30 meters, and the differences between the batch-least-squares ephemerides and the sequentially estimated smoothed ephemerides

were no larger than 12 meters. The application of a smoother algorithm to the filter solutions consistently reduced the difference with the batch-least-squares solutions. These results demonstrate that smoother postprocessing offers the potential for significant improvement in sequential estimation solution accuracy.

References

1. Goddard Space Flight Center, Flight Dynamics Division, FDD/552-89/001, *Goddard Trajectory Determination System (GTDS) Mathematical Theory, Revision 1*, A. C. Long and J. O. Cappellari, Jr. (CSC) and C. E. Velez and A. J. Fuchs (GSFC) (editors), prepared by Computer Sciences Corporation, July 1989
2. Goddard Space Flight Center, Flight Dynamics Division, FDD/554-91/064, *Enhanced RTOD Demonstration System User's Guide*, W. Chuba (ATA), prepared by Applied Technology Associates, Inc., March 1991
3. D. H. Oza, T. L. Jones, S. M. Fabien, G. D. Mistretta, R. C. Hart, and C. E. Doll, "Comparison of ERBS Orbit Determination Using Batch Least-Squares and Sequential Methods," NASA Conference Publication 3123, *Proceedings of the Flight Mechanics/Estimation Theory Symposium*, p. 79, Paper No. 5, presented at Goddard Space Flight Center, Greenbelt, Maryland, May 21–23, 1991
4. D. H. Oza, M. Hodjatzadeh, M. S. Radomski, C. E. Doll, and C. J. Gramling, "Evaluation of Orbit Determination Using Dual-TDRS Tracking," Paper No. AIAA-90-2925-CP, *A Collection of Technical Papers Part 1*, p. 410, published by the AIAA; presented at the AIAA/AAS Astrodynamics Conference, Portland, Oregon, August 20–22, 1990
5. D. H. Oza, T. L. Jones, M. Hodjatzadeh, M. V. Samii, C. E. Doll, G. D. Mistretta, and R. C. Hart, "Evaluation of TDRSS-User Orbit Determination Accuracy Using Batch Least-Squares and Sequential Method," paper presented at the Third International Symposium on Spacecraft Flight Dynamics, Darmstadt, Germany, September 30–October 4, 1991
6. Goddard Space Flight Center, Flight Dynamics Division, 554-FDD-91/105R3UD0, *Tracking and Data Relay Satellite System (TDRSS) Onboard Navigation System (TONS) Flight Software Mathematical Specifications, Revision 3*, A. C. Long, D. H. Oza, et al. (CSC), prepared by Computer Sciences Corporation, March 1992
7. J. R. Wright, "Sequential Orbit Determination with Auto-Correlated Gravity Modeling Errors," *Journal of Guidance and Control*, vol. 4, 1981, p. 304
8. A. Gelb (editor), *Applied Optimal Estimation*. Cambridge, Massachusetts: M.I.T. Press, 1974
9. C. E. Doll et al., "Improved Solution Accuracy for TDRSS-Based TOPEX/Poseidon Orbit Determination," Paper No. 15, presented at the Flight Mechanics/Estimation Theory Symposium, Goddard Space Flight Center, Greenbelt, Maryland, May 17–19, 1994
10. Goddard Space Flight Center, Flight Dynamics Division, FDD/554-90/103, "Effects of Polar Motion and Earth Tides on High-Accuracy Orbit Determination of the Earth Radiation Budget Satellite (ERBS)," *Operational Orbit Techniques, 1990 Flight Dynamics Analysis Report 1*, D. H. Oza and T. Mo (CSC), prepared by Computer Sciences Corporation, May 1990
11. D. H. Oza et al., "Tracking Schedule Dependence of High-Accuracy TDRSS-User Orbit Determination Solutions," Paper No. AAS 93-600, presented at the AAS/AIAA Astrodynamics Specialist Conference, Victoria, British Columbia, August 16–19, 1993
12. D. H. Oza et al., "Evaluation of Landsat-4 Orbit Determination Accuracy Using Batch Least-Squares and Sequential Methods," Paper No. AAS 93-161, presented at the AAS/AIAA Spaceflight Mechanics Meeting, Pasadena, California, February 22–24, 1993

OPTIMUM SATELLITE RELAY POSITIONS

WITH APPLICATION TO A TDRS-1 INDIAN OCEAN RELAY

A. H. Jackson
 NASA Goddard Space Flight Center
 Greenbelt, MD 20771

P. Christopher
 Stanford Telecom
 Reston, VA 22090

Abstract

An Indian Ocean satellite relay is examined. The relay satellite position is optimized by minimizing the sum of downlink and satellite to satellite link losses. Osculating orbital elements are used for fast intensive orbital computation. Integrated Van Vleck gaseous attenuation and a Crane rain model are used for downlink attenuation. Circular polarization losses on the satellite to satellite link are found dynamically. Space to ground link antenna pointing losses are included as a function of yaw and spacecraft limits. Relay satellite positions between 90 to 100 degrees East are found attractive for further study.

1.0 BACKGROUND

The Tracking and Data Relay Satellite System (TDRSS) has provided vital communication relay service between low altitude satellites and White Sands, New Mexico. Figure 1 shows a polar view of the Earth and relative positions of TDRS East and TDRS West. The ground station at White Sands looks southwest toward TDRS West and southeast to TDRS East. The complementary coverage of western and eastern relays allows nearly full time communication links with low altitude satellites. The complementary coverage is implied by the view of the Earth as seen from TDRS West as shown in Figure 2 and the view from TDRS East (Figure 3). Figures 2 and 3 imply that the Indian Ocean region is a region of concern for marginal communication. Indeed, viewers who watched the Hubble Space Telescope (HST) repair saw excellent video until HST passed over the Indian Ocean. The video flickered and was gone, just that quickly. Approximately four minutes later the link to TDRS West was established as HST approached Malaysia.

We examine the possibility of an Indian Ocean relay to augment TDRSS communication. Figure 4 shows the view from a possible Indian Ocean relay. A ground station in southeastern Australia may be considered for the uplink. The ground station, Tidbinbilla (35.402S, 148.981E), is marginally within view of the relay at 90

degrees East. The ground station would be expected to suffer signal attenuation at low antenna elevation angle. Here we see the first part of a two horned dilemma. The ground station attenuation could be relieved by transferring the Indian Ocean relay eastward to raise the Australian ground station elevation angle. However, this would aggravate the space-space link (SSL) losses in terms of both free space loss and multipath loss. (Multipath loss was related to the video flicker from HST before the signal disappeared). It is difficult to reach a compromise between these competing demands unless the system designer defines some overall system objective function.

Here, we choose a conceptually simple and useful objective function composed of the sum of downlink and SSL losses. We seek to minimize this "Total Loss" objective function to optimize system performance. This concept will apply to any ground station, any relay, and any low altitude user for very general results.

The optimization is computationally intensive. The simulation for the relay must include the SSL link to a low altitude satellite such as the Gamma Ray Observer (GRO) at 5 second intervals. Multipath statistics are compiled for periods of at least 24 hours at each relay position. The intensive computations require efficient, accurate algorithms at every step. We begin by using a method of osculating elements to simulate orbits quickly and accurately for altitudes ranging from 200 to over 42000 km. At each time, a number of losses must also be calculated on both the space to ground link (SGL) and the space-space link (SSL).

The space to ground losses include:

- Gaseous attenuation
 - Water vapor
 - Oxygen
 - Crane rain attenuation
- SGL antenna loss due to limit imposed by antenna stops and yaw
- Free space loss

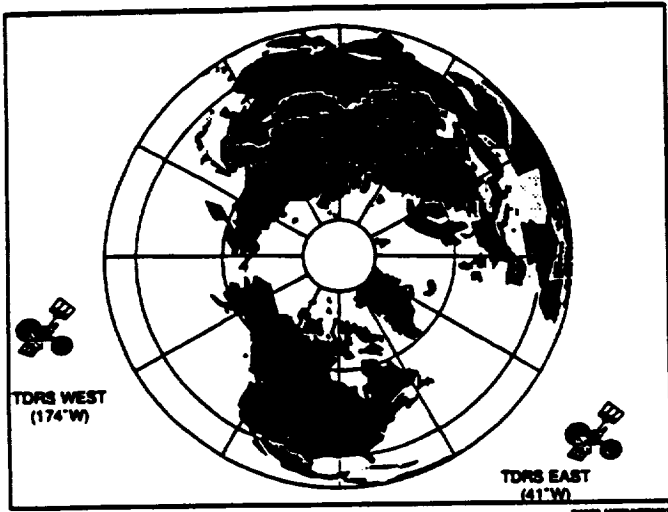
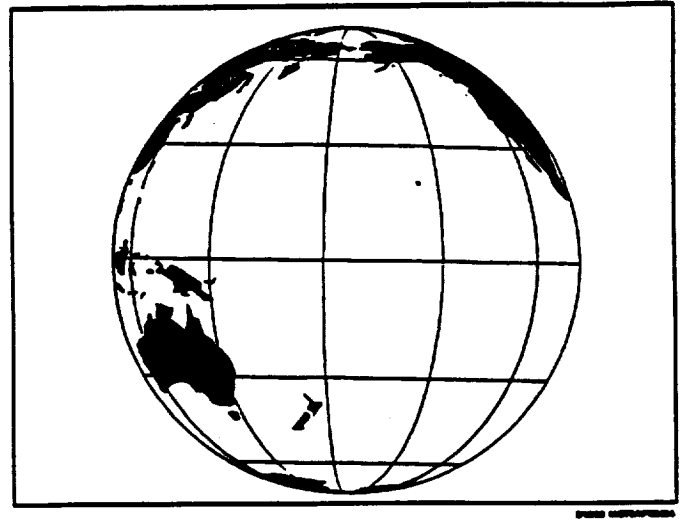
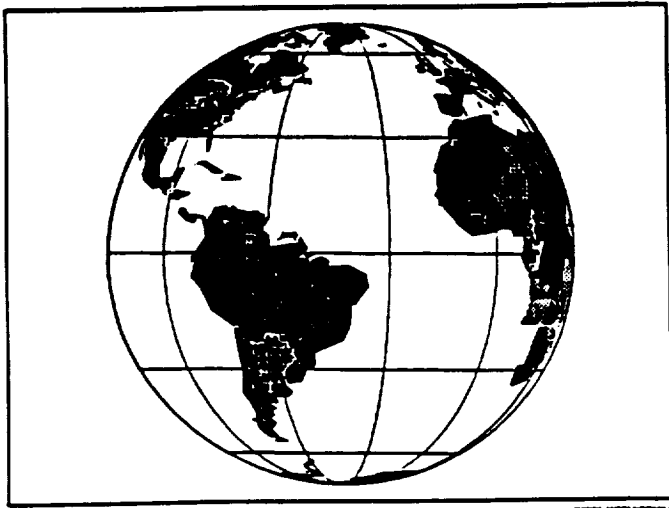


Figure 1: Polar View Showing TDRS Positions at 41°W, 174°W



**Figure 2: View of Earth from TDRS West (174°W)
Mathematica Orthographic Projection**



**Figure 3: View of Earth from TDRS East (41°W)
Mathematica Orthographic Projection**

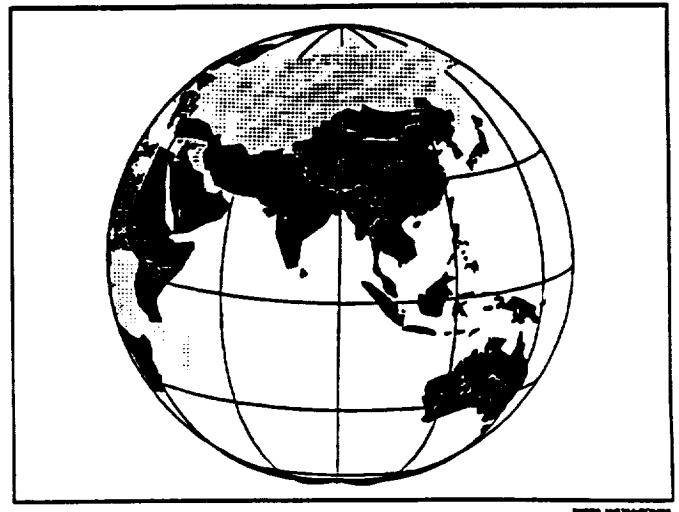


**Figure 4: View of Earth from an Indian Ocean Relay at 80°E
Note Southeastern Australia is Barely Visible**

SSL losses include:

- Two ray interference for multipath loss
 - Earth grazing ray attenuated by TDRS antenna pattern, gaseous attenuation
- Free space loss

We first show some key results for the method of osculating elements, along with a relatively new and unused result for lunar perturbations. Short expressions for the loss terms follow. Intermediate level results are shown for a relay which has no yaw or SGL antenna restrictions. The paper concludes with three dimensional plots of total loss as a function of longitude and relay yaw for a relay at 8 degree inclination. A TDRS1/GRO example demonstrates the method and indicates practical optimum relay positions.

2.0 ORBITAL ANALYSIS

The method of osculating elements is used here for speed and accuracy in orbital computation. This method has been used by classical astronomers [1]. The method relies on an initial set of Keplerian elements which changes continuously due to a non-central force field. Typical non-central forces to be considered are:

- | | |
|---|---|
| 1. Oblate earth gravitational force | (included here) |
| 2. Higher earth gravitational force terms | (no available result for osculating elements) |
| 3. Moon and sun perturbations | (Ash 1974) |
| 4. Air drag | (omitted here) |
| 5. Radiation pressure | (omitted here) |

The method of osculating elements has often been avoided because it requires analytic derivations for rates of change for the classical orbital elements. Ash [2] has removed some of these objections with a derivation of the smoothed rates of change of orbital elements due to lunar perturbations. Other rates of change were discussed previously in a 1976 SCSC paper [3]. The higher earth gravitational perturbation terms have not yielded short analytic relations, to our knowledge.

2.1 Oblateness Effects. The oblateness effects have been found to give a regression of nodes

$$\dot{W} = -\frac{3}{2a} \sqrt{\frac{\mu}{a}} J_2 \left(\frac{R}{P_{SL}}\right)^2 \cos(i) \text{ rad/sec} \quad (2-1)$$

The argument of perigee changes as

$$\dot{W}_p = \frac{3}{4a} \sqrt{\frac{\mu}{a}} J_2 \left(\frac{R}{P_{SL}}\right)^2 (-1 + 5\cos^2(i)) \text{ rad/sec} \quad (2-2)$$

and the mean anomaly changes as

$$\dot{M} = \frac{3}{4a} \sqrt{\frac{\mu}{a}} J_2 \left(\frac{R}{P_{SL}}\right)^2 \sqrt{1-e^2} (-1 + 3\cos^2(i)) \text{ rad/sec} \quad (2-3)$$

- W = right ascension, rad
- W_p = argument of perigee, rad
- R = earth radius, km

- Where μ = earth gravitational constant
= 0.39860064 * 10⁶ km³/sec²
- P_{SL} = a (1-e²) = semilatus rectum
- J₂ = 1.082635 * 10⁻³

- a = semimajor axis, km
- e = eccentricity
- i = inclination (deg.)

These are the three main perturbing effects which will concern us as we implement the method of osculating elements. Even these first order effects are interesting. The argument of perigee has a stationary point (at cos²i = 1/5, or i = 63.43°). This is the basis of a stable "Molniya" satellite communication orbit which has been serving the USSR for over two decades. The stability at i = 63.43° has been a concern for decades, and it is still being studied.

2.2 Lunar Perturbations

In the early 1970's, MIT's Lincoln Lab was concerned with satellites at geosynchronous altitudes and higher. The moon is a leading source of perturbations at geosynchronous altitude. Lincoln Lab had a Planetary Ephemeris Program (PEP) developed in that period which allowed discrete simulations for the 3 body problem (earth-moon-satellite). PEP required exorbitant amounts of computer time, and Lincoln Lab soon realized that a leading orbital dynamicist should examine the problem, in an attempt to get good orbital solutions in a reasonable runtime. M. Ash found that reasonable solutions could be found by spreading the moon into a ring of equivalent lunar mass. His leading terms for the following satellite perturbations were:

$$\Delta W = -2\pi \left(\frac{\mu_m}{\mu} \right) \left(\frac{a}{P_m} \right)^2 \cos(I_m) \left[\frac{3}{4} + \left(\frac{a}{P_m} \right)^2 - \left[\frac{135}{128} + \frac{315}{128} \cos^2(I_m) \right] \right] \text{ rad/orbit}$$

$$\Delta c = -\pi \left(\frac{\mu_m}{\mu} \right) \left(\frac{a}{P_m} \right)^2 c \sin(2W_p) \left[-\frac{15}{4} \sin^2(I_m) + \frac{a^2}{P_m^2} \left[\frac{315}{128} - \frac{315}{16} \cos^2(I_m) + \frac{2205}{128} \cos^4(I_m) \right] \right] \text{ rad/orbit}$$

$$\Delta W_p = \pi \left(\frac{\mu_m}{\mu} \right) \left(\frac{a}{P_m} \right)^2 \left[3 - \frac{15}{2} \sin^2(W_p) \sin^2(I_m) \right] + \frac{a^2}{P_m^2} \text{ (continued)}$$

$$\left[-\frac{45}{32} + \frac{315}{64} \sin^2(W_p) + \left(\frac{225}{32} - \frac{315}{8} \sin^2(W_p) \right) \cos^2(I_m) \right] \text{ rad/orbit}$$

Where $\left(\frac{\mu_m}{\mu} \right) = \frac{\text{lunar gravitational constant}}{\text{earth gravitational constant}} = 0.012288$

$I_m =$ inclination with respect to lunar plane

$P_m =$ mean lunar distance = $3.844 \cdot 10^5$ km from geocenter

This spreading of lunar mass into an equivalent thin lunar annulus allowed these relatively short, computationally efficient equations. However, actual runs of the PEP revealed a difference in stability between prograde and retrograde satellite orbits. The difference in stability was traced to unstable semimajor axis and eccentricity. Figure 5 shows retrograde orbits as more stable than prograde.

2.3 Comparison of Prediction Methods

Numerical integration techniques may be broadly compared to the method of osculating orbital elements as in Figure 6. The first two numerical integration methods are found in NASA SP-33 [4,5]. The last entry, for osculating orbital elements, is our own addition to the table. The osculating elements offer a good speed comparison, but a different kind of error is seen. A particular 8 hour orbit may resonate as a harmonic of the Earth's third order gravitational potential, and grievous error may result from this latter method.

In practice, the method of osculating elements has shown good accuracy for TDRS and all users with altitude greater than 200 km.

3.0 PROPAGATION EFFECTS

The signal loss on the space-to-space link (SSL) and the attenuation losses at Tidbinbilla are interesting in their own right. The SSL losses are seen to increase as the relay shifts eastward, and the ground station losses to increase as the relay shifts westward. They must be studied in detail in order to minimize the sum of losses by shifting the longitude of the Indian Ocean relay.

3.1 Multipath for an Earth Grazing Ray

The space-to-space link between TDRS and the user may be degraded by a variety of mechanisms. Figure 7 shows the signal degradation mechanisms which we consider here. The ray tangent height (HGRAZ) is a key influence on multipath interference. Two ray multipath interference is the dominant effect. The reflected ray is considered as a specular reflection which interferes with the direct ray. Three ray interference models have been shown by Rummel to give good comparisons to actual multipath conditions, but we use only two rays here for simplicity and for maximum constructive and destructive interference. Minimum signal results when the reflected ray is 180 degrees out of phase with the direct ray. These effects would be severe for linearly polarized rays, with large variations in received signal amplitude for the TDRS-user link. Horizontal polarization gives deeper signal fades than vertical polarization. Fortunately, the TDRSS SSLs have avoided these deep fading possibilities by using circular polarization.

Circularly polarized links, such as the TDRSS SSLs, have more benign fading than linear polarization. H. R. Reed [6] has shown the vector sum of the direct and interfering circularly polarized rays. His general analysis concludes with:

$$\frac{E_r}{E_o} = \left[1 + \left(\frac{D}{2} \frac{E_r'}{E_o} \right)^2 + 2D \left(\frac{E_r'}{2E_o} \right) \cos(\theta - \phi_h + \alpha) \right]^{1/2} \quad (3-1)$$

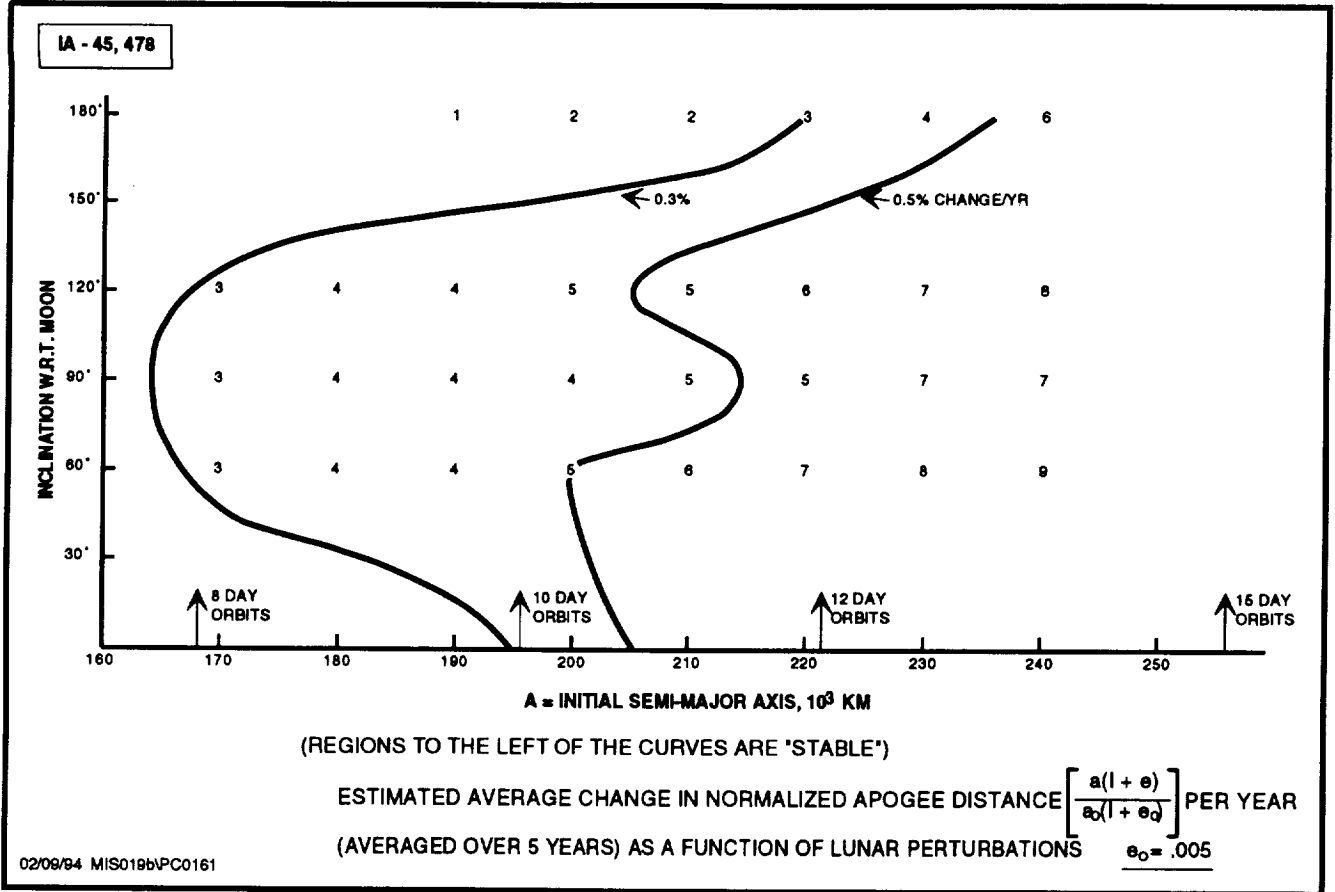


Figure 5: Instability Regions Due to Lunar Perturbations

Method	Ease of Changing Step Size	Speed	Stability	Error
Runge-Kutta Numerical Integration	*	Slow	Stable	Satisfactory Roundoff
Bowie Numerical Integration	Easy	Fast	Stable	Satisfactory Roundoff
Method of Osculating Elements	Easy	Very Fast	Stable	**

* Difficult to determine proper step size.

** No roundoff error, but missing higher order earth gravitational terms (usually unimportant unless orbit is a harmonic of a third order perturbation, as for an 8 hour inclined orbit).

Figure 6: Short Comparison of Prediction Methods

and

$$E_r' = E_o [R_v^2 + R_h^2 + 2R_v R_h \cos(\phi_h - \phi_v)]^{1/2} \text{ volts/meter} \quad (3-2)$$

where

- E_R = received voltage amplitude
- E_o = received voltage amplitude in absence of reflection
- D = divergence factor
- E_R' = received reflection voltage amplitude
- α = additional phase lag, rad. = 0
- θ = path lag of reflected wave, rad
- ϕ_h = reflection phase lag of horizontal component, rad
- ϕ_v = reflection phase lag of vertical component, rad
- R_h = magnitude of horizontal reflection coefficient
- R_v = magnitude of vertical reflection coefficient

For low reflection angles, ϕ_h is assumed equal to π rad and ϕ_v equal to zero for this simplified analysis. In addition D is assumed as unity. With these simplifications and the introduction of a front-to-side power ratio (F) (3-2) reduces to:

$$E_r' = \frac{E_o}{\sqrt{F}} [-R_v + R_h] \quad (3-3)$$

The front-to-side power ratio consists of both antenna gain and atmospheric attenuation terms.

(3-2) may be substituted into (3-1) to yield:

$$\frac{E_r}{E_o} = \left[1 + \left(\frac{1}{2\sqrt{F}} \right)^2 [R_h - R_v]^2 + \frac{[R_h - R_v]}{\sqrt{F}} \cos(\theta - \pi) \right]^{1/2} \quad (3-4)$$

At a given front-to-side ratio (F) and reflection coefficients, $\left(\frac{E_r}{E_o} \right)^2$ is seen to follow the same distribution as a uniformly distributed cosine.

Reed and Russell's result is a good start in describing the received signal amplitude. However, other important signal degradation occurs on the TDRS link, too. Many interesting phenomena occur in the upper atmosphere, as elucidated by a recent IEEE Transactions [7]. This key issue on astronomy and remote sensing has outlined the atmospheric constituents that have been measured at millimeter wavelengths. These include ozone, chlorine monoxide, water vapor, nitrous oxide (N₂O), HO₂, and carbon monoxide in the stratosphere. Measurements in the troposphere (altitudes less than 10 km) have concentrated on water vapor at 22.2 GHz and oxygen transitions at 60 GHz. The primary measurement objectives for future missions, as given by Joe Waters, are shown in Figure 8. Note the entire range of objectives extends to 80 km altitude. We treat only oxygen and water vapor attenuation here, and ray tangent heights less than 50 km will usually be required for noticeable attenuation (multipath fading is another matter, and S-band multipath may occur for ray tangent heights of hundreds of km).

The amplitude of the direct ray suffers attenuation in the upper parts of the atmosphere and the reflected ray is attenuated even more than the direct ray. The reflected ray suffers integrated Van Vleck gaseous attenuation as found in earlier papers [8,9].

$$A_o = \frac{.34}{\lambda^2} \left(\frac{-H_o}{\sin E} \right) \left[\frac{1}{2K_1} \ln \left(\frac{\left(\frac{1}{\lambda} \right)^2}{\left(\frac{1}{\lambda} \right)^2 + K_1 v_1^2} \right) + \frac{1}{2K_2} \ln \left(\frac{\left(2 + \frac{1}{\lambda} \right)^2}{v_1^2 K_2^2 + \left(2 + \frac{1}{\lambda} \right)^2} \right) + \frac{1}{2K_2} \ln \left(\frac{\left(2 - \frac{1}{\lambda} \right)^2}{\left(2 - \frac{1}{\lambda} \right)^2 + K_2^2 v_1^2} \right) \right] \quad (3-5)$$

dB, total oxygen attenuation (1 GHz < f < 50 GHz)

- where K_1 = 0.018
- K_2 = 0.049
- λ = wavelength in cm
- E = elevation angle, radians

H_0 = 7 km (oxygen scale height)
 v_1 = $\exp(-h_1/H_0)$
 h_1 = height of ground reflection point above sea level, km

$$A_{H_2O} = \left(\frac{0.0035}{\lambda^2} \right) \frac{\rho_o}{K_3} \left(\frac{H_0}{\sin E} \right) \left[+ \frac{2v_1^3}{3} - \frac{a_1}{K_3^2} \left[v_1 - \frac{\sqrt{a_1}}{K_3} \tan^{-1} \frac{K_3 v_1}{\sqrt{a_1}} \right] - \frac{a_2}{K_3^2} \left[v_1 - \frac{\sqrt{a_2}}{K_3} \tan^{-1} \left(\frac{K_3 v_1}{\sqrt{a_2}} \right) \right] \right] \quad (3-6)$$

dB H₂O attenuation.

where K_3 = 0.087,
 ρ_o = water vapor density at the earth's surface, g/m³.

$$a_1 = \left(\frac{1}{\lambda} - \frac{1}{1.35} \right)^2; \quad a_2 = \left(\frac{1}{\lambda} + \frac{1}{1.35} \right)^2$$

The total gaseous attenuation will be assumed to be the sum of Equations 3-5 and 3-6.

Crane's rain attenuation [10,11,12] may also be introduced for earth grazing ray attenuation. It is usually omitted because it is representative of rays less than 4 km altitude.

The TDRS antenna pattern is the final item considered here. The general antenna pattern given by Silver for a uniformly illuminated parabolic dish has been found useful in previous TDRS interference studies [13]. The antenna off-boresight loss for the reflected ray may then be described by:

$$G(U) = 10 \log_{10} \left[2 \frac{J_1(U)}{U} \right]^2 \text{ dB} \quad (3-7)$$

where $U = \frac{\pi D}{\lambda} \sin$ (off-boresight angle)

D = antenna diameter, same units as wavelength
 λ

Equation (4-7) has been found to be useful at the TDRS S, Ku, and Ka-bands.

With

A_a = Gain loss for reflected ray (off-boresight), dB (Equation 3-7).
 A_{atm} = Atmospheric loss for reflected ray - Atmospheric loss for direct ray, dB (Equation 3-5 plus Equation 3-6).

The front-to-side ratio can be found from

$$F_s = 10^{\left[\frac{(A_a + A_{atm})}{10} \right]} \quad (3-8)$$

and substituted into Equation 3-4 for the magnitude of the received signal amplitude.

Figure 9 shows potential multipath regions in the polar regions. In addition, Reed and Russell show considerable multipath effects within the satellite horizon. We also consider these effects in the results section.

3.2 Ground Station Attenuation

The integrated gaseous attenuation equations of Section 3.1 may also be used for the ground station at Tidbinbilla. The appropriate substitutions are made for ground station elevation angle and ground station altitude above sea level. The rain model proposed by R. K. Crane is used here in the following form:

$$A_R = \frac{H_R}{\sin(E)} \alpha_1 \gamma \beta R_p^{(\beta - \alpha_e)} \text{ dB} \quad (3-9)$$

where:

H_R = Rain model height above ground station, km

E = elevation angle of ground antenna, degrees

α_1 = $0.01 \left(\frac{F_G}{10} \right)^{2.3502}$

F_G = Frequency, GHz

γ = $2.3 \log_{10}[v]$

$$\begin{aligned} v &= H_r / (\tan(e)) \\ \beta &= 1.18 - 0.00475 (F-10) \\ de &= 0.3 \log_{10}[v] \end{aligned}$$

The height of the model rain cell is typically more than 3 km and is a function of ground station latitude. Dr. Ippolito of Stanford Telecom has pointed out that rain cell height is a function of intensity.

Rain attenuation is intrinsically a probabilistic phenomenon. It has been the subject of many excellent theoretical studies over several decades. Lin [14] has described rain attenuation as lognormal over several orders of magnitude. Our primary interest here is only in the two orders of magnitude between 0.01 and 0.0001 rainfall probability, and a much simpler function is adequate for us.

Rain attenuation may often be treated as a two-parameter exponential probability density function over two orders of magnitude. This is apparent in a form of the Rice Holmberg relations for attenuation given by Dutton [15], and the exponential function has been useful in other derivations. For example, constant elevation angle experiments conducted with Applications Technology Satellite-6 (ATS-6) were quantitatively different at each ground location, but they would be represented approximately by:

$$P(A_R \geq A) = \phi \exp - \frac{(A - \lambda)}{\beta}, \text{ for } A \geq \lambda \quad (3-10)$$

where rain attenuation $A_R \geq$ an arbitrary attenuation A , dB.

- ϕ = fraction of time noticeable rain or cloud attenuation occurs, typically A dB.
- λ = lower cut-off for exponential distribution, dB.
- β = standard deviation of exponential distribution, dB.

We assume that λ and β can be weighted by (cosecant elevation) so that equation (3-9) can apply to other elevation angles. We also assume that attenuation has a frequency dependence described by Crane's rain model.

A rain region F is assumed for Tidbinbilla. (This will be subject to change). The rain rate at 0.99 exceedance probability is 1.7 min/hr and the corresponding rain rate at the 0.999 level is 5.5 min/hr.

The total atmospheric attenuation (rain attenuation + gaseous attenuation) at Tidbinbilla is seen on Figure 10 to be a strong function of elevation angle. If ground station attenuation were the only concern, the Indian Ocean relay would be located near Australia. However, this would cause multipath losses on the space-space link to increase sharply.

Overall relay communication performance is more closely related to the sum of ground station losses and SSL losses than to any single loss.

4.0 GEOSTATIONARY RESULTS

All three relay satellites are geostationary for these examples. This rare event would occur when TDRS East, TDRS West, and the Indian Ocean relay have 42164 km semimajor axis, zero inclination, and zero eccentricity. The elevation angle from Tidbinbilla to the Indian Ocean relay is therefore constant once the Indian Ocean longitude is chosen. The SSL link to a low orbiter is simulated at 5 second intervals. All three relays are checked for visibility and multipath loss, and the relay which is visible and has minimum loss is chosen as the preferred relay. The minimum loss is saved from interval to interval, and loss statistics are compiled. After 24 hours of orbital simulation, the maximum (of the minimum losses) is added to the uplink loss and saved as SUMLOSS.

Figure 11 shows SUMLOSS results for a range of Indian Ocean relay longitudes. The Gamma Ray Observatory (GRO) is chosen both for its important mission and for its characteristic orbital elements. The GRO semimajor axis is approximately 6829 km and has 28.5 deg. orbital inclination. The downlink losses at 99.9 percentile level are used for the top curve SUMLOSS999. The top curve clearly favors relay positions east of 95 east for S-band SSLs. An absolute minimum is reached in the vicinity of 125 East. The downlink loss is indicated by SGL999 and the average space-space loss is shown as AVSSL. Figure 12 shows conceptually similar results, but for a Ku band SSL. The average SSL loss is lower than the corresponding loss at S band, but the optimum relay position is in the same 125 East vicinity as the S band case.

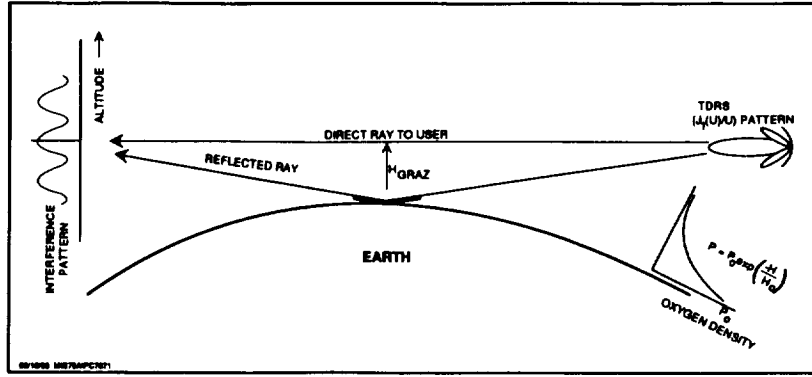


Figure 7: Interference Pattern (Multipath) for a Marginal TDRS - User Link

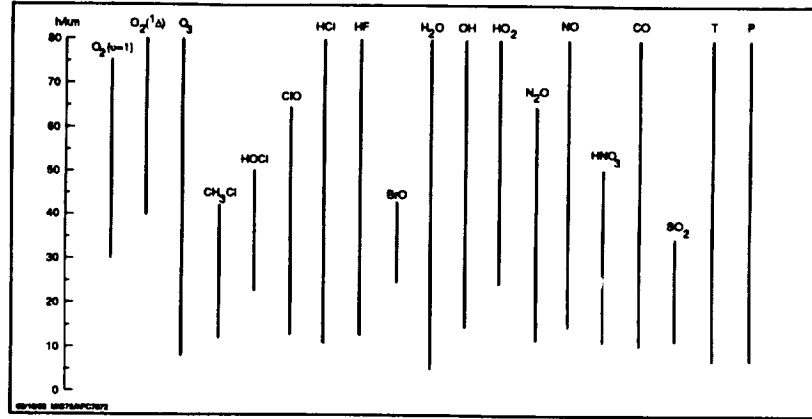


Figure 8: Measurement Objectives for Future NASA Millimeter/Submillimeter Wave Earth Observations (Joe W. Waters, 1992)

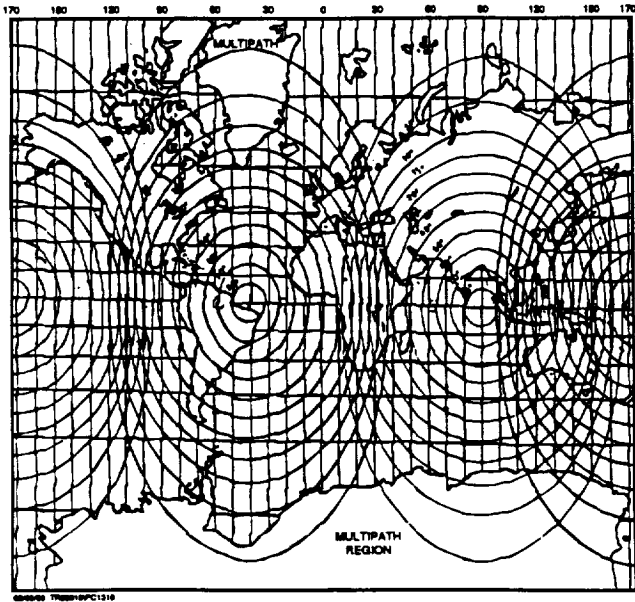
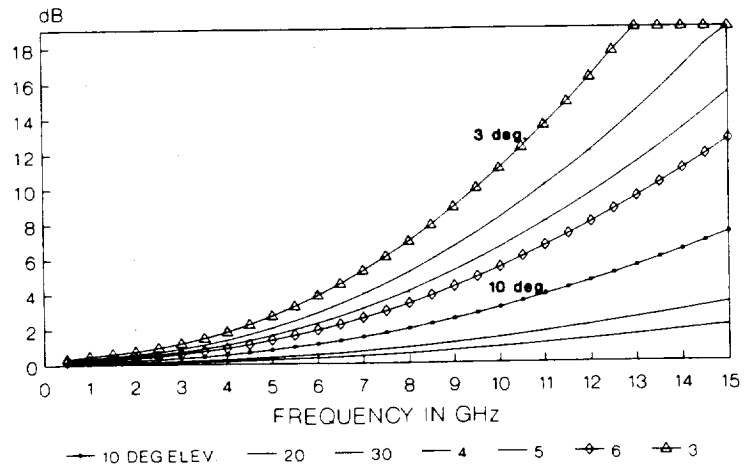


Figure 9: Potential Multipath Regions TDRS at 180°E, 317°E and 90°E



TIDBINBILLA ASSUMED IN CRANE'S REGION F

PC 3/4/84
ATM07

Figure 10: Tiddinbilla Atmospheric Attenuation
 $P=0.999$, Region F, Rain Rate=5.5 MM/HR

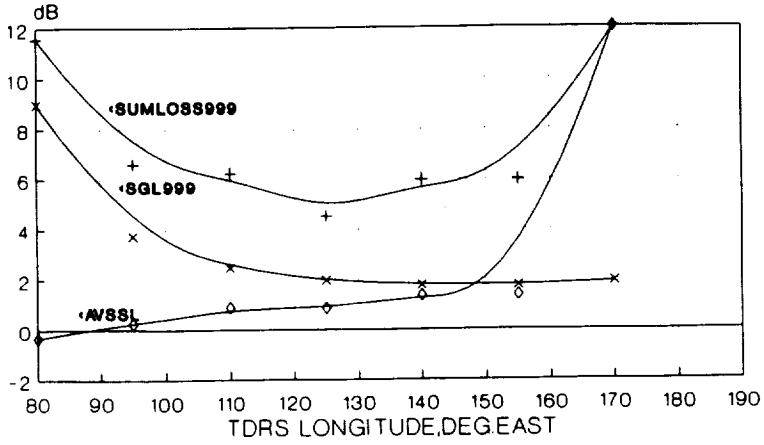


Figure 11: Tidbinbilla-TDRS-GRO Sumloss
2.2875 GHz SSL $I_{TDRS}=0$

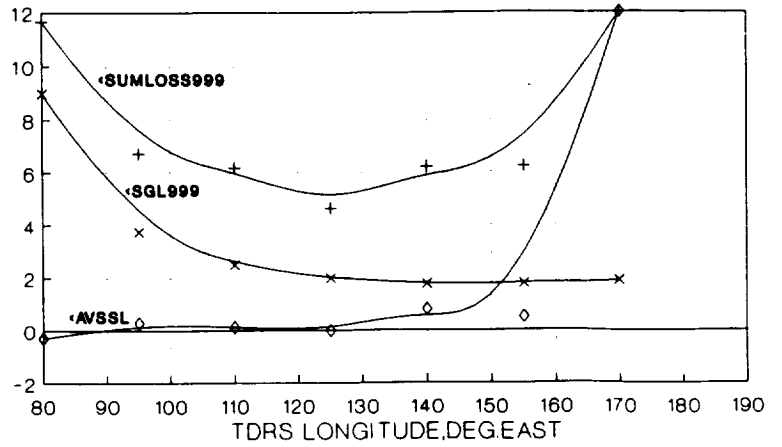


Figure 12: Tidbinbilla-TDRS-15 GHz SSL $I_{TDRS}=0$

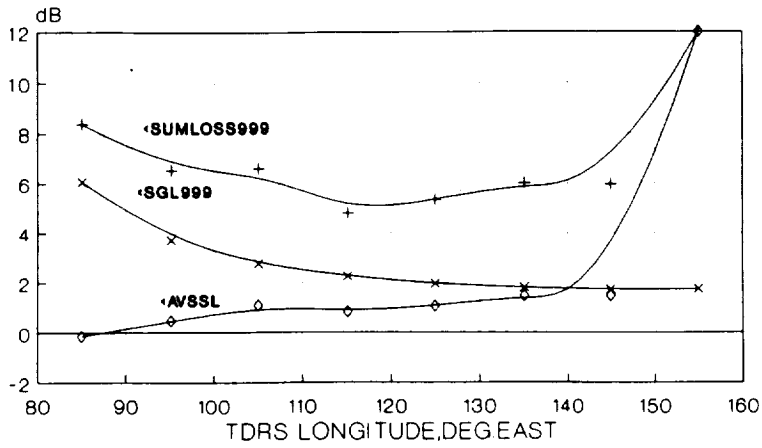
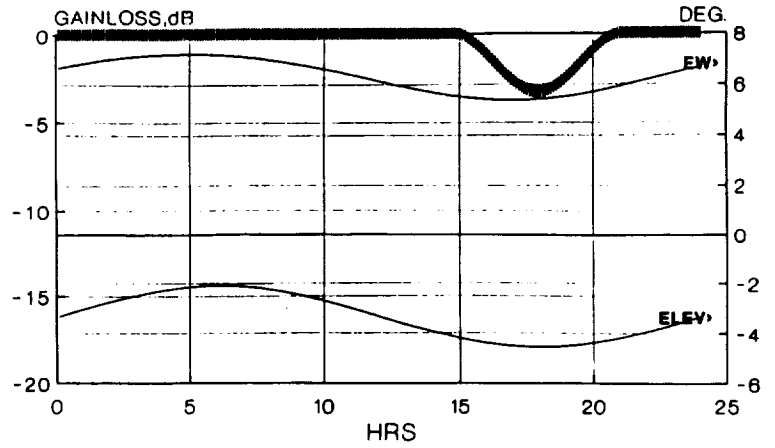


Figure 13: Tidbinbilla-TDRS-Shuttle Sumloss
2.2875 GHz SSL $I_{TDRS}=0$



+ GAINLOSS,dB — EW,DEG. — ELEV,DEG.
 WORST GAINLOSS--3.26dB
 MIN ELEV---4.639DEG.

PC 10/7/9:
ASB

Figure 14: 85E to Tidbinbilla $I=10$ Deg
Roll=-2, Yaw=-1.0 Deg, SW2 Limit=-4.155 Deg
SGL BW=0.7 Deg $F=13.73$ GHz

Figure 13 shows results for links to a 200 km altitude satellite, such as the shuttle. The inclination is again 28.5 deg. The optimum relay position is near 115 East for both S band SSL and Ku band SSL.

5.0 TOTAL LOSS FOR NON-GEOSTATIONARY RELAYS

TDRS-1 may have some difficulty in pointing the space to ground (SGL) link antenna toward Tidbinbilla. The antenna is software limited at 4.15 deg. South, and some conditions may require more southerly pointing. Figure 14 shows the diurnal gainloss effects due to mispointing the SGL antenna. The SGL elevation angle is seen to dip below -4.15 deg. elevation (right scale) at 16 hours and the resultant SGL antenna gain (top curve) suffers. Over 3 dB gain loss would be expected in this case. This "worst gain loss" is actually a function of relay longitude, inclination, roll and yaw.

The NASA Flight Dynamics Facility has supplied long term calculations for TDRS-1 inclination. They may be approximated by an equation as [16]

$$i = 4.79178 + 0.393246 x + 0.128427 x^2 - 0.0209437 x^3 + 0.00133576 x^4 + 0.0000383016 x^5 + 4.04173 \cdot 10^{-7} x^6 \text{ deg.}$$

where i = inclination, deg.
 X = year after 1990

The inclination may be plotted as Figure 15.

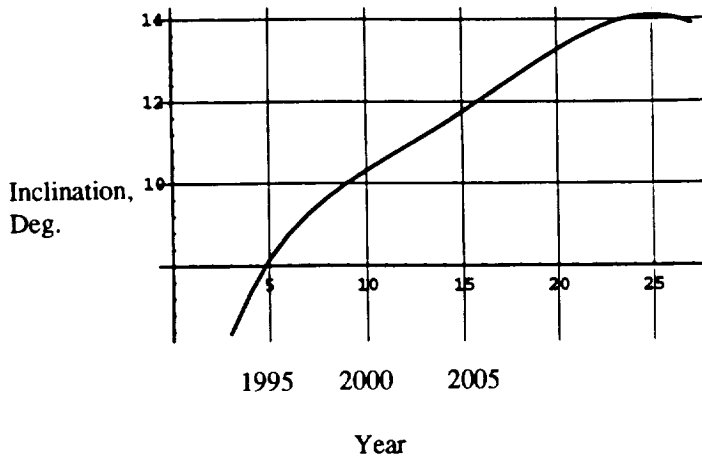


Figure 15 : TDRS-1 Inclination vs. Time

Figure 15 implies an 8 degree inclination in late 1994. An 8 deg. inclination and negative 1.8 deg. roll may be used to examine alternative relay positions. A large array of

runs conceptually similar to Figure 14 may be used to generate the gain loss results of Figure 16. The Mathematica two dimensional curve fit for gain loss yields

$$\begin{aligned} \text{SGL Gain Loss=} & 5.63641 \cdot 10^{-6} + 0.000204767 \text{ LON} + 0.00450539 \text{ LON}^2 - \\ & 0.000185253 \text{ LON}^3 + 2.61605 \cdot 10^{-6} \text{ LON}^4 - 1.4523 \cdot 10^{-8} \\ & \text{LON}^5 + 2.77005 \cdot 10^{-11} \text{ LON}^6 + 3.63655 \cdot 10^{-8} Y - 3.56642 \\ & 10^{-6} \text{ LON} Y - 0.000547018 \text{ LON}^2 Y + 3.43689 \cdot 10^{-6} \text{ LON}^3 \\ & Y + 0.000166314 Y^2 + 0.00910266 \text{ LON} Y^2 - \\ & 0.0000636192 \text{ LON}^2 Y^2 + 7.02275 \cdot 10^{-6} Y^3 + 0.00079983 \\ & \text{LON} Y^3 + 0.000391586 Y^4 + 0.0000232073 Y^5 \end{aligned}$$

where LON = relay longitude deg.
and Y = YAW, deg.

Figure 16 is difficult to examine quantitatively. Figure 17 shows 1.0 dB contour intervals for a wide range of longitudes and spacecraft yaw. Less than 4.0 dB SGL gain loss is seen for most yaw conditions at relay positions west of 90E.

This provides an interesting contrast for the loss results of Figure 11. The sum of downlink and forward link losses increased sharply for relay positions west of 90E. The sum of uplink losses, forward losses, and SGL gain loss may be shown as total loss in Figure 18, or the Mathematica functional approximation for total loss as

$$\begin{aligned} \text{Total Loss=} & 0.000301945 + 0.0109703 \text{ LON} + 0.241427 \text{ LON}^2 - \\ & 0.00795836 \text{ LON}^3 + 0.0000979854 \text{ LON}^4 - 5.32179 \cdot 10^{-7} \\ & \text{LON}^5 + 1.07592 \cdot 10^{-9} \text{ LON}^6 + 3.61795 \cdot 10^{-8} Y - 3.57324 \cdot 10^{-6} \\ & \text{LON} Y - 0.00547041 \text{ LON}^2 Y + 3.43711 \cdot 10^{-6} \text{ LON}^3 Y + \\ & 0.000340661 Y^2 + 0.0092383 \text{ LON} Y^2 - 0.0000647599 \\ & \text{LON}^2 Y^2 + 7.01938 \cdot 10^{-6} Y^3 + 0.000799475 \text{ LON} Y^3 + \\ & 0.000566351 Y^4 + 0.0000231966 Y^5 \end{aligned}$$

Figure 19 is a contour plot of Figure 18 with 1 dB intervals. A near-minimum total loss condition exists between 98-105 E. The contour plot shows the interesting case of optimum position shifting to 102E for perfect spacecraft attitude control and zero yaw.

Figure 20 allows a closer look at the optimum longitude regions. Finer increments were chosen for the runs, and the entire 90°-100° E region is attractive. It also shows the interesting shift westward for negative yaw.

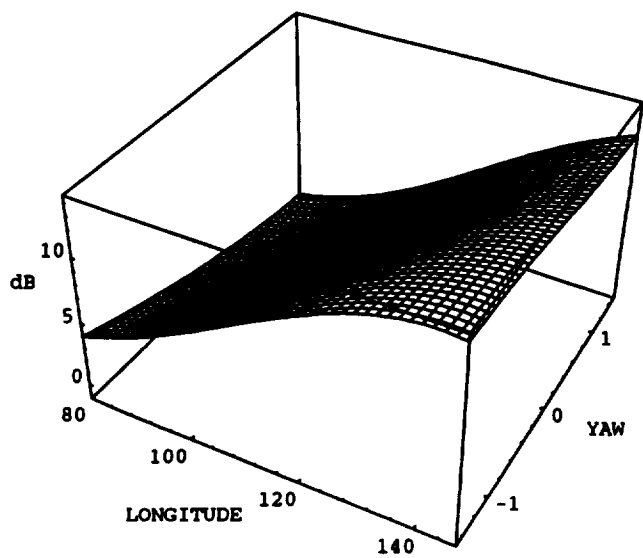


Figure 16: Maximum Gain Loss (dB) as a Function of Longitude and Spacecraft Yaw $l = 8^\circ$, November 1994

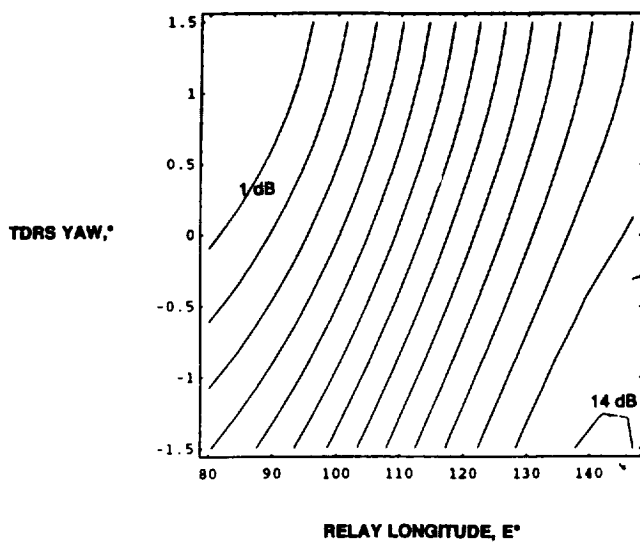


Figure 17: SGL Maximum Gain Loss at 1.0 dB Intervals $l = 8^\circ$, November 1994

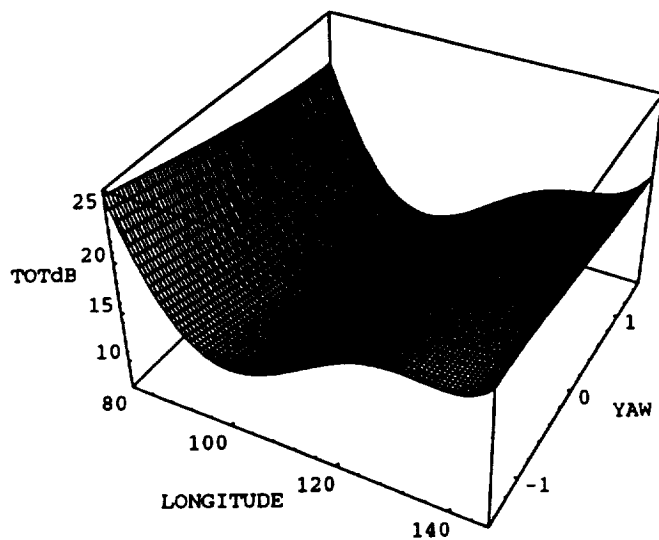


Figure 18: Total Loss as a Function of Longitude and Yaw $l = 8^\circ$, November 1994

MIS019B

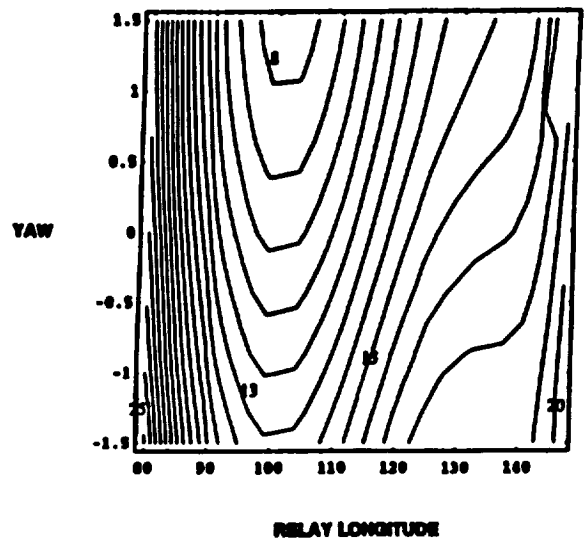


Figure 19: Total Loss at 1 dB Intervals

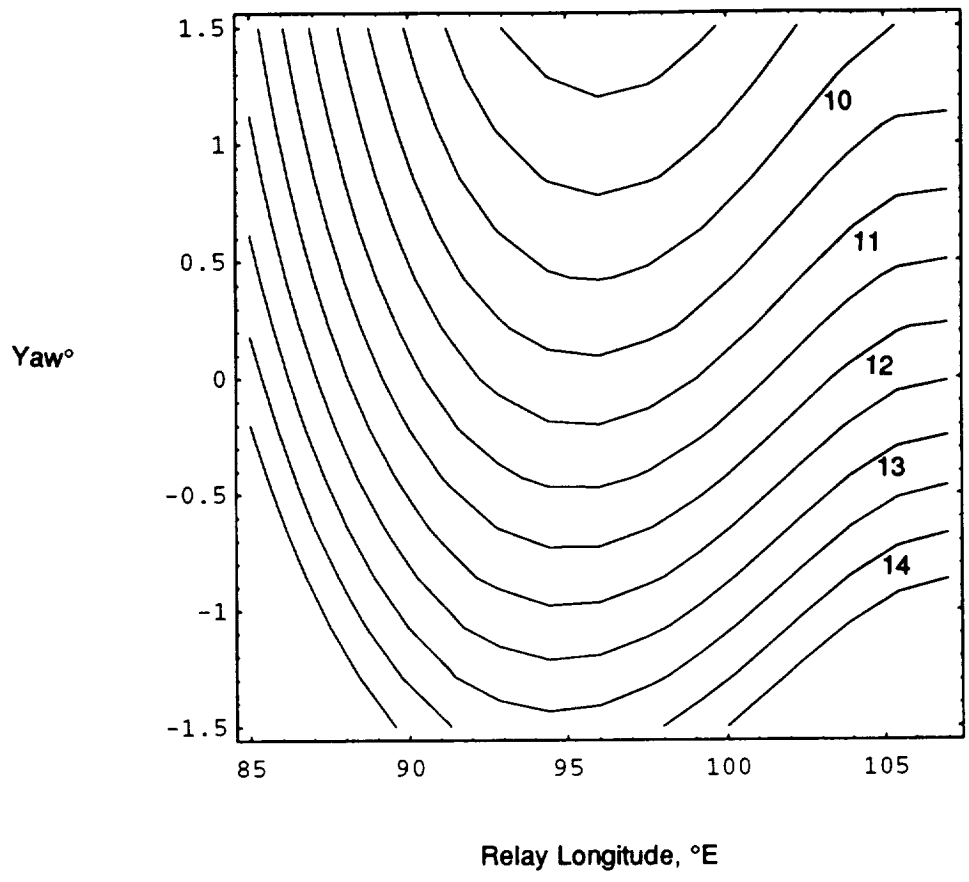


Figure 20: Details of Optimum Relay Region, with Total Loss at 0.5 dB Intervals $l=8^\circ$, November 1994

The benefits of optimizing TDRS-1 mean longitude continue to grow throughout the decade. Inclination will continue to grow with time (Figure 15), and the Tidbinbilla elevation angle would be expected to drop below 6 degrees for a relay mean longitude of 85°E in August 1998 at an inclination of 10 degrees. This would imply a large gaseous and rain attenuation at the ground station. Relay positions in the 90-100°E region would have sizeable advantages in total loss, as shown in the figures of the Appendix.

6.0 CONCLUSIONS

We have discussed a way to optimize relay satellite positions. The conflicting requirements of good downlinks and good satellite to satellite links were reconciled by minimizing the sum of link losses. This method clearly discriminated against any relay position which offered excessive loss, whether as a low elevation angle at a ground station or as an Earth grazing ray on the relay to satellite link.

The method required fast, accurate orbital computation and concise equations for signal loss on the downlink and the SSL. The method of osculating elements was used to calculate all satellite positions at 5 second intervals for a day at each relay longitude. The analytic rates of change of Keplerian elements were shown in succinct form. The oblate Earth perturbations were very important for low orbiting satellites and Ash's lunar perturbation terms became important at geosynchronous altitude and above.

Gaseous attenuation on both the SSL and the downlink was represented by integrated Van Vleck attenuation for oxygen and water vapor. The downlink also included rain attenuation, as modeled by R.K. Crane. The downlink attenuation typically became excessive at low ground elevation angles. Two ray multipath interference was included on the SSL. The SSL fading became excessive for Earth grazing rays. A special space to ground antenna pointing loss was modeled as a function of roll, pitch, and yaw with the aid of the Euler Theorem and experimental TDRS SGL gain patterns.

The utility of the method was shown with examples of TDRS-1 as an Indian Ocean relay. Optimum TDRS longitudes were seen to be dependent on the orbit of the low altitude satellite user, the SSL frequency, the ground station climate, and the TDRS roll and yaw. TDRS-1 longitudes between 90-100E were seen to be attractive for further study.

The method will be useful for a number of other cases. A variety of downlink and SSL conditions apply not only to future TDRSS concepts, but also to new low altitude satellite communication concepts. Ground stations at a variety of locations may be considered by changing the rain region and coordinates. Space-space link frequencies between 1-55 GHz may be used with the current set of integrated Van Vleck attenuation equations.

Acknowledgements

Shannan Bloomquist solved the Gordian Knot of long equations in narrow columns. George McKay suggested key ways to simplify the figures. Charlo Mullen offered invaluable tips on the legibility of reduced text. Charles Downs of BFEC provided checks on TDRS-1 orbital elements.

REFERENCES

1. Moulton, F. R. (1914). *An Introduction to Celestial Mechanics*, MacMillan Co., N.Y., 1914.
2. Ash, M. (1974). "Doubly Averaged Effect of the Moon and Sun on a High Altitude Earth Satellite Orbit," TN 1974-5, Lincoln Laboratory, 1 March, 1974.
3. Christopher, P., S. M. Maciorowski, and L. Allen (1976). "High Altitude Satellite Communication, with Crosslinks." Proceedings of Summer Computer Simulation Conference, July 1976.
4. Townsend, G. E., Jr. (1963). *Orbital Flight Handbook*, Vol. 1, Part 1, NASA SP-33, NASA, Washington, D.C., 1963.
5. Bate, Roger D., Donald D. Mueller, and Jerry E. White (1971). *Fundamentals of Astrodynamics*, Dover Pubs, N.Y., 1971.
6. Reed, H. R. and Russell, C. M. (1964). *Ultra High Frequency Propagation*, Boston Technical Publishers, Inc. Lexington, MA, 1964.
7. Waters, J. W. (1992). "Submillimeter-Wavelength Heterodyne Spectroscopy and Remote Sensing of the Upper Atmosphere," IEEE Proc., November, 1992, p. 1679.
8. Kerr, D. 1965. *Propagation of Short Radio Waves*, Dover Publications, N.Y., N.Y., (1965). (Originally

published as Vol. 13 of the MIT Rad Laboratory Series, McGraw-Hill, 1951.)

9. Kamal, A. K. and Christopher, P. (1981). "Communications at Millimeter Wavelengths," Proc. ICC, June, 1981.
10. Frediani, D. J. (1979). "Technology Assessment for Future MILSATCOM Systems: The EHF Band," Lincoln Laboratory Project Report DCA-5, 12 April 1979.
11. Crane, R. K. (1980). "Prediction of Attenuation by Rain," IEEE Transactions on Communications, Vol. Com-28, No. 9, September 1980.
12. Ippolito, L. J., R. D. Kaul, and R. G. Wallace (1981). "Propagation Effects Handbook for Satellite Systems Design," NASA Reference Publication 1082 (Second Edition), December 1981.
13. Silver, S. (1965). *Microwave Antenna Theory and Design*, Dover, N.Y., 1965.
14. Lin, S. H. (1979). "Statistical Behavior of Rain Attenuation, Bell System Technical Journal, Vol. 52, No. 4, pp. 557-581.
15. Bean, B. R. and E. J. Dutton (1966). *Radio Meteorology*, NBS Monograph 92, U.S. Department of Commerce, 1966, pp. 270-274.
16. Wolfram, S. (1991). *MATHEMATICA a System for Doing Mathematics by Computer*, Second Edition, Addison Wesley Publishing Co., Inc., 1991.

Appendix: Total Loss in 1998, with $I=10$ Degrees

Figure A-1 shows expected total loss vs. TDRS-1 relay longitude and yaw for a Tidbinbilla ground station. Approximately 4 to 5 dB advantage is shown on the contour plot of Figure A-2 for a relay at 93E versus a relay at 85E.

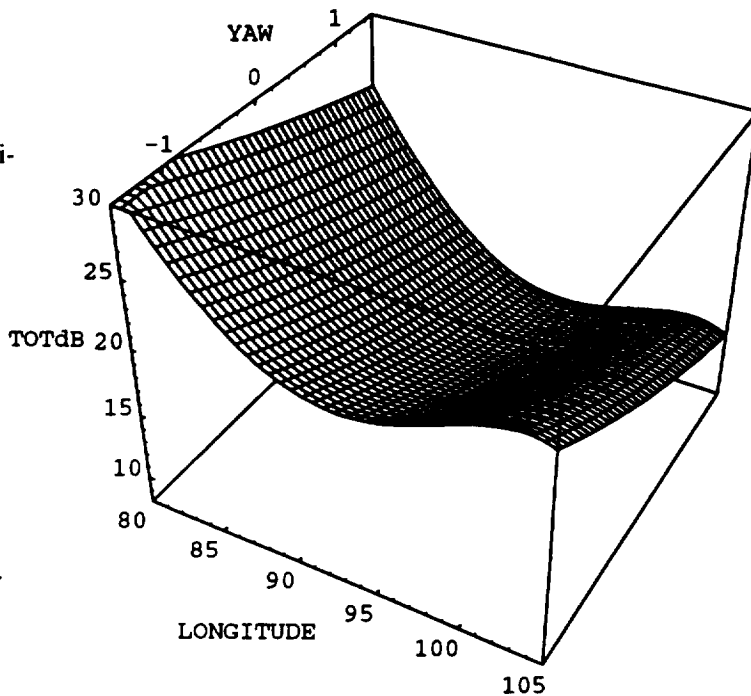


Figure A-1: Total Loss as a Function of Longitude and Yaw $I=10^\circ$, August 1998

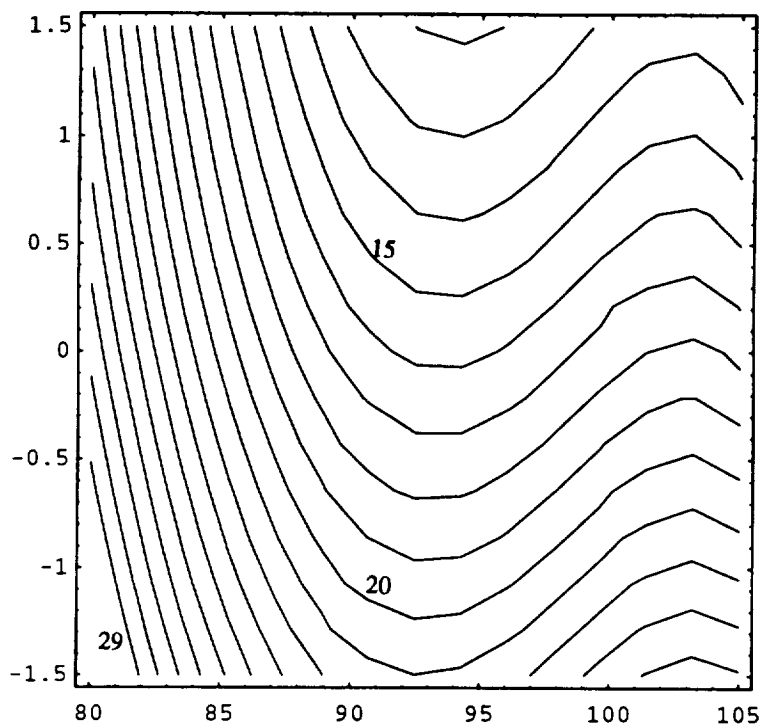


Figure A-2: Total Attenuation with 1 dB Contour Intervals $I=10^\circ$, August 1998

TDRSS Onboard Navigation System (TONS) Flight Qualification Experiment*

C. J. Gramling, R. C. Hart, and D. C. Folta
Goddard Space Flight Center (GSFC)
Greenbelt, Maryland, USA

A. C. Long
Computer Sciences Corporation (CSC)
Lanham-Seabrook, Maryland, USA

Abstract

The National Aeronautics and Space Administration (NASA) Goddard Space Flight Center (GSFC) is currently developing an operational Tracking and Data Relay Satellite (TDRS) System (TDRSS) Onboard Navigation System (TONS) to provide realtime, autonomous, high-accuracy navigation products to users of TDRSS. A TONS experiment was implemented on the Explorer Platform/Extreme Ultraviolet Explorer (EP/EUVE) spacecraft, launched June 7, 1992, to flight qualify the TONS operational system using TDRSS forward-link communications services. This paper provides a detailed evaluation of the flight hardware, an ultrastable oscillator (USO) and Doppler extractor (DE) card in one of the TDRSS user transponders, and the ground-based prototype flight software performance, based on the 1 year of TONS experiment operation. The TONS experiment results are used to project the expected performance of the TONS I operational system. TONS I processes Doppler data derived from scheduled forward-link S-band services using a sequential estimation algorithm enhanced by a sophisticated process noise model to provide onboard orbit and frequency determination and time maintenance. TONS I will be the prime navigation system on the Earth Observing System (EOS)-AM1 spacecraft, currently scheduled for launch in 1998.

Inflight evaluation of the USO and DE short-term and long-term stability indicates that the performance is excellent. Analysis of the TONS prototype flight software performance indicates that realtime onboard position accuracies of better than 25 meters root-mean-square are achievable with one tracking contact every one to two orbits for the EP/EUVE 525-kilometer altitude, 28.5-degree inclination orbit. The success of the TONS experiment demonstrates the flight readiness of TONS to support the EOS-AM1 mission.

Introduction

The Tracking and Data Relay Satellite (TDRS) System (TDRSS) provides National Aeronautics and Space Administration (NASA) low Earth-orbiting spacecraft with telemetry, command, and tracking services. These user spacecraft require position, time, and frequency knowledge to maintain precise attitude control, antenna pointing to each TDRS, and operational health and safety and to annotate their science data. Currently, TDRSS supports user orbit, frequency, and time determination through ground-based extraction and processing of range and either two-way or one-way return-link Doppler tracking data. Future TDRSS user mission profiles forecast the need for onboard, realtime, high-accuracy position knowledge to 10 meters (1σ), time determination to 1 microsecond (1σ), and frequency determination to 1 part in 10^{12} (1σ). These missions also require systems that can be easily integrated into a user's onboard environment, with minimal power, weight, and volume penalty to the spacecraft subsystems and low budgetary impact. The TDRSS Onboard Navigation System (TONS), developed by NASA, can meet these objectives via the onboard extraction of high-fidelity tracking measurements from a forward-link signal using components already available on a TDRSS user spacecraft.

The ultimate objective is to develop an autonomous user navigation system that (1) supports accurate onboard orbit, time, and frequency determination, based on observation of a continuously available, unscheduled navigation beacon signal; (2) decreases the user's reliance on TDRSS ground operations and scheduled TDRSS resources; and (3) provides

* This work was supported by the National Aeronautics and Space Administration (NASA)/Goddard Space Flight Center (GSFC), Greenbelt, Maryland, under Contract NAS 5-31500.

sufficient failure recovery modes to maintain or extend the user lifetime to accomplish science objectives. TONS is being developed in stages: the one-way return-link Doppler navigation experiment hosted on the Cosmic Background Explorer (COBE) spacecraft; the TONS experiment successfully flown on Explorer Platform (EP)/Extreme Ultraviolet Explorer (EUVE); and the TONS I, TONS II-A, and TONS II operational systems. This paper discusses the TONS experiment implementation and provides an assessment of the performance of the TONS hardware and software components as the predecessor to an operational TONS I implementation.

TONS Development

Future NASA mission navigation requirements, such as those for the Earth Observing System (EOS)-AM1 mission, point to the need for autonomous onboard navigation. By offering various levels of upgrades to TDRSS user spacecraft and TDRSS capabilities, TONS allows corresponding increases in the degree of user navigation autonomy, navigation services, and failure recovery modes. In addition, TDRSS onboard navigation options will provide graceful degradation modes to maintain user autonomy and/or extend spacecraft mission lifetime, with little impact on the user spacecraft itself. The operations concept for each of the TONS stages is explained in Reference 1 and is summarized below.

The first stage was the navigation experiment on the COBE spacecraft, in which an external ultrastable oscillator (USO) provided a reference frequency to a second-generation TDRSS user transponder to supply accurate one-way return-link Doppler measurements for ground-based orbit and frequency determination. This experiment demonstrated that one-way return-link noncoherent Doppler tracking provides equivalent accuracy to two-way coherent Doppler tracking. This tracking method became operational on COBE and later on the Ocean Topography Experiment (TOPEX)/Poseidon spacecraft. Processing accurate one-way and two-way Doppler tracking of TOPEX provided orbit determination accuracies of better than 10 meters (3σ).

Components for the TONS experiment were integrated into the EP, launched with the EUVE on June 7, 1992. The TONS experiment provided an opportunity to flight qualify TONS by processing Doppler measurements extracted on-orbit in a ground-based flight-emulation environment. The TONS experiment required an S-band multiple-access (MA) or S-band single-access (SA) forward-link scheduled reference signal from TDRSS, a Doppler extractor (DE) card in the second-generation TDRSS user transponder, a USO, and a ground-based navigation processor to process the Doppler measurements downlinked in the user spacecraft telemetry. In addition, software onboard the user spacecraft demonstrated onboard control of user signal acquisition. TDRS ephemerides, computed separately on the ground, are provided as input to the navigation processor. The TONS experiment provided a ground-based version of user spacecraft orbit and frequency determination and onboard control of user signal acquisition, necessary for an operational TONS system.

TONS I uses Doppler measurements derived from an S-band forward-link scheduled TDRSS service to provide onboard orbit and frequency determination and uses the frequency bias estimate for onboard time maintenance. The timetag of the pseudorandom noise (PN) code epoch received by the transponder is used in the User Spacecraft Clock Calibration System (USCCS) to perform time determination on the ground. Figure 1 illustrates the TONS I navigation scenario. TONS I requires the user to have a stable frequency reference, a Doppler measurement capability and PN code epoch receipt timetagging in the user transponder, and onboard navigation processing and signal acquisition software. TONS I is compatible with the current TDRSS configuration and currently available user spacecraft components.

TONS II-A is an augmented version of TONS I that provides the user spacecraft with additional Doppler measurements derived from a forward-link S-band beacon signal, when the TDRSS service is not scheduled for a user, to provide nearly continuous, realtime orbit and frequency determination. This signal can be provided by the current TDRSS using the interservice radiated multiple-access signal available between scheduled user services. The interservice signal is available about 80 percent of the time. Figure 1 also illustrates the TONS II-A navigation scenario with the beacon signal.

All TONS-related upgrades to TDRSS are being designed to be transparent to the standard TDRSS user. The TONS I system is discussed in more detail in Reference 2.

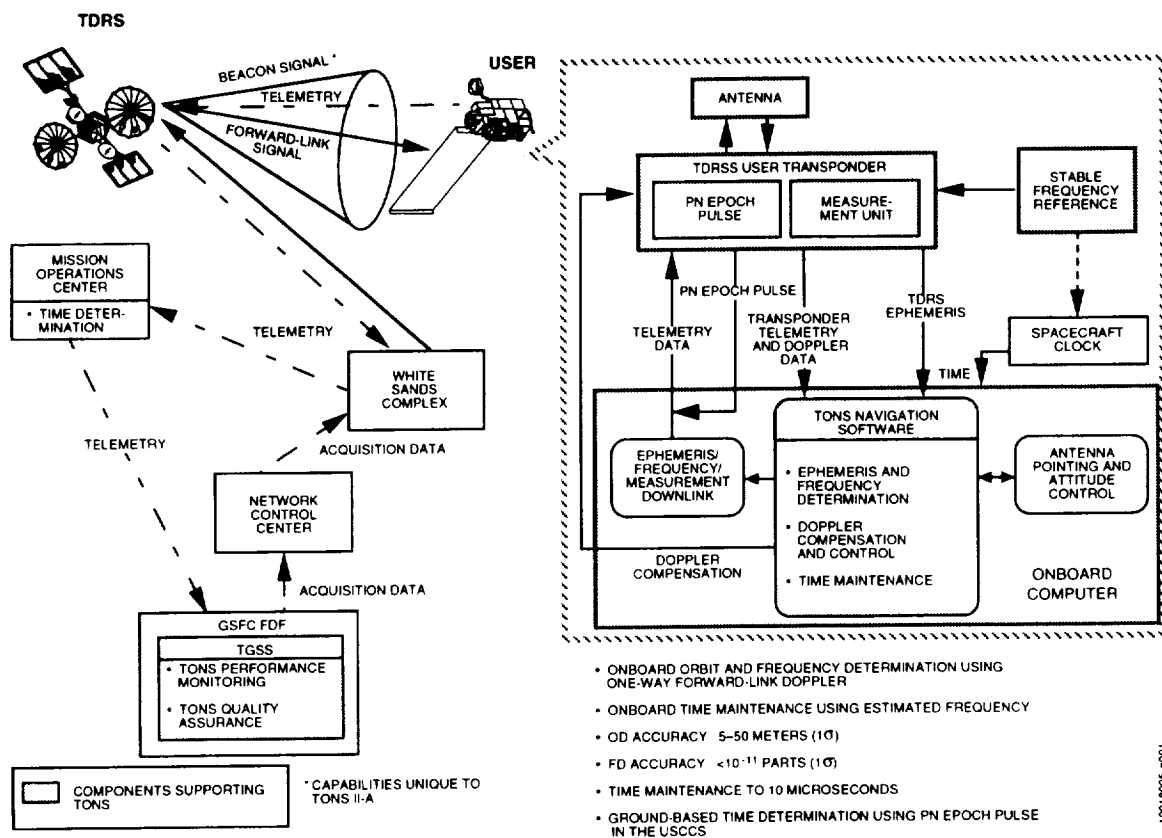


Figure 1. TONS Navigation Scenarios

TONS Experiment Description

The TONS experiment involves flight systems onboard EP/EUVE and ground systems for experiment data processing and performance analysis. Figure 2 provides an overview of the TONS experiment configuration. During the 1 year of the TONS experiment, all major experiment objectives were accomplished:

- The TONS flight hardware components, the USO and DE card, were successfully activated and provided excellent performance well within specifications.
- The onboard Doppler compensation (OBDC) application resident in the EP/EUVE 1750A coprocessor was successfully activated and demonstrated onboard signal acquisition for more than 90 TDRSS contacts with a 100-percent success rate.
- The accuracy and processing efficiency of the TONS prototype flight software was demonstrated using the Doppler measurements extracted onboard.
- Modifications to the baseline TONS navigation algorithms were evaluated with respect to improved accuracy and processing efficiency.
- The accuracy of the TONS prototype flight software was verified by comparison with independent high-accuracy EP/EUVE ephemerides determined by Jet Propulsion Laboratory (JPL) personnel by processing Global-Positioning-System (GPS)-derived measurements.

This paper discusses these accomplishments and presents the conclusions and recommendations. Detailed discussions are provided in References 3 and 4.

The EP, TDRSS, and ground segments for the experiment are described in the following paragraphs. The space and ground segments of this configuration are described in detail in References 5 through 8.

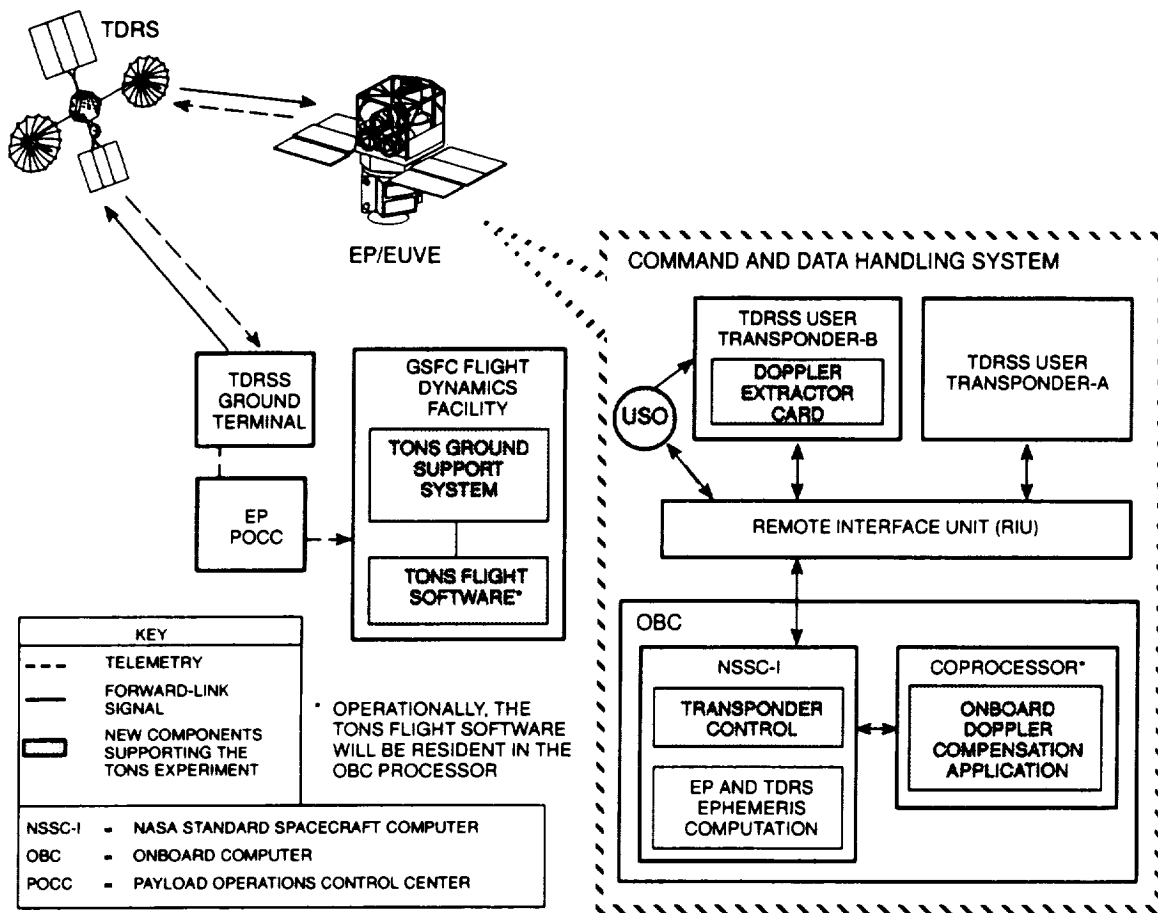


Figure 2. TONS Experiment Overview

EP and TDRSS Segments

Two second-generation TDRSS user transponders are onboard EP/EUVE, one of which, Transponder-B, is augmented with a DE card. An external USO supplies a stable frequency reference to Transponder-B for Doppler measurement. Both the transponder and the USO are controlled via a Remote Interface Unit (RIU) on EP. The transponder/DE/RIU configuration implemented for the TONS/EUVE experiment is not optimal. Three different oscillators provide the timing and frequency references supporting the Doppler measurement, Doppler count accumulation, and telemetry data collection operations via the RIU. This configuration produces unnecessary timing ambiguities.

The transponder's microprocessor sends 24-bit frequency control words (FCWs) to the receiver's numerically controlled oscillator (NCO) every 500 microseconds to maintain lock with the received TDRSS forward-link signal. The DE card accumulates 20480 of these internal FCWs to a resolution of 0.01 hertz at S-band in a 40-bit accumulator. The aggregate count is latched at 10.24-second intervals.

The nondestruct 40-bit Doppler count measurement, along with additional transponder status telemetry bits, is placed in the EP/EUVE downlink engineering telemetry stream and transmitted to the Goddard Space Flight Center (GSFC) Flight Dynamics Facility (FDF) via the POCC. The average Doppler frequency over 10.24 seconds is computed from the nondestruct Doppler counts and processed using the TONS prototype flight software to estimate the EP/EUVE orbit and onboard reference (USO) frequency offset.

In addition, EP/EUVE has the capability for onboard Doppler compensation and control of TDRSS forward-link signal acquisition to within the transponder's ± 1500 -hertz bandwidth using an OBDC application resident in the EP/EUVE coprocessor (a MIL STD 1750A microprocessor) and stored commands. The OBDC application computes the predicted instantaneous Doppler shift of the forward-link signal based on TDRS and user spacecraft vectors and converts the

predicted shift to an external transponder FCW. This 16-bit FCW is input as a serial command to the transponder and is updated every 8.192 seconds on EP/EUVE throughout the contact. At EP/EUVE's maximum Doppler rate of 55 hertz per second, an 8.192-second update rate changes the FCW to offset the receiver by approximately 450 hertz. After the transponder achieves signal acquisition, new FCWs are processed only if the receiver loses lock. The OBDC process replaces the current method of signal acquisition, in which the ground terminal must dynamically compensate the forward-link signal to eliminate the apparent Doppler shift at the spacecraft. The POCC then requests that this frequency variation be inhibited when acquisition is verified so that a valid tracking service can be initiated.

EP/EUVE also hosts a Motorola GPS Demonstration Standard Positioning System (SPS)/L1 receiver/processor (GPSDR) assembly unit as a secondary experiment in the Payload Equipment Deck (PED). The downlink telemetry includes the GPS tracking measurements, which were used by JPL experimenters to determine a high-accuracy EP/EUVE solution in a sophisticated ground-based system.

Experiment Ground Segment

To support the ground-based flight demonstration, the GSFC/Flight Dynamics Division (FDD) developed the TONS Ground Support System (TGSS) and TONS prototype flight software. The TGSS processes the EP/EUVE telemetry data, analyzes tracking data quality, and provides tools for assessing performance of the onboard hardware and software experiment components. The TONS prototype flight software performs the navigation processing in an emulated flight environment created by the TGSS. The TONS flight software schedules and executes the navigation processing tasks, including the processing of TDRSS one-way forward-link Doppler measurements and other data required by the navigation algorithm (e.g., TDRS ephemerides, tracking schedule), state vector propagation and estimation, Doppler compensation prediction, and output of navigation-related data. The design for the TGSS and prototype flight software is presented in Reference 6.

The flight software environment approximates the flight processing environment on EP/EUVE to achieve a major objective of the TONS experiment, i.e., developing and demonstrating the prototype TONS I flight software. The prototype flight software was developed in Ada on a Digital Equipment Corporation (DEC) MicroVAX 3100. The software was crosscompiled using the Tartan Ada crosscompiler for execution in the onboard coprocessor, a MIL STD 1750A architecture microprocessor that runs at 15 megahertz and executes at a peak rate of approximately 2 million instructions per second (MIPS). In the TONS operational systems, the TONS flight software will reside in the user spacecraft's onboard processor.

The accuracy of the navigation process depends on the quantity and quality of the Doppler measurements extracted onboard, the accuracy of the TDRS ephemerides, and the algorithms and models used for processing. The TONS flight software algorithms were selected (1) to provide a realtime ephemeris accuracy of 10 meters (1σ), with continuous tracking of low Earth-orbiting spacecraft; (2) to require a maximum of 256K bytes for the navigation processing; (3) to consume no more than 20 percent of the available central processing unit (CPU) of a 2-MIPS MIL STD 1750A microprocessor; and (4) to provide operational simplicity and ease of adaptability to a beacon tracking environment. To meet these goals, a sequential estimation algorithm was selected and provided with a sophisticated process noise model to improve performance and robustness. These algorithms are defined in Reference 9.

TONS Experiment Flight Hardware Performance

To support the experiment, EP/EUVE includes the hardware components necessary to perform onboard extraction of accurate one-way forward-link TDRSS Doppler measurements. These components consist of a USO to provide a precision frequency reference for onboard Doppler extraction and a DE card in one of the TDRSS second-generation transponders. Table 1 lists the associated hardware performance specifications and summarizes the measured performance statistics.

The USO performance was monitored and evaluated starting with its power-on on June 9, 1992, 2 days after the EP/EUVE launch. After the stability warm-up period was complete, the USO was selected as the frequency reference for Transponder-B on June 18, 1992. Figure 3 shows the USO's receive frequency offset relative to the nominal S-band receive frequency of 2106.40625 megahertz, estimated based on one-way forward-link Doppler measurements. Note that the increase of approximately 0.6 hertz on December 16 is due to the inclusion of general and special relativistic

Table 1. TONS Flight Hardware Performance

Performance Measure	Specification	On-Orbit Performance
USO long-term drift (parts/day fractional frequency)	1.0×10^{-10}	0.98×10^{-10} * 0.81×10^{-10} ** 0.62×10^{-10} ***
Allan variance (fractional frequency)	2.0×10^{-12} (USO only, 10-second interval)	2.5×10^{-12} (combined USO and DE, 10.24-second interval)
Doppler noise (hertz-RMS over 10.24-second interval)	0.0033	0.0026

* Value on June 18, 1992

** Value on November 30, 1992

*** Value on May 31, 1993

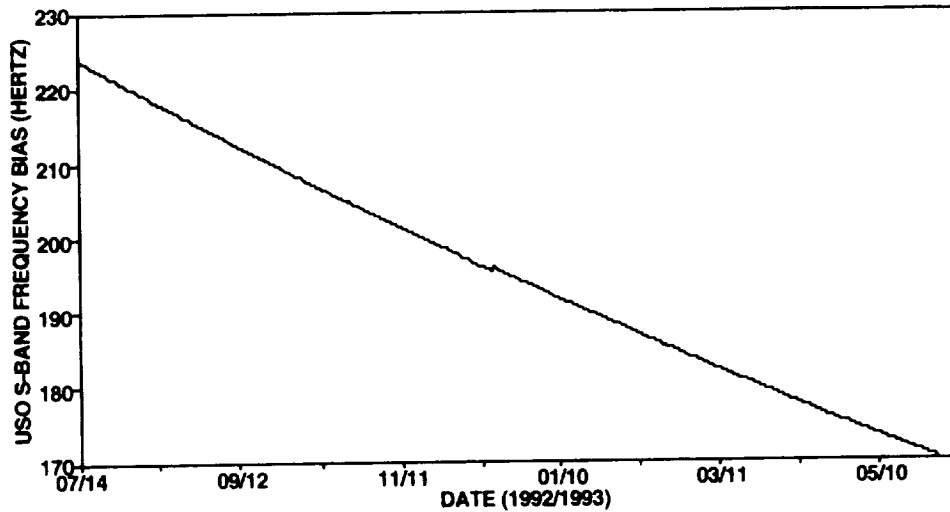


Figure 3. USO S-Band Receive Frequency Offset Estimated From One-Way Forward-Link Doppler Measurements

corrections starting at that time. The systematic characteristic change in the offset is equivalent to a near-linear long-term drift of approximately -0.98×10^{-10} parts per day (or equivalently -0.21 hertz per day) when the USO was selected as the reference frequency, decreasing to -0.62×10^{-10} parts per day (or equivalently -0.14 hertz per day) by May 31, 1993.

DE performance was monitored and evaluated starting with the initial measurements extracted during the first TDRSS contact after launch prior to enabling of the USO. The DE demonstrated excellent performance, producing Doppler measurements of comparable quality to the standard TDRSS two-way and one-way return-link Doppler measurements. Evaluation of the combined USO and DE short-term stability after launch indicates that the Allan variance is on the order of 2.5 parts in 10^{12} . The one-way forward-link Doppler noise is approximately 2.6 millihertz-root-mean-square (RMS) at S-band (2106.40625 megahertz), which is equivalent to 0.35 millimeter per second. The corresponding noise for the one-way return-link Doppler measurements via the Tracking Subsystem at the TDRSS White Sands Ground Terminal (WSGT) is 2.3 millihertz-RMS at S-band. Analysis of TDRSS two-way Doppler measurements for EP/EUVE provided a Doppler noise of 5.2 millihertz-RMS at S-band.

TONS Experiment OBDC Performance

On March 30, 1993, an OBDC acquisition test was performed, in which the application was enabled by a stored command prior to the scheduled TDRSS contact and acquisition was monitored on the ground. In this test, the FCWs computed in the OBDC application were used to shift the transponder center frequency to acquire a fixed-frequency (i.e., 2106.40625 megahertz) forward-link signal transmitted from the TDRSS ground terminal. OBDC proved successful in offsetting the Transponder-B receiver by approximately 38,000 hertz to acquire the signal within the nominal 15 seconds. Comparison of the telemetered FCWs with the measured Doppler shift indicates that OBDC-computed frequency offsets follow the

Doppler measurements to provide an accurate acquisition aid throughout the orbit. During April and May 1993, more than 90 TDRSS contacts were scheduled using OBDC with a 100-percent success rate. Figure 4 illustrates the OBDC application performance during the OBDC acquisition test, in terms of the predicted and measured Doppler shift. The predicted Doppler shift based on the computed FCWs is within ± 150 hertz of the actual frequency compared with the acquisition requirement of ± 1500 hertz.

TONS Experiment Navigation Software Performance

An indepth evaluation of the prototype flight software performance was a primary objective of the TONS experiment. This section presents the performance results using the baseline flight software algorithms, as well as an evaluation of modifications to improve accuracy and efficiency.

TDRS Ephemeris Accuracy

To process the one-way forward-link Doppler measurements, the TONS flight software uses routine TDRS state vectors uplinked daily and postmaneuver state vectors uplinked approximately 2 hours following a TDRS maneuver. During the July 14 through August 31, 1992, time period, the routine TDRS vectors were uplinked at 0:00 coordinated universal time (UTC), 10 hours before the end of the routine operational definitive solution. Starting on September 1, a more operationally realistic procedure was followed in which the routine TDRS vectors were uplinked at 12:00 UTC, 2 hours after the end of the routine operational definitive solution and were then used by the TONS flight software to predict the TDRS positions for the next 24 hours.

Comparison of the 26-hour TDRS-4 (TDRS-East) predictions with the corresponding definitive ephemerides over the January 1 through March 31, 1993, time period, yielded daily maximum differences varying from 10 to 130 meters, excluding predictions through periods with north/south stationkeeping maneuvers. A similar comparison of the 26-hour TDRS-5 (TDRS-West) ephemeris predictions yielded daily maximum differences varying from 10 to 60 meters. A covariance analysis of the routine operational TDRS definitive solutions indicates that ground-to-space ionospheric errors from the Bilateral Ranging Transponder System (BRTS) at the White Sands Complex, measurement noise, and range bias are the dominant error sources in the routine operational TDRS definitive solutions.

EP/EUVE Definitive Ephemeris Accuracy

The accuracy of the TONS flight software is assessed by comparing the flight software solutions with EP/EUVE definitive orbit determination solutions computed daily using a batch-least-squares estimator with high-fidelity modeling. The definitive estimator processed 34-hour spans of standard TDRSS tracking data and used definitive TDRS

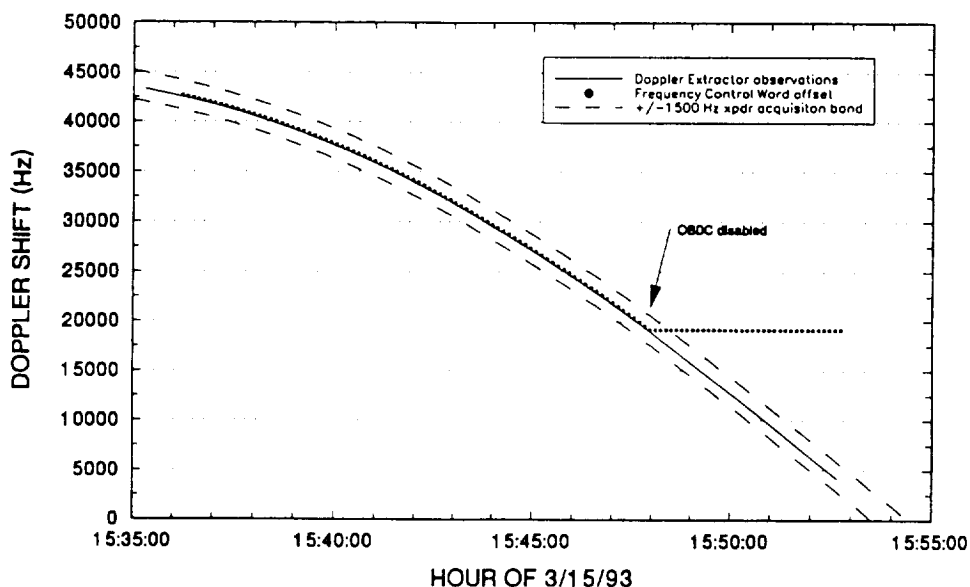


Figure 4. OBDC Performance Results

ephemerides. More accurate orbit propagation models were used in the definitive orbit determination than in the TONS flight software. The definitive solution uses a larger geopotential model [the Goddard Earth Model (GEM)-T3 50 × 50], a Jacchia atmospheric density model with historical solar activity data, solar and lunar ephemerides derived from the Jet Propulsion Laboratory's Development Ephemeris (DE)-200, Earth tides, and polar motion corrections.

A covariance analysis of the EP/EUVE definitive solution accuracy indicates that geopotential modeling error is the dominant error source, followed by TDRS-ephemeris-related errors and TDRS-to-EUVE ionospheric delay. The covariance analysis did not model TDRS-maneuver-induced errors and geomagnetic activity effects. The covariance analysis also indicates that the RMS position differences measured over the overlapping time periods are comparable to the RMS solution errors, indicating that the measurement of overlapping differences provides an approximate estimate of the definitive solution accuracy.

Figure 5 shows the measured daily maximum and RMS overlap position differences of the definitive solutions, for July 14, 1992, through May 31, 1993. In general, the daily maximum overlap differences are below 60 meters, and the daily RMS difference is approximately 20 meters. Large TDRS ephemeris errors arising from TDRS north/south stationkeeping maneuvers and/or large fluctuations in geomagnetic activity occurred on the days for which the maximum and RMS differences were larger than nominal.

To provide an independent check on the accuracy of the EP/EUVE definitive batch-least-squares solutions, these definitive solutions for September 15, 16, 22, 23, and 24, 1992, were compared with JPL-provided high-accuracy solutions computed by processing the GPS measurements from EP/EUVE in a sophisticated ground-based system (Reference 10). The mean differences were about 15 meters RMS and 30 meters maximum, very similar to the corresponding TDRSS definitive overlap differences for the same timeframe. Therefore, based on measured overlap differences, covariance analysis, and comparisons with GPS-derived ephemerides, the accuracy of the definitive batch-least-squares solutions is estimated to be 65 meters (3 σ) over the entire experiment timespan, with daily maximum differences always below 130 meters.

Baseline Flight Software Accuracy

Starting on July 14, 1992, the EP/EUVE POCC began to inhibit Doppler compensation during all TDRSS contacts via the high-gain antenna (HGA) when OBDC was not used. The resulting daily TDRSS contact schedule provided six to seven 30-minute coherent passes and six to seven 20-minute noncoherent passes via the HGA. Typically, 10 to 12 of these passes were usable in the TONS flight software; however, on several days there were eight or fewer usable passes, producing data gaps as long as 24 hours. Due to HGA visibility constraints associated with the slowly spinning EP attitude configuration, there was a gap of about 4 to 6 hours each day in the Doppler data that were processed by the TONS flight software prior to January 24, 1993, when the spacecraft attitude was changed to a three-axis stabilized attitude configuration. In the three-axis stabilized attitude configuration, the HGA has TDRSS visibility periods, but not necessarily tracking contacts, every EP orbit.

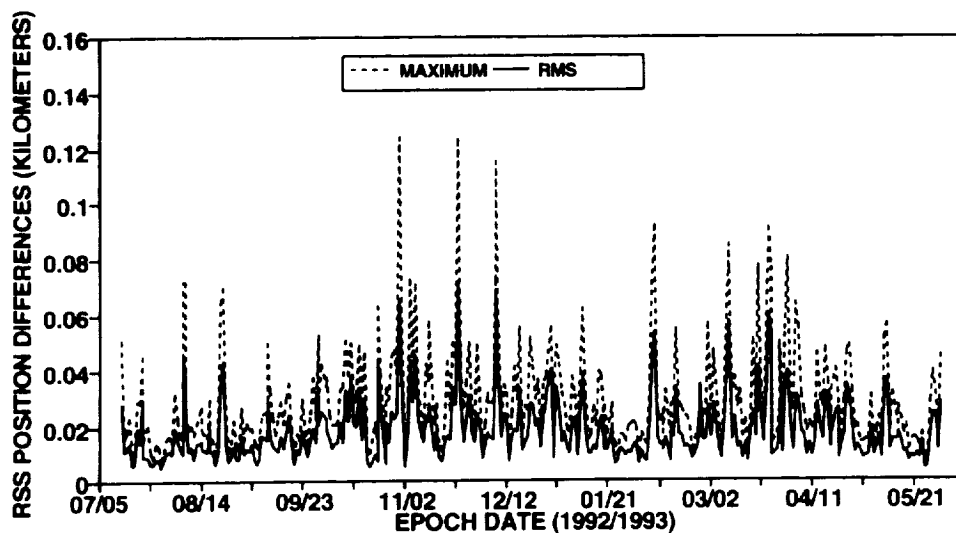


Figure 5. EP/EUVE Definitive Overlap Comparisons

On July 14, 1992, the TONS flight software was initialized using the batch-least-squares-derived EP/EUVE position, velocity, and USO bias estimates and a USO drift rate based on the rate of change of the USO bias through July 13. Table 2 lists the baseline estimation and propagation parameters used in the TONS flight software processing. A more detailed description is provided in References 3 and 4. The robustness of the filter processing was excellent. The filter stabilized within 12 hours of initialization and recovered immediately after data gaps of up to 24 hours. Filter processing was run continuously for 155 days without reinitialization or any parameter changes, except for an increase in the measurement editing multiplier. On December 16, 1992, the flight software's filter was reinitialized to accommodate a software upgrade to model special and general relativistic effects in the computation of the USO frequency bias. The filter converged to a steady-state solution after processing four tracking passes without exceeding a difference of 200 meters versus the definitive solution and was then run continuously for 165 additional days.

Sequential covariance analysis to assess the accuracy of the TONS flight software solutions indicates that the flight software solution accuracy should be comparable to the definitive solution accuracy excluding the effects of measurement timetagging errors, geomagnetic fluctuations, and TDRS maneuver-induced errors, which were not modeled. The dominant error source is the geopotential modeling error, with significant contributions from TDRS ephemeris prediction errors and small contributions from TDRS-to-user ionospheric refraction effects and atmospheric density modeling errors.

In the TONS/EUVE experiment implementation, measurement timetag ambiguities result from the sum of the RIU clock offset from UTC, the DE accumulation delay, the DE/RIU synchronization delay at the start of the accumulation interval, and the instability of the transponder's A1 module oscillator, which provides the DE accumulation interval. The expected magnitude and characteristics of these timetagging errors is discussed in References 11 and 12. For example, the addition of onboard measurement timetagging errors of 3 milliseconds increases the along-track error component by 20 meters and the total RMS error by approximately 10 meters.

Figure 6 shows the daily maximum and RMS position differences between the flight software and definitive estimates during periods with tracking every one to two orbits. Figure 7 shows the monthly mean values of the daily RMS differences between the TONS flight software and definitive estimates in the case of tracking every one to two orbits. These values are 5 to 15 meters larger than the definitive solution overlap RMS differences. As shown in Figure 8, the monthly mean values of the daily maximum differences between the TONS flight software and definitive estimates in the case of tracking every one to two orbits are about 10 to 30 meters larger than the definitive solution overlap maximum differences. These larger differences are expected because the measured difference between the TONS flight software and the definitive ground-based estimates reflects the errors in both the flight software and definitive batch-least-squares estimates. Measurement timetagging uncertainties also contribute to the difference between the two estimates.

Table 2. Baseline TONS Flight Software Parameters

Parameter or Option	EP/EUVE Values	TDRS Values
Estimated Parameters	User position and velocity Drag coefficient correction USO frequency bias correction	N/A
Tracking data	One-way forward-link Doppler	N/A
Data rate	One per 10.24 seconds	N/A
Sigma editing multiplier	3 (through November 4, 1992) 6 (after November 4, 1992)	N/A
Doppler measurement weight	0.1 hertz	N/A
Integrator type (step size)	Runge-Kutta 3(4+) (10.24 seconds)	Runge-Kutta 3(4+) (102.4 seconds)
Integration coordinate system	Mean of J2000.0	Mean of J2000.0
Geopotential model	GEM-T3 (30 × 30)	GEM-T3 (8 × 8)
Atmospheric density model (F _{10.7} solar flux, power of cosine)	Analytic Harris-Priester (135, 2)	N/A
Solar and lunar ephemerides	Analytic	Analytic
Solar radiation pressure	No	Yes

NOTE: GEM = Goddard Earth Model

N/A = not applicable

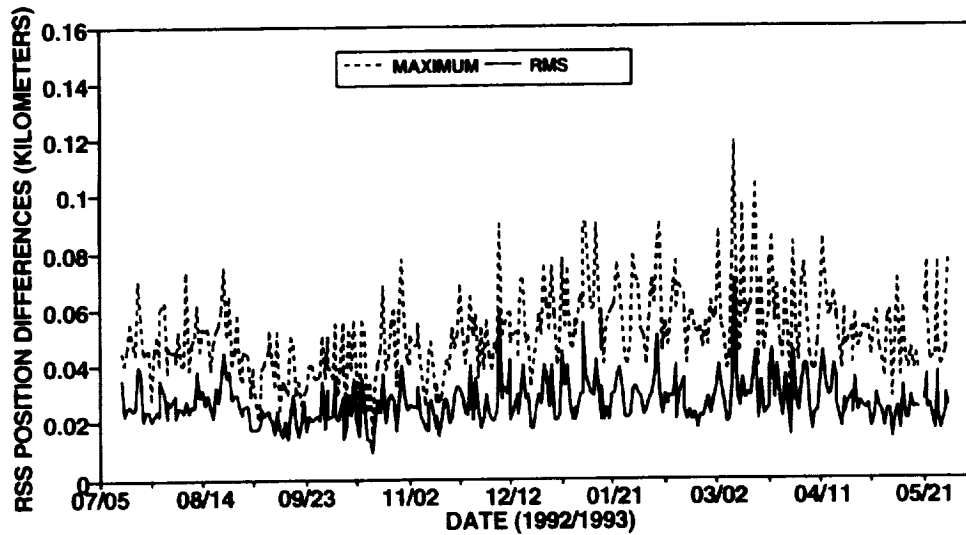


Figure 6. TONS Flight Software Versus Definitive EP/EUVE Position Differences During Periods With Tracking Every One to Two Orbits

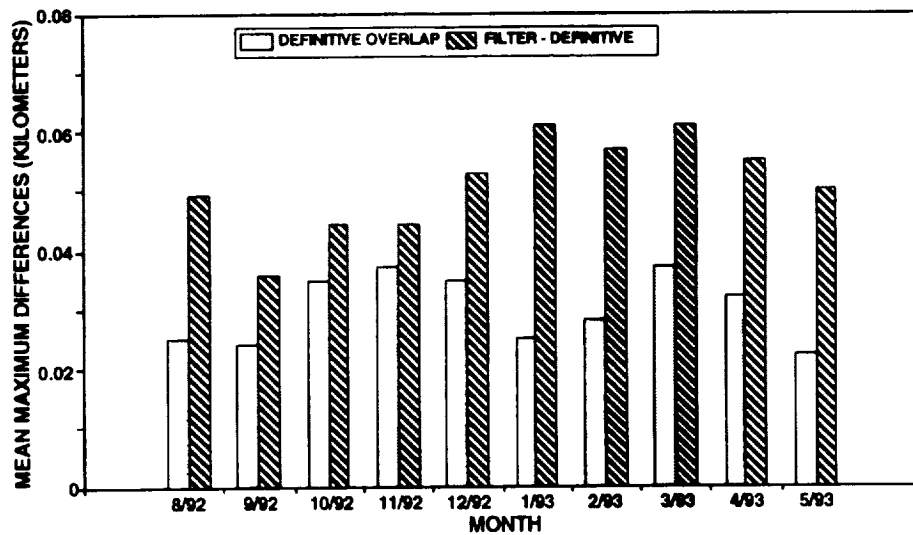


Figure 7. Mean Monthly RMS Values for TONS Flight Software Versus Definitive EP/EUVE Position Comparisons and Definitive Overlap Comparisons During Periods With Tracking Every One to Two Orbits

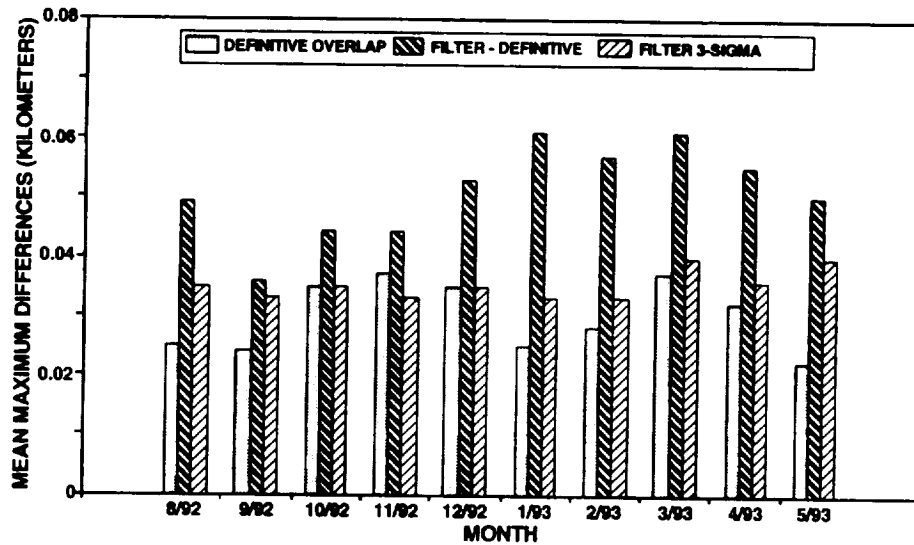


Figure 8. Mean Monthly Maximum Values for TONS Flight Software Versus Definitive EP/EUVE Position Comparisons and Definitive Overlap Comparisons During Periods with Tracking Every One to Two Orbits

To provide an independent check on the accuracy of the EP/EUVE filter solutions, TONS experiment filter solutions for September 15, 16, 22, 23, and 24, 1992, were compared with GPS-derived solutions. The GPS-derived solutions were provided by JPL, based on their ground-based postprocessing of the GPS measurements extracted onboard EP/EUVE, using differential GPS techniques. Reference 10 states that these GPS-derived solutions had overlap RMS differences of approximately 5 meters for the 5-day period processed. Figure 9 shows the total position differences between the TONS flight software and the GPS-derived estimate for the September 22–24, 1992, timespan. The mean differences were about 17 meters RMS and 35 meters maximum for periods with tracking every one to two orbits, 4 meters RMS and 7 meters maximum less than the measured difference from the definitive solution for the same timeframe. In general, these differences are consistent with the following relationship:

$$|\vec{r}_{FSW} - \vec{r}_{DEF}| = \left(|\vec{r}_{FSW} - \vec{r}_{GPS}|^2 + |\vec{r}_{DEF} - \vec{r}_{GPS}|^2 \right)^{\frac{1}{2}}$$

where \vec{r}_{FSW} = TONS flight software position estimate

\vec{r}_{DEF} = definitive position estimate

\vec{r}_{GPS} = GPS-derived position estimate

Based on this relationship and the data presented in Figure 8, the mean monthly values of the daily maximum flight software solution errors would be expected to be approximately 40 meters. Figure 8 shows the mean monthly values of the flight software's 3σ daily position maximum error estimates, which are approximately 35 meters. This optimistic error estimate is probably due to the fact that the flight software error estimates do not include timetag errors, TDRS-ephemeris-related errors, and errors in the coefficients used in the gravitational model (also referred to as errors of commission).

Therefore, based on measured differences versus definitive solutions, covariance analysis, and comparisons with GPS-derived ephemerides, the baseline TONS filter solution accuracy is approximately 75 meters (3σ) during periods with tracking every one to two orbits. The largest errors occur in conjunction with large TDRS postmaneuver ephemeris errors and/or significant fluctuations in geomagnetic activity (when the definitive solution errors are also larger).

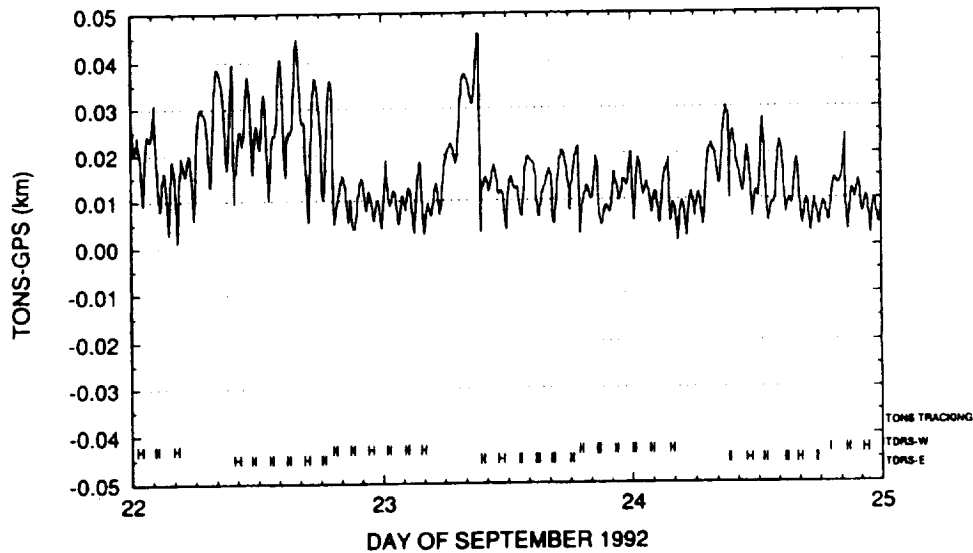


Figure 9. TONS Flight Software Versus GPS-Derived EP/EUVE Position Differences for September 22–24, 1992

Because the impact of TDRS ephemeris errors following north/south (N/S) maneuvers can be significant, the recommended operational concept for handling these maneuvers onboard is to use tracking from the nonmaneuvered TDRSs until an accurate postmaneuver TDRS vector can be uplinked. It is expected that the differences between the TONS flight software and definitive solutions would be further reduced if timetag errors were not present.

Figure 3 (given earlier) shows the TONS flight software estimate for the USO S-band receive frequency offset for July 14, 1992, through May 1, 1993. Note that the increase of approximately 0.6 hertz on December 16 is due to the inclusion of general and special relativistic corrections starting at that time. The USO drift rate was not estimated but applied using the initial value of -0.211 hertz per day, which was adjusted in February and April 1993. The corresponding estimate for the standard deviation of the offset is 1 part in 10^{11} (or equivalently 0.02 hertz). The USO S-band receive frequency offset estimate is consistent with the USO S-band receive frequency offset computed based on one-way return-link Doppler measurement residuals to within 0.1 hertz, the precision of the estimate computed using the one-way return-link Doppler measurement residuals.

Baseline Flight Software Processing Efficiency

The measured memory usage and peak CPU usage of the 1750A-hosted flight software are 233K bytes and 12 percent of the available CPU of a 2-MIPS processor, respectively. Algorithm optimization enhancements associated with the frequency of computation of coordinate rotation matrices and solar and lunar ephemeris and streamlining the geopotential computations have reduced peak CPU utilization from that reported in Reference 1 by approximately 40 percent without compromising accuracy. EP/EUVE ephemeris propagation, TDRS propagation, and measurement processing now require 6 percent, 1.75 percent per TDRS, and 2.5 percent of the peak CPU, respectively. The 48-bit 1750A software was used to process actual EP/EUVE TONS tracking data and the results compared with results obtained using the 64-bit VAX-based version of the flight software. The mean RSS position difference observed over the 31-day period processed was 0.22 meter, with a maximum of 1.6 meter. The largest differences occurred (1) when processing was continued using the results from the previous day, due to timing roundoff errors introduced in initiating the continuation of processing, which would not occur in the onboard environment; and (2) after propagation of more than 7 hours. Based on these results, there is no indication that there is a significant accuracy impact from the reduced precision of the 1750A processor.

Performance With Algorithm Improvements

Modifications to the baseline TONS navigation algorithms were investigated with the following objectives:

- Improved accuracy of the state estimate and the state covariance estimate
- Simplification of the onboard algorithms without accuracy degradation
- Reduction in the peak processing CPU requirements

The results from this investigation are discussed in this section.

Table 3 summarizes the algorithm modifications that were studied to improve navigation accuracy. Significant accuracy improvements of up to 20 meters were achieved by either estimating or applying an accurate value for the USO frequency drift. However, estimating the USO frequency drift increased the time required for the estimator to converge to an accurate state estimate, while applying a calibrated drift value would require a monthly uplink of this value to the onboard software. The addition of gravity errors of commission to the state process noise model increased the filter's error estimate to a more realistic level.

Table 4 summarizes the algorithm modifications that have been studied to improve processing efficiency and their projected performance based on the baseline CPU utilization measurements. Based on this analysis, the following modifications can be used to reduce peak CPU usage to less than 5 percent:

- Peak CPU utilization can be decreased by 20 percent by replacing the baseline integrator with a fourth-order Runge-Kutta (RK4) algorithm
- Peak CPU utilization can be decreased by 50 percent by doubling the maximum EP integration stepsize and doubling the Doppler averaging interval

Summary

Stage two of NASA's stepwise approach to providing high-accuracy, autonomous navigation to TDRSS users is complete. With the successful implementation of the TONS experiment on EP/EUVE, the flight demonstration of onboard Doppler extraction, onboard signal acquisition, and the qualification of the TONS flight software have been accomplished. The TONS experiment has provided the following major conclusions:

- The USO performance is excellent, demonstrating a predictable near-linear decrease in frequency and a reliable reference frequency for one-way navigation.

Table 3. Algorithm Modifications

Modification	Objective	Performance
Estimation of frequency drift	Improve accuracy	Reduces RMS differences by up to 20 meters but increases convergence time
Application of accurate USO frequency drift	Improve accuracy	Reduces RMS differences by up to 20 meters with monthly update of calibrated frequency drift
Addition of gravity errors of commission	Improve accuracy of state and covariance	Increases position covariance by 10 meters (3 σ) but does not improve solution accuracy
Application of timetag bias	Improve state accuracy	Reduces along-track differences
Estimation of timetag bias	Improve accuracy of state and covariance	Timetag bias is not observable using only Doppler measurements
Estimation of TDRS measurement biases	Improve accuracy of state and covariance	Reduces filter stability; can reduce the impact of TDRS ephemeris errors larger than 75 meters but provides no significant improvement if TDRS ephemeris errors are below 75 meters (3 σ)
Random-walk model for drag coefficient correction	Simplified algorithm	Provides accuracy comparable to more complex Gauss-Markov model
Random-walk model for USO bias correction	Simplified algorithm	Provides accuracy comparable to more complex Gauss-Markov model
Random-walk model for USO frequency drift correction	Simplified algorithm	Provides accuracy comparable to more complex Gauss-Markov model

Table 4. Projected Processing Reductions

Integration Step size (seconds)	Integrator*	Doppler Averaging Interval (seconds)	Peak EUVE Position Differences† (meters)	Peak CPU for 2 MIPS 1750A (%)
10.24	RK3(4+)	10.24	0.0	12 over 10.24 seconds
10.24	RK4	10.24	< 1	9.6 over 10.24 seconds
20.48	RK3(4+)	20.48	10	6.0 over 20.48 seconds
20.48	RK4	20.48	10**	4.8 over 20.48 seconds
30.72	RK3(4+)	30.72	15	4 over 30.72 seconds
61.44	RK3(4+)	61.44	20	2 over 61.44 seconds

* RK3(4+) = Runge-Kutta 3(4+); RK4 = Runge-Kutta 4

** Estimated result

† Peak differences over 5 days versus baseline run

- The stability characteristics of the onboard system allow for time maintenance to the 10-microsecond level.
- The DE card in the second-generation TDRSS transponder produced Doppler measurements of comparable quality to the standard TDRSS two-way and one-way return-link Doppler measurements, with very low noise and no interference with user operations due to its passive activity.
- The capability to perform autonomous signal acquisition onboard EP/EUVE was demonstrated and used to aid signal acquisition in more than 90 TDRSS contacts with a 100-percent success rate.
- The TONS flight software performance was excellent. During periods with tracking of approximately one contact every one to two orbits, RMS position differences of 27 meters, RMS velocity differences of 0.03 meter per second, and frequency accuracies of better than 5 parts in 10^{11} (1σ) were achieved for EP/EUVE, compared to the corresponding definitive solutions with an estimated 65 meters (3σ) accuracy. Based on measured differences versus definitive solutions, covariance analysis, and comparisons with GPS-derived ephemerides, the baseline TONS filter solution accuracy is approximately 75 meters (3σ) during periods with tracking every one to two orbits.
- The robustness of the filter processing was remarkable. The filter stabilized within 24 hours of initialization and recovered immediately after data gaps of more than 24 hours. Starting on July 14, 1992, filter processing was performed continuously for 320 days with one reinitialization to accomplish a software upgrade and one parameter change, an increase in the sigma editing multiplier.

It is worthwhile to note that JPL's GPS-derived solutions, with RMS overlap differences of 5 meters for the 5 days processed, were computed in a ground-based postprocessing environment using differential GPS techniques. However, the TONS-derived solutions, with an estimated accuracy of 75 meters (3σ), are provided in realtime onboard the user spacecraft.

Synchronization of onboard time and frequency references in an operational implementation, improvements available in the third-generation TDRSS transponder, impending significant improvements in available geopotential modeling, and refinement of the navigation algorithms can be implemented to significantly improve navigation performance for TONS I and TONS II-A operational users. Based on the results of this experiment, the TONS I operational system will meet the EOS-AM1 navigation accuracy requirements of 50 meters (1σ) and allow EOS-AM1 to meet their navigation goal of 20 meters (1σ), especially if enhanced by the TONS II-A option.

In summary, TDRSS provides a means by which TDRSS users can obtain low-cost, realtime, high-accuracy onboard navigation to meet their requirements with little impact to user spacecraft weight, power, and volume, since TONS uses hardware components already available on the spacecraft. The capabilities are progressive with associated user enhancements and provide failure modes to maintain user autonomy or extend spacecraft lifetime.

Acknowledgments

The authors wish to acknowledge the following contributions. For contributions to TONS experiment data processing and analysis—Michael Maher of AlliedSignal Technical Services Corporation; Jerome Teles, Ernest Santoro, Gregory Horstcamp, Neil Ottenstein, Edward Smith-Rowland, Taesul Lee, Christopher Cox, Allan Schanzle,

Diane Gentry, Dipak Oza, and Mina Samii of Computer Sciences Corporation; and Ronald Bruno and Bryant Elrod of Stanford Telecommunications, Incorporated. For participating in the TONS software development effort—Terri Wood of NASA/GSFC and Warren Steger, Edward Joyce, Jay Bugenhagen, and John Chung of CSC. For encouragement and support of TONS—Rhoda Hornstein of NASA Headquarters and Kathy Hartman and James A. Jackson of NASA/GSFC.

References

1. C. J. Gramling et al., "Performance Assessment of the TDRSS Onboard Navigation System (TONS) Experiment on EP/EUVE," Paper No. AAS 93-256, presented at the AAS/GSFC International Symposium on Space Flight Dynamics, Goddard Space Flight Center, Greenbelt MD, April 26–30, 1993
2. C. J. Gramling et al., "Tracking and Data Relay Satellite System (TDRSS) Onboard Navigation System (TONS) Experiment on the Explorer Platform/Extreme Ultraviolet Explorer (EP/EUVE)," Paper No. IAF-92-0056, presented at the 43rd Congress of the International Astronautical Federation, Washington, DC, August 28–September 5, 1992
3. Goddard Space Flight Center, Flight Dynamics Division, 553-FDD-92/111R0UD0, *Tracking and Data Relay Satellite System (TDRSS) Onboard Navigation System (TONS) Experiment First Quarter Status Report*, A. C. Long et al., prepared by Computer Sciences Corporation, October 1992
4. Goddard Space Flight Center, Flight Dynamics Division, 553-FDD-94/007R0UD0, *Tracking and Data Relay Satellite System (TDRSS) Onboard Navigation System (TONS) Experiment Final Report*, A. C. Long et al., prepared by Computer Sciences Corporation, March 1994
5. Goddard Space Flight Center, Flight Dynamics Division, 554-FDD-91/059R4UD0, *Tracking and Data Relay Satellite System (TDRSS) Onboard Navigation System (TONS) Experiment Ground Support and Flight Software Requirements and Functional Specifications, Revision 4*, A. C. Long et al. (CSC), prepared by Computer Sciences Corporation, March 1992
6. Goddard Space Flight Center, Flight Dynamics Division, 552-FDD-91/039R0UD0, *TDRSS Onboard Navigation System (TONS) Experiment Ground Support System System Description*, W. Steger et al. (CSC), prepared by Computer Sciences Corporation, July 1992
7. C. J. Gramling et al., "Navigation Accuracy Analysis for the TDRSS Onboard Navigation System (TONS) Experiment on EP/EUVE," Paper No. AAS 91-354, presented at the AAS/AIAA Astrodynamics Specialist Conference, Durango, Colorado, August 19–22, 1991
8. C. J. Gramling and R. C. Hart, "Onboard Configuration and Operation of the TDRSS Onboard Navigation System (TONS)," Paper No. AAS 92-010, presented at the AAS Guidance and Control Conference, Keystone, Colorado, February 8–12, 1992
9. Goddard Space Flight Center, Flight Dynamics Division, 554-FDD-91/105R3UD0, *Tracking and Data Relay Satellite System (TDRSS) Onboard Navigation System (TONS) Flight Software Mathematical Specifications, Revision 3*, A. C. Long et al. (CSC), prepared by Computer Sciences Corporation, March 1992
10. K. Gold et al., "GPS Orbit Determination for the Extreme Ultraviolet Explorer (EUVE)," *Proceedings of GPS IONU93*, September 22–24, 1993, Salt Lake City, Utah
11. Stanford Telecommunications, Incorporated, TR 91065, *Assessment of Doppler Measurement Time Tagging Errors in the TONS Experiment*, B. D. Elrod et al., July 1991
12. Stanford Telecommunications, Incorporated, TR 92034, *TDRSS Onboard Navigation System (TONS) Pre-flight Engineering Test Report Volume I: Pre-shipment Testing*, R. C. Bruno et al., April 1992

FLIGHT MECHANICS/ESTIMATION THEORY SYMPOSIUM

MAY 17-19, 1994

SESSION 4

ATLAS SOLAR POINTING OPERATIONS

C. A. Tyler¹ and C. J. Zimmerman²

The ATLAS-series Spacelab missions is comprised of a diverse group of scientific instruments, including instruments studying the sun and how the sun's energy changes across an eleven-year solar cycle. The ATLAS solar instruments are located on one or more pallets in the Orbiter payload bay and use the Orbiter as a pointing platform for their examinations of the sun. One of the ATLAS instruments contained a sun sensor allowing the scientists and engineers on the ground to see the pointing error of the sun with respect to the instrument and correct for the error based upon the information coming from the sun sensor. This paper presents the solar operation activities and flight experience from the ATLAS 1 and ATLAS 2 missions with particular attention given to identifying the sources of pointing discrepancies of the solar instruments and to describe the crew and ground controller procedures that were developed to correct for these discrepancies. The Orbiter pointing behavior from the ATLAS 1 and ATLAS 2 flights presented in this paper can be applied to future flights which use the Orbiter as a pointing platform.

INTRODUCTION

The Atmospheric Laboratory for Applications and Science (ATLAS) series of Spacelab missions, an element of NASA's Mission to Planet Earth, is chartered to study the composition of the middle atmosphere and the possible atmospheric variations due to solar changes across an eleven-year solar cycle. The first and second missions in the ATLAS series successfully flew in March 1992 and April 1993 and mission planning has begun to support the ATLAS 3 launch scheduled for October 1994.

The ATLAS payload complement comprises investigations for both solar sciences and atmospheric sciences. The ATLAS instruments are also co-manifested with other payloads. As a result, the solar operations are scheduled during the orbital day portion of 20 to 30 orbits during the flight. The orbital night portion of each revolution is devoted to other non-solar science operations or to instrument cooling.

OVERVIEW OF ATLAS SOLAR OPERATIONS

In order to better understand the driving force behind global atmospheric changes, the solar science portion of the ATLAS payload intends to measure the total solar irradiance and the solar energy distribution and how these properties vary with time. Two of the ATLAS solar instruments, the Active Cavity Radiometer Irradiance Monitor (ACRIM) and the Measurement of Solar Constant experiment (SOLCON) examine the solar irradiance, also known as the solar constant, and how this value changes with time. The Solar Spectrum Measurement experiment (SOLSPEC) and the Solar Ultraviolet Spectral Irradiance Monitor (SUSIM) study the solar energy variations at various wavelengths. Although the ATLAS solar science instruments operate only briefly in the context of an eleven year solar cycle, their ability to be precisely calibrated before and after flight provides an excellent calibration source for satellites operating for extended periods of time. Three of the ATLAS solar instruments have sister instruments on free-flying satellites. During the ATLAS missions, ACRIM and SUSIM took coincident measurements with their counterparts on the Upper Atmospheric Research Satellite (UARS) which was launched in 1991. SOLCON provided comparison data for the Nimbus-7, the Earth Radiation Budget Satellites, as well as the ACRIM instrument on ATLAS and UARS. [1]

¹Teledyne Brown Engineering, Huntsville, Alabama 35807-7007

²EO43, Marshall Space Flight Center, Huntsville, Alabama 35812

Implementation of solar experiment operations on ATLAS missions typically calls for dedicated blocks of time in units of one orbital revolution of approximately 90 minutes. During each revolution, the orbiter experiences a 90 minute "day" where a portion of time is spent in darkness and the rest of the time is in daylight. A minimum of 45 minutes of orbital daylight is required for a standard solar observation which consists of all of the solar instruments operating simultaneously. The amount of day/night time during each revolution is a function of the solar beta angle and may be controlled by selecting a certain launch time of day.

A group of consecutive revolutions dedicated to solar science, referred to as a solar period, is constructed and laid out under several general guidelines. First of all, a majority of the solar instruments desire as many consecutive revolutions as possible in order to observe short term solar variations. One of the instruments, SUSIM, requires at least 4 consecutive revolutions to assure an effective observation session. The desire for consecutive observations is offset however by the need to keep instruments from overheating. Thus an individual solar period is limited to 8 revolutions or less. An additional guideline expressed by the solar science group states that the individual solar periods should be scheduled throughout the mission to provide the greatest possible separation between the first and last observations. This guideline is accomplished by placing the first solar period directly after mandatory 24-hour out-gassing. The last solar period is scheduled such that the final observation occurs just before the required Passive Thermal Conditioning period prior to de-orbit. The remaining solar period(s) is distributed as equally as possible between the first and last solar periods.

A summary of the ATLAS 1 and ATLAS 2 solar periods is shown in Figure 1. ATLAS 1 nominally planned for 20 solar observations occurring in groups of 8,4, and 8 revolutions each. Once the payload had been in orbit for several days, flight controllers at Johnson Space Center granted an extension day to be used by the payload. Solar experiments were allocated a group of 4 revolutions on the extension day of which they were able to use three for a total of 23 solar observations. ATLAS 2 performed 26 solar observations in groups of 8,6,4 and 6 revolutions each and an additional 2 solar observations during an extension day.

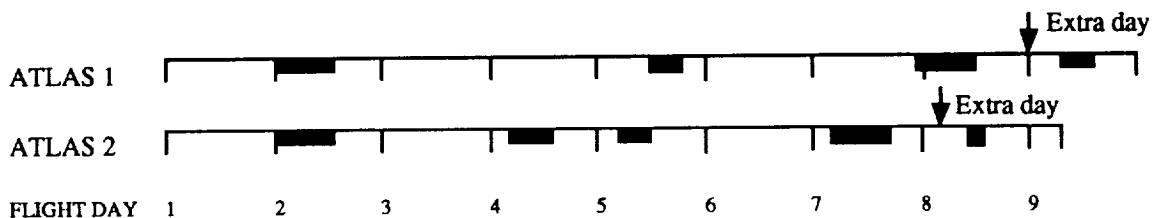


Figure 1. Layout of Solar Observation Periods for ATLAS 1 and ATLAS 2

ATLAS SOLAR OPERATIONS

Once the overall layout of solar periods has been set, details regarding what type of observations are performed can be planned. Solar observations on ATLAS missions are regarded by the payload planning team to fall into two general categories: nominal and special.

Normal Solar Operations

The first category, which is used for the majority of observations, simply points the instrument viewing axes directly at the sun and holds this orientation for the duration of the orbit day. At this point it is assumed that all of the solar instruments are aligned with each other and in turn aligned with the orbiter -Z body axis (directly out the payload bay). The orbiter azimuth-co-elevation coordinate system is shown in Figure 2. This system locates the origin along the -Z axis and may be used to conveniently describe solar pointing vectors in the orbiter body system.

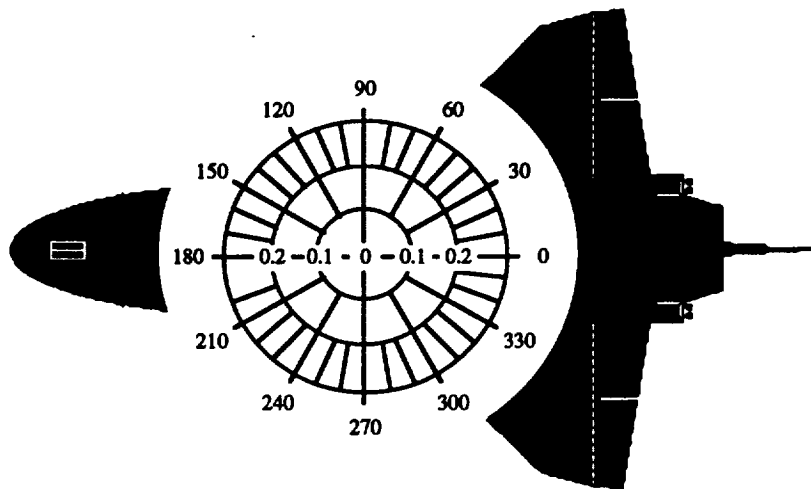


Figure 2. Orbiter Azimuth Co-elevation coordinate system

Although the solar criss-cross was designed specifically for the SOLCON experiment, the other The apparent movement of the sun is taken into account (removed) by using the orbiter Digital Auto Pilot (DAP) sun target logic which allows any orbiter body axis to be pointed toward the sun. Since the DAP depends on information from the Inertial Measurement Unit (IMU) to derive a predicted sun location, an IMU alignment is desired prior to the beginning of each solar period.

Figure 3 shows actual and predicted sun positions during the fourth and fifth observations of the first solar period of ATLAS 1. Note the rectangular shape created from the $0.1^\circ/\text{axis}$. attitude deadband standard for solar observations. The first plot, solar observation number four, has clearly two separate locations for actual and predicted sun position. The second plot, solar observation number five, shows the actual and predicted sun positions collapsed onto one location after an IMU alignment was performed just prior to the observation. The $0.1^\circ/\text{axis}$. deadband for solar observations can be decreased as far as $0.033^\circ/\text{axis}$ in special circumstances assuming propellant budget is available. The rate deadband was fixed at $0.01^\circ/\text{sec}/\text{axis}$ on ATLAS 1 and $0.02^\circ/\text{sec}/\text{axis}$ on ATLAS 2. With one exception, instrument fields of view are large enough to tolerate these minor pointing errors. The SUSIM instrument with an operational field of view of $\pm 0.75^\circ$ requires a fair amount of attention to be given to pointing precision during real time. [2]

Special Observations

Special observations, the second category, are used for any performances which require the orbiter to execute a maneuver during an observation. ATLAS 1 planned for the performance of two special observations nicknamed "criss-cross" designed for the SOLCON experiment and "5-point scan" for the SUSIM experiment. ATLAS 2 planned for these maneuvers as well as a third special observation nicknamed "asterisk". These procedures were developed separately under guidelines specified by individual experiments as a way to verify instrument/detector responses.

The solar criss-cross consists of two single axis maneuvers each designed to sweep the instrument axes through an eight degree arc with sun center located at the midpoint of the arc. Although the solar criss-cross was designed specifically for the SOLCON experiment, the other solar experiments are not excluded from taking data. Solar criss-cross maneuvers were planned for the first observation of the first solar period and the last observation of the last solar period for both ATLAS 1 and ATLAS 2.

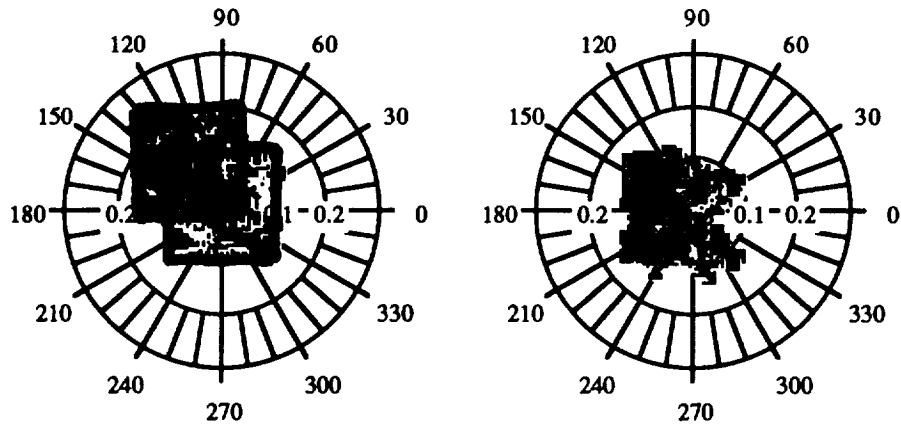


Figure 3. Actual and predicted sun position during solar observations 4 and 5 on ATLAS 1

The SUSIM Alignment Verification or 5-point scan is performed to provide data for assessing degradation of the instrument sensitivity and to map the sensitivity throughout the instrument field-of-view (FOV). The instrument FOV is mapped by observing the sun center in different regions of the FOV by pointing the instrument line-of-sight at different five points on the sun. The SUSIM Alignment Verification is performed twice: once early in the mission during the first solar period and again during the last solar period. The SUSIM instrument pointing for the alignment verification is performed using five different solar inertial attitudes with very small 0.033° attitude deadbands. [3]

Figure 4 shows examples of the solar criss-cross maneuver and the SUSIM 5-point scan generated from ATLAS 1 IMU telemetry data.

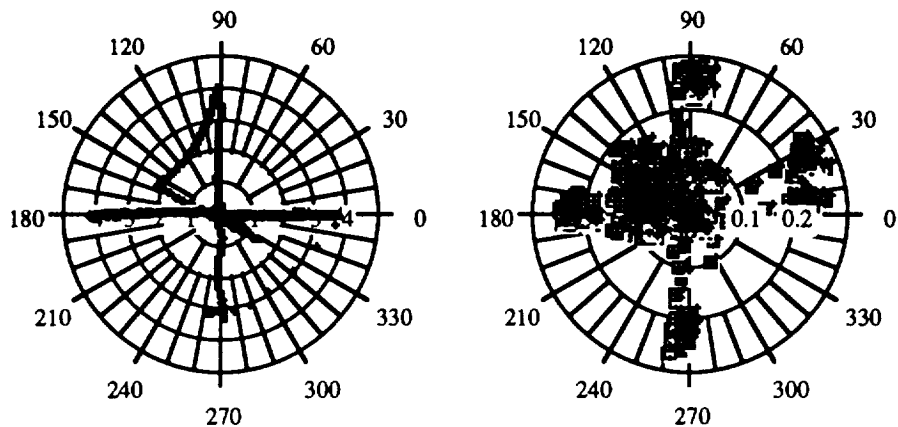


Figure 4. Solar criss-cross maneuver and SUSIM 5 point scan

ORIGIN OF POINTING ERROR

Before the ATLAS-1 mission, very little accurate information was available describing the on-orbit pointing environment within the payload bay. Accurate pointing information is essential to the processing of data gathered by the ATLAS instruments. For one ATLAS instrument, the Millimeter Wave Atmospheric Sounder (MAS), a pointing error of 0.1° will cause an uncertainty of 3 kilometers in position for the experiment's examination of the atmosphere at the earth's limb. [4]

This need for accurate pointing information caused the creation of the Pointing and Alignment Workstation (PAWS) which brought together a small team of engineers to gather realtime pointing information from Orbiter and payload sources and to examine the pointing behavior of the Orbiter and the ATLAS instruments. The PAWS engineers were also tasked to determine the magnitudes of the instrument pointing errors resulting from the various contributing sources.

Prior to the ATLAS-1 flight, possible errors sources and their advertised limits were researched. The pointing error sources were identified and grouped as Orbiter-related and instrument-related. The primary Orbiter-related error sources are the IMU uncertainty and Orbiter thermal distortions. The payload-related pointing errors sources are thermal distortions and misalignment of the pallet, instrument calibration errors and mechanical misalignments. [5]

Using the identified pointing error sources and advertised accuracies from Orbiter and ATLAS payload documentation, a pre-mission error tree was constructed to provide the only prediction to the on-orbit pointing environment. The pre-mission predictions of an example ACRIM instrument pointing errors budget are shown in Figure 5.

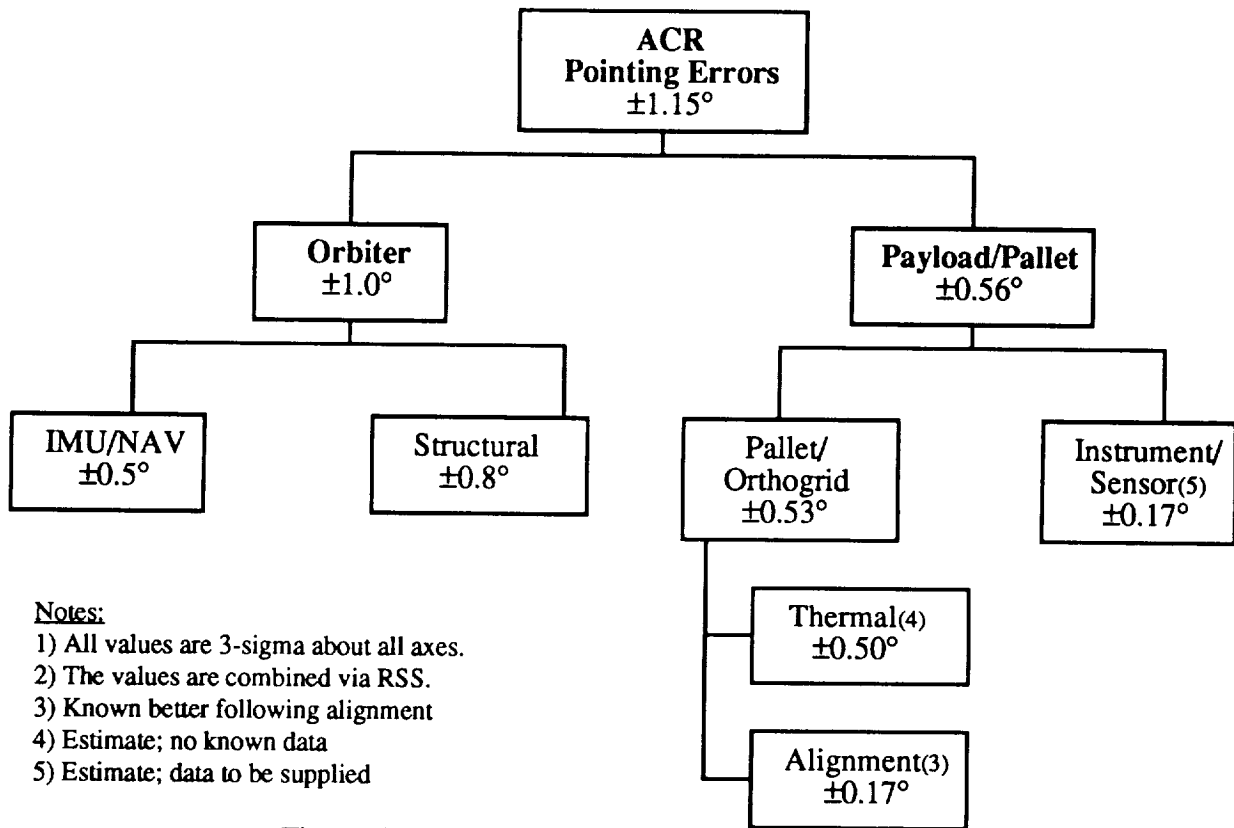


Figure 5. Pre-mission Pointing Error Budget Tree [5]

Orbiter-based Pointing Error

The Orbiter uses three Inertial Measurement Units (IMUs) to determine the *believed* orientation of the Orbiter within the capability of the IMUs. The IMUs can be operated in a shared mode whereby the IMU information is selected from the units using the Redundancy Management (RM) logic, or by prime-selecting an IMU. For the ATLAS series, IMU alignments are performed approximately every twelve hours. This frequency is a compromise between the desired increase in pointing accuracy that IMU alignments provide and the time consumed by these alignments which reduce the available on-orbit time for the experiments.

Orbiter pointing errors also result from structural thermal distortions caused by solar heating along the distance between the Orbiter Inertial Measurement Units (IMUs) and the ATLAS pallet. Since, for the most part, this distance lies along the long axis of the Orbiter, the pointing error is most significant in the pitch axis. Prior to the first ATLAS flight, predicting the pointing error due to thermal distortions was difficult due to the changing thermal environment and the uncertainty of the effect on the Orbiter structure. The structural thermal distortions were actually the largest contribution to the pointing error seen by the ATLAS solar instruments.

Payload-based Pointing Error

The payload-related errors can be a result of mechanical misalignments at assembly, calibration errors due to internal instrument misalignments, or due to thermal distortions and misalignment of the pallet where the ATLAS instruments are mounted. [5]

The assembly mechanical misalignment errors are unavoidable due to the inherent inaccuracies of the optical alignment measuring devices and the instrument alignment which is performed in a 1-g environment. [5]

Another problem which increased the difficulty of pointing during the ATLAS missions is the misalignment of the solar instruments' line of sight with respect to each other. Figure 6 illustrates the instrument line of sight with respect to the SUSIM alignment cube on ATLAS 1. For ATLAS 1, the solar instrument pointing problem was even greater since the SUSIM alignment cube was aligned to the -Z axis rather than the center of the SUSIM field of view (SUSIM Science), complicating solar pointing. During assembly and alignment for ATLAS 2, the SUSIM field of view was properly aligned with the -Z axis so that an offset was not required.

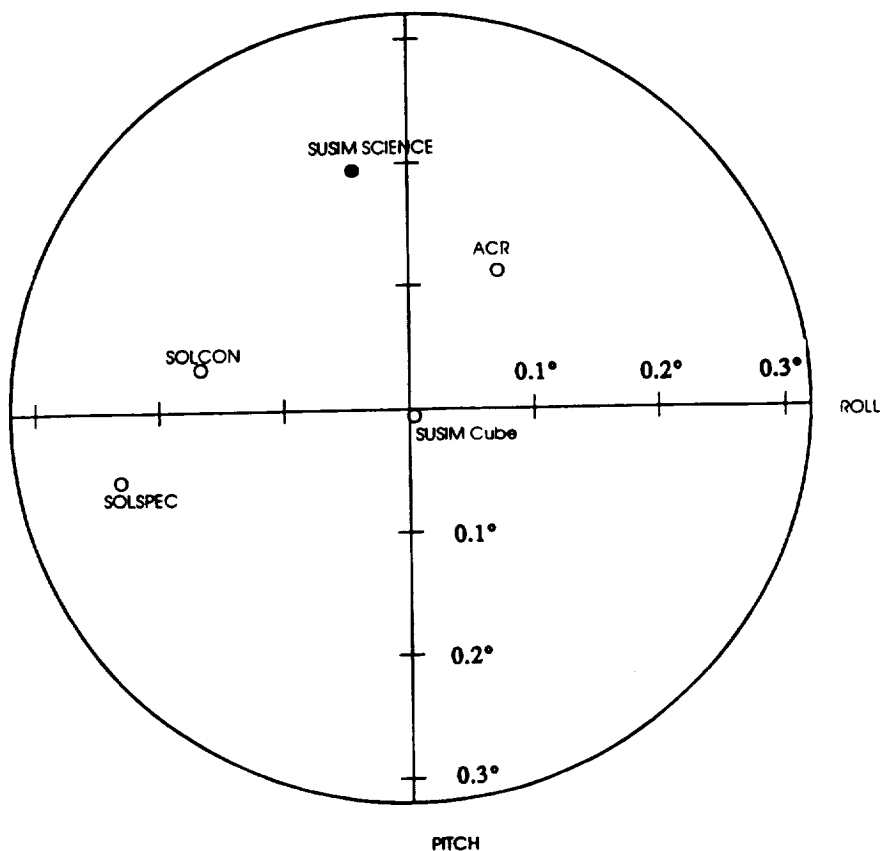


Figure 6. Solar Instrument Relative Alignment

POINTING BEHAVIOR DURING ATLAS SOLAR OPERATIONS

During any given solar observation, pointing errors may accumulate due to instrument misalignment, IMU uncertainty and drift, as well as other sources. If these errors become too great data may be lost or degraded as a result of the sun tracking outside of an instrument field of view. Prior to the flight of ATLAS 1, the payload planning team developed a procedure to allow for the solar experimenters to request pointing corrections in the event of instrument misalignment. One of the ATLAS solar instruments, SUSIM, was equipped with a sensor to determine the relative position of the sun in the instrument field of view. During ATLAS 1, it became clear that the SUSIM sun sensor would be used as the basis for determining pointing accuracy for the solar experiment complement. Fortunately, the majority of solar observations were performed without difficulty. However, at the beginning of the third solar period, SUSIM noted from their data that a pointing correction would be necessary. This initiated a call/response loop between the planning team and SUSIM which proved only marginal effectiveness at fixing the problem and in some cases made it worse. Figure 7 shows a histogram of the SUSIM sun sensor data for the first four observations of the third solar period on ATLAS 1 [5].

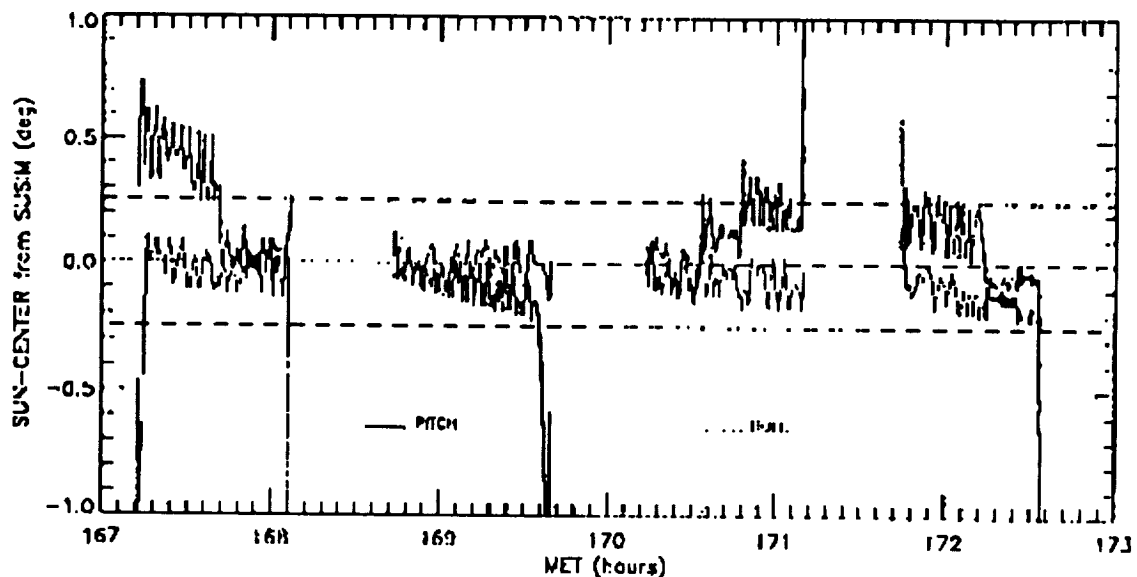


Figure 7. SUSIM Sun Sensor data from ATLAS 1

Clearly, from Figure 7, instrument pointing during the first observation begins with a pitch offset well away from sun center. A pitch correction based on this information was computed by the payload planners and executed by the orbiter crew halfway through the observation.

The first plot of Figure 8 shows IMU telemetry data during this observation. Point A in Figure 8 is sun centered according the IMU. The pitch correction maneuver applied halfway through the solar observation is shown by point B. This correction places sun center approximately 0.25° toward the nose of the orbiter. The same pitch offset applied to the following observation appears at first to have completely corrected the problem; however, returning to Figure 7, the end of the observation has drifted enough in pitch to require a further correction on the following pass.

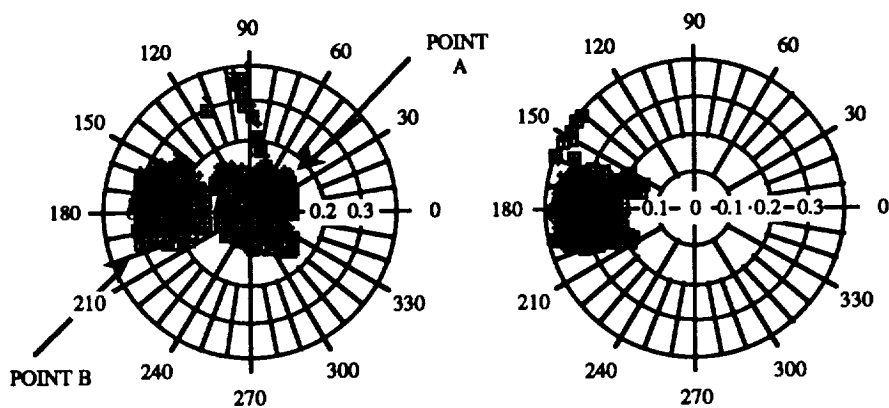


Figure 8. First and second observations of the third solar period.

Pointing behavior during the third solar period was confusing to the planning team mainly due to the fact that all of the data shown here was not available in real time. The large drift rate was at first attributed to orbiter IMU; however, the Guidance, Navigation, and Control (GNC) officer denied that the magnitude of error being suggested by the SUSIM sun sensor could have this cause. The actual cause of the large pitch drift during these observations turns out to be mainly related to thermal bending. Since the solar instruments became misaligned relative to the IMU reference system, the attitude adjustments did not correct the position of the sun in the instrument fields-of-view. Corrections which were performed before the misalignment trends were well-established or understood resulted in incorrect adjustments illustrated by the final observations of Figure 7.

During both ATLAS 1 and ATLAS 2, a sinusoidal variation in instrument pointing was observed by several PIs and by the PAWS engineers. The amplitude and phase of the sinusoidal variations changed when maneuvering from +X/VV to -X/VV. Investigations of the cause of this pointing error has shown that during ATLAS 2 one of the aging KT-70 units performed poorly and when the Redundancy management (RM) logic computed the pointing information, the RM logic caused rapid switching between the three IMU units when one IMU was not "prime-selected". The roll drift between the "good" and "bad" IMUs was 0.12° to 0.20°. The sinusoidal pointing error can be explained, in part, by the on-board computer shifting between one IMU unit's reference system to another unit's system. [6]

New HAINS IMU units are beginning to replace the older KT-70 units. The new units are expected to have an IMU drift rate for small dispersions (1-sigma) of approximately 0.006°/hour. This new capability will provide reduced IMU pointing error. Also, to minimize the IMU drift during the solar operations, an IMU alignment is scheduled immediately before the start of the solar period. Another IMU alignment is scheduled immediately following the last sun observation of the solar period to characterize the IMU drift throughout the period.

An on-orbit crew procedure called SUSIM nulling was developed for ATLAS 2 to center the -Z body axis using the SUSIM sun sensor. Pitch and roll fly-to angles were used to correct the instrument pointing misalignments from the planned solar attitudes since these values would be more meaningful to the Orbiter crew making the corrections. Using this procedure, the misalignment was properly corrected. One problem with the SUSIM nulling procedure was that the process required a crewman to reposition the monitor to allow the pilot to see the SUSIM sun sensor information. The nulling process could not be performed if the crew was busy at other tasks.

In addition to the new SUSIM nulling crew procedure developed for ATLAS-2, the SUSIM 5-point alignment verification crew procedure was added. Previously, the pilot followed a long list of attitudes and maneuvers in the attitude timeline (ATL) to orient the Orbiter -Z body axis at a sequence of five fixed points on the solar disk. The maneuvers were very small, approximately 0.3° , and were extremely difficult to perform manually. Consequently, the ATLAS-2 SUSIM alignment verifications were performed from a detailed list of procedures for the complex operations, and by using the DAP, the pilot performed precise Orbiter pointing.

The solar criss-cross activities are much less complex than the 5-point alignment verification and are directed from the attitude timeline. A special solar crisscross on ATLAS-2 was developed to perform eight scans across the sun in a pattern resembling an asterisk. Since this complex sun scan was developed during the flight, it was not possible to develop a crew procedure and so it was scheduled using the attitude timeline. For future ATLAS missions, a crew procedure will be developed to simplify the complex sun scan activities.

CONCLUSIONS

There was much pressure during the ATLAS 1 on-orbit operations to quickly assess and correct the pointing errors. Immediate action caused two problems: to understand the pointing behavior, time was required to let the trends develop and to examine these trends; the second, is to properly coordinate the necessary changes to the solar operations through a number of different groups located at different NASA centers and ultimately to the crew.

Resulting from lessons learned during ATLAS 1, hardware and procedural changes were made to allow the ATLAS 2 crew to view on-board instrument pointing data and to correct the instrument pointing errors immediately. The crew and flight planners were extensively trained prior to the second ATLAS flight to perform the correction procedures.

The flight of ATLAS 1 for payload planners provided many lessons for understanding the behavior of the Orbiter as a pointing platform. This experience permitted improved solar operations for ATLAS 2 and can be applied to future flights which use the Orbiter as a pointing platform.

ACKNOWLEDGEMENTS

The author's would like to thank the JSC Pointing Officers, JSC Guidance, Navigation, and Control Officers, and the PAWS engineers for providing insight and experience when we needed help and suggestions.

This work was supported by the National Aeronautic and Space Administration (NASA)/ Marshall Space Flight Center (MSFC), Huntsville, Alabama, under Contract NAS8-41000.

REFERENCES

- [1] ATLAS Brochure, NASA/MSFC Payload Project Office, 1993.
- [2] SUSIM Instrument Interface Agreement, NASA/MSFC Document JA-606E Rev. A, July 1992.
- [3] VanHoosier, M., ATLAS-3 Crew Training Presentation, Naval Research Laboratory, February 23, 1994.
- [4] Degenhardt, W., ATLAS 1 S/C Position and Attitude (MAS HK Plots), Max-Planck-Institut fur Aeronome, December 1992.
- [5] ATLAS 1 Pointing and Alignment Workstation (PAWS) Final Report, Teledyne Brown Engineering Report 410RPT0146, September 1992.
- [6] ATLAS Postmission Attitude/Ephemeris Data Products Study, Teledyne Brown Engineering Report 410RPT0375, November 1993.

Overview of the Miniature Sensor Technology Integration (MSTI) Spacecraft Attitude Control System

Rob McEwen

Integrated Systems, Inc.

3260 Jay St. Santa Clara, CA 95054

May, 1994

ABSTRACT

Msti2 is a small, 164 kg (362 lb), 3-axis stabilized, low-Earth-orbiting satellite whose mission is missile booster tracking. The spacecraft is actuated by 3 reaction wheels and 12 hot gas thrusters. It carries enough fuel for a projected life of 6 months. The sensor complement consists of a Horizon Sensor, a Sun Sensor, low-rate gyros, and a high rate gyro for despin. The total pointing control error allocation is 6 mRad (.34 Deg), and this is while tracking a target on the Earth's surface. This paper describes the Attitude Control System (ACS) algorithms which include: attitude acquisition (despin, Sun and Earth acquisition), attitude determination, attitude control, and linear stability analysis.

INTRODUCTION

Msti2 is a small, relatively inexpensive spacecraft that was designed, built and tested in 16 months. It is 3-axis stabilized, and will be able to track a point on the Earth's surface to within 6 *m*-rad, (.34°) total pointing error. The control system pointing error allocation (excluding sensor errors) is 1.7 *m*-rad (.1°). The vehicle carries enough fuel for a projected life of 6 months.

Msti2 will be placed in a low-Earth, Sun-synchronous (polar) orbit. The orbital period is 92 minutes. Msti2 will come into contact with a ground station approximately once every 1-2 hours, with a typical contact duration of 8-12 minutes. The infrequent contacts require that the vehicle have a relatively autonomous high-level (mode) controller.

The Msti2 flight code has been designed, coded, and tested in 13 months. This short schedule was, in large part, made possible by the use of automatic code generation. The controls algorithms were first realized in block-diagram form, then automatically converted to Ada code. The generated code comprises approximately 40% of the total flight code. The rest consists mostly of command and telemetry functions, and device specific I/O code, which do not lend themselves readily to block diagram form and hence were hand written. The entire Ada source code is 25,000 lines, not including comments. The executable is slightly less than 128k bytes.

This paper introduces the Msti2 spacecraft from an Attitude Control System (ACS) and software point-of-view. The paper then describes various aspects of the ACS design, such as attitude determination, attitude control, linear analysis and design, and robustness.

PHYSICAL CHARACTERISTICS, SENSORS AND ACTUATORS

The vehicle is octagonal in shape, and weighs 164 kg (362 lb) including fuel and payload. The principle moments of inertia are (17, 20 14) kg-m². It is approximately .8 m (2.5 ft) in diameter, and 1.4 (4.5 ft) in height. The average power consumption is 145 watts.

The CPU is a 1750A with 1 M-byte of sRAM, and 512 k-bytes of E²PROM. It can process approximately .8 MIPS. The CPU communicates with the interface boards through a VME bus.

Three reaction wheels provide actuation for fine pointing control. The wheel motor torque capacity is at 25 milli-Newton-meters. The drag torque ranges from 2 to 15 *m*-Nm. The wheel can spin up to 530 rad/sec (5100 rpm), which corresponds to a momentum storage capacity of 4 Newton-meters-seconds. A digital tachometer measures wheel speed at 54 counts per revolution.

The vehicle carries 12 monopropellant hydrazine thrusters for wheel desaturation, orbit adjust, and backup attitude control. There are 8 ACS thrusters at .9 Newtons (.2 lb), and 4 Delta-*v* thrusters at 4 Newtons (1 lb).

The Sun sensor has a 128° field of view in each of two axes, with a quantization step of 34 μ -rad per lsb. Static error is about 26 lsb, 3σ . The sun sensor faces out along the +*y* vehicle axis.

The Horizon sensor has a conical scan of 60° at 5 Hz, with a blanking region of 81°. Quantization is 96 μ -rad/lsb. Sensor error is 154 lsb, 3σ . The scan cone faces out along the -*y* vehicle axis.

The high resolution gyros are rate-integrating, with a quantization step of 20 μ -rad/lsb. Noise is approximately .7 lsb, 3σ . The saturation level is $\pm 5^\circ$ /sec (87 μ -rad/sec).

DESCRIPTION OF THE MSTI2 ATTITUDE CONTROL SYSTEM

Overview

This section introduces the major components of the Msti2 Attitude Control System (ACS). Each component is discussed in further detail in subsequent sections.

Figure 1 shows an overview of the Msti2 ACS. Each block represents a distinct part of the control system. All blocks represent software, except the Watchdog Timer, and the sensors.

The architecture in Figure 1 is due to the basic control requirements, which are:

1. Despin the vehicle after separation from the booster.
2. Point the +*y* vehicle axis at the Sun to illuminate the solar array, and to obtain a Sun sensor measurement.
3. Point the +*z* axis of the vehicle at nadir to obtain a Horizon Sensor measurement, and to establish communication with the primary antenna.
4. Perform an orbit adjust maneuver.
5. Track a point on the Earth's surface to within 6 *m*-rad total pointing error, and 100 μ -rad/sec rate stability.

The block "Modes" contains algorithms that accept signals from the sensors, and compute position and rate error. The purpose of the first 6 modes is to despin the vehicle, after separation from the Scout booster, and then locate the Sun and the Earth. This process takes about 10 minutes.

All modes output position and rate error in the form of a normalized quaternion, and an angular velocity vector.

Only one mode may be active at a time. Mode selection is based on boolean variables such as: body rates small, Sun present, Earth present, etc. The block "Mode Control Logic" accepts

inputs from the sensors and activates the appropriate mode. Automatic mode selection may be overridden by ground controllers at any time by either time-tagged or immediate commands. The Modes and Mode Controller are described further in the following section.

The remaining four Mission modes control precision pointing and maneuvering during payload operation. These modes differ from the others in that they have a complete, large-angle attitude reference, and will maintain attitude reference should the Sun or the Earth or both go out of the field of view during a maneuver.

The “Command Generator” block computes the desired attitude and body rates for each of the four Mission modes. The output of this block is an inertial quaternion and inertial body rates.

The “Attitude Controller” block takes the position and rate error computed by one of the modes, and requests a torque. This block performs a proportional derivative (PD) computation when the angular position error is small enough. Otherwise, it does a constant rate slew about the Euler axis until the error is small enough to switch to PD.

The requested torque vector is routed to either the wheel controller, or the thruster controller. Either, or both, may be enabled.

The “Thruster Controller” converts the requested torque vector into on-times for each of the 12 thrusters, using pulse width modulation. Any subset of the 12 thrusters may be enabled by ground commands. This controller also contains logic to maintain attitude control during orbit adjust by off-modulating the 4 delta-v thrusters.

The “Wheel Controller” takes the requested torque from the Attitude Controller, and computes wheel motor commands. This controller contains a speed feedback loop based on the wheel tachometer. The wheel controller also will accept speed set-point commands from the ground for desaturation.

Modes and Mode Controller

Figure 2 shows the Mode Controller, which is a set of recursive boolean equations in state diagram form. This is an actual block diagram, from which Ada code was generated, and not a cartoon representation.

Each of the small rectangular boxes along the transition path represent the conditions which must be satisfied for transition.

The mode transition conditions are summarized in Table 1. Whenever a comparison of a sensor value to a commandable threshold is made, it is simply stated as “big” or “small.”

Two important mode controller commands are MODELIM and MODEFORC. MODELIM sets an upper limit beyond which the mode controller cannot go. For example, MODELIM is initially set to 6 for orbit injection, because the orbit propagator must first be manually initialized by the ground controllers before any of the Mission modes can have a valid attitude reference. For this reason, once the vehicle gets to Mode 6 it must wait for ground commands at a subsequent pass.

MODEFORC overrides the transition conditions and forces the mode controller to enable a commanded mode.

These two commands are not shown Table 1 because they apply to every mode. Keep in mind, for example, that mode 1 is reached by setting MODELIM to 1.

There is safemode logic which can override the Mode Controller at any time. The logic checks the following 6 conditions against commandable thresholds:

1. Sun absent too long

Transition	Up	Down
1 ↔ 2	None.	None.
2 ↔ 3	Body rates small.	Body rates large.
3 ↔ 4	Sun Present.	Sun not present or Body rates large.
4 ↔ 5	Body rates small and Sun pointing error small.	Sun not present or Sun pointing error large or Body rates large.
5 ↔ 6	Earth present and Pitch error small.	Sun not present or Earth not present or Body rates large.
> 6	Body rates small.	None.

Table 1: Mode Transition Conditions

2. Earth absent too long
3. Body rates too large
4. Pointing error too great
5. Wheel speed too high
6. Thrusters on too long

Should any of these conditions be met, a corresponding safemode delay queue will execute. These queues contain sequences of preset commands. Additionally, ground controllers can reprogram these queues, so that the vehicle can be set up to react properly should there be any specifically anticipated anomalies.

Each of the modes is described below. Recall that only one mode may be active at a time, and that each mode puts out position and rate error in the form of an error quaternion and an error angular velocity.

The attitude determination algorithm is enabled for all modes, that is, it is always running, although the attitude it computes is ignored for Mode 6 or less.

Mode1: Idle. The requested torque output of the attitude controller is set to zero. The wheel controller will maintain wheel speeds. No sensors are used for feedback.

Mode2: Capture. The requested torque is proportional to the body rates as measured by the despun gyro. Nominally, the actuators are thrusters 1-4, but this can be reset to any combination of thrusters by ground commands. This mode will damp nutation for the expected range of nutation frequency.

Mode3: Sun Search. The mode controller activates this mode when the measured body rates drop below a commanded threshold. This mode propagates gyro rates to form a large angle quaternion. The initial reference frame is inertially fixed, and is taken to be wherever the vehicle is when the mode is enabled. Relative to this initial frame, the vehicle performs a series of 3 slews designed to pass the entire sky through the field-of-view of the Sun sensor. The sequence is a -270° yaw, followed by a 90° roll, followed by a 180° yaw.

As soon as the Sun present flag is set, the mode controller transitions to Sun point. If the Sun is not found, the vehicle does a final maneuver to return to the initial orientation, and sets a "Sun Not Found" flag in telemetry.

The mode uses only gyros for input.

Mode4: Sun Point. The vehicle will slew its $+y$ axis, where the solar array is, into coincidence with the Sun-line. The Sun sensor outputs are then passed through for roll and yaw position control. Pitch angle is derived by essentially accumulating the pitch gyro channel. A command will set a pitch rotation rate.

The Sun pointing mode uses both the gyro and the Sun sensor for input. When both the body rates and the Sun pointing error are below commandable thresholds, the mode controller transitions to Earth Search.

Mode5: Earth Search. This is basically the same as the previous mode, except that the pitch rate is increased, and the mode controller will activate Sun/Earth pointing mode as soon as the Earth is far enough within the field-of-view of the Horizon sensor.

Mode6: Sun/Earth Point. Here, the pitch angle is now computed from the horizon sensor. Each vehicle axis now has a measured position and rate term. All three attitude determination sensors are in use.

This mode forms the three measured position signals into an approximate small angle quaternion. The quaternion represents the angular displacement of the vehicle from a reference frame which has its y axis centered on the Sun, and z axis as close to the Earth as possible. The z axis of this frame will vary seasonally from approximately 7° to 30° off Earth nadir due to orbit geometry and the inclination of the Earth to the Ecliptic.

The following "Mission" modes use an exact, large angle quaternion computed by the attitude determination. This computation requires on-board propagation of the Sun vector and the vehicle orbit state. After orbit injection, the orbit propagator must be initialized with a measured ephemeris before the attitude determination is valid. Once this is accomplished, any of the following modes may be selected by ground commands.

The attitude determination propagates gyro outputs in order to compute position when the Sun or the Earth or both are out of the field-of-view of their respective sensors.

The Mission modes have the following function:

Mode7: Mission-Local Vertical Hold. The vehicle is held fixed with respect to the Local-Vertical Local-Horizontal reference frame. Ground controllers may command the vehicle to a constant offset from this frame, while in this mode.

Mode8: Mission-Slew. In addition to the automatic slew submode of the attitude control, ground controllers may explicitly command a slew. The slew acceleration, rate, total slew angle, and slew axis are all commandable. The slew profile is a constant acceleration, a constant rate, and a constant deceleration about an inertially fixed Euler axis.

Once the slew is completed, the vehicle maintains the final inertial orientation and awaits ground commands.

Mode9: Mission-Surface Point Track. For the payload to acquire its target, its line-of-sight must remain on a predetermined point on the surface of the Earth. This mode takes target latitude, longitude and altitude as input. It then maneuvers the vehicle so that the z body axis points at the target. It also keeps the vehicle yz plane centered on the Sun to maintain solar array power.

Mode10: Mission-Inertial Hold. The vehicle is held fixed with respect to the ECI frame.

The flexibility and capability of these modes is greatly expanded by use of the delay queues.

Delay queues are buffers in which ground controllers may store a series of time-tagged commands. The flight code will then automatically execute these commands at the prespecified times. Time-tagged commands may then enable or disable modes, or reset parameters. For example, LV hold, Mode 7, can be given a series of offsets, at regular intervals, so that the vehicle in effect can be made to track a prespecified orientation profile.

CONTROL DESIGN

Attitude Determination and Command Generation

The attitude determination involves four frames of reference, shown in Figure 3.

The first is the Earth Centered Inertial (ECI) frame, which has its x - y vectors in the equatorial plane, and the x vector points at the Sun on the vernal equinox. The on-board orbit and Sun propagators output vectors coordinatized in these frames.

The local vertical (LV) frame has the z axis pointing to the center of the Earth, and the x axis in the direction of flight.

The Mission frame represents the desired vehicle orientation, and may move with respect to the local vertical frame. For example, during payload operation, the z axis of the Mission frame will track a point on the Earth's surface. In the Local Vertical Hold mode, the Mission frame is coincident with the local vertical frame.

The fourth frame is fixed in the vehicle body. The objective of the attitude control is to minimize the angular error between the Mission frame and the body frame.

A quaternion with subscript notation specifies the orientation of one frame with respect to another. For example, the orientation of the Body frame with respect to the Mission frame is denoted $q_{B/M}$. The angular velocity of the Body frame with respect to the Mission frame is ${}^M\omega^B$. This nomenclature is used throughout this paper.

The attitude determination propagates gyro outputs in order to compute position when the Sun or the Earth or both are out of the field-of-view of their respective sensors.

In typical control design procedure, one would linearize the plant, and then implement a linear state estimator for attitude determination. For Msti2, payload operation requires that the vehicle z axis track a point on the Earth's surface, which in turn requires that the vehicle have angular acceleration and deceleration over large angles. This makes linearization of Euler's equation infeasible. For this reason, the algebraic method, as described in Wertz, page 424, was chosen for attitude determination. This method provides an exact large angle quaternion over a wide range of vehicle orientations, and does not require a linearized model of the vehicle dynamics.

The attitude determination algorithm passes the algebraically computed quaternion through a low-pass filter to reduce quantization noise.

The algorithm produces $q_{B/ECI}$, the quaternion expressing body attitude with respect to the Earth Centered Inertial (ECI) reference frame. This computation requires orbital location and Sun position (coordinatized in ECI) as input. For this reason, the flight software contains both Sun and vehicle orbit propagation algorithms.

The orbit propagation algorithm must be initialized with a measured ephemeris after orbit injection. Ground operators must subsequently perform periodic ephemeris updates to correct propagator drift. The propagator contains an aerodynamic drag term, which has a commandable value that will be used to adjust the propagator to minimize drift.

The command generator computes desired vehicle orientation and rates with respect to the ECI frame. This orientation is expressed as $q_{M/ECI}$, where M symbolizes the "mission"

(or desired) reference frame. The attitude error is then

$$q_{B/M} = Q_{B/ECI} q_{ECI/M} \quad (1)$$

This quaternion multiply is expressed here as a matrix multiply where Q is the 4 by 4 matrix representation, and $q_{ECI/M}$ is the conjugate of $q_{M/ECI}$. $q_{B/M}$ is passed to the attitude control compensation, and represents pointing error.

The command generator can generate 4 different orientation and rate profiles for the mission frame, which correspond to the 4 Mission Modes described previously.

Attitude Control

The attitude control algorithm, as shown in Figure 4, computes a requested torque T_r , based on position and rate errors. The basic scheme is proportional-derivative, with slightly different variations for despin, large angular error, and small angular error.

During despin, requested torque is based on angular velocity:

$$\vec{T}_r = -I^B 2K_r {}^{ECI}\vec{\omega}^B \quad (2)$$

where I^B is the vehicle inertia matrix, K_r is the rate gain, and ${}^{ECI}\vec{\omega}^B$ is the angular velocity of the body (vehicle) with respect to the ECI frame.

Nutation motion is damped by this control because the applied torque is always proportional to the negative of the angular velocity. However, the control system sampling rate must be significantly faster than the nutation frequency or else the sampling process will cause a potentially destabilizing delay.

The nutation frequency ω_N , is defined here as the frequency at which the angular velocity vector rotates around the principal axis *as viewed by an observer fixed in the body frame*. Then,

$$\omega_N = \left| \frac{I_s}{I_t} - 1 \right| \omega_{sp} \quad (3)$$

where ω_{sp} is the spin frequency, and I_s, I_t are the spin and tangential inertias, respectively. For Msti2, $\omega_N \approx 4$, or about .6 Hz, which is sufficiently less than the control system sampling frequency of 5 Hz.

When the control is passed a large angle $q_{B/M}$, the requested torque is

$$\vec{T}_r = I^B \left(\omega_s \frac{\vec{q}}{\|\vec{q}\|} - {}^{ECI}\vec{\omega}^B \right) K_r + {}^{ECI}\vec{\omega}^B \times I^W {}^B\vec{\omega}^W \quad (4)$$

where \vec{q} is the vector part of $q_{B/M}$, I^W is the inertia matrix of the three reaction wheels, and ${}^B\vec{\omega}^W$ is the angular velocity of the wheels with respect to the body frame. ω_s is a (scalar) commanded slew rate.

This causes a rate controlled slew about the Euler axis. The second term above accounts for stored wheel momentum.

When $q_{B/M}$ represents a small angular error, the requested torque is

$$\vec{T}_r = -I^B (2K_p \vec{q}_{B/M} + K_r {}^M\vec{\omega}^B) + {}^{ECI}\vec{\omega}^B \times I^W {}^B\vec{\omega}^W \quad (5)$$

This essentially is PD control. K_p and K_r are position and rate gains, and ${}^M\vec{\omega}^B$ is the angular velocity of the body (vehicle) with respect to the mission frame.

Linear Modelling and Stability Analysis

Figure 5 shows the small-signal linear model of the attitude control loop. The following analysis is for the fine pointing case, which uses wheel control. Thruster actuated attitude control is not discussed here.

The outer loop two loops represent the small signal behavior of the attitude control. The inner loop, from \bar{T}_{in} to the zero order hold, is the wheel controller.

The Wheel Controller takes the requested torque from the Attitude Controller, and computes wheel torquer motor commands.

The wheel controller contains a feedforward path that passes the requested torque to the wheel motors, after a conversion to counts. A feedback term, based on the tachometer, is added to the motor command. The primary purpose of the feedback loop is to compensate for wheel bearing drag, which is a nonlinear function of wheel speed, and is also temperature dependent.

The feedback term is computed by first scaling the requested torque by the wheel inertia matrix, and then accumulating (integrating) it to produce a wheel speed command. The filtered tachometer output is differenced with the speed command to produce an error signal, which is passed through a compensator.

The compensator contains a proportional term and an integral (accumulated) term. The purpose of the accumulator is to command just enough torque to cancel the drag torque.

The accumulator state is limited because the controller may ask for more torque than the wheel motor can provide (this is nonlinear behavior). For example, this will happen during wheel desaturation when the wheel speed set point is reset to zero. During the time the wheel is spinning down, the accumulator, if not limited, would be "winding up," or accruing a large state, which would cause a large, slow, and undesirable transient.

The tachometer measurement is passed through a first order filter to reduce quantization noise.

The initial ACS design iteration was done by a series of simplifying approximations. The quantization filters have a bandwidth of .5 Hz, which is much higher than the expected closed loop bandwidth, so they may be neglected for approximate analysis. The torque control (T_o/T_i) has an approximately unity transfer function so it may be neglected as well. The closed loop bandwidth is much lower than the sampling frequency, so the whole system may be approximated by its continuous-time equivalent. These approximations result in the standard second order continuous-time transfer function shown below:

$$\frac{\theta_C}{\theta_R} = \frac{K_p}{s^2 + K_r s + K_p} \quad (6)$$

This is a type 1 system, and has no steady-state error for step inputs.

The specifications for control system performance are 1.7 *m*-rad pointing error and 100 μ rad/sec rate stability during payload operation. The vehicle will probably be maneuvering during payload operation, and so the natural frequencies of the control loop should be much higher than the frequency content of the commanded angles and rates. This indicates that the dominant time constants should be less than about 5 seconds.

As an initial value, the time constant is chosen to be 2.5 sec, which implies that $K_r = .8 \text{ sec}^{-1}$. It is desirable to keep

$$\frac{1}{\sqrt{2}} \leq \zeta \leq 1 \quad (7)$$

which implies that that

$$.16 \leq K_p \leq .32 \quad (8)$$

$$.04 \leq f_{BW} \leq .09 \quad (9)$$

where f_{BW} is the closed loop bandwidth in Hz. The velocity error constant indicates that pointing performance will improve as K_p increases, however, stability margins decrease and sensor noise amplification increases.

The loop transfer function, with the loop opened at the torque command input to the plant (K_p gain in Figure 5) is

$$l(s) = \frac{K_r s + K_p}{s^2} \quad (10)$$

This system has an infinite gain margin, and a phase margin between 65° and 75° . Of course, these values discussed above are approximate, and the stability margins in particular are suspect, because the loop must be opened at the zero-order-hold in Figure 5, instead of at K_p , to get a realistic measure. Accurate values can be obtained by a numerical analysis of the system in Figure 5.

Starting with the (K_p , K_r) values above, the system in Figure 5 was numerically discretized and analyzed. Then several trial-and-error simulation runs were made, involving both the linear analysis program, and the nonlinear truth simulation, to slightly adjust the gains to achieve the desired performance and robustness. The final results are summarized below.

```
Kp = 2.5000D-01  1/sec**2, Position Gain
Kr = 9.0000D-01  1/sec, Rate Gain
fquant = 5.0000D-01  Hz, Quantization Filter Bandwidth
Krw = 6.0000D-02  1/sec, Wheel Rate Gain
Kiw = 1.0000D-03  1/sec**2, Wheel Integrator Gain
fwhl = 1.0000D-01  Hz, Wheel Tach Filter Bandwidth
The drag torque coefficient (viscous) is 4.5000D-05 Nm/rad/sec.
```

```
The order of the open loop system is: 7
The open loop roots are:
```

```
---Z Root Information Algorithm-----
1 eigenvalues at z=0 have been removed.
There is (are) 6 real evals, 0 complex pairs
and 0 s=0 evals.
```

```
Magnitude and Phase (Deg):
0.5335  0.0000  (Quantization filter pole)
0.8819  0.0000  (Wheel tach filter pole)
0.9988  0.0000  (Drag Torque pole)
1.0000  0.0000
1.0000  0.0000
1.0000  0.0000
```

```
Time constant, 3 time constants (seconds):
0.3183  0.9549
1.5915  4.7746
171.1135  513.3406  (Wheel drag time constant)
```

```
---End Z Root Information Algorithm-----
```

The gain crossover frequency is 1.5180D-01 Hz.
The gain margin is: -2.4418D+01 1.3529D+01 dB.
The phase margin is: 4.1615D+01degrees.

The order of the closed loop system is: 7
The closed loop roots are:

---Z Root Information Algorithm-----
1 eigenvalues at z=0 have been removed.
There is (are) 2 real evals, 2 complex pairs
and 0 s=0 evals.

Magnitude and Phase (Deg):

0.8165	0.0000
0.8501	9.0693
0.8501	-9.0693
0.9307	0.0000
0.9940	0.1137
0.9940	-0.1137

Damping ratio, Natural Frequency (Hz), time constant, 3*T.C.:

0.7161	0.1805	1.2315	3.6944
0.9493	0.0050	33.3692	100.1075

Time constant, 3 time constants (seconds):

0.9868	2.9604
2.7852	8.3555

---End Z Root Information Algorithm-----

The closed loop bandwidth is 6.8405D-02 Hz.

The wheel accumulator time constant shows up here as 33 seconds. From a transfer function point of view, these poles are nearly cancelled by zeros, so the effect on the input-output response is small. The wheel accumulator state is limited to a commandable value between 4-15 *m*-Nm, so this transient will not show up anyway.

Simulations show that the step response is dominated by the 2.9 second time constant.

Robustness

This discussion pertains to the fine pointing wheel control loop in Figure 5. Thruster control is not analyzed here.

The above linear analysis showed a gain margin of 13 db, and a phase margin of 47°, with the loop opened at the wheel motor interface. This point is inside both the attitude control and the wheel control loops. It is important to measure the stability margin at this point since it is where the uncertainty in the plant is best represented. The uncertainty is caused by the torquer motor coefficient, vehicle and wheel inertias, etc.

The linear analysis also shows a lower gain margin of 24 dB. This is due to the accumulator pole which produces the commanded wheel speed setpoint. It is acceptable because if the gain at that point should drop by 24 dB, the wheel control would be so weak that the vehicle would have to be switched to thruster control anyway.

Another point of interest is the drag torque, since it is not constant, and may vary by a factor of about 7. It is known to be a function of both wheel speed and temperature. The stability margin at the drag torque coefficient, with all other loops closed, is 66 dB gain

margin, and infinite phase margin. This shows that the system is stable for all realistic drag torque values.

ACKNOWLEDGEMENTS

I would like to acknowledge the other members of the Msti2 ACS and Software design team, who have contributed significantly to this project. They are: Fred Tubb, Keiko Chevray, Andy Waddell, John Farazian, and Chris Rygaard.

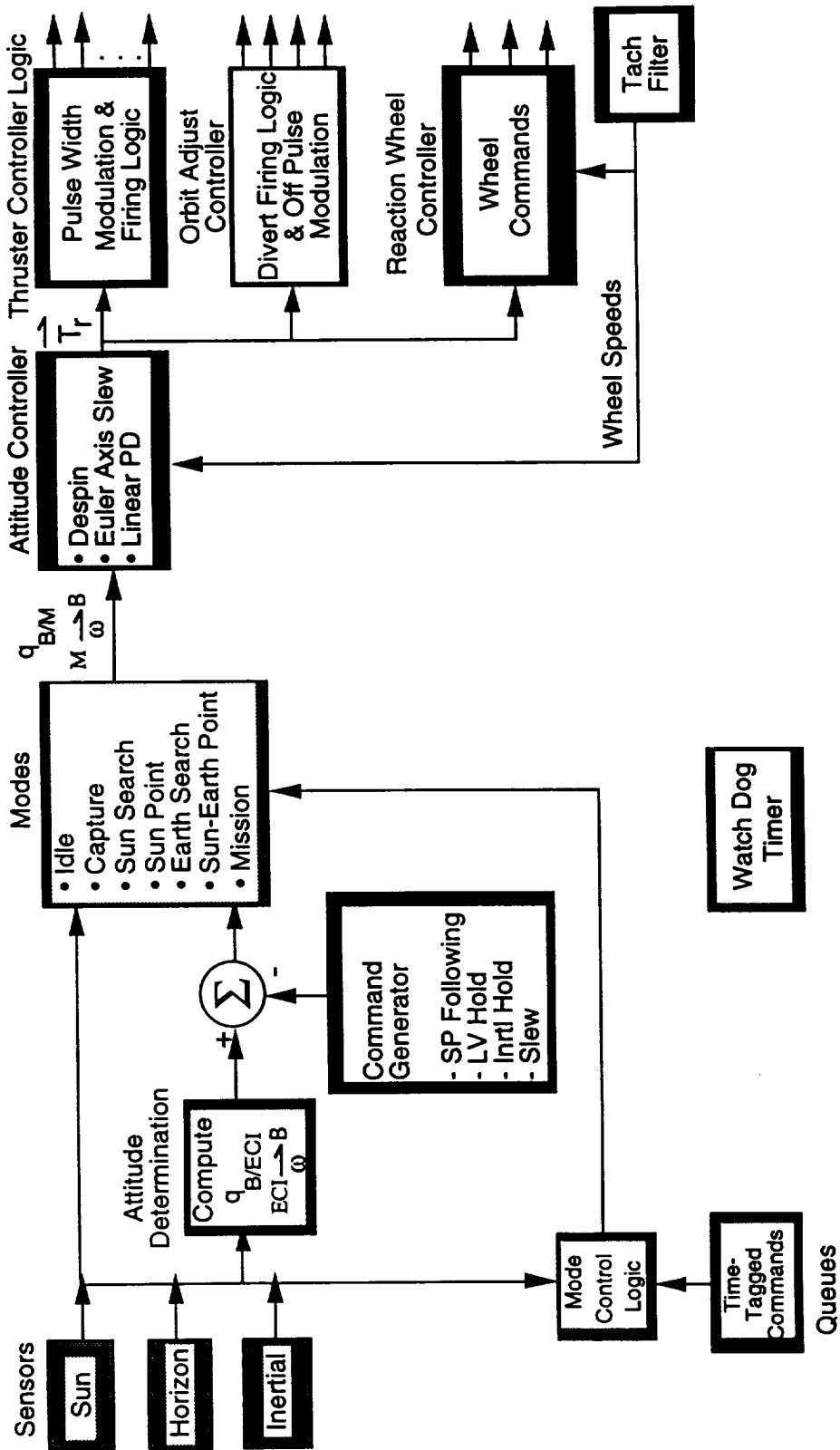


Figure 1: Overview of Msti2 ACS

State Diagram	STD.Inputs	STD.Outputs	SuperBubble	Level
Mode Controller	10	10	TOP_LEVEL	1

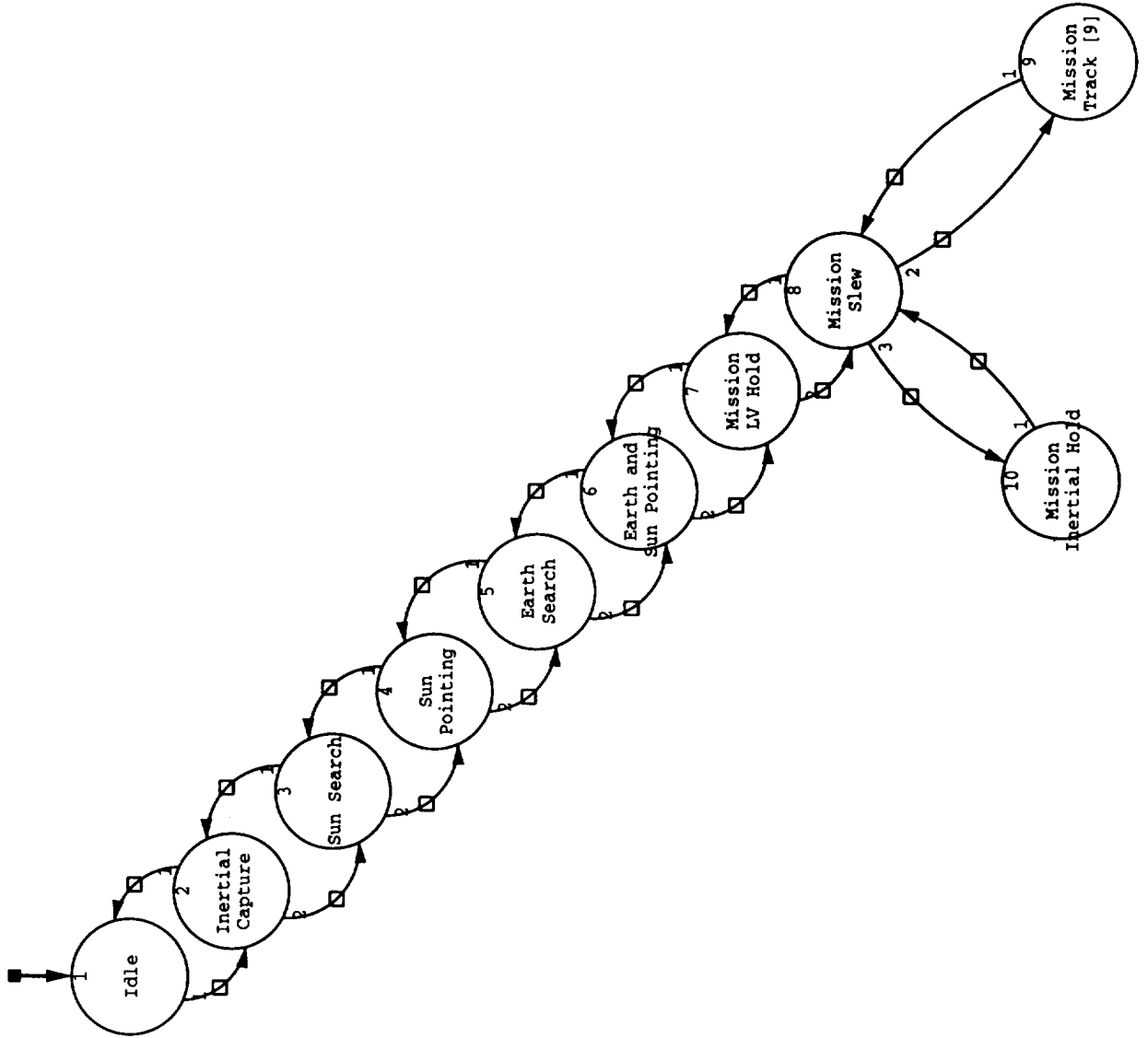


Figure 2: Mode Controller State Diagram

A Geometric Model of a V-Slit Sun Sensor Correcting for Spacecraft Wobble

W. P. McMartin and S. S. Gambhir
The Analytic Sciences Corporation (TASC)
12100 Sunset Hills Road
Reston, Virginia 22090
(703) 834-5000

Abstract

A V-Slit sun sensor is body-mounted on a spin-stabilized spacecraft. During injection from a parking or transfer orbit to some final orbit, the spacecraft may not be dynamically balanced. This may result in wobble about the spacecraft spin axis as the spin axis may not be aligned with the spacecraft axis of symmetry. While the widely used models in *Spacecraft Attitude Determination and Control* edited by Wertz correct for separation, elevation, and azimuthal mounting biases, spacecraft wobble is not taken into consideration. A geometric approach is used to develop a method for measurement of the sun angle which corrects for the magnitude and phase of spacecraft wobble. The algorithm was implemented using a set standard mathematical routines for spherical geometry on a unit sphere.

1 Introduction

Spin-stabilized spacecraft will exhibit wobble or coning if the principal axes of the vehicle are not aligned with the body axes. This condition exists for some dual spin spacecraft when they are in an all-spun condition before the platform is despun. For vehicles that use integral propulsion to achieve operational orbit, attitude determination while in an all-spun condition can be important, since the attitude determination accuracy will determine the accuracy of the direction of the integral propulsion injection maneuvers.

For our problem the principal axes are well known in the vehicle body system; all that remains is to model the sensors taking vehicle coning into account. The sensors include a V-slit sun sensor and an infrared body mounted horizon sensor measuring earth chord. We will discuss the development of a V-slit sun sensor model accounting for vehicle coning.

2 V-Slit Sun Sensor Model

We wish to produce a model that generates predicted sun sensor measurements given an orbital position, an attitude, and the location of the principal axes in body coordinates. This is what many attitude determination processes require.

We start with the discussion of V-slit sensors in Wertz[1]. The model developed in Wertz is not intended to take vehicle coning into account, but the development does provide the insight required to find a model that does account for coning. **Figure 1** shows the geometry of V-slit sensor with no coning. As seen from the vehicle body coordinate system, the sun will describe a small circle of radius β . That is, the sun describes a small circle about the spin axis of the vehicle as seen from the vehicle body coordinate system.

To develop the V-slit sensor model accounting for a coning vehicle, observe that the small circle that describes the sun motion is no longer centered at the pole of the figure; it is centered about the spin axis of the vehicle, just as in the case without coning. The only difference is that the spin axis is no longer the body z axis. This is shown in **Figure 2**. In Figure 2 P is the spin axis of the vehicle, S_1 is the sun-slit 1 intersection, and S_2 is the sun-slit 2 intersection. The rotation angle, S_1PS_2 is the desired sensor prediction.

To calculate S_1PS_2 the points S_1 and S_2 must first be found. Then the rotation angle S_1PS_2 can be calculated. This task is simple if the analyst's software toolkit includes routines for finding the intersections of small circles and routines for finding rotation angles. The intersections of the sun small circle with the two great circles that define the V-slit fields of view are the

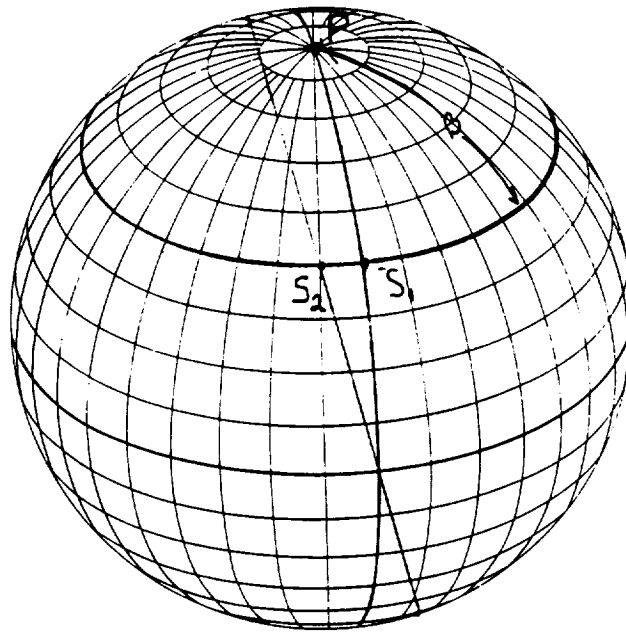


Figure 1 V-Slit Sun Sensor Geometry with No Wobble

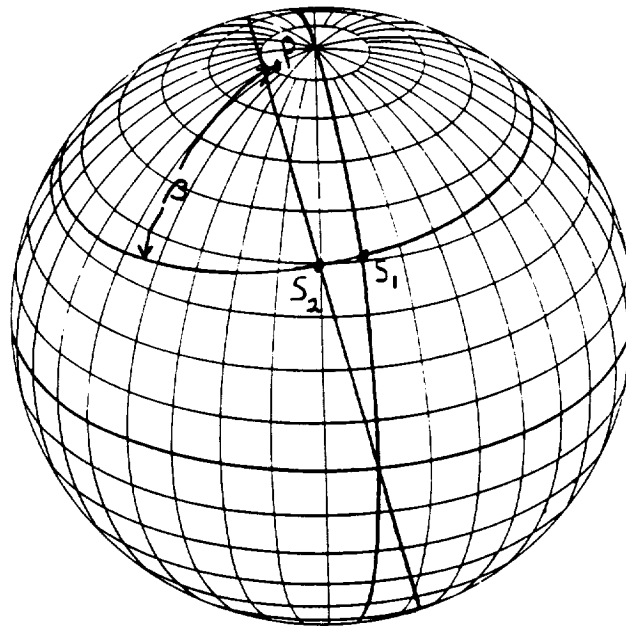


Figure 2 V-Slit Sun Sensor Geometry with Vehicle Wobble

points S_1 and S_2 . The rotation angle from first slit crossing to the second slit crossing about the axis of rotation is the rotation angle S_1PS_2 , the predicted sensor measurement.

This approach to modeling the V-slit sensor also makes dealing with slit misalignments quite easy, since the slit alignments are described by the location of the poles of the great circles that describe the slit fields of view. Inclusion of slit alignment biases reduces to simple changes to the coordinates describing the poles of the slit great circles. The resulting FORTRAN code is shown in Figure 3.

3 Results

Figure 4 compares the predictions of the coning and non-coning V-slit models. The x-axis shows the azimuth of the principal axis in the body coordinate system (the vertical slit of the V-slit sensor is assumed to be at azimuth 0°). The cases shown are for a 3° coning angle; the different lines show different β angles. The size of the model error increases for the extreme elevation angles. Since injection scenarios can involve extreme sun angles, this increases the desirability of using the more sophisticated model.

4 Conclusions

Inclusion of coning effects in V-slit sensor predictions produces a marked improvement in the model accuracy. The adjustment to the V-slit model developed in Wertz is simple and intuitive. Model development is simplified when software utilities for finding rotation angles and intersections of small circles are a part of the analysis environment.

5 References

1. Wertz, James R. (Editor), Spacecraft Attitude Determination and Control, Norwell, MA, Kluwer Academic Publishers, 1978, pp. 217-221.

```

function vslit(ral,decl,rad1,ra2,dec2,rad2,beta,wobble,phi)

c ral, decl      right asc. and declination of slit #1 pole
c rad1          radius of the small circle that describes slit #1
c ra2, dec2     right asc. and declination of slit #2 pole
c rad2          radius of the small circle that describes slit #2
c beta         sun angle measured from axis of rotation
c wobble       coning magnitude (deg)
c phi          coning phase (deg)

      real*8 ral,decl,rad1,ra2,dec2,rad2,beta,wobble,phi,vslit
      real*8 sun(3),sens1(3),sens2(3)
      real*8 vecout1(3),vecout2(3),usens1(3),usens2(3)
      real*8 cross1(3),cross2(3)
      real*8 rad,dang,rotang
      integer flag

c RADECV forms a vector from a right ascension, declination, and magnitude
      call radecv(rad(ral),rad(decl),1.d0,sens1)
      call radecv(rad(ra2),rad(dec2),1.d0,sens2)
      call radecv(rad(phi),rad(90.0d0-wobble),1.0d0,sun)

c CONES8 finds the intersections of two small circles
c DANG finds the included angle between two vectors
      call cones8(sens1,rad(rad1),sun,rad(beta),flag,vecout1,vecout2)
      call radecv(rad(ral-90),rad(decl),1.0d0,usens1)
      if(dang(usens1,vecout1).gt.dang(usens1,vecout2)) then
          call dup(vecout2,cross1)
      else
          call dup(vecout1,cross1)
      endif

      call cones8(sens2,rad(rad2),sun,rad(beta),flag,vecout1,vecout2)
      call radecv(rad(ra2-90),rad(dec2),1.0d0,usens2)
      if(dang(usens2,vecout1).gt.dang(usens2,vecout2)) then
          call dup(vecout2,cross2)
      else
          call dup(vecout1,cross2)
      endif

c ROTANG finds the rotation angle from vector1 to vector2 about vector3
      vslit = rotang(cross2,cross1,sun)

      return
      end

```

Figure 3 FORTRAN Code for V-slit Sun Sensor Model Accounting for Vehicle Wobble

Error Magnitude vs. Coning Phase for 5 Sun Angles

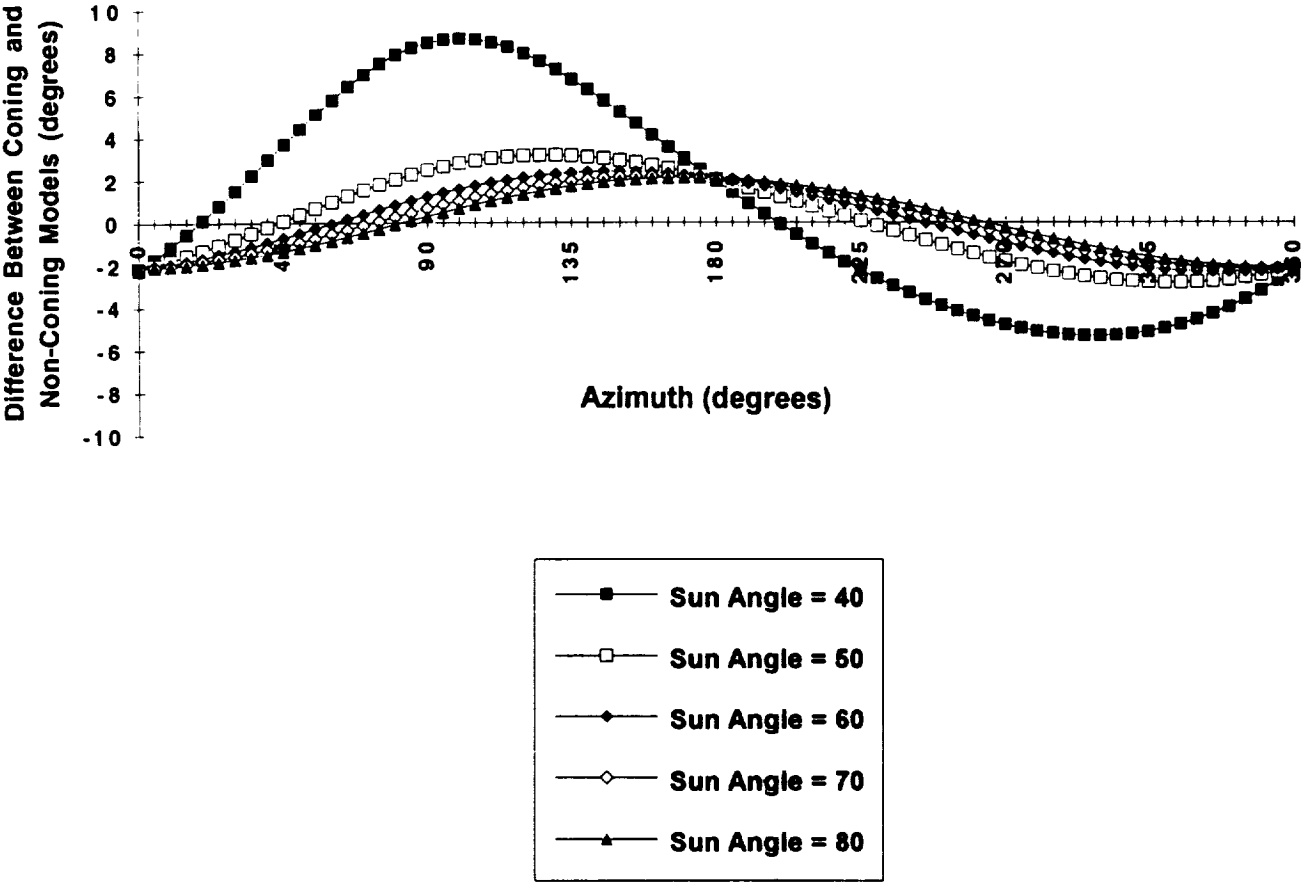


Figure 4 V-Slit Sun Sensor Model Predictions for Coning and Non-Coning Models

Overview of the MSTI 2 On-Orbit Alignment

Christopher A. Rygaard
Fred W. Smith
M. Michael Briggs

Integrated Systems, Inc.
Santa Clara, CA

Abstract

The Miniature Sensor Technology Integration (MSTI) 2 spacecraft is a small 3-axis stabilized spacecraft designed to track mid-range missiles and estimate their state vectors. In order to accurately estimate the target state vector, the MSTI 2 spacecraft must have high accuracy knowledge of its own attitude. Errors in its attitude knowledge arise primarily from the errors in its Attitude Control System (ACS) sensors. The ACS sensors on the spacecraft include a scanning Earth Sensor (ES), a Sun Sensor (SS), and two 2-axis gyros.

The On-Orbit Alignment (OOA) generated an error map of the ES, and estimated the biases of the SS and the misalignment of the gyros. This paper discusses some of the error sources, and the techniques used to reduce the effects of these errors, including estimating errors so that they could be analytically eliminated, and mission design to avoid these errors.

The payload carried by the MSTI 2 spacecraft is a high fidelity camera, which was aimed at the target using gimballed mirrors. By aiming it at a celestial target, the payload was used as a high-accuracy single-axis attitude reference. This attitude reference was compared to the attitude reference of the ACS sensors, and the errors were attributed to the ACS sensors.

Introduction

The MSTI 2 spacecraft (see Figure 1) was designed to track theater ballistic missiles and estimate their state vector. This requires that the attitude knowledge of the spacecraft be on the order of 100 microradians.

The payload is a high accuracy camera with a gimballed mirror. The payload can lock onto a target and track it independently of the MSTI 2 bus. By using the payload to track Venus, it provided a high-fidelity single-axis attitude reference. The ACS sensor data was compared to this attitude reference in order to estimate their respective errors.

This paper discusses some of the error sources, and the techniques used to reduce the effects of these errors, including the estimation techniques to determine some of these errors, and the mission design techniques to avoid other of these errors.

The ACS sensors include two 2-axis gyros, an earth sensor, and a sun sensor. Each of these sensors was calibrated independently, and this paper presents the approach used in each of these calibrations.

Error sources

The gyros underwent extensive ground testing, and were very well characterized prior to launch. The primary error source for the gyros is due to geometric misalignment in their mounting on the spacecraft.

The ground testing of the sun sensor indicated errors on the order of 0.2° , while ground testing of the earth sensor indicated errors on the order of 0.1° . It was unclear if these errors were within the sensor itself, or if they were due to inaccuracies in the test apparatus. In addition, the ground testing included no statistical characterization. Also, the time-tagging of the SS data and ES included a uniform-distribution error 0.2 seconds wide. The SS and ES also had errors due to geometric misalignment their mounting on the spacecraft.

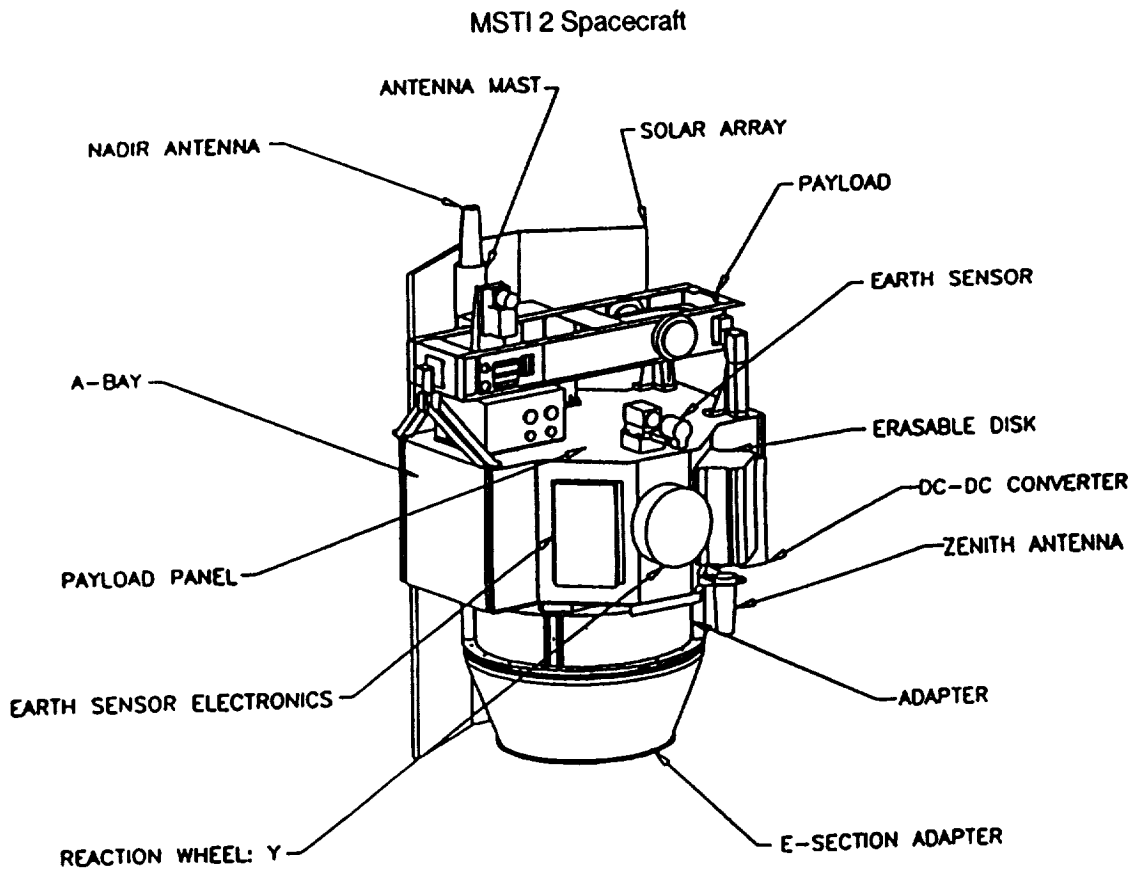


Figure 1

The earth sensor had two other error sources. First, the relatively slow scan rate of the ES caused an error source in its attitude information. If the spacecraft is slewing, the spacecraft will slew a certain amount during the time between sensing the leading edge of the earth signal and sensing the trailing edge of the earth signal. The amount of this slew would introduce errors in the attitude knowledge. Second, the flight software analyzed the ES data under a spherical earth shape approximation. This can introduce errors as large as 1° . The OOA and the mission design had to account for this error source by utilizing an oblate earth shape approximation.

The goal of the MSTI 2 bus is to accurately point the payload. Therefore it was decided that the ACS sensors would be calibrated relative to the p_1 , p_2 , and p_3 unit vectors which define the payload reference frame, and not relative to the S/C frame. This eliminated any errors due to uncertainties in the precise location of the S/C reference frame. In fact, the attitude of the S/C reference frame is irrelevant during a target encounter; only the attitude of the payload is of interest. The S/C reference frame is completely fictitious; it is a purely mathematical construct to facilitate analysis, design, and construction.

Mission Design to Avoid Errors

The problem of the slow ES scan rate is eliminated if the spacecraft is not slewing, because there will be no change in attitude between the times of the leading edge and the trailing edge of the earth signal. Also, the time-tagging problem of the ES and the SS is eliminated if the spacecraft is not slewing, because the signals they generate are constant. Therefore it was decided that immediately prior to a target encounter, the spacecraft would hold its attitude fixed in inertial space long enough to obtain a high accuracy attitude reference, and then proceed with the target encounter using only gyro propagation. This maneuver was called the "Gyro Nulling Attitude" (GNA). The GNA effectively eliminated the error sources due to time tagging and slow ES scan rate. This in turn eliminated the need to analytically remove the errors due to these source.

The primary purpose of the GNA was to hold the spacecraft fixed in inertial space in some attitude. This maneuver would be effective in any orientation. Therefore, it was decided to select the GNA orientation to reduce the OOA effort. Ideally, it would be necessary to calibrate only one point in the SS FOV, and one single ES orientation, and then select the GNA to place the sun and earth at these points. With this technique, the error estimation effort of the

OOA would be greatly reduced. However, the Sun-S/C-Earth angle changes during the spacecraft's orbit around the earth, and it changes during the earth's orbit around the sun. Therefore, these sensors had to be calibrated to accommodate a range of Sun-S/C-Earth angles. Nonetheless, this approach reduced the error estimation effort significantly.

Celestial Attitude Reference

The only celestial bodies which are bright enough to be seen by the MSTI 2 payload are the sun, the moon, and Venus. The sun could not be used because it would quickly damage the focal plane of the payload.

The moon is bright enough to be tracked by the payload, but it has a significant angular extent as seen from orbit. In addition, its image on the MSTI 2 payload focal plane will have some unknown shape due to the cooling of the moon as it changes phases, and it is unclear exactly how the tracker would compute the centroid this shape. The only feasible technique to use the moon as an attitude reference would have required that the outer arc of the crescent of the moon be estimated, so that its center could be used as an accurate attitude reference. This implies an extensive development effort with high risk.

Therefore, it was decided that Venus would be used as the celestial attitude reference. This presented its own set of problems. The off-axis sensitivity of the MSTI 2 payload is such that if it is pointed within 20° of the sun, any image it has would be washed out. Figure 2 shows the separation between Venus and the sun during the period of interest. Prior to April 9, 1994, Venus is within 20° of the sun. This was only a few days prior to the MSTI 2 OOA maneuvers.

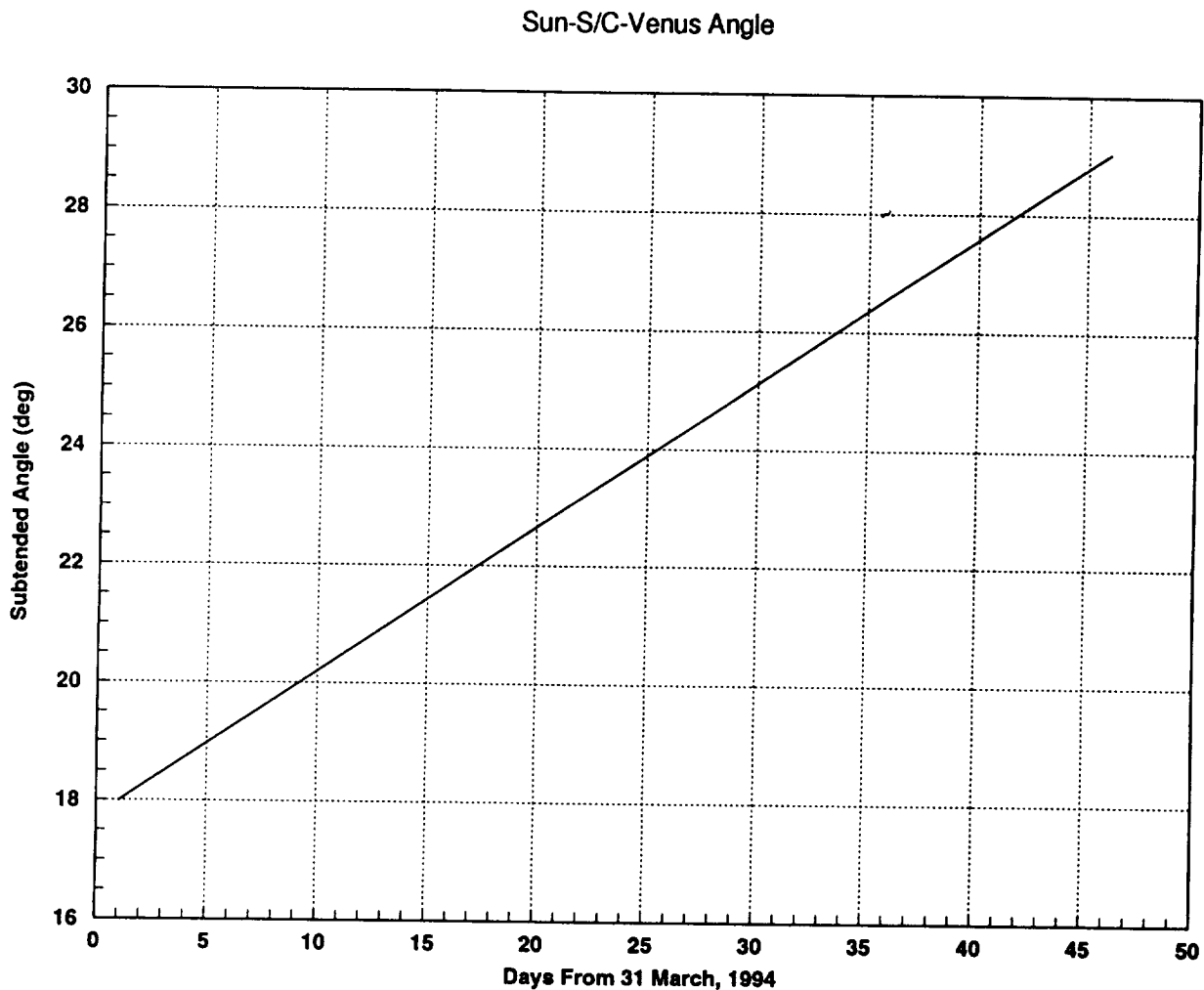


Figure 2

In addition, this small subtended angle between the sun and Venus presented problems arising from the geometry of the MSTI 2 spacecraft, as will be described in the discussion on SS calibration.

Sun Sensor Calibration

The SS has a "square" Field Of View (FOV), nominally centered along the S/C Y axis. The sun sensor would report the position of the sun by transmitting two signed angles representing the location of the sun in the FOV. These are (1) SS Z, the angle between the projection of a unit vector pointing toward the sun onto the S/C X-Y plane, and the S/C X axis, and (2) SS X, the angle between the projection of a unit vector pointing toward the sun onto the S/C Z-Y plane and the S/C Z axis.

Due to geometry constraints, it was decided that only one point in the SS FOV would be calibrated, as described below. A complete calibration at this single point could be characterized by a simple bias on each of the two outputs. Because it is a single point, all of the non-temporal error sources could be corrected by these simple biases.

The approach utilized to estimate these biases was purely geometric. With this approach, in order to measure the errors with a single experiment, the full 3-axis attitude of the payload reference frame would have to be known. However, the only high-accuracy attitude reference available was Venus, and this was only a single-axis attitude reference. Therefore, multiple experiments were required in order to make the biases observable. This purely geometric approach ignores the information provided by the gyros, but it also keeps the gyro alignment estimation and the SS calibration independent of each other.

The approach utilized is illustrated in Figures 3 and 4. These figures are for descriptive purposes only, and are not drawn to scale. Figure 3 illustrates one procedure, and Figure 4 illustrates another procedure. These two procedures alone are enough to algebraically determine the biases. Multiple executions of these two procedures provided statistical data and required a least-squares estimator.

In Figure 3 (Procedure #1), the sun is located in the SS FOV at the calibration point. Also Venus is in the FOR of the payload at one location, which provides only one axis of attitude information. Using astronomical databases, β_1 , the subtended angle between the sun and Venus, is known very accurately. Therefore it is known that the sun must lie somewhere along the arc shown in Figure 3. The exact location of the sun along this arc is unknown because the Venus vector provides only one axis of attitude information. This procedure, by itself, provides only partial error information. In particular, it provides only ϵ_{p1} , the component of the error normal to the arc in Figure 3.

In Figure 4 (Procedure #2), the S/C is oriented so that the sun is still at the calibration point, but Venus is located at a different point in the payload FOR. In effect, the S/C has slewed about the S/C-sun line from Procedure #1 to Procedure #2. Again, this procedure, by itself, only provides partial error information, ϵ_{p2} . Combining the results from Procedure #1 and #2 will provide full error information, because the errors measured in the two experiments are in different directions.

The procedures depicted in Figures 3 and 4 were each executed several times in order to obtain some statistical characterization of the results.

In addition to estimating the SS errors, the combination of Procedures #1 and #2 will also provide enough information to determine the slew angle about the S/C-Venus line for each experiment.

In the least-squares estimator, the vector of estimated parameters was

$$\mathbf{x} = \begin{bmatrix} \zeta_1 \\ \vdots \\ \zeta_n \\ \epsilon_x \\ \epsilon_z \end{bmatrix}$$

Where ζ_i is the slew angle about the S/C-Venus line for procedure #i ($i=1, \dots, n$), ϵ_x is the bias in the SS X measurement at the calibration point and ϵ_z is the SS Z measurement bias at the calibration point. It was necessary to estimate the individual slew angles because it indirectly provided a 3-axis attitude determination for each procedure, and this is what is required for measuring the SS errors.

Sun Sensor Estimation Procedure #1

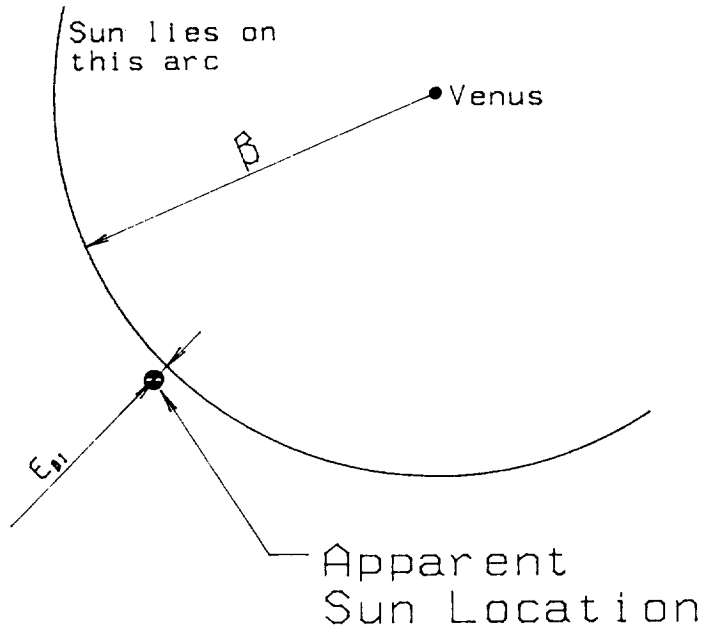


Figure 3

Sun Sensor Estimation Procedure #2

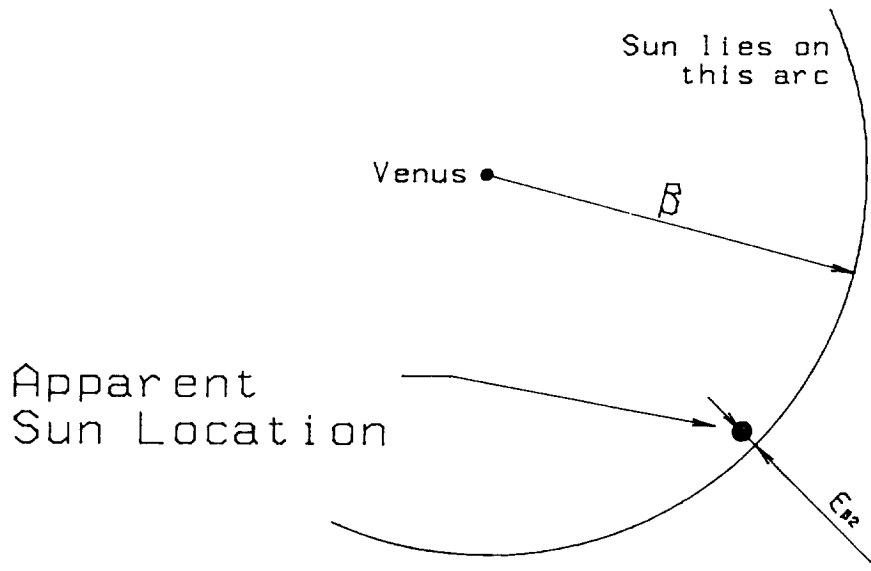


Figure 4

The measurement vector used for the SS estimation was:

$$m = \begin{bmatrix} SSX_1 \\ SSZ_1 \\ SSX_2 \\ SSZ_2 \\ \vdots \\ SSX_n \\ SSZ_n \end{bmatrix}$$

Where SSX_i and SSZ_i are the two outputs of the SS for procedure #i ($i=1, \dots, n$).

Because only data from the SS and the payload were used, the calibration was necessarily relative to the frame defined by the payload, and not relative to the S/C frame.

Figure 5 shows the geometry of the payload FOR relative to the SS FOV. In this polar plot, the radial dimension represents the angle from the payload Z axis, and the angular dimension represents the azimuth from the payload X axis. The solid line represents the limits of the payload FOR, and the dashed line represents the limits of the SS FOV. Not all of the SS FOV is shown in Figure 5. The Field Of Regard of the MSTI 2 payload was limited by the amount of travel allowed in the gimbals.

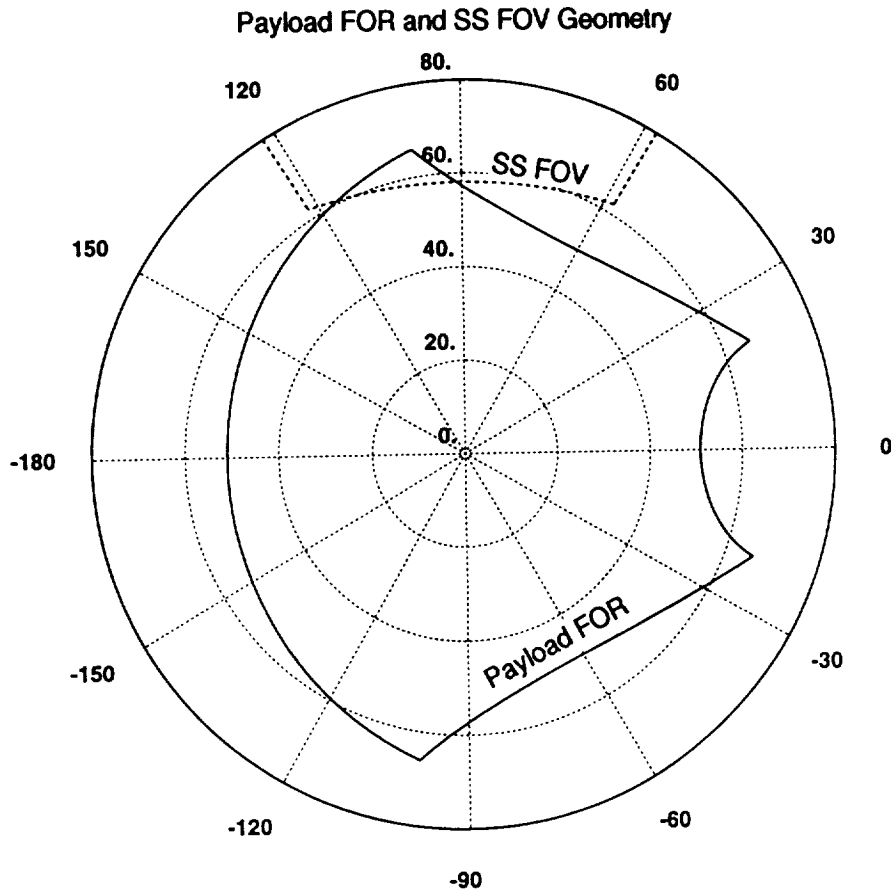


Figure 5

When the payload is pointed near the edge of its FOR, its image will be partially obscured by the S/C structure, resulting in a dimmer image. Therefore, it is desirable to point the S/C so that Venus is as far away from the edge of the FOR of the payload as possible. This places a limitation on the geometries which will simultaneously place the sun in the SS FOV and Venus in the payload FOR.

During the time of the OOA maneuvers, the Venus was 20° to 30° away from the sun, as indicated in Figure 2. This, coupled with Figure 5, indicates additional limitations on geometries which will simultaneously place Venus in the payload FOR and the sun in the SS FOV.

These limitations were the driving factors in the decision to calibrate the SS at only one point. The calibration point, and the geometries of the SS calibration experiments, are illustrated in Figure 6. By selecting the calibration point at $SSX = 30^\circ$ and $SSZ = 10^\circ$, Venus was kept as far away as possible from the edges of the payload FOR, while still allowing a 90° slew about the S/C-sun line between the two procedures. The small circle is the chosen location of the SS calibration point, and the two "x"s represent the location of Venus for the two SS Calibration maneuvers.

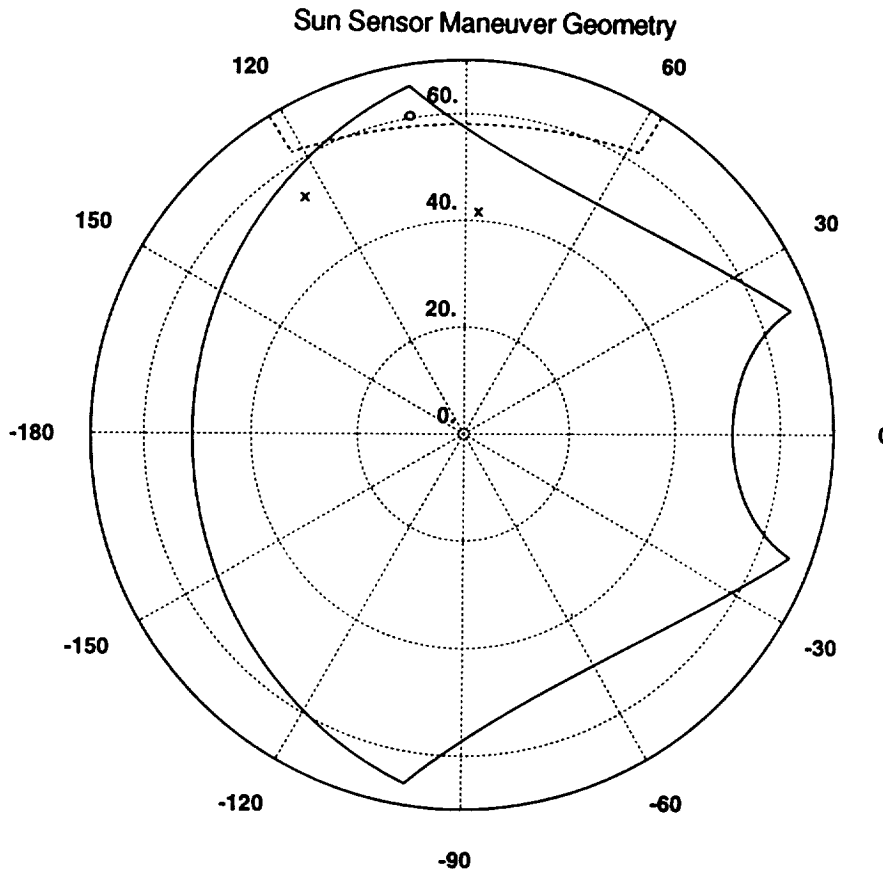


Figure 6

For maximum observability, the slew angle about the S/C-sun line between the two experiments should be 90° . The two Venus locations indicated in Figure 5 satisfy this requirement.

Earth Sensor Calibration

The ES is a scanning horizon sensor. It has a 2° conical field of view which sweeps out a cone with a 60° half-cone angle every 0.2 seconds. The axis of the ES scan cone is nominally along the S/C -Y axis. The ES measures the size and location of the "earth chord", which is that portion of the scan cone which intersects the earth. The outputs of the ES consist of Φ , the scan angle from a zero-reference scan angle to the center of the earth chord, and Ω , the width of the earth chord.

The basic technique to calibrate the ES is similar to the SS calibration. The primary differences are:

- (1) The geometry of a scanning horizon sensor is different from the geometry of the SS,
- (2) The ES had to be calibrated along a locus of points to accommodate a range of earth-S/C-sun angles,
- (3) No analytic horizon sensor model incorporating an oblate earth shape model was available.

Because of the complicated geometry of a scanning horizon sensor, the location of the earth in the S/C frame was deduced only indirectly. Because an oblate earth shape model was required, there were no analytic expressions relating the location of the earth to the ES sensor readings. An iterative search was employed, using the spherical

earth shape approximation as a first guess.

Because the Sun-S/C-earth angle changes during the orbit and during the year, and because only one point of the SS FOV was calibrated, it was necessary to calibrate a locus of ES output pairs to cover the range of possible angles. Each "point" in the locus corresponded to one location of the earth relative to the payload frame.

The multiple procedure technique described above for the SS calibration was modified for the ES calibration. There were two sets of procedures, instead of two discrete procedures. For each procedure in the first set, the S/C was oriented so that the earth was at various points along the calibration locus, and all of these procedures used approximately the same slew angle about the S/C-earth line. For the second set of procedures, the earth was again located at various points along the calibration line, but the slew angle about the S/C-earth line was approximately 90° from the slew angle used for the first set.

Because the ground testing included no statistical characterization, an assumed function with unknown parameters was used to model the ES errors. The Φ and Ω errors were each assumed to vary as a function of the distance along the locus of points. Because an assumed form of the error model was used, it was unnecessary to calibrate individual points with pairs of parameters, as was done with the SS calibration. Instead, the error function parameters were estimated collectively. It was only necessary that each individual procedure placed the earth at some location along the locus. It was not necessary for each procedure in the second set of procedures to place the earth at the same location along the locus as an procedure in the first set.

In the least-squares estimator, the vector of estimated parameters was:

$$\mathbf{x} = \begin{bmatrix} \alpha_1 \\ \alpha_2 \\ \vdots \\ \alpha_{n-1} \\ \alpha_n \\ c_{\phi 0} \\ c_{\phi 1} \\ c_{\phi 2} \\ c_{\Omega 0} \\ c_{\Omega 1} \\ c_{\Omega 2} \end{bmatrix}$$

Where α_i is the slew angle about the S/C-Venus line for experiment #i ($i=1, \dots, n$), and $c_{\Omega 0}$, $c_{\Omega 1}$, $c_{\Omega 2}$, $c_{\phi 0}$, $c_{\phi 1}$, and $c_{\phi 2}$ are the unknown parameters of the ES error model. It was necessary to estimate the individual slew angles because it indirectly provided a 3-axis attitude determination for each experiment, and this is what is required for measuring the ES errors.

The measurement vector used was:

$$\mathbf{m} = \begin{bmatrix} \Phi_1 \\ \Omega_1 \\ \Phi_2 \\ \Omega_2 \\ \vdots \\ \Phi_n \\ \Omega_n \end{bmatrix}$$

Where Φ_i and Ω_i are the two outputs of the ES for experiment #i ($i=1, \dots, n$).

The least-squares estimator requires derivatives of the measurement vector elements with respect to the state vector elements. Because no analytic function relating Φ and Ω to the estimated parameters was available, there was no analytic expression for the related derivatives. However, the spherical earth shape model is very nearly equal to the oblate earth shape model, so the derivatives based on the spherical earth shape model were used, while the measurement model used the oblate earth shape model.

Because only data from the ES and the payload were used, the calibration was necessarily relative to the frame defined by the payload, and not relative to the S/C frame.

Gyro Misalignment Estimation

The ground testing of the MSTI 2 gyros was very extensive, and provided very good characterization of the gyros. The gyro models, and their parameters, were determined with very good accuracy, and it was felt that no further of the gyros themselves was needed. The only significant error source in the gyros was their geometric misalignment relative to the MSTI 2 S/C.

The sensitive axes of the one of the X-Y gyro are nominally aligned with the payload frame X- and Y-axes, and the sensitive axes of the X-Z gyro are nominally aligned with the payload frame X- and Z-axes. The X-axis rate information, for both attitude control and telemetry, comes from only one gyro at any given time, as selected by ground commands. The nominal mission called for using both channels of the X-Y gyro, and only the Z-axis information of the X-Z gyro. Therefore, it was necessary to estimate all three misalignment angles for the X-Y gyro, and only two misalignment angles for the X-Z gyro.

In order to make the gyro misalignments observable, three simple Euler-axis slews were executed by the S/C. While performing these slews, the payload was tracking Venus in order to make the estimated parameters observable. Ideally, for maximum observability, the three slew axes should be mutually orthogonal. However, the limited extent of the payload FOR constrained the slew axes to be non-orthogonal. The geometry of the three slews is illustrated in Figure 7. The orientation of the angular velocity vector for each slew is indicated by the small "o"s, and the dashed circles indicate the path followed by Venus through the payload FOR.

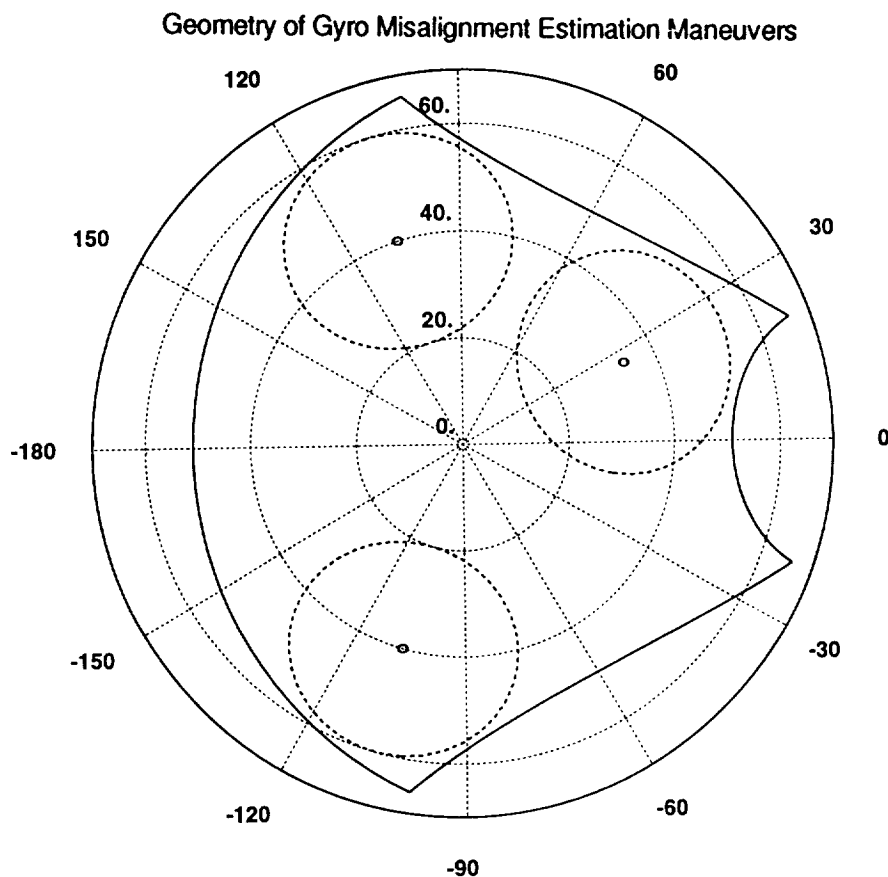


Figure 7

For this estimation, it was assumed that the two axes of each gyro are perfectly perpendicular. It was also assumed that the misalignment of each gyro was independent of the misalignment of the other gyro.

When the S/C was commanded to perform the three slew maneuvers, it complied by using the misaligned gyros. Therefore, it was necessary to also estimate the parameters of the Euler-axis slew as well as the gyro misalignments. The estimated parameters were:

- (1) The orientation and magnitude of each slew axis in the payload frame coordinates,
- (2) The orientation of each slew axis in inertial space,

- (3) The initial slew angle of each slew maneuver,
- (4) The X, Y, and Z angular misalignments of the X-Y gyro relative to the payload frame, and
- (5) The X and Y angular misalignments of the X-Z gyro relative to the payload frame.

It was necessary to express the equations describing the slew maneuvers in terms of the orientation of the slew axes in inertial space, in order to force the resulting slew parameters to apply to an Euler-axis slew fixed in inertial space. It was necessary to estimate these orientations because they were not directly measurable.

In the least-squares estimator, the vector of estimated parameters was:

$$x = \begin{bmatrix} \theta_{z01} \\ \omega_{11} \\ \omega_{21} \\ \omega_{31} \\ RA_{a1} \\ Decl_{a1} \\ \theta_{z02} \\ \omega_{12} \\ \omega_{22} \\ \omega_{32} \\ RA_{a2} \\ Decl_{a2} \\ \theta_{z03} \\ \omega_{13} \\ \omega_{23} \\ \omega_{33} \\ RA_{a3} \\ Decl_{a3} \\ \gamma_{11} \\ \gamma_{12} \\ \gamma_{13} \\ \gamma_{21} \\ \gamma_{22} \end{bmatrix}$$

Where θ_{z0i} is the initial slew angle of the S/C at the beginning of slew maneuver #i (i=1,2,3), ω_j is the component of the angular velocity vector along the p_i axis for slew maneuver #j (i=1,2,3; j=1,2,3), RA_{ai} is the right ascension of the angular velocity vector for slew maneuver #i (i=1,2,3), $Decl_{ai}$ is the declination of the angular velocity vector for slew maneuver #i (i=1,2,3), γ_{ii} are the three misalignment angles of the X-Y gyro (i=1,2,3), and γ_{2i} are two of the three misalignment angles of the the X-Z gyro (i=1,2).

The X axis data from the X-Z gyro was not available, so the third misalignment angle of the X-Z gyro, γ_{23} , is neither required nor observable.

The measurement vector used was:

$$m = \begin{bmatrix} v_{p11} \\ v_{p21} \\ v_{p31} \\ \hat{\omega}_{11} \\ \hat{\omega}_{21} \\ \hat{\omega}_{31} \\ v_{p12} \\ v_{p22} \\ v_{p32} \\ \hat{\omega}_{12} \\ \hat{\omega}_{22} \\ \hat{\omega}_{32} \\ \vdots \\ v_{p1n} \\ v_{p2n} \\ v_{p3n} \\ \hat{\omega}_{1n} \\ \hat{\omega}_{2n} \\ \hat{\omega}_{3n} \end{bmatrix}$$

Where v_{p_i} is the component of the Venus unit vector along the p_i direction at time t_i ($i=1,2,3; j=1,\dots,n$), $\hat{\omega}_{1i}$ is the angular velocity measured by the X axis of the X-Y gyro at time t_i ($i=1,\dots,n$), $\hat{\omega}_{2i}$ is the angular velocity measured by the Y axis of the X-Y gyro at time t_i ($i=1,\dots,n$), and $\hat{\omega}_{3i}$ is the angular velocity measured by the Z axis of the X-Z gyro at time t_i ($i=1,\dots,n$).

Conclusion

Most of the error sources in the attitude knowledge of the MSTI 2 spacecraft were removed analytically by using the payload as a high fidelity attitude reference, and using this information to deduce the errors in the ACS sensors. This determined the errors relative to the payload, and eliminated the need to align the sensors relative to the spacecraft. Those errors which could not be eliminated analytically were avoided by careful mission design.

Measuring Attitude with a Gradiometer

David Sonnabend*

Thomas G. Gardner†

Abstract

This paper explores an idea of S. Kant of Goddard — can a gravity gradiometer measure the attitude of a satellite, given that the gravity field is accurately known? Since gradiometers actually measure a combination of the gradient and attitude rate and acceleration terms, the answer is far from obvious. The paper demonstrates yes, and at microradian accuracy. The technique employed is dynamic estimation, based on the momentum biased Euler equations. The satellite is assumed nominally planet pointed, and subject to control, gravity gradient, and partly random drag torques. The attitude estimator is unusual. While the standard method of feeding back measurement residuals is used, the feedback gain matrix isn't derived from Kalman theory. Instead, it's chosen to minimize a measure of the terminal covariance of the error in the estimate. This depends on the gain matrix, and the power spectra of all the process and measurement noises. An integration is required over multiple solutions of Lyapunov equations.

1 Notation & Units

Uppercase bold roman letters are 2 dimensional arrays; e.g., \mathbf{F} . Lowercase bold roman or greek letters are column vectors; e.g., \mathbf{r} . Magnitudes of vectors are non-bold; e.g., $r = |\mathbf{r}|$. Lowercase greek subscripts are indices. The Einstein summation convention is used for repeated lower case greek indices. Overdots signify time derivatives; e.g., $\dot{x} = dx/dt$. A T superscript denotes transpose. Primes denote scaled variables. Sines and cosines are denoted by s and c respectively.

\mathbf{A} = constant matrix in Riccati equation

$\mathbf{a}_e = \mathbf{f}_e/m$ = external non-gravitational acceleration on spacecraft

\mathbf{a}_i = inertial acceleration of the i th accelerometer

\mathbf{B} = process noise state distribution matrix

\mathbf{C} = vector of state concern values; C_t = settling time concern value

$\mathbf{D}(\omega)$ = matrix satisfying Lyapunov equation (72)

$E(\mathbf{x})$ = expectation of \mathbf{x} ; \mathbf{e}_α^x = unit vector along axis α in coordinate system x

\mathbf{F} = plant matrix; \mathbf{f}_e = external non-gravitational force on spacecraft

G = universal gravitational constant = 6.67259×10^{-11} N-m²/kg²

\mathbf{g} = gravity field vector at \mathbf{r} ; \mathbf{g}_i = gravitational acceleration at the i th accelerometer

\mathbf{H} = measurement partials matrix; h = spacecraft pitch momentum bias

\mathbf{I}_n = identity tensor of order n ; \mathbf{J} = overall spacecraft inertia tensor

\mathbf{K} = filter feedback gain matrix; $\mathbf{L} = \mathbf{H}^T \mathbf{M}^{-1} \mathbf{H}$ in Riccati equation

k_{1-4} = constants defined in (23); k_f = air drag force constant defined in (33)

\mathbf{M} = combined "equivalent" white noise matrix defined in (80)

m = spacecraft mass; also field source mass

$\mathbf{N}(\omega)$ = matrix defined in (75); \mathbf{P}_ξ = terminal covariance of the error of the estimate

$\mathbf{Q}(\omega)$ = function of power spectra defined in (68); q = performance index; also dynamic pressure

$\mathbf{R}(\tau)$ = autocorrelation matrix with delay τ ; $R(0)$ = average power

\mathbf{r} = field position vector relative to m ; \mathbf{r}_{cp} = spacecraft center of pressure

$\mathbf{S}(\omega)$ = general noise power spectrum; \mathbf{S}_v , \mathbf{S}_w = white noise spectra

s , t superscripts signify spacecraft and trajectory coordinates

t = time in seconds; $t' = t/C_t$ = scaled time; t_s = filter settling time

\mathbf{U} = process noise measurement distribution matrix; \mathbf{u} = vector of controls

$\mathbf{V} = \mathbf{B} \mathbf{S}_w \mathbf{U}^T$ = white process noise effect matrix

*President, Analytical Engineering Co., Boulder, CO, 303-530-9641

†Ph. D. Candidate, University of Colorado

v_o = satellite orbital speed
 $\mathbf{W} = \mathbf{B} - \mathbf{K}\mathbf{U}$ = process noise effect matrix
 \mathbf{w} = process noise vector; w_d = dimensionless air drag random process
 $\mathbf{X} = \mathbf{F} - \mathbf{V}\mathbf{M}^{-1}\mathbf{H}$ = linear term matrix in Riccati equation
 \mathbf{x} = state vector; $\hat{\mathbf{x}}$ = estimate of \mathbf{x} ; $\dot{\hat{\mathbf{x}}} = d\hat{\mathbf{x}}/dt'$
 \mathbf{Y} = measurement noise distribution matrix
 $\mathbf{Z} = \mathbf{F} - \mathbf{K}\mathbf{H}$ = observer system matrix; \mathbf{z} = vector of measurements
 ϵ = variation in spacecraft ω
 Γ = gravity gradient tensor; $\Gamma_0 = Gm/r^3$ = gradient scalar due to mass m at distance r
 $\lambda(\mathbf{Z})$ = eigenvalue of \mathbf{Z} ; $\sigma = \Re(\lambda)$ = real part of eigenvalue
 $\mu_e = Gm_e$ = gravitational constant of the earth = $3.98603 \times 10^{14} \text{ m}^3/\text{s}^2$
 $\boldsymbol{\xi} = \hat{\mathbf{x}} - \mathbf{x}$ = error in the state estimate; $\boldsymbol{\tau}_e$ = non-gravitational external torque
 ω = spacecraft angular velocity; ω = angular frequency used in power spectra
 ω_c = break frequency in power spectrum; ω_o = orbital mean motion

Unless otherwise stated, the units used in this paper are SI. However, we have also followed common practice in the field of gradiometry on the units of gravity gradient. The natural SI unit is $(\text{m}/\text{s}^2)/\text{m}$, or just s^{-2} . Since gradient components at the earth's surface are on the order of $1.5 \times 10^{-6} \text{ s}^{-2}$, and are routinely measured to 10^{-9} s^{-2} , or better, this has proved unwieldy. There has now been world wide acceptance of the Eötvös unit: $1 \text{ E} = 10^{-9} \text{ s}^{-2}$. Here, the SI unit will be used everywhere in the formulas; but Eötvös units will be generally employed in the text.

2 Static Attitude Estimation

The gravitational potential due to a particle of mass m at a distance r is:

$$\Phi = -Gm/r \quad (1)$$

The vector gravitational field at this point, due to m , is the acceleration of a free test particle there:

$$\mathbf{g} = -\nabla\Phi = -Gmr^{-3}\mathbf{r} \equiv -\Gamma_0\mathbf{r} \quad (2)$$

Finally, the gravity gradient tensor field due to m , is:

$$\Gamma = \nabla\mathbf{g} = \Gamma_0 \left(\frac{3\mathbf{r}\mathbf{r}^T}{r^2} - \mathbf{I}_3 \right) \quad (3)$$

Outside the earth, the fields are closely approximated by these formulas. If the test mass is a spacecraft, in circular orbit about the earth at radius r , then the orbital angular velocity ω_o is given by:

$$\omega_o^2 = \Gamma_0 = \mu_e/r^3 \quad (4)$$

in which μ_e is the gravitational constant of the earth. The actual potential of the earth is complicated; but differs from (1) by only about 1 part in 1000 in low earth orbit, less at higher altitudes. The variations in turn are known to better than 1 part in 1000. Thus, if spacecraft attitude is actually inferred from gradiometer measurements, this error in knowledge of the field would lead to corresponding attitude determination errors on the order of 10^{-6} rad, almost surely not the worst error contribution. In any case, the intent of the study is to find the accuracy with which a gradiometer can measure attitude, *given that the field is known*; so the study neglects field knowledge errors.

On the other hand, neglect of the known deviation from sphericity (mainly oblateness) would lead to attitude errors on the order of 10^{-3} rad, usually unacceptable. However, our intent is to determine feasibility; so the form of the necessary oblateness correction is outside the scope. A real system would also have to deal with eccentric orbits; but as the orbit is not solved for, the observability of the attitude can't be seriously affected by eccentricity; and the spacecraft orbit is taken here as circular.

In general, coordinate systems are described by sets of right handed orthonormal base vectors \mathbf{e}_α^x , where $\alpha = 1, 2, \text{ or } 3$ denotes the axis, and x indicates the system. 1st, the spacecraft system \mathbf{e}^s . This is the

physical system in the spacecraft to which all the accelerometer input axes, and all other instruments, are aligned. For simplicity, it will be assumed that the origin of \mathbf{e}^s is at the spacecraft center of mass. The term “spacecraft attitude” means the rotation that connects \mathbf{e}^s to a trajectory system \mathbf{e}^t . \mathbf{e}_1^t is defined as the local upward vertical, through the origin of \mathbf{e}^s , and \mathbf{e}_3^t is parallel to the orbital angular momentum. \mathbf{e}_2^t completes a right handed system, and is along the spacecraft velocity vector. \mathbf{e}^t rotates uniformly at a rate ω_o about \mathbf{e}_3^t relative to an inertial system that won't need to be identified further.

The connection between systems may be described by a matrix of direction cosines \mathbf{A} :

$$\mathbf{e}_\alpha^s = A_{\alpha\beta} \mathbf{e}_\beta^t \quad (5)$$

In this study, the spacecraft is assumed to be earth pointing; so \mathbf{A} will be taken as a small rotation. It then can be expressed in terms of small yaw (ψ), roll (ϕ), and pitch (θ) angles; about \mathbf{e}_1^t , \mathbf{e}_2^t , and \mathbf{e}_3^t , respectively. In these terms, and to 1st order in the angles:

$$\mathbf{A} = \begin{bmatrix} 1 & \theta & -\phi \\ -\theta & 1 & \psi \\ \phi & -\psi & 1 \end{bmatrix} \quad (6)$$

The need for \mathbf{e}^t is that the earth fields \mathbf{g} and $\mathbf{\Gamma}$ are most conveniently expressed there:

$$\mathbf{g}^t = -\Gamma_0 \mathbf{e}_1^t = \Gamma_0 r [-1, 0, 0]^T \quad (7)$$

$$\mathbf{\Gamma}^t = \Gamma_0 \text{diag} [2, -1, -1] \quad (8)$$

and expressing these in \mathbf{e}^s , where the instruments reside:

$$\mathbf{g}^s = \mathbf{A} \mathbf{g}^t = \Gamma_0 r [-1, \theta, -\phi]^T \quad (9)$$

$$\mathbf{\Gamma}^s = \mathbf{A} \mathbf{\Gamma}^t \mathbf{A}^T = \Gamma_0 \begin{bmatrix} 2 & -3\theta & 3\phi \\ -3\theta & -1 & 0 \\ 3\phi & 0 & -1 \end{bmatrix} \quad (10)$$

again to 1st order in the angles. Note first, that while pitch and roll turn up in these expressions, yaw does not. Physically, this is because \mathbf{r} is an axis of symmetry of the fields.

If we could measure either \mathbf{g} or $\mathbf{\Gamma}$ in \mathbf{e}^s , we could infer both θ and ϕ . Alas, accelerometers don't measure gravitational acceleration at all, and gradiometers are strongly perturbed by angular velocities and accelerations (see below). What if dynamic effects could be removed? For example, if a spot measurement of Γ_{13}^s could somehow be made, the error in ϕ would be:

$$\delta\phi = \delta\Gamma / (3\Gamma_0) + 3\phi\delta r / r \quad (11)$$

Suppose an orbit altitude of 500 km. Then $r = 6.867 \times 10^6$ m, and $\Gamma_0 = 1231$ E. A gradient measurement accuracy of .01 E would then contribute 2.708×10^{-6} rad to $\delta\phi$. The analysis of $\delta\theta$ is similar, given a measurement of Γ_{12}^s . In each case, the 2nd contribution to the error comes from the uncertainty in the knowledge of r . Supposing $\delta r = 10$ m, and $\phi = 0.1$ rad, this contribution to $\delta\phi$ comes to 4.37×10^{-7} rad. Since satellite tracking usually determines r rather better; and attitude control is typically much tighter; the tracking contribution may be regarded as conservative, and won't be considered further. Thus, if spot measurements of the gradient could be made at the .01 E level, then roll and pitch determination at the microradian level would be possible. If this gradient measurement came from a pair of accelerometers, with an 0.5 m separation and independent errors, their required accuracy would be

$$\delta a = 0.5(10^{-11})/2^{1/2} = 3.536 \times 10^{-12} \text{ m/s}^2$$

within the capability of the best room temperature accelerometers today, operating in space.

3 Dynamic Attitude Estimation

If gradiometers actually measured the gradient, then a model would be something like $\mathbf{z} = \mathbf{\Gamma}$ plus noise, or a subset of its components. A least squares analysis would then yield the covariance of the errors in the estimate of the desired ϕ and θ , for each discrete sample \mathbf{z} . However, as any real gradiometer measurement \mathbf{z} contains functions of ω and $\dot{\omega}$, least squares analysis won't suffice; and we have to resort

to dynamic estimation. The plant equations consist of the Euler equations of more or less rigid body motion, plus kinematic equations relating ω to the attitude angular rates. Actually, as there is very little process noise (external torque variations), these equations add considerable strength to the estimates; thus turning a practical necessity into a virtue. These plant equations are developed and linearized below, a process noise model is spelled out, a filter is synthesized, and it's shown how the terminal covariance of the errors in the estimates may be determined. A few results are given.

A major variation from the earlier gradiometer dynamic estimation studies, [5] and [4], is that, instead of treating gradiometers as measuring the intrinsic tensor (see below), this study follows [8] in treating the instrument as an array of accelerometers. The measurement models consist of what each accelerometer should measure, plus noise. One advantage of this is that the measurement noises are now uncorrelated, avoiding the careful treatment needed in [5]. For simplicity, the spacecraft is supposed to be a box, with edges l_α aligned along the \mathbf{e}_α^s . Supposing a uniform density ρ , the spacecraft mass is:

$$m = \rho l_1 l_2 l_3 \quad (12)$$

A typical density might be $\rho = 1000 \text{ kg/m}^3$; and the principal moments of inertia are:

$$J_1 = m(l_2^2 + l_3^2)/12 \quad ; \quad J_2 = m(l_1^2 + l_3^2)/12 \quad ; \quad J_3 = m(l_1^2 + l_2^2)/12 \quad (13)$$

The orbit is assumed circular, at a radius r . Assuming an altitude of 500 km, $r = 6.867 \times 10^6 \text{ m}$, $\omega_o = .0011095 \text{ rad/s}$, and $\Gamma_0 = 1231 \text{ E}$. Also, the spacecraft speed in orbit is $v_o = r\omega_o = 7614 \text{ m/s}$.

In [4] it's shown that the Euler equations of rigid body motion, when modified to include an arbitrary bias momentum \mathbf{h}_W , can be written as:

$$\mathbf{J}\dot{\boldsymbol{\omega}} = (\mathbf{J}\boldsymbol{\omega} + \mathbf{h}_W) \times \boldsymbol{\omega} + \boldsymbol{\tau}_{gg} + \boldsymbol{\tau}_e \quad (14)$$

in which the external torque has been separated into the gravity gradient torque $\boldsymbol{\tau}_{gg}$ and the nongravitational torque $\boldsymbol{\tau}_e$, the latter mostly due to air drag. Note that the derivative is the rate of change as seen in \mathbf{e}^s . Control torques could be included in $\boldsymbol{\tau}_e$; but as they would then reappear in the filter structure equations, they cancel out in the covariance study. Unfortunately, this system is nonlinear in $\boldsymbol{\omega}$. Since we are analyzing a nominally earth pointing satellite, the nominal value of $\boldsymbol{\omega}$ is $\omega_o \mathbf{e}_3^s$. However, because of the body derivatives, a much simpler procedure is to define the variation $\boldsymbol{\epsilon}$ by:

$$\boldsymbol{\omega} = \omega_o \mathbf{e}_3^s + \boldsymbol{\epsilon} \quad (15)$$

Another simplification comes by arguing that, in an earth pointing satellite, bias momentum, if any, is usually confined to the pitch axis:

$$\mathbf{h}_W = h \mathbf{e}_3^s \quad (16)$$

Additional wheels for control aren't precluded; it's only required that their nominal momentum is zero. Substituting these relations into (14), and deleting quadratic terms in $\boldsymbol{\epsilon}$, yields

$$\mathbf{J}\dot{\boldsymbol{\epsilon}} = \omega_o(\mathbf{J}\boldsymbol{\epsilon}) \times \mathbf{e}_3^s + \omega_o(\mathbf{J}\mathbf{e}_3^s) \times (\omega_o \mathbf{e}_3^s + \boldsymbol{\epsilon}) + h \mathbf{e}_3^s \times \boldsymbol{\epsilon} + \boldsymbol{\tau}_{gg} + \boldsymbol{\tau}_e \quad (17)$$

We also need $\boldsymbol{\tau}_{gg}$. The well known formula in \mathbf{e}^t may be put in the form:

$$\boldsymbol{\tau}_{gg}^t = 3\Gamma_0 \mathbf{e}_1^t \times (\mathbf{J}^t \mathbf{e}_1^t) \quad (18)$$

Since only \mathbf{J}^s is readily available, and as what we really need is $\boldsymbol{\tau}_{gg}^s$, we need to work out

$$\boldsymbol{\tau}_{gg}^s = 3\Gamma_0 \mathbf{A}[\mathbf{e}_1^t \times (\mathbf{A}^T \mathbf{J}^s \mathbf{A} \mathbf{e}_1^t)] = 3\Gamma_0 \begin{bmatrix} -J_{12}\phi - J_{13}\theta \\ (J_{11} - J_{33})\phi + J_{23}\theta - J_{13} \\ (J_{11} - J_{22})\theta + J_{23}\phi + J_{12} \end{bmatrix} \quad (19)$$

Note that, while nothing depends on ψ , there is a yaw torque, arising from off diagonal components of \mathbf{J} . These also produce bias torques in roll and pitch. That's why, for earth pointing satellites, it's generally

preferable to point some principal axis up. Moreover, by making this axis (\mathbf{e}_1^s) have the least J , τ_{gg} is restoring. Here, where the main issue is observability, it's assumed that this condition is met, when

$$\mathbf{J}^s = \text{diag}[J_1, J_2, J_3] \quad (20)$$

In the examples, it's further assumed that $J_1 < J_2 < J_3$, known to be the best configuration for gravity gradient stabilized satellites. With the principal axis assumption, the torque reduces to:

$$\boldsymbol{\tau}_{gg}^s = 3\Gamma_0[0, (J_1 - J_3)\phi, (J_1 - J_2)\theta]^T \quad (21)$$

On putting this into (17), and expressing it in standard form, the Euler equations become:

$$\begin{aligned} \dot{\epsilon}_1 &= k_1\epsilon_2 + J_1^{-1}\tau_{e1} \\ \dot{\epsilon}_2 &= k_2\epsilon_1 + k_3\phi + J_2^{-1}\tau_{e2} \\ \dot{\epsilon}_3 &= k_4\theta + J_3^{-1}\tau_{e3} \end{aligned} \quad (22)$$

in which the constants are defined as:

$$k_1 = [\omega_o(J_2 - J_3) - h]/J_1 ; k_2 = [\omega_o(J_3 - J_1) + h]/J_2 ; k_3 = 3\Gamma_o(J_1 - J_3)/J_2 ; k_4 = 3\Gamma_o(J_1 - J_2)/J_3 \quad (23)$$

If the gravity gradient and other external torques are neglected, then ϵ_1 and ϵ_2 decouple from ϵ_3 in (22), resulting in a harmonic oscillator with frequency ω_N given by:

$$\omega_N^2 = -k_1k_2 \quad (24)$$

This is the natural nutation frequency, arising mainly from the momentum bias h .

To complete the plant equations we must add the kinematical relations. With the same linearizing assumptions, these are easily shown to be (see for instance [4]):

$$\dot{\psi} = \epsilon_1 + \omega_o\phi ; \dot{\phi} = \epsilon_2 - \omega_o\psi ; \dot{\theta} = \epsilon_3 \quad (25)$$

We now have a linear system of plant equations of 6th order in ϵ , ψ , ϕ , and θ .

The random process appearing in the Euler equations (22) is the external non-gravitational torque $\boldsymbol{\tau}_e$. At 500 km, this is largely due to air drag; and the random component is largely from variations in air density ρ_a . For gradiometer studies, a flat earth barometric model was adopted in [4]:

$$\rho_a(r + \delta r) = \rho_a(r)e^{-\delta r/h_s} \quad (26)$$

where h_s is the density scale height. At 500 km, [9] lists $\rho_a = 1.905 \times 10^{-12}$ kg/m³, $h_s = 83,000$ m, and a mean free path of 25,000 m. These numbers are, admittedly, quite shaky. In any case, the dynamic pressure then comes from the speed:

$$q = \rho_a v_o^2 / 2 \quad (27)$$

and with the above numbers, $q = 1.106 \times 10^{-4}$ N/m². Since the speed is along \mathbf{e}_2^t , and the spacecraft attitude is not far from nominal, the steady force from air drag is very nearly:

$$\mathbf{f}_e = -ql_1l_3C_D\mathbf{e}_2^s \quad (28)$$

Because the mean free path is much larger than the spacecraft, drag is essentially Newtonian, with a coefficient $C_D = 2$. However, since some inelastic, oblique, and diffuse scattering of air molecules is likely, this C_D may be high, and $C_D = 1.5$ is adopted. We should also consider radiation pressure. Corresponding to q is I_s/c , where $I_s = 1360$ w/m² the mean insolation outside the earth, and c is the speed of light. Thus, the mean "radiation dynamic pressure" is 4.54×10^{-6} N/m², well below q ; and as the variations are much slower than for air drag, radiation pressure is ignored. [4] goes on to develop a statistical model. It supposes that ρ_a is actually the mean of a distribution, to which a random component is added:

$$\rho_r = \rho_a w_d(t) \quad (29)$$

$w_d(t)$ is a dimensionless, zero mean, random function of position and time. At satellite speed, the spatial variation dominates. Suppose that $w_d(t)$ has a standard deviation σ_w . Still, we need a power spectrum. Physically, we are looking at dynamic variations in density, with scale lengths of order h_s , plus the orbital frequency variation due to solar heating of the atmosphere. The latter, while reaching substantial amplitudes, is confined to such low frequencies as to have little effect on the attitude estimates, and is ignored. As for dynamic variations, we can imagine variability on all length scales, but petering out below distances of order h_s . This situation led to the development of the cubic power spectrum in [2]:

$$S(\omega) = \frac{\pi R(0)}{\omega_c} \left(1 - \frac{\omega}{2\omega_c}\right)^2 \left(1 + \frac{\omega}{\omega_c}\right) \quad (0 \leq \omega \leq 2\omega_c) \quad (30)$$

and zero otherwise. Suppose the autocorrelation of variations falls by half at a distance αh_s . The time to travel this distance is $\lambda = \alpha h_s / v_o$, and [2] shows that, for the cubic spectrum, we should choose:

$$\omega_{cw} = \frac{\pi}{2\lambda} = \frac{\pi v_o}{2\alpha h_s} \quad (31)$$

We must also pick $R_w(0)$ and α . The best information presently available to us is an analysis of CACTUS data in [10]. Accelerometer data over approximately 800 s intervals was analyzed at altitudes between 270 and 320 km. Density variations of $\sim 4\%$, peak to peak were typical; rising sometimes to $\sim 15\%$, during severe magnetic disturbances. The corresponding σ_w values are .014 and .05. A reasonable balance between these values would be $\sim .02$; but, allowing for a bit greater variability at higher altitudes, we have taken $\sigma_w = .025$. Then, as these time series meet the oversampling conditions discussed in the Appendix, $R_w(0) = \sigma_w^2 = 6.25 \times 10^{-4}$. As for α , [10] doesn't show a power spectrum, but does give representative time series of a normal and a disturbed interval; and states that the apparent wavelengths concentrate in the range of 700 to 1500 km. Examination of the time series suggests that $R(\tau)$ falls to 0.5 at $\tau \sim 50$ s. Translating to our altitude, the corresponding distance is 381 km, when $\alpha = 4.6$. Since for a sinusoid, $R(\tau)$ falls by half at 1/3 of a wavelength, these numbers are at least consistent. Again, to allow for a bit more variability at 500 km, we have taken $\alpha = 4$, leading to $\omega_{cw} = 0.03606$ rad/s.

It remains to convert this to torque. The overall drag force is very nearly:

$$\mathbf{f}_e = -k_f [1 + w_d(t)] \mathbf{e}_2^s \quad (32)$$

where

$$k_f \equiv \rho_a v_o^2 l_1 l_3 C_D / 2 \quad (33)$$

Supposing a center of pressure at a location \mathbf{r}_{cp} in the spacecraft, the torque due this is:

$$\boldsymbol{\tau}_e = \mathbf{r}_{cp} \times \mathbf{f}_e = k_f [1 + w_d(t)] [r_{cp3}, 0, -r_{cp1}]^T \quad (34)$$

Note that there a deterministic bias force and torque, which must be treated correctly in the filter. Also, while our box structure has no torque along \mathbf{e}_2^s , an actual spacecraft would likely have a small propeller torque on this axis. To allow for this below, a component r_{cp2} replaces the zero in (34).

4 Measurement Model

In [5] and [3], the instrument was modeled as measuring elements of the "intrinsic" tensor:

$$\mathbf{T} = \boldsymbol{\Gamma} + \omega^2 \mathbf{I}_3 - \omega \boldsymbol{\omega}^T + \boldsymbol{\varepsilon} \dot{\boldsymbol{\omega}} \quad (35)$$

where $\boldsymbol{\varepsilon}$ is the 3-index permutation symbol. The quadratic ω terms are centrifugal effects. Because the instrument is fixed in \mathbf{e}^s , there is no coriolis. Here, the instrument is dissolved into its component accelerometers, partly to avoid the noise correlations required in [5] and [3], but mainly to prepare for later studies. The gradiometer is taken as an array of 3 axis accelerometers, with input axes aligned along the \mathbf{e}_α^s . For entering symmetrical arrays, it's convenient to identify a "center" of the instrument \mathbf{r}_c , relative to the origin of \mathbf{e}^s . Then, the i th accelerometer will have a position \mathbf{r}_{ai} , relative to the center. Thus, its location relative to the center of mass is:

$$\mathbf{r}_i = \mathbf{r}_c + \mathbf{r}_{ai} \quad (36)$$

For a perfectly circular orbit, the center of mass is subject to $-\omega_o^2 r \mathbf{e}_1^t$. As for rotation effects, \mathbf{e}^s is rotating at a rate ω , relative to an inertial frame \mathbf{e}^n . So, purely due to rotation, the inertial velocity of the i th accelerometer is (the superscripts indicate the frame in which the derivative is observed):

$$\dot{\mathbf{r}}_i = \frac{d^n}{dt} \mathbf{r}_i = \frac{d^s}{dt} \mathbf{r}_i + \omega \times \mathbf{r}_i = \omega \times \mathbf{r}_i \quad (37)$$

the latter because \mathbf{r}_i is invariant in \mathbf{e}^s . Going to the next derivative

$$\ddot{\mathbf{r}}_i = \frac{d^n}{dt} \dot{\mathbf{r}}_i = \dot{\omega} \times \mathbf{r}_i + \omega \times \frac{d^n}{dt} \mathbf{r}_i = \dot{\omega} \times \mathbf{r}_i + \omega \times (\omega \times \mathbf{r}_i) \quad (38)$$

Note that $\dot{\omega}$ is the same, whether viewed from \mathbf{e}^n or \mathbf{e}^s . Finally, on including the external non-gravitational acceleration \mathbf{a}_e , the i th accelerometer is subject to:

$$\mathbf{a}_i = -\omega_o^2 r \mathbf{e}_1^t + \omega \times (\omega \times \mathbf{r}_i) + \dot{\omega} \times \mathbf{r}_i + \mathbf{a}_e \quad (39)$$

On the other hand, the gravitational acceleration of the i th accelerometer is \mathbf{g}^t plus the correction at \mathbf{r}_i due to the gradient. From (7) and (4), this comes to:

$$\mathbf{g}_i = -\omega_o^2 r \mathbf{e}_1^t + \Gamma \mathbf{r}_i \quad (40)$$

Actual accelerometers measure only non-gravitational acceleration; i.e., the difference between inertial and gravitational acceleration. These are identical in free fall, when an accelerometer measures zero. Conversely, an accelerometer on a table on earth measures the acceleration imposed by the table that keeps the instrument from falling through the floor. Thus, the i th accelerometer model is:

$$\mathbf{z}_i = \mathbf{a}_i - \mathbf{g}_i + \mathbf{v}_i \quad (41)$$

where \mathbf{v}_i is the noise in the 3 measurements. On substituting from above this becomes:

$$\mathbf{z}_i = \omega \times (\omega \times \mathbf{r}_i) + \dot{\omega} \times \mathbf{r}_i - \Gamma \mathbf{r}_i + \mathbf{a}_e + \mathbf{v}_i \quad (42)$$

Note that the acceleration of the center of mass has dropped out. The next step is to linearize this using (15). On neglecting the quadratic terms, and recalling that $\dot{\omega}$ is the same in \mathbf{e}^n and \mathbf{e}^s , we get:

$$\mathbf{z}_i = \omega_o (\omega_o \mathbf{e}_3^s + \boldsymbol{\epsilon}) \times (\mathbf{e}_3^s \times \mathbf{r}_i) + \omega_o \mathbf{e}_3^s \times (\boldsymbol{\epsilon} \times \mathbf{r}_i) + \dot{\boldsymbol{\epsilon}} \times \mathbf{r}_i - \Gamma \mathbf{r}_i + \mathbf{a}_e + \mathbf{v}_i \quad (43)$$

We'll work this out term by term, in the form of matrices of constants times the state variables, plus whatever is left over. Starting on the left:

$$\mathbf{e}_3^s \times (\mathbf{e}_3^s \times \mathbf{r}_i) = r_{i3} \mathbf{e}_3^s - \mathbf{r}_i = -[r_{i1}, r_{i2}, 0]^T \quad (44)$$

$$\boldsymbol{\epsilon} \times (\mathbf{e}_3^s \times \mathbf{r}_i) = (\mathbf{r}_i \cdot \boldsymbol{\epsilon}) \mathbf{e}_3^s - \epsilon_3 \mathbf{r}_i = \begin{bmatrix} 0 & 0 & -r_{i1} \\ 0 & 0 & -r_{i2} \\ r_{i1} & r_{i2} & 0 \end{bmatrix} \begin{bmatrix} \epsilon_1 \\ \epsilon_2 \\ \epsilon_3 \end{bmatrix} \quad (45)$$

$$\mathbf{e}_3^s \times (\boldsymbol{\epsilon} \times \mathbf{r}_i) = r_{i3} \boldsymbol{\epsilon} - \epsilon_3 \mathbf{r}_i = \begin{bmatrix} r_{i3} & 0 & -r_{i1} \\ 0 & r_{i3} & -r_{i2} \\ 0 & 0 & 0 \end{bmatrix} \begin{bmatrix} \epsilon_1 \\ \epsilon_2 \\ \epsilon_3 \end{bmatrix} \quad (46)$$

The $\dot{\boldsymbol{\epsilon}}$ term can't be expressed directly in the state variables; however, from (22), there follows:

$$\dot{\boldsymbol{\epsilon}} \times \mathbf{r}_i = \begin{bmatrix} k_2 r_{i3} & 0 & k_3 r_{i3} & -k_4 r_{i2} \\ 0 & -k_1 r_{i3} & 0 & k_4 r_{i1} \\ -k_2 r_{i1} & k_1 r_{i2} & -k_3 r_{i1} & 0 \end{bmatrix} \begin{bmatrix} \epsilon_1 \\ \epsilon_2 \\ \phi \\ \theta \end{bmatrix} + \begin{bmatrix} J_2^{-1} r_{i3} \tau_{e2} - J_3^{-1} r_{i2} \tau_{e3} \\ J_3^{-1} r_{i1} \tau_{e3} - J_1^{-1} r_{i3} \tau_{e1} \\ J_1^{-1} r_{i2} \tau_{e1} - J_2^{-1} r_{i1} \tau_{e2} \end{bmatrix} \quad (47)$$

The Γ term comes directly from (10):

$$\Gamma \mathbf{r}_i = 3\Gamma_o \begin{bmatrix} r_{i3} & -r_{i2} \\ 0 & -r_{i1} \\ r_{i1} & 0 \end{bmatrix} \begin{bmatrix} \phi \\ \theta \end{bmatrix} + \Gamma_o \begin{bmatrix} 2r_{i1} \\ -r_{i2} \\ -r_{i3} \end{bmatrix} \quad (48)$$

and on combining all these, and substituting from the process noise model:

$$\mathbf{z}_i = \begin{bmatrix} (k_3 + \omega_o)r_{i3} & 0 & -2\omega_o r_{i1} & 0 & (k_3 - 3\Gamma_o)r_{i3} & (3\Gamma_o - k_4)r_{i2} \\ 0 & (\omega_o - k_1)r_{i3} & -2\omega_o r_{i2} & 0 & 0 & (k_4 + 3\Gamma_o)r_{i1} \\ (\omega_o - k_2)r_{i1} & (k_1 + \omega_o)r_{i1} & 0 & 0 & -(k_3 + 3\Gamma_o)r_{i1} & 0 \end{bmatrix} \begin{bmatrix} \epsilon_1 \\ \epsilon_2 \\ \epsilon_3 \\ \psi \\ \phi \\ \theta \end{bmatrix} + \Gamma_o \begin{bmatrix} -3r_{i1} \\ 0 \\ r_{i3} \end{bmatrix} + k_f \begin{bmatrix} J_2^{-1}r_{i3}r_{cp2} + J_3^{-1}r_{i2}r_{cp1} \\ -J_3^{-1}r_{i1}r_{cp1} - J_1^{-1}r_{i3}r_{cp3} - m^{-1} \\ J_1^{-1}r_{i2}r_{cp3} - J_2^{-1}r_{i1}r_{cp2} \end{bmatrix} [1 + w_d(t)] + \mathbf{v}_i \quad (49)$$

This completes the description of the accelerometers. There is 1 such 3 vector for each accelerometer. The noise depends critically on instrument design; but as we are interested only in feasibility, no particular instrument is used. Since a power spectrum is needed even for a generic instrument, a cubic spectrum similar to (30) is assumed. The Appendix shows how the average power $R_v(0)$, and the break frequency ω_{cv} , are determined from the rms acceleration error and the averaging time τ of the measurement.

5 Filter Structure

The 1st step in calculating the terminal covariance in a dynamic estimation problem is to determine the structure of the filter. This starts with identifying the set of state variables that appear in the plant and measurement equations. From (22) and (25), it's clear that we should choose:

$$\mathbf{x} = [\epsilon_1, \epsilon_2, \epsilon_3, \psi, \phi, \theta]^T \quad (50)$$

Following [7], it's conventional to consolidate the plant equations in standard linearized form:

$$\dot{\mathbf{x}} = \mathbf{F}\mathbf{x} + \mathbf{G}(\mathbf{u}) + \mathbf{B}\mathbf{w} \quad (51)$$

Here, \mathbf{F} is the plant matrix, \mathbf{u} is a vector of controls, $\mathbf{G}(\mathbf{u})$, a possibly nonlinear vector function, distributes the controls, \mathbf{w} is a vector of independent process noises, and \mathbf{B} is the process noise state distribution matrix. The matrices are readily identified. From (22) and (25), we find:

$$\mathbf{F} = \begin{bmatrix} 0 & k_1 & 0 & 0 & 0 & 0 \\ k_2 & 0 & 0 & 0 & k_3 & 0 \\ 0 & 0 & 0 & 0 & 0 & k_4 \\ 1 & 0 & 0 & 0 & \omega_o & 0 \\ 0 & 1 & 0 & -\omega_o & 0 & 0 \\ 0 & 0 & 1 & 0 & 0 & 0 \end{bmatrix} \quad (52)$$

As for the control and process noise terms, it's convenient to separate the deterministic process noise bias from the random components, and combine them with the actual controls, if any, to produce the $\mathbf{G}(\mathbf{u})$ used here. Since these terms will eventually cancel out in the analysis below, the actual controls have no effect on filter performance, and there is no need to spell out $\mathbf{G}(\mathbf{u})$. Finally, by identifying \mathbf{w} with $w_d(t)$ in (34), and including propeller torque, we have:

$$\mathbf{B} = k_f [r_{cp3}/J_1, r_{cp2}/J_2, -r_{cp1}/J_3, 0, 0, 0]^T \quad (53)$$

Turning now to the measurement model, the direct appearance of the process noise in each of the accelerometer measurements requires a modification of the usual standard model:

$$\mathbf{z} = \mathbf{H}\mathbf{x} + \mathbf{Y}\mathbf{v} + \mathbf{U}\mathbf{w} + \mathbf{z}_B \quad (54)$$

Here, \mathbf{H} is the measurement partials matrix, developed above. From (49), this is:

$$\mathbf{H}_i = \begin{bmatrix} (k_3 + \omega_o)r_{i3} & 0 & -2\omega_o r_{i1} & 0 & (k_3 - 3\Gamma_o)r_{i3} & (3\Gamma_o - k_4)r_{i2} \\ 0 & (\omega_o - k_1)r_{i3} & -2\omega_o r_{i2} & 0 & 0 & (k_4 + 3\Gamma_o)r_{i1} \\ (\omega_o - k_2)r_{i1} & (k_1 + \omega_o)r_{i1} & 0 & 0 & -(k_3 + 3\Gamma_o)r_{i1} & 0 \end{bmatrix} \quad (55)$$

and the complete measurement partials matrix is:

$$\mathbf{H} = [\mathbf{H}_1^T, \mathbf{H}_2^T, \dots]^T \quad (56)$$

For example, if there are 7 vector accelerometers, \mathbf{H} will be a 21×6 matrix.

For measurement noise, it's assumed that each axis of each accelerometer has separate independent noise. Thus, $\mathbf{v}(t)$ has one element for each element of \mathbf{z} , and \mathbf{Y} is just an identity. A more elaborate model may be found in [1]; so \mathbf{Y} is retained in what follows. The spectral properties of $\mathbf{v}(t)$ were developed above. As for the process noise term, having established that \mathbf{w} is $w_d(t)$, \mathbf{U} comes immediately from (49):

$$\mathbf{U}_i = k_f \begin{bmatrix} J_2^{-1} r_{i3} r_{cp2} + J_3^{-1} r_{i2} r_{cp1} \\ -J_3^{-1} r_{i1} r_{cp1} - J_1^{-1} r_{i3} r_{cp3} - m^{-1} \\ J_1^{-1} r_{i2} r_{cp3} - J_2^{-1} r_{i1} r_{cp2} \end{bmatrix} \quad (57)$$

The overall \mathbf{U} is a column vector with 3 such elements for each accelerometer. The remaining terms in (49) constitute the bias \mathbf{z}_B . As it doesn't affect the covariance analysis below, it's not spelled out.

An observer based on these models starts with an estimate $\hat{\mathbf{x}}$ of the state \mathbf{x} . This is caused to follow the deterministic parts of the plant equations (51), corrected by feeding back the residuals, i.e., the actual measurements \mathbf{z} minus the measurement model (54). The filter structure then takes the form:

$$\dot{\hat{\mathbf{x}}} = \mathbf{F}\hat{\mathbf{x}} + \mathbf{G}(\mathbf{u}) + \mathbf{K}(\mathbf{z} - \mathbf{H}\hat{\mathbf{x}} - \mathbf{z}_B) \quad (58)$$

Note that this structure assumes that the control and bias terms are known, and available to the filter. The issue buried here is that $\mathbf{G}(\mathbf{u})$ is accurately modeled, and that the biases have been accurately determined by some sort of in flight calibration. Pursuing these points is beyond our scope.

6 Terminal Covariance

The performance of a dynamic filter is generally examined by determining the statistics of the error in the estimate, defined by:

$$\boldsymbol{\xi} \equiv \hat{\mathbf{x}} - \mathbf{x} \quad (59)$$

The evolution of $\boldsymbol{\xi}$ comes from subtracting (51) from (58):

$$\dot{\boldsymbol{\xi}} = \mathbf{Z}\boldsymbol{\xi} + \mathbf{K}\mathbf{Y}\mathbf{v}(t) - \mathbf{W}\mathbf{w}(t) \quad (60)$$

where the observer system matrix and the process noise effect matrix are defined by:

$$\mathbf{Z} \equiv \mathbf{F} - \mathbf{K}\mathbf{H} \quad ; \quad \mathbf{W} \equiv \mathbf{B} - \mathbf{K}\mathbf{U} \quad (61)$$

There's lots to learn from (60). 1st, \mathbf{x} , $\hat{\mathbf{x}}$, and all the control and bias terms have disappeared. Thus, the quality of the estimate doesn't depend on the controls, even if they fail to stabilize the plant — the "Separation Theorem" in the controls business. 2nd, filter stability requires \mathbf{Z} to be stable; i.e., all its eigenvalues are in the left half plane, a standard requirement in any negative feedback system. Filter theory puts this differently: if a \mathbf{K} can be found such that \mathbf{Z} is stable, then the state \mathbf{x} is said to be observable by the measurements \mathbf{z} . 3rd, the diagonal elements and the eigenvalues of \mathbf{Z} have the dimensions of inverse time; and filter settling time is essentially given by the inverse of its least negative eigenvalue. This is used below to insure that the "optimal" filter has a reasonable settling time. Finally, since the noises are unbiased, so is $\boldsymbol{\xi}(t)$.

Various measures have been proposed to study the quality of the estimate. Here, and generally in the references, attention has centered on the covariance of the error:

$$\mathbf{P}_\xi(t) \equiv E[\boldsymbol{\xi}(t)\boldsymbol{\xi}^T(t)] \quad (62)$$

where E is the expectation operator. The idea that, in a stationary system, $\mathbf{P}_\xi(t)$ would have a terminal or asymptotic value, has been around a long time, but finding it could be quite tedious, if the settling time was long. About 4 years ago, William McEneaney, in unpublished notes, showed that this terminal value

\mathbf{P}_ξ could be calculated directly from the structural information and the noise statistics. On generalizing to arbitrary power spectra, his ideas led to [6] and [7].

The present problem differs from [7] primarily by including process noise in the measurement model. Also, [7] dealt with the autocovariances of all the noises, and it has since been found much easier to work with power spectra directly. Since none of this appears in print, the algorithm for calculating \mathbf{P}_ξ is derived here. To begin, it may be supposed that the filter has been running for all past time; when the initial conditions have settled out. Then (60) is solved for "now" in this form:

$$\xi(0) = \int_0^\infty e^{\mathbf{Z}\mu} [\mathbf{K}\mathbf{Y}\mathbf{v}(\mu) - \mathbf{B}\mathbf{w}(\mu)] d\mu \quad (63)$$

where the dummy variable μ may be interpreted as past time. Strictly, the noise terms should be $v(-\mu)$ and $w(-\mu)$; but, as only the statistical properties of ξ matter, it makes no difference. An apparently graver problem is $e^{\mathbf{Z}\mu}$ — the dimensions of $\mathbf{Z}\mu$ depend on those of \mathbf{x} , thus calling into question the validity of the formal expansion. However, from (60), the dimensions of the vector $t\mathbf{Z}\mathbf{x}$ are just those of \mathbf{x} . Thus, all terms of the form $\mu^i \mathbf{Z}^i \mathbf{x}$ have the same dimensions, and if the exponential is merely viewed as shorthand for the formal expansion, there are no dimensional difficulties.

The terminal covariance may now be found by substituting this into (62):

$$\mathbf{P}_\xi = \int_0^\infty \int_0^\infty e^{\mathbf{Z}\mu} \{ \mathbf{K}\mathbf{Y}E[\mathbf{v}(\mu)\mathbf{v}^T(\nu)]\mathbf{Y}^T\mathbf{K}^T + \mathbf{W}E[\mathbf{w}(\mu)\mathbf{w}^T(\nu)]\mathbf{W}^T \} e^{\mathbf{Z}^T\nu} d\mu d\nu \quad (64)$$

This supposes that the expectation and integration operators may be commuted, and uses the assumption that \mathbf{w} and \mathbf{v} are independent and free of bias. On recognizing the autocorrelations of the noises, this is:

$$\mathbf{P}_\xi = \int_0^\infty \int_0^\infty e^{\mathbf{Z}\mu} [\mathbf{K}\mathbf{Y}\mathbf{R}_v(\mu - \nu)\mathbf{Y}^T\mathbf{K}^T + \mathbf{W}\mathbf{R}_w(\mu - \nu)\mathbf{W}^T] e^{\mathbf{Z}^T\nu} d\mu d\nu \quad (65)$$

Well, autocorrelations and power spectra are Fourier transforms of each other. Using the one sided spectra of [6], these relations for any noise component are:

$$R(\tau) = \frac{1}{\pi} \int_0^\infty S(\omega) c(\tau\omega) d\omega \quad ; \quad S(\omega) = 2 \int_0^\infty R(\eta) c(\omega\tau) d\tau \quad (66)$$

After using the former in (65), and interchanging the order of integrations, there follows:

$$\mathbf{P}_\xi = \frac{1}{\pi} \int_0^\infty \int_0^\infty \int_0^\infty e^{\mathbf{Z}\mu} \mathbf{Q}(\omega) e^{\mathbf{Z}^T\nu} c[\omega(\mu - \nu)] d\mu d\nu d\omega \quad (67)$$

in which:

$$\mathbf{Q}(\omega) \equiv \mathbf{K}\mathbf{Y}\mathbf{S}_v(\omega)\mathbf{Y}^T\mathbf{K}^T + \mathbf{W}\mathbf{S}_w(\omega)\mathbf{W}^T \quad (68)$$

Considerable progress can now be made by a change of coordinates:

$$\theta \equiv \mu + \nu \quad ; \quad \eta \equiv \mu - \nu \quad (69)$$

the double integration region is now the quadrant surrounding the $+\theta$ axis, so

$$\begin{aligned} \mathbf{P}_\xi = & \frac{1}{2\pi} \int_0^\infty \left[\int_{-\infty}^0 e^{\mathbf{Z}\eta/2} \int_{-\eta}^\infty e^{\mathbf{Z}\theta/2} \mathbf{Q}(\omega) e^{\mathbf{Z}^T\theta/2} d\theta e^{-\mathbf{Z}^T\eta/2} c(\omega\eta) d\eta \right. \\ & \left. + \int_0^\infty e^{\mathbf{Z}\eta/2} \int_\eta^\infty e^{\mathbf{Z}\theta/2} \mathbf{Q}(\omega) e^{\mathbf{Z}^T\theta/2} d\theta e^{-\mathbf{Z}^T\eta/2} c(\omega\eta) d\eta \right] d\omega \end{aligned} \quad (70)$$

Now, it's not hard to establish that

$$\int e^{\mathbf{Z}\theta/2} \mathbf{Q}(\omega) e^{\mathbf{Z}^T\theta/2} d\theta = 2e^{\mathbf{Z}\theta/2} \mathbf{D}(\omega) e^{\mathbf{Z}^T\theta/2} + \text{constant} \quad (71)$$

where $\mathbf{D}(\omega)$ satisfies the Lyapunov equation:

$$\mathbf{Z}\mathbf{D}(\omega) + \mathbf{D}(\omega)\mathbf{Z}^T = \mathbf{Q}(\omega) \quad (72)$$

Putting this into (70), setting $\eta \rightarrow -\eta$ in the 1st integral, and evaluating at the required limits, a considerable simplification results:

$$\mathbf{P}_\xi = -\frac{1}{\pi} \int_0^\infty \left[\mathbf{D}(\omega) \int_0^\infty e^{\mathbf{Z}^T \eta c(\omega \eta)} d\eta + \int_0^\infty e^{\mathbf{Z} \eta c(\omega \eta)} d\eta \mathbf{D}(\omega) \right] d\omega \quad (73)$$

when another analytic integral has surfaced:

$$\int_0^\infty e^{\mathbf{Z} \eta c(\omega \eta)} d\eta = -(\mathbf{Z} + \omega^2 \mathbf{Z}^{-1})^{-1} \quad (74)$$

leading finally to:

$$\mathbf{P}_\xi = \frac{1}{\pi} \int_0^\infty [\mathbf{N}(\omega) + \mathbf{N}^T(\omega)] d\omega ; \quad \mathbf{N}(\omega) \equiv (\mathbf{Z} + \omega^2 \mathbf{Z}^{-1})^{-1} \mathbf{D}(\omega) \quad (75)$$

It may be noted that this analysis would break down in several places but for \mathbf{Z} being stable. Once again, especially in (74), the dimensions may look flaky. However, letting u_i represent the dimensions of x_i , it is readily shown from the differential equations that the expressions $Z_{ij}t$, Z_{ij}/ω , and ωZ_{ij}^{-1} all have the dimensions u_i/u_j . By extension, the ij th element of (74) has the dimensions tu_i/u_j . This work has established the forward procedure. For a given \mathbf{K} , \mathbf{Z} and \mathbf{W} are computed from (61) and (61). A set of ω values is chosen to cover the region where any of the noise spectra are nonzero, with reasonable density. $\mathbf{Q}(\omega)$ is then determined over this set from (68). Each $\mathbf{Q}(\omega)$ yields a corresponding $\mathbf{D}(\omega)$ by solution of the Lyapunov equation (72), and a corresponding $\mathbf{N}(\omega)$ from (75). \mathbf{P}_ξ is then found by integrating (75).

7 Optimal Feedback Gains

Having found how to compute \mathbf{P}_ξ from \mathbf{K} , we still need to find the \mathbf{K} that yields optimal filter performance, whatever that means. While \mathbf{P}_ξ certainly contains the necessary information, in this 6th order problem there are 21 independent matrix elements; so some sort of scalar measure of \mathbf{P}_ξ is needed. The software used here is based on a performance index q , constructed from the weighted trace of \mathbf{P}_ξ :

$$q = P_{\xi\alpha\alpha}/C_\alpha^2 \quad (76)$$

In this technique, known as ‘‘Bryson weighting’’, each C_i is the ‘‘level of concern’’ for the error ξ_i . For example, if x_i were a position, the level of concern might be $C_i = 1$ m. $C_i = 10$ m would show less concern, and cause the optimization to put less weight on the variance of ξ_i . Note that the Bryson technique has the virtue that q is the sum of dimensionless terms — it doesn’t add apples and oranges.

A further concern can be added to the performance index — filter settling time. If the \mathbf{K} that minimizes (76) leads to a \mathbf{Z} with a small (though negative) eigenvalue, then we may see from (60) that the settling time of the filter will be long, perhaps excessively so. To avoid such a problem, a term may be added to (76) penalizing the filter settling time. To see how to do this, consider the behavior of the filter evolution equation (60). If λ_α symbolizes the eigenvalues of \mathbf{Z} , and $\sigma_\alpha \equiv \Re(\lambda_\alpha)$, then the filter response to initial conditions or perturbations may be regarded as a set of n exponentially decaying modes, with individual settling times $-1/\sigma_\alpha$. Since all n modes decay simultaneously, the overall settling time is:

$$t_s = \max_\alpha [-\Re(\lambda_\alpha)]^{-1} = - \left[\max_\alpha \Re(\lambda_\alpha) \right]^{-1} \quad (77)$$

Now suppose we introduce a concern level C_t in seconds for the settling time t_s . Then the overall performance index may be taken as:

$$q = (P_{\xi\alpha\alpha}/C_\alpha^2) + t_s/C_t \quad (78)$$

The added term serves another function. The stability boundary for \mathbf{Z} is that all $\sigma_\alpha < 0$. Thus, as some $\sigma_\alpha \rightarrow 0$ from the left, $t_s \rightarrow \infty$. So, adding the t_s term erects a barrier against \mathbf{Z} going unstable. If we have picked the concerns C_i and C_t , and have a \mathbf{K} , such that \mathbf{Z} is stable, then \mathbf{P}_ξ may be found as detailed above, and q computed. Next, each element of \mathbf{K} is varied, to get a δq . Taken together, these constitute a ∇q , relative to the elements of \mathbf{K} . A minimum q is then found by searching along $-\nabla q$. This whole process is iterated until q bottoms out. The final \mathbf{K} is the "optimal" feedback gain, and the final \mathbf{P}_ξ and t_s comprise the filter performance at that gain. However, this result could just be local.

$C_{4,5,8}$ weight the variances in the attitude angular errors. Since our sponsor feels that 5×10^{-5} rad is a reasonable goal for θ and ϕ , these are the adopted concern levels, with .001 rad for ψ . As for $C_{1,2,3}$, an uncontrolled gravity stabilized satellite might sway by .05 rad at frequencies of order $2\omega_o$. Thus, the actual rates ϵ would be $\sim 10^{-4}$ rad/s. If we needed to know them to, say, 1%, our level of concern would be 10^{-6} rad/s; and this is taken as the concern level. However, an unusually stringent rate jitter requirement, would shrink the rate concern levels.

There is one serious loose end — the starting \mathbf{K} must yield a stable \mathbf{Z} . The method we use is based on Kalman theory. Suppose each noise component $S(\omega)$ is replaced by a flat bounded spectrum with the same average power $R(0)$, and with cutoff frequency Ω where $S(\omega)$ vanishes for good. This level is $S = \pi R(0)/\Omega$. The white noise "equivalent" to $S(\omega)$ has level S out to infinity. Replacing all the noise components with these "equivalents" causes \mathbf{Q} , and thus \mathbf{D} to be independent of ω . This allows \mathbf{P}_ξ to be integrated analytically, leading to $\mathbf{P}_\xi = -\mathbf{D}$, when there is a clean connection between \mathbf{K} and \mathbf{P}_ξ . On reorganizing with the help of (61) and (61), so as to make the dependence on \mathbf{K} explicit, we have:

$$\mathbf{KHP}_\xi + \mathbf{P}_\xi \mathbf{H}^T \mathbf{K}^T - \mathbf{FP}_\xi - \mathbf{P}_\xi \mathbf{F}^T = \mathbf{KMK}^T - \mathbf{KV}^T - \mathbf{VK}^T + \mathbf{BS}_w \mathbf{B}^T \quad (79)$$

where:

$$\mathbf{M} \equiv \mathbf{YS}_v \mathbf{Y}^T + \mathbf{US}_w \mathbf{U}^T \quad ; \quad \mathbf{V} \equiv \mathbf{BS}_w \mathbf{U}^T \quad (80)$$

Since an optimum \mathbf{P}_ξ is necessarily stationary relative to variations in \mathbf{K} , (79) may be expressed in components, and differentiated relative to each $K_{\mu\nu}$, leading to this stationarity condition for \mathbf{P}_ξ :

$$\mathbf{KM} = \mathbf{P}_\xi \mathbf{H}^T + \mathbf{V} \quad (81)$$

While this can't be used directly to eliminate either \mathbf{K} or \mathbf{P}_ξ from (79), we need only assume that some noise contaminates every measurement component to insure that \mathbf{M} is non-singular. Thus:

$$\mathbf{K} = (\mathbf{P}_\xi \mathbf{H}^T + \mathbf{V}) \mathbf{M}^{-1} \quad (82)$$

which, except for the \mathbf{V} term, is a staple of Kalman theory. When this is substituted back into (79), an equally well known algebraic Riccati equation emerges:

$$\mathbf{A} + \mathbf{XP}_\xi + \mathbf{P}_\xi \mathbf{X}^T = \mathbf{P}_\xi \mathbf{H}^T \mathbf{M}^{-1} \mathbf{HP}_\xi \equiv \mathbf{P}_\xi \mathbf{LP}_\xi \quad (83)$$

where:

$$\mathbf{A} \equiv \mathbf{B}(\mathbf{S}_w - \mathbf{S}_w \mathbf{U}^T \mathbf{M}^{-1} \mathbf{US}_w) \mathbf{B}^T \quad ; \quad \mathbf{X} \equiv \mathbf{F} - \mathbf{VM}^{-1} \mathbf{H} \quad (84)$$

All this reduces to Kalman theory when the measurements don't depend on $\mathbf{w}(t)$; i.e., $\mathbf{U} = \mathbf{V} = \mathbf{0}$. In the software, (83) is solved for \mathbf{P}_ξ , and \mathbf{K} is computed from (82). While this \mathbf{K} is far from optimal for real power spectra, it does guarantee a stable \mathbf{Z} to start the iteration. A potential difficulty is that the Riccati equation has many solutions; but it's known that at most 1 yields $\mathbf{P} > \mathbf{0}$.

This is quite a large optimization. For example, if the gradiometer is composed of 4 vector accelerometers, \mathbf{K} has 72 elements, all of which must be determined. Such problems are touchy, and the difficulties are aggravated by poor conditioning in \mathbf{P}_ξ or \mathbf{Z} . Some sort of scaling is usually applied to alleviate this. Here, a natural scaling already exists — the Bryson concern levels. On the hypothesis that the variance $P_{\xi ii}$ is on the same order of magnitude as C_i^2 , consider scaling the state variables and time:

$$x'_i = x_i / C_i \quad ; \quad t' = t / C_t \quad (85)$$

which are non-dimensional. Recall that, in the convention adopted in this paper, summation is only over lower case *greek* indices. The covariance of the scaled variables is then:

$$P'_{\xi_{ij}} = E(x'_i x'_j) = P_{\xi_{ij}} / (C_i C_j) \quad (86)$$

The real virtue of such a scaling is that the eigenvalues of \mathbf{P}'_{ξ} should be much closer together than those of \mathbf{P}_{ξ} , with a corresponding improvement in the condition number. To carry out this scaling, (85) is substituted into (51), leading to:

$$\dot{\mathbf{x}}' = \mathbf{F}' \mathbf{x}' + \mathbf{G}'(\mathbf{u}) + \mathbf{B}' \mathbf{w} \quad (87)$$

in which

$$F'_{ij} = F_{ij} C_t C_j / C_i \quad ; \quad B'_{ij} = B_{ij} C_t / C_i \quad ; \quad G'_i = G_i C_t / C_i \quad (88)$$

It's not hard to show that the scaling makes all these arrays dimensionless. While it's not necessary to scale the measurements, in the model we must set

$$\mathbf{H}\mathbf{x} = \mathbf{H}'\mathbf{x}' \quad (89)$$

from which

$$H'_{ij} = C_j H_{ij} \quad (90)$$

The filter structure then becomes:

$$\dot{\hat{\mathbf{x}}}' = \mathbf{F}' \hat{\mathbf{x}}' + \mathbf{G}'(\mathbf{u}) + \mathbf{K}'(\mathbf{z} - \mathbf{H}' \hat{\mathbf{x}}' - \mathbf{z}_B) \quad (91)$$

in which the derivatives are with respect to t' , and

$$K'_{ij} = K_{ij} C_t / C_i \quad (92)$$

and the error in the estimate

$$\xi'_i = \hat{x}'_i - x'_i = \xi_i / C_i \quad (93)$$

evolves as

$$\dot{\xi}' = \mathbf{Z}' \xi' + \mathbf{K}' \mathbf{Y} \mathbf{v}(t) - \mathbf{W}' \mathbf{w}(t) \quad (94)$$

where

$$\mathbf{W}' \equiv \mathbf{B}' - \mathbf{K}' \mathbf{U} \quad ; \quad \mathbf{Z}' \equiv \mathbf{F}' - \mathbf{K}' \mathbf{H}' \quad (95)$$

In components, these matrices are related to the unscaled versions by:

$$W'_{ij} = W_{ij} C_t / C_i \quad ; \quad Z'_{ij} = Z_{ij} C_t C_j / C_i \quad (96)$$

Note that the matrices \mathbf{Y} and \mathbf{U} , and thus \mathbf{M} aren't affected by scaling. From the determinant relation for eigenvalues, it's not hard to show that those of \mathbf{Z}' obey

$$\lambda'_\alpha = C_t \lambda_\alpha \Rightarrow \sigma'_\alpha = C_t \sigma_\alpha \Rightarrow t'_s = t_s / C_t \quad (97)$$

On substituting these scaling relations into (78), q becomes rather simple:

$$q = \text{Tr}(\mathbf{P}'_{\xi}) + t'_s \quad (98)$$

The modified iteration starts by forming \mathbf{B}' and \mathbf{F}' . Then, the transformed algebraic Riccati equation is

$$\mathbf{A}' + \mathbf{X}' \mathbf{P}'_{\xi} + \mathbf{P}'_{\xi} \mathbf{X}'^T = \mathbf{P}'_{\xi} \mathbf{L}' \mathbf{P}'_{\xi} \quad (99)$$

in which \mathbf{A}' , \mathbf{X}' , and \mathbf{L}' are computed as above, except that \mathbf{F} , \mathbf{B} , and \mathbf{H} are replaced by their primed equivalents. Note that $\mathbf{V} \rightarrow \mathbf{V}'$, but no scaling of \mathbf{M} is required. Solving this leads to a starting value \mathbf{P}'_{ξ} for the main iteration. Applying the scaling everywhere, the iteration becomes:

$$\mathbf{Q}'(\omega) \equiv \mathbf{K}' \mathbf{Y} \mathbf{S}_v(\omega) \mathbf{Y}^T \mathbf{K}'^T + \mathbf{W}' \mathbf{S}_w(\omega) \mathbf{W}'^T \quad (100)$$

The Lyapunov equation is then:

$$\mathbf{Z}' \mathbf{D}'(\omega) + \mathbf{D}'(\omega) \mathbf{Z}'^T = \mathbf{Q}'(\omega) \quad (101)$$

whose solution leads to \mathbf{N}' and \mathbf{P}'_{ξ} . Finally, when q has settled, yielding the terminal \mathbf{K}' and \mathbf{P}'_{ξ} , the unscaled values are

$$P_{\xi_{ij}} = C_i C_j P'_{\xi_{ij}} \quad ; \quad K_{ij} = C_i K'_{ij} / C_t \quad (102)$$

8 Results

The calculation of the terminal covariance for a given set of input data requires the exercise of several programs in sequence, all more or less interactive. The programs are all written in APL, and implemented on a 486DX 33 Mhz computer. A typical run requires several hours, almost entirely for the minimization of q , but including all the interactive input and output routines. All the results cited here are based on the numbers in the text. The spacecraft dimensions are 2.0, 0.7, and 0.5 m; with a mass of 140 kg. A momentum bias of 10 N-m-s is added, yielding a natural nutation frequency of 0.48458 rad/s. From the air data in the text, $\omega_{c\omega d} = .036046$ rad/s. For numerical integration, 63 points were used in the ω vector; but a couple of runs were repeated with more points, to insure the accuracy. The instrument consists of 4 accelerometers at the corners of a regular tetrahedron, whose circumscribed sphere has a radius of 0.25 m. The noise levels ranged from 2×10^{-10} to 10^{-8} m/s². The averaging time was 1 s, for $\omega_{cv} = 62.832$ rad/s. The C_i are as in the text; $C_t = 10$ s.

In all cases, q was dominated by t_s ; although this dominance wanes at higher measurement noise levels. Our interpretation is that ψ is observable only through roll-yaw coupling in the kinematic equations, at a natural frequency ω_o , and thus causes long settling times. As the noise increases, so must P_ξ ; and t_s rises to maintain the concern balance. Presumably, a filter simulation would show that roll and pitch would settle much more quickly. This behavior is seen in the following table:

$10^9 \times \text{rms error} - \text{m/s}^2$	0.2	0.5	1	2	5	10
σ yaw - μrad	56.3	11.9	34.5	51.0	22.8	82.1
σ roll - μrad	3.04	3.33	7.06	32.0	20.1	72.5
σ pitch - μrad	4.18	2.92	3.74	16.7	34.5	138
t_s - s	223	315	336	670	695	1378

The progression to higher noise seems rather erratic. We believe that this is due in part to the t_s dominance, but much more to the $\lambda(\mathbf{Z})$. In the 2nd and 3rd runs, t_s comes from complex twins. The 1st and 4th run produced triplets, 1 of which was real; while the last 2 runs yielded quadruplets, composed of 2 complex pairs. In most cases, coalescence signaled that further iteration is unproductive. In all cases there were dramatic improvements from the Riccati equation starting \mathbf{K} to the final value. Clearly, there is a great deal of room for further research; and many more runs are planned, varying other parameters.

The authors would like to acknowledge the considerable assistance of Prof. Penina Axelrad of the Univ. of Colorado. Most of the work was performed under a contract to Analytical Engineering from the Univ. of Colorado, in turn supported by a Grant from Goddard Space Flight Center.

Appendix — Averaged Measurement Noise

The instruments studied here are modeled as measuring the acceleration of their case, plus noise. In practice, they generally average the analog output for some time interval τ , and deliver a digital result after each interval. The study considers only analog instruments, and thus takes $\tau = 0$. On the other hand, the instrument manufacturers often characterize their devices as delivering "samples" (really averages) every τ seconds, or alternatively, at a sample rate of $1/\tau$ Hz. The noise associated with these averages is then specified by a standard deviation σ . This appendix deals with relating this type of specification to the parameters of the assumed cubic power spectrum. This situation was examined in [11], where it was found that for an arbitrary noise power spectrum $S(\omega)$, the variance of the averages is:

$$\sigma^2 = \frac{2}{\pi\tau^2} \int_0^\infty S(\omega) [1 - c(\tau\omega)] \frac{d\omega}{\omega^2} \quad (103)$$

Assuming the cubic spectrum (30) for the analog noise, the variance can be put in the form:

$$\sigma^2 = R(0) f_s(\tau\omega_c) \quad (104)$$

where, in terms of the sine integral function:

$$f_s(x) = \frac{2}{x} \text{Si}(2x) + \frac{8x}{x^3} \left(\frac{8x}{x} + cx \right) - \frac{2}{x^2} (1 + s^2 x) \quad (105)$$

in which:

$$\text{Si}(y) = \int_0^y \frac{\text{s}z}{z} dz = y - \frac{y^3}{3 \cdot 3!} + \frac{y^5}{5 \cdot 5!} - \dots \quad (106)$$

The function looks ghastly for $x \ll 1$; but it actually behaves quite well:

$$f_s(x) = 1 - \frac{x^2}{9} + O(x^4) \quad (107)$$

This is the oversampling limit; i.e., if a time series is very frequently measured, but is long enough to cover many cycles of the highest noise frequency, then $R(0)$ is the variance of the samples, and the distinction between sample and average disappears. Actually, this limit holds for any $S(\omega)$. The other limit, $x \gg 1$ is also clean: $\text{Si}(x) \rightarrow \pi/2$ and $f_s(x) \rightarrow \pi/x$. Overall, $f_s(x)$ is a monotonic decreasing function, whose behavior can be seen from the table:

x	0	0.1	0.2	0.5	1	2	3
$f_s(x)$	1	0.99956	0.99823	0.98901	0.9574	0.84917	0.71822
x	5	10	20	50	100	200	500
$f_s(x)$	0.50907	0.28422	0.14958	.061632	.031116	.015633	.006271

When σ was measured by the manufacturer, the repetition frequency $1/\tau$ was probably chosen about an order of magnitude below the half power frequency $\omega_c/(2\pi)$. Adapting this reasoning, we can pick:

$$\omega_c = 20\pi/\tau \quad (108)$$

so that $\tau\omega_c = 20\pi = 62.832$ rad; and $R(0) = .0492401\sigma^2$. This assumed structure has been used to determine the measurement noise power spectrum in the study.

References

- [1] D Sonnabend, "A Simple GRADIO Accelerometer Model", JPL EM 314-495, 1-24-91.
- [2] D Sonnabend, "Cubic Power Spectra", JPL EM 314-507, 6-18-91.
- [3] AM San Martín, "SGGM In Flight Calibration", JPL IOM 343-90-601, 11-3-90.
- [4] D Sonnabend, "Realistic Gradiometer Dynamics", Proc. IUGG Meeting, Vienna Austria, 8-91; also JPL EM 314-508, 7-26-91.
- [5] D Sonnabend & WM McEneaney, "Gravity Gradient Measurements", Proc. IEEE Meeting on Decision and Control, Bierman Memorial Symposium, Austin TX, 12-88.
- [6] D Sonnabend, "Who Needs Markov?", JPL EM 314-478, 6-8-90.
- [7] D Sonnabend, "Terminal Covariance", JPL EM 314-481, 6-11-90.
- [8] D Sonnabend, "Locating a Free Mass", JPL EM 314-465, 9-17-90.
- [9] CW Allen, "Astrophysical Quantities", 2nd Ed., Athlone Press, 1963.
- [10] F Barlier & C Berger, "Rapid density variations — Statistical analysis; Applications to gradiometry", CIGAR CERGA 140/CMTR/s, 6-12-88.
- [11] D Sonnabend, "Time Averaged Noise", JPL EM 314-494, 12-12-90.

Overview of the MSTI 2 Processor-In-The-Loop Simulator

Christopher A. Rygaard

Integrated Systems, Inc.

Abstract

To thoroughly test the on-board software for the MSTI 2 spacecraft, it was necessary to generate an environment for the software which accurately simulated the on-orbit conditions of the spacecraft. To achieve this, the MSTI 2 Processor-In-The-Loop (PIL) high-fidelity simulator was developed. The entire development was completed in 3 months, and required 4 man-months of effort. This paper describes the design and development of this simulator, and the methodology employed.

Introduction

Thorough testing of the MSTI 2 on-board software required that the software be placed in an environment which accurately reproduces the conditions which the software will encounter while it is on orbit. This was achieved by using a flight processor with flight I/O boards, in conjunction with an AC-100 real-time simulator (see Figure 1). The unmodified on-board software was loaded onto the flight processor, and the I/O boards were utilized in their flight configuration. The AC-100 captured the output signals from the I/O boards, updated its simulation accordingly, and emitted the input signals to the flight processor. This process occurred in real time.

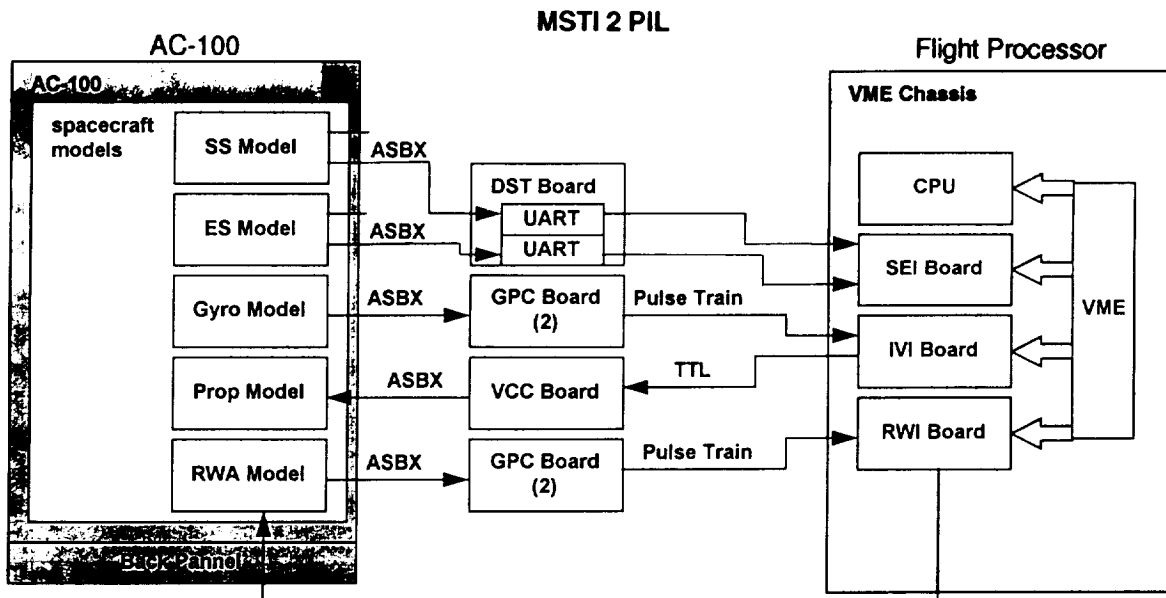


Figure 1

This paper discusses the design of the PIL, including an architectural overview, and the development of the PIL, including the methodology which was employed for rapid development. This paper focuses on the

real-time simulator, running on the AC-100, which emulated the on-orbit environment. The flight processor and the on-board software are not discussed in detail in this paper.

Overview

The MSTI 2 PIL provided a real-time simulation of the spacecraft environment for testing the on-board software running real-time on the flight processor (see Figure 2). The primary task of the MSTI 2 on-board software was attitude control, so the PIL was limited primarily to those functions relating to the Attitude Control System (ACS). The subsystems which were emulated by the AC-100 include attitude dynamics, ACS sensors and actuators, and orbit dynamics.

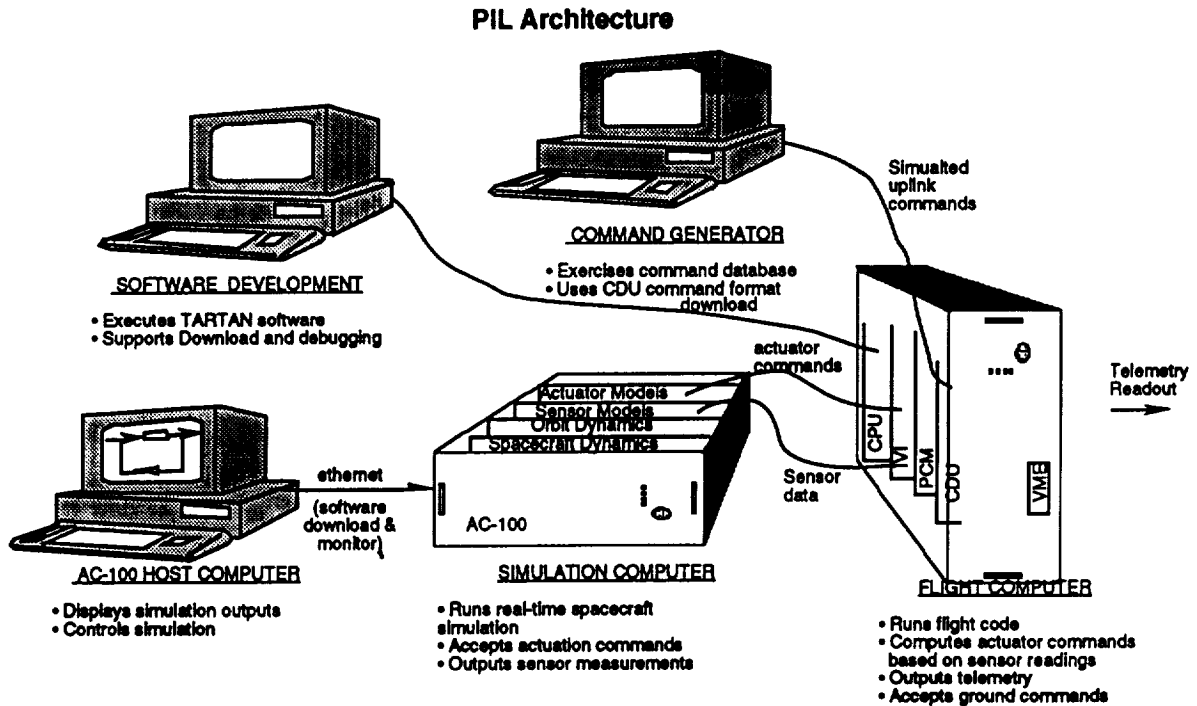


Figure 2

The PIL was designed to provide a realistic environment for the on-board software which accurately emulates the interactions between the processor and the rest of the spacecraft. The interfaces between the processor and the AC-100 were restricted to the ACS sensors and actuators, because these are the only ACS interfaces on the spacecraft available to the flight processor. The AC-100 intercepted those commands generated by the flight processor which were intended for the ACS actuators, and passed these commands to the spacecraft models. These models processed the commands, and the propagated dynamical subsystems, in order to generate realistic ACS sensor data. This data was passed along to the AC-100 output hardware, which emulated the electrical characteristics of the sensors.

The simulator hardware includes the AC-100 off-the-shelf real-time simulator, the custom I/O boards for the AC-100, and the host workstation. The simulator software includes the development environment, the automatically generated software, and the handwritten C code. In addition, a dynamics analysis software program, AutoLev, was used to develop the attitude equations of motion and generate the attitude dynamics subroutines.

The AC-100 System

As indicated in Figure 2, the hardware in the PIL consists of the AC-100 real-time simulator, the host workstation, and the custom I/O electronics boards in the AC-100. The PIL software consists of the Matrixx/SystemBuild development environment, the automatically generated C code, the custom hardware

interface routines, and the C code reused from other projects.

Matrix_x/SystemBuild is a single program which provides two environments: Matrix_x and SystemBuild. Matrix_x provides a command line environment for numerical design and analysis, while SystemBuild is an environment which allows the user to model systems with block diagrams, and then simulate the systems directly from the block diagrams. The results of the simulations can be analyzed in the Matrix_x environment.

As an example, Figure 3 shows a block diagram from the earth sensor subsystem. The data flow is indicated by the interconnections between the blocks, and the operations on the data are indicated by the blocks. Figure 3 shows gain blocks, data path switches, logic blocks, trigonometric blocks, and others. Many other blocks are available in the SystemBuild environment. The block labeled "ES Blanking Logic" is a Superblock, and within it is an entire subsystem, which is in turn built of blocks and superblocks. The superblocks can be nested in this way without limit.

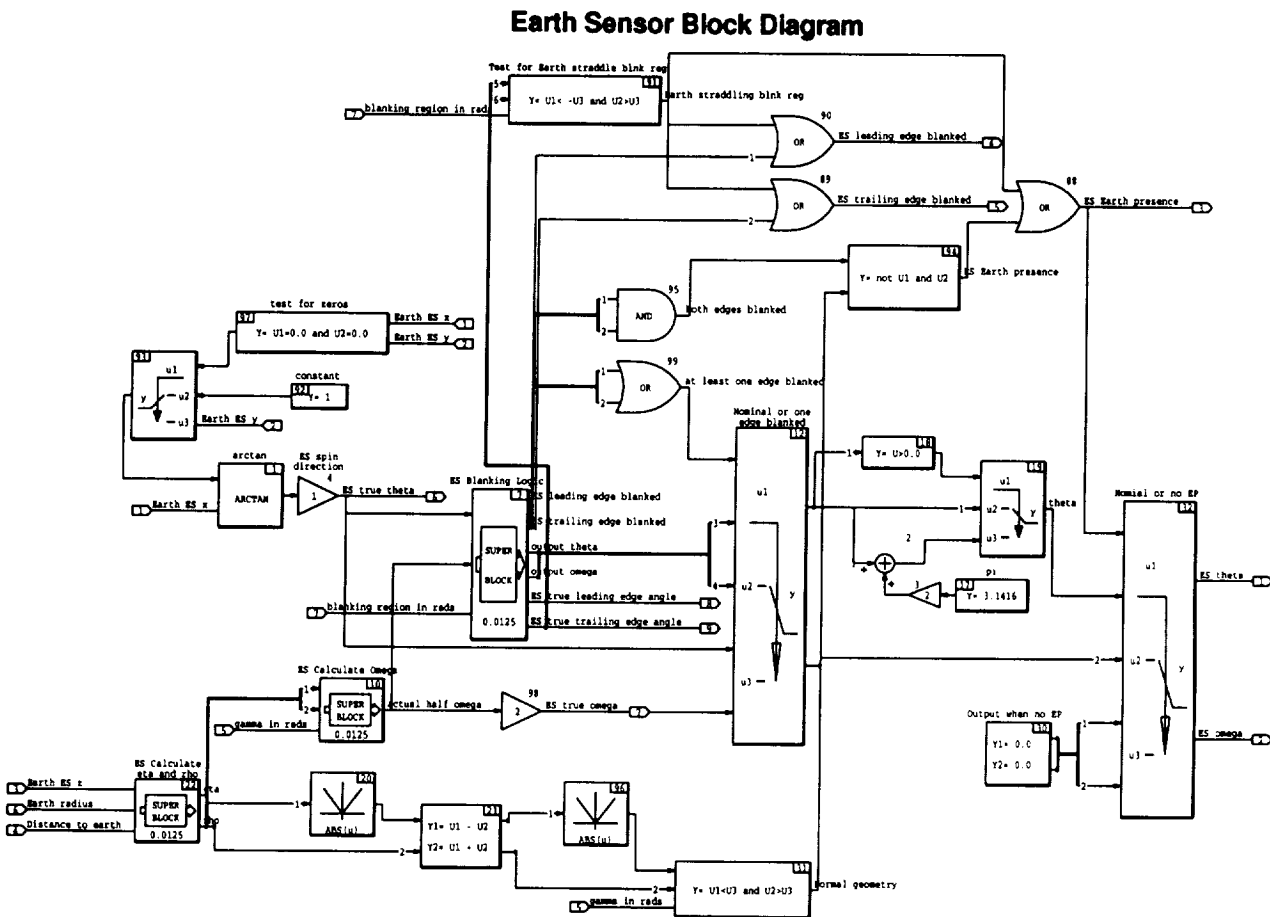


Figure 3

AutoCode converts the block diagrams developed under SystemBuild directly into real-time executable C code, which can be downloaded to the AC-100 real-time processor, or any other real-time processor. IA is a graphical environment which allows the user to build control panels to provide real-time interaction with the simulations executing on the AC-100.

The development of the PIL simulator software began under the Matrix_x/SystemBuild environment, starting with the MSTI 1 PIL models. In this environment, the various S/C subsystems were modeled using block diagrams. While in this environment, individual subsystems, or the entire spacecraft model, could be simulated non-real-time. Because the block diagrams could be simulated on the host workstation, it was possible to develop and debug the spacecraft models without needing to develop source code, and without porting the software to the AC-100 platform.

Not all of the spacecraft models were in block diagram form. The orbit dynamics models and the sun ephemeris had already been developed on earlier projects in handwritten C code, so it was not desirable to redevelop them. The SystemBuild a capability, called "User Code Blocks", which provides a standardized interface so that the user's handwritten C code can be used within the block diagrams. This provides a migration path from handwritten software to automatically generated simulations. The existing orbit dynamics models and sun ephemeris were incorporated into the block diagram this way.

Once the spacecraft block diagrams were developed and debugged, they were ready for the code generation process for execution on the AC-100. AutoCode converted the block diagrams directly into executable real-time source code, so moving these block diagrams to the AC-100 required no more than a few minutes.

Certain portions of the I/O were also readily ported to the AC-100, because the standard I/O capabilities of the AC-100 are tightly integrated into the software, so that connecting the AC-100 standard I/O was no more difficult than editing the block diagrams.

Other portions of the MSTI 2 PIL I/O had to emulate the specialized interfaces of the various ACS sensors and actuators, which required custom hardware interfaces to be developed for the AC-100. These hardware interfaces required the development of routines to allow the automatically generated code to communicate with the custom-designed I/O boards. These were 5 short C subroutines which called low-level I/O routines which are supplied with the AC-100. These custom routines were developed using the ordinary compile-link-debug cycle.

In addition, the equations of motion of the spacecraft were developed using AutoLev. This software package develops the equations of motion of a dynamical system using Kane's method, and automatically generates source code to simulate these equations. This code was integrated into the SystemBuild models as a User Code Block.

Spacecraft Subsystem Models

The models which were implemented in the MSTI 2 PIL included attitude dynamics, a sun sensor, an earth sensor, low rate gyros, a high rate gyro, thrusters, reaction wheels, orbit dynamics, and sun ephemeris.

The PIL setup operated at 80 Hz, which provided a sufficiently fast response to the on-board code which was operating at 5 Hz. Throughput testing started by running the models at 20 Hz, and then increasing the rate. The rate was increased to 120 Hz, and the AC-100 had not overflowed, so testing was stopped. It was decided that operating the model at 80 Hz. would allow a growth in model complexity of 50% or more, and this rate was more than sufficient for a quick response to the 5 Hz. on-board software.

The 80 Hz. rate of the PIL was also chosen because the on-board software operated at 5 Hz., it was not necessary to model any phenomena much faster than this. No phenomena which responded faster than about 0.05 seconds was modeled, and the 80 Hz. rate supported this.

Sun Sensor

The MSTI 2 sun sensor had a square field of view, 64° by 64° in extent. The output of this sensor was two numbers representing the angular position of the sun in the Field Of View (FOV), a single bit to indicate the sun is present in the FOV, and some housekeeping information. This information was encoded in a data frame which was transmitted 5 times per second to the processor. This was transmitted on an ordinary serial data stream, using RS-422 voltage levels. No commands were transmitted from the processor to the sun sensor.

Figure 4 shows the highest level block diagram of the Sun Sensor model. This model used the output of the attitude dynamics models, along with the sun ephemeris model, to compute the sensor data. The model had to check for sun presence in the SS FOV. If the sun was in the field of view, the angles were calculated, otherwise the default values were used. In addition, the "sun present" bit had to be set properly. The housekeeping information was hard-coded to its default value, and was not variable.

The error models included in the sun sensor model included geometric misalignment of the sensor on the spacecraft, and a bias on each output angle.

The data bytes for the serial data stream were formatted in the SystemBuild models, and passed on to the serial output of the AC-100.

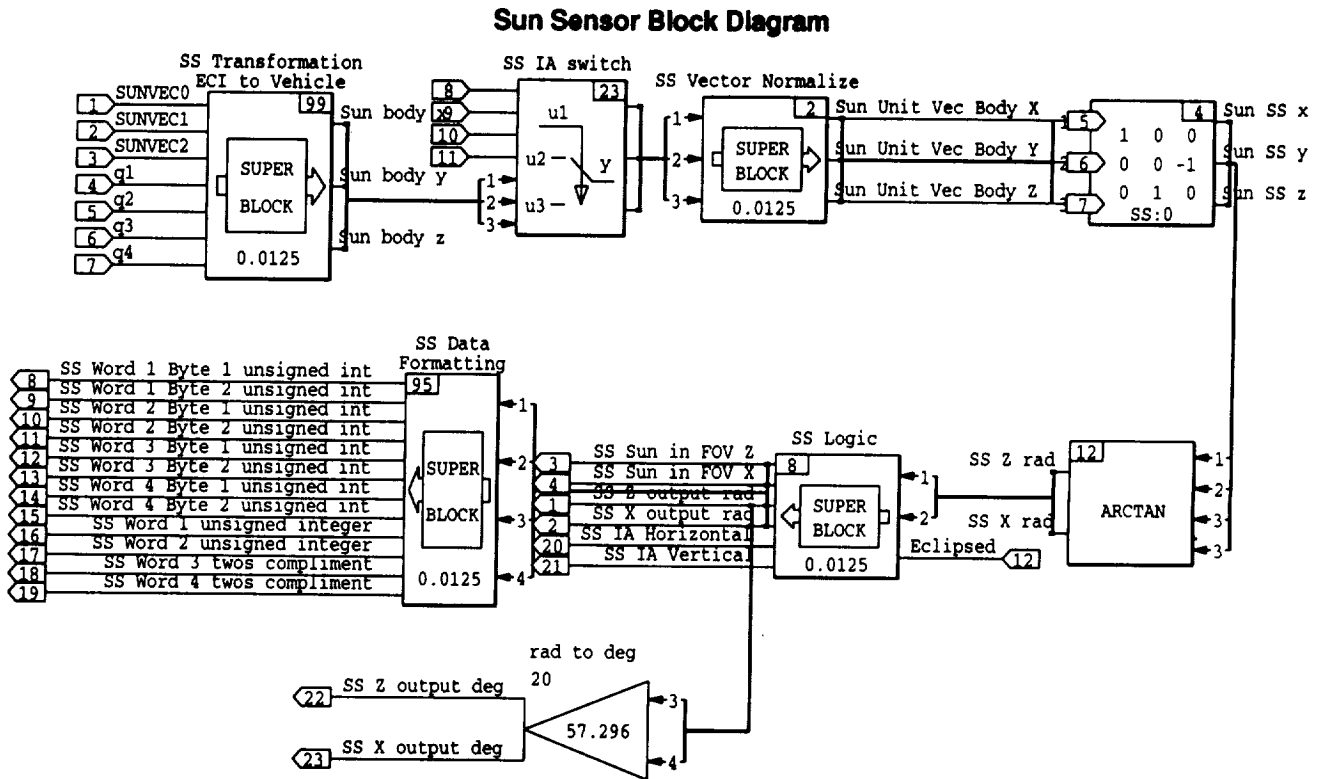


Figure 4

Earth Sensor

The MSTI 2 earth sensor was a scanning horizon sensor with a 60° half-cone angle. Due to the mechanical structure of the sensor, 81° of the scan cone were obstructed.

The outputs of this sensor included two angles, representing the phase and the chord of the earth in the scan cone. In addition, there were three individual informational bits: one bit indicated the earth was present in the scan cone, another single bit indicated that the leading edge of the earth chord was blocked by the obstruction, and the third single bit indicated that the trailing edge of the earth chord was blocked by the obstruction. This information, along with some housekeeping information, was encoded in a data frame which was transmitted 5 times per second to the processor. This was transmitted on an ordinary serial data stream using RS-422 voltage levels. No commands were transmitted from the processor to the earth sensor.

Figure 3 shows the block diagram of the Earth Sensor model. This model used the output of the attitude dynamics model, along with the orbit dynamics model, to compute the sensor data. If the scan cone intersected the earth, the chord and phase were computed, and the three bits described above, were set appropriately. If the scan cone did not intersect the earth, the default values for the angles were used, and the default values were used for the blanking bits. The housekeeping information was hard-coded to its default value, and was not variable.

The error models for the earth sensor included geometric misalignment of the sensor on the spacecraft, and a bias on each of the angle outputs.

The data bytes for the serial data stream were formatted in the SystemBuild models, and passed on to the serial output of the AC-100.

Low Rate Gyro

The primary source of attitude rate information on the MSTI 2 spacecraft was two high accuracy 2-axis gyros. However, they would saturate at a relatively low angular rate.

Each sensitive axis of each gyro had two pulse streams: one for positive rotation, and one for negative rotation. Only one of these two pulse streams was active at any moment. The frequency of these pulse streams was proportional to the angular rate about the sensitive axis. In addition, each pulse stream had a redundant transmitter for reliability. These pulse streams were transmitted on a RS-422 differential pair. There were a total of 32 conductors transmitting the gyro data.

There was no housekeeping information transmitted from the gyros to the processor, and there were no commands transmitted from the processor to the gyros.

The gyro models on the AC-100 used data only from the attitude dynamics models. The error models included geometric misalignment of the gyro on the spacecraft, and gyro biases.

Because the gyros had to be emulated with very high precision, and because the gyro outputs were specialized, it was necessary to build a custom output board for the AC-100, the GPC board. This board provided closed-loop control of the frequency. A counter was placed on each pulse stream, and these counters could be read by the AC-100 to provide a feedback path. The angular rate of the spacecraft about each gyro axis was integrated over time, and this accumulated value was compared to the counters during each 80 Hz. step. The frequency of each step was adjusted to make sure that the gyro outputs were never more than one pulse in error, when compared against the software models. The feedback path allowed the GPC board to generate smooth pulse trains which were lower than 80 Hz., by shutting down the pulse stream altogether during one or more 80 Hz. periods, and only occasionally commanding one pulse to be transmitted.

Each GPC board could transmit all of the signals coming from one gyro, so 2 GPC boards were required in the PIL to emulate these gyros.

It was necessary to develop a small handwritten C routine to drive the GPC boards. This routine handled the feedback control of the GPC board. This routine took the integrated angular rate from the block diagrams, and read the feedback counters on the GPC boards. After applying appropriate scale factors, the two values were compared for errors. Any differences were compensated by adjusting the frequency during the next 80 Hz cycle. With this feedback scheme, the accumulated errors of the gyro emulators, compared to the desired values, never exceeded 8 arcseconds.

This interface routine interacted with the hardware by calling simple low-level I/O routines, which are bundled with the AC-100. This routine was incorporated into the SystemBuild block diagram as a User Code Block.

High Rate Gyro

The MSTI 2 spacecraft included one low fidelity 3-axis gyro which had favorable saturation characteristics in order to handle that portion of the mission in which the spacecraft had high angular rates. The output of this gyro was three voltage levels, one for each axis. The voltage level was proportional to the angular rate of the spacecraft about the respective axis. There was no housekeeping information transmitted by this gyro, and there were no commands from the flight processor to this gyro.

The high rate gyro model used data from the attitude dynamics model to compute the gyro output. The standard AC-100 configuration includes several digital-to-analog outputs, so emulating the gyro electrical interface was quite simple. Using the standard I/O connection editor, this entire model, along with its I/O, required about one half of a day to implement.

Reaction Wheel Assembly

The MSTI 2 spacecraft had three reaction wheels, one along each primary axis of the spacecraft. These reaction wheels accepted an analog electrical signal as a torque command from the flight processor, and emitted an electrical pulse stream whose frequency was proportional to the wheel speed. In addition, there were various housekeeping commands which the processor could transmit to the wheels, and there were

various housekeeping signals which the wheels could transmit to the processor.

The reaction wheel models incorporated two torque sources. First, the motor torque was directly proportional to the analog torque command, so this was modeled by a simple gain. Second, the frictional torque varied as a function of wheel speed, and this was modeled using a simple table lookup block. The net torque acting on the wheel was the signed sum of these two torques.

The net torque computed by the wheel model was passed along to the attitude dynamics model, which would compute the wheel angular accelerations relative to the spacecraft. The reaction wheel model would integrate this acceleration to determine the wheel speed.

The standard AC-100 configuration includes several analog-to-digital inputs, so the input to this model was quite easy to implement. The output from this model was a pulse stream. While it was not necessary to control this pulse stream with high accuracy, the pulse stream generator from the gyro subsystem had already been developed, so it was easiest to simply reuse the gyro software and hardware with only changes in a few parameters in the software. Each GPC board could emulate two reaction wheels, so two additional copies of this board were required to emulate the RWAs. The housekeeping inputs and outputs of the reaction wheels were not modeled in the PIL.

Thrusters

The MSTI 2 spacecraft included 12 thrusters: 8 low-force thrusters for attitude control and 4 high-force thrusters for orbit adjust and orbit maintenance. These were simple on-off thrusters, and could not be throttled for proportional control. The flight processor issued no commands directly to the thrusters. Instead, the propulsion valves were controlled by the processor. A high TTL level signal opened the valves, and a low TTL level signal closed the valves. There were many housekeeping signals to and from the spacecraft propulsion system.

The fuel system on the MSTI 2 spacecraft regulated the pressure of the fuel being fed to the thrusters.

The interface board in the flight processor could command a thruster burn duration in increments of 250 μ s. These TTL level signals were issued by the on-board software once per 5 Hz. period. The MSTI 2 thrusters had a very short thrust buildup at the beginning of each thrust pulse, followed by a very short thrust tail-off at the end of each thrust pulse.

The thruster models in the MSTI 2 PIL were modeled with no thrust buildup or tail-off. The models simply applied a force and a moment on the spacecraft, based on the thrust capability and location of the individual thrusters. The forces were summed and passed along to the orbit dynamics models, and the torques were summed and passed along to the attitude dynamics models. The propulsion models did not include blowdown of the fuel system, because this was a pressure regulated system.

In order to maintain sufficient fidelity of the attitude dynamics, it was decided that the thruster commands should be captured with a resolution finer than one 80 Hz. period. This required a custom interface board, the Valve Command Capture (VCC) board. This board sampled the TTL thruster signals at 6 MHz., and accumulated the results over each 80 Hz. period. The PIL software would sample the VCC board once per 80 Hz. cycle, and fold the results into the thruster models. 6 MHz. was a much higher sample rate than required by this simulation, but this high rate was no more difficult to implement than a lower rate.

This board required a short C interface routine, which was handwritten code. This routine did little more than call the low-level I/O routines supplied by the AC-100, and pass the results along to the block diagram. This routine was implemented in the block diagram as a User Code Block.

Attitude Dynamics Models

The MSTI 2 spacecraft was modeled as four interacting rigid bodies: The main spacecraft structure and three reaction wheels. The main attitude dynamics block diagram is shown in Figure 5. The equations of motion of these bodies were developed using Kane's method, with the AutoLev software package. Kane's method allowed the models to include all forces of interest on the bodies, including non-conservative frictional forces and arbitrary actuator forces.

The spacecraft structure was modeled as a rigid body with misalignment of the principal axes of inertia. The wheels were modeled as axisymmetric bodies with their axis of symmetry aligned with their spin axis.

The moments and products of inertia of each body were set as parameters in the block diagram.

Using AutoLev, the equations describing the interaction of the bodies was described vectorially, and then AutoLev automatically generated a complete stand-alone implementation of these equations. One of the routines which AutoLev generated computes the algebraic relation between (1) the current state of the system and the actuator forces and (2) the angular accelerations of the bodies.

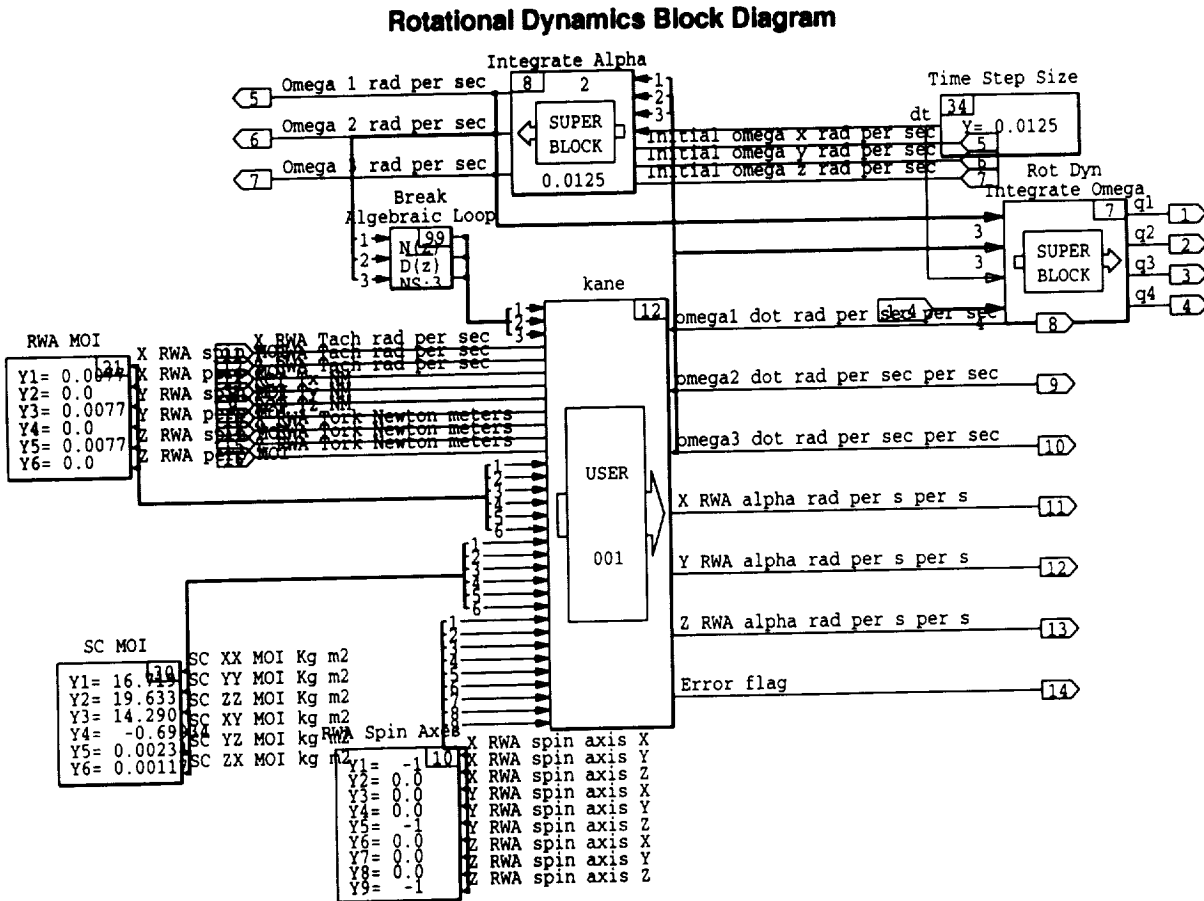


Figure 5

This routine was extracted from the AutoLev-generated program, and incorporated into the block diagrams as a User Code Block. The inputs to this routine were (1) the total torque due to the thrusters, (2) the total torque acting on each of the reaction wheels, (3) The current angular velocity of the spacecraft frame, (4) the current angular rate of each wheel, (5) the mass properties of the spacecraft structure, (6) the mass properties of the individual wheels, and (7) the orientation of each wheel in the spacecraft. The outputs from this User Code Block were the angular accelerations of the spacecraft structure and the angular accelerations of the individual wheels.

The angular accelerations were fed into discrete-time integrators to compute the angular rate of the spacecraft and the speed of the wheels. The spacecraft rates were fed into a discrete-time quaternion propagator to compute the spacecraft attitude.

Orbit Dynamics Models and Sun Ephemeris

These are two high fidelity models which were developed several years ago for other programs. They were developed as handwritten C source code. Sometime after their original development, they were modified to be User Code Blocks for use in the SystemBuild environment. Both of these models were used without

further modification in the MSTI 2 PIL.

The Orbit dynamics model includes a fifth order gravity model, and incorporates accelerations due to thrusting. Its propagator is a fixed-step fourth-order Runge-Kutta integrator. The input to the sun ephemeris is the time, expressed as year, month, day, hour, minute, second, and millisecond, and the output is the sun location in ECI, accurate to a few arcseconds.

User Interface

While the PIL is executing, an interface was presented to the user which allowed the operator to interact with the real-time simulation. This interface was built under Interactive Animation (IA). Using the Interactive Animation editor, the screens were built up graphically and connected to the various inputs and outputs of the block diagram.

Interactive Animation User Interface

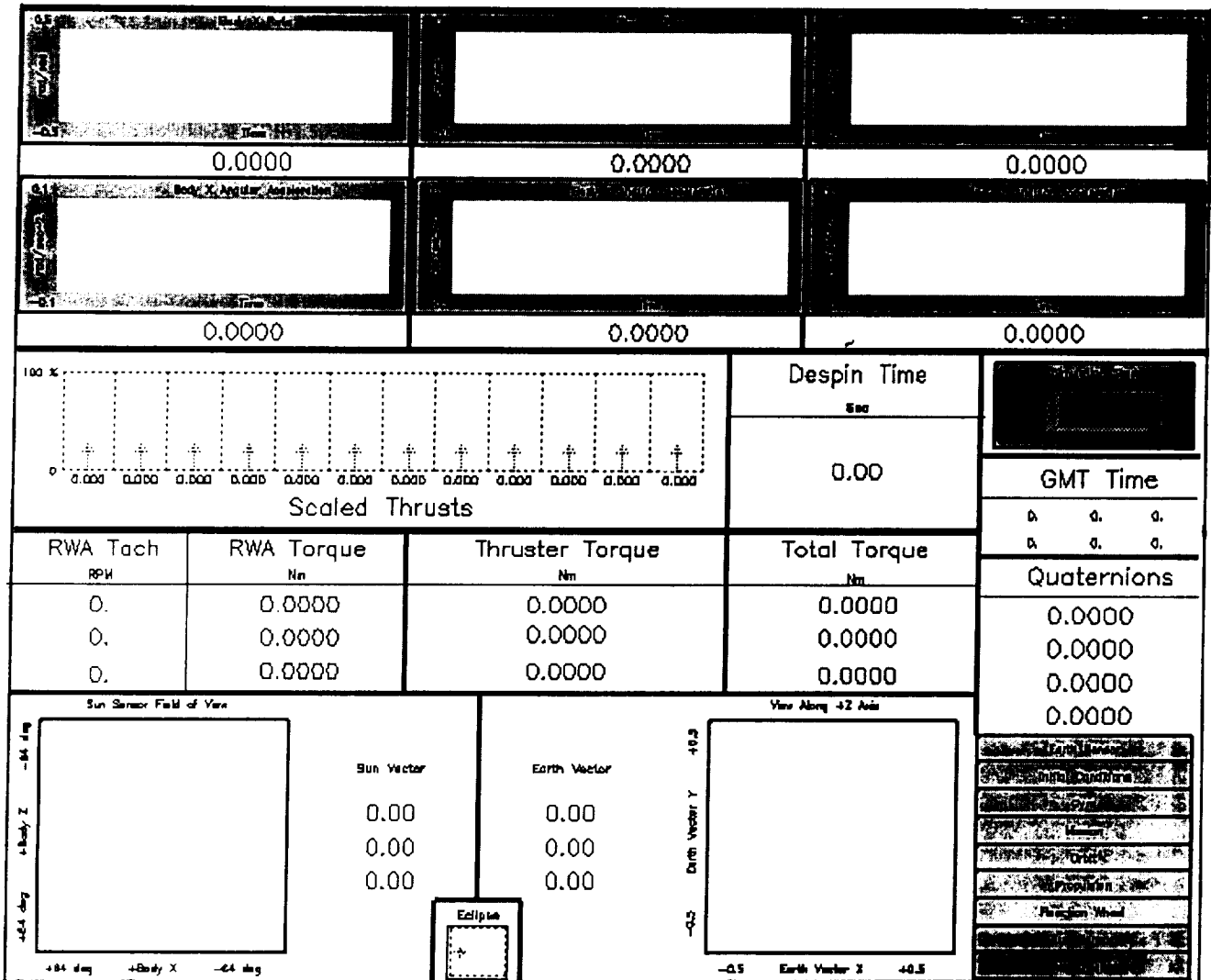


Figure 6

The main executive PIL screen is shown in Figure 6. From this screen, the user could invoke any one of many different screens at any time. With these screens, the user could monitor various internal variables in the PIL simulator real-time, or the user could interact with the simulation by varying parameters and adjust-

ing various settings, again in real-time. This capability was used primarily to simulate faults in the spacecraft, in order to test the response of the on-board software to off-nominal conditions.

A different screen dedicated to each subsystem was included in the Interactive Animation interface. With each screen dedicated to an actuator, the user could override the commands coming from the flight processor and inject his or her own commands. The user could command individual thruster firings, and could command reaction wheel torques directly. Similarly, with each screen dedicated to a sensor, the user could override the sensor data computed by the PIL simulation and inject his or her own values. The user could place the sun in any orientation relative to the spacecraft coordinates, could place the earth in any orientation relative to the spacecraft coordinates, or could inject any body rates into the gyro models.

Outside of the flight processor, the variables internal to the on-board software are not available to the spacecraft. In order to keep the PIL a true environment emulator, it also had no access to the variables internal to the processor. Therefore, the Interactive Animation screens could not present all of the information of interest in the spacecraft. Most significantly, the PIL provided no direct method to determine what attitude control mode the processor was currently using.

Custom Interface Boards

As described above, several custom electronics boards were developed for this project. These boards were prototyped and debugged by the primary engineer, and the artwork and fabrication was subcontracted to an electronics design house.

The boards included the GPC board, and the VCC board. The MSTI 2 PIL was implemented on an older model of the AC-100 which did not have an efficient serial interface, so it was necessary to build a custom serial interface, the Dual Serial Transmitter (DST). In addition, a simple executive board, the ASBX, was build to control the interactions of the other boards with the AC-100.

Because the graphical programming environment of SystemBuild provides such rapid software development, most of the time spent developing the MSTI 2 PIL went toward hardware development.

Conclusion

By taking maximum advantage of the AC-100 development environment, one engineer spent three months, with one month of help from a second engineer, to develop a high fidelity spacecraft simulator. This included all initial design, all model development, all software development, the design and development of four custom electronics boards, integration of the subsystems, and refinement of the system. This was due primarily to the graphical programming environment of SystemBuild, along with the code generation capability of AutoCode. Another prime factor in this success was the ability of the AC-100 system to reuse existing code.

By spending very little time on software development, the engineer was allowed to focus on the more difficult task of hardware development.

The Control of Satellites with Microgravity Constraints:
The COMET Control System

Walter Grossman
Madison Guidance, Navigation & Control
616 Madison Court
Yorktown Heights, NY 10598-3722
e-mail: w.grossman@ieee.org

Douglas Freesland
CTA Space System
1521 Westbranch Drive
McLean, VA 22102-3201

I. Nomenclature

- \hat{b} - Unit vector in direction of local magnetic field.
- g_p - Proportional control gain.
- g_d - Derivative control gain.
- g_i - Integral control gain.
- g_w - Wheel speed control feedback gain.
- G - Gravity gradient torque.
- h - Spacecraft internal angular momentum.
- J - Spacecraft inertia matrix.
- \hat{n} - Momentum management axis. Unit vector along intersection of magnetic control subspace and wheel control subspace.
- n_{\perp} - \mathcal{R}^2 space perpendicular to \hat{n} .
- q - Attitude quaternion.
- R_i - Saturation ratio of i th actuator. $R_i = |\tau_i|/\tau_{max\ i}$.
- v - Linear control of dynamics-inverted system.
- w - Wheel speed vector $[0 \ w_y \ w_z]'$.
- w_y, w_z - y and z momentum wheel speeds, respectively.
- \hat{x} - Unit vector along spacecraft x -axis.
- ϵ_p - Euler axis attitude error derived from ϵ_q . $\epsilon_p = 2\epsilon_q(0)[\epsilon_q(1) \ \epsilon_q(2) \ \epsilon_q(3)]'$.
- ϵ_q - Quaternion error. $\epsilon_q = q \otimes q_{ref}^{-1}$.
- ϵ_w - Wheel speed error. $\epsilon_w = w - w_{ref}$.
- ϵ_{ω} - Spacecraft angular velocity error. $\epsilon_{\omega} = \omega - \omega_{ref}$.
- τ - Spacecraft control torque.
- τ_1 - Attitude control torque projected onto \hat{n} .
- τ_2 - Attitude control torque projected onto n_{\perp} .
- τ_i - Actuation command for i th actuator.
- $\tau_{max\ i}$ - Saturation value of i th actuator.
- τ_{m1} - Attitude control torque projected onto n_{\perp} effectuated by magnetic torquers.

- τ_{m2} - Momentum management torque parallel to \hat{n} effectuated by magnetic dipole torquers.
- τ_{w1} - Attitude control torque projected onto n_{\perp} effected by momentum wheel actuators.
- τ_{w2} - Momentum management control torque parallel to \hat{n} effectuated by momentum wheels.
- ω - Spacecraft angular velocity.
- \otimes - Quaternion multiplication operator.

II. Introduction

The COMmercial Experimental Transporter (COMET) satellite provides a microgravity environment for experimental payloads. For the first thirty days of the mission the satellite is operated in a solar-inertial fixed attitude to maximize the power profile. The spacecraft is then pointed along the velocity vector and the experiment carrier is released for deboosting and recovery. The spacecraft is then nadir pointed and additional microgravity experiments are conducted.

The COMET Attitude Determination and Control System (ADACS) supports these mission requirements by combining inverse dynamics nonlinear feedback with a novel momentum management technique.

Inverse dynamics was developed in the middle 1980's for multi-mission, multi-configuration aircraft [1, 2] and subsequently applied to spacecraft [3].

The technique uses nonlinear feedback to *globally* transform nonlinear system dynamics into a linear system described by a linear second-order differential equation. Since the transfor-

mation is global and exact only a single set of control gains is required for both small-angle attitude maintenance and large-angle attitude maneuvers. The technique inherently accomodates multiple spacecraft mass configurations without the need for multiple sets of control gains. The inverse dynamics technique compensates for and exploits spacecraft precession to achieve three-axis attitude control using two reaction wheels.

The COMET momentum management system controls reaction wheel speed while preserving the satellite microgravity environment. Unlike the inner-loop/outer-loop structure common to most satellites, the COMET momentum management system calculates the momentum management torques as an integral part of the attitude control torque.

III. Inverse Dynamics Control

The spacecraft dynamics are written

$$J(q)\dot{\omega} + \underbrace{\omega^\times [J(q)\omega + h]}_{\text{precession}} + \underbrace{G(q)}_{\text{grav grad}} = \tau. \quad (1)$$

The plant dynamics described by (1) are inverted and *globally* linearized

$$\tau = J(q)v + \omega^\times [J(q)\omega + h] + G(q) \quad (2)$$

$$v = -g_p \epsilon_q - g_d \epsilon_\omega - g_i \int_0^t \epsilon_q(\lambda) d\lambda. \quad (3)$$

Substituting equations (2) and (3) into (1) yields the linear differential equation

$$\dot{\omega} = -g_p \epsilon_q - g_d \epsilon_\omega - g_i \int_0^t \epsilon_q(\lambda) d\lambda. \quad (4)$$

The feedback gains, g_p , g_d , and g_i are chosen using LQR design methods.

Implementation of the inverse dynamics control law described by equations (2) and (3), requires full-state feedback of spacecraft attitude and angular velocity. Many spacecraft lack the inertial measurement unit (IMU) necessary to measure angular rates. COMET has an IMU but its use is necessarily limited to conserve power.

It was shown [4, 5] that inverse dynamics can be robustly implemented with only partial-state

feedback using a Kalman observer to estimate the unmeasured velocity state. Including the position and velocity estimates from the Kalman observer, the control law described by equations (2) and (3) is modified

$$\tau = J(\hat{q})v + \hat{\omega}^\times [J(\hat{q})\hat{\omega} + h] + G(\hat{q}) \quad (5)$$

$$v = -g_p \hat{\epsilon}_q - g_d \hat{\epsilon}_\omega - g_i \int_0^t \hat{\epsilon}_q(\lambda) d\lambda, \quad (6)$$

where the $\hat{\cdot}$ indicates the observer-estimated value.

The torque vector derived from the control law, equations (5) and (6), is applied to the COMET microgravity attitude actuators.

IV. Torque Distribution & Momentum Management

A. The Actuator Suite

The COMET microgravity actuator suite consists of three 100 $a\cdot m^2$ electromagnetic torque coils along the spacecraft x , y , and z body axes and two 2 newton-meter-second momentum wheels along the spacecraft y and z body axes. There is no momentum wheel parallel to the spacecraft x -axis. (COMET is equipped with six 44 newton (10 lb) cold gas thrusters. They impart accelerations which exceed microgravity limits so their use is restricted to initial acquisition and recovery system reaction control.)

At the nominal 250 nautical mile altitude the magnetic torques deliver approximately 1×10^{-3} newton-meter torque in the plane perpendicular to the local magnetic field. The momentum wheels deliver approximately 8.5×10^{-3} newton-meter torque.

B. Momentum Management by Torque Decomposition

Three wheel and four wheel momentum management schemes are usually implemented as a feedback outer-loop external to the attitude control system inner-loop controller. Gas jets provide instantaneous three-axis desaturation control authority. For non-equatorial orbits mag-

netic dipoles provide instantaneous two-axis desaturation and over-orbit three-axis momentum management.

Inner-loop/outer-loop control structure separation works with spacecraft having three or four wheels because the wheel axes span \mathcal{R}^3 . The attitude control torque is exactly decomposed onto the wheel axes and effectuated entirely with the momentum wheel actuators. The instantaneous momentum error is projected onto the magnetic control subspace \mathcal{R}^2 normal to the local external field and is removed. Over orbit the magnet control subspace spans \mathcal{R}^3 and wheel momentum is maintained. The control problem separates whereby high-bandwidth attitude control is effected by the momentum wheels and low-bandwidth momentum control is effect by the magnetic torque coils.

Having only two wheels, the COMET microgravity control system cannot be partitioned into this inner-loop/outer-loop structure. The COMET attitude control torque must be applied using a combination of the wheels and torque coils while momentum is simultaneously maintained over orbit. The momentum control torques are calculated continuously and as an integral part of the attitude control torques.

The wheel torque subspace spans \mathcal{R}^2 . When the spacecraft x -axis is not colinear with the local magnetic field the magnetic torque subspace spans a different \mathcal{R}^2 and the actuator torque space is overdetermined. The intersection of the two subspaces represents a direction in \mathcal{R}^3 where the attitude control torque can be applied *either using the magnetic torquers or the momentum wheels*. This axis is the “momentum management axis” where some portion of the momentum error can be removed without disturbing spacecraft attitude. See figure 1.

The COMET momentum management and attitude control torque distribution technique is captured mathematically by solving a system of linear constraints. The decomposition steps are summarized:

$$\hat{n} = \frac{\hat{x} \times \hat{b}}{|\hat{x} \times \hat{b}|} \quad (7)$$

$$\tau_1 = \hat{n}' \tau. \quad (8)$$

$$\tau_2 = (I - \hat{n} \hat{n}') \tau. \quad (9)$$

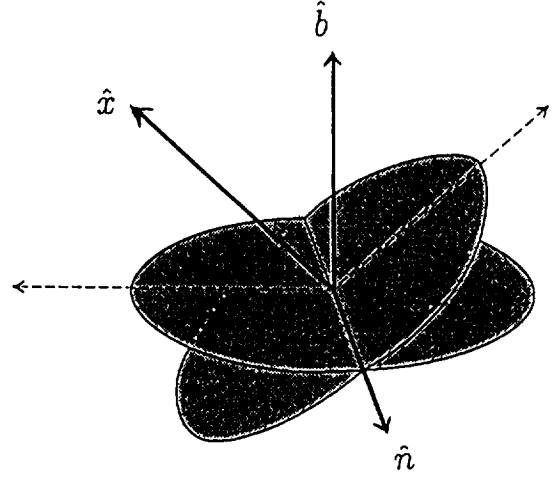


Figure 1: The “torque space” and the momentum management axis.

$$\begin{pmatrix} 0 \\ 0 \\ \tau_2 \\ 0 \\ 0 \end{pmatrix} = \begin{pmatrix} \hat{b}' & 0 \\ 0 & \hat{x}' \\ I - \hat{b} \hat{b}' & I - \hat{x} \hat{x}' \\ \hat{n}' & 0 \\ 0 & \hat{n}' \end{pmatrix} \begin{pmatrix} \tau_{m1} \\ \tau_{w1} \end{pmatrix} \quad (10)$$

$$\tau_1 = (\hat{n}' \quad \hat{n}') \begin{pmatrix} \tau_{m1} \\ \tau_{w1} \end{pmatrix} \quad (11)$$

Equation (10) represents the constraints for solving for the torque in subspace n_{\perp} . These constraints are:

1. Zero magnetic torque in direction of \hat{b} .
2. Zero wheel torque in direction of \hat{x} .
3. The sum of the wheel and magnetic torque in their respective subspaces equals the component of the attitude control torque in space n_{\perp} .
4. Zero magnetic torque in direction of \hat{n} .
5. Zero wheel torque in direction of \hat{n} .

The 7×6 matrix in (10) is a rank 6 matrix and the equation has a unique solution. (In COMET these equations are solved using the numerically robust QR decomposition.) Equation (11) is underdetermined. *Any combination of magnetic and wheel torque in the direction \hat{n} which equals τ_1 will correctly maintain the spacecraft attitude.*

The momentum management torque is proportional to the wheel speed error projected onto \hat{n} . A wheel speed corrective torque and

a compensating magnetic torque are applied in the \hat{n} and $-\hat{n}$ direction, respectively.

$$\tau_{w2} = -g_w \hat{n} \hat{n}' \epsilon_w \quad (12)$$

$$\tau_{m2} = \tau_1 - \tau_{w2}. \quad (13)$$

The final actuator torques are the sum of the components in the \hat{n} and n_{\perp} spaces

$$\tau_w = \tau_{w1} + \tau_{w2} \quad (14)$$

$$\tau_m = \tau_{m1} + \tau_{m2}. \quad (15)$$

C. Saturation Control

The computed wheel torques and magnetic dipole moments may drive the actuators into saturation. Saturation does not usually occur uniformly across all the actuators. The effect of saturation is to misdirect the corrective rotation of the satellite.

Saturation control in COMET is based upon the heuristic that it is preferable to maintain the *direction* of the control torque at reduced magnitude than to apply maximum control authority in the wrong direction.

The five actuator commands (two wheel torques, three magnetic dipole values) are calculated and five saturation ratios $R_i = |\tau_i|/\tau_{max\ i}$ are calculated. If any of these five ratios exceeds unity then *all* the actuator commands are scaled by the largest of these five ratios.

The effect of occasional actuator saturation upon linear systems is generally benign and not destabilizing. The effect of actuator saturation upon an inverse dynamics control system is complicated in that saturation leads to incomplete inversion. Simulation has demonstrated good system performance even with occasional saturation. The effect of saturation on incomplete dynamics inversion and control system performance is an area which requires future research.

V. Simulation

Simulations demonstrate the performance of the COMET microgravity control system.

Gravity gradient and aerodynamic torques are the dominant disturbances and are simulated. The simulation orbit is circular at 463 km (250 NM) altitude. The F10.7 solar flux level is 116.

Spacecraft state estimates generated by attitude determination system are used for calculation the attitude and rate errors. Except where noted, the IMU is off and feedback linearization is achieved using angular velocity estimates.

Simulation series (1) demonstrates COMET solar-pointing performance with a momentum bias. The spacecraft attitude recovers from the initial 15° error. Momentum wheel rates converge to their nominal 1500 RPM bias levels.

Lack of sensor input combined with unmodelled aerodynamic torques cause the attitude error to increase in the umbra. This pointing error is due to attitude estimation error developed in the Kalman Filter extrapolation step. Simulation series (2) shows represents the same run as series (1) except the IMU is on and satellite body rates are directly measured. Umbra performance is greatly improved.

Simulation series (3) demonstrates COMET solar-pointing performance without momentum bias. The spacecraft attitude recovers from the initial error. Momentum wheel mean rates converge to zero. The attitude control system in series (3) is identical to that of series (1) demonstrating control system flexibility in accommodating different momentum configurations. This flexibility is a consequence of the exact *global* linearization provided by the inverse dynamics control law. With equal flexibility the control system accommodates spacecraft with varying mass properties. COMET is a multi-configuration spacecraft which uses the same control law for all its mass configurations.

Simulation series (4) demonstrates COMET Earth-pointing performance¹.

Simulation series (5) demonstrates the COMET large-slew microgravity transition

¹In Earth-pointing mode the COMET spacecraft coordinate system differs from the conventional local vertical system. In this mode the roll axis (*x*-axis) is nadir-pointing, the yaw axis (*z*-axis) is aligned anti-parallel to the orbit normal, and the pitch axis (*y*-axis) completes the triad, pointing approximately in the velocity direction.

from solar-pointing to Earth-pointing. Note the rate quenching of the COMET pitch momentum wheel (yaw wheel by conventional terminology). Spacecraft acceleration is maintained within the $10^{-5}g$ microgravity acceleration limit *during the slew*.

Simulation series (6) demonstrates COMET slewing 90° in pitch and yaw and holding to an arbitrary attitude. Momentum wheels maintain their 1500 RPM bias during the slew. This mode is used for reentry attitude control prior to recovery capsule deboosting.

Simulation series (7) demonstrates the synthesized roll control performed without a roll wheel. This synthesized roll is a consequence of the inclusion of the precession term in the inverse dynamics. Series (7a) shows the large roll when the precession term is not included. Simulation series (7b) shows the roll error reduction caused by inclusion of the precession term.

Simulations (1)-(7) demonstrate the performance of the COMET attitude control system. Slewing of the the reaction wheel during transition and maintenance of their speeds in the steady-state demonstrates the performance of the novel COMET momentum management technique. Operational flexibility to the variety mass properties, momentum biases and command attitudes is a feature inherent to the method of inverse dynamics control.

From simulation experiments, inverse dynamics control is empirically known to be robust to large variations in the "model" plant. Simulation series (8) demonstrates that COMET is robust to large uncertainty to mass properties. In this simulation the three mass principle axes of the true satellite are skewed 15° from their "model" orientation. The system remains stable and within specification. The mass properties mismatch does causes a 50% increase RMS attitude error (see simulation series 1 for comparison.)

VI. Conclusion

The COMET attitude determination and control system, using inverse dynamics and a

novel torque distribution/momentum management technique, has shown great flexibility, performance, and robustness.

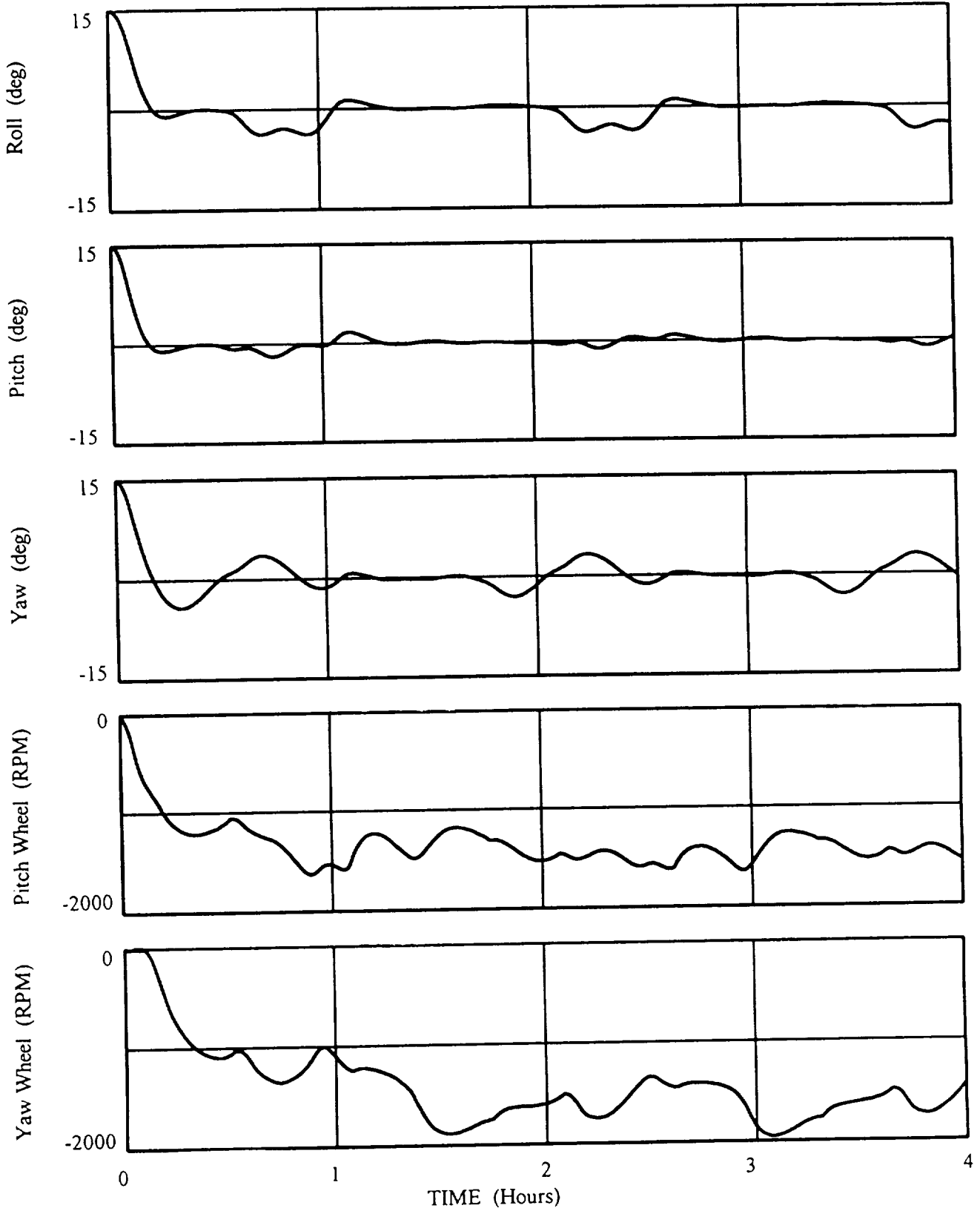
Three-axis control with two wheels is an inherent consequence of inverse dynamics control which allows for reduction in spacecraft weight and cost, or alternatively, provides a simple means of failure-redundancy for three-wheel spacecraft.

The control system, *without modification*, has continued to perform well in spite of large changes in spacecraft mass properties and mission orbit altitude that have occurred during development². This flexibility has obviated imposition of early stringent ADACS design constraints and has greatly reduced commonly incurred ADACS modification costs and delay associated with program maturation.

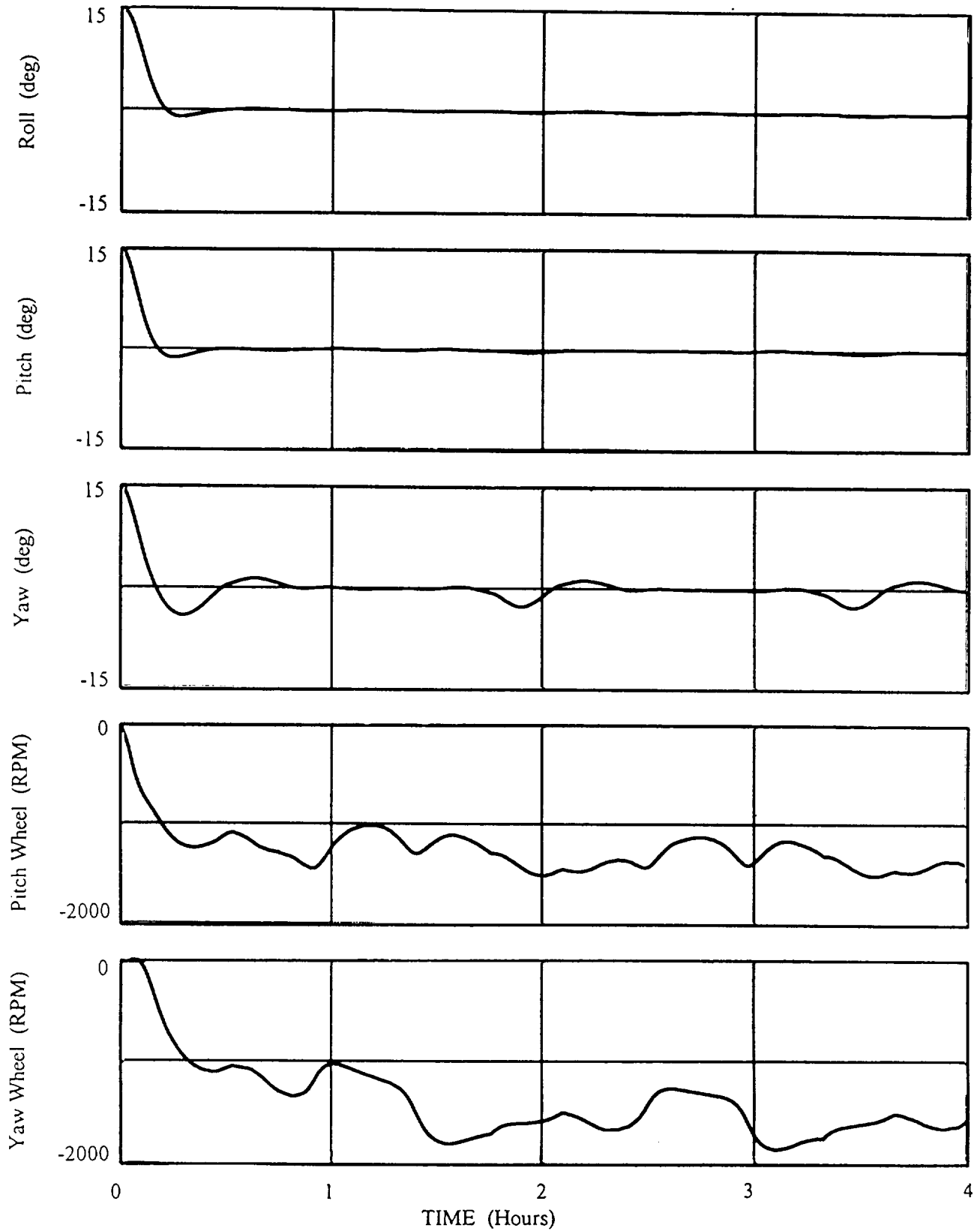
-
- [1] G. Meyer, R. Su, and L. R. Hunt, "Application of nonlinear transformations to automatic flight control," *Automatica*, vol. 20, no. 1, pp. 103-107, 1984.
 - [2] A. Isidori, "Nonlinear control systems," in *Lecture Notes in Control and Information (2nd edition)*, Springer-Verlag, 1989.
 - [3] T. A. W. Dwyer, "Exact nonlinear control of large angle rotational maneuvers," *IEEE Trans. Automatic Control*, vol. AC-29, no. 9, pp. 769-774, 1984.
 - [4] W. Grossman, F. Khorrami, and B. Friedland, "Observer-based design for robust control of robot manipulators," in *Proceedings of the 1990 American Control Conference*, (San Diego, California), pp. 731-736, May 1990.
 - [5] W. D. Grossman, *An Observer-based Design for Control of Nonlinear Systems and Applications to Robot Manipulators*. Degree of Engineer thesis, Polytechnic University, Brooklyn, New York, 1992.

²Increases in spacecraft mass has lead to reduction of orbit altitude from the original 556 km (300 nm) altitude to the 463 km (250 nm) altitude. The control system was designed for the original altitude.

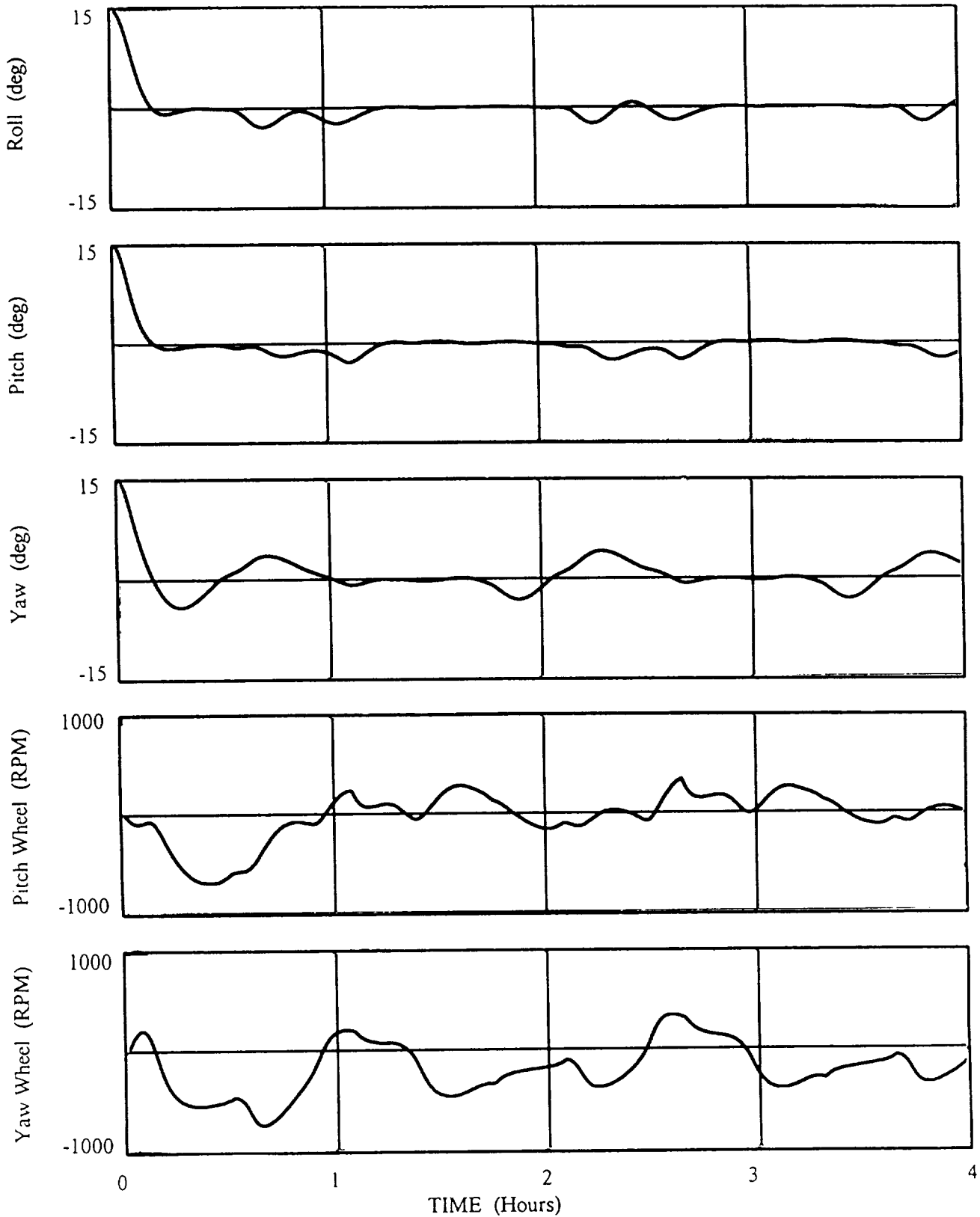
Simulation Series 1



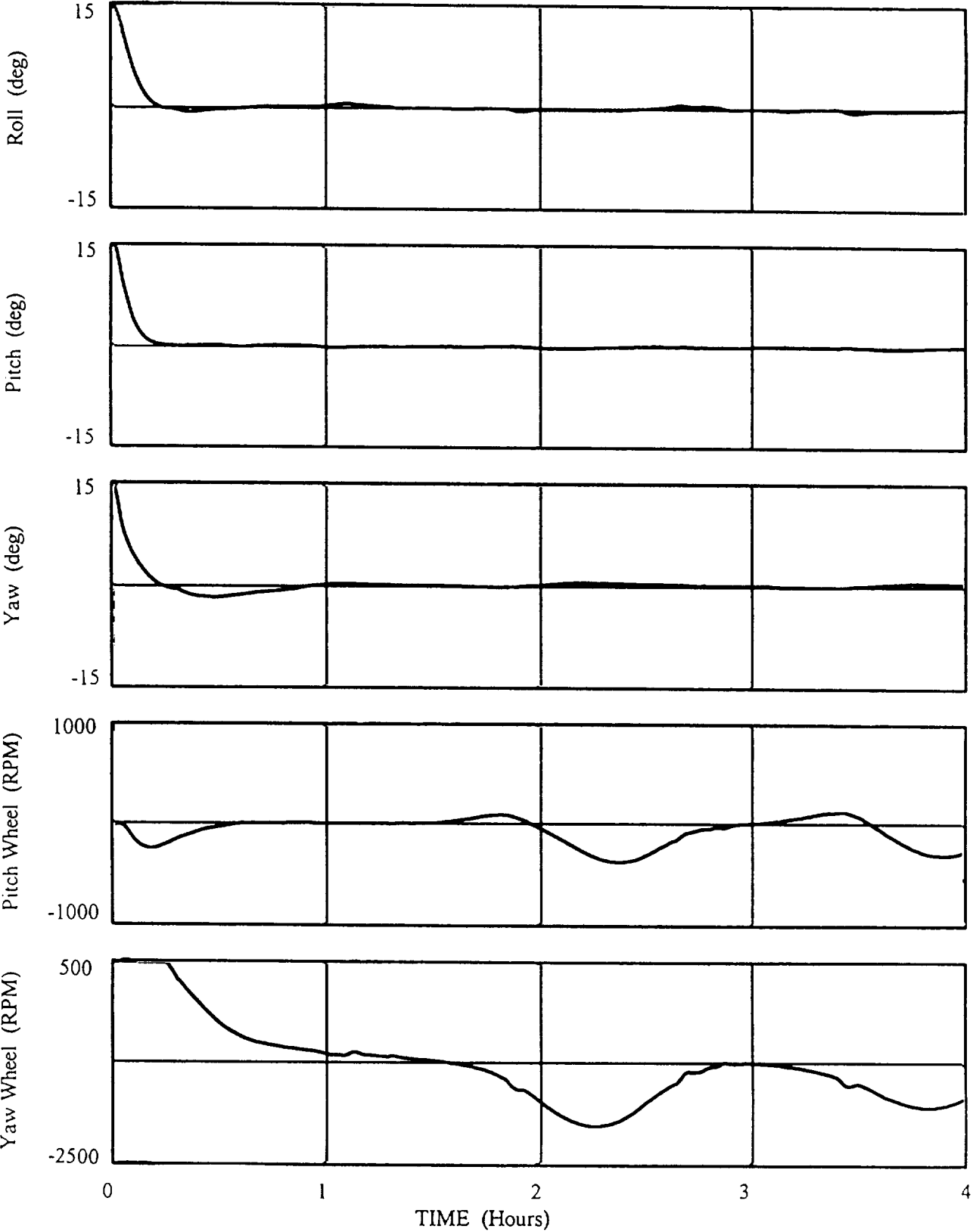
Simulation Series 2



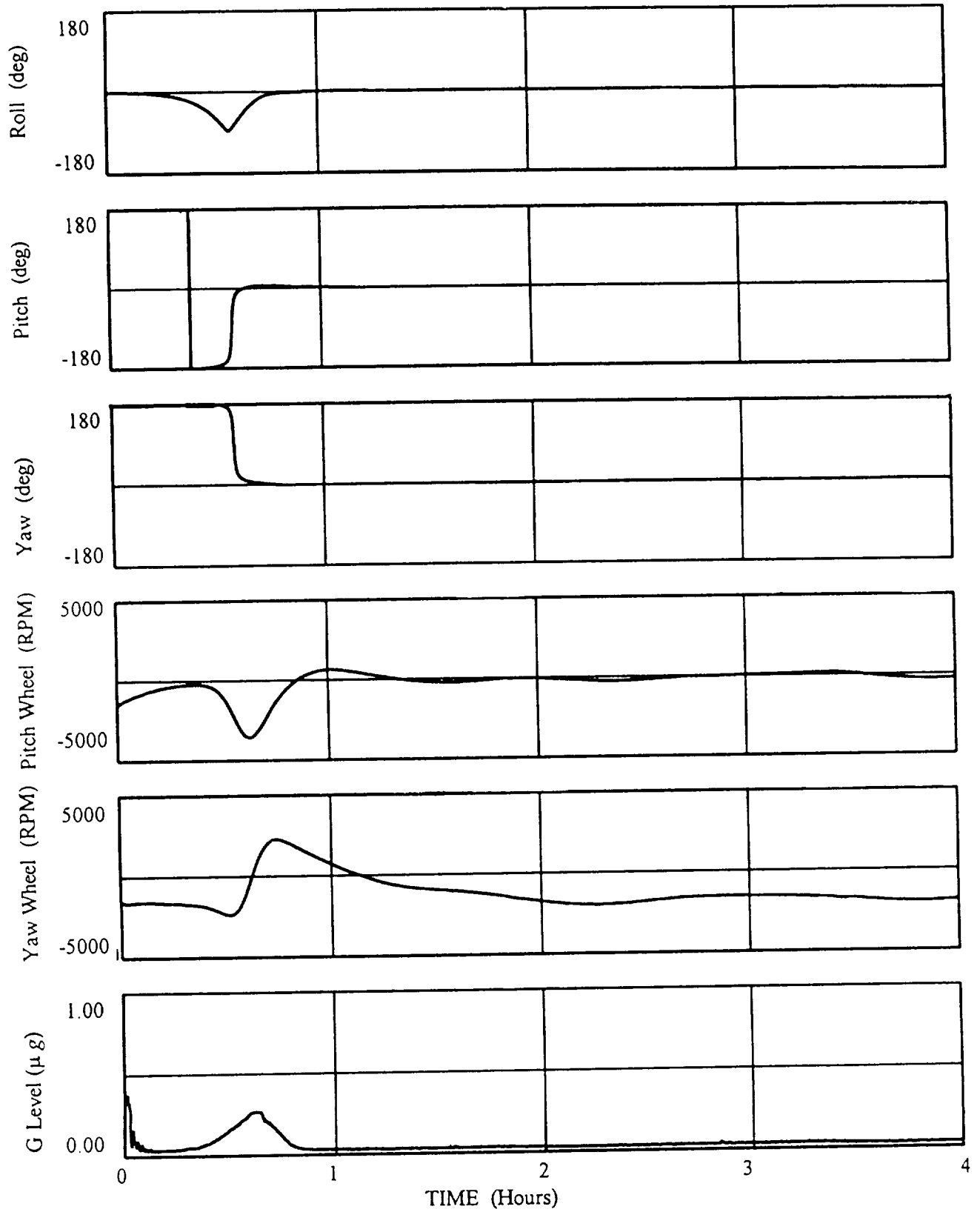
Simulation Series 3



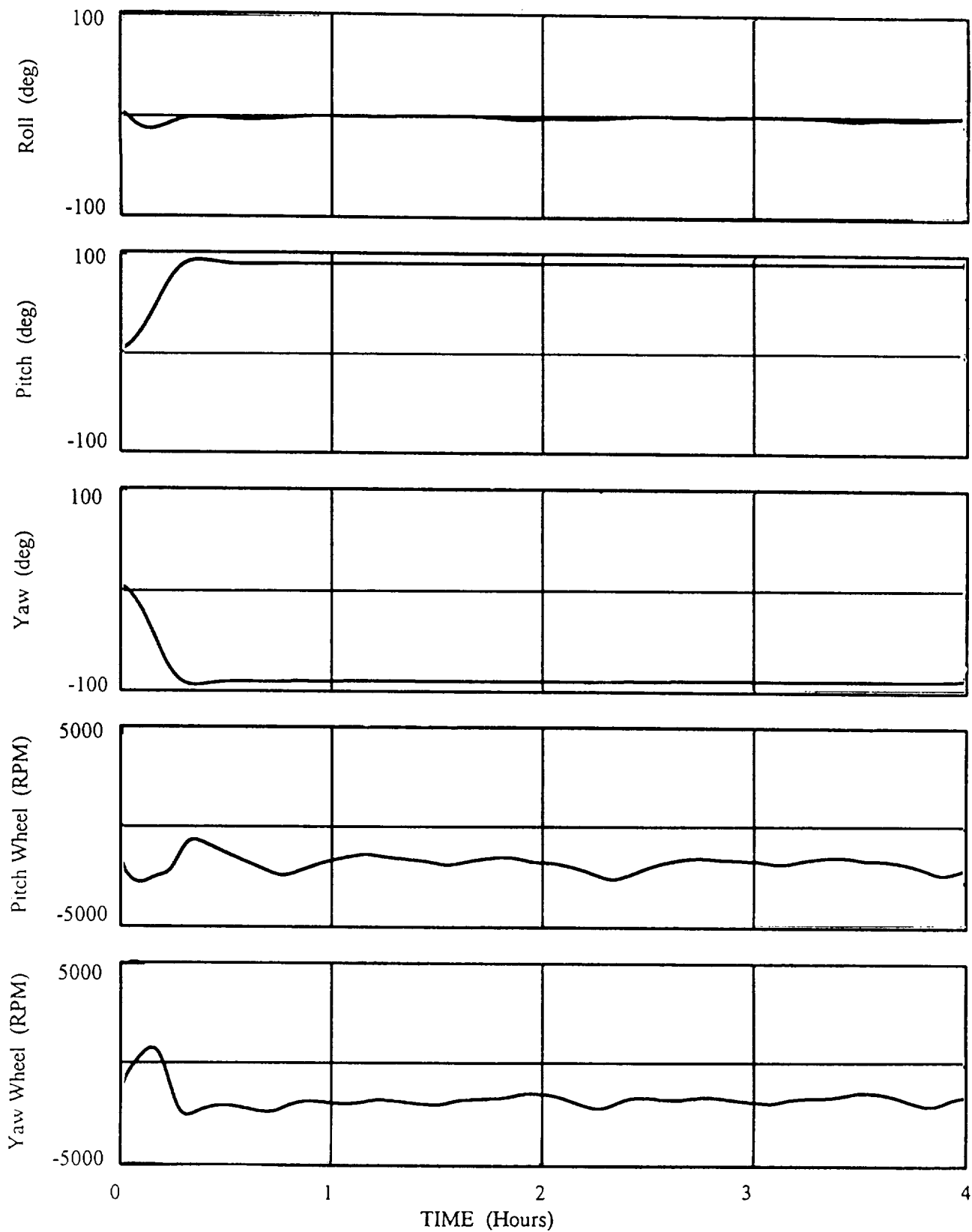
Simulation Series 4



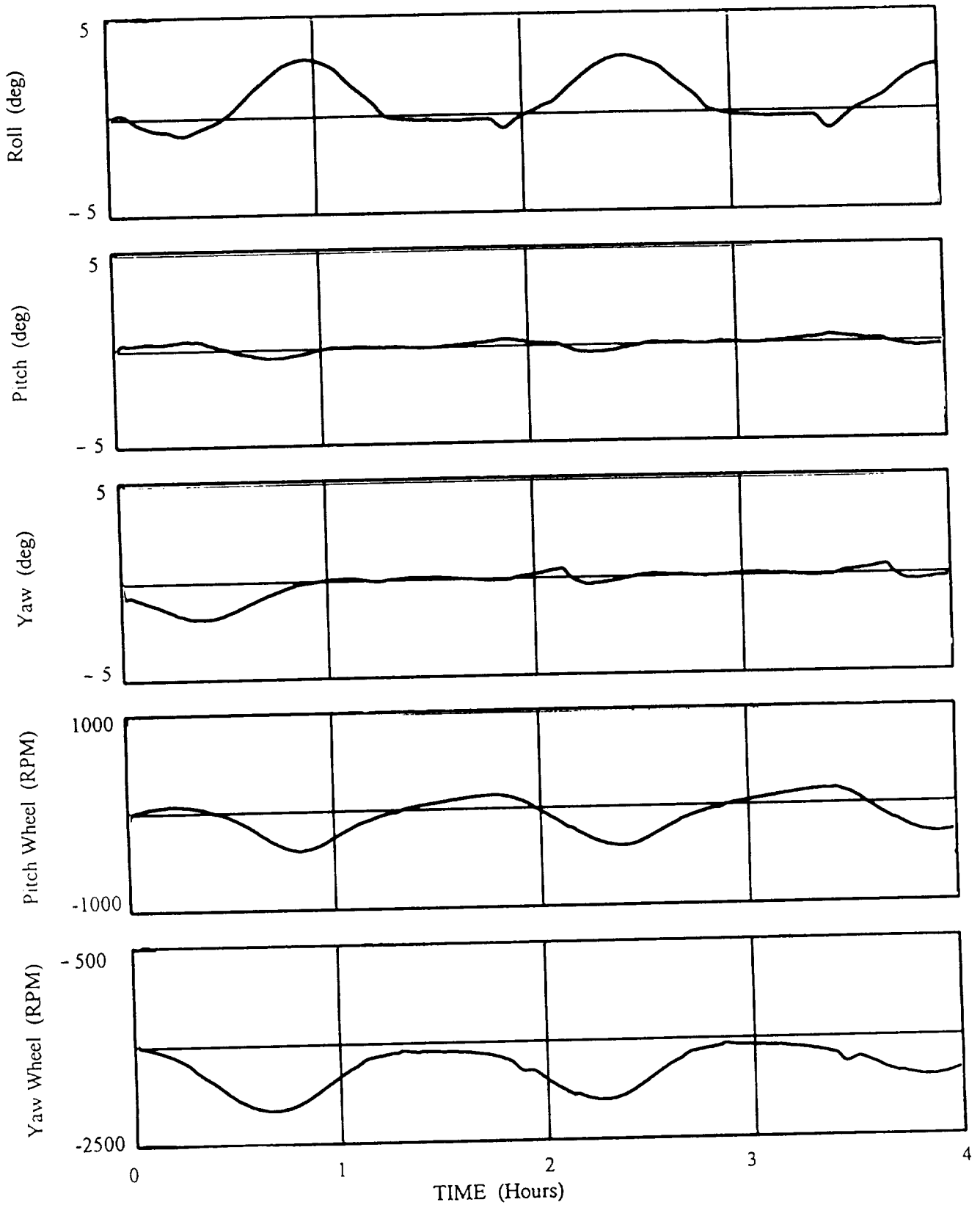
Simulation Series 5



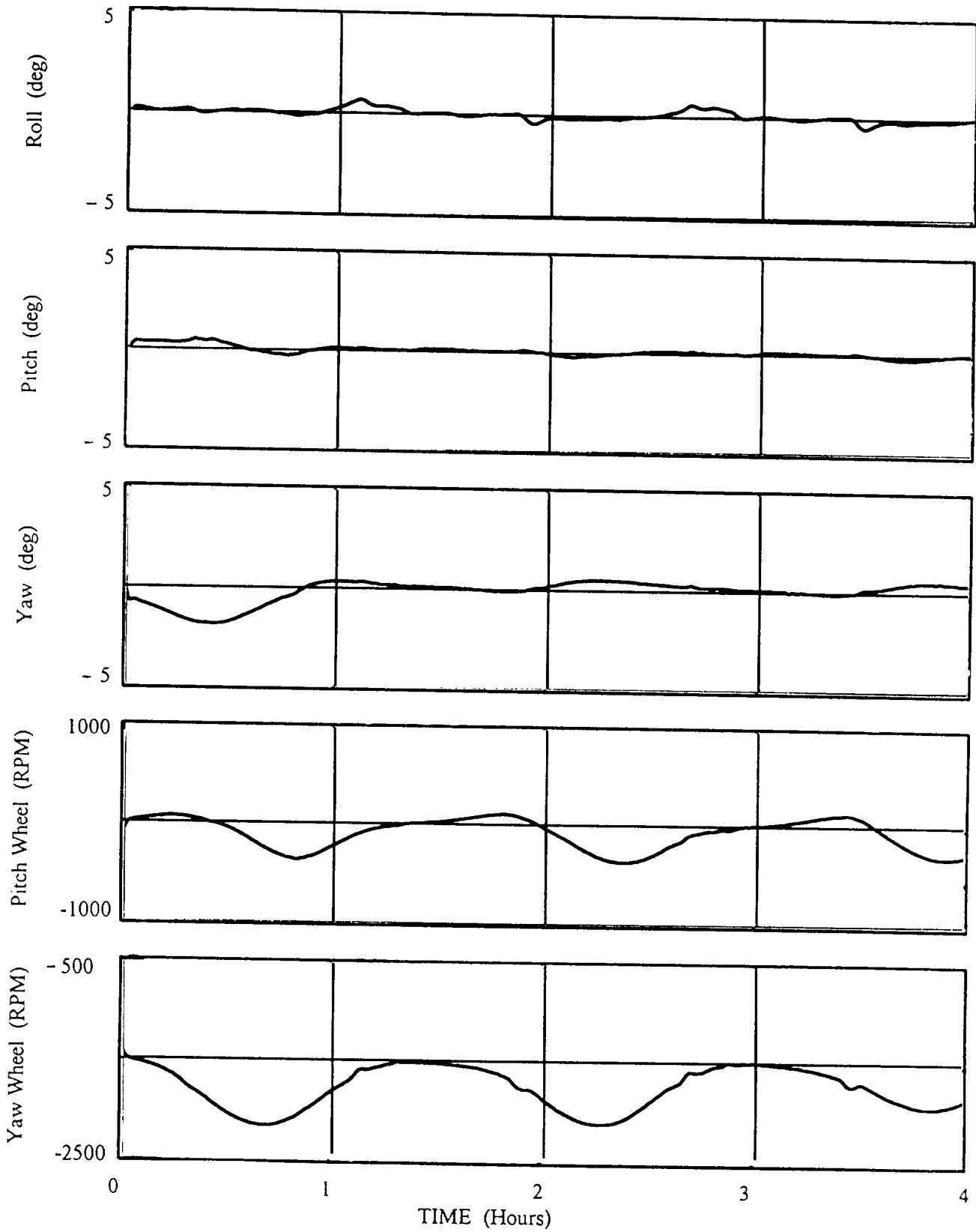
Simulation Series 6



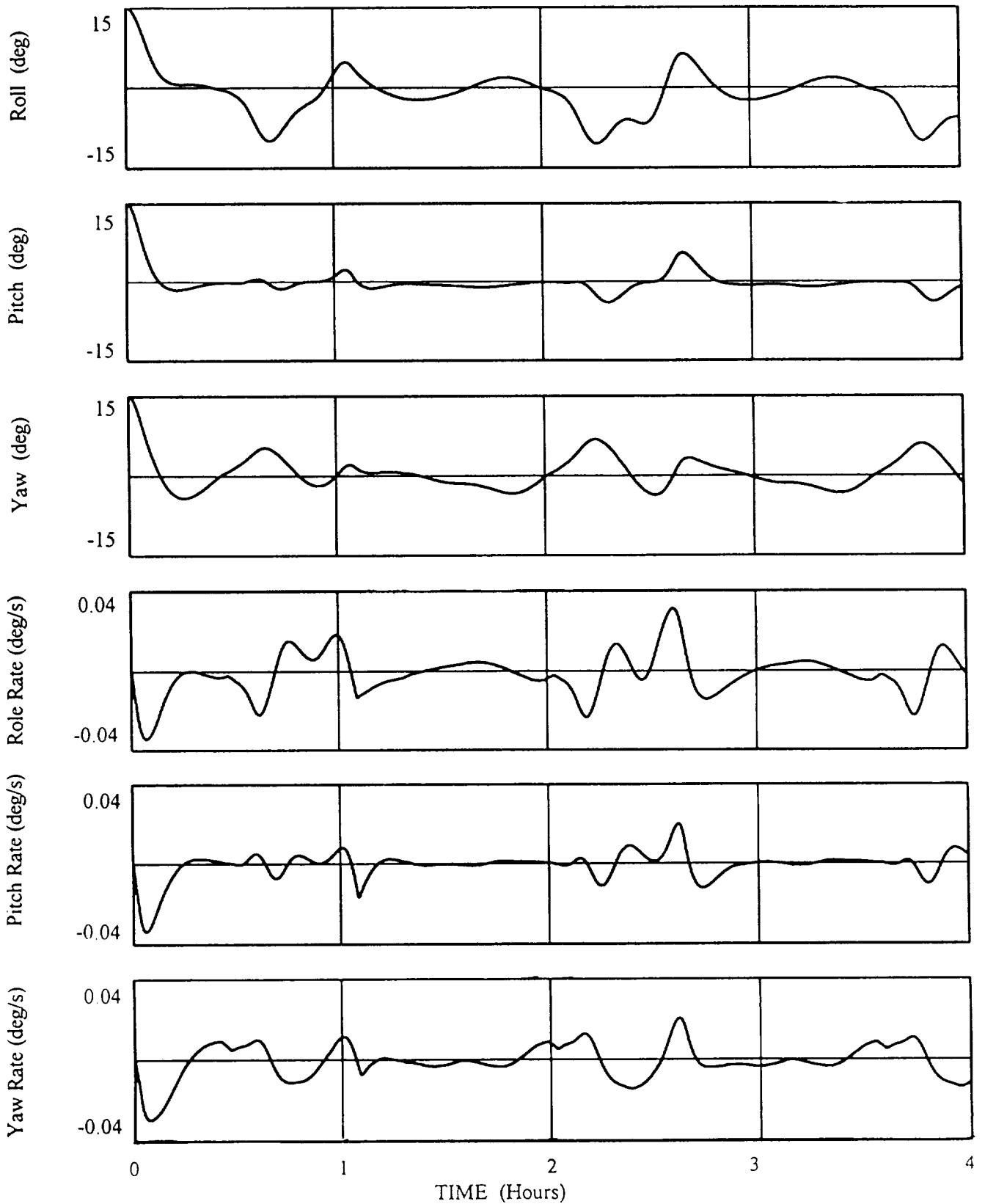
Simulation Series 7A



Simulation Series 7B



Simulation Series 8



FLIGHT MECHANICS/ESTIMATION THEORY SYMPOSIUM

MAY 17-19, 1994

SESSION 5

SELF-RESCUE STRATEGIES FOR EVA CREWMEMBERS EQUIPPED WITH THE SAFER BACKPACK

Trevor Williams¹ and David Baughman²

An extravehicular astronaut who becomes separated from a space station has three basic options available: grappling the station immediately by means of a "shepherd's crook" device; rescue by either a second crewmember flying an MMU or a robotic-controlled MMU; or self-rescue by means of a propulsive system. The first option requires very fast response by a tumbling astronaut; the second requires constant availability of an MMU, as well as a rendezvous procedure thousands of feet from the station. This paper will consider the third option, propulsive self-rescue.

In particular, the capabilities of the new Simplified Aid for EVA Rescue (SAFER) propulsive backpack, which is to be tested on STS-64 in September 1994, will be studied. This system possesses an attitude hold function, so can automatically detumble an astronaut after separation. On-orbit tests of candidate self-rescue systems have demonstrated the need for such a feature. SAFER has a total Δv capability of about 10 fps, to cover both rotations and translations, compared with a possible separation rate of 2.5 fps. But the Δv required for self-rescue is critically dependent on the delay before return can be initiated, as a consequence of orbital effects. A very important practical question is then whether the total Δv of SAFER is adequate to perform self-rescue for worst case values of separation speed, time to detumble and time for the astronaut to visually acquire the station.

This paper shows that SAFER does indeed have sufficient propellant to carry out self-rescue in all realistic separation cases, as well as in cases which are considerably more severe than anything likely to be encountered in practice. The return trajectories and total Δv s discussed are obtained by means of an "inertial line-of-sight targeting" scheme, derived in the paper, which allows orbital effects to be corrected for with only the visual information available to the pilot, namely the line-of-sight direction to the station relative to the stars.

INTRODUCTION

A space station which is in orbit for an extended period of time will require a great deal of Extra-Vehicular Activity (EVA) by astronauts for service and repair work. There is therefore a significant possibility that an EVA crewmember will at some point become separated from the station. Such a separation could occur, for instance, if a safety tether

¹ Associate Professor, Department of Aerospace Engineering, University of Cincinnati, Cincinnati, Ohio 45221. Phone: (513) 556-3221; e-mail: twilliam@uceng.uc.edu. Senior Member, AIAA and AAS.

² Acoustics and Vibration Associate Engineer, General Dynamics Electric Boat Division, 75 Eastern Point Road, Groton, Connecticut. Phone: (203) 433-1696. Member, AIAA.

broke or were not fastened correctly. Examination of data from the Weightless Environment Training Facility (WETF) at NASA Johnson Space Center suggests¹ that this may be expected to occur about once every 1,000 EVA hours. Unfortunately, unlike the Space Shuttle Orbiter, a station is not a maneuverable spacecraft. It therefore cannot chase and recover a drifting astronaut. Also, even if an Orbiter or Soyuz spacecraft were docked to the station when a separation occurred, the long lead time required for undocking and backing away from the station would make these vehicles unsuitable for EVA rescue. Some other rescue technique is therefore required.

The various types of system studied to date for EVA rescue can be summarized as follows. The first possibility is to have the separated crewmember rescued by another astronaut flying the Manned Maneuvering Unit (MMU)². However, this requires constant availability of both the MMU and the second crewmember, as the reaction time of such a system is critical. Even allowing only 10 minutes for the second astronaut to reach, ingress, checkout and launch the MMU, rendezvous with the drifting crewmember occurs³ thousands of feet from the station. At these distances, orbital effects play an important role, making it necessary to use a closed-loop rendezvous targeting scheme⁴ if rescue is to be achieved without exhausting MMU propellant. This would likely require the addition of hardware, for instance ranging equipment or a Global Positioning System (GPS) receiver, to the MMU. The EVA Retriever⁵, a proposed robotic-controlled MMU, would allow the initial reaction time to be reduced; however, this vehicle would be expensive to develop, and so is not likely to be available for near-term space station applications.

The other available alternatives all involve some form of *self-rescue* of the drifting astronaut. The simplest type of approach makes use of a "shepherd's crook" to allow the crewmember to grapple the station. Four examples of this type of system were flown, but not actually tested, on the STS-49 mission in 1992^{6,7}. These devices, which are typically 12 - 20 feet long when fully deployed, would be useful in cases where the initial separation velocity and tumble rates are comparatively low. However, there are many credible separation scenarios where this will not be the case⁸. For these cases, it is necessary to consider propulsive self-rescue systems. The simplest such system is a Hand-Held Maneuvering Unit (HHMU), or "gas gun", of the type flown on Gemini⁹, Skylab^{2,10}, and on STS-49 as the Crew Propulsive Device (CPD)⁷. These work adequately for short translations. However, a major difficulty for the self-rescue application is that they require the crewmember to visually determine his tumble rates about all three axes, and then position the HHMU in such a way as to null these rates. This would be likely to prove very challenging in practice, given the limited visual cues available to a crewmember tumbling away from the station, possibly at night. For this reason, one of the recommendations that followed from the CPD on-orbit test was⁷ that any self-rescue device provide an automatic detumble function.

The Simplified Aid for EVA Rescue (SAFER) backpack¹¹⁻¹³, to be flown on STS-64 in September 1994, is planned to satisfy this requirement. This system, essentially a minimized derivative of the MMU, provides full six degree-of-freedom control by means of a set of 24 cold-gas thrusters. It also possesses an automatic attitude hold function, so allowing detumbling to be achieved automatically, and provides a total Δv of 10 - 12 fps. Self-rescue strategies based on the capabilities of this system are the subject of this paper. These make use of an "inertial line-of-sight targeting" scheme which does not require that either range or range rate data be accessible to the pilot. Instead, only the visual cues that are readily available to the astronaut, namely the motion of the line-of-sight to the target relative to the stars, are required. Both realistic separation cases, which may actually occur in practice, and more extreme cases will be examined. The extreme cases, with either quite

high initial Δv s or long delay times until return can be initiated, serve to clarify the boundaries of the performance envelope of SAFER-equipped self-rescue. This study will show that all credible separation cases, and many extreme ones, are easily within the capabilities of SAFER.

EVA SELF-RESCUE DETAILS

Analysis carried out early in the Space Station Freedom program suggested that it would be possible for an EVA crewmember to separate from the station at rates of up to 3.5 fps. However, considerable uncertainty existed in this value; furthermore, estimates of the associated tumble rates were difficult to derive analytically. For these reasons, a series of tests were carried out on the Precision Air-Bearing Floor (PABF) at NASA Johnson, as well as in the KC-135 aircraft while flying zero-gravity parabolas⁸. Various types of possible separation scenarios were tested with four test subjects of differing sizes. Based on input from a test subject astronaut with EVA experience, the following two of these scenarios were deemed to be the most representative of possible actual on-orbit separations:

one-arm moderate push-off, simulating a translational maneuver carried out untethered;

breakaway, simulating the failure of a tether, or an article to which the astronaut is tethered, while under tension.

The separation speeds and tumble rates obtained in these tests varied considerably from individual to individual, and indeed from run to run for each individual. Taking all results together, the following values appear to be reasonable upper limits for use in practice:

Separation speed: 2.5 fps;
Pitch rate: 55 deg/s;
Roll and yaw rates: 20 deg/s.

It should be noted that these limits are somewhat conservative, in that a separation that yields a high linear velocity may well only produce low angular rates, and *vice versa*. The test case currently being used in Space Station self-rescue studies at NASA Johnson, namely a speed of 2.0 fps and angular rates of 30 deg/s about all three axes, is in line with this observation.

For comparatively benign separations (velocity less than 1.0 fps; total tumble rate less than 10 deg/s), some form of "shepherd's crook" may suffice to perform a self-rescue by grappling the station. Four versions of this basic type of system were flown on STS-49 in May 1992 as part of the Crew Self-Rescue (CSR) flight experiment⁷: these were the Inflatable Pole (IP), the Bi-Stem Pole (BP), the Telescopic Pole (TP), and the Astro-rope (AR). The ranges of these devices were between 12 and 20 feet. The first three involved poles which were extended by nitrogen pressure (IP), an EVA power tool (BP) and manually (TP); all three could be fitted with an end effector designed to grapple a handrail or strut. The AR consisted of two cleat-like end effectors at the end of a Kevlar cord; this was intended to be thrown bola-fashion. Unfortunately, none of these devices were able to be tested on STS-49: the Intelsat capture and repair took three EVAs rather than the planned one, leaving less time than planned for CSR tests. However, it is clear from ground studies and tests that none of these devices is an adequate solution for crew self-rescue in all credible separation cases: they are too bulky when stowed, would be difficult for a tumbling astronaut to aim, and are not guaranteed to successfully grapple the station in the

brief time available. Consequently, some form of propulsive system seems necessary to completely satisfy the requirement for self-rescue.

One such system was flown, and actually tested, on STS-49 as part of the CSR experiment. This is the Crew Propulsive Device, a redesign of the Gemini Hand-Held Maneuvering Unit. The HHMU is a pistol-like device which can provide positive or negative thrust directed along a single line. In principle, the crewmember can produce pure translational commands by holding the HHMU so that it thrusts through his center of mass. Attitude control is obtained by offsetting the thrust axis so as to produce the desired torque; unfortunately, translational inputs also inevitably result from the non-zero applied force. An HHMU was tested⁹ during the first U.S. EVA, on the Gemini 4 mission, and a more capable unit flown on Gemini 10. This was found² to be adequate for short, straight-ahead translations where precise control was not required. However, it demanded a high level of crewmember concentration, as well as physical exertion due to the resistance of the pressure suit arm to bending. Similar conclusions were drawn as a result of the HHMU tests carried out inside the large Skylab workshop as a part of the M509 experiment¹⁰, as well as after the tests of the CPD^{7,14}.

One of the main conclusions reached after the CSR tests⁷ was that any self-rescue system should provide an automatic detumbling facility. The crewmember who tested the CPD felt that it was quite challenging to correctly identify multi-axis tumbles purely by eye. In fact, he estimated that he was only correct about half the time, despite being in the Orbiter payload bay with its rich visual cues. This identification problem would be considerably worse for a drifting astronaut, especially at night. An HHMU-based system with automatic detumbling was described and studied in¹⁶: this had an HHMU for translation, and a system of dedicated attitude jets and rate gyros for detumble built into the upper backpack of the proposed advanced Space Station suit. However, this is quite a complicated hybrid system, and still suffers from the extensive cross-coupling problems and high pilot workload of any HHMU. A much better approach appears to be to use a propulsive backpack such as SAFER. The background to this new system is the subject of the next section.

SAFER BACKGROUND AND DESCRIPTION

A propulsive backpack makes use of a set of fixed thrusters to provide the EVA astronaut with independent attitude and translational control, typically about all six axes simultaneously. Pilot workload is consequently greatly reduced; it is reduced even further if an attitude hold feature is provided. The Gemini Astronaut Maneuvering Unit (AMU) was the first example of a space-qualified backpack: this was carried on Gemini 9, but problems encountered when the pilot attempted to don the AMU prevented it from being tested⁹. The first on-orbit tests of an AMU vehicle were then carried out during Skylab, as part of the M509 experiment¹⁰. As was the case for the HHMU, these tests were conducted inside the Skylab workshop. The Skylab AMU proved to be very successful, and led directly to the development of the Space Shuttle MMU¹⁵. It was this vehicle that performed the first ever self-propelled untethered EVA, as a part of the STS-41B mission in early 1984. On two subsequent shuttle flights that same year, the MMU was used to participate in the Solar Maximum Mission spacecraft repair and to capture the Palapa B-2 and Westar-VI communications satellites for their return to Earth.

Although the MMU is an extremely versatile spacecraft, it is too bulky and expensive to be carried on all shuttle flights. There is therefore a need for a propulsive system which is small enough to be flown on every mission, and which is adequate for performing

inspection or repair EVAs to otherwise inaccessible external surfaces of the Orbiter. Ideally, it would provide an attitude hold capability, in order to facilitate work in areas without handholds. This system would also be extremely desirable for the space station self-rescue requirement.

SAFER¹¹, shown shaded in Figure 1, is designed to satisfy both shuttle and station EVA requirements. It is a small, lightweight system which attaches to the underside of the standard Primary Life Support Subsystem (PLSS) backpack. It provides full six-axis control, as well as attitude hold, by means of a set of 0.8 lbf cold-gas nitrogen thrusters. Total Δv is at least 12 fps after the initial ground charge of the tanks, and at least 10 fps after subsequent on-orbit recharges. SAFER can be stored in the Orbiter middeck or airlock on a routine basis, then donned if needed for a contingency EVA. This type of operation is scheduled to be first tested on the STS-64 mission in September of this year. It is also envisioned that SAFER will be worn by all crewmembers on station EVAs.

Note that SAFER uses, for compactness, a single modified Apollo translational hand controller, together with a translation/rotation mode switch, to command all six degrees-of-freedom. On the station production version, this hand controller will be stowed in the side of the main SAFER compartment during normal EVA operations. In the event of separation from the station, automatic attitude hold is immediately engaged once the crewmember unstows the hand controller. Thus, the only delay before detumble of the astronaut is begun is the time that is required for him to free his hand of any equipment he may be carrying and reach the hand controller. This has the very desirable consequence of reducing the self-rescue reaction time as much as possible.

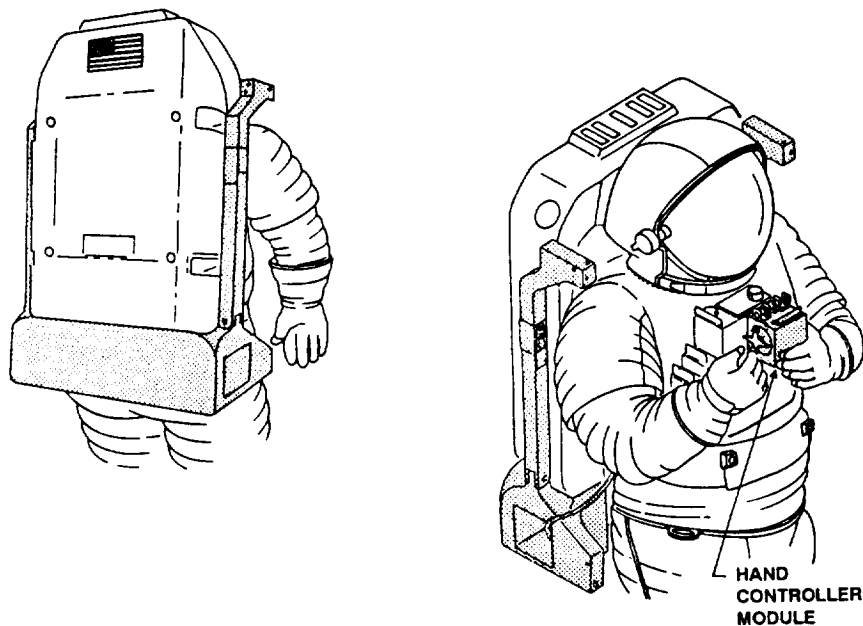


Figure 1 SAFER General View

ORBITAL DYNAMICS OF SELF-RESCUE

The motion of an object relative to another in a nearby circular reference orbit of angular rate ω is described by Hill's equations¹⁷. In the Local Vertical/Local Horizontal (LVLH) coordinate system that is normally used to describe on-orbit proximity operations, these become

$$\begin{aligned}\ddot{x} &= 2\omega\dot{z}, \\ \ddot{y} &= -\omega^2 y, \\ \ddot{z} &= 3\omega^2 z - 2\omega\dot{x},\end{aligned}\tag{1}$$

where the x -axis is directed along the velocity vector (or VBAR) of the reference body, the z -axis along the negative local vertical (or RBAR), and the y -axis along the orbit normal. Note that the equation in y is decoupled from those in x and z ; it represents simple harmonic motion out of the orbital plane. These equations have closed-form solutions, known as the Clohessy-Wiltshire (CW) equations¹⁸, which can be used to determine in a straightforward way the motion that results from an initial known velocity. These expressions are

$$\begin{aligned}x(t) &= \{-2\dot{z}_0 \cos \omega t + (4\dot{x}_0 - 6\omega z_0) \sin \omega t - (3\dot{x}_0 - 6\omega z_0) \omega t + (2\dot{z}_0 + \omega x_0)\} / \omega, \\ y(t) &= \{\omega y_0 \cos \omega t + \dot{y}_0 \sin \omega t\} / \omega, \\ z(t) &= \{(2\dot{x}_0 - 3\omega z_0) \cos \omega t + \dot{z}_0 \sin \omega t - (2\dot{x}_0 - 4\omega z_0)\} / \omega,\end{aligned}\tag{2}$$

where $\{x_0, y_0, z_0\}$ and $\{\dot{x}_0, \dot{y}_0, \dot{z}_0\}$ are the initial relative position and velocity of the body, respectively. Eq. (2) can of course be differentiated to give equally simple closed-form velocity expressions. The CW equations also lead to closed-form expressions for the magnitude and direction of the initial velocity required to transfer from a given position to a desired one in a specified time. This property makes them extremely useful in the terminal approach phase of the rendezvous problem. (See, for instance, ⁴ for details.)

The CW equations form the basis for a preliminary study of the self-rescue problem. First, Eq. (2) can be used to compute the position of an astronaut, who separated from the station with known initial velocity, after some drift time t_d . The net velocity required to return after some additional return time t_r can then also be found. Hence, as the velocity at the end of drift period is known from differentiating Eq. (2), the magnitude and direction of the burn required to initiate return can be found by subtracting these two velocities. While such a scheme is not usable in practice, as the EVA crewmember knows neither his velocity nor his position with great precision, it will serve to illustrate some important trends in the self-rescue problem. These will now be described, with special emphasis given to the in-plane motion. Out-of-plane behavior, being decoupled and sinusoidal, is quite simple to analyze separately and adds nothing of substance to what follows.

The first point to be made is the critical importance of initiating return as soon as possible. Consider the case of an astronaut who separates from the station (taken to be at an altitude of 185 n.mi.) at a rate of 3.0 fps in some arbitrary direction in the orbital plane, drifts while getting ready to maneuver back, and then applies an impulse derived from CW targeting. Figure 2 shows the dependence of the total Δv on both the drift and return times for the worst-case departure direction. It can be seen that total Δv increases extremely rapidly with increasing drift time. By contrast, increasing the return time reduces Δv

slowly; note the different scales on the two axes. Thus, it is very important to keep the drift time as short as possible; return time can be extended somewhat if Δv must be reduced modestly. (Note that, in this example, the total Δv included both the burn to initiate return and a final braking burn to null approach rates. In practice, the braking burn could be deleted if necessary.)

The second point that follows from a CW analysis of self-rescue is that, if drift and return times are long enough, a simple burn directly back towards the station no longer gives a successful return trajectory. This can be seen from Figures 3 and 4 for a separation rate of 3.0 fps, a drift time of 5 min and a return time of 10 min. The solid curve in Figure 3 shows the offset between the line-of-sight (LOS) to the station and the direction along which the Δv should be applied as a function of departure angle (measured counter-clockwise from VBAR); the dashed curve gives the magnitude of the burn. The trajectories in Figure 4 then are as follows: outbound (solid); return after correct CW burn (dashed); return after a burn of the correct CW magnitude, but directed along the LOS (dash-dot). It can be seen that a pointing error in the return burn of only about 6 deg leads, in this case, to miss distances of about 200 ft.

It should be noted that the initial velocity, drift time and return time are all somewhat unrealistically high in this example, so as to more clearly illustrate the effects of orbital mechanics. However, it does serve to highlight a practical difficulty. On the one hand, a separated astronaut cannot implement a CW rendezvous scheme, as he has neither precise position and velocity information nor the computing capability required. On the other hand, if he fires directly along the LOS, he may miss the station altogether. Fortunately though, looking at the trajectories of Figure 4 in a "pseudo-inertial" coordinate system, i.e. one that has its origin fixed on the station but does not rotate to follow the LVLH frame, suggests quite a straightforward solution. In these coordinates (Figure 5), the outbound and desirable CW return trajectories can be seen to follow approximately straight paths. Therefore, a maneuver technique which produces nearly straight trajectories in these non-rotating coordinates and makes use only of the limited visual cues available to the astronaut, namely the LOS direction to the station, should lead to a good practical solution to the self-rescue problem.

The following "inertial LOS targeting" scheme satisfies these requirements. Beginning at the end of the drift phase, it proceeds as follows:

- (1) Apply a Δv perpendicular to the LOS to (approximately) null any rotation of this line in inertial coordinates, i.e. relative to the stars.
- (2) Apply a Δv along the LOS sufficient to set up a closing rate which will give recontact after roughly the desired return time.
- (3) At periodic intervals (taken here as every 30 sec), the pilot checks the position of the station relative to the stars. If the inertial LOS direction has shifted by more than some deadband (taken here as 0.5 deg, the diameter of the Moon), a small Δv is applied perpendicular to the LOS and in the same direction as the shift. The magnitude of these corrective burns is taken here as 0.1 fps, which corresponds¹¹ to 0.5 sec of SAFER thrusting.
- (4) (Optional) Apply a final braking burn along the LOS to reduce the final contact speed.

This scheme sacrifices some efficiency for the sake of feasibility. For instance, combining the two burns in steps (1) and (2) into a single one would lead to a reduced total

Δv . However, it would also make it harder for the astronaut to determine the correct direction along which to fire. Simulation studies to date suggest that inertial LOS targeting typically requires about 10 - 20% more propellant than would CW targeting. This modest increase seems well worthwhile, given the greatly improved robustness properties of the new scheme that result from its man-in-the-loop feedback. (A similar point was made in ¹⁹ concerning the sensitivity of Lambert rendezvous targeting.) As a final comment on efficiency, it should be noted that the parameters of the LOS scheme, i.e. interval length, deadband and transverse Δv magnitude, were all selected, after extensive simulation studies, so as to reduce the total Δv as much as possible while still ensuring recontact with the station.

SELF-RESCUE USING SAFER

The example in the previous section used a relatively large separation rate and drift and return times, in order to better illustrate orbital effects. More realistic values for these quantities will now be used, so as to demonstrate the most challenging return cases that may reasonably be expected to occur in practice.

The sequence of events involved in using SAFER for self-rescue is as follows:

- (a) Astronaut frees right hand (if initially carrying equipment or tools) and unstows the hand controller. This automatically initiates SAFER automatic attitude hold (AAH), so beginning the detumbling phase.
- (b) Once detumbling is complete, astronaut performs a visual search for the station.
- (c) Astronaut carries out the inertial LOS targeting scheme described above.

The worst-case delays and Δv requirements for each of these stages can be found from the characteristics of SAFER and those of the self-rescue problem. On the basis of discussions with EVA personnel, a delay of 30 sec appears to be the longest that may be expected for step (a); this phase of course requires no Δv . For single-axis rotations, SAFER has angular acceleration magnitudes²⁰ of approximately 4.25 deg/s² in pitch, 4.5 deg/s² in roll and 9.8 deg/s² in yaw; each second of such thrusting consumes propellant equivalent to a linear Δv of 0.1 fps. Consequently, nulling the worst expected tumbling rates (55 deg/s in pitch; 20 deg/s in each of roll and yaw) should take no more than about 19 sec and equate to a Δv of 1.9 fps.

A visual search pattern for step (b) that appears reasonable, again after discussions with EVA personnel, is to first perform a yaw scan at 20 deg/s. In the worst case, the station may be either directly above or directly below the crewmember, so this scan will not bring it into view. In that case, the yaw scan is halted after covering 360 deg and a pitch scan, again at 20 deg/s, is initiated instead. The field-of-view of the EVA helmet is large enough that these two scans should guarantee that the station will be visually acquired. In the worst case, this acquisition will occur near the end of the pitch scan.

Taking these considerations into account, the worst-case delay time to be expected in practice is as given below. Also listed is the propellant consumption required for the various "non-translational" maneuvers involved.

	Time (s)	Δv (fps)
<i>Initial delay before activating AAH:</i>	30	0.0
<i>Stabilizing attitude using AAH:</i>	20	1.9
<i>Search pattern to find station:</i>	50	1.2
<i>Attitude control during return:</i>	--	0.5
<i>Sub-total:</i>	100	3.6

Thus, a total delay time of 2 min appears to be a conservative worst-case value. (Of the numbers tabulated above, the only one for which significant uncertainty exists is the allocation of 0.5 fps for attitude control during the return cruise. This appears to be a reasonable value, but is subject to further analysis.)

Figure 6 shows the trajectories that result, in rotating LVLH coordinates, for an initial separation rate of 2.5 fps, a delay time of 2 min and a time for the return leg of 5 min. The solid curves are the outbound trajectories, and the dash-dot ones the returns obtained using the inertial LOS targeting scheme described previously. For completeness, departure angles ranging from 0 to 315 deg, in steps of 45 deg, are shown. Figure 7 gives the same trajectories in non-rotating coordinates, showing how close to straight both outbound and return trajectories are. The minimum Δv required for return (with no final braking burn) for the various departure angles is 4.08 fps and the maximum 4.16 fps, giving a grand total self-rescue Δv of about 7.7 - 7.8 fps. This is clearly easily within the capability (at least 10 fps) of SAFER. It is interesting to note that using a classical CW scheme would require a return Δv ranging between 3.44 and 3.63 fps for this example. Thus, the greatly enhanced feasibility of the new inertial LOS scheme was achieved with a performance penalty of only 15 - 19 %. Also, increasing the return time up to about 8 min or so modestly reduces the inertial LOS return Δv . Going beyond this time causes the Δv to increase again, as a result of the more numerous trajectory corrections required. This contrasts somewhat with the CW case, where increasing return time continues to reduce Δv (see Figure 2).

Two rather more extreme cases will now be considered. Although these should never actually be encountered in practice, they serve to quantify the performance reserves that SAFER possesses for self-rescue. In the first of these, the same 2.5 fps separation as above is assumed, but the delay is increased from 2 to 5 min and the return leg from 5 to 7 min. The resulting trajectories, in LVLH rotating coordinates, are given as Figure 8. Note that the inertial LOS targeting scheme achieves a successful return here despite the increased orbital effects introduced by the greater delay (compare the return trajectories in Figure 8 with those in Figure 4). The return Δv required in this case ranges between 4.98 and 5.49 fps, giving a grand total range of about 8.6 - 9.1 fps. This is still within the minimum specified capability of SAFER. (The performance penalty range of the inertial LOS scheme relative to CW targeting widened somewhat to 12 - 24 % in this example.)

Finally, Figure 9 shows the trajectories obtained for a drift time of 2 min, a return leg of 5 min, and a very high initial separation rate of 5 fps. Inertial LOS targeting again achieves successful returns in this case, with return leg Δv s now of between 6.38 and 6.16 fps; these are 7 to 16 % higher than the corresponding CW values. Once again, SAFER can be seen to be able to deal successfully with a rather extreme separation scenario.

CONCLUSIONS

This paper has studied the problem of self-rescue for an EVA crewmember who becomes separated from a non-maneuverable spacecraft such as a space station. As a first step, a discussion of plausible separation cases was given, yielding upper limits on expected separation speeds and tumble rates. The performance of the SAFER propulsive backpack was then described; of particular importance for self-rescue applications are its automatic detumble feature and its full six degree-of-freedom control. It was then noted that return to a space station after separation is complicated by the effects of orbital mechanics, as well as by the comparatively low Δv capability of SAFER. However, an "inertial line-of-sight targeting" scheme to accomplish this return was then described which requires only the visual cues that are readily available to the pilot, namely the motion of the line-of-sight to the station relative to the stars. This simple scheme was shown to allow successful return to the station with the Δv available using SAFER for all credible, and indeed some quite extreme, EVA separation cases.

ACKNOWLEDGMENTS

This work was motivated by discussions with Cliff Hess, Carl Meade, Calvin Seaman and the late C.E. Whitsett and Matt Hines, all of NASA Johnson Space Center, and Gary Slater of the University of Cincinnati.

REFERENCES

1. A.R. Brody, R. Jacoby and S.R. Ellis, "Man Overboard! What Next?", Paper IAA-91-584, International Astronautical Federation Congress, Montreal, Canada, October 5-11, 1991
2. C.E. Whitsett, "Role of the Manned Maneuvering Unit for the Space Station", SAE Paper 861012, 16th Intersociety Conference on Environmental Systems, San Diego, California, July 14-16, 1986
3. J.M. Neff and W.T. Fowler, "Minimum-Fuel Rescue Trajectories for the Extravehicular Excursion Unit", *Journal of the Astronautical Sciences*, Vol. 39, 1991, pp. 21-45
4. M.C. Jensen, J.M. Hines and C.M. Foale, "Man Overboard Rescue", *Simulation*, Vol. 57, 1991, pp. 39-47
5. G.J. Reuter, C.W. Hess, D.E. Rhoades, L.W. McFadin, K.J. Healey and J.D. Erickson, "An Intelligent, Free-Flying Robot", SPIE Symposium on Advances in Intelligent Robotic Systems, Space Station Automation IV, Cambridge, Massachusetts, November 6-11, 1988
6. K.R. Armstrong, R.K. Fullerton and S.A. Bleisath, "EVA Operational Enhancements and ASEM", SAE Paper 921341, 22nd International Conference on Environmental Systems, Seattle, Washington, July 13-16, 1992
7. *Final Report for the STS-49 Crew Self Rescue (CSR) Flight Experiment*, JSC-25762, NASA Johnson Space Center, August 1992
8. *EVA Crew Separation Dynamics Final Test Report*, CTSD-SS-278, Lockheed Engineering & Sciences Company, March 1989
9. *Summary of Gemini Extravehicular Activity*, NASA SP-149, 1967
10. C.E. Whitsett and B. McCandless II, "Skylab Experiment M509: Astronaut Maneuvering Equipment Orbital Test Results and Future Applications", AAS Paper AAS74-137, in *The Skylab Results (Advances in the Astronautical Sciences*, Vol. 31), Part 1, pp. 385-416

11. "SAFER Flight Test Project", NASA Johnson Space Center Automation and Robotics Division presentation, July 14, 1992
12. *Simplified Aid for EVA Rescue (SAFER) Training Manual*, JSC-26283, NASA Johnson Space Center, July 1993
13. T. Williams and D. Baughman, "Exploiting Orbital Effects for Short-Range Extravehicular Transfers", AAS Paper 93-181, in *Spaceflight Mechanics 1993 (Advances in the Astronautical Sciences, Vol. 82)*, Part II, pp. 1201-1214
14. *STS-49 EVA Operations and Training Report*, JSC-25995, NASA Johnson Space Center, April 1993
15. *Manned Maneuvering Unit Operational Data Book*, MMU-SE-17-73 Rev. B, Martin Marietta, July 1985
16. J.M. Neff and W.T. Fowler, "Six Degree-of-Freedom Simulation of an Astronaut Detumble System", *Journal of the Astronautical Sciences*, Vol. 39, 1991, pp. 3-20
17. M.H. Kaplan, *Modern Spacecraft Dynamics and Control*, John Wiley & Sons, New York, 1976
18. W.H. Clohessy and R.S. Wiltshire, "Terminal Guidance System for Satellite Rendezvous", *Journal of the Aerospace Sciences*, Vol. 27, 1960, pp. 653-658
19. B. Newman, "Robustness Evaluation of Classical vs Lambert-Based Midcourse Guidance for Exoatmospheric Intercepts", AAS Paper 94-167, AAS/AIAA Spaceflight Mechanics Meeting, Cocoa Beach, Florida, February 14-16, 1994
20. T. Williams, "On-Orbit Mass Properties Determination for the SAFER/Astronaut System", AAS Paper 94-187, AAS/AIAA Spaceflight Mechanics Meeting, Cocoa Beach, Florida, February 14-16, 1994

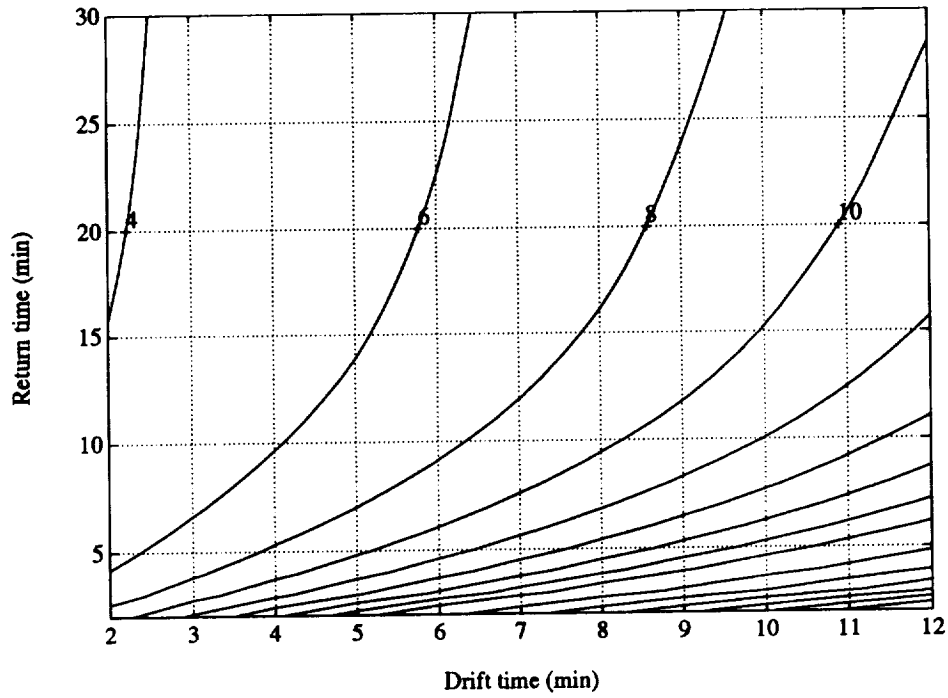


Figure 2 Worst Case Δv (fps) for Return Plus Braking

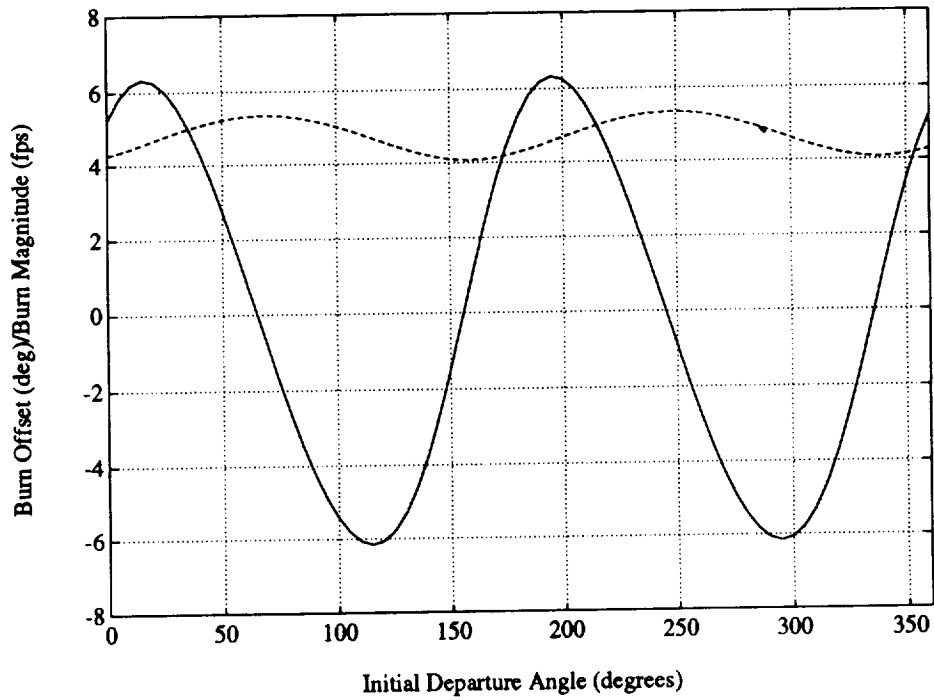


Figure 3 Direction and Magnitude of Return Δv

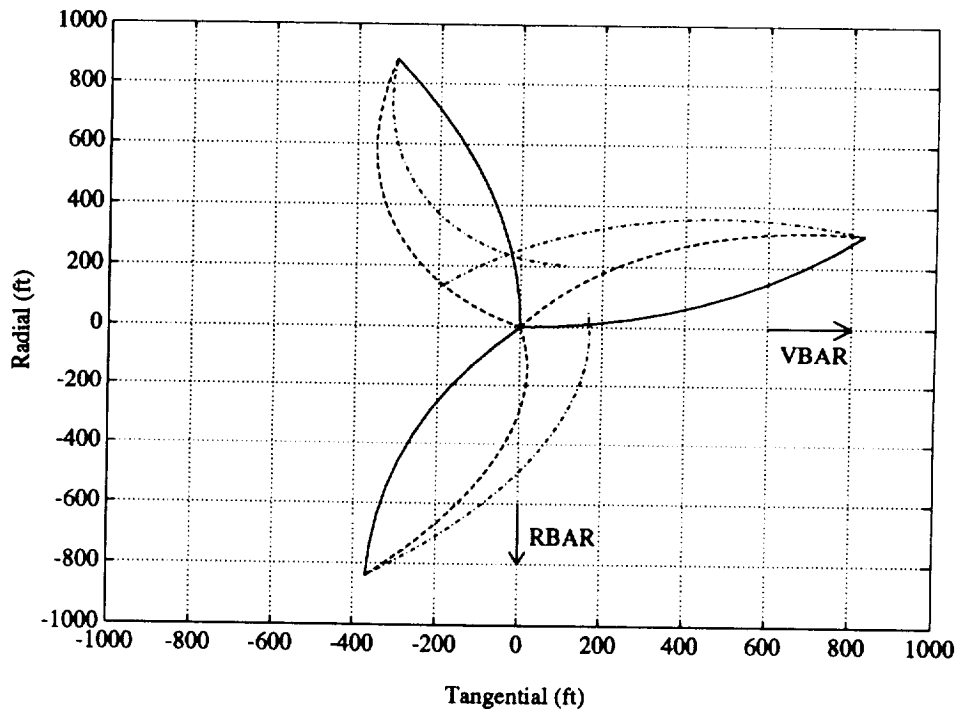


Figure 4 LVLH Outbound and Return Trajectories

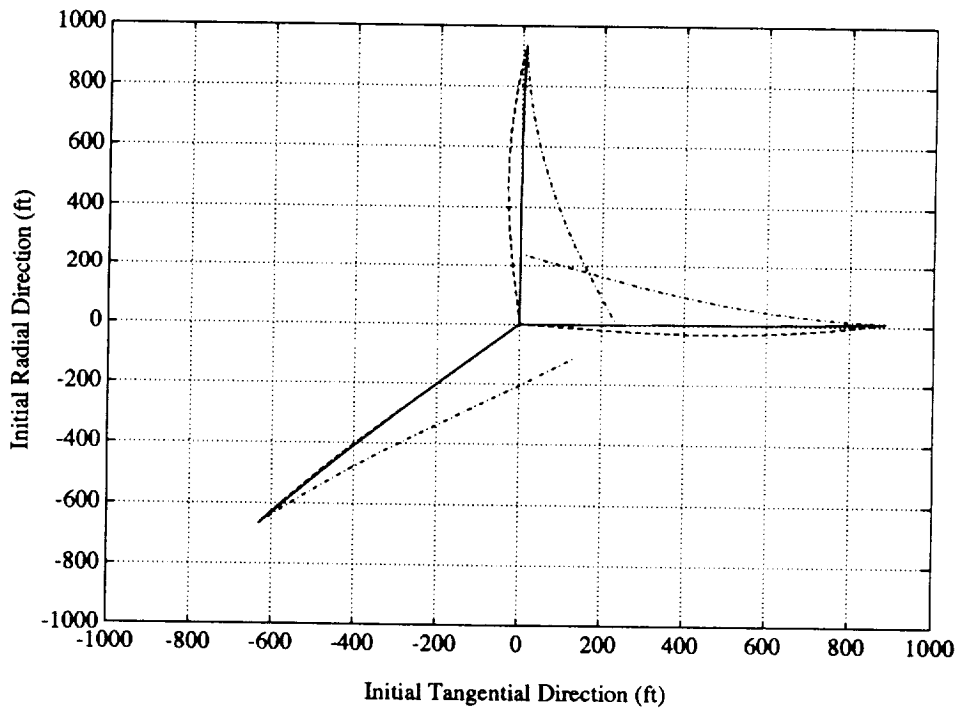


Figure 5 Trajectories in Non-Rotating Coordinates

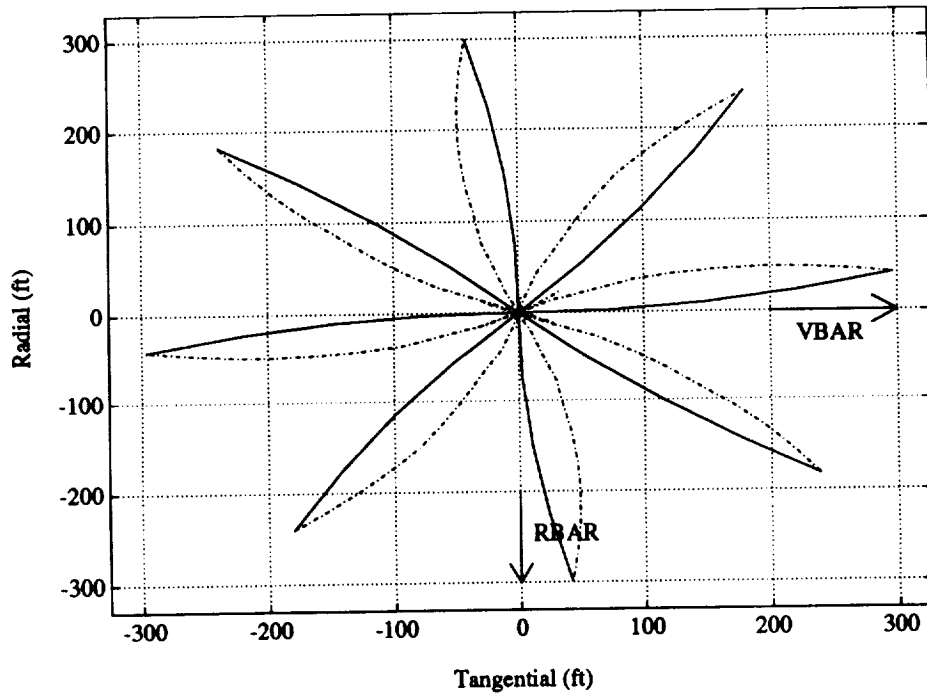


Figure 6 LVLH Trajectories, Worst Practical Case

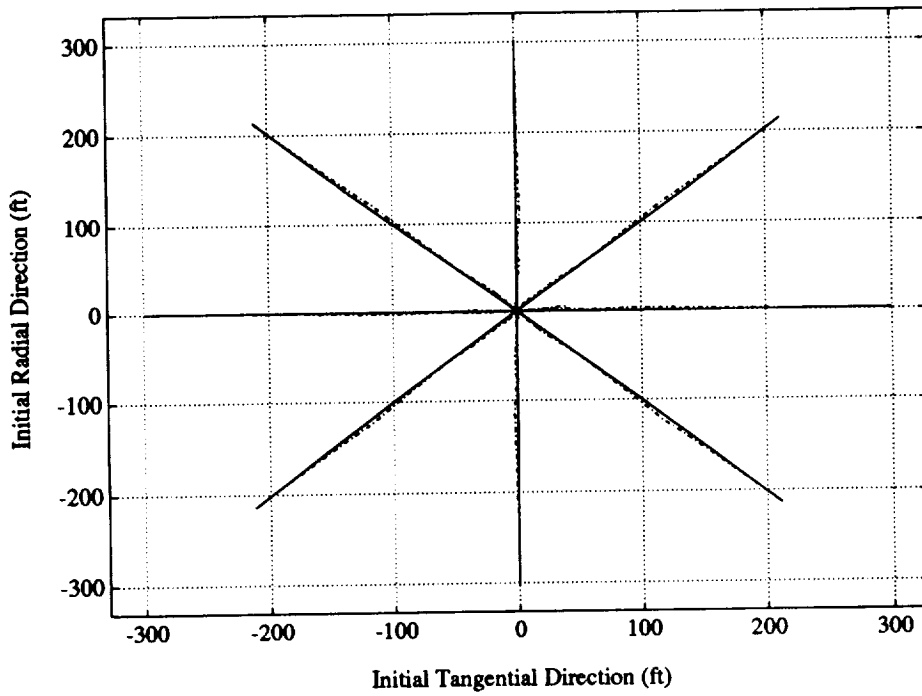


Figure 7 Trajectories in Non-Rotating Coordinates

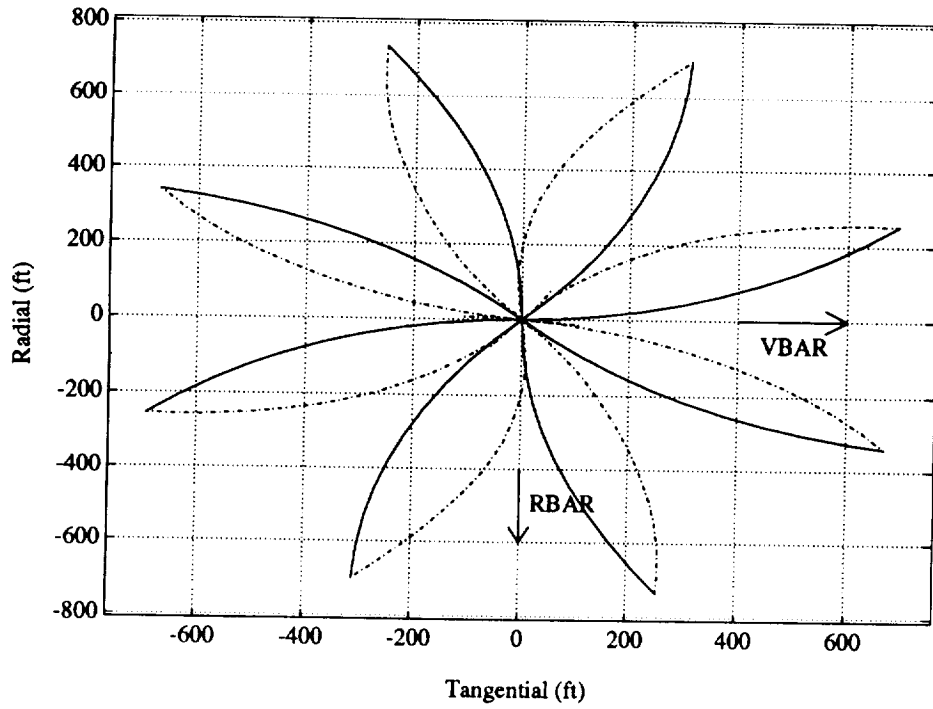


Figure 8 LVLH Trajectories, Long Delay Case

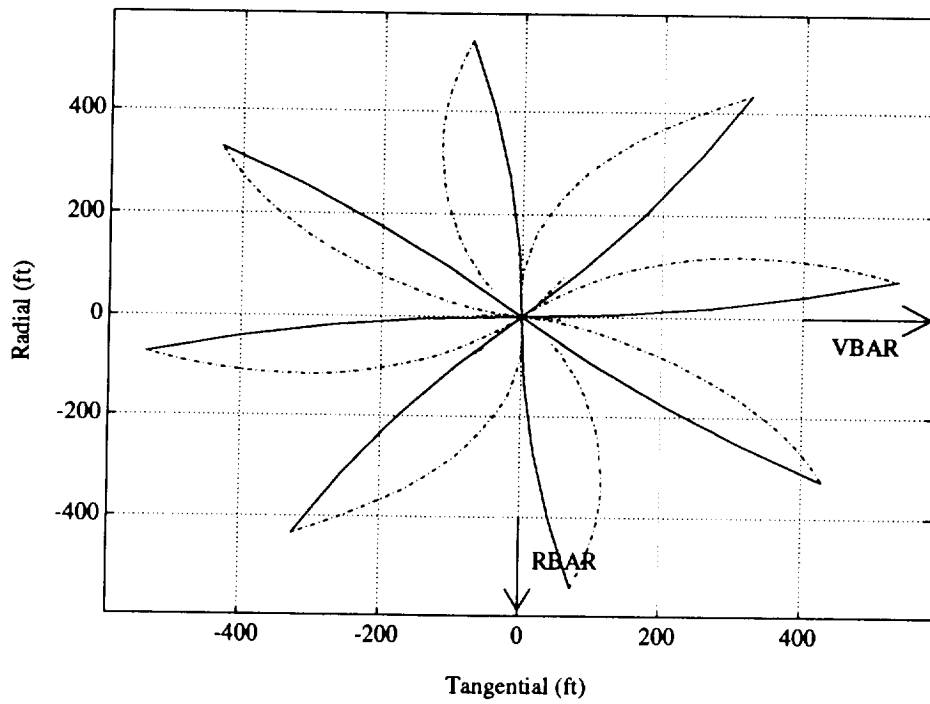


Figure 9 LVLH Trajectories, High Separation Rate Case

SPACE SHUTTLE ORBIT DETERMINATION
USING EMPIRICAL FORCE MODELING OF ATTITUDE MANEUVERS
FOR THE GERMAN MOMS-02/D2 MISSION

C. von Braun[†] and Ch. Reigber[‡]

In the spring of 1993, the MOMS-02 (Modular Optoelectronic Multispectral Scanner) camera, as part of the second German Spacelab mission aboard STS-55, successfully took digital threefold stereo images of the surface of the Earth. While the mission is experimental in nature, its primary goals are to produce high quality maps and three-dimensional digital terrain models of the Earth's surface. Considerable improvement in the quality of the terrain model can be attained if information about the position and attitude of the camera is included during the adjustment of the image data.

One of the primary sources of error in the Shuttle's position is due to the significant attitude maneuvers conducted during the course of the mission. Various arcs, using actual Tracking and Data Relay Satellite (TDRSS) Doppler data of STS-55, were processed to determine how effectively empirical force modeling could be used to solve for the radial, transverse and normal components of the orbit perturbations caused by these routine maneuvers. Results are presented in terms of overlap-orbit differences in the three components. Comparisons of these differences, before and after the maneuvers are estimated, show that the quality of an orbit can be greatly enhanced with this technique, even if several maneuvers are present. Finally, a discussion is made of some of the difficulties encountered with this approach, and some ideas for future studies are presented.

INTRODUCTION

During the course of the second German Spacelab mission flown aboard the U. S. Space Shuttle in the spring of 1993, the MOMS-02/D2 camera performed digital

[†] Technical Staff, MIT Lincoln Laboratory, Lexington, Massachusetts; formerly with the GeoForschungsZentrum Potsdam, c/o DLR, Oberpfaffenhofen, Germany

[‡] Director, Division I, GeoForschungsZentrum Potsdam, Potsdam, Germany

mapping of the Earth's surface. The special characteristics of the camera combine high resolution panchromatic images for three-dimensional geometric information with multispectral images for thematic information. This experimental project has been funded by the German Federal Minister for Research and Technology (BMFT) with the aim of producing high quality maps, acquiring digital data for geographic databases and information systems, and generating digital terrain models with an accuracy of 5 m or better. To attain these accuracies in the terrain models, estimates of the camera's position and attitude during its operation must be introduced into the least squares adjustment of the image data. While it is not the intent of this paper to discuss the operation of the camera or of the mathematical modeling of the relevant phenomena, excellent explanations of these aspects can be found in (Ref. 1) and (Ref. 2). It is, however, the goal of this work to discuss the process by which position estimates of the Shuttle were established, and how these estimates can be improved by employing empirical forces to estimate the effects of routine attitude maneuvers.

The paper will begin by briefly reviewing the basic features of the primary on-orbit tracking system used during Shuttle missions: the Tracking and Data Relay Satellite System (TDRSS). This will help establish some perspective on one of the difficulties in estimating attitude maneuvers. This is followed by a summary of some of the key results from simulations performed in an earlier work (Ref. 10) to determine an appropriate dynamical model to be used for the processing of arcs. Then, a fairly detailed discussion is made regarding the effects and estimation process of the significant attitude maneuvers, which occur throughout the mission. Finally, a presentation of the quality of each orbit and the degree to which it was improved by estimating maneuvers is given.

TRACKING SYSTEM

The launch and subsequent deployment of TDRS-A from STS-6 (Space Transportation System) in April, 1983 established the first of five near-geostationary satellites making up the current TDRS System. The system was established by the National Aeronautics and Space Administration (NASA) as its fundamental means for relaying tracking, telemetry, voice and image data between a user-satellite and the ground. Nominally, two TDRSS satellites provide near-global coverage; but, due to the existence of only one ground terminal in White Sands, New Mexico, the use of additional satellites does not enhance the coverage. These two satellites, located at longitudes of 41° and 171° W, are always in view of the ground terminal and provide a link with the user-spacecraft for over 85% of the orbit. Fig. 1 shows the zone of exclusion for typical TDRSS users.

The Space Shuttle is equipped with S- and Ku-Band antennas for sending and receiving information via the TDRSS link. While this link provides for various forms of communication, the only tracking observable is a two-way Doppler signal. Fig. 2 shows the basic geometry of the TDRSS-user configuration and of the Doppler signal. A detailed explanation of the construction of the signal can be found in (Ref. 10), or, if an in-depth understanding of the entire TDRS System is sought, in (Ref. 8).

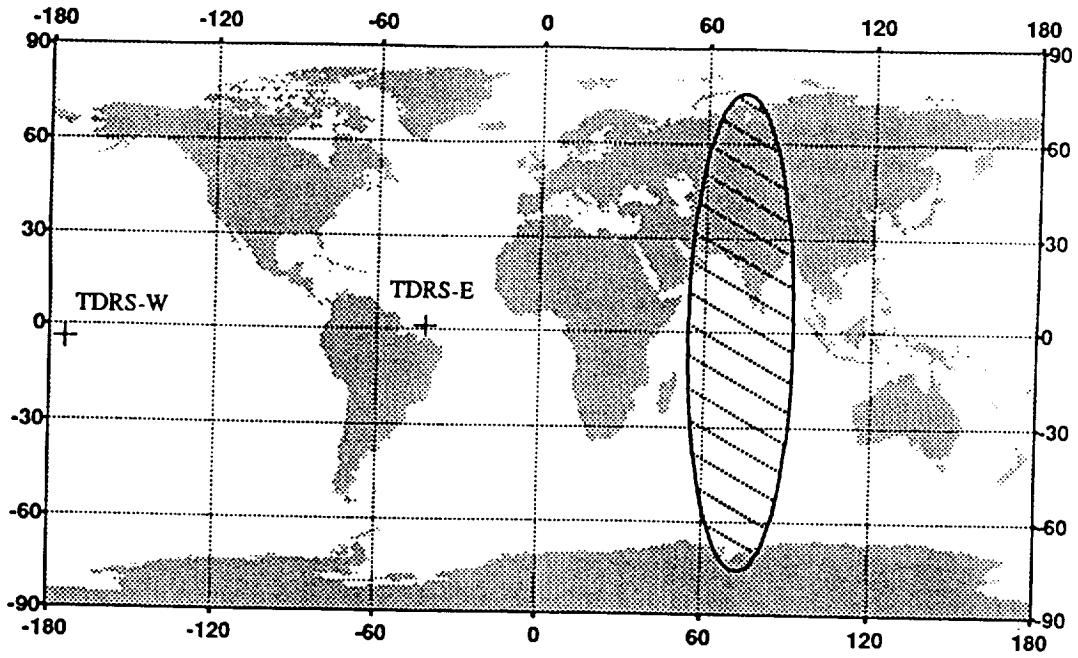


Fig. 1 Zone of Exclusion for TDRS Users (200 km Altitude)

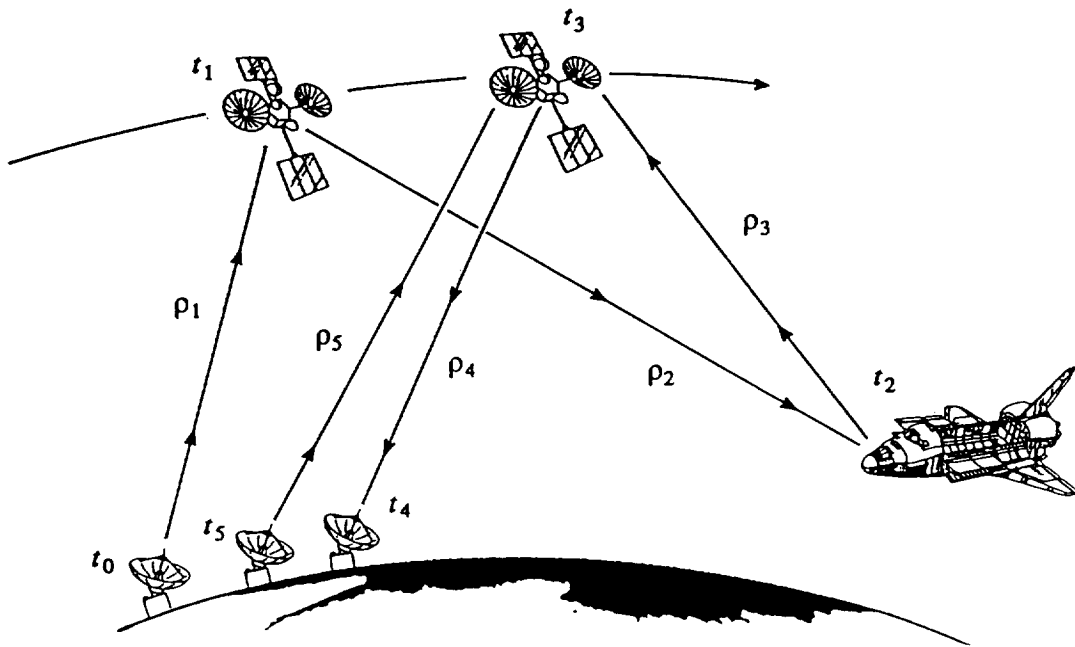


Fig. 2 TDRS-Shuttle Tracking Geometry

DYNAMICAL MODEL AND ORBIT PERTURBATIONS

One of the primary concerns in any analysis regarding orbit determination is to establish good mathematical models describing the response of the spacecraft to both natural and man-made forces. Any deficiencies in these models will be reflected in the comparison of the observed with the predicted behavior. Additionally, errors in the geometric and dynamic modeling of the observations, stochastic corruption of the signal and uncertainties in the model parameters will also degrade the quality of the orbit. The following sections briefly describe the dynamical force models used in this study, the degree to which these forces affect the motion of the Shuttle and the sources of any additional uncertainties in the model or observation type.

Dynamical Model

The forces which, in some reasonable way, affect the motion of the Shuttle can be separated into gravitational forces, surfaces forces and artificially-induced forces, such as maneuvers. Mathematically, the total force, F , can be expressed simply as

$$F = F_G + F_S + F_M + F_e \quad (1)$$

where F_G comprises the forces which are gravitational in nature, such as the Earth's solid-body gravitational field, variations in that field due to solid Earth and ocean tides, and luni-solar and planetary perturbations; F_S represents the forces which act on the surface of the Shuttle, such as those due to the atmospheric effects of drag and lift and that of solar radiation; F_M consists of forces arising from orbit and attitude maneuvers; and F_e encompasses all remaining forces, which are considered negligible in this study. Unlike the other forces, maneuvers do not occur continuously, but, clearly, only at selected times during the mission. While a detailed description of the mathematical modeling of each of these forces can be found in an earlier work (Ref. 10), a brief summary of the models and the degree to which the forces perturb the orbit will be given here, for the sake of clarity.

Perturbations due to the inhomogeneous mass distribution of the Earth are some of the most significant affecting the Shuttle orbit. The geopotential model used for the simulations and for the orbit determination of the Shuttle for the MOMS-02 mission is the JGM-1 (Joint Gravity Model) developed for use during the TOPEX/Poseidon mission. It has evolved from the GEM-T3 geopotential model (Ref. 5) and is one of the most complete developed to date, with harmonic coefficients up to degree and order 70.

The atmospheric effects of drag and lift also play a significant role on the behavior of the Shuttle. The model used in this investigation incorporates knowledge of the attitude of the Shuttle as a function of time and, thus, accounts for the variation of the surface area exposed to the relative wind. In this case, three primary surfaces, each oriented normal to one of the Shuttle body-fixed axes' unit vectors, were used. This technique was used to establish the effect of both drag and lift. The CIRA '86 (Ref. 4) model of the atmosphere, which relies on atmospheric data, solar flux values and indices of the geomagnetic activity, was the empirical model used to estimate the local density.

The remaining gravitational forces due to solid Earth and ocean tides, lunar, solar and planetary perturbations, and the surface force of solar radiation were shown to be below the levels of realistic Shuttle position determination (Ref. 10). Table 1, extracted from the same reference, shows the orbit perturbations on a 300 km Shuttle orbit over the course of three hours. In addition, the effect of the offset between the location of the Shuttle's S-Band antennas and its center of mass is given.

Table 1
 RADIAL, TRANSVERSE AND NORMAL (RMS) ORBIT PERTURBATIONS

MODEL	orbit perturbation (m) for 3 hour arc lengths		
	r	τ	η
Ocean Tides	0.02	0.05	0.07
Earth Tides	0.04	0.07	0.25
Solar Radiation	0.01	0.05	0.06
Luni-solar and Planetary	0.14	0.28	1.05
Geopotential (50x50)	0.56	1.70	1.06
Geopotential (36x36)	0.55	1.27	2.31
Geopotential (8x8)	14.73	19.50	20.32
Antenna Offsets	0.53	3.59	2.81
Drag (spherical model) LVLH; C_D not est.	33.78	79.90	82.34
Drag (spherical model) LVLH; C_D est.	0.09	0.15	0.13
Drag (spherical model) IH; C_D not est.	12.94	31.88	32.86
Drag (spherical model) IH; C_D est.	8.76	18.96	9.56

It should be noted for clarity that these results were established by fitting an arc to simulated TDRSS Doppler data, with any given effect removed. The arc was then differenced with an arc that had been fit to the same data, but with all possible effects modeled.

Unmodeled Error Sources

The previous section discussed the modeling and orbit perturbations of forces which could be classified as gravitational or surface-dependent in nature. While several of these effects contributed non-negligible perturbations to the orbit, additional forces and error sources can produce comparable uncertainties, if left unmodeled.

In the case of a satellite-to-satellite tracking system such as TDRSS, one primary concern is of the quality to which the positions of these satellites can be estimated. Although these uncertainties will be naturally scaled down by the ratio of the tracking

satellite's orbital radius to the user's orbital radius (Ref. 3), significant errors can still remain. It has been established that generated ephemerides of the TDRSS satellites, as performed at the Goddard Space Flight Center, possess errors of approximately 50 m (Ref. 9). Since the radii of TDRSS satellites are five to six times those of the Shuttle in low Earth orbit, these errors will manifest themselves as approximately 10 m errors in the position of the Shuttle. To incorporate these errors properly, it is necessary to perform a simultaneous solution for the positions of the TDRSS satellites and of the Shuttle, using a combination of TDRSS bilateration and Shuttle Doppler data. In this work, the TDRS positions were interpolated from an ephemeris in which data was available at 60 second intervals. It was assumed that there were no sources of error in the ephemeris.

Depending on the objective of any given mission, the Space Shuttle will perform fairly regular orbit and attitude adjustments. During the course of STS-55, two significant orbit burns or trim maneuvers were performed. Since these maneuvers tend to be so large that an arc is usually not fit directly through them, the modeling of their perturbations is not of primary concern. However, the same cannot be said for the attitude maneuvers. In most cases, their effect, or the effect of a series of routine maneuvers, will create perturbations considerably larger than any of the aforementioned effects, over a short arc. It is the modeling of these perturbations which is the major thrust of this work and the topic of the next section.

ESTIMATION OF ATTITUDE MANEUVERS

Description

Throughout the course of any mission, the Space Shuttle is in one of two types of attitude holds: those referred to as Local Vertical Local Horizontal holds (LVLH), in which the orientation of the vehicle is fixed relative to the surface of the Earth, and those referred to as Inertial Holds (IH), in which the spacecraft does not rotate with respect to the stars. Which hold is used at any given time, depends predominantly on the experiments which are being conducted, and which requirements, if any, these have placed on the orientation of the vehicle in space. However, usually both classes of holds will be required and, thus, significant maneuvers must be employed to rotate the spacecraft from one to the other. Since the Shuttle uses rockets and not momentum wheels to perform these maneuvers, and since the rockets are not aligned in such a way as to purely rotate the vehicle, each firing will contribute some degree of acceleration to the spacecraft, as a whole. The direction in which this acceleration occurs depends on a number of factors: which rockets are used, how long they fire and the initial and final orientation. Because the rockets are fixed to the body of the Shuttle, the overall perturbation on the orbit will be an integrated effect over the period of the burn, as a function of the vehicle's orientation during the maneuver. Clearly, if momentum wheels were used in the Shuttle, as is the case with most other satellites, the coupling between the orbit and the attitude would be reduced to that of natural dynamical coupling, which is completely negligible.

Neither the LVLH nor the IH configuration is very stable; drag, gravity gradient effects, and even crew activity tend to drive the vehicle away from these attitudes. As a consequence, fairly small but frequent attitude adjustment maneuvers

are required to maintain any given hold. Typically, a deadband angle of about 2° is allowed for drift, but once this angle is exceeded, a small adjustment will be performed to correct the attitude. During the periods of the MOMS camera observation, this deadband angle was increased to 5° to maintain a more passive environment.

Both the large attitude maneuvers and the smaller control thrusting realignments can perturb the orbit to a non-negligible level, especially if they occur frequently. Typically, it is the cumulative effect of many unmodeled maneuvers that leads to large errors. Fig. 3 shows a typical timeline of the pitch angle of the Shuttle over a three hour span. The angle is given with respect to an inertial frame, so an IH configuration can be easily identified as periods during which the angle is, essentially, constant. The circles identify times when large attitude maneuvers occur, while control thrusting can be seen by the wave-like appearance during either of the two IH configurations.

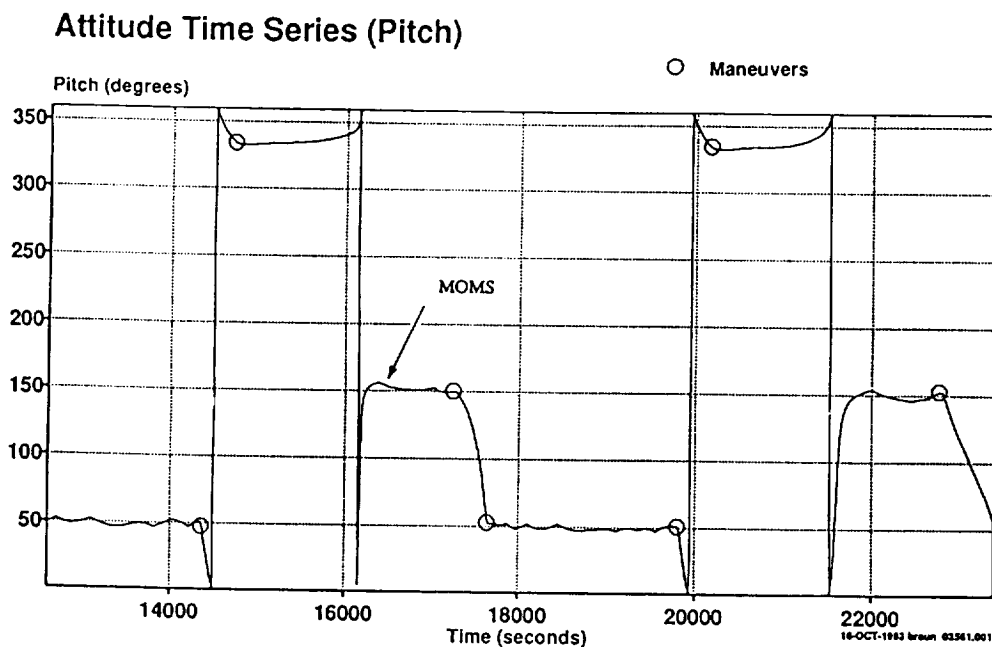


Fig. 3 Typical Shuttle Attitude Timeline (Pitch)

Any maneuver between an IH attitude and an LVLH hold consists of, firstly, an accelerative burn, followed by a period of a rapid change in the any given angle, and, secondly, a decelerative burn, once the new attitude is reached. This period can be identified as times when the slope of the angle is very high (the sudden jumps from 0° to 360° are of no relevance). Following each final braking maneuver, the Shuttle is then held in either an LVLH or an IH configuration for up to 30 minutes, before another significant maneuver occurs.

Approach

It will be seen in one of following sections that, because these attitude maneuvers are so highly coupled with the orbit, completely ignoring them will lead to errors of up

to several hundred meters in the position after three hours. As a consequence, it was attempted to estimate some of the larger maneuvers by introducing so-called empirical forces during the isolated times of the burns.

Empirical forces act, essentially, as a mechanism by which unknown or unmodeled effects can be introduced into the model at any given time and acting over any given duration. In this case, they consist of three forces, one in each of the radial, transverse and normal (identical to the radial, along-track and cross-track) orbit directions. The magnitude of the force in any given direction can be established as an *a priori* value, if there is some knowledge of the phenomenon, or by simply estimating its value during the filtering process, if very little is known.

The technique used in this study was to isolate, from information of the as-flown attitude timeline and the actual time series of the pitch, yaw and roll angles of the Shuttle, the times at which each of the large attitude maneuvers between an IH configuration and an LVLH hold were conducted. Empirical force parameters were then estimated during the course of a maneuver, which, typically, lasts 10 to 15 seconds. As discussed earlier, each maneuver will contribute perturbations in each of the radial, transverse and normal directions, and any estimate of these, using this approach, will only yield an average value over the period of the burn. It was also found that a reasonable estimate of all three components was usually not possible, due to high correlations. Thus, since the energy required to perturb the orbit in the normal direction is considerably greater than that required to perturb it an equivalent amount in either the radial or transverse direction, it was always the case that the normal component of any given maneuver was not estimated. Even so, a good estimate of the transverse and radial components can also greatly improve the internal consistency of the orbit in the normal direction.

PROCESSING OF STS-55 ORBITS

Goals

Actual TDRSS Doppler tracking data from STS-55 were processed using the same force models discussed in the previous sections. Twelve arcs, each between two and a half and three hours in duration and centered around the brief period of operation of the MOMS camera, were selected for processing. Table 2 gives both the Shuttle and orbit parameters for the D2 mission; these are identical to those used during the simulations, the results of which were summarized in Table 1. It is the goal of this work to establish the best estimates possible for the position of the Shuttle during the operation of the camera, and, in doing so, assess the degree to which empirical force estimates of the significant maneuvers can be established.

Quality Assessment

In any batch or Kalman filtering technique, such as ones used in orbit determination, the theoretical accuracy of the estimates of the state is given by the state covariance. This, however, assumes that there exists a good understanding of the errors associated with the observations, the force models and the dynamic parameters.

Table 2
SHUTTLE AND ORBIT PARAMETERS OF THE SIMULATIONS

Semi-major axis	6678 km
Eccentricity	0.001
Inclination	28.5°
Shuttle mass	109090 kg
Shuttle cross-section (Bay doors open)	
Normal to u_x :	68.19 m ²
Normal to u_y :	222.60 m ²
Normal to u_z :	413.42 m ²
Reflectivity coefficient (nominal for all surfaces)	0.7
S-Band antenna x :	13.9 m
y :	3.39 m
z :	-1.76 m

If such error models are not known or if forces exist which are not well-modeled, as is the case with attitude maneuvers, then the covariance values will tend to be optimistic. As a consequence, another technique which is commonly used for assessing the quality of an orbit is to compare the arc with an overlapping arc generated with mostly independent tracking data (Ref. 6).

In this investigation, overlap arcs, similar in duration to the main arcs, were processed. The target overlap, in terms of the percentage of the main arc of which the secondary arc overlapped, was 25%; the number varied slightly, depending on the quality and supply of the tracking data and on the timing of the maneuvers. The quality of the orbit is then quantified as the root mean square (rms) of the radial, transverse and normal overlap differences.

Results

The results of processing 12 MOMS arcs are summarized in Table 3, where the improvements in the overlap values before and after maneuvers were estimated is given. For any given arc, the parameters estimated were the initial state, a combined scaling coefficient for lift and drag, and various radial and transverse empirical force values for the significant attitude maneuvers. Table 3 also shows the number of large maneuvers which existed in each of the main and overlap arcs. This, however, does not always directly correspond to the number of maneuvers estimated. This is the case for two primary reasons. Firstly, it is not always possible to estimate a maneuver if there is a poor supply of tracking data at the time of the burn. As mentioned earlier, there is a period over India, usually lasting about 10 minutes, for which there is no tracking data available. In addition, data is lost during the switch from one TDRS to another, often creating gaps of several minutes. If a maneuver occurs during or around the time of these gaps, it is very difficult to get a good estimate of its magnitude; any attempt will often corrupt estimates of the other maneuvers or simply degrade the quality of the orbit. The second reason it may not be possible to reliably estimate a maneuver is if it occurs near the end of an arc. Because there is not data beyond the

end of the arc, the quality of the orbit tends to degrade in these areas. Any attempt to estimate maneuvers during these times will tend to yield magnitudes which are much too large, and overlap differences are likely to be too pessimistic. This is also very evident by the relative magnitudes of the estimated value for the maneuver and its uncertainty; clearly, the latter must be considerably smaller than the former if any confidence is to be placed on the estimate. Due to these shortcomings, only maneuvers which occurred during periods for which there was a good supply of tracking data and which were not near the ends of the arc were estimated. It is clear, however, from results in Table 3 that, even if a considerably large number of maneuvers is present, a significant improvement in the quality of the orbit can be made by carefully estimating their values.

Table 3
 RADIAL, NORMAL AND TRANSVERSE (RMS) ORBIT OVERLAPS,
 BEFORE AND AFTER MANEUVER ESTIMATION

Rev No.	Maneuvers		Rms Doppler Residual (Hz)		Rms Overlaps (r, η, τ) (m)	
	Main	Overlap	Before	After	Before	After
9	6	6	1.52	0.83	88,201,186	15,23,18
10	6	6	0.92	0.79	88,201,186	15,23,18
11	8	6	1.29	0.84	120,268,289	38,67,21
12	6	6	0.80	0.77	48,107,96	17,49,25
14	4	6	1.14	0.81	153,178,337	40,73,61
75	4	2	1.18	1.04	82,48,110	14,32,31
82	4	3	0.88	0.82	23,155,160	35,45,20
91	4	2	1.30	0.85	54,23,121	52,39,62
97	6	4	0.88	0.86	42,120,80	17,53,31
105	6	0	0.92	0.86	120,134,119	40,43,56
115	4	4	0.93	0.87	96,51,107	10,15,16
146	6	3	0.81	0.71	121,154,256	15,47,46

This current discussion has, so far, said nothing of the frequent control thrustings that are needed to maintain an attitude hold. As was evident in Fig. 3, these occur every few minutes throughout the mission. There is very little hope of being able to estimate each of these maneuvers, as was done for the more significant burns, due to the frequency at which they are conducted. What tends to happen for small perturbations, particularly their along-track, or transverse, components, is that the scaling parameter for drag will absorb some of the errors. In fact, this term will assume the role of a junk parameter, and take on values which may not be realistic of a drag or lift coefficient. This was often seen to be the case here; but, in allowing the parameter to vary freely, i.e. without an *a priori* value, the overlaps differences could be modestly decreased.

CONCLUSIONS

Orbit Determination of the U.S. Space Shuttle during STS-55 was performed to assist in the processing of digital image data from the German MOMS-02 remote sensing camera on-board. Simulations from an earlier work (Ref. 10) have shown that the remaining unmodeled effects on the motion of the Shuttle are due to both attitude maneuver thrusting and attitude hold control thrusting; all other significant effects have been accounted for. In addition to the errors introduced due to the maneuvers, errors from uncertainties in the TDRSS satellite positions are at the 10 m level.

An attempt was made to absorb some of the most significant errors by estimating empirical force accelerations during many of the largest attitude maneuvers. Radial and transverse accelerations were estimated for up to six maneuvers during a three hour arc for 12 selected arcs during the mission. It was found that overlap differences could be greatly reduced in all cases, anywhere from two to 10 times, by estimating the maneuvers.

The primary difficulties in applying this technique are encountered if maneuvers occur during periods of poor or no tracking, and in areas near the beginning and end of the arc. It is also not feasible to estimate control thrusting maneuvers during attitude holds, due to the frequency at which they occur.

Clearly, if further significant improvements are to be made in Space Shuttle orbit determination, it will be necessary to completely model each maneuver that occurs. Since these attitude maneuvers couple the attitude with the orbit, this would require incorporating information about the instantaneous orientation of the Shuttle with knowledge of which rockets were used, their mean thrust values and the duration of each burn. Then, a numerical algorithm for determining the integrated effect of each burn as a function of orientation would have to be implemented into the orbit determination software, in order to establish the radial, transverse and normal orbit perturbation from each burn. Further improvements beyond this would need to focus on the quality of the TDRS position ephemerides.

ACKNOWLEDGMENT

This research was supported under a contract from the German Federal Minister for Research and Technology and the Department of Photogrammetry at the University of Stuttgart, in conjunction with MOMS-02/D2 mission. The authors would like to thank C. Rajasenan and F.-H. Massmann of the GeoForschungsZentrum for their informative suggestions, and to Ed Brown of Rockwell International for his tremendous assistance in supplying the Shuttle data and for sharing his knowledge of Shuttle navigation.

REFERENCES

1. Ackermann, F., J. Bodechtel, F. Lanzl, D. Meissner, P. Seige and H. Winkenbach, "MOMS-02 A Multispectral Stereo Imager for the Second German

Spacelab Mission D2", *International Archives of Photogrammetry and Remote Sensing*, Vol. 28, Part 1, 1990, pp. 110-116.

2. Ebner, H., and F. Müller, "Processing of Digital Three-Line Imagery Using a Generalized Model for Combined Point Determination", *Photogrammetria*, Vol. 3, 1987, pp. 173-182.
3. Fang, B.T., "Satellite-to-Satellite Tracking Orbit Determination", *J. Guidance and Control*, Vol. 2, No. 1, 1979, pp. 57-64.
4. Hedin, A.E., "MSIS-86 Thermospheric Model", *J. Geophys. Res.*, Vol. 92, No. A5, 1987, pp. 4649-4662.
5. Lerch, F.J., R.S. Nerem, B.H. Putney, T.L. Felsentreger, B.V. Sanchez, S.M. Klosko, G.B. Patel, R.G. Williamson, D.S. Chinn, J.C. Chan, K.E. Rachlin, N.L. Chandler, J.J. McCarthy, J.A. Marshall, S.B. Luthcke, D.W. Pavlis, J.W. Robbins, S. Kapoor, and E.C. Pavlis, Geopotential Models of the Earth From Satellite Tracking, Altimeter and Surface Gravity Observations: GEM-T3 and GEM-T3S, NASA Technical Memorandum 104555, 1992.
6. Massmann, F.-H., Ch. Reigber, R. König, J.C. Raimondo and C. Rajasenan, "ERS-1 Orbit Information Provided by D-PAF", ERS-1 Second ERS-1 Symposium, Hamburg, Germany, October 11-14, 1993
7. Pallaschke, S., and J. Housden, "Tracking Accuracy Evaluation for Data Relay and User Satellites", *Acta Astronautica*, Vol. 21, No. 1, 1990, pp. 13-22.
8. Phung, P.B., V.S. Guedeney, and J. Teles, "Tracking and Data Relay Satellite System (TDRSS) Range and Doppler Tracking System Observation Measurement and Modeling", Technical Memorandum X-572-80-26, Goddard Space Flight Center, 1980.
9. Teles, J., Goddard Space Flight Center, personal communication, 1991.
10. von Braun, C. and Ch. Reigber, "Space Shuttle Orbit Determination Using TDRSS Doppler Data In Preparation for the German MOMS-02/D2 Mission", Paper AAS 93-281 at the AAS/GSFC International Symposium on Space Flight Dynamics, Goddard Space Flight Center, Greenbelt, MD, April 26-30, 1993.

APPLICATION OF A MONTE CARLO ACCURACY ASSESSMENT TOOL TO TDRS AND GPS

Michael S. Pavloff

The MITRE Corporation, Bedford, MA 01730

ABSTRACT

In support of a NASA study on the application of radio interferometry to satellite orbit determination, MITRE developed a simulation tool for assessing interferometric tracking accuracy. Initially, the tool was applied to the problem of determining optimal interferometric station siting for orbit determination of the Tracking and Data Relay Satellite (TDRS). Subsequently, the Orbit Determination Accuracy Estimator (ODAE) was expanded to model the general batch maximum likelihood orbit determination algorithms of the Goddard Trajectory Determination System (GTDS) with measurement types including not only group and phase delay from radio interferometry, but also range, range rate, angular measurements, and satellite-to-satellite measurements. The user of ODAE specifies the statistical properties of error sources, including inherent observable imprecision, atmospheric delays, station location uncertainty, and measurement biases. Upon Monte Carlo simulation of the orbit determination process, ODAE calculates the statistical properties of the error in the satellite state vector and any other parameters for which a solution was obtained in the orbit determination.

This paper presents results from ODAE application to two different problems: (1) determination of optimal geometry for interferometric tracking of TDRS, and (2) expected orbit determination accuracy for Global Positioning System (GPS) tracking of low-earth orbit (LEO) satellites. Conclusions about optimal ground station locations for TDRS orbit determination by radio interferometry are presented, and the feasibility of GPS-based tracking for IRIDIUM, a LEO mobile satellite communications (MOBILSATCOM) system, is demonstrated.

INTRODUCTION

As part of its effort to assess cost and performance benefits of various emerging technologies, NASA Headquarters sponsored a series of studies on the application of radio interferometry to satellite tracking. Though astronomers had used radio interferometry for decades prior, it was not until the late 1960s that interferometry was proposed for use in satellite orbit determination. In an experiment devised by Irwin Shapiro, Alan Whitney, and others, very long baseline interferometric (VLBI) measurements were made on the TACSAT I communications satellite in geosynchronous orbit (GEO), and the semi-major axis of the orbit was measured with accuracy on the order of several hundred meters [1]. Subsequent experiments performed in the 1980s by Jim Ray, Curt Knight, and others to determine the position of the Tracking and Data Relay Satellite (TDRS) yielded accuracy on the order of 75 meters [2]. Such orbit determination accuracy, which derives from the extremely high precision of the group delay and phase delay observables, make radio interferometry an attractive option for satellite tracking.

Operational considerations are also a benefit of radio interferometry in satellite orbit determination, because the group and phase delay measurements are made completely passively. Whereas the existing Bilateral Ranging Transponder System (BRTS) is taxing on TDRS communications resources, radio interferometry can derive its measurements from any signal, including the signal intended for the TDRS user community. Therefore, an interferometric orbit determination system for TDRS would eliminate traffic for tracking on the TDRS transponder. Because an interferometric tracking system would be passive, it would place no design constraints on the space segment, and it would therefore provide backward compatibility with all generations of TDRS. Thus, NASA found radio interferometry to be an attractive technology to pursue for future TDRS tracking applications.

NASA sponsored a series of studies to investigate whether an operational radio interferometry system could provide TDRS orbit determination services (1) at lower cost, (2) at greater accuracy, and (3) across considerably smaller baselines than BRTS. Contributors to these studies included Interferometrics, Inc., where a Small Business Initiative Research (SBIR) contract with NASA was executed to demonstrate hardware and software that would provide group delay measurements on TDRS with VLBI. CSC performed an assessment for the Goddard Space Flight Center (GSFC) on a variety of TDRS tracking alternatives, including VLBI and Connected Element Interferometry (CEI) systems. The Jet Propulsion Laboratory (JPL) sponsored a series of experiments to determine CEI accuracy from its Goldstone facility. For its part of the effort, MITRE assessed optimal site locations and expected life-cycle costs of an operational interferometric TDRS orbit determination system.

For accuracy assessment purposes, MITRE developed a Monte Carlo simulation tool, the Orbit Determination Accuracy Estimator (ODAE), that initially modeled error sources in orbit determination with VLBI and CEI systems. In ODAE, the user can specify a satellite orbit, any set of ground stations between which group or phase delay measurements are to be made, and the statistical properties of the error in those measurements. Upon each iteration of the Monte Carlo simulation, the orbit of the satellite is determined based on measurements with errors added, and the errors in the resulting satellite ephemerides are recorded. Thus, the user may study the statistical properties of the error in the batch orbit determination process resulting from the use of group or phase delay measurements. The initial application of ODAE was to study the effects of varying satellite and measuring station geometries on orbit determination accuracy and to propose optimal siting for TDRS tracking by radio interferometry. The results of that study are presented in this paper.

Subsequent studies for the United States Air Force (USAF) on Space Surveillance Network (SSN) accuracy and Global Positioning System (GPS) accuracy led to the expansion of ODAE to include range, range rate, azimuth and elevation angle, and satellite-to-satellite measurement

types. The potential application of GPS to satellite tracking has been under consideration for a number of years (e.g., [3]). For GEO satellites, which have higher orbits than GPS satellites, the problems of low GPS satellite visibility and weak signal strength present limitations [4]. However, for LEO satellites, which have lower orbits than GPS satellites, visibility and signal strength are greatly improved. Attention has been focused recently on LEO satellites in the arena of mobile communications. A number of LEO MOBILSATCOM systems are currently in planning or development, including Motorola's IRIDIUM, Loral's Globalstar, TRW's Odyssey, and, most recently, Teledesic, a joint venture of Kinship Partners with William Gates and Craig McCaw [5]. We used ODAE to study the accuracy of GPS tracking for the IRIDIUM system, the results of which are shown herein.

THE ODAE MODEL

ODAE models the batch maximum likelihood orbit determination process applied in the Goddard Trajectory Determination System (GTDS) [6]. The user specifies a reference true satellite orbit, a set of observing stations (earth-based or space-based), the observation types, and the times at which measurements are to be made. Given a set of observations on the satellite (e.g., radar measurements, group or phase delay measurements, or pseudorange measurements), ODAE determines the set of parameters (e.g., state vector, clock offsets, or atmospheric parameters) that best fit the observations. Upon each iteration of its Monte Carlo simulation, ODAE injects errors of user-specified statistical properties into various parts of the orbit determination process. ODAE computes the error of the measured parameters at each iteration, and at the end of the simulation, ODAE computes the statistical characteristics of the error.

Error sources that can be modeled by ODAE include inherent measurement imprecision, station location uncertainty, atmospheric delays, and clock offsets. The user must specify the statistical properties of the error sources. Trajectory propagation schemes for dynamic orbit determination range from the two-body approximation to numerical integration of the fully disturbed equations of motion. A detailed mathematical specification of the coordinate frame, force models, and numerical integration techniques used in ODAE are given in Reference 7. The only significant deviation from the GTDS approach to orbit determination is the use of Bulirsch-Stoer rational function extrapolation for numerical integration [8, 9]. For the numerical integration of the equations of satellite motion, the Bulirsch-Stoer technique has been shown to provide the same precision as more traditional techniques, such as predictor-corrector integration or Runge-Kutta integration, but at reduced computational cost [7, 10]. For short-term dynamic orbit determination accuracy studies to assess the relative effects of changes in station geometry or measurement errors, it is often sufficient to apply simplified trajectory propagation schemes for the sake of reducing computation time.

ODAE was implemented in Mathematica to allow maximum flexibility of the model. Since its initial application to the problem of optimal ground station siting for interferometric tracking of TDRS, MITRE has applied ODAE to a variety of problems. Most recently, MITRE has proposed the use of ODAE for assessment of initial orbit determination accuracy with the HAVE STARE radar. Existing applications include the assessment of orbit determination accuracy for the Space Surveillance Network Improvement Program (SSNIP) for various classes of orbits, and to the determination of GPS accuracy for various scenarios. Although computational time is increased by using Mathematica, it allows for very natural representation of the equations of motion, numerical integration schemes, and the batch orbit determination algorithm. Also, because ODAE is written in Mathematica, it is very quickly adaptable to a variety of problems, including satellite-to-satellite tracking and GPS navigation. After an overview of the group and phase delay measurement functions, applications of ODAE to TDRS tracking and to GPS navigation for a LEO satellite system are described.

GROUP DELAY AND PHASE DELAY MEASUREMENT FUNCTIONS

Consider an interferometric orbit determination scenario in which O is the origin of an earth-centered inertial (ECI) coordinate system, \mathbf{r} is the position vector of a satellite with respect to O , \mathbf{b}_1 and \mathbf{b}_2 are the position vectors of two ground stations from which measurements are to be made, and \mathbf{d}_1 and \mathbf{d}_2 are the position vectors of the satellite with respect to those ground stations, as pictured in Figure 1. The position vectors \mathbf{r} , \mathbf{b}_1 , \mathbf{b}_2 , \mathbf{d}_1 , and \mathbf{d}_2 are all functions of time. The sum of a station position vector, \mathbf{b}_k , and the satellite position vector measured from that station, \mathbf{d}_k , is simply the satellite position vector \mathbf{r} ; therefore, $\mathbf{d}_k = \mathbf{r} - \mathbf{b}_k$. If the propagation rate, c , of the signal through the atmosphere is known, then the transit time, T_k , of the signal from the satellite at point P to ground station number k at point B_k will be given by

$$T_k = \frac{1}{c} |\mathbf{d}_k| = \frac{1}{c} \sqrt{(\mathbf{r} - \mathbf{b}_k) \cdot (\mathbf{r} - \mathbf{b}_k)}$$

The true group delay, τ , between stations 2 and 1 is the differential transit time of the signal between these two sites:

$$\tau = T_2 - T_1 = \frac{1}{c} (|\mathbf{d}_2| - |\mathbf{d}_1|) = \frac{1}{c} \left[\sqrt{(\mathbf{r} - \mathbf{b}_2) \cdot (\mathbf{r} - \mathbf{b}_2)} - \sqrt{(\mathbf{r} - \mathbf{b}_1) \cdot (\mathbf{r} - \mathbf{b}_1)} \right] \quad (1)$$

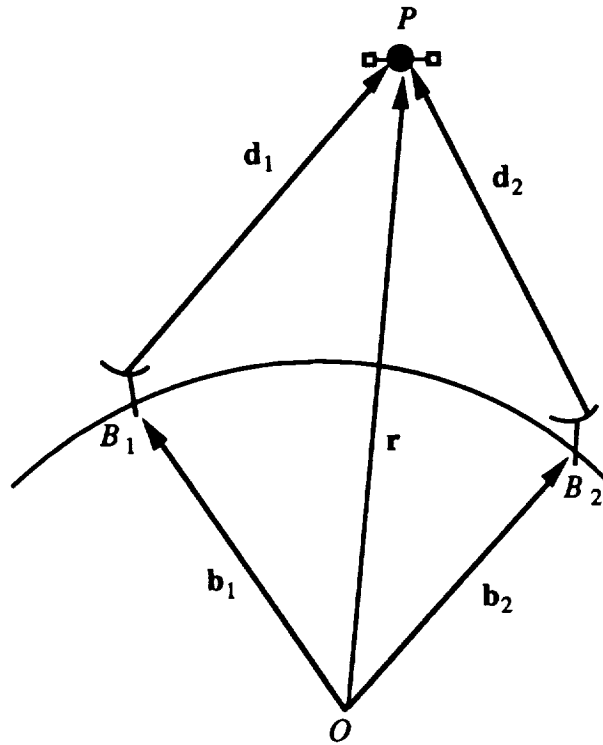


Figure 1. Illustration of the Interferometric Measurement Scenario

A subtlety of equation (1) is that the satellite position vector, \mathbf{r} , the station 1 position vector, \mathbf{b}_1 , and the station 2 position vector, \mathbf{b}_2 , are all referenced to different times. If the measured signal emanates from the satellite at time t , then it will arrive at station 1 at time $t + T_1$, and it will

arrive at station 2 at time $t + T + \tau$, where T is the signal transit time from the satellite to station 1, and τ is the true group delay between stations 1 and 2. If the satellite position vector \mathbf{r} is measured at time t , then the station 1 position vector is measured at time $t + T$, and the station 2 position vector is measured at time $t + T + \tau$. Thus, we write $\mathbf{r} = \mathbf{r}(t)$, $\mathbf{b}_1 = \mathbf{b}_1(t + T)$, and $\mathbf{b}_2 = \mathbf{b}_2(t + T + \tau)$. The group delay equation (1) is, therefore, more properly written as follows:

$$\tau = \frac{1}{c} \sqrt{[\mathbf{r}(t) - \mathbf{b}_2(t + T + \tau)] \cdot [\mathbf{r}(t) - \mathbf{b}_2(t + T + \tau)]} - \frac{1}{c} \sqrt{[\mathbf{r}(t) - \mathbf{b}_1(t + T)] \cdot [\mathbf{r}(t) - \mathbf{b}_1(t + T)]} \quad (2)$$

In ODAE, a user specifies a scenario that includes epoch time, satellite state vector at epoch, latitude, longitude, and altitude of interferometer sites, and times at which measurements are to be taken. ODAE must then calculate the true group delay observables from equation (2), but as can be seen, the right-hand side of (2) is a function of τ . Therefore, ODAE solves equation (2) for τ iteratively, as described in Reference 7. During the Monte Carlo simulation, ODAE computes measured group delay by adding measurement or atmospheric fluctuation errors to the true group delay as computed above. The solution of the orbit determination problem on each iteration of the simulation, as described in Reference 7, follows the GTDS maximum likelihood estimation approach, one step of which is the computation of the Jacobian, or matrix of partial derivatives of equation (2) with respect to the state vector parameters at epoch.

For phase delay measurements, ODAE converts phase delay into equivalent group delay. If ν is the reference center frequency of the phase delay measurement, N is an integer number of signal cycles, and ϕ is the true phase delay, then the equivalent true group delay τ can be computed as follows:

$$\tau = \frac{\phi + 2\pi N}{2\pi\nu} \quad (3)$$

This computation can be accomplished so long as the cycle ambiguity N can be determined from *a priori* information about the satellite's position vector. ODAE allows the user to model clock offsets or local oscillator offsets for group or phase delay measurements, respectively. In such cases, the offset is taken as an additional parameter in the orbit determination process.

APPLICATION TO TDRS

In this section, the level of GEO satellite orbit determination accuracy that can be attained with radio interferometry is demonstrated, and conclusions about optimal station-satellite geometry are drawn. The results are applied to recommend optimal ground station siting for orbit determination of TDRS by radio interferometry.

Radio interferometry with baselines the size of BRTS's, which are intercontinental, would translate the high level of observable group delay accuracy into greatly improved TDRS tracking accuracy. However, it was NASA's desire instead to accept only a modest improvement in accuracy while reducing system cost and ameliorating other operational considerations by greatly shortening the baselines. This led naturally to the study of a CEI-based system, where baselines are very short. Because of the requirement for a CEI system to have interferometer sites connected by fiberoptic cable in a temperature-controlled environment, the cost of lengthening baselines is very high. We constrained our baselines to 20 km maximum length for the purposes of this study.

We used ODAE to assess position determination accuracy for a baseline scenario and to determine the effects of varying the relative satellite to ground station geometry. Because the effect only of relative geometry was to be studied initially, it was not necessary to select true TDRS ephemerides or true potential ground station locations. The reference orbit chosen was geosynchronous with a 4° inclination and a subsatellite longitude of 18°W. To provide three independent baselines across which phase delay could be measured, we constrained four CEI sites to lie on the vertices of a square with a 20 km baseline, as shown in Figure 2. The site latitudes, longitudes, and altitudes for this reference scenario are given in Table 1. ODAE modeled simultaneous phase delay measurements across the baselines from station 2 to station 1, station 3 to station 1, and station 4 to station 1 (denoted 2-1, 3-1, and 4-1, respectively). These baselines are illustrated in bold in Figure 2.

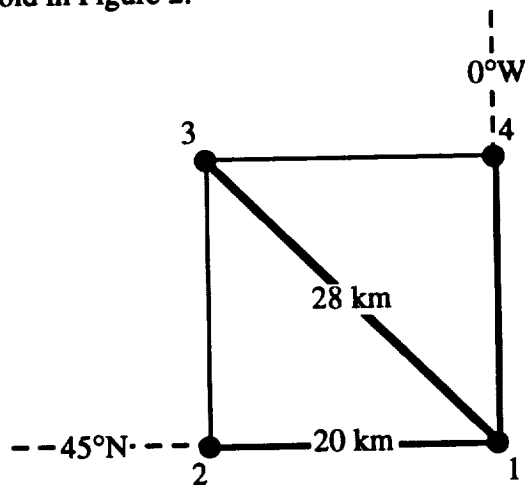


Figure 2. CEI Station Locations

Table 1. CEI Station Locations for Reference Scenario

Station Number	Geodetic Latitude (°)	Longitude (°E)	Altitude (km)
1	45.00000	0.0000	0.1
2	45.00000	-0.2545	0.1
3	45.17997	0.0000	0.1
4	45.17997	-0.2545	0.1

An extension of Alan Whitney’s work [11] shows that the theoretically achievable precision of the phase delay observable, σ_ϕ , is given by

$$\sigma_\phi = \frac{1}{2\pi(SNR)\nu} \quad (4)$$

where ν is the center frequency, in Hz, sampled by the interferometer. Since the TDRS downlink to White Sands is centered at 14 GHz, the theoretically achievable precision of the phase delay observable is 0.23 picosec. While no TDRS tracking experiments were performed with JPL’s

CEI equipment at Goldstone, observations were made on natural radio sources at 8.4 GHz to assess the precision of the phase delay observable [12]. The statistical phase error, expressed in radians, is roughly $1/SNR$, and JPL's experiments at Goldstone demonstrated a typical phase error of 0.005 cycles [13]. The achieved SNR was therefore $1/(2\pi \times 0.005) \approx 32$. At 8.4 GHz, relationship (4) predicts a phase delay observable precision of 0.59 picosec. JPL demonstrated the standard deviation in the phase delay observable to be approximately 1 picosec [12], which is a factor of 1.7 larger than the theoretically achievable value. Applying this factor to the theoretically achievable phase delay precision for TDRS, we estimated the practically achievable precision to be $0.23 \times 1.7 \approx 0.4$ picosec. We took this measurement error to be independently normally distributed across each baseline. For the initial study, it was assumed that there were no equipment biases, that there were no atmospheric delay errors, that all stations were connected by fiberoptic cable to one clock and frequency standard, that there were no local oscillator offsets between the four stations, and that station positions were known with perfect accuracy. Thus, the pure effect of measurement geometry and observable precision on orbit determination could be assessed.

ODAE Monte Carlo simulation of the orbit determination scenario described above with 200 iterations showed a 1σ root-mean-squared (RMS) position vector accuracy of 3.2 km. We also assessed the accuracy that can be attained with the use of other combinations of baselines. It is practical to have one site in common for all three measurements so that the common site can act as the correlation center at which the phase delay observables are generated. For the particular satellite and ground station locations in this scenario, selection of three measurements where one station is common to each pair (i.e., 2-1, 3-1, 4-1; or 1-2, 3-2, 4-2; or 1-3, 2-3, 4-3; or 1-4, 2-4, 3-4) results in a 1σ RMS position vector accuracy of 3.2 km. Thus, there is no geometrically-preferred common site for the measurements.

The orbit determination scenario described above was the starting point for the assessment of the effects of varying interferometric measurement geometry on orbit determination accuracy. Since only relative geometry matters, and since it would have been more cumbersome to vary the positions of four ground stations, we instead varied the satellite's initial position vector. First, we studied the effect of relative interferometer baseline size on orbit determination accuracy. Satellite range from station 1 was varied while keeping the elevation angle and azimuth angle from that station constant. Because the baseline sizes are small relative to the range to GEO, the range, elevation angle, and azimuth angle from each of the other three stations is close to that of the first. For this particular orbit determination scenario, range from each site to the satellite is approximately 37,850 km, the elevation angle is approximately 39° , and the azimuth angle is approximately 155° . As shown in Figure 3, the smaller the range to the satellite for a constant baseline length (or, equivalently, the longer the baselines across which phase delay is measured relative to the range to the satellite), the greater the position vector accuracy.

Next, we assessed the effect of satellite azimuth angle on orbit determination accuracy. The azimuth angle of the satellite at station 1 in the original scenario was varied while keeping the range and elevation angle from that station constant. Figure 4 shows the variation in position determination accuracy with satellite azimuth angle. The results indicate that for a configuration of four interferometric ground stations at the vertices of a square, position error is maximized when the satellite's azimuth angle is an integer multiple of 90° , and position error is minimized when the satellite's azimuth angle is an integer multiple of 45° .

Finally, we assessed the effect of satellite elevation angle on orbit determination accuracy in this scenario. The elevation angle of the satellite at station 1 was varied while keeping the range and azimuth angle from that station constant. As can be seen in Figure 5, for this particular orbit determination scenario, position error increases monotonically with elevation angle. Thus, based

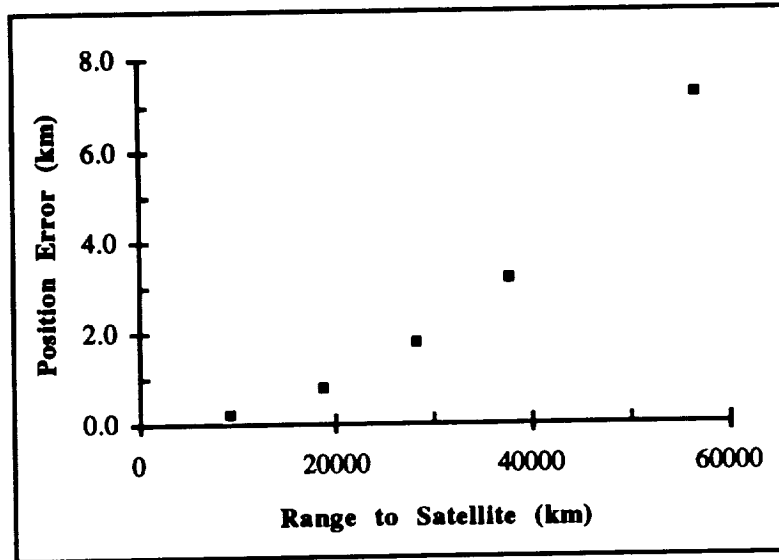


Figure 3. Position Error vs. Range to Satellite

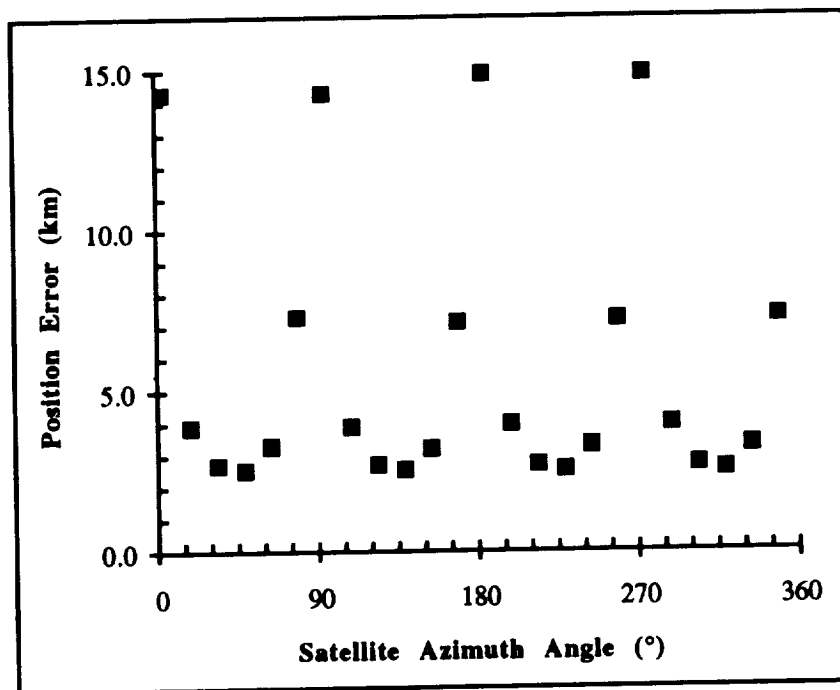


Figure 4. Position Error vs. Satellite Azimuth Angle

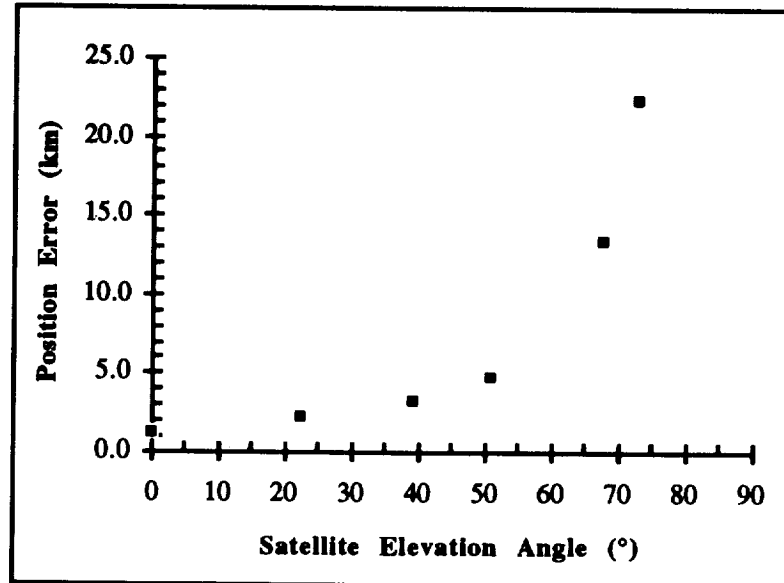


Figure 5. Position Error vs. Satellite Elevation Angle

on the criterion of minimizing ephemeris error due only to error in the phase delay measurement, optimal viewing geometry is at the lowest possible elevation angle, and the scenario becomes degenerate when the satellite is at zenith.

A tradeoff is suggested by the geometrical result that greater orbit determination accuracy is attained at lower elevation angles. The tradeoff arises because statistical models of the variation in signal propagation rate through the troposphere show that errors in predicting signal propagation rate increase as elevation angle decreases [14, 15]. Moreover, errors in predicting propagation rate due to tropospheric fluctuations tend to be the dominant error source in overall accuracy for CEI systems [15]. Thus, we sought to determine the optimal elevation angle for CEI measurements with consideration of both measurement error and tropospheric delay error.

We modeled tropospheric fluctuations between each interferometer site and the satellite as being independently normally distributed. The assumption of independence is based on the fact that water vapor cells can be of several kilometers in diameter, and so tropospheric delay errors from each site can in fact be independent. For an elevation angle of 20° and for a 100 second measurement duration, the magnitude of the standard deviation in tropospheric delay error was estimated to be 4 picosec [14]. The elevation angle dependence of the standard deviation in tropospheric delay error follows the square root of the structure function calculated in Reference [14]. Also, under the assumption of independent errors along each station-to-satellite path, the variance in phase delay error for a particular measurement pair will be the sum of the variances along each path. Since elevation angles are roughly equal along each path, the standard deviation of the phase delay error will, therefore, be $\sqrt{2}$ times the standard deviation along one path. From these assumptions and the results in Reference [14], we computed the values of standard deviation in phase delay error due to tropospheric fluctuations shown in Table 2.

For varying satellite elevation angles, we used ODAE to model error due to tropospheric fluctuations as well as inherent phase delay imprecision. The resulting 1σ position errors are shown in Figure 6. As can be seen, the optimal satellite elevation angle is approximately 30° . In the conclusions section of this paper, we show how these results can be applied to optimally siting a CEI system for TDRS orbit determination.

Table 2. Standard deviation in phase delay error due to tropospheric fluctuations as a function of elevation angle

Elevation Angle (°)	Tropospheric Delay Error (picosec)
10	7.5
20	5.7
30	4.6
40	3.9
50	3.3
60	3.0

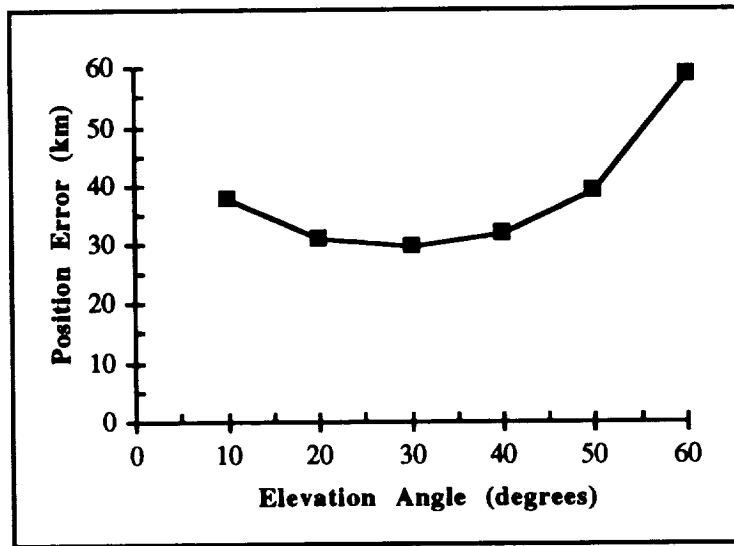


Figure 6. Position Error vs. Elevation Angle with Tropospheric Effects Included

APPLICATION TO GPS

Studies of GPS accuracy for a precision landing system and other GPS-related studies for the Department of Defense led to the application of ODAE to GPS accuracy problems. ODAE models the GPS navigation problem in much the same way as it models the satellite orbit determination problem. In the case of GPS navigation, a “station location” is the position of a GPS satellite at a particular time. GPS almanac data are loaded into ODAE and propagated to the desired measurement times. The unknown receiver position can be on the surface of the earth or on a satellite, and in the case of the former, the satellite orbit is also propagated to the desired measurement time. ODAE tests the visibility of satellites in the GPS constellation from the receiver position, and if the number of visible satellites exceeds the number of available channels in the receiver, ODAE determines the optimal subset of satellites for measurement.

GPS has been considered an attractive option for satellite orbit determination, in part because of the potential for cost and weight savings on a satellite's telemetry, tracking, and command (TT&C) subsystem. In the NASA study of TDRS tracking alternatives, GPS suffered from the problems of limited visibility from GEO. However, for LEO systems, GPS is a more viable alternative for orbit determination. To demonstrate potential accuracy, we considered the tracking of IRIDIUM by GPS.

The IRIDIUM constellation is currently designed to consist of 66 satellites in orbits with a semi-major axis of 7,143 km [16]. Satellites will be divided into six orbital planes spaced by 31.58° in right ascension of the ascending node. Orbital inclinations will be 86.4° , and eccentricities will be 0.0013. Satellites will be spaced equally within each plane, and adjacent planes will be half-way out of phase with one another. We selected an arbitrary satellite from the IRIDIUM constellation (right ascension of the node 31.58° , initial mean anomaly 0°) for analysis. We used ODAE to determine the number of GPS satellites visible to this IRIDIUM satellite as a function of time, and we used ODAE to determine position accuracy as a function of time.

The most recent GPS almanac data (2/13/94 at this time of this study) included the full constellation of 26 satellites. For the purposes of assessing GPS satellite visibility, we assumed a GPS beam width of approximately 27° , which is the angle subtended by the earth from a GPS satellite. Because the beam width is, in fact, larger than 27° , it would be possible to acquire a GPS signal from a satellite on the opposite side of the earth. However, since larger antennas would be required to achieve the necessary gain, the TT&C weight savings would be compromised. Consequently, for the purposes of this study, we considered GPS satellites to be visible to an IRIDIUM satellite only if they are on the same side of the earth.

Figure 7 shows the number of GPS satellites visible as a function of time from the reference IRIDIUM satellite. As can be seen, for four hours, fewer than four GPS satellites are visible; therefore, the GPS system availability to the IRIDIUM satellite would be 0.83. However, with an accurate clock, IRIDIUM could maintain continuous positioning services through GPS because only three visible satellites would be required.

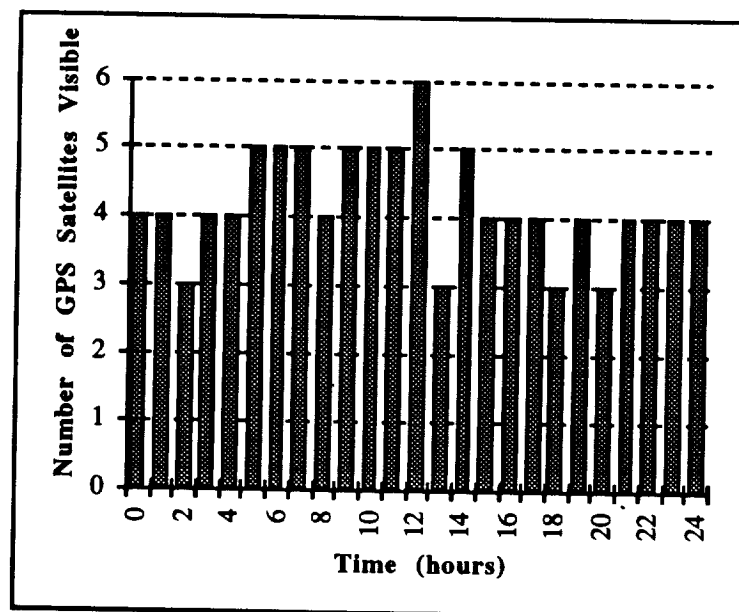


Figure 7. GPS Satellites Visible from an IRIDIUM Satellite Over a One-Day Period

We next computed position accuracy as a function of time for IRIDIUM tracking by GPS. Figure 8 shows position dilution of precision (PDOP) across a 24-hour period for instantaneous position fixes. For the points where only three GPS satellites were visible, we assumed that an accurate clock was available and that the navigation solution could, therefore, be obtained. As expected, Figure 8 shows poorest accuracy at the times when fewer GPS satellites are visible. Except for those times, baseline PDOP appears to be on the order of 2 or 3.

Finally, we used ODAE to compute dynamic orbit determination accuracy for IRIDIUM tracking by GPS. Figure 9 shows PDOP across a 24-hour period where measurements are taken on the hour, added to the previous pool of measurements, and processed in batch. After four hours, PDOP decreases below a value of one, and after 10 hours, a value of roughly 0.5 is obtained. For a low-accuracy situation where the precision of the pseudorange measurement is on the order of 3 meters, the resulting long-term IRIDIUM tracking accuracy would be on the order of $0.5 \times (3 \text{ meters}) = 1.5 \text{ meters}$. Such accuracy is likely to be sufficient, even with IRIDIUM's stringent formationkeeping requirements [16].

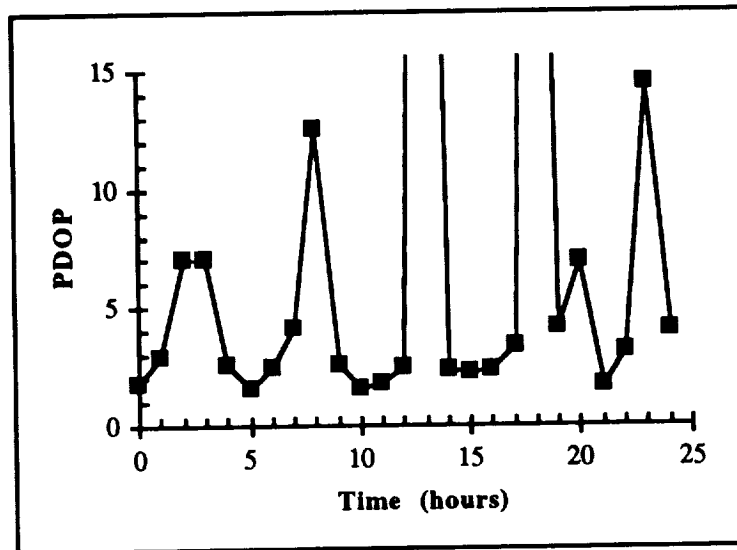


Figure 8. Position Accuracy over a One-Day Period for an IRIDIUM Satellite

CONCLUSIONS

In the first part of this report, we derived conclusions about optimal geometry for orbit determination of a GEO satellite by radio interferometry. Those results can be applied to the problem of optimally siting a CEI system to track TDRS. For a particular TDRS satellite, and for a configuration of four interferometer sites located at the vertices of a square, a geographical position should be chosen so that the satellite's elevation angle is as close to 30° as possible, and the square should be oriented so that the satellite's azimuth angle is an integer multiple of 45° . For TDRS-W at 171°W , the maximum elevation angle visible within the -20 dB contour of the White Sands downlink is in southern California at approximately 20° elevation. For TDRS-E at 41°W , an elevation angle near 30° can be attained within the -20 dB contour of the White Sands downlink by siting a CEI system in eastern Louisiana or western Mississippi.

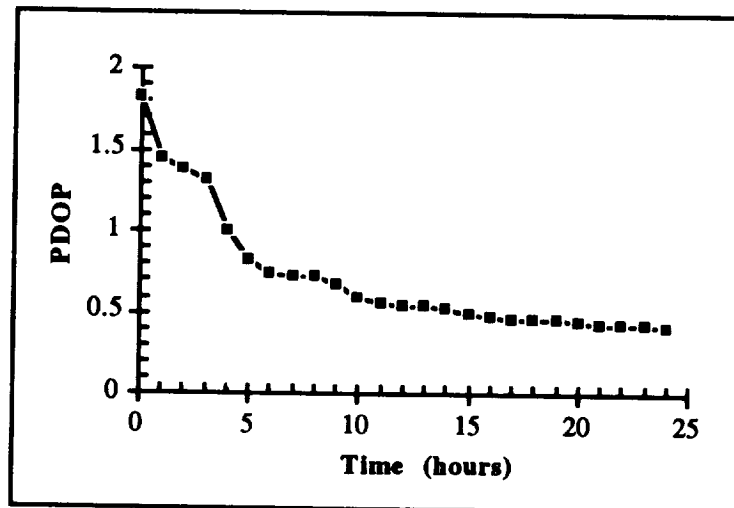


Figure 9. Dynamic Orbit Determination Accuracy over a One-Day Period for an IRIDIUM Satellite

In the second part of this report, we assessed GPS availability and accuracy for tracking a LEO satellite. In particular, for IRIDIUM, where the proposed constellation consists of satellites in near-polar orbits at altitudes of 785 km, instantaneous orbit determination accuracy is available at the level of 9 meters (1σ), and long-term dynamic orbit determination can reduce errors to the level of 1.5 meters. Because GPS receiver equipment has the potential of offering reduced weight and cost by comparison with traditional TT&C equipment, GPS provides an attractive tracking alternative for LEO satellites such as IRIDIUM.

LIST OF REFERENCES

1. Preston, R. A., et al, 27 October 1972, "Interferometric Observations of an Artificial Satellite," *Science*, Vol. 178, pp. 407-409.
2. Ray, J., et al., October-December 1988, "VLBI Tracking of the TDRS," *The Journal of the Astronautical Sciences*, Vol. 36, No. 4, pp. 347-364.
3. Leeuwen, A. V., E. Rosen, and L. Carrier, 1980, "The Global Positioning System and its Application in Spacecraft Navigation," Washington, D.C.: The Institute of Navigation, reprints from *Navigation*, Vol. I.
4. Potash, R., et al, September 1989, *Advanced Tracking Systems Design and Analysis*, CSC/TM-88/6060.
5. Tucci, L., 28 March - 3 April 1994, "Teledesic System Proposal Awaits FCC Approval," *Space News*, Vol. 5, No. 13.
6. Long, A. C., et al (ed.), July 1989, *Goddard Trajectory Determination System (GTDS) Mathematical Theory, Revision 1*, FDD/552-89/001, Greenbelt, MD: Goddard Space Flight Center.
7. Pavloff, M. S., September 1993, *A Monte Carlo Tool for Simulation of Satellite Orbit Determination by Radio Interferometry*, Cambridge, MA: The Massachusetts Institute of Technology, Master's Thesis, Department of Aeronautics and Astronautics.
8. Bulirsch, R., and J. Stoer, 1966, "Numerical Treatment of Ordinary Differential Equations by Extrapolation Methods," *Numerische Mathematik*, Vol. 8, pp. 1-13.
9. Stoer, J., and R. Bulirsch, 1980, *Introduction to Numerical Analysis*, New York: Springer-Verlag Inc.
10. Pavloff, M. S., September 1992, *Analysis of Orbit Prediction Algorithms for the Universal Modem System*, WP-92B0000263V1, Bedford, MA: The MITRE Corporation.
11. Whitney, A. R., January 1974, *Precision Geodesy and Astrometry Via Very Long Baseline Interferometry*, Cambridge, MA: The Massachusetts Institute of Technology, PhD Dissertation, Department of Electrical Engineering.
12. Edwards, C. D., "Angular Navigation on Short Baselines Using Phase Delay Interferometry," *IEEE Transactions on Instrumentation and Measurement*, Vol. 38, No. 2, April 1989.
13. Edwards, C. D., "Development of Realtime Connected Element Interferometry at the Goldstone Deep Space Communications Complex," AIAA 90-2903, *AIAA/AAS Astrodynamics Conference*, August 1990.
14. Treuhaft, R. N., and G. E. Lanyi, "The Effect of Wet Troposphere on Radio Interferometric Measurements," *Radio Science*, Vol. 22, No. 2, March-April 1987, pp. 251-265.
15. Edwards, C. D., "The Effect of Spatial and Temporal Wet-Troposphere Fluctuations on Connected Element Interferometry," TDA Progress Report 42-97, January-March 1989.
16. Gaffney, L. M., et al, February 1994, *A Reevaluation of Selected Mobile Satellite Communications Systems: Ellipso, Globalstar, IRIDIUM, and Odyssey*, MTR-93B0000157, Bedford, MA: The MITRE Corporation.

Evaluation of Semiempirical Atmospheric Density Models for Orbit Determination Applications*

C. M. Cox, R. J. Feiertag, and D. H. Oza
Computer Sciences Corporation (CSC)
Lanham-Seabrook, Maryland, USA

C. E. Doll
National Aeronautics and Space Administration (NASA)
Goddard Space Flight Center (GSFC)
Greenbelt, Maryland, USA

Abstract

This paper presents the results of an investigation of the orbit determination performance of the Jacchia-Roberts (JR), Mass-Spectrometer-Incoherent-Scatter-1986 (MSIS-86), and Drag-Temperature-Model (DTM) atmospheric density models. Evaluation of the models was performed to assess the modeling of the total atmospheric density. This study was made generic by using six spacecraft and selecting time periods of study representative of all portions of the 11-year solar cycle. Performance of the models was measured for multiple spacecraft, representing a selection of orbit geometries from near-equatorial to polar inclinations and altitudes from 400 kilometers to 900 kilometers. The orbit geometries represent typical low Earth-orbiting spacecraft supported by the Goddard Space Flight Center (GSFC) Flight Dynamics Division (FDD).

The best available modeling and orbit determination techniques using the Goddard Trajectory Determination System (GTDS) were employed to minimize the effects of modeling errors. The latest geopotential model available during the analysis, the Goddard Earth Model-T3 (GEM-T3), was employed to minimize geopotential model error effects on the drag estimation. Improved-accuracy techniques identified for TOPEX/Poseidon orbit determination analysis were used to improve the Tracking and Data Relay Satellite System (TDRSS)-based orbit determination used for most of the spacecraft chosen for this analysis.

This paper shows that during periods of relatively quiet solar flux and geomagnetic activity near the solar minimum, the choice of atmospheric density model used for orbit determination is relatively inconsequential. During typical solar flux conditions near the solar maximum, the differences between the JR, DTM, and MSIS-86 models begin to become apparent. Time periods of extreme solar activity, those in which the daily and 81-day mean solar flux are high and change rapidly, result in significant differences between the models. During periods of high geomagnetic activity, the standard JR model was outperformed by DTM. Modification of the JR model to use a geomagnetic heating delay of 3 hours, as used in DTM, instead of the 6.7-hour delay produced results comparable to or better than the DTM performance, reducing definitive orbit solution ephemeris overlap differences by 30 to 50 percent. The reduction in the overlap differences would be useful for mitigating the impact of geomagnetic storms on orbit prediction.

1.0 Introduction

Orbit determination for spacecraft whose perigee heights are less than 2000 kilometers (km) requires a comprehensive atmospheric density model because atmospheric drag effects exert significant perturbation forces on spacecraft at these altitudes. Currently, the Goddard Trajectory Determination System (GTDS) provides the user with two atmospheric density models. One model is the Jacchia 1970 model (Reference 1) with analytical modifications given by Roberts (Reference 2), also referred to as the Jacchia-Roberts (JR) model. The JR model was updated to reflect the Jacchia 1971 model constants (Reference 3). The other model is the modified Harris-Priester (HP) model (Reference 4). At the current time, the JR model is used operationally by the Goddard Space Flight Center (GSFC) Flight Dynamics Division (FDD).

Over the past few years, other atmospheric density models, notably the Drag-Temperature Model (DTM) (Reference 5) and the Mass-Spectrometer-Incoherent-Scatter-1986 (MSIS-86) (Reference 6) atmospheric density model, have been constructed based on data unavailable to the JR and HP models and were expected to perform better under

* This work was supported by the National Aeronautics and Space Administration (NASA)/Goddard Space Flight Center (GSFC), Greenbelt, Maryland, under Contract NAS 5-31500.

varying conditions of solar, geomagnetic, and seasonal-variational activity. It is of interest to evaluate these atmospheric models to determine their potential roles in supporting orbit determination efforts in the GSFC Flight Dynamics Facility (FDF), particularly in future mission planning. It was also desirable to test these models in GTDS where an evaluation of model performance could be ascertained by trending of the GTDS solution fit parameters, such as weighted root-mean-square (WRMS) residuals, estimated drag correction factors, and definitive ephemeris overlap comparisons, under various solar and geomagnetic conditions, orbit geometries, and spacecraft area and ballistic coefficients.

1.1 Overview

GTDS is used for current operational orbit determination support by the GSFC FDD. GTDS employs a batch-least-squares algorithm which estimates the set of orbital elements, force modeling parameters, and measurement-related parameters that minimizes the sum of the squared differences between observed and calculated values of selected tracking data measurements over a solution arc (Reference 7). Of interest for this study is the ability of GTDS to estimate a drag scaling parameter ρ_1 , defined by

$$\vec{F}_D = -\frac{1}{2} C_D \rho \vec{V} |\vec{V}| A (1 + \rho_1)$$

where

- ρ = density of atmosphere surrounding the spacecraft
- ρ_1 = drag scaling parameter, here assumed to be a constant
- C_D = coefficient of drag
- A = cross-sectional area of spacecraft
- V = velocity of spacecraft relative to local atmosphere

Assuming that the solar flux and geomagnetic index (GMI) input values are correct and that the ballistic coefficient is calibrated, then the estimated ρ_1 values should be near zero if the model correctly accounts for the density. The density model that yields the smallest average ρ_1 value would generally be assumed to be the most accurate model. A model that accurately describes the density magnitudes and variations over any given set of solutions should result in minimal definitive ephemeris overlap comparisons. Higher overlap comparison values would represent poorer model performance. Also, if a model accurately describes the density magnitudes and variations over any given set of solutions, then the WRMS values of the solutions should be reduced for each spacecraft. Higher WRMS values for each individual spacecraft would represent poorer model performance. Finally, all results were scrutinized for consistency with the predicted model behavior as determined from comparisons of the densities produced by the models.

1.2 Summary of the Models

Atmospheric models are formulated using theoretical and semiempirical methods to obtain equations interrelating the properties of the atmosphere. As accuracy requirements increase, greater reliance is placed on empirical techniques. Dynamic models, also called time-varying models, attempt to predict the structure of the atmosphere in space and time as the atmosphere responds to varying conditions. Changing atmospheric structure is attributable to solar, geomagnetic, diurnal, semiannual, seasonal-latitudinal, and unpredicted day-to-day variations (Reference 8).

The era of semiempirical models began with the Jacchia 1965 model (Reference 9), a dynamic model, where the prime data were derived from atmospheric drag on satellites. Although the Jacchia model was built around a static model derived by integration of the diffusion equations, thermospheric variations were introduced by use of empirical formulas. The MSIS series of models began with the analysis of atmospheric composition data from the mass spectrometer onboard the Orbital Geophysical Observatory-6 (OGO-6) and a comparison of these data with data derived from a ground-based radar incoherent scattering technique. The MSIS-77 model (Reference 10) eventually gave rise to both the MSIS-86 and DTM models. All are based on the Bates type of analytic temperature profile with boundary conditions on temperature and composition given by spherical harmonic expansions that have been fit to in situ measurements. Table 1 summarizes some major features of the models evaluated here.

Table 1. Features of the JR, MSIS-86, and DTM Models

Model Features	Jacchia-Roberts (Updated to Jacchia 1971 Standard)	MSIS-86	DTM
Variations with solar flux	Daily and 81-day centered average	Daily and 81-day centered average	Daily and 81-day centered average
Geomagnetic heating delay	6.7 hours	0-59 hours, with local variations	3 hours
Density for each constituent gas	Only for total	Yes	Yes
Local variations in density	No	Yes, by constituents	Yes, by constituents
Diurnal variations	Yes	Yes, by constituents	Yes, by constituents
Semiannual variation	Yes	Yes, by constituents	Yes, by constituents
Seasonal latitudinal variations of lower thermosphere boundary	Limited to heights from 90-120 km	Yes, expressed as spherical harmonics	Yes, expressed as spherical harmonics
Seasonal latitudinal variations of helium	Yes	Yes	Yes
Hydrogen effects (important above 1200 km)	No	Yes	Yes

In general, the best data coverage is in the 150-km to 600-km range. Jacchia does have some data from higher altitudes; however, in general, reliable data outside this range are very sparse, and density extrapolations based on several assumptions become increasingly inaccurate for all models as altitudes vary from this region.

1.3 Direct Comparison of the Models

Atmospheric densities predicted by the JR, HP, and MSIS-86 models at various altitudes for common input values of solar and geomagnetic activity were compared for June 22, 1992. The solar activity is characterized by the 10.7-centimeter solar flux, designated in this paper as $F_{10.7}$ (with implied units of 10^{-22} watts per meter² per hertz). The geomagnetic activity is characterized by the K_p and A_p geomagnetic indices (unitless, where K_p values are expressed in a logarithmic scale and A_p values are expressed in a linear scale). Analysis (Reference 11) revealed that the local atmospheric density variations between the MSIS-86 and JR models ranged between -40 percent and +80 percent for low solar activity ($F_{10.7} = 100$, $K_p = 2$) and between -40 percent and +40 percent for high solar activity ($F_{10.7} = 200$, $K_p = 2$). These differences represent many subtle differences among the models, the most significant local variation being in the behavior of the diurnal bulge. As altitudes increase, the diurnal bulge movement is generally southward and is primarily related to the seasonal-latitudinal helium effect, which generally dominates at altitudes above 500 km, where helium flows toward the winter pole.

Differences between static global averages of densities produced by the JR and MSIS-86 models are less than 15 percent during low solar activity time periods ($F_{10.7} = 100$, $K_p = 2$). The differences are most pronounced for the averages representing polar orbits, where values just under 25 percent were observed. At higher solar flux values ($F_{10.7} = 200$, $K_p = 2$) and altitudes above 400 km, MSIS-86 predicts smaller densities than JR. Increasing GMI ($F_{10.7} = 200$, $K_p = 5$) results in a similar effect.

Average density plots as a function of time (for altitudes of 300 km, 700 km, and 1300 km) show marked differences between the models, particularly in response to GMI fluctuations. The JR model employs a single K_p value 6.7 hours prior to the current time, whereas the MSIS-86 model employs 21 3-hour A_p values spanning 59 hours prior to the desired time. Comparison of the time-dependent densities reveal that MSIS-86 and JR are similar in density magnitude in the lower and middle altitudes for moderate GMI activity but tend to have the strongest reactions to high GMI activity in the middle to high altitudes. At high altitudes, JR densities are always greater than MSIS-86 densities due to a spiking effect in JR, where the tendency is for JR to exhibit a rapid and large peak density spike and for MSIS-86 to display a broad-based spike. The timing of the MSIS-86 density peak precedes the JR peak by approximately 6 hours. In general, the JR model response to solar and geomagnetic activity was greater than that of the MSIS-86 model. Overall, the largest difference in the models was in their reaction to high GMI activity conditions, although their reactions to the solar flux also differed. The large differences observed in the densities produced by the different models can have a significant effect on areas such as mission planning, where the density is important in determining orbit decay rates.

Table 4. Parameters and Options Used in the GTDS Solutions

Orbit Determination Parameter or Option	User Spacecraft	TDRS
Estimated parameters	Orbital state, ρ_1 , and station measurement biases (USO bias and drift, COBE only)	Orbital state, coefficient of solar radiation pressure (C_R), BRTS range bias
Integration type	Cowell 12th order	Cowell 12th order
Coordinate system of integration	Mean of J2000.0	Mean of J2000.0
Integration step size (seconds)	60 seconds	600 seconds
Tracking measurements	TDRSS two-way Doppler (TD2S) TDRSS two-way range (TR2S) TDRSS one-way Doppler (TD1S) Ground S-band range rate (URDF)	BRTS two-way range
Data span	2 days (4 for COBE)	See text
Data rate	1 per 10 seconds	1 per 10 seconds
Editing criterion	3σ Central angle to local horizon	3σ
Measurement weight sigmas	TD2S: 0.25 hertz TR2S: 30 meters TD1S: 0.13 hertz URDF: 10 centimeters/second	10 meters
Satellite area model (all constant)	COBE: 17.8 meters ² ERBS: 4.7 meters ² HST: 74.0 meters ² LA4: 12.3 meters ² LA5: 12.7 meters ² SMM: 17.5 meters ²	40 meters ²
Satellite mass	COBE: 2155.00 kilograms ERBS: 2116.00 kilograms HST: 11328.00 kilograms LA4: 1900.32 kilograms LA5: 1913.25 kilograms SMM: 2315.59 kilograms	TDRS-4 ~ 1900 kilograms TDRS-3 ~ 1990 kilograms TDRS-1 ~ 1730 kilograms
Geopotential model	50 x 50 GEM-T3	20 x 20 GEM-T3
Atmospheric density model	JR, MSIS-86, DTM	N/A
Solar and lunar ephemerides	DE 200	DE 200
Coefficient of drag (C_D)	2.2 (2.3 for COBE)	N/A
User-spacecraft antenna offset	Constant radial	No
Tropospheric refraction correction	Yes	Yes
Ionospheric refraction correction		
Ground-to-spacecraft	Yes	Yes
Spacecraft-to-spacecraft	No (central angle edit instead)	N/A
Polar motion correction	Yes	Yes
Solid Earth tides	Yes	Yes

NOTE: GEM = Goddard Earth Model
DE = Developmental Ephemeris
LA = Landsat
N/A = not applicable
URDF = unified S-band range differencing
USO = ultrastable oscillator

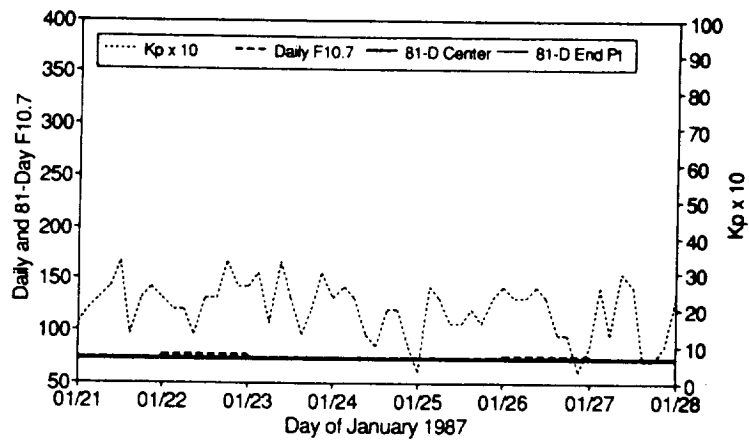


Figure 1. Solar Flux and GMI for Period A

Table 5. Summary of Orbit Determination Solution Results for Period A

Spacecraft	Density Model	ρ_1	WRMS	Overlap MPD (meters)
ERBS	JR	-0.01 ± 0.22	0.21 ± 0.04	23.5 ± 6.6
	MSIS-86	-0.07 ± 0.25	0.21 ± 0.04	23.5 ± 6.6
	DTM	-0.24 ± 0.18	0.21 ± 0.04	23.5 ± 6.6
Landsat-5	JR	-0.01 ± 0.31	0.21 ± 0.05	27.7 ± 10.9
	MSIS-86	-0.01 ± 0.31	0.21 ± 0.05	27.3 ± 10.3
	DTM	-0.16 ± 0.26	0.21 ± 0.05	27.3 ± 10.5
SMM	JR	-0.27 ± 0.04	0.26 ± 0.03	26.7 ± 7.8
	MSIS-86	-0.14 ± 0.03	0.24 ± 0.02	23.9 ± 9.2
	DTM	-0.37 ± 0.02	0.25 ± 0.02	24.6 ± 9.3

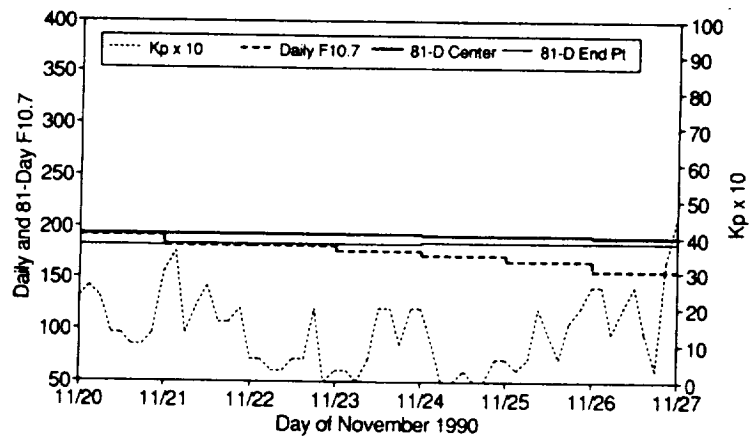


Figure 2. Solar Flux and GMI for Period B

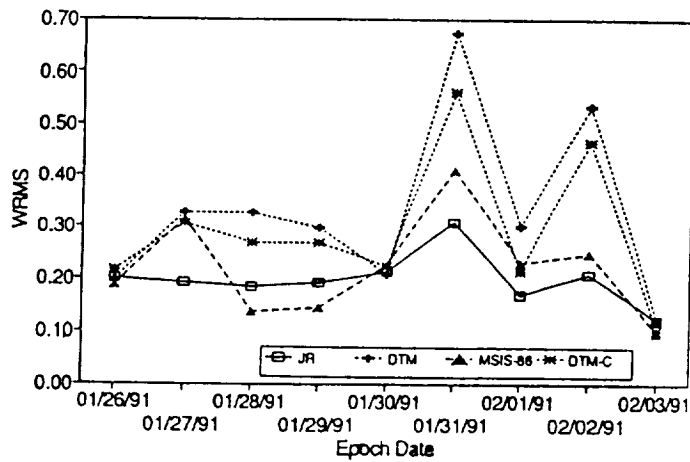


Figure 6. ERBS Solution WRMS Results for Period C

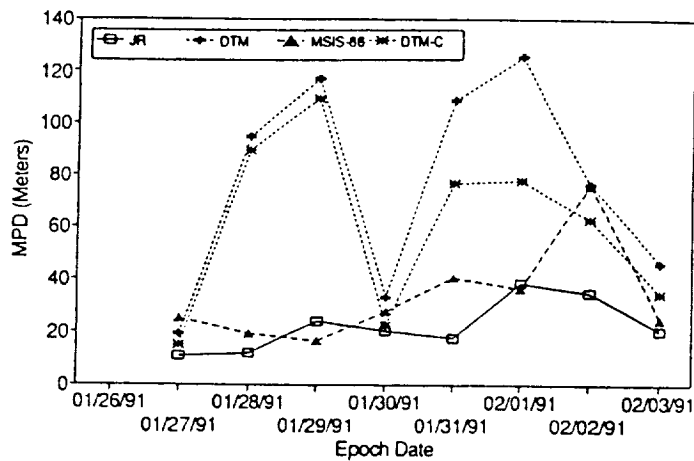


Figure 7. ERBS Solution Overlap MPD Results for Period C

Table 7. Summary of Orbit Determination Solution Results for Period C

Spacecraft	Density Model	ρ_1	WRMS	Overlap MPD (meters)
COBE	JR	-0.21 ± 0.04	0.22 ± 0.02	30.4 ± 12.4
	MSIS-86	-0.01 ± 0.06	0.23 ± 0.01	41.8 ± 17.2
	DTM	-0.82 ± 0.34	0.36 ± 0.07	103.4 ± 34.1
	DTM-C	-0.14 ± 0.15	0.32 ± 0.04	82.4 ± 21.8
ERBS	JR	-0.08 ± 0.05	0.20 ± 0.05	22.4 ± 9.3
	MSIS-86	-0.04 ± 0.08	0.22 ± 0.09	33.3 ± 17.7
	DTM	-0.50 ± 0.38	0.33 ± 0.16	77.6 ± 37.9
	DTM-C	-0.07 ± 0.18	0.29 ± 0.13	61.2 ± 31.6
HST	JR	-0.24 ± 0.05	0.28 ± 0.10	39.6 ± 24.0
	MSIS-86	-0.13 ± 0.05	0.28 ± 0.09	50.8 ± 36.6
	DTM	-0.27 ± 0.26	0.55 ± 0.31	115.5 ± 84.5
	DTM-C	-0.20 ± 0.12	0.45 ± 0.24	85.1 ± 70.3
Landsat-4	JR	-0.23 ± 0.04	0.17 ± 0.09	21.5 ± 7.9
	MSIS-86	-0.00 ± 0.10	0.19 ± 0.10	37.9 ± 23.9
	DTM	-0.60 ± 0.42	0.26 ± 0.15	87.4 ± 45.4
	DTM-C	-0.03 ± 0.20	0.24 ± 0.12	69.3 ± 32.2

Overall, the JR and MSIS-86 models were comparable in performance, while both versions of the DTM model resulted in the worst WRMS and overlap MPD values, on average. All the models had some difficulty with the GMI activity on February 1. Ranked best to worst were JR, MSIS-86, the modified DTM, and the implemented DTM. For all models, the peak solar flux time period is the worst; however, both DTM versions produced overlap differences greater than 200 m (the mission requirement) for HST near the GMI activity on February 1 (see Figure 8).

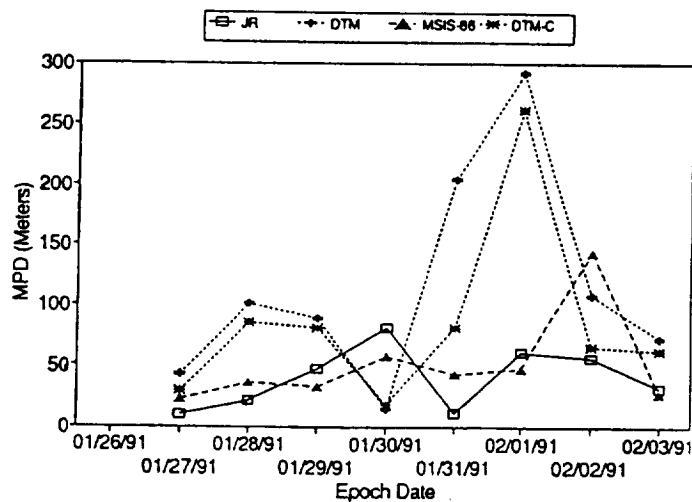


Figure 8. HST Solution Overlap MDP Results for Period C

The ρ_1 values resulting from the originally implemented DTM model based on the 81-day endpoint average solar flux are significantly higher than the JR and MSIS-86 ρ_1 values, while the modified DTM model using the 81-day centered average solar flux resulted in an average ρ_1 comparable to JR and MSIS-86. Daily trends for the solved-for JR and MSIS-86 ρ_1 values are nearly constant. The DTM ρ_1 values start near 0, peak at approximately 0.7 for HST (higher for the other spacecraft), and then return to the -0.2 to 0.2 range. The modified DTM model showed a similar peak; however, the relative height of the peak from the base was only half that seen in the implemented model. The atmospheric density modeled by the DTM model was consistently low during the peak in the daily solar flux activity, as indicated by the ρ_1 trends in both of the DTM cases. This is consistent with a situation in which a portion of the daily solar flux is applied as a daily difference from the mean, as opposed to being correctly applied as part of the mean value. The mean solar flux has a greater effect on the resulting density than the daily contribution. During this time period, the use of an 81-day endpoint-averaged $F_{10.7}$ value will result in a significant portion of the solar flux during the peak activity being applied as the daily solar flux input, resulting in a lower density. The fact that the phenomenon is still apparent with the modified DTM indicates that the DTM model may not handle extreme solar flux input values as well as the JR or MSIS-86 models.

3.4 Period D: Effects of Geomagnetic Activity

Period D was chosen from a time period in which the daily and average solar flux values were behaving in the nominal 27-day period pattern, as in period B, but also included extremely high geomagnetic activity. As shown in Figure 9, the average solar flux was approximately 200, while the daily value was approximately 240, near the maximum of the current 27-day solar rotation. In general, GMI activity was very high, with K_p actually reaching 8.7 (9.3 is the nominal maximum on the logarithmic K_p scale) on one occasion. The behavior of the atmospheric models during such geomagnetic storms is important because the ability or inability to accurately model GMI activity effects can affect the orbit determination and prediction process adversely, as has been observed during the operational and TDRSS Onboard Navigation System (TONS) experiment use of the JR model (Reference 13).

Based on the generally good performance of the DTM model during this period, a second set of results was generated for the JR model; in this case, the delay in the geomagnetic activity was modified from the original 6.7 hours to

3 hours. This change was made based on previous analysis of the performance of the models (Reference 11), which showed JR to have the longest delay in GMI, and because the value Jacchia applied in the original model was an assumed value meant to reflect an average time for the geomagnetic heating effect (Reference 3). The modified JR model is referred to as the JR-3 model in this paper.

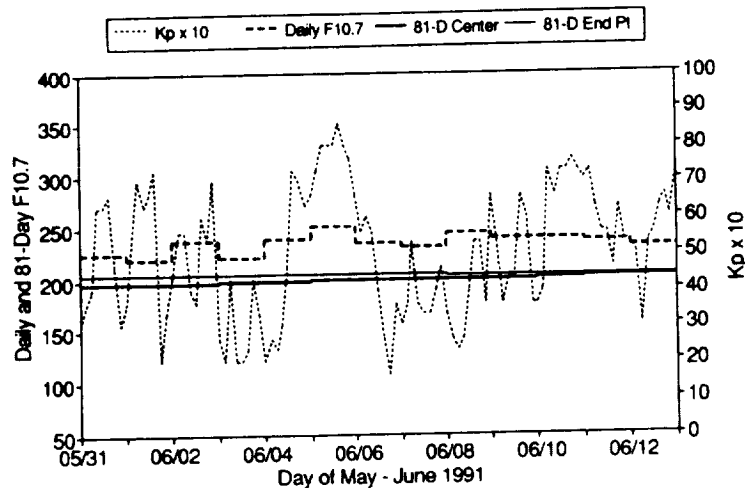


Figure 9. Solar Flux and GMI for Period D

As is evident from Table 8, there were significant variations in the ρ_1 values. The ρ_1 values resulting from the original JR and the modified JR models are comparable. The relatively large negative ρ_1 indicates that the DTM model produced an average density that was too high. The daily trends in the solved-for ρ_1 values, shown in Figure 10 for the ERBS spacecraft, are more active than for other periods, due to the geomagnetic activity. In this case, the MSIS-86 model appears to produce a consistently lower average density than either JR or DTM for those spacecraft that are under 700 km.

Table 8. Summary of Orbit Determination Solution Results for Period D

Spacecraft	Density Model	ρ_1	WRMS	Overlap MPD (meters)
COBE	JR	-0.28 ± 0.06	0.25 ± 0.05	49.1 ± 19.6
	JR-3	-0.28 ± 0.04	0.23 ± 0.02	30.9 ± 11.5
	MSIS-86	-0.18 ± 0.06	0.20 ± 0.02	28.0 ± 6.6
	DTM	-0.16 ± 0.06	0.21 ± 0.01	19.1 ± 5.9
ERBS	JR	-0.21 ± 0.10	0.22 ± 0.08	58.7 ± 56.4
	JR-3	-0.20 ± 0.06	0.20 ± 0.04	33.0 ± 27.2
	MSIS-86	-0.06 ± 0.09	0.23 ± 0.08	53.3 ± 43.2
	DTM	-0.27 ± 0.06	0.22 ± 0.06	35.8 ± 31.5
HST	JR	-0.37 ± 0.09	0.55 ± 0.19	62.9 ± 47.0
	JR-3	-0.38 ± 0.07	0.45 ± 0.28	49.8 ± 26.3
	MSIS-86	-0.27 ± 0.09	0.50 ± 0.25	77.4 ± 60.5
	DTM	-0.52 ± 0.05	0.35 ± 0.24	51.2 ± 26.8
Landsat-4	JR	-0.29 ± 0.10	0.18 ± 0.05	36.2 ± 13.2
	JR-3	-0.38 ± 0.07	0.16 ± 0.04	31.1 ± 22.2
	MSIS-86	-0.16 ± 0.15	0.17 ± 0.03	37.5 ± 25.7
	DTM	-0.29 ± 0.06	0.17 ± 0.04	33.4 ± 19.4

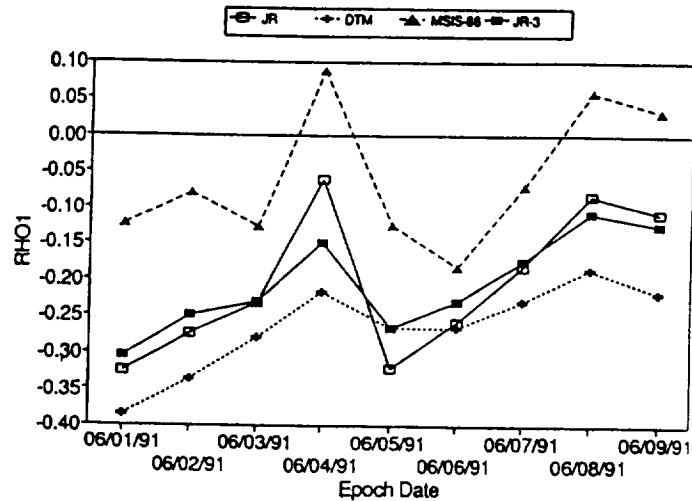


Figure 10. ERBS Solution ρ_1 Results for Period D

The increased WRMS and MPD values during the GMI storm on June 4 through June 7 show that there was sensitivity to the GMI, especially for the models with the longer delay in GMI modeling (JR and MSIS-86). Solution WRMS values showed significant variations between the models and were adversely affected by the GMI activity during this period. Surprisingly, the COBE WRMS values from the DTM model were little affected by the change in GMI activity on June 6 and June 9, unlike the JR and MSIS-86 models, both of which showed increased WRMS values. The modified JR produced individual solution WRMS values similar in trend to DTM.

For all models the worst overlaps are seen at the onset and ends of the large storm from June 5 through June 9. The unmodified JR and MSIS-86 models produced overlaps of approximately 175 meters in the 2σ to 3σ range. The JR-3 MPDs are generally improved over the standard JR model. The Landsat-4 overlap values are significantly lower than the HST and ERBS MPD values for this period due to the absence of the overlap for the June 4 and June 5 solutions because of an orbit maintenance maneuver. This period shows an improvement when the JR-3 model is used instead of the standard JR model; however, it is not clear that it is the best performer when compared with DTM and MSIS 86.

3.5 Long-Term Changes in Density Model Performance

The long-term behavior of the estimated ρ_1 values is of interest because it indicates long-term variations in the modeling of the atmospheric density. To do this accurately, it is necessary to consider the ρ_1 values for those spacecraft for which the ballistic coefficient remained constant. In this study the only spacecraft that fit this requirement are ERBS and COBE. Figure 11 illustrates the average ρ_1 values (Rho1 in Figure 11) for each model used in the ERBS orbit solutions. (JR-3 applies to period D only, while DTM-C applies to period C only). The ρ_1 values for both the JR and MSIS-86 models change significantly depending on the study period. The total range of the JR ρ_1 is from approximately 0 to -0.4, representing up to 67 percent of the actual atmospheric density. DTM varies also, but the total range is somewhat smaller assuming that the DTM using the 81-day centered average solar flux is the correct implementation (for Period C). COBE does not exhibit as wide a range of change in the average ρ_1 , but the average changes by up to 0.3 for DTM. Overall, the change in the average ρ_1 indicates that calibrating the ballistic coefficient for use in long-term ephemeris propagations will need to be a routine process with regular updates. Failure to update the ballistic coefficient periodically will result in propagation errors because there would be no accounting for long-term errors in the atmospheric models.

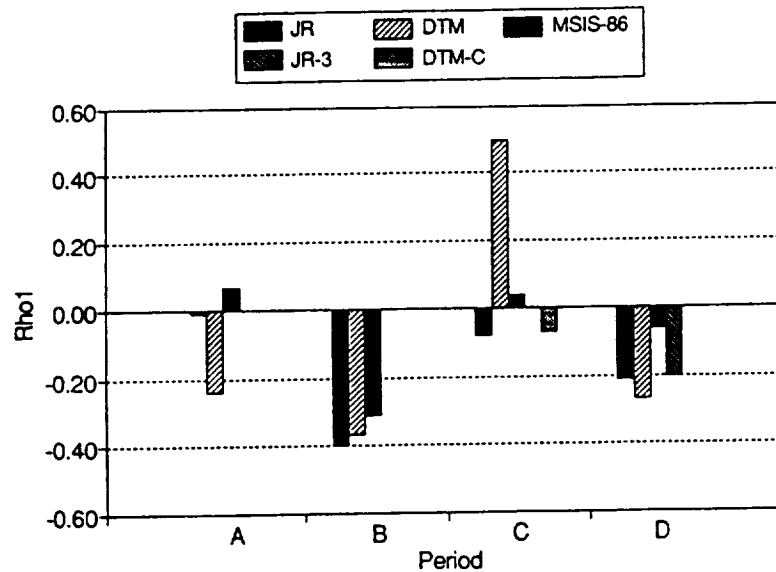


Figure 11. ERBS Long-Term Solution ρ_1 Changes

4.0 Summary and Conclusions

Performance of the three atmospheric density models was measured for multiple spacecraft, representing a selection of orbit geometries from near-equatorial to polar inclination; altitudes from 400 km to 900 km; and inclinations of 28, 57, and 99 degrees. The orbit geometries chosen represent typical low Earth-orbiting spacecraft supported by the GSFC FDD.

Overall, evaluation of the relative performance of the atmospheric models was based primarily on the solution overlap maximum position differences. The solution WRMS values showed less difference between the models, indicating that the relative level of error in the orbit solutions is still high compared with the relative level of improvement between the models. However, in some instances there was significant change in the solution WRMS values. In most cases, the WRMS values and the overlap MPDs result in similar conclusions.

During periods of relatively quiet $F_{10.7}$ activity near the solar minimum, without extreme geomagnetic activity, the choice of atmospheric density model is relatively inconsequential. During typical solar flux conditions near the solar maximum, the differences between the JR, DTM, and MSIS-86 models begin to become apparent, with JR providing marginally improved results. Time periods of extreme solar activity, i.e., those in which the daily and 81-day mean solar flux are high ($F_{10.7}$ greater than 270+) and changing rapidly, result in significant differences between the models. Generally, the JR model performed the best, while DTM performed the worst.

The choice of an 81-day centered average solar flux for use in the DTM model resulted in substantial improvement in performance. This demonstrates that the 81-day centered average solar flux should be used as specified in the original paper for optimal model performance. However, the improvements in the DTM performance resulting from this change were not enough for the model to outperform the JR model.

Geomagnetic activity produced the largest differences in performance of the models. The analysis results show that the standard JR model, which has a 6.7-hour delay for geomagnetic effects, was outperformed by DTM, which has a 3-hour delay. Modification of JR to use a 3-hour delay produces results comparable to or better than the DTM performance, with definitive overlaps typically being reduced by 30 to 50 percent. The reduction in the overlap differences would help mitigate the impact of GMI storms on FDD deliverables. Given that significant GMI activity is present throughout the solar cycle and that the relative contribution of the solar flux to the atmospheric density is greatly reduced during the solar minimum, the ability of an atmospheric density model to accurately reflect the GMI effects is particularly critical.

Under most circumstances, the differences in the orbit determination performances of these models is negligible. Under conditions of unsettled geomagnetic activity, the JR model currently implemented in GTDS did not provide optimal performance. With the exception of COBE, the DTM model appeared to handle GMI activity best for the spacecraft used during that period. Modification of the JR model geomagnetic activity modeling to reflect a 3-hour delay instead of the default 6.7-hour delay produced results that were similar to or marginally better than the DTM results. This modification to the JR model is not in conflict with Jacchia's published works and is further supported by previous FDF analysis (Reference 14)

References

1. Smithsonian Astrophysical Observatory Special Report No. 313, *New Static Models of the Thermosphere and Exosphere With Empirical Temperature Profiles*, L. G. Jacchia, 1970
2. E. R. Roberts, Jr., "An Analytical Model for Upper Atmosphere Densities Based Upon Jacchia's 1970 Models," *Celestial Mechanics*, Vol. 4, No. 3, 1971, pp. 368-377
3. L. G. Jacchia, Smithsonian Astrophysical Observatory Special Report No. 332, *Revised Static Models of the Thermosphere and Exosphere with Empirical Temperature Profile*, May 1971
4. I. Harris and W. Priester, "Time-Dependent Structure of the Upper Atmosphere," *Journal of the Atmospheric Sciences*, Vol. 19, No. 4, 1962, pp. 286-301
5. F. Barlier, C. Berger, J. L. Falin, G. Kockarts, and G. Thuillier, "A Thermospheric Model Based on Satellite Drag Data," Institut D'Aeronomic Spatiale de Belgique, *Aeronomica Acta*, 1977
6. A. E. Hedin, "The Atmospheric Model in the Region 90 to 2000 km," *Advanced Space Research*, Vol. 8, No. 5-6, 1988, pp. 5(9)-5(25)
7. Goddard Space Flight Center, Flight Dynamics Division, FDD/552-89/001, *Goddard Trajectory Determination System (GTDS) Mathematical Theory, Revision 1*, A. C. Long and J. O. Cappellari, Jr., (CSC) and A. J. Fuchs and C. E. Velez (GSFC) (editors), prepared by Computer Sciences Corporation, July 1989
8. National Oceanic and Atmospheric Administration, Prompt Report No. 515, *Solar-Geophysical Data* (Supplement), H. E. Coffey, John A. McKinnon (editors), et al., July 1987
9. L. G. Jacchia, "Static Diffusion Models of the Upper Atmosphere With Empirical Temperature Profiles," *Smithsonian Contribution to Astrophysics*, Vol. 8, 1965, pp. 215-257
10. G. Thuillier, J. L. Falin, and F. Barlier, "Global Experiment Model of the Exospheric Temperature Using Optical and Incoherent Scatter Measurements," *Journal of Atmospheric and Terrestrial Physics*, Vol. 39, 1977, p. 1195
11. Goddard Space Flight Center, Flight Dynamics Division, 553-FDD-93/014R0UD0, *Schatten Solar Flux Prediction and Jacchia-Roberts Atmospheric Density Model Analysis*, C. Cox, R. Feiertag, and M. Radomski (CSC), prepared by Computer Sciences Corporation, September 1993
12. Goddard Space Flight Center, Flight Dynamics Division, 553-FDD-93/086R0UD0, *Orbit Determination Performance Analysis of the Jacchia-Roberts, Mass-Spectrometer-Incoherent Scatter-1986, and Drag-Temperature Model Atmospheric Density Models*, C. Cox and R. Feiertag (CSC), prepared by Computer Sciences Corporation, December 1993
13. Goddard Space Flight Center, Flight Dynamics Division, 553-FDD-93/005R0UD0, *Tracking and Data Relay Satellite System (TDRSS) Onboard Navigation System (TONS) Experiment Second Quarter Status Report*, A. Long et al., prepared by Computer Sciences Corporation, March 1993
14. Computer Sciences Corporation, CSC/TM-80/6173, *An Evaluation of the Geomagnetic Activity Effect in the GTDS Jacchia-Roberts Atmospheric Density Model*, T. Lee and K. Willig, September 1980

Filter Parameter Tuning Analysis for Operational Orbit Determination Support*

J. Dunham, C. Cox, and D. Niklewski
Computer Sciences Corporation (CSC)
Lanham-Seabrook, Maryland, USA

G. Mistretta and R. Hart
National Aeronautics and Space Administration (NASA)
Goddard Space Flight Center (GSFC)
Greenbelt, Maryland, USA

Abstract

The use of an extended Kalman filter (EKF) for operational orbit determination support is being considered by the Goddard Space Flight Center (GSFC) Flight Dynamics Division (FDD). To support that investigation, analysis was performed to determine how an EKF can be tuned for operational support of a set of Earth-orbiting spacecraft. The objectives of this analysis were to design and test a general purpose scheme for filter tuning, evaluate the solution accuracies, and develop practical methods to test the consistency of the EKF solutions in an operational environment. The filter was found to be easily tuned to produce estimates that were consistent, agreed with results from batch estimation, and compared well among the common parameters estimated for several spacecraft. The analysis indicates that there is not a sharply defined "best" tunable parameter set, especially when considering only the position estimates over the data arc. The comparison of the EKF estimates for the user spacecraft showed that the filter is capable of high-accuracy results and can easily meet the current accuracy requirements for the spacecraft included in the investigation. The conclusion is that the EKF is a viable option for FDD operational support.

Introduction

This paper discusses the results of a filter parameter tuning analysis for operational orbit determination support. The filter program used in the analysis was the personal computer (PC)-based Real-Time Orbit Determination/Enhanced (RTOD/E)** System. This program provides orbit determination capabilities for Tracking and Data Relay (TDRS) System (TDRSS)-supported user spacecraft and simultaneously estimates the states for two relay and one user spacecraft using TDRSS and the Bilateral Ranging Transponder System (BRTS) range and Doppler data. The data used in the analysis included one-way return-link Doppler tracking data for those spacecraft equipped with an ultra-stable oscillator (USO), which provides an accurate reference frequency. A more detailed discussion of the analysis is presented in Reference 1.

The analysis had the following three objectives:

- **To design a general purpose scheme** for tuning an extended Kalman filter (EKF) for operational support of a spacecraft
- **To evaluate the accuracies** achievable with RTOD/E against the accuracies attained with the batch least-squares orbit determination program of the Goddard Trajectory Determination System (GTDS)
- **To develop methods to test the consistency** of the EKF solutions independently of external results

*This work was supported by the National Aeronautics and Space Administration (NASA)/Goddard Space Flight Center (GSFC), Greenbelt, Maryland, under Contract NAS 5-31500

**RTOD/E is a copyrighted product of Applied Technology Associates, Inc.

Parameter Tuning

The tunable parameters of RTOD/E are the following:

- **Gauss-Markov process noise model parameters** (base parameter value, decay time, and parameter variances) for the following estimation parameters:
 - **Tracking data biases** on the BRTS and the two-way tracking measurements, with separate biases by data type, estimated separately by data pass
 - **Drag and solar radiation pressure coefficients**
- **Random-walk process noise model parameters for the USO frequency bias** (base parameter value, additive deweighting variance, and associated time interval) and the **constant oscillator frequency drift** (for one-way data only)
- **Gravity auto-correlation parameters** for user spacecraft
- **Measurement noise standard deviation, measurement data rate, and data editing criteria**
- **Omission and commission degree variances** for Earth gravity models and **Error in the Earth's central body term** for the TDRS gravity process noise model

The analysis was designed assuming that the characteristics of a filter that performs orbit estimation satisfactorily are as listed below. A well-tuned filter should:

- Apply the majority of the correction from the first few measurements of a pass to the spacecraft position-velocity states.
- Bound the drag and solar radiation pressure coefficients and data biases to acceptable limits, which can be established from other estimates.
- Allow the estimates for the drag and solar radiation pressure coefficient to vary within a range of approximately 5-20 percent over a period of 1 to several days. Also, do not return to the "base" value but keep the estimate when propagating after the end of a data pass.
- Edit anomalous data.
- Produce realistic estimates of errors, consistent with comparisons with other estimates, as well as consistent with past experience in orbit determination and results from error analysis studies.

A parameter tuning procedure was developed with these characteristics in mind, and results from following the procedure were tested and evaluated as described in the following sections of this paper.

Analysis and Results

The data used for the tunable parameter analysis were TDRSS tracking data collected at GSFC for use in Flight Dynamics Division (FDD) orbit determination for periods from October 1990 to mid-December 1992. The TDRSS user spacecraft were the Earth Radiation Budget Spacecraft (ERBS), the Cosmic Background Explorer (COBE), the Explorer Platform/Extreme Ultraviolet Explorer (EP/EUVE), Landsat-4, and the Ocean Topography Experiment (TOPEX)/Poseidon. These spacecraft were tracked by TDRS-3, -4, and -5 in east-west pairs. This report primarily discusses analysis for orbit determination of ERBS, COBE, EUVE, Landsat-4, and TOPEX supported by TDRS-4 and TDRS-5 for the early weeks of November, 1992. The spacecraft-specific parameters and findings for the RTOD/E results are summarized for the user spacecraft in Table 1 and for the TDRSs in Table 2.

Table 1. Filter Run Descriptions and Parameters for User Spacecraft (1 of 3)

General		
Parameters	Values	Comments
Force Model Parameters:	Reference frame = B1950.0 Solar, lunar third-body perturbations Solar radiation pressure Drag with Jacchia model Integration Step 1 min GEM T3 Gravity Model (50x50)	Solar radiation pressure is computed for all spacecraft; drag only for user spacecraft.
Data-Related Parameters	Editing criteria = 3σ Data available = TDRSS range and Doppler, one-way return-link Doppler, BRTS range and Doppler Data corrections = tropospheric	RTOD/E also can use one-way forward-link Doppler; ionospheric corrections not available, but data biases are an estimation option.
ERBS		
Parameters	Values	Comments
Mission Description:	Altitude = 530 km Inclination = 57 deg Maneuvers w/thrusters = Yes during data span, modeled w/RTOD/E Mass = 2116.0 kg Area = 4.6 m² User tracking data = TDRSS range, Doppler Data span = Nov 5-15	Maneuver November 9 between 19 ^h 08 ^m 49 ^s and 19 ^h 16 ^m 37 ^s , caused some difficulty.
Tunable Parameters: Data Related	Measurement Data Biases Decay time = 10 min $\sigma = 4.5$ m for range and 0.02 Hz for Doppler Data rate = 10 sec	
Tunable Parameters: Other	$C_r = 1.2$, applied C_D Gauss-Markov $\sigma=0.5$, time interval = 14400 min Auto-correlation Values (R, I, C) (min) = (15.226, 0.001, 30.153)	Sensitive to base value of C_D ; change of 30% in value caused estimation failure. Auto-correlation parameters had to be inflated by 10 times nominal values.
Results:	Data edited = 6% Position RSS 1σ estimated error = 9-36 m	Reasonable agreement with GTDS solutions.
EUVE		
Parameters	Values	Comments
Mission Description:	Altitude = 520 km Inclination = 28 deg No orbit maneuvers USO on board Mass = 3245.05 kg Area = 16.3 m² User Tracking data = TDRSS Doppler, one-way return-link Doppler Data span = Nov 5-15	
Tunable Parameters: Data Related	Data biases Decay time = 10 min $\sigma = 0.02$ Hz for Doppler Data rate = 10 sec	
Tunable Parameters: USO	a_1 deweighting $\sigma = 5 \times 10^{-14}$ parts, interval = 10 sec $a_2 = -8.1 \times 10^{-11}$ parts/day	Changing USO a_1 deweighting σ from 1×10^{-11} to 5×10^{-14} parts removed a daily oscillation in S-band Doppler bias solutions.
Tunable Parameters: Other	$C_r = 1.2$, applied C_D Gauss-Markov $\sigma=0.5$, time interval = 14400 min Auto-correlation values (R, I, C) (min) = (1.384, 0.0002, 2.7518)	

Table 1. Filter Run Descriptions and Parameters for User Spacecraft (2 of 3)

EUVE (Cont'd)		
Parameters	Values	Comments
Results:	Data edited = 4% Position RSS 1 σ estimated error = 5-31 m	Sensitive to base value of C_D ; change of 5% in value caused estimation failure. Including/not including the TDRSS range data made a maximum difference of 24 m.
Landsat-4		
Parameters	Values	Comments
Mission Description:	Altitude = 690 km Inclination = 98 deg Maneuvers with thrusters = none during data span Mass = 1869.45 kg Area = 12.2644 m² User Tracking data: TDRSS range, Doppler Data span = Nov 5-15	
Tunable Parameters: Data Related	Data biases Decay time = 10 min $\sigma = 4.5$ m for range; 0.02 Hz for Doppler Data rate = 10 sec	
Tunable parameters: Other	$C_R = 1.5$, applied C_D Gauss-Markov $\sigma=1.0$, time interval = 14400 min Auto-correlation values (R, I, C) (min) = (1.7887, 0.0003, 3.5391)	Insensitive to changes in TDRS C_R Gauss-Markov and GM error parameters, as long as one or the other was set to enlarge the TDRS covariances
Results	Data edited = 2% Position RSS 1 σ estimated error = 4-13 m	
TOPEX/Poseidon		
Parameters	Values	Comments
Mission Description	Altitude = 1336 km Inclination = 66 deg Orbit maneuver capability, none performed during data span USO on board Mass = 2417.2 kg Area = 32 m² User Tracking data = TDRSS Doppler, one-way return-link Doppler Data span = Nov 5-19	Venting was not modeled.
Tunable Parameters: Data Related	Data biases Decay time = 10 min $\sigma = 0.02$ Hz for Doppler Data rate = 20 sec	
Tunable Parameters: USO	a_1 deweighting $\sigma = 2.5 \times 10^{-14}$ parts, interval = 20 sec $a_2 = 1.8 \times 10^{-11}$ parts/day	Slope of estimated S-band Doppler bias indicates a_2 changed to $\approx 2.6 \times 10^{-11}$ parts/day about Nov 11, 1992. Long-term filter behavior sensitive to changes in this term. A daily oscillation was seen in estimated S-band Doppler bias, not removed by changing USO a_1 deweighting σ .
Tunable Parameters: Other	C_R Gauss-Markov $\sigma=0.25$, time interval = 14400 min C_D Gauss-Markov $\sigma=1.0$, time interval = 14400 min Auto-correlation values (R, I, C) (min) = (3.2043, 0.0172, 6.3120)	
Results	Data edited = 3% Position RSS 1 σ estimated error = 1.5-2.2 m	Best results when parameters set for a small position/velocity covariance.

Table 1. Filter Run Descriptions and Parameters for User Spacecraft (3 of 3)

COBE		
Parameters	Values	Comments
Mission Description	Altitude = 880 km Inclination = 99 deg No orbit maneuver capability Mass = 2055. kg Area = 17.8 m² User tracking data: return-link one-way Doppler Data span = Nov 5–15	
Tunable Parameters: Data Related	Data rate = 10 sec	
Tunable Parameters: USO	a₁ deweighting $\sigma = 5.0 \times 10^{-14}$ parts, interval of 10 sec a₂ = -3.0^{-11} parts/day	S-band Doppler bias estimate improved, but not significantly, by changing a ₁ noise; estimator follows noise in data by changing USO frequency bias estimates.
Tunable parameters: Other	C_R = 1.42, applied C_D Gauss-Markov $\sigma=0.5$, time interval = 14400 min Auto-correlation values (R, I, C) (min) = (2.1739, 0.0020, 4.2959)	
Results	Data edited = 3% Position RSS 1 σ estimated error = 6-10 m	S-band Doppler bias estimate of significantly poorer quality than GTDS estimates.

Table 2. Filter Run Descriptions and Tunable Parameters for Relay Spacecraft

Parameters	Values	Comments
Mission Description:	Geosynchronous, low-inclination, tracking relay spacecraft; no orbit maneuvers during data spans	Momentum unloading maneuvers (attitude maneuvers performed with thrusters) occurred.
Force Model Parameters	Integration step 1 min GEM T3 gravity model (8x8)	
Tunable Parameters: Data-Related	BRTS data biases Decay time = 60 min $\sigma = 4.5$ m for range; 0.02 Hz for Doppler Measurement noise Range = 4.0 m Doppler = 0.02 Hz (0.004 for TOPEX)	Measurement noise does not differentiate by type (i.e., range noise applies to all ranges, Doppler noise applies to all Doppler).
Tunable Parameters: Other	C_R Gauss-Markov $\sigma=0.05$, time interval = 14400 min GM error = 5.0	Increasing GM error from 0.05 to 5.0 (2 orders of magnitude) increased TDRS position σ by a factor of 2–3. Trajectories estimated using a C _R noise of 0.3 plus a GM error of 0.05 were very close to estimates with a C _R noise of 0.05 plus a GM error of 5.0. Both terms increase the TDRS position/velocity covariance; decreasing one while increasing the other left the covariance approximately the same.
Results:	Position RSS 1 σ estimated error: 10–30 m (slightly lower with TOPEX/Poseidon)	

RTOD/E computes the user spacecraft position/velocity noise covariance matrix contribution arising from the geopotential errors using the auto-correlated gravity modeling technique described in Reference 2. The gravity error is approximated with an integration of a matrix product that includes a diagonal 3x3 matrix with diagonal elements equal to the constant auto-correlation integrals for the spacecraft. The auto-correlation integrals are computed for each spacecraft based on its approximate orbit and the geopotential model used.

Experiments with the geopotential error process noise matrices for the user spacecraft showed that the computed values for the auto-correlation integrals using this technique produced a spacecraft position-velocity covariance that was small in comparison to the expected errors in the solutions. However, further experimentation showed that better results were obtained for the estimator with a somewhat small covariance. The ERBS processing needed an inflation of the auto-correlation parameters by 10 times to continue past both the November 9 ERBS yaw maneuver and TDRS-4 momentum unloading. ERBS was the only spacecraft for which this inflation was necessary.

Three of the spacecraft in this analysis carried USOs. In RTOD/E, the USO oscillator bias is modeled as a random-walk process with a linear drift term. The bias is propagated as

$$b(t_{i+1}) = b(t_i) + a_2 \cdot \Delta t \quad (1)$$

where

$$\begin{aligned} b(t_{i+1}) &= \text{fractional frequency bias at time } t_{i+1}, \text{ initialized as } a_1 \text{ from the user input} \\ a_2 &= \text{constant oscillator frequency drift, input by the user} \\ t_{i+1}, t_i &= \text{times of current and previous updates, respectively} \\ \Delta t &= t_{i+1} - t_i \end{aligned}$$

The USO frequency bias variance is propagated from t_i to t_{i+1} as

$$P(t_{i+1}) = \hat{P}(t_i) + d \quad (2)$$

where

$$\begin{aligned} \hat{P}(t_i) &= \text{updated bias variance at } t_i \\ P(t_{i+1}) &= \text{predicted bias variance at } t_{i+1} \\ d &= \text{filter deweighting variance} = [N + (\nu/D)]\sigma^2 \\ D &= \text{time interval associated with the deweighting} \\ N &= \text{number of intervals of length } D \text{ in } (t_{i+1} - t_i) \\ \nu &= \text{fractional part of } D \text{ in } (t_{i+1} - t_i) \text{ so that } t_{i+1} - t_i = ND + \nu \\ \sigma &= \text{deweighting standard deviation} \end{aligned}$$

The effect of this random walk model is to add a process noise of σ^2 every D time interval. The values for the USO parameters used for the final EUVE estimates add an error of 5×10^{-14} parts (0.00011 Hz) in a 10-second time interval, which adds a total of approximately 1.0 Hz per day. Similar levels of error were used for TOPEX/Poseidon and COBE.

TOPEX/Poseidon science data processing requires accurate orbit estimation for the ocean topography data analysis. For that reason, highly precise orbit ephemerides (POEs) were computed by the GSFC Space Geodesy Branch from laser ranging and Doppler Orbitography and Radiopositioning Integrated by Satellite (DORIS) tracking data. The POEs provided a highly accurate independent comparison for the RTOD/E solutions. The details of how these solutions were generated are presented in Reference 3. Four cases are extracted and presented in Figure 1 and Table 3 to show the effects of changes in the tunable parameters on the comparisons. The daily root mean square (RMS) of the total position differences between these four cases and the trajectories from the POEs are plotted in Figure 1. These values have been computed on a daily basis, and are plotted for the comparisons made for November 7-18, 1992. Table 3 shows the variations among the tunable parameters for these cases. Of these terms, the solar radiation pressure coefficient (C_R), the GM error, and the range measurement noise primarily affected the TDRSs solutions. The USO noise in Case A, 1×10^{-14} parts, was too small, and excessive one-way data were edited. As seen in Figure 1, after November 8 this case compares the least well with the POE. Case B does not begin to compare well with the POE until November 11. Case C had the best of the comparisons, coming to within 2.3 meters of the POE solution on November 12. Case D did not compare as well as Case C with the POE, but its TDRS trajectories agreed better with the GTDS for TDRS-4 and about as well for TDRS 5. The plot shows the long timespan necessary to distinguish the performance of the filter with different sets of tunable parameters.

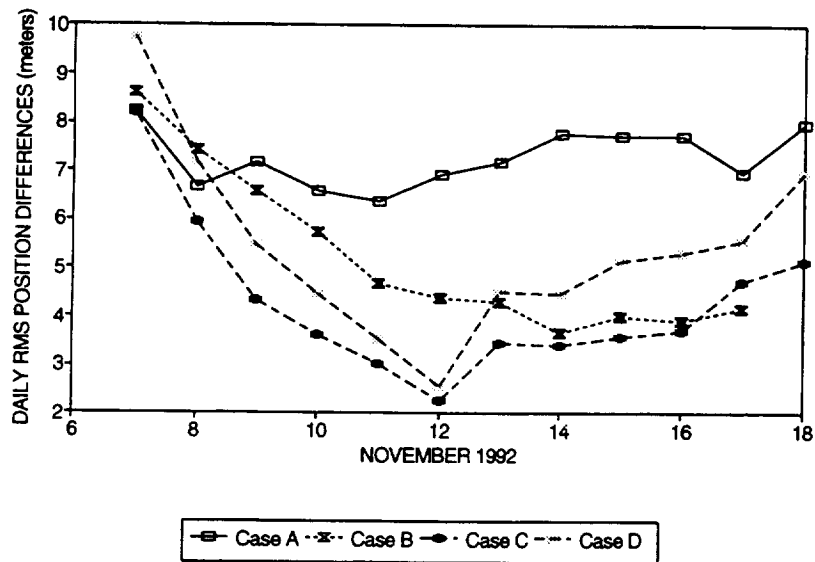


Figure 1. Daily RMS Values From Differences Between RTOD/E and POE TOPEX/Poseidon Trajectories

Table 3. Effects of Changing TOPEX/Poseidon Tunable Parameters

	Case A	Case B	Case C	Case D
C_R Gauss-Markov σ	0.3	0.3	0.3	0.01
GM Error	0.05	0.05	5.0	5.0
a_1 Deweighting σ (10^{-12} parts) Time Interval	0.01 10	0.1 10	0.1 10	0.025 20
a_2 (10^{-11} parts/day)	1.7	1.7	2.0	1.8
BRTS Range Noise	0.4	0.4	4.0	4.0
Comparison With GTDS Solution (best daily RMS)	NA	3 m	2.07 m	3.6 m
Comparison With TDRS GTDS Solutions (best daily RMS)	NA	20 m	18.1 m	17.4 m
Comments	Deletes excessive data	Fair POE comparison	Best POE comparison	Final tunable parameter set

Figure 2 shows the estimated S-band Doppler bias from Case D, and, for comparison, the estimated bias from the GTDS solution from November 7–17. An oscillation with a frequency of .8 to .9 day was present in all of the TOPEX/Poseidon solutions, and was not diminished by decreasing the value of the a_1 deweighting σ . This is in contrast with the EUVE results, where a similar oscillation was removed by decreasing the deweighting σ . Other effects of changes to the tunable parameters on the TOPEX/Poseidon solutions are summarized in Table 1.

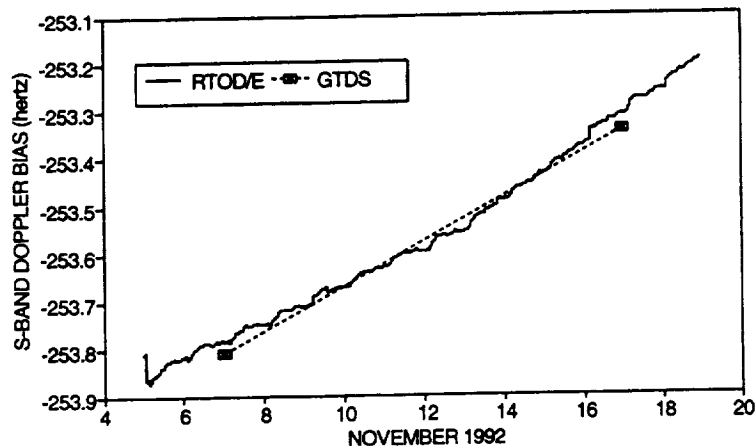


Figure 2. Estimated S-Band Doppler Bias for TOPEX/Poseidon USO From RTOD/E and GTDS

The scheme for setting the tunable parameters which resulted from the analysis is as follows:

1. Obtain the auto-correlation integrals for omission plus commission errors appropriate to the geopotential model, and degree and order of that model, that will be used. Propagate the user and covariance to determine the rate of covariance growth. Also, inspect the TDRS covariance growth to determine if it will be sufficient, or will need an inflation of the GM error. It may be necessary to increase the default auto-correlation integrals if the user spacecraft has an attitude maneuver performed with thrusters or the GM error if one or both TDRSs perform a momentum unloading maneuver (which uses thrusters).
2. Set the user spacecraft drag process noise σ to a value between 0.5 (for drag-perturbed spacecraft such as EUVE) and 1.0 (for spacecraft such as TOPEX in orbits with less drag perturbation), and set the associated Gauss-Markov time interval to a long enough time to make the model effectively a random walk model.
3. Set the TDRS solar radiation pressure process noise standard deviation to a relatively small value (0.05 was one example) and also set the time interval to a large number. This gives C_R estimates that compare well with GTDS estimates for TDRS solutions done with BRTS data only. The only user spacecraft for which C_R was estimated was TOPEX. The process noise standard deviation was set to 0.25, a value that gave results that allowed (along with the drag noise used) RTOD/E to accommodate the anomalous thrusting TOPEX experienced.
4. Set the standard deviations on the biases for BRTS range and Doppler data to accommodate the unmodeled effects of ionospheric refraction and station location errors. The values used in this analysis were 4.5 m for the range and 0.02 Hz for the Doppler. The time interval used was immaterial, since these are local solve-for parameters that are reset to the a priori values at the end of each pass. The biases on the TDRSS range and Doppler are set similarly, except that they are not local parameters in this implementation, and need a time value larger than a pass length, but small enough to return to the a priori before the next pass begins.
5. Set the USO estimation parameters to be commensurate with previous estimates, or the oscillator specifications if no previous estimate exists. The drift needs to be calibrated by evaluating long frequency bias estimates, and changed as necessary.

The appropriate level of the tunable parameters was checked with the assessment criteria, with particular attention to the variances on the estimated parameters.

GTDS Solutions

GTDS was used to compute batch-estimation orbit solutions for the TDRSS user and TDRSs for comparison with the RTOD/E solutions. The user spacecraft orbit determination solutions were computed separately from the TDRS orbit solutions, with all user spacecraft estimation performed with the same TDRS orbits. The TDRS spacecraft orbit determination was performed using techniques identified for the TOPEX/Poseidon analysis described in Reference 3. To improve the estimation accuracy, the TDRS data spans were selected to avoid all maneuvers and momentum unloads. Only BRTS range data were used. The ground tracking [White Sands Ground Terminal (WSGT)] antenna biases were estimated to correct for errors in the calibration of the range-zero sets and the measurement of the applied user and TDRS spacecraft transponder delays. Specific force and observation modeling options used in the analysis are given in Table 4.

In general, in the user spacecraft orbit determination solutions, the state, station range biases or USO transmit frequency and frequency drift biases, and two (sometimes three) drag modeling correction terms were estimated. The TOPEX/Poseidon solutions estimated eight thrust factors, instead of drag, to compensate for an anomalous unmodeled force acting on the spacecraft.

As with the TDRSs, station range biases were estimated for each of the WSGT antennas. The software used for the analysis had limitations (since removed) preventing the use of station range bias solve-fors in conjunction with the USO bias and drift estimation. Therefore, TDRSS range data were not used when USO-based one-way return Doppler data were available.

The EUVE batch estimation options are generally the same as those used in the TDRSS Onboard Navigation System (TONS) experiment for comparison with the TONS filter (Reference 3). In particular, the standard deviations for the included tracking data types are the same as the TONS processing, which differ from the nominal operational values used for the other spacecraft.

The batch orbit determination solution performance was quantified using solution overlaps and data type mean and standard deviations of the solution residuals. User solutions were overlapped by 50 percent of the data span, with the exceptions of COBE, which had no overlapping solutions, and ERBS, which experienced a yaw turn on November 9. TDRS solution ephemeris consistency was measured by comparing a 12-hour predictive extension to the next definitive period.

Figure 3 shows results of the overlap comparisons of the GTDS solutions for Landsat-4, EUVE, and ERBS. These solutions were 2-day arcs with 1-day overlaps, except for ERBS, around the yaw maneuver on November 9. The TOPEX comparison shown in Figure 3 is against the POE. The COBE solution was a single arc through the entire data span, so there were no overlaps.

Assessment Summary

The assessment criteria and results are summarized in the following:

Anomalous behavior: Criteria: The anomalies noted were divergence, editing of much or all of the tracking data for a satellite, or extreme values of C_D or C_R . Results: Anomalous data editing was often traced to inappropriate values of C_D , or to unmodeled attitude maneuvers of the user or TDRS spacecraft.

Comparison with external solutions: Criteria: Comparisons were made with GTDS solutions and with precision ephemerides provided for TOPEX. When the RTOD/E and GTDS solutions are made on the same basis (same reference frame, same atmospheric model data, and same Earth orientation data), the results should agree to within their cumulative accuracies. Results: All of the user- and TDRS-estimated trajectories from the final parameter set for the November data have been compared to the companion GTDS solutions. The comparisons for TOPEX were

Table 4. Parameters and Options Used in the GTDS Solutions

Orbit Determination Option	User Spacecraft	TDRS
Estimated Parameters	Orbital state: position and velocity Drag ($a_{1,2}$): all except TOPEX Thrust (8 constants): TOPEX C_R : COBE and TOPEX WSGT range biases: ERBS and Landsat-4 USO bias and drift: COBE, EUVE and TOPEX	Position and velocity C_R WSGT range biases
System of Integration	Mean-of-J2000	Mean-of-J2000
Integration Step Size	60 sec	600 sec
Tracking Measurements	Two-way Doppler (TD2S): all except COBE Two-way range (TR2S): ERBS and Landsat-4 One-way Doppler (TD1S): COBE, EUVE, TOPEX	BRTS range
Data Span	2 Days: ERBS, Landsat-4, and EUVE 8 Days: COBE 10 Days: TOPEX	See text
Data Rate	1 per 10 sec (1 per 60 sec for TOPEX)	1 per 10 sec
Editing Criterion	3σ Central angle to local horizon	3σ
Measurement Weight σ	TD2S: .25 Hz (.1 Hz for EUVE) TR2S: 30 m (10 m for EUVE) TD1S: .13 Hz (.075 Hz for EUVE)	10 m
Area	COBE: 17.8 m ² ERBS: 4.7 m ² Landsat-4: 12.3 m ² EUVE: 16.3 m ² TOPEX: variable mean area model	40 m ²
Mass	COBE: 2155.00 kg ERBS: 2116.00 kg Landsat-4: 1869.45 kg EUVE: 3243.05 kg TOPEX: 2417.20 kg	Approximately 1950 kg, as appropriate for fuel state
C_D	2.2 (2.3 for COBE)	N/A
C_R	COBE: Estimated ERBS: 1.2 Landsat-4: 1.5 EUVE: 1.2 TOPEX: Estimated	Estimated
Atmospheric Density Model	Jacchia-Roberts	N/A
Geopotential Model	GEM-T3 50x50	GEM-T3 20x20
Ionospheric Refraction Ground-to-S/C S/C-to-S/C	Yes No (central angle edit instead)	Yes N/A
Antenna Offset	Constant radial—cobe: -1.0 m (positive up) ERBS: 0.0 m Landsat-4: 2.5 m EUVE: 0.0 m TOPEX: 3.0 m	No
Tropospheric Refraction	Yes	Yes
Polar Motion	Yes	Yes
Solid Earth Tides	Yes	Yes

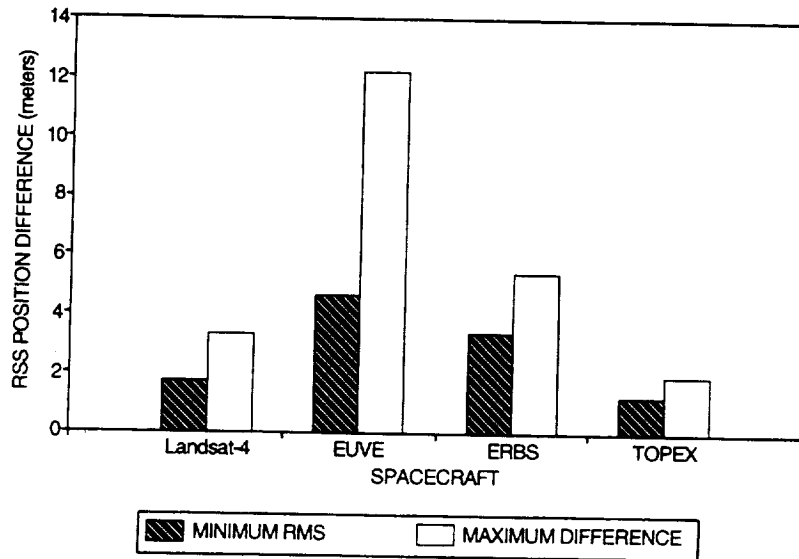


Figure 3. GTDS Overlap Comparisons

consistent with the comparisons with the POE solutions. The comparisons for COBE, EUVE, ERBS, Landsat-4, TDRS-4, and TDRS-5 all were considered reasonable. There was no evidence of a bias in the differences, as they were evenly distributed about zero. Figure 4 shows a plot of the daily RMS values for the differences of the RTOD/E and GTDS solutions for these spacecraft. The COBE estimate shows significantly more disagreement due to poor tracking geometry. Figure 1, given earlier, shows a comparison of RTOD/E and POE results for TOPEX.

Comparison of TDRS solutions: Criteria: Since the same TDRSs are used to support several spacecraft, the various estimates of the same TDRS orbits can be compared. Agreement to within the accuracies of the TDRS solutions (approximately 50 m) is expected from the filter estimates. Results: The TDRS solutions prepared by RTOD/E from the final set of tunable parameters for October and November were compared with TDRS solutions from RTOD/E solutions for other user spacecraft. These generally show mutual agreement to within 50 m (1σ), with some excursions.

C_D values for user spacecraft: Criteria: The GTDS DC solutions were used for comparison of the drag parameter estimates. Results: It was observed that RTOD/E was sometimes quite sensitive to the value for the C_D Gauss-Markov base parameter. Comparisons with the GTDS results were generally acceptable. Figure 5 shows the comparison of the EUVE RTOD/E results with the GTDS estimates.

C_R values for TDRSs: Criteria: The GTDS solutions provide estimates of these values used for comparison. In addition, since the same TDRS will be estimated repeatedly with different spacecraft, the different C_R estimates can be compared, and their mutual agreement used as a measure of filter solution quality. Results: The comparison of the RTOD/E estimates of C_R with the GTDS solutions for the November 12–19 data span showed significantly more variation from RTOD/E than from GTDS. For both the October and November data sets, the RTOD/E solutions showed reasonable mutual agreement.

Biases on the BRTS range: Criteria: A bias in excess of 15 m is unacceptable. Results: Isolated instances of large range biases were observed in otherwise acceptable cases following TDRS momentum unloading maneuvers.

S-band bias: Criteria: The S-band bias is the effect of the USO bias on the one-way return-link Doppler tracking data. The RTOD/E results were compared with GTDS estimates of this bias. Results: The values for the S-band bias were all acceptable. An example was shown in Figure 2. The filter was sensitive to the a_2 constant value (frequency drift). It could not accommodate values in error by 25 percent in long data arcs, and would delete excessive one-way data at the end.

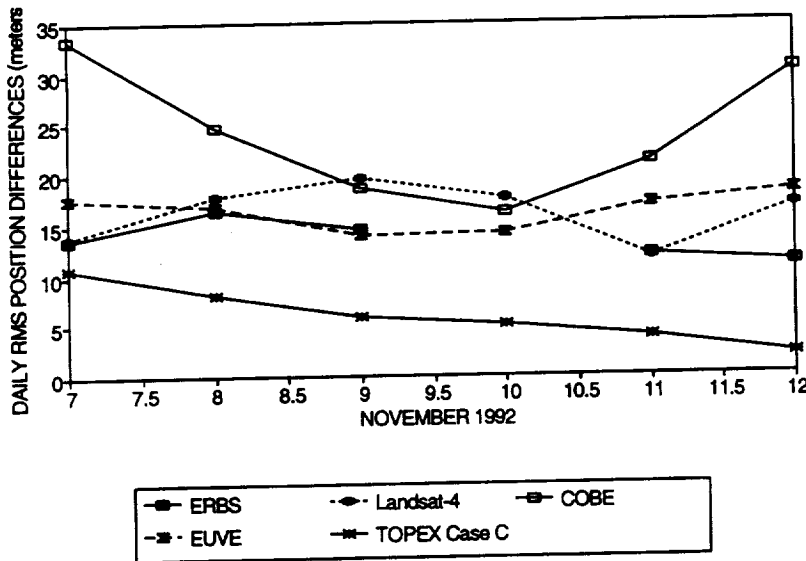


Figure 4. Daily Root-Mean-Square Differences for RTOD/E and GTDS Estimated Trajectories

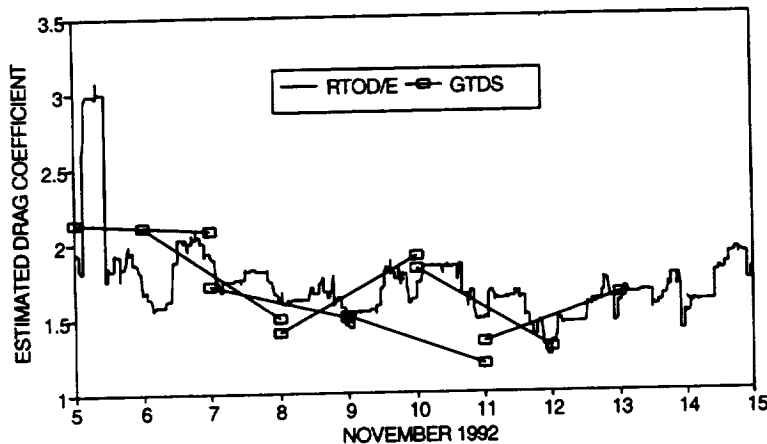


Figure 5. Estimated EUVE C_D From RTOD/E and GTDS

Data statistics: Criteria: The numbers of accepted and rejected observations of valid data are examined after the filter has stabilized, and the residuals are examined to look for any patterns in data rejection. **Results:** Deleting a significant portion of the data or deleting data in specific patterns were found to be good indicators of problems in the solution quality. Solutions with excessive amounts of data deleted did not compare well with the external results.

Covariance magnitudes: Criteria: The standard deviations of the estimated positions, C_D , C_R , and USO bias were examined. These are expected to stay within reasonable values, based on previous experience with orbit determination and orbit determination error analysis. Once the filter has completed the initial stabilization process, the covariance is expected to stay bounded in both maximum and minimum values as long as the data rate and frequency stay approximately the same and there are no spacecraft maneuvers. Unacceptable behavior includes taking extremely small or continuously decreasing values during the entire data span. **Results:** Acceptable values for the covariances were achieved for all parameters. It was observed that the best comparisons were obtained when the covariance was tuned to be somewhat small as judged by comparisons with external solutions, so that the filter did not react rapidly

to new data. Unfortunately, then the covariance does not respond quickly to anomalous events, leading to some cases in which the residuals were outside the acceptance criteria for multiple passes, sometimes rejecting all data and diverging.

Solution propagation: Criteria: Vectors were extracted from the estimated trajectories and propagated for comparison with later estimated trajectories. Changes in the maximum differences can be used to measure the effect of changes to the tunable parameters on the filter. A procedure was developed that automatically generated a 24-hour predicted ephemeris and a definitive ephemeris for this comparison. **Results:** The comparison of the predicted versus the estimated was also a major indicator of the relative merits of the runs. However, it can not be blindly applied, as instances arose in which significant amounts of data were deleted for the day selected for the comparison, producing a very good comparison between the predicted and estimated trajectories—since they were basically both predicted. Also, for some cases in which excessive data were deleted at the end, the comparison was done before that part of the data arc, and did not reveal the problem.

The results for November for each of the user spacecraft from the application of these criteria are summarized in Table 5.

Table 5. Summary of Final Results for November Data

Results	ERBS	EUVE	COBE	Landsat-4	TOPEX/ Poseidon
User Data Edited	6%	4%	<1%	2%	3%
Estimated Position Error (1 σ) (m)					
TDRS 4	19-31	17-32	16-30	14-31	8-12
TDRS 5	11-27	11-27	10-26	9-26	7-19
User S/C	9-36	5-31	5-10	4-13	1.5-2.2
Predicted vs Estimated (m) (24 hours)					
TDRS 4	261	262	226	261	250
TDRS 5	75	106	118	126	109
User S/C	34 (18-Hour)	327	41	53	15
GTDS Solution Comparisons (best RMS, m)					
TDRS -4	26.7	27.8	40.4	16.6	17.4
TDRS -5	8.4	19.9	64.5	11.7	23.4
User spacecraft	11.1	14.0	16.2	11.7	2.47
TOPEX POE Comparison (best RMS, m)					2.26

Conclusions

The objectives of this filter parameter timing analysis were met. (1) A general purpose scheme for tuning the filter for operational support has been developed and tested. (2) Results are presented for the comparison with GTDS solutions, which are in agreement with the accuracy of the estimation as found by comparison with the TOPEX/Poseidon POE solutions. The comparison of the RTOD/E estimates for EUVE, ERBS, COBE, Landsat-4, and TOPEX/Poseidon with external results shows that the filter is capable of quite accurate results, and can certainly meet the accuracy requirements for daily operational support for the TDRSS user spacecraft and the TDRSs. (3) Methods for testing the consistency of the EKF solutions independently of external results have been proposed and tested.

The following is a summary of the results of the tunable parameter analysis for TOPEX/Poseidon, ERBS, EUVE, Landsat-4, and COBE:

- The best TOPEX/Poseidon comparisons with the POE were obtained when the tunable parameters were set to provide a small covariance, equal to about half the accuracy of the estimated trajectory.

- Very long (2–3 weeks as opposed to 3–4 days) estimation spans may be necessary to distinguish among tunable parameter options. The effect of the USO bias drift parameter on the solution, for example, was not evident with short spans.
- All maneuvers, both attitude and orbit, done with thrusters must be accommodated, either by specific use of maneuver modeling, and/or by enlarging the covariance matrix with the tunable parameters for success in estimating the spacecraft trajectory.
- Drag base value, noise, and decay time—Extremely important for drag-perturbed spacecraft. The decay time must be set long enough for this term to act like a random walk. The test filter is not very tolerant of poor guesses for the base value (a priori value). This would not be acceptable for an operational filter, which must accommodate poor initial estimates.
- C_R Gauss-Markov parameters for TDRSs (base value, noise, and decay time)—Physical reasons would imply that the decay time should be set to a long value, so that this model acts more like a random walk than a Gauss-Markov parameter. The C_R Gauss-Markov standard deviation was adjusted until the estimates were in acceptable agreement with the GTDS results.
- Gravity auto-correlation parameters—These directly affect the size of the user covariance in propagation. The tests have included values from 1 to 100 times the base values for a given spacecraft. The most accurate results were obtained with the unscaled nominal. This produces a position/velocity covariance that is somewhat small considering the comparisons with external results.
- Error in GM —This directly affects the size of the TDRS covariances in propagation. The model value for the gravitational model used based on the estimated error in GM ($.005 \text{ km}^2/\text{cm}^3$) is so small that it only adds about a meter over a day of prediction. A value of 5.0 was needed to assist in estimating through TDRS momentum unloading maneuvers.
- Data sampling—Not much of an effect for two-way tracking. The data rate needs to be at least 1-per-20 seconds for 1-way Doppler data for the most accurate results.
- Data editing criteria—Increasing the editing criteria from 3 to 100 or 1000 to get past problems in initialization produced problems with the TDRS solutions (such as spikes in the C_R estimates and exceptionally large range bias estimates) when a bad observation or two was accepted.
- USO bias—RTOD/E appears to estimate the bias with little difficulty for arc lengths of a week or less, but can have difficulty for longer arcs if the drift is not set to a high degree of accuracy. The RTOD/E model cannot accommodate changes in the drift. The bias deweighting factor standard deviation, σ , must be tuned very carefully, in concert with the frequency drift.

Acknowledgments

The authors would like to thank Anne Long and Dipak Oza of CSC for their many helpful discussions and suggestions during the course of this analysis and the preparation of this paper.

References:

1. Goddard Space Flight Center, Flight Dynamics Division, 553-FDD-93/100R0UD0, *Sequential Orbit Determination Final Analysis Report*, M. Nemesure, J. Dunham, D. Nikewski, and D. Hartley (CSC), prepared by Computer Sciences Corporation, March 1993
2. J.C. Wright, "Sequential Orbit Determination With Auto-Correlated Gravity Modeling Errors," *Journal of Guidance and Control*, Vol. 4, Washington: American Institute of Aeronautics and Astronautics, 1981

3. C. Doll et al., "Comparison of TOPEX/Poseidon Orbit Determination Solutions Obtained by the Goddard Space Flight Center Flight Dynamics Division and Precision Orbit Determination Teams," Paper No. AAS 93-265, presented at the AAS/GSFC International Symposium on Space Flight Dynamics, Goddard Space Flight Center, Greenbelt, Maryland, April 26–30, 1993
4. Goddard Space Flight Center, Flight Dynamics Division, 553-FDD-93/005R0UD0, *Tracking and Data Relay Satellite System TDRSS On-Board Navigation System (TONS) Experiment Second Quarter Status Report*, A.C. Long et al. (CSC), prepared by Computer Sciences Corporation, March 1993

Comparison of Kalman Filter and Optimal Smoother Estimates of Spacecraft Attitude*

J. Sedlak

Computer Sciences Corporation (CSC)
Lanham-Seabrook, Maryland, USA

Abstract

Given a valid system model and adequate observability, a Kalman filter will converge toward the true system state with error statistics given by the estimated error covariance matrix. The errors generally do not continue to decrease. Rather, a balance is reached between the gain of information from new measurements and the loss of information during propagation. The errors can be further reduced, however, by a second pass through the data with an optimal smoother. This algorithm obtains the optimally weighted average of forward and backward propagating Kalman filters. It roughly halves the error covariance by including future as well as past measurements in each estimate. This paper investigates whether such benefits actually accrue in the application of an optimal smoother to spacecraft attitude determination. Tests are performed both with actual spacecraft data from the Extreme Ultraviolet Explorer (EUVE) and with simulated data for which the true state vector and noise statistics are exactly known.

1. Introduction

Spacecraft attitude determination and sensor calibration are major functions of the Goddard Space Flight Center's (GSFC) Flight Dynamics Facility (FDF). The problem is to extract information about the system state in the presence of perturbing noise. There are a number of ways to attack the problem. These divide broadly into batch and sequential filter methods. While batch methods have been used extensively in the past, sequential filters are also playing an increasingly important role in FDF operations. In particular, real-time extended Kalman filters are currently in use for the Solar, Anomalous, and Magnetospheric Particle Explorer (SAMPEX), the Extreme Ultraviolet Explorer (EUVE) (prototype only), and the soon-to-be-launched next-generation Geostationary Operational Environmental Satellite-I (GOES-I). These are real-time systems designed to solve only for the attitude and the rate bias on each axis.

More elaborate filters are planned for some future missions, such as the X-Ray Timing Explorer (XTE) and the Submillimeter Wave Astronomy Satellite (SWAS). These will include a sequential filter as the central engine of their Attitude Ground Support Systems (AGSS). Various AGSS subsystems are generally responsible for gyro and sensor calibrations. For XTE and SWAS, the gyro calibration will be performed by the AGSS Kalman filter, simultaneously with the attitude. The filter optionally will solve for elements of an expanded state vector, including rate bias, scale factor corrections, and misalignments.

One obvious deficiency of a sequential filter is that only the final state estimate makes use of data throughout the given data span. The XTE and SWAS software will generate improved attitude estimates for an entire data span by using optimal smoothing. A smoother is a sequential method that makes a second pass through the data, so that all the sensor information is available for estimating the state at each time step. Smoothed estimates can be, in effect, weighted averages of forward and backward propagating filters. The uncertainty in the estimate at each step is reduced, compared to the Kalman filter, since it makes use of future as well as past data.

Thus, there are two new aspects to the planned AGSSs: the noise modeling for the expanded state vector in the context of an extended Kalman filter and the smoother algorithm itself. This paper focuses on the smoother algorithm and does not consider the expanded state. The thrust of current investigations is to verify the filter/smoother design, to experiment with tuning parameters, and to examine the improvements in the estimates. It should be stressed that this work is not intended as a definitive statement about the use of smoothing methods for attitude determination. Rather, as just one part

*This work was supported by the National Aeronautics and Space Administration (NASA)/ Goddard Space Flight Center (GSFC), Greenbelt, Maryland, under Contract NAS 5-31500

of a continuing investigation (see References 1 and 2), it is expected that the smoother results obtained here may be improved in several ways in the future.

The next section presents the extended Kalman filter equations and shows how forward and backward filter results can be combined to form an optimally smoothed estimate. Section 3 discusses some results and comparisons for test cases using EUVE data. The final section gives a summary and conclusions.

2. Theory

As stated above, the smoother can simply form an average of forward and backward filter estimates. What is not obvious is that the optimally smoothed estimate can be written as a linear combination of optimal (i.e., Kalman) filter solutions using only the forward, backward, and smoother error covariance matrices in the weighting coefficients (Reference 3). Conveniently, the smoother error covariance matrix is easily obtainable from the forward and backward filter error covariances.

The starting point for the smoother considered here is the "Unit Vector Filter" (UVF) described in Reference 2. This extended Kalman filter solves for attitude and gyro bias using a particularly simple observation noise model. Onboard measurements of Sun and star unit vectors are assumed to be perturbed by random noise uniformly on all three axes; hence, the sensor noise covariance matrix is a constant times the identity matrix.

For both the UVF and the smoother described below, a distinction must be made between the full 7-component state vector, comprised of the attitude quaternion and the gyro bias vector, and the 6-component error state (Reference 4). The small-angle rotation from the true to the estimated attitude can be written as a 3-component error vector, one dimension less than the 4-component quaternion needed for an unambiguous representation of the attitude in inertial space.

Thus, in outline, the UVF proceeds as follows for either forward or backward processing: The full state vector and the 6x6-dimensional state error covariance matrix are propagated from the current time to the next sensor measurement. A prediction vector, based on the estimated attitude and a reference vector, is subtracted from the observation to obtain a residual vector. The residual, weighted by the Kalman gain matrix, yields the new estimated error state. The propagated quaternion is rotated by the estimated attitude error, and the gyro bias is corrected by the bias error. The error state then is discarded since its information has been incorporated into the full state. Finally, the Kalman gain also is used to update the state error covariance matrix.

Kalman Filter

The state evolution can be integrated over a time step Δt to obtain discrete-step propagation equations. Derivations can be found in Reference 5 and in those previously cited. For the backward filter, the index k increases as the time t_k decreases. The attitude quaternion is propagated as

$$q_{k|k-1} = \left\{ \cos\left(\frac{\theta}{2}\right)I_4 + \frac{1}{\omega_{k,k-1}} \sin\left(\frac{\theta}{2}\right)\Omega(\bar{\omega}_{k|k-1}) \right\} q_{k-1|k-1} \quad (1)$$

where the time interval is $\Delta t = t_k - t_{k-1}$, and

$$\theta = \omega_{k|k-1} \Delta t \quad (2)$$

The $k|j$ notation indicates a quantity estimated using sensor data through time t_j , and propagated (if $k \neq j$) to time t_k .

Equation (1) is approximate in that it assumes the angular rate is constant over Δt . The estimated rate for this interval is the gyro output \bar{u}_k , corrected with the latest bias estimate:

$$\bar{\omega}_{k|k-1} = \bar{u}_k - \bar{b}_{k|k-1} \quad (3)$$

In many cases, \bar{u}_k is an average for the time interval, generated by a rate integrating gyro unit.

The matrix Ω is

$$\Omega(\bar{\omega}) = \begin{bmatrix} 0 & \omega_z & -\omega_y & \omega_x \\ -\omega_z & 0 & \omega_x & \omega_y \\ \omega_y & -\omega_x & 0 & \omega_z \\ -\omega_x & -\omega_y & -\omega_z & 0 \end{bmatrix} \quad (4)$$

The estimated gyro bias propagates as a constant:

$$\bar{b}_{k|k-1} = \bar{b}_{k-1|k-1} \quad (5)$$

The error state is

$$x_k = \begin{bmatrix} \bar{a}_k \\ \Delta \bar{b}_k \end{bmatrix} \quad (6)$$

where the true (but unknown) error rotation vector \bar{a} is related to the true and estimated quaternions by

$$q_k = \delta q_k^{-1} \otimes q_{k|k-1} \quad (7)$$

with

$$\delta q_k^{-1} \approx \begin{bmatrix} -\bar{a}_k/2 \\ 1 \end{bmatrix} \quad (8)$$

The product in Equation (7) is defined so as to combine quaternions in the same order as attitude matrices. Also, the inverse quaternion is used in Equation (7) to simplify signs elsewhere. For brevity, only the first order approximation is shown in Equation (8) and elsewhere for the error quaternion. In practice, one must either add a normalization step or use the full trigonometric relationship in Equation (8).

Similarly, the true gyro bias, its estimate, and the unknown correction are related additively:

$$\bar{b}_k = \bar{b}_{k|k-1} + \Delta \bar{b}_k \quad (9)$$

Although dynamics noise does not affect the mean propagation of the full state described above, it is needed for the error covariance propagation. Perturbations are assumed to enter the problem as zero-mean white noise in the true angular rate

$$\bar{\omega} = \bar{u} - \bar{b} - \bar{\eta}_1 \quad (10)$$

and in the true gyro bias evolution

$$\frac{d\bar{b}}{dt} = \bar{\eta}_2 \quad (11)$$

From these, one can form a 6-component noise vector $\eta^T = [\bar{\eta}_1^T, \bar{\eta}_2^T]$. Its 2-time expectation is

$$E[\eta(t)\eta^T(t')] = Q(t)\delta(t-t') \quad (12)$$

The matrix $Q(t)$ is the spectral density

$$Q(t) = \begin{bmatrix} \sigma_1^2 I_3 & 0 \\ 0 & \sigma_2^2 I_3 \end{bmatrix} \quad (13)$$

where I_3 is the 3×3 identity matrix, and σ_1^2, σ_2^2 model the gyro drift rate noise and drift rate ramp noise, respectively.

From this noise model, one can show that the state error covariance

$$P_{k|j} = E[x_{k|j} x_{k|j}^T] \quad (14)$$

propagates according to

$$P_{k|k-1} = \Phi P_{k-1|k-1} \Phi^T \pm Q_k \quad (15)$$

where the plus sign is used when $\Delta t > 0$ and the minus sign when $\Delta t < 0$. The propagation matrix is

$$\Phi = \begin{bmatrix} \phi & \psi \\ 0_{3 \times 3} & I_3 \end{bmatrix} \quad (16)$$

where the submatrices are

$$\phi = I_3 - \sin \theta \frac{[\bar{\omega} \times]}{\omega} + (1 - \cos \theta) \frac{[\bar{\omega} \times]^2}{\omega^2} \quad (17)$$

and its integral

$$\psi = I_3 \Delta t + (\cos \theta - 1) \frac{[\bar{\omega} \times]}{\omega^2} + (\theta - \sin \theta) \frac{[\bar{\omega} \times]^2}{\omega^3} \quad (18)$$

The antisymmetric cross-product matrix is denoted

$$[\bar{\omega} \times] = \begin{bmatrix} 0 & -\omega_z & \omega_y \\ \omega_z & 0 & -\omega_x \\ -\omega_y & \omega_x & 0 \end{bmatrix} \quad (19)$$

The process noise matrix is

$$Q_k = \begin{bmatrix} C & \sigma_2^2 \chi \\ \sigma_2^2 \chi^T & \sigma_2^2 \Delta t \end{bmatrix} \quad (20)$$

where the matrix χ is the integral of ψ

$$\chi = I_3 \frac{\Delta t^2}{2} + (\sin \theta - \theta) \frac{[\bar{\omega} \times]}{\omega^3} + \left(\cos \theta - 1 + \frac{\theta^2}{2} \right) \frac{[\bar{\omega} \times]^2}{\omega^4} \quad (21)$$

and C is the integral of a constant plus $\psi \psi^T$

$$C = \sigma_1^2 I_3 \Delta t + \sigma_2^2 \left[\frac{I_3 \Delta t^3}{3} + 2 \frac{[\bar{\omega} \times]^2}{\omega^5} \left(\sin \theta - \theta + \frac{\theta^3}{6} \right) \right] \quad (22)$$

The update step uses the standard Kalman filter equations (Reference 5):

$$x_{k|k} = K_k \bar{y}_k \quad (23)$$

where the a priori state is zero since x is an error state. The residual \bar{y}_k is discussed below. The Joseph-stabilized error covariance update is

$$P_{k|k} = (I_3 - K_k H_k) P_{k|k-1} (I_3 - K_k H_k)^T + K_k R_k K_k^T \quad (24)$$

The Kalman gain matrix is

$$K_k = P_{k|k-1} H_k^T [H_k P_{k|k-1} H_k^T + R_k]^{-1} \quad (25)$$

and the UVF observation model assumes the sensor noise covariance matrix to be

$$R_k = \sigma_k^2 I_3 \quad (26)$$

where σ_k here is the noise standard deviation on each component of the unit vector.

The residual

$$\bar{y}_k = \hat{w}_k - \hat{w}_{k|k-1} \quad (27)$$

is the difference between the observed unit vector and the prediction

$$\hat{w}_{k|k-1} = A_{k|k-1} \hat{v}_k \quad (28)$$

where A is the attitude matrix and \hat{v}_k is the reference vector. Model the actual observation as

$$\hat{w}_k = \frac{A_k \hat{v}_k + \bar{n}_k}{|A_k \hat{v}_k + \bar{n}_k|} \quad (29)$$

where \bar{n}_k is a Gaussian distributed white noise sequence of strength σ_k on each axis. References 2 and 6 show that one can safely neglect the difference between the covariance of the sensor noise implied by Equation (29) and that given in Equation (26). (This freedom arises because the filter is totally insensitive to the noise component along the observed vector.)

The observation sensitivity matrix is the partial of the observation vector with respect to the error state vector, evaluated at the current estimate. Analogous to Equation (7), the true attitude matrix is related to its estimate by the small-angle rotation, $-\bar{\alpha}_k$. Representing the rotation as a matrix exponential, one has

$$\begin{aligned} A_k \hat{v}_k &= \exp([\bar{\alpha}_k \times]) A_{k|k-1} \hat{v}_k \\ &\approx (I + [\bar{\alpha}_k \times]) \hat{w}_{k|k-1} \\ &= \hat{w}_{k|k-1} - [\hat{w}_{k|k-1} \times] \bar{\alpha}_k \end{aligned} \quad (30)$$

where the sign flip occurs when \hat{w} and $\bar{\alpha}$ are interchanged through the cross product. Inserting this into Equation (29) and expanding, one finds the sensitivity matrix is

$$H_k = (-[\hat{w}_{k|k-1} \times] \quad 0_{3 \times 3}) \quad (31)$$

The zero submatrix appears because the observation is independent of the gyro bias part of the error state.

Optimal Smoother

As the forward filter proceeds, the a posteriori (post-update) full state and error covariance are periodically saved. Observation data and reference vectors are also saved so that star identification and data adjustment need not be repeated. To run the backward Kalman filter, the saved values are read and processed in reverse order. The only difference from the forward filter is that the sign of the process noise must be flipped for the covariance propagation, as indicated in Equation (15). This ensures that the uncertainty in the estimate grows whichever way one propagates.

The smoother runs simultaneously with the backward filter. The backward state estimate is propagated to the time of a saved forward solution. If this is also a measurement time, the state vectors are combined prior to updating the backward estimate (the information from that measurement having already been used in the forward filter).

One complication is that the smoother cannot combine the state vectors directly. The 6×6 -covariance matrices apply to the rotation vector and bias correction, not to the full state. It is necessary to express the smoother algorithm also in terms of a small-angle rotation. Were it not for this complication, one would simply form the smoother covariance

$$P_k^s = (P_{k|k}^f^{-1} + P_{k|k-1}^b)^{-1} \quad (32)$$

and obtain the smoothed state (generically referred to as X here) as the weighted average:

$$X_k^s = P_k^s (P_{k|k}^f^{-1} X_{k|k}^f + P_{k|k-1}^b^{-1} X_{k|k-1}^b) \quad (33)$$

The f, b, s notation refers to forward, backward, and smoothed values, and some care must be taken in interpreting the $k|k-1$ subscript on the backward estimates (the indices refer to the update sequence, not the time sequence). Rearranging Equation (32) yields

$$P_k^s P_{k|k}^f^{-1} = I - P_k^s P_{k|k-1}^b^{-1} \quad (34)$$

hence

$$X_k^s = X_{k|k}^f + P_k^s P_{k|k-1}^b^{-1} (X_{k|k-1}^b - X_{k|k}^f) \quad (35)$$

Thus, the smoothed state is the forward state plus a correction proportional to the difference between the states.

Analogously, one can use the small-angle rotation between the attitudes and the gyro bias difference to correct the forward state. Noting that it is $-\bar{\alpha}$ in Equations (7) and (8) that rotates from the estimated to the true state, one defines Δq and $\Delta \bar{\alpha}$ by

$$\Delta q = (q^b \otimes q^{f*})^* = q^f \otimes q^{b*} \quad (36)$$

and

$$\Delta q \approx \begin{bmatrix} \Delta \bar{\alpha}/2 \\ 1 \end{bmatrix} \quad (37)$$

The sequence indices have been suppressed in these and the following equations. So, $-\Delta \bar{\alpha}$ rotates from the forward to the backward attitude estimate. Similarly, $\Delta \bar{b}$ is the difference from the forward to the backward bias estimate

$$\Delta \bar{b} = \bar{b}^b - \bar{b}^f \quad (38)$$

This is then weighted using the covariances

$$\begin{bmatrix} \delta \bar{\alpha} \\ \delta \bar{b} \end{bmatrix} = P^s P^{b-1} \begin{bmatrix} \Delta \bar{\alpha} \\ \Delta \bar{b} \end{bmatrix} \quad (39)$$

Finally, these are combined with the forward estimate, as in Equation (35), to obtain the smoothed state

$$q^s \approx \begin{bmatrix} -\delta \bar{\alpha}/2 \\ 1 \end{bmatrix} \otimes q^f \quad (40)$$

and

$$\bar{b}^s = \bar{b}^f + \delta \bar{b} \quad (41)$$

One can see how the smoother works most easily by inspecting Equations (32) and (33). If one of the forward or backward error covariances is much larger than the other, then its inverse contributes little to the sum in Equation (32). In that case the smoother error covariance approximately equals the smaller of P^f and P^b . In Equation (33), the inverse of the large covariance suppresses the contribution from that state, and P^s times the inverse of the other covariance is close to the identity. Thus, the smoothed state closely equals the state with the smaller covariance. Alternatively, when P^f and P^b are similar, the inverse of the sum in Equation (32) yields a smoother covariance half as large, and the smoothed state is roughly the average of the forward and backward states.

The forward filter starts with a relatively large uncertainty, thus the smoothed state should be dominated by the backward estimate until observation data bring the forward covariance down. Similarly, the backward state is initialized with a very large covariance, so the smoothed state should nearly equal the forward solution near the end of the data span.

3. Results

This section presents results from two sets of tests run on the first version of the optimal smoother. The first tests make use of actual flight data from the EUVE spacecraft. These data span two orbits on December 16, 1992, when EUVE was in Survey mode. In this mode, the spacecraft has its body x -axis (the roll axis) pointed away from the Sun, and it maintains a steady 3-revolution-per-orbit (3-rpo) roll rate. It remains nearly stationary about its y - and z -axes (pitch and yaw).

The only measurements used in these tests are from two fixed-head star trackers (FHSTs) and the rate-integrating gyros. When not in Earth shadow, the Sun vector is used to help identify stars by a dot product test, but it is not included in

the filter update. The FHST 1σ noise parameters are set to 0.01 deg, due mainly to the time tag uncertainty times the roll rate. The gyro noise parameters are taken to be $\sigma_1^2 = 10^{-13} \text{ rad}^2/\text{sec}$ and $\sigma_2^2 = 10^{-19} \text{ rad}^2/\text{sec}^3$.

Figure 1 shows the forward filter solutions for the pitch and yaw axes as solid lines. The roll angle varies from 0 to 360 deg six times during this period and is not shown. These are similar to results presented in Reference 2, except for some significant improvements in the gyro processing in the current version. For comparison, the solutions generated by the onboard computer (OBC) filter are shown as dashed lines. These two filters are fairly similar in design. The steps in the yaw angle near $t = 5000$ sec and 11000 sec are small maneuvers performed each orbit to keep the roll axis pointing away from the Sun. At the same time, there is a roll adjustment to maintain the roll phase relative to the orbital position.

The sensor update history is shown in Figure 2. The points indicate the times of occurrence of filter updates for the two star trackers. The gaps in the update history appear when the trackers are facing the Earth.

The small-angle deviations between the OBC and the forward filter solutions are presented in Figure 3. On this scale, initial transients and the jitter due to gyro noise are more apparent. The backward filter results look quite similar, except that the "initial" transients occur at the end of the data span. The relatively large deviations in roll angle at the times of the roll phase adjustment are errors in the OBC solution, probably caused by its gyro smoothing algorithm. The 3-rpo oscillation derives from a small difference between the UVF and OBC estimated Euler axes, which leads to body frame errors being modulated at the rotation rate.

Figure 4 shows the smoother attitude estimates in the same format as Figure 3. It is clear that the smoother has had only a small effect on the solutions. Some apparent improvement is visible near $t = 3000$ sec (where a gyro counter rollover occurs) and the forward and backward transients are completely removed.

Gyro biases shown in Figure 5 are in excellent agreement with OBC-determined biases (not shown) and with those obtained from the ground support system for a similar time span (dashed lines). The offset of roughly 0.01 deg/hr is comparable to the 1σ uncertainty in the AGSS estimate (Reference 7). Forward, backward, and smoothed solutions are shown for the body frame z-axis gyro drift rate. Solutions are similar for the x- and y-axes. The transients apparent in the forward and backward estimates are completely removed in the smoothed bias. There also is a visible reduction in noise.

One internal figure of merit for the filter and smoother is the error covariance. Uncertainties for the attitude and bias are obtained separately as the square root of the sum of the first three and the last three elements of the covariance matrix. Figure 6 overlays these uncertainties for the forward, backward, and smoothed solutions. Several features are apparent: the smoother errors equal the forward errors at the end of the time span, and equal the backward errors at the beginning, as expected from Equation (32). The errors grow due to process noise during the data gaps between star observations. The Kalman filter errors are lowest at the beginning or ending times, after each has had access to all of the data. The smoother always has access to the entire data span, but its errors are lowest near the middle since that point is closest in time to all the data, on average. This minimizes the contribution from the process noise.

A second internal check is to obtain the mean gyro bias and the root-mean-square (RMS) deviation from the mean. This is useful since the bias is expected to be very nearly constant. As Figure 5 shows, the deviations are very small. Statistics are gathered from the second orbit for the forward filter, the first orbit for the backward filter, and from the middle for the smoother. The three-axis root-sum-square averages of these orbit-averaged RMS deviations are 0.0026 deg/hr for both the forward and backward filters, and 0.0011 deg/hr for the smoother, somewhat smaller than the uncertainties deduced from the covariances shown in Figure 6. The filter/smoothing covariance ratio is close to 2, as expected (see Equation (32) and the discussion at the end of Section 2).

A similar statistical check of the attitude is not useful because there is no available truth model. The deviations in Figure 3 are caused equally by errors in the UVF and the OBC filters. The OBC errors mask any improvements due to the smoother. For this reason, the smoother was tested using a simulated data set for which the true state is known. The true rates are taken to be (3 rpo, 0, 0), but the gyro output is perturbed by white noise and a randomly walking gyro bias as in Equation (10). The noise on the simulated star observations is Gaussian distributed, with width $\sigma = 0.01 \text{ deg}$. The resulting deviations with the truth model are shown in Figure 7. In this case, the uncertainty (as defined for Figure 6) and the deviation from the truth model are in fairly close agreement. When averaged over an orbit, and averaging the

three axes, the forward and backward filters both have uncertainties of 3.8 arc sec, and RMS deviations of 3 to 4 arc sec. The smoother uncertainty is 2.4 arc sec and RMS deviation is 2.1 arc sec.

4. Conclusions

An optimal smoother for estimating spacecraft attitude and gyro bias has been developed and tested using both EUVE flight data and simulated data. It has been shown that the algorithm converges and yields reasonable results. The solutions have been tested for internal consistency by examining the error covariances and the RMS variations of those parameters that are expected to be constant (the gyro biases). In addition, the smoother was tested using a simple simulation. The tuning parameters then could be chosen exactly to match the model, and the resulting error covariances were found to match the actual solution statistics.

Continuing investigations may go in two different directions. The expanded state vector to be used by some future missions for full gyro calibrations should be tested for convergence under varying observability conditions. Designs for those filter/smoother also include a more general process noise matrix that allows for a different noise parameter on each axis. This should be tested for its ability to obtain good attitudes in the presence of gyro degradation on selected axes.

Another direction for future studies is to look at alternative smoother algorithms. There are a few different ways to re-express the simple forward/backward average implemented here. There are expected advantages to these other methods in terms of central processing unit (CPU)-time efficiency. There also is a theoretical difference that may be significant. The current smoother uses the final forward state estimate as the initial value for the backward filter. This imposes strong correlations between the forward and backward states that should not be there. To cure this, the backward error covariance is taken to be the forward covariance times a large factor (typically 10^{12} in the test cases). It is expected that this large covariance forces the backward filter to put full confidence in the sensor data, and almost instantly forget its initial value. However, there may be correlations that persist and leave the smoother state suboptimal. The problem can be avoided by redefining the backward filter in terms of P^{-1} and a new state variable, $P^{-1}x$. Initializing these to zero implies zero a priori information and no correlation with the forward filter.

References

1. M. Challa, et al., "Real-Time Attitude Determination and Gyro Calibration," in *Proceedings, Flight Mechanics/Estimation Theory Symposium*, NASA Goddard Space Flight Center, May 1991
2. J. Sedlak and D. Chu, "Kalman Filter Estimation of Attitude and Gyro Bias With the QUEST Observation Model," in *Proceedings, AAS/GSFC International Symposium on Space Flight Dynamics*, April 1993
3. D. C. Fraser and J. E. Potter, "The Optimum Linear Smoother as a Combination of Two Optimum Linear Filters," *IEEE Trans. on Automatic Control*, Vol. 7, No. 8, August 1969
4. E. J. Lefferts, F. L. Markley, and M. D. Shuster, "Kalman Filtering for Spacecraft Attitude Estimation," *J. Guidance, Control, and Dynamics*, Vol. 5, No. 5, Sept.–Oct. 1982
5. A. Gelb, ed., *Applied Optimal Estimation*, Cambridge: MIT Press, 1974
6. M. D. Shuster, "Kalman Filtering of Spacecraft Attitude and the QUEST Model," *J. Astronaut. Sci.*, Vol. 38, No. 3, July–Sept. 1990
7. W. Davis, et al., "Postlaunch Calibration of Spacecraft Attitude Instruments," in *Proceedings, AAS/GSFC International Symposium on Space Flight Dynamics*, April 1993

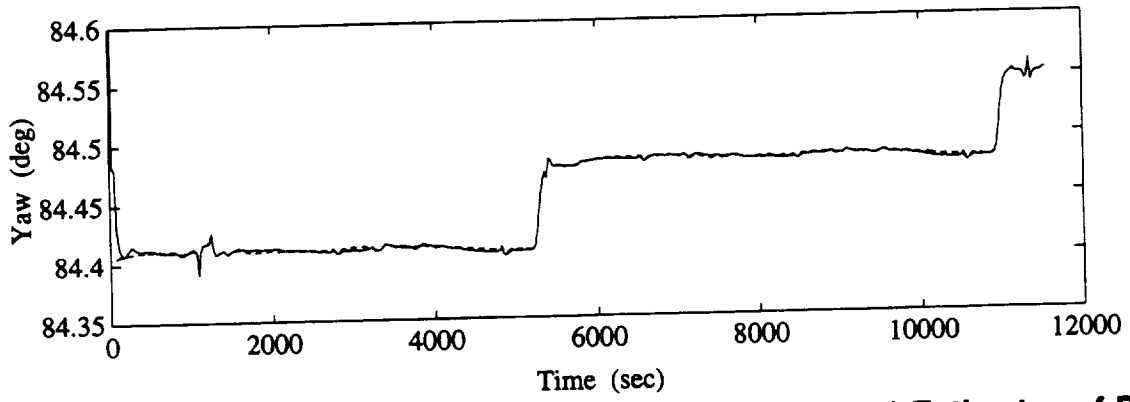
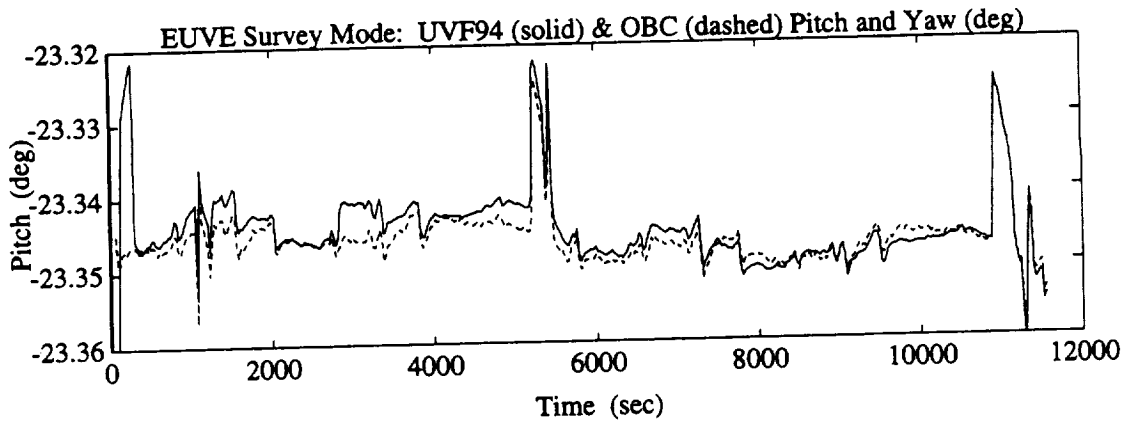


Figure 1. Forward Filter (solid lines) and OBC (dashed lines) Estimates of Pitch and Yaw Angles Versus Time

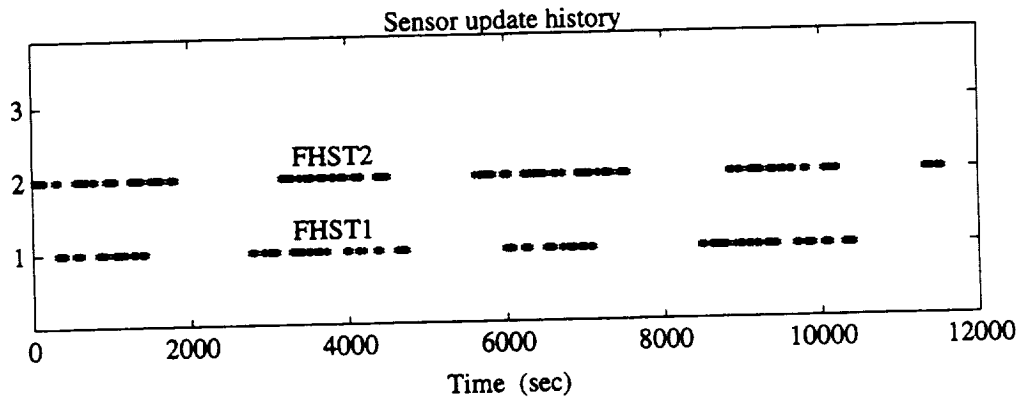


Figure 2. Sensor Update History

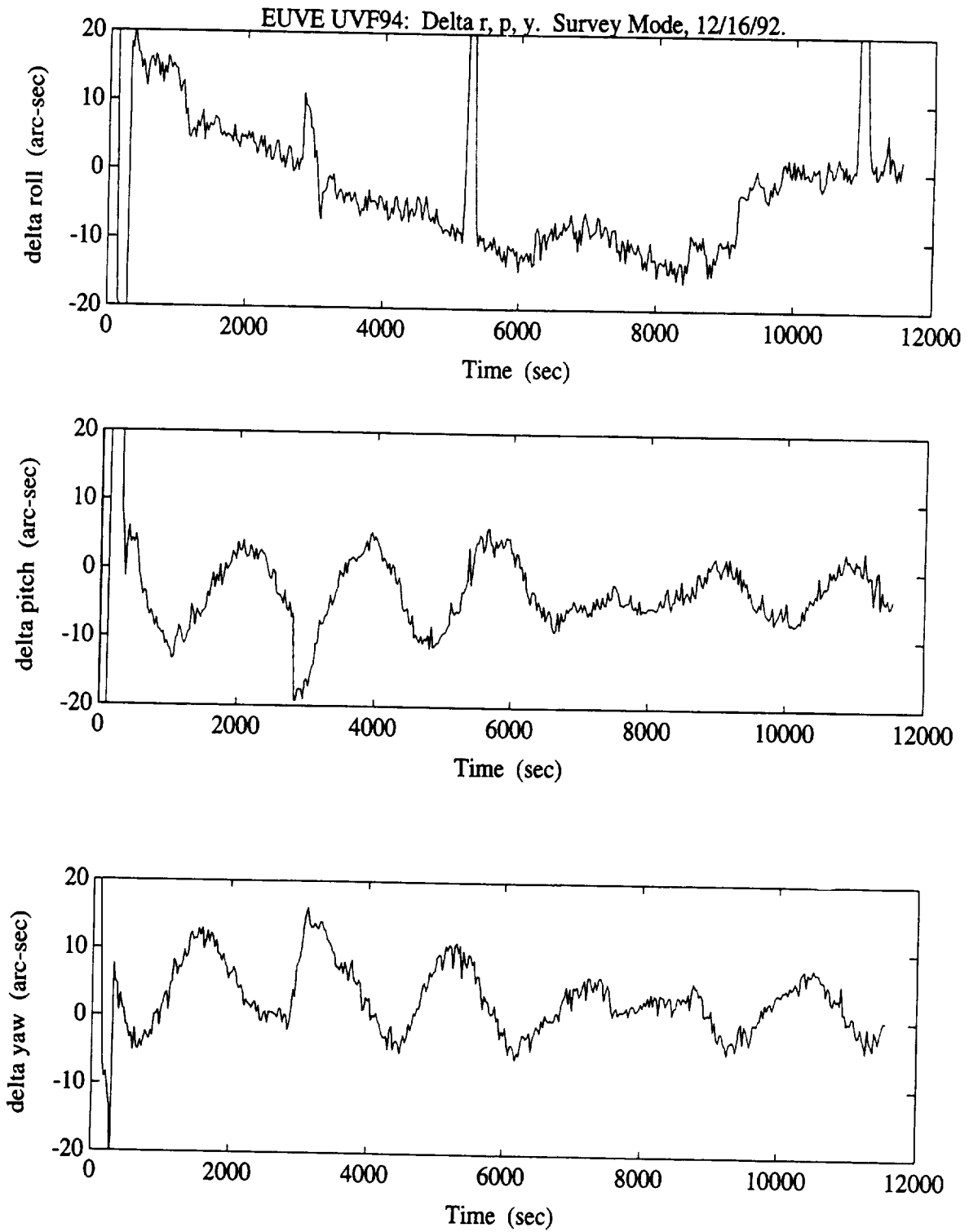


Figure 3. Delta Roll, Pitch, and Yaw Versus Time From Comparison of EUVE Forward Filter and OBC Quaternion Estimates

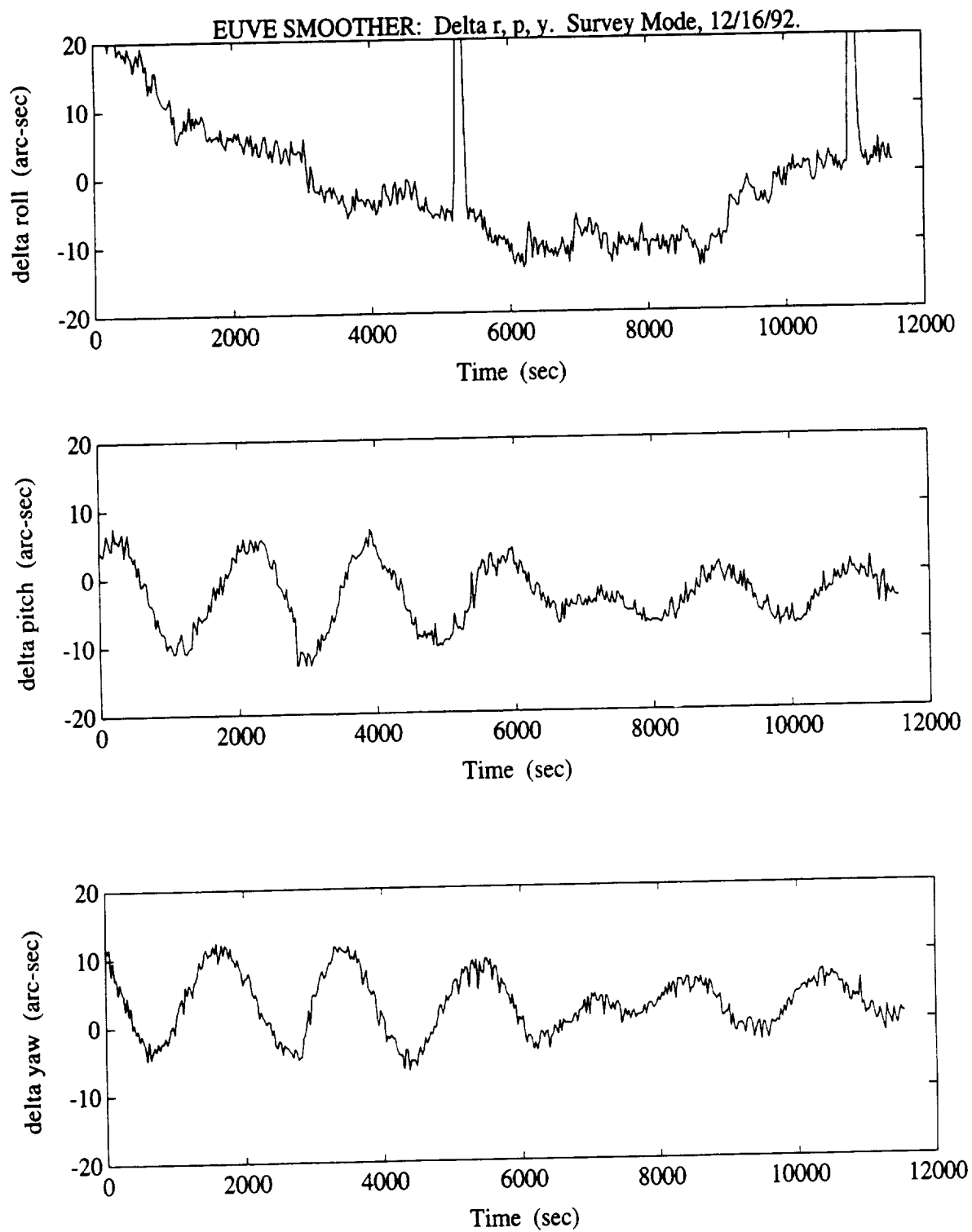


Figure 4. Delta Roll, Pitch, and Yaw Versus Time From Comparison of EUVE Optimal Smoother and OBC Quaternion Estimates

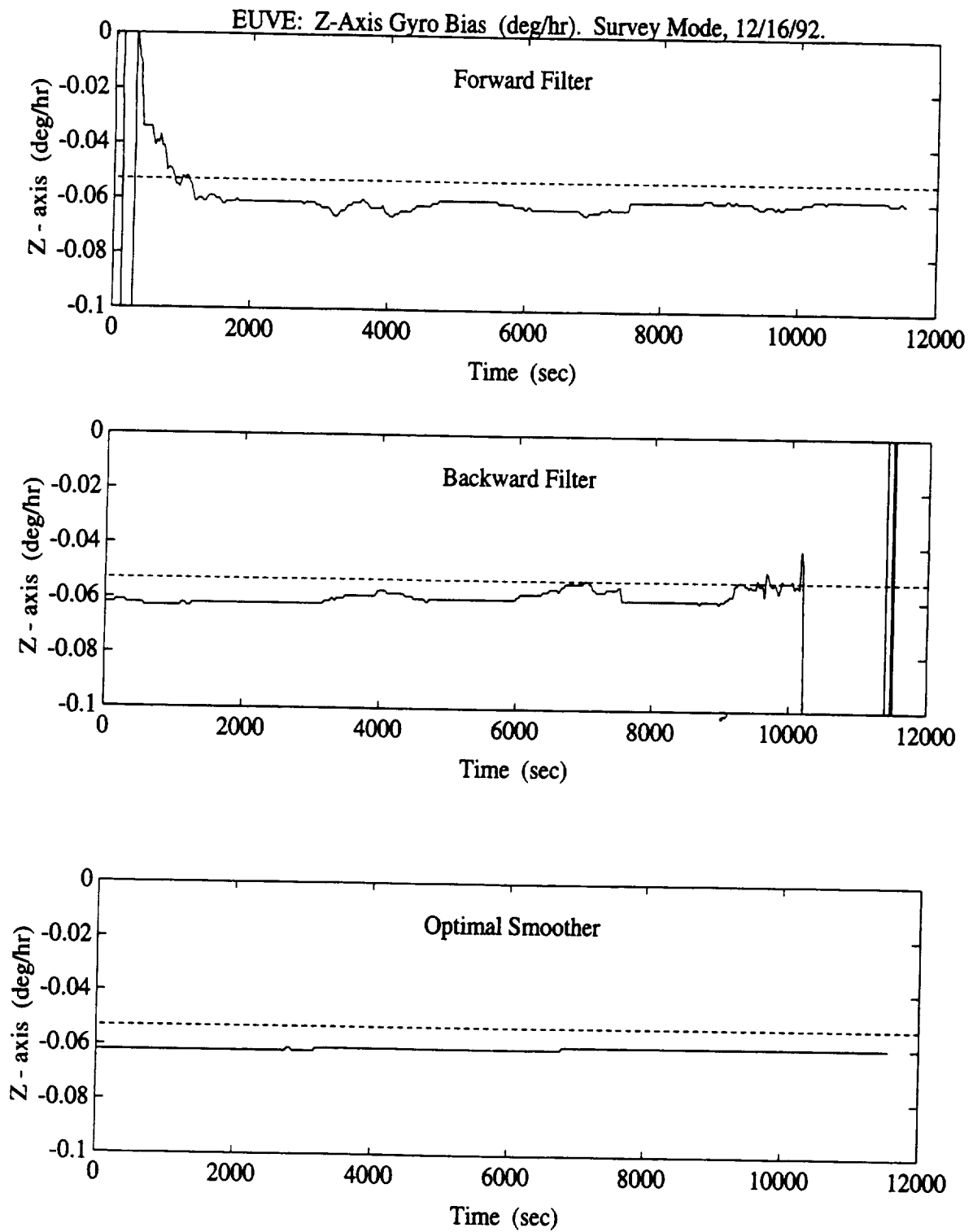


Figure 5. Forward Filter, Backward Filter, and Optimal Smoother Estimates of Body Z-Axis Gyro Drift Bias Versus Time (dashed lines indicate AGSS estimate)

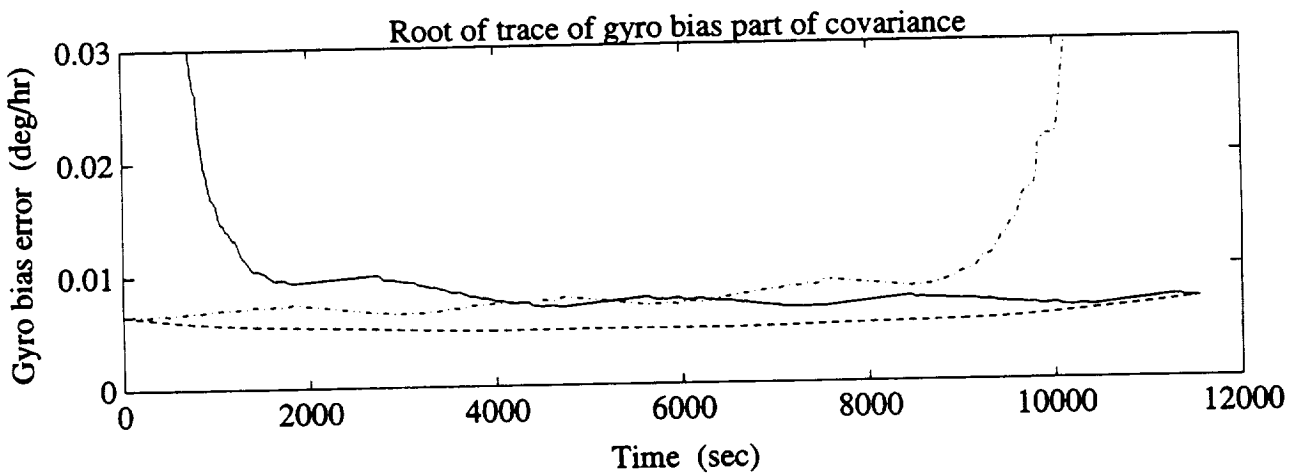
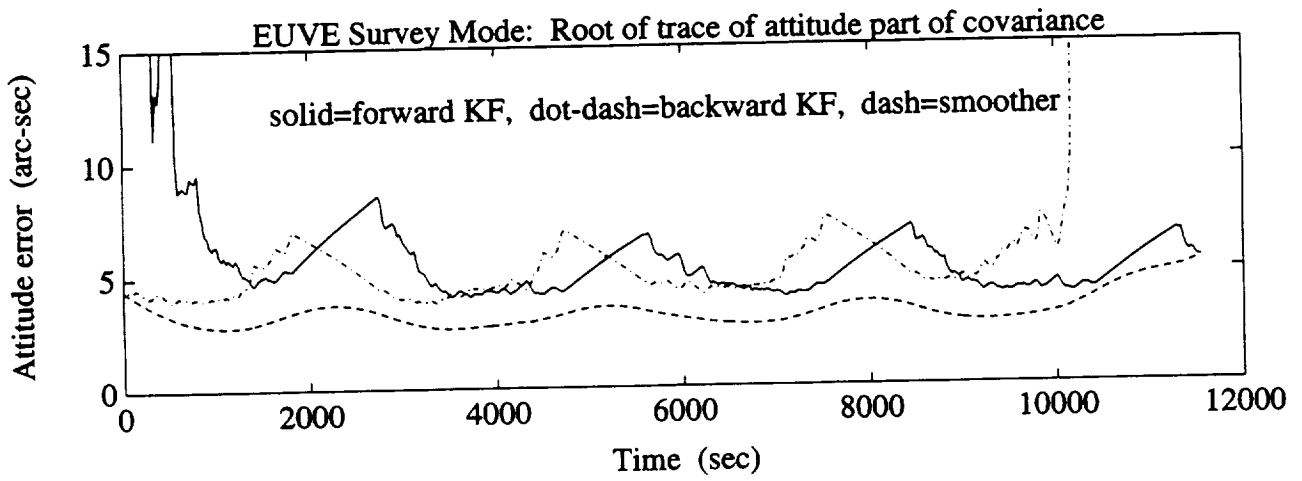


Figure 6. Forward (solid), Backward (dot-dash), and Smoother (dashed) Attitude and Gyro Bias Uncertainties Versus Time

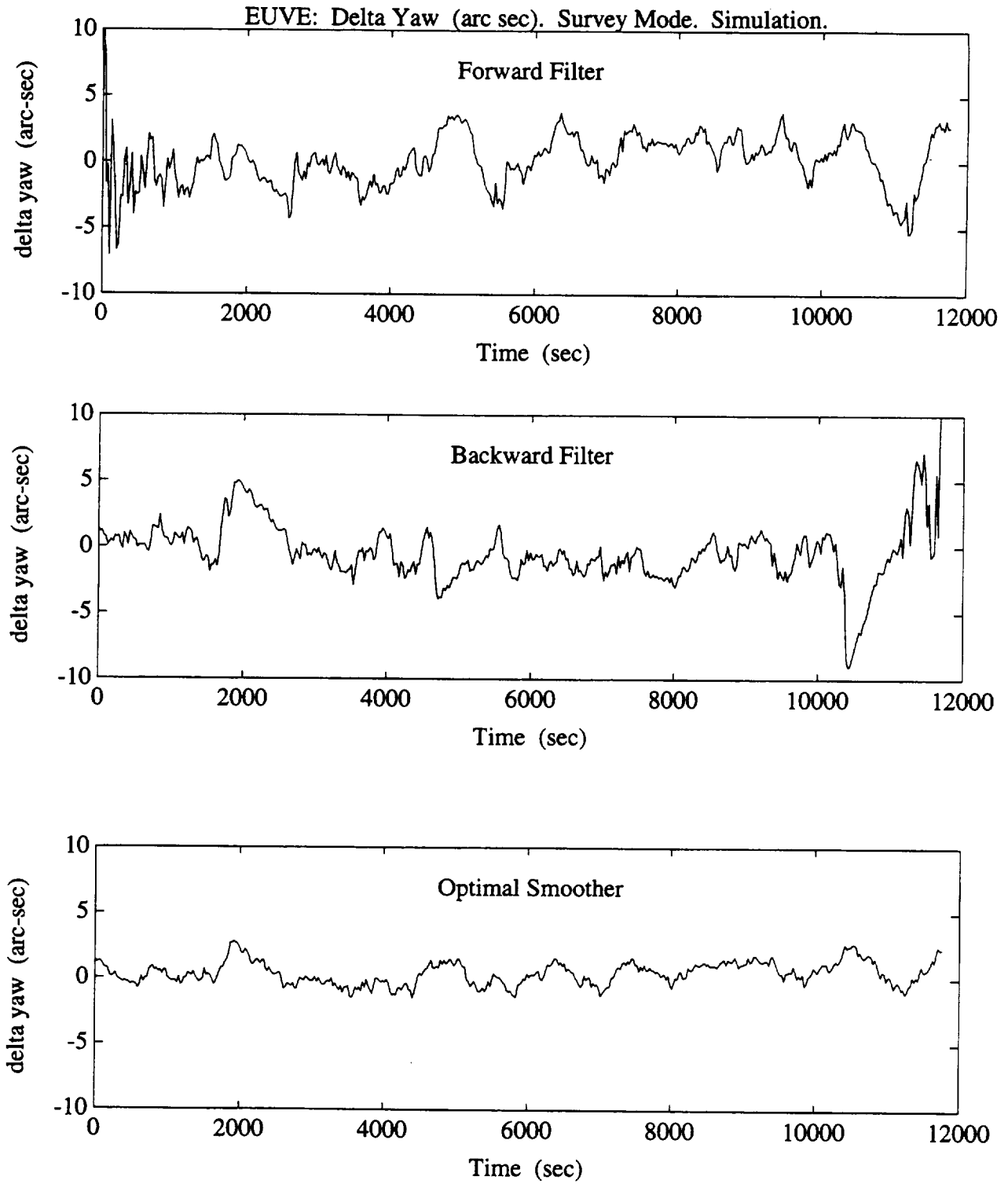


Figure 7. Delta Yaw Versus Time From Comparison of Estimates and Simulation Truth Model

Attitude Stability of a Spinning Spacecraft During Appendage Deployment/Retraction

Norman Fitz-Coy* and Wayne Fullerton**
AeMES Department
University of Florida

The work presented in this paper is motivated by the need for a national satellite rescue policy, not the ad hoc policy now in place. In studying different approaches for a national policy, the issue of capture and stabilization of a tumbling spacecraft must be addressed. For a rescue mission involving a tumbling spacecraft, it may be advantageous to have a rescue vehicle which is compact and "rigid" during the rendezvous/capture phase [1]. After capture, passive stabilization techniques could be utilized as an efficient means of detumbling the resulting system (i.e., both the rescue vehicle and captured spacecraft). Since the rescue vehicle is initially compact and "rigid", significant passive stabilization through energy dissipation can only be achieved through the deployment of flexible appendages. Once stabilization is accomplished, retraction of the appendages before maneuvering the system to its final destination may also prove advantageous. It is therefore of paramount interest that we study the effect of appendage deployment/retraction on the attitude stability of a spacecraft. Particular interest should be paid to appendage retraction, since if this process is destabilizing, passive stabilization as proposed may not be useful.

Over the past three decades, it has been an "on-again-off-again affair" with the problem of spacecraft appendage deployment [2-7]. In most instances, these studies have been numerical simulations of specific spacecraft configurations for which there were specific concerns. The primary focus of these studies was the behavior of the appendage during deployment; the effects of appendage retraction was considered only in one of these studies. What is missing in the literature is a thorough study of the effects of appendage deployment/retraction on the attitude stability of a spacecraft.

This paper presents a rigorous analysis of the stability of a spinning spacecraft during the deployment or the retraction of an appendage. The analysis is simplified such that meaningful insights into the problem can be inferred--it is not overly simplified such that critical dynamical behavior is neglected.

The system is analyzed assuming that the spacecraft hub is rigid. The appendage deployment mechanism is modelled as a point mass on a massless rod whose length undergoes prescribed changes. Simplified flexibility effects of the appendage are included. The system is examined for stability by linearizing the equations in terms of small deviations from steady, non-interfering coning motion. Routh's procedure [8] for analyzing small deviations from steady motion in dynamical systems is utilized in the analysis. The system of equations are nondimensionalized to facilitate parametric studies. The results are presented in terms of a reduced number of nondimensional parameters so that some general conclusions may be drawn. Verification of the linear analysis is presented through numerical simulations of the complete nonlinear, nonautonomous, coupled equations.

* Assistant Professor

** Graduate Research Assistant

1. Fitz-Coy, N. G., and Chatterjee, A., "Spacecraft Detumbling Through Energy Dissipation," Proceedings of the 1992 Flight Mechanics/Estimation Theory Symposium (NASA CP?3186), May 1992, pp. 23-37.
2. Gluck, R., and Gale, E. H., "Motion of a Spinning Satellite during the Deployment of Asymmetrical Appendages," *Journal of Spacecraft*, Vol. 3, No. 10, Oct. 1966, pp. 1463-1469.
3. Cloutier, G. J., "Dynamics of Deployment of Extendible Booms from Spinning Space Vehicles," *Journal of Spacecraft*, Vol. 5, No. 5, May 1968, pp. 547-552.
4. Cherchas, D. B., "Dynamics of Spin-Stabilized Satellites during Extension of Long Flexible Booms," *Journal of Spacecraft*, Vol. 8, No. 7, July 1971, pp. 802-804.
5. Modi, V. J., and Ibrahim, A. M., "A General Formulation for Librational Dynamics of Spacecraft with Deployable Appendages," *Journal of Guidance, Control, and Dynamics*, Vol. 7, No. 5, Sept.-Oct. 1984, pp. 563-596.
6. Banerjee, A., and Kane, T. R., "Extrusion of a Beam from a Rotating Base," *Journal of Guidance, Control, and Dynamics*, Vol. 12, No. 2, March-April 1989, pp. 140-146.
7. Shen, Q., and Modi, V. J., "On the Dynamics of Spacecraft with Flexible, Deployable and Slewing Appendages," Paper AAS 93?644 presented at the 1993 AAS/AIAA Astrodynamics Specialist Conference, Victoria, B.C., Aug. 1993.
8. Goldstein, H., *Classical Mechanics, 2nd Ed.*, Addison Wesley Publishing Co., MA., 1980.

FLIGHT MECHANICS/ESTIMATION THEORY SYMPOSIUM

MAY 17-19, 1994

SESSION 6

Application of Star Identification Using Pattern Matching to Space Ground Systems at GSFC*

D. Fink and D. Shoup
Computer Sciences Corporation (CSC)
Lanham-Seabrook, Maryland

Abstract

This paper reports the application of pattern recognition techniques for star identification based on those proposed by Van Bezooijen to space ground systems for near-real-time attitude determination. A prototype was developed using these algorithms, which was used to assess the suitability of these techniques for support of the X-Ray Timing Explorer (XTE), Submillimeter Wave Astronomy Satellite (SWAS), and the Solar and Heliospheric Observatory (SOHO) missions. Experience with the prototype was used to refine specifications for the operational system. Different geometry tests appropriate to the mission requirements of XTE, SWAS, and SOHO were adopted. The applications of these techniques to upcoming mission support of XTE, SWAS, and SOHO are discussed.

1.0 Introduction

The Van Bezooijen pattern-matching technique is based on a series of tests, as are most star identification algorithms. Each test compares the scalar value of an observable characteristic of the observed stars with the scalar value of the same characteristic of candidate reference stars, with the test being not for strict equality between the two numeric values but for a match within specified tolerances (i.e., using an inexact, or "fuzzy," comparison). Each such characteristic that can be represented as a scalar quantity is termed a pattern dimension. The pattern dimensions that were used in this study to identify a star are the separation angles between it and all other stars in the region viewed by a tracker and within a larger catalog region, the brightness of a star within some wavelength band (e.g., visual or instrument magnitude), and the angle between a star and some reference direction (e.g., the Sun vector). Tests are performed to compare the values of potential candidates in each pattern dimension against the values of the observed stars, and in every such comparison those candidate pairs that can be ruled out with certainty are eliminated. When all such tests have been completed, the candidate stars that remain are voted for by counting up the number of times that each candidate star has survived as a possible match to one of the observed stars. The candidate with the highest vote tally for a given observed star (if any) is declared the winner. We suspected that Van Bezooijen's techniques would be especially well suited to the multiple, simultaneous, high-accuracy star observations possible with the Charge-Coupled Device (CCD) star trackers to be flown on the X-Ray Timing Explorer (XTE), Submillimeter Wave Astronomy Satellite (SWAS), and Solar and Heliospheric Observatory (SOHO) missions.

Clearly, this is a probabilistic method that assumes that the odds of some other candidate star being found which has a score equal to the correct star is small, based on the set of tests and votes used. A principal objective of this analysis was to establish that the odds of identifying the observed stars correctly are sufficiently great to consider this method reliable in an automated, real-time setting, assuming realistic levels of error in the observed data. The other principal objective was to determine whether the algorithm and associated data structures could execute and be regenerated quickly enough to fit into a real-time system with a 4-sec update limit when running on an HP 715/50 workstation supporting XTE/SWAS. The timing requirements for SOHO were less stringent, but identification results within 10 min were desired.

Performing this analysis required a prototype, as the algorithms previously had not been implemented in the Flight Dynamics Facility (FDF). Building the prototype provided an opportunity to observe the performance of the algorithm and to take advantage of the lessons learned from the preliminary analysis to prepare the specifications for the operational system. The prototype was originally built using only the first two of the pattern dimensions (separation and magnitude), with a separation test as described in Van Bezooijen's special algorithm. In the special algorithm separation test, observed stars are compared in separation only pairwise with separations of candidate stars, rather than the more exacting comparison of "match groups" composed of up to all the observed stars considered as one geometric element, as used in Van Bezooijen's general algorithm. Van Bezooijen's special algorithm includes a

*This work was supported by the National Aeronautics and Space Administration (NASA)/Goddard Space Flight Center (GSFC), Greenbelt, Maryland, under Contract NAS 5-31500.

"field of view (FOV) rotation tolerance" test which was not implemented in this prototype. We omitted that test because initially, one goal was to use spacecraft attitude only to ensure that a tracker boresight would lie within the confines of the zone catalog being used as the source of candidate stars. Two types of zone catalog were required to meet the mission requirements of XTE/SWAS and SOHO: a small circle region (or cap catalog) for XTE/SWAS, and a band centered around either a small or great circle (a band catalog) for SOHO. Analysis of these early results led to a decision to implement additional geometric tests based on partial a priori knowledge of the spacecraft attitude to improve recognition accuracy, as Van Bezooijen had done, although these tests are somewhat different from his: these tests were designed to accommodate the different identification geometries for cap and band catalogs.

2.0 Method

Both the star identification (STARID) prototype itself and the simulator that drives it were written in FORTRAN 77 and were compiled and executed on a 33 MHz, 486 PC, equipped with 16 MB of RAM. Comparison of PC industry literature indicated this machine is several times slower than the target HP 715/50 computer at floating point operations of the sort that make up the bulk of the algorithm's computations. We used the 33 MHz 486 time as a conservative measure of whether we were satisfying our 4-sec update limit, since the operational system on the HP platform must do more than just star identification. For the final timing runs, the compiler performance options were enabled. Input and output files resided remotely on a PC network file server. All position and magnitude variables obtained from the star catalog were stored as REAL*4 variables. All separation values were also maintained in REAL*4 precision, and angular data were processed using trigonometric functions without any particular attempt to minimize memory use and computation time.

The PC version of the operational Multimission Three-Axis Support System (MTASS) Run Catalog (MMS_RCAT) currently in use for ground support of the Upper Atmosphere Research Satellite (UARS) and Extreme Ultraviolet Explorer (EUVE) was used for all XTE/SWAS-type cap catalog runs. The PC version of the SOHO catalog (SOHO_RUN) was used for the SOHO-type band catalog runs. In all the results presented in this paper for XTE/SWAS, all stars down to magnitude 6.5 were used from the MMS_RCAT catalog; for SOHO, all stars down to magnitude 8.0 were used from the SOHO_RUN catalog. These magnitude limits were hardcoded in the XTE/SWAS and SOHO versions of the prototype and were not input parameters.

STARID attempts to determine the SKYMAP numbers (*SKYMAP Star Catalog System Description*, Slater, 1992) of the observed stars by matching them pairwise with the catalog star pairs it generates. STARID returns the SKYMAP number of the catalog star it believes matches the observed star; it returns a flag value for observed stars which ended up matching more than one candidate catalog star equally well; and it returns another flag for observed stars which it determines did not match a catalog star at all. The simulator then tabulates the results.

A summary of the input parameters is provided in Table 1 and parameter descriptions accompany each test. The values used in the table are close to the expected mission tolerances, with a margin in whatever direction would affect the identification process adversely, while still providing a semblance of nominal behavior.

In each simulation the simulator selects random directions to generate main cap or band catalogs, and sensor FOV catalogs (which are cap catalogs in these simulations) within those main catalogs. The set of stars available in each FOV catalog, if any, is sampled at random for up to five simulated observed stars, to whose position and magnitude noise is added. For the results presented in this paper, Gaussian white noise was used. Note that measurement noise and sensor FOV calibration error were not modeled separately but were treated as a single Gaussian white noise process. The position errors are uniformly and randomly distributed in direction, in addition to being Gaussian-distributed in magnitude. These simulated observed star positions and magnitudes are then passed anonymously from the simulator to STARID, along with the cap or band catalog within which they and their view catalog all lie. All observations used for each identification attempt can be considered to be from a single time, made from a single inertially-fixed circular tracker FOV.

The random direction of the star tracker FOV can be controlled by reading an input base direction and a bound from that desired direction, within which the catalog generation vector must lie. An option is also provided to misalign the spacecraft-centered inertial reference frame from the true geocentric inertial (GCI) frame, to produce the sort of large, systematic observed star position error one sees in flight data when the spacecraft-body-to-GCI transformation has large errors.

Following the identification of candidate pairs based on separation tests, either star in the observed pair could be either star in any of the identified candidate pairs. The following section summarizes the magnitude and geometry tests used to determine which of the candidates should be given a vote of confidence as being each observed star, which will subsequently be counted and compared to the tallies for competing candidates for the same observed star. Note that a given pair of candidates may fail these tests entirely, in which case there will be no votes cast for either candidate in the pair. Depending on the geometry and the setting of the tolerances, a given pair may also obtain ambiguous results from the geometry tests, in which case a vote is cast for each of the candidates as being each of the observed stars in the pair, in the expectation that other pairings provide votes to resolve the ambiguity, or the user may need to resolve the ambiguity through changing test tolerances.

Table 1. Basic Input Parameters

Input Parameter Definition	Variable Name	Cap Catalog Baseline Value	Band Catalog Baseline Value
For cap catalog runs, the angle, in degrees, within which to restrict the uniformly and randomly distributed catalog a priori boresight. For band catalog runs, the angle, in degrees, within which to restrict the uniformly and randomly distributed pole axis of the band catalog.	<i>RCCAT</i>	180.00°	180.00°
For cap catalog runs, the angle, in degrees, within which to restrict the uniformly and randomly distributed sensor boresight vector, measured from the catalog a priori boresight. For band catalog runs, the angle, in degrees, within which to restrict the uniformly and randomly distributed sensor boresight vector, measured from the center of the band catalog.	<i>RCVIEW</i>	6.66°	0.10°
Simulated observation position noise, 1σ	<i>SIGOBS</i>	0.00083° (3")	0.00083° (3")
Simulated observation magnitude noise, 1σ	<i>SIGMAG</i>	0.10	0.10
+ - Bound on error in simulated observed magnitudes	<i>RCMAG</i>	0.6	0.6
Cap catalog radius (only applies to cap catalog case)	<i>CCAP</i>	10.66°	N/A
Half width of band catalog (only applies to band catalog)	<i>WBAND</i>	N/A	2.1°
Coelevation of sensor boresight for band catalog generation	<i>COEL</i>	N/A	90.0°
Half width of tracker boresight	<i>FOVMAX</i>	4.0°	2.0°
Maximum-range-of-separation hashing function used to select catalog star pairs, e.g., $2^{\circ}FOVMAX$ (deg)	<i>HMAX</i>	8.0°	4.0°
Separation tolerance to use in building hashing tables, and in final separation tolerance test (deg)	<i>SEPTOL</i>	0.0066°	0.0066°
Magnitude tolerance for rejection of a candidate star by the magnitude check	<i>XMTOL</i>	0.6	0.6
Magnitude tolerance to use in determining which star in a pair of observed stars is brighter	<i>TMAGMX</i>	0.6	0.6
Angular threshold at which two cross-product vectors are considered parallel in cap catalog cross-product tests	<i>CAPMAX</i>	90.0°	N/A
Angular threshold at which the difference in star vector-to-catalog generation vector angles are considered large enough for the closeness-to-pole test, and considered too large for the cross-product test to be applied (deg)	<i>BANTOL1</i>	N/A	0.13°
Angular threshold used in the closeness to pole test, at which star vector-to-catalog generation vector angles of the closer stars or further stars are considered more different than they should be, considering the error in the position of the pole of the band catalog (deg)	<i>BANTOL2</i>	N/A	7.2°
Angular threshold at which two cross-product vectors are considered parallel in band catalog cross-product test (deg)	<i>BANMAX</i>	N/A	90.0°
Flag to perform a 3-2-1 rotation on observed vectors, with respect to body coordinate axes (logical)	<i>LIBROT</i>	T	T
For <i>LIBROT</i> = T, the first rotation angle	<i>PHI</i>	0.0116667°	0.1000000°
For <i>LIBROT</i> = T, the second rotation angle	<i>THETA</i>	0.0116667°	0.1000000°
For <i>LIBROT</i> = T, the third rotation angle	<i>PSI</i>	0.0166667°	180.0000000°

In the following summary we use the input variable names as defined in Table 1 for brevity and clarity. In this discussion we refer to the candidate pairs as indexed by J , and the observed pairs as being indexed by I . We refer to a candidate acceptability flag $IFLAG(J,I)$, initialized to -1 , and a relative order flag $LORD(J,I)$, initialized to 0 .

2.1 Magnitude Tests

STEP 1: On option, attempt to determine the matching order using relative magnitude. If the magnitude test is not selected, then set $LMAGT$ to $FALSE$, for the benefit of the logic used below in the geometry tests, to indicate that none of the candidates has been prescreened by a magnitude test. If the magnitude of a pair of observed stars differs by less than $TMAGMX$ then set $LMAGT$ to $FALSE$, skip this test, and proceed to the geometry tests below.

STEP 2: If the magnitude difference between this pair of observed stars is $TMAGMX$ or greater, then set $LMAGT$ to $TRUE$, and test each of the candidate pairs for that observed pair as follows: Compare the brighter of the observed stars to the first star in the candidate pair (candidate pairs were created with the brighter star first). If the difference in magnitude is greater than $XMTOL$, set the acceptability flag for this candidate for this pair to the "no" value, $IFLAG(J,I) = 0$, and go on to the next candidate pair. If the difference in magnitude is acceptable, compare the dimmer star of the observed pair with the dimmer candidate.

STEP 3: If the difference in magnitude between the dimmer observed star and the dimmer candidate star is greater than $XMTOL$, reject the J th candidate by setting $IFLAG(J,I) = 0$, and go on to the next candidate pair. If the difference is acceptable, set an order flag $LORD(J,I) = +1$ if the matching order was found to be that the first observed star matches the first candidate and the second observed star matches the second candidate, or set the $LORD(J,I) = -1$ if the reverse order was found. When all candidates have been checked, proceed on to the next candidate pair, then proceed to the geometry tests.

2.2 Geometry Tests: Perform the following tests as indicated, depending on whether a cap or band catalog is being used.

Cap Catalog:

STEP 4: Form the unit cross product of the two observed star vectors and the unit cross product of the two candidate star vectors. Compute the angular difference $CRSSEP$ between these two unit cross-product vectors, and its supplement $CRSSEN = 180.0 \text{ deg} - CRSSEP$. If $LMAGT$ is $FALSE$, the order of multiplication that gives the cross products within a user-specified angular tolerance $CAPMAX$ determines the proper pairing of the observed and candidate vectors. If $CRSSEP \leq CAPMAX$, set $LORD(J,I) = 1$ to record that the first observed star matches the first candidate and the second observed star matches the second candidate, or if $CRSSEN \leq CAPMAX$, set $LORD(J,I) = -1$ to record that the order is the reverse. If neither order of multiplication satisfies the angular tolerance, set $IFLAG(J,I) = 0$, and go on to the next candidate pair.

STEP 5: If $LMAGT$ is $TRUE$, check the order flag $LORD(J,I)$; if it is zero as it was earlier initialized, proceed with the test as above in STEP 4. However, if $LORD(J,I)$ is 1 or -1 , just check that order of the cross-product multiplication to confirm or refute it. If the cross products are not within the user specified angle $CAPMAX$, set $IFLAG(J,I) = 0$, and go on to the next candidate pair. If the angle is within $CAPMAX$, the order is confirmed to be that given by the magnitude test. Continue on with the next candidate pair.

Band Catalog:

STEP 6: First determine whether the observed and candidate stars can be distinguished based on their angular distance from the one axis which is known with some certainty, the pole of the band catalog. Find the angle between each observed star vector and the catalog generation vector, and the angle between each reference star vector and the catalog generation vector. Compute the angles $GTO1$ and $GTO2$ from each member of the pair of observed stars to the catalog generation vector. Compute $GTODIF$, the absolute value of the difference between $GTO1$ and $GTO2$. Compute the angles $GTR1$ and $GTR2$ from each member of the pair of candidate stars to the catalog generation vector. Compute $GTRDIF$, the absolute value of the difference between $GTR1$ and $GTR2$. If both $GTODIF$ and $GTRDIF$ are greater than $BANTOL1$, proceed with the test at STEP 7 below. If either $GTODIF$ or $GTRDIF$ is less than or equal to $BANTOL1$, check the absolute difference between $GTODIF$ and $GTRDIF$; if it is greater than $BANTOL1$, set $IFLAG(J,I) = 0$, and go on to the next candidate pair. If the absolute difference between $GTODIF$ and $GTRDIF$ is less than or equal to $BANTOL1$ proceed instead to the cross-product test below at STEP 10.

STEP 7: If both $GTODIF$ and $GTRDIF$ are greater than $BANTOL1$, compute the absolute difference between $GTODIF$ and $GTRDIF$; if it is greater than $BANTOL1$, set $IFLAG(J,I) = 0$, and go on to the next candidate pair. If the absolute difference between $GTODIF$ and $GTRDIF$ is less than or equal to $BANTOL1$, then determine the greater of $GTO1$ and $GTO2$ and the greater of $GTR1$ and $GTR2$. Compare the greater angles with one another. If the absolute difference is not within $BANTOL2$, set $IFLAG(J,I) = 0$, and go on to the next candidate pair. Compare the lesser angles to one another; if the absolute difference is not within $BANTOL2$, set $IFLAG(J,I) = 0$, and go on to the next candidate pair. If, however, both the greater and the lesser angles were within $BANTOL2$ of one another, then this geometry test has established a probable matching order of each observed star in the pair to a single candidate: the observed

star with the greater angle to the pole going with the candidate with the greater angle to the pole and the observed star with the lesser angle to the pole going with the candidate with the lesser angle to the pole.

STEP 8: If *LMAGT* is *FALSE*, the probable matching order determined above is judged valid, we have paired the observed star that is closer to the catalog generation vector with the reference star that is closer to the catalog generation vector, and the further with the further, with *BANTOL2* used to confirm that the angles were in fact in the expected range. Proceed with the next candidate pair.

STEP 9: If *LMAGT* is *TRUE*, compare the probable matching order based on the closeness to the catalog generation vector to the order determined by the magnitude test. If they do not agree, set *IFLAG(J,I) = 0*, and go on to the next candidate. If the order is confirmed, proceed to the next step.

STEP 10: If the difference between the observed and reference angles is less than *BANTOL1*, check the cross product of the two observation vectors and the cross product of the two reference vectors as is done for cap catalogs.

3.0 Full Sky Tests and Results

For the first series of cap catalog tests there were 10 randomly selected large cap catalogs, 10 randomly selected viewing attitudes within each large cap catalog, and up to 5 observed stars per view, for a total of 498 observed stars. The same random number seed was used to begin each test, so the same sequence of attitudes and stars is represented in these cap catalog tests.

For the first series of band catalog tests there were 10 randomly selected directions for the pole of the band catalog, with 10 randomly selected viewing attitudes within each band catalog, and up to 5 observed stars per view, for a total of 495 observed stars. The same random number seed was used to begin each test, so the same sequence of attitudes and stars is represented in these band catalog tests.

3.1 Effect of Increasing Attitude Error

Simulating Attitude Error and Tracker Off-Pointing

The effects of attitude error and tracker off-pointing were also examined in this study because they constitute systematic error sources differing from the random errors in star position and magnitude.

Attitude Error

Attitude error is simulated by generating a nominal GCI-to-body transformation, obtaining the observed star positions in that body frame, and then perturbing those observations by rotating them by the angles given in the indicated 3-2-1 rotation sequence $(\Delta\phi, \Delta\theta, \Delta\psi)$. The observations are converted back to GCI using the inverse transformation of the unperturbed GCI-to-body transformation. The error that is simulated by introducing this rotation is similar to what happens when the transformation matrix used to convert from spacecraft body coordinates to GCI is in error by the respective rotation angles used (i.e., an error in the knowledge of the spacecraft attitude).

This error corresponds to the situation if one were given an a priori spacecraft attitude for the initial attitude acquisition: this attitude would be loaded into mission support software and would be used for the transformation from body to GCI. When the actual spacecraft inertial attitude differs from that expected, the observations made in sensor coordinates are converted to body coordinates using a presumably good transformation, then converted to GCI coordinates using the faulty transformation. The final GCI components of the observations will differ from those in the reference catalog because of this attitude error, even if all other position-related errors are zero. This effect matters because the geometry tests in the STARID algorithm are not fully coordinate-frame independent. Therefore, we needed to ensure that the expected range of attitude errors is tolerated by the STARID algorithm and does not cause the geometry tests to produce erroneous results. In the XTE/SWAS cap catalog case, we expect the initial attitude to differ from the a priori by no more than several degrees about each body axis. For the SOHO band catalog case, we expect any possible rotation about the X-axis but expect no more than 0.1 deg of off-pointing of the X-axis from the Sun.

Tracker Off-Pointing

Another effect studied is that due to the tracker pointing in an unexpected direction, observing other than the expected stars. The STARID algorithm is intended to operate autonomously, so it is desirable that a considerable degree of off-pointing be accommodated without human intervention. The STARID algorithm accommodates off-pointing by maintaining an indexed zone catalog larger than the sensor FOV, which is chosen to contain the actual FOV as a subset. The zone catalog should be large enough to encompass the actual sensor FOV, but it should not be any larger than necessary because the odds of a coincidental match between an observed star pair and some random, incorrect candidate star pair increases as the size of the zone catalog increases. In addition, a larger zone catalog requires greater memory and processing overhead. We can simulate this effect simply by choosing the sensor boresight

randomly within a specified bound. We can choose the bound to keep the sensor FOV safely within the zone catalog, given expected errors. For example, the XTE/SWAS-type cap catalog simulations use a simulated tracker FOV with a radius of 4 deg, and a nominal tracker off-pointing value of 6.66 deg, so the corresponding cap catalog must be at least 10.66 deg in radius.

Attitude Error Versus Tracker Off-Pointing

In practice, both of these effects will be present. To accommodate them, the STARID geometry test parameters must be set according to the expected magnitude of the attitude error and the expected magnitude of the tracker off-pointing error. The size of the zone catalog also needs to be selected according to the expected tracker off-pointing error. The first series of tests attempted to uncover the effect of attitude error, in the presence of a nominal amount of tracker off-pointing. The nominal values chosen are given in Table 1. In the cap catalog runs, a random error is introduced of up to 6.66 deg in the body X-axis position from the nominal boresight of the cap catalog. In the band catalog runs, a random error is introduced of up to 0.1 deg in the X-axis position from the nominal pole of the band catalog, with the Z-axis selected randomly about the X-axis.

3.1.1 Cap Catalog Case

In the cap catalog case, the view direction was confined to within 6.66 deg of the catalog center. To simulate the effect of an error in the conversion from spacecraft body frame to GCI, the LIBROT option to perform 3-2-1 ($\Delta\phi, \Delta\theta, \Delta\psi$) rotations was used to introduce increasing attitude errors in the body frame prior to the nominal body-frame-to-GCI transformation being applied to the observed star positions. Attitude errors significantly larger than the diameter of the cap catalog were tested. The results are given in Table 2. In the cap catalog case, the body X-axis direction is defined to be the tracker boresight direction. Note that misidentifications did not occur until the rotation angles began to equal the tolerance CAPMAX, and the assumptions required for STEP 4 of the geometry test described earlier broke down. Consider the results in Table 2, Run 6. There, we see that an error in the knowledge of the rotation of the tracker about its boresight of 100 deg led to catastrophic failure. If one simply turned off the geometry tests in that case, the result would instead be 1 ambiguous star, 497 stars identified correctly, and no misidentifications.

3.1.2 Band Catalog Case

If, as for SOHO attitude acquisition, only the position of the body axis assumed to lie along the pole of the band catalog is known with any certainty (the pole is nominally Sun-pointing), the ability of the algorithm to tolerate the presence of an error in the body-to-GCI transformation is especially important. Therefore, the band catalog geometry tests need to be effective through the entire range of rotation about the pole. Note in the band catalog case, the body X-axis nominally lies along the direction of the pole of the band catalog, and the body Z-axis is defined to be the tracker boresight direction. The results are given in Table 3. The results show good tolerance for rotation about the pole of the band catalog, as was desired. Significant tilting of the attitude away from the pole is also accommodated, but more than a few degrees begins to produce a significant number of misidentifications. Taking Run 16 from Table 3, and turning the geometry tests off for this band catalog case, the results are not improved: 159 ambiguous stars, only 259 correctly identified stars, and 77 misidentifications resulted. This trial run shows that the separation and magnitude tests alone are not sufficient for the band catalog cases with the levels of position and magnitude noise used as nominal in this analysis.

Table 2. Increasing Simulated Attitude Error and Nominal Tracker Off-Pointing, Cap Catalog Case (1 of 2)

Run #	$\Delta\phi$	$\Delta\theta$	$\Delta\psi$	# Ambiguous Stars	# Stars Identified Correctly (uniquely)	# Stars Misidentified
1	40°	40°	60°	0 (0.00%)	498 (100.00%)	0 (0.00%)
2	40°	40°	10°	0 (0.00%)	498 (100.00%)	0 (0.00%)
3	40°	40°	30°	0 (0.00%)	498 (100.00%)	0 (0.00%)
4	40°	40°	85°	0 (0.00%)	498 (100.00%)	0 (0.00%)
5	40°	40°	90°	22 (4.42%)	474 (95.18%)	2 (0.40%)
6	40°	40°	100°	379 (76.10%)	2 (0.40%)	117 (23.49%)
7	10°	40°	60°	0 (0.00%)	498 (100%)	0 (0.010%)
8	30°	40°	60°	0 (0.00%)	498 (100.00%)	0 (0.00%)
9	90°	40°	60°	0 (0.00%)	498 (100.00%)	0 (0.00%)
10	100°	40°	60°	55 (11.04%)	438 (87.95%)	5 (1.00%)

Table 2. Increasing Simulated Attitude Error and Nominal Tracker Off-Pointing, Cap Catalog Case (2 of 2)

Run #	$\Delta\phi$	$\Delta\theta$	$\Delta\psi$	# Ambiguous Stars	# Stars Identified Correctly (uniquely)	# Stars Misidentified
11	110°	40°	60°	71 (14.26%)	410 (82.33%)	17 (3.41%)
12	40°	10°	60°	0 (0.00%)	498 (100.00%)	0 (0.00%)
13	40°	30°	60°	0 (0.00%)	498 (100.00%)	0 (0.00%)
14	40°	90°	60°	0 (0.00%)	498 (100.00%)	0 (0.00%)
15	40°	100°	60°	31 (6.22%)	463 (92.97%)	4 (0.80%)
16	40°	110°	60°	73 (14.66%)	412 (82.73%)	13 (2.61%)

Table 3. Increasing Simulated Attitude Error and Nominal Tracker Off-Pointing, Band Catalog Case

Run #	$\Delta\phi$	$\Delta\theta$	$\Delta\psi$	# Ambiguous Stars	# Stars Identified Correctly (uniquely)	# Stars Misidentified
1	0.1°	0.1°	0.1°	3 (0.61%)	492 (99.39%)	0 (0.00%)
2	0.1°	0.1°	90°	3 (0.61%)	492 (99.39%)	0 (0.00%)
3	0.1°	0.1°	180°	4 (0.81%)	491 (99.19%)	0 (0.00%)
4	0.1°	0.1°	270°	3 (0.61%)	492 (99.39%)	0 (0.00%)
5	3°	3°	3°	14 (2.83%)	479 (96.77%)	2 (0.40%)
6	3°	3°	90°	14 (2.83%)	480 (96.97%)	1 (0.20%)
7	3°	3°	180°	19 (3.84%)	476 (96.16%)	0 (0.00%)
8	3°	3°	270°	18 (3.64%)	476 (96.16%)	1 (0.20%)
9	4°	4°	4°	72 (14.54%)	414 (83.64%)	9 (1.82%)
10	4°	4°	90°	78 (15.76%)	409 (82.63%)	8 (1.62%)
11	4°	4°	180°	75 (15.15%)	415 (83.84%)	5 (1.01%)
12	4°	4°	270°	77 (15.56%)	412 (83.23%)	6 (1.21%)
13	5°	5°	5°	115 (23.23%)	361 (72.93%)	19 (3.84%)
14	5°	5°	90°	121 (24.44%)	356 (71.92%)	18 (3.64%)
15	5°	5°	180°	121 (24.44%)	356 (71.92%)	18 (3.64%)
16	5°	5°	270°	122 (24.65%)	356 (71.92%)	17 (3.43%)

3.2 Effect of Increasing Star Magnitude Error

The STARID algorithm input parameters must be consistent with the expected error in the observed magnitudes for the magnitude information to be used effectively as a pattern dimension. The next series of runs was performed with the tolerance $XMTOL$, the maximum difference between the magnitude of an observed star and the magnitude of any of its candidates, above which a candidate star is eliminated from consideration, fixed at 0.6. This value is a reasonable bound for the match between the predicted and actual instrumental magnitude for the majority of cataloged stars. The tolerance $TMAGMX$, the minimum magnitude difference indicating which is the brighter of the two observed stars, was also fixed at 0.6. The upper limit on simulated magnitude error was set to 6, to ensure that the distribution of the magnitude errors was not cut off for the higher values of $SIGMAG$ (the simulated observed star magnitude noise standard deviation, 1σ) that were tested. The results are shown in Table 4 for the cap catalog case and in Table 5 for the band catalog case. The first few runs in each table have a simulated magnitude error within the range for which the fixed

Table 4. Increasing Simulated Magnitude Error, Cap Catalog Case

Run #	SIGMAG (simulated magnitude noise, 1σ)	# Ambiguous Stars	# Stars Identify Correctly (uniquely)	# Stars Misidentified
1	0.10	0 (0.00%)	498 (100.00%)	0 (0.00%)
2	0.15	0 (0.00%)	498 (100.00%)	0 (0.00%)
3	0.20	1 (0.20%)	497 (99.80%)	0 (0.00%)
4	0.25	2 (0.40%)	496 (99.60%)	0 (0.00%)
5	0.30	7 (1.41%)	490 (98.39%)	1 (0.20%)
6	0.35	23 (4.65%)	473 (94.98%)	2 (0.40%)
7	0.40	35 (7.03%)	458 (91.97%)	5 (1.00%)
8	0.45	48 (9.64%)	445 (89.36%)	5 (1.00%)
9	0.50	63 (12.65%)	431 (86.55%)	4 (0.80%)
10	1.00	208 (41.77%)	275 (55.22%)	15 (3.01%)

Table 5. Increasing Simulated Magnitude Error, Band Catalog Case

Run #	SIGMAG (simulated magnitude noise, 1σ)	# Ambiguous Stars	# Stars Identified Correctly (uniquely)	# Stars Misidentified
1	0.10	4 (0.81%)	491 (99.19%)	0 (0.00%)
2	0.15	4 (0.81%)	491 (99.19%)	0 (0.00%)
3	0.20	4 (0.81%)	491 (99.19%)	0 (0.00%)
4	0.25	5 (1.01%)	490 (98.99%)	0 (0.00%)
5	0.30	13 (2.63%)	479 (96.77%)	3 (0.61%)
6	0.35	21 (4.24%)	470 (94.95%)	4 (0.81%)
7	0.40	35 (7.07%)	451 (91.11%)	9 (1.82%)
8	0.45	64 (12.93%)	419 (84.65%)	12 (2.42%)
9	0.50	83 (16.77%)	390 (78.79%)	22 (4.44%)
10	1.00	273 (55.15%)	170 (34.34%)	52 (10.50%)

reasonable tolerances are valid, or nearly so. The later runs show the effect of the magnitude error rising past the point where the fixed tolerances become invalid, showing what might happen if predicted instrumental magnitude and actual were not in as good an agreement as expected. These results also show a general feature of the pattern-matching algorithm: the smooth degradation of identification results as error increases. This feature should be helpful in monitoring during operations, since the number of ambiguous identifications can be watched, and a high number can alert the user that tolerances may need to be adjusted.

3.3 Effect of Increasing Simulated Observed Star Position Error

In this series of runs, the amount of simulated observed star position error was increased while the related STARID input parameters remained fixed at the nominal values given in Table 1. The results are given in Table 6 for the cap catalog case and in Table 7 for the band catalog case.

Table 6. Increasing Simulated Observed Star Position Error, Cap Catalog Case

Run #	SIGOBS (simulated position noise, 1σ , sec)	# Ambiguous Stars	# Stars Identified Correctly (uniquely)	# Stars Misidentified
1	0	0 (0.00%)	498 (100.00%)	0 (0.00%)
2	3	0 (0.00%)	498 (100.00%)	0 (0.00%)
3	6	0 (0.00%)	498 (100.00%)	0 (0.00%)
4	9	0 (0.00%)	497 (99.80%)	1 (0.20%)
5	12	3 (0.60%)	493 (99.00%)	2 (0.40%)
6	15	12 (2.41%)	482 (96.79%)	4 (0.80%)
7	18	26 (5.22%)	469 (94.18%)	3 (0.60%)
8	21	48 (9.64%)	446 (89.56%)	4 (0.80%)

Table 7. Increasing Simulated Observed Star Position Error, Band Catalog Case

Run #	SIGOBS (simulated position noise, 1σ , sec)	# Ambiguous Stars	# Stars Identified Correctly (uniquely)	# Stars Misidentified
1	0	4 (0.81%)	491 (99.19%)	0 (0.00%)
2	3	4 (0.81%)	491 (99.19%)	0 (0.00%)
3	6	4 (0.81%)	485 (97.98%)	0 (0.00%)
4	9	5 (1.01%)	485 (97.98%)	0 (0.00%)
5	12	16 (3.23%)	478 (96.57%)	1 (0.20%)
6	15	30 (6.06%)	461 (93.13%)	4 (0.81%)
7	18	61 (12.32%)	424 (85.66%)	10 (2.02%)
8	21	83 (16.77%)	396 (80.00%)	16 (3.23%)

The increasing position errors become apparent both through the effect of the observed separations becoming erroneous, causing invalid indexing into the list of candidates, and from the separation tolerance test for candidates being applied without accounting for the increased error. Note that a value of SIGOBS, the simulated observed star position error (1σ), of 3 sec or less is consistent with the expected tracker measurement noise for XTE, SWAS and SOHO missions.

4.0 Band Catalog With Sun-Oriented Pole Tests and Results

This series of tests explores the algorithm performance for a SOHO-type mission where the body X-axis is nominally aligned toward the Sun. Since for this mission the Sun-oriented band catalog geometry repeats itself every 6 months, unit vectors toward the Sun were generated from solar-lunar-planetary (SLP) files over the interval of 950701 to 960101 at 1-month intervals. The Sun unit vectors were selected for use as the a priori catalog generation vectors. The body X-axis was chosen to lie within a uniform random error of 0.1 deg from the Sun unit vector, and the body Z-axis was chosen in a uniformly random direction perpendicular to the X-axis. The 3-2-1 rotation of 0.1, 0.1, and 180 deg used previously was applied to simulate the effect of attitude error. Table 8 summarizes the results for this series of runs that used the nominal parameters shown in Table 1, for 4 runs, each with a different seed for the linear congruential generator, to obtain a larger total set of tests. Each individual run generated 6 band catalogs, and used each band catalog for 10 randomly selected views. From these results we see that with nominal errors, the algorithm performed well for the Sun-oriented geometries tested. At the higher levels of error, the results were within a percent or so of the results obtained in the randomly-oriented full sky band catalog tests at the same error level.

Table 8. Sun-Oriented Band Catalog Tests

Test Description	#Stars Total	# Ambiguous Stars	# Stars Identified Correctly (uniquely)	# Stars Misidentified
Nominal Sun-Oriented Band Catalog Series	1192	8 (0.67%)	1184 (99.33%)	0 (0.00%)
Sun-Oriented Band Catalog Series With Serious Attitude Errors: The simulated attitude error rotation was $(\Delta\phi, \Delta\theta, \Delta\psi) = (3^\circ, 3^\circ, 3^\circ)$, the value at which misidentifications began to occur in Section 3.1.	1192	49 (4.11%)	1137 (95.38%)	6 (0.50%)
Sun-Oriented Band Catalog Series With Serious Magnitude Errors: <i>SIGMAG</i> was set to 0.3, the value at which misidentifications began to occur in Section 3.2. The upper limit on simulated magnitude error was set to 6.	1192	43 (3.61%)	1138 (95.47%)	11 (0.92%)
Sun-Oriented Band Catalog Series With Serious Simulated Observed Star Position Errors: <i>SIGOBS</i> was set to 12 sec, the value at which misidentifications began to occur in Section 3.3.	1192	22 (1.85%)	1167 (97.90%)	3 (0.25%)

5.0 Star Desert and Star Forest Tests

Study of the pattern-matching algorithms suggested that the reliability and execution time of the methods would likely be affected by the varying stellar density encountered from region to region within a given full-sky star catalog. We used the natural variation of stellar density to evaluate the effects of this factor by looking at regions with fewer stars than average ("star deserts") and regions with more stars than average ("star forests").

5.1 Star Desert and Star Forest Tests, Cap Catalog Case

Table 9 summarizes the results of star desert and star forest tests using a cap catalog. The most interesting result is the decrease in ambiguous identifications in the star desert compared to the star forest. Likewise, there was an increase in misidentifications in the serious error cases in the star forest compared to the star desert.

5.2 Star Desert and Star Forest Tests, Band Catalog Case

Table 10 summarizes the results of star desert and star forest tests using a band catalog. Again we see the decrease in ambiguous identifications in the star desert compared to the star forest, and an increase in misidentifications in the serious error cases in the star forest compared to the star desert. The effects are significantly larger, however, than in the cap catalog tests. This is apparently simply due to the larger number of stars in the zone catalog in the band catalog case. The number of candidate pairs is proportional to the number of combinations of *NCAP* items taken 2 at a time, equal to $(NCAP^2 - NCAP)/2$, where *NCAP* is the number of stars in the zone catalog. A given error in the value of an observed star's measurement along a pattern dimension has a much higher probability of leading to misidentification of the observed star pair when using a large zone catalog than when using a small one because of the greatly increased density of candidate pairs with respect to each unit of pattern dimension.

6.0 Performance Considerations

6.1 Execution Time

It is useful to consider the prototype execution times with respect to the values of *NCAP*, the number of stars in the zone catalog, and *NTOT*, the number of candidate pairs from that zone catalog with separation less than the effective FOV width. Recall that in these simulations, all observations used for each identification attempt can be considered to be from a single time, made from a single inertially-fixed circular tracker FOV. Thus, the effective FOV width is just the tracker diameter (8 deg for XTE/SWAS, 4 deg for SOHO). Execution times from a representative set of runs described above are given in Table 11 for cap catalog cases and in Table 12 for band catalog cases. Note that the software wall clock time has a resolution of about 0.055 sec, so "buckets" are noticeable on short times. In the runs we examined, the wall clock time required to reassemble the same zone catalog varies slightly, most likely due to the varying load on the LAN. The first access is almost always the longest, as one would expect, due to overhead in establishing the file connection. The subsequent zone catalog generation times for the same zone catalog were generally more

Table 9. Star Desert and Star Forest Tests, Cap Catalog Case

Test Description	#Stars Total	# Ambiguous Stars	# Stars Identified Correctly (uniquely)	# Stars Misidentified
Star Desert With Nominal Errors: The direction for the cap catalog generation was $(\alpha, \delta) = (12.25^\circ, -27.4^\circ)$, the approximate position of the Southern Galactic Pole (SGP)	1861	19 (1.02%)	1842 (98.98%)	0 (0.00%)
Star Forest With Nominal Errors: The direction for the cap catalog generation was $(\alpha, \delta) = (265.6^\circ, -28.917^\circ)$, the approximate position of the Galactic Center (GC).	2000	0 (0.00%)	2000 (100.00%)	0 (0.00%)
Star Desert With Serious Attitude Errors: Rotations about each axis were set to values at which misidentifications began to occur in Section 3.1. ($\Delta\phi=40'', \Delta\theta=40'', \Delta\psi=90^\circ$)	1861	118 (6.34%)	1726 (92.74%)	17 (0.91%)
($\Delta\phi=100^\circ, \Delta\theta=40'', \Delta\psi=60''$)	1861	199 (10.69%)	1643 (88.29%)	19 (1.02%)
($\Delta\phi=40'', \Delta\theta=100^\circ, \Delta\psi=60''$)	1861	212 (11.39%)	1614 (86.73%)	35 (1.88%)
Star Forest With Serious Attitude Errors: Rotations about each axis were set to values at which misidentifications began to occur in Section 3.1. ($\Delta\phi=40'', \Delta\theta=40'', \Delta\psi=90^\circ$)	2000	106 (5.30%)	1868 (93.40%)	26 (1.30%)
($\Delta\phi=100^\circ, \Delta\theta=40'', \Delta\psi=60''$)	2000	235 (11.75%)	1726 (86.30%)	39 (1.95%)
($\Delta\phi=40'', \Delta\theta=100^\circ, \Delta\psi=60''$)	2000	210 (10.50%)	1735 (86.75%)	55 (2.75%)
Star Desert Series With Serious Magnitude Errors: SIGMAG was set to 0.3, and the upper limit on simulated magnitude error was set to 6.	1861	51 (2.74%)	1803 (96.88%)	7 (0.38%)
Star Forest Series With Serious Magnitude Errors: SIGMAG was set to 0.3, and the upper limit on simulated magnitude error was set to 6.	2000	48 (2.40%)	1945 (97.25%)	7 (0.35%)
Star Desert Series With Serious Simulated Observed Star Position Errors: SIGOBS was set to 12 sec	1861	40 (2.15%)	1803 (97.80%)	1 (0.05%)
Star Forest Series With Serious Simulated Observed Star Position Errors: SIGOBS was set to 12 sec	2000	21 (1.05%)	1972 (98.60%)	7 (0.35%)

Table 10. Star Desert and Star Forest Tests, Band Catalog Case

Test Description	#Stars Total	# Ambiguous Stars	# Stars Identified Correctly (uniquely)	# Stars Misidentified
Star Desert With Nominal Errors: The direction for the pole of the band catalog was $(\alpha, \delta) = (292.3894^\circ, 80.0740^\circ)$, a position selected because it gave fewer stars (1,292) and fewer candidate pairs with separations up to 4 deg (18,768) than other directions found. This number of stars and candidate pairs is assumed to be near the minimum possible given this input catalog.	1965	11 (0.56%)	1954 (99.44%)	0 (0.00%)
Star Forest With Nominal Errors: The direction for the pole of the band catalog was $(\alpha, \delta) = (191.1942^\circ, 27.6408^\circ)$, a position near the North Galactic Pole (NGP), selected because it gave almost the maximum number of stars (3,124 versus 3,125) and more candidate pairs with separations up to 4° (106,802 vs 106,592 for the 3,125 star case) than other directions found during our random search. This number of stars and candidate pairs is assumed to be near the maximum possible given this input catalog.	2000	40 (2.00%)	1956 (97.80%)	4 (0.20%)
Star Desert With Serious Attitude Errors: Rotations were set to $(\Delta\phi, \Delta\theta, \Delta\psi) = (3^\circ, 3^\circ, 3^\circ)$, the values at which misidentifications began to occur in Section 3.1.	1965	47 (2.39%)	1917 (97.56%)	1 (0.05%)
Star Forest With Serious Attitude Errors: Rotations were set to $(\Delta\phi, \Delta\theta, \Delta\psi) = (3^\circ, 3^\circ, 3^\circ)$, the values at which misidentifications began to occur in Section 3.1.	2000	157 (7.85%)	1813 (90.65%)	30 (1.50%)
Star Desert Series With Serious Magnitude Errors: <i>SIGMAG</i> was set to 0.3, and the upper limit on simulated magnitude error was set to 6.	1965	60 (3.05%)	1897 (96.54%)	8 (0.41%)
Star Forest Series With Serious Magnitude Errors: <i>SIGMAG</i> was set to 0.3, and the upper limit on simulated magnitude error was set to 6.	2000	108 (5.40%)	1860 (93.00%)	32 (1.60%)
Star Desert Series With Serious Simulated Observed Star Position Errors: <i>SIGOBS</i> was set to 12 sec	1965	39 (1.98%)	1923 (97.86%)	3 (0.15%)
Star Forest Series With Serious Simulated Observed Star Position Errors: <i>SIGOBS</i> was set to 12 sec	2000	122 (6.10%)	1863 (93.15%)	15 (0.75%)

**Table 11. Wall Clock Execution Times for Selected Cap Catalog Cases
(Platform: 33 MHz, 486 CPU)**

Case Description	Generate Catalog		Create Star Identification Data Structure (SIDS) and Do 1st Star Identification			Subsequent ID Times With Existing SIDS		
	Time	NCAP	Time	NCAP	NTOT	Time	NCAP	NTOT
1st Run from Table 2, Cap Catalog, Random Pointing, Nominal Errors	Min 0.22 s Max 0.49 s	63 67	Min 0.17 s Max 0.22 s	63 84	697 1467	Min 0.10 s Max 0.22 s	63 63	697 697
Total Time = Sum of all 10 catalogs: (time to generate catalog + time to create SIDS and 1st ID + time for subsequent 9 IDs with existing SIDS) = 18.55 s, 1.9 s average for a new catalog and 10 views/catalog								
1st Run from Table 9, Cap Catalog Case, Star Desert, Nominal Errors	Min 0.17 s Max 0.27 s	49 49	Min 0.16 s Max 0.22 s	49 49	483 483	Min 0.10 s Max 0.22 s	49 49	483 483
Total Time = Sum of all 10 catalogs: (time to generate catalog + time to create SIDS and 1st ID + time for subsequent 9 IDs with existing SIDS) = 17.86 s, 1.8 s average for a new catalog and 10 views/catalog								
1st Run from Table 9, Cap Catalog Case, Star Forest, Nominal Errors	Min 0.22 s Max 0.38 s	116 116	Min 0.33 s Max 0.39 s	116 116	2701 2701	Min 0.11 s Max 0.33 s	116 116	2701 2701
Total Time = Sum of all 10 catalogs: (time to generate catalog + time to create SIDS and 1st ID + time for subsequent 9 IDs with existing SIDS) = 20.67 s, 2.1 s average for a new catalog and 10 views/catalog								

**Table 12. Wall Clock Execution Times for Selected Band Catalog Cases
(Platform: 33 MHz, 486 CPU)**

Case Description	Generate Catalog		Create SIDS and Do 1st Star Identification			Subsequent ID Times With Existing SIDS		
	Time	NCAP	Time	NCAP	NTOT	Time	NCAP	NTOT
1st Run from Table 8, Band Catalog Case, Sun-Oriented, Nominal Errors	Min 8.02 s Max 11.48 s	1534 1947	Min 6.97 s Max 11.20 s	1534 2009	28676 42067	Min 0.17 s Max 0.50 s	1534 1747	28676 37616
Total Time = Sum of all 6 catalogs: (time to generate catalog + time to create SIDS and 1st ID + time for subsequent 9 IDs with existing SIDS) = 135.45 s, 22.6 s average for a new catalog and 10 views/catalog								
1st Run from Table 10 Band Catalog Case, Star Desert, Nominal Errors	Min 4.56 s Max 6.42 s	1292 1292	Min 4.72 s Max 4.89 s	1292 1292	18768 18768	Min 0.11 s Max 0.33 s	1292 1292	18768 18768
Total Time = Sum of all 10 catalogs: (time to generate catalog + time to create SIDS and 1st ID + time for subsequent 9 IDs with existing SIDS) = 121.19 s, 12.2 s average for a new catalog and 10 views/catalog								
1st Run from Table 10 Band Catalog Case, Star Forest, Nominal Errors	Min 15.32 s Max 22.02 s	3124 3124	Min 28.28 s Max 28.62 s	3124 3124	106802 106802	Min 0.66 s Max 1.10 s	3124 3124	106802 106802
Total Time = Sum of all 10 catalogs: (time to generate catalog + time to create SIDS and 1st ID + time for subsequent 9 IDs with existing SIDS) = 528.21 s, 52.8 s average for a new catalog and 10 views/catalog								

consistent. The operational systems for support of XTE/SWAS will also have remote access to files, which saves space; but our experience suggests that, to avoid this problem, separate copies of the star catalogs should be kept on each HP 715/50 workstation that may need to run the support software. In the star desert cases, the minimum star identification times were typically those for which the fewest stars were in the simulated sensor FOV, give or take the wall clock resolution.

6.2 Memory Requirements

The largest storage requirements in the prototype are for those arrays that need to be sized larger than the expected number of candidate pairs $NTOT$. $NTOT$ is related to $NCAP$ by:

$$NTOT = k_g \frac{(NCAP^2 - NCAP)}{2} \quad (1)$$

Pairs of zone catalog stars whose separation exceeds the effective tracker FOV are unobservable, so $k_g \leq 1$.

We have observed that for the range of effective tracker FOV widths and zone catalog sizes used in this study, the constant of proportionality k_g is approximated by

$$k_g \approx 3 \frac{AREA_{TRACKERFOV}}{AREA_{ZONECATALOG}} \quad (2)$$

As stars are not uniformly distributed, the observed values necessarily vary about this or any other approximation. Values of geometric k_g calculated using (2), and apparent k_g calculated using (1) with the $NCAP$ and $NTOT$ values given in Tables 11 and 12 are given below in Tables 13 and 14, respectively. The approximation gives a conservatively large value of k_g for the range of relative tracker FOV and zone catalog areas we considered.

The relationship between $NCAP$ and $NTOT$ must be kept in mind to ensure that arrays are dimensioned according to the expected worst-case $NTOT$ value. To find the memory requirements of this algorithm for a given catalog if the worst-case stellar density for the catalog is available, multiply that density by the area of the zone-catalog to get an estimate for $NCAP$, and use the approximation for k_g in (1) to calculate a bound for $NTOT$. In practice, a safety margin seems warranted: we used a dimension of 150,000, which was never exceeded in our tests. The $NTOT = 106802$ band catalog case was the largest we found with the SOHO catalog and a 4.2-deg edge-to-edge band.

Table 13. Values of k_g Obtained for Selected Cap Catalog Cases

Geometric k_g	$NCAP$	$NTOT$	Apparent k_g
0.4224	63	697	0.357
0.4224	84	1467	0.421
0.4224	49	483	0.411
0.4224	116	2701	0.405

Table 14. Values of k_g Obtained for Selected Band Catalog Cases

Geometric k_g	$NCAP$	$NTOT$	Apparent k_g
0.0249	1534	28676	0.024
0.0249	2009	42067	0.021
0.0249	1292	18768	0.022
0.0249	3124	106802	0.022

7.0 Conclusions

Based on these results, the prototype algorithm is fast enough for both XTE/SWAS and SOHO mission requirements. Even the periodic updates to the zone catalog and corresponding SIDS initialization for XTE/SWAS-type cases can be accomplished in under 1 sec on the 33 MHz 486, so should not present a problem on the HP 715/50. Initialization does take longer for SOHO-type band catalog cases, but still completed in under 60 sec even for the star forest case.

When operating within XTE/SWAS and SOHO mission parameters, the identification process was almost always successful and was found not to produce incorrect identifications. It was found to degrade smoothly when errors grow above tolerances. However, the degradation was steep for the cap catalog geometry tests once the tolerances were exceeded. With the nominal values of position and magnitude noise, it appears that the separation and magnitude tests alone are often sufficient for good identification results in such a cap catalog case, as we saw with the results in Table 2, Run 6. However, as with the results in Table 3, Run 16, we found that the band catalog geometry tests, even when their tolerances were exceeded, produced significant improvement in identification accuracy over that achieved with separation and magnitude tests alone, with the levels of position and magnitude noise used as nominal in this analysis.

References

Van Bezooijen, R. W. H., "Autonomous Star Referenced Attitude Determination," AAS 89-03, *Guidance and Control, Proceedings of the Annual Rocky Mountain Guidance and Control Conference*, Keystone, CO, 1989

Slater, M. and Hashmall, J. (CSC), *SKYMAP Star Catalog Data Base Generation and Utilization System Description, Revision 3, Update 1*, 554-FDD-89/001R3UD1, Goddard Space Flight Center, Flight Dynamics Division, prepared by Computer Sciences Corporation, August 1992

Color/Magnitude Calibration for National Aeronautics and Space Administration (NASA) Standard Fixed-Head Star Trackers (FHST)*

J. Landis, T. Leid, A. Garber
Computer Sciences Corporation (CSC)
Lanham-Seabrook, Maryland, USA

M. Lee
National Aeronautics and Space Administration (NASA)
Goddard Space Flight Center (GSFC)
Greenbelt, Maryland, USA

Abstract

This paper characterizes and analyzes the spectral response of Ball Aerospace Fixed-Head Star Trackers (FHSTs) currently in use on some three-axis stabilized spacecraft. The FHST output is a function of the frequency and intensity of the incident light and the position of the star image in the field of view. The FHSTs on board the Extreme Ultraviolet Explorer (EUVE) have had occasional problems identifying stars with a high B-V value. These problems are characterized by inaccurate intensity counts observed by the tracker. The inaccuracies are due to errors in the observed star magnitude values. These errors are unique to each individual FHST. For this reason, data were also collected and analyzed from the Upper Atmosphere Research Satellite (UARS). As a consequence of this work, the Goddard Space Flight Center (GSFC) Flight Dynamics Division (FDD) hopes to improve the attitude accuracy on these missions and to adopt better star selection procedures for catalogs.

Introduction

The Extreme Ultraviolet Explorer (EUVE) satellite was launched in June 1992. It began its mission operations during the survey mode phase, where EUVE scanned the entire sky in the extreme ultraviolet wavelength to make a complete extreme ultraviolet sky map. After the mapping phase was completed, EUVE went on to observe specific ultraviolet sources. This was the spectroscopy or inertial phase of the mission. Survey mode is also the mission configuration where the attitude determination instruments are calibrated, so EUVE enters survey mode periodically for calibration.

The primary instrument used for attitude determination (AD) on EUVE are the two National Aeronautics and Space Administration (NASA) Standard Fixed-Head Star Trackers (FHSTs). If a problem were to occur with the one or both of the FHSTs, the AD would have to be done using the fine Sun sensor (FSS), which is less accurate (60 arcseconds (arcsec) as opposed to 10 arcsec for FHSTs). Therefore, it has been standard practice to analyze thoroughly any anomalies with the FHSTs to ensure their proper performance. Most star acquisition problems with the FHSTs can be attributed to stars in the field of view (FOV) being optical binaries or to a bright star in the FOV. But since EUVE's launch, there have been several anomalies in FHST1 that could not be explained by either of these two explanations. The FHST would scan the FOV for a cataloged guide star and would never identify any stars. When EUVE is in inertial mode, it usually has no more than one or two stars in the FOV of each FHST that can be used for AD. If one of the FHSTs is unable to acquire a star in its FOV, the AD must be done using only one FHST and the FSS, therefore making the attitude determination less accurate.

*This work was supported by the National Aeronautics and Space Administration (NASA)/Goddard Space Flight Center (GSFC), Greenbelt, Maryland, under Contract NAS 5-31500.

Preliminary analysis indicated that the FHST was unable to maintain a lock on the stars. When an FHST scans for stars, it returns two pieces of data: (1) an observed intensity count value and (2) a position in the FOV. The FHST scanning the FOV for the cataloged guide star would actually "see" the star. The OBC would not identify the star because of an error in the observed intensity of the star (Reference 1) and would break track on the star. This led to the FHST continuously scanning the FOV but never having the OBC identify anything. Many times when this problem occurred, the star in the FOV was a dim star with a high blue minus visual (B-V) value. A star's B-V value is defined as its color index. Because stars have different temperatures, their spectral energy curves peak at different wavelengths. Therefore, hotter stars are bluish, and cooler stars are reddish. Using the B-V color index, it can be seen that a bluish star has a negative B-V value because it is brighter in blue (smaller B magnitude) than at longer wavelengths (larger V magnitude). Conversely, a reddish star has a positive color index because it is brighter in V than in B (Reference 2). This color index value considers the interstellar medium. It measures the star temperature and the scattering of blue wavelengths due to interstellar gas and dust. The following Hirshfeld table (Table 1) provides the approximate correspondence between the value of the color index and the observed color.

Table 1. Hirshfeld Table

Color Index	Visual Color
Less than 0.0	Blue
0.0 to 0.3	Blue to White
0.3 to 0.6	White
0.6 to 1.1	White to Yellow
1.1 to 1.5	Orange to Red
Greater than 1.5	Red

Because EUVE and the Gamma Ray Observatory (GRO) FHSTs have both experienced these types of problems (Reference 3), it was decided to evaluate the Upper Atmosphere Research Satellite's (UARS) FHSTs to determine if it was experiencing similar problems. The UARS, which was launched in September 1991, is an Earth-pointing satellite with a constant pitch rate of 1 revolution per orbit (RPO). This creates a scenario where the FHSTs are constantly acquiring new stars in their FOV. Therefore, a problem with observed magnitudes could go unnoticed unless specifically tracked. It should be noted that since each FHST has its own spectral response, analysis must be performed on each FHST independently.

EUVE/UARS Spacecraft Overview

The EUVE spacecraft (Figure 1) consists of a Multi-Mission Modular Spacecraft (MMS), a Platform Equipment Deck (PED), and a Payload Module. The MMS is triangular prism in shape with three basic submodules attached: the Modular Power Subsystem (MPS), Modular Attitude Control Subsystem (MACS), and Communications and Data Handling (C&DH) Subsystem. The MMS components are used for attitude/orbit determination and control and for communications with the ground through the Tracking and Data Relay Satellite System (TDRSS).

The coordinate system of the Attitude Control System (ACS) is defined as follows: the X-axis points toward the payload module and is aligned with the Deep Survey Photometer/Spectrometer pointing direction (opposite the high-gain antenna); the Y-axis points toward the FHSTs; and the Z-axis is normal to the outward face of the Signal Conditioning and Control Unit (SC&CU). The coordinate system is often referred to as the ACS coordinate system. The FHSTs are attached to the MACS module. The EUVE FHSTs boresights are approximately 76 degrees (deg) apart.

The EUVE spacecraft has two nominal modes of operation: survey mode and inertial pointing mode. During survey mode, the spacecraft is rotating about the ACS X-axis at 3 revolutions per orbital period corresponding to a roll rate of 0.19 degrees/second (deg/sec). The 3 revolutions per orbital period ensure that one revolution will occur every orbit night. At every orbit sunrise, the -X-axis is repointed at the Sun and held in that direction until the next orbit sunrise. The 1-deg per day average motion of the Earth about the Sun allowed EUVE to scan the entire celestial sphere in 6 months. In inertial mode the spacecraft is three-axis stabilized, and the ACS X-axis points at the target extreme ultraviolet source.

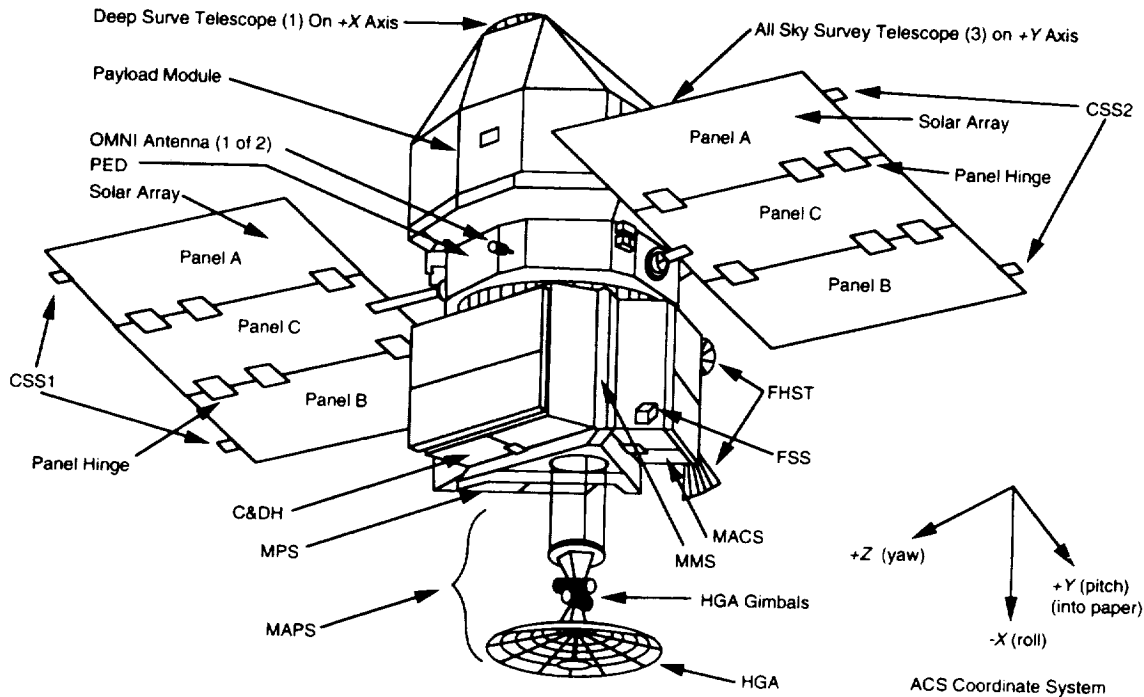


Figure 1. EUVE Spacecraft

The UARS spacecraft (Figure 2) is also an MMS. The nominal MCS is defined by the MACS alignment cube and is nominally parallel to the body coordinate system (BCS). The coordinate system of the MACS is defined as follows: the X-axis points toward the Solar Stellar Pointing Platform (SSPP); the Y-axis points towards the FHSTs; and the Z-axis is nadir pointing toward the Earth. The coordinate system is often referred to as the ACS coordinate system. As with EUVE, the FHSTs are attached to the MACS module and are approximately 76 deg apart.

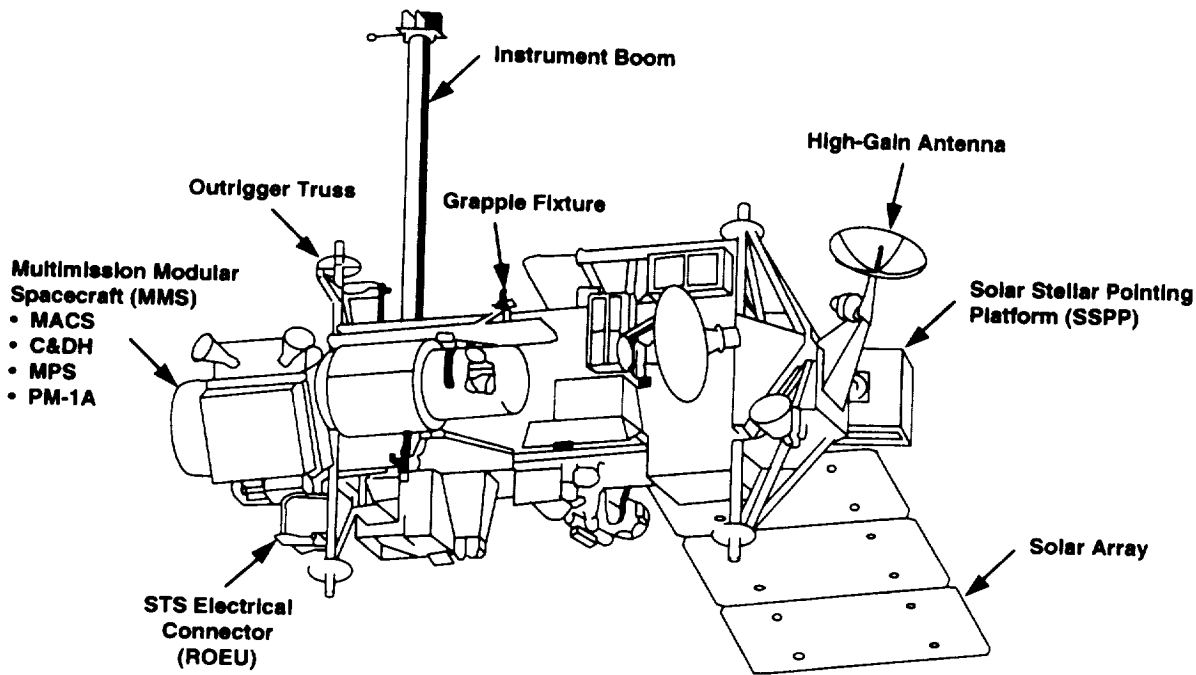


Figure 2. UARS Spacecraft

The UARS spacecraft normally operates in Earth-pointing mode. During Earth-pointing mode at 0 deg yaw, the spacecraft is rotating at 1 RPO about the ACS Y-axis, with the X-axis pointing along the velocity vector and the Z-axis nadir pointing at all times. Approximately once every 35 days, a 180-deg yaw maneuver is performed to keep the solar arrays aligned with the Sun and the science instruments out of the Sun. When the spacecraft is at 180 deg yaw, rotation at 1 RPO occurs about the ACS negative (-) Y-axis, with the X-axis pointing along the negative velocity vector, while the Z-axis maintains nadir pointing.

FHST Overview

The primary attitude sensors included on board EUVE and UARS are two pairs of FHSTs. The FHSTs used are NASA standard star trackers built by Ball Electro-Optics/Cryogenics Division. These sensors search for, detect, and track stars by focusing light from the object being tracked on the photocathode of an image dissector tube determining the intensity and position of the star. The FHSTs can track stars in the instrumental magnitude range of 2.0 to 5.7. (The instrumental magnitude is the magnitude that is expected of a star based on its intensity and color along with an averaged standard spectral response of an FHST.) As a star passes through the FOV of the FHST, a 0.2 magnitude fluctuation is expected.

For use on EUVE, the magnitudes of allowable stars to track is limited by the flight operations team (FOT), depending on the mission phase. While in survey mode, the magnitudes are limited to a range from 2 to 4.25. When the spacecraft is rotating, a narrow magnitude limit is preferable because of the large numbers of stars passing through the FOV of the FHSTs. While EUVE is inertial-pointing mode, however, the magnitude limits are increased to include stars to a magnitude of 5.25 because of the lower numbers of stars available to ensure that there is a star available in each tracker.

Each FHST has an 8-deg-by-8-deg square FOV, with a digital resolution of 7.78 arcsec. The manufacturer's specified position accuracy is 10 arcsec (1σ) within an 8-deg circular central FOV. Each telemetry count is equivalent to 7 arcsec of position in the FOV. For consistency, the FOV's coordinate system is defined as follows. From the inside of the FHST looking outward, the vertical position is referred to as theta with negative theta being in the upward direction. The horizontal position is referred to as phi with negative phi being to the left.

On the ground, the FHST's measurements are handled as follows. The FHST position output consists of two angles measured sequentially, each requiring a 50 milliseconds (msec) measurement time. The position determined is approximately that of the star at the middle of the measurement period, 25 msec before the measurement becomes available for sampling. Since the 100 msec FHST measurement cycle is independent of the onboard computer (OBC) sampling cycle, and, therefore, the time since the measurements were updated is unknown; the time of the star position measurement is at least 25 msec and as much as 125 msec before the time at which the measurement is sampled. Due to this timing error in conjunction with the roll rate, position errors can be in the range of +/- 20.3 arcsec. The position is then corrected for using known alignments and calibrated misalignments.

The FHST manufacturer provides a transfer function for the calibration of the star tracker's FOV. It consists of a polynomial in tracker temperature, ambient magnetic field, star intensity, and star position in the FOV. Each FHST also has a FOV scale factor. These values are used to convert from horizontal and vertical counts in the FOV to angular measurements. Nominally, these values are 0.002162 deg per count. The scale factor value for UARS FHST1 is drifting at a quasi-linear rate making the FHST1 values 0.002130 deg per count as of October 28, 1993. The values for the EUVE FHSTs presently show no drifting. This drift in the UARS value must be accounted for when analyzing any FHST1 data.

The intensity information is also unpacked and converted from counts to volts (0.02 volt per count) and eventually to star instrumental magnitude. The conversion equations are given below as

$$I_{obs} = 0.02 * (\text{intensity counts}) \quad (1)$$

$$M_I = A * \text{Log}_{10}(I_{obs} - I_{ref}) + M_{bias} \quad (2)$$

where I_{obs} is the observed intensity in volts, I_{ref} is the reference intensity, M_{bias} is the magnitude bias, M_I is the calculated observed magnitude, and A is a constant. Since each FHST needs to be calibrated independently, each FHST can have its own values. The values for both spacecraft and each FHST are listed in Table 2.

Table 2. Intensity Conversion Constants

Intensity Conversion Constants	EUVE	UARS
A(FHST1)	-2.5	-2.5
A(FHST2)	-2.5	-2.5
M_{bias} (FHST1)	3.500	3.533
M_{bias} (FHST2)	3.423	3.533
I_{ref} (Both)	0.0	0.0

The star observations are later corrected for stellar aberration and identified by propagating all star observations to a common time and then comparing the positions of the stars with the reference positions and magnitudes of known stars included in the onboard star catalog. The positions are determined assuming a known a priori attitude, usually the OBC attitude.

Analysis

Because of the large volume of FHST data collected during the EUVE/UARS mission, data reduction was necessary. It was assumed that any processes that changed the FHST readings were not instantaneous and that noticeable changes took 6 months to a year to occur (Reference 4). Currently, EUVE has been in orbit for just over 1-1/2 years and UARS for almost 2.5 years. Since there is no definite amount of time for a FHST to degrade, it was uncertain whether time degradation effects could even be noticed.

Data were chosen for EUVE from the survey phase of the mission. More different stars are acquired during survey mode, so trends and patterns become more evident than with inertial mode data. Approximately one-orbit of data for seven different timespans were chosen for analysis. For processing of UARS data, five 1-orbit spans of data were chosen, spanning approximately 15 months (see Table 3). Data were chosen throughout the length of the missions to determine if there were any time dependencies or degradation effects involved.

Table 3. Data Spans

EUVE Greenwich mean time (YYMMDD.HHMMSS)	UARS Greenwich mean time (YYMMDD.HHMMSS)
921217.114517-134517	920819.162835-.182349
930207.041018-061017	921119.163604-.182315
930325.015017-035017	930219.163002-.182411
930425.080017-100017	930715.163105-.181727
930517.024517-044517	931102.163033-.182320
930613.024517-044517	
930717.084518-104518	

Each timespan was processed using the Multimission Three-Axis Stabilized Spacecraft (MTASS) Attitude Determination System (ADS). Uncorrected counts for star intensity and horizontal and vertical positions in the FOV were extracted from spacecraft telemetry data using the Telemetry Processor (TP) subsystem. These data were then converted from counts to engineering units, adjusted for biases, and corrected for temperature and magnetic effects using the Data Adjuster (DA) subsystem. For UARS, a new FOV scale factor was used for each timespan due to its quasi-linear degradation (about 1 percent). After all the data were corrected, the FHST-observed positions and magnitudes were used to identify the stars using the Star Identification (SI) subsystem. Once the stars were identified, the data were converted to the sensor reference frames using known FHST alignments and misalignments.

The difference between the instrumental magnitude and the observed magnitude is referred to here as the delta magnitude (Instrumental Magnitude – Observed Magnitude) or magnitude error. A positive error implies that the FHST is seeing the star too bright. The primary plots and comparisons analyzed here are as follows:

- Delta Magnitude versus B-V
- Delta Magnitude versus Instrumental Magnitude
- Delta Magnitude versus FOV Position

The first type was chosen because it demonstrates the FHST's inaccuracies as a function of the color index of the stars. The second shows the FHST's accuracy as a function of the brightness of the incident light. The third displays any position dependencies in the FHST's FOV.

Table 4 provides basic statistics for the magnitude errors of each FHST for each spacecraft.

Table 4. Magnitude Error Statistics

Star Tracker	Average Error	Standard Deviation of Error
EUVE FHST 1	-0.131	0.199
EUVE FHST 2	0.042	0.112
UARS FHST 1	0.106	0.113
UARS FHST 2	-0.103	0.105

As evident in Table 4, EUVE's FHST 1 is experiencing the most problems with magnitude errors, and EUVE's FHST2 is having the least.

EUVE Data and Results

When data were examined for EUVE for degradation effects, a plot of the delta magnitude versus FOV position for December 1992 was compared to the same plot for July 1993 (for each FHST). Data were averaged across the FOV to determine any sensitive regions. The plots showed less than a +/-0.1 magnitude difference between them across the FOV. Since a star traveling through the FOV can be expected to have a 0.2 magnitude fluctuation, no time dependence is evident for FOV position. When plots were also analyzed as a function of the B-V value, still no time dependence showed. Therefore, the remainder of the EUVE analysis was performed by combining all data spans together into one database. Also, EUVE magnitude errors were averaged for each star passing through the FOV to eliminate the 0.2 magnitude fluctuations seen across the FOV.

Table 5. Statistics for Regression of Delta Magnitude Versus B-V

Parameter	EUVE FHST1	EUVE FHST2	UARS FHST1	UARS FHST2
Intercept	-0.048	0.064	0.177	-0.112
Slope	-0.188	-0.041	-0.100	0.013
R Square	0.535	0.062	0.286	0.005
Stand. Error	0.106	0.100	0.095	0.105

EUVE's FHST1 was the FHST that prompted this study. As illustrated in Figure 3, the FHST1 has an almost linear dependence on B-V value. Conversely, FHST2 has no evident color dependence. Table 5 shows statistics for regression analysis with these data. This analysis shows that FHST1 has a high slope value and a high dependence on the B-V value, with the R Square value indicating more than 50 percent of the correlation coming from the B-V value. FHST2 has almost zero slope in comparison, with a much lower dependence on the B-V value. (R Square is a measure of how much influence X has on the Y value.)

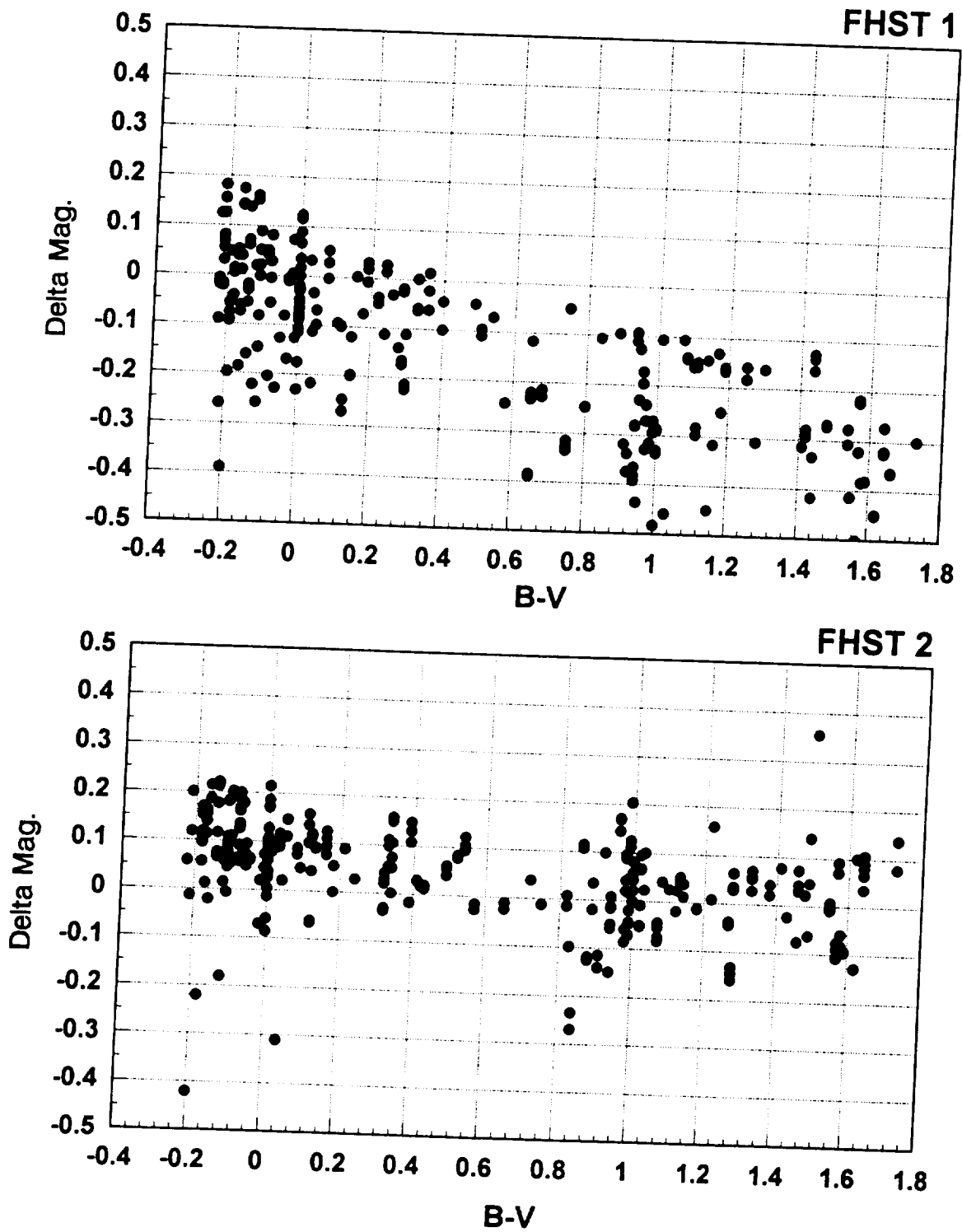


Figure 3. Delta Magnitude Versus B-V (EUVE)

EUVE's FHST1 does display a trend in the position in the FOV. Figure 4 shows that the negative theta position (the top half of the FOV) displays a definite shift in the magnitude error. Also, visual inspection of the surface plot may seem to show a problem with the outermost corner of the first quadrant. Since that area is outside the central FOV, where the OBC is supposed to break track, more data are required in that position to make an accurate determination of any trend. When the position in the FOV was examined as a function of the star's B-V values, no trend was evident. Of the stars sampled in the negative theta region of the FOV, only 21 percent of them had B-V values greater than 1.0, while in the upper half. This demonstrates that the magnitude errors that occur in the upper half of the FOV do not occur just because there is a high sampling of high B-V stars in that region. That portion of the FOV is actually giving erroneous measurements. Twenty-five percent had high B-V values.

Figure 5 shows magnitude error versus instrumental magnitude. Data for FHST1 shows no correlation between magnitude and magnitude error, while FHST2 does show a slight correlation. With FHST1, magnitude errors can occur at any magnitude. FHST2 shows the general trend of being less accurate at dimmer magnitudes. This is expected as the visual to instrumental magnitude conversions are less accurate at dimmer magnitudes.

UARS Data and Results

As with EUVE, when data were analyzed to look for any time-related effects, none were evident. Once again, data were combined and viewed as a whole, rather than as time dependent. UARS data were not averaged since its data rate is 64 times less than EUVE's.

For UARS, the color dependencies looked surprising upon first glance (Figure 6). FHST1 shows UARS to be seeing low B-V value stars that are too bright, while FHST2 shows no correlation with color. Table 5 shows statistics similar to EUVE. For FHST1, there is a higher dependence upon B-V value with 30 percent of the correlation due to the B-V value. The slope is also higher for FHST1 by about a factor of seven. FHST2 indicates no color dependence. These numbers and visual inspection seem to demonstrate a problem similar to EUVE's, with the exception that it is unlikely that FHST1 is seeing low B-V stars too bright. For an FHST to see stars that are too bright would require the electronics to be better than 100 percent efficient. It is more likely that the M_{bias} value in the magnitude calibration equation, Equation (2) is in error. A change in this value will move the data downward on the graph. This will show the FHST as actually seeing high B-V stars that are too dim, as with EUVE. To be sure, this will require some future analysis.

UARS's FHST2 also displays a trend in the position in the FOV. Since FHST2 shows no color dependencies, no color dependency versus FOV position needs to be analyzed. Figure 7 shows that the problem areas are the second quadrant (negative theta, positive phi), and the outermost corner of the first quadrant. These seem to be actual problem regions of the FOV. Once again, as with EUVE, the erroneous data in the first quadrant is outside the central FOV and is never used by the OBC for attitude determination.

Figure 8 shows plots of magnitude error versus instrumental magnitude. Both plots show higher magnitude errors as the magnitude gets dimmer. It is expected that as stars get dimmer, there should be larger standard deviation in the error measurements. These plots indicate a slope in the error measurements for both FHSTs. This implies a calibration coefficient problem for the A value in the magnitude calibration equation, Equation (2). More analysis is necessary to determine what the corrected values should be.

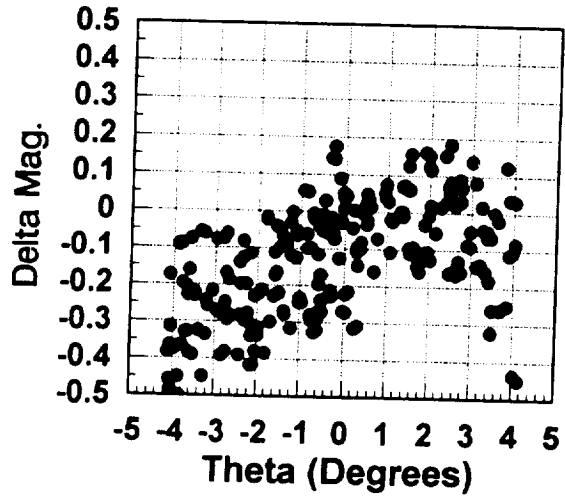
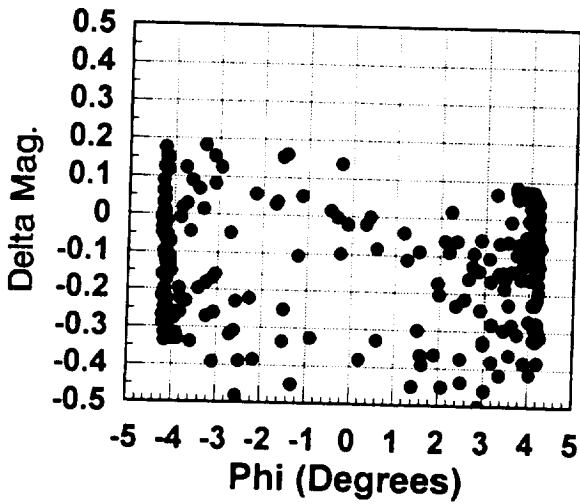
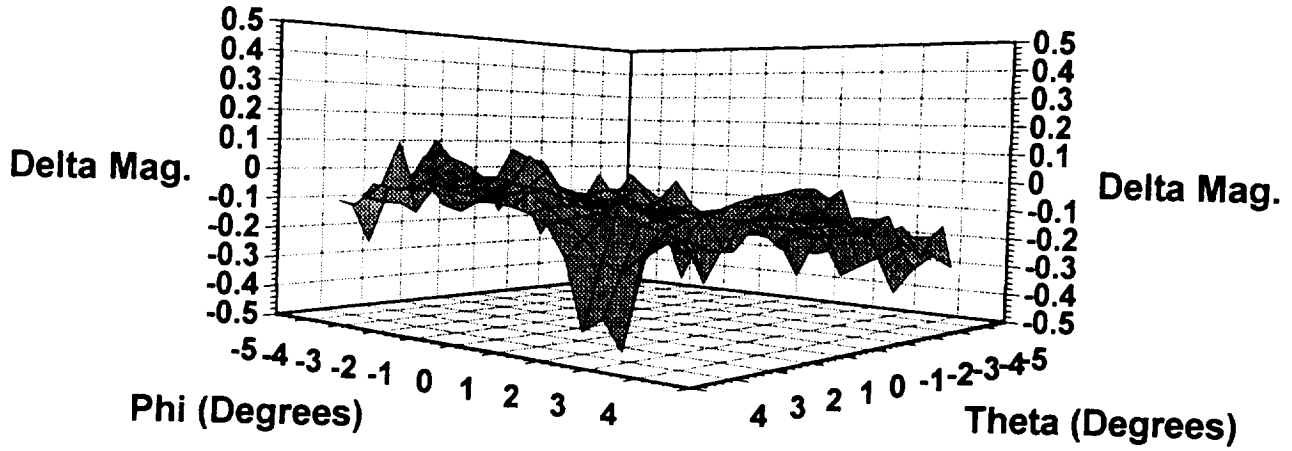


Figure 4. Delta Magnitude Versus FOV Position (EUVE, FHST1, Averaged)

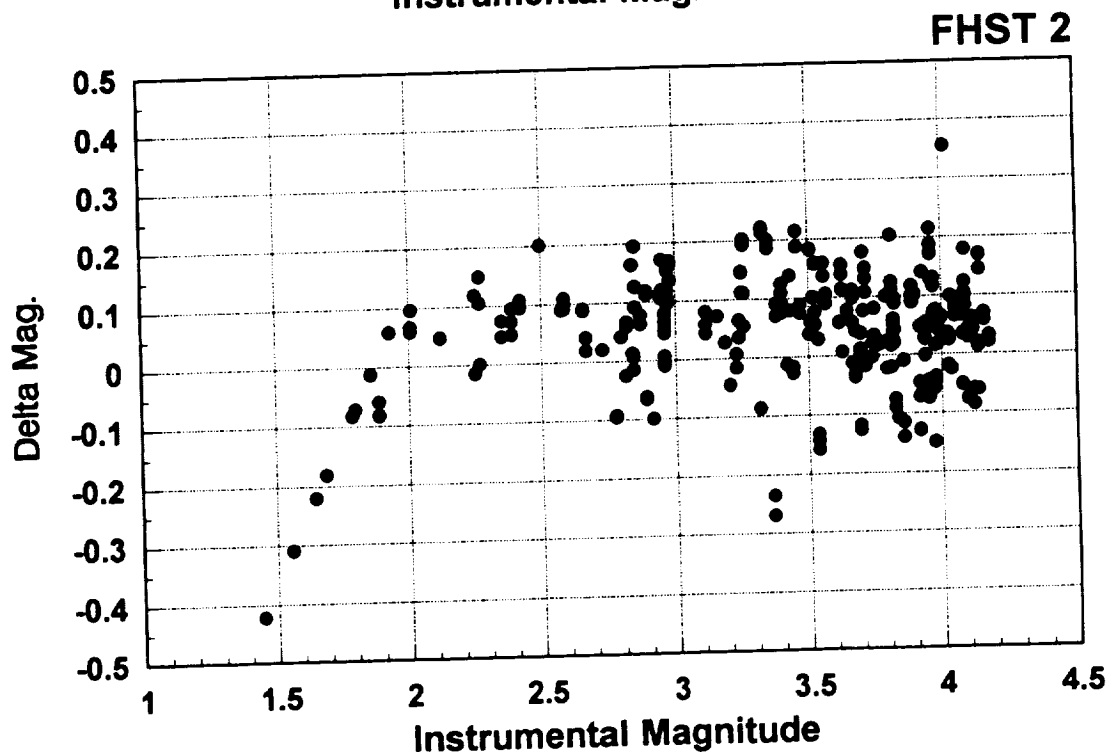
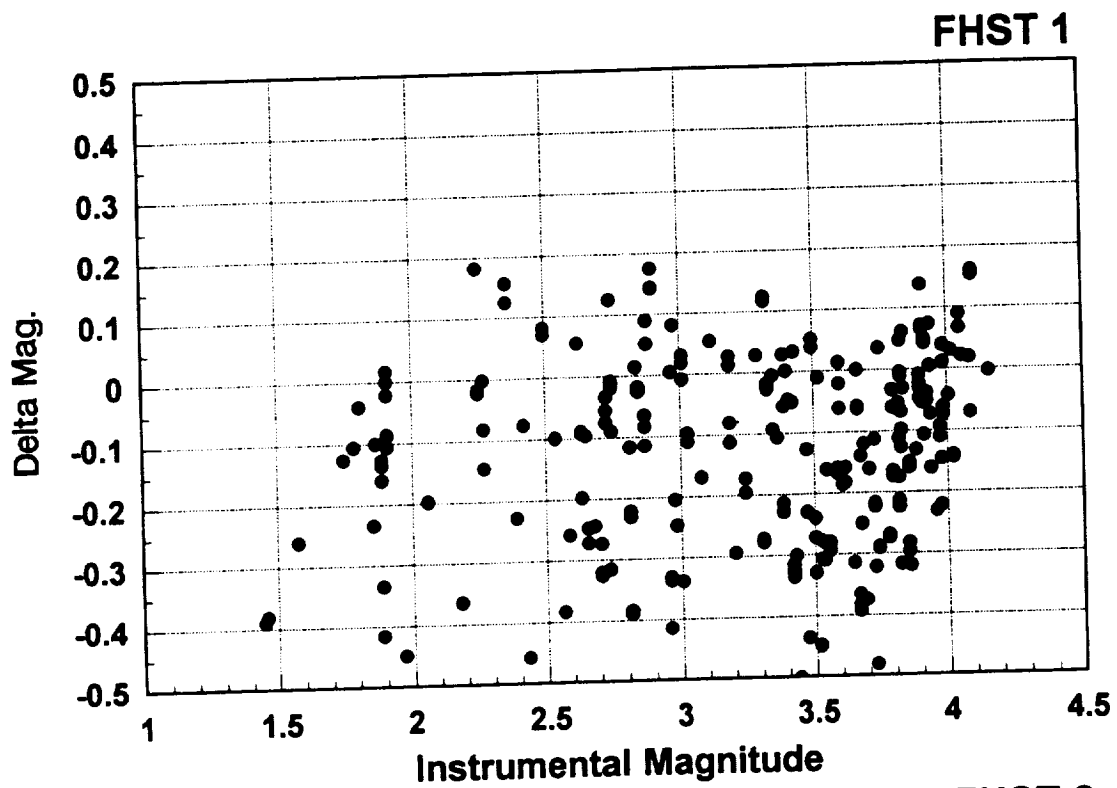


Figure 5. Delta Magnitude Versus Instrumental Magnitude (EUVE, Averaged)

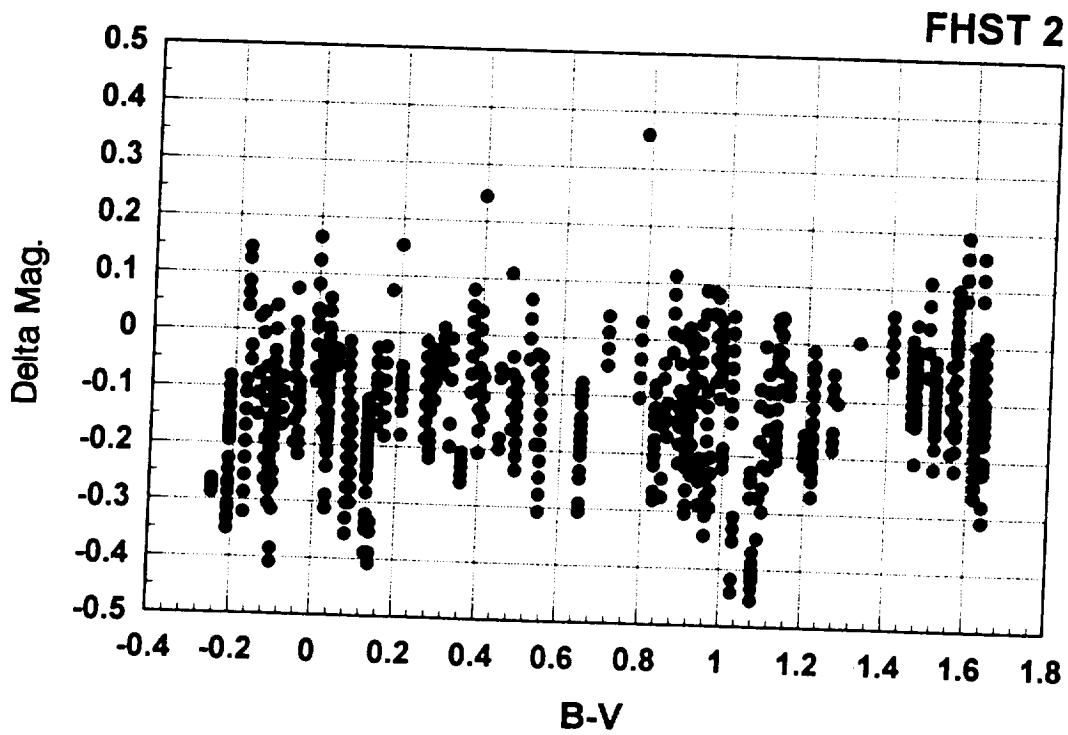
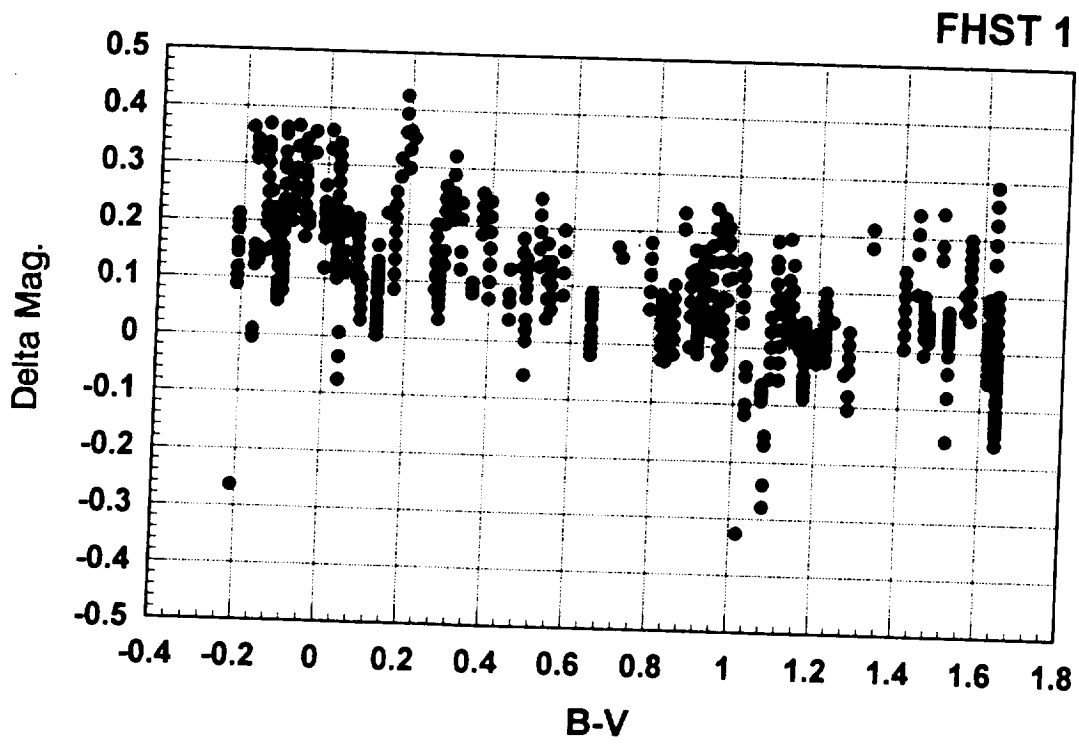


Figure 6. Delta Magnitude Versus B-V (UARS)

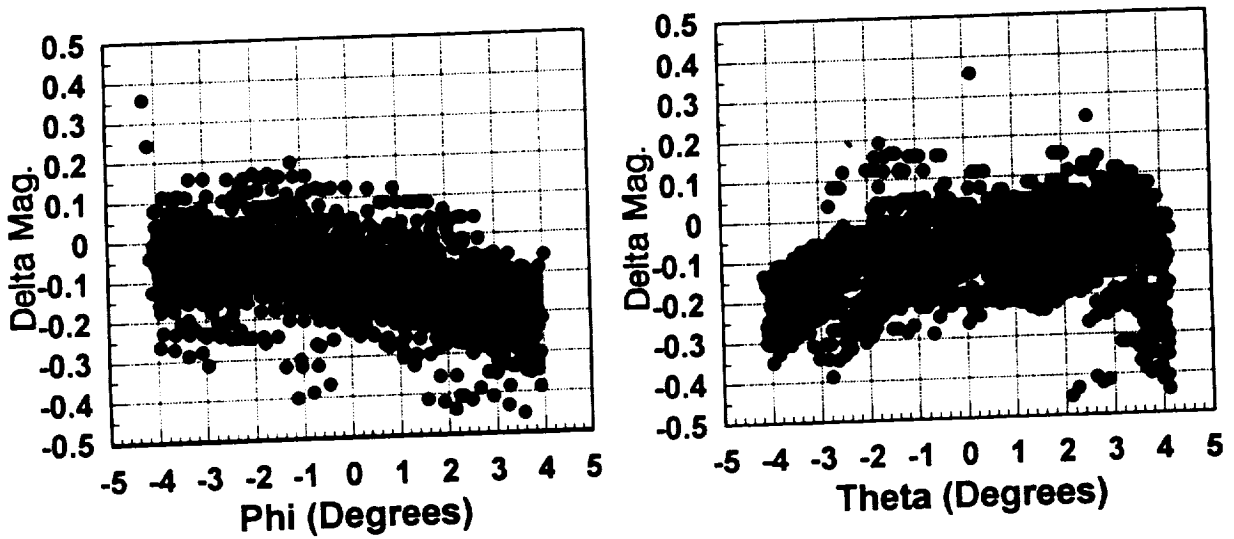
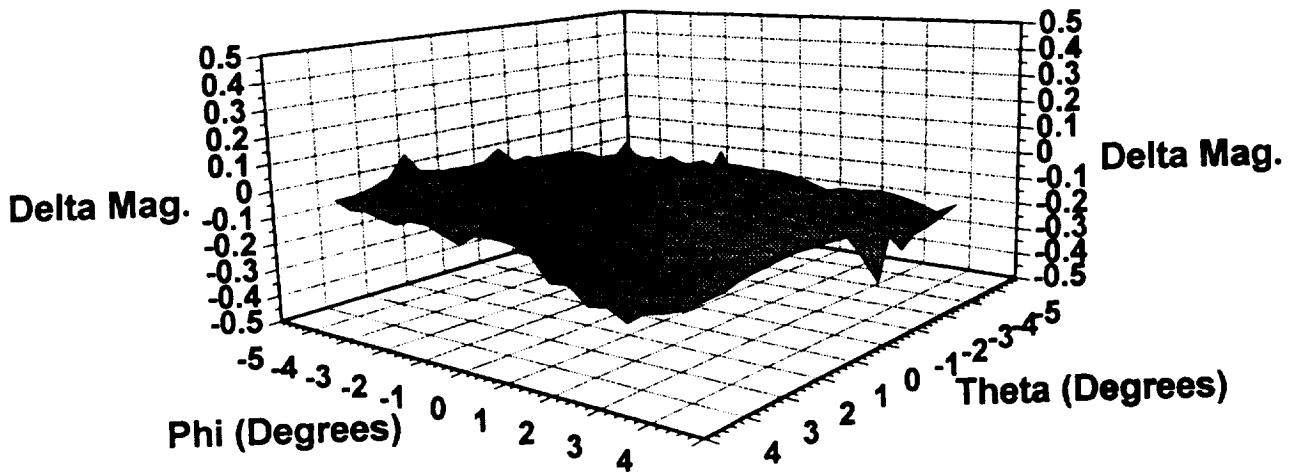


Figure 7. Delta Magnitude Versus FOV Position (UARS, FHST2)

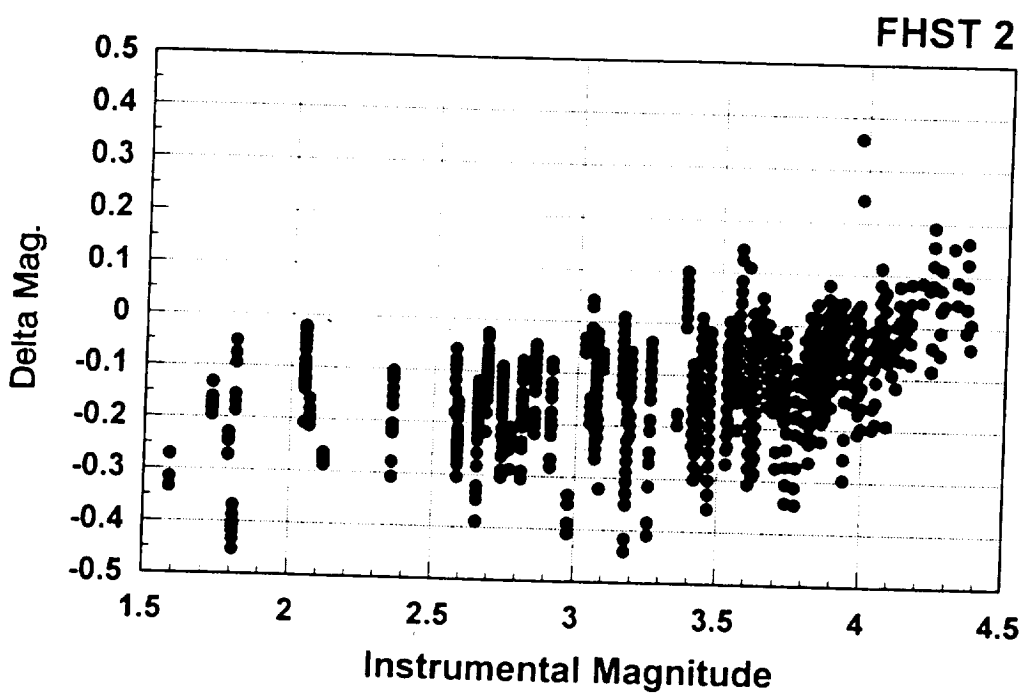
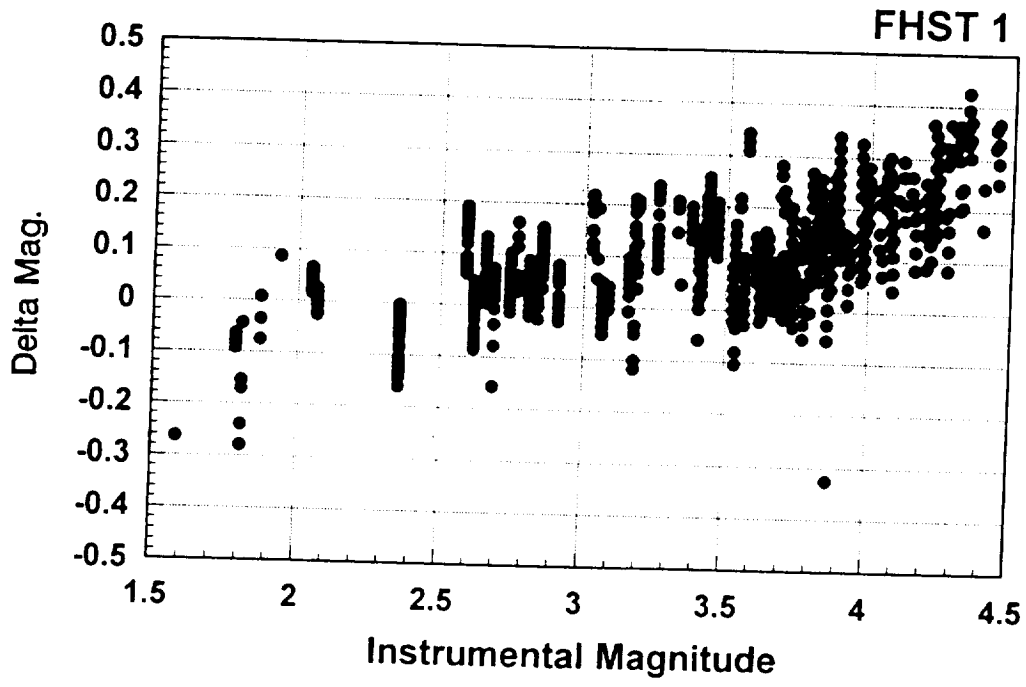


Figure 8. Delta Magnitude Versus Instrumental Magnitude (UARS)

Conclusions

Plots of theta versus phi indicate that the study has used a uniform distribution of stars across each FHST's FOV. None of the FHSTs analyzed in this paper have displayed a noticeable time dependence. Since EUVE's data spans covered 8 months and UARS's covered over a year, the processes that influence an FHST's degradation take longer than these spans.

Color index has an effect on two of the FHSTs: EUVE FHST 1 and UARS FHST 1. Both show a significant correlation between magnitude error and B-V value. It should be noted that these two FHSTs have serial numbers of SN005 (UARS FHST1) and SN006 (EUVE FHST1). EUVE and UARS swapped star trackers before launch due to a problem with the SN006 FHST. UARS was launched with EUVE's original FHST1 in place of its original FHST2. Once the problem with SN006 was repaired, it was put onboard EUVE as its FHST1. It is assumed that since these two FHSTs were the original ones built for UARS, they were built at the same time. These color-caused magnitude errors could have some dependence upon the manufacturing process of the FHSTs. This should be considered in the future when new missions are launched using the Charged Coupled Device (CCD) star trackers since these are even more sensitive to reddish colors than the Image Dissector Tube FHSTs.

Position dependence due to magnitude errors is evident in two of the FHSTs: EUVE FHST 1 and UARS FHST 2. Both FHSTs display position dependencies with similar results. Currently, it is unknown why certain areas in the FOV seem to have more errors than the other since no time dependence is seen, but future analysis may provide answers.

More analysis of the magnitude calibration equation for UARS is necessary. Data from the Delta Magnitude/B-V and Delta Magnitude/Instrumental Magnitude plots supports the need for new coefficients in Equation (2). This has already been done for EUVE. These calibrations should allow for more stars to be identified properly and, therefore, more accurate attitude determinations.

References

1. M. Lee, "The Extreme Ultraviolet Explorer (EUVE)/Explorer Platform (EP) Fixed Head Star Tracker (FHST) Sensitivity Study," internal memorandum, June 1993
2. Smith, and M. Zeilik, *Introductory Astronomy and Astrophysics*, Philadelphia: Saunders College Publishing, 1987
3. Goddard Space Flight Center, Flight Dynamics Division, GRO-743-93021, V. Lu, *GRO FHST Performance Analysis*, prepared by Computer Sciences Corporation, April 1993
4. D. Pitone, B. Twambly, A. Eudell, and D. Roberts, "Fixed Head Star Tracker Magnitude Calibration on the Solar Maximum Mission," paper presented at the Flight Mechanics Estimation Theory (FMET) Symposium, April 1990

Advantages of Estimating Rate Corrections During Dynamic Propagation of Spacecraft Rates—Applications to Real-Time Attitude Determination of SAMPEX*

M. S. Challa and G. A. Natanson
Computer Sciences Corporation (CSC)
Lanham-Seabrook, Maryland

D. F. Baker and J. K. Deutschmann
Goddard Space Flight Center (GSFC)
Greenbelt, Maryland

Abstract

This paper describes real-time attitude determination results for the Solar, Anomalous, and Magnetospheric Particle Explorer (SAMPEX), a gyroless spacecraft, using a Kalman filter/Euler equation approach denoted the Real-Time Sequential Filter (RTSF). The RTSF is an extended Kalman filter whose state vector includes the attitude quaternion and corrections to the rates, which are modeled as Markov processes with small time constants. The rate corrections impart a significant robustness to the RTSF against errors in modeling the environmental and control torques, as well as errors in the initial attitude and rates, while maintaining a small state vector.

SAMPEX flight data from various mission phases are used to demonstrate the robustness of the RTSF against a priori attitude and rate errors of up to 90 deg and 0.5 deg/sec, respectively, as well as a sensitivity of 0.0003 deg/sec in estimating rate corrections in torque computations. In contrast, it is shown that the RTSF attitude estimates without the rate corrections can degrade rapidly. RTSF advantages over single-frame attitude determination algorithms are also demonstrated through (1) substantial improvements in attitude solutions during Sun-magnetic field coalignment and (2) magnetic-field-only attitude and rate estimation during the spacecraft's Sun-acquisition mode.

A robust magnetometer-only attitude-and-rate determination method is also developed to provide for the contingency when both Sun data as well as a priori knowledge of the spacecraft state are unavailable. This method includes a deterministic algorithm used to initialize the RTSF with coarse estimates of the spacecraft attitude and rates. The combined algorithm has been found effective, yielding accuracies of 1.5 deg in attitude and 0.01 deg/sec in the rates and convergence times as little as 400 sec.

1. Introduction

A crucial aspect of an attitude Kalman filter is that the attitude quaternion q and the covariance matrix must be propagated between measurements using the spacecraft's angular velocity (also referred to here as the rates), ω . Thus, q is propagated via

$$\frac{dq}{dt} = \frac{1}{2} \mathbf{\Omega}(\omega) q \quad (1)$$

where

$$\mathbf{\Omega}(\omega) = \begin{bmatrix} -[\omega \times] & \omega \\ -\omega^T & 0 \end{bmatrix} \quad (2)$$

and ω_x , ω_y , and ω_z are the components of ω along the spacecraft's body axes. Note that matrices, including vectors (column matrices), are denoted in boldface in this paper, matrix transposes are denoted by the superscript T , and

*This work was supported by the National Aeronautics and Space Administration (NASA)/Goddard Space Flight Center (GSFC), Greenbelt, Maryland, under Contract NAS 5-31500.

$$[\boldsymbol{\omega} \times] = \begin{bmatrix} 0 & -\omega_z & \omega_y \\ \omega_z & 0 & -\omega_x \\ -\omega_y & \omega_x & 0 \end{bmatrix} \quad (3)$$

Equation (3) defines a cross product-to-matrix equivalence that will be used elsewhere in this paper. Attitude here denotes the orientation of the spacecraft body frame with respect to the geocentric inertial frame (GCI), $\boldsymbol{\omega}$ describes the rate of change of the attitude, and all vectors are resolved along the body axes unless specified otherwise.

For a gyro-based spacecraft, gyros accurately measure $\boldsymbol{\omega}$, and accurate results can be obtained by integrating Equation (1) alone. For a gyroless spacecraft such as the Solar, Anomalous, and Magnetospheric Particle Explorer (SAMPEX), however, we must propagate the rates via the following Euler equation (References 1 and 2):

$$\frac{d\mathbf{L}}{dt} = \mathbf{N}_{\text{ext}} - \boldsymbol{\omega} \times \mathbf{L} \quad (4)$$

where \mathbf{N}_{ext} is the sum of the external torques acting on the spacecraft, and \mathbf{L} is the total angular momentum of the spacecraft. If \mathbf{I} is the inertia tensor of the rigid part of the spacecraft and \mathbf{h} denotes angular momentum contribution from rotating parts such as momentum wheels, \mathbf{L} is given by

$$\mathbf{L} = \mathbf{I}\boldsymbol{\omega} + \mathbf{h} \quad (5)$$

Equations (1) and (4) generally pose a difficult initial-value problem, because significant errors in $\boldsymbol{\omega}$ can arise from spacecraft and torque models, as well as the initial values of \mathbf{q} and $\boldsymbol{\omega}$ used in the integration.

Of course, we may avoid rate propagation altogether by using only single-frame algorithms such as TRIAD (algebraic method in Reference 1) and QUEST (Reference 3), which determine the attitude using at least two simultaneous measurements. But these methods do not provide accurate solutions when all of the observed vectors are nearly collinear. A Kalman filter is superior in such a situation, as will be demonstrated later, since it can use propagation to estimate the unobservable elements of the state. Additionally, modeling the spacecraft's dynamics is advantageous because it accounts for other physical phenomena such as nutational frequencies.

A Kalman filter scheme that corrects for the errors in $\boldsymbol{\omega}$ is thus desirable. This paper presents results from such a filter developed for the PC-based SAMPEX real-time attitude determination system (Reference 4), denoted the Real-Time Sequential Filter (RTSF). Only pertinent aspects of the SAMPEX RTSF are discussed here; complete details, including system aspects, mathematics, and models for the environmental torques, are given in References 5–7.

The basic features of the SAMPEX RTSF are as follows. Let $\boldsymbol{\omega}_{\text{prop}}$ denote the rates generated through Equation (4), and let $\boldsymbol{\omega}_{\text{true}}$ denote the true rates. The errors are the difference of the two, and these errors are modeled as being of two types: a zero-mean white noise vector, $\boldsymbol{\eta}_{\boldsymbol{\omega}}$, and a systematic error, \mathbf{b}_{true} , i.e.,

$$\boldsymbol{\omega}_{\text{prop}} = \boldsymbol{\omega}_{\text{true}} + \mathbf{b}_{\text{true}} + \boldsymbol{\eta}_{\boldsymbol{\omega}} \quad (6)$$

In addition to the quaternion, we wish to estimate the rate errors \mathbf{b} using the following Kalman state vector:

$$\mathbf{X} = [\mathbf{q}^T \ \mathbf{b}^T]^T \quad (7)$$

together with the following general principles:

- Model \mathbf{N}_{ext} as accurately as possible.
- Model noise terms such as $\boldsymbol{\eta}_{\boldsymbol{\omega}}$ by treating them as a noisy background arising from torque uncertainties and accounting for them statistically in the Kalman filter formulation.
- Estimate \mathbf{b} optimally by using the sensor residuals, and propagate \mathbf{b} between measurements using a suitable dynamics model.

To formulate a dynamics model for \mathbf{b} , we first note the following aspect of Equation (4): It is not reasonable to treat \mathbf{b} as constant because even constant errors in \mathbf{N}_{ext} do not necessarily generate constant \mathbf{b} . In fact, in view of the sporadic nature of the control torques as well as the attitude dependence of the environmental torques, it is uncertain whether a simple dynamic model can be developed for \mathbf{b} . We avoid this issue by arguing that we are interested not in the origin of \mathbf{b} , but in its instantaneous value that would reconcile the differences between the propagated and observed

values of \mathbf{q} . Consider now propagation between measurement times t_k and t_{k+1} and use the following notation: filter estimates are denoted by carets; estimates before and after updates (via measurements) are denoted by minus signs and plus signs, respectively; and the times are denoted by subscripts k and $k+1$. In this notation, $\hat{\omega}_k(-) \equiv \omega_{prop}(t_k)$, and we seek to correct the rates using

$$\hat{\omega}_k(+) = \hat{\omega}_k(-) - \hat{\mathbf{b}}_k(+) \quad (8)$$

Propagation of \mathbf{q} , ω , and the covariance matrix, \mathbf{P} , to t_{k+1} is then done using $\hat{\omega}_k(+)$. Since Equation (8) corrects the rates at t_k , it follows that $\hat{\mathbf{b}}_{k+1}(+)$ must reflect only errors that accumulated during the intervening period, $\Delta t = t_{k+1} - t_k$.

Kalman filter updates, however, are of the form:

$$\hat{\mathbf{b}}_{k+1}(+) = \hat{\mathbf{b}}_{k+1}(-) + \Delta \mathbf{b}_{k+1}^* \quad (9)$$

where $\Delta \mathbf{b}_{k+1}^*$ denotes the correction estimated by the filter. It follows that $\hat{\mathbf{b}}_{k+1}(+)$ (and $\Delta \mathbf{b}_{k+1}^*$) will denote the errors in $\hat{\omega}_{k+1}(-)$ if $\hat{\mathbf{b}}_{k+1}(-) \approx 0$. This is achieved in the RTSF by specifying that $\hat{\mathbf{b}}$ decays exponentially with a time constant, τ , of the order of Δt . That is, we model the dynamics of $\hat{\mathbf{b}}$ through the first-order Markov model:

$$\frac{d\hat{\mathbf{b}}}{dt} = -\tau^{-1}\hat{\mathbf{b}} + \boldsymbol{\eta}_b \quad (10)$$

where $\boldsymbol{\eta}_b$ is another zero-mean white noise vector.

The above Markov model also assists in tuning the filter through the following useful feature: The diagonal elements of \mathbf{P} corresponding to $\hat{\mathbf{b}}$ would then converge to a constant value that depends on τ and the statistical properties of $\boldsymbol{\eta}_b$. For simplicity, take $\hat{\mathbf{b}}$ and $\boldsymbol{\eta}_b$ as scalars, and define Q , through $\langle \eta_b(t) \eta_b(t')^T \rangle = Q(t) \delta(t-t')$, where $\delta(t-t')$ is the Dirac delta function. Then p_{ω} , the Kalman filter's covariance matrix element for $\hat{\mathbf{b}}$, converges to p_{ω} given by

$$p_{\omega} = Q \tau^2 \quad (11)$$

Let us now suppose that the $\langle |\boldsymbol{\eta}_\omega|^2 \rangle$ is known by examining the model uncertainties in Equation (4). We argue that p_{ω} is also of this order of magnitude since $\hat{\mathbf{b}}$ cannot be known to a greater degree of precision than ω itself. Thus, we use p_{ω} and τ together to fix the numerical value of Q in Equation (11), and then use Q in the Kalman filter computations.

This formulation for estimating $\hat{\mathbf{b}}$ has many similarities to gyro-bias estimation (References 8–10), where $\hat{\mathbf{b}}$ denotes the gyro drift-rate biases and $\hat{\omega}(-)$ denotes uncorrected gyro rates. In view of the slow variation of these biases over time (see, e.g., Reference 11), it is then possible to approximate their dynamics by Equation (10) using a *large* value for τ . There is one important difference, though, between the two situations. Gyros accurately measure ω , and the leading errors in the gyro rates are indeed removed by estimating essentially constant biases. Thus, for example, $\hat{\mathbf{b}}_k(+)$ is subtracted from *both* $\hat{\omega}_k(-)$ and $\hat{\omega}_{k+1}(-)$ and before their mean is used to propagate \mathbf{q} via Equation (1). Consequently, the increments, $\Delta \hat{\mathbf{b}}$, to $\hat{\mathbf{b}}$ provided by the Kalman updates take $\hat{\mathbf{b}}$ progressively closer to that constant.

The rest of this paper is organized as follows. Sections 2 and 3 summarize details of the spacecraft, the data used here, and the theory. Sections 4 and 5 are devoted to tuning, accuracy, and robustness of the filter. Section 6 demonstrates the advantages of the RTSF over single-frame solutions by (1) showing its stability when Sun and magnetic field vectors are nearly parallel and (2) determining attitude and rates using only magnetic field data. Section 7 shows that combining the RTSF with the deterministic algorithm of References 12 and 13 yields a robust magnetometer-only attitude-and-rate determination scheme. Section 8 summarizes the conclusions.

2. Description of SAMPEX and Data Characteristics

SAMPEX is the first of the Small Explorer satellites and is designed to study elemental and isotopic composition of energetic particles of solar and cosmic origin. It has a 550×675 km orbit with an 82-deg inclination. SAMPEX nominally is Sun-pointing and has a rate of 1 rotation per orbit (RPO) about the spacecraft-to-Sun vector. The attitude accuracy

requirement of 2 deg is achieved using a fine Sun sensor (FSS) and a three-axis magnetometer (TAM). The control hardware consists of a momentum wheel and a magnetic torquer assembly (MTA).

The nominal body y -axis is the Sun vector, and the nominal x - and z -body axes are defined by the Sun/orbital frame of Reference 14. For our purposes, it suffices to note the following:

- The body y -axis is the pitch axis and also the FSS boresight, and the angular deviations of this axis from the Sun vector are defined as the roll and yaw angles, which are measured by the FSS.
- The pitch angle denotes angular errors about the y -axis and is measured by the TAM.
- Pitch control is derived through the wheel whose axis coincides with the body y -axis, whereas the MTA primarily provides roll and yaw control, and angular momentum dumping.
- During the nominal 1-RPO mode, roll, pitch, and yaw angles are all 0, and $\omega \approx (0, 0.06, 0)$ deg/sec.

SAMPEX telemetry datasets of Table 1 are used here and, with the exception of SIM722, they all contain inflight data. SIM722 was constructed (Reference 7) using SAMPEX ephemerides and the wheel data from PB722 and is useful in calibrating the accuracy of the \hat{b} estimates.

Table 1. Highlights of the SAMPEX Telemetry Datasets Used for Evaluating the RTSF

Name of Dataset	Features
PB705	Transition from Sun-acquisition mode to nominal 1-RPO mode on the day of launch, 7/4/92
PASS53	Nominal 1-RPO mode data of 7/8/92
SIM722	Simulated data for duration of eclipse (Earth shadow) on 7/21/92
PB825	Near-coalignment of Sun and magnetic field vectors on 8/23/92
PB722	Inflight data for the eclipse of SIM722

No significant differences were noticed between QUEST and TRIAD attitude solutions. The TRIAD attitude solutions were differenced to provide rates, and the single-frame results are often taken as the truth models accurate to: 0.5 deg for roll/yaw, 1.5 deg for pitch, and 0.5 deg/sec for rates.

3. Theoretical Aspects of the RTSF

Definition of Errors:

The Kalman filter formalism here follows the scheme of Reference 15; i.e., state errors before and after an update are considered, and the differential equation for \mathbf{P} is derived by demanding optimality. The following notation is used in addition to that in Section 1. \mathbf{A} generally denote an orthogonal matrix; $\mathbf{A}(\mathbf{q})$ is then the orthogonal matrix parameterized by a quaternion \mathbf{q} . Quaternion multiplication, denoted by \otimes , is defined here in the reverse order of the corresponding attitude matrices; i.e., $\mathbf{q} = \mathbf{q}_1 \otimes \mathbf{q}_2$ is equivalent to $\mathbf{A}(\mathbf{q}) = \mathbf{A}(\mathbf{q}_2)\mathbf{A}(\mathbf{q}_1)$.

The attitude error is linearized, and is taken as a vector of three small independent Euler angles, $\boldsymbol{\alpha} = (\alpha_x, \alpha_y, \alpha_z)$, needed to rotate the true body frame onto the estimated body frame. That is, if

$$\delta\mathbf{q} \approx \begin{bmatrix} \boldsymbol{\alpha}^T \\ 1 \end{bmatrix}^T \quad (12)$$

then $\mathbf{A}(\hat{\mathbf{q}}) = \mathbf{A}(\delta\mathbf{q})\mathbf{A}(\mathbf{q}_{true})$. The error \mathbf{x} in the state vector \mathbf{X} of Equation (7) is then

$$\mathbf{x} = [\boldsymbol{\alpha}^T \quad \Delta\mathbf{b}^T]^T \quad (13)$$

The 6x6 covariance matrix \mathbf{P} is then defined as $\mathbf{P} = \langle \mathbf{x}\mathbf{x}^T \rangle$. If $\mathbf{X}_{true} = [\mathbf{q}_{true}^T \ \mathbf{b}_{true}^T]^T$ is the true state vector, the following relationships hold:

$$\begin{aligned}\hat{\mathbf{q}}(\pm) &= \mathbf{q}_{true} \otimes \delta \mathbf{q}(\pm) \\ \hat{\mathbf{b}}(\pm) &= \mathbf{b}_{true} - \Delta \mathbf{b}(\pm)\end{aligned}\quad (14)$$

The sign convention for $\Delta \mathbf{b}$ ensures that, from Equations (6) and (8), the rate estimates are of the following form:

$$\hat{\boldsymbol{\omega}} = \boldsymbol{\omega}_{true} + \Delta \mathbf{b} + \boldsymbol{\eta}_\omega \quad (15)$$

Let

$$\mathbf{x}^* = [\boldsymbol{\alpha}^{*T} \ \Delta \mathbf{b}^{*T}]^T \quad (16)$$

be the errors estimated by the filter. $\hat{\mathbf{X}}$ is then updated through

$$\begin{aligned}\hat{\mathbf{q}}(+) &= \hat{\mathbf{q}}(-) \otimes (\delta \mathbf{q}^*)^{-1} \\ \hat{\mathbf{b}}(+) &= \hat{\mathbf{b}}(-) + \Delta \mathbf{b}^*\end{aligned}\quad (17)$$

The relation between the state errors before and after an update follows as $\mathbf{x}(+) = \mathbf{x}(-) - \mathbf{x}^*$.

Propagation From t_k to t_{k+1} :

$\hat{\mathbf{b}}$ is propagated readily after ignoring $\boldsymbol{\eta}_b$ in Equation (9), i.e.,

$$\hat{\mathbf{b}}_{k+1}(-) = \hat{\mathbf{b}}_k(+) \exp\left[-\left(\frac{t_{k+1} - t_k}{\tau}\right)\right]$$

Regarding the rates, $\hat{\boldsymbol{\omega}}$ is first updated via Equation (8), and $\hat{\mathbf{L}}$ is updated using Equation (5): $\hat{\mathbf{L}}_k(+) = \mathbf{I} \hat{\boldsymbol{\omega}}_k(+) + \mathbf{h}_k$. Here \mathbf{h} is the wheel momentum given by $\mathbf{h} = [0 \ I_{wheel} \omega_{wheel} \ 0]^T$, where I_{wheel} is the moment of inertia of the wheel about its axis and ω_{wheel} is the wheel speed. $\hat{\boldsymbol{\omega}}_k(+) and $\hat{\mathbf{L}}_k(+) are then used to numerically integrate Equations (1) and (4) to obtain $\hat{\mathbf{q}}_{k+1}(-)$ and $\hat{\mathbf{L}}_{k+1}(-)$, along with the differential equation for \mathbf{P} to be given shortly. The uncorrected rates at t_{k+1} are then obtained by inverting Equation (5), i.e., $\hat{\boldsymbol{\omega}}_{k+1}(-) = \mathbf{I}^{-1}[\hat{\mathbf{L}}_{k+1}(-) - \mathbf{h}_{k+1}]$.$$

While propagating $\hat{\mathbf{L}}$, N_{tot} is modeled as the sum of four external torques: magnetic control (N_{mag}), gravity gradient, aerodynamic, and radiation pressure. (The wheel torque is implicit through \mathbf{h}_{k+1} in the above propagation scheme.) The environmental torques are computed in the RTSF using a detailed spacecraft model as well as accurate algorithms; in particular, the aerodynamic torque is computed using the FREEMAC algorithm (Reference 16), which generates velocity-dependent drag coefficients. We note, however, that the noise in SAMPEX wheel speed obscures the effects of the environmental torques. Thus, only N_{mag} is noticeable; this is given by $N_{mag} = \boldsymbol{\mu} \times \mathbf{B}$, where $\boldsymbol{\mu}$ is the dipole moment of the MTA and \mathbf{B} is the magnetic field.

The differential equation for \mathbf{P} can be derived by noting that the error in $\hat{\mathbf{X}}$ after propagation comes from two sources: (1) the error before propagation and (2) the random vectors, $\boldsymbol{\eta}_\omega$ and $\boldsymbol{\eta}_b$, which are ignored in propagation. The linearized propagation equations for the errors follow as

$$\begin{aligned}\frac{d\mathbf{x}}{dt} &= \begin{bmatrix} -[\hat{\boldsymbol{\omega}} \times] & \mathbf{I}_{3 \times 3} \\ \mathbf{0}_{3 \times 3} & -\tau^{-1} \mathbf{I}_{3 \times 3} \end{bmatrix} \mathbf{x} + \begin{bmatrix} \boldsymbol{\eta}_\omega \\ \boldsymbol{\eta}_b \end{bmatrix} \\ &= \mathbf{F}(\hat{\boldsymbol{\omega}}) \mathbf{x} + \boldsymbol{\eta}\end{aligned}\quad (18)$$

Equation (18) defines \mathbf{F} and $\boldsymbol{\eta}$. Introducing \mathbf{Q} , the diagonal spectral density matrix of $\boldsymbol{\eta}$, through $\langle \boldsymbol{\eta}(t) \boldsymbol{\eta}(t')^T \rangle = \mathbf{Q} \delta(t-t')$ it can then be shown (Reference 15) that the covariance matrix evolves according to

$$\frac{d\mathbf{P}}{dt} = \mathbf{F}\mathbf{P} + \mathbf{P}\mathbf{F}^T + \mathbf{Q} \quad (19)$$

Equation (19) is integrated numerically in the RTSF to obtain $\mathbf{P}_{k+1}(-)$.

Updates Using Sensor Measurements:

Let V_B and V_I be the measured (body frame) and reference (GCI) vectors corresponding to a particular sensor and let $\hat{V}_B = A(\hat{q}(-))V_I$. The residual y is defined as $y = V_B - \hat{V}_B$. Linearizing the attitude errors about q_{true} yields

$$y = Hx(-) + \Delta V_B \quad (20)$$

where $H = [-\hat{V}_B \times] \mathbf{0}_{3 \times 3}$ and ΔV_B is random measurement error. The following optimality requirements can then be used to obtain the usual Kalman gain and covariance-update equations: (1) if the error is unbiased before a measurement ($\langle x(-) \rangle = \mathbf{0}$), it should remain so after the update ($\langle x(+) \rangle = \mathbf{0}$), and (2) the statistical average of the total error, $\langle x(+)^T x(+) \rangle$, should be a minimum:

$$K = P(-)H^T [HP(-)H^T + R]^{-1} \quad (21)$$

$$P(+) = [I_{6 \times 6} - KH]P(-)$$

where $R = \langle \Delta V_B \Delta V_B^T \rangle$. The correction x^* is then given by

$$x^* = Ky \quad (22)$$

for use in Equations (16) and (17). The covariance update in Equation (21) was chosen over more numerically stable algorithms due to memory and speed considerations on personal computers. To partially mitigate the risks, $P(+)$ is symmetrized after the update. No adverse effects have been noticed to date.

For SAMPEX, no special treatment is necessary to construct R for the TAM, since independent magnetic field measurements are made along each body axis. The FSS, however, measures only two independent angles, and only the corresponding components of y are used in the computations. Details are given in Reference 5.

4. Tuning and Accuracy of the Rate Corrections

The telemetry digitization of the FSS is 0.5 deg; this value was used to construct R for FSS measurements. For the TAM, uncertainties in the reference magnetic field calculations are larger than the digitization errors of 0.3 mG; after the residuals were examined, a TAM noise of 3 mG was used to construct R .

A distinctive feature of telemetered SAMPEX data is the large wheel noise (~ 1 rad/sec). This noise yields torques of the order of 10^{-2} N-m, far in excess of the maximum values of the environmental torques ($\sim 10^{-6}$ N-m), and results in a noise of about 1.7×10^{-4} rad/sec in ω_y . The pitch covariance P_{22} thus grows by about $3 \times 10^{-8} (\Delta t)^2$ rad² between measurements. Since Q is the rate of change of P due to the process noise (Equations (19)), Q_{22} was correspondingly assigned a value of $3 \times 10^{-8} \Delta t$ rad²/sec. To provide for the situation in which ω_x and ω_z are substantial (as during Sun acquisition), the same value was also assigned for Q_{11} and Q_{33} .

The discussion of Equations (8-11) then fixes the bottom three elements of Q , which correspond to η_b . Thus, p_{ii} in Equation (11) was chosen as 3×10^{-8} rad²/sec², so that

$$Q_{ii} = \frac{6 \times 10^{-8} \text{ rad}^2}{\tau \text{ sec}^3}, \quad i = 4, 5, 6$$

τ is chosen equal to the telemetry period: 0.5 sec for real-time data and 5.0 sec for playback data. As can be seen from Figure 1, the rate-error elements of P converge to the above value of p_{ii} very well.

Figure 2 clarifies the discussion of Equations (9) and (10), by examining the dependence of τ on t_{upd} , the update period for \hat{b} . That is, \hat{b} is updated via Equation (17) only after every t_{upd} sec, as opposed to the telemetry period of 5 sec here. (\hat{q} is always updated every 5 sec.) Here "Sun angle" is the angle between the predicted and measured Sun vectors; thus, for a fixed set of measurements, larger Sun angles indicate larger propagation errors. Plots a and b show that, when $\tau = t_{upd} = 5$, the mean Sun angle is about 0.25 deg and rate corrections of the order of 10 deg/hour are estimated. In plots c and d, τ is lowered to 1 sec while retaining the same value for p_{ii} . Thus, Q is now larger, and the RTSF does not correct for errors below this noise level. However, the mean Sun angle is now larger, about 1 deg, indicating that larger propagation errors arise if rates are not corrected. Plots e and f show the results for a larger value of τ : 25 sec. If t_{upd} is retained at 5 sec (plot e), the RTSF quickly diverges and the Sun angle even reaches 180 deg. This happens

because \hat{b} does not decay to zero during the time between the updates, so that the updates, $\hat{b}(+)$, in Equation (9) also include past rate errors. The divergences are eliminated by choosing $t_{\text{upd}} = 25$ sec, as shown in plot f. However, since \hat{b} is now updated infrequently, the Sun angles in plot f are generally larger than those in plot a.

The accuracy of the \hat{b} estimates was ascertained by using simulated data. These results are shown in Figure 3. In plot a, the truth model for ω_y is noisy due to fluctuations in the inflight wheel data used to generate SIM722. The simulated data were input to the RTSF *but with a constant wheel speed equal to the value at 0 sec*, and we see that the RTSF's ω_y estimates generally reflect the true mean values. However, significant differences occur around 100 and 450 sec, where changes in ω_{whl} cause changes in the true ω_y . This information is not available to the RTSF and leads to significant Sun angles, together with nonzero values for \hat{b}_y around these times in plot b. We see from plots a and b that the signs of these \hat{b}_y estimates agree with Equation (6). Quantitatively also, the \hat{b}_y estimates are reasonable; for example, the corrections total about 0.01 deg/sec during 0-200 sec, which compares well with the rate differences in plot a.

We thus see that tuning results confirm the arguments of Section 1 and that the rate corrections \hat{b} are accurate to 1 deg/hour.

5. Robustness of the RTSF Against A Priori Errors and Torque Errors

The RTSF was evaluated extensively with PB705 data where SAMPEX is in Sun acquisition soon after launch. The spacecraft is initially nutating rapidly— ω_y constant at about 0.3 deg/sec and ω_x and ω_z sinusoidal with amplitudes of about 0.6 deg/sec—before transitioning to the nominal 1-RPO mission mode. (The transition is clearly visible in Figure 10.) Thus, the Sun-acquisition part of PB705 is a rapidly varying situation and provides a stringent test of the RTSF's performance. In most results here, the RTSF was started with what we term *zero initial conditions*; i.e., the body frame is aligned with GCI and $\omega = (0, 0, 0)$.

Figure 4 shows the convergence of the RTSF results to single-frame solutions using both FSS and TAM data. Although the a priori errors are large—(−27, −91, 21) deg in attitude and (−0.5, 0.3, 0.4) deg/sec in the rates—the RTSF's estimates converge in about 300 sec. The effects of the a priori errors clearly show up in plot c, where \hat{b} is extremely large during convergence.

Figures 5 and 6 show another useful aspect of the RTSF: the ability to compensate for torque errors. Figure 5 shows results with PB705 during the transition to 1-RPO mode, with the TRIAD rates serving as the truth model. Here ω_y drops from 0.3 deg/sec to the 1-RPO value of 0.06 deg/sec partly due to a substantial wheel torque. The wheel speeds input to the RTSF, however, were deliberately given the *wrong sign* during this run. Thus, around 200 sec, the RTSF's ω_y estimate initially *increases*. This gives rise to large Sun angles, and significant \hat{b}_y are estimated (plot b) that eventually correct ω_y ; the time lag needed to correct $\hat{\omega}$ is finally eliminated in the 1-RPO mode where ω_y is nearly constant. Similar results were, in fact, used during prelaunch tests of ground software to detect and rectify the conversion factor for telemetered wheel data.

Figure 6 presents results with PASS53 data where rate errors of about 1 deg/hour appear in phase with MTA activity. Unlike the data in Figure 5, the data here are unmodified, and the RTSF results suggest that the MTA needs to be calibrated.

Figure 7 presents results with PASS53 data highlighting the usefulness of estimating \hat{b} even in a slowly varying situation. Here propagation of ω via Equation (4) was completely omitted, and the RTSF was run using zero initial conditions; the ω_y estimate quickly converges to the 1-RPO value. In contrast, Figure 8 shows the results with PB705 data where the reverse situation holds: The a priori errors were small, ω was propagated, but \hat{b} was not estimated. Large rate errors (which we ascribe to N_{mag} errors) accumulate over time and eventually degrade the attitude accuracy.

6. RTSF Advantages Over Single-Frame Algorithms

As mentioned in the introduction, a Kalman filter yields estimates via propagation of \hat{X} for state vector elements that are not observable. This is demonstrated here for two situations: (1) near-coalignment of the Sun and magnetic field vectors whereby the pitch angle is nearly unobservable and (2) attitude and rate estimation using only magnetic field data. (Note that Figure 3 is also a *magnetic-field-only* situation, since SIM722 models an eclipse.)

vectors whereby the pitch angle is nearly unobservable and (2) attitude and rate estimation using only magnetic field data. (Note that Figure 3 is also a *magnetic-field-only* situation, since SIM722 models an eclipse.)

Figure 9 presents the former case, with the top plot showing peaks of nearly 25 deg in both QUEST and TRIAD solutions for the pitch angle when the Sun-magnetic field angle falls below 5 deg. This occurs despite nominal values for all sensor and control data (not shown here) during this period. In contrast, the RTSF pitch estimates vary very little over the timespan, with these estimates now being generated using propagation alone. The absence of pitch observability does affect the RTSF pitch covariance P_{22} , whose growth due to Q in Equation (19) is not offset by measurements. Thus, P_{22} first rises steeply in plot b and then falls when the TAM data again provide useful information.

Figure 10 presents RTSF results using PB705 data but without using the available FSS data. The starting conditions here were the zero initial conditions as in Figure 4, but now attitude information is obtained through only the magnetic field B . Although a single measurement of B can yield only information regarding rotations perpendicular to it, B changes direction sufficiently during an orbit, so that all three attitude angles are observable over a sufficiently long span of data. This is indeed seen in Figure 10, where the RTSF's yaw angle estimates converge after about 1000 sec. After convergence, the RTSF attitude and rate estimates remain within 1.5 deg and 0.01 deg/sec, respectively, of the single-frame estimates (not apparent here). We attribute this difference to magnetic field model uncertainties since RTSF attitude accuracies of 0.1 deg were obtained using simulated data (Reference 7).

7. Robust TAM-Only Attitude and Rate Determination

Motivated by the successful TAM-only attitude-and-rate estimation by the RTSF (Figures 3 and 10), we have developed a robust TAM-only method that overcomes the following shortcomings of the RTSF: (1) Convergence of the RTSF estimates is not guaranteed since it is an extended Kalman filter, and (2) the TAM-only convergence is slow, about 1000 sec in Figure 10. These difficulties are overcome here by initializing the RTSF with the solution from the TAM-only deterministic algorithm (DA) of References 12 and 13.

The DA considers the following two time derivatives of the magnetic field B : the one in the reference frame, \dot{B}_R , and the one in the body frame, \dot{B}_A . (The notation used here conforms with that of References 12 and 13.) They are related formally by the vector equation:

$$\dot{B}_R = \dot{B}_A + \omega \times B \quad (23)$$

Noting that $|B|$ is invariant under orthogonal transformations, two special orthogonal axes perpendicular to B (Reference 12) can be chosen such that the projections ω_2 and ω_3 of ω along these axes are restricted to lie on a circle. The DA then extracts the radius and center of this circle from TAM data.

The constraint on ω_2 and ω_3 can be parameterized by an angle Φ so that ω is described by two unknown parameters: ω_1 , the projection of ω onto B , and Φ . These are then determined using $\dot{\omega}$ and the second time derivatives of B as evaluated in the two frames. From Equation (4), $\dot{\omega}$ is expressed as a function of ω and N_{tot} , yielding

$$\Lambda_0(\Phi) + \omega_1 \Lambda_1(\Phi) + \omega_1^2 \Lambda_2(\Phi) = 0 \quad (24)$$

where the vectors $\Lambda_k(\Phi)$, $k = 0, 1, 2$, are defined in Reference 13. Projecting Equation (24) onto the plane perpendicular to B yields two transcendental equations for Φ and ω_1 , generally yielding at least two solutions. The ambiguity in the solutions can be removed if N_{tot} can be neglected, so that we can demand that the reference frame components of the angular momentum L be constant. For SAMPEX, in particular, this requirement holds during eclipses when there is no magnetic control.

The efficacy of the DA calculations was tested using eclipse data from PB722, and evaluating \dot{B}_R and \dot{B}_A using 100-sec batches of TAM data. Figure 11 presents attitude and rate results from this calculation, using a 2-3-2 Euler sequence to parameterize the attitude. The advantage of this parameterization is that the third Euler angle directly reflects the 1-RPO rate of the spacecraft, whereas the other two angles are very nearly constant for small nutational amplitudes. We see that, although up to four solutions appear toward the middle of the timespan, only two solutions appear toward the extremities. Demanding the constancy of L in the reference frame then unambiguously selects the correct solution

To understand why we usually have only two solutions, it is useful to approximate $L \approx h$, which holds very well for SAMPEX. Then

$$\dot{\omega}(\Phi, \omega_1) = \Omega_0^0(\Phi) + \omega_1 \Omega_1^0 \quad (25)$$

where $\Omega_0^0(\Phi) = -I^{-1}[\omega_1(\Phi) \times h]$, $\Omega_1^0 |B| = -I^{-1}[B \times h]$, and ω_1 denotes the projection of the ω onto the plane perpendicular to B . This linearizes Equation (24) and yields:

$$\Lambda_0(\Phi) + \omega_1 \Lambda_1(\Phi) = 0 \quad (26)$$

One can then exclude ω_1 by projecting these equations onto the vector $C_3^* |B| = B \times \Lambda_1(\Phi)$. This leads to a quadratic equation with respect to $x = \tan(\Phi/2)$, analogous to that in Reference 12 for the constant- ω limit. (The quadratic equation turns into Equation (3-11) in Reference 12 if one sets $h = 0$.)

The DA yields multiple solutions when B is approximately antiparallel to the roll axis. Since h for SAMPEX is directed along the pitch axis, $\Omega_0^0(\Phi)$ is approximately antiparallel to B for any value of Φ . Contributions to $\Omega_0^0(\Phi)$ cannot then be neglected in $B \times \dot{\omega}$, and this gives rise to the multiple solutions, at about 600 sec in Figure 11.

Figure 12 compares the RTSF roll angle results obtained by initializing the filter with two different schemes: (1) zero initial conditions and (2) with the correct DA solution from Figure 11. It is evident that using the DA for initialization significantly improves the attitude accuracy by reducing the convergence time of the RTSF. Note that results with both initial conditions reflect oscillations with the spacecraft's nutational period (≈ 120 sec). To illustrate the importance of the initial conditions, we note that the RTSF solutions diverged when the spurious solution of Figure 11 was used to initialize the filter. In this context the successful convergence with zero initial conditions is also noteworthy. (The large nutational amplitudes for zero initial conditions are eventually damped by the RTSF's rate corrections.)

8. Conclusions

We find that the SAMPEX RTSF's method of estimating the rate errors b that accumulated during the period between rate updates yields accurate results while minimizing the computational load. The tuning scheme, which exploited the relationship between the converged covariances, noise characteristics of SAMPEX data, and the Markov time constant, was simple but effective, and resulted in estimates of b accurate to 0.0003 deg/sec (1 deg/hour). Consequently, estimating b significantly enhanced the performance of the SAMPEX RTSF by providing robustness against

- Large a priori attitude and rate errors
- Errors in the control torques

In fact, we see that rates were generated accurately in slowly varying situations even when the Euler equation is not used.

The RTSF's advantages over single-frame algorithms were demonstrated through

- Stability of pitch angle estimates during Sun-magnetic field near-coalignment, where both QUEST and TRIAD solutions were incorrect by nearly 25 deg
- Magnetic-field-only attitude and rate determination to within 1.5 deg and 0.01 deg/sec of the single-frame solutions using zero initial conditions

The deterministic magnetic-field-only algorithm significantly enhanced the robustness and accuracy of the filter by generating coarse estimates of the a priori attitude and rates. This results in an important contingency algorithm for spacecraft like SAMPEX which have no sensor redundancy.

References

1. J. S. Wertz (ed.), *Spacecraft Attitude Determination and Control*, D. Reidel Publishing Co., Dordrecht, Holland, 1984
2. E. Harvie and D. Chu, "Dynamics Modelling for ERBS Attitude Propagation," Proceedings of Third International Symposium on Spacecraft Flight Dynamics, European Space Agency Conference Publication No. ESA-ST 326, Darmstadt, Germany, December 1991
3. M. D. Shuster and S. D. Oh, "Three-Axis Attitude Determination from Vector Observations," *Journal of Guidance and Control*, Vol. 4, p. 70-77, 1981
4. NASA Goddard Space Flight Center (GSFC), Flight Dynamics Division, 554-FDD-91/145, *Solar, Anomalous, and Magnetospheric Particle Explorer (SAMPEX) Real-Time Attitude Determination System for Personal Computer (SRTADS/PC) Specifications Document*, P. Crouse (GSFC), September 1991
5. NASA Goddard Space Flight Center, Flight Dynamics Division, 553-FDD-93/024R0UD0, *Solar, Anomalous, and Magnetospheric Particle Explorer (SAMPEX) Real Time Sequential Filter (RTSF): Evaluation Report*, M. Challa (CSC), prepared by Computer Sciences Corporation, April 1993
6. NASA Goddard Space Flight Center, Flight Dynamics Division, FDD-554-91/030, *Real Time Sequential Filter (RTSF) Mathematical Model for Dynamic Propagation of Angular Rates*, M. Challa (CSC) and M. Rokni (CSC), prepared by Computer Sciences Corporation, January 1991
7. NASA Goddard Space Flight Center, Flight Dynamics Division, 553-FDD-93/076R0UD0, *Attitude Dynamics Task: Attitude Determination Using Only Magnetometer Data for the Solar, Anomalous, and Magnetospheric Particle Explorer (SAMPEX)*, G. Natanson (CSC), M. Challa (CSC), S. Kotaru (CSC), and C. Woodruff (CSC), prepared by Computer Sciences Corporation, August 1993
8. E. J. Lefferts, F. L. Markley, and M. D. Shuster, "Kalman Filtering for Spacecraft Attitude Estimation," *Journal of Guidance, Control, and Dynamics*, Vol. 5, No. 5, Sept.-Oct. 1982, pp. 417-429
9. J. Deutschmann, I. Y. Bar-Itzhack, and M. Rokni, "Comparison and Testing of Extended Kalman Filters for Attitude and Estimation of the Earth Radiation Budget Satellite," Flight Mechanics and Estimation Theory Symposium, NASA Conference Publication 3102, Greenbelt, MD, May 1990
10. J. Sedlak and D. Chu, "Kalman Filter Formulation of Attitude and Gyro Bias with the QUEST Observation Model," Paper No. AAS 93-297, Proceedings of the AAS/GSFC International Symposium on Space Flight Dynamics, NASA Goddard Space Flight Center, Greenbelt, MD, April 1993
11. R. Hammon, "An Application of Random Process Theory to Gyro Drift Analysis," *IRE Transactions on Aerospace and Navigational Electronics*, Vol. 7, pp. 84-91, September 1960
12. G. A. Natanson, S. F. McLaughlin, and R. C. Nicklas, "A Method of Determining Attitude From Magnetometer Data Only," Flight Mechanics and Estimation Theory Symposium, NASA Goddard Space Flight Center, Greenbelt MD, May 1990
13. G. A. Natanson, "A Deterministic Method for Estimating Attitude From Magnetometer Data Only," Paper No. IAF-92-0036, Proceedings of the World Space Congress, Washington DC, August-September 1992
14. J. K. Forden, T. W. Flatley, D. A. Henretty, and E. G. Lightsey, "On-board Attitude Determination and Control Algorithms for SAMPEX," Flight Mechanics and Estimation Theory Symposium, NASA Conference Publication 3102, May 1990
15. A. Gelb (ed.), *Applied Optimal Estimation*, The MIT Press, Cambridge, Massachusetts, 1974
16. D. C. Folta and D. F. Baker, *Increased Ephemeris Accuracy Using Attitude-dependent Aerodynamic Force Coefficients for Inertially Stabilized Spacecraft*, Flight Mechanics and Estimation Theory Symposium, NASA Conference Publication No. 3123, May 1991

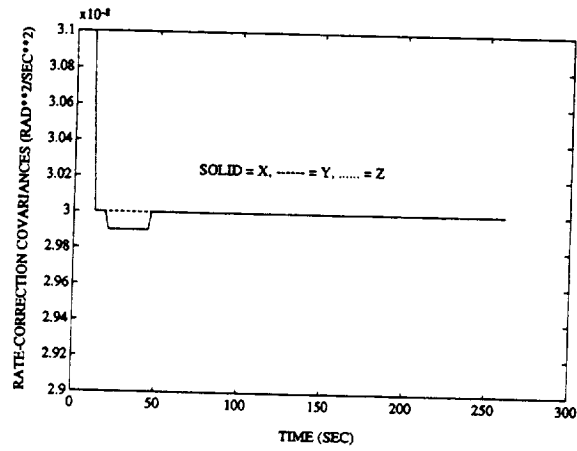
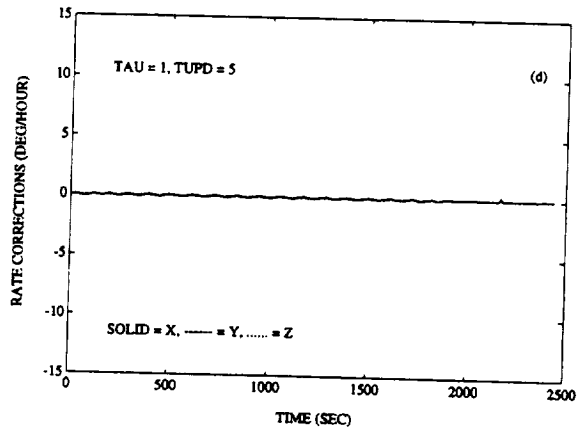
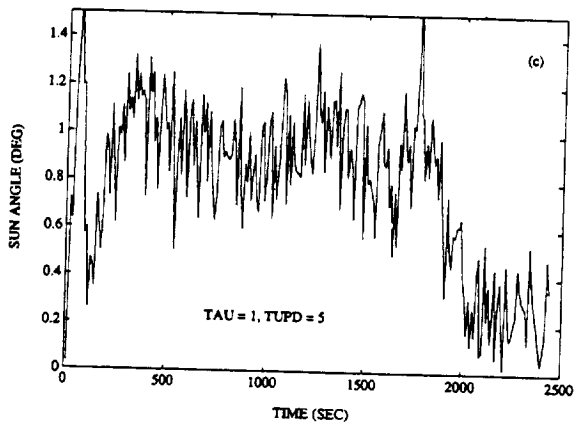
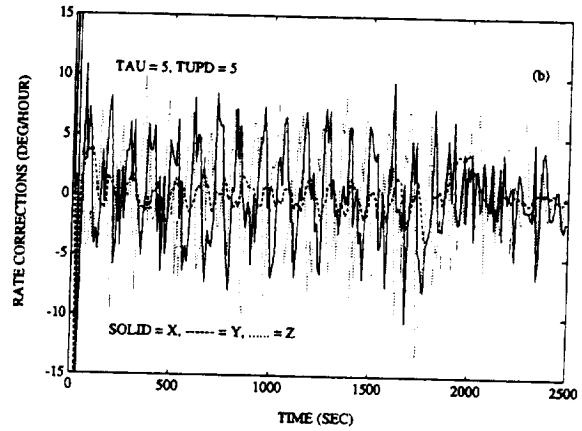
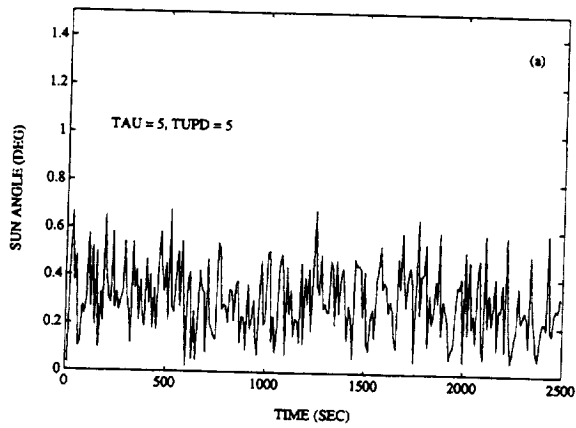
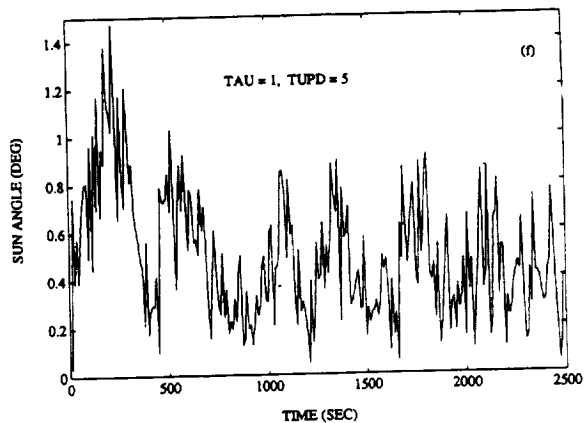
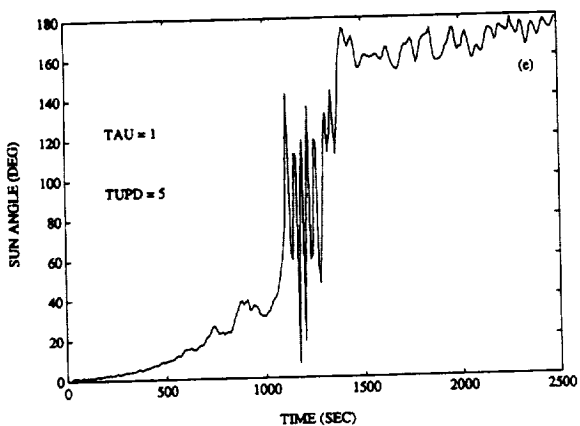


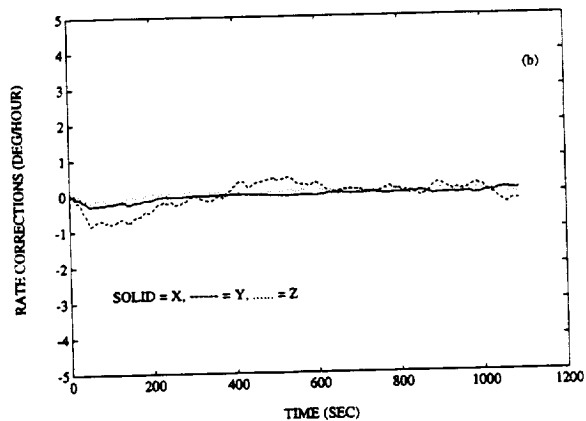
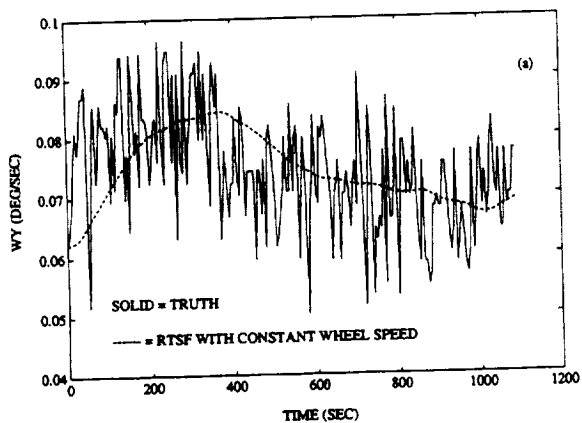
Figure 1. Results Using PB705 Data Showing Convergence of Rate Correction Covariances to the Theoretical Value



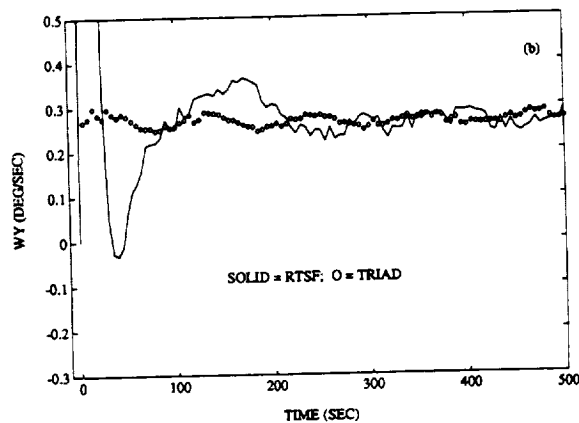
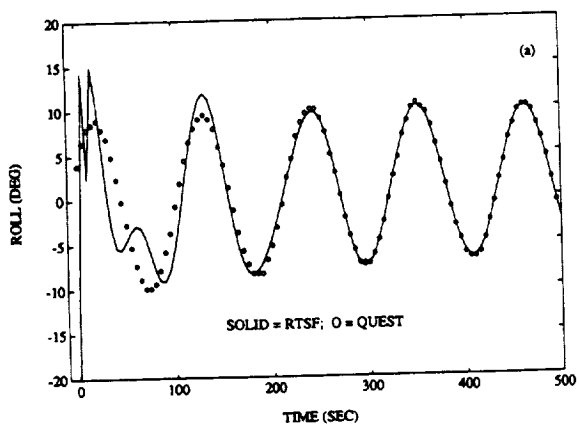
Figures 2a-2d. RTSF Results Using PB705 Data Showing That Tuning is Optimal When Both τ and t_{upd} Equal the Telemetry Period of 5 sec



Figures 2e and 2f. RTSF Results Using PB705 Data Showing That Tuning is Optimal When Both τ and t_{upd} Equal the Telemetry Period of 5 Sec



Figures 3a and 3b. Results Using SIM722 Data Showing Accuracy of the Rate Corrections



Figures 4a and 4b. Results Using PB705 Data Showing Convergence of RTSF Estimates to Single-Frame Results Despite Large a Prior Errors

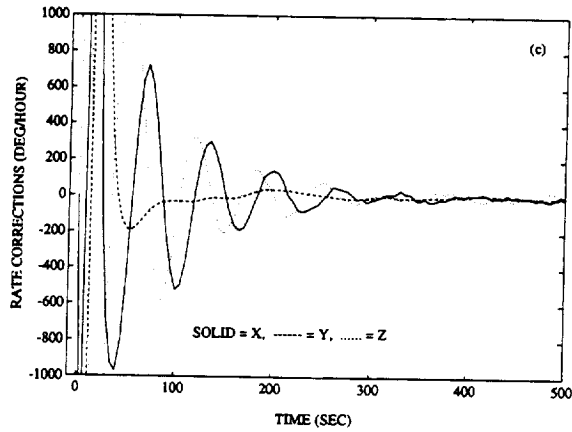
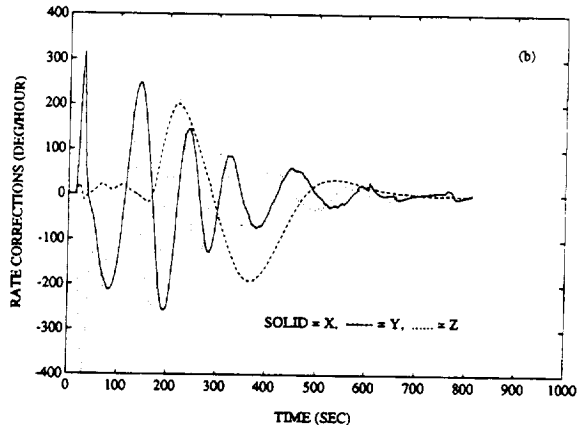
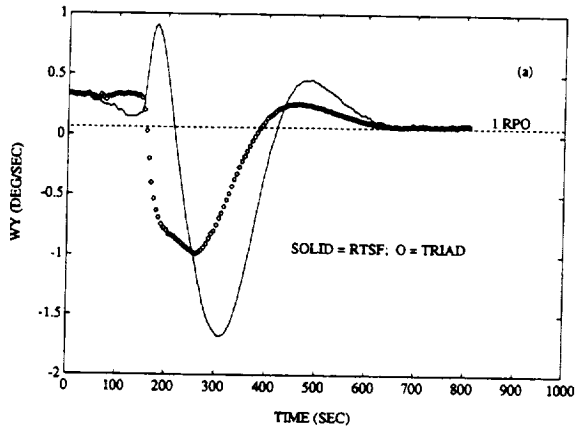
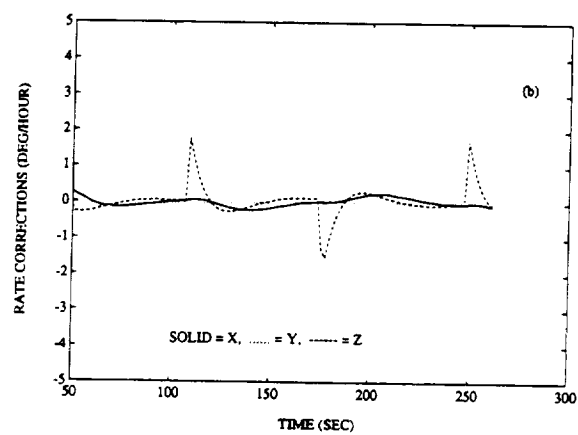
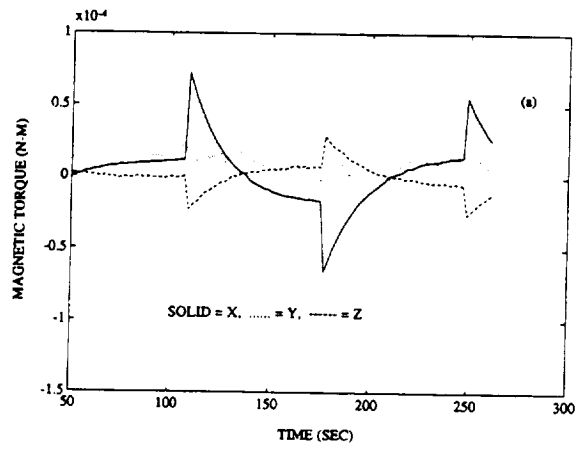


Figure 4c. Results Using PB705 Data Showing Convergence of RTSF Estimates to Single-Frame Results Despite Large a Priori Errors



Figures 5a and 5b. Compensation by the Rate Corrections for Wheel Torque Errors in Modified PB705 Data



Figures 6a and 6b. Results Using PASS53 Data Suggesting Errors in Magnetic Control Torques

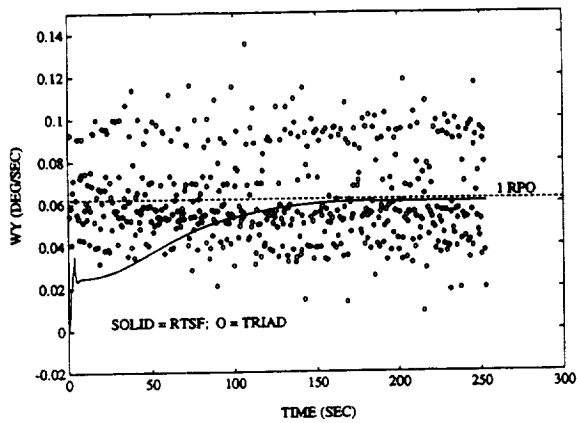


Figure 7. Results Using PASS53 Data Showing Robustness of RTSF When Rate Propagation Is Suppressed

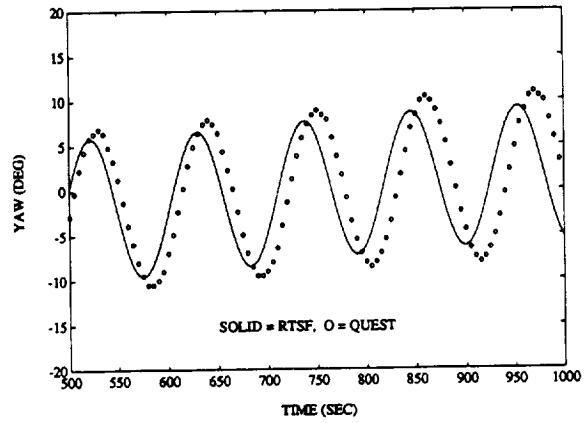


Figure 8. Results Using PB705 Data Showing Significant RTSF Errors When Rate Corrections Are Not Estimated

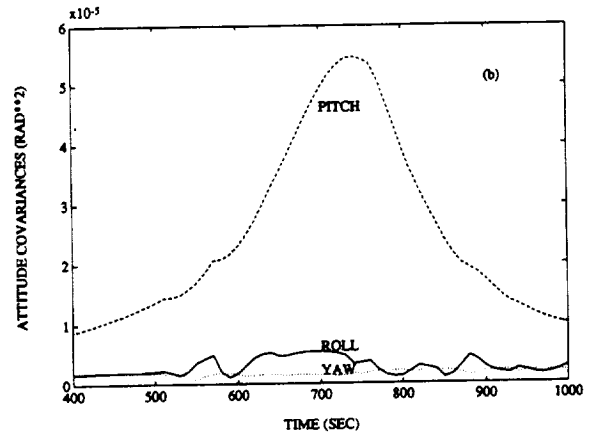
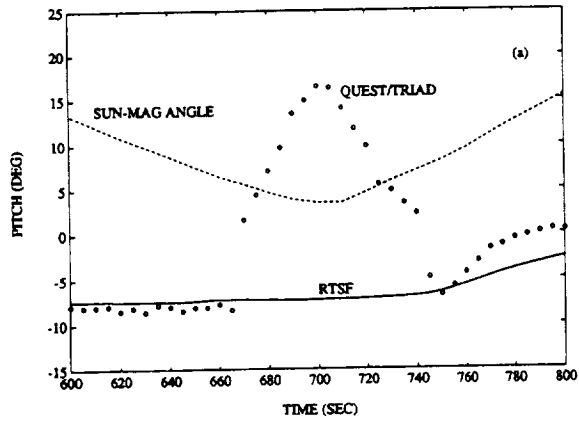
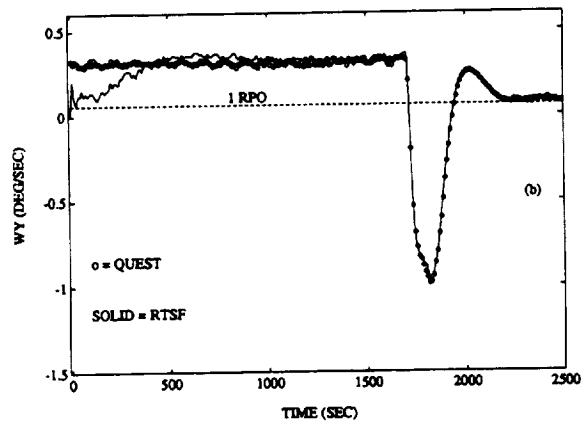
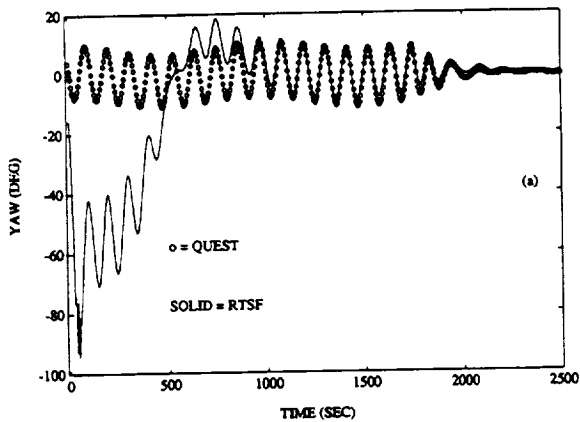
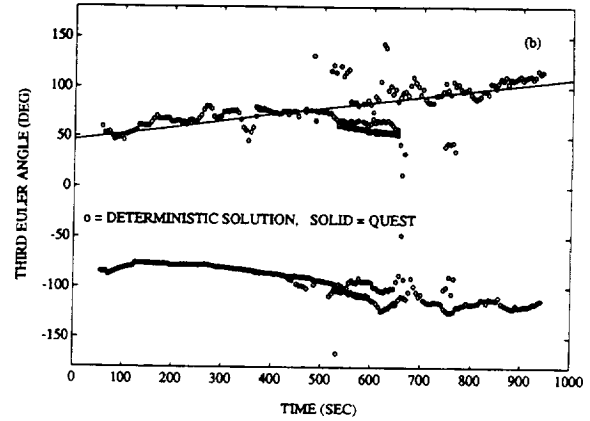
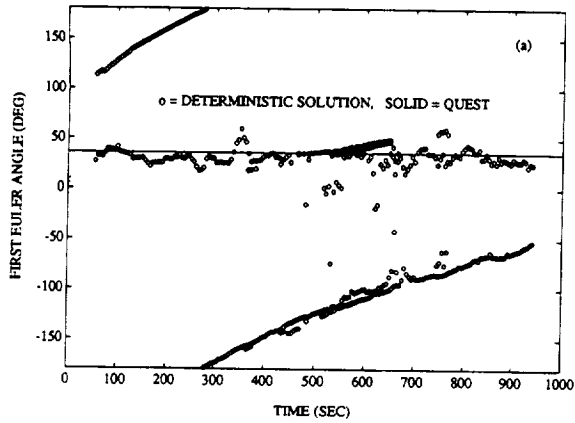


Figure 9a and 9b. Results Using PB825 Data Showing Robustness of RTSF During Near-Coalignment of Sun and Magnetic Field Vectors



Figures 10a and 10b. Convergence of RTSF Estimates for PB705 Data When Only TAM Data and Large a Priori Errors Are Used



Figures 11a and 11b. TAM-Only Attitude and Rate Solutions Generated by the Deterministic Method During an Eclipse in PB722 Data

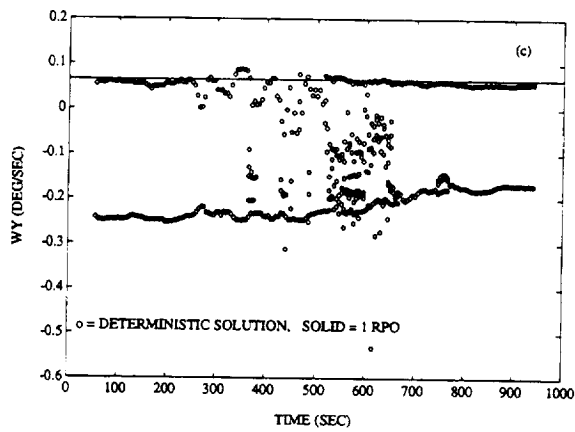


Figure 11c. TAM-Only Attitude and Rate Solutions Generated by the Deterministic Method During an Eclipse in PB722 Data

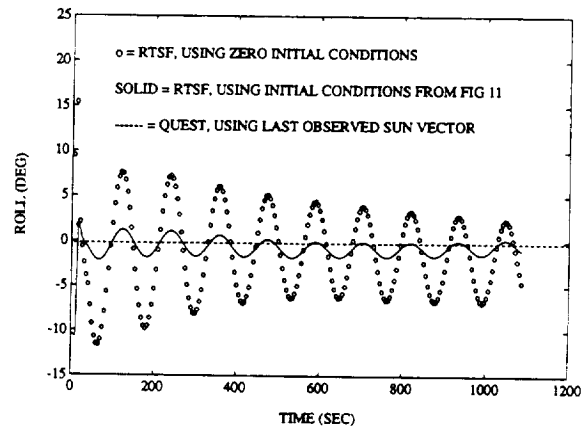


Figure 12. RTSF TAM-Only Results for PB722 Data Showing Faster Convergence Using the Correct Solutions of Figure 11

MME-BASED ATTITUDE DYNAMICS IDENTIFICATION AND ESTIMATION FOR SAMPEX

Juan De Peña*

John L. Crassidis†

Michael D. McPartland‡

Thomas J. Meyer§

D. Joseph Mook||

ABSTRACT

A method is described for obtaining optimal attitude estimation algorithms for spacecraft lacking attitude rate measurement devices (rate gyros), and then demonstrated using actual flight data from the Solar, Anomalous, and Magnetospheric Particle Explorer (SAMPEX) spacecraft. SAMPEX does not have on-board rate sensing, and relies on sun sensors and a three-axis magnetometer for attitude determination. Problems arise since typical attitude estimation is accomplished by filtering measurements of both attitude and attitude rates. Rates are nearly always sampled much more densely than are attitudes. Thus, the absence/loss of rate data normally reduces both the total amount of data available and the sampling density (in time) by a substantial fraction. As a result, the sensitivity of the estimates to model uncertainty and to measurement noise increases. In order to maintain accuracy in the attitude estimates, there is increased need for accurate models of the rotational dynamics. The proposed approach is based on the Minimum Model Error (MME) optimal estimation strategy, which has been successfully applied to estimation of poorly-modeled dynamic systems which are relatively sparsely and/or noisily measured. The MME estimates may be used to construct accurate models of the system dynamics (i.e. perform system model identification). Thus, an MME-based approach directly addresses the problems created by absence of attitude rate measurements.

-
- * NASA Graduate Research Fellow; Student Member AIAA
Department of Mechanical and Aerospace Engineering, State University of New York at Buffalo, Buffalo, NY 14260
 - † NRC Postdoctoral Research Fellow; Member AIAA
Goddard Space Flight Center, Code 712, Greenbelt, MD 20771
 - ‡ Postdoctoral Research Assistant; Member AIAA
Department of Mechanical and Aerospace Engineering, State University of New York at Buffalo, Buffalo, NY 14260
 - § Research Assistant; Student Member AIAA
Department of Mechanical and Aerospace Engineering, State University of New York at Buffalo, Buffalo, NY 14260
 - || Associate Professor; Senior Member AIAA
Department of Mechanical and Aerospace Engineering, State University of New York at Buffalo, Buffalo, NY 14260

INTRODUCTION

The attitude of a spacecraft can be estimated by either single-frame deterministic methods (such as TRIAD and QUEST [1-2]) or algorithms which combine analytical models with attitude measurements and, for most spacecraft, attitude rates (such as the Kalman filter [3]). Generally, the use of rate gyros significantly improves the attitude estimation, because the densely-measured rates may virtually eliminate the need for dynamic models. However, the intentional omission of rate gyros in the design of satellites is increasingly likely as resources become more scarce (for example, the Solar, Anomalous, and Magnetospheric Particle Explorer (SAMPEX) satellite does not have rate gyros on board). In addition, existing satellites with rate gyros on board may experience gyro degradation or failure (such as the failure of four of the six rate gyros on the Earth Radiation Budget Satellite (ERBS) [4]). When rate gyro data is either not available or not dependable, the attitude estimation accuracy becomes much more heavily dependent on accurate dynamic models since the attitude measurements are typically much less dense and less accurate than the rate data. In these cases, dynamic models may be required to provide estimates between and/or in addition to the attitude measurements.

Unfortunately, accurate models of spacecraft rotational dynamics are often unavailable. In cases where the spacecraft was launched with rate gyros, the attitude estimation algorithm likely did not require an accurate dynamics model since dense rate measurements were available. Even for spacecraft which do not have rate gyros, determining an accurate rotational dynamics model may be difficult. If an accurate model is necessary in the attitude estimation algorithm, estimation accuracy is compromised. This is especially true for spacecraft launched with rate gyros which subsequently fail.

To circumvent the problem of rate gyro omission or failure, analytical models of gyro biases can be used. An example of a commonly used gyro bias model is the model based on a Markov (exponential decay) process. This simple model has been successfully used in a Real-Time Sequential Filter (RTSF) algorithm in order to propagate dynamic state estimates and error covariances for the SAMPEX satellite (see [5]). A clear advantage to using dynamic models for gyro biases was shown for the case of Sun-magnetic near-co-alignment. For this case, the single-frame algorithms, TRIAD and QUEST, showed anomalous behaviors with extreme deviations in attitude estimations. However, since the RTSF propagates an analytical model of the gyro bias, the attitude estimates are improved even when data from only one sensor is available (i.e., only magnetometer measurements).

In theory, perfect, solvable models of the spacecraft rotational dynamics could be used to obtain perfect attitude estimates. When accurate rate gyros are present, they can often take the place of the dynamic models. When rate gyros are either absent or excessively noisy, attitude estimation accuracy becomes critically dependent on the accuracy of the rotational dynamic models. The ERBS studies [6-8] showed, for an existing satellite, that modeling of the attitude dynamics leads to accurate attitude estimation algorithms. However, the authors concluded that in order to be operationally useful, "automatic" methods for determining these dynamic models must be available.

In this paper, a technique is described which directly addresses the problem of attitude estimation when rate data is not available (or severely degraded), regardless of the cause. The method described herein addresses this problem directly in two distinct but related approaches. First, the MME [9–12] method may be used simply to obtain accurate state estimates for dynamic systems which are both poorly modeled and sparsely measured. This is accomplished through explicit accounting for errors in the dynamic model. Thus, attitude estimation using existing satellite dynamic models (which may not be particularly accurate) is possible. However, the MME estimates may also be used to construct accurate models of the system dynamics (i.e., perform system model identification). Thus, the second, and main, thrust of the approach is the use of the MME to create more accurate dynamic models for use in ANY estimation algorithm (batch, sequential, or MME).

An optimal attitude estimation algorithm is described which is capable of robust and accurate estimates for spacecraft lacking both accurate attitude rate measurements and accurate rotational dynamics models. The current approach is based on the Minimum Model Error (MME) optimal estimation strategy, which has been successfully applied to estimation of numerous poorly-modeled dynamic systems which are relatively sparsely and/or noisily measured. The MME-based approach described in this paper has the capability to automatically determine accurate rotational dynamic models, resulting in algorithms which exhibit the high accuracy of estimation using accurate dynamic models, as shown in [9], while eliminating the practical limitations currently imposed by the requirement that the models be determined manually for each orbit.

The organization of this paper is as follows. First, a brief description of the SAMPEX satellite and associated (model) equations of motion is shown. Then, a brief summary of the MME estimation algorithm for nonlinear systems is shown. An MME estimator, which incorporates the SAMPEX model, is next applied to estimate the dynamics (attitudes, angular rates, and angular momentum) of SAMPEX using actual telemetry measurements. Lastly, candidate functional forms for the model error trajectories given by the MME estimator are investigated. Results are compared with actual telemetry data.

SAMPEX MISSION DESCRIPTION

The Goddard Space Flight Center (GSFC) Small Explorer (SMEX) program was developed to provide relatively inexpensive, frequent space science missions. The Solar, Anomalous, and Magnetospheric Particle Explorer (SAMPEX) satellite is the first of the SMEX class missions. The SAMPEX [5] general mission is to study energetic particles and various types of rays. The duration of the mission is 3 years with a possible extension of up to 3 more years.

The spacecraft is three-axis stabilized in a 550 by 675 km elliptical orbit with an 82° inclination. The nominal mode is a one rotation per orbit about the Sun vector. The body z-axis is defined by the instrument boresights and is required to be within 15° of zenith near the magnetic poles. The body y-axis nominally is aligned with the Sun vector.

The attitude determination hardware consists of five coarse Sun sensors (CSS) (primarily for Sun-acquisition), one fine Sun sensor (FSS) (for roll and yaw), and a three-axis magnetometer (TAM) (for pitch). The attitude control hardware consists of a magnetic torquer assembly (MTA) (for roll and yaw), and a reaction wheel assembly (RWA) (for pitch). The nominal attitude determination accuracy is $\pm 2^\circ$.

SRTADS

The SAMPEX Real-Time-Attitude-Determination-System (SRTADS) is a graphical-user-interface program which computes and displays attitude solutions along with telemetry measurements in a real-time mode during real-time contacts. One of the functions of the system is to serve as a testing platform for filtering methods used in attitude determination.

The current version of the SRTADS program implements three different attitude determination methods: 1) the TRIAD algorithm; 2) the QUEST algorithm; and 3) the Real-Time Sequential Filter (RTSF). Both TRIAD and QUEST are single-frame deterministic methods which primarily rely on a pair of measured vectors for attitude determination. The RTSF is an extended Kalman filter which combines both measured data and a system model to obtain an attitude solution.

THE MME APPROACH

The Minimum Model Error (MME) estimation algorithm was developed for optimal state estimation of poorly modeled dynamic systems ([9]). Motivated by problems in satellite orbit/attitude determination (see [13]), in which significant unmodeled dynamics may be present, the MME was formulated to rigorously account for both significant modeling error and significant measurement noise.

The MME state and model error estimations have been shown to be extremely accurate in previous work [9–10], [12] and the algorithm shown to be robust with respect to modeling errors, measurement errors, and measurement sparsity [12]. The true state trajectories are accurately estimated, $\hat{\mathbf{x}}(t) \approx \mathbf{x}(t)$, and, most important for the realization/identification problem, $\hat{\mathbf{d}}(t)$ approaches the correct model error trajectory. Another key feature of the MME (explained in [10]) is that the state estimates are free of jump discontinuities evident in Kalman filters, for example.

The MME solution yields the optimal state estimates $\hat{\mathbf{x}}(t)$ and the optimal model error estimates $\hat{\mathbf{d}}(t)$. Results presented in [12], [13] showed that for poorly modeled systems, the MME state estimates are of considerably higher accuracy than those obtained using standard approaches based on Kalman filtering. In addition, the MME has been used as the basis for highly accurate and robust system identification algorithms, both linear [11], [14–16], and nonlinear [12], [17–18], based on the combination of state and model error estimates.

MODEL EQUATIONS

The following is a brief summary of the kinematic and dynamic equations of motion for a three-axis stabilized spacecraft. The rotational orientation of the spacecraft (kinematic equations) may be represented by the quaternion attitude parameterization as

$$\dot{\underline{q}} = \frac{1}{2} \underline{\Omega} \underline{q} \quad (6)$$

where

$$\underline{\Omega} = \begin{bmatrix} 0 & \omega_3 & -\omega_2 & \omega_1 \\ -\omega_3 & 0 & \omega_1 & \omega_2 \\ \omega_2 & -\omega_1 & 0 & \omega_3 \\ -\omega_1 & -\omega_2 & -\omega_3 & 0 \end{bmatrix} \quad (7)$$

The elements of $\underline{\Omega}$ are the components of the instantaneous spacecraft angular velocity defined relative to the body frame.

The dynamic equations of motion (Euler's Equations of Motion) for a non-rigid spacecraft (SAMPEX is not modeled as a rigid body because it contains a reaction-wheel assembly), may be defined as

$$\frac{d\underline{L}}{dt} = \underline{N} - \underline{\omega} \times \underline{L} \quad (8a)$$

$$\underline{L} = \underline{L}_{body} + [I_{rw} \times \omega_{rw}] \hat{j} \quad (8b)$$

where

\underline{N} = total external torque

$\underline{\omega}$ = instantaneous angular velocity

\underline{L} = total angular momentum

\underline{L}_{body} = angular momentum of the body

I_{rw} = inertia of the reaction wheel

ω_{rw} = angular velocity of the reaction wheel

Here, again, all vectors are resolved in a body-fixed coordinate system. The angular momentum of the reaction wheel only acts along the y-body axis. The nonlinear state-

space representation of the dynamic equations of motion is given by

$$\begin{Bmatrix} \dot{q}_1 \\ \dot{q}_2 \\ \dot{q}_3 \\ \dot{q}_4 \\ \dot{L}_1 \\ \dot{L}_2 \\ \dot{L}_3 \end{Bmatrix} = \frac{1}{2} \begin{bmatrix} 0 & \omega_3 & -\omega_2 & \omega_1 & 0 & 0 & 0 \\ -\omega_3 & 0 & \omega_1 & \omega_2 & 0 & 0 & 0 \\ \omega_2 & -\omega_1 & 0 & \omega_3 & 0 & 0 & 0 \\ -\omega_1 & -\omega_2 & -\omega_3 & 0 & 0 & 0 & 0 \\ 0 & 0 & 0 & 0 & 0 & 2\omega_3 & -2\omega_2 \\ 0 & 0 & 0 & 0 & -2\omega_3 & 0 & 2\omega_1 \\ 0 & 0 & 0 & 0 & 2\omega_2 & -2\omega_1 & 0 \end{bmatrix} \begin{Bmatrix} q_1 \\ q_2 \\ q_3 \\ q_4 \\ L_1 \\ L_2 \\ L_3 \end{Bmatrix} + \begin{bmatrix} 0 & 0 & 0 \\ 0 & 0 & 0 \\ 0 & 0 & 0 \\ 0 & 0 & 0 \\ 1 & 0 & 0 \\ 0 & 1 & 0 \\ 0 & 0 & 1 \end{bmatrix} \begin{Bmatrix} N_1 \\ N_2 \\ N_3 \end{Bmatrix} \quad (9)$$

The body angular rates can be determined using the angular momentum, reaction wheel momentum, and known inertia:

$$\begin{Bmatrix} \omega_1 \\ \omega_2 \\ \omega_3 \end{Bmatrix} = I^{-1} \begin{Bmatrix} L_1 \\ L_2 - I_{rw} \times w_{rw} \\ L_3 \end{Bmatrix} \quad (10)$$

where I represents the inertia tensor of the satellite.

SRTADS provides time histories for all external torques (aerodynamic, gravitational, solar, magnetic, etc) and the reaction wheel input. The nominal numerical values for the SAMPEX inertia tensor and reaction wheel inertia are given by [5]

$$I = \begin{bmatrix} 15.516 & 0 & 0 \\ 0 & 21.621 & -0.194 \\ 0 & -0.194 & 15.234 \end{bmatrix} \text{ kg} - \text{m}^2 \quad I_{rw} = 0.0041488 \text{ kg} - \text{m}^2$$

RESULTS

A nominal satellite pass is used to compare the MME estimator to the deterministic method (e.g., TRIAD). Nominally, both FSS and TAM data is available throughout the orbit. Anomalous behavior occurs during either sun occultation and/or co-alignment of the measurement vectors. However, this test case involves a non-event pass (i.e., no anomalous behavior). SRTADS utilizes telemetry and ephemeris data from an orbital pass and determines the Euler attitudes using TRIAD, QUEST, and the RTSF in 5 second intervals.

The MME estimator uses a priori values from the single-frame solutions (i.e., the TRIAD solution for the spacecraft's attitude). The MME estimator is then used to obtain

estimates for both the three-axis attitudes and the dynamic rates. Since this test case involves a non-event pass, the TRIAD solution for the spacecraft's attitude is assumed to be the actual (nominal) solution. Figures 1–3 show the TRIAD solutions for the SAMPEX Euler attitudes. These attitude time histories are assumed to be the “true” attitudes for this test case.

The MME model error term $\underline{d}(t)$ is added only to the last three (angular momentum) states of the dynamic model, represented by Equation (9). The first four states (i.e., the quaternions) are assumed to be perfect kinematic relationships so that no model correction is added to these states. This formulation avoids any difficulties encountered by the normalization constraint of the quaternions [2]. Therefore, no pre-conditioning of the estimator model for the normalization constraint of the quaternion states is required. This formulation has clear advantages over the Kalman filter method for attitude estimation (see Reference [3]).

Results indicate that the attitude time estimates given by the MME estimator are exactly identical to the TRIAD solutions, shown in Figures 1–3. Therefore, the MME estimator provides accurate attitude estimates in this non-event case (i.e., the estimates parallel the TRIAD solution throughout the entire time interval).

The angular momentum estimates from the MME are shown in Figures 4–6. These trajectories are used to determine the instantaneous spacecraft angular rates resolved along the body frame, which propagate the quaternions. The associated model error trajectories ($\underline{d}(t)$) from the MME estimator are shown in Figure 7. It is important to note that the correction is only applied to the angular momentum states. This formulation provides accurate MME state estimates of the Euler angles (see Figures 1–3), and also maintains the quaternion normalization constraint.

The model error trajectories can now be used to correlate a linear or nonlinear correction to the SAMPEX dynamic model. To identify mathematical expressions that describe these trajectories, the Least-Squares-Correlation (LSC) algorithm is used [19]. This algorithm develops a set of mathematical expressions that describe the model error histories as a combination of the state estimates. This algorithm can be implemented in two ways: (1) the code can be allowed to form combinations of simple mathematical functions, or (2) a library of functions may be supplied by the user to augment the search process (i.e., by supplying known functions from intuitive implementations or past studies). This library is a list of functions which the user expects will appear in the system under investigation. These functions may be common occurring functions from initial runs of the LSC algorithm.

A method for identifying possible library functions involves plotting the model error trajectories versus the state estimates. These plots may offer significant mathematical insight on how to formulate library expressions. Plots of the second model error versus the first and second state estimates are shown in Figures 8–9. From these figures, a possible functional form may be a Lemniscate geometric function with internal oscillations. This geometric function is implemented into the library set (along with previous internal

functions). Table 1 contains example candidate functions obtained to this point. The second model error candidate expression shows a high correlation coefficient of 0.99. Figure 10 shows the second model error and the example candidate function that describes it. From the high correlation value, and the presence of only minor discrepancies in this figure the second model error is assumed to be correctly identified by the function shown in Table 1. Note that this model error candidate expression has been identified without the use of any library terms.

The next step in the study is to create a library starting with known attitude dynamical model components and external disturbances (e.g., aerodynamic torque, radiation torque, orbit maneuvering torques, solar radiation pressure, etc). These can be used to further and more accurately identify nonlinear terms for the remaining model error trajectories (i.e., to obtain higher correlations). Once dynamical error models are obtained, they can be used to determine actual trajectories during anomalous periods such as Sun occultation and/or measurement vector co-alignment.

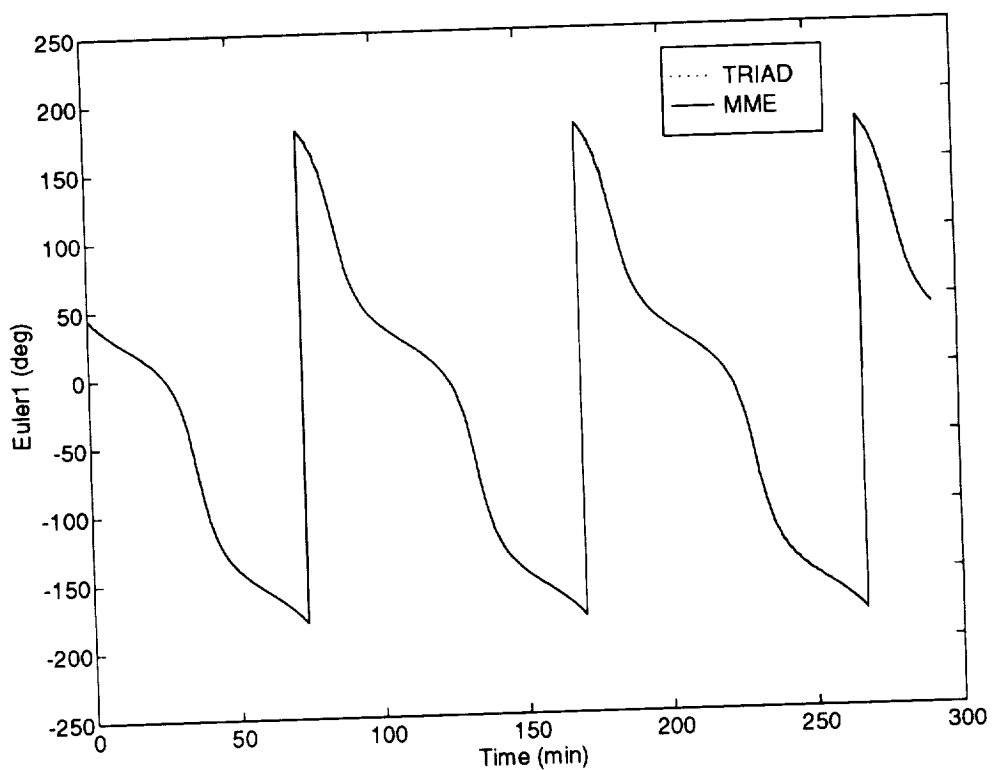


Figure 1 TRIAD and MME Euler1 Angle Solutions

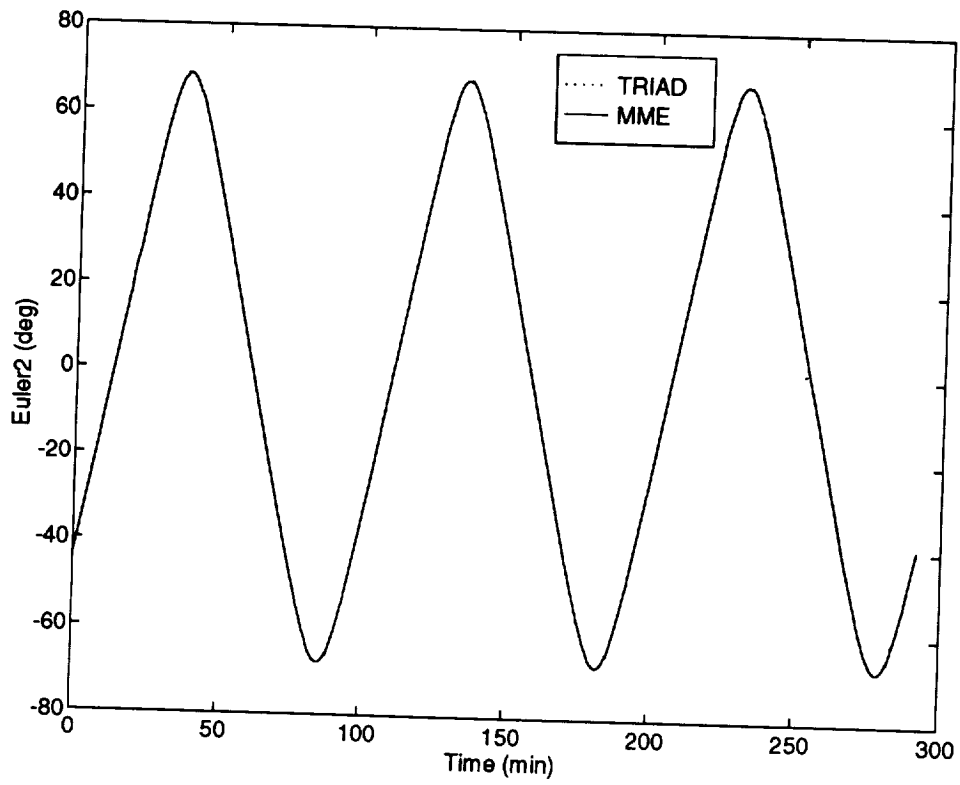


Figure 2 TRIAD and MME Euler2 Angle Solutions

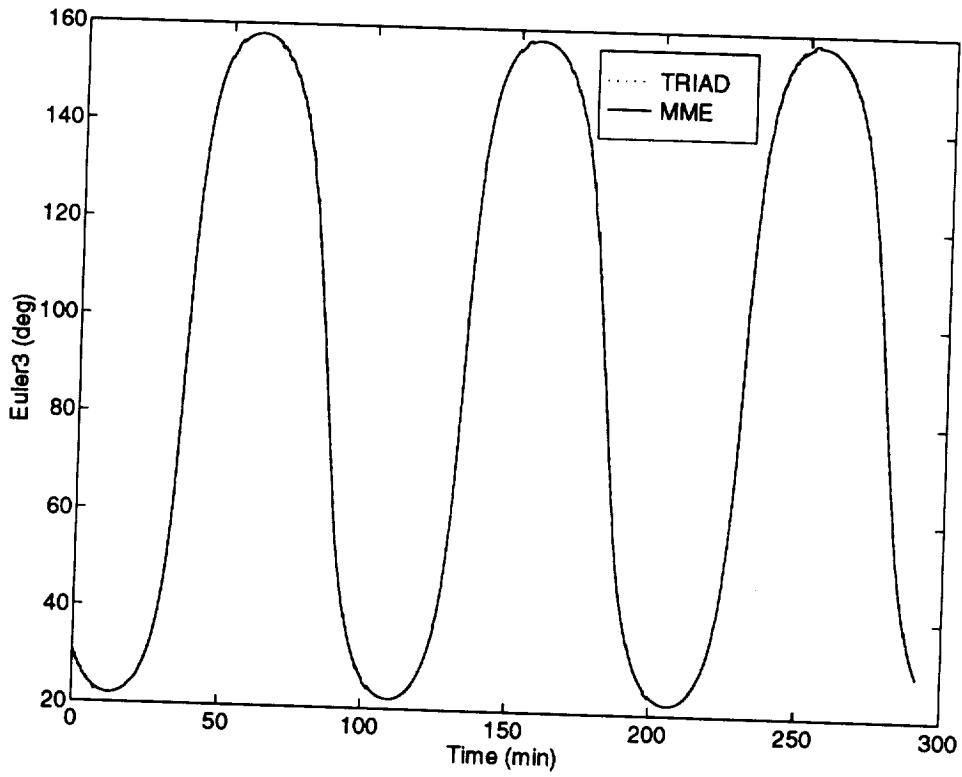


Figure 3 TRIAD and MME Euler3 Angle Solutions

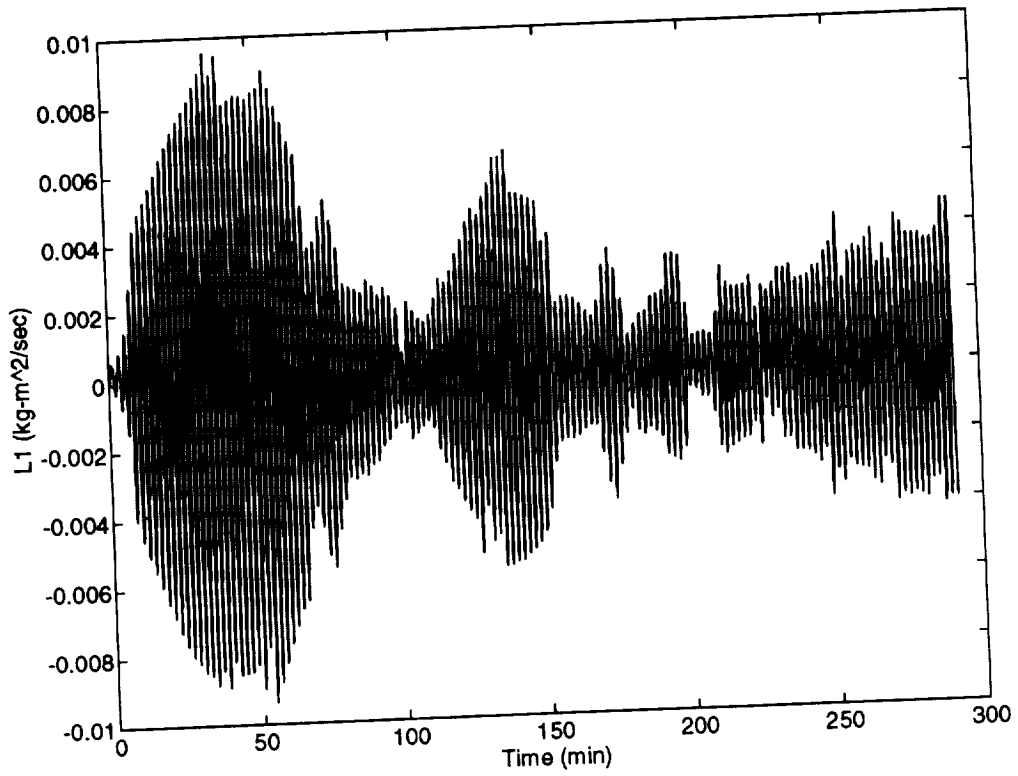


Figure 4 MME L_1 Angular Momentum State Estimate

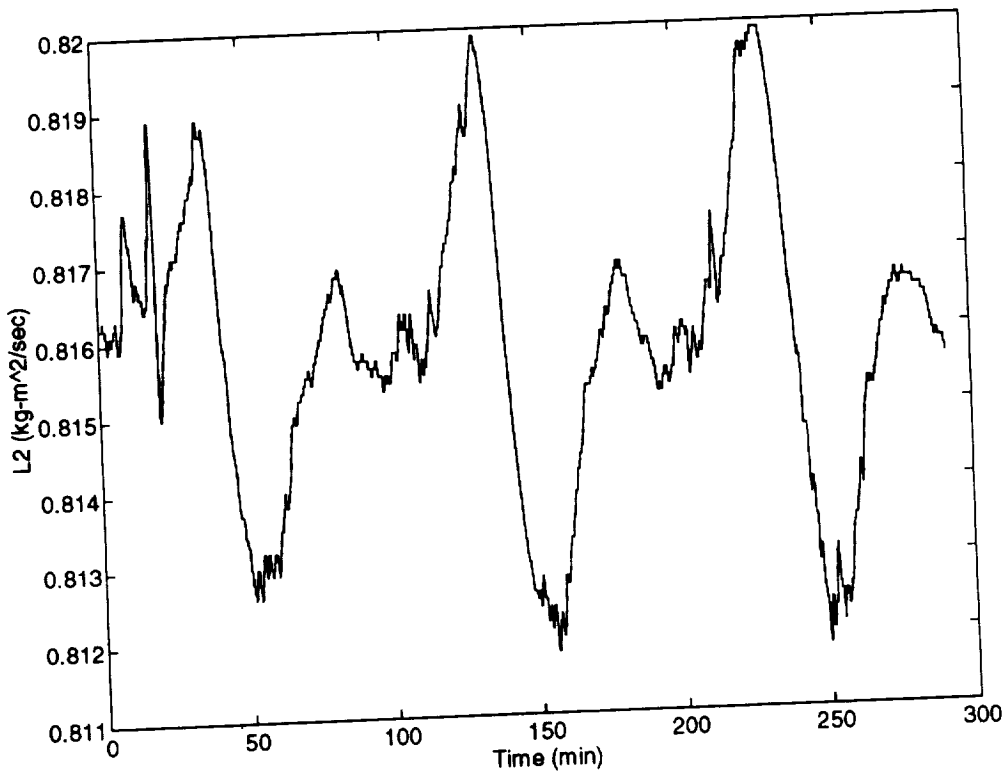


Figure 5 MME L_2 Angular Momentum State Estimate

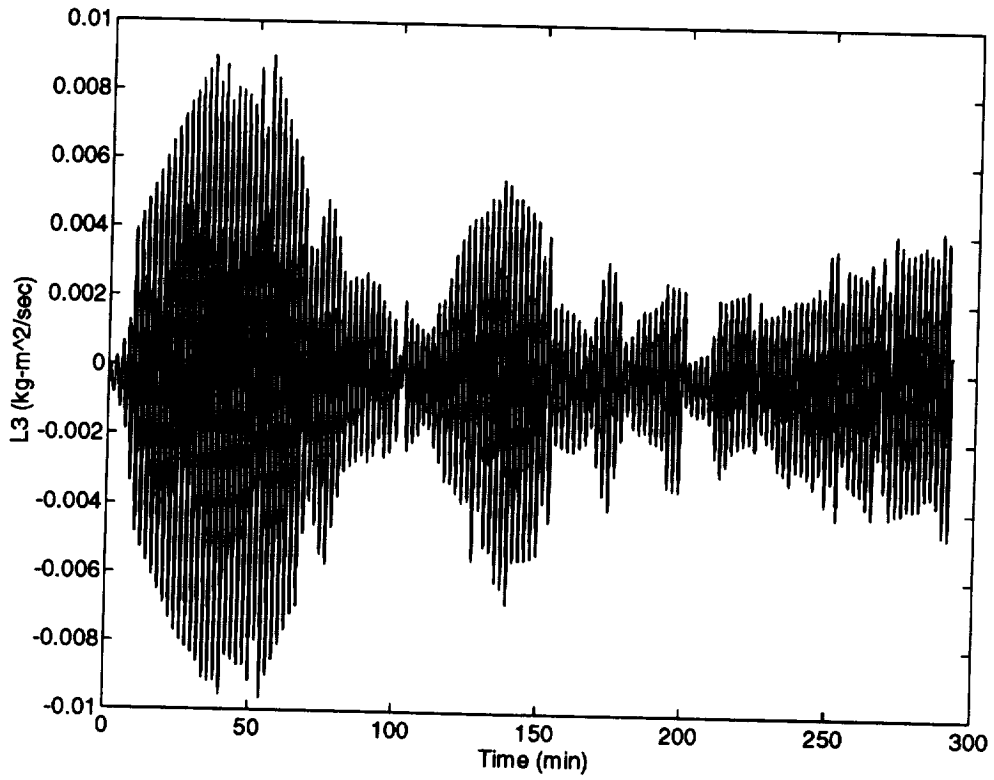


Figure 6 MME L_3 Angular Momentum State Estimate

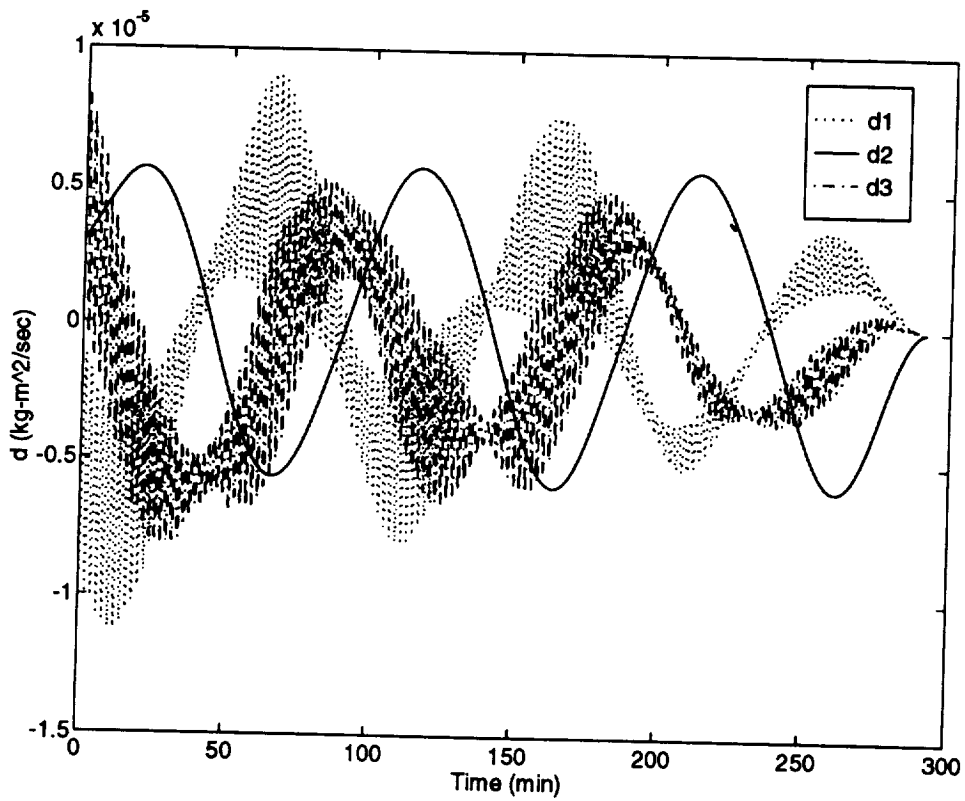


Figure 7 MME Angular Momentum Model Error Trajectories

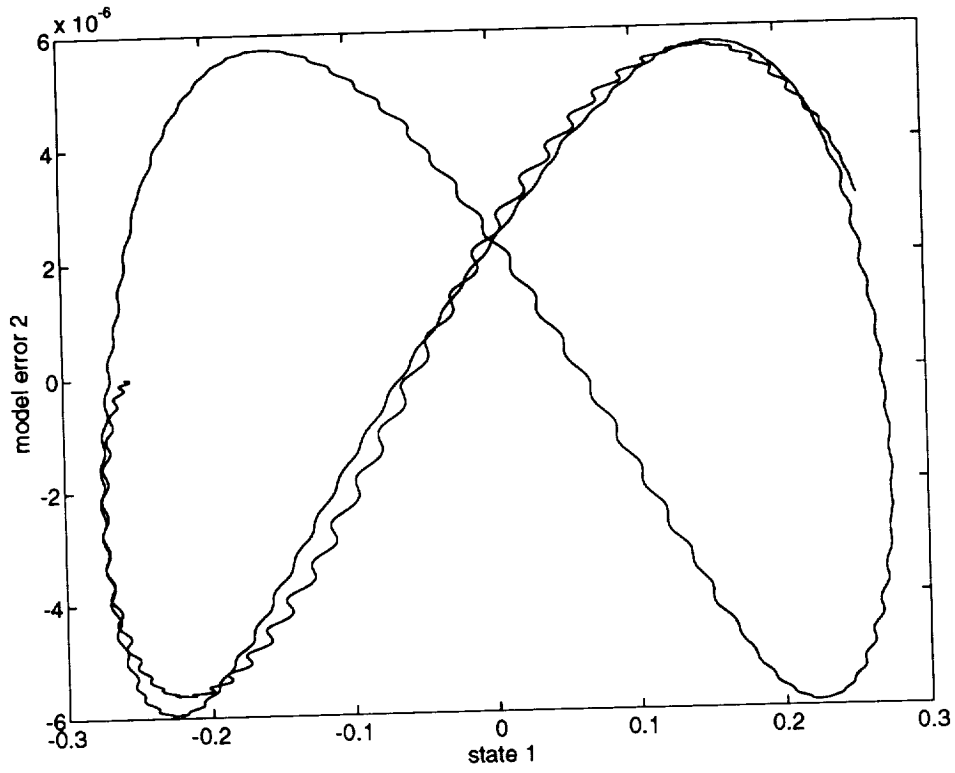


Figure 8 Second Model Error versus First Estimated State

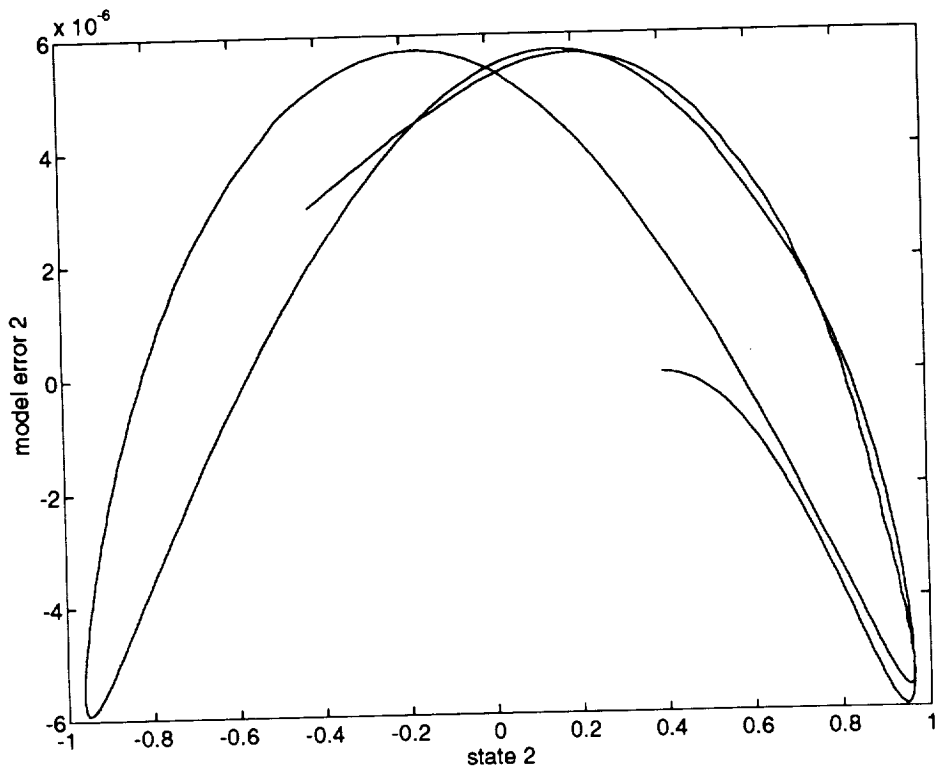


Figure 9 Second Model Error versus Second Estimated State

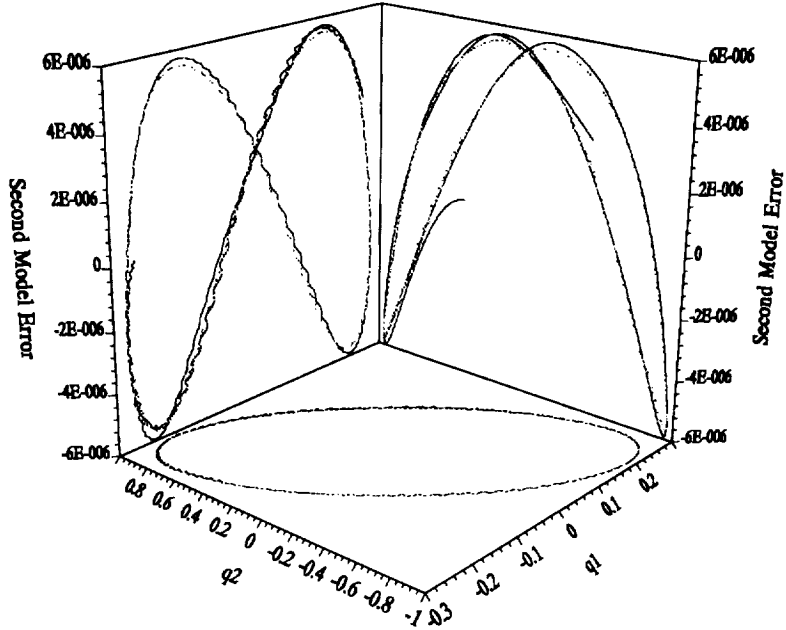


Figure 10 Identified Candidate Function and Second Model Error

Table 1 Example Candidate Functions for the Model Error Histories

Error	Candidate Function	Correlation
d_1	$-2.416 \times 10^{-6} e^{[q_2]^2} e^{[q_4]^4} - 2.120 \times 10^{-3} e^{[L_1]^4} e^{[L_3]^2} + 2.130 \times 10^{-3}$	0.8647
d_2	$-4.581 \times 10^{-6} e^{[q_2]^2} q_2^2 - 9.737 \times 10^{-3} q_1^6 + 5.780 \times 10^{-6}$	0.9963
d_3	$5.250 \times 10^{-4} q_4^2 L_3^2 - 5.163 \times 10^{-5} e^{[L_3]^2} e^{[q_3]^2} + 5.163 \times 10^{-5}$	0.8074

SUMMARY

A technique has been described which leads to algorithms capable of accurate attitude estimation in the presence of significant model error and/or sparse/noisy data. In many satellites, such as SAMPEX, attitude rate measurements are not available either by design or by failure of existing rate gyros. The absence of rate measurements increases the estimation sensitivity to modeling uncertainty and measurement noise in the remaining, relatively sparse attitude measurements. The technique described directly addresses the problem of attitude estimation without rate gyro data.

Results using actual SAMPEX data and corrected models indicate that the technique described in this paper produces accurate estimates for both the spacecraft's position and attitude rate. Also, the formulation described in this paper avoids any difficulties encountered when using quaternions to represent the attitude of the satellite. The new technique may be used directly as an estimator, or, as described in the paper, as a robust method of automatically obtaining accurate dynamic models for existing satellites. Nonlinear candidate functions have been identified with fairly high correlation for SAMPEX. Later studies will utilize more candidate functions in order to obtain unity correlations for all model error trajectories. Therefore, these identified functions can be used to propagate the model accurately in order to determine attitude and rate motion during anomalous conditions.

ACKNOWLEDGMENT

This authors wish to acknowledge the financial support of the Flight Dynamics Division at Goddard Space Flight Center, under a National Aeronautics and Space Administration (NASA) grant #NAG52181. The second author's research was conducted under a National Research Council Associateship. This support is greatly appreciated.

REFERENCES

1. Shuster, M.D., and Oh, S.D., "Three-Axis Attitude Determination from Vector Observations," *AIAA Journal of Guidance, Control and Dynamics*, Vol. 4, No. 1, Jan.-Feb. 1981, pp. 70-77.
2. Wertz, J.S. (ed.), *Spacecraft Attitude Determination and Control*, D. Reidel Publishing Co., Dordrecht, The Netherlands, 1984.
3. Lefferts, E.J., Markley, F.L., and Shuster, M.D., "Kalman Filtering for Spacecraft Attitude Estimation," *AIAA Journal of Guidance, Control and Dynamics*, Vol. 5, No. 5, Sept.-Oct. 1982, pp. 417-429.
4. Harvie, E., Glickman, J., and Tran, K., *Earth Radiation Budget Satellite (ERBS) Inertial Reference Unit (IRU) Performance Analysis*, Computer Sciences Corporation, 553-FDD-91/025R0ud0 (CSC/TM-91/6080R0UD0), February 1992.

5. Challa, M., *Solar, Anomalous, and Magnetospheric Particle Explorer (SAMPEX) Real-Time Sequential Filter (RTSF)*, Evaluation Report, NASA Goddard Space Flight Center, April 1993.
6. Chu, D., and Harvie, E., "Accuracy of the ERBS Definitive Attitude Determination System in the Presence of Propagation Noise," *Proceedings of the Flight Mechanics/Estimation Theory Symposium*, Goddard Space Flight Center, 1990, pp. 97-114.
7. Harvie, E., Chu, D., and Woodard, M., "The Accuracy of Dynamic Attitude Propagation," *Proceedings of the Flight Mechanics/Estimation Theory Symposium*, Goddard Space Flight Center, 1990, pp. 213-232.
8. Chu, D., Glickman, J., and Harvie, E., "Improvements in ERBS Attitude Determination Without Gyros," *Proceedings of the Flight Mechanics/Estimation Theory Symposium*, Goddard Space Flight Center, 1992, pp. 185-200.
9. Mook, D.J., and Junkins, J.L., "Minimum Model Error Estimation for Poorly Modeled Dynamic Systems," *AIAA Journal of Guidance, Control and Dynamics*, Vol. 11, No. 3, pp. 256-261, May-June 1988.
10. Mook, D. J., "Measurement Covariance Constrained Estimation for Poorly Modeled Dynamic Systems," *Proceedings of the AIAA Aerospace Sciences Meeting*, Reno, NV 1986.
11. Mook, D.J., "Optimal Post-Experiment Estimation of Poorly Modeled Dynamic Systems," *Proceedings of the Seventh NASA Flight Mechanics/Estimation Theory Symposium*, pp. 131-152, Goddard Space Flight Center, May 1988.
12. Mook, D.J., "Estimation and Identification of Nonlinear Dynamic Systems," *AIAA Journal*, Vol. 27, No. 7, pp. 968-974, July 1989.
13. Junkins, J.L., and Mook, D.J., *Enhanced Spacecraft Attitude Estimation*, Final Report, Contract #60921-83-G-9-A165, performed for the Naval Surface Weapons Center, Dahlgren, VA, November 1985, 124 pages.
14. Mook, D.J. and Lew, J.H., "A Robust Algorithm for System Realization/Identification," *AAS Journal of the Astronautical Sciences*, Vol. 38, No. 2, pp. 229-243, April-June 1990.
15. Roemer, M.J., and Mook, D.J., "Enhanced Realization/Identification of Physical Modes," *ASCE Journal of Aerospace Engineering*, Vol. 3, No. 2, pp. 122-136, April 1990.
16. Roemer, M.J., and Mook, D.J., "Robust Modal Identification/Estimation of the Minimast Testbed", *AIAA Journal of Guidance, Control, and Dynamics*, Vol. 15, No. 3, pp. 642-647, May-June 1992.
17. Mook, D.J., and Stry, G.I., "An Analog Experimental Study of Nonlinear Identification", *Nonlinear Dynamics*, Vol. 3, No. 1, 1991.
18. Stry, G. I., and Mook, D. J., "An Experimental Study of Nonlinear Dynamic System Identification," *Nonlinear Dynamics*, Vol. 3, pp. 1-11, 1992.
19. McPartland, M.D., and Mook, D.J., "Nonlinear Model Identification of Electrically Stimulated Muscle," *Proceedings of the IFAC Symposium on Modeling and Control in Biomedical Systems*, Galveston, TX, pp. 23-24, March 1994.

A NEW ALGORITHM FOR ATTITUDE-INDEPENDENT MAGNETOMETER CALIBRATION

Roberto Alonso * and Malcolm D. Shuster †

A new algorithm is developed for inflight magnetometer bias determination without knowledge of the attitude. This algorithm combines the fast convergence of an heuristic algorithm currently in use with the correct treatment of the statistics and without discarding data. The algorithm performance is examined using simulated data and compared with previous algorithms.

Introduction

At orbit injection, the only attitude sensor which may be operating is often the vector magnetometer. Frequently, the spacecraft is spinning rapidly, and, if the spacecraft is not in an equatorial orbit or at too high an altitude, it is possible on the basis of this sensor alone to determine the spin rate and the spin-axis attitude of the spacecraft. At the same time, the accuracy of the magnetometer data may be compromised by large systematic magnetic disturbances on the spacecraft, often the result of space charging during launch or from electrical currents within the spacecraft. Thus, some means is usually needed to quickly determine this bias. Since the three-axis attitude of the spacecraft usually cannot be determined at this stage, the desired algorithm must not require a knowledge of the attitude as input.

A number of algorithms have been proposed for estimating the magnetometer bias. The simplest is to solve for the bias vector by minimizing the weighted sum of the squares of residuals which are the differences in the squares of the magnitudes of the measured and modeled magnetic fields [1]. This approach has the disadvantage that the cost function is quartic in the magnetometer bias, and therefore admits multiple minima. If these solutions are close to one another, then convergence of the algorithm may be poor. Typically, one initiates the least-

* Head, Attitude Control Group, Comisión Nacional de Actividades Espaciales, 1425 Buenos Aires, Argentina

† Senior Professional Staff, Space Department, The Johns Hopkins University Applied Physics Laboratory, Laurel, Maryland 20723.

squares procedure by assuming that the initial magnetometer bias vector vanishes, which may lead to slow convergence if the magnetometer bias is large compared to the ambient magnetic field.

Gambhir [1, 2] advocated centering the data to remove the quartic dependence. This leads to a cost function which is quadratic in the bias and, therefore, has a unique solution. The algorithm embodying this centering is called RESIDG (supposedly, "G" for Gambhir) and has been employed with good results for nearly two decades. The centering, however, necessarily discards part of the data, and the effect of this loss of data on the accuracy has never been studied. In addition, RESIDG does not make any attempt to treat the statistics correctly, so that it is not possible to assess the accuracy of the estimation adequately.

A second approach has been put forth by Thompson [3, 4], who preferred to construct a fixed-point algorithm, which he chose to call, with obvious reference, RESIDT. Fixed-point algorithms have the advantage of converging quickly when one is far from the solution, but can become intolerably slow as one approaches the solution. Thompson's algorithm was successfully employed in support of the AMPTE spacecraft.

Davenport [5] has proposed another approach to solving the quartic cost function by finding an approximate solution for the magnetometer bias and using this as an initial value for the iterative solution of the least-squares problem. The approximate solution produced by this algorithm, unfortunately, makes approximations which destroy its consistency. Hence, the approximate solution cannot approach the true solution as the number of data becomes infinite. However, the inconsistency seems to be no worse than about ten per cent for biases as large as one third of the ambient field. Higher accuracy can then be obtained by an iterative procedure, using the approximate estimate as a starting value. This algorithm has been applied to the magnetometers of the Hubble Space Telescope.

The present work proposes a superior solution which: is almost as fast as the centered algorithm of Refs. 1 and 2, without discarding data or ignoring the correlations introduced by centering; does not suffer from the convergence problems of a fixed-point algorithm such as in Ref. 3 and 4; is much more direct than the algorithm of Ref. 5; and is consistent as well at every stage. It does this in several important ways by (1) treating the statistics more completely and correctly, (2) correcting for the centering operation, and (3) estimating scale factors as well as biases. The authors do not call this algorithm either RESIDA or RESIDS.

The Model

All treatments begin with the model

$$\mathbf{B}_k = A_k \mathbf{H}_k + \mathbf{b} + \epsilon_k, \quad k = 1, \dots, N, \quad (1)$$

where \mathbf{B}_k is the measurement of the magnetic field (more exactly, magnetic induction) by the magnetometer at time t_k ; \mathbf{H}_k is the corresponding value of the geomagnetic field with respect to an Earth-fixed coordinate system; A_k is the attitude of the magnetometer with respect to the Earth-fixed coordinates; \mathbf{b} is the magnetometer bias; and ϵ_k is the measurement noise. The measurement noise, which includes both sensor errors and geomagnetic field model uncertainties, is generally assumed to be white and Gaussian. This is probably a poor approximation,

since the errors in the geomagnetic field model are certainly highly correlated, and, in fact, generally dominate the instrument errors. However, for the sake of argument we shall assume here that the errors are white and Gaussian.

To eliminate the dependence on the attitude, we transpose terms in equation (1) and compute the square, so that at each time

$$|\mathbf{H}_k|^2 = |A_k \mathbf{H}_k|^2 = |\mathbf{B}_k - \mathbf{b} - \boldsymbol{\epsilon}_k|^2 \quad (2ab)$$

$$= |\mathbf{B}_k|^2 - 2\mathbf{B}_k \cdot \mathbf{b} + |\mathbf{b}|^2 - 2(\mathbf{B}_k - \mathbf{b}) \cdot \boldsymbol{\epsilon}_k + |\boldsymbol{\epsilon}_k|^2. \quad (2c)$$

If we now define effective measurements and measurement noise according to

$$z_k \equiv |\mathbf{B}_k|^2 - |\mathbf{H}_k|^2, \quad (3a)$$

$$v_k \equiv 2(\mathbf{B}_k - \mathbf{b}) \cdot \boldsymbol{\epsilon}_k - |\boldsymbol{\epsilon}_k|^2, \quad (3b)$$

then we can write

$$z_k = 2\mathbf{B}_k \cdot \mathbf{b} - |\mathbf{b}|^2 + v_k, \quad k = 1, \dots, N. \quad (4)$$

This is the starting point for the derivation of all of the algorithms. (Note that in equations (3b) and (4), \mathbf{B}_k is the value about which the measurement is linearized and therefore must be interpreted as the sample value of the measured magnetic field and not a random variable.)

Even with the assumption that the original measurement noise is white and Gaussian, the effective measurement noise is not white and Gaussian. Assuming that $\boldsymbol{\epsilon}_k$ is white and Gaussian, so that

$$\boldsymbol{\epsilon}_k \sim \mathcal{N}(\mathbf{0}, \Sigma_k), \quad (5)$$

and

$$E\{\boldsymbol{\epsilon}_k \boldsymbol{\epsilon}_\ell^T\} = 0 \quad \text{for } k \neq \ell, \quad (6)$$

then

$$\mu_k \equiv E\{v_k\} = -\text{tr}(\Sigma_k), \quad (7a)$$

$$\sigma_k^2 \equiv E\{v_k^2\} - \mu_k^2 = 4(\mathbf{B}_k - \mathbf{b})^T \Sigma_k (\mathbf{B}_k - \mathbf{b}) + 2 \sum_{i=1}^3 (\Sigma_k)_{ii}^2, \quad (7b)$$

so that v_k must contain both Gaussian and χ^2 components, as is evident from equation (3b). Here $\text{tr}(\cdot)$ denotes the trace operation. In addition,

$$E\{v_k v_\ell\} = \mu_k \mu_\ell, \quad (8)$$

so that the v_k are uncorrelated but not white. If we assume, however, that the noise $\boldsymbol{\epsilon}_k$ is small compared to the geomagnetic field, then to a large degree v_k is Gaussian and we can write approximately

$$v_k \sim \mathcal{N}(\mu_k, \sigma_k^2), \quad (9)$$

keeping only the first term in equation (7b).

Maximum Likelihood Estimate of the Bias and Scoring

Given the statistical model above, the negative-log-likelihood function [6] for the magnetometer bias is given by

$$J(\mathbf{b}) = \frac{1}{2} \sum_{k=1}^N \left[\frac{1}{\sigma_k^2} (z_k - 2 \mathbf{B}_k \cdot \mathbf{b} + |\mathbf{b}|^2 - \mu_k)^2 + \log \sigma_k^2 + \log 2\pi \right], \quad (10)$$

which is quartic in \mathbf{b} . The maximum-likelihood estimate maximizes the likelihood of the estimate, which is the probability density of the measurements (evaluated at their sampled values) given as a function of the magnetometer bias. Hence, it minimizes the negative logarithm of the likelihood (equation (10)), which thus provides a cost function.

Since the domain of \mathbf{b} has no boundaries, the maximum-likelihood estimate for \mathbf{b} , which we denote by \mathbf{b}^* , which minimizes the negative-log-likelihood function, must satisfy

$$\left. \frac{\partial J}{\partial \mathbf{b}} \right|_{\mathbf{b}^*} = \mathbf{0}. \quad (11)$$

Note that only the first of the three terms under the summation depends on the magnetometer bias. Unless one wishes to estimate parameters of the measurement noise, there is no reason to retain the remaining two terms. This quartic dependence can be avoided if complete three-axis attitude information is available, since the bias term then enters linearly into the measurement model (q.v. equation (1)) as in the work of Lerner and Shuster [7].

The most direct solution is obtained by scoring, which in this case is the Newton-Raphson approximation. We consider the sequence¹

$$\mathbf{b}_0^{\text{NR}} = \mathbf{0}, \quad \mathbf{b}_{i+1}^{\text{NR}} = \mathbf{b}_i^{\text{NR}} - \left[\frac{\partial^2 J}{\partial \mathbf{b} \partial \mathbf{b}^T} (\mathbf{b}_i^{\text{NR}}) \right]^{-1} \frac{\partial J}{\partial \mathbf{b}} (\mathbf{b}_i^{\text{NR}}). \quad (12)$$

This series is obtained by expanding $J(\mathbf{b})$ to quadratic order in $(\mathbf{b} - \mathbf{b}_i^{\text{NR}})$, setting the gradient of the truncated series to zero, and solving for \mathbf{b}_{i+1} . If for some value of i we are sufficiently close to the maximum-likelihood estimate, then it will be true that

$$\lim_{i \rightarrow \infty} \mathbf{b}_i^{\text{NR}} \rightarrow \mathbf{b}^*. \quad (13)$$

We have made the convention here that the partial derivative of a scalar function with respect to a column vector is again a column vector. The gradient vector $\partial J / \partial \mathbf{b}$ is the 3×1 matrix

$$\frac{\partial J}{\partial \mathbf{b}} = - \sum_{k=1}^N \frac{1}{\sigma_k^2} (z_k - 2 \mathbf{B}_k \cdot \mathbf{b} + |\mathbf{b}|^2 - \mu_k) 2 (\mathbf{B}_k - \mathbf{b}), \quad (14)$$

and the Hessian matrix $\partial^2 J / \partial \mathbf{b} \partial \mathbf{b}^T$ is given by the 3×3 matrix

$$\frac{\partial^2 J}{\partial \mathbf{b} \partial \mathbf{b}^T} = \sum_{k=1}^N \frac{1}{\sigma_k^2} [4 (\mathbf{B}_k - \mathbf{b})(\mathbf{B}_k - \mathbf{b})^T + 2 (z_k - 2 \mathbf{B}_k \cdot \mathbf{b} + |\mathbf{b}|^2 - \mu_k) I_{3 \times 3}]. \quad (15)$$

¹ Throughout this work we shall use k as the time index and i as the iteration index.

Generally, the second term in the brackets will be much smaller than the first and can be discarded.

A second approach to scoring is the Gauss–Newton approximation [8]. In this case, we replace the Hessian matrix by its expectation, the Fisher information matrix F . Since

$$E\{(z_k + 2 \mathbf{B}_k \cdot \mathbf{b} + |\mathbf{b}|^2 - \mu_k)\} = 0, \quad (16)$$

this amounts to discarding the second term. According to the law of large numbers, as the number of independent identically distributed (i.i.d.) samples of a random variable becomes infinite (the asymptotic limit), the average of these samples approaches the expectation value of the random variable. Our measurements are not identically distributed because of the dependence on \mathbf{B}_k . However, if the distribution of the values of $A_k \mathbf{H}_k$ is regularly repeated, then we may regard the measurements as being i.i.d. for each value of $A_k \mathbf{H}_k$. Except for the replacement of the Hessian matrix in equations (12) by the Fisher information matrix, the iteration proceeds as before.

For both the Newton–Raphson and the Gauss–Newton method, the estimate error covariance matrix is given in the limit of infinitely large data samples by

$$P_{bb} \rightarrow F_{bb}^{-1} = \left[\sum_{k=1}^N \frac{1}{\sigma_k^2} 4 (\mathbf{B}_k - \mathbf{b})(\mathbf{B}_k - \mathbf{b})^T \right]^{-1}. \quad (17)$$

If the measurement noise is Gaussian, then the asymptotic limit is true, in fact, for finite data samples. In most cases, the Fisher information matrix is simpler to evaluate than the Hessian matrix of the negative-log-likelihood function, and often can be evaluated independently of the data.

The earliest estimates of the magnetometer bias were accomplished by the method culminating in equations (12) though usually the weights were not chosen according to a statistical criterion.

The Centered Estimate

In order to avoid the minimization of a quartic cost function, let us define the following weighted averages

$$\bar{z} \equiv \bar{\sigma}^2 \sum_{k=1}^N \frac{1}{\sigma_k^2} z_k, \quad \bar{\mathbf{B}} \equiv \bar{\sigma}^2 \sum_{k=1}^N \frac{1}{\sigma_k^2} \mathbf{B}_k, \quad \bar{v} \equiv \bar{\sigma}^2 \sum_{k=1}^N \frac{1}{\sigma_k^2} v_k, \quad \bar{\mu} \equiv \bar{\sigma}^2 \sum_{k=1}^N \frac{1}{\sigma_k^2} \mu_k, \quad (18)$$

where

$$\frac{1}{\bar{\sigma}^2} \equiv \sum_{k=1}^N \frac{1}{\sigma_k^2}. \quad (19)$$

This is similar to the centering approximation of Gambhir [1, 2], who, however, did not determine the weights from any statistical quantities. It follows that

$$\bar{z} = 2 \bar{\mathbf{B}} \cdot \mathbf{b} - |\mathbf{b}|^2 + \bar{v}. \quad (20)$$

If we define now

$$\tilde{z}_k \equiv z_k - \bar{z}, \quad \tilde{\mathbf{B}}_k \equiv \mathbf{B}_k - \bar{\mathbf{B}}, \quad \tilde{v}_k \equiv v_k - \bar{v}, \quad \tilde{\mu}_k \equiv \mu_k - \bar{\mu}, \quad (21)$$

then subtracting equation (20) from equation (4) leads to

$$\tilde{z}_k = 2 \tilde{\mathbf{B}}_k \cdot \mathbf{b} + \tilde{v}_k, \quad k = 1, \dots, N. \quad (22)$$

This operation is called *centering*.

The centered measurement is no longer quadratic in the magnetometer bias vector. However, the centered measurement noise is no longer uncorrelated. Thus, one can no longer write the negative-log-likelihood function in the form of equation (10). Nonetheless, in practice one has ignored this and determined the bias from a cost function of the form²

$$J^{\text{approx}}(\mathbf{b}) = \frac{1}{2} \sum_{k=1}^{N-1} \frac{1}{\sigma_k^2} (\tilde{z}_k - 2 \tilde{\mathbf{B}}_k \cdot \mathbf{b} - \tilde{\mu}_k)^2, \quad (23)$$

and achieved reasonable results in spite of the lack of consistency, arguing that one was only discarding a single measurement out of many. We shall see below that one can discard much more than $1/N$ of the accuracy by this operation, but we shall see also that equation (23) is closer to being correct than one might have imagined. Note that the sum is from 1 to $N - 1$, since the centered measurements are not independent.

$$\sum_{k=1}^N \tilde{z}_k = 0. \quad (24)$$

Minimizing $J^{\text{approx}}(\mathbf{b})$ over \mathbf{b} leads to

$$\mathbf{b}^{\text{approx}} = P_{bb}^{\text{approx}} \sum_{k=1}^{N-1} \frac{1}{\sigma_k^2} (\tilde{z}_k - \tilde{\mu}_k) 2 \tilde{\mathbf{B}}_k, \quad (25)$$

with the estimate error covariance matrix given approximately by

$$P_{bb}^{\text{approx}} \approx (F_{bb}^{\text{approx}})^{-1} = \left[\sum_{k=1}^{N-1} \frac{1}{\sigma_k^2} 4 \tilde{\mathbf{B}}_k \tilde{\mathbf{B}}_k^T \right]^{-1} \quad (26)$$

Note that $\tilde{\mu}_k$ will vanish if the original measurement noise ϵ_k , $k = 1, \dots, N$, is identically distributed. The centered estimator converges in a single iteration because the cost function is exactly quadratic.

²In actual fact, these calculations have almost always assumed a constant weighting and neglected the contribution of μ_k .

Fixed-Point Method

To avoid the loss of data from centering, Thompson, Neal and Shuster [3, 4] proposed a fixed-point algorithm. Define the quantities

$$G \equiv \sum_{k=1}^N \frac{1}{\sigma_k^2} [4 \mathbf{B}_k \mathbf{B}_k^T + 2(z_k - \mu_k) I_{3 \times 3}] , \quad (27a)$$

$$\mathbf{a} \equiv \sum_{k=1}^N \frac{1}{\sigma_k^2} (z_k - \mu_k) 2\mathbf{B}_k , \quad (27b)$$

$$\mathbf{f}(\mathbf{b}) \equiv \sum_{k=1}^N \frac{1}{\sigma_k^2} [4(\mathbf{B}_k \cdot \mathbf{b})\mathbf{b} + 2|\mathbf{b}|^2(\mathbf{B}_k - \mathbf{b})] . \quad (27c)$$

Then the gradient of the negative-log-likelihood function becomes

$$\frac{\partial J(\mathbf{b})}{\partial \mathbf{b}} = G \mathbf{b} - \mathbf{a} - \mathbf{f}(\mathbf{b}) = 0 . \quad (28)$$

which can be solved implicitly to yield

$$\mathbf{b}^* = G^{-1} [\mathbf{a} + \mathbf{f}(\mathbf{b}^*)] . \quad (29)$$

This equation must be solved iteratively,

$$\mathbf{b}_0^{\text{FP}} = \mathbf{0} , \quad \mathbf{b}_{i+1}^{\text{FP}} = G^{-1} [\mathbf{a} + \mathbf{f}(\mathbf{b}_i^{\text{FP}})] , \quad (30)$$

and we expect that once \mathbf{b}_i^{FP} is sufficiently close to the solution that

$$\lim_{i \rightarrow \infty} \mathbf{b}_i^{\text{FP}} = \mathbf{b}^* . \quad (31)$$

Davenport's Approximation

Davenport and his collaborators [5] have offered an approximate form for the bias vector estimator. He begins by writing an approximate cost function as

$$J_D(\mathbf{b}) = \frac{1}{2} \sum_{k=1}^N \frac{1}{\sigma_k^2} (z_k - 2\mathbf{B}_k \cdot \mathbf{b} + \lambda^2 - \mu_k)^2 , \quad (32)$$

where λ is a constant. This cost function would agree with that of equation (10) when $\lambda = |\mathbf{b}|$. Davenport, however, allows λ to be a free parameter.

The cost function of equation (32) is only quadratic in \mathbf{b} . Differentiating this cost function with respect to \mathbf{b} and setting the gradient equal to zero leads to a solution of the form

$$\mathbf{b}_D^* = \mathbf{f}_D(\lambda), \quad (33)$$

that is, the estimate of the bias is a function of the parameter λ . The “consistent” value of this parameter is obtained by solving

$$|\mathbf{f}_D(\lambda)|^2 = \lambda^2. \quad (34)$$

Because Davenport’s algorithm effectively changes the dependence of the non-random part of the measurement on the bias even in the absence of noise, it cannot be consistent. Thus, as more data is accumulated the accuracy will not improve. However, it can be used as the starting point for a Newton-Raphson or Gauss-Newton iteration of the quartic cost function.

A Statistically Correct Centered Algorithm

The original data, z_k , $k = 1, \dots, N$, may be replaced by the centered data, \tilde{z}_k , $k = 1, \dots, N - 1$, and the center value \bar{z} . The measurement equations are given by equations (20) and (22). The centered data have the advantage of depending only linearly on the magnetometer bias. However, they have the disadvantage that the centered measurement noise is correlated. Therefore, the cost function for the centered data alone cannot be written as the sum of $N - 1$ squares. To write a statistically correct cost function for the centered data (making the approximation that the measurement noise v_k is Gaussian) we define

$$\tilde{\mathbf{Z}} \equiv [\tilde{z}_1, \tilde{z}_2, \dots, \tilde{z}_{N-1}]^T, \quad \tilde{\mathbf{B}} \equiv [\tilde{\mathbf{B}}_1, \tilde{\mathbf{B}}_2, \dots, \tilde{\mathbf{B}}_{N-1}]^T, \quad (35ab)$$

$$\tilde{\mathbf{M}} \equiv [\tilde{\mu}_1, \tilde{\mu}_2, \dots, \tilde{\mu}_{N-1}]^T, \quad \tilde{\mathbf{V}} \equiv [\tilde{v}_1, \tilde{v}_2, \dots, \tilde{v}_{N-1}]^T, \quad (35cd)$$

and write formally

$$\tilde{\mathbf{Z}} = 2\tilde{\mathbf{B}}\mathbf{b} + \tilde{\mathbf{V}}, \quad (36)$$

with

$$\tilde{\mathbf{V}} \sim \mathcal{N}(\tilde{\mathbf{M}}, \tilde{\mathcal{R}}). \quad (37)$$

Here $\tilde{\mathcal{R}}$ is the covariance matrix of $\tilde{\mathbf{V}}$. (Note that $\tilde{\mathbf{B}}$ is an $(N - 1) \times 3$ matrix.)

The negative-log-likelihood function for this stacked centered measurement is simply

$$\tilde{J}(\mathbf{b}) = \frac{1}{2} \left[(\tilde{\mathbf{Z}} - 2\tilde{\mathbf{B}}\mathbf{b} - \tilde{\mathbf{M}})^T \tilde{\mathcal{R}}^{-1} (\tilde{\mathbf{Z}} - 2\tilde{\mathbf{B}}\mathbf{b} - \tilde{\mathbf{M}}) + \log \det \tilde{\mathcal{R}} + (N - 1) \log 2\pi \right]. \quad (38)$$

Equation (23) made the assumption that $\tilde{\mathcal{R}}$ was diagonal. We do not make this approximation here. Minimizing this negative-log-likelihood function leads directly to

$$\tilde{\mathbf{b}}^* = \left(4\tilde{\mathbf{B}}^T \tilde{\mathcal{R}}^{-1} \tilde{\mathbf{B}} \right)^{-1} 2\tilde{\mathbf{B}}^T \tilde{\mathcal{R}}^{-1} (\tilde{\mathbf{Z}} - \tilde{\mathbf{M}}), \quad (39)$$

with estimate error covariance matrix

$$\tilde{P}_{bb} = \left(4 \tilde{\mathbf{B}}^T \tilde{\mathcal{R}}^{-1} \tilde{\mathbf{B}} \right)^{-1}. \quad (40)$$

For large quantities of data, the naive evaluation of equations (39) and (36) can be a formidable task. Therefore, we seek the means of inverting the matrix in equation (38) explicitly. Clearly,

$$\tilde{\mathcal{R}}_{k\ell} = E\{(\tilde{v}_k - \tilde{\mu}_k)(\tilde{v}_\ell - \tilde{\mu}_\ell)\} = \sigma_k^2 \delta_{k\ell} - \bar{\sigma}^2, \quad (41)$$

which shows the correlation explicitly. However, this matrix has the simple inverse

$$\left(\tilde{\mathcal{R}}^{-1} \right)_{k\ell} = \frac{1}{\sigma_k^2} \delta_{k\ell} + \frac{\sigma_N^2}{\sigma_k^2 \sigma_\ell^2}, \quad (42)$$

where σ_N^2 is the variance of v_N . Substituting this expression into equation (38) leads to

$$\tilde{J}(\mathbf{b}) = \frac{1}{2} \sum_{k=1}^N \frac{1}{\sigma_k^2} (\tilde{z}_k - 2\tilde{\mathbf{B}}_k \cdot \mathbf{b} - \tilde{\mu}_k)^2 + \text{terms independent of } \mathbf{b}. \quad (43)$$

The statistically correct cost function for the centered data looks exactly like the naive expression of equation (23) except that the summation is now from 1 to N . The minimization is simple and leads directly to

$$\tilde{\mathbf{b}}^* = \tilde{P}_{bb} \sum_{k=1}^N \frac{1}{\sigma_k^2} (\tilde{z}_k - \tilde{\mu}_k) 2\tilde{\mathbf{B}}_k, \quad (44)$$

and the estimate error covariance of the centered estimate is given by

$$\tilde{P}_{bb} = \tilde{F}_{bb}^{-1} = \left[\sum_{k=1}^N \frac{1}{\sigma_k^2} 4 \tilde{\mathbf{B}}_k \tilde{\mathbf{B}}_k^T \right]^{-1}. \quad (45)$$

The centered estimate is seen now to be much more attractive than before. It is simple, and by a very trivial alteration (replacing the sum from 1 to $N - 1$ by a sum from 1 to N) it can be made to treat the statistics of the measurement noise correctly. It is very different in character from that the centered estimate of Gambhir [1,2]. It is thus to be preferred to Thompson's algorithm [3,4], whose convergence can be problematic, and to Davenport's approximation [5], which is not consistent. The greatest drawback to the centered algorithm lies in the exclusion of certain data, the effect of which we now investigate.

The Complete Solution

For N large, the naive centered algorithm presented earlier is hardly worse than the rigorously centered algorithm derived above. From the standpoint of computation burden, the

more rigorous treatment of the statistics has merely added one more term (out of N) to the summation. However, equation (45), because it has been derived rigorously, will afford us the possibility of computing the correction from the discarded measurement \bar{z} .

Instead of the measurement set $\bar{z}_k, k = 1, \dots, N - 1, \bar{z}$, we may now consider the measurements to be effectively $\tilde{\mathbf{b}}^*$ and \bar{z} . Therefore, to determine the exact maximum likelihood estimate \mathbf{b}^* , we must develop the statistics of these two effective measurements more completely.

Let us substitute equation (22) into equation (44). This leads to

$$\tilde{\mathbf{b}}^* = \tilde{P}_{bb} \sum_{k=1}^N \frac{1}{\sigma_k^2} (2\tilde{\mathbf{B}}_k \cdot \mathbf{b} + \tilde{v}_k - \tilde{\mu}_k) 2\tilde{\mathbf{B}}_k, \quad (46)$$

which we may rewrite as

$$\tilde{\mathbf{b}}^* = \mathbf{b} + \tilde{P}_{bb} \sum_{k=1}^N \frac{1}{\sigma_k^2} 2\tilde{\mathbf{B}}_k (\tilde{v}_k - \tilde{\mu}_k) \quad (47a)$$

$$= \mathbf{b} + \tilde{\mathbf{v}}_b. \quad (47b)$$

The last term is just the (zero-mean) estimate error. Obviously,

$$\tilde{\mathbf{v}}_b \sim \mathcal{N}(\mathbf{0}, \tilde{P}_{bb}). \quad (48)$$

It follows that we can write

$$\tilde{J}(\mathbf{b}) = \frac{1}{2} (\mathbf{b} - \tilde{\mathbf{b}}^*)^T \tilde{P}_{bb}^{-1} (\mathbf{b} - \tilde{\mathbf{b}}^*) + \text{terms independent of } \mathbf{b}, \quad (49)$$

which can be verified by expanding equation (43) and completing the square in \mathbf{b} . The estimate $\tilde{\mathbf{b}}^*$ is thus a sufficient statistic for \mathbf{b} [6]. Equation (49) is very useful, because it allows us to investigate the effect of corrections to the centered formula using only our knowledge of $\tilde{\mathbf{b}}^*$ and \tilde{P} . We do not have to refer again to the N centered measurements $\bar{z}_k, k = 1, \dots, N$.

We must now combine $\tilde{\mathbf{b}}^*$ and \bar{z} to obtain a complete representation of our data for the computation of \mathbf{b} . Recall equation (20),

$$\bar{z} = 2\bar{\mathbf{B}} \cdot \mathbf{b} - |\mathbf{b}|^2 + \bar{v}, \quad (20)$$

with

$$\bar{v} \sim \mathcal{N}(\bar{\mu}, \bar{\sigma}^2). \quad (50)$$

Note that \bar{z} , which, unfortunately, is a nonlinear function of \mathbf{b} , is nonetheless an extremely accurate measurement, more accurate than the other measurements by typically a factor of $1/\sqrt{N}$, because $\bar{\sigma}$ is smaller typically than the other variances by this factor. Thus, simply centering the data can entail a significant loss of accuracy if $\bar{\mathbf{B}} - \mathbf{b}$ is not significantly smaller than typical values of \mathbf{B}_k .

What is the correlation between $\tilde{\mathbf{v}}_b$ and \bar{v} ? Calculating this explicitly, gives

$$E\{\tilde{\mathbf{v}}_b(\bar{v} - \bar{\mu})\} = \tilde{P} \sum_{k=1}^N \frac{1}{\sigma_k^2} \tilde{\mathbf{B}}_k E\{(\tilde{v}_k - \tilde{\mu}_k)(\bar{v} - \bar{\mu})\} \quad (51a)$$

$$= \tilde{P} \sum_{k=1}^N \frac{1}{\sigma_k^2} \tilde{\mathbf{B}}_k \bar{\sigma}^2 = \mathbf{0}, \quad (51bc)$$

and we have used equation (21). Thus, $\tilde{\mathbf{v}}_b$ and \bar{v} are uncorrelated. It follows, that the negative-log-likelihood functions add and

$$J(\mathbf{b}) = \tilde{J}(\mathbf{b}) + \bar{J}(\mathbf{b}), \quad (52)$$

with $\tilde{J}(\mathbf{b})$ given by equation (49) and

$$\bar{J}(\mathbf{b}) = \frac{1}{2} \left[\frac{1}{\bar{\sigma}^2} (\bar{z} - 2\bar{\mathbf{B}} \cdot \mathbf{b} + |\mathbf{b}|^2 - \bar{\mu})^2 + \log \bar{\sigma}^2 + \log 2\pi \right] \quad (53)$$

The weight associated with the center term $\bar{J}(\mathbf{b})$ is equal to the sum of all the weights of $\tilde{J}(\mathbf{b})$. Thus, when $\bar{\mathbf{B}}$ is not small, the loss of accuracy from discarding the center time can be substantial. We can determine the relative importance of these terms to the estimate accuracy by computing the Fisher information matrix F_{bb} to obtain

$$F_{bb} = \tilde{P}_{bb}^{-1} + \frac{4}{\bar{\sigma}^2} (\bar{\mathbf{B}} - \mathbf{b})(\bar{\mathbf{B}} - \mathbf{b})^T = P_{bb}^{-1}. \quad (54)$$

The estimate error covariance matrix will be the inverse of this quantity. If the distribution of the magnetometer measurements is "isotropic," that is, if $\bar{\mathbf{B}} - \mathbf{b}$ vanishes, then $\bar{J}(\mathbf{b})$ will be insensitive to \mathbf{b} . It is in this case that the centering approximation obviously leads to the best results. If, however, one attempts to determine the magnetometer bias from a short data span, say, from an inertially stabilized or Earth-pointing spacecraft, then $\bar{\mathbf{B}} - \mathbf{b}$ will be equal to the similar expression for a typical value of the magnetic field, and the formerly discarded center term which will provide half of the accuracy, especially for the component along $\bar{\mathbf{B}} - \mathbf{b}$.

Thus, our new algorithm is as follows:

- We compute the centered estimate $\tilde{\mathbf{b}}^*$ of the magnetometer bias and the covariance matrix \tilde{P}_{bb} using the centered data and equations (44) and (45).
- Using the centered estimate $\tilde{\mathbf{b}}^*$ as an initial estimate, the correction due to the center term is computed using the Gauss-Newton method

$$\mathbf{b}_{i+1} = \mathbf{b}_i - F_{bb}^{-1}(\mathbf{b}_i) \mathbf{g}(\mathbf{b}_i), \quad (55)$$

where the Fisher information matrix $F_{bb}(\mathbf{b})$ is given by equation (54), and the gradient vector is given by the sum of the gradients of equations (49) and (53)

$$\mathbf{g}(\mathbf{b}) = \tilde{P}_{bb}^{-1} (\mathbf{b} - \tilde{\mathbf{b}}^*) - \frac{1}{\bar{\sigma}^2} (\bar{z} - 2\bar{\mathbf{B}} \cdot \mathbf{b} + |\mathbf{b}|^2 - \bar{\mu}) 2(\bar{\mathbf{B}} - \mathbf{b}). \quad (56)$$

- The iteration is continued until

$$\eta_i \equiv (\mathbf{b}_i - \mathbf{b}_{i-1})^T F_{bb}(\mathbf{b}_{i-1}) (\mathbf{b}_i - \mathbf{b}_{i-1}) \quad (57)$$

is less than some predetermined small quantity.

Numerical Examples

The algorithms treated in this work have been examined for an inertially stabilized spacecraft. The spacecraft orbit has been chosen to be circular with an altitude of 560 km and an inclination of 38 deg. This is, in fact, the orbit of the SAC-B spacecraft (Satelites de Aplicaciones Científicas), the first spacecraft to be developed by Argentina, which will be inertially stabilized to observe the Sun. The geomagnetic field in our studies has been simulated using the International Geomagnetic Reference Field (IGRF (1985)) [9], which has been extrapolated to 1994. More recent field models are available, but IGRF (1985) is adequate for our simulation needs.

For purposes of simulation we have assumed an effective white Gaussian magnetometer measurement error with a standard deviation per axis of 2.0 mG, corresponding to an angular error of approximately 0.5 deg at the equator. We have assumed that no axis of the magnetometer is predominantly parallel to the spacecraft spin axis or the geomagnetic field. The data were sampled once every ten seconds.

We examine first Davenport's approximation. To highlight the inconsistency of this method, we examine its behavior and that of the centered estimate for noise-free data. The results for half an orbit of data for the spinning spacecraft are shown in Table 1. The equivalent results for noisy data are presented in Table 2.

For small values of the magnetometer bias, Davenport's approximation yields acceptable results. For values of the magnetometer bias comparable to or greater than the magnitude of the ambient magnetic field, the errors in Davenport's approximation become unacceptably large. These statements hold both for the noise-free and the noisy data.

We can gain a greater appreciation of the behavior of these two algorithms if we examine the normalized errors, $\tilde{\eta}$ and η_D defined by

Table 1. Comparison of Davenport's Approximation and Centered Estimate for Noise-Free Data

Model Bias (mG)	Centered Estimate	Davenport's Approximation
[10., 20., 30.]	[10., 20., 30.]	[10., 20., 30.]
[30., 60., 90.]	[30., 60., 90.]	[30., 50., 90.]
[60., 129., 180.]	[60., 129., 180.]	[60., 129., 180.]
[100., 200., 300.]	[100., 200., 300.]	[101., 208., 261.]
[200., 400., 600.]	[200., 400., 600.]	[180., 539., 161.]

Table 2. Comparison of Davenport's Approximation and Centered Estimate for Noisy Data

Model Bias (mG)	Centered Estimate	Davenport's Approximation
[10., 20., 30.]	[9.88 ± 0.35, 20.47 ± 0.82, 27.77 ± 2.44]	[10.27, 19.88, 29.70]
[30., 60., 90.]	[29.69 ± 0.30, 60.52 ± 0.69, 89.95 ± 2.03]	[29.66, 60.60, 89.66]
[60., 129., 180.]	[59.47 ± 0.25, 130.98 ± 0.65, 174.54 ± 1.58]	[54.88, 129.28, 179.75]
[100., 200., 300.]	[100.33 ± 0.22, 201.13 ± 0.56, 296.78 ± 1.60]	[101.94, 214.30, 230.13]
[200., 400., 600.]	[199.82 ± 0.37, 400.76 ± 6.34, 598.28 ± 3.44]	[178.92, 538.68, 160.33]

$$\eta \equiv \frac{1}{\sqrt{6}} \left[(\mathbf{b}^{\text{true}} - \mathbf{b}^*)^T \tilde{P}_{bb}^{-1} (\mathbf{b}^{\text{true}} - \mathbf{b}) - 3 \right], \quad (58)$$

which should have mean zero and standard deviation unity. A comparison of these quantities is given in Table 3. The inconsistency of Davenport's algorithm is evident.

To see the advantages of this algorithm over naive quartic scoring consider the estimation of a magnetometer bias whose true value is (10., 20., 30.) mG. The results of successive iterations for naive quartic scoring and the new algorithm are shown in Table 4. For the new algorithm, the first algorithm is the statistically correct centered algorithm and successive iterations are obtained by applying the Gauss-Newton method to the complete cost function as given by equation (53). The 1σ error brackets, computed from the Fisher information matrix, are ($\pm 0.13, \pm 0.19, \pm 0.12$) mG. The results of the two methods are nearly identical in this case and the convergence is equally rapid. Small differences in the results are due to the slightly different treatment of the roundoff errors.

Consider now the case where the magnetometer bias vector is large compared with the ambient field, say (100., 200., 300.) mG. In this case we obtain the value presented in Table 5. The 1σ error brackets here are found to be ($\pm 0.12, \pm 0.10, \pm 0.12$) mG.

In this case naive quartic scoring does not even converge to the correct answer, nor does the method of Thompson, Neal and Shuster [3, 4], which does not converge at all. Naive quartic scoring converges, in fact, to a local minimum. The new algorithm, on the other hand, works

Table 3. Comparison of Normalized Errors for Davenport's Approximation and the Centered Estimate for Noisy Data

Model Bias (mG)	$\tilde{\eta}$	η_D
[10., 20., 30.]	0.82	-1.18
[30., 60., 90.]	0.68	3.87
[60., 129., 180.]	0.814	0.81
[100., 200., 300.]	2.66	2.86×10^3
[200., 400., 600.]	-0.83	0.65×10^3

Table 4. Comparison of Naive Quartic Scoring and the New Algorithm. The true value of the magnetometer bias vector is (10., 20., 30.) mG.

Iteration	Naive Quartic Scoring	New Algorithm
1	[10.08, 19.27, 33.04]	[9.82, 20.08, 29.05]
2	[9.84, 20.18, 29.91]	[9.90, 19.83, 29.94]
3	[9.84, 20.19, 29.89]	[9.90, 19.83, 29.93]
4	[9.84, 20.19, 29.89]	[9.90, 19.83, 29.93]

very well. Note that a single iteration of the center correction is sufficient. The errors for the new algorithm are clearly consistent with the computed confidence intervals.

Discussion

The new algorithm for attitude-independent magnetometer bias determination produces excellent results in all situations. Since it begins with a very good initial estimate for the bias, it is more likely to converge to the correct minimum than does naive scoring [1] or the fixed-point method of Thompson *et al.* [3,4], which begin at $\mathbf{b} = \mathbf{0}$. Unlike the centered algorithm of RESIDG fame [2], it does not discard data and does the centering in a statistically correct way, apart from the approximation that the measurement errors on the attitude-independent derived measurement are Gaussian and uncorrelated, which is almost certainly not the case. It is amusing to speculate that the statistically correctly centered cost function of equation (43) would probably be rejected as statistically incorrect by heuristic algorithm developers unschooled in Statistics, because it appears to use redundant data. Its initial centered estimate for the magnetometer bias is clearly a better approximation than ignoring the quadratic behavior of $|\mathbf{b}|^2$ as in the work of Davenport *et al.* [5]. The new algorithm is certainly more sophisticated statistically than its predecessors, and more efficient computationally. Perhaps, most importantly, the new algorithm makes manifest the physical quantities which

Table 5. Comparison of Naive Quartic Scoring and the New Algorithm. The true value of the magnetometer bias vector is (100., 200., 300.) mG.

Iteration	Naive Quartic Scoring	New Algorithm
1	[107.62, 259.77, 2.85]	[99.82, 200.63, 298.02]
2	[51.51, 398.62, -368.88]	[99.97, 200.11, 299.81]
3	[70.35, 358.17, -196.33]	[99.97, 200.11, 299.81]
4	[72.13, 340.88, -145.65]	...
5	[71.78, 338.71, -140.60]	...
6	[71.70, 338.64, -140.62]	...
7	[71.70, 338.64, -140.62]	...

determine the behavior of the bias estimator. It is also understandable.

Acknowledgments

The authors are grateful to F. Landis Markley for interesting discussions and helpful criticisms. R. Alonso is grateful to the Guidance and Control Branch of NASA Goddard Space Flight Center (GSFC), NASA, for their hospitality during which this work was carried out. He is thankful also to the Comisión Nacional de Actividades Espaciales (CONAE) and the Consejo Nacional de Investigaciones Científicas y Técnicas (CONICET) for their financial support during this period.

References

- [1] GAMBHIR, B. "Determination of Magnetometer Biases Using Module RESIDG," Computer Sciences Corporation, Report No. 3000-32700-01TN, March 1975.
- [2] LERNER, G. M. "Scalar Checking," in Wertz, J. R. (editor) *Spacecraft Attitude Determination and Control*, Kluwer Academic, Dordrecht, 1978, pp. 328-334.
- [3] THOMPSON, R. H., NEAL, G. N., and SHUSTER, M. D. "Spin-Axis Attitude Estimation and Magnetometer Bias Determination for the AMPTE Mission," *Proceedings, Flight Mechanics/Estimation Theory Symposium*, NASA Goddard Space Flight Center, Greenbelt, Maryland, October 1981.
- [4] THOMPSON, R. H., NEAL, G. N., and SHUSTER, M. D. "Magnetometer Bias Determination and Spin-Axis Attitude Estimation for the AMPTE Mission," *Journal of Guidance Control and Dynamics*, Vol. 7, No. 4, 1984, pp. 505-507.
- [5] DAVENPORT, P. B., RUMPL, W. M., and WELTER, G. L. "In-Flight Determination of Spacecraft Magnetic Bias Independent of Attitude," *Proceedings, Flight Mechanics/Estimation Theory Symposium*, NASA Goddard Space Flight Center, Greenbelt, Maryland, May 10-11, 1988, pp. 326-343.
- [6] SORENSON, H. W. *Parameter Estimation*, Marcel Dekker, New York, 1980.
- [7] LERNER, G. M., and SHUSTER, M. D. "Inflight Magnetometer Calibration and Attitude Determination for Near-Earth Spacecraft," *Journal of Guidance and Control*, Vol. 4, No. 5, 1981, pp. 518-522.
- [8] GUPTA, N. K., and MEHRA, R. K. "Computational Aspects of Maximum Likelihood Estimation and Reduction in Sensitivity Function Calculations," *IEEE Transactions on Automatic Control*, Vol. AC-19, No. 6, 1974, pp. 774-783.
- [9] LANGEL, R. A. "The Main Field," in J. A. JACOBS (editor), *Geomagnetism*, Academic Press, New York, 1987, pp. 348-349.

A Simple Suboptimal Least-Squares Algorithm for Attitude Determination with Multiple Sensors

Thomas F. Brozenec and Douglas J. Bender

ABSTRACT

Three-axis attitude determination is equivalent to finding a coordinate transformation matrix which transforms a set of reference vectors fixed in inertial space to a set of measurement vectors fixed in the spacecraft. The attitude determination problem can be expressed as a constrained optimization problem. The constraint is that a coordinate transformation matrix must be proper, real, and orthogonal. A transformation matrix can be thought of as optimal in the least-squares sense if it maps the measurement vectors to the reference vectors with minimal 2-norm errors and meets the above constraint. This constrained optimization problem is known as Wahba's problem. Several algorithms which solve Wahba's problem exactly have been developed and used. These algorithms, while steadily improving, are all rather complicated. Furthermore, they involve such numerically unstable or sensitive operations as matrix determinant, matrix adjoint, and Newton-Raphson iterations.

This paper describes an algorithm which minimizes Wahba's loss function, but without the constraint. When the constraint is ignored, the problem can be solved by a straightforward, numerically stable least-squares algorithm such as QR decomposition. Even though the algorithm does not explicitly take the constraint into account, it still yields a nearly orthogonal matrix for most practical cases; orthogonality only becomes corrupted when the sensor measurements are very noisy, on the same order of magnitude as the attitude rotations. The algorithm can be simplified if the attitude rotations are small enough so that the approximation $\sin\theta \approx \theta$ holds.

We then compare the computational requirements for several well-known algorithms. For the general large-angle case, the QR least-squares algorithm is competitive with all other known algorithms and faster than most. If attitude rotations are small, the least-squares algorithm can be modified to run faster, and this modified algorithm is faster than all but a similarly specialized version of the QUEST algorithm.

We also introduce a novel measurement averaging technique which reduces the n -measurement case to the two measurement case for our particular application, a star tracker and earth sensor mounted on an earth-pointed geosynchronous communications satellite. Using this technique, many n -measurement problems to reduce to ≤ 3 measurements; this reduces the amount of required calculation without significant degradation in accuracy.

Finally, we present the results of some tests which compare the least-squares algorithm with the QUEST and FOAM algorithms in the two-measurement case. For our example case, all three algorithms performed with similar accuracy.

The authors are with Hughes Aircraft Company, Bldg E1, MS D110, POB 92919, Los Angeles, CA 90009

1. INTRODUCTION

This paper discusses a new sub-optimal algorithm for attitude determination. It also introduces a novel measurement averaging technique which effectively reduces the number of vector measurements that must be processed by any attitude determination algorithm. It is organized as follows: first a brief statement of the attitude determination problem is given, followed by a formal statement of Wahba's attitude determination problem. In Section 2, we introduce a new suboptimal least-squares algorithm which minimizes Wahba's loss function, but without the orthogonality constraint on the attitude matrix solution. In Section 3 the computational requirements for the new algorithm are presented and compared with several other attitude solutions (optimal & suboptimal). Section 4 discusses a technique for reducing the number of vector measurements. Finally, Section 5 presents simulation results for a specific example of a geosynchronous communications satellite with a star tracker and an earth sensor. We end with a brief conclusion.

Attitude Determination Problem Statement

Consider a set of reference vectors r_i , $i = 1, \dots, n$ expressed in an inertially defined coordinate system I . Consider the same set of vectors, but denoted s_i , $i = 1, \dots, n$ when expressed in a spacecraft body defined coordinate system B . These vectors are related by the attitude (or direction cosine) matrix A , i.e.

$$s_i = Ar_i \quad i = 1, \dots, n \quad (1)$$

In one application, for example, the measurement vectors s_i would be provided by earth sensor and star tracker measurements (corrupted by error sources such as noise and biases) while the reference vectors r_i would correspond to known directions of the stars and earth nadir expressed in I .

The vectors s_i and r_i (for $i = 1, \dots, n$) can be concatenated to form the columns of matrices

$$S = [s_1 | s_2 | \dots | s_n] \quad R = [r_1 | r_2 | \dots | r_n]. \quad (2)$$

Then (1) can be written as one matrix equation

$$S = AR \quad (3)$$

where S and R are $3 \times n$ matrices and A is a 3×3 proper real orthogonal matrix [1], i.e.

$$A^T = A^{-1} \quad \& \quad \det(A) = 1 \quad (4)$$

Since A satisfies the properties of (4), it represents a rotation transformation which preserves the lengths of vectors and the angles between them.

The problem is to find an estimate \hat{A} of the attitude matrix A using the measurement matrix S and the reference matrix R (both possibly corrupted by noise). It is a fundamental fact that at least two non-collinear vectors are needed to determine attitude; thus, it is necessary that $n > 1$ to obtain a solution.

The problem thus described has a long history ([3]-[14]). A number of solutions have been proposed, both approximate and optimal. Approximate algorithms such as TRIAD cannot accommodate more than two observations and even throw away part of this information; therefore, they don't provide an optimal estimate of the attitude.

Optimal algorithms, on the other hand, compute a best estimate of the spacecraft attitude based on a loss function which takes into account all n measurements. One particular loss function which has found a prominent place in the literature is the so-called Wahba loss function, which was first proposed by Wahba in 1965 [2]:

$$L(\hat{A}) = \frac{1}{2} \sum_{i=1}^n a_i \|s_i - \hat{A}r_i\|_2^2 = \frac{1}{2} \left\| (S - \hat{A}R) \Lambda^{1/2} \right\|_2^2 = \frac{1}{2} \text{tr} \left[\Lambda^{1/2} (S - \hat{A}R)^T (S - \hat{A}R) \Lambda^{1/2} \right], \quad (5)$$

where $\|\cdot\|_2$ denotes the vector 2-norm, $\Lambda = \text{diag}(a_1, a_2, \dots, a_n)$, and the a_i , $i = 1, \dots, n$ are non-negative weights, whose sum can be set to unity without loss of generality (and will be in the sequel).

Wahba's Problem

Wahba's problem is formally stated as follows: *Find a proper real orthogonal matrix satisfying (4) which minimizes the cost function (5).*

Solutions to Wahba's problem

The early solutions, as reported in [2], involve a polar decomposition of SR^T ; a complete set of eigenvalues and eigenvectors of the symmetric part is then required. Therefore, these solutions required a large amount of calculation.

Davenport [4] has shown that the quadratic loss function in the attitude matrix can be transformed into a quadratic loss function in the corresponding quaternion. This is a great simplification of the problem proposed by Wahba since the quaternion is subject to fewer constraints than the nine elements of the attitude matrix. Davenport's substitution leads directly to an eigenvalue equation for the quaternion. This substitution and the resulting eigenvalue equation form the basis for much of the work presented in the literature; for example, it is the starting point for the derivation of the well-known QUEST algorithm. The QUEST algorithm provides an efficient closed-form solution to the eigenvalue problem.

The TRIAD algorithm is a deterministic, suboptimal algorithm which can accommodate only two measurements. It involves very simple and straightforward calculations, has been in existence for at least two decades, and has been implemented in a number of missions; these include, among others, Small Astronomy Satellite (SAS), Seasat, Atmospheric Explorer Mission (AEM), and Dynamics Explorer.

Markley's SVD algorithm [6] provides a very robust method for solving Wahba's problem. It is not very efficient since it requires the singular value decomposition of the attitude profile matrix (a 3×3 matrix constructed from the measurement and reference vectors). Markley's FOAM algorithm [9] provides a related solution which does not require the singular value decomposition and is, therefore, very efficient. Markley reports execution times faster even than for QUEST, previously the fastest known algorithm. In a very recent paper [10], Markley introduces a variant of FOAM. The iteration normally required for solving the usual quartic is avoided at the cost of losing orthogonality of the solution. However, orthogonality is recovered using an original technique; simulations show no loss of accuracy in most cases.

Another solution recently described is the polar decomposition (PD) algorithm of Bar-Itzhack [12]. As the name suggests, it obtains a solution by performing a polar decomposition of the attitude profile matrix; i.e. a decomposition into orthogonal and symmetric parts. The orthogonal part is precisely the solution to Wahba's problem.

In the next sections we explore the use of standard linear least-squares techniques to minimize (5) while relaxing the constraint (4).

2. THE NEW SUBOPTIMAL ALGORITHM

Least squares estimation theory can be used to obtain an approximate solution to the problem posed in Section 1. To be perfectly clear, the algorithm presented here is not a solution of Wahba's problem; it minimizes Wahba's loss function, but *without* constraint. Therefore, this solution is suboptimal. We first present the general form of the algorithm after which it is specialized for the case of small rotations. The general algorithm requires three non-collinear vector measurements in the general case, while the small-angle least-squares algorithm works with as few as two measurements.

2.1 General Case

Consider the attitude matrix A of (1). We wish to estimate A using r_i and s_i (for $i = 1, \dots, n, n \geq 3$). Given Equation (3), the problem we address is

$$\text{minimize } \|S - \hat{A}R\|_2^2 \quad (6)$$

over all possible \hat{A} . The objective function of (6) is equivalent to Wahba's loss function with all weights a_i set to unity for simplicity; the results in this paper can easily be extended to the weighted least-squares case. The least squares estimator minimizing this objective function is given by [16]:

$$\hat{A} = SR^+ \quad (7)$$

where R^+ denotes the pseudo-inverse of R . If the columns of R are linearly independent (as they would be with ≥ 3 nonredundant measurements), R^+ can be written

$$R^+ = R^T (RR^T)^{-1} \quad (8)$$

In practice, rather than directly computing (8), it is much more numerically robust and computationally efficient to perform an orthogonal triangularization of R ; from this the attitude estimate, \hat{A} , can be computed. An orthogonal matrix Q exists which transforms R to an lower triangular matrix Γ :

$$RQ = \begin{bmatrix} \Gamma & 0 \end{bmatrix} \quad (9)$$

Ref. [15] describes some standard, numerically stable algorithms exist for computing the orthogonal transformation of R ; two of the more popular algorithms are Householder rotations and modified Gram-Schmidt. Equation 9 is slightly different from the "usual" orthogonal triangularization in two ways: first, in the more typical setup, Q would operate from the left instead of the right and Γ would be upper instead of lower triangular, and second, the notation is perturbed because we already used the symbol R and here we use Γ to represent the matrix that would usually be called R .

Now, partitioning Q as $[Q_1 \ Q_2]$, yields

$$R = \begin{bmatrix} \Gamma & 0 \end{bmatrix} \begin{bmatrix} Q_1^T \\ Q_2^T \end{bmatrix} = \Gamma Q_1^T \quad (10)$$

We now show how this factorization can be used to minimize the 2-norm of $E \triangleq S - \hat{A}R$. Denote

$$SQ = \begin{bmatrix} C & D \end{bmatrix} \quad (11)$$

Then, calculate

$$EQ = \begin{bmatrix} C - \hat{A}\Gamma & D \end{bmatrix} \quad (12)$$

So, the least squares solution is obtained by choosing \hat{A} to satisfy

$$\hat{A}\Gamma = C \quad \text{or} \quad \hat{A} = C\Gamma^{-1} \quad (13)$$

which is a matrix equation whose matrix-valued solution can be obtained using standard techniques from linear algebra. Equations (9), (11) & (13) give an algorithm for solving the linear least squares problem (6). Equation (7) is a batch solution of a static estimation problem. It can be used to update each time step of a recursive algorithm such as a Kalman Filter, such as in [11].

Advantages of the General Least-Squares Algorithm

- (1) The algorithm can be carried out using well-known, numerically stable algorithms.

Disadvantages of the General Algorithm

- (1) Implementing the QR decomposition requires a relatively large number of calculations in the general case, so the algorithm trades speed for numerical robustness.
- (2) The solution technique ignores the constraints of (4); thus the estimated attitude matrix will not necessarily be a true attitude matrix (i.e. orthogonal). This can be alleviated by using the orthogonalization procedure of Bar-Itzhack [11]. More importantly, as sensor errors approach zero the estimated attitude matrix will approach orthogonality. This is because the least-squares algorithm minimizes the objective function of (6); since the true attitude matrix zeros this objective function, in the error-free (no noise) case, the least squares solution will equal the exact solution to Wahba's constrained problem. We have observed this in a number of simulations.
- (3) The algorithm is only usable when three or more (non-collinear) measurements are available; otherwise the inverse of (8) doesn't exist.

Summary: The general least-squares algorithm does not appear to be very interesting in its own right; its main interest is that in the special case of small attitude rotations it can be simplified, yielding a very attractive algorithm. We discuss this below.

2.2 Small Rotations Case

If small attitude rotations are assumed, the attitude matrix A of (1) can be written as

$$A \approx \begin{bmatrix} 1 & \psi & -\theta \\ -\psi & 1 & \phi \\ \theta & -\phi & 1 \end{bmatrix} \quad (14)$$

where ϕ , θ , and ψ are the usual Euler angles and are the quantities we wish to estimate (all Euler angle sets are essentially equivalent for small angles; these are the so-called body roll, pitch, and yaw pointing errors).

Combining Equations (1) & (14) as in Bar-Itzhack [11], the least-squares problem (6) reduces to:

$$\text{minimize } \|\tilde{S}_{small} - \tilde{R}_{small} \Theta\|, \quad (15)$$

where

$$\tilde{S}_{small} \triangleq \begin{bmatrix} s_1 - r_1 \\ s_2 - r_2 \\ \vdots \\ s_n - r_n \end{bmatrix}, \quad \tilde{R}_{small} \triangleq \begin{bmatrix} 0 & -r_{13} & r_{12} \\ r_{13} & 0 & r_{11} \\ -r_{12} & r_{11} & 0 \\ 0 & -r_{23} & r_{22} \\ r_{23} & 0 & r_{21} \\ -r_{22} & r_{21} & 0 \\ \vdots & \vdots & \vdots \\ 0 & -r_{n3} & r_{n2} \\ r_{n3} & 0 & r_{n1} \\ -r_{n2} & r_{n1} & 0 \end{bmatrix}, \quad \text{and } \Theta \triangleq \begin{bmatrix} \phi \\ \theta \\ \psi \end{bmatrix}.$$

Equation (15) represents a linear measurement equation where the parameters to be estimated are the desired body roll, pitch, and yaw angles. The least squares attitude estimate in this case is given by

$$\hat{\Theta} = \tilde{R}_{small}^+ \tilde{S}_{small} = \left[\tilde{R}_{small}^T \tilde{R}_{small} \right]^{-1} \tilde{R}_{small}^T \tilde{S}_{small}. \quad (16)$$

Equation (16) gives the least-squares solution to the linear system of equations in (15); a solution exists for $n \geq 2$ measurements. Again, instead of computing (16) directly, a QR decomposition of \tilde{R}_{small} is used to calculate the attitude solution. More explicitly, there exists an orthonormal matrix Q and an upper triangular matrix Γ such that

$$Q \tilde{R}_{small} = \begin{bmatrix} \Gamma \\ 0 \end{bmatrix}. \quad (17)$$

(Note that in this case, the "QR" decomposition is in its usual form except that Γ takes the place of R). Now, partition $Q = \begin{bmatrix} Q_1 \\ Q_2 \end{bmatrix}$; then,

$$\tilde{R}_{small} = [Q_1^T \quad Q_2^T] \begin{bmatrix} \Gamma \\ 0 \end{bmatrix} = Q_1^T \Gamma. \quad (18)$$

As above, this factorization can be used to minimize the 2-norm of $e = \tilde{S}_{small} - \tilde{R}_{small} \Theta$. Denote

$$Q \tilde{S}_{small} = \begin{bmatrix} c \\ d \end{bmatrix}. \quad (19)$$

Then, calculate

$$Qe = \begin{bmatrix} c - \Gamma \Theta \\ d \end{bmatrix}. \quad (20)$$

The least squares solution is then obtained by choosing Θ such that

$$\Gamma \Theta = c, \quad (21)$$

which is a 3×3 system of linear equations easily solved using standard techniques such as Gaussian elimination [15]. Therefore, having computed the QR decomposition of \tilde{R}_{small} , Equations (19) & (21) give an algorithm for solving the linear least squares problem considered.

Advantages of the Small-Angle Least-Squares Algorithm

- (1) For small angles, this algorithm provides a nearly optimal attitude estimate using an efficient and numerically stable algorithm.
- (2) The small angle algorithm explicitly estimates the roll, pitch, and yaw angles (not the full attitude matrix). Thus additional calculations are not required to obtain the roll, pitch, and yaw angles from the attitude matrix.
- (3) The matrix \tilde{R}_{small} contains many zeros and one can take advantage of this known structure to reduce the required computation. This algorithm's computational requirement compares favorably with other algorithms as shown below.
- (4) This algorithm works with $n \geq 2$ measurements, unlike the general algorithm which needs at least three measurements.

Disadvantages of the Small-Angle Algorithm

- (1) The primary disadvantage is introduction of errors due to the small-angle approximation, and thus applicability limited to only those cases where small angle approximations are valid. For attitude rotations in all three coordinate axes of less than 5° , the error due to the small angle approximations is bounded by 0.006° , which is acceptable in many cases.
- (2) As for the general least-squares algorithm, this algorithm is not an exact solution of the Wahba problem and does not guarantee an orthogonal attitude matrix. If no measurement noise is present (and there are no roundoff errors), the only errors are due to the small angle assumptions. If the amount of measurement noise is small compared to the size of the attitude rotations, the linearization is the main source of error and nonoptimality is not an issue.

3. COMPUTATIONAL REQUIREMENTS

In this section, we present the computational requirements for the least squares algorithm and compare these with the computational requirements of several well-known algorithms. Table 1 below summarizes the computational requirements.

For each algorithm, we address both the general case and the small rotation case. We specifically address the cases of two and three vector measurements (i.e. $n = 2, 3$). The two and three measurement cases are the most important because most typical spacecraft have either two or three sensors active at a time. Two vector measurements are sufficient to determine attitude. The three measurement case is important because many systems seeking maximal accuracy will include an orthogonal (or near orthogonal) triad of sensing devices. In the next section we present a technique for reducing more than three measurements to no more than three for cases where the additional measurements can be conveniently clustered (for example, one star tracker tracking and measuring multiple stars).

The computational requirements in this table do not include the calculations needed to compute the so-called attitude profile matrix, thus making general QUEST and SVD operations counts independent of n , the number of measurements. The least-squares operations counts, on the contrary, do grow with larger n . For the general (large-angle) least squares algorithm, only the three-measurement case is included because three vector measurements are required to obtain a solution. The SOMA (slower optimal matrix) algorithm [9], a variant of FOAM, is included for completeness.

Observations From Table 1

- (1) TRIAD is the fastest two-measurement algorithm, but is error prone because it actually throws away some of the measurement information.
- (2) Of small-angle algorithms (excluding TRIAD), QUEST is the fastest, both for two and three measurements. It is followed by least squares and then FOAM.
- (3) Of the general large-angle algorithms, FOAM is the fastest, followed by QUEST and then least squares. SVD is the slowest.

Table 2 summarizes the primary characteristics of each algorithm. The second column indicates the nature of the solution by construction. The third column indicates the types of calculations which make up the bulk of the computation for each algorithm. We make one more observation:

Algorithm	Operations						
	cosine	sine	add	multiply	arccos	arcsin	sqrt
Least Squares							
General, $n=3$ msmts	0	0	267	264	0	0	6
Small Angles, $n=2$ msmts	0	0	81	78	0	0	3
Small Angles, $n=3$ msmts	0	0	117	114	0	0	3
TRIAD, $n=2$ msmts	0	0	34	59	0	0	2
QUEST							
General Case, $n=2$ & 3 msmts	0	0	217	209	0	0	1
Small Angles, $n=2$ msmts	0	0	42	71	0	0	1
Small Angles, $n=3$ msmts	0	0	64	95	0	0	1
SVD, $n=2$ & 3 msmts	0	0	299	336	0	0	0
FOAM, $n=2$ msmts	0	0	81	112	0	0	1
FOAM*, $n=3$ msmts	0	0	117	148	0	0	1
SOMA**, 3 msmts	1	0	94	155	1	0	4

* assumes one Newton-Raphson iteration

** SOMA identical to FOAM in two measurement case

(4) As a preview of Section 5, FOAM appears to have more numerical error. Both QUEST and FOAM include some computations which might be sensitive to numerical round-off errors such as trace, adjoint, determinant, and Newton-Raphson iteration.

Algorithm	Solution Characteristic	Primary Computations
Least Squares		
Small Angles	solves for ϕ , θ , & ψ directly; near-optimal	QR decomposition
General Case	minimizes Wahba's loss function without constraint	QR decomposition
TRIAD	non-optimal; deterministic	cross products, matrix multiply
QUEST		
Small Angles	solves Wahba's problem	solve $Ax = b$, $A \in \mathbb{R}^{3 \times 3}$
General Case	solves Wahba's problem	trace, adjoint, determinant, Newton-Raphson iteration
SVD	solves Wahba's problem	singular value decomposition (iterative)
FOAM	solves Wahba's problem	adjoint, Newton-Raphson iteration, frobenius norm
Polar Decomposition	solves Wahba's problem	polar decomposition, linear equation solution, matrix multiply

4. AVERAGING OF MEASUREMENTS FOR NEARLY COLLINEAR SENSORS

In this section we describe a technique for combining the measurements of nearly collinear sensors to reduce the number of independent measurements which must be processed by the attitude determination algorithm. This is

motivated by the following observation: given two or three (non-collinear) vector measurements, additional, independent measurements which are nearly collinear to any of the original two or three provide very little additional information. For example, consider a spacecraft with two star trackers whose boresights are well-separated from each other. Further assume that each tracker tracks several stars within its field of view and produces independent vector measurements for every star it tracks. The stars within each star tracker's boresight are separated by only a few degrees. Therefore, each star tracker is essentially a two-axis sensing device, with a weak measurement of the axis of rotation about its boresight. A much better three-axis attitude measurement is available by combining the measurements of the two star trackers, and two axes of measurement from each is sufficient.

The central concept of this section is to combine collections of nearly collinear measurements by *averaging* them, and then using that averaged measurement (along with at least one other measurement) in the attitude determination algorithm of choice.

To carry out this concept, the nearly collinear measurements (for example, the measurements of all stars in a star tracker) are averaged and normalized in Cartesian coordinates. This results in one measurement vector (and its corresponding reference vector) as follows:

$$\text{measurement vector: } s_{avg}^m = \frac{s_1 + s_2 + \dots + s_m}{\|s_1 + s_2 + \dots + s_m\|_2} \quad (22)$$

$$\text{reference vector: } r_{avg} = \frac{r_1 + r_2 + \dots + r_m}{\|r_1 + r_2 + \dots + r_m\|_2} \quad (23)$$

It is easy to verify that if the original measurements satisfy (3), then the resulting averages from (22) & (23) also satisfy (3). Therefore, if there are at least two widely separated sets of coaligned or nearly coaligned attitude measurements, these sets of measurements can be grouped and averaged as above. This results in just a few (typically two or three) measurements, each of which might be aggregates of several sets of nearly coaligned measurements. Reducing the number of measurements this way has two main benefits:

- (1) It reduces the operations necessary in the attitude determination algorithm (at least if the least squares algorithm is used; some algorithms' operations counts do not grow with additional measurements).
- (2) It reduces the data flow required across the interface between the star sensor and the central processor.

5. SIMULATION RESULTS : COMPARISON OF LEAST-SQUARES, QUEST, and FOAM

In this section we present the results of a simulation which demonstrates several of the concepts in this paper. We compare the performance of the least-squares algorithm with the well-known QUEST and FOAM algorithms for the case of small attitude rotations with two vector measurements. We also demonstrate the use of the measurement averaging technique of Section 4.

The particular example studied here is a geosynchronous satellite with a star tracker and an earth sensor. The star tracker can track up to m stars, but the m star measurements are averaged by the technique of Section 4 to produce one vector measurement. The star tracker boresight is assumed to be 53° from the earth sensor boresight, and these two sensors provide two well-separated vector measurements for attitude determination. We simulate only the small-angle version of the least-squares algorithm since the general algorithm needs at least three measurement vectors. It is reasonable to use the small-angle algorithm, because during normal operations geosynchronous satellites typically maintain their attitudes to within small perturbations from the nominal attitude. We also simulate both the general and small-angle QUEST algorithms, and the FOAM algorithm.

To study the effects of finite precision arithmetic, the simulation includes a model of the round-off error which is exhibited in a typical processor. The algorithms are assumed to be implemented in single precision floating-point arithmetic, with numbers stored as 23-bit mantissa, sign, and 8-bit exponent. This corresponds to the popular 1750a architecture.

First, coordinate frames will be defined after which the detailed implementation of the algorithm will be described. Figure 1 depicts the geometry.

5.1 Coordinate Frame Definitions

The right-handed coordinate frames considered are defined below.

orbiting reference frame, $R=(1,2,3)$

body frame, $B=(x,y,z)$

Star sensor frame, $S=(a,b,c)$

inertial frame, $I=(\gamma, II, N)$

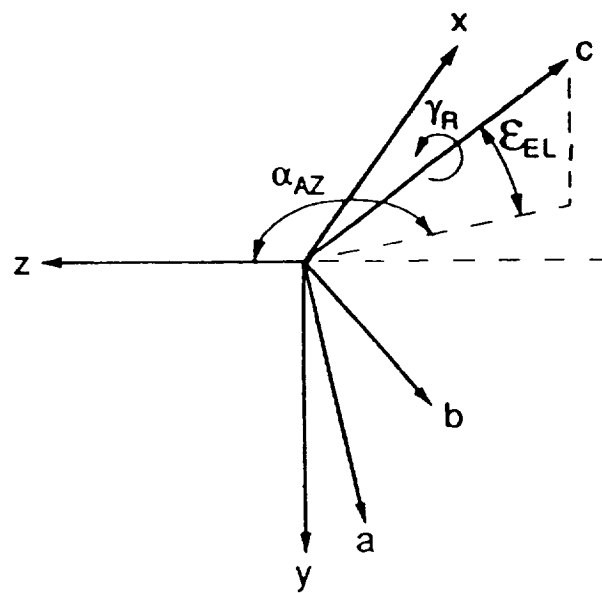
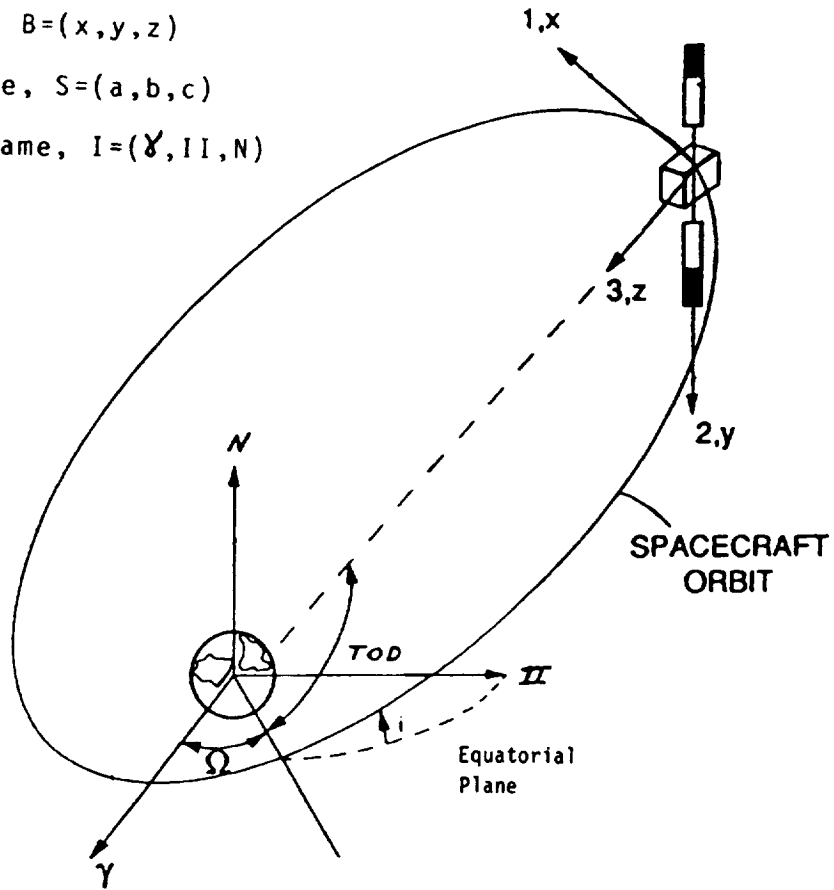


Figure 1 - Geometry & Coordinate Frames

1. **S = Star Sensor Frame**
This frame has its 3-axis in the direction of the star sensor boresight, its 1-axis in the positive azimuth direction of the star sensor, and its 2-axis completes the right-handed triad.
2. **B = Spacecraft Body Frame**
This frame has the spacecraft yaw axis as its 3-axis, the spacecraft pitch axis as its 2-axis, and the spacecraft roll axis as its 1-axis.
3. **R = Orbiting Reference Frame**
This frame has its 3-axis nadir pointed, its 2-axis orbit normal south, while its 1-axis completes the right-handed triad.
4. **I = Celestial Frame**
This frame, commonly referred to as the Earth Centered Inertial (ECI) frame, has its 3-axis parallel to the rotation axis of the earth and pointed north, its 1-axis towards the vernal equinox, and its 2-axis in the plane of the equator completing the right-handed triad.

5.2 Coordinate Frame Transformations

The coordinate frame transformations considered are defined below. A 3x3 direction cosine matrix is a transformation from one coordinate frame to another. In the following, a direction cosine matrix will be written $A = A(\alpha_1, \dots, \alpha_n)$ where arguments α_i , $i = 1, \dots, n$ indicate a functional dependence (not explicitly shown) of the direction cosine matrix on the arguments.

1. Transformation From Spacecraft Body To Star Sensor Coordinates

$$M : B \rightarrow S \quad M = M(\alpha_{AZ}, \epsilon_{EL}, \gamma_R) \quad (24)$$

where

$$\alpha_{AZ}, \epsilon_{EL}, \gamma_R = \text{Azimuth, Elevation, \& Rotation Mounting Angles Of The Star Sensor}$$

2. Transformation From Orbiting Reference Frame To Body Frame

$$A : R \rightarrow B \quad A = A(\phi, \theta, \psi) \quad (25)$$

3. Transformation From Celestial Frame To Orbiting Reference Frame

$$C : I \rightarrow R \quad C = C(i, \Omega, TOD) \quad (26)$$

where TOD denotes the time-of-day angle, i = orbit inclination, and Ω = right ascension of the ascending node.

5.3 Measurements

The following measurements are available from the star sensor and the earth sensor to estimate the spacecraft attitude.

1. Star vector measurements expressed in the star sensor coordinate frame S , $s_i^m \in S$ $i = 1, 2, \dots, m$.
2. The corresponding star vectors expressed in the celestial coordinate frame I from the star catalog (obtained as a result of performing star identification), $r_i^c \in I$ $i = 1, 2, \dots, m$.
3. Earth vector measurements expressed in spacecraft body coordinates B from the earth sensor, $s_E^m \in B$.

$$s_E^m = \begin{bmatrix} -\sin\theta_{AZ} \cos\phi_{EL} \\ \sin\phi_{EL} \\ \cos\theta_{AZ} \cos\phi_{EL} \end{bmatrix} \quad (27)$$

where θ_{AZ} and ϕ_{EL} are the earth sensor azimuth and elevation measurements, respectively, with respect to earth nadir. Our earth "ephemeris" data which is analogous to star reference positions given from the catalog is $r_E^c = (0, 0, 1)^T \in R$.

5.4 Collection and Averaging Of Measurements

Our ultimate goal is to find an attitude matrix $A(\phi, \theta, \psi)$ which transforms from the orbiting reference frame \mathbf{R} to the body frame \mathbf{B} and equates the measurement vectors in \mathbf{R} to the reference vectors in \mathbf{R} (see equations (6) and (24), or (30) and (32) below). The measurement and reference vectors for the earth sensor are:

$$s_E^m \in \mathbf{B} \text{ and } r_E^e \in \mathbf{R}, \quad (28)$$

and the measurement and reference vectors for the star tracker are:

$$M^T s_i^m \in \mathbf{B} \text{ and } C r_i^e \in \mathbf{R}, \quad i = 1, 2, \dots, m. \quad (29)$$

The star sensor measurements and reference vectors are then averaged using equations (22) and (23) to make one aggregate star sensor measurement.

5.5 Implementing the Suboptimal Algorithm

In this case, the least-squares problem (15) is to minimize the difference between the the measurements (expressed in the body frame) and the references (expressed in the orbiting reference frame) through attitude rotation A (the desired quantity). For the star sensor measurements,

$$\text{minimize } \|S_{avg} - A(\phi, \theta, \psi) R_{avg}\|, \quad (30)$$

where

$$S_{avg} = M^T s_{avg}^m \text{ and } R_{avg} = C r_{avg}^e. \quad (31)$$

For the earth sensor measurement,

$$\text{minimize } \|s_E^m - A(\phi, \theta, \psi) r_E^e\|, \text{ where } r_E^e = \begin{bmatrix} 0 \\ 0 \\ 1 \end{bmatrix} \quad (32)$$

Combining Equations (28) (28), and (29), rearranging terms, and removing one extraneous equation, the least-squares problem (15) reduces to

$$\text{minimize } \|\bar{S} - \bar{R} \Theta\|, \text{ or minimize } \left\| \begin{bmatrix} S_{avg,1} - R_{avg,1} \\ S_{avg,2} - R_{avg,2} \\ S_{avg,3} - R_{avg,3} \\ s_{E,1}^m \\ s_{E,2}^m \end{bmatrix} - \begin{bmatrix} 0 & -R_{avg,3} & R_{avg,2} \\ R_{avg,3} & 0 & -R_{avg,1} \\ -R_{avg,2} & R_{avg,1} & 0 \\ 0 & -1 & 0 \\ 1 & 0 & 0 \end{bmatrix} \begin{bmatrix} \phi \\ \theta \\ \psi \end{bmatrix} \right\| \quad (33)$$

which is a linear measurement equation in ϕ , θ , and ψ . $X_{avg,i}$ denotes the i 'th entry of the vector X_{avg} . The least squares solution is then obtained by factoring \bar{R} and implementing Equations (19) and (21) as discussed in Section 2 above.

Small angle approximations are used to provide the simple form of the attitude matrix in Equation (33). Because of the orbit normal steering law of many geosynchronous satellites, the small angle assumption is valid; the satellite body axes will not deviate from the orbiting reference frame more than a few tenths of a degree during normal operations (including stationkeeping). The star sensor measurements and references are averaged in cartesian coordinates using equations (22) and (23) providing one single "measurement" from the star sensor which reduces subsequent computation and limits data flow at the interface.

5.6 Simulation Results

For our simulations, we use the following reference vectors:

$$R_{avg1} = \begin{bmatrix} 0 \\ 0 \\ 1 \end{bmatrix}, \quad R_{avg2} = \begin{bmatrix} 0 \\ -\sin 53^\circ \\ -\cos 53^\circ \end{bmatrix} \quad (34)$$

The reference vector R_{avg1} is the direction of earth nadir in the orbiting reference frame while R_{avg2} is the direction of a star expressed in the orbiting reference frame. The measurement vectors are computed as

$$S_{avg i} = A_{att} R_{avg i} + n_i, \quad i = 1, 2 \quad (35)$$

where

$$A_{att} = \begin{bmatrix} \cos\psi\cos\theta & \cos\psi\sin\theta\sin\phi + \sin\psi\cos\phi & -\cos\psi\sin\theta\cos\phi + \sin\psi\sin\phi \\ -\sin\psi\cos\theta & -\sin\psi\sin\theta\sin\phi + \cos\psi\cos\phi & \sin\psi\sin\theta\cos\phi + \cos\psi\sin\phi \\ \sin\theta & -\cos\theta\sin\phi & \cos\theta\cos\phi \end{bmatrix} \quad \phi = \theta = \psi = \theta_{rot} \quad (36)$$

and n_i is a vector of zero-mean Gaussian white noise measurement errors on the components of n_i . For simplicity, the measurement noise is assumed to have equal magnitude in every direction. We denote its equivalent angular size by θ_n . In all cases, the measurement vectors thus produced are normalized to have unity 2-norm. The parameter θ_{rot} represents the size of the true attitude rotation.

The simulation results are summarized in Table 3. All algorithms were simulated with $n_i = 0$, to assess the effect of round-off errors, and with $n_i \neq 0$ to assess estimation accuracy in the presence of sensor noise (and round-off error). Algorithm accuracy is computed by

$$\epsilon_{att} = \left[(\hat{\phi} - \theta_{rot})^2 + (\hat{\theta} - \theta_{rot})^2 + (\hat{\psi} - \theta_{rot})^2 \right]^{1/2} \quad (37)$$

Of course, when no measurement noise is included, the algorithm need be executed only once; however, when measurement noise is included, we execute the algorithm 250 times to capture the statistical effects and then take RMS values. When $n_i = 0$ (i.e. $\theta_n = 0$), this gives the effect of round-off errors; when $n_i \neq 0$, the metric of (37) is a measure of total estimation error. We stress that the numerical results are merely experimental, not validated by any rigorous numerical analysis.

CASE	ROTATION SIZE θ_{rot} , degrees	MEASUREMENT NOISE LEVEL θ_n , degrees	ESTIMATION ERROR, ϵ_{att} , degrees			
			SMALL ANGLE LEAST SQUARES	GENERAL QUEST	SMALL ANGLE QUEST	FOAM
A	0	0	2.0×10^{-6}	0.0	0.0	0.0
B	0.001	0	3.1×10^{-8}	4.0×10^{-6}	4.0×10^{-6}	2.5×10^{-5}
C	0.01	0	3.6×10^{-6}	1.8×10^{-6}	1.6×10^{-6}	2.8×10^{-5}
D	0.1	0	2.7×10^{-4}	1.9×10^{-6}	1.5×10^{-4}	5.8×10^{-6}
E	0.1	0.0001	2.8×10^{-4}	1.4×10^{-4}	1.9×10^{-4}	1.4×10^{-4}
F	0.1	0.01	0.014	0.014	0.014	0.014
G	0	0.001	0.0014	0.0014	0.0014	0.0014
H	0	0.01	0.014	0.014	0.014	0.014

The results summarized in Table 3 are representative of a fairly wide range of attitude errors and noises, although all would be considered "small-angle" cases. We see that, for these cases, the least-squares algorithm is less affected by finite precision arithmetic than the other algorithms (except, mysteriously, in Case A). Its accuracy is comparable with the other algorithms in the presence of sensor noise. So, from Table 3, we conclude that for this special case, the least squares algorithm provides accuracy essentially identical to QUEST and FOAM.

The FOAM algorithm appears to be most susceptible to round-off error and, thus, its estimation accuracy degrades as measurement noise decreases.

6. CONCLUSION

A number of algorithms exist for solving the attitude determination problem. In this paper we introduce a new suboptimal least-squares algorithm for the solution of Wahba's problem. It is especially attractive for cases where attitude rotations are known to be small. In the small-angle case, the least-squares algorithm is quite efficient and can be performed with numerically stable operations. The computational requirements of the least squares algorithm are compared with other well-known algorithms for the two and three measurement cases. If the angle of rotation is known *a priori* to be small, small angle QUEST is the most efficient algorithm, followed closely by the least squares algorithm. In the general n -measurement, large-angle case, QUEST and FOAM are still preferable as they are fast optimal algorithms which have been shown to work well in practice. Finally, we introduce a measurement averaging technique which reduces the number of vector measurements that any

algorithm must process. Performance degradations using the averaging technique are small as long as at least two sensors with large angular separations and similar accuracies are available.

REFERENCES

- [1] G.M. Lerner, "Three-Axis Attitude Determination," in *Spacecraft Attitude Determination & Control*, Ed. by J.R. Wertz, D. Reidel, 1985, pp. 420-28.
- [2] G. Wahba, *A Least Squares Estimate Of Spacecraft Attitude*, SIAM Rev., v. 7, no. 3, Jul 1965, p. 409.
- [3] J.E. Brock, *Optimal Matrices Describing Linear Systems*, AIAA J., v. 6, no. 7, Jul 1968.
- [4] P.B. Davenport, *A Vector Approach To The Algebra Of Rotations With Applications*, NASA X-546-65-437, Nov., 1965.
- [5] M.D. Shuster & S.D. Oh, *Three-Axis Attitude Determination From Vector Observations*, J. Guid. & Contr., v. 4, no. 1, Jan-Feb 1981.
- [6] F.L. Markley, *Attitude Determination Using Vector Observations And The Singular Value Decomposition*, J. Astro. Sci., v. 36, no. 3, Jul-Sep 1988, pp. 245-258.
- [7] F.L. Markley, *Attitude Determination & Parameter Estimation Using Vector Observations : Theory*, J. Astro. Sciences, v. 37, no. 1, Jan - Mar, 1989, pp. 41-58.
- [8] F.L. Markley, *Attitude Determination & Parameter Estimation Using Vector Observations : Application*, AAS Paper 89-364.
- [9] F.L. Markley, *Attitude Determination Using Vector Observations : A Fast Optimal Matrix Algorithm*, Flight Mech./Est. Theory Symp., Greenbelt, MD, 5-7 May 1992.
- [10] F.L. Markley, *New Quaternion Attitude Estimation Method*, J. Guid., Contr., & Dyn., v. 17, no. 2, Mar-Apr 1994.
- [11] Itzhack Y. Bar-Itzhack & J. Reiner, *Recursive Attitude Determination From Vector Observations : Direction Cosine Matrix Identification*, J. Guid. & Contr., v. 7, no. 1, Jan-Feb 1984.
- [12] Itzhack Y. Bar-Itzhack, *Polar Decomposition For Attitude Determination From Vector Observations*, Flight Mech./Est. Theory Symp., Greenbelt, MD, 5-7 May 1992.
- [13] M.D. Shuster, *Approximate Algorithms For Fast Optimal Attitude Computation*. AIAA Guidance & Control Conference, Palo Alto, CA, Aug 1978.
- [14] M.D. Shuster, *Maximum Likelihood Estimation Of Spacecraft Attitude*, J. Astro. Sci., v. 37, no. 1, Jan-Mar 1989, pp. 79-88.
- [15] G.W. Stewart, *Introduction To Matrix Computations*. Academic, 1973.
- [16] J.M. Mendel, *Lessons In Digital Estimation Theory*, Prentice-Hall, 1986.

APPENDIX - ALGORITHM OPERATIONS COUNTS

In this appendix, we present the details of some of the operations counts for the case of two measurements. These results are presented in Table 1 of the main body of this paper. This appendix is included to justify the claims of Table 1, document the assumptions used to do the operations counts for the various algorithms, and illustrate the general method used to obtain the results of Table 3 of the main body. It is not exhaustive due to lack of space.

Small Angle Least Squares Count

The operations count for the least squares solution using a QR decomposition is taken from Stewart [15] who provides a count of the number of multiplies required by each algorithm; we assume the same number of additions are required. The results are shown in Table A1.

OPERATION TYPE	additions	multiplies	sqrt
QR Decomposition (Stewart [15], Alg. 3.8, p. 236)	36	36	3
Use QR for Least Squares (Stewart [15], Alg. 3.7, p. 234, three times)	30	30	0
Solve upper triangular system	3	6	0
form "measurement"	6	0	0
TOTAL	81	78	3

The calculations required to solve an upper triangle 3×3 system were counted by hand. The form "measurement" operation of the last row is the calculation required to form \tilde{S} of Equation (15) in the main body of this paper.

Small Angle QUEST Operations Count

The bulk of the computations required for small angle QUEST are those involved with solving a 3×3 system of linear equations. We assume that Gaussian elimination is used for which Stewart [15] provides a count of the multiplies (we assume the number of additions is the same). The calculations are summarized in Table A2. The notation is from [5].

OPERATION TYPE	additions	multiplies	sqrt
form S_0	9	24	0
calculate $A = 2I - S_0$	3	0	0
form Z	9	18	0
solve $Ax = z$ using gaussian elimination (Stewart [15], Alg. 1.3, p. 131)	18	18	0
form \tilde{q}	3	8	1
multiply elements by 2	0	3	0
TOTAL	42	71	1

General QUEST Operations Count

The general QUEST operations count is summarized in Table A3 below. The notation in the table is consistent with [5].

OPERATION TYPE	additions	multiplies	sqrt
form S 4 times	36	0	0
form σ 4 times	8	0	0
form $\det(S)$ 4 times	20	36	0
form κ 4 times	48	72	0
form ω 4 times	16	8	0
form Z	9	18	0
form $\sigma^2 - \kappa$	1	0	0
form $\sigma^2 + Z^T Z$	3	3	0
form $\delta + Z^T S Z$	9	12	0
form $Z^T S^2 Z$	14	15	0
one newton-raphson iteration	10	4	0
form α, β, ω	5	2	0
form $(\alpha I + \beta S + S^2)Z$	36	33	0
form \bar{q}	2	4	1
post rotate	0	2	0
TOTAL	217	209	1

A number of the operations are done four times to find and implement pre-rotations which avoid the 180° rotation case.

FOAM Operations Count

Table A4 below summarizes the operations count for the FOAM algorithm. Notation in the table is consistent with [9].

OPERATION TYPE	additions	multiplies	sqrt
form λ	1	1	1
form κ	1	2	0
form ζ	0	1	0
form $\ B\ _F^2$	8	9	0
form $\ adj(B)\ _F^2$	17	27	0
form $(\kappa + \ B\ _F^2)\zeta$	1	10	0
form $\lambda adj(B^T)\zeta$	0	10	0
form $BB^T B$	36	54	0
divide above by ζ	0	9	0
add and subtract three matrices	18	0	0
TOTAL	81	112	1

For the two measurement case, no Newton-Raphson iteration is required since λ admits a closed form solution in this case.

Motion Models in Attitude Estimation*

D. Chu, Z. Wheeler, and J. Sedlak
Computer Sciences Corporation (CSC)
Lanham-Seabrook, Maryland, USA

Abstract

Attitude estimators use observations from different times to reduce the effects of noise. If the vehicle is rotating, the attitude at one time needs to be propagated to that at another time. If the vehicle measures its angular velocity, attitude propagation entails integrating a rotational kinematics equation only. If a measured angular velocity is not available, torques can be computed and an additional rotational dynamics equation integrated to give the angular velocity.

Initial conditions for either of these integrations come from the estimation process. Sometimes additional quantities, such as gyro and torque parameters, are also solved for. Although the partial derivatives of attitude with respect to initial attitude and gyro parameters are well known, the corresponding partial derivatives with respect to initial angular velocity and torque parameters are less familiar. They can be derived and computed numerically in a way that is analogous to that used for the initial attitude and gyro parameters.

Previous papers have demonstrated the feasibility of using dynamics models for attitude estimation but have not provided details of how much angular velocity and torque parameters can be estimated. This tutorial paper provides some of that detail, notably how to compute the state transition matrix when closed form expressions are not available. It also attempts to put dynamics estimation in perspective by showing the progression from constant to gyro-propagated to dynamics-propagated attitude motion models. Readers not already familiar with attitude estimation will find this paper an introduction to the subject, and attitude specialists may appreciate the collection of heretofore scattered results brought together in a single place.

*This work was supported by the National Aeronautics and Space Administration (NASA)/Goddard Space Flight Center (GSFC), Greenbelt, Maryland, under Contract NAS 5-31500.

Attitude Estimation

Modeling attitude motion makes it possible to use observations taken at different attitudes over longer time spans. Having more data reduces the effect of noise and generally improves estimate accuracy. Estimation is explained by Sorenson (Ref. 1) but is reviewed here to establish notation.

Least Squares

To determine some parameter of interest, such as attitude, the "best" least-squares value is the one that minimizes the squared difference between the observations and values computed from the state. Observations \bar{z}_i at times t_i are a function of the state \bar{x} and time t_i but also include noise \bar{v}_i :

$$\bar{z}_i = \bar{h}(\bar{x}, t_i) + \bar{v}_i$$

If the noise has constant variance (second order stationary) and is uncorrelated in time (white), its autocorrelation is

$$E(\bar{v}_i \bar{v}_j^T) = R \delta(t_i - t_j)$$

If each noise component is also independent, the matrix R is diagonal. The Dirac delta function $\delta(t)$ is defined to be zero everywhere but at the origin and to integrate to 1:

$$\int_{0^-}^{0^+} \delta(t) dt = 1$$

The correct value of the state should minimize the residuals $\Delta \bar{z}_i$; that is, the difference between the observed and computed observation values:

$$\Delta \bar{z}_i = \bar{z}_i - \bar{h}(\bar{x}, t_i)$$

The optimal value for the state is determined by minimizing a loss function defined as the sum of the squared observation residuals:

$$J = \frac{1}{2} \sum_{i=1}^N \Delta \bar{z}_i^T R_i^{-1} \Delta \bar{z}_i$$

Newton-Raphson Solution

Least-squares problems may be solved in several ways. The method used here is the Newton-Raphson method as described by Wertz (Ref. 2). It begins by taking the derivative of the loss function with respect to the state and setting it to zero:

$$\frac{\partial J}{\partial \bar{x}} = - \sum_{i=1}^N \Delta \bar{z}_i^T R_i^{-1} H_i = \bar{0}$$

where the derivative of the modeled observation with respect to the state is

$$H = \frac{\partial \bar{h}}{\partial \bar{x}}$$

If the observations are linear functions of the state, this equation can be solved as follows:

$$\Delta \bar{x} = \frac{\partial J}{\partial \bar{x}} \left(\frac{\partial^2 J}{\partial \bar{x}^2} \right)^{-1}$$

where—ignoring the second derivative of observations with respect to the state—the second derivative of the loss function is

$$\frac{\partial^2 J}{\partial \bar{x}^2} = \sum_{i=1}^N H_i^T R_i^{-1} H_i$$

This matrix is called the normal or information matrix and is the inverse of the covariance matrix P :

$$P^{-1} = \sum_{i=1}^N H_i^T R_i^{-1} H_i$$

If the observations are nonlinear functions of the state, the solution is computed recursively:

$$\bar{x} \leftarrow \bar{x} + \Delta \bar{x}$$

This iteration is explicit in the batch estimator, where all observations are processed together. It can be implicit in the sequential estimator, where numerical convergence at a given time is combined with observability convergence with increasing time.

If one already has a state estimate based on past information, that estimate can be updated to reflect additional observations without having to process all the observations over again. The resultant solution \bar{x} is an average in which the two solutions are weighted by their respective information matrices:

$$\bar{x} \leftarrow P(P_1^{-1} \bar{x}_1 + P_0^{-1} \bar{x}_0) = \bar{x}_1 + PP_1^{-1}(\bar{x}_1 - \bar{x}_0)$$

and the total information P^{-1} is equal to the sum of the information in the two sets of observations:

$$P^{-1} = P_0^{-1} + P_1^{-1}$$

Parameterizing Attitude

To conform to the approach outlined above, the quantity being estimated must be expressed as a vector. For attitude, this means that the familiar matrix representation is inappropriate. Attitude could be expressed as a quaternion, but because the four components are not independent, the corresponding covariance matrix would be singular; it would not be invertible.

Attitude can also be expressed in axis-angle or rotation vector form, where the three components are all independent (Ref. 2). Rotation vectors still have the unavoidable problem that finite rotations are not additive; they are very nonlinear. This problem can be circumvented by estimating the attitude error rather than the attitude itself. As long as the attitude error is small, the linear approximations made so far are justified.

The attitude error vector in body coordinates $\Delta \vec{a}$ takes the true attitude A to the estimated attitude A' :

$$A' = R(\Delta \vec{a})A$$

The rotation matrix $R(\Delta \vec{a})$ is given by the formula

$$R(\Delta \vec{a}) = I - \sin(\Delta a) \left(\frac{\Delta \vec{a}}{\Delta a} \right) + [1 - \cos(\Delta a)] \left(\frac{\Delta \vec{a}}{\Delta a} \right)^2$$

where Δa is the error magnitude, $\Delta \vec{a}$ is the error direction, and I is the 3 by 3 identity matrix. The tilde denotes the antisymmetric matrix

$$\tilde{a} = \begin{bmatrix} 0 & -a_3 & a_2 \\ a_3 & 0 & -a_1 \\ -a_2 & a_1 & 0 \end{bmatrix}$$

which is also the cross product operator

$$\vec{a} \times \vec{b} = \tilde{a}\vec{b}$$

$R(\Delta \vec{a})$ can also be expressed as

$$R(\Delta \vec{a}) = \cos(\Delta a)I + [1 - \cos(\Delta a)]\Delta \vec{a}\Delta \vec{a}^T - \sin(\Delta a)\left(\frac{\Delta \vec{a}}{\Delta a}\right)$$

by using the identity

$$\Delta \vec{a}^2 = \Delta a^2(\Delta \vec{a}\Delta \vec{a}^T - I)$$

Once the state has been solved for and the attitude error vector obtained, the attitude matrix is updated with the rotation matrix

$$A' = R(-\Delta \vec{a}) A'$$

Estimation With a Drift Model

Modeling Motion

Attitude may not remain constant over the data spans necessary to average out long-term errors. If differential equations can be written to model the attitude motion, observations may be predicted more accurately than with a constant attitude model. As in Gelb (Ref. 3), these equations are linearized to make them easier to solve:

$$\frac{d\vec{x}}{dt} = F(\vec{x}, t)\vec{x} + G(\vec{x}, t)\vec{w}$$

Here, \bar{w} is a noise term reflecting that the uncertainty is the state propagation. Even though these equations may not be exact, their solution, in particular the state transition matrix Φ , makes it possible to propagate the state from the past to the present.

$$\bar{x}(t_i) = \Phi(t_i, t_{i-1})\bar{x}(t_{i-1})$$

If the attitude drifts at random, it can be modeled as the Markov process

$$\frac{d\Delta\bar{a}}{dt} = -\frac{\Delta\bar{a}}{\tau} + \bar{w}$$

where τ is a characteristic time for the drift. The larger τ is, the larger the variance. As τ increases, the Markov model approaches the random walk model

$$\frac{d\Delta\bar{a}}{dt} = \bar{w}$$

Process Noise

Whatever the motion model, the state cannot be propagated with certainty. Farrenkopf (Ref. 4) gives a very clear discussion of this "process noise," and Lefferts et al. (Ref. 5) demonstrate how it can be reflected in the covariance matrix for the sequential estimator. The propagation covariance ΔP can be defined as

$$\Delta P = E[\bar{x}(\sigma)\bar{x}(\tau)^T]_{|\sigma=\tau}$$

and evaluated by substituting for \bar{x} :

$$\Delta P = E \left[\left(\int_0^t G(\tau)\bar{w}(\tau)d\tau \right) \left(\int_0^t G(\sigma)\bar{w}(\sigma)d\sigma \right)^T \right]$$

If the components of \bar{w} are independent, white, and stationary, the process noise is

$$E[\bar{w}(\tau)\bar{w}^T(\sigma)] = Q \delta(\sigma - \tau)$$

where Q is diagonal. This expression can be simplified by making the two integrals a double integral and by bringing the expectation operator inside. The result is

$$\Delta P = \int_0^t G(\tau)Q G^T(\tau)d\tau$$

After propagation, the total covariance is just the sum of the propagated covariance and the process noise contribution:

$$P = \Phi P \Phi^T + \Delta P$$

Estimation With Gyro Propagation

Attitude Error Equation

The attitude error equation is derived by perturbing the kinematic equation for attitude matrix propagation

$$\frac{dA}{dt} = -\bar{\omega}A$$

(Ref. 6). Given the angular velocity $\bar{\omega}$ and initial attitude, one can integrate to find the attitude at any later time. A small change in the attitude matrix can be approximated as

$$A' \approx (I - \Delta\bar{a})A$$

Error can be introduced into the true angular velocity $\bar{\omega}$ as

$$\bar{\omega}' = \bar{\omega} + \Delta\bar{\omega}$$

Substituting these expressions into the kinematic equation and subtracting the unperturbed equation gives

$$-\frac{d\Delta\bar{a}}{dt}A - \Delta\bar{a}\frac{dA}{dt} = (\bar{\omega}\Delta\bar{a} - \Delta\bar{\omega} + \Delta\bar{\omega}\Delta\bar{a})A$$

Ignoring errors that are the product of two small quantities gives

$$\frac{d\Delta\bar{a}}{dt}A + \Delta\bar{a}\frac{dA}{dt} = (-\bar{\omega}\Delta\bar{a} + \Delta\bar{\omega})A$$

Substituting for $\frac{dA}{dt}$ and postmultiplying by A^T gives

$$\frac{d\Delta\bar{a}}{dt} - \Delta\bar{a}\bar{\omega} = -\bar{\omega}\Delta\bar{a} + \Delta\bar{\omega}$$

Isolating $\frac{d\Delta\bar{a}}{dt}$ and postmultiplying by $\Delta\bar{a}$ gives

$$\frac{d\Delta\bar{a}}{dt}\Delta\bar{a} = (\Delta\bar{a}\bar{\omega} + \Delta\bar{\omega})\Delta\bar{a}$$

Because $\Delta\bar{a}\Delta\bar{a}$ is identically zero, its derivative is zero as well:

$$\Delta\bar{a}\frac{d\Delta\bar{a}}{dt} = -\Delta\bar{a}\bar{\omega}\Delta\bar{a} - \Delta\bar{\omega}\Delta\bar{a}$$

Changing multiplication order in the first term on the right and factoring out the matrix $\Delta \bar{a}$ gives the attitude error equation

$$\frac{d\Delta \bar{a}}{dt} = -\bar{\omega} \Delta \bar{a} + \Delta \bar{\omega}$$

Modeling Gyro Parameters

Gyro errors are ascribed to parameters, including biases \bar{b}_g , scale factor errors \bar{k}_g , misalignments \bar{m}_g , and noise \bar{w}_v :

$$\Delta \bar{\omega} = G_b \bar{b} + G_k(\bar{\omega}) \bar{k} + G_m(\bar{\omega}) \bar{m} + \bar{w}_v$$

Like attitude drift, gyro parameter drift $\Delta \bar{g}$ can be modeled as a Markov process plus white noise. To estimate some set of gyro parameters \bar{g} , the state equations become

$$\frac{d}{dt} \begin{bmatrix} \Delta \bar{a} \\ \Delta \bar{g} \end{bmatrix} = \begin{bmatrix} -\bar{\omega} & G_g \\ 0 & -\frac{I}{\tau} \end{bmatrix} \begin{bmatrix} \Delta \bar{a} \\ \Delta \bar{g} \end{bmatrix} + \begin{bmatrix} I & 0 \\ 0 & I \end{bmatrix} \begin{bmatrix} \bar{w}_v \\ \bar{w}_g \end{bmatrix}$$

where the matrix G_g is constructed such that the modeled angular velocity error is

$$\Delta \bar{\omega} = G_g \Delta \bar{g}$$

For batch estimation, the transition matrix also serves as the partial derivative of current state variables with respect to their epoch values. If the transition matrix has the form

$$\Phi = \begin{bmatrix} \phi & \psi \\ 0 & \chi \end{bmatrix}$$

the derivatives of the current attitude error with respect to the epoch attitude error $\Delta \bar{a}_0$ and gyro parameter errors $\Delta \bar{g}$ are

$$\frac{\partial \Delta \bar{a}}{\partial \Delta \bar{a}_0} \Big|_{t=t_1} = \phi(t_1, t_0)$$

$$\frac{\partial \Delta \bar{a}}{\partial \Delta \bar{g}} \Big|_{t=t_1} = \psi(t_1, t_0)$$

After the gyro parameter errors have been solved for, the gyro parameters are updated as

$$\bar{g} \leftarrow \bar{g} - \Delta \bar{g}$$

Estimation With Torque Modeling

Angular Velocity Error Equation

Harvie (Ref. 7) has demonstrated the feasibility of accurately modeling torques for attitude propagation, but there he estimates angular velocity bias rather than epoch angular velocity. The following development yields the partial derivatives for epoch angular velocity.

Given accurate torque models, the angular velocity can be found by integrating Euler's equation for rotational motion

$$\vec{N} = \vec{\omega} \times \vec{L} + \frac{d\vec{L}}{dt}$$

where \vec{N} is the external torque and \vec{L} is the total angular momentum both expressed in the rotating body frame. The angular momentum is composed of two parts, one due to the rotation of the body with its inertia tensor J and one due to any internal angular momentum \vec{h}

$$\vec{L} = J\vec{\omega} + \vec{h}$$

To reduce the possibility of confusion over units, the angular acceleration $\vec{\alpha}$ can replace the torque as the state variable

$$\vec{\alpha} = J^{-1}\vec{N}$$

to give the differential equation for the angular velocity as

$$\frac{d\vec{\omega}}{dt} = \vec{\alpha} - J^{-1} \left[\vec{\omega} \times (J\vec{\omega} + \vec{h}) + \frac{d\vec{h}}{dt} \right]$$

Along with the initial attitude, the integrated angular velocity now serves as input to the kinematic propagation equation. An error in the predicted angular acceleration $\Delta\vec{\alpha}$ causes a corresponding error in the angular velocity $\Delta\vec{\omega}$:

$$\frac{d(\vec{\omega} + \Delta\vec{\omega})}{dt} = (\vec{\alpha} + \Delta\vec{\alpha}) - J^{-1} \left\{ (\vec{\omega} + \Delta\vec{\omega}) [J(\vec{\omega} + \Delta\vec{\omega}) + \vec{h}] + \frac{d\vec{h}}{dt} \right\}$$

Subtracting the original differential equation and discarding terms that are the product of two small quantities leaves

$$\frac{d\Delta\vec{\omega}}{dt} = \Delta\vec{\alpha} - J^{-1} (\vec{\omega}J\Delta\vec{\omega} + \Delta\vec{\omega}J\vec{\omega} + \Delta\vec{\omega}\vec{h})$$

Reversing multiplication order in the second and third terms in parentheses and factoring out $\Delta\vec{\omega}$ gives

$$\frac{d\Delta\vec{\omega}}{dt} = J^{-1}(-\vec{\omega}J + \vec{L})\Delta\vec{\omega} + \Delta\vec{\alpha}$$

The corrected angular velocity is computed as

$$\vec{\omega} = \vec{\omega} - \Delta\vec{\omega}$$

Modeling Dynamics Parameters

As for angular velocity errors, angular acceleration errors can be attributed to poorly known dynamics parameters such as the moments \bar{J}_u , the products of inertia \bar{J}_{uv} , the residual magnetic dipoles \bar{m}_r , and noise \bar{w}_v :

$$\Delta \bar{a} = J^{-1} (G_{J_u} \Delta \bar{J}_u + G_{J_{uv}} \Delta \bar{J}_{uv} + G_{m_r} \Delta \bar{m}_r) + \bar{w}_v$$

To estimate some set of dynamics parameter errors $\Delta \bar{d}$, the state equations become

$$\frac{d}{dt} \begin{bmatrix} \Delta \bar{a} \\ \Delta \bar{\omega} \\ \Delta \bar{d} \end{bmatrix} = \begin{bmatrix} -\bar{\omega} & I & 0 \\ 0 & J^{-1}(\bar{L} - \bar{\omega}J) & G_d \\ 0 & 0 & -\frac{I}{\tau} \end{bmatrix} \begin{bmatrix} \Delta \bar{a} \\ \Delta \bar{\omega} \\ \Delta \bar{d} \end{bmatrix} + \begin{bmatrix} 0 & 0 & 0 \\ 0 & I & 0 \\ 0 & 0 & I \end{bmatrix} \begin{bmatrix} \bar{0} \\ \bar{w}_v \\ \bar{w}_u \end{bmatrix}$$

where G_d comes from the coefficient matrices above such that the modeled angular acceleration is

$$\Delta \bar{a} = G_d \Delta \bar{d}$$

If the state transition matrix has the form

$$\Phi = \begin{bmatrix} \phi & \zeta & \xi \\ 0 & \nu & \nu \\ 0 & 0 & \kappa \end{bmatrix}$$

the derivatives of the current attitude error with respect to the initial angular velocity error $\Delta \bar{\omega}_0$ and dynamics parameter error $\Delta \bar{d}$ are

$$\frac{\partial \Delta \bar{a}}{\partial \Delta \bar{\omega}_0} \Big|_{t=t_i} = \zeta(t_i, t_0)$$

$$\frac{\partial \Delta \bar{a}}{\partial \Delta \bar{d}} \Big|_{t=t_i} = \xi(t_i, t_0)$$

When the dynamics parameter errors are found, the dynamics parameters are corrected as

$$\bar{d} = \bar{d} - \Delta \bar{d}$$

Computing the State Transition Matrix

Short Time Steps

The state transition matrix is needed to chain derivatives back to epoch and to propagate the covariance matrix. Brogan (Ref. 8) discusses its evaluation, as do other texts on linear system theory. If the coefficient matrix F is constant over the time step, the transition matrix is simply the exponential of the product of the coefficient matrix and the time step:

$$\Phi(t, t_0) = e^{F(t-t_0)}$$

For simple coefficient matrices, a closed form solution can sometimes be obtained by simplifying the infinite series

$$e^{Ft} = I + tF + \frac{t^2}{2}F^2 + \frac{t^3}{3!}F^3 + \frac{t^4}{4!}F^4 + \dots$$

Harvie (Ref. 7) simply truncated the series without ill effect. With this approach, one always wonders how many terms to include. If the coefficient matrix has all zeros on the main diagonal, the infinite series terminates after n or fewer terms. Writing the matrix as the sum of an upper U and a lower triangular matrix L and using the binomial theorem to express powers of their sum

$$(U + L)^n = \sum_{r=0}^n \frac{n!}{r!(n-r)!} U^r L^{n-r}$$

and substituting into the series

$$e^{Ft} = \sum_{n=0}^{\infty} \frac{t^n}{n!} \sum_{r=0}^n \frac{n!}{r!(n-r)!} U^r L^{n-r}$$

the infinite series terminates after at most n terms, since the triangular matrices U and L are nilpotent.

Exact formulas exist which involve only moderate additional effort. Using the Cayley-Hamilton theorem, it can be shown that the exponential of an n by n matrix is equal to the $n - 1$ order polynomial in tF :

$$e^{Ft} = \alpha_0 I + \alpha_1 tF + \alpha_2 t^2 F^2 + \dots + \alpha_{n-1} t^{n-1} F^{n-1}$$

where the α_i are scalar coefficients that are determined by solving a set of linear equations. This is the form of the attitude propagation matrix given above. This equation shows that the reduction to three terms is not due to the antisymmetric nature of the coefficient matrix.

The coefficients α_i come from a system of equations of the form

$$e^{\lambda_i t} = \alpha_0 + \alpha_1 \lambda_i t + \alpha_2 \lambda_i^2 t^2 + \dots + \alpha_{n-1} \lambda_i^{n-1} t^{n-1}$$

where the λ_i are the eigenvalues of F . If repeated eigenvalues exist, the repeated equation can be differentiated with respect to the eigenvalue to give an additional equation.

Another eigenvalue approach exponentiates the diagonal matrix whose elements are the eigenvalues of Ft :

$$e^{At} = \begin{bmatrix} e^{\lambda_1 t} & 0 & \dots & 0 \\ 0 & e^{\lambda_2 t} & \dots & 0 \\ \vdots & \vdots & \ddots & \vdots \\ 0 & 0 & \dots & e^{\lambda_n t} \end{bmatrix}$$

We then perform a similarity transformation using matrices formed from the eigenvectors

$$e^{Ft} = S e^{At} S^{-1}$$

where the S matrix is made up of the eigenvectors \hat{v}_i :

$$S = (\hat{v}_1 \vdots \hat{v}_2 \vdots \dots \vdots \hat{v}_n)$$

Again, when a full set of eigenvalues does not exist, the diagonal matrix becomes block diagonal, and generalized eigenvectors must be found.

Closed Form Expressions

Solutions for the attitude error $\Delta \vec{a}$ can be written in terms of the transition submatrices ϕ and ψ as

$$\Delta \vec{a}(t) = \phi(t,0) \Delta \vec{a}(0) + \psi(t,0) \Delta \vec{\omega}(0)$$

A closed form expression for the transition matrix ϕ can be obtained directly from the infinite series definition by collapsing the series with the identity

$$\vec{\omega}^3 = -\omega^2 \vec{\omega}$$

or by using the Cayley-Hamilton eigenvalue method outlined above. The eigenvalues λ_i of the antisymmetric matrix are 0 and $\pm i\omega t$. The three equations for the α_i become

$$\begin{aligned} e^0 &= \alpha_0 \\ e^{i\omega t} &= \alpha_0 + \alpha_1(i\omega t) + \alpha_2(i\omega t)^2 \\ e^{-i\omega t} &= \alpha_0 + \alpha_1(-i\omega t) + \alpha_2(-i\omega t)^2 \end{aligned}$$

giving the transition submatrix ϕ as

$$\phi(t,0) = I - \sin \omega t \left(\frac{\vec{\omega}}{\omega} \right) + (1 - \cos \omega t) \left(\frac{\vec{\omega}}{\omega} \right)^2$$

In addition to propagating the attitude error using angular velocity, the same expressions can be used to propagate the angular velocity error for an axisymmetric spinning spacecraft using the angular acceleration error.

The transition submatrix ψ for the inhomogeneous solution is the convolution of the transition matrix ϕ found above with the "forcing function" coefficient matrix G_x :

$$\psi(t,0) = \int_0^t \phi(t,\tau) G_x(\tau) d\tau$$

and for constant G_x is equal to

$$\psi(t,0) = \left[tI - \frac{1 - \cos \omega t}{\omega} \left(\frac{\bar{\omega}}{\omega} \right) + \left(t - \frac{\sin \omega t}{\omega} \right) \left(\frac{\bar{\omega}}{\omega} \right)^2 \right] G_x$$

Recursion Relations

For batch estimation, the transition matrix must be accumulated over the length of the batch. Over such long times, the assumption that the coefficient matrix F remains constant may not be valid. In this case, the transition matrix can be computed recursively:

$$\Phi(t_p, t_0) = \Phi(t_p, t_{i-1}) \Phi(t_{i-1}, t_0)$$

where the initial value of the Φ is the identity matrix

$$\Phi(t_0, t_0) = I$$

Because the batch estimator needs derivatives of the attitude error only, it is not necessary to form the entire transition matrix. The submatrices can also be computed recursively. For gyro propagation, the recursion relations are

$$\begin{aligned} \phi(t_p, t_0) &= \phi(t_p, t_{i-1}) \phi(t_{i-1}, t_0) \\ \psi(t_p, t_0) &= \phi(t_p, t_{i-1}) \psi(t_{i-1}, t_0) + \psi(t_p, t_{i-1}) \end{aligned}$$

where the initial values of these matrices are

$$\begin{aligned} \phi(t_0, t_0) &= I \\ \psi(t_0, t_0) &= 0 \end{aligned}$$

For dynamic propagation, the attitude error recursion is unchanged, but two additional recursion relations exist:

$$\begin{aligned} \zeta(t_p, t_0) &= \phi(t_p, t_{i-1}) \zeta(t_{i-1}, t_0) + \zeta(t_p, t_{i-1}) v(t_{i-1}, t_0) \\ \xi(t_p, t_0) &= \phi(t_p, t_{i-1}) \xi(t_{i-1}, t_0) + \zeta(t_p, t_{i-1}) v(t_{i-1}, t_0) + \xi(t_p, t_{i-1}) \end{aligned}$$

where these matrices are initially zero:

$$\zeta(t_0, t_0) = \xi(t_0, t_0) = 0$$

Summary

Modeling attitude motion can improve accuracy by allowing the estimate to follow the changing state. The model may be random, as in Markov drift; deterministic, as in gyro propagation; or a combination of both types. Differential equations for the attitude error provide a means for propagating covariance in the sequential estimator and for chaining derivatives back to epoch in the batch estimator. Closed form expressions are available for the state transition matrix solutions to those equations, and the state can be augmented to include propagation parameters, such as gyro biases.

These methods reflect attitude estimation as traditionally practiced by the NASA/Goddard Space Flight Center Flight Dynamics Facility. The recent addition of dynamics motion models has required new expressions for the derivatives of the attitude with respect to dynamics parameters, such as products of inertia, and numerical evaluation of the state transition matrices. It is hoped that the expressions for these derivatives, the transition matrix methods, and unified treatment of motion models provided here will be useful to those who follow in the practice of attitude estimation.

References

1. H. W. Sorenson, *Parameter Estimation*, Marcel Dekker, 1980
2. J. R. Wertz, ed., *Attitude Determination and Control*, D. Reidel, 1980
3. A. Gelb, *Applied Optimal Estimation*, MIT Press, 1986
4. R. L. Farrenkopf, "Analytic Steady-State Accuracy Solutions for Two Common Spacecraft Attitude Estimators," *J. Guidance and Control*, vol. 1, no. 4, pp. 282–284, July–August 1978
5. E. J. Lefferts, F. L. Markley, and M. D. Shuster, "Kalman Filtering for Spacecraft Attitude Estimation," *J. Guidance*, vol. 5, no. 5, September–October 1982
6. K. Hall, CSC/TM-87/6041, *Cosmic Background Explorer (COBE) Flight Dynamics Support System (FDSS) Mathematical Background*, Computer Sciences Corporation, October 1987
7. E. Harvie, "Dynamics Modeling for ERBS Attitude Propagation," ESA SP-326, European Space Agency, December 1991
8. W. L. Brogan, *Modern Control Theory*, Prentice-Hall, 1985



REPORT DOCUMENTATION PAGE

Form Approved
OMB No. 0704-0188

Public reporting burden for this collection of information is estimated to average 1 hour per response, including the time for reviewing instructions, searching existing data sources, gathering and maintaining the data needed, and completing and reviewing the collection of information. Send comments regarding this burden estimate or any other aspect of this collection of information, including suggestions for reducing this burden, to Washington Headquarters Services, Directorate for Information Operations and Reports, 1215 Jefferson Davis Highway, Suite 1204, Arlington, VA 22202-4302, and to the Office of Management and Budget, Paperwork Reduction Project (0704-0188), Washington, DC 20503.

1. AGENCY USE ONLY (Leave blank)		2. REPORT DATE May 1994	3. REPORT TYPE AND DATES COVERED Conference Publication - May 17-19, 1994	
4. TITLE AND SUBTITLE Flight Mechanics/Estimation Theory Symposium - 1994			5. FUNDING NUMBERS 550	
6. AUTHOR(S) Kathy R. Hartman, Editor			8. PERFORMING ORGANIZATION REPORT NUMBER 94B00060	
7. PERFORMING ORGANIZATION NAME(S) AND ADDRESS (ES) Goddard Space Flight Center Greenbelt, Maryland 20771				
9. SPONSORING / MONITORING AGENCY NAME(S) AND ADDRESS (ES) National Aeronautics and Space Administration Washington, DC 20546-0001			10. SPONSORING / MONITORING AGENCY REPORT NUMBER NASA CP-3265	
11. SUPPLEMENTARY NOTES K. Hartman is Head, Trajectory Section, Flight Dynamics Support Branch, at the Goddard Space Flight Center, Greenbelt, Maryland				
12a. DISTRIBUTION / AVAILABILITY STATEMENT Unclassified - Unlimited Subject Category 13			12b. DISTRIBUTION CODE	
13. ABSTRACT (Maximum 200 words) This conference publication includes 41 papers and abstracts presented at the Flight Mechanics/ Estimation Theory Symposium on May 17-19, 1994. Sponsored by the Flight Dynamics Division of Goddard Space Flight Center, this symposium featured technical papers on a wide range of issues related to orbit-attitude prediction, determination and control; attitude sensor calibration; attitude determination error analysis; attitude dynamics; and orbit decay and maneuver strategy. Government, industry, and the academic community participated in the preparation and presentation of these papers.				
14. SUBJECT TERMS Flight Mechanics, Estimation Theory, Attitude Determination, Mission Analysis, Spacecraft Dynamics, Orbit Determination			15. NUMBER OF PAGES 568	
			16. PRICE CODE	
17. SECURITY CLASSIFICATION OF REPORT Unclassified	18. SECURITY CLASSIFICATION OF THIS PAGE Unclassified	19. SECURITY CLASSIFICATION OF ABSTRACT Unclassified	20. LIMITATION OF ABSTRACT UL	